



**Vitor Hugo da Silva  
Magalhães**

**Carbonatos autigénicos e estruturas de escape de  
fluidos no Golfo de Cádiz**

**Authigenic carbonates and fluid escape structures in  
the Gulf of Cadiz**





**Vitor Hugo da Silva  
Magalhães**

**Carbonatos autigénicos e estruturas de escape de  
fluidos no Golfo de Cádiz**

**Authigenic carbonates and fluid escape structures in  
the Gulf of Cadiz**

Tese apresentada à Universidade de Aveiro para cumprimento dos requisitos necessários à obtenção do grau de Doutor em Geociências, realizada sob a orientação científica do Professor Doutor Luis Menezes Pinheiro, Professor associado do Departamento de Geociências da Universidade de Aveiro, com co-orientação científica do Professor Doutor Michael Ivanov, Professor da Faculdade de Geologia da Universidade de Moscovo, Rússia.

Apoio financeiro da FCT

O trabalho desenvolvido no decorrer desta tese foi suportado pelos Projectos INGMAR (PLE/4/98) e MVSEIS-Euromargins (01-LEC-EMA24F), com financiamento da Fundação para a Ciência e a Tecnologia (FCT) e pela Bolsa de Doutoramento da FCT SFRH/BD/11747/2003.

This work was supported by the INGMAR (PLE/4/98) and MVSEIS - Euromargins (01-LEC-EMA24F) projects, financed by the Portuguese Foundation for Science and Technology (FCT) and by the FCT fellowship SFRH/BD/11747/2003.



Dedico este trabalho à minha esposa e a meus pais.



## **o júri**

presidente

Professor Doutor Eduardo Anselmo Ferreira da Silva  
Professor Catedrático do Departamento de Geociências da Universidade Aveiro

Professor Doutor Luís Filipe Fuentefria de Menezes Pinheiro  
Professor Associado do Departamento de Geociências da Universidade Aveiro

Professora Doutora Maria Cármen Comas  
Professora de Investigación do Instituto Andaluz de Ciências da Terra, CSIC y Univ.  
Granada, Espanha

Professor Doutor Michael Ivanov  
Professor of the Geology Faculty of the Moscow State University, Russia

Professora Doutora Beatriz Valle Aguado  
Professora Auxiliar do Departamento de Geociências da Universidade Aveiro

Professor Doutor José Francisco Horta Pacheco dos Santos  
Professor Auxiliar do Departamento de Geociências da Universidade Aveiro

Professor Doutor Pedro Gancedo Terrinha  
Investigador Auxiliar do Departamento de Geologia Marinha do INETI; Professor  
Auxiliar Convidado do Departamento de Geologia da Faculdade de Ciências da  
Universidade de Lisboa



## agradecimentos

Esta tese de doutoramento beneficiou da ajuda e apoio de muitas pessoas e instituições a quem expresso o meu agradecimento. Todas elas constantemente me encorajaram e contribuíram com sugestões e discussões pertinentes ao longo do desenvolvimento deste trabalho.

Ao Professor Luís Menezes Pinheiro e ao Professor Michael Ivanov, com quem muito aprendi, agradeço toda a orientação e ensinamentos prestados ao longo deste projecto. Estou-lhes muito grato pelo apoio despendido, revisões, proveitosas discussões e críticas que visivelmente melhoraram este trabalho em diferentes aspectos.

As actividades de investigação desenvolvidas no decorrer desta tese foram realizadas principalmente no Departamento de Geologia Marinha do Instituto Nacional de Engenharia, Tecnologia e Inovação, I.P. (DGM-INETI), anterior Instituto Geológico e Mineiro. A todos os membros do DGM o meu obrigado por toda a colaboração prestada. Ao Dr. Hipólito Monteiro e à Dra. Fátima Abrantes, directores do departamento durante este período, agradeço todo o apoio e entusiasmo que me deram. Gostaria também de agradecer ao Dr. Luís Gaspar por todos conselhos e ensinamentos na geoquímica dos carbonatos, que foram muito importantes para este trabalho. Estou também grato à Dra. Antje Voelker e aos meus antigos e actuais colegas de gabinete, Drs. Mário Mil-Homens, António Ferreira, Henrique Duarte e Susana Muiños, pela sua amizade e pelos importantes comentários e discussões que tivemos.

Aos colegas do Departamento de Geocências da Universidade de Aveiro quero agradecer pela forma sempre prestável e disponível como sempre me receberam. O meu muito obrigado.

Um especial agradecimento a todos os membros do UNESCO – MSU Research and Training Centre for Marine Geology and Geophysics of the Faculty of Geology at the University of Moscow (Russia) pela forma sempre amiga como me receberam tanto em Moscovo como a bordo do Navio Professor Logachev.

Ao Dr. Crisogono Vasconcelos, Professora Judith McKenzie, Dr. Rolf Warthmann e Dr. Stefano Bernasconi do ETH em Zurique, agradeço-lhes pela forma como me receberam e me ajudaram em vários trabalhos de laboratório e pelas construtivas discussões científicas que aumentaram consideravelmente a qualidade de deste trabalho.

Um especial agradecimento vai para o Professor Jorn Peckmann e Dr. Daniel Birgel do RCOM em Bremen por me ensinarem a parte laboratorial dos biomarcadores e pelas importantes discussões dos resultados obtidos.

Também gostaria de agradecer aos Drs. Warner Bruckmann, Anton Eisenhauer, Ana Kolevica e Jan Fietzk do IFM-Geomar em Kiel pelo seu constante apoio e orientação durante a preparação de amostras para datações com U/Th.

## **agradecimentos**

Aos Drs. Victor Díaz-del-Río, Luiz Samoza e a toda a equipa do Anastasya o meu obrigado pela sua amizade e camaradagem a bordo do Navio Cornide de Saavedra.

Um muito obrigado aos meus pais, irmã e cunhado pelo permanente e incondicional apoio e encorajamento.

Finalmente, quero agradecer à minha esposa Emília todo o apoio e estímulo constante durante estes anos e que foi crucial no desenvolvimento deste trabalho.

O trabalho desenvolvido no decorrer desta tese foi suportado pelos Projectos INGMAR (PLE/4/98) e MVSEIS-Euromargins (01-LEC-EMA24F), com financiamento da Fundação para a Ciência e a Tecnologia (FCT) e pela Bolsa de Doutoramento da FCT SFRH/BD/11747/2003.

## palavras-chave

Estruturas de escape de fluidos, carbonatos autigénicos, carbonatos autigénicos derivados de oxidação de metano, vulcões de lama, hidratos de gás, Golfo de Cádiz.

## resumo

Este trabalho foca-se no estudo das ocorrências de carbonatos autigénicos do Golfo de Cádiz. A mineralogia, textura e valores de  $\delta^{13}\text{C}_{\text{carbonatos}}$  indica que as diferentes litologias são formadas a partir de oxidação de metano que induz a cimentação dos sedimentos por precipitação de dolomite, calcite magnesiana, calcite e aragonite autigénicas.

Os diferentes carbonatos autigénicos derivados de metano (CADM) ocorrem associados a vulcões e cones de lama, cristas diapiricas ou ao longo de falhas. Dois grupos distintos de CADM foram descritos. Um grupo cuja mineralogia é dominada por dolomite e que ocorrem como crostas, chaminés ou nódulos, e um outro grupo com a mineralogia dominada por aragonite e que ocorrem sub a forma de crostas, pavimentos ou montículos, no fundo do mar.

Os diferentes grupos de CADM reflectem diferentes ambientes geoquímicos de formação. Os CADM aragoníticos formam-se próximo da interface sedimento/água, enquanto que os CADM dolomíticos formam-se por cimentação ao longo de condutas por onde o fluido circulou dentro da coluna sedimentar em ambientes confinados relativamente à água do mar.

A ocorrência destes CADM é interpretada como indicadora de extenso escape de metano na área do Golfo de Cádiz.

Biomarcadores indicadores de Archaea capaz de realizar oxidação anaeróbica de metano (OAM) e biomarcadores indicadores de bactérias sulfato-redutoras foram identificados nas amostras de CADM. Estes resultados, apoiados também pelas observações de microscópio electrónico e micro-texturas características dos CADM, confirmam um activo envolvimento microbiano na formação destes CADM.

A composição isotópica destes CADM indica que na sua formação estiveram envolvidos fluidos intersticiais com um claro contributo de água resultante da dissociação de hidratos de metano.

As idades de amostras representativas de CADM, calculadas pela análise de U/Th indica que estes carbonatos se formaram no decorrer dos últimos 250 ka, em períodos correlacionados com rápidas variações paleoceanográficas, como as terminações dos períodos glaciares.



## Acknowledgments

This PhD thesis benefited from the help and support of many people and research institutes that I had the pleasure to work with. I am thankful to everybody that in any way contributed with encouragement, discussions and suggestions along the development of this work.

I am grateful to Professor Luís Menezes Pinheiro and Professor Michael Ivanov who initiated this project and from whom I learned immensely. I am very grateful for their support, reviews and many fertile discussions that greatly improved this work in many different ways.

The research activities were carried out mainly at the Marine Geology Department of the National Institute of Engineering, Technology and Innovation, I.P. (DGM - INETI), former Geological and Mining Institute (IGM), therefore my thanks to all the DGM members. To Dr. Hipólito Monteiro and Dr. Fátima Abrantes, directors of the department during this time, my appreciation for all the support, enthusiasm and strength that gave me. I gratefully acknowledge Dr. Luís Gaspar for his constructive advises and explanations on the carbonate geochemistry that were crucial during this work. I am also grateful to Dr. Antje Voelker and my former and actual roommates, Mário Mil-Homens, António Ferreira, Henrique Duarte and Susana Muiños, for their friendship and helpful comments and discussions.

I am also grateful to the colleagues at the Geosciences Department of the University of Aveiro where I was always welcome.

I would express my thanks to the UNESCO – MSU Research and Training Centre for Marine Geology and Geophysics of the Faculty of Geology of the Moscow State University (Russia) for the friendship that I found in Moscow and onboard of the R/V Professor Logachev.

Thanks also to Dr. Crisogono Vasconcelos, Professor Judith McKenzie, Dr. Rolf Warthmann, and Dr. Stefano Bernasconi from the ETH in Zurich for their support with the several laboratory work and for their constructive scientific discussions that greatly improved the quality of the present dissertation.

A special acknowledgement to Professor Jorn Peckmann and Dr. Daniel Birgel from the RCOM in Bremen for initiating me in biomarker analysis and for the valuable discussions of the results.

Thanks also to Drs. Warner Bruckmann, Anton Eisenhauer, Ana Kolevica, and Jan Fietzk from the IFM-Geomar in Kiel for their constant support and supervision during the sample preparation for U/Th dating.

## **Acknowledgments**

To Drs. Victor Díaz-del-Río, Luiz Samoza and all the Anastasya team also my thanks for their friendship onboard the R/V Cornide de Saavedra.

I gratefully thank my parents, sister and brother-in-law for their permanent unconditional support and encouragement.

Finally, I would like to thank my wife Emília for all her support and motivation that was of crucial importance for the development of this work along these years.

This work was supported by the INGMAR (PLE/4/98) and MVSEIS - Euromargins (01-LEC-EMA24F) projects, financed by the Portuguese Foundation for Science and Technology (FCT) and by the FCT fellowship SFRH/BD/11747/2003.

**keywords**

Fluid escape structures, Authigenic carbonates, Methane-derived authigenic carbonates, Mud volcanoes, gas hydrates, Gulf of Cadiz.

**abstract**

This work focus on the occurrences of authigenic carbonates in the Gulf of Cadiz. Mineralogy, texture and  $\delta^{13}\text{C}_{\text{carbonate}}$  values clearly indicate that the different carbonate lithologies are methane-derived (MDAC), formed by the lithification of sediments as result of the precipitation of authigenic dolomite, calcite, Mg-calcite and aragonite.

The MDAC are found associated with mud volcanoes and mud cones, diapiric ridges or along faults.

Two distinct groups of MDAC were described in the Gulf of Cadiz. A group dominated by dolomite mineralogy (dolomite crusts, nodules and chimneys) and a group of aragonite dominated carbonates (aragonite pavements, slabs, crusts and buildups).

The different MDAC morphologic types reflect different geochemical formation environments. The aragonite pavements represent precipitation of authigenic carbonates at the sediment-seawater interface or close to it. The dolomite nodules, crusts and chimneys result from the cementation along fluid conduits inside the sediment column, in more confined geochemical environments.

The widespread abundance of MDAC is interpreted as an evidence of several episodes of extensive methane seepage in the Gulf of Cadiz.

Specific  $^{13}\text{C}$ -depleted lipid biomarkers indicating archaea involvement in the anaerobic oxidation of methane and bacterial lipid biomarkers also  $^{13}\text{C}$ -depleted and related to sulphate reducing bacteria were both identified on the MDAC. These results, substantiated by SEM observations and by microbial related microfabrics, confirm that microbial activity has played an important role in carbonate authigenesis.

Considering the minimum and maximum temperature limits admitted to be possible to occur in the Gulf of Cadiz, some of the MDAC samples indicate a formation from  $^{18}\text{O}$ -enriched pore fluids, interpreted as resulting from a contribution of dissociated gas hydrates to the pore waters from which the authigenic carbonates were formed.

The estimated U/Th ages of selected dolomite chimneys indicate episodes of intense precipitation of the authigenic carbonates, at least during the last 250 ka, that correlate with periods of rapid paleoceanographic changes as the onsets of glacial/interglacial terminations.



## Table of contents

<b>Agradecimentos</b>	
<b>Palavras-chave</b>	
<b>Resumo</b>	
<b>Acknowledgements</b>	
<b>Keywords</b>	
<b>Abstract</b>	
<b>Table of contents</b>	<i>i</i>
<b>List of tables</b>	<i>ix</i>
<b>List of figures</b>	<i>xi</i>
<b>Chapter 1. Introduction</b>	<b>1</b>
1.1 Nature and scope of this research	1
1.2 Geographical location and physiography of the study area	3
1.3 Main objectives	7
1.4 Database	7
1.5 Methodology	8
1.6 Thesis outline	9
<b>Chapter 2. Fluid escape processes and manifestations at continental margins</b>	<b>13</b>
2.1 Mud volcanism and mud diapirism	13
2.1.1 Introduction	13
2.1.2 Formation mechanisms	19
2.1.3 Detection of submarine mud volcanoes	21
2.1.4 Worldwide distribution	21
2.1.5 Global significance, potential interest and environmental impacts	24
Influence on the global carbon budget	24
A window to the deep sedimentary section and hydrocarbon potential	24
A window to the deep biosphere	25
Geological hazards	25
2.2 Pockmarks	25
2.3 Active hydrocarbon seepage	27
2.3.1 Cold seeps: Definition and characteristics	28
2.3.2 Methane oxidation and main biogeochemical processes in cold seeps	29
2.3.2.1 The methanogenic zone	30
2.3.2.2 The sulphate reduction zone	30
2.3.2.3 The aerobic zone	34
2.3.3 Geologic setting and worldwide occurrences of cold seeps	34
2.3.4 Cold seepage manifestations and detection	36
2.4 Methane-derived authigenic carbonates	38
2.5 Gas Hydrates and BSRs	41
2.5.1 Definition, characteristics and formation mechanisms	41

2.5.2	Significance	42
2.5.3	Detection	43
2.5.4	Occurrences	46
2.5.5	Global estimations	47
2.6	Associated ecosystems	48
<b>Chapter 3. Geodynamic and oceanographic settings of the Gulf of Cadiz</b>		<b>51</b>
3.1	Plate tectonic setting	51
3.2	Seismicity (present day stress pattern and tectonic regime)	55
3.3	Geodynamic evolution of the study area	56
3.3.1	Mesozoic	56
3.3.2	Cenozoic	57
3.3.2.1	Paleogene	57
3.3.2.2	Neogene	57
3.3.2.2.1	Early and Middle Miocene	57
3.3.2.2.2	Late Miocene and Pliocene	58
3.3.2.3	Quaternary	60
3.4	Different geological domains in the Gulf of Cadiz	61
3.4.1	Flysch domain	61
3.4.2	Sub-Betic domain	61
3.4.3	Cadiz Basin	61
3.4.4	Allochthonous units (Olistostrome/Accretionary wedge)	63
3.4.5	Plio-Quaternary morpho-sedimentary domains	64
3.5	Oceanographic setting and the Mediterranean Outflow	65
3.5.1	Present day oceanographic setting	65
3.5.2	Brief overview of the paleoceanographic evolution of the MO	71
<b>Chapter 4. Characterization of areas of MDAC occurrence in the Gulf of Cadiz and their relation to other fluid escape structures</b>		<b>73</b>
4.1	Introduction	73
4.2	Methods	76
4.2.1	Positioning systems	76
4.2.2	Seafloor sampling	77
4.2.3	Underwater observations	77
4.2.4	Side-scan sonar mapping	77
4.3	Results: Geological and geophysical cartography	78
4.3.1	MDAC occurrences in the GDR Field and their relationship with mud volcanoes and mud cones	80
4.3.1.1	Guadalquivir Diapiric Ridge	80
4.3.1.1.1	Coruña mud cone	82
4.3.1.1.2	Profile in the GDR North of the Coruña mud cone	83
4.3.1.2	Formoza Ridge	85
4.3.1.3	Hormigas Ridge	91
4.3.1.3.1	Iberico	92
4.3.1.3.2	Cornide	98
4.3.1.3.3	Arcos	101

4.3.2	The Tasyo Field	101
4.3.2.1	Hesperides	102
4.3.2.2	Faro, Cibeles and Almazan	112
4.3.3	Mediterranean Outflow channels	122
4.3.3.1	Cadiz Channel W of Iberico	122
4.4	Discussion	126
4.4.1	Fluid and gas escape manifestations in the Gulf of Cadiz	126
4.4.2	MDAC occurrence and characterization	128
4.4.2.1	Dolomite crusts and chimneys	129
4.4.2.2	Aragonite pavements	132
4.4.3	Chemosynthetic fauna: occurrence and underwater observations	132
4.4.4	Characteristics of mud volcanoes, mud cones and diapiric ridges	133
4.4.5	Temporal and spatial relationship between the MDAC, chemosynthetic organisms and the MV, MD and diapiric ridges	137
4.5	Conclusions	140

## **Chapter 5. Methane-derived authigenic carbonates from the Gulf of Cadiz:**

	<b>Characterization and formation model</b>	<b>143</b>
5.1	Introduction	143
5.2	Material and methods	145
5.3	Results	148
5.3.1	Types and morphologies of the MDAC	148
5.3.1.1	Dolomite chimneys (DChy)	148
5.3.1.2	Dolomite crusts (DCr)	151
5.3.1.3	Dolomite nodules (Nod)	153
5.3.1.4	Aragonite crusts and pavements (AragPav)	154
5.3.1.4.1	Lithified mud volcano breccias (LMb)	154
5.3.1.4.2	Shell crusts (SCr)	156
5.3.1.4.3	Intraformational breccias (IBr)	157
5.3.1.4.4	Lithified fragments of dolomite chimneys/crusts (LDChy)	158
5.3.1.4.5	Stromatolitic layers (SL)	159
5.3.1.4.6	Fossilised biofilms (Fbf)	160
5.3.2	Occurrence and Underwater observations	160
5.3.2.1	Dolomite crusts and chimneys	161
5.3.2.2	Aragonite pavements	162
5.3.3	Mineralogy, petrography and SEM	165
5.3.3.1	Dolomite crusts, chimneys and nodules	165
5.3.3.2	Aragonite crusts and pavements	168
5.3.4	CaCO <sub>3</sub> and Total Organic Carbon	171
5.3.5	C and O stable isotopes	174
5.3.6	Sr Isotopes and seawater Influence	176
5.3.7	Biomarker analyses	178
5.4	Discussion	179
5.4.1	MDAC and their relation with MVs and deep faults	179
5.4.2	Estimation of fluids composition and evolution	180
5.4.2.1	Estimation of Pore water composition	180
5.4.2.2	Anaerobic oxidation of methane and carbonate precipitation	182

5.4.3	Carbonate mineralogy and geochemical environments	183
5.4.3.1	Dolomite	184
5.4.3.2	Aragonite	185
5.4.3.3	Calcite and Mg-calcite	185
5.4.4	Biogeochemistry - the microbial factor	186
5.4.5	Formation of the different MDAC lithologies	187
5.4.5.1	Isotopic zonation	187
5.4.5.2	Formation of dolomite crusts, chimneys and nodules	187
5.4.5.3	Formation of the aragonite pavements	190
5.5	Conclusions	192

**Chapter 6. Origin, paleo-temperature and composition reconstruction of fluids associated with the formation of MDAC in the Gulf of Cadiz** **195**

6.1	Introduction	195
6.1.1	Fractionation factor	196
6.1.2	The delta value ( $\delta$ )	197
6.1.3	Oxygen isotopic standards	198
6.1.4	Temperature equations	199
6.1.4.1	Calcite and Mg-Calcite	203
6.1.4.2	Protodolomite and Dolomite	205
6.1.4.3	Aragonite	209
6.1.4.4	Comparison of the Aragonite with the Calcite fractionation equations	211
6.1.4.5	Comparison of the Dolomite with the Calcite fractionation equations	213
6.2	Present day oceanographic conditions in the Gulf of Cadiz	214
6.3	Methods	215
6.4	Results	218
6.4.1	Oxygen and carbon isotopes	218
6.4.1.1	EDTA	218
6.4.1.2	Calcite and Mg-calcite vs Dolomite in bulk samples of the dolomite crusts, chimneys and nodules	219
6.4.1.3	Calcite and Mg-calcite vs Aragonite in aragonite pavements	221
6.4.2	Strontium isotopes	223
6.5	Discussion	225
6.5.1	Methane rich pore waters	225
6.5.2	Paleo-temperatures and fluid composition on dolomite crusts, chimneys and nodules	226
6.5.2.1	Calcite and high Mg-calcite	228
6.5.2.2	Protodolomite and dolomite	233
6.5.2.3	Dolomite crusts, chimneys and nodules carbonates	235
6.5.3	Paleo-temperatures and fluid composition on aragonite pavements	237
6.5.3.1	Calcite and high Mg-calcite	237
6.5.3.2	Aragonite	241
6.5.3.3	Aragonite pavement carbonates	244
6.5.4	Comparison of aragonite pavements and dolomite crusts, chimneys and nodules	247
6.6	Conclusions	248

<b>Chapter 7. U/Th Ages of dolomite chimneys from the Gulf of Cadiz: record of intense past fluid escape episodes</b>	<b>251</b>
7.1 Introduction	251
7.2 Materials and methods	253
7.2.1 Samples used	253
7.2.2 Petrography, mineralogy and geochemistry of the authigenic carbonates	256
7.2.2.1 Petrography of the two dolomite chimneys	256
7.2.2.2 XRD results	257
7.2.2.3 Carbon and Oxygen Isotopic analysis	257
7.2.3 Sample preparation and analytical methods	258
7.3 Results and Discussion	259
7.3.1 Constrains on the origin of the uranium in the MDAC	259
7.3.2 Age determination	262
7.3.2.1 Sample 3463-A08	269
7.3.2.2 Sample 3463-A03	269
7.3.2.3 Samples 3463-A03 and 3463-A08	270
7.3.3 $^{230}\text{Th}/^{234}\text{U}$ ages of the MDAC and their relationship to the global sealevel record	271
7.3.4 Potential controls on the $\delta^{18}\text{O}$ signal in the chimneys	275
7.3.4.1 Sample 3463-A03	278
7.3.4.2 Sample 3463-A08	281
7.3.5 Formation model of the two chimneys	282
7.4 Conclusions	284
<b>Chapter 8. Biomarker and SEM evidences of microbial mediation in the formation of MDAC in the Gulf of Cadiz</b>	<b>285</b>
8.1 Introduction	285
8.2 Materials and Methods	289
8.2.1 Petrography, SEM and EDS	292
8.2.2 Lipid Biomarkers	292
8.2.2.1 Sample preparation	292
8.2.2.2 Analytical procedure	293
8.2.2.3 Gas chromatography and coupled mass spectrometry (GC-MS)	293
8.3 Results	294
8.3.1 Petrographic and SEM evidences of bacterial activity	294
8.3.1.1 Dolomite chimneys	295
8.3.1.2 Aragonite pavements	309
8.3.2 Lipid biomarkers	324
8.3.2.1 Dolomite chimneys	324
8.3.2.2 Aragonite pavements	327
8.4 Discussion	330
8.4.1 Textural and fabric implications on the MDAC formation processes	330
8.4.2 Microfabrics and microbial fossil evidences	332
8.4.3 Biomarker significance	335
8.5 Conclusions	336

<b>Chapter 9. Main Conclusions, Future work and Open questions</b>	<b>339</b>
9.1 Main conclusions	339
9.2 Future work and open questions	345
<b>10. References</b>	<b>349</b>
<b>11. Publications</b>	<b>373</b>
<b>Appendix A. Geophysical data acquisition and processing, sample collection and underwater observations</b>	<b>A-1</b>
A.1 Oceanographic cruises	A-1
A.2 Navigation	A-4
A.3 Multibeam bathymetry and backscatter reflectivity	A-5
A.3.1 Matespro and Delila 1 cruises (NRP D. carlos I)	A-5
A.3.1.1 Data acquisition	A-5
A.3.1.2 Data processing	A-6
A.3.2 GAP cruise (RV Sonne)	A-7
A.4 Seismic profiles	A-7
A.4.1 PSAT seismic profiles	A-7
A.4.1.1 Data acquisition	A-7
A.4.1.2 Post-cruise data processing	A-8
A.4.2 Multichannel seismics	A-9
A.5 Side-scan Sonar	A-11
A.5.1 NRL Seemap side-scan sonar mosaic	A-11
A.5.2 OKEAN	A-11
A.5.3 OREtech	A-11
A.5.4 MAK-1M	A-13
A.6 Sub-bottom profiler	A-13
A.6.1 TTR hull-mounted acoustic profiler	A-13
A.6.2 Parametric parasound	A-14
A.7 Heat flow measurements	A-14
A.8 Underwater video observations	A-15
A.9 Gravity cores	A-16
A.10 TV controlled grabs	A-19
A.11 Box-cores	A-19
A.12 Kasten box-cores	A-19
A.13 Dredges	A-20
<b>Appendix B. Analytical methods and Results (tables)</b>	<b>B-1</b>
<b>Appendix C. EDTA Differentiation of calcite and high Mg-calcite from dolomite for stable isotope measurements</b>	<b>C-1</b>
C.1 Introduction	C-1

C.2	Methods	C-2
C.3	Results and Discussion	C-4
C.3.1	XRD results	C-4
C.3.2	Carbon and Oxygen Isotopic analysis	C-8
C.4	Conclusions	C-13

**Appendix D. Biomarkers: samples preparation and analysis** **D-1**

D.1	Introduction	D-1
D.1	Sample preparation	D-2
D.2	Decalcification	D-3
D.3	Saponification	D-4
D.4	Extraction	D-4
D.5	Column chromatography	D-6
D.5	Gas chromatography and coupled mass spectrometry (GC-MS)	D-9



## List of tables

<b>Table 5.1.</b> Mineralogy, carbonate content and stable isotopic composition of the different defined types of MDAC samples collected in the Gulf of Cadiz. (Complete table of values is given in Appendix B)	<b>163</b>
<b>Table 5.2.</b> Strontium isotope values of MDAC samples.	<b>176</b>
<b>Table 6.1.</b> $\delta^{18}\text{O}$ values of commonly used O-isotope standards (Hoefs, 1997).	<b>198</b>
<b>Table 6.2.</b> Oxygen isotope fractionation factors for carbonates. Calibrations based on experiments or natural samples. Modified from (Chacko <i>et al.</i> , 2001).	<b>200</b>
<b>Table 6.3.</b> Strontium isotope values of MDAC samples.	<b>224</b>
<b>Table 6.4.</b> Summary table of the minimum, maximum and average estimated values of oxygen isotopic composition of the end-members calcite and aragonite phases in the aragonite pavements and of the end-members calcite and dolomite of the dolomite crusts, chimneys and nodules.	<b>227</b>
<b>Table 6.5.</b> Dolomite crusts, chimneys and nodules estimated isotopic composition of seawater or pore fluid from which the end-members calcite and dolomite had precipitated considering several temperature values.	<b>234</b>
<b>Table 6.6.</b> Aragonite pavements estimated isotopic composition of seawater or pore fluid from with the end-members calcite and aragonite had precipitated considering several temperature values.	<b>245</b>
<b>Table 7.1.</b> MDAC samples used for U/Th dating.	<b>254</b>
<b>Table 7.2.</b> Mineralogy and detrital fraction present in the analysed samples. See Figure 7.1 for location.	<b>257</b>
<b>Table 7.3.</b> Stable carbon and oxygen isotopic composition, estimated isotopic values of the calcite and dolomite pure phases and theoretical $\delta^{18}\text{O}$ composition of pure calcite and dolomite phases, calculated for the present day temperature (Ambar <i>et al.</i> , 2002) and the $\delta^{18}\text{O}_{\text{SMOW}}$ isotopic values of seawater collected from the lower core of the MO at locations close to the sampling site (Voelker, 2005).	<b>254</b>
<b>Table 7.4.</b> U and Th isotopic compositions and $^{230}\text{Th}/^{234}\text{U}$ ages determined for the authigenic carbonates analysed in this study.	<b>263</b>
<b>Table 7.5.</b> Osmond isochrones ages determined for the analysed samples.	<b>266</b>
<b>Table 7.6.</b> Calculated $\delta^{18}\text{O}_{\text{SMOW}}$ values of pure phases calcite and dolomite, for temperature values of 4, 8, 11, 12 and 14°C. For calcite, the Kim and O'Neil (1997) fractionation equation was used, and for dolomite the one by Vasconcelos <i>et al.</i> , (2005). $\delta^{18}\text{O}$ values of sub-samples 9 and 10 were not measured.	<b>280</b>
<b>Table 8.1.</b> Samples selected for biomarker analyses and SEM observations. (TS: thin section; SEM: scanning electron microscopy; BK: biomarker analysis)	<b>291</b>
<b>Table 8.2.</b> Main biomarker compounds identified on the studied samples and their carbon isotopic compositions (values in ‰ VPDB). Diagnostic lipid biomarkers are highlighted in grey, red colour values identify probable AOM compounds. (n.d. = not detected).	<b>326</b>
<b>Table 8.3.</b> Main biomarker compounds identified on aragonite pavements collected from the Hesperides and Faro mud volcanoes (data from Duarte, 2005; Niemann <i>et al.</i> , 2006). Abundances of fatty acids were normalised to i-C <sub>15:0</sub> , archaeal diethers to archaeol and archaeal isoprenoidal hydrocarbons to PMI:0. Diagnostic lipid biomarkers are highlighted in grey. (n.d. = not detected).	<b>329</b>
<b>Table B.1.</b> Carbonate mineralogy, carbon and oxygen stable isotopes of MDAC samples, by lithologic type.	<b>B-2</b>
<b>Table C.1.</b> Mineral content prior and after EDTA leaching and mole% MgCO <sub>3</sub> in the present carbonate phases.	<b>C-4</b>

**Table C.2.** EDTA leaching method results. Efficiency of the leaching technique and stable carbon and oxygen isotope composition of the bulk, dolomite and high Mg-calcite fractions obtained with 0.25 M EDTA treatment. **C-9**

**Table D.1.** Samples selected for biomarker analyses and SEM observations. (TS: thin section; SEM: scanning electron microscopy; BK: biomarker analysis) **D-2**

## List of figures

- Figure 1.1.** Geographic location of the study area (gold dashed line) with the indication of the targets focused of this study: methane-derived authigenic carbonates and mud volcanoes occurrences. (Mercator projection, true scale at 35°N) Bathymetry from the GEBCO Digital Atlas (2003 edition) and from the multibeam surveys: Matespro, Delila, Tasyo and GAP. 4
- Figure 1.2.** Topography, physiography and morphology of the study area and surrounds, with the indication of the main physiographic elements that are referred to in this work. Bathymetry from the GEBCO Digital Atlas (2003 edition) and from the multibeam surveys: Matespro, Delila, Tasyo and GAP. 6
- Figure 2.1.** Schematic diagrams (scale-independent) illustrating the structure and the main elements of a cone-shaped mud volcano. (A) Schematic cross-section profile, modified from Dimitrov (2002) and Kopf (2002). Note the “Christmas-tree” structure indicating multiple episodes of mud extrusion. (B) Schematic map illustrating the radial pattern of mud flows accumulation away from the crater, modified from Rensbergen *et al.*, (2005a). 15
- Figure 2.2.** Images of MVs and processes related to mud volcanism. (A to D) the Salse di Milano, Italy. (A) gryphons of about 3 m high within the main MV crater; (B) crater of a gryphon, 25 cm wide, with rings created by gas bubbles. (C) crater of a gryphon, about 25 cm wide, from where fresh mud flows are spreading out. (D) mud pie. (E) 500 m high Toragai MV, Azerbaijan (Aliyev *et al.*, 2002). (F) Everlasting fires, Baku, Azerbaijan (Aliyev *et al.*, 2002). (G) Swath bathymetry 3D model of the Bonjardim MV. (H) Side-scan sonar imagery overlaid on the bathymetric 3D model of the Bonjardim MV, showing high reflectivity of the fresh mud breccia material at the top and central crater. G and H were produced in this work. 16
- Figure 2.3.** Schematic diagram illustrating the different basic mechanisms of formation of submarine MVs (from Milkov, 2000). (A) seafloor piercing shale diapir without a MV; (B) MV formed on top of a shale diapir; (C) seafloor seepage; (D1) MV formed by the rise of a fluidized sediments along a fault connected to an diapir; (D2) MV formed by the rise of a fluidized sediments along a fault directly connected to the mud source bed. 20
- Figure 2.4.** Worldwide occurrence of mud volcanoes, modified after Kholodov (2002), Kopf (2002) and Judd and Hovland (2007); plate boundaries from Coffin *et al* (2000). 22
- Figure 2.5.** Pockmarks. (A) Schematic illustration (left column) and correspondent 5 kHz seismic reflection profiles of different evolution stages of pockmarks (Çifçi *et al.*, 2003) Note: BP denotes a buried pockmark. (B) MAK-1 side-scan sonar record of pockmarks (pm) and corresponding seabottom profile (Dimitrov and Woodside, 2003). (C) morphological model with chemical and biological features within a pockmark. The centre is dominated by methane-derived authigenic carbonate build-ups and endemic bacteria and fauna. The periphery is dominated by sulphide-dependent Vesicomylidia-type fauna living on black reduced sediments and white bacterial mats. In this model, the upper boundary of methane hydrates is concordant with the sulphate-methane interface (SMI) and gas hydrates can only outcrop in the centre of a pockmark if the upward flux of methane is strong enough (Gay *et al.*, 2006c). 26
- Figure 2.6.** Schematic diagram of depth distributions of methane, sulphate, total dioxide and carbon isotope ratio of carbon dioxide in interstitial waters of anoxic marine sediments. All distributions show breaks or slope changes in the sulphate-methane transition zone (SMTZ), which represents the zone of maximum anaerobic methane oxidation. Modified from Reeburg (1980). 32
- Figure 2.7.** In situ identification of archaea-sulphate reducing bacteria consortium aggregates with fluorescence in situ hybridization (FISH) with specific 16S rRNA-target oligonucleotide probes. The archaea are shown in red and the SRB in green. Confocal laser scanning micrograph of the

- hybridization with CY3-labelled probe EelMS932 (archaea) and the FLUOS-labelled probe DSS658 (SRB). Scale bar is 5  $\mu\text{m}$ . From Boetius *et al.*, (2000). 33
- Figure 2.8.** World-wide distribution map of modern and ancient (Archaean to recent) hydrothermal vent and hydrocarbon seep occurrences with chemosynthetic community associations. Plate boundary (PB) symbols include: double line - constructive PB; tooth pattern - destructive PB; single line - strike-slip PB. Data compiled from numerous literature sources (Campbell, 2006). 35
- Figure 2.9.** Cold seepage detection. (A, B and C) Still pictures of bubble discharge at the Håkon Mosby Mud Volcano (1250 m water depth) (from Sauter *et al.*, 2006). (B) Detail showing perforated sediments indicative of transient gas release. (C) Zoomed image showing bubbles in more detail. (D and E) Gas seepage in the Gulf of Mexico illustrating (D) gas bubbles seeping from a shallow gas hydrate deposit, with about 1 m across, at 570 m water depth and (E) large gas bubble rising (arrow) from a pool of brine at the crater, 25 cm across, of a small MV (D and E from MacDonald *et al.*, 2002). (F and G) Gas flares on single-beam echograms (Greinert *et al.*, 2006; Sauter *et al.*, 2006). (H) Gas plumes (arrows) in the water column imaged by side-scan sonar (Rollet *et al.*, 2006). 37
- Figure 2.10.** MDAC: examples of seafloor pictures and on land outcrops. (A to C) MDAC from a complex pockmark off Mid-Norway (Hovland *et al.*, 2005b), (A) a large, up to 24 m<sup>3</sup> carbonate slab inside the pockmark that serves as fixed substrate for benthic fauna, (B) carbonate cemented sediments with layered and friable structures that serves as substrate for benthic fauna, (C) thin carbonate crusts (inset shows one of this crusts recovered). (D to F) Seafloor images of MDAC from Hydrate Ridge (Greinert *et al.*, 2001), showing, (D) block and slab-like mudstones and bioturbation casts, (E) irregular chemoherm block with white bacterial overgrowth and white clams, and (F) aragonite pavement in direct contact with outcropping gas hydrates and also with bacterial mats and scattered with clams on the sediment. (G to I) Bottom photographs taken from the R/V Prof. Logachev underwater video camera on the Iberico mud cone and on the Formosa ridge. The field of view is approximately 2 m. (J to L) The “stone forest” from Varna, Bulgaria showing Lower Eocene massive carbonate cemented columns or chimneys, up to 1.5 m diameter and 8 m high and horizontal interbeds (De Boever *et al.*, 2006), pictures from Dimitrov (2000). (M to O) Miocene seep carbonates in the uppermost Santa Cruz Mudstone Formation in Santa Cruz, Monterey, California (M) circular conduits that extends along the opal CT horizontal porcelanite layers. Area of view is about 15 m<sup>2</sup> (Aiello *et al.*, 2001). (N and O) carbonate pipes with ~70 cm tall that protrude from the fractured opal CT horizontal porcelanite layers, (N) from Aiello (2001) and (O) from Aiello (2005). 40
- Figure 2.11.** (A, B and C) Natural GHs occurrences at the seafloor, (A) and (B) from Cascadia margin (Suess *et al.*, 1999), (C) GH mound ~1.5 m across in 543 m water depth in central Gulf of Mexico (Sassen *et al.*, 2001). (D to F) GH samples collected from the Gulf of Mexico. (G) Schematic diagram of GH cubic crystalline structure I. (H) Scheme illustrating the conventional model for GH stability and bottom simulating reflectors in submarine sediments. The base of the hydrate stability is marked by a univariant phase boundary as temperature increases with depth. At this point methane in excess of solubility in pore water may exist as free gas and potentially produce a distinct seismic reflector due to the reduced velocity (Clennell *et al.*, 1999). (I) BSR seismic record over Cascadia Margin, also illustrating the methane plumes over the seepage area (Suess *et al.*, 1999). 44
- Figure 2.12.** Global occurrences of natural gas hydrates in the ocean floor (dots) and permafrost (dashed polygons). Modified from Kvenvolden and Lorenson (2000), with additions. 47
- Figure 2.13.** (A to F) Bottom photographs of cold seep fauna (Suess *et al.*, 1998). (A to C) Pogonophoran tubes amongst clam and gastropods. (B and C) detail of the pogonophorans. (D) cold seep community. (E and F) detail of vesicomid clams. 49
- Figure 3.1.** Atlantic Africa-Eurasia plate boundary with the present day stress fields. Plate boundary adapted from Coffin *et al.*, (2000) and relative movements from Jiménez-Munt *et al.*, (2001). 52
- Figure 3.2.** Simplified lithospheric cross-section with a W-E direction crossing the Gulf of Cadiz at the Gibraltar Strait (36°N) showing the geometry of the east dipping fault plane between the subducting slab and the upper plate (Gibraltar block) with the distribution of earthquake hypocenters. Box on the Gulf of Cadiz shows the location of the simplified line draw of Sismar seismic profile 16 interpretations presented in Figure 3.3 (Gutscher *et al.*, 2002; Thiebot and Gutscher, 2006). 54
- Figure 3.3.** Multichannel Sismar seismic profile 16 and interpretation, showing the E dipping decollement, E dipping trusts and the general westward verging tectonic shortening of the area. Upper panels show zooms of ramp thrusts emerging at the seafloor and the basal un-deformed strata beneath the decollement (Thiebot and Gutscher, 2006). 54

- Figure 3.4.** Distribution of the epicentres for the years 1963 to 2006 (magnitude > 0.1) taken from the USGE-ANSS catalogue. Shallow earthquakes (depth < 20 km) are represented in blue colour, intermediate earthquakes (20 < depth < 40 km) are represented in green and deep earthquakes (depth > 40 km) are represented in red colour. The size of the points is proportional to the magnitude of the earthquake according to the scale. 55
- Figure 3.5.** (A) Simplified geological setting of the Gulf of Cadiz during the Late Jurassic and Early Cretaceous (Maldonado and Nelson, 1999). (B) Simplified geological sketch of the Gulf of Cadiz and surrounding domains during the early part of the Middle Miocene (Maldonado and Nelson, 1999). The present shorelines of southern Europe and Africa are outlined for reference. A.G.F.Z. D Azores-Gibraltar Fracture Zone. 58
- Figure 3.6.** Paleogeographic and geodynamic evolution of the Mediterranean region and the Gulf of Cadiz (Jolivet *et al.*, 2006). To be noted that the oceanic crust is shown only in the Mediterranean domain, not in the Atlantic Ocean and Black Sea. 59
- Figure 3.7.** Paleogeographic and geodynamic evolution of the Mediterranean region and the Gulf of Cadiz from the Pliocene to Present day conditions and the timing of the main geodynamic events, as described in the text (Jolivet *et al.*, 2006). 60
- Figure 3.8.** Different geologic domains in the Gulf of Cadiz as defined by Somoza *et al.*,(1999) and Medialdea *et al.*,(2004). (A) map modified from Medialdea *et al.*,(2004). (B-C) cross sections long the Gulf of Cadiz (Medialdea *et al.*, 2004). Location of profiles is given on the map in (A). 62
- Figure 3.9.** Morphosedimentary map of the Contourite Depositional System on the middle slope of the Gulf of Cadiz (Hernández-Molina *et al.*, 2006). Morphosedimentary sectors: (1) proximal scour and sand ribbons sector; (2) overflow sedimentary lobe sector; (3) channels and ridges sector; (4) contourite depositional sector; and (5) submarine canyon sector. 65
- Figure 3.10.** Main water masses in the eastern Atlantic and in the Gulf of Cadiz and their circulation pattern. Modified from Fiuza (1984) and Perez *et al.*,(1998). 67
- Figure 3.11.** General circulation pattern of the Mediterranean Outflow water (MO) in the Gulf of Cadiz (Hernández-Molina *et al.*, 2006). 69
- Figure 3.12.** General circulation pattern of the Mediterranean Outflow water (MO) in the eastern North Atlantic (Iorga and Lozier, 1999). 71
- Figure 4.1.** Location of the mud volcanoes and MDAC occurrences in the Gulf of Cadiz. Boxes indicate the main mud volcano fields defined in previous works and described in the text. 74
- Figure 4.2.** Multibeam relief of the Guadalquivir Diapiric Ridge mud volcano field and northern Tasyo Field. Boxes shows the locations of detailed investigation areas (figures 9.4 to 9.8) and open circles indicate the locations where MDAC were identified. Bathymetry with a slope and hillshade with illumination from the NW. 81
- Figure 4.3.** Multibeam relief, with slope and hillshade with illumination from the NW, of the Guadalquivir Diapiric Ridge mud volcano field. Boxes show the location of the detailed investigation areas and open circles indicate the locations where MDAC were identified. 81
- Figure 4.4.** (A) GDR in the area of the Curunã cone with the location of the dredge done during the Anastasya campaign and the seismic profile Psat-215 (TTR11). TV-profile TTR11-TV-22 crosses the GDR north of the Coruña mound. Bathymetric relief with a slope and hillshade with illumination from the NW. (B) NRL Seamap side-scan sonar imagery of the GDR and Coruña mound with superimposed bathymetry. 82
- Figure 4.5.** (A) Slope gradient of the GDR and the Coruña mound. (B) Single channel seismic line TTR11-Psat215. Location of the seismic line is given in Figure 4.4. To be noted the chaotic and indistinct seismic reflection pattern below the conical expression of the GDR, contrasting with the parallel reflections of the sedimentary basin sequences to the W. 83
- Figure 4.6.** Facies interpretation of the underwater video profile TTR11-TV22. See location in Figure 4.4. 84
- Figure 4.7.** Bathymetric relief with a slope and hillshade with illumination from the NW of the Formosa Ridge, Iberico mud cone, the Cadiz Channel and the Lolita structure. Also shown in the figure the seismic lines, underwater TV observation profiles and samples collected in this area which were used for this study. 85
- Figure 4.8.** Bathymetry, with a slope gradient and a hillshade with illumination from the NW, of the southern termination of the Formosa Ridge with the location of the dredge, TV-grab and underwater video observation profile collected during the TTR12. 87

- Figure 4.9.** NRL Seamap side-scan sonar imagery of the Formoza Ridge with the seafloor facies interpretation of the video profile TTR12-TV-29. (see Figure 4.10). 88
- Figure 4.10.** Facies interpretation of the underwater video profile TTR12-TV29. Letters (A-I) in blue indicate pictures in Figure 4.11 and 9.13. 88
- Figure 4.11.** Pictures taken from the underwater video profile TTR12-TV29 over the Formoza Ridge. (A-C) Pictures illustrate the dolomite chimneys covering the seafloor. Image (C) illustrates a chimney in a vertical position protruding from the seabed; these occurrences are statistically much less frequent than the typical occurrence of the chimneys lying broken on the seabed. (D-F) probably aragonite pavements, not sampled. To be noted that the MDAC are used as hard-grounds for fixation of benthic organisms. Pictures are about 1.5 m wide. 89
- Figure 4.12.** Pictures taken from the underwater video profile over the Formoza Ridge. (A-C) Pictures illustrate the rippled seabed with coarse sediment and where strong currents can be observed from the movement of suspended particles. Chimneys occur frequently within rippled seabed sediments as illustrated in (C). (D-F) rock outcrops, most probably of the blue marls from the Early-Middle Miocene (see text for discussion). Pictures are about 1.5 m wide. 90
- Figure 4.13.** Methane-derived authigenic carbonate samples collected from the TTR12-388Gr TV-controlled grab station on the Formoza Ridge. 91
- Figure 4.14.** Bathymetric relief with a slope and hillshade with illumination from the NW and work performed on the Hormigas Ridge (marked by the dashed red line and with the limits are marked by the arrows). 92
- Figure 4.15.** 3D bathymetric morphology of the Iberico mud cone. (A) view from SW of Iberico. (B) view from NE of the Iberico. 93
- Figure 4.16.** Slope gradient of the Iberico mud cone. See location in Figure 4.14. 94
- Figure 4.17.** Profiler and single channel seismic lines TTR11-Psat 211 and TTR11-Psat 212. Location of seismic lines is given in Figure 4.18A. To be noted the chaotic and indistinct seismic reflection pattern below the surface conical expression of the Iberico cone, contrasting with the parallel reflections of the sedimentary basin sequences. 94
- Figure 4.18.** Iberico mud cone and the Cadiz Channel, south of Iberico. (A) EM-12 multibeam bathymetry with underwater video observation profiles plotted in blue, Anastasya 2000 dredge station plotted in yellow and seismic reflection profiles plotted in light blue. (B) NRL Seamap 12 kHz SSS (low resolution) and MAK SSS imagery (high resolution) with the bottom facies interpretation plotted over it. Labels A and B pinpoint the location of still video camera pictures presented in Figure 4.19. On the SSS imagery, high backscatter is dark. (C-E) bottom facies interpretation of the underwater video profiles. 96
- Figure 4.19.** Pictures taken from the underwater video profiles over the Iberico mud cone. Pictures illustrate the dolomite chimneys recovering the seafloor. (B1) vertical carbonate chimneys. Pictures A and B2 correspond to an area approximately 1.5 m wide. Picture B1 correspond to an area approximately 75 cm wide. 97
- Figure 4.20.** Methane-derived authigenic carbonate samples collected by the TTR11-335D dredge station. (A) dolomite chimneys. (B) dolomite crusts. 98
- Figure 4.21.** Bathymetry of the Hormigas ridge in the area of Cornide and Arcos. The location of the dredge stations, heat flow measurements and gravity coring performed during the Anastasya campaigns are represented by the yellow dots and lines, respectively. Bathymetric relief with a slope and hillshade with illumination from the NW. 99
- Figure 4.22.** NRL Seamap imagery on the Hormigas ridge ver Cornide and Arcos structures. High backscatter is represented as dark. 100
- Figure 4.23.** Anastasya 2001 heat-flow station ANA01-SC06C. Temperature profile and calculated conductivity and heat flux (Gardner *et al.*, 2001). To be noted the temperature anomaly recorded in the first meter of sediments, interpreted as the result of short term fluctuations of the anomalously high temperature of the MO. 100
- Figure 4.24.** Hesperides mud volcano EM-12 multibeam bathymetry with OFOS underwater track plotted in blue, Anastasya sampling stations in yellow, GAP stations in brown and single channel seismic line Psat155 in green. Bathymetry, with a slope gradient and a hillshade with illumination from the NW. 103
- Figure 4.25.** (A) Slope gradient image of the Hesperides MV. (B) Single channel seismic line TTR10-Psat155. Location of the seismic line is shown in Figure 4.24. To be noted the chaotic and indistinct seismic reflection pattern below the complex, contrasting with the parallel reflections of the sedimentary basin sequences to the S. 103
- Figure 4.26.** NRL Seamap long range SSS with the facies interpretation plotted over it. 104

- Figure 4.27.** Facies interpretation of the OFOS 16 video profile. Labels 1, 2 and 3 indicate the location of still video camera pictures presented in Figure 4.29. **105**
- Figure 4.28.** Facies interpretation of the OFOS 17 video profile. Labels 1, 2 and 3 show the location of still video camera pictures presented in Figure 4.29. **106**
- Figure 4.29.** Still photograph taken with the video sledge OFOS16. (A-B) large number of chimneys and other carbonate rubble. (B-C) pavements, pavement slabs and mounded buildups. (E-F) corals and coral rubble in a chimneys field. Most probably the corals use the chimneys as hardground for fixation. **107**
- Figure 4.30.** Photographs of samples collected by the TV-controlled grab during the GAP cruise. (A-B) station GeoB 9024. (C-D) station GeoB 9023. (E-F) station GeoB 9022. See Figure 4.24 for location of the sampling stations. **108**
- Figure 4.31.** Gravity cores ANA00-Gc10 and ANA00-Gc12 retrieved during the Anastasya 2000 cruise, with mud breccia, which indicates the mud volcanic nature of Hesperides. **109**
- Figure 4.32.** Gravity cores GeoB 9019 and GeoB 9021 retrieved during the GAP cruise (Kopf *et al.*, 2004) with mud breccia that indicate the mud volcano nature of the Hesperides. **110**
- Figure 4.33.** Heat flow station ANA01-Sc15 collected during the Anastasya survey in 2001 in the pool-like depression at the base of the Hesperides MV, south of cone C1 (see Figure 4.24 for location). **111**
- Figure 4.34.** Heat flow stations GeoB 9025 collected during the GAP cruise (Kopf *et al.*, 2004) along a profile on the Hesperides MV, see Figure 4.24 for location. **111**
- Figure 4.35.** Bathymetry of the Faro, Cibeles and Almazam MV with the sampling stations and underwater OFOS track of station GeoB 9028. Bathymetry, with a slope gradient and a hillshade with illumination from the NW. **112**
- Figure 4.36.** (A) NRL Seamap long-range side-scan sonar. (B) Slope gradient of the arcuate structure where the Cibeles, Faro and Almazan MVs are located. **113**
- Figure 4.37.** Single channel seismic lines TTR09-Psat 120 and TTR11-Psat 213. The location of the seismic lines is depicted in Figure 4.35. To be noted the chaotic and indistinct seismic reflection pattern bellow the surface conical expression of the Faro MV, contrasting with the parallel reflections of the sedimentary basin sequences. **114**
- Figure 4.38.** Heat-flow stations ANA01-Sc08 and ANA01-Sc14 collected, respectively, at the summit of Almazan and Faro MVs during the Anastasya survey in 2001 (Gardner *et al.*, 2001), see Figure 4.35 and Figure 4.39 for location. **115**
- Figure 4.39.** Bathymetry of the Faro MV with the sampling stations and the facies interpretation of the underwater OFOS track station GeoB 9028. Legend of the interpretation is depicted in Figure 4.40. Circles correspond to gravity cores, boxes correspond to TV-grab stations and hexagons correspond to TV-multicorer stations. Anastasya stations: heat-flow probe and gravity core, are plotted in yellow; GAP stations are plotted in brown; white letters represent the underwater seafloor pictures shown in Figure 4.41. (see text for description). **116**
- Figure 4.40.** NRL Seamap long range SSS with the seafloor facies interpretation from the OFOS28 video observations. **117**
- Figure 4.41.** Photographs taken from the video profile OFOS28. (A-B) carbonate buildups, crusts, slabs and pavements. (C-D) Clam and shell fields with dead and live organisms. (E-F) Bacterial mats recovering pavement slabs and pogonophora tubes occurring as isolated individuals or in small clusters. See Figure 4.39 for location of the photographs. Pictures are about 1.5 m wide. **120**
- Figure 4.42.** (A) gravity core ANA2000-Gc09 collected at the SW flank of the Cibeles MV. (B-F) Samples collected from Faro MV. (B) TV-Grab GeoB 9029-3 with detail images illustrating Vestimentifera tubes, aragonite pavement samples and shells. Aragonite pavement samples and mytilid bivalves in (C), and live *Acharax* sp. and *Lucinoma* sp. bivalves in (D), are indicating active hydrocarbon gas escape. (E-F) live corals collected from the TV-Grab GeoB 9030-3. **121**
- Figure 4.43.** Bathymetry of the Cadiz Channel W of Iberico where the underwater profile TTR11-TV-21 was acquired which allowed the interpretation of the seabed nature. Bathymetry, with a slope gradient and a hillshade with illumination from the NW. **123**
- Figure 4.44.** NRL Seamap long range SSS (low resolution) and TTR11-MAK41 SSS imagery (high resolution) with the bottom facies interpretation overlaid. **123**
- Figure 4.45.** Bottom facies interpretation of the underwater TTR11-TV 21 video profile. **124**
- Figure 4.46.** (A) 5 kHz profiler of the deep towed TTR11-MAK 42 illustrated in Figure 4.44. (B) seismic profile TTR11-Psat 210 whose location in shown in Figure 4.43. **124**
- Figure 4.47.** Underwater pictures from the video profile TTR11-TV 21. Location of the pictures is plotted in Figure 4.43. (A-B) illustrate the aspect of the chimneys and carbonate rubble. (C-D)

- illustrate the aspect of the chimneys and carbonate rubble lying over the claystone rocky outcrops where meter-size scarps and faults are frequent along the channel scarp headwall. (E-F) illustrate the pavements, pavement slabs, chimneys and other carbonate rubble over the rocky outcrops. Pictures are about 1.5 m wide. 125
- Figure 4.48.** Samples collected by the dredge TTR11-339D, with dolomite chimneys and carbonate rubble, composed of fragments of the dolomite chimneys and crusts; also some fragments of claystone interpreted as fragments of the rocky outcrops. 126
- Figure 4.49.** Schematic summary of the qualitative relationships between the flux of fluids and gases to the seafloor and the resultant escape structures (Roberts and Carney, 1997). (A) pictures illustrating the rapid flux (mud-prone) end-member corresponding to the mud volcanoes and mud flows. (B) pictures illustrating an intermediate case with moderate flux rates, corresponding to surface exposures or shallow gas hydrates and well-developed chemosynthetic ecosystems and local areas of occurrence of MDAC. (C) pictures corresponding to slow flux cases (mineral-prone case) characterized by a sparse or absent chemosynthetic communities and dominance of the MDAC, occurring as pavements, slabs, buildups, mounds, chimneys and other forms of lithified seafloor. 128
- Figure 4.50.** (A) Carlos Ribeiro MV showing a recent mud flow characterized by a strong backscatter MAK 1 side-scan sonar imagery. (B) Gravity core GeoB 9037-1 where is possible to recognize three mud flows. (C) bathymetry of the mini-basin where the Sonne mud cone, the Captain Arutyunov and the Atlas MVs are located. Also shown the location of gravity core GeoB 3937-1. 136
- Figure 4.51.** Schematic representation of a mud volcano illustrating a succession of different phases of its evolution. (A) phase of rapid flux with a mud-prone dominated event. (B) phase of intermediate flux with a flux dominated by water and gas and subsequent formation of MDAC, accumulation of gas hydrates and the establishment of large chemosynthetic communities. (C) phase of slow flux rate with a mineral-prone dominated features. (D) new phase of rapid flux with a mud-prone dominated event that covers the previous MDAC and chemosynthetic communities. 139
- Figure 5.1.** Map of the Gulf of Cadiz, showing the location of mud volcanoes, mud diapirs and carbonate crusts and chimneys. 144
- Figure 5.2.** Area of the Guadalquivir Diapiric Ridge (GDR) and Formosa Ridge (FR) where the samples described in this study were collected. Also shown the location of underwater video camera profiles and the pathway of the Mediterranean Outflow Water (MO) that in this area runs near the sea bottom causing a strong erosive effect. 144
- Figure 5.3.** Illustration of the different morphologic types of dolomite carbonate samples recovered. A: Dolomite crust type; B: Tubular DChy; C: Conical DChy; D: Spiral DChy; E: Branched DChy; F: Nodular or massive type (Nod). 152
- Figure 5.4.** Illustration of the different types of vent channel. (A) open vent channel; (B) open vent channel exhibiting oxidation fronts spreading out from the exterior of the sample and from the interior open vent channel and also from open holes of burrows, as the one illustrated where is possible to observe the oxidation front spreading from this hole; (C) completely filled chimney sample exhibiting concentric grow layers; (D) chimney with 2 parallel vent channels that are jointed at an intermediate length; (E) chimney with two parallel and open vent channels. 153
- Figure 5.5.** Illustration of the different aragonite pavement types. (A) Lithified mud volcano mud breccias (LMb); (B) Shell crusts (SCr); (C) intraformational breccias (IBr); (D) Lithified clasts of dolomite chimneys crusts fragments (LDChy); (E) Stromatolitic layers (SL). 155
- Figure 5.6.** Bottom photographs taken from the R/V Prof. Logachev underwater video camera from the video profiles: TV AT-18 and TV AT-19 (B) on the Iberico mud diapir; TV AT-20 and TV AT-21 (A) on the MO channel; and TV AT-29 on the Formosa Ridge (C to H) (see location in Figure 5.2). The field of view is approximately 1m for picture A, approximately 2 m for B and approximately 2.5 m for pictures C to H. 162
- Figure 5.7.** Frequency histogram of the distribution of the  $d(104)$  values for calcites and dolomites of the studied dolomite dominated samples. 166
- Figure 5.8.** Box-whisker diagrams of the mineralogical composition and carbonate content of the dolomite dominated samples. 167
- Figure 5.9.** Box-whisker diagrams of the mineralogical composition and carbonate content of the aragonite dominated samples. 171
- Figure 5.10.** Box-whisker diagrams of the mineralogical composition and carbonate content of the different types of aragonite dominated samples. 172

- Figure 5.11.** Box-whisker diagrams of the mineralogical composition and carbonate content of sediment samples collected at the places near the MDAC occurrences and of shells and corals collected from the MDAC. **173**
- Figure 5.12.** Isotopic composition of the authigenic carbonates. **175**
- Figure 5.13.** Radial and longitudinal profiles along dolomite chimneys. **175**
- Figure 5.14.** Radial and longitudinal profiles along dolomite chimneys. **176**
- Figure 5.15.** Strontium isotope values of MDAC samples with reference to the present day seawater strontium isotopic composition (Paytan *et al.*, 1993). **177**
- Figure 5.16.** Hydrocarbon fraction gas chromatograms of a dolomite chimney (on top) and of an aragonite pavement (bottom). Isotope compositions of individual biomarkers are presented in  $\delta^{13}\text{C}$  ‰ relative to PDB. **179**
- Figure 5.17.** Proposed schematic model for the formation of the methane-derived authigenic carbonates in the Gulf of Cadiz. **189**
- Figure 6.1.** Carbon isotopic composition of some geologically important materials. Modified from (Hoefs, 1997) **196**
- Figure 6.2.**  $^{18}\text{O}$ -fractionation equations defined for calcite and Mg-calcite. **205**
- Figure 6.3.**  $^{18}\text{O}$ -fractionation equations for dolomite and proto-dolomite. **208**
- Figure 6.4.**  $^{18}\text{O}$ -fractionation equations for aragonite. **210**
- Figure 6.5.** Differences in the oxygen isotopic fractionation ( $\Delta^{18}\text{O}_{\text{arag-calc}}$ ) of calcite (red lines) and aragonite (blue lines) in equilibrium with water with  $\delta^{18}\text{O} = 0\text{‰}$  SMOW, as a function of temperature. The difference between aragonite and calcite according to the Bohm *et al.*, (2000) and the Kim and O'Neil (1997) equations is 1.40‰. The maximum difference in the oxygen isotopic fractionation is 1.60‰ considering the Grossman and Ku (1986) equation for aragonite. **212**
- Figure 6.6.** Differences in the oxygen isotopic fractionation ( $\Delta^{18}\text{O}_{\text{arag-calc}}$ ) of calcite (red lines) and aragonite (blue lines) in equilibrium with water with  $\delta^{18}\text{O} = 1\text{‰}$  SMOW, as a function of temperature. The difference between aragonite and calcite according to the Bohm *et al.*, (2000) and the Kim and O'Neil (1997) equations is 1.40‰. The maximum difference in the oxygen isotopic fractionation is 1.60‰ considering the Grossman and Ku (1986) equation for aragonite. **212**
- Figure 6.7.** Differences in the oxygen isotopic fractionation ( $\Delta^{18}\text{O}_{\text{arag-calc}}$ ) of calcite (red lines) and aragonite (blue lines) in equilibrium with water with  $\delta^{18}\text{O} = 2\text{‰}$  SMOW, as a function of temperature. The difference between aragonite and calcite according to the Bohm *et al.*, (2000) and the Kim and O'Neil (1997) equations is 1.40‰. The maximum difference in the oxygen isotopic fractionation is 1.60‰ considering the Grossman and Ku (1986) equation for aragonite. **213**
- Figure 6.8.** Differences in the oxygen isotopic fractionation ( $\Delta^{18}\text{O}_{\text{dol-calc}}$ ) of calcite (red lines) and dolomite (blue lines) in equilibrium with water with  $\delta^{18}\text{O} = 0\text{‰}$  SMOW, as a function of temperature. **214**
- Figure 6.9.** (a) Temperature profile close to the Iberico mud cone, where MDAC were collected. Data presented correspond to summer and winter profiles from the CANIGO data base and shows the two main water masses in the Gulf of Cadiz. At the depth range between 400 and 1600 meters, the NACW is characterized by temperatures ranging from 6 to 12°C. The MO is characterized by temperatures ranging from 10 to 14°C. (b) Map showing the location of sites where MDAC were collected and temperature values of the deepest CTD measurement from the CANIGO data set. To be noted the scarceness of measurements in the Moroccan margin. The temperature values on this margin were extrapolated from the temperature values from the northern part of the Gulf of Cadiz which most probably corresponds to an underestimation of the temperature values for the Morocco margin. **215**
- Figure 6.10.** Correlation between the dolomite/(calcite + Mg-calcite) ratio and the  $\delta^{18}\text{O}$  values of the group of samples treated with EDTA leaching. Pure dolomite yields 5.6‰  $\delta^{18}\text{O}$  PDB, whereas  $^{18}\text{O}$  is strongly depleted in the calcite and Mg-calcite phases. There is no clear relationship between the mineralogy and the  $\delta^{13}\text{C}$  values. **219**
- Figure 6.11.** Correlation between the dolomite/calcite + Mg-calcite ratio and the  $\delta^{18}\text{O}$  values of the dolomite crusts, chimneys and nodular samples. Also plotted (in red dashed line) the trend line and the calculated (red circles) isotopic composition of the pure calcite and pure dolomite phases determined with the EDTA leaching methodology (Appendix C). Grey arrows indicate the considered extreme isotopic maximum and minimum values for the pure calcite and pure dolomite end-members. **220**
- Figure 6.12.** Correlation between the dolomite/calcite + Mg-calcite ratio and the  $\delta^{13}\text{C}$  values of the dolomite crusts, chimneys and nodular samples. **220**
- Figure 6.13.** Correlation between the Aragonite/calcite+Mg-calcite ratio and the  $\delta^{18}\text{O}$  values for the aragonite pavement samples. A pure aragonite mineral yields about 4.2‰  $\delta^{18}\text{O}$  (PDB), whereas  $^{18}\text{O}$  is

- lighter in the pure calcite phase (2.3‰). Also plotted (in green) the isotopic composition of shells cemented within the shell pavement-type samples and corals and shells (dark brown colour) attached to the external surface of dolomite chimney samples. Labels on the Aragonite pavement samples correspond to the sample ID number see text for explanation. 222
- Figure 6.14.** Aragonite pavement samples do not reveal any clear correlation between the Aragonite/calcite ratio and the  $\delta^{13}\text{C}$  values. Also plotted (in green) the isotopic composition of shells cemented within the shell pavement type samples. In dark brown colour is shown the isotopic composition of corals and shells attached to the external surface of dolomite chimney samples. 223
- Figure 6.15.** Strontium isotope values of MDAC samples plotted with reference to the seawater and to the pore fluids end member compositions from the Captain Arutyunov, Ginsburg and Bonjardim MVs (Hensen *et al.*, Submitted). 224
- Figure 6.16.** Strontium isotope values of MDAC samples plotted over the ODP site 758 Farrel *et al.*, (1995) seawater  $^{87}\text{Sr}/^{86}\text{Sr}$  reference curve and the respective confidence interval ( $\pm 19 \times 10^{-6}$  from 5-order fit of the curve). Dcr - Dolomite crust sample; Scr - stromatolitic crust of an aragonite pavement; Dchy - Dolomite chimney sample. To be noted that the Age axis is valid only for the Farrel *et al.*, (1995) seawater  $^{87}\text{Sr}/^{86}\text{Sr}$  reference curve, the age of the MDAC samples is not established and their position over the X axis on this plot is positioned only for reading convenience. On the graph is also plotted the Present day seawater strontium value from Payton *et al.*, (1993). 225
- Figure 6.17.** Plot showing the relation between oxygen isotope composition estimated for the end-member pure calcite of the dolomite crust, chimney and nodule samples, versus the temperature of precipitation with seawater oxygen isotope composition of -1.5, -1.0, 0, 1, 2, and 2.8‰ vs. SMOW. The relation is based on the equation given by Kim and O'Neil (1997). 227
- Figure 6.18.** Different  $^{18}\text{O}$ -fractionation equations defined for calcite and Mg-calcite and the extrapolated range of  $\delta^{18}\text{O}$  values of the dolomite crusts, chimneys and nodules for different oxygen isotope compositions of water (-2 to +3‰ SMOW). Also shown in the plots the present day temperature range at the sites where the MDAC where collected. 231
- Figure 6.19.** Different  $^{18}\text{O}$ -fractionation equations defined for protodolomite and dolomite and the extrapolated range of  $\delta^{18}\text{O}$  values of the dolomite crusts, chimneys and nodules for different oxygen isotope compositions of water (-2 to +3‰ SMOW). Also shown in the plots the present day temperature range at the sites where the MDAC where collected. 232
- Figure 6.20.** Plot showing the relation between oxygen isotope composition estimated for dolomite and temperature of precipitation, for oxygen isotope composition of seawater of -2, -1, 0, 1, 2, and 3‰ vs. SMOW. The relation is based on the equation given by Vasconcelos *et al.*, (2005). 233
- Figure 6.21.** Plot showing the dolomite crusts, chimneys and nodules estimated average and extreme limit values of the isotopic composition of seawater or pore fluid from with the end-members calcite and dolomite had precipitated. 237
- Figure 6.22.** Plot showing the relation between oxygen isotope composition estimated for calcite and/or high Mg-calcite in aragonite pavement samples and temperature of precipitation with oxygen isotope composition of seawater are -2, -1, 0, 1, 2, and 3‰ vs. SMOW. The relation is based on the equation given by Kim and O'Neil (1997). 238
- Figure 6.23.** Different  $^{18}\text{O}$ -fractionation equations defined for calcite and Mg-calcite and the extrapolated range of  $\delta^{18}\text{O}$  values of the aragonite pavements for different oxygen isotope compositions of water -2 to +3‰ SMOW. Also shown in the plots the present day temperature range at the sites where the MDAC where collected. 239
- Figure 6.24.** Different  $^{18}\text{O}$ -fractionation equations defined for aragonite and the extrapolated range of  $\delta^{18}\text{O}$  values of the aragonite pavements for different oxygen isotope compositions of water -2 to +3‰ SMOW. Also shown in the plots the present day temperature range at the sites where the MDAC where collected. 242
- Figure 6.25.** Plot showing the relation between oxygen isotope composition estimated for pure phase aragonite in aragonite pavement samples and temperature of precipitation with oxygen isotope composition of seawater are -2, -1, 0, 1, 2, 3 and 4‰ vs. SMOW. The relation is based on the equation given by Bohm *et al.*, (2000). 243
- Figure 6.26.** Plot showing the aragonite pavements estimated average and extreme limit values of the isotopic composition of seawater or pore fluid from with the end-members calcite and aragonite had precipitated. 245
- Figure 6.27.** Plot comparing the estimated average and extreme limit values of the isotopic composition of seawater or pore fluid from with the end-members calcite – aragonite and calcite - dolomite had

precipitated on the aragonite pavement samples (bottom frame) and the dolomite crusts, chimneys and nodules (top frame). 247

- Figure 7.1.** (A) Sample location and seabottom water temperature grid, calculated based on the deepest measurements from the CTD (stations Co-68 and Co-69 acquired during the winter at the same positions of the equivalent summer stations: Th-53 and Th-54) database from the CANIGO project (Ambar *et al.*, 2002). (B) CTD profiles closer to the sampling site, are plotted over the P-T stability domain of gas hydrates. To be noted that the sampling location are bathed by the lower core of the Mediterranean Outflow (MOW) with a temperature of 11°C, but the seasonal variations on the temperature values close to the seafloor are in the order of magnitude of 0.5°C to 1°C; therefore, the gas hydrate stability zone (GHSZ) plotted in the graph represents the temperature in winter conditions and it can be significantly reduced or even null during part of the year. In red are plotted the salinity profiles and in blue the temperature profiles. 254
- Figure 7.2.** Samples analysed for U/Th age determination. (A) and (B): sample 3463-A03. (C), (D) and (E): sample 3463-A08. Numbers in (B) and (E) represent locations of analysed sub-samples collected with a hand micro-drilling. 255
- Figure 7.3.** Thin section photomicrographs of dolomite chimney 3463-A03 (A and B) and sample 3463-A08 (C and D) where it is evident that sample 3463-A03 have a sand size grain supported texture while sample 3463-A08 that corresponds to a mudstone/wackstone have a cement/clay matrix supported texture. Therefore the initial permeability of sample 3463-A03 is much higher than sample 3463-A08. 256
- Figure 7.4.** Uranium concentrations of the analysed samples, compared with modern seawater U concentration (c.a. 3.238 ng/g) from Chen *et al.*, (1986), uranium average values from fossil and modern corals (Cheng *et al.*, 2000), and aragonite authigenic carbonates (chemoherms) from Hydrate Ridge (Teichert *et al.*, 2003). 261
- Figure 7.5.**  $\delta^{234}\text{U}$  ratios of the analysed samples and  $\delta^{234}\text{U}$  average value from modern seawater, c.a. 144  $\pm 2\%$  (Chen *et al.*, 1986). 261
- Figure 7.6.** Inverse U concentration as a function of  $\delta^{234}\text{U}$  values in the analysed chimney samples. The seawater average value (Cheng *et al.*, 2000) is also plotted, for reference. 261
- Figure 7.7.** U/Th ages determined along radial and longitudinal profiles on the analysed samples. 265
- Figure 7.8.** Rosholt type II isochron diagrams. To be noted the good linear correlation of the trend lines. To be noted that the graphs on the right correspond to a zoom of the lower values [0-20] of the graphs in the left. 266
- Figure 7.9.** Osmond type II isochron diagrams. To be noted the reasonable linear correlation of the trend lines, with the exception of sample 3463-A03. To be noted that the graphs on the right correspond to a zoom of the lower values [0-1.2] of the graphs in the left. 267
- Figure 7.10.** Osmond type isochron diagrams. To be noted the good linear correlation of the trend lines, with the exception of sample 3463-A03. To be noted that the graphs on the right correspond to a zoom of the lower values [0-1.2] of the graphs in the left. 268
- Figure 7.11.**  $^{230}\text{Th}/^{234}\text{U}$  ages of individual sub-samples and isochron ages determined by the Osmond isochron method. 271
- Figure 7.12.** Ages of the two dolomite chimney samples projected over the  $\delta^{18}\text{O}_{\text{SMOW}}$  estimated sealevel variation curve. The sealevel variation curve is based on the assumption that the global seawater  $\delta^{18}\text{O}_{\text{SMOW}}$  variation resultant from glacial-interglacial ice volume change is of about 1‰ (Schrag *et al.*, 1996; Duplessy *et al.*, 2002) and that the entire sealevel scale is 125 m (Fairbanks and Matthews, 1978; Fairbanks, 1989). The plotted  $\delta^{18}\text{O}$  curve corresponds to the normalized “LR04” stack (Lisiecki and Raymo, 2005). The MIS ages and nomenclature are the ones defined by the SPECMAP, Martinson *et al.*, (1987) and (Shackleton, 2000). 275
- Figure 7.13.** Mineralogy (dolomite/calcite ratio) and  $\delta^{18}\text{O}$  values of the analysed sub-samples and extrapolated values of calcite and dolomite pure phases. Red line represents the trend line that indicates the relationship of the estimated isotopic compositions of pure calcite and dolomite phases, calculated from the group of samples leached with EDTA, according to Figure 6.10 in chapter 6. Grey arrows point to the pure calcite and dolomite phases isotopic, minimum and maximum, estimated isotopic values. 277
- Figure 7.14.** Plot of the determined ages of the analysed dolomite chimneys over the normalized  $\delta^{18}\text{O}_{\text{SMOW}}$  “LR04” stack curve (Lisiecki and Raymo, 2005). Age values are projected onto the normalized  $\delta^{18}\text{O}_{\text{SMOW}}$  curve. The estimated  $\delta^{18}\text{O}_{\text{SMOW}}$  fluid composition from which the calcite (in blue) and the dolomite (in red) pure phases end-members precipitated are plotted for fluid temperature

values of 4, 8, 11, 12 and 14°C, respectively (Table 7.6). In magenta are plotted the temperatures of precipitation considering a constant  $\delta^{18}\text{O}$  fluid composition value of 0.6‰ (SMOW), the open circles correspond to calcite and the X symbols correspond to dolomite. Note the different age scale and the scale hiatus in the graph. Green numbers indicate sub-sample labels. 280

**Figure 8.1.** Occurrences of MDAC in the Gulf of Cadiz. The samples analysed for biomarkers in this work are highlighted with open blue circles. Black triangles indicate the location of known mud volcanoes. 287

**Figure 8.2.** Samples analysed for biomarkers. Sample 3340-5001 (TTR09-218Gr): aragonite pavement, from which a sub-sample was collected for biomarker analyses, by cutting a 7 cm thick slice off the interior of the crust. Sample 3463-A08 (TTR11-339D-A08): dolomite chimney with no signs or very weak signs of oxidation. Sample 3722-A33 (ANA00-DA10.33): dolomite chimney with weak signs of oxidation in the internal chimney material. To avoid the oxidation fronts, sub-samples were collected by cutting a 7 cm thick slice in the internal, less oxidized area. 290

**Figure 8.3.** Dolomite chimneys general textural characteristics. Sandstone (A, C, D and F) and wackestone (B, E) thin section microphotographs, where it is possible to recognise that the detrital fraction, composed of bioclasts and terrigenous detritus, is cemented by a micrite to micro-spar carbonate cement with a peloidal and clotted microfabric. The detrital grains range from clast-supported to matrix-supported. The cement shows a clotted microfabric (cm) where peloidal-like structures (p) are identified. Pyrite (py), some times replaced by oxy-hydroxides, occurs speckled in the clotted micrite cement and within bioclasts (b) of foraminifera tests. All microphotographs are in plane-polarized light except for image D which is in crossed-polarized light. 296

**Figure 8.4.** SEM imagery illustrating the general textural characteristics of the dolomite chimney samples. Authigenic calcite, high Mg-calcite and dolomite compose the cement whereas the detrital fraction is composed of quartz, feldspars, clays and bioclasts. (A to C) general characteristics where it is possible to recognise different detrital grains and the authigenic carbonate minerals with rhombohedra shapes less than 5  $\mu\text{m}$  in size. (D-E) details of euhedral carbonate minerals. (F) carbonate cement minerals with less than 0.5  $\mu\text{m}$  in size that have sub-round shapes, contrasting with the euhedral crystal shapes on the images (D) and (E). Scale and acquisition parameters of pictures are shown in the pictures footnotes. 297

**Figure 8.5.** SEM imagery and EDS chemical composition of the authigenic dolomite and high Mg-calcites in the dolomite chimney samples. Note that the detection of Fe in the EDS chemical analysis is considered to result from the crystal structure and also from the iron oxy-hydroxides that pervasively exist coating the sample. Scale and acquisition parameters are shown in the pictures footnotes. 299

**Figure 8.6.** SEM imagery and EDS chemical composition of framboidal pyrite (Py) within dolomite chimney samples. The pyrite framboids are surrounded by euhedral dolomite crystals (Dol). (B) is a detailed image of the pyrite framboid in (A) where the EDS chemical analysis (C) was performed. Scale and acquisition parameters are shown in pictures footnotes. 299

**Figure 8.7.** Thin section micrograph of peloidal and clotted microfabric in dolomite chimney samples. (A) peloidal and clotted microfabric on oxidized and non oxidized material. Arrow pinpoints the oxidation front. (B) peloidal (p) and clotted microfabric (cm) where it is possible to recognise high density of speckled pyrite framboids (py) also present on the micrite cement. (C) detail image of (B) where the indistinct and diffuse margins of the peloid (p1) is compared with an more well defined margin of the peloid (p2). (D and E) shows micritic clots surrounded by micritic cement and also show foraminifera bioclasts with oxidized pyrite infillings. (F) peloidal and clotted microfabric of the cement where it is possible to recognise speckled pyrite framboids (py). All microphotographs are in plane-polarized light. 301

**Figure 8.8.** SEM imagery illustrating microbial filaments on dolomite chimney samples. (Scale and acquisition parameters are shown in pictures footnotes). See text for description and discussion. 303

**Figure 8.9.** SEM imagery illustrating calcified structures on dolomite chimney samples that are interpreted to have a biological origin. (Scale and acquisition parameters are shown in pictures footnotes). 304

**Figure 8.10.** SEM imagery illustrating calcitic globular and rod-shaped structures (scale and acquisition parameters are shown on the pictures footnotes). (A and C) globular and rod-shaped structures that are possibly biological in origin. (C) is a detail image of (A) showing the boundary between the rod-shaped agglomerate and the cement. (B and D) EDS chemical analyses on (B) calcite cement crystal and (D) rod-shaped structures, indicating a calcite mineralogy. See text for discussion. 304

- Figure 8.11.** Dolomite chimney samples SEM imagery, illustrating the similarity between the (A) globular and rod-shaped structures that are possibly biological in origin and (B-E) the radial structures, possibly of sections of spiculas. (Scale and acquisition parameters are shown in pictures footnotes). See text for discussion. **305**
- Figure 8.12.** SEM imagery illustrating linear filamentous structures (batons) interpreted as possible fossilised bacteria. (Scale and acquisition parameters are shown in pictures footnotes). (A-C) baton like structures with bacterial equivalent sizes, some of which are being incorporated in the carbonate crystals. The structure pointed by the white arrow in (C) is a cocolith disk. (D) detail of one of the baton structures. **306**
- Figure 8.13.** SEM imagery illustrating globular, tubular and dumbbell like structures that are interpreted to have a biological origin. (Scale and acquisition parameters of pictures are shown in pictures footnotes). (A-B) globular morphology possible a dumbbell? (C-D) globular sub-spherical grains. (E) fragment of a tubular structure. (F) clotted surface with globular grains and pyrite framboids being cemented on these clotted surface. **307**
- Figure 8.14.** SEM imagery illustrating globular and structures that are interpreted to have a biological origin on dolomite crystals. (Scale and acquisition parameters of pictures are shown in picture footnote). **308**
- Figure 8.15.** SEM imagery illustrating high Mg-calcite globular and framboidal structures that are interpreted to have a biological origin. (Scale and acquisition parameters are shown in pictures footnotes). (B) is a detail of the area framed by the green rectangle in (A). Arrow in (B) pinpoints a sub-spherical agglomerate of euhedral crystals that are being incorporated by the larger cement crystal. Both sub-spherical agglomerate and the large cement crystal have similar chemical compositions, as indicated by the EDS analysis presented in (C) and (D) respectively. **309**
- Figure 8.16.** (A) Transversal cut of an aragonite pavement where is possible to recognise a dissolution surface and veins filled by pure aragonite cement (B) with botryoidal and stromatolitic layers (C). **310**
- Figure 8.17.** Thin section micrograph of the lithified mud volcano mud breccias and shell crusts. (A) shows the two carbonate cement phases: the clotted micrite or microbial pelmicrite cement (cm) composed of calcite, high Mg-calcite and aragonite; and a later cementation stage by acicular (almost pure) aragonite that fills the pore spaces, fractures and open cracks, frequently forming botryoidal cements. (B) detail of (A) where is possible to recognise clotted peloidal-like (p) microfabric of the aragonite and calcite cement that is very similar to the fabric of the dolomite chimneys illustrated in Figure 8.7B and C. Arrows in (A) and in (B) indicate coincident locations. (C) pyrite (py) and micritic to spar aragonite (a) cementing bioclasts and leaving some open voids (v). (D-F) details of the contact between the acicular aragonite and the peloidal clotted microfabric (cm) with abundant pyrite framboids and from where the botryoidal acicular aragonite initiates from. In some occasions this contact is characterized by intense pyrite (and organic matter) layer that can show locally finer intercalations of aragonite cement, as illustrated by the arrows in (E) and in Figure 8.18C. (E) is a detail image of (D). All microphotographs are in plane-polarized light except for images (C) and (F) that are crossed polarized light. **314**
- Figure 8.18.** Thin section micrograph of aragonite pavement samples with re-cemented megaclasts (up to 3 cm size) of previous authigenic carbonate fragments. These samples correspond to the intraformational breccias (described in Chapter 5). (A) biopelmicrite megaclasts (Cm clast), interpreted as previously cemented mud to sands with textural characteristics as described on the dolomite chimneys and other aragonite pavements, fractured and cemented by acicular aragonite (ac) and pyrite (py) probably later replaced by oxy-hydroxids (Fe oxy) and also by clotted micritic cement (cm) with aragonite, calcite and Mg-calcite that can incorporate also bioclasts and other detrital components, as illustrated in (B) and (C). Voids and open cracks are also observed (C) Arrows in (C) pinpoints to the mega-clasts borders. Some of the mega-clasts show sub-rounded shapes (D) and frequently have signs of dissolution, pinpointed by the arrows in (D) and (E). (F) illustrates the radial botryoidal cement (ab) with radial aragonite fabric growing from the clotted pelmicrite cement (cm); to be noted the cloudy fabric at the base of the botryoidal aragonite that is also frequently observed at their ends and that is interpreted as resulting from the incorporation of organic matter of microbial origin. All microphotographs are in plane-polarized light except for images (C) that is crossed polarized light. **315**
- Figure 8.19.** Thin section micrograph of aragonite pavement peloidal and clotted microfabrics. (A) Clots containing framboidal pyrite (smack black spots) cementing detrital grains (d) and bioclasts some of them containing pyritised interiors (py). (B) detail of the clot from (A). (C - F) clotted microfabric and micritic cement with peloidal-like structures and spackled by pyrite framboids forming clusters or

- dispersed in the cement. Arrows in (F) pinpoint to intercalations of aragonitic layers in the clotted microfabric. All microphotographs are in plane-polarized light except for images (A) that is crossed polarized light. 316
- Figure 8.20.** Thin section micrographs illustrating peloidal, clotted microfabric and aragonite botryoidal infilling voids, cavities and cracks of the lithified mud volcano breccias and shell crusts. (A and C) details of peloids (p) where botryoidal aragonite (ab) cement, with radial fabric, initiates and grow, infilling open spaces. (C) detail of a peloid from (A and B) where is possible to recognise the margin of the peloid and the initiation of the botryoidal aragonite, showing zoned concentric isopachous layers that are interpreted as being layers of higher organic matter content and pyrite. (D) botryoidal aragonite infilling of voids where is botryoidal aragonite grows over clotted micrite cement. (F) detail of image (E) showing the botryoidal infilling of open space showing zoned concentric isopachous layers of brownish yellowish material speckled by small black spots interpreted as pyrite. These layers are interpreted as corresponding to high content in organic matter probably the biofilms and preserved bacterial rods that are imagined by SEM images in Figure 8.22D and E and in Figure 8.26. 317
- Figure 8.21.** SEM imagery illustrating general textural characteristics of the micrite and pelmicritic fabric of the aragonite pavements. Arrows in (A) pinpoint detrital grains. (Scale and acquisition parameters are shown in pictures footnotes). 318
- Figure 8.22.** SEM imagery illustrating textural characteristics of the aragonite botryoidal and stromatolitic layers fabric of the aragonite pavements. (D) arrows pinpoint to different aragonite layers within the stromatolitic layer fabric (Scale and acquisition parameters are shown in pictures footnotes). 319
- Figure 8.23.** SEM imagery illustrating aragonite pavements microbial filaments. (Scale and acquisition parameters are shown in the pictures footnotes). 321
- Figure 8.24.** SEM imagery illustrating aragonite pavements tubular and microbial scavenger holes. (Scale and acquisition parameters are shown in pictures footnotes). 322
- Figure 8.25.** SEM imagery illustrating general textural characteristics of the aragonite pavement type with mucilage or calcified biomucous within the aragonite needles pinpointed by the arrows. (Scale and acquisition parameters are shown in pictures footnotes). 322
- Figure 8.26.** SEM imagery illustrating aragonite needles stromatolitic layer filing a cavity with biofilms and biomucos. (Scale and acquisition parameters are shown in pictures footnotes). 323
- Figure 8.27.** Gas chromatograms of hydrocarbon fractions obtained from samples 3722-A33 (A) and 3463-A08 (B). n-Alkanes are indicated by solid circles. Numbers represent total number of carbon atoms. (Hydrocarbon compounds: Pr= 2, 6, 10, 14-tetramethylpentadecane; Ph= 2, 6, 10, 14-tetramethylhexadecane; Cr= Crocetane; Cr:1, Cr:2 = Crocetane containing one or two double bonds, respectively; PMI= 2, 6, 10, 15, 19-pentamethylcosane; PMI:3, PMI:4, PMI:5 = pentamethylcosenes containing three, four or five double bonds, respectively; SI= internal standards; ?= unknown cyclic compounds). Italicized values in red indicate  $\delta^{13}\text{C}$  isotopic composition of individual biomarkers in ‰ VPDB. 325
- Figure 8.28.** Gas chromatograms of hydrocarbon fractions obtained from the aragonite pavement sample 3340. n-Alkanes are indicated by solid circles. Numbers represent total number of carbon atoms. (Hydrocarbon compounds: Pr= 2, 6, 10, 14-tetramethylpentadecane; Ph= 2, 6, 10, 14-tetramethylhexadecane; Cr= Crocetane; Cr:1, Cr:2 = Crocetane containing one or two double bonds, respectively; PMI= 2, 6, 10, 15, 19-pentamethylcosane; PMI:3, PMI:4, PMI:5 = pentamethylcosenes containing three, four or five double bonds, respectively; SI= internal standards; ?= unknown cyclic compounds). Italicized values in red indicate  $\delta^{13}\text{C}$  isotopic composition of individual biomarkers in ‰ VPDB. 327
- Figure 8.29.** Schematic diagram illustrating the chemical environment during the formation of the authigenic carbonates (phase A and B). In (C) a change in the chemical environment occurs due to destabilization of gas hydrate layers that promotes the fracturation of the incipient aragonite pavements and subsequent ventilation of the system by seawater and consequent change of the environment to an oxic phase. This phase can be followed by a new phase (D) of authigenic carbonate formation leading to the re-cementation of the MDAC fragments. 331
- Figure 8.30.** Schematic diagram illustrating the chemical environment during the formation of the authigenic carbonates considering multiple episodes of mud volcano mud breccia extrusion episodes. 331
- Figure A.1.** Research vessels used in some of the cruises that allowed the collection of data used in this work. (A) Professor Logachev used on the TTR09 to TTR16 cruises. (B) R/V Cornide de Saavedra where the Anastasya cruises were performed. (C) R/V Belgica where the cruises Cadipor 1 and 2 were

- performed. (D) R/V D. Carlos I used during the swath bathymetry surveys Matespro and Delila 1. (E) R/V Sonne, GAP cruise. **A-4**
- Figure A.2.** SPW processing flow for TTR11 Psat211 line. **A-9**
- Figure A.3.** Side-scan sonar equipments used on board the R/V Professor Logachev. (A) OKEAN side-scan sonar fish used in all the TTR cruises. (B) OREtech deep-towed side-scan sonar used during the TTR09 and TTR10 cruises. (C) MAK-1M deep-towed side-scan sonar used from the TTR11 to the TTR16 cruises. **A-12**
- Figure A.4.** Heat flow probes. (A) Lister type heat flow probe with a violin bow design used in the GAP cruise and of the same type as the one used during the Anastasya-2001 cruise. (B) mini-temperature logger installed on a gravity corer. **A-15**
- Figure A.5.** Underwater video systems. (A) TTR underwater video unit. In the picture is possible to recognise mounted in the frame the light system and the high-pressure housing containing the power supply. (B) OFOS system used during the GAP cruise. **A-16**
- Figure A.6.** Sampling devices used during the several cruises whose where used for this thesis. (A) Gravity corer used onboard the R/V Professor Logachev during the TTR cruises. (B) Gravity corer used onboard the R/V Sonne, GAP cruise. (C) TV-controlled grab used onboard the R/V Professor Logachev during the TTR10, 11, 12 and 15 cruises. (D) TV-controlled grab used onboard the R/V Professor Logachev during the TTR09, and TTR14 cruises. (E) TV-controlled grab used onboard the R/V Sonne, GAP cruise. (F) Box corer used onboard the R/V Professor Logachev during the TTR cruises. (G) Kasten box corer used onboard the R/V Professor Logachev during the TTR14 and TTR15 cruises. (H) circular dredge and (I) rectangular dredge used onboard the R/V Professor Logachev during the TTR cruises. (J) dredge used onboard the R/V Cornide de Saavedra during the Anastasya cruises. **A-18**
- Figure C.1.** X-ray diffraction pattern of high Mg-calcite – dolomite carbonate mixture of a dolomite chimney sample (3463-A03). The sample was leached with a 0.25 M EDTA solution of pH 11 and aliquots were taken after 24 hours. The  $2\theta$  positions for high Mg-calcite and dolomite are marked on the graphs. To be noted that the calcite peak almost completely disappears with the EDTA leaching. **C-5**
- Figure C.2.** X-ray diffraction pattern of high Mg-calcite – dolomite carbonate mixture of a dolomite chimney sample (3463-A03). The sample was leached with a 0.25 M EDTA solution of pH 11 and aliquots were taken after 24 hours. The  $2\theta$  positions for high Mg-calcite and dolomite are marked on the graphs. **C-5**
- Figure C.3.** X-ray diffraction pattern of high Mg-calcite – dolomite carbonate mixture of a dolomite chimney sample (3463-A03). The sample was leached with a 0.25 M EDTA solution of pH 11 and aliquots were taken after 24 hours. The  $2\theta$  positions for high Mg-calcite and dolomite are marked on the graphs. **C-6**
- Figure C.4.** X-ray diffraction pattern of high Mg-calcite – dolomite carbonate mixture of a dolomite chimney sample (3463-A03). The sample was leached with a 0.25 M EDTA solution of pH 11 and aliquots were taken after 24 hours. The  $2\theta$  positions for high Mg-calcite and dolomite are marked on the graphs. **C-6**
- Figure C.5.** X-ray diffraction pattern of high Mg-calcite – dolomite carbonate mixture of a dolomite chimney sample (3463-A03). The sample was leached with a 0.25 M EDTA solution of pH 11 and aliquots were taken after 24 hours. The  $2\theta$  positions for high Mg-calcite and dolomite are marked on the graphs. **C-7**
- Figure C.6.** X-ray diffraction pattern of high Mg-calcite – dolomite carbonate mixture of a dolomite chimney sample (3463-A03). The sample was leached with a 0.25 M EDTA solution of pH 11 and aliquots were taken after 24 hours. The  $2\theta$  positions for high Mg-calcite and dolomite are marked on the graphs. **C-7**
- Figure C.7.** X-ray diffraction pattern of high Mg-calcite – dolomite carbonate mixture of a dolomite chimney sample (3463-A03). The sample was leached with a 0.25 M EDTA solution of pH 11 and aliquots were taken after 24 hours. The  $2\theta$  positions for high Mg-calcite and dolomite are marked on the graphs. **C-8**
- Figure C.8.** Carbon and Oxygen isotopic composition of bulk samples (open symbols) and after EDTA leaching (filled symbols). All the samples exception to the sample 3463-B02.24 where the leaching process was not successfully completed, present a similar trend on the isotopic shift. **C-9**
- Figure C.9.** Group of samples treated with EDTA leaching reveal linear correlation between the dolomite/(calcite + Mg-calcite) ratio and the  $\delta^{18}\text{O}$  values. Pure dolomite yields 5.6‰  $\delta^{18}\text{O}$  PDB,

whereas  $^{18}\text{O}$  is strongly depleted in the calcite and Mg-calcite phases. There is no clear relationship between the mineralogy and  $\delta^{13}\text{C}$  values. **C-10**

**Figure C.10.** Plot of the dolomite/(calcite + Mg-calcite) ratio and the  $\delta^{18}\text{O}$  values on all the samples of dolomite crusts, chimneys and Nodules. The correlation is not clear probably because of the high compositional variability of the samples but the general trend calculated from the EDTA leaching (red dashed line) can be inferred indicating heavier values toward higher abundance of dolomite and lighter oxygen isotopic values toward the dominated calcite samples. **C-11**

**Figure C.11.** Dolomite crusts, chimneys and Nodules reveal linear correlation between the dolomite/(calcite + Mg-calcite) ratio and the  $\delta^{13}\text{C}$  values. Pure dolomite yields  $-38 \pm 0.1\%$   $\delta^{13}\text{C}$  (PDB), whereas  $^{13}\text{C}$  is strongly enriched in the calcite and Mg-calcite phases. **C-11**

**Figure C.12.** Plot of the extrapolations of the  $\delta^{13}\text{C}$  values for pure dolomite and pure calcite phases, based on the  $\delta^{13}\text{C}$  values of bulk and leached material. Also is plotted the function obtained by the linear fit for all bulk samples from Figure C.11. The extrapolated  $\delta^{13}\text{C}$  values for pure dolomite phase ranges from  $-57\%$  to  $-28\%$  (PDB), whereas  $^{13}\text{C}$  is strongly enriched in the calcite and Mg-calcite phases with the extrapolated values ranging from  $-2$  to  $-23\%$  (PDB). **C-12**

**Figure D.1.** Flowchart of the analytical procedure for biomarker analyses of cold seep carbonates. Modified from Peckmann *et al.*, (2004). **D-5**

**Figure D.2.** Flowchart of the analytical procedure of biomarker analyses with a previous extraction, used on the dolomite chimney 3463-A08. **D-8**

## Chapter 1. Introduction

### 1.1 Nature and scope of this research

The Gulf of Cadiz is located south of Iberia, in an area where a broad spectrum of geological processes of global importance are active. These include: (1) the tectonic evolution of the Africa-Iberia plate boundary; (2) the formation of the Gibraltar orogenic arc; (3) various sedimentological and oceanographic processes related to the Mediterranean Outflow; (4) the formation and dissociation of methane hydrates and associated deep water ecosystems; (5) the widespread occurrence of mud volcanism and methane-derived authigenic carbonates.

The return flow and the impact of volatiles (especially methane) and other fluids at continental margins such as the Gulf of Cadiz, where sediment and sedimentary rock sequences of a continental crust with a thicknesses of 11 to 30 km are observed (Medialdea *et al.*, 2004) have complex effects on the geosphere, biosphere, ocean and atmosphere, and are high priority objectives in present day geosciences. Sediment compaction and geochemical processes during diagenesis are responsible for the major fluid input into the sedimentary basins and subduction zones, together with the alteration products of the oceanic crust and the trench-fill from down-slope mass wasting. The output of the volatile phases from the sedimentary pile is done via fluid venting at the deformation front of accretionary complexes, together with widespread mud diapirism, mud volcanism, cold seepage and gas hydrate dynamics. These volatile phases are either ejected into the biosphere, ocean and atmosphere, accreted to the edges of continental plates or transported into the lower mantle.

This work focuses on the study of fluid escape structures and processes in the South Portuguese margin and the Gulf of Cadiz. It aims to contribute to a better understanding of the nature, structural control and the characteristics of the fluid escape structures in the Gulf of Cadiz. It is especially focused on the study of the methane-derived authigenic

carbonates associated with modern and fossil methane seepage in an area of extensive mud volcanism. The gas hydrates occurrence, formation and dissociation, the tectonic implications and significance of the fluid escape structures are also investigated.

Gas charged sediments, revealed by acoustic blanking zones and acoustic turbidity, surface and buried pockmarks and acoustic anomalies in the water column have been also identified and described in the central eastern continental shelf and upper slope areas of the Gulf of Cadiz (Baraza and Ercilla, 1996; Baraza *et al.*, 1999). Both were interpreted as indicating active fluid escape in this region.

In 1992, during the Kane cruise, organized by the Marine Physics Branch of the Naval Research Laboratory, USA (NRL) in cooperation with the Hawaii Mapping Research Group and the Naval Oceanographic Office, a high quality side-scan sonar mosaic was acquired for a large part of the slope, upper and lower continental rise of the central part of the Gulf of Cadiz. This coverage revealed a large number of structures that were inferred to be mud volcanoes (Gardner, 2001; Gardner, 2002). In 1999, during the Training Through Research Cruise (TTR09), ground-truthing in some of these structures retrieved gas charged mud breccia and confirmed their mud volcanic nature (Gardner, 2001).

Since 1999, a strong effort has been made by several scientific research teams to investigate the fluid escape processes in the Gulf of Cadiz, and several Portuguese and international projects have focused this topic in this area. The research presented in this thesis was developed in the framework of the INGMAR (PLE/4/98), the Training Through Research program (IOC/UNESCO – Moscow State University), and the MVSEIS - Euromargins (01-LEC-EMA24F) projects. The INGMAR project (“*Reforço da Capacidade de Investigação no Domínio da Geologia Marinha*”, Sub-project: Geology and resources of the Portuguese Margin) was developed at the Marine Geology Department of the Geological and Mining Institute, now National Institute of Engineering, Technology and Innovation, I.P. (INETI) with financial support from the *Fundação para a Ciência e a Tecnologia* (FCT) and was coordinated by one of the supervisors of this thesis (L. M. Pinheiro). The INGMAR project started in 1998 with the objective of investigate the geology and the resources of the Portuguese margin and finished in 2003. The UNESCO-IOC Training Through Research (TTR) program employs an innovative concept that directly interlinks two major components: scientific research and education. This

program provides to students advanced training in marine science, from the phases of data collection, processing, laboratory analyses and, ultimately, the presentation and publication of the research results, under supervision of senior top researchers from several European top research institutions. The Euromargins/Eurocores programme project MVSEIS “Tectonic control, deep crustal structure and fluid escape pathways in the Gulf of Cadiz mud volcano field” started on June 2003 and integrates Portuguese, Spanish, Belgium and French teams under the coordination of the Portuguese team (L. M. Pinheiro). The Portuguese work package has been founded by the Portuguese Science Foundation - FCT. The objective of the MVSEIS project is to investigate the deep crustal structure, the sedimentary section and sediment dynamics, the tectonic control and the detailed geometry of the fluid escape pathways in this area with active mud volcanism and cold seeps, using a multidisciplinary approach. The multidisciplinary approach gives the opportunity to link the tectonic, sedimentological, geochemical and biological processes associated with the mud volcanism and gas seepage.

## **1.2 Geographical location and physiography of the study area**

The study area of this work corresponds to the South Portuguese Margin and the Gulf of Cadiz (Figure 1.1 and Figure 1.2). It is delimited by the parallels 34°45'N and 36°45'N and by the meridians 6°25'W and 10°W. The water depth in the study area ranges from 200 m to 4000 m. It corresponds mainly to the upper and lower continental slopes and the uppermost part of the Horseshoe and Seine abyssal plains in the South Iberian Atlantic margin and the North African Atlantic margin of Morocco.

The morphology of the Gulf of Cadiz is characterized by a complex tectonic structure with an accretionary wedge (Gutscher *et al.*, 2002) and olistostrome complex emplacement (Maldonado *et al.*, 1999) that results in a wide development of the continental slope and rise in this area.

The northern continental margin of the Gulf of Cadiz extends from the Gibraltar straight, to the West of Tarifa, until Cape Saint Vicente. The southern continental margin of the Gulf of Cadiz extends from Tangier to North of Casa Blanca, to the on-land

prolongation of the Rharb Valley that defines the southern limit of the Accretionary wedge. In this continental margin several sectors can be defined, with different shelf, slope and rise characteristics. These characteristics are controlled by tectonic, diapiric and sedimentary/erosive processes related to slump processes and related to the strong effect of the outflow of the Mediterranean Water (MW) on the seafloor.

The continental shelf in this area has a variable width but it is in general fairly wide (ranging from 10 to 50 km) with the exception of the Gibraltar strait where it is less than 8 km wide. The slope of the continental shelf (out of the Gibraltar strait area) can reach up to  $0.5^\circ$ , but it is flatter ( $0.3^\circ$ ) in the Moroccan and Spanish margins. The shelf break occurs at depths ranging from 100 to 200 m. In the Portuguese margin it is located at about 130 m except offshore Faro where it is found at about 100 m water depth. To the West of Faro, in the Spanish margin, the depth of the shelf break is located between 140 and 150 m diminishing again to the South of Cadiz (Vanney and Mougnot, 1981).

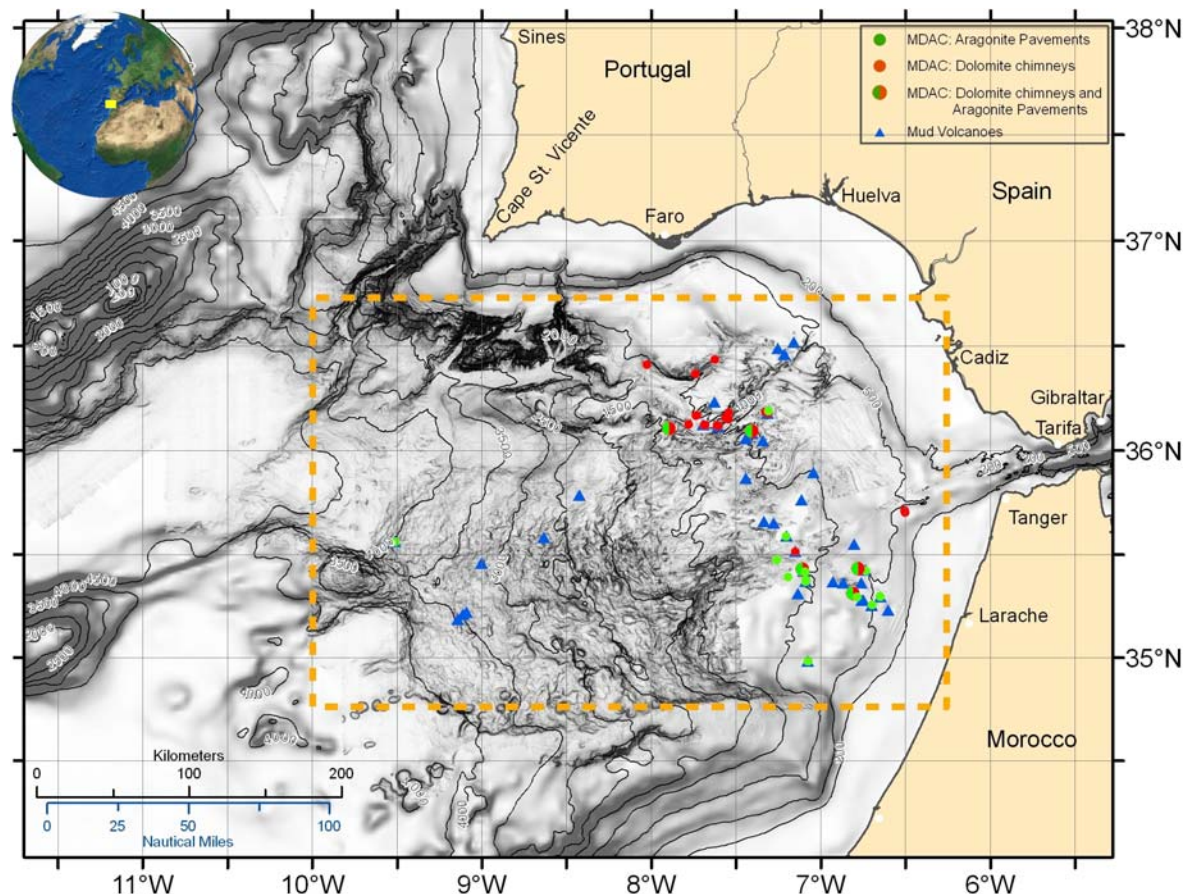


**Figure 1.1.** Geographic location of the study area (gold dashed line) with the indication of the targets focused of this thesis: methane-derived authigenic carbonates and mud volcanoes occurrences. (Mercator projection, true scale at  $35^\circ\text{N}$ ) Bathymetry from the GEBCO Digital Atlas (2003 edition) and from the multibeam surveys: Matespro, Delila, Tasyo and GAP.

The Gulf of Cadiz slope and rise are the physiographic domains in which this thesis is focused on. They are characterized by an irregular seafloor morphology shaped by active sedimentary and tectonic processes. The South Portuguese margin to the West of Faro is characterized by the presence of several incisive canyons that shape this sector of the margin. To the East of Faro, the Spanish and Moroccan margins are characterized by the accretionary wedge/olistostrome complex domain. The upper slope, between 130 and 400 m water depth, is narrow and characterized by depositional processes related to the prograding edge of the continental shelf break, erosive processes related to the canyons and channels, gravitational structures related to slumping processes, tectonic processes revealed by recent fractures and diapiric processes, gas-charged sediments and fluid escape structures as pockmarks (Baraza and Ercilla, 1996). The middle slope, from 400 to 1200 m water depth, is characterized by its large extension except in the South Portuguese margin, in the Portimão and Faro Canyons area, where it is narrower. It is characterized by the strong erosive/depositional influence of the Mediterranean Outflow (MO) with large contourite deposits and erosive channels (Hernandez-Molina *et al.*, 2003). The central part of this area is characterized by the presence of important ridge systems associated with diapiric structures with a preferential NE-SW direction and by the occurrence of mud volcanoes and other fluid escape structures that are frequent in this domain (Figure 1.2). The lower slope, ranging from 1200 to 4000 m water depth, shows a large extension on the accretionary/olistostrome domain but, on the South Portuguese margin West of Faro, in the sector dominated by the presence of canyons, the middle and lower slopes are narrower. The dominant seafloor morphology within the accretionary domain is characterized by the presence of small-scale bottom features such as mini-basins, some of them with polygonal shapes, mud volcanoes and salt diapirs. The Horseshoe and Seine abyssal plains have flat seafloor morphologies. The Horseshoes Abyssal Plain is limited to the North by the Gorringe Bank and to the South by the Ampere and Coral Patch seamounts which, together with the Coral Patch Ridge define the northern limits of the Seine Abyssal Plain. In the East, both abyssal plains are limited from the continental rise by scarps. The Horseshoe Abyssal plain is limited to the East by the Horseshoe fault that delimits a domain of the foot of the rise that has a gentle and constant slope, limited to the East by the accretionary wedge deformation front scarp. The Seine Abyssal plain is limited by the accretionary wedge deformation front scarp (Figure 1.2).

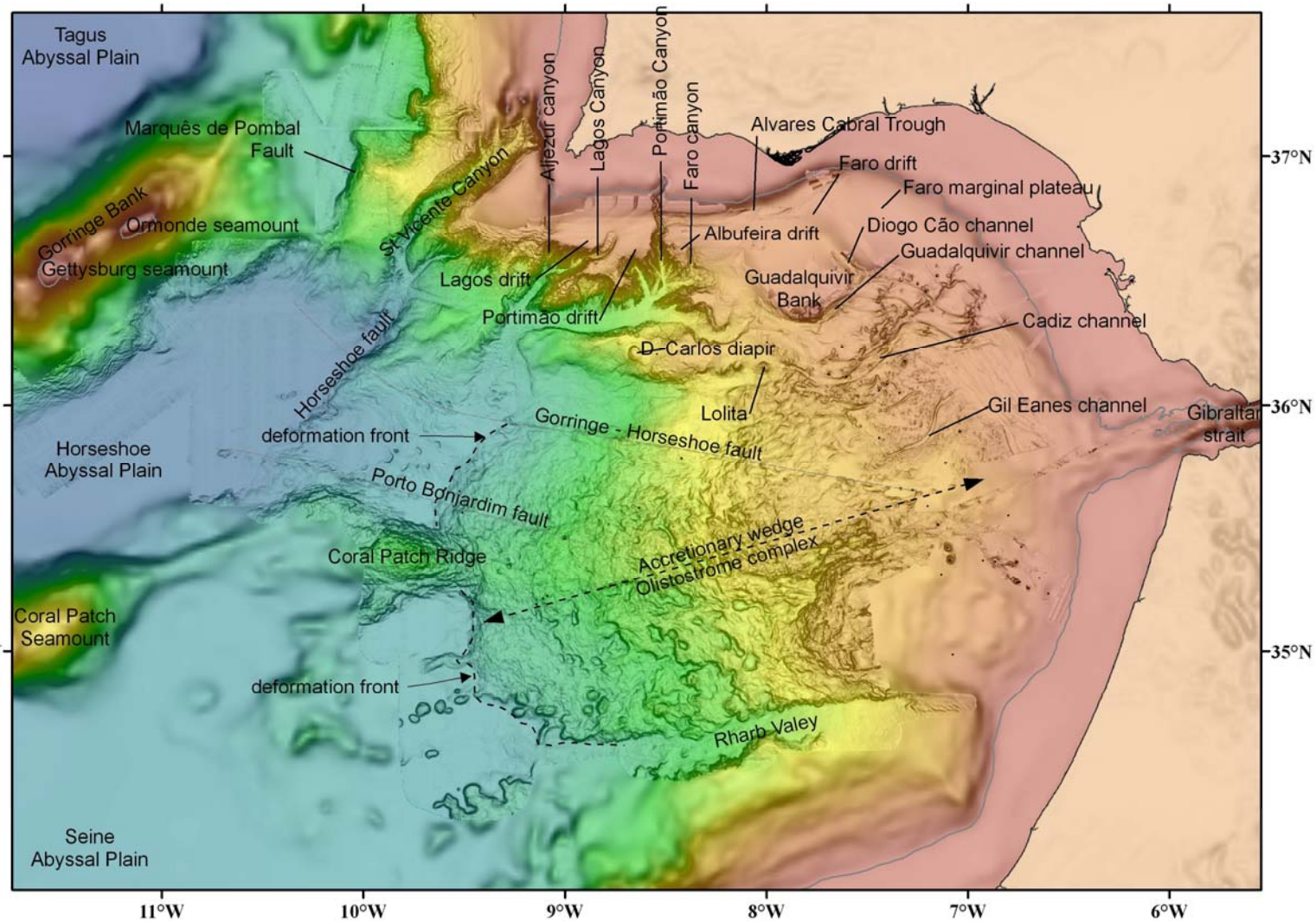


**Figure 1.2.** Topography, physiography and morphology of the study area and surrounds, with the indication of the main physiographic elements that are referred to in this work. Bathymetry from the GEBCO Digital Atlas (2003 edition) and from the multibeam surveys: Matespro, Delila, Tasyo and GAP.

### **1.3 Main objectives**

The main objectives of this thesis are to investigate the fluid escape structures in the Gulf of Cadiz, related to the formation of methane-derived authigenic carbonates (MDAC) and to contribute to a better understanding of their nature, characteristics and occurrences. The characterization of these fluid escape structures, their evolution and significance on the regional geology, their impact on the biosphere, hydrosphere and atmosphere were also addressed, as the tectonic and sedimentary control on the fluid escape processes and manifestations. The specific scientific objectives of this thesis are:

1. To identify and to describe the morphology and characteristics of the fluid escape structures in the Gulf of Cadiz, especially the occurrences of MDAC and to investigate their possible structural control and their relationship with major fluid escape structures;
2. To identify the various types of MDAC observed in the study area and to characterize their mineralogy and geochemistry, in order to establish the main physical, chemical and bio-geochemical processes involved in their formation;
3. To investigate the role of hydrocarbon-rich fluid venting in the formation of the MDAC;
4. To investigate the role of microbial consortia on the anaerobic oxidation of methane and the precipitation of the MDAC;
5. To determine the age and growth rates of the MDAC;
6. To identify any major episodes of formation and to correlate them with past climate changes and eustatic sea-level fluctuations;
7. To propose a model of formation for the different MDAC.

### **1.4 Database**

The database for this PhD Thesis consists of data collected largely by the author from 14 scientific cruises: TTR09, TTR10, TTR11A, TTR11, TTR12, TTR14, TTR15, TTR16, Anastasya-2000, Anastasya-2001, GAP, Cadipor, Matespro and Delila (see details

in Appendix A). During these cruises a large dataset was collected in the Gulf of Cadiz, including seismic lines (that were added to the previous existing seismic dataset), side-scan sonar data (both surface and deep-towed), heat flow, multibeam bathymetry, underwater video observations and a large number of sediment and rock (mud breccia clasts and MDAC) samples, from gravity cores, dredges and grabs. A description of the different geophysical data, its acquisition parameters and processing, and a description of the sample collection and underwater video observation equipments are presented in Appendix A. For this thesis, about 2700 km of seismic reflection profiles were used, together with more than 2700 km of ecosounder profiles, 58422 km<sup>2</sup> of low resolution side-scan sonar, and 578 km<sup>2</sup> of high resolution deep-towed side-scan sonar. Multibeam bathymetry data from 5 surveys was used for the construction of regional and detailed bathymetric 3D models. 331 sampling stations (including gravity cores, TV-grabs and dredges) and 70 underwater video observation profiles were used to constrain the nature of seafloor and sub-seafloor.

## **1.5 Methodology**

All the data collected in the Gulf of Cadiz, relative to geophysical investigations, video observations and retrieved samples, was integrated into a Geographic Information System (GIS) database. The positioning of all the data acquisition operations was calculated and integrated on the GIS database, together with information relative to the acquired data and subsequent analytical results. This allowed the analysis and interpretation of all the georeferenced data and the investigation of relationships between the different datasets. The GIS database allowed the location, characterization and interpretation of the fluid escape structures morphology, elaboration of 3D models and map production. GIS analyse tools applied on the database were used to investigate the spatial relationships between the different fluid escape structures and the geological, tectonic and oceanographic settings.

To identify and characterize the different types of MDAC and to establish their formation processes, the different samples were described in hand-specimens, under binocular and by thin section petrographic and cathodoluminescence microscopy. The

mineralogy was determined and quantified by X-ray diffraction and chemical analysis (total carbon content, total organic carbon and carbonate content). Carbon and oxygen stable isotopic composition of selected samples were also determined as the strontium isotopic compositions of the representative MDAC types.

Based on the mineralogical and geochemical characterization of the MDAC, the nature of the hydrocarbon-rich diagenetic fluids involved in their formation was investigated and estimated together with other environmental properties (temperature of formation and geochemical setting).

The presence and the active role of microbes involved in the formation of the MDAC was interpreted based on the mineralogy, texture and microfabric of the carbonates, as investigated on petrographic microscopy, complemented with cathodoluminescence characterization and scanning electron microscopy (SEM). The active role of microbial consortia on the anaerobic oxidation of methane and precipitation of the MDAC was investigated by stable carbon isotopic composition of the different carbonate phases and by the determination of the presence of characteristic biomarkers with diagnostic depleted carbon isotopic composition.

The U/Th dating method was used to define the age of formation and growth velocities of selected MDAC samples. Their age determinations allowed to estimate the processes potentially involved in their formation, as the climatic changes and eustatic sea-level fluctuations. This method was the one that fitted to the geochemistry of the formation environment and on the estimated time range of the MDAC from the Gulf of Cadiz.

The different analytical methods and techniques are reported and described in more detail within the different chapters, according to their use.

## **1.6 Thesis outline**

The first chapter presents an introduction to the nature and scope of this research, describes the main objectives, the database and the methodology used. This is followed by a brief outline of the thesis chapters.

The second chapter presents a review of the state of the art and the global significance of fluid escape processes and manifestations at continental margins.

The third chapter introduces the geological and oceanographical setting of the study area. The geodynamic setting, the present day seismicity and stress pattern, and the tectonic regime are then described followed by a short discussion of the nature of the accretionary prism/olistostrome complex. Next, the paleogeographic and geodynamic evolution of the Gulf of Cadiz and the geology of the Betic-Rifean Domains and adjacent basin are described, as well as the morpho-sedimentary domains in the study area. This chapter concludes with a description of the present day oceanographic setting of the study area, with a particular focus on the importance of the Mediterranean Outflow Water on the seafloor morphology and sedimentary dynamics.

In Chapter four the characteristics and the distribution of the MDAC occurrences in the Gulf of Cadiz are analyzed and correlated with the other fluid escape manifestations and associated structures (mud volcanoes, diapiric ridges and faults). This includes the interpretation of the underwater video profiles and the correlation of the observations and samples retrieved with the geophysical and bathymetric data. A cartography of the MDAC occurrences was produced and the evaluation of the sedimentological and tectonic processes that potentially can control the occurrence of the MDAC and cold seeps in the Gulf of Cadiz are discussed.

Chapter five presents the petrographic, mineralogical, geochemical, isotopic and lipid biomarker studies performed on the MDAC samples collected in the Gulf of Cadiz. Based on these data, together with the macroscopic sample description and the underwater video observations, a model for the formation of the different authigenic carbonates is proposed.

Chapter six presents a detailed carbon and oxygen stable isotopic study of the MDAC and a reconstruction of the original pore water composition from which the different carbonate minerals precipitated.

Chapter seven describes the results of the dating of selected samples of MDAC and their interpretation. A link between MDAC formation and the corresponding fluid flow episodes are correlated with past oceanographic conditions and eustatic sea-level changes in the Gulf of Cadiz.

In chapter eight, the evidences of the microbial mediation in the formation of the MDAC are investigated, based on textural microscopy interpretation, electron microscopy observations and on biomarker analyses.

Finally, Chapter nine presents a summary of the main conclusions presented in the different chapters, integrated on a regional setting. The thesis concludes with a list of questions that could not be covered in this work and new and open questions that arose during this research.



## **Chapter 2. Fluid escape processes and manifestations at continental margins**

### **2.1 Mud volcanism and mud diapirism**

#### **2.1.1 Introduction**

Mud volcanism, or sedimentary volcanism, as defined by (Kugler, 1933, 1975) is a worldwide and common geological process. It refers to a series of sedimentary processes that result in the episodic extrusion to the surface or to the seafloor of a sedimentary mixture of gases, water and solid material (mud and clasts) originated from deep sources in the sedimentary column (Higgins and Saunders, 1974). Different mud volcanic structures can be defined (Brown and Westbrook, 1988; Brown, 1990). Mud volcanoes (MVs) are defined as conical shape positive morphological features in relation to the regional topography, with a central feeder chimney or conduit and extrusive features such as mud flows. The mud mounds and mud ridges are defined as positive morphological features, with conical shapes but, without any central feeder chimney or extrusive features at the surface (Brown and Westbrook, 1988). Therefore, the MVs are formed when a mud rich material with clasts and other fluids reaches the seafloor or the surface, where extrusive features (such as mud flows, craters, gryphons, mud pools or salses) will be formed. The shale or mud diapirs are formed like the mud volcanoes by the intrusion of mud rich fluids through the sedimentary column that can possibly reach the surface, but unlike the mud volcanoes, the mud diapirs are characterized by a slow intrusion and ascension of the material. In the case of the seafloor-piercing mud diapirs, called mud mounds or mud cones, there will be an absence of the extrusive features that are present on the mud volcanoes. In this work the mud cone terminology will be preferably used to name mud volcanic structures that were not positively confirmed as mud volcanoes. The difference

between the mud cones and mud volcanoes is therefore revealed by their surface expression. The mud cones show, like the MVs, superficial conical shape morphologies but, unlike MVs, they do not exhibit extrusive features such as mud flows, craters or gryphons.

The material extruded from the MVs is composed of a fluidized mixture of sediments dominated by clays, liquids and gases that, in general, incorporates rock fragments (clasts) pulled up from the pierced sedimentary sections. This mixture called a diapiric melange, argille scaliuse or, more commonly, mud breccia (Cita *et al.*, 1981). The mud breccia is composed of a clayish matrix (that can be up to 90% volume) that can contain exotic rock fragments, called mud breccia clasts, that present a variable lithology, size and shapes, which depends of the nature of the original source layers from where they were pulled up by the piercing of the mud volcano (Ivanov *et al.*, 1996).

Several morphologic elements can be defined on the MVs, such as the mud flows, crater and flanks, the surrounding moat, gryphons, mud pools and the feeder channel. The extrusion of the mud breccia at the surface produces the characteristic out-flowing masses or mudflows (Figure 2.1 and Figure 2.2C). Depending on the viscosity of the material, the mud flows can be elongated and can travel long distances; if the mud breccia material is more viscous, it will produce short mud flows that in general are deposited at a short distance from their extrusion point (Figure 2.1B). The stacking of successive mud flows, generally produces topographic conical elevations of variable sizes and shapes, analogous to the morphology and activity of igneous volcanoes and therefore these features are called MVs. If the extruded material is very fluid, as a result of high amount of water, then there will not be an edification of a conical structure with steep flanks, and the formed edifice will preferably have a flat topography with low angle slopes. When the flanks are very flat (less than 5°), the structure is preferably named a mud pie (Cita *et al.*, 1981). In general, the mud breccia extrudes from a central vent, the feeder channel, chimney or conduit, that connects the parent bed of the mud source (the deepest source of the material extruded) to the surface of the main crater, or to secondary craters (Figure 2.1). The crater corresponds to the superficial expression of the central chimney and in general corresponds to a depression that results from the post-activity episodes of stress relax and subsidence at the MV summit. To be noted that the crater can have a diameter that can be significantly larger than the diameter of the feeder channel. Mud extrusion can also occur from parasitic vents

or gryphons (Figure 2.2A, B and C) that can be located within the central crater or on the flanks of the mud cone edifice (Figure 2.1). At the central crater different types of features can occur. It is frequent the formation of gryphons, that correspond to meter size positive morphologic conical edifices from witch mud extrusion occurs; mud pools (Figure 2.2D) that correspond to depressions where soupy mud is extruded; salses, extrusion of high salinity solutions or brines forming pools in depressions.

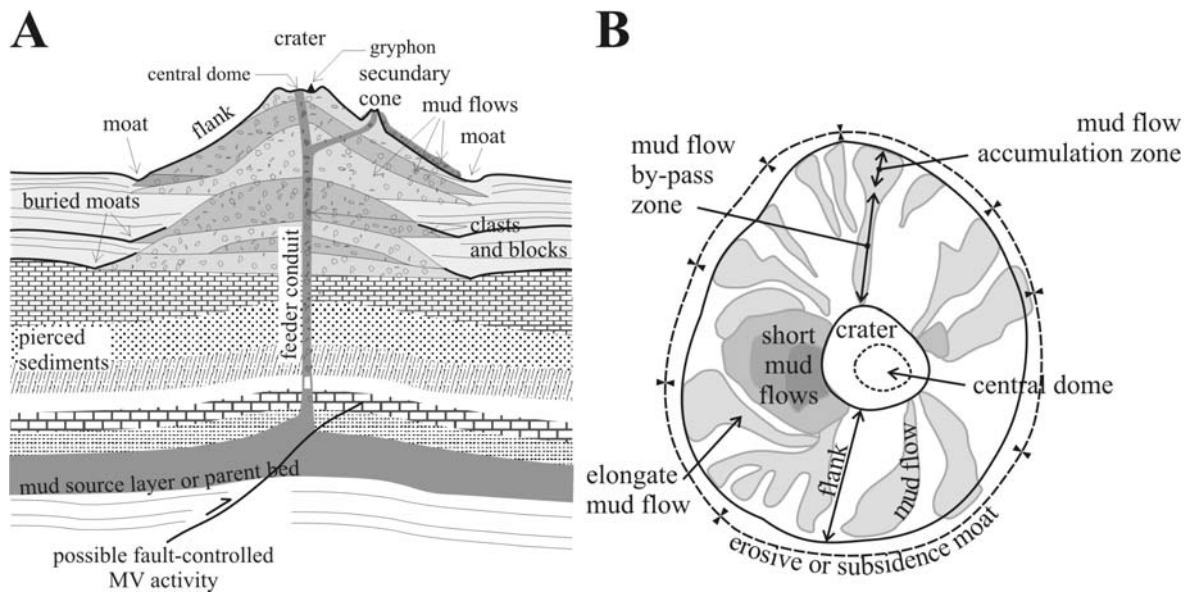


**Figure 2.1.** Schematic diagrams (scale-independent) illustrating the structure and the main elements of a cone-shaped mud volcano. (A) Schematic cross-section profile, modified from Dimitrov (2002) and Kopf (2002). Note the “Christmas-tree” structure indicating multiple episodes of mud extrusion. (B) Schematic map illustrating the radial pattern of mud flows accumulation away from the crater, modified from Rensbergen *et al.* (2005a).

Some submarine mud volcanoes are characterized by the presence of a surrounding moat at their base. The moat corresponds to a depression that totally or partially surrounds the base of the mud volcano. The moat can be erosive in origin (consequence of the erosive effect of currents that contour the mud volcano); it can also result from the over-pressuring over the surrounding sediments, consequence of the overburden of the mud volcano edifice; alternatively the moat can be formed as consequence of the stress release after the mud volcano activity and edification; or can result from the collapse or depression of sedimentary layers as result of the remotion of sediments from the sedimentary layers under the mud volcanic edifice.

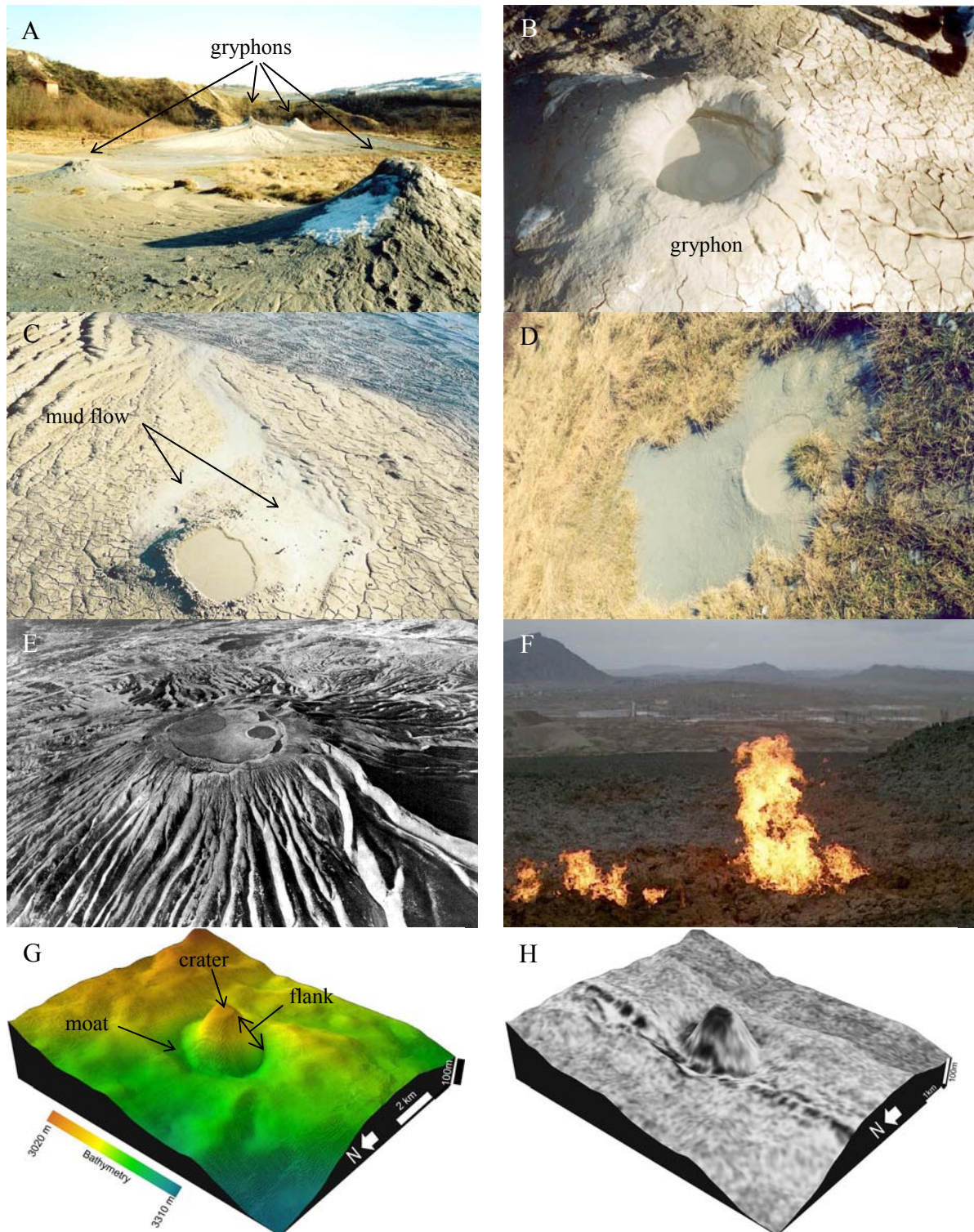


**Figure 2.2.** Images of MVs and processes related to mud volcanism. (A to D) the *Salse di Milano*, Italy. (A) gryphons of about 3 m high within the main MV crater; (B) crater of a gryphon, 25 cm wide, with rings created by gas bubbles. (C) crater of a gryphon, about 25 cm wide, from where fresh mud flows are spreading out. (D) mud pie. (E) 500 m high Toragai MV, Azerbaijan (Aliyev *et al.*, 2002). (F) Everlasting fires, Baku, Azerbaijan (Aliyev *et al.*, 2002). (G) Swath bathymetry 3D model of the Bonjardim MV. (H) Side-scan sonar imagery overlaid on the bathymetric 3D model of the Bonjardim MV, showing high reflectivity of the fresh mud breccia material at the top and central crater. G and H were produced in this work.

Mud volcano (MV) activity can occur at a wide range of scales, with eruptive cones ranging from some centimetres (Figure 2.2B) to hundreds of meters high (e.g. Toragai MV in Azerbaijan with 500 m high, Figure 2.2E) and several km in diameter, e.g. Al-Idrisi MV in the Gulf of Cadiz with 5.4 km wide (Rensbergen *et al.*, 2005b). The MV mud flows can have decimetres to kilometres in length. Four types of MV activity have been recognized on land in Azerbaijan (State Oil of the Republic of Azerbaijan (SOCAR), 1996; Fowler *et al.*, 2000). These are: (1) Explosive activity, characterized by violent extrusion of large amounts of mud breccia with high amounts of mud breccia clasts and powerful flow of gas that spontaneously ignites producing explosions of variable strength; (2) Effusive activity, with the ejection of large amounts of mud breccia with or without less non-ignited gas emissions; (3) Effusive activity with the outflow of low viscosity mud breccias and without intense gas emissions; (4) Extrusive activity that corresponds to the slow extrusion of viscous mud with negligible emission of gas. Submarine MVs can have different activity characteristics but, most probably, episodes of powerful and rapid extrusion of large volumes of mud breccias possibly accompanied by gas release will alternate with quieter effusive episodes of fluidized mud breccia eruption with small amounts of gas. As illustrated in Figure 2.1, the different episodes can succeed over long periods of the MV activity and can intercalate with periods of MV inactivity (Graue, 2000). Fluid and gas emissions are commonly associated with MVs, but can also occur outside the mud edifice, along deep faults. These gases are expelled at localized venting sites, either as free gas in the case of terrestrial MVs (Figure 2.2E) or, in the case of submarine MVs as dissolved in pore waters, trapped as gas hydrates or as free gas (even in the gas hydrate stability zone gas can be preserved as free gas and not completely crystallized as gas hydrate).

The mud volcano morphology is a function of its past activity and evolution, local lithology and of the tectonic framework of the host sediments. Therefore, there is no strict and universal classification for MVs but, based on the classification defined for land MVs, three types of MVs were defined by Kalinko (1964) and Dimitrov (2002), based on their morphology and eruptive activity. The *Lokbatan type* corresponds to MVs with frequent explosive activity, as a consequence of the rapid eruption of low viscosity mud breccias with abundant clasts and high amounts of gas. The morphology corresponds to well developed steep conical shapes. The activity episodes are short and alternate with longer periods of inactivity. Blocking of the feeder chimney by mud breccia clasts and high

viscosity mud breccia is frequent, forming a mud cork and the fluid pressure increases below it. When the fluid pressure overcomes the resistance of the mud cork the MV retakes the activity with an explosive episode. Once the pressure is released the feeder chimney can be blocked again until the repetition of the process. This activity favours the edification of complex morphologies with secondary feeder chimneys and abundant gryphons. The *Chikishlyar type* corresponds to MVs with continuous and relatively weak and not violent extrusive activity. This type of MV is strongly affected by the presence of water saturated layers and in general forms numerous vents of gassy mud and water. They form very low or flat domes. The *Schugin type* corresponds to a transitional type of MV activity, with intermediate characteristics between the two previous types. The eruptive periods are replaced by weak activity. This type of MV is characterized by a great variety of forms, but most commonly they build composite craters.

The submarine mud volcanoes are difficult to classify and not always fit the Kalinko (1964) classification types. However, some assumptions can be made, based on their morphology character such as the shape of the MV, the structure of the crater, the shape and characteristics of the mud flows, etc. (Ivanov *et al.*, 1996). Recent activity episodes can be identified by several peculiarities, most prominent at the summit of the MV, such as: fluid emissions (visible as gas bubbling, water discharge, diffusive flux, gas hydrates presence); biological indicators (bacterial mats and chemosynthetic communities); geological indicators (carbonate build-ups of methane-derived authigenic carbonates, recent mud breccia at the seafloor); geophysical and geochemical anomalies (such as thermal anomalies, high geothermal gradient, pore fluid and pore water chemical anomalies).

In the literature, several terms (diatreme, gas dome, mud lump, mud mound, mud pot, mud cone) have been proposed as synonyms for the different main mud volcanic structures: mud volcanoes, mud diapirs, seafloor-piercing mud diapirs and mud ridges. In this work, the term mud volcano will be used to identify mud volcanic structures that, as confirmed by ground truthing, are characterized by a the presence of mud breccia (that can be covered by a layer of pelagic sediments with variable thickness) and high fluid and high gas (essentially methane) contents, or the geophysical data shows without a doubt the extrusive activity of the MV (e.g. high backscatter mud flows). Structures that show geophysical and morphologic characteristics similar to MVs but were not sampled, or

where sampling did not clearly reveal the presence of mud breccia or high fluid and methane contents, are preferably classified here as mud cones. As such, mud cones correspond to either seafloor-piercing diapirs or to MVs (when they were not confirmed by sampling or sampling was not conclusive due to e.g. a thick pelagic sedimentary cover over a MV inactive for a long period of time). The mud diapirs are intrusive structures (emplaced during a longer span of time than the MVs) that on seismic profiles can exhibit mud volcanic similar seismic facies with acoustic chaotic reflection patterns but that do not reach the seafloor and pelagic sediment layers are identified on top of it or, if they are piercing to the seafloor they do not show evidences of extrusion of mud breccias or other extrusive features.

### **2.1.2 Formation mechanisms**

Mud volcanism corresponds to the ascent of buried sediments as the result of density inversion or buoyancy forces (Brown, 1990) and pore fluids overpressure generated on buried sediments. The mud ascension and extrusion to the surface will occur whenever the pore fluid pressure exceeds the lithostatic pressure, causing hydraulic fracturing. The mechanisms through which buried sediments can ascend and form MVs are related with: (1) high pore fluids and gas pore pressures developed within the sedimentary sequences (Kugler, 1933; Ridd, 1970; Hedberg, 1974; Kugler, 1975; Milkov, 2000); (2) density inversions within the sedimentary sequences (Brown, 1990); (3) tectonic loading resulting from lateral tectonic shortening, accretion and overthrusting (Higgins and Saunders, 1974); (4) occurrence of diapiric structures or anticlinal folds and the occurrence of faults, along which the ascension and migration of fluidized sediments can occur (Brown, 1990).

The development of the necessary high pore fluid pressure to induce the migration of the fluidised sediments can be reached as a result of several processes, some of them acting simultaneously, such as: (i) tectonic loading resulting from lateral tectonic shortening, accretion and overthrusting; (ii) sediment loading (resulting from high sedimentation rates, slumps, debris flows or overriding thrust sheets); (iii) diagenetic reactions of dehydration (such as smectite to illite and montmorillonite to illite dehydration (Brown *et al.*, 2001) and opal A to opal CT diagenetic transformation); (iv) hydrocarbon formation and changes of phase of the hydrocarbons such as reactions of creaking of heavier hydrocarbons into

lighter hydrocarbons; and (v) hydrothermal pressuring (Barber *et al.*, 1986; Dimitrov, 2002; Kopf, 2002). Fluidization and subsequent rapid flow of pore fluids through the sedimentary column can be reached through gas expansion, gas and water flux and shearing stresses (Brown, 1990). Over-pressuring of light, plastic, undercompacted fine-grained layers from deeper sedimentary sections is the major factor for the formation of MVs. Most of these causes are closely related to each other and, in general, occur simultaneously.

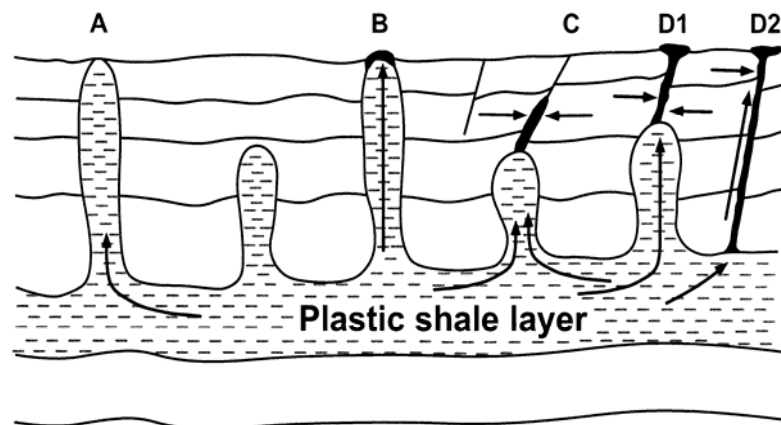


**Figure 2.3.** Schematic diagram illustrating the different basic mechanisms of formation of submarine MVs (from Milkov, 2000). (A) seafloor piercing shale diapir without a MV; (B) MV formed on top of a shale diapir; (C) seafloor seepage; (D1) MV formed by the rise of a fluidized sediments along a fault connected to an diapir; (D2) MV formed by the rise of a fluidized sediments along a fault directly connected to the mud source bed.

Figure 2.3 illustrates the more frequent mechanisms of formation of MVs (Milkov, 2000). Figure 2.3B corresponds to MVs formed directly on top of a seafloor-piercing mud diapir as consequence of fluid migration along the body of the diapir (e.g. Ivanov *et al.*, 1996). It should be noted that, during active diapiric stages, the increase of the tectonic pressure will favour MV generation (Rensbergen *et al.*, 1999).

The most common mechanism of the formation of MVs, corresponds to the rise of fluidized mud along faults and fractures (situation D1 and D2 in Figure 2.3). The mud breccias from these MVs are characterized by high fluid contents. The MVs can be connected with diapirs within the sedimentary sequence (case D1 in Figure 2.3) or they can be directly connected to the source layers (case D2 in Figure 2.3). Fluid migration plays the principal role in this mechanism and, in particular stages of the evolution of the system, when fluids (brine, water or gas) are the main or the only material to migrate, they will

produce at the surface not MVs but pockmarks, pockmark structures and methane-derived authigenic carbonates (case C in Figure 2.3).

### **2.1.3 Detection of submarine mud volcanoes**

There are several methods used for the detection of submarine MVs. Direct methods include: (1) direct observations from a submersible, remotely operated vehicle (ROV) or through underwater video or photo survey that allows the identification of mud breccia mud flows at the seafloor, and (2) sampling of the seafloor and retrieval of mud breccia sediment. Indirect methods include: (1) multibeam bathymetric characterization of the seafloor topography, which allows the identification of positive conical topographic features (MVVs or mud cones); or in some high resolution bathymetric data it is sometimes possible to identify specific morphologic elements of the MVs, such as the crater, mud flows and moats; (2) side-scan sonar imagery, which is also a widely used method for the identification of submarine MVs, since the mud breccia is characterized by strong backscatter returns when compared with the normal seabottom pelagic sediments; (3) MVs are also detected by reflection seismics (single channel or multi-channel), as the MVs are characterized by having a positive expression and an acoustic transparent or chaotic acoustic facies on seismic profiles.

### **2.1.4 Worldwide distribution**

Mud volcanoes are found worldwide, onshore and offshore, on continental shelves, continental and insular slopes and in the abyssal parts of inland seas (Figure 2.4). Estimated total number of known and inferred MVs have been put forward by several authors and range from  $10^3$  to  $10^5$  (Milkov, 2000), to approximately 1800 (Dimitrov, 2002). And estimations of annual amounts of methane globally emanated through MVs are of the order of  $\sim 10^8$  to  $2 \times 10^9$  m<sup>3</sup> (Kopf, 2002). The technical advances in marine geophysical equipment and the increase in deep-water exploration resulted in an increasing number of identified submarine MVs. In spite of the increasing number of underwater surveys, the amount of investigated Earth seafloor is still very sparse, and it is therefore probable that a very significant number of MV fields are yet to be discovered.

Mud volcanism occurs predominately at: (1) active margins, compressional tectonic settings and accretionary prisms; (2) passive margins associated with thick sedimentary sequences that have undergone rapid deposition and have become over-pressurized, such as in deep-sea fans; (3) associated with diapir formation several km bellow the seafloor; and (4) associated with hydrocarbon provinces, where the above mentioned processes of high pore pressure fluids generation dominate.

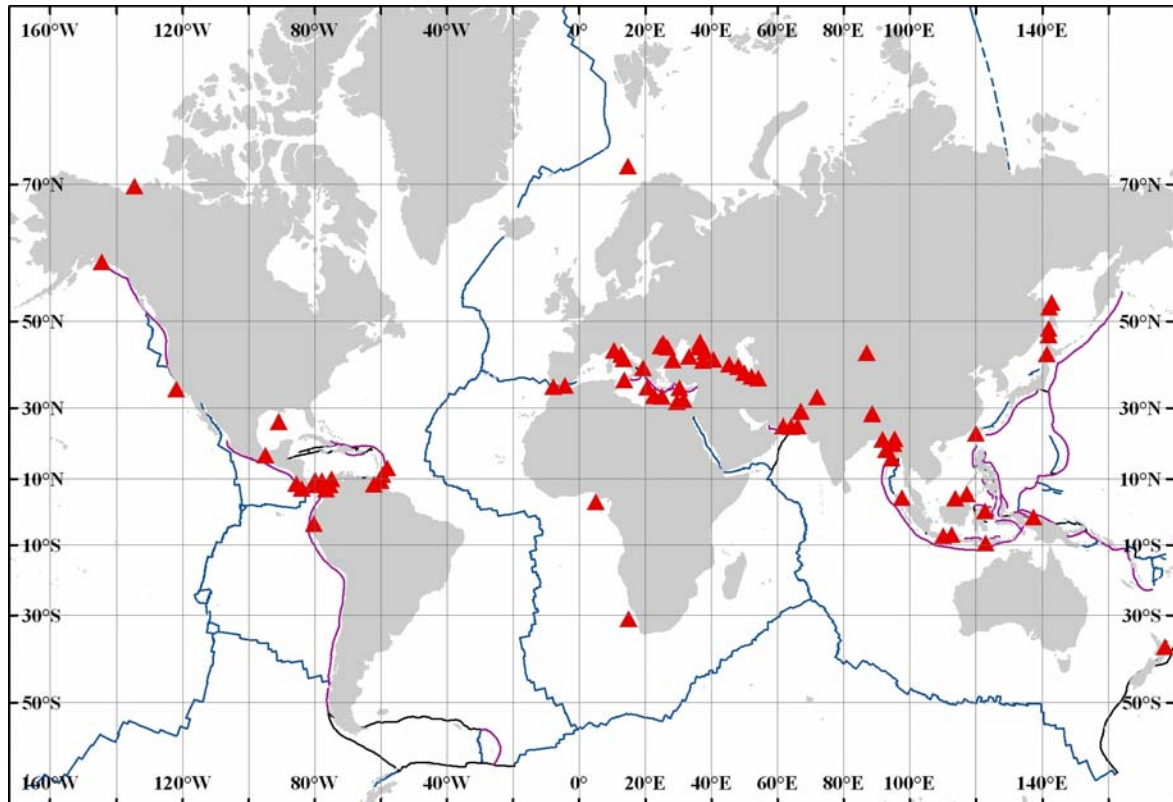


**Figure 2.4.** Worldwide occurrence of mud volcanoes, modified after Kholodov (2002), Kopf (2002) and Judd and Hovland (2007); plate boundaries from Coffin *et al.* (2000).

Figure 2.4 shows a compilation of MV occurrences modified and confirmed from Milkov (2000), Kholodov (2002), Kopf (2002) and from Judd and Hovland (2007). It can be observed that, the MVs occur predominately in active margins, in regions of tectonic compressive settings, not only within the limits of the accretionary wedges but also at their toe. They also occur along the Alpine-Himalayan collision belt, extending from the Gulf of Cadiz (Kenyon *et al.*, 2000; Gardner, 2001; Kenyon *et al.*, 2001, 2002, 2003; Pinheiro *et al.*, 2003; Somoza *et al.*, 2003; Depreiter *et al.*, 2005; Rensbergen *et al.*, 2005a; Rensbergen *et al.*, 2005b; Rooij *et al.*, 2005) and the Alboran Sea (Perez-Belzuz *et al.*, 1997; Sautkin *et al.*, 2003; Talukder, 2003), through the Mediterranean Sea (Cita *et al.*,

1981; Limonov *et al.*, 1994; Ivanov *et al.*, 1996; Limonov *et al.*, 1996; Robertson *et al.*, 1996; Limonov *et al.*, 1997; Woodside *et al.*, 1997a, b; De Lange and Brumsack, 1998; Kopf *et al.*, 1998; Robertson and Kopf, 1998; Woodside *et al.*, 1998; Kopf *et al.*, 2000), in the Black and Caspian Seas (Ivanov *et al.*, 1992; Ivanov *et al.*, 1996; Woodside *et al.*, 1997a, b), in the Crimea and Taman peninsulas (Ivanov and Woodside, 1996; Ivanov *et al.*, 1998; Lavrushin *et al.*, 2005), Azerbaijan (which has the biggest land mud volcanoes in the world (Hovland *et al.*, 1997; Fowler *et al.*, 2000; Aliyev *et al.*, 2002), Turkmenistan and Iran, as far as into the Makran coast (von Rad *et al.*, 2000; Wiedicke *et al.*, 2001). They also occur along collisional zones in most parts of the Indian Ocean, such as the Indonesian Sunda fore-arc (Wiedicke *et al.*, 2002), Sumatra, Borneo (Rensbergen *et al.*, 1999), Timor (Teixeira, 1950; Gageonnet and Lemoine, 1958; Leme, 1968; Barber *et al.*, 1986). They also occur in Taiwan and in the Nankai trench (Yamano *et al.*, 1992; Kuramoto *et al.*, 2001) and in the Barbados accretionary prism (Westbrook and Smith, 1983; Brown and Westbrook, 1988; Henry *et al.*, 1990; Le Pichon *et al.*, 1990), in the Trinidad island, Colombia, Ecuador, Mexico (Higgins and Saunders, 1974) and in the southern Caribbean thrust belts (Reed *et al.*, 1990; Vernet *et al.*, 1992), as well as along the northeastern American coast (Orange *et al.*, 1999).

At passive margins, MVs are mainly associated with environments with high sedimentation rates, such as deep sea fans and deltaic systems, like the Niger delta (Graue, 2000), in the Gulf of Mexico (Hovland and Judd, 1988; Prior *et al.*, 1989; Sager *et al.*, 2003), in the Nile deep-sea fan (Masclé *et al.*, 2001), in the Norwegian Sea (Vogt *et al.*, 1999), and in the Orinoco Delta, Eastern Venezuela (Aslan *et al.*, 2001).

As shown in Figure 2.4, MVs occur mainly in regions where hydrocarbons (oil and gas) have been or are actively generated, such as the Caspian Sea (Kopf, 2002; Huseynov and Guliyev, 2004; Yusifov and Rabinowitz, 2004), Trinidad (Higgins and Saunders, 1974), Azerbaijan (Hovland *et al.*, 1997), the Makran accretionary prism (Wiedicke *et al.*, 2001; Delisle *et al.*, 2002; Schluter *et al.*, 2002), the Caucasus, Indonesia (Barber *et al.*, 1986; Barber and Brown, 1988), the Caribbean and the North Sea.

The high number of modern MVs suggests that they should also be frequent in the geological record. In fact, some palaeo-cones are imaged at depth on seismic sections (Fowler *et al.*, 2000), but MV descriptions in the geologic record are scarce. The re-interpretation of some chaotic melange deposits, mixtures of blocks in a clay matrix, such

as melanges, olistostromes, submarine slumps or debris flow deposits showed that they were probably generated from mud volcanism related processes (Barber *et al.*, 1986; Barber and Brown, 1988). However, the vulnerability towards erosion of these structures makes it difficult to preserve them through geological times.

### **2.1.5 Global significance, potential interest and environmental impacts**

Mud volcanism, being a fluid escape process, has a significant role in degassing and dewatering of buried sediments (Kopf *et al.*, 2001; Dimitrov, 2002); therefore, they contribute with an important parcel to the fluid and gas budget and in the geochemical cycle within the sedimentary basins and in the subduction factory (Kopf and Deyhle, 2002).

#### **Influence on the global carbon budget**

Mud volcanoes are also a significant natural source for atmospheric methane, through massive episodic eruptions and dissociation of associated shallow gas hydrates. They have an important contribution and an important role on the world greenhouse gas budget and their quantification is of significant importance for the climatic change models (Dimitrov, 2003).

#### **A window to the deep sedimentary section and hydrocarbon potential**

As MVs bring materials originated within the sub-seafloor to the seafloor, they can give us direct and indirect information about processes occurring in the deep sub-seafloor (Ivanov *et al.*, 1996). The study of the mud breccia clasts, since they correspond to rock fragments pulled up from deeper sections of the sedimentary column to the surface, they provide easy access to important information of the deep sedimentary sequences of the basin, namely on the composition, genesis, age and geochemistry of the sediments and processes occurring at depth e.g. Akhmanov *et al.*,(2003); Ovsyannikov *et al.*, (2003). As most of the oil and natural gas production areas are associated with mud volcanism, the MVs were firstly interpreted and studied as direct indicators of hydrocarbon migration, providing information of the petroleum potential in the deep subsurface (Ivanov *et al.*, 1998; Stadnitskaia *et al.*, 2006).

### **A window to the deep biosphere**

The sub-seafloor sedimentary layers harbour over half of all the prokaryotic cells on Earth (Whitman *et al.*, 1998). Live sub-seafloor prokaryotes are found even in very old (16 Ma) and deep (> 400 m) sediments (Schippers *et al.*, 2005) and they can have high activity rates and be active over geological timescales (Parkes *et al.*, 2005). As MVs bring material from the sub-seafloor, they are also a window into the deep biosphere and related biogeochemical processes. They indeed represent an important deep biosphere habitat as they supply source energy (CH<sub>4</sub> and HS<sup>-</sup>) that can fuel chemoautotrophic ecosystems. They can also transport faunal assemblages from the deep sub-seafloor.

### **Geological hazards**

Submarine MVs are also important hazardous structures for seafloor operations and infrastructures. They can have a damaging impact on drilling operations, rig installations, pipelines and communication routings.

Other scientific issues that can be addressed through the study of MVs are the role of fluid flow and hydrate dissociation in sediment stability, the interplay between microbial life and fluid seepage, and the dynamics of the gas hydrate system.

## **2.2. Pockmarks**

Pockmarks are negative morphological structures, craterlike or cone shaped depressions at the seafloor, that are the expression of high fluid discharge (seepage) through a conduit (Figure 2.5). Seepage in the water column can be manifested by bubble streams and columns of coloured or shimmering water. As the migration of fluids through unlithified sediments has a relatively powerful erosive effect and pockmarks are features that record the erosive effect of seepage in suitable types of seabed sediments (Hovland and Judd, 1988).

Pockmarks were described for the first time in the continental shelf of Nova Scotia, Canada, based on side-scan sonar imagery (King and MacLean, 1970); since then, pockmarks have been recognised not merely as morphologic features, but as indicators of dynamic geological processes of seepage of fluids at the seabed. The pockmarks occur in a

wide variety of geological settings: on continental shelves, slopes, rises and in the deep ocean.

Because pockmarks can be located relatively easily (inclusive buried pockmarks are detectable on reflection seismic records), while seepage activity is more difficult to detect, pockmarks are used as indicators of active or inactive seepage. In general, the pockmarks are generated by methane, of biogenic or of thermogenic origin, that seeps at the seabed. It is also possible that some pockmarks are caused by venting of destabilized gas hydrates or deep-earth originated gas, but their percentage in this case should be smaller, compared with the other fluid supplies, as both fluid supplies should be much less abundant.

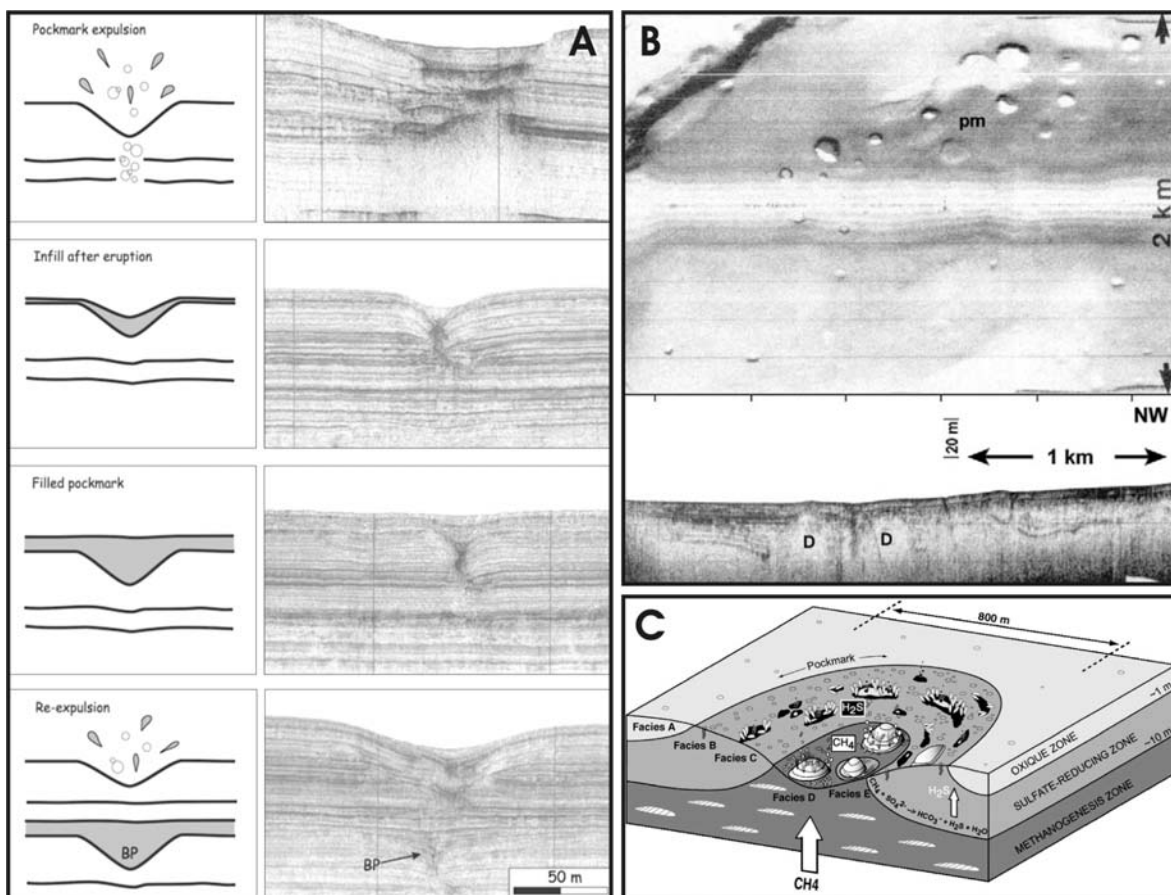


**Figure 2.5.** Pockmarks. (A) Schematic illustration (left column) and correspondent 5 kHz seismic reflection profiles of different evolution stages of pockmarks (Çifçi *et al.*, 2003) Note: BP denotes a buried pockmark. (B) MAK-1 side-scan sonar record of pockmarks (pm) and corresponding seabottom profile (Dimitrov and Woodside, 2003). (C) morphological model with chemical and biological features within a pockmark. The centre is dominated by methane-derived authigenic carbonate build-ups and endemic bacteria and fauna. The periphery is dominated by sulphide-dependent Vesicomylidia-type fauna living on black reduced sediments and white bacterial mats. In this model, the upper boundary of methane hydrates is concordant with the sulphate-methane interface (SMI) and gas hydrates can only outcrop in the centre of a pockmark if the upward flux of methane is strong enough (Gay *et al.*, 2006c).

### 2.3 Active hydrocarbon seepage

The term seepage embraces a wide spectrum of fluid escape processes that occur on different geologic settings, both onshore and offshore. Seepage intensity ranges from the vigorous bubbling of gas (a gas macro seepage) to small scale emanation of microscopic bubbles, to water dominated fluids or hydrocarbon compounds in solution, detected only by geochemical instruments. Seepage activity can be continuous or episodically with short periods of activity between long periods of dormancy.

The seeping fluids may be: (1) hydrocarbons (thermogenic or biogenic), that are in general dominated by methane and light hydrocarbons (as gas or dissolved), although seepage of heavier compounds can also occur; (2) hydrothermal or volcanic fluids; (3) groundwater; (4) fluids resulting from the decomposition of gas hydrates; and (5) deep-earth gas (such as methane, carbon dioxide and some other compounds that could be rising from deep within the Earth, according to the “deep-earth gas hypothesis” (Gold and Soter, 1980).

The seepage of volcanic hydrothermal fluids is a common phenomenon at plate boundaries and at spreading centres on mid ocean ridges, where submarine volcanic eruptions take place and fluids originated by volcanic activity, modified through fluid circulation through volcanic and sedimentary host rocks, are expelled at elevated temperatures (up to 350°C) representing positive temperature anomalies in relation to the ambient background temperature values (Corliss *et al.*, 1979). The sites of active volcanic fluid seepage are called hydrothermal vents.

Groundwater seepage occurs when migration paths, hydrostatic pressure and adequate aquifer recharge from land results in seepage of meteoric water at the seabed in areas close to land. Discharge of aqueous fluids resulting from the compaction of sediments can also be considered as groundwater seepage.

In general, the occurrence of shallow gas, gas chimneys and gassy sediments are associated with cold seepage, gas hydrates, pockmarks or mud volcanoes. The shallow gas and gassy sediments are recognised on the seismic records by acoustic blanking, acoustic turbidity and enhanced reflectors (Hovland and Judd, 1988).

The term cold seeps refers to the sites along convergent plate boundaries and passive continental margins, where near ambient bottom water temperature gas or fluids enriched

in hydrocarbons reach the seafloor. This term is defined in opposition to the hydrothermal seepage or hydrothermal vents, where the seepage fluids are characterized by positive temperature anomalies in relation to the ambient seawater.

### **2.3.1 Cold seeps: Definition and characteristics**

Different types of fluids with different hydrocarbons can be expelled at cold seeps: light hydrocarbons, as free gas or dissolved (that in adequate pressure and temperature conditions can form gas hydrates); heavier hydrocarbons, such as oil; water dominated brines; and saline brines. Liquid oil seepage, accompanied by light hydrocarbons dissolved or as gas, occur in general associated with oil reservoirs e.g. Gulf of Mexico (Aharon *et al.*, 1992; Sassen *et al.*, 2003). The leakage of the oil into the water column and into the surface waters produces oil slicks that can be observed at the sea surface (Kornacki *et al.*, 1994; MacDonald *et al.*, 2002). Oil and heavier hydrocarbon seepage, accompanied by asphalt or producing asphalt as result of their oxidation, as observed in the Campeche Knolls in the southern Gulf of Mexico, can result in lava-like flows of solidified asphalt associated with oil seepage, gas hydrates and authigenic carbonates (MacDonald *et al.*, 2004; Hovland *et al.*, 2005a). These asphalt flows are colonized by chemosynthetic tubeworms and bivalves.

Methane is the dominant hydrocarbon at the majority of cold seeps, in general accompanied by smaller quantities of CO<sub>2</sub>, H<sub>2</sub>S and heavier hydrocarbons such as ethane, propane, butane and pentane (Hovland *et al.*, 1987; Hovland and Judd, 1988). Methane is the second most abundant compound in the sediments (after water) and the global flux of methane in the sediment column can have significant importance to the biosphere, hydrosphere and to the atmosphere. Large amounts of methane are produced in marine sediments but most of it is consumed within the sediments and does not reach the bottom waters or the atmosphere. Methane seeps are places where high flux of methane reaches the seabottom and sustains ecological systems and particular geological features.

Three different origins can be considered for methane: microbial, thermogenic or abiogenic. Microbial methane is generated by bacterial anaerobic decomposition of organic matter at low temperatures within the sediments in the anaerobic methanogenic zone, such as the thermophilic methanogens fermenting VFAs or reducing CO<sub>2</sub>/formate coupled with

H<sub>2</sub> oxidation (Thauer, 1998). The methanogenic zone is supposed to extend over the first 1000 m below surface (Whiticar, 1999) or even deeper (Ivanov, personal communication). Thermogenic methane is generated by thermo-catalytic breakdown of organic matter (kerogen) at high temperatures and pressures (of about 110°C) and is usually accompanied by heavier hydrocarbons. Abiogenic methane can be generated by chemical reactions such as clay metamorphism, abiogenic reduction of CO<sub>2</sub>, CO or formate with H<sub>2</sub> (Lollar *et al.*, 2002), hydrothermal alteration of sedimentary organic matter (Des Marais *et al.*, 1981), Fischer-Tropsch reactions in aqueous solution at elevated temperature (390°C) in the presence of metallic catalysts, which is common during the serpentinization and hydration of ultramafic rocks (Lollar *et al.*, 1993; Foustoukos and Seyfried Jr., 2004), methane generation can also be mediated by deep hydrothermal processes (Hensen *et al.*, in press; Nuzzo *et al.*, Submitted); and, according to the “deep-earth gas hypothesis”, methane derived from the mantle, where it was an original component of the accretion Earth (Gold and Soter, 1980).

Thermogenic, abiogenic and, to some extent, biogenic hydrocarbons have to migrate vertically along the sedimentary column from the source rocks and reservoirs to the seafloor. Gaseous hydrocarbons C<sub>1</sub> to C<sub>6</sub> are the most mobile and methane having the smallest molecular size, is the most mobile and can reach the surface more easily (Hovland and Judd, 1988). The methane reaching the upper part of the sediment column is in general oxidized anaerobically as described in the section below.

### **2.3.2 Methane oxidation and main biogeochemical processes in cold seeps**

The flux of methane from the sediments to the atmosphere is controlled by the microbial-mediated process of anaerobic oxidation of methane (AOM). AOM is identified as a major sink of methane (Reeburgh, 1980) and it also accounts for a substantial fraction of sulphate reduction in marine sediments and in anoxic waters. The identification and quantification of the mechanisms by which methane is being oxidized in natural environments is very important both in terms of the global carbon budget and for reconstruction of the relationships between gas hydrate carbon pools and concentrations of greenhouse gases in ancient atmospheres (Kvenvolden, 1993; Henriot and Mienert, 1998).

Along the sedimentary column, from depth to the seawater, three main zones (Figure 2.6) with distinctive biogeochemical processes can be defined: the methanogenic zone, the sulphate reduction zone and the aerobic zone.

### 2.3.2.1 The methanogenic zone

The methanogenic zone is the deepest of the three zones described above and in normal marine sediments it is usually located deeper than a few meters below the seafloor. At seepage sites this zone is pulled up and can occur very close to the seafloor or even reach the seafloor at very active seepage sites. This zone is anaerobic and methane is generated biologically by methanogenic archaea. Several intermediates of the breakdown of organic matter, as acetate, are converted to methane, following the simplified reaction illustrated by equation 2.1.



### 2.3.2.2 The sulphate reduction zone

The anaerobic sulphate reduction zone extends from the top of the methanogenic zone to the bottom of the oxic zone. In general this zone extends few centimetres to few meters below the seafloor. At cold seeps the thickness of this zone is highly variable and in active seepage systems the sulphate reduction zone can be very thin and is in general pulled up to the seafloor or very close to it. The biogeochemical processes at this zone are characterized by two main reactions: the anaerobic oxidation of methane (AOM) which occurs in combination with sulphate reduction (SR) according to equation 2.2, and the oxidation of organic matter (equation 2.3).

AOM is the primary process by which biomass is generated and accumulates at methane seeps (Boetius *et al.*, 2000; Elvert *et al.*, 2000; Michaelis *et al.*, 2002). AOM has been found to be performed by a consortium of methanotrophic archaea and sulphate-reducing bacteria (SRB), in which sulphate acts as the terminal oxidant (Boetius *et al.*, 2000). AOM in cold seeps sediments is indicated by geochemical (Thiel *et al.*, 1999; Elvert *et al.*, 2000) and by direct microscopic evidence (Boetius *et al.*, 2000; Orphan *et al.*, 2001). This process is estimated to globally consume the methane equivalent to 5 - 20% of

the net modern atmospheric methane flux ( $20 - 100 \times 10^{12} \text{ g year}^{-1}$ ) (Valentine and Reeburgh, 2000). AOM-SR process is also recognised to be the predominant anaerobic methane oxidation metabolic process at methane-seeps in the geologic record (Peckmann *et al.*, 1999a; Peckmann *et al.*, 1999b; Peckmann *et al.*, 1999c; Thiel *et al.*, 1999; Elvert *et al.*, 2000; Goedert *et al.*, 2000; Valentine and Reeburgh, 2000; Peckmann *et al.*, 2001a; Peckmann *et al.*, 2001b; Peckmann *et al.*, 2001c; Thiel *et al.*, 2001; Campbell *et al.*, 2002; Michaelis *et al.*, 2002; Peckmann *et al.*, 2002; Gischler *et al.*, 2003; Goedert *et al.*, 2003; Peckmann *et al.*, 2003; Peckmann and Thiel, 2004; Peckmann *et al.*, 2004). The understanding of the microbial processes is therefore most important for the understanding of element cycling at modern and ancient seeps. Ancient methane seepage processes can be revealed by geochemical evidence: biomarkers, C and S stable isotopes and microbial-induced sedimentary fabrics and microbial precipitates. Stromatolitic fabrics have been found at seep deposits as old as the Devonian age (Peckmann and Thiel, 2004). Microbial-induced precipitates have been reported from a Tertiary seep limestone (Cavagna *et al.*, 1999; Peckmann *et al.*, 1999b). Fossilised biofilms were recognised in the same limestone (Peckmann *et al.*, 1999b) as well as in Cretaceous seep deposits which contain structures interpreted to represent prokaryotic body fossils (Shapiro, 2004).

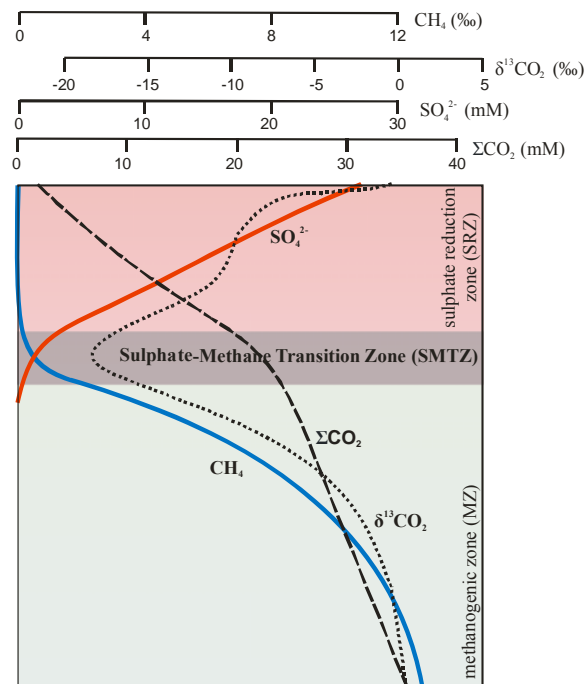
Three lines of evidence have traditionally been used to support the existence of AOM-SR: (i) diagenetic (advection-diffusion-reaction) models of methane concentration profiles in anoxic sediments and water column (Barnes and Goldberg, 1976); (ii) tracer measurements using  $^{14}\text{C} - \text{CH}_4$ ,  $^3\text{H} - \text{CH}_4$  and  $^{35}\text{S} - \text{SO}_4^{2-}$  (Reeburgh, 1980); and (iii) stable isotope distributions (Whiticar, 1999).

Figure 2.6 schematically summarizes the depth distributions of  $\text{CH}_4$ , total carbon dioxide ( $\Sigma\text{CO}_2$ ), sulphate ( $\text{SO}_4^{2-}$ ) and the stable carbon isotope ratio of carbon dioxide ( $\delta^{13}\text{CO}_2$ ) in anoxic marine sediments. The distributions of all species show slope changes or minima at a specific depth, suggesting that most of the methane consumption takes place in a thin subsurface depth interval. The  $\delta^{13}\text{CO}_2$  minimum appears to be the result of local injection of methane-derived carbon dioxide. AOM occurs throughout the sulphate reduction zone (SRZ) reaching the maximum at the base of the SRZ, at the sulphate-methane transition zone (SMTZ). The low methane concentration zone observed at the surface of marine sediments results from the distribution of anaerobic methane oxidation rates in the sulphate reduction zone. Methane oxidation rates are highest at the SMTZ.

The anaerobic oxidation of methane has been described geochemically by the following net reaction (Reeburgh, 1980):



It should be noted that, as consequence of AOM-SR, in particular as result of the sulphate reducing bacteria, the pore water dissolved sulphate is consumed, the alkalinity increases and sulphide accumulates in concentrations equivalent to those of sulphate consumption. Intense sulphide production supports the occurrence of sulphide-based communities such as *Beggiatoa*, *Calyptogenia*, bivalves of the families Vesicomidae, Mytilidae, Solemyidae, Thyasiridae and Lucinidae, hosting endosymbiotic chemoautotrophic bacteria, pogonophoran worms, Cladorhizidae and Hymedesmiidae sponges (Sibuet and Olu, 1998). In the Gulf of Cadiz the common chemosynthetic community is composed of *Siboglinum* sp., *Polybrachia* and *Oligograchia* (pogonophora), *Acharax* sp. (solemydae) and *Lucinoma* (Lucinidae) (Cunha *et al.*, 2005; Rodrigues and Cunha, 2005).



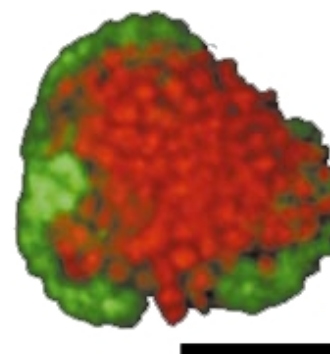
**Figure 2.6.** Schematic diagram of depth distributions of methane, sulphate, total dioxide and carbon isotope ratio of carbon dioxide in interstitial waters of anoxic marine sediments. All distributions show breaks or slope changes in the sulphate-methane transition zone (SMTZ), which represents the zone of maximum anaerobic methane oxidation. Modified from Reeburgh (1980).

Also as a consequence of the net reaction (2.2), methane-derived bicarbonate precipitates as carbonate and forms methane-derived authigenic carbonate structures, such

as aragonite pavements and dolomite conduits (Magalhães *et al.*, 2005a). This process will be discussed in chapters 5 to 8 of this thesis.

The microorganisms that mediate this reaction are composed by a consortium of certain archaea that are capable of reverse the process of methanogenesis by interaction with sulphate-reducing bacteria (Hoehler *et al.*, 1994; Hansen *et al.*, 1998; Hinrichs *et al.*, 1999), with sulphate as the terminal electron acceptor, according to equation (2.2). Microscopic evidence of the structured consortium of archaea and sulphate-reducing bacteria, identified by Boetius *et al.* (2000) using fluorescence in situ hybridization (FISH) with specific 16S rRNA-target oligonucleotides has shown that the archaea-bacterial symbiosis is structured in dense aggregates in general of about 100 cells (although these aggregates can contain a smaller or a much larger number of cells) of archaea surrounded by sulphate-reducing bacteria, as illustrated in Figure 2.7.

**Figure 2.7.** In situ identification of archaea-sulphate reducing bacteria consortium aggregates with fluorescence in situ hybridization (FISH) with specific 16S rRNA-target oligonucleotide probes. The archaea are shown in red and the SRB in green. Confocal laser scanning micrograph of the hybridization with CY3-labelled probe EelMS932 (archaea) and the FLUOS-labelled probe DSS658 (SRB). Scale bar is 5  $\mu\text{m}$ . From Boetius *et al.* (2000).



These aggregates are abundant in gas hydrate rich sediments and in methane seep areas with high rates of methane-based sulphate reduction. An average archaea/SRB consortium, illustrated in Figure 2.7, consists of an inner sphere of  $2.3 \pm 1.3 \mu\text{m}$  diameter containing about 100 coccoid archaeal cells, each  $0.5 \mu\text{m}$  in diameter. These are partially or fully surrounded by about 200 cells of SRB ( $0.3 - 0.5 \mu\text{m}$  in diameter), which form an outer shell of mostly 1-2 cell layers. The size spectrum of 100 archaea/SRB consortia ranged from 1 to  $11 \mu\text{m}$  in diameter with an average of  $3.2 \pm 1.5 \mu\text{m}$ . The smallest aggregates identified were composed of 1-3 archaea cells and 1-3 cells of SRB, and may represent early stages of the consortium development, while the largest aggregates contained about 10000 cells. These consortia are highly abundant in surface sediments at sulphide concentrations  $< 10 \text{ mM}$ , with a maximum of  $7 \times 10^7$  aggregates  $\text{cm}^{-3}$  at 1-2 cm depth (Boetius *et al.*, 2000).

The anaerobic oxidation of organic matter, that can be described by the simplified equation 3, is the result of different types of bacteria.



This reaction produces  $CO_2$  and increases the alkalinity in the sediments. Similar to the AOM-SR the anaerobic oxidation of organic matter also can drive carbonate precipitation and replacement reactions producing calcite and or dolomite.

### 2.3.2.3 The aerobic zone

The aerobic zone extends from the top of the sulphate reduction zone to the seafloor and within the water column, in normal seawater. In sites of high methane flux, such as active mud volcanoes, the oxygenated zone can be of just a few millimetres thick e.g. 4 mm thick of the aerobic zone at the Captain Arutyunov MV (Pfannkuche and Fahrteilnehmer, 2006). The aerobic oxidation of methane can be represented by the following reaction:



It should be noted that the aerobic oxidation of methane produces  $CO_2$  which, reacting with the  $H_2O$ , generates  $H_2CO_3$ , reducing the pore water pH and inhibiting the precipitation of carbonates, leading to their dissolution.

### 2.3.3 Geologic setting and worldwide occurrences of cold seeps

Cold seepage is recognized to occur in a diversity of geological and tectonic settings. The occurrence of cold seeps is in general associated with other fluid escape structures. They are in general directly associated with: mud volcanoes (Brown, 1990; Aloisi *et al.*, 2000; Magalhães *et al.*, 2004); mud cones (Díaz-del-Río *et al.*, 2003); mud diapirs (Brown, 1990); pockmarks (Hovland *et al.*, 1987; Hovland and Judd, 1988); salt diapirs (Acosta *et al.*, 2003); coral reefs, although not proved and still in debate, a possibly link between methane seepage and carbonate mount formation by coral reef *Lophelia Pertusa* growth was been proposed (Hovland, 1990; Hovland and Thomsen, 1997; Henriet *et al.*, 2003);

seamounts; eroded platforms or escarpments (Paull *et al.*, 1992); faults (Ritger *et al.*, 1987; Kauffman *et al.*, 1996; Rad *et al.*, 1996); polygonal faults, a non-tectonic class of layer-bound faults that are organized in a polygonal map pattern and are related to sediment compaction and fluid expulsion (Gay *et al.*, 2006a; Gay *et al.*, 2006b); sedimentary structures, such as sand injections (sandstone dykes and sills), and inclined bedding (Jonk *et al.*, 2003; Mazzini *et al.*, 2003). It should be noted that the sandstone dykes and sills are not distinct processes that originate other fluid escape structures but form a related continuum of mobilization features or of fluid escape structures. These structures, when formed, also represent conduits for preferential fluid transport to the seafloor.

An worldwide compilation of occurrences of modern and ancient seeps was presented by Campbell *et al.*, (2002) and is illustrated in Figure 2.8.

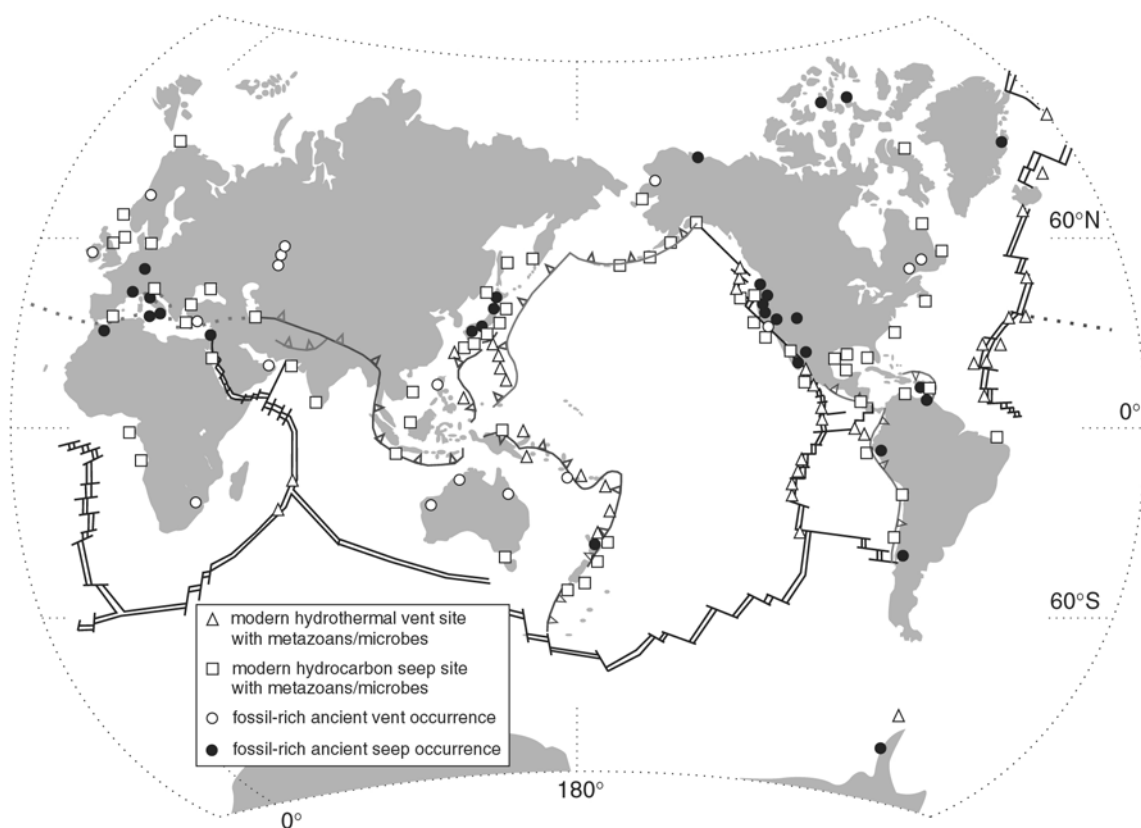


**Figure 2.8.** World-wide distribution map of modern and ancient (Archaean to recent) hydrothermal vent and hydrocarbon seep occurrences with chemosynthetic community associations. Plate boundary (PB) symbols include: double line - constructive PB; tooth pattern - destructive PB; single line - strike-slip PB. Data compiled from numerous literature sources (Campbell, 2006).

### 2.3.4 Cold seepage manifestations and detection

Cold seeps, in particular methane seepage can be detected by visual, hydro-acoustic and by geochemical observations. Visual inspection of the seafloor by submersible/ROV or underwater video systems allow the observation of gas hydrates at the seafloor (that indicate methane flux to the near seafloor where it crystallises as clathrates), plumes of gas bubbles streams ascending from the seafloor (Figure 2.9A, C, F and G). Gas bubbles can also be revealed by acoustic observations, specially the cases of gas hydrate coated methane bubbles that can be imaged by echo sounders (Greinert *et al.*, 2006; Sauter *et al.*, 2006) where they form flares in the water column (Figure 2.9F and G) that can also be imaged by side-scan sonar (Figure 2.9H). Geochemical profiles of methane (Figure 2.6), hydrocarbons, chlorinity and specific elements allow the measurement of fluxes of hydrocarbon gas measurements and the calculation of the rates of consumption or seepage to the bottom waters.

Both hydrothermal and cold seeps, in general, support chemoautotrophic fauna (section 2.6) that supports very specific ecosystems that clearly differ from the normal surrounding environment. As the distinction between hydrothermal vents and cold seeps is chemically and geologically simple, the identification of such chemosynthetic communities is used as a strong indicator of cold seepage on the geological record.

The most important manifestation of seepage of hydrocarbons is the formation of methane-derived authigenic carbonates (MDAC). The deposits of MDAC together with the identification of chemosynthetic communities are the most important criteria used to the identification of palaeo-cold seeps in the geological record.

Fossil cold seep deposits were recognised as far as into the Devonian (Campbell and Bottjer, 1995; Peckmann *et al.*, 1999c; Peckmann *et al.*, 2005). Examples of fossil cold seeps include the Lower Eocene carbonate cemented chimneys in Varna, NE Bulgaria (De Boever *et al.*, 2006), the Eocene–Miocene fossiliferous carbonates from Barbados, Trinidad and northern Venezuela (Gill *et al.*, 2005), the Late Cretaceous in the (Campanian) submarine springs (Tepee Buttes) of Colorado (Kauffman *et al.*, 1996), the Miocene Marmorito and *Lucina* limestones of Monferrato, NW Italy (Clari *et al.*, 1994; Cavagna *et al.*, 1999; Peckmann *et al.*, 1999b; Pierre *et al.*, 2002), the Oxfordian seep carbonates from Beauvoisin, southeastern France (Peckmann *et al.*, 1999b), the Upper Jurassic Methane-Seep Limestone from the Fossil Bluff Group Fore-Arc Basin of

Alexander Island, Antarctica (Kelly *et al.*, 1995), the Miocene fossil seep structures of the Monterey Bay region (Aiello *et al.*, 2001; Aiello, 2005), the hydrocarbon seep-carbonate occurrences in late Jurassic to late Cretaceous forearc and accretionary prism strata in western California (Campbell *et al.*, 2002), the Cretaceous cold seep mounds from the Canadian Arctic (Savard *et al.*, 1996), and others.

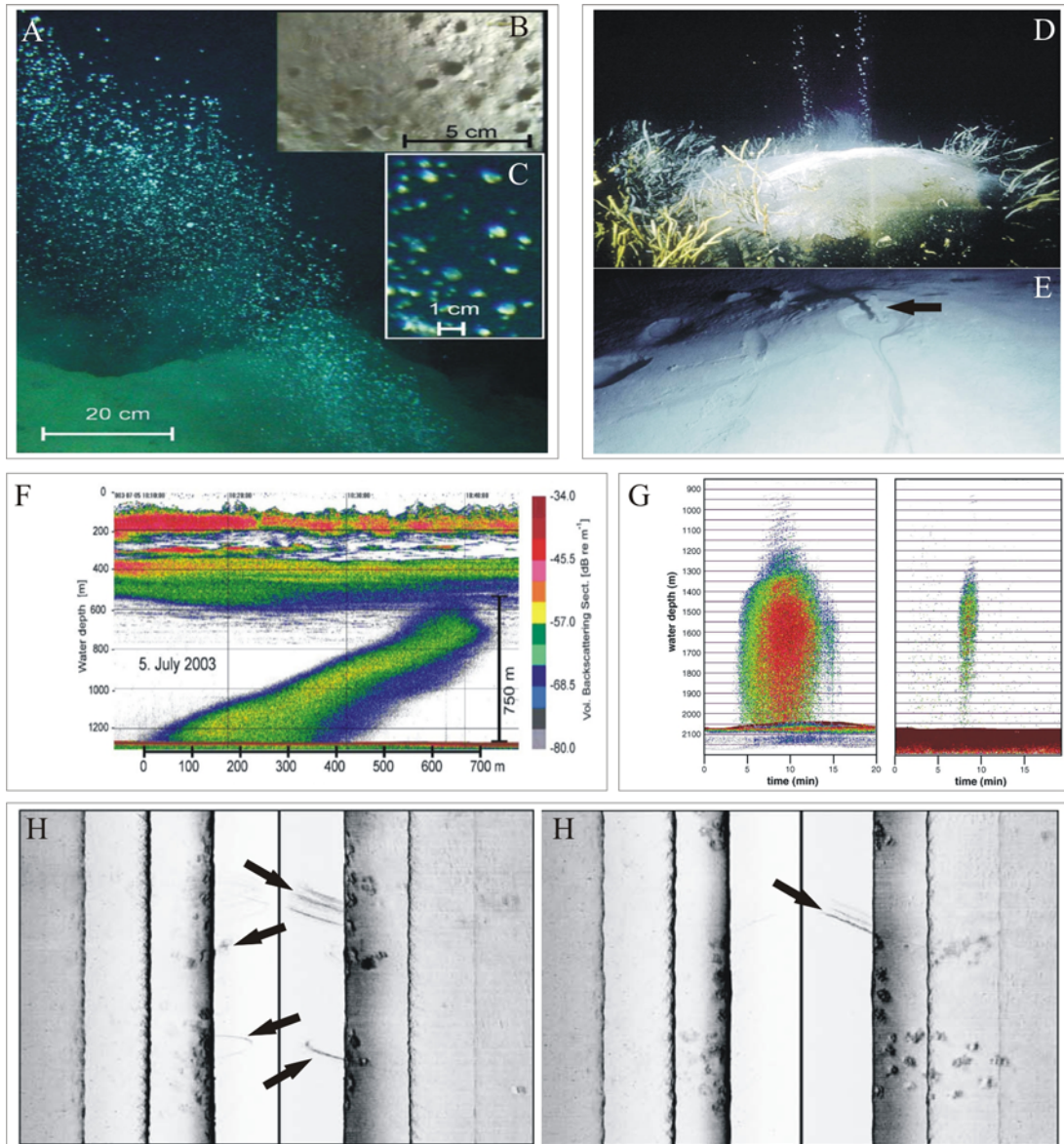
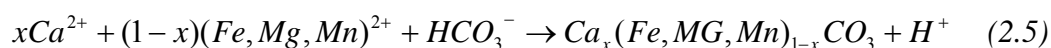


**Figure 2.9.** Cold seepage detection. (A, B and C) Still pictures of bubble discharge at the Håkon Mosby Mud Volcano (1250 m water depth) (from Sauter *et al.*, 2006). (B) Detail showing perforated sediments indicative of transient gas release. (C) Zoomed image showing bubbles in more detail. (D and E) Gas seepage in the Gulf of Mexico illustrating (D) gas bubbles seeping from a shallow gas hydrate deposit, with about 1 m across, at 570 m water depth and (E) large gas bubble rising (arrow) from a pool of brine at the crater, 25 cm across, of a small MV (D and E from MacDonald *et al.*, 2002). (F and G) Gas flares on single-beam echograms (Greinert *et al.*, 2006; Sauter *et al.*, 2006). (H) Gas plumes (arrows) in the water column imaged by side-scan sonar (Rollet *et al.*, 2006).

## 2.4 Methane-derived authigenic carbonates

Methane-derived authigenic carbonates (MDAC) are carbonates formed by microbially-mediated processes that occur at the seafloor or in subsurface, at sites of hydrocarbon-rich fluid seepage (e.g. Hovland *et al.*, 1987; Hovland and Judd, 1988). The precipitation of the carbonates is assigned to the sulphate reduction zone or to the transition between the sulphate reduction zone with the methanogenic zone, where the microbial sulphate reduction is coupled with anaerobic methane oxidation (Ritger *et al.*, 1987; Paull *et al.*, 1992), as described in section 2.3.2. According to the Reeburgh (1980) net equation (equation 2.2), bicarbonate is produced and increases the alkalinity promoting the precipitation of carbonates. The precipitation of carbonate can be envisaged as follows:



with  $0 < x < 1$ .

Thus, for carbonate precipitation to occur, a cation (Ca, Fe, Mg or Mn) is required. Calcite precipitation occurs when pore fluids are supersaturated with respect to this mineral. The mineralogy of the carbonate cement is possibly controlled by the geochemical environment such as the concentration of  $SO_4^{2-}$  in pore waters. Strong concentrations of  $SO_4^{2-}$  in the sediments will inhibit the precipitation of dolomite or Mg-calcite (which are the more soluble and thermodynamically more stable), enhancing instead the precipitation of aragonite.

The understanding of the formation of dolomite in the MDAC can bring an important contribution to the understanding of the so called “dolomite problem”. Dolomite is the thermodynamically stable carbonate phase in seawater, but it is a rather rare mineral in modern marine depositional environments. Nevertheless, dolomite is one of the three most common sedimentary carbonate minerals (Baker and Kastner, 1981). This abundance of dolomite over the geological record can not be explained by the diagenetic dolomitization process of calcite and aragonite, as there are marked irregularities in the dolomite distribution with time. Therefore, dolomite had to be a common, extensive and widespread rock forming mineral in ancient sediments, in particular in late Precambrian and Paleozoic times, but it is rather scarce in the Holocene (Kastner, 1984).

The formulation of the microbial dolomite model (Vasconcelos and McKenzie, 1997; Warthmann *et al.*, 2000) introduced a biogeochemical approach to the understanding of the dolomite formation. A plausible correlation was established between the geochemical cycles and dolomite formation with a positive correlation between extensive dolomitization periods and decreased oxygen levels at the oceans and atmosphere (Burns *et al.*, 2000). The low oxygen levels would have fostered a more active community of anaerobic microbes, including the sulphate-reducing bacteria, that are involved in mediating the dolomite nucleation in the formation of dolomite in natural environments (Vasconcelos *et al.*, 1995). The understanding of the formation process of the authigenic dolomite in cold seeps environments can contribute to the understanding of the biogeochemical environmental conditions of dolomite formation (see chapters 5, 6 and 7).

The carbonates in these environments are formed by cementation of seafloor or shallow sediments by precipitation of authigenic carbonates. The formed carbonates can present variable morphologies and shapes: (1) cemented sedimentary layers (Hovland *et al.*, 1987; Hovland and Judd, 1988) (Figure 2.10, e.g. A to F); (2) thin crusts (few centimetres) to thick slabs (up to several meters in size) that pave the seafloor for several square meters (Aloisi *et al.*, 2000; Greinert *et al.*, 2001; Greinert *et al.*, 2002; Magalhães *et al.*, 2005b) (Figure 2.10B, C E and F); (3) irregular edifices and build-ups that can be several meters high (Magalhães *et al.*, 2005b) (Figure 2.10A) and that can be formed by chemical authigenic precipitation (called chemoherms) and by cemented calcareous skeletal debris of chemo-symbiotic fauna (Aharon, 1994; Clari *et al.*, 1994); (4) chimneys or pipe-like structures (Kulm *et al.*, 1986; Kulm and Suess, 1990; Aiello *et al.*, 2001; Díaz-del-Río *et al.*, 2003; Magalhães *et al.*, 2005b) (Figure 2.10G to I). The MDAC are typically found on the seafloor or at shallow depths below the sediment water interface.

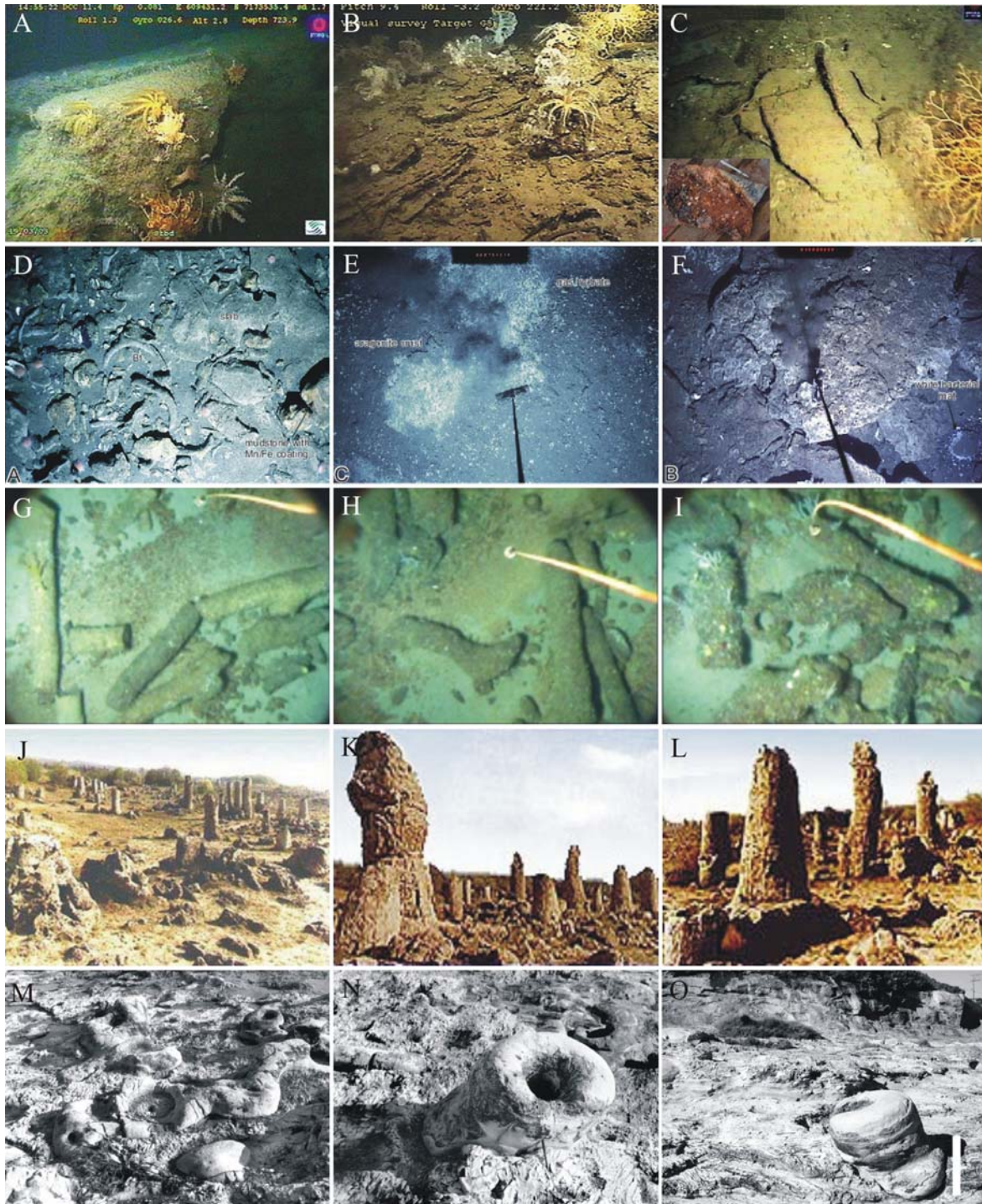


**Figure 2.10.** MDAC: examples of seafloor pictures and on land outcrops. (A to C) MDAC from a complex pockmark off Mid-Norway (Hovland *et al.*, 2005b), (A) a large, up to 24 m<sup>3</sup> carbonate slab inside the pockmark that serves as fixed substratum for benthic fauna, (B) carbonate cemented sediments with layered and friable structures that serves as substratum for benthic fauna, (C) thin carbonate crusts (inset shows one of these crusts recovered). (D to F) Seafloor images of MDAC from Hydrate Ridge (Greinert *et al.*, 2001), showing, (D) block and slab-like mudstones and bioturbation casts, (E) irregular chemoherm block with white bacterial overgrowth and white clams, and (F) aragonite pavement in direct contact with outcropping gas hydrates and also with bacterial mats and scattered with clams on the sediment. (G to I) Bottom photographs taken from the R/V Prof. Logachev underwater video camera on the Iberico mud cone and on the Formosa ridge. The field of view is approximately 2 m. (J to L) The “stone forest” from Varna, Bulgaria showing Lower Eocene massive carbonate cemented columns or chimneys, up to 1.5 m diameter and 8 m high and horizontal

interbeds (De Boever *et al.*, 2006), pictures from Dimitrov (2000). (M to O) Miocene seep carbonates in the uppermost Santa Cruz Mudstone Formation in Santa Cruz, Monterey, California (M) circular conduits that extends along the opal CT horizontal porcelanite layers. Area of view is about 15 m<sup>2</sup> (Aiello *et al.*, 2001). (N and O) carbonate pipes with ~70 cm tall that protrude from the fractured opal CT horizontal porcelanite layers, (N) from Aiello (2001) and (O) from Aiello (2005).

## 2.5 Gas Hydrates and BSRs

### 2.5.1 Definition, characteristics and formation mechanisms

Natural gas hydrate (Figure 2.11A to B) is a mineral composed of water and natural gas (of relatively light molecular weight and that usually is methane, but can also be C<sub>2</sub>H<sub>6</sub>, C<sub>3</sub>H<sub>8</sub>, C<sub>4</sub>H<sub>10</sub>, CO<sub>2</sub> or H<sub>2</sub>S), where the water molecules hydrogen-bonded are arranged in a rigid framework of cages. The interior of the water cages is occupied by the gas molecules that give the stability to the structure (Kvenvolden and Lorenson, 2001). Natural gas hydrates can have three possible structures: structure I (Figure 2.11G) and II, of the cubic crystallographic system, and structure H, of the hexagonal crystallographic system. The gas hydrate structure depends on the size of the guest gas molecules (Sloan, 1998).

Since 1810, with the discovery of chlorine hydrate by Sir Humphrey Davy, gas hydrates have been looked as a scientific curiosity, in which gas and water are transformed into a solid. Since 1934, with the recognition of the occurrence of gas hydrate plugs in pipelines, gas hydrates started to be looked as a hazard concern in the gas and oil industry. From the mid-1960s, with the discovery of natural gas hydrates in deep oceans, permafrost regions and also in extraterrestrial environments, gas hydrates started to be of increasing interest in the geosciences (Sloan, 1998). The first recognition of natural gas hydrates was in 1965 in the Siberian permafrost, northern Russia (Makogon *et al.*, 1971). On the seabed environment, gas hydrates were later inferred from pore water analysis during the DSDP Leg 11 drill in the Blake Ridge, in the early 1970s (Lancelot and Ewing, 1972). More discoveries were reported from the Black Sea (Yefremova and Zhizhchenko, 1974), from the Caspian Sea (Ginsburg and Soloviev, 1998), from the MacKenzie Delta and offshore Mexico (Shipley *et al.*, 1979; Shipley and Didyk, 1982). Since then, gas hydrates have been increasingly recognised in many offshore areas of both active and passive margins.

Natural gas hydrates can be formed and are stable in conditions illustrated in Figure 2.11H, which depend on the temperature, pressure, the chemistry (salinity) of the pore water and the composition of the guest gas molecules. Favourable conditions for the formation of natural gas hydrates occur over a greater part of the shallow subsurface of the Earth beneath the ocean at water depths exceeding about 500 m (shallower beneath colder Arctic seas) and on land beneath high-latitude permafrost. Gas hydrates will be present in such conditions only if there is adequate water within the sediments to form the host molecules, and the adequate supply of gas (in general methane). In the Arctic, gas hydrate occurrences are often associated with petroleum deposits, whereas at continental margins, where the greatest amounts of gas hydrate occur, the gas is mainly microbial in origin. The ocean margins are characterized by the greatest flux of organic carbon to the seafloor because of the high biologic productivity and the highest organic detritus accumulation from the continents. Furthermore, continental margins are characterized by high sedimentation rates that have the effect of covering and sealing the organic material preventing it from being oxidized. Lateral microbial degradation of the organic matter in the sediments produces methane which, if the pressure and temperature conditions are appropriated, will form gas hydrates.

### **2.5.2 Significance**

Natural gas hydrates (GHs) are of great importance and their formation/dissociation can constrain several sedimentological processes.

The dissociation of GHs can create overpressures in the sediments that can trigger landslides (Huhnerbach and Masson, 2004), blowouts, seafloor collapse events and seafloor mass movements that represent a potential geohazard for seafloor pipelines, oilrig anchors and other seafloor structures (Hovland and Gudmestad, 2001). The dissociation of GHs during drilling operations can cause sediment mobilization and represent also a safety hazard for seafloor and sub-seafloor operations. Moreover, GHs in sediments are sensitive to small temperature changes. A temperature increase of 1.0-1.5°C has the potential to cause gas hydrate (GH) dissociation. Small fluctuations in fluid flow were also recorded at the tidal frequency, indicating that very small perturbations in the ambient pressure conditions may lead to GH dissociation.

The proximity of the GH methane reservoir to the seafloor and its restricted thermodynamic stability domain has motivated large speculations about the release of methane in response to climatic changes (MacDonald, 1990). Increases of seabottom temperature (as result of regional oceanographic condition changes) and decreases in pressure (e.g. through sea level changes) can destabilize GHs, releasing methane into the near-surface environment and having an important impact on the carbon cycle (Buffett and Archer, 2004; Archer and Buffett, 2005). According to the “clathrate gun” hypothesis (Kennett *et al.*, 2003), episodic emissions of methane to the atmosphere (a powerful greenhouse gas), as a consequence of the destabilisation of GH reservoirs may have had significant impact on past climatic changes (Kennett *et al.*, 1996; Judd *et al.*, 1997; Kennett *et al.*, 2000; Judd *et al.*, 2002; Judd, 2003; Kennett *et al.*, 2003; Judd, 2004).

In particular sites, where GHs may occur in adequate concentrations, GHs may also be a significant energy resource as a hydrocarbon fuel. Mud volcanoes are one of these particular sites where GHs can occur in high concentrations.

Gas hydrates may also play an important role on the distribution of chemosynthetic communities (Carney, 1994), as revealed during the ODP Leg 164 at Blake Ridge where high bacterial activity were reported near the bottom simulating reflector (BSR) (Wellsbury *et al.*, 2000) demonstrating that the sediments near the BSR form a biogeochemical dynamic zone.

### **2.5.3 Detection**

While gas hydrates have been recovered and directly observed at the seafloor, they are generally identified in the marine environment through geochemical and geophysical (mainly seismic) indirect evidences.

The geochemical indicators consist of decreases of the interstitial water chlorinity values, stable isotopic  $^{18}\text{O}$ -enrichment of the pore waters, and salinity and temperature anomalies registered along gravity cores and boreholes (Hesse and Harrison, 1981; Davidson *et al.*, 1983; Hesse *et al.*, 2000; Hesse, 2003). During the crystallization of the hydrates, like in the formation of ice, salt ions are excluded from the solid structure and there is a preferential uptake of the heavy isotopes. During the retrieval of gas hydrate

bearing cores, the destabilization of the gas hydrates releases fresh water that produces the chlorinity and salinity anomalies associated with  $^{18}\text{O}$ -enrichment of the pore waters.

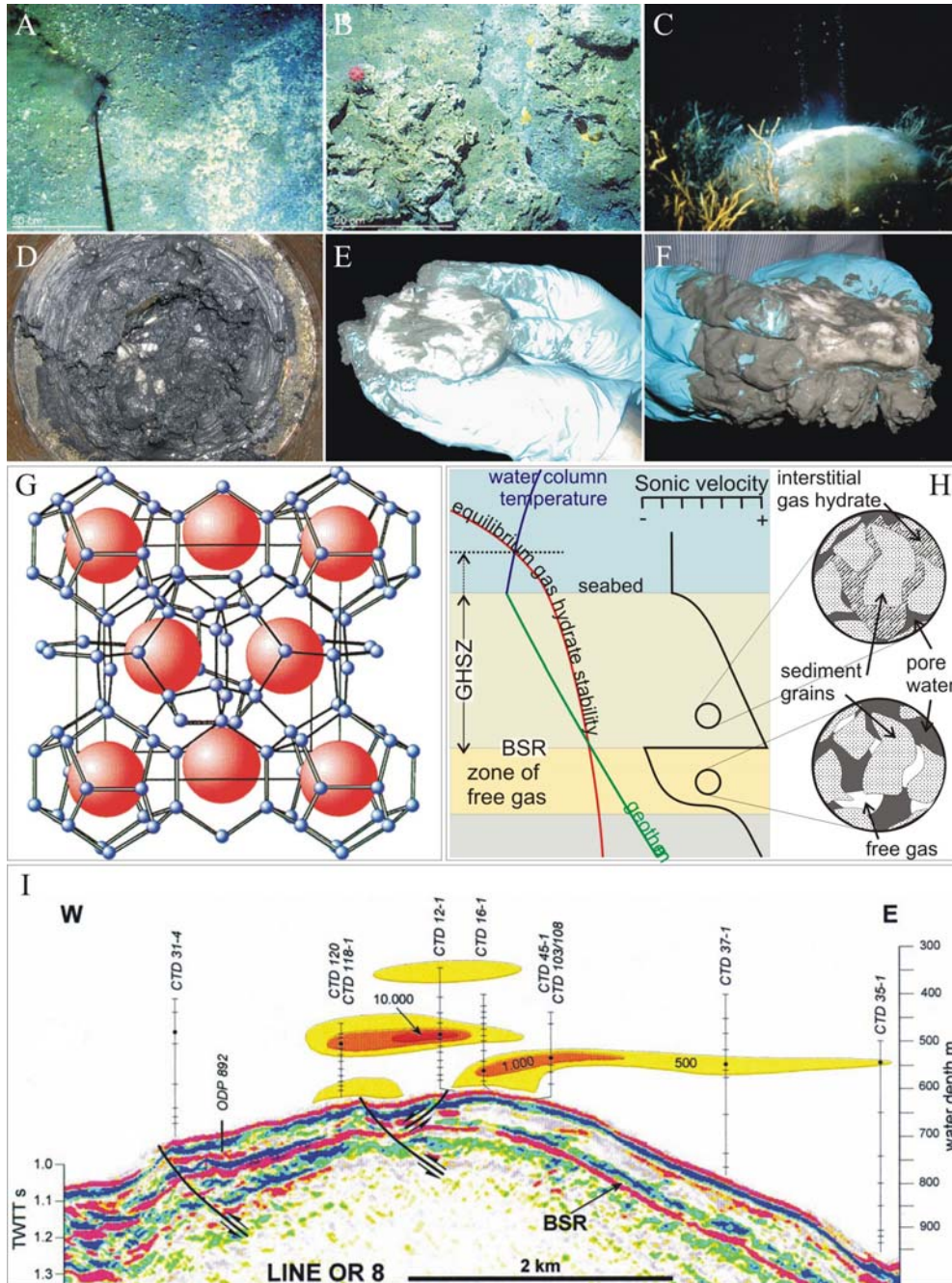


**Figure 2.11.** (A, B and C) Natural GHs occurrences at the seafloor, (A) and (B) from Cascadia margin (Suess *et al.*, 1999), (C) GH mound ~1.5 m across in 543 m water depth in central Gulf of Mexico (Sassen *et al.*, 2001). (D to F) GH samples collected from the Gulf of Mexico. (G) Schematic diagram of GH cubic crystalline structure I. (H) Scheme illustrating the conventional model for GH stability and bottom simulating reflectors in submarine sediments. The base of the hydrate stability is marked by a univariant phase boundary as temperature increases with depth. At this point methane in excess of solubility in pore water may exist as free gas and potentially produce a distinct seismic reflector due to the reduced velocity (Clennell *et al.*, 1999). (I) BSR seismic record over Cascadia Margin, also illustrating the methane plumes over the seepage area (Suess *et al.*, 1999).

Geophysical evidence of gas hydrates are the so called gas hydrate-related bottom-simulating reflectors (BSRs) detected with seismic reflection methods (Figure 2.11H and I). The BSR are a class of seismic reflectors that cross-cut sedimentary strata and that are generally related to processes that occur after the deposition of the sediments. The BSRs are caused by processes depending on sub-bottom depth, which in turn influences the pressure and the temperature within the sediments. A common BSR not related with GH is caused by the diagenetic transformation of opal A to opal CT and quartz. This process results in a positive acoustic impedance contrast between the silicate rich sediments with different diagenetic evolution stages (Kastner *et al.*, 1977). In the mid-Norwegian margin, a similar diagenetic-related BSR has been observed underneath the opal A to opal CT transition and interpreted as resulting from the diagenetic smectite to illite transformation or as resulting from an increase in the abundance of authigenic carbonates (Berndt *et al.*, 2004). These diagenetic-related BSRs have the same polarity as the seafloor reflection, a criteria that differentiates this class of BSRs from the gas hydrate-related BSRs.

The gas hydrate-related BSRs are formed as a consequence of the acoustic contrast between the relatively high velocity hydrate-charged sediments within the gas hydrate stability zone, below which is located a low velocity gas charged sediments, where free gas can occur underneath the gas hydrate stability zone (Singh *et al.*, 1993). The gas hydrate-related BSR corresponds to a reflection caused by these negative impedance contrasts (Pecher *et al.*, 1996). The gas hydrate-related BSRs present four main characteristics: (1) The depth of the BSR below the seafloor is more or less constant, indicating that the BSR is temperature dependent rather than pressure dependent; (2) the BSRs are anomalously high reflective events, indicating an abrupt change in the acoustic impedance, i.e., a strong contrast in density and/or sound velocity with depth; (3) the BSRs often cross-cut the lithological reflections, indicating that it is a diagenetic feature (fluid/gas), rather than related to changes in lithology; (4) the BSRs present a reverse acoustic polarity with respect to the seafloor reflection, indicating that the P waves are being reflected from a boundary with an negative impedance contrast, i.e., where in general the density is reduced and/or the sound velocity is reduced with depth. Sedimentary strata below the BSRs are usually more strongly defined i.e. enhanced, compared to those above, where the lithological layers are weakly reflective. This upper

zone is therefore referred to as *seismically transparent* or *blanking zone* and, it is suspected to be caused by hydrate cementation and its relatively high acoustic velocity.

Although the gas hydrate-related BSRs are widely interpreted as *in situ* gas hydrates indicators, they are not necessary and always adequate indicators of gas hydrates and their absence does not exclude the possibility to find gas hydrates. Some areas with gas hydrates do not have BSRs and in some areas drilling through BSRs failed to find gas hydrates. Off the coast of Norway, where drilling through BSRs had failed to find gas hydrates, it was proposed that the observed BSR represented a palaeo-BSR, and although the gases and gas hydrates may once have been present, they are no longer there in significant quantities, in spite of the fact that the diagenetic and consequently acoustic properties changes induced by the BSR are still present.

In conclusion, BSRs can be interpreted as representing a physicochemical and a biogeochemical intense reaction zone, where gas hydrates are formed above the BSR in the gas hydrate stability zone (GHSZ) and free gas occurs below it.

#### **2.5.4 Occurrences**

Natural gas hydrates occur worldwide in oceanic sediments of continental and insular slopes and rises of active and passive margins, in deep-water sediment of inland lakes and seas, and in polar sediment on both continents and continental shelves. Their occurrence is controlled by the conjugation of factors that include temperature, pressure and the composition of the gas and water (Kvenvolden, 1993). In marine sediments, gas hydrates are found where the water depths that exceed about 300 m and the bottom water temperatures approach 0° C, found at the seafloor down to sediment depths of about 1100 m. In polar continental regions of permafrost, gas hydrates can be present in sediments at depths between about 150 and 2000 m (Kvenvolden and Lorenson, 2000, 2001). As can be seen from Figure 2.12 and comparing it with the global occurrences of mud volcanism (Figure 2.4) and cold seeps (Figure 2.8), it is possible to conclude that many of these locations coincide, putting in evidence the interconnection between all the different fluid escape occurrences and manifestations.



that will input significant amount of carbon to the ocean/atmosphere, a process important enough to unbalance the carbon cycle. During the geological record this process is recognized as having a important role in the global carbon cycle and that could have triggered rapid climatic changes such as the intense global warming at the Paleocene/Eocene thermal maximum (PETM) (Schiermeier, 2003).

## 2.6 Associated ecosystems

Since their discovery, chemoautotrophic or methanotrophic-based communities associated with seafloor seepage have been found in various settings and appear to be common along continental margins. Chemosynthetic primary production forms the base of the hydrocarbon seep community food web. These comprise the sulphate-reducing bacteria, methanogens, methane and sulphide oxidizing bacteria.

The most characteristic and indicative seep biota consists of bacterial mats, pogonophorans (Figure 2.13A-C) and Vestimentifera tubeworms, mollusca modiolid mussels, lucinid and vesicomid clams (Figure 2.13D-F). Their presence indicates the expulsion of hydrocarbon-rich fluids. Certain types of bivalves are frequently used for the detection of active seepage sites by visual inspection due their large size, their light colour and their general high abundance and characteristics arrangements in clusters and alignments (Suess *et al.*, 1998).

Chemosynthetic endosymbioses occur ubiquitously at oxic-anoxic interfaces in marine environments. In these mutualisms, bacteria living directly within the cell of a eukaryotic host oxidize reduced chemicals (sulphur or methane), fuelling their own energetic and biosynthetic needs, in addition to those of their host (Stewart *et al.*, 2005). The oldest metazoans populated with microbes in vent settings are Silurian in age, as the metazoan fossils of seep deposits (Campbell, 2006).

The nutrition of the Vesicomidae clams and solemyids is based on the thiotrophic chemoautotrophy of the endosymbionts. Vestimentiferans and pogonophorans are also chemoautotrophic, with most species being thiotrophic, but some clear methanotrophic (Suess *et al.*, 1998). Stable isotopic compositions of tissues ( $\delta^{13}\text{C}$ ,  $\delta^{15}\text{N}$ ,  $\delta^{34}\text{S}$ ) are used as

indicators of the food source. Large depletions of  $\delta^{13}\text{C}$  (-30 to -70‰) in the tissues of organisms, such as vestimentiferans, bivalves and gastropods, have been proposed to indicate methanotrophy or sulphide oxidation by symbionts in seep and vent taxa (Levin, 2005). The carbon isotopic composition of soft tissues and chitinous hard parts of seep biota exhibit  $^{13}\text{C}$ -depleted stable isotopic compositions, reflecting thiotrophic and methanotrophic origin as the dominant carbon metabolizing pathway. For instance, the  $\delta^{13}\text{C}$  values of non calcareous parts of seep fauna from the Aleutian subduction zone range from -28.6‰ to -64.3‰ Pee Dee belemnite (PDB) (Suess *et al.*, 1998) and the chemosynthetic communities from the Florida Escarpment have  $\delta^{13}\text{C}$  values as low as -76.4‰ (Paull *et al.*, 1992). The carbonate shells also exhibit evidence for chemoautotrophic derived carbon. Usually the seep bivalve shells are only slightly depleted in  $\delta^{13}\text{C}$  because they preferably incorporate bicarbonate from seawater. The vesicomyid clams usually show complex cross-laminar layer structure with differential  $\delta^{13}\text{C}$  compositions that due to metabolic factor are more enriched in the inner lamellas. The solemyid shells in general present isotopically lighter carbonate than the carbonate of the vesicomyid clam shells. This is interpreted as consequence of the solemyids metabolism as they utilize a mixture of metabolic and bottom water  $\text{CO}_2$  in building their shells, probably because they live buried in the vent sediments and pump bottom water through their borrows (Suess *et al.*, 1998).

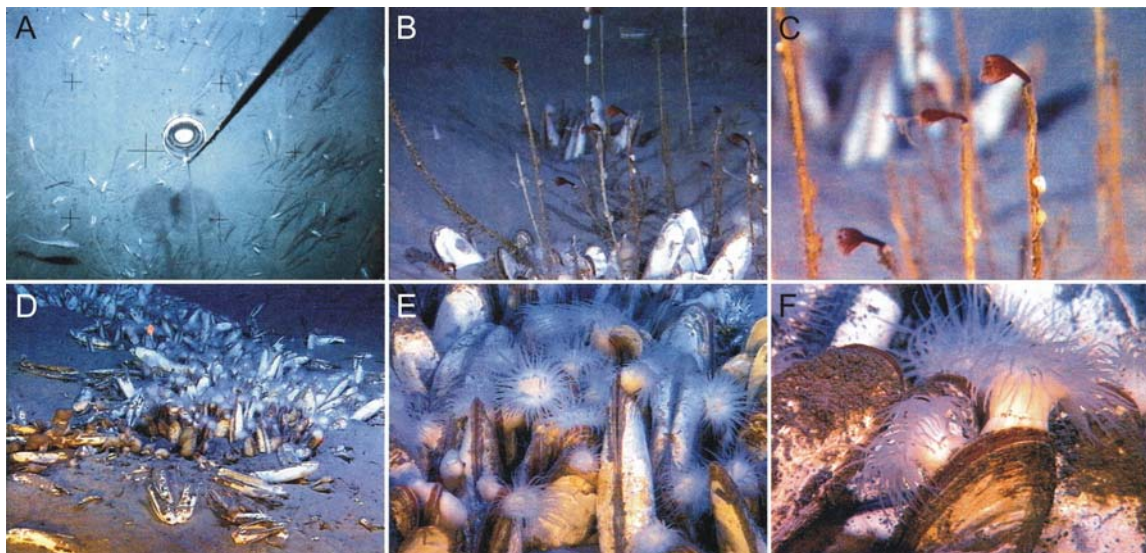


**Figure 2.13.** (A to F) Bottom photographs of cold seep fauna (Suess *et al.*, 1998). (A to C) Pogonophoran tubes amongst clam and gastropods. (B and C) detail of the pogonophorans. (D) cold seep community. (E and F) detail of vesicomyid clams.



## **Chapter 3. Geodynamic and oceanographic settings of the Gulf of Cadiz**

### **3.1 Plate tectonic setting**

The Gulf of Cadiz is located between the southern limit of the Iberia continental margin and the northern limit of the Africa Atlantic margin. The regional geodynamic setting in the Gulf of Cadiz is dominated by the slow convergence of about 4 mm/year between the African and the Eurasian plates (Argus *et al.*, 1989).

The boundary between the Eurasia and the Africa tectonic plates (Figure 3.1) extends from the Azores archipelago, in the West, across the Gibraltar area in the Gulf of Cadiz, and to the East through the Alboran Sea, into the Mediterranean region in the north of Morocco, Algeria and Tunisia (Bufo *et al.*, 1995). This plate boundary has a complex nature due to its proximity to the pole of rotation of the African plate (Bufo *et al.*, 2004a; Bufo *et al.*, 2004b). The Atlantic sector of the Azores-Gibraltar Plate Boundary (AGPB) has a variable stress pattern along its length. In the western sector, from the Mid-Atlantic Ridge until 25°W, the Azores plateau (Figure 3.1), it is characterized by a divergent behaviour with crustal extension and normal faulting (Jiménez-Munt *et al.*, 2001). In the central sector, the Gloria fault, between 25° and 15°W, the boundary has a transcurrent motion with dextral strike-slip faulting (Jiménez-Munt *et al.*, 2001). The eastern sector, delimited from the Gloria Fault by the Tore-Madeira Ridge, is composed of two distinct regions: the Gorringe Bank region, that has oceanic affinities (Sartori *et al.*, 1994); and the Gulf of Cadiz region, more likely of continental nature. Both regions of this AGPL sector are characterised by a general NW-directed compressive behaviour with plate convergence and reverse faulting (Tortella *et al.*, 1997) with a transpressional regime in the Gulf of Cadiz. This sector of the AGPL is more complex than the ones to the west and neither the plate limits nor the lithosphere structure are yet well constrained (Sartori *et al.*, 1994).

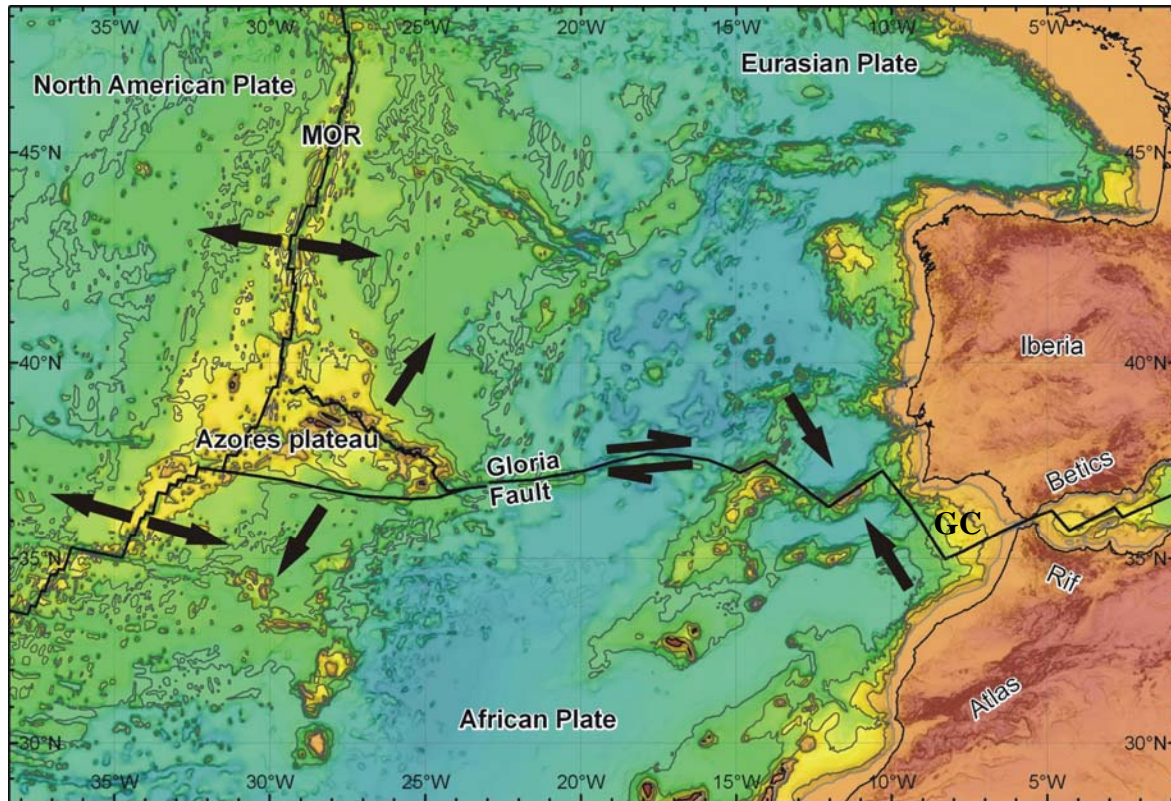


**Figure 3.1.** Atlantic Africa-Eurasia plate boundary with the present day stress fields. Plate boundary adapted from Coffin *et al.* (2000) and relative movements from Jiménez-Munt *et al.* (2001). The Gulf of Cadiz location is shown by the letters: GC.

The main regional features in the Gulf of Cadiz are related with the Rif-Betic mountain belt, with westward directed thrusting (Maldonado *et al.*, 1999), that establishes the eastern limit of the Azores-Gibraltar transform. The arcuate mountain belt of the Rif-Betic surrounds a zone of strong Neogene subsidence and crustal thinning in the Western Alboran Sea.

In the Gulf of Cadiz, the Eurasia-Africa boundary or, more precisely, the Iberia-Africa (Nubia) boundary, corresponds to a NNW-SSE directed continental-continental collisional setting, with a slow convergence of 2 to 4 mm/year (Argus *et al.*, 1989; Sartori *et al.*, 1994), and with a diffuse nature (Jiménez-Munt *et al.*, 2001). The deformation is expressed by a large number of lithospheric blocks delimited by deep accidents with variable main orientations: E-W to ENE-WSW; NW-SE; and NE-SW (Cabral, 1995). The complex interaction of these microplates is expressed by a diffuse seismicity in the Gulf of Cadiz and Gibraltar region (Jiménez-Munt *et al.*, 2001) with superficial epicentres and with important intermediate-depth epicentres (Figure 3.4). The focal mechanisms indicate

predominantly inverse fault systems and oblique NW-SE convergence (Grimison and Chen, 1986; Buforn *et al.*, 1995).

The Gulf of Cadiz area comprises the ocean-continent boundaries of the African and Iberian plates. The exact location of the continental-ocean boundary is not exactly known but it is accepted that most of the Gulf of Cadiz basement is continental crust that thins to the west and oceanic crust is probably found at the Gorringe Bank, Horseshoe and Seine Abyssal Plains (Gonzalez-Fernandez *et al.*, 2001).

Several tectonic models have been proposed to explain the different geologic characteristics of the Gulf of Cadiz. Subduction models involving either: a southward-dip (Sanz de Galdeano, 1990; Morales *et al.*, 1999), a northward-dip (Torres-Roldan *et al.*, 1986), an eastward-dip (Royden, 1993; Lonergan and White, 1997; Gutscher *et al.*, 2002; Gutscher *et al.*, 2006; Thiebot and Gutscher, 2006), and a westward-dip (Docherty and Banda, 1995) have been proposed. Maldonado *et al.* (1999) propose the subduction of intermediate-type crust from the Iberian margin under the Alboran microplate in a western Alboran subduction zone with subsequent deformation of the lower plate in the form of crustal slices. Alternatively, Sartori *et al.* (1994) proposed that the tectonic stress from the Iberia-Africa convergence was released across a 200 km long area between the Seine Abyssal plain and the Gorringe Bank, without a defined plate margin and without any subduction been developed in the area.

While both tectonic regimes: subduction and distributed compression deformation, have not been demonstrated and strong debate is still going on, the Gutscher *et al.* (2002) (active) subduction model proposes the Gulf of Cadiz as an (active) accretionary wedge resulting from the east dipping subduction zone beneath the Gibraltar Arc and the Alboran domain. This subduction would be the result of slab rollback towards the west causing extension and subsidence in the Alboran domain and westward advance of the Gibraltar Arc resulting in compressional deformation of the Gulf of Cadiz accretionary wedge. This model is based on the tomography data that images a slab of cold and dense material, interpreted as oceanic lithosphere, dipping from the Atlantic domain of the Gulf of Cadiz, passing through intermediate depths (60-120 km) beneath the westernmost Alboran Sea (region dominated by intermediate depth seismicity) and that is proposed to merge with a region of deep-focus earthquakes (600-660 km) below Granada, Spain (Figure 3.2). The observation of active thrust faults dipping to the east, above an east dipping decollement

and an eastern dipping basement (Figure 3.3) is interpreted as indicating an active accretionary wedge in the Gulf of Cadiz region supporting the tectonic model of Gutscher (2002).

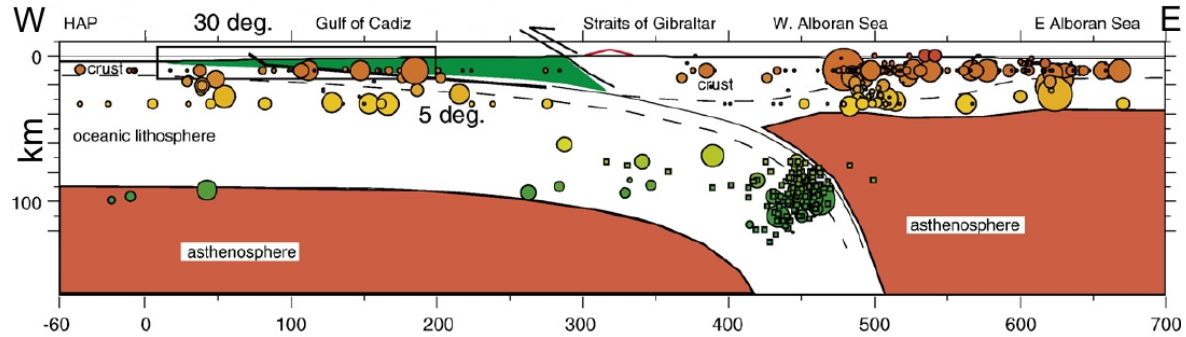


**Figure 3.2.** Simplified lithospheric cross-section with a W-E direction crossing the Gulf of Cadiz at the Gibraltar Strait (36°N) showing the geometry of the east dipping fault plane between the subducting slab and the upper plate (Gibraltar block) with the distribution of earthquake hypocenters. Box on the Gulf of Cadiz shows the location of the simplified line draw of Sismar seismic profile 16 interpretations presented in Figure 3.3 (Gutscher *et al.*, 2002; Thiebot and Gutscher, 2006).

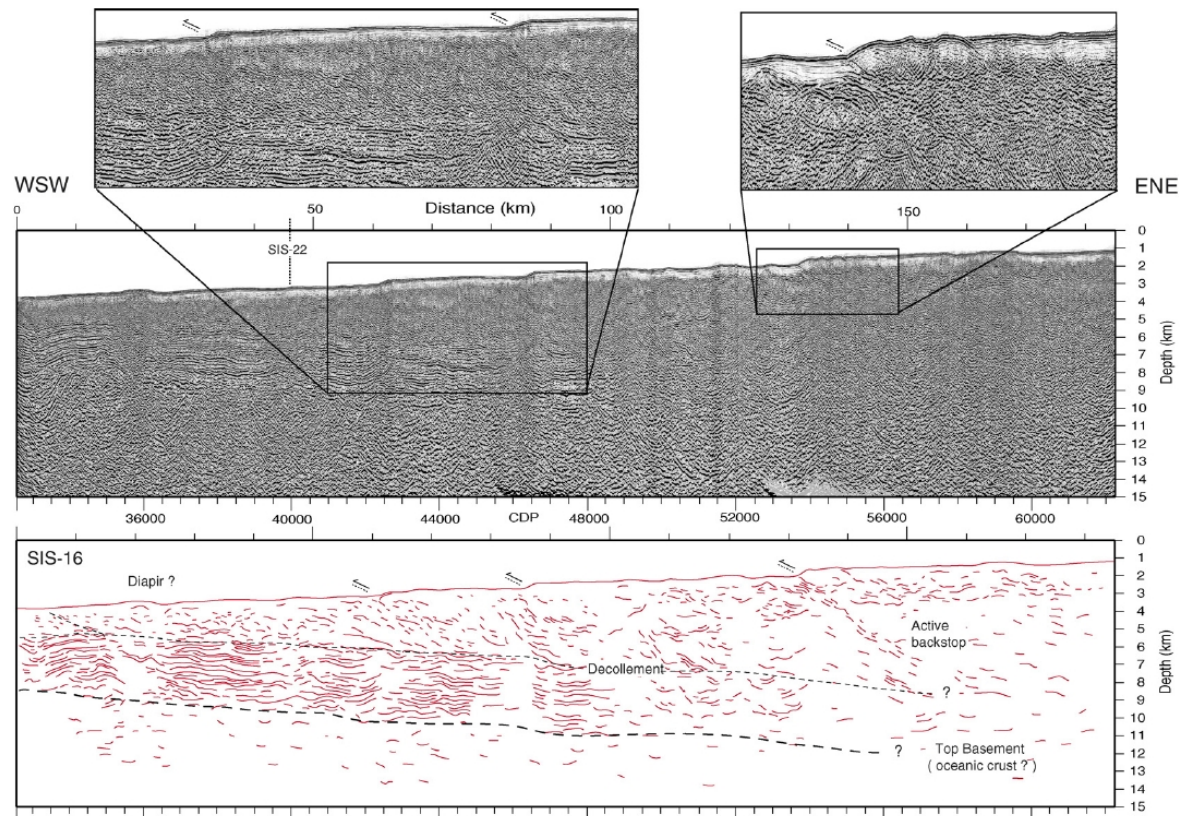


**Figure 3.3.** Multichannel Sismar seismic profile 16 and interpretation, showing the E-dipping decollement, E-dipping thrusts and the general westward verging tectonic shortening of the area. Upper panels show zooms of ramp thrusts emerging at the seafloor and the basal un-deformed strata beneath the decollement (Thiebot and Gutscher, 2006).

### 3.2 Seismicity (present day stress pattern and tectonic regime)

The seismicity distribution can be used to constrain the Africa-Eurasia plate boundary. The main characteristic of the distribution of the epicentres in the Gulf of Cadiz is the asymmetry between the North and South margins. The seismicity is clearly concentrated in the Iberia margin (between the latitude 36° and 37°N) while along the Moroccan margin the seismicity is found on the Rif, including the Larache area, but out of this domain the seismicity is very scarce (Figure 3.4). This indicates that the deformation caused by the present day active collision between Africa (Nubia) and Iberia is being concentrated on the northern sector of the Gulf of Cadiz where most probably the plate boundary is located.

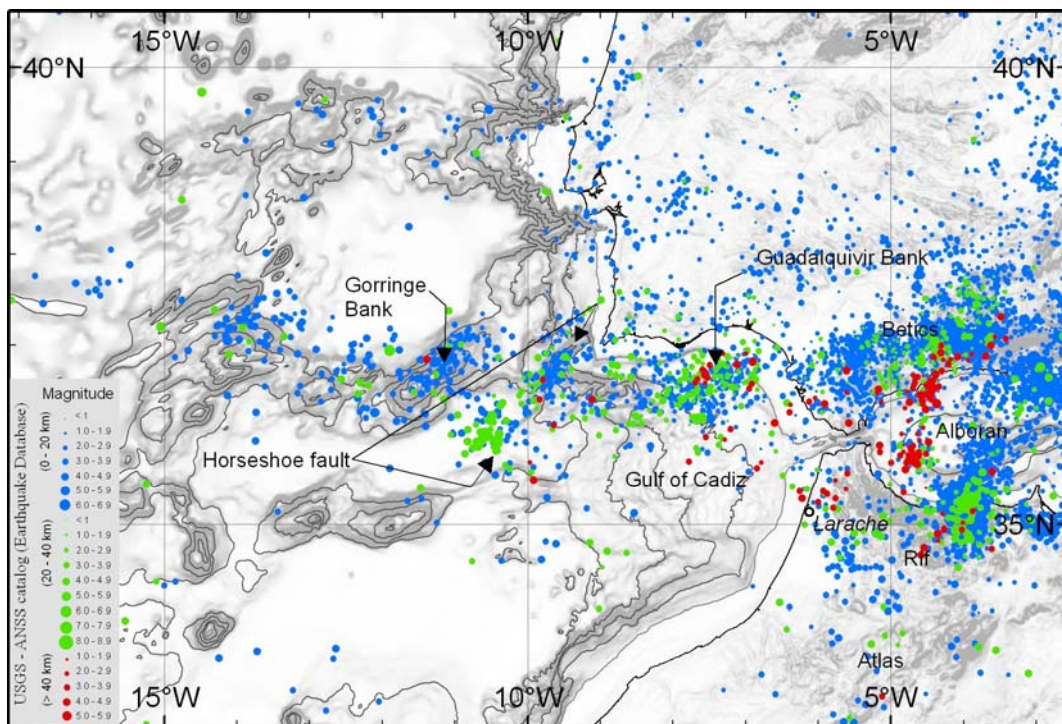


**Figure 3.4.** Distribution of the epicentres between 1963 and 2006 (magnitude > 0.1) taken from the USGE-ANSS catalogue. Shallow earthquakes (depth < 20 km) are represented in blue, intermediate earthquakes (20 < depth < 40 km) are represented in green and deep earthquakes (depth > 40 km) are represented in red. The size of the points is proportional to the magnitude of the earthquake according to the scale.

In the area of the Gulf of Cadiz the distribution of the epicentres shows a complex behaviour, with shallow (depth < 20 km) earthquakes showing a diffuse distribution but where some clusters can be identified. These clusters seem to correlate with main

topographic and structural highs, such as the Gorringe Bank with a NE-SW orientation, the Guadalquivir Bank, where the epicentres are scattered but the general orientation NE-SW is still possible to be identified; clusters of the epicentres are also found located along some faults as the Horseshoe fault also with the NE-SW trend (Figure 3.4). The distribution of the intermediate depth (between 20 and 40 km) and the deep epicentres show a similar pattern (Vázquez *et al.*, 2000; Vázquez *et al.*, 2003). The location of the epicentres in this location are in agreement with the main tectonic trend described for this area (Torelli *et al.*, 1997; Hayward *et al.*, 1999; Maldonado *et al.*, 1999). The seismicity also shows conspicuous evidences of particular lineaments with a NW-SE direction or with the NE-SW direction (Figure 3.4). Some of those lineaments on the seismicity can be correlated with tectonic lineaments that correspond to the limits and the direction of some of the channels and ridges recognised on the bathymetry and on the side-scan sonar imagery.

### **3.3 Geodynamic evolution of the study area**

The geodynamic evolution of the Gulf of Cadiz involved multiphase extensional and compressional episodes, the last of which is related with the development of the Gibraltar Arc associated with the termination of the Betic-Rif orogen, in the W sector of the Mediterranean Alpine belt (Roberts, 1970).

#### **3.3.1 Mesozoic**

During the Mesozoic, from the Permo-Triassic, the geodynamic evolution of the South Iberia margin, as a passive margin, was related with a generalized period of extension, related with the break-up of the Pangaea and the opening of the central and north Atlantic ocean. During the Triassic and Jurassic pre-rift and rift phases, a regional oblique extension and rifting, with sinistral strike-slip motion characterized the South Iberia margin (García-Dueñas *et al.*, 1994; Tortella *et al.*, 1997). As result of this extensive phase, during the Late Jurassic and Early Cretaceous (see Figure 3.5A) this area acted as a continental passive margin (Mauffret *et al.*, 1989). During the Late Cretaceous the area start to change to a compressive setting associated with the convergence of Iberia with Africa (Rosenbaum *et al.*, 2002).

### **3.3.2 Cenozoic**

During the Cenozoic the South Iberia margin was in a compressive setting with N-S convergence resultant from the rotation of Africa (Srivastava *et al.*, 1990). From this phase resulted subduction processes with the closure of the Tethys, subsequent continental collision and lithospheric deformation started to develop (Rosenbaum *et al.*, 2002). At the meridional Iberia Margin, this process resulted in the formation of the Rif-Betics orogenic belt, that defines the western domain of the Alpine orogen (Roberts, 1970).

#### **3.3.2.1 Paleogene**

During the Late Cretaceous to the Middle Eocene, Iberia and Africa behave as a solid plate. During the Late Eocene and Early Oligocene, Iberia became again independent from the Africa plate and at the beginning of the Oligocene the area south Iberia margin goes through a new compressive phase as result of the Euroasiatic-Africa plates convergence (Srivastava *et al.*, 1990), as illustrated in Figure 3.6A-B. At this time the boundary of the two plates is defined by the Azores-Gibraltar Fracture Zone with characteristics very similar to the present day.

#### **3.3.2.2 Neogene**

During the Neogene three different phases can be defined in the geodynamic evolution of the Gulf of Cadiz. The first phase corresponds to the last phase of the Rif-Betic orogen during the Early and Middle Miocene. The second phase, in the Late Miocene and Pliocene, is characterized by subsidence and extensional regime in the area, with the formation of normal faults with a NNE-SSW direction. The last phase, in the Quaternary is characterized by an inversion of the tectonic regime that became compressive.

##### **3.3.2.2.1 *Early and Middle Miocene***

During the Early Miocene the area goes under a compressive regime with the beginning of the formation of the Betic orogen (Figure 3.5B and Figure 3.6B). The Iberia-Africa compression is along a NNW-SSE direction (Srivastava *et al.*, 1990). This compressive regime resulted in a convergence of more than 200 km in an N-S direction since the Oligocene to the Late Miocene, resulting in the complete closure of the Tethys and the displacement of the Gibraltar Arc to the West (Dewey *et al.*, 1989), and the development of the Alboran micro-plate to the East (Figure 3.6B-H).

As result of this westward migration of the Gibraltar arc front, the instability of the continental shelf was promoted and the emplacement of chaotic bodies occurred during the Miocene, the so called olistostrome, (Tortella *et al.*, 1997). The emplacement of the chaotic bodies was also promoted by the development, during his emplacement, of trusts in its front and extensional structures in its back, as a result of fast subsidence in the basin (Maldonado and Nelson, 1999).

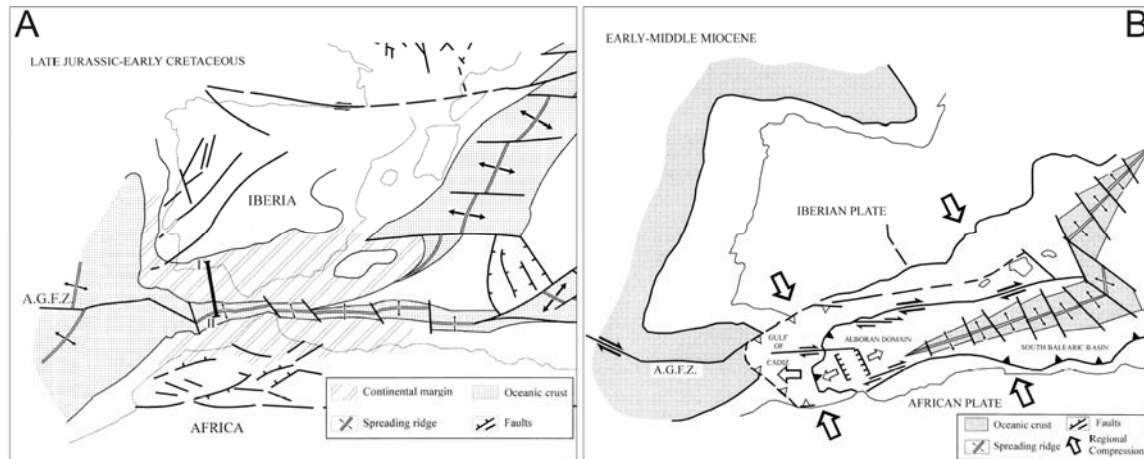


**Figure 3.5.** (A) Simplified geological setting of the Gulf of Cadiz during the Late Jurassic and Early Cretaceous (Maldonado and Nelson, 1999). (B) Simplified geological sketch of the Gulf of Cadiz and surrounding domains during the early part of the Middle Miocene (Maldonado and Nelson, 1999). The present shorelines of southern Europe and Africa are outlined for reference. AGFZ: Azores-Gibraltar Fracture Zone.

### 3.3.2.2 Late Miocene and Pliocene

During the Early and Middle Miocene the connection between the Atlantic and the Alboran domain (Figure 3.6C-F) was established through the Guadalquivir basin north of the Betic range and through the Guercif, South of the Rif (Mulder and Parry, 1977). The migration to the West of the Alboran domain resulted in the closure of these connections that can be associated with a period of low sealevel stand and resulted in the closure of the connection of the Mediterranean Sea with the Atlantic (Haq *et al.*, 1987), leading to the desiccation of the Mediterranean, between 5.96 and 5.33 Ma (Figure 3.6H): the so-called Messinian salinity crisis (Krijgsman *et al.*, 1999).

During the Early Pliocene, the tectonic regime became transtensional resulting in local extension in the area, and leading to the opening of the Gibraltar strait, re-establishing the connection between the Atlantic and the Mediterranean (Figure 3.7A).

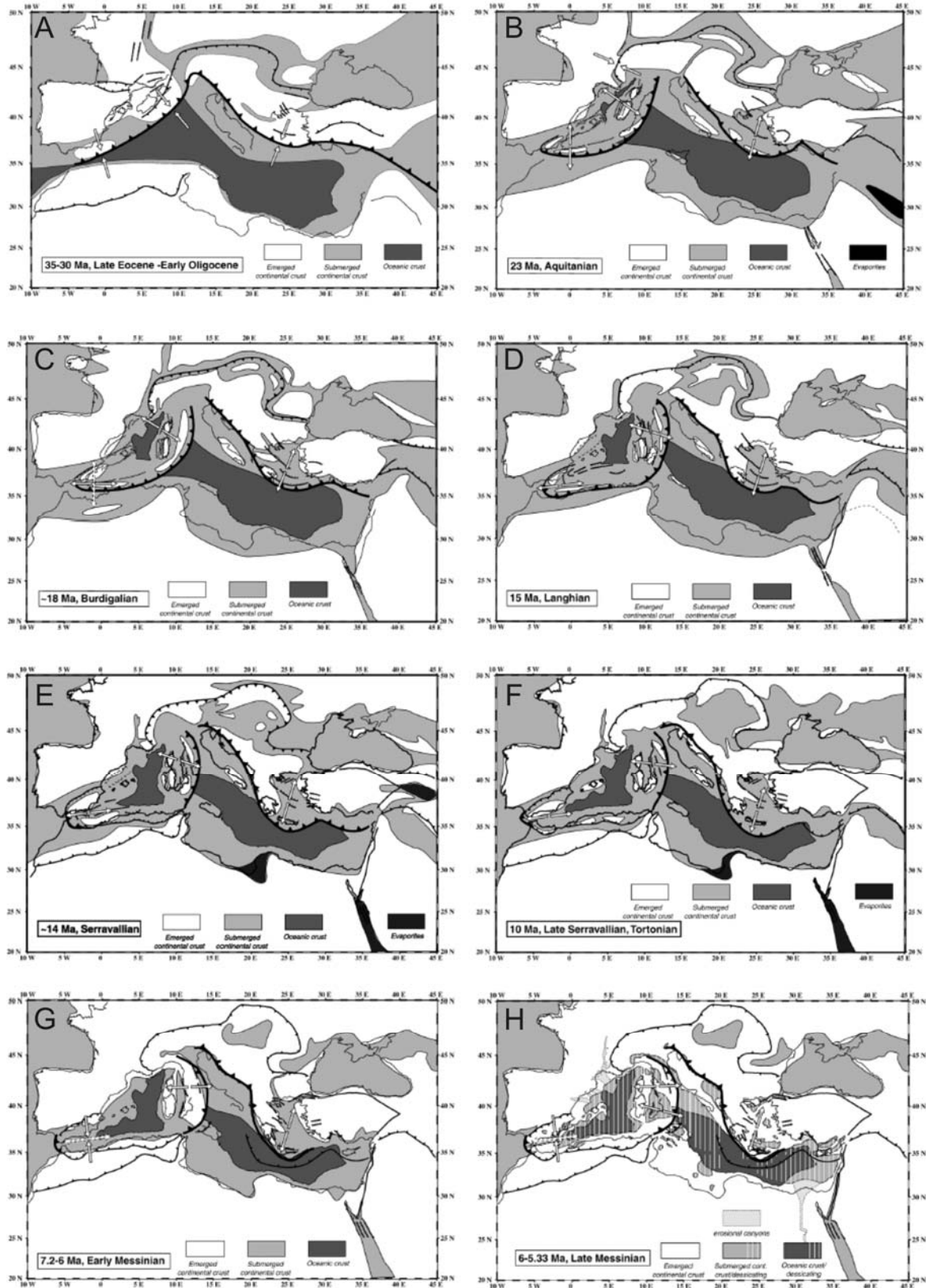


**Figure 3.6.** Paleogeographic and geodynamic evolution of the Mediterranean region and the Gulf of Cadiz (Jolivet *et al.*, 2006). To be noted that the oceanic crust is shown only in the Mediterranean domain, not in the Atlantic Ocean and Black Sea.

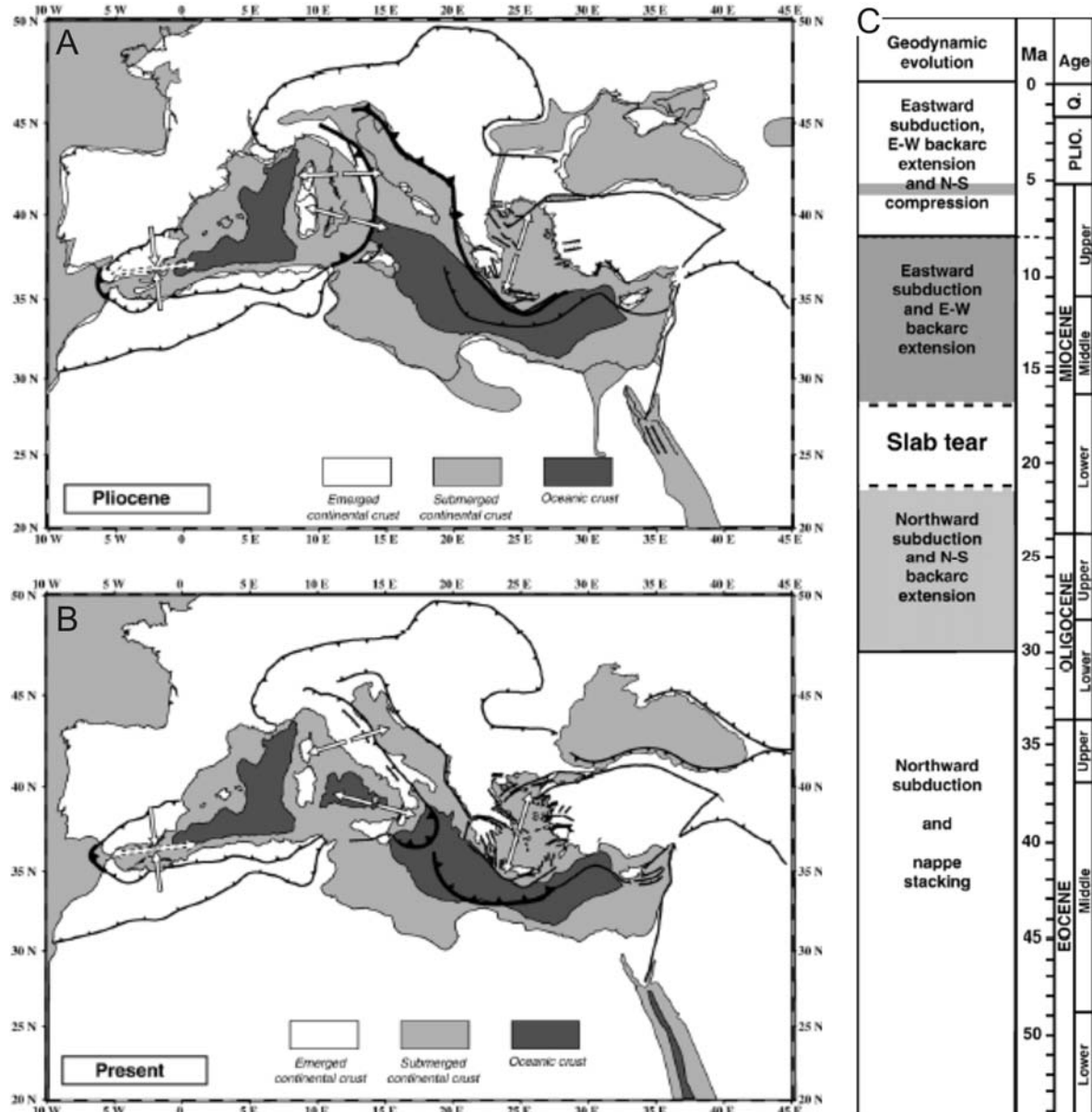


**Figure 3.7.** Paleogeographic and geodynamic evolution of the Mediterranean region and the Gulf of Cadiz from the Pliocene to Present day conditions and the timing of the main geodynamic events, as described in the text (Jolivet *et al.*, 2006).

### 3.3.2.3 Quaternary

Since the Late Pliocene, the tectonic regime in the Gulf of Cadiz becomes transpressive, with major compression with NNW-SSE direction (Maldonado *et al.*, 1999), and the regional geodynamic setting became dominated by the slow convergence of about 4 mm/year between Africa and Iberia (Figure 3.7A-B).

### **3.4 Different geological domains in the Gulf of Cadiz**

Several geologic domains can be defined in the Gulf of Cadiz. These domains include, from the Gibraltar strait towards the abyssal plains: the Flysh domain, the Sub-Betics, the Cadiz Basin, the allocthonous units, and the accretionary wedge (Figure 3.8).

#### **3.4.1 Flysch domain**

The Flysch domain occurs both on land and offshore and corresponds to the SE sector of the Iberia margin and the NW sector of the Moroccan margin (Figure 3.8) located close to and in the Strait of Gibraltar. It is composed of siliciclastic deposits, mostly turbidites of Cretaceous to Miocene age, indicating deep deposition in a trough located between the Iberian margin and the Alboran domain, later translated and incorporated into the Gibraltar Arc. This domain is delimited to the W by a major thrust with an arcuate shape, indicating displacement to the NW and overthrusting of the sub-Betic domain (Puga, 2004). This thrust can be mapped offshore and onshore in southern Spain and in northern Morocco.

#### **3.4.2 Sub-Betic domain**

The sub-Betic domain is located externally around the Flysch domain. Its front is delimited by a major thrust that defines the arcuate shape of this domain. It corresponds to the external domain of the Rif-Betics orogen. This domain consists of Triassic to lower Miocene deposits that represents the south Iberian Mesozoic paleo-margin, later incorporated into the Rif-Betic orogen.

#### **3.4.3 Cadiz Basin**

This domain is located in front and externally to the sub-Betic domain. This domain is characterized by the infilling of the depocenters along the NE-SW direction of the trusts from the sub-Betic domain. This domain is filled by deposits of the Neogene, corresponding to the infilling by sediments from the main emerged areas. The Cadiz basin developed during the Early Miocene and the oldest deposits are deformed and overlain by the emplacement of the Allocthonous Unit of the Guadalquivir (Puga, 2004) marking therefore the age of the emplacement of the first allocthonous units.

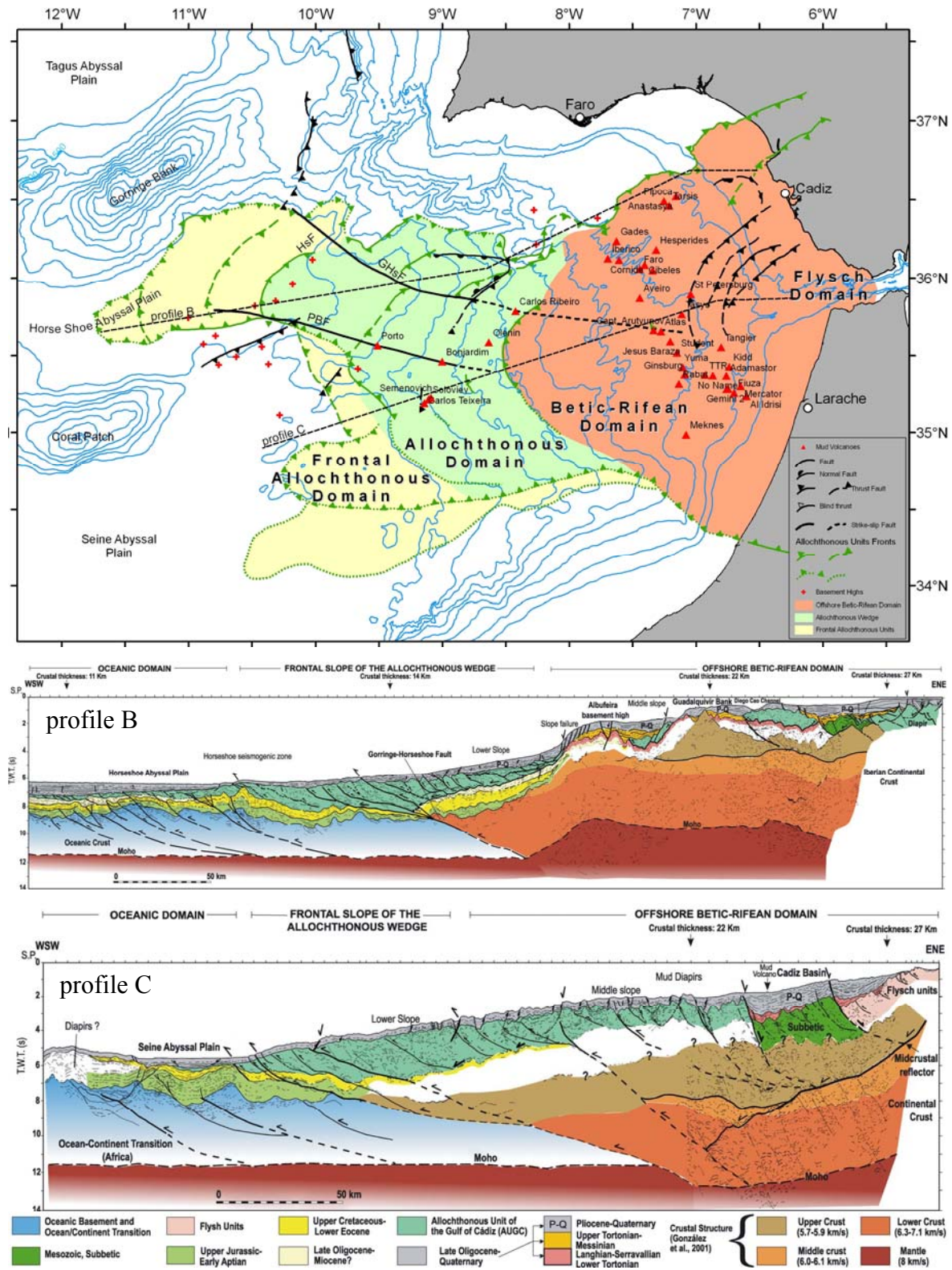


**Figure 3.8.** Different geologic domains in the Gulf of Cadiz as defined by Somoza *et al.* (1999) and Medialdea *et al.* (2004). (A) map modified from Medialdea *et al.* (2004) and from Hensen *et al.* (in press). (B-C) cross sections long the Gulf of Cadiz (Medialdea *et al.*, 2004). Location of profiles in given on the map in (A).

The basin has a maximum width of 35 km and a rectangular geometry. The NE limit is subdivided by three main diapiric ridges that subdivide the basin into several sub-basins located between the diapiric ridges. In general the direction of these basins coincides with the direction of the main Cadiz basin.

On the seismic profiles, these basins have up to 1.7 s (TWT) in thicknesses, an asymmetric geometry and they have been deformed by the diapiric emplacements during the Pliocene and the Quaternary.

#### **3.4.4 Allochthonous units (Olistostrome/Accretionary wedge)**

The allochthonous deposits in the Gulf of Cadiz (the so-called Olistostrome, chaotic body, Guadalquivir allochthon, Guadalquivir accretionary wedge or melange of the Gulf of Cadiz), recognized onland and offshore (Roberts, 1970), have been interpreted as resulting from gravitational processes, debris-flow mechanisms, diapirism and tectonic melanges. Medialdea *et al.* (2004) defined three different domains of the allochthonous units, based on their seismic architecture, the main tectonic features and the nature of the basement (oceanic or continental), corresponding to different evolutionary steps in the mechanisms of emplacement of the allochthonous units.

The eastern domain extends along the continental shelf and upper and middle slope and corresponds to the offshore extension of the Betic–Rifean external front. This domain was emplaced as part of the pre-Messinian orogenic wedge related to the collision that gave rise to the Betic–Rifean belt by a combined gravitational and tectonic mechanism. It is characterized by salt and shale nappes later affected by extensional collapses.

The central domain develops along the lower slope between the Betic–Rifean front and the abyssal plains and is characterized by a change in dip of the allochthonous basal surface and the basement. The northern boundary of this domain is marked by the occurrence of a major WNW–ESE-trending thrust fault with a strike-slip component, known as the Gorringer–Horseshoe fault (Medialdea *et al.*, 2004).

The westernmost domain corresponds to the abyssal plains, where the distal emplacement of the allochthonous body takes place; it is characterized by thrust faults affecting both the sedimentary cover and the possible oceanic basement. The allochthonous units of the central and western domains were emplaced after the emplacement of the

eastern domain, as a consequence of the Iberia-Africa NE–SW compression since the Late Miocene until present.

### **3.4.5 Plio-Quaternary morpho-sedimentary domains**

Since the Late Pliocene until present the tectonic setting in the Gulf of Cadiz became mainly transpressive with the main compression in the NNW-SSE direction (Maldonado *et al.*, 1999). The Quaternary sediment cover of the Gulf of Cadiz was conditioned by the sealevel fluctuations with the deposition of thick terrigenous deposits originated from the Guadalquivir and Guadiana rivers which on the continental shelf form progradant wedges toward the shelf edge. The northern margin of the Gulf of Cadiz is characterized by an active compressive framework where the allochthonous units provide an unstable basement for Late Miocene, Pliocene and Quaternary sedimentation. The Quaternary sedimentation in the Gulf of Cadiz is a combination of a contourite-turbidite system with combined drift-fan morphologies. The presence of a high density of canyons (St. Vicente, Aljesur, Lagos, Portimão and Faro Canyons and the Guadalquivir and Cadiz Channels) in the western part of the South Portuguese margin that drain sediment directly to the Horseshoe Abyssal Plain resulted in the turbiditic sedimentation of the Abyssal plain with slump debris flow deposits along this part of the margin. The middle slope is dominated by along-slope processes driven by the Mediterranean Outflow water (MO) that during the Pliocene and the Quaternary produced the edification of a complex contourite depositional system (Mougenot and Vanney, 1982; Faugères *et al.*, 1984; Nelson *et al.*, 1993; Hernandez-Molina *et al.*, 2003). This contourite system is composed of both depositional and erosive features (Figure 3.9). The main depositional features are composed of sedimentary wave fields, sedimentary lobes, mixed drifts, plastered drifts, elongated mounded, separated drifts and sheeted drifts. The main erosive features of the contourite system are the contourite channels, furrows, marginal valleys and moats (Llave *et al.*, 2001; Hernandez-Molina *et al.*, 2003; Hernández-Molina *et al.*, 2006; Llave *et al.*, 2006). The development of this contourite system is controlled by the Pliocene and Quaternary environmental and paleoceanographic changes and by the morphology of the margin. The lower slope with an irregular morphology and the Abyssal plains are dominated by down-slope depositional processes. A present day morphosedimentary characterization of the Gulf of Cadiz is presented in Figure 3.9.

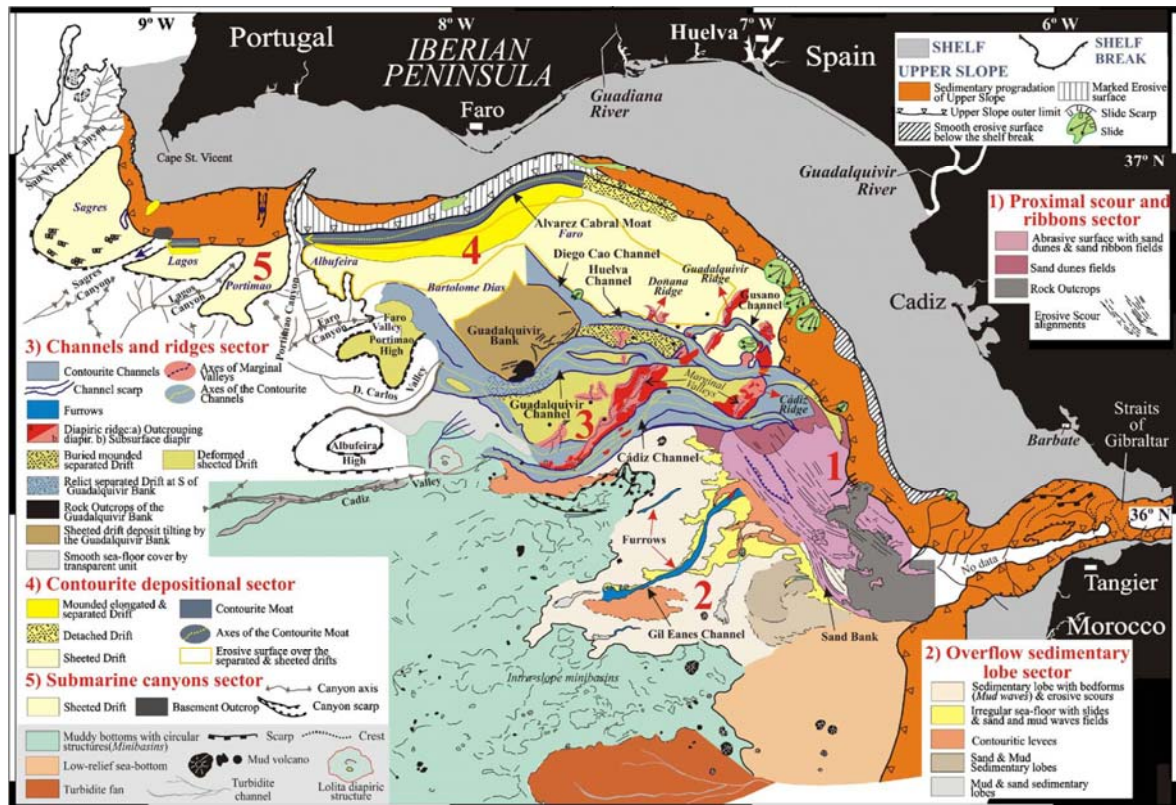


**Figure 3.9.** Morphosedimentary map of the Contourite Depositional System on the middle slope of the Gulf of Cadiz (Hernández-Molina *et al.*, 2006). Morphosedimentary sectors: (1) proximal scour and sand ribbons sector; (2) overflow sedimentary lobe sector; (3) channels and ridges sector; (4) contourite depositional sector; and (5) submarine canyon sector.

### 3.5 Oceanographic setting and the Mediterranean Outflow

#### 3.5.1 Present day oceanographic setting

The present day circulation patterns and the hydrographical conditions in the Gulf of Cadiz are dominated by the exchange of water masses through the Strait of Gibraltar. The Atlantic Ocean at the latitude of the Gulf of Cadiz and off Iberia is characterized by four main water masses:

(~100-600 m depth) The Eastern North Atlantic Central Water (Fiuza, 1984) is represented by the descending branch of the Gulf Stream.

(~600 to 1400 m depth) The Mediterranean Water (MW) that corresponds to the Western Mediterranean Intermediate and Bottom Waters characterized by high salinity, relatively high temperature and reduced concentration of dissolved oxygen.

(2000 to 4000 m) The North Atlantic Deep Water

(>4000 m) The Antarctic Bottom Water

A regional subdivision of these water masses into four layers can be established and to each of these layers corresponds a particular transport direction.

In the ocean surface, two sub-layers can be defined: the mixture layer or the thermocline layer, which is the superficial layer (0-100 m), under direct influence of the atmosphere dynamics and that shows considerable seasonal variability. Above the thermocline layer that corresponds to the Eastern North Atlantic Water (Fiuza, 1984).

Bellow the Eastern North Atlantic Water is located under the Eastern North Atlantic Central Water (ENACW) and presents in the eastern sector of the North Atlantic two main components (Figure 3.10), with distinctive origins, that split at a latitude of about 40°N (Fiuza, 1984). A water mass with a setentrional subpolar source, the Eastern North Atlantic Central Water subpolar (ENACWp), formed by cold convection of deep water at the north and northwest of the Iberian Peninsula. The second component of the ENACW has a subtropical origin and is therefore called the Eastern North Atlantic Central Water subtropical (ENACWt). The ENACWt is the central water at the SW and S Portuguese margins, in the Gulf of Cadiz and in the Atlantic Moroccan margin. In the Gulf of Cadiz, this segment of the ENACWt is characterized by temperature values that range from 8 to 18°C and salinities between 32.2 and 36.7 (Emery and Meincke, 1986). The ENACWt is described as moving at intermediate depths under the Azores current and circulates in the Gulf of Cadiz between 100 and 850 m (Fiuza, 1984; Fiuza *et al.*, 1998) but its velocity is considered to be significant only bellow depths of about 500 m, under the surface layer characterized by a strong seasonal variation (Fiuza, 1984).

The hydrology, morphology and the sedimentary dynamics of the Gulf of Cadiz are intensely modulated by the intermediate water mass of the Mediterranean Water (MW). The MW is characterized by temperatures of about 13°C, high salinities (~36.5), and an oxygen content of about 176  $\mu\text{mol kg}^{-1}$  (Madelain, 1970; Ambar and Howe, 1979a; Ambar *et al.*, 2002). The MW that outflows into the Gulf of Cadiz is composed mainly (about

90%) by the Levantine Intermediate Water and by the Western Mediterranean Deep Water (Bryden and Stommel, 1984).

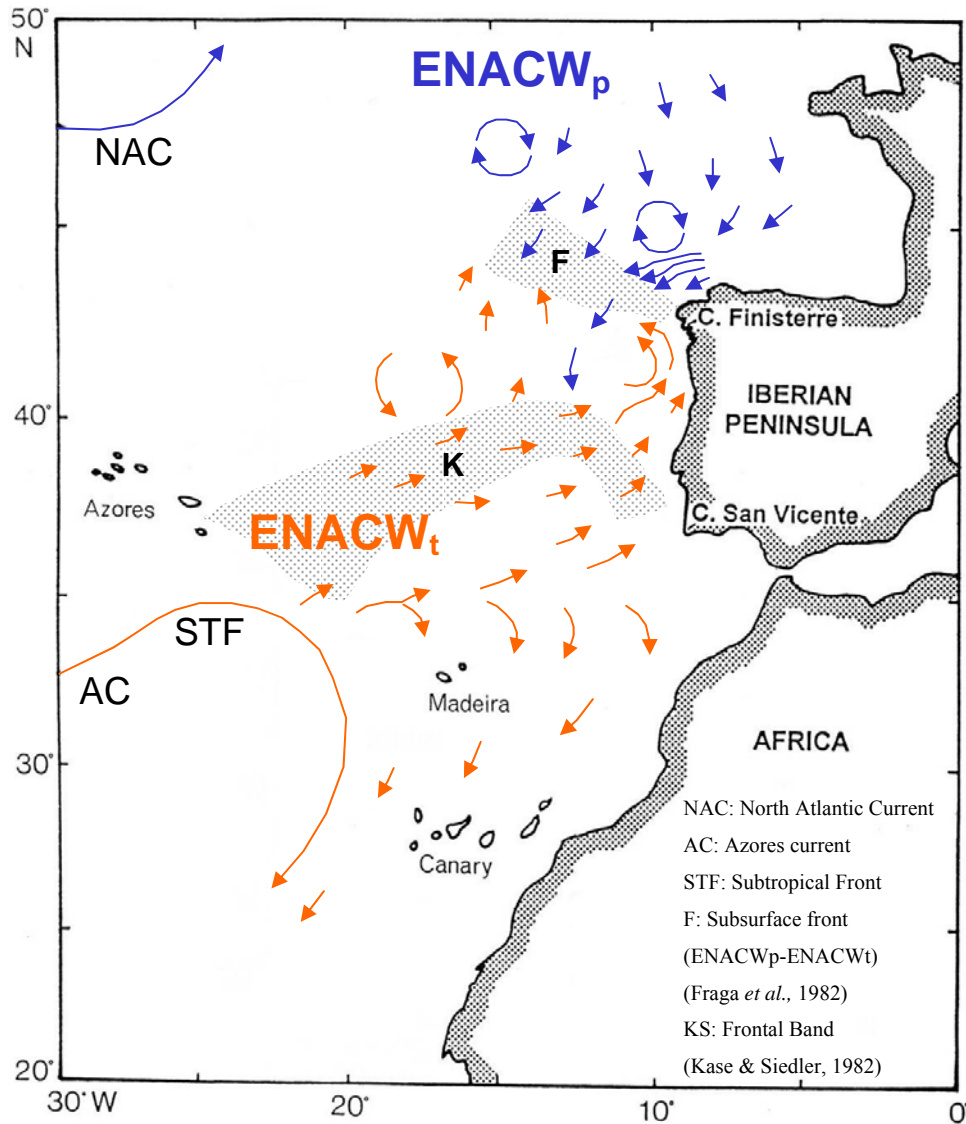


**Figure 3.10.** Main water masses in the eastern Atlantic and in the Gulf of Cadiz and their circulation pattern. Modified from Fiuza (1984) and Perez *et al.* (1998). ENACW<sub>p</sub>: subpolar branch of the Eastern North Atlantic Central Water; ENACW<sub>t</sub>: subtropical branch of the Eastern North Atlantic Central Water.

In the Strait of Gibraltar a two-layer circulation system is established, where the less saline water from the Atlantic enters into the Mediterranean as an upper layer and the more saline Mediterranean water outflows from the Mediterranean into the Atlantic as a bottom layer. The Atlantic Influx corresponds to water from the ENACW<sub>t</sub> that crosses the Strait of Gibraltar at the surface while the MW crosses the Strait beneath the Atlantic Influx at

depths of 40 to 200 m, depending on the bottom strait topography (Gascard and Richez, 1985). After passing the Strait, the Mediterranean Outflow (MO) descends into the Gulf of Cadiz as a density current, forming a turbulent flux 150 to 200 m wide and moves in contact with the seafloor along a channel within the Gibraltar gateway in a WSW direction, at a speed of more than 200 cm/s (Ambar and Howe, 1979a), locally reaching 300 cm/s (Mulder *et al.*, 2003). The MO velocity is strongly affected by the bottom topography and it decreases as result of the friction with the seafloor and as the mixing with the ENACW diminishes the MW density anomaly. Most probably, this flux influences the site where methane-derived authigenic carbonates (MDAC) were identified and sampled in front of the Gibraltar Strait, and in which strong bottom currents were evident on the underwater video profiles (see description in section 4.4.3.3, of Chapter 4). Thereafter, the MO spreads westward into the Gulf of Cadiz and due to the Coriolis effect the MO is deflected to the right of its pathway, i.e. along the slope, rather than directly to the west. There it flows against the upper slope of the South Iberian margin, in a NW direction, along the MO Channel (Figure 3.11) where it flows as a strong bottom current and where the friction with the seabottom is an important process controlling the MO behaviour (Baringer and Price, 1999). Due to horizontal variations of the outflow properties and as the upper and middle slope is characterized by a complex bottom topography with several canyons, plateau and mounds that steer the MO, these factors favour the splitting of the plume into several veins (Madelain, 1970; Zenk and Armi, 1990) and flows are distributed at constant depths along the Cadiz channel and Guadalquivir channel. Divergences of the MO from the main current direction, that flow down-slope are also observed such as the one that flows along the Gil Eanes channel (Figure 3.11). On its pathway, the MW gradually decreases its high thermohaline properties with the correspondent decrease in density, as it mixes with the surrounding fresher and colder ENACWt (Price *et al.*, 1993; Price and Baringer, 1994). Until approximately the longitude of 8°W, the MO behaves as a density current and from here it changes into a wall-bounded jet. Downstream from this area the MW reaches a density equilibrium with the surrounding ENACWt and the MO flows at mid-depths (Ambar *et al.*, 1999).

As the MO changes the direction from a westward direction to a north-westward direction (Figure 3.11) due to the Coriolis effect, it is divided into two main cores: the

Mediterranean Upper core - MU and the Mediterranean Lower core – ML (Madelain, 1970; Ambar and Howe, 1979b; Gardner and Kidd, 1983; Zenk and Armi, 1990).

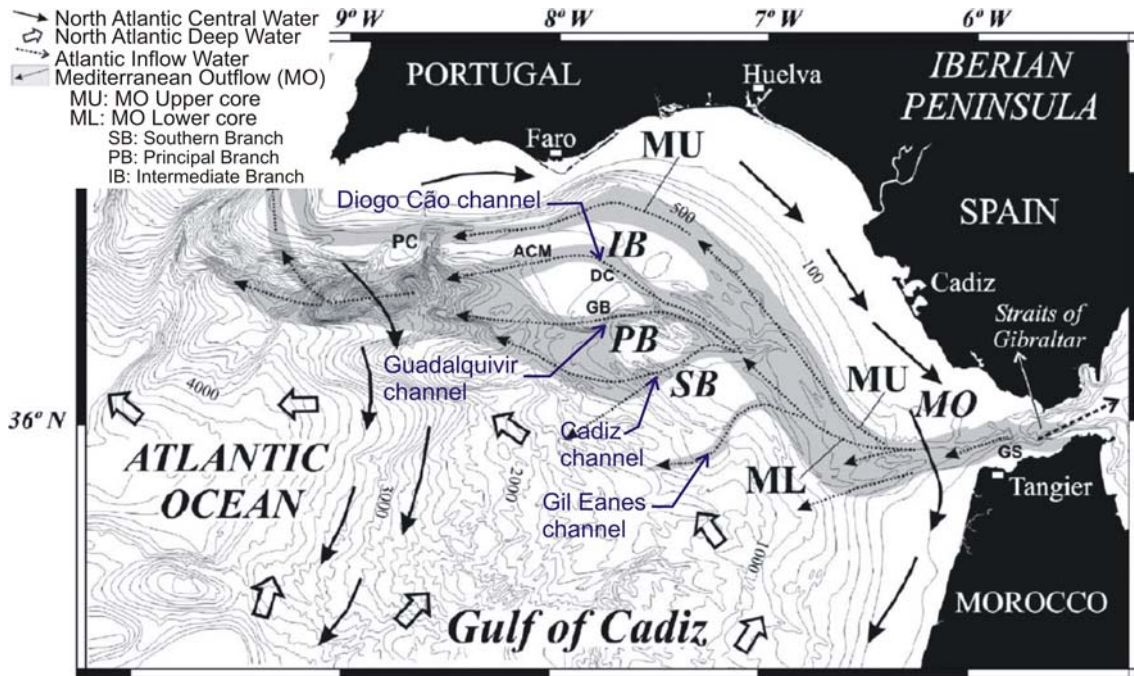


**Figure 3.11.** General circulation pattern of the Mediterranean Outflow water (MO) in the Gulf of Cadiz (Hernández-Molina *et al.*, 2006).

The MU upper core corresponds to the less dense core and is located between 500 and 800 m depth and is characterized by a density of  $27.6 (\sigma_0)$ . Until Cape St. Vicente it is characterized by an average velocity of 46 cm/s, a mean temperature of  $13.4^\circ\text{C}$  and salinity of 37.07 (Ambar *et al.*, 1999).

The ML is denser than the MU and corresponds to the main water flux of the MO in the Gulf of Cadiz. It is centred at about 1200 m depth and is characterized by a density of  $27.8 (\sigma_0)$ . Between  $6^\circ20'W$  and  $7^\circ W$  (Figure 3.11), the ML is divided into three minor branches that flow along different channels (Madelain, 1970; Nelson *et al.*, 1993; García *et al.*, 2003): the intermediate branch (IB), which flows north-westward along the Diogo Cão channel; the principal branch (PB), which is, at present, responsible for the main transport of the MO and flows south of the Guadalquivir Bank along the Guadalquivir channel; and the southern branch (SB), that flows along several steep valleys with an important flow along the Cadiz channel.

A third core of the MW, not so conspicuous, with a shallower depth between 400 and 600 m depth, was identified in the southern (Ambar, 1983) and western (Ambar, 1983; Hinrichsen *et al.*, 1993) Portuguese coast, not extending further offshore than about 50 km.

Mapping the thermohaline field and the sedimentary structures in the Northern margin of the Gulf of Cadiz have shown that the MO in general flows at the seabottom and has a strong erosional effect on the seafloor, especially to the East of Portimão Canyon (E of 8°30'W). It is proposed as a reference that the MO becomes neutrally buoyant and loses contact with the seafloor at 1000 m depth in the easternmost area and at 1400 m depth in the westernmost area (Baringer and Price, 1999). To the west of the Portimão canyon the margin becomes dominated by submarine valleys and canyons that strongly influence the MO current causing stronger instability (Chérubin *et al.*, 2003), diverging and inducing the meandering of the MO, producing their offshore extension (Ambar and Howe, 1979a, b; Zenk and Armi, 1990) and giving origin to vortices or eddies of MW, the so-called meddies (Serra *et al.*, 2005). Meddies generation is also promoted at the St. Vicente Promontory and Cape (Serra *et al.*, 2005). The spreading of the MO is reinforced by the development of these meddies that detach from the Mediterranean undercurrent mass (Figure 3.12). The meddies play an important role in the dispersion of the Mediterranean water into the Atlantic (Armi and Zenk, 1984; Armi *et al.*, 1989; Richardson *et al.*, 1989; Serra *et al.*, 2005) but also in the transport of particulate and dissolved matter (Freitas and Abrantes, 2002).

Underneath the Mediterranean Water flows the North Atlantic Deep Water (NADW). In the Gulf of Cadiz the NADW flows southward, below 2000 m water depth. The NADW is a multiple-source water mass, characterized by a low stratification and with temperatures ranging from 4-8°C, salinity values between 24.95 and 35.2 and a high oxygen content (Emery and Meincke, 1986).

The bottom water mass in the eastern Atlantic basin is the Antarctic Bottom Water (ABW) that circulates under the NADW at depths greater than 4000 m (Emery and Meincke, 1986) and that therefore does not have direct influence in the Gulf of Cadiz accretionary wedge region.

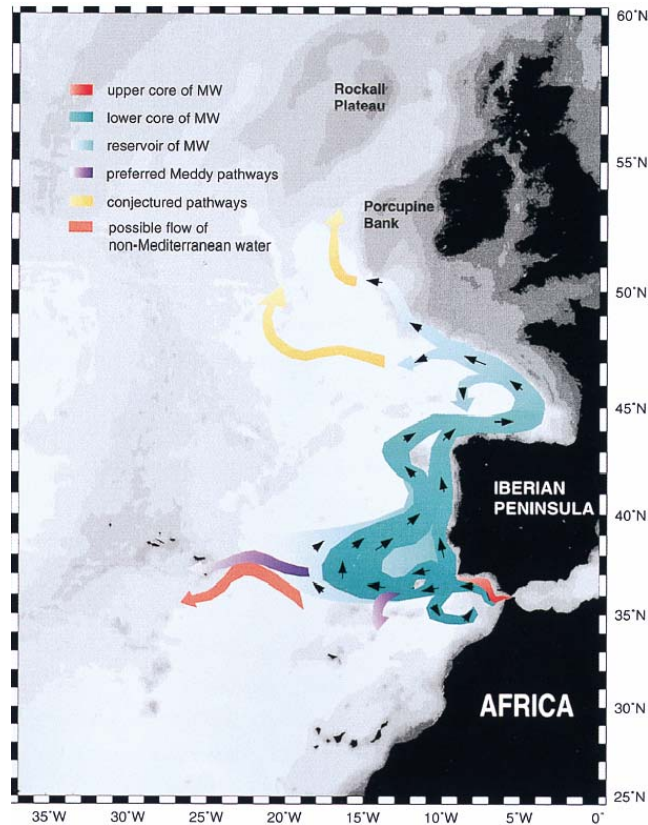


**Figure 3.12.** General circulation pattern of the Mediterranean Outflow water (MO) in the eastern North Atlantic (Iorga and Lozier, 1999).

### 3.5.2 Brief overview of the paleoceanographic evolution of the MO

The MO started with the opening of the Strait of Gibraltar at the end of the Miocene (Maldonado *et al.*, 1999) but a similar to the present day oceanographic configuration was established after the global cooling event in the Late Pliocene at 2.4 Ma (Loubere, 1987; Thunell *et al.*, 1991). This cooling event triggered a shift to more arid conditions and established a negative water balance in the Mediterranean and an anti-estuarine water exchange between the Mediterranean and the Atlantic. Since 2.4 Ma the MO has undergone significant variations as the result of the climate and sea-level fluctuations (Nelson *et al.*, 1993; Voelker *et al.*, 2006).

Recent paleoceanographic studies have concluded that global climate and oceanographic changes have caused vertical and spatial fluctuations of the MO in the Gulf of Cadiz. An enhancement of the MO occurred during cold periods when compared with the warmer periods (Cacho *et al.*, 2000; Llave *et al.*, 2006). It has been proposed that

during cool stages and low-stands of glacial sea level, the cross section at the Gibraltar Strait was reduced and the MO volume was lower than at present day conditions (Gardner and Kidd, 1983; Matthiesen and Haines, 2003). Such a setting may well have diminished the water exchange between the Mediterranean and the Atlantic but, the lower temperature and the generally dryer Mediterranean would result in a significantly higher salinity and density of the MW (Schonfeld, 1997; Cacho *et al.*, 2000; Schonfeld and Zahn, 2000). This would then result in a more intense and deeper-flowing MO i.e. in an enhancement of the Lower core of the MO during cool low-sealevel periods (Thomson *et al.*, 1999; Rogerson *et al.*, 2005; Llave *et al.*, 2006). During the warm periods of high sealevel the density of the MO would be lower than during the cold periods, and therefore the interaction of the upper MO cores would be more intense at shallower water depths (Thomson *et al.*, 1999; Rogerson *et al.*, 2005; Llave *et al.*, 2006).

## **Chapter 4. Characterization of areas of MDAC occurrence in the Gulf of Cadiz and their relation to other fluid escape structures**

### **4.1 Introduction**

Fluid seepage structures are characterized by housing and sustaining unique consortia of benthic organisms (Suess *et al.*, 1985; Olu *et al.*, 1997; Sibuet and Olu, 1998; Levin, 2005), geochemical and geothermal anomalies in the seafloor sediments (Kastner *et al.*, 1991; Wallmann *et al.*, 1997; Henry *et al.*, 2002; Henrys *et al.*, 2003; Sassen *et al.*, 2003), formation of massive authigenic carbonates (Kulm *et al.*, 1986; Hovland *et al.*, 1987; Ritger *et al.*, 1987; Hovland and Judd, 1988; Kulm and Suess, 1990; Paull *et al.*, 1992), methane plumes in the ocean column (Roberts and Aharon, 1994; Roberts, 2001; Greinert *et al.*, 2002; Greinert and Nutzal, 2004; Greinert *et al.*, 2006; Sauter *et al.*, 2006) and the occurrence of gas hydrates (Shipley and Didyk, 1982; Sassen *et al.*, 2001a; Sassen *et al.*, 2001b; Sassen *et al.*, 2004). The occurrence of fluid escape processes at continental margins is now recognized as widespread in a variety of different marine settings and throughout the geological record (Campbell *et al.*, 2002; Peckmann and Thiel, 2004). The nature and composition of the expelled fluids and materials from the fluid escape structures and mud volcanoes provides fundamental information on the geology and geochemistry of the deeper sediments.

Fluid escape structures in the Gulf of Cadiz (GC) were first reported in the shelf break and in the upper continental slope of the eastern-central part of the GC in areas covered by muddy sediments (Baraza and Ercilla, 1996; Baraza *et al.*, 1999). In the last 6 years extensive work was carried out by several research groups with the objective to study the fluid escape structures and processes in the GC, specially within the middle and lower slope (Kenyon *et al.*, 2000; Gardner, 2001; Kenyon *et al.*, 2001, 2002; Somoza *et al.*,

2002; Van Rooij *et al.*, 2002; Díaz-del-Río *et al.*, 2003; Kenyon *et al.*, 2003; Pinheiro *et al.*, 2003; Somoza *et al.*, 2003; Kopf *et al.*, 2004; Depreiter *et al.*, 2005; Henriët *et al.*, 2005; Rensbergen *et al.*, 2005a; Rensbergen *et al.*, 2005b; Rooij *et al.*, 2005; Kenyon *et al.*, 2006; Masson and Berndt, 2006). As a result, 41 mud volcanoes (confirmed by coring), with gas hydrates being recovered from 3 of them, as well as many other fluid escape features, were described and studied. Figure 4.1 illustrates the location of the mud volcanoes, mud cones and the occurrences of MDAC in the Gulf of Cadiz.

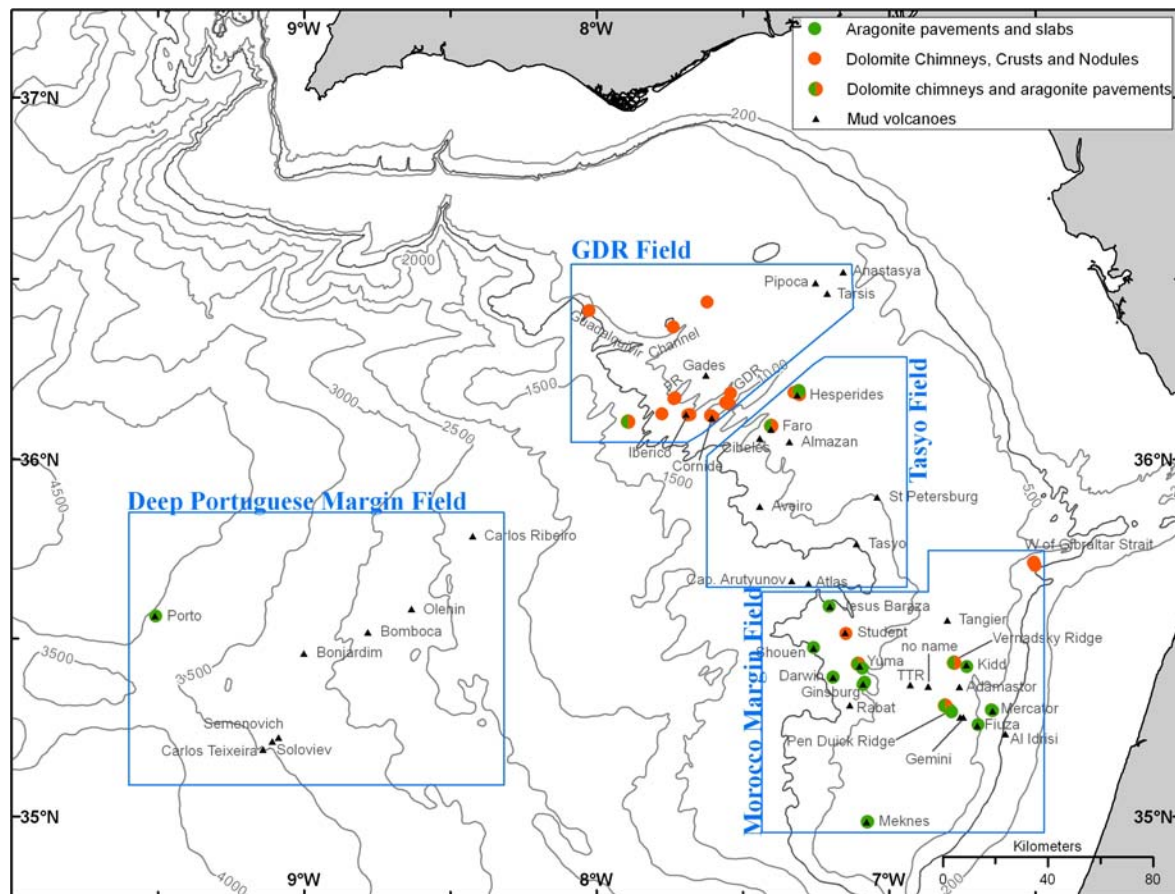


**Figure 4.1.** Location of the mud volcanoes and MDAC occurrences in the Gulf of Cadiz. Boxes indicate the main mud volcano fields defined in previous works and described in the text.

Based on geophysical data, seafloor video observations and samples collected during the TTR10 (Leg 1), TTR11 (Leg 3), TTR12 (Leg 2), TTR14 (Leg 1), TTR15 (Leg 4) and TTR16 (Leg2) cruises (2000, 2001, 2002, 2004, 2005 and 2006 respectively), complemented with data from the Anastasya 2000, Anastasya 2001 and GAP cruises, several areas have been shown to be characterized by the widespread occurrence of MDAC: (1) on the Guadalquivir Diapiric Ridge (GDR) and the Formosa Ridge (FR); (2)

along several erosional features associated with the Mediterranean outflow (MO) on the Cadiz Channel; (3) on the Pen Duick Escarpment and the Vernadsky Ridge; (4) on some mud volcanoes and mud diapirs located on the pathway of the MO, Iberico, Faro, Hesperides, Student and Yuma (Kenyon *et al.*, 2002; Magalhães *et al.*, 2002; Somoza *et al.*, 2002; Díaz-del-Río *et al.*, 2003; Kenyon *et al.*, 2003; Pinheiro *et al.*, 2003; Pinheiro *et al.*, 2004); (5) dense fields of MDAC were also discovered during the TTR14 cruise on the main channel of the MO in front of the Strait of Gibraltar (Magalhães *et al.*, 2005; Kenyon *et al.*, 2006); (6) the re-examination of samples collected during an earlier (1976) Hesperides cruise on the northern slope of the Guadalquivir Channel also showed the presence of similar dolomite chimneys; and (7) MDAC occurring as aragonite and calcite crusts and pavements, were also discovered and sampled, associated with the Pen Duick and the Vernadsky Ridges, within the Cadiz Channel and associated with several mud volcanoes: Jesus Baraza, Yuma, Ginsburg, Kid, Mercator, Fiuza, Darwin, Shouen, Adamastor, Meknes, Hesperides Faro and Porto (Figure 4.1). The present day survey coverage shows that fluid escape structures in the GC are far more common features than previously anticipated and they now have been found in many locations between 500 and 4000 m water depth.

As described in Chapter 5, two main lithologic types of MDAC were identified in the collected samples from the Gulf of Cadiz: (i) dolomite-dominated carbonates and (ii) aragonite-dominated carbonates. The dolomite-dominated carbonates form crusts, irregular massive or nodular aggregates, and chimneys (fluid conduits or filled burrows) with tubular or pipe-like morphologies. The aragonitic MDAC occur as pavements, crusts or slabs that pave the seafloor for several square meters, or form buildups and irregular blocks, up to 2 m high, at the seabottom.

The geological characteristics of the seafloor at the several fluid escape structures is highly variable and is a function of the rate and duration of the seepage episodes as well as the nature and composition of the material (solid, fluid and gas) expelled (Roberts, 2001). In this Chapter will be presented a synthesis of the different geophysical, visual, geochemical and mineralogical data collected from fluid escape structures where MDAC have been identified. It is discussed the superficial geology, and to a lesser extent biology, related to the fluid escape structures where MDAC were found. It is also discussed the relationship between the seafloor morphology, the seafloor acoustic facies (SSS

reflectivity) and the nature of the seafloor recognised from underwater video profiles and from the samples retrieved by tv-controlled grab, dredging and gravity coring. A relationship between the occurrences of the authigenic carbonates and other fluid escape structures, such as mud volcanoes and mud cones, is postulated and the controls of their occurrence is investigated. Another objective of this chapter is to assess the intensity of the upward fluid migration, the dynamics and the morphology of the seepage structures and to relate them with the different observed seafloor features and products.

## **4.2 Methods**

### **4.2.1 Positioning systems**

Positioning during the TTR cruises was obtained with an Ashtech GG24 DPS + GLONASS receiver, allowing an optimal static accuracy of  $\pm 35$  cm (75 cm at 95% confidence limits). The normal accuracy in the Gulf of Cadiz area, under normal satellite configuration, is assumed to be ca. 5 m. Navigation on board the D. Carlos I (Matespro and Delila 1 cruises), Sonne, Cornide de Saavedra and Belgica research ships was obtained using both Global Positioning System (GPS) and Differential Global Positioning System (DGPS), installed in one or in multiple positions of the vessel. The two systems were used in order to obtain the necessary accuracy in position determination, as well as the necessary yaw corrections to be used by the multibeam systems.

Underwater navigation during deep-towed operations onboard the RV Professor Logachev, such as with deep-towed side-scan sonar (MAK1 and OREtech), the deep-towed video system and the TV-controlled grab were based on the Sigma-1001 hydro-acoustic system. This system consists on a pinger fitted to the deep-towed equipment, operating between 7-15 kHz, and four stationary hull-mounted acoustic receivers, spaced 14 m apart. The signal emitted by the deep-towed pinger is tracked on board and accurate *x,y* position of the device is computed in relation to the vessel, taking into account the vessel roll, trim and speed. The error of the estimated position of the deep-towed equipment by this system usually does not exceed 1-2% of the water depth.

During the GAP cruise, on board the R/V Sonne, underwater navigation for the Ocean Floor Observation System (OFOS) and of the TV-controlled grab was similar to the

one used onboard the RV Professor Logachev. Given the inferior number of acoustic receivers and their closer separation the precision on the underwater determination on board the RV Sonne was less accurate than the one achieved with the RV Professor Logachev.

For gravity corer seabed sampling, the error in positioning is normally 5% of the accuracy of the vessel position, due to the rapid deployment.

Detailed descriptions of the positioning systems are presented in Appendix A.

#### **4.2.2 Seafloor sampling**

The seafloor samples used for this work were collected during several cruises (TTR 09, TTR 10, TTR 11, TTR 12, TTR 14, TTR15, TTR16, Anastasya 2000, Anastasya 2001 and GAP) using several devices (gravity corer, box corer, multi-corer, Kasten corer, dredge, grab, and video controlled grab). Sediment sample descriptions from other cruises were also used when available and relevant for this study. Detailed descriptions of the sampling devices are presented in Appendix A.

#### **4.2.3 Underwater observations**

Underwater observations during the TTR cruises were carried out with an underwater video cameras (analogical or digital), with a video controlled grab (during the TTR and the GAP cruises) and with the Ocean Floor Observation System (OFOS, GAP cruise). Detailed descriptions of these systems are presented in Appendix A.

#### **4.2.4 Side-scan sonar mapping**

Side-scan sonar mapping was performed with the NRL Seemap long range side-scan sonar, a low frequency 12 KHz system, and with the OKEAN system, which operates at a frequency of 9.5 kHz. Both systems have fairly similar resolutions. When no other coverage was available and in areas with multibeam coverage, the backscatter imagery from the EM12 swath bathymetry system was used.

High resolution deep-towed side-scan sonar imagery (MAK-1M or OREtech) was also acquired in areas of detailed investigations. Both MAK and OREtech systems were

used on board the R/V Professor Logachev during the TTR cruises. They are both equipped with a subbottom profiler, operating at a frequency of 5 kHz. The maximum swath coverage is 2 km (1 km per side) for a towing altitude of 150 m above the seafloor, operating at a frequency of 30 kHz, and about 50 m above the seafloor for 100 kHz surveys. The resolution of the system ranges from 7 to 1 m across and along the track.

Detailed descriptions of both systems are given in Appendix A.

### **4.3 Results: Geological and geophysical cartography**

Based on the underwater video observations several bottom facies have been defined and mapped. Whenever possible, these facies were calibrated with sampling information. The main bottom facies defined were:

1. Pelagic sediments
2. Rippled pelagic sediments
3. Unrippled pelagic sediments
4. Sediment clogged dead coral framework
5. Live-coral covered sediments
6. Coral rubble, dense coverage of mostly dead coral
7. Patches of mainly dead coral
8. Rock outcrops
9. Mud volcano mud breccia
10. Sediment covered with pogonophora tube worms
11. Sediment covered with clams and clam fields
12. Bacterial mat
13. MDAC chimney fields: chimneys, pipelike or conduits, corresponding most probably to the dolomitic crusts, chimneys and nodules
14. MDAC pavements and buildups: most probably correspond to the aragonitic pavements mineralogies
15. Gas bubbles
16. Gas hydrate patches

The underwater video profiles were interpreted and each segment of about 1 minute was classified according to the dominant seabottom facies classification defined above. The facies classification was then plotted on the navigation and correlated with other seafloor information as the backscatter intensity and collected samples.

Four main areas or fields of fluid escape structures have been defined for the Gulf of Cadiz (Figure 4.1): (1) the Deep Portuguese Margin Field (DPF); (2) the Guadalquivir Diapiric Ridge Field (GDRF); (3) the Tasyo Field; and (4) the Morocco Margin Field - MMF (Kenyon *et al.*, 2000; Gardner, 2001; Kenyon *et al.*, 2001, 2002, 2003). The latter was further subdivided into the West MMF, the Central MMF and the East MMF (Gardner, 2001). More recently, the Eastern MMF was defined as the El Arraiche Mud Volcano Field, which includes the Al Isidri, Mercator Fiuza, Don Quichote, Gemini, Kidd, Lazarilho de Tornos and Adamastor mud volcanoes, and the Vernadsky and the Pen Duick ridges (Rensbergen *et al.*, 2005a; Rensbergen *et al.*, 2005b).

The middle slope of the northern central part of the Gulf of Cadiz corresponds to the GDRF (Figure 4.2) where the MDAC were first identified and sampled (Diaz-del-Rio *et al.*, 2001; Somoza *et al.*, 2002). The GDRF is characterized by several regionally important diapiric ridges: the Guadalquivir diapiric ridge (GDR), the Cadiz Ridge (CDR), the Hormigas Ridge (HR) and the Formosa Ridge (FR). The GDR, CDR, HR and FR are interpreted as diapiric ridges resulting from lateral compression and by the pressing up of the plastic marly clay deposits (blue marls) of the front units of the Early-Middle Miocene pre-olistostrome units, unit M1 of Maldonado *et al.* (1999), of the front of the olistostrome/accretionary complex (Somoza *et al.*, 2003). Several fluid escape structures, such as mud volcanoes, mud mounds with high abundance of MDAC and pockmarks were identified in the GDR. Based on the multibeam bathymetry and geophysical information, specific target areas were selected for detailed underwater video observation and sampling. Such areas include several mud volcanoes, mud cones, diapiric ridges and high reflectivity areas in side-scan sonar backscatter, such as the Iberico and the Cornide mud cones; the FR, the Coruña cone of the GDR; on the Cadiz Channel E of Lolita and at the Cadiz Channel W of the Iberico. These areas are described above in more detail.

The Tasyo MV Field (Somoza *et al.*, 2003) is located south of the GDR and corresponds to the Central Gulf of Cadiz. In this area MDAC were identified associated with the Hesperides, Faro, Cibeles and Almazan MVs.

In the southern part of the Gulf of Cadiz, the Morocco Margin Field (MMF) is characterized by large mud volcanoes, ridges and fault escarpments. MDAC were identified and collected along the Pen Duick and the Vernarsky ridges and escarpments and on the Darwin, Fiuza, Yuma, Ginsburg, Jesus Baraza, Kidd, Meknes, Mercator, Shouen and Student mud volcanoes.

In the DPF, which includes the Carlos Ribeiro, Olenin, Bomboca, Bonjardim, Semenovich, Soloviev, Carlos Teixeira and Porto mud volcanoes, until present, MDAC were only identified in the Porto mud volcano, although their presence in other sites cannot be excluded.

### **4.3.1 MDAC occurrences in the GDR Field and their relationship with mud volcanoes and mud cones**

MDAC were identified on mud cones and mud volcanoes (MV) along two parallel linear ridges clearly evident in the bathymetry (Figure 4.2): along the Guadalquivir Diapiric Ridge (GDR) and along the Formosa Ridge (FR).

Other prominent diapiric ridge, the Cadiz Diapiric Ridge (CDR) which range from 370 to 700 m water depth have a relief of 250 to 300 m high and up to 4500 m wide and extends for 27 km with a NNE-SSW orientation (Figure 4.2) was not investigated for the occurrences of MDAC.

#### **4.3.1.1 Guadalquivir Diapiric Ridge**

The GDR crest is located between 380 and 940 m water depth, have an average relief of 250 m, up to 4000 m wide and extends for 85 km with an NE-SW orientation (Figure 4.2). The area close to the GDR exhibit several features with their bathymetric expression indicated to be mud volcanoes (Somoza *et al.*, 2003). Ground-truthing of some of these structures confirmed their mud volcanic nature. Therefore, the Anastasya, Tarsis and Pipoca MV were confirmed in the northern end of the GDR by the presence of mud breccia, sediments with high gas content and strong H<sub>2</sub>S smell in gravity cores (Somoza *et al.*, 2003). Similar sediment characteristics were recorded from gravity cores in the Gades MV, located at the northern termination of the FR (Somoza *et al.*, 2003). In the GDR, MDAC were identified and sampled from the Coruña mud cone (Díaz-del-Río *et al.*, 2003; Somoza *et al.*, 2003; León *et al.*, 2006).

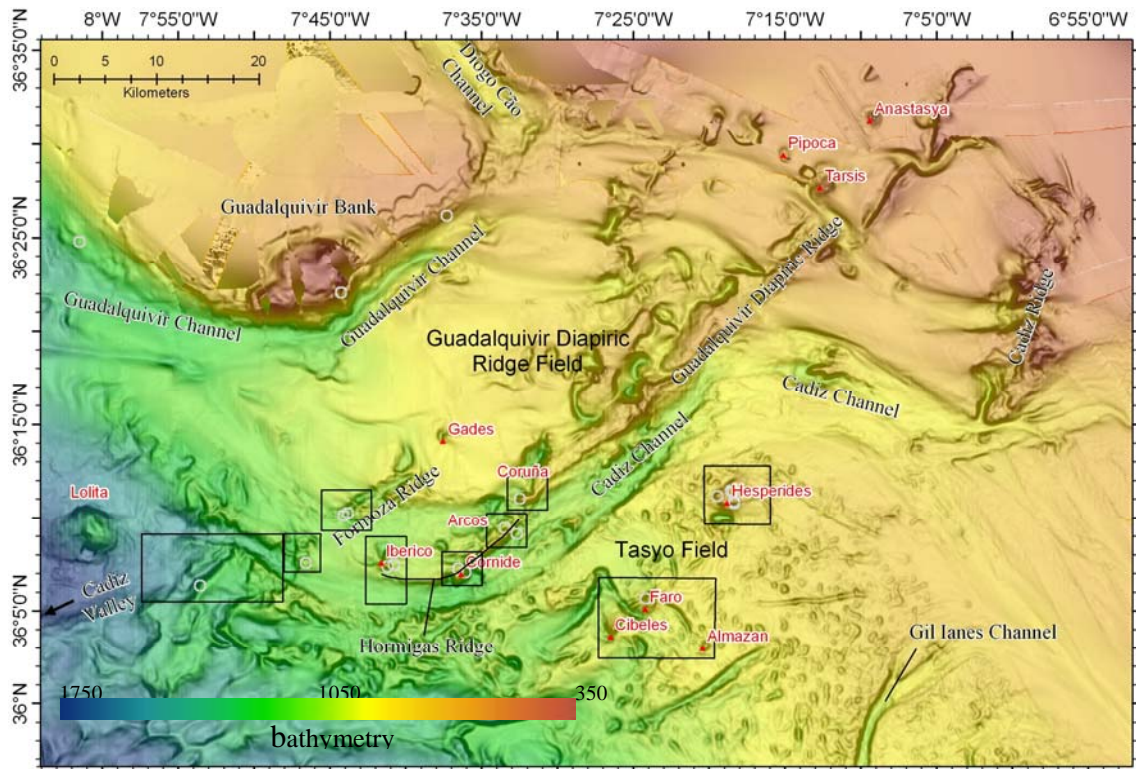


**Figure 4.2.** Multibeam relief of the Guadalquivir Diapiric Ridge mud volcano field and northern Tasyo Field. Boxes shows the locations of detailed investigation areas (figures 9.4 to 9.8) and open circles indicate the locations where MDAC were identified. Bathymetry with a slope and hillshade with illumination from the NW.

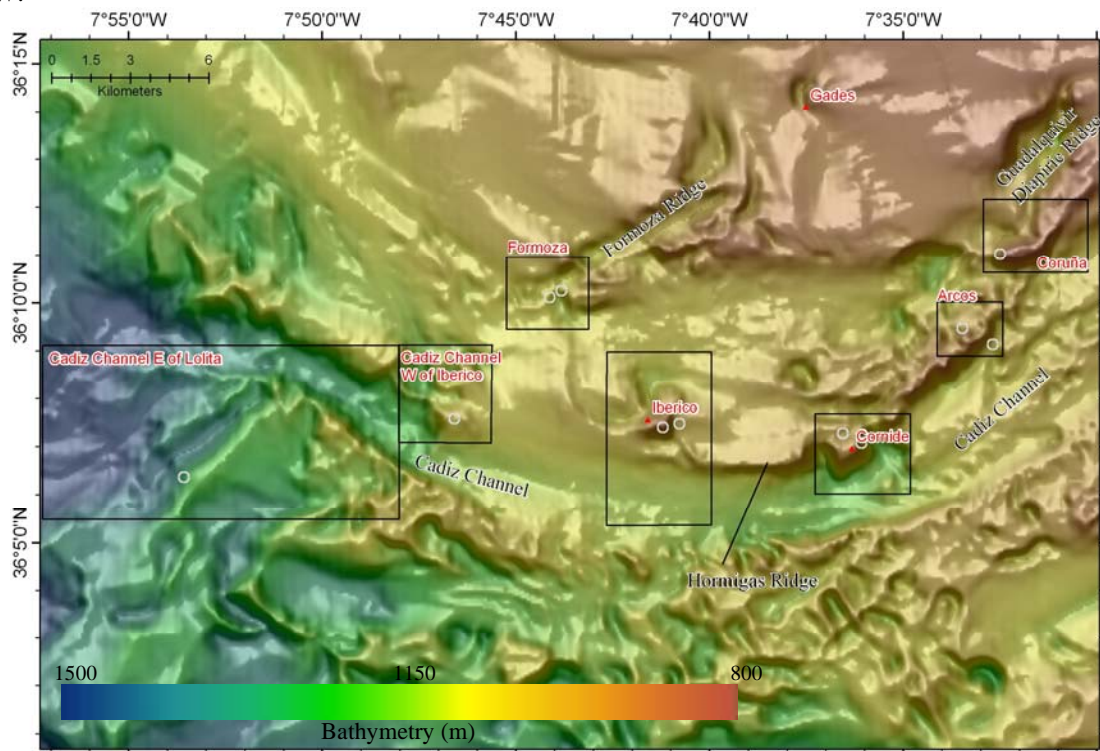


**Figure 4.3.** Multibeam relief, with slope and hillshade with illumination from the NW, of the Guadalquivir Diapiric Ridge mud volcano field. Boxes show the location of the detailed investigation areas and open circles indicate the locations where MDAC were identified.

#### 4.3.1.1.1 Coruña mud cone

The Coruña mud cone was surveyed during the Anastasya campaign in 2001. This area was investigated with multibeam, seismics, underwater seabottom photography and dredging (Díaz-del-Río *et al.*, 2003; Somoza *et al.*, 2003; León *et al.*, 2006).

The Coruña is an asymmetric cone shaped mound with a relief of 233 m with asymmetric flanks and slope gradients up to 24° (Figure 4.5A). The mound summit is located at 830 m water depth (Figure 4.4A). The bathymetry and the backscatter imagery do not show any structures at the mound summit, nor any moat or mud flows. The NRL Seamap side-scan sonar shows a highly reflectivity surface (Figure 4.4B), similar to the backscatter reflectivity of the remaining GDR, with high acoustic reflectivity at the ridge summit and on the flanks, contrasting with the lower reflectivity characteristic of the sedimentary contourite deposits like the ones north of the GDR (compare the contourite deposit, c.a. shot point 1200 in profile Psat-125 with the low backscatter reflectivity on the NRL Seamap, in Figure 4.4B, corresponding to the basin north of the Coruña mound). The seismic profile Psat-215 (Figure 4.5B) illustrates the typical seismic character of chaotic reflectors and transparent facies typical of the GDR, compared with the coherent reflectors of the contiguous sediments. The GDR shows a strong seafloor reflection that is interpreted as being caused by the high abundance of MDAC.

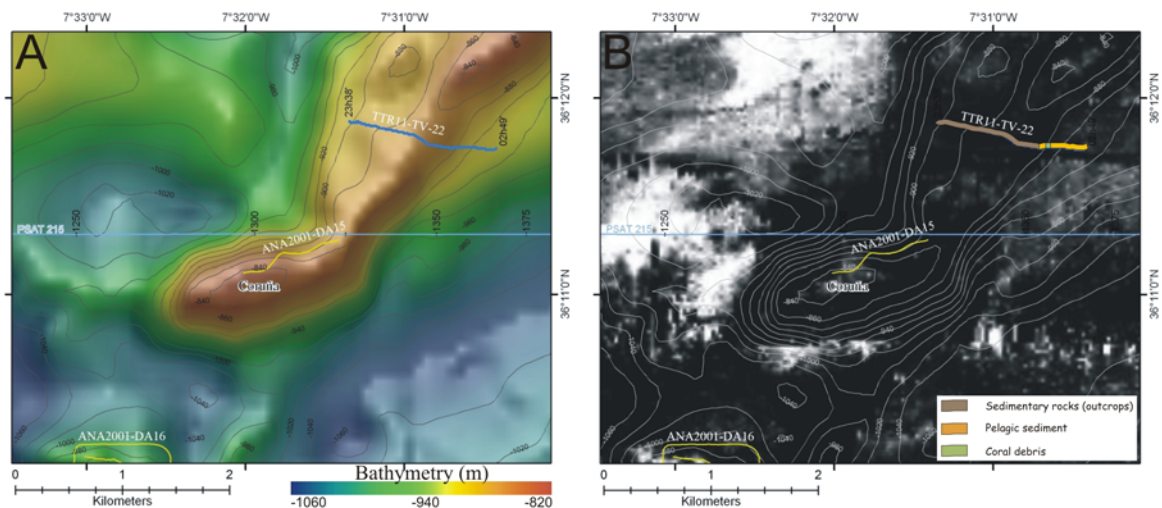


**Figure 4.4.** (A) GDR in the area of the Curuña cone with the location of the dredge done during the Anastasya campaign and the seismic profile Psat-215 (TTR11). TV-profile TTR11-TV-22 crosses the GDR north of the Coruña mound. Bathymetric relief with a slope and hillshade with illumination from the NW. (B) NRL Seamap side-scan sonar imagery of the GDR and Coruña mound with superimposed bathymetry.

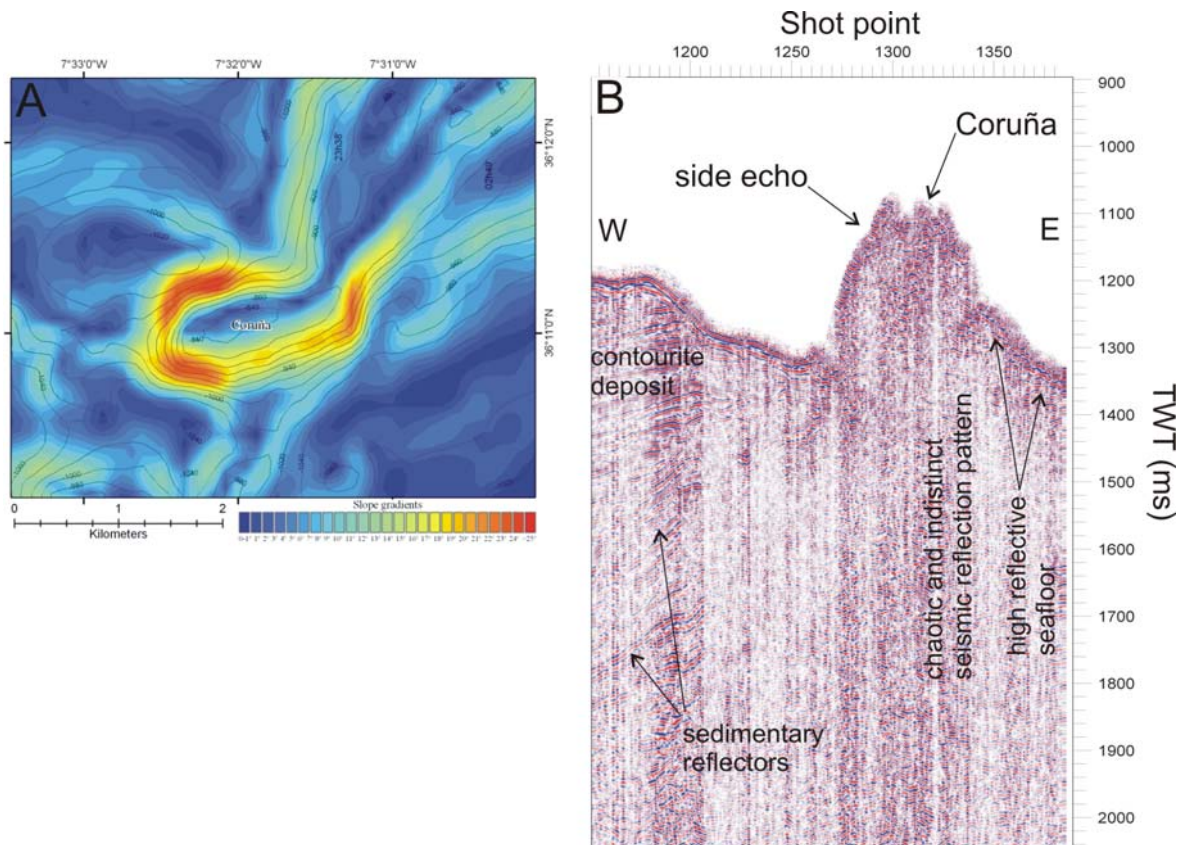


**Figure 4.5.** (A) Slope gradient of the GDR and the Coruña mound. (B) Single channel seismic line TTR11-Psat215. Location of the seismic line is given in Figure 4.4. To be noted the chaotic and indistinct seismic reflection pattern below the conical expression of the GDR, contrasting with the parallel reflections of the sedimentary basin sequences to the W.

The dredge ANA2001-DA15 allowed the collection of MDAC samples dominated by dolomite chimneys and slabs (Díaz-del-Río *et al.*, 2003). Plastic mud and blue marls clasts were also retrieved from the Coruña mound. The blue marls were interpreted as being of Early-Middle Miocene age and associated with the tectonic compression of the wedge front of the olistostrome/accretionary complex (Maldonado *et al.*, 1999; Somoza *et al.*, 2001; Díaz-del-Río *et al.*, 2003). Fragments of corals were also retrieved from this dredge.

#### 4.3.1.1.2 Profile in the GDR North of the Coruña mud cone

A profile of underwater TV across the GDR was collected during the TTR11 cruise. The interpretation of the seafloor observations are illustrated in Figure 4.6. This profile started in middle slope of the northern flank of the GDR, crossed the ridge summit and

descended along the southern flank to the base of the Cadiz Channel. The northern flank, the summit and the top part of the southern flank (at a water depth of 880 m) is characterized by outcropping of well lithified rocks with evident parallel bedding, with absent or very thin pelagic sediment drape. The stratification appears to be sub-vertical and the sedimentary rocks are dominated by claystones. Abundant sub-rounded clasts, probably fragments of the outcropping rocks are found along the slope. In the southern flank, above 880 m water depth the seafloor is characterized by a sedimentary cover dominated by sandy sediments with ripples and sand waves. These sedimentary facies are interpreted as corresponding to the contourite deposits resultant from the MO that flows with a strong velocity at the seafloor along the southern flank of the GDR and along the Cadiz Channel. During the video observations, especially along the southern flank of the GDR, a strong current could be observed from the movement of particles put in suspension by the video camera. Clasts of the outcropping material found scattered on the sandy sediment are interpreted as fragments from the upper slope that rolled downwards. In the mid slope a patch of coral debris was found, about one hundred meters long. This patch is characterized by a dense coverage of coral rubble, composed of abundant fragments of coral branches (dead coral; no live coral was positively identified) that partially cover by sediments. In this patch some gastropods were also identified and fragments of not yet identified shells.

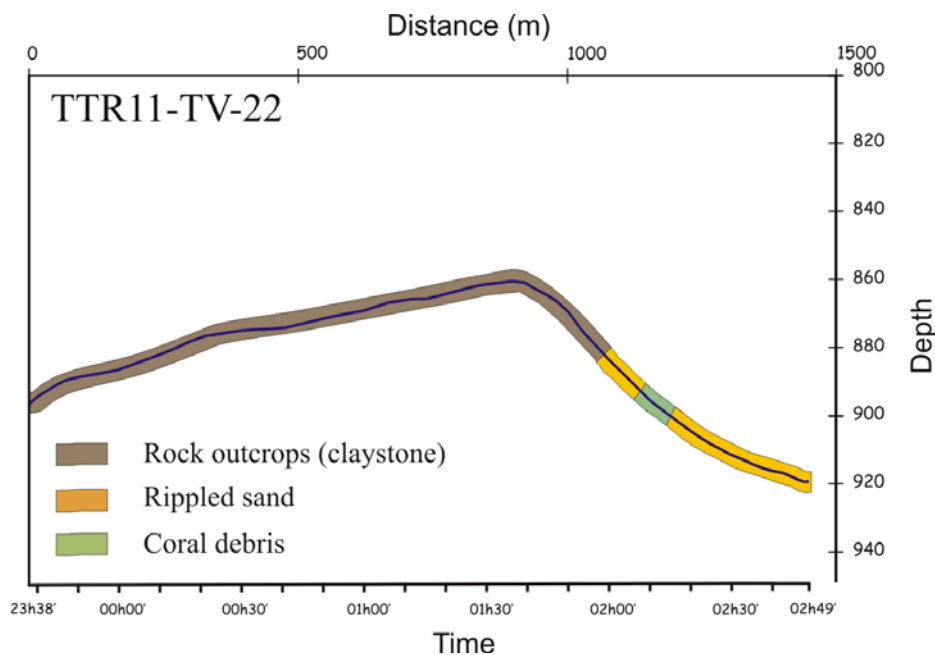


**Figure 4.6.** Facies interpretation of the underwater video profile TTR11-TV22. See location in Figure 4.4.



During the TTR12 cruise (Kenyon *et al.*, 2003) one underwater TV line (TTR-TV-AT-29) was collected and samples were retrieved by dredging (TTR12-AT-389D) and with a TV-controlled grab (TTR12-388Gr) on the southern end on the FR (Figure 4.7). The TV line video observation started from the north towards the SW along the northern flank of the southern termination of the Formoza ridge, in an area of strong acoustic backscatter (Figure 4.9), and continued along the small crest between the depressions that delimit the ridge. The profile is dominated by the occurrence of MDAC at the seafloor, as pipe-like structures or chimneys that are broken and lies on the seafloor, as illustrated in Figure 4.11(A-C). In general, these chimneys are intensely fragmented and accompanied by rubble of small fragments of broken chimneys. The chimneys have variable sizes, up to 2 meters long and up to about 0.5 m in diameter. Some of them have clear open central orifices while others are completely filled, as illustrated in Figure 4.11(B-C) and also recognised on the samples retrieved and described in Chapter 5. The chimneys are intensely colonized by benthic fauna of sessile organisms like sponges, sea urchins, Cidaridae and Asterinidae sea stars. Live corals were not collected from this site but some probable individual colonies were identified on the video observations occurring over some chimneys. Chimneys in the vertical position, protruding from the seafloor, like the one illustrated in Figure 4.11C were identified, but this occurrence is much less frequent than the occurrence of the chimneys lying on the seafloor. The chimneys in the vertical position also show strong colonization by benthic fauna and their colour and characteristics indicate that they do not represent active venting structures but are interpreted instead as representing fossil venting conduits, inactive for a long time. In some of them it was possible to recognise that at the foot of some vertical chimneys there were often linear pipe-like chimneys lying on the seafloor and aligned, indicating that they represent a longer chimneys that has fall down and broken into several fragments. On this profile it was also possible to recognise a strong bottom current, with velocities of 1-2 m/s, estimated from the movement of suspended particles. These bottom currents were also evident from the movement of some of the benthic fauna that bent due to the current, and also from the cable that was hanging from the TV frame that was sometimes bent in a different direction from that of the movement of the camera. The strong bottom current was interpreted as sufficient to remobilise the unconsolidated sediments, resulting in active erosion of the soft sediments and to promote the exhumation of the MDAC to the seafloor.

The slope gradients along the ridge promoted the remobilization of the MDAC and their consequent fragmentation.

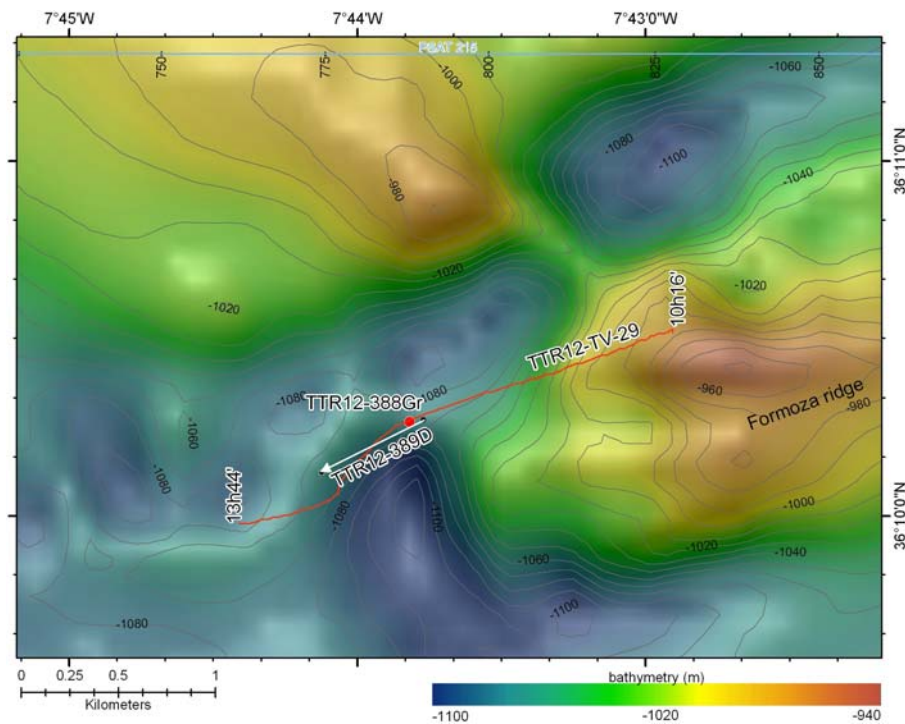


**Figure 4.8.** Bathymetry, with a slope gradient and a hillshade with illumination from the NW, of the southern termination of the Formoza Ridge with the location of the dredge, TV-grab and underwater video observation profile collected during the TTR12.

Pavements, crusts and irregular buildups were identified on the video observations, sometimes occurring simultaneous with the chimneys and MDAC rubble. The pavements (illustrated in Figure 4.11D-F) occur as thin (several cm thick) crusts that can extend for several square meters, paving the seafloor or occurring as fragmented slabs. These pavements show a coarse texture interpreted as resulting from the incorporation of shells and fragments of shells in the cemented crust. Their surface was in general irregular with irregular contours. Compared to the chimneys, the pavements exhibit less intense colonization of benthic fauna, which is interpreted as indicating a smaller period of contact with the seawater (probably also a younger age).

The chimneys and crusts were found, in general, within coarse sediments, sometimes with a high amount of shell fragments and frequently characterized by ripples and decimetre size sand waves (Figure 4.12G-I). In some places, in the northern flank of the ridge and along the crest south of the ridge, outcrops of lithified rock were observed, probably claystone, interpreted as corresponding most probably to the blue marls of Early-

Middle Miocene age, not sampled at this site but sampled along the GDR and in the Iberico mud cone (Somoza *et al.*, 2001). Some chimneys and pavements were also found on these outcrop sites, but it was not clear that the chimneys and crusts were formed within these rocks. It is possible that the chimneys and crusts were remobilized to these sites by bottom currents and through gravity flows from other sites upslope.

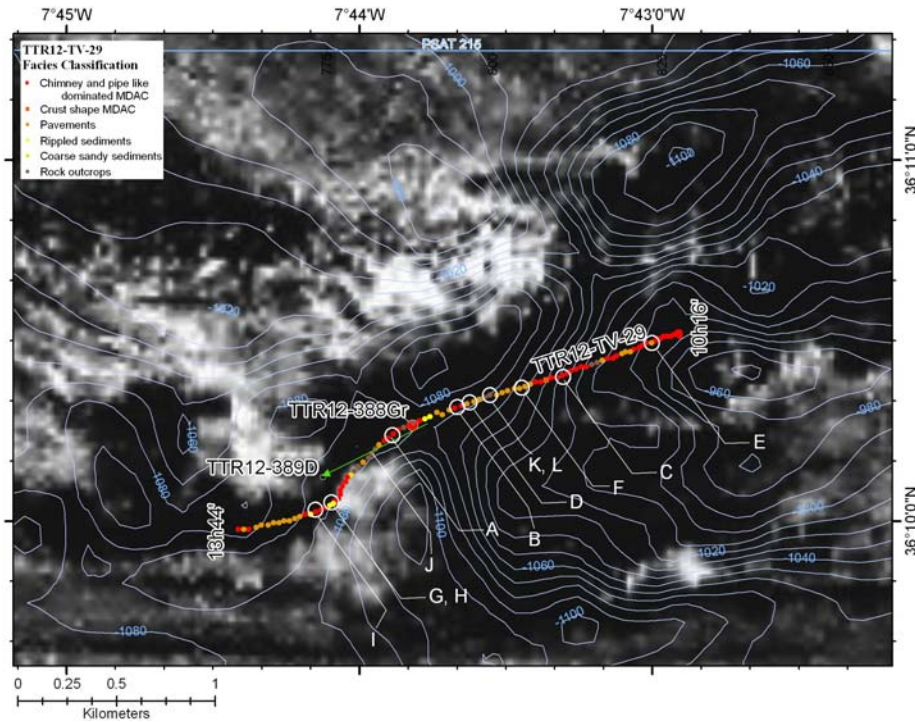


**Figure 4.9.** NRL Seamap side-scan sonar imagery of the Formoza Ridge with the seafloor facies interpretation of the video profile TTR12-TV-29. (see Figure 4.10).  
Distance (m)

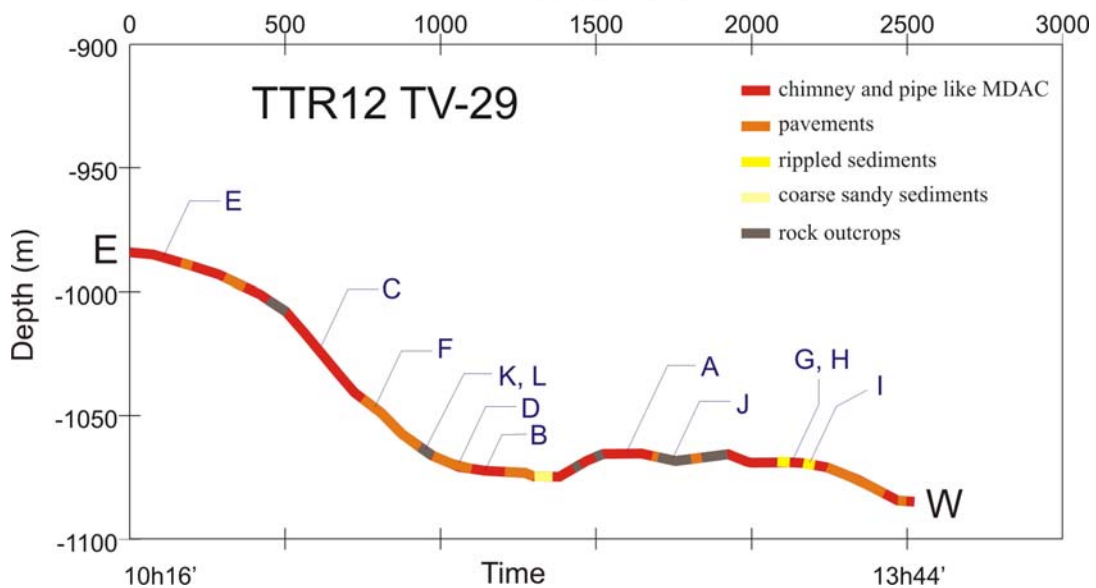


**Figure 4.10.** Facies interpretation of the underwater video profile TTR12-TV29. Letters (A-I) in blue indicate pictures in Figure 4.11 and 9.13.

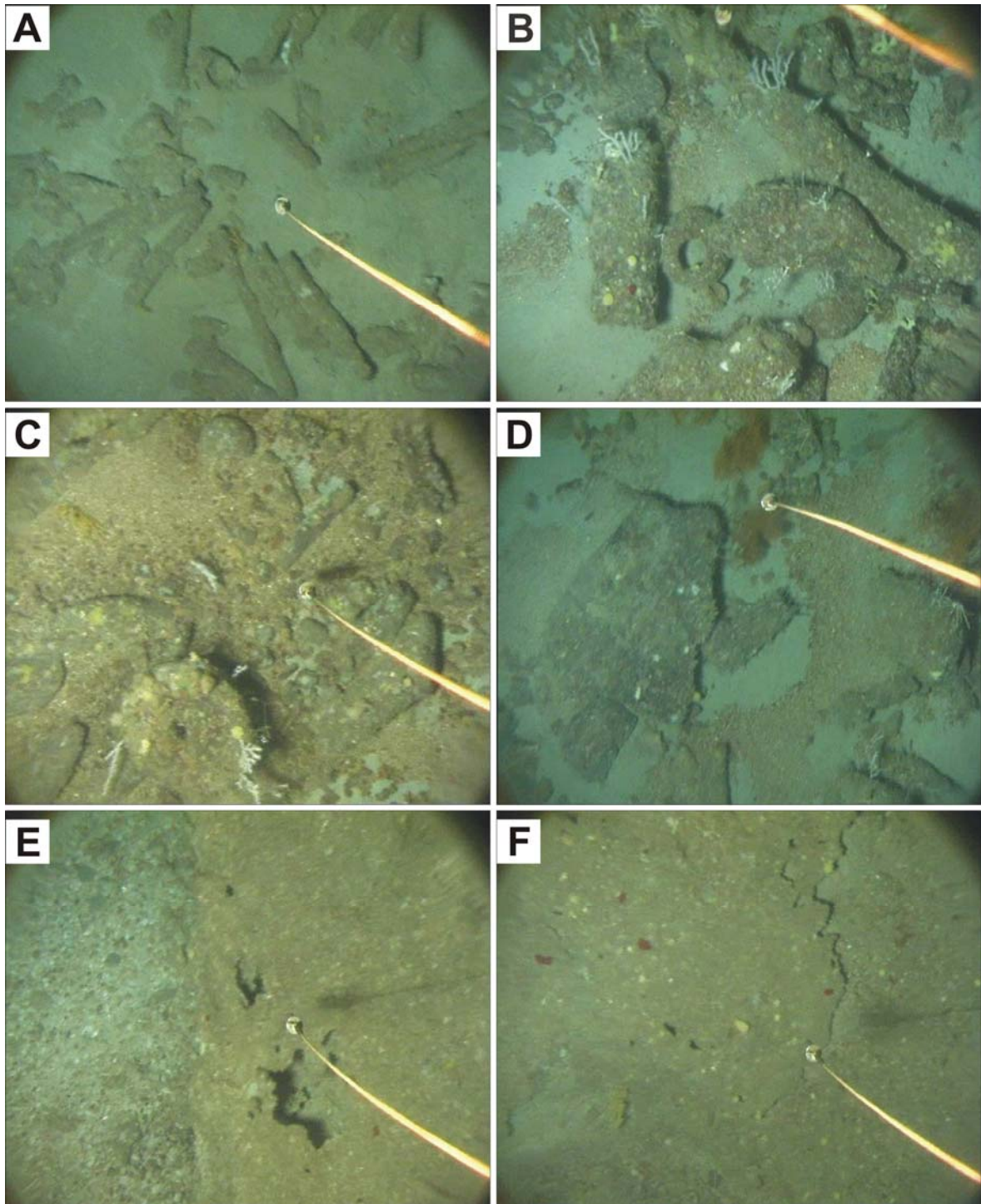


**Figure 4.11.** Pictures taken from the underwater video profile TTR12-TV29 over the Formosa Ridge. (A-C) Pictures illustrate the dolomite chimneys covering the seafloor. Image (C) illustrates a chimney in a vertical position protruding from the seabed; these occurrences are statistically much less frequent than the typical occurrence of the chimneys lying broken on the seabed. (D-F) probably aragonite pavements, not sampled. To be noted that the MDAC are used as hard-grounds for fixation of benthic organisms. Pictures are about 1.5 m wide.

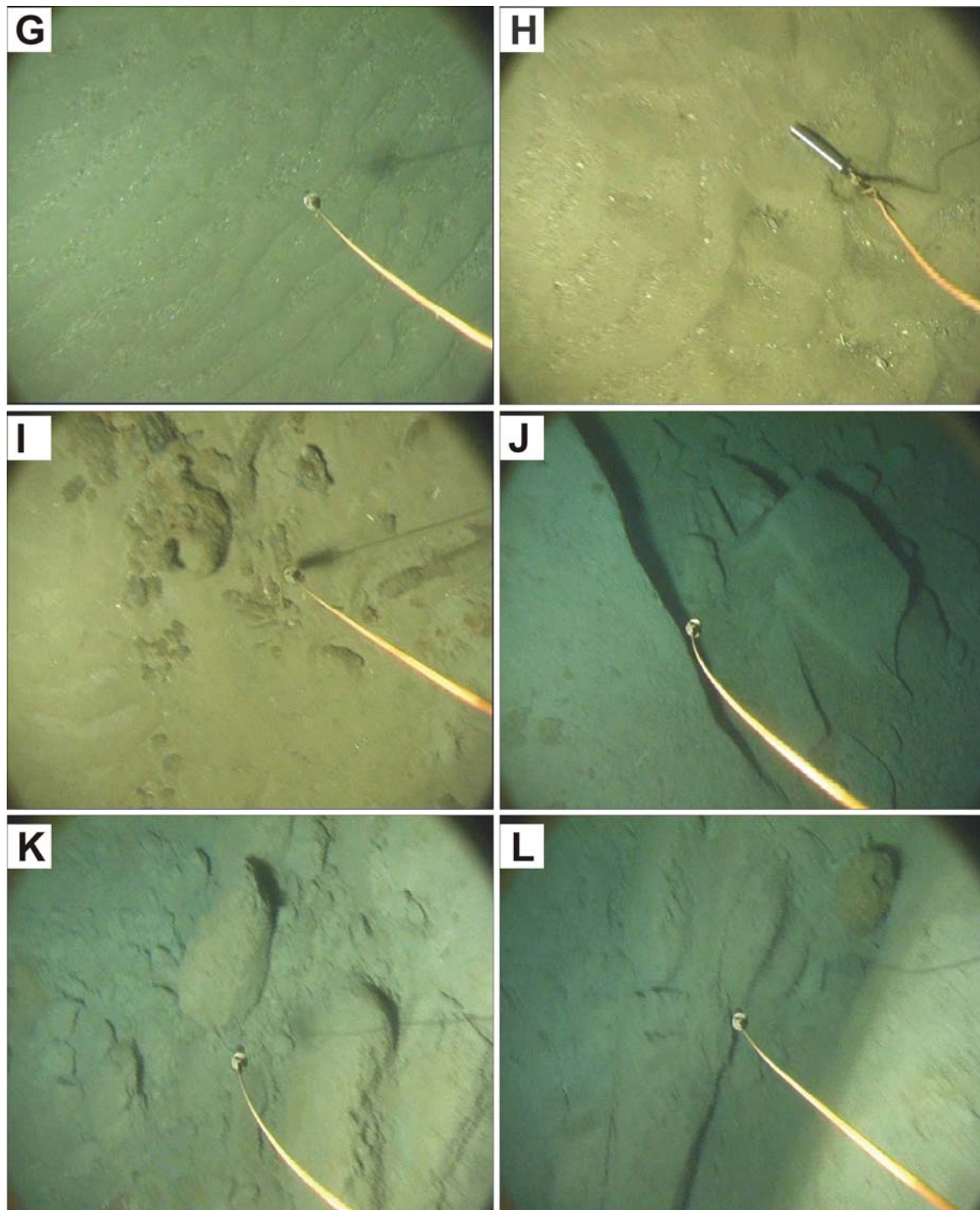


**Figure 4.12.** Pictures taken from the underwater video profile over the Formoza Ridge. (A-C) Pictures illustrate the rippled seabed with coarse sediment and where strong currents can be observed from the movement of suspended particles. Chimneys occur frequently within rippled seabed sediments as illustrated in (C). (D-F) rock outcrops, most probably of the blue marls from the Early-Middle Miocene (see text for discussion). Pictures are about 1.5 m wide.

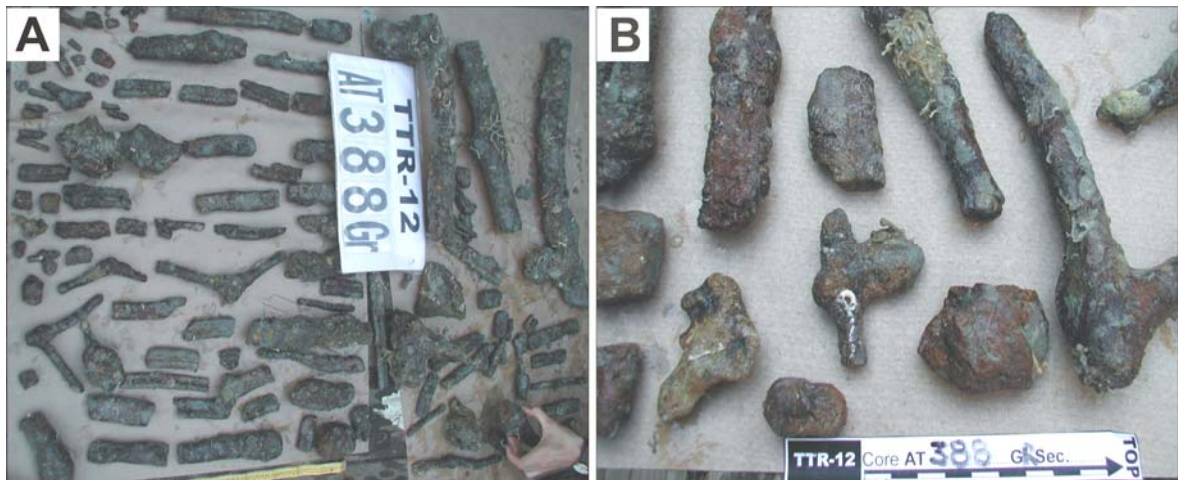


**Figure 4.13.** Methane-derived authigenic carbonate samples collected from the TTR12-388Gr TV-controlled grab station on the Formosa Ridge.

#### 4.3.1.3 Hormigas Ridge

The southern termination of the GDR is marked by the Coruña mound (Figure 4.14). To the southwest of the GDR, between 7°41'W and 7°33'W, the bottom topography is characterized by an arcuate-shaped ridge that defines the northern boundary of the Cadiz Channel (Figure 4.14). This arcuate-shaped ridge, called Hormigas Ridge (Díaz-del-Río *et al.*, 2003; Somoza *et al.*, 2003), is characterized by the presence of a series of mounds from which Iberico, Cornide and Arcos exhibit the highest relieves and strongest acoustic backscatter reflectivity on the NRL Seamap imagery.

The Iberico mud cone was surveyed during the TTR11 and Anastasya campaigns and the Cornide, Arcos and Coruña were surveyed during the Anastasya campaigns. The surveys of these structures included seismics, deep towed side-scan sonar, underwater observations and sampling with dredges (Kenyon *et al.*, 2002; Díaz-del-Río *et al.*, 2003; Somoza *et al.*, 2003).

These mounds (Iberico, Cornide, Arcos and Coruña) are characterized by the occurrence of MDAC, dominated by dolomite chimneys (Díaz-del-Río *et al.*, 2003) as illustrated in Figure 4.20, which occur as dense fields that cover most of the structures area.

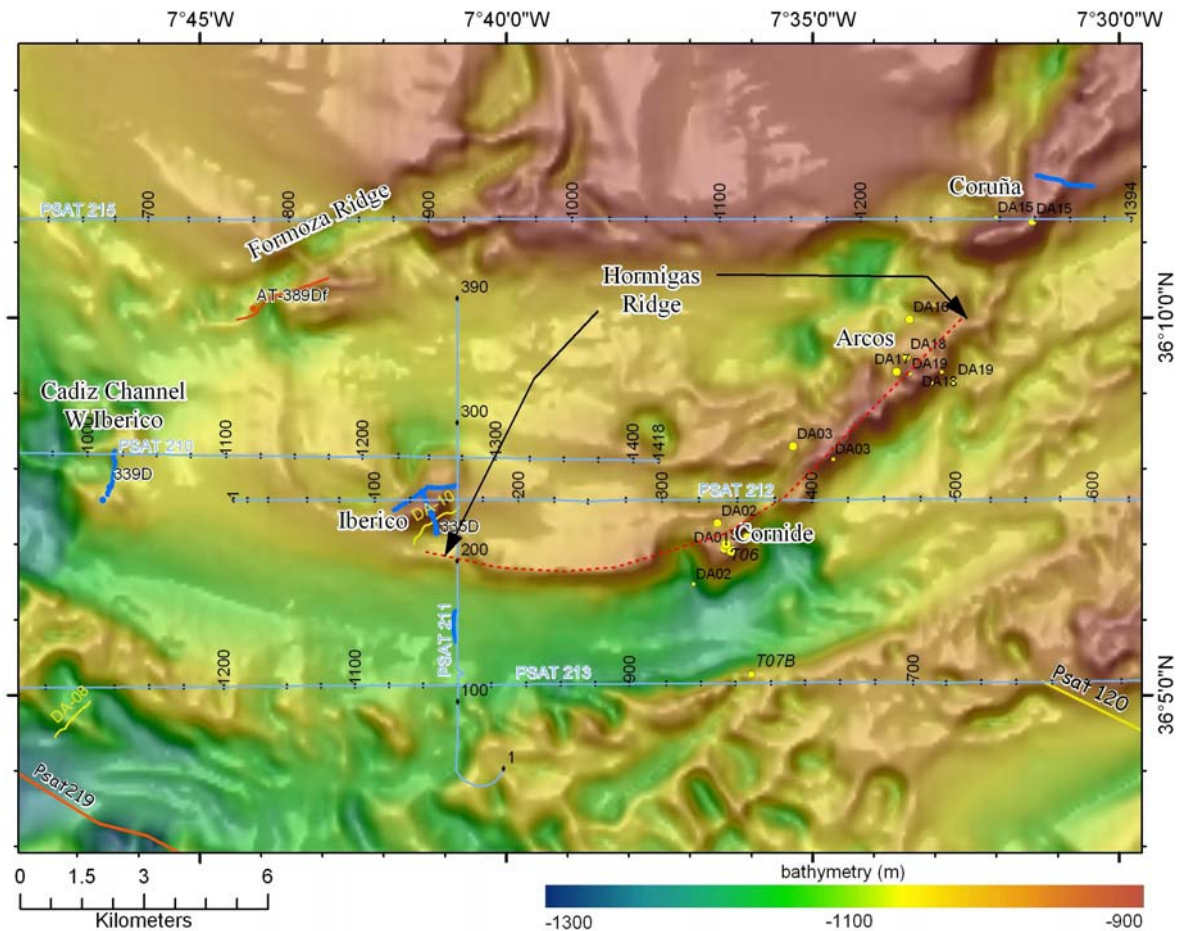


**Figure 4.14.** Bathymetric relief with a slope and hillshade with illumination from the NW and work performed on the Hormigas Ridge (marked by the dashed red line and with the limits are marked by the arrows).

#### 4.3.1.3.1 Iberico

The Iberico mud cone has a conical, asymmetric morphology (Figure 4.15), with a triangular section shape. Their summit is located at 874 m water depth and it is 156 m high in relation to the surrounding ridge in which it is located. The diameter of the cone ranges from 1200 to 1700 m. The southward and the eastward flanks have the steepest gradients, up to 26.7°, while the northward flank has slopes of 8 to 17° (Figure 4.16). The summit of the cone does not show any particular distinct feature from the flanks.

Iberico is located on the western end of the Hormigas ridge that borders the northern limit of the Cadiz MO Channel. In relation to the ridge morphology, the Iberico mount is bordered in the southern flank by a 40 m depression or moat (feature M<sub>s</sub> marked by the white dashed line in Figure 4.18B). The northern flank is also bordered by a larger and

deeper depression where a smaller asymmetrical depression, a pockmark, or an erosional scour hole is observed on both the bathymetry and the MAK side-scan sonar imagery (feature P<sub>1</sub> and P<sub>2</sub> in Figure 4.18A).

The seafloor reflection of the Iberico mound is higher than the seafloor reflection of the surrounding sediments. While the acoustic penetration obtained with the used system, in the Iberico and within the ridge area, was not sufficient to discriminate the nature and dimensions of the contact between the feeder channel under the Iberico and the surrounding sedimentary sequence, it is possible to distinguish the chaotic and indistinct seismic reflection pattern under the Iberico from the stratified host sediment reflectors (Figure 4.17).

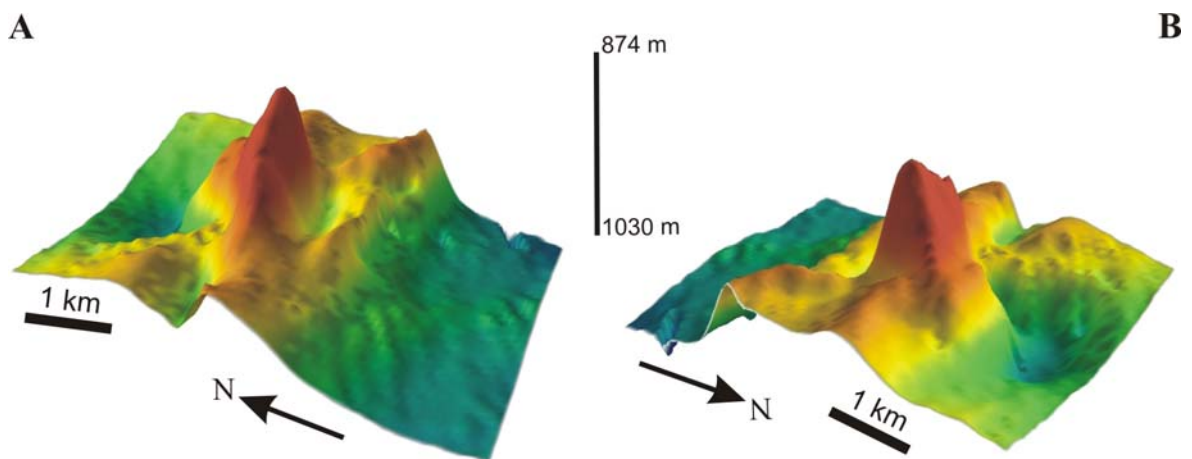


**Figure 4.15.** 3D bathymetric morphology of the Iberico mud cone. (A) view from SW of Iberico. (B) view from NE of the Iberico.

In the Iberico mud cone several samples (as illustrated in Figure 4.20) were collected by dredging along the south flank during the TTR11 cruise (sample TTR11-335D, with the position of this dredge plotted by the black arrow in Figure 4.18A) and during the Ana00-DA10 dredge (Díaz-del-Río *et al.*, 2003) from the Anastasya 2000 cruise (ship navigation corresponds to the yellow line in Figure 4.18A). Both dredges allowed the collection of large number of MDAC of dolomite-dominated chimneys and dolomite-dominated crusts (the study of these samples is described in Chapter 5). Plastic mud and blue marls clasts were also retrieved from these dredges. The blue marls have been interpreted as being of Early-Middle Miocene age and expressing the wedge front of the olistostrome/accretionary complex (Somoza *et al.*, 2001; Díaz-del-Río *et al.*, 2003).

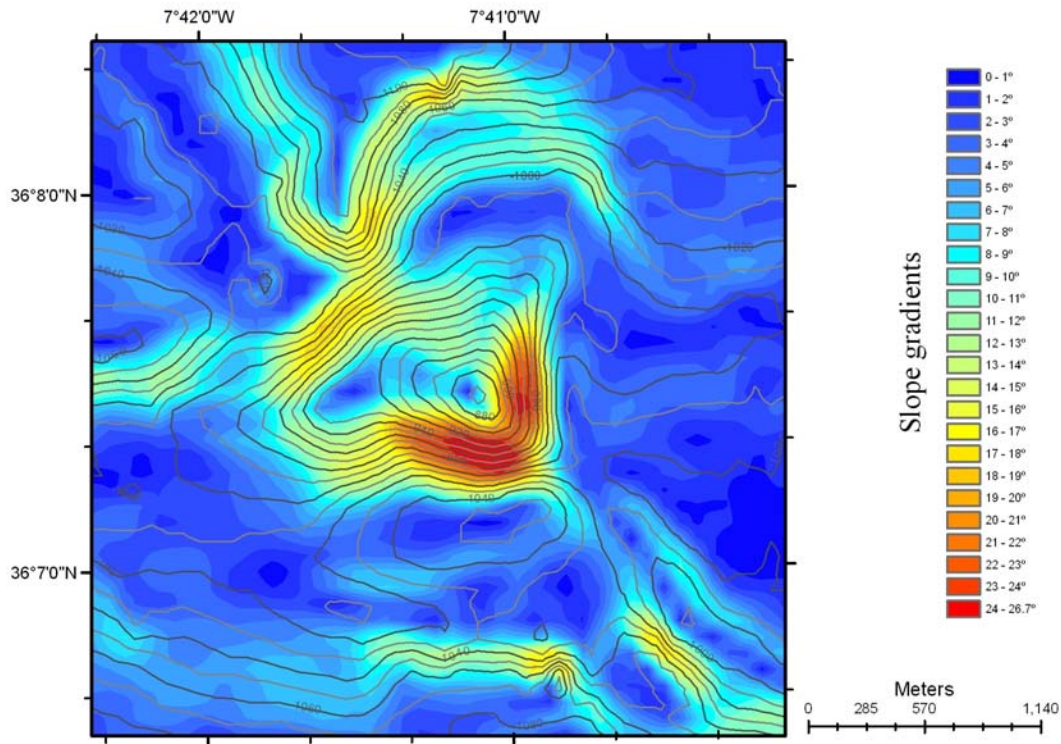


Figure 4.16. Slope gradient of the Iberico mud cone. See location in Figure 4.14.

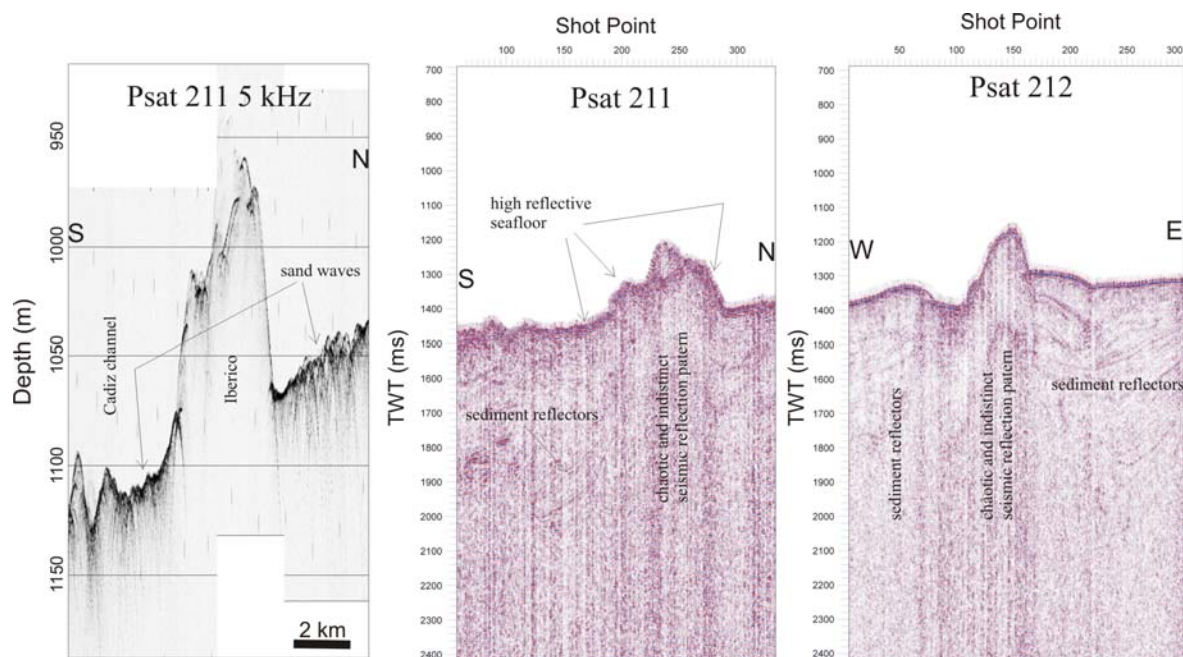
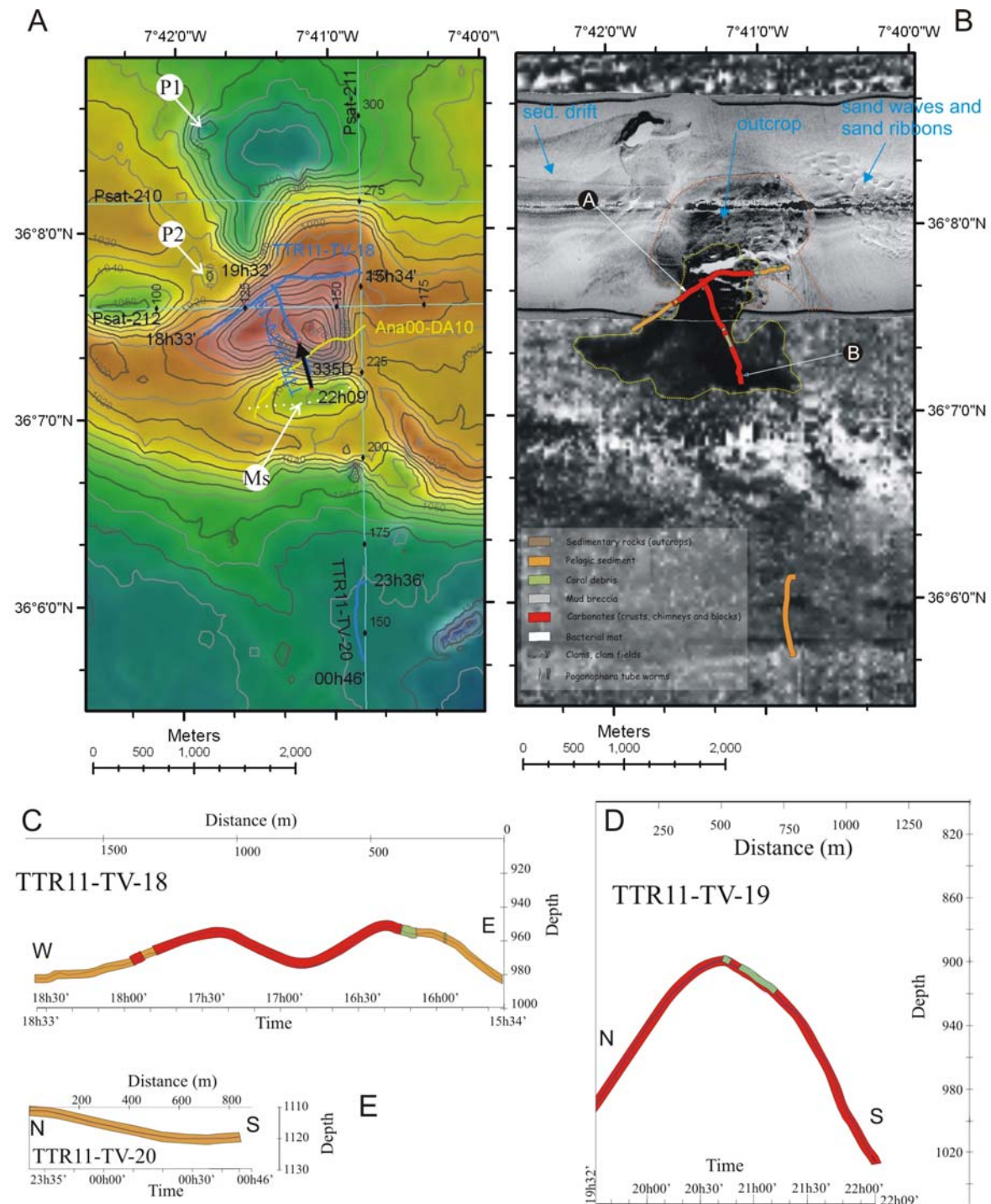


Figure 4.17. Profiler and single channel seismic lines TTR11-Psat 211 and TTR11-Psat 212. Location of seismic lines is given in Figure 4.18A. To be noted the chaotic and indistinct seismic reflection pattern below the surface conical expression of the Iberico cone, contrasting with the parallel reflections of the sedimentary basin sequences.

The Iberico mud cone exhibits a strong but differential acoustic backscatter on the NRL 12 kHz Seamap side-scan sonar imagery and also on the deep-towed high resolution 30 kHz MAK profile TTR11-42 (Figure 4.18B). The southern and the northern flanks of the cone are characterized by a strong backscatter but with distinctive patterns. While the southern flank and the upper part of the northern flank (area highlighted by the yellow dashed line in Figure 4.18B) are characterized by a very strong backscatter with an homogeneous pattern, which is interpreted as corresponding to areas recovered by MDAC (pictures A and C from Figure 4.19) the northern and the western lower slopes of the mound are characterized by a strong backscatter with sharp, near parallel shadows interpreted as indicating rock outcrops with bedding faulting and folding (area highlighted by the brown dashed line in Figure 4.18B). To the eastern of the mound, the side-scan sonar images show a weaker reflectivity that, also according to the seafloor observations, is interpreted as corresponding to pelagic sediment cover with sand waves and sand ribbons with absence of MDAC. To the W off the Iberico the seafloor is characterized by sediment drift deposits (as observed on the 5 kHz MAK profiler).

On the Iberico mud cone two underwater video camera lines (TTR11-TV-18 and TTR11-TV-19) were carried out during the TTR11 cruise (Kenyon *et al.*, 2002; Magalhães *et al.*, 2005). Profile TTR11-TV-18 was acquired from E to W, approximately at a constant depth, along the mid slope of the northern flank of the mud cone. The profile initially showed a seafloor covered by pelagic oxidized sediments, with scattered occurrence of fragments of carbonate clasts and some scarce chimneys and coral debris. This portion of the profile corresponds to an intermediate backscatter reflectivity in the MAK SSS. A larger occurrence of coral debris was observed when a water depth of 960 m was reached and from there on the profile was characterized by an almost continuous occurrence of chimneys, most of them very fragmented and lying broken at the seafloor, as illustrated in Figure 4.19A. When approaching the base of the cone, the occurrence of carbonate chimneys becomes less frequent and then pelagic sediment with scarce fragments of chimneys and scarce clasts, similar to the observed at the beginning of this profile is observed.



**Figure 4.18.** Iberico mud cone and the Cadiz Channel, south of Iberico. (A) EM-12 multibeam bathymetry with underwater video observation profiles plotted in blue, Anastasya 2000 dredge station plotted in yellow and seismic reflection profiles plotted in light blue. (B) NRL Seamap 12 kHz SSS (low resolution) and MAK SSS imagery (high resolution) with the bottom facies interpretation plotted over it. Labels A and B pinpoint the location of still video camera pictures presented in Figure 4.19. On the SSS imagery, high backscatter is dark. (C-E) bottom facies interpretation of the underwater video profiles.

Profile TTR11-TV-19 was acquired from the base of the moat in the southern flank to the middle of the northern flank of the Iberico mud cone, crossing the cone summit. All along the profile the seafloor was characterized by high density of chimneys and crusts as illustrated in Figure 4.19B. At the summit and at the top of the S flank, close to the summit, the seafloor was characterized by the presence of coral debris. No live coral was positively identified and only died coral rubble was observed. The Northern flank, similarly to the southern flank, was covered by chimneys and crusts, most of them fragmented and lying at the seafloor. Chimneys in a vertical position, protruding from the seafloor as illustrated in Figure 4.19B<sub>1</sub> was very rare to be observed.

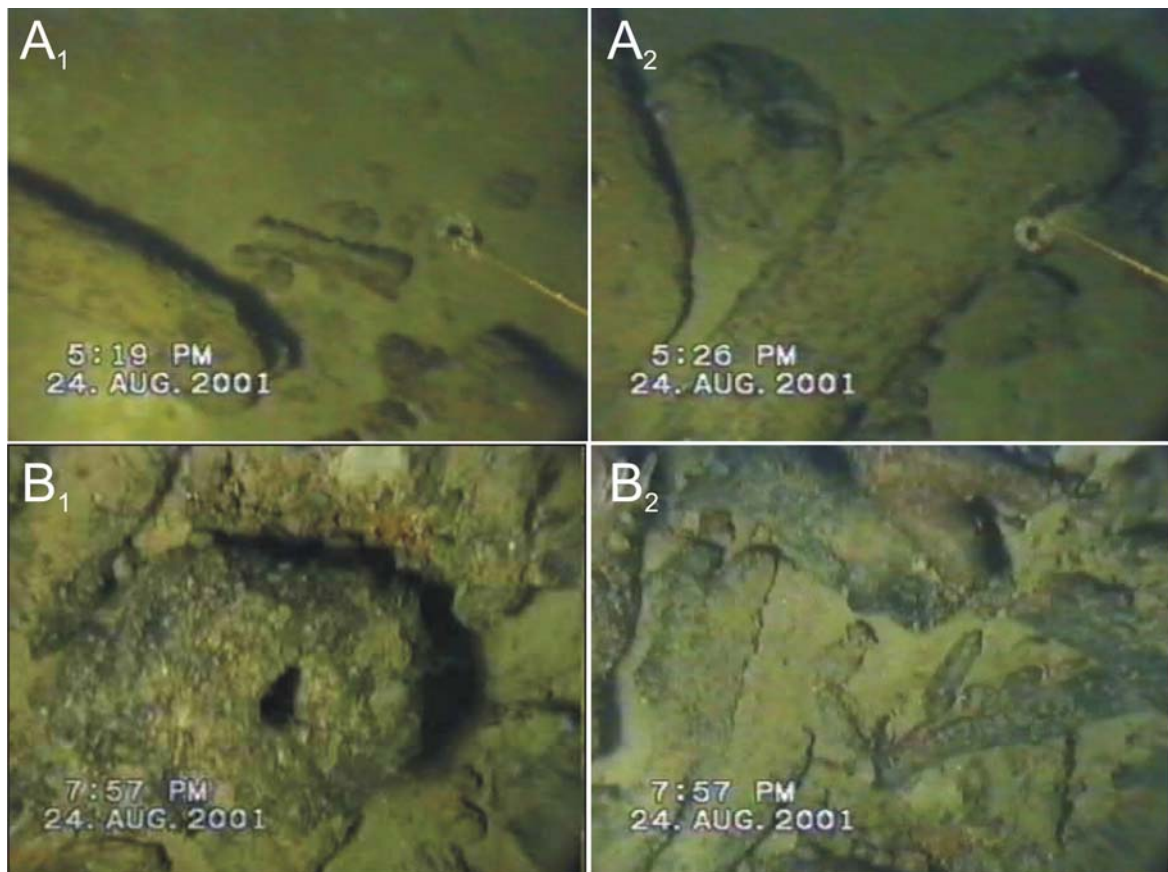


**Figure 4.19.** Pictures taken from the underwater video profiles over the Iberico mud cone. Pictures illustrate the dolomite chimneys recovering the seafloor. (B<sub>1</sub>) vertical carbonate chimneys. Pictures A and B<sub>2</sub> correspond to an area approximately 1.5 m wide. Picture B<sub>1</sub> correspond to an area approximately 75 cm wide.

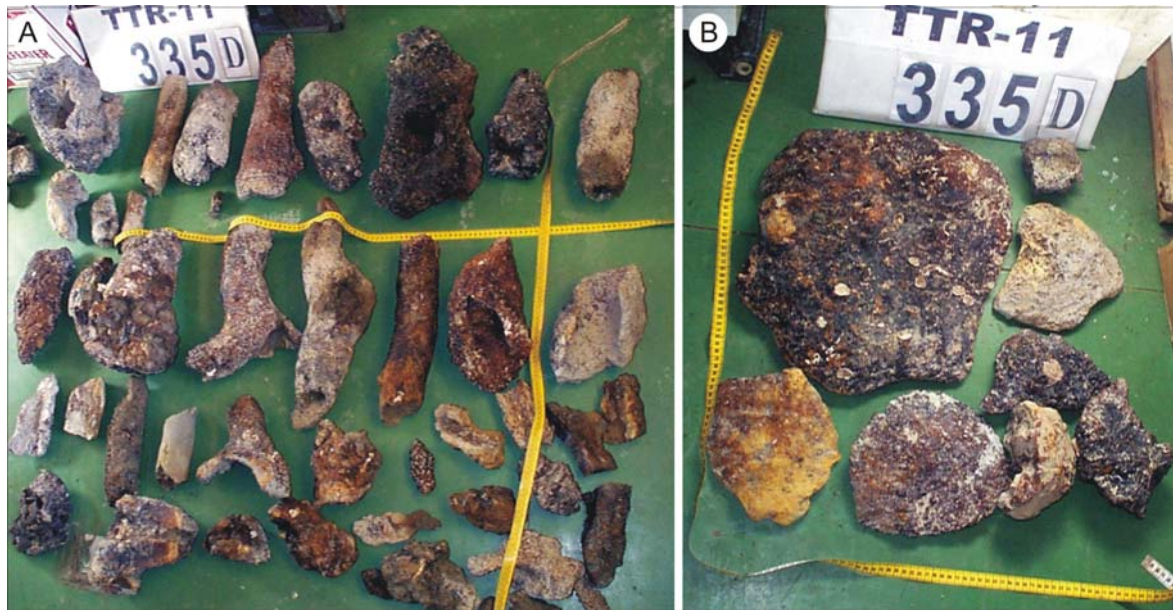


**Figure 4.20.** Methane-derived authigenic carbonate samples collected by the TTR11-335D dredge station. (A) dolomite chimneys. (B) dolomite crusts.

#### 4.3.1.3.2 *Cornide*

Cornide is a cone shaped mound with a maximum basal diameter of 1.8 km and 220 m high in relation to the base of the Cadiz channel. It has SW and SE steep slopes with gradients up to 25°, and smooth northern flanks. The top of the mound is located at 920 m water depth and the summit of the mound has a smoothed conical shaped where no collapse rims are evident. On this mound no structures typical of a mud volcano edifice, evidencing mud flows are found (Figure 4.21). On the NRL Seamap side-scan sonar imagery the Cornide is characterized by very strong backscatter intensity on the steep slopes and on its summit. The northern smooth flanks are characterized by a moderate backscatter intensity (Figure 4.22).

During the Anastasya campaigns, two dredge sampling stations were carried out on Cornide. Dredge ANA01-Dr01 was acquired along the summit and top of the eastern flank and allowed the collection of crusts and chimneys similar to the ones collected on the Iberico mud cone. Dredge ANA01-Dr02 was acquired along the western and northern flanks, crossing the top of the mound, west of the summit. This dredge, like the previous ones allowed the collection of pipe-like dolomite chimneys and slabs, and clasts of blue marls (Somoza *et al.*, 2002; Díaz-del-Río *et al.*, 2003) similar to the ones collected on the Iberico mud cone. On the cone summit, a gravity core allowed the identification of mud

sediment with a strong H<sub>2</sub>S smell, an high vacuolization of the sediment, interpreted as indicating a high gas content in the core, but no mud breccia typical of mud volcanoes was positively identified (Diaz del Rio *et al.*, 2001).

Underwater photographs taken during the Anastasya 2001 campaign also allowed recognizing that the summit of the Cornide was covered by pipe-like chimneys with a similar aspect to the underwater pictures from the Formosa ridge and from the Iberico cone (Somoza *et al.*, 2002).

On the Cornide summit, heat flow stations were also performed allowing the measure of a seabottom sediment temperature of 12°C and the estimation of a thermal gradient of 23.68, an heat flow value of 29.34 (mW/m<sup>2</sup>) and a conductivity of 1.239 W/m-K (Gardner *et al.*, 2001). The heat flow data revealed fluctuations in the upper meters of the sediment column (Figure 4.23) reflecting short term bottom water temperature changes of the order of less than a year. From the estimated thermal gradient, Gardner *et al.* (2001) estimated a gas hydrate stability zone (GHSZ) with a thickness of 125 m at 1052 m water depth.

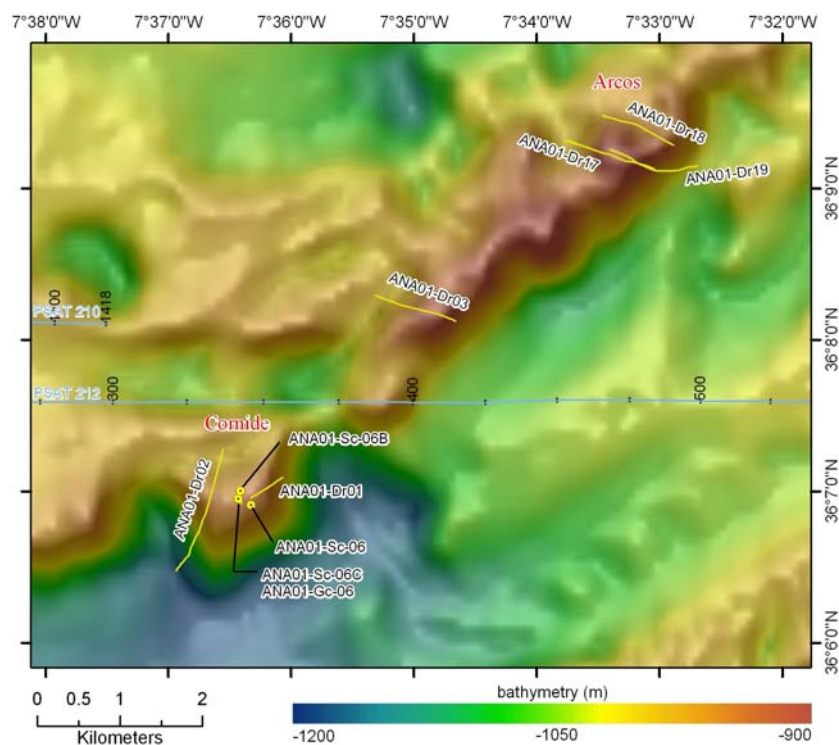


**Figure 4.21.** Bathymetry of the Hormigas ridge in the area of Cornide and Arcos. The location of the dredge stations, heat flow measurements and gravity coring performed during the Anastasya campaigns are represented by the yellow dots and lines, respectively. Bathymetric relief with a slope and hillshade with illumination from the NW.

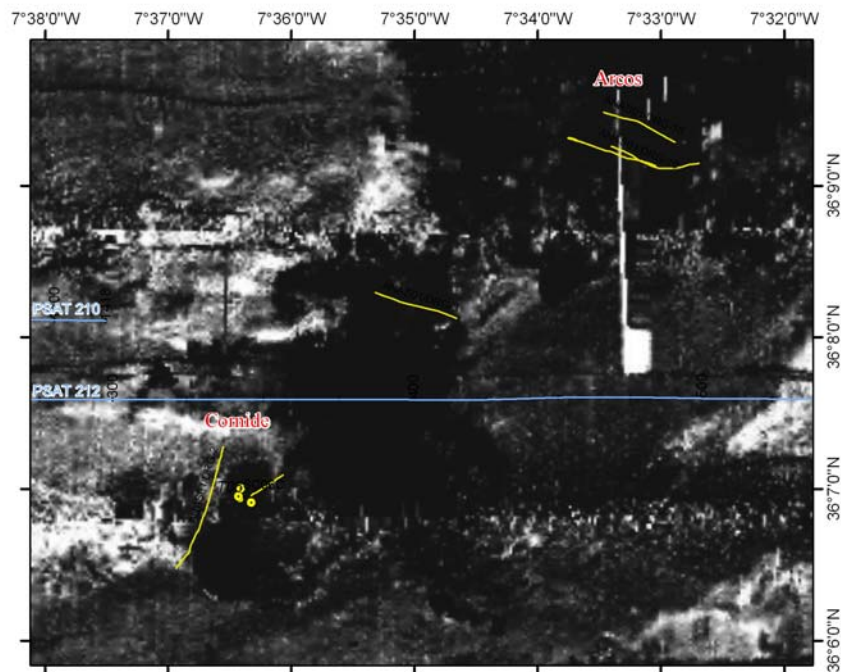


**Figure 4.22.** NRL Seamap imagery on the Hormigas ridge ver Cornide and Arcos structures. High backscatter is represented as dark.

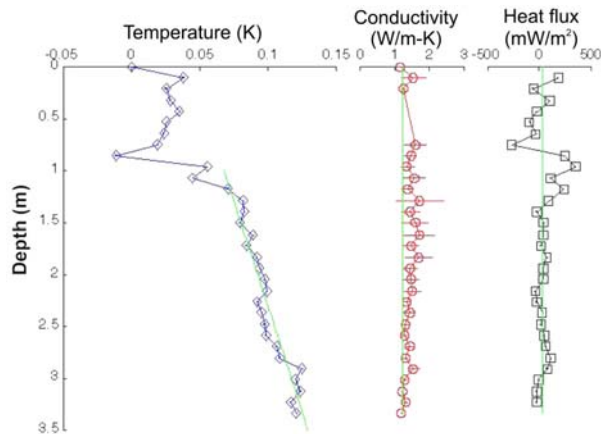


**Figure 4.23.** Anastasya 2001 heat-flow station ANA01-SC06C. Temperature profile and calculated conductivity and heat flux (Gardner *et al.*, 2001). To be noted the temperature anomaly recorded in the first meter of sediments, interpreted as the result of short term fluctuations of the anomalously high temperature of the MO.

During the Anastasya 2001 campaign a dredge (ANA01-Dr03) was also performed across the Hormigas ridge between Cornide and Arcos mounds (Figure 4.21). The dredge did not allow the collection of any material as the cable broke during the retrieval of

the dredge, due to excess of loading of the dredge container. However, underwater photography from this area allowed the recognition of carbonate chimneys and crusts, similar to the ones from Cornide.

#### **4.3.1.3.3 Arcos**

On the northern termination of the Hormigas ridge, the Arcos mound is characterized by an irregular topography with a height of 100 m relative to the base of the Cadiz channel and steep gradient slopes. The summit of the Hormigas ridge in this area exhibits crests with an irregular linear shape and with horizontal steps to the north flank that intercalate the ridge crest (Figure 4.21). This area is characterized by strong backscatter on the NRL Seemap side-scan sonar imagery (Figure 4.22) and 3 dredge profiles were acquired in this area during the Anastasya 2001 cruise. Dredges ANA01-Dr18 and 19 allowed the recovering of crusts and chimneys, similar to the ones collected in Formoza, Iberico and Cornide. During the Dredge ANA01-Dr19 clasts of blue marls and limestones were also collected, which were interpreted as corresponding to fragments of rock outcrops.

### **4.3.2 The Tasyo Field**

The Tasyo Field is considered to be delimited to the north by the southern edge of the Cadiz Channel and its southern limit is defined by the Captain Arutyunov and the Atlas mud volcanoes. The morphology of the Tasyo Field area is characterized by the interfingering of several distinct processes. Several fluid escape structures, such as mud volcanoes and pockmarks can be distinguished on the bathymetry and sonar backscatter. This area is dominated by erosional and sedimentary features related to the outflow of the Mediterranean water. On its eastern sector, within the main Channel of the MO, there is a dominance of proximal scour and ribbon features with abrasive surfaces with rock outcrops, sand dunes and sand ribbon fields. Outside of the main Channel of the MO, the overflow sedimentary lobe sector is characterized by the presence of mud waves and erosive scours, seafloor slides, mud waves fields, contouritic levees and overflow MO channels and furrows (Hernandez-Molina *et al.*, 2003; Hernandez-Molina *et al.*, 2006). This sector is also characterized by large negative depressions, some of which resemble scars of sediment slides that transport material towards the lower slope and to the Horseshoe Abyssal Plain. Intra-slope mini-basins with a diameter of 800 - 4000 m are also

observed in this area.

In the Tasyo Field, the Hesperides, Cibeles, Faro and Almazan mud volcanoes were investigated in detail for the occurrence of MDAC.

#### 4.3.2.1 Hesperides

The Hesperides mud volcano (Figure 4.24) is the largest mud volcanic structure identified in the Tasyo Field (Somoza *et al.*, 2003). It has a complex morphology with six single cone-shaped domes (labelled C 1 to C6 in Figure 4.24), with diameters ranging from 400 m to 1.1 km. These cones sit over a small plateau that defines the mud volcano complex and has a total seafloor diameter of about 3 km (Figure 4.24). The global shape of the complex is irregular, but most of the cones exhibit a regular symmetrical conical shape (Figure 4.24). The summits of the complex range from 685 to 740 m water depth, and have a maximum height of 75 m (c.a. for the cone C1) in relation to the plateau and about 200 m in relation to the surrounding seafloor. The Hesperides MV has slopes with smooth gradients, up to 16° but in general less than 10° within the plateau (Figure 4.25A). Nearby of the MV complex, it is possible to identify several depressions or mini-basins on the bathymetry, up to 2.4 km wide (structure B1 in Figure 4.24). It is also possible to identify low-relief sub-circular depressions, some of which have a small positive relief at their base (e.g. structure P1 in Figure 4.24), which are interpreted as possible pockmarks.

The Seamap imagery of the complex exhibits strong acoustic backscatter intensity over some of the cones (C1, C2, C5 and C6) and moderate backscatter over the remaining plateau area, with a stronger intensity at the summits of the C3 and C4 cones (Figure 4.26). This is also confirmed by the acoustic seismic seafloor reflection of the parametric parasound, 5 kHz profiler and even by the single channel seismic profile TTR10-Psat155 over the Hesperides complex, which exhibits a strong surface reflectivity (Figure 4.25B). On the seismic profiles, the subsurface under the MV is characterized by a non-reflective transparent facies with chaotic reflectors, typical of the mud volcanic nature of the structure (Figure 4.25B). From the seismic reflection profile it is also possible to recognise that the MV emplacement produced a deformation of the adjacent contourites, producing low amplitude folds of the adjacent host sediments, SE of the MV.

Two underwater video profiles with Ocean Floor Observation System (OFOS) were acquired on the Hesperides MV during the GAP cruise (Kopf *et al.*, 2004). OFOS 16 and OFOS 17 crossed this complex from NE to SW and from S-N respectively (Figure 4.24).

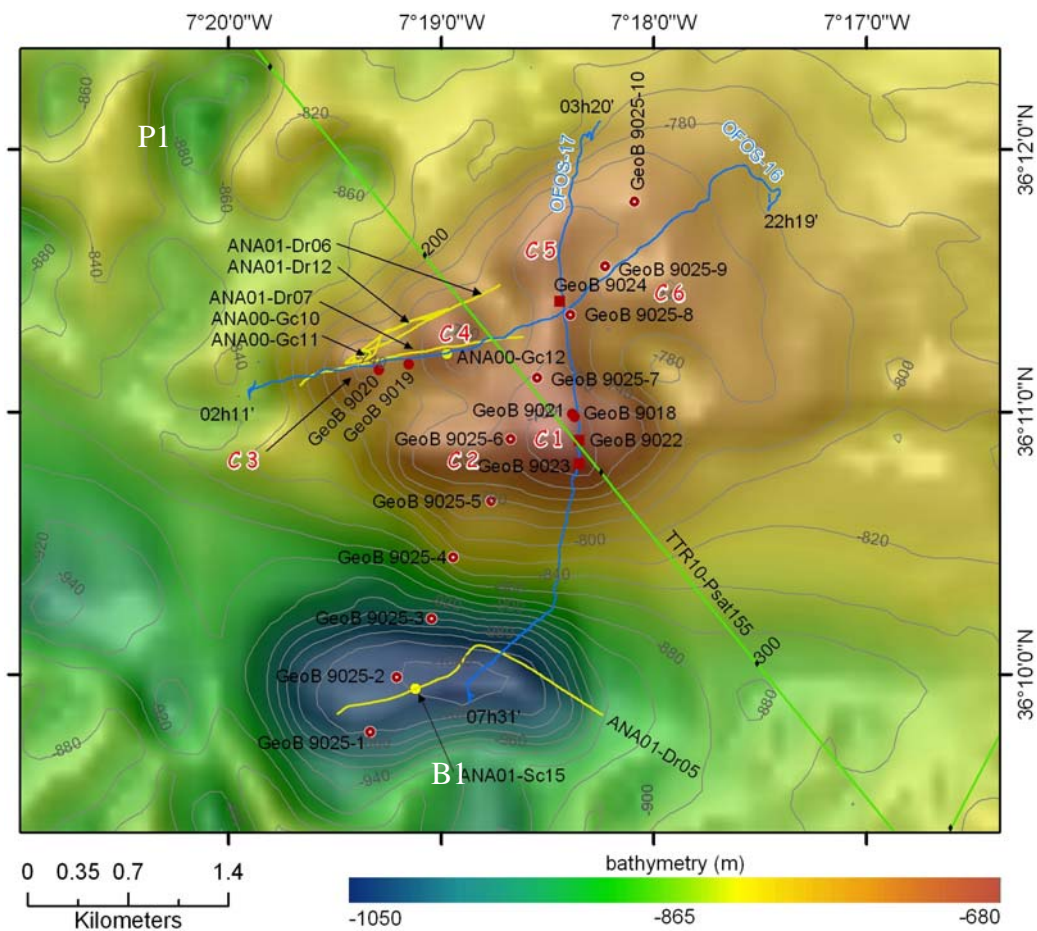


**Figure 4.24.** Hesperides mud volcano EM-12 multibeam bathymetry with OFOS underwater track plotted in blue, Anastasya sampling stations in yellow, GAP stations in brown and single channel seismic line Psat155 in green. Bathymetry, with a slope gradient and a hillshade with illumination from the NW.

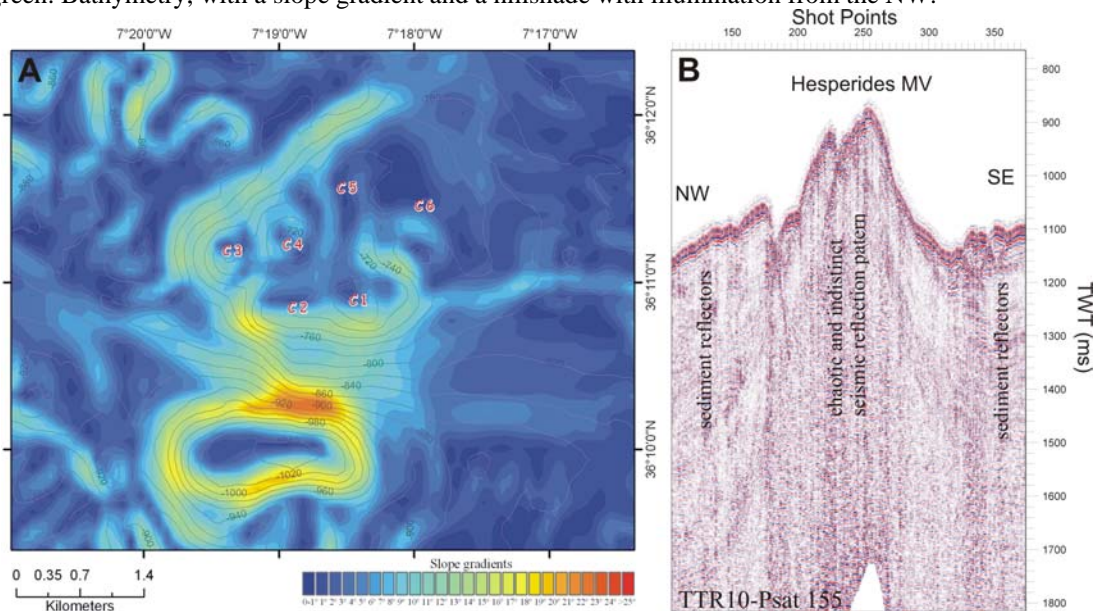


**Figure 4.25.** (A) Slope gradient image of the Hesperides MV. (B) Single channel seismic line TTR10-Psat155. Location of the seismic line is shown in Figure 4.24. To be noted the chaotic and indistinct seismic reflection pattern below the complex, contrasting with the parallel reflections of the sedimentary basin sequences to the S.

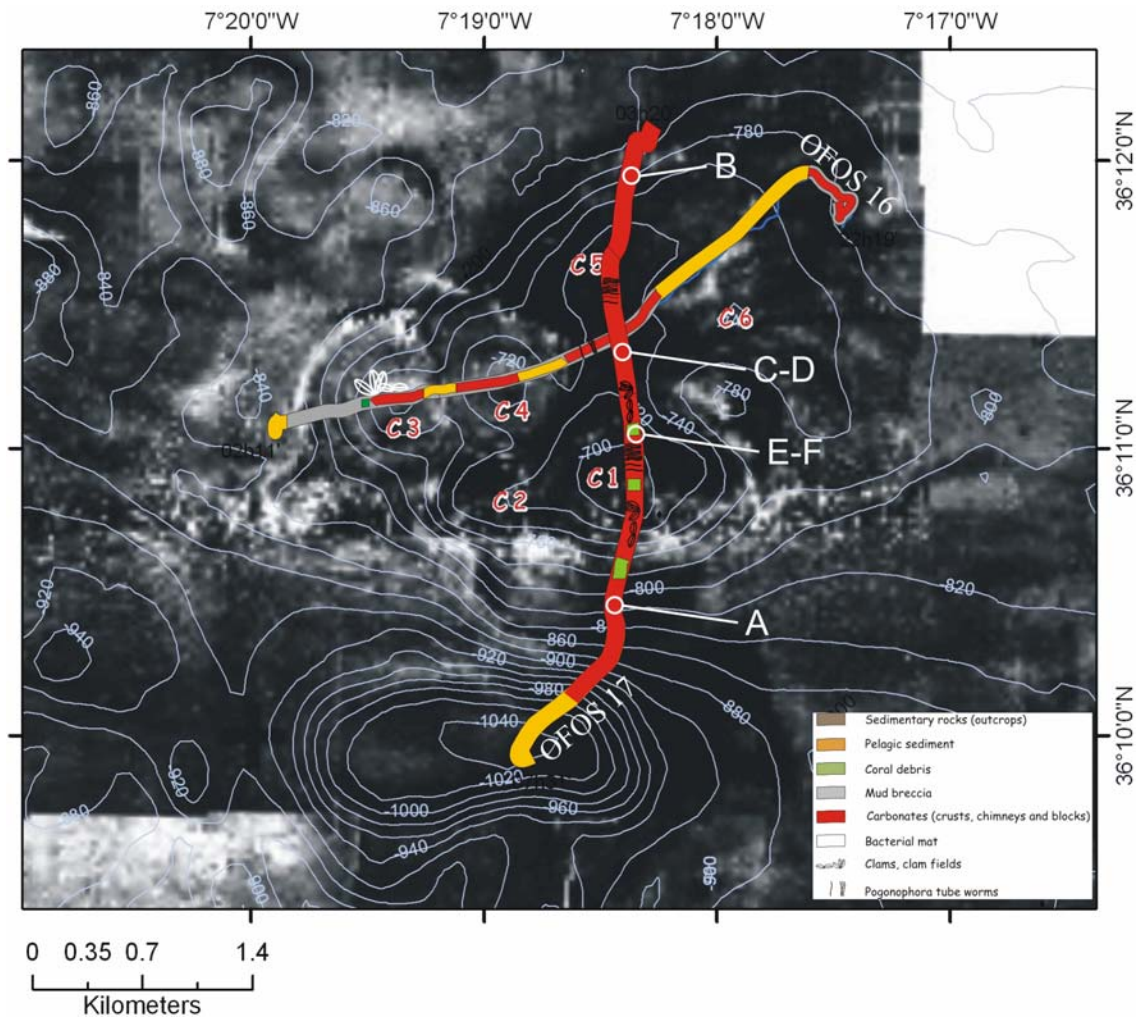


**Figure 4.26.** NRL Seamap long range SSS with the facies interpretation plotted over it.

The profile OFOS 16 began at the foot of the flank of cone C6, and showed gravel horizons interbedded with mud, interpreted as outcrops of older mud-breccia flows. Chimney fragments and carbonated rubble were also found scattered on the mud sediments but sometimes they occurred as dense patches on the seafloor. The chimneys and boulders occur fragmented, laid on the seafloor, colonized by benthic fauna, similar to those observed in the Iberico, Cornide or Formoza. Some larger boulders also occur. In the slope, rising through a broad plateau at the easternmost portion of the complex, in between the cones C5 and C6, this gently sloping plateau is characterized by the occurrence of scattered carbonate clasts within rippled sandy and muddy patches. At the central crest between the cones C1 and C5, this summit region is characterized by vast carbonate slabs with some scattered carbonate chimneys. Tubes of Pogonophora sp. were observed overlying the carbonate slabs and small bubbles coming up from some fissures were observed in this

area during the GAP cruise, but to date there is no confirmation of such venting. This area was the target of TV grab Station GeoB 9024, which allowed the collection of considerable amounts of carbonate crusts and slabs with numerous interbedded bivalves (Figure 4.30A-B). Numerous sessile organisms such as small corals, brachiopods, small sponges, were attached to carbonate crusts. As the track descends to the western flank of the cone into the depression between the crest and cone C4, only scattered carbonate crusts and muddy patches were observed. This depression is characterized by pelagic sediment, with sand and gravel, probably fragments of carbonates that roll downslope, and mud breccia clasts. Along the upper slope and summit of cone C4, chimneys and carbonate rubble and boulders were again observed at the seafloor of mud breccia-like sediment (as confirmed by the gravity core ANA00-Gc12, Figure 4.31). Patches of coral debris were also observed. The southwestern flank of cone C4 is characterized by the dominance of mud breccia sediments alternating with patches of sand and gravel. Carbonate fragments occur very rarely. This facies is also characteristic of the northeastern flank of cone C3. Near and at the summit of C3 the seafloor is characterized by the occurrence of scattered clasts, probably of mud breccia clasts. The southwestern flank of C3 is characterized by mud breccia-type sediments (as confirmed by the gravity cores ANA00-Gr10, ANA00-Gr11, GeoB 9019 and GeoB 9019; Figure 4.31) with occurrence of slabs and crusts, large carbonate boulders, small patches of fragmented shells and fields of gastropods, some of these patches of gastropods; extend for about 10 m. Coral debris were also found along this slope. At the base of the Hesperides plateau, close to the end of this profile, the seafloor is characterized by sandy sediments, sometimes with ripples.

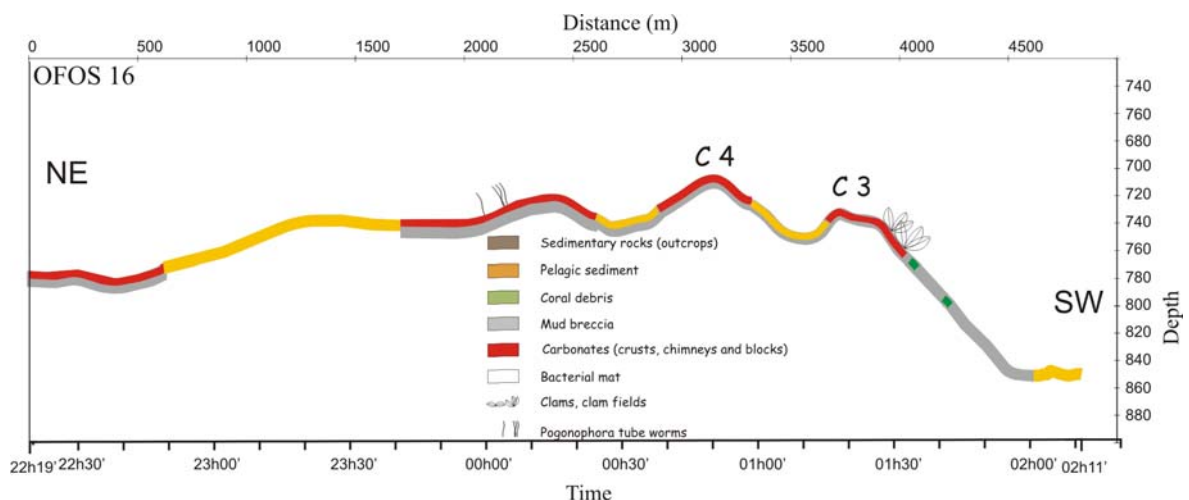


**Figure 4.27.** Facies interpretation of the OFOS 16 video profile. Labels 1, 2 and 3 indicate the location of still video camera pictures presented in Figure 4.29.

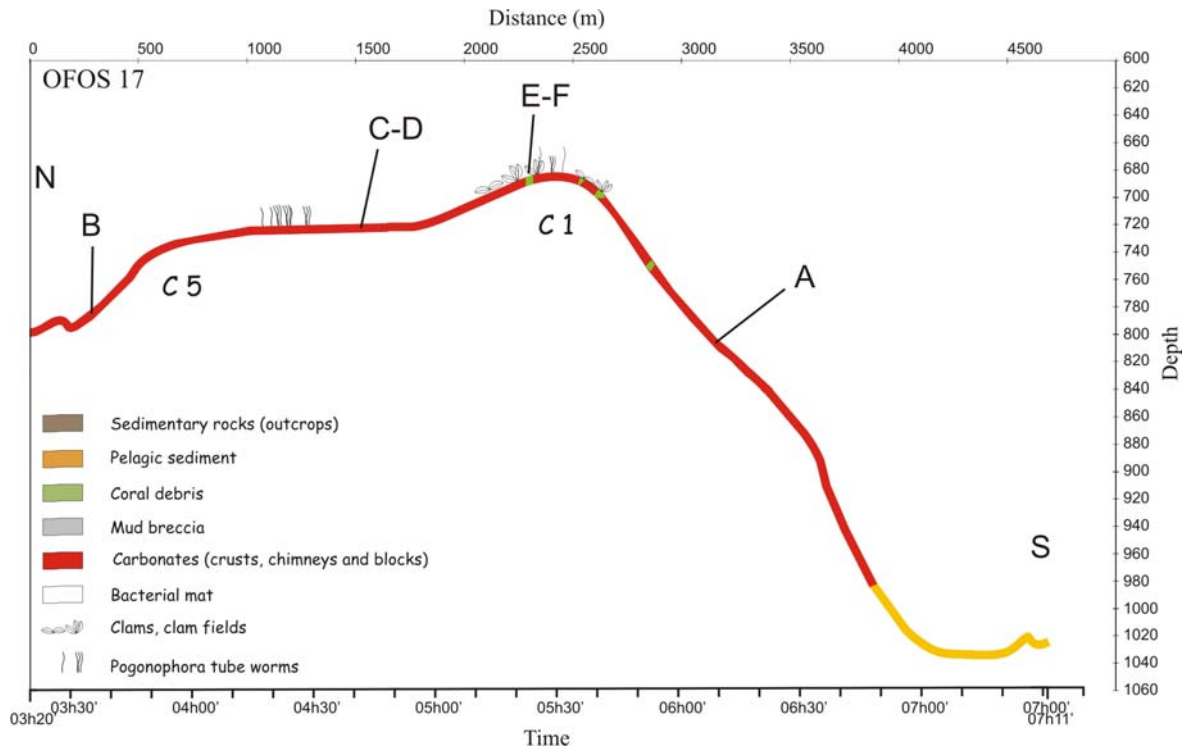


**Figure 4.28.** Facies interpretation of the OFOS 17 video profile. Labels 1, 2 and 3 show the location of still video camera pictures presented in Figure 4.29.

OFOS 17 began at the northernmost flank of the Hesperides mud volcano complex. The seafloor was covered by a high density of carbonate chimneys, lying broken on the seafloor and highly fragmented. The northern flank of the cone C5 is characterized mainly by muddy areas with patches of rippled sands and scattered carbonate crusts and chimneys. The summit of cone C5 and the crest between cones C5 and C1 is characterized by a dense coverage by carbonate pavements and crusts. This OFOS crossed the previous profile at the crest confirming the previous observation of abundant tubes of *Pogonophora* sp. tube worms. At the northern flank of cone C1 and at the summit, patches of coral debris were observed but the summit of C1 is characterized by extensive fields of pavements and carbonate crusts, sampled by TV-controlled grab at stations GeoB 9022 and GeoB 9023 (samples are illustrated in Figure 4.30). The summit of C1 is characterized by the occurrence of extensive coverage of deep water coral, forming reef-like patches. A patch of this coral debris was sampled with TV grab GeoB 9022 (Figure 4.30). It consists of dead coral rubble with small broken coral pieces and coral branches up to 30 cm in length and probably originating from species such as *Lophelia pertusa*, *Madrepora oculata*, and *Desmophyllum*. Several gastropods, brachiopods and small hydrozoa were found attached

to the dead coral pieces. Some small living coral species settled on the dead coral branches occasionally. Numerous carbonate slabs, crusts and fragments of chimneys were also collected in this grab sample (Figure 4.30). Most of the chimney pieces are oxidized as indicated by the brown to light brown colours, and vary in shape and size from a few centimetres up to 40 cm across. Small corals and encrusting organisms are attached to the chimneys. Along the southern flank of the cone C1, a high density of carbonate chimneys, some about 2 meters long, were observed together with some coral debris patches similar to the ones on the summit.

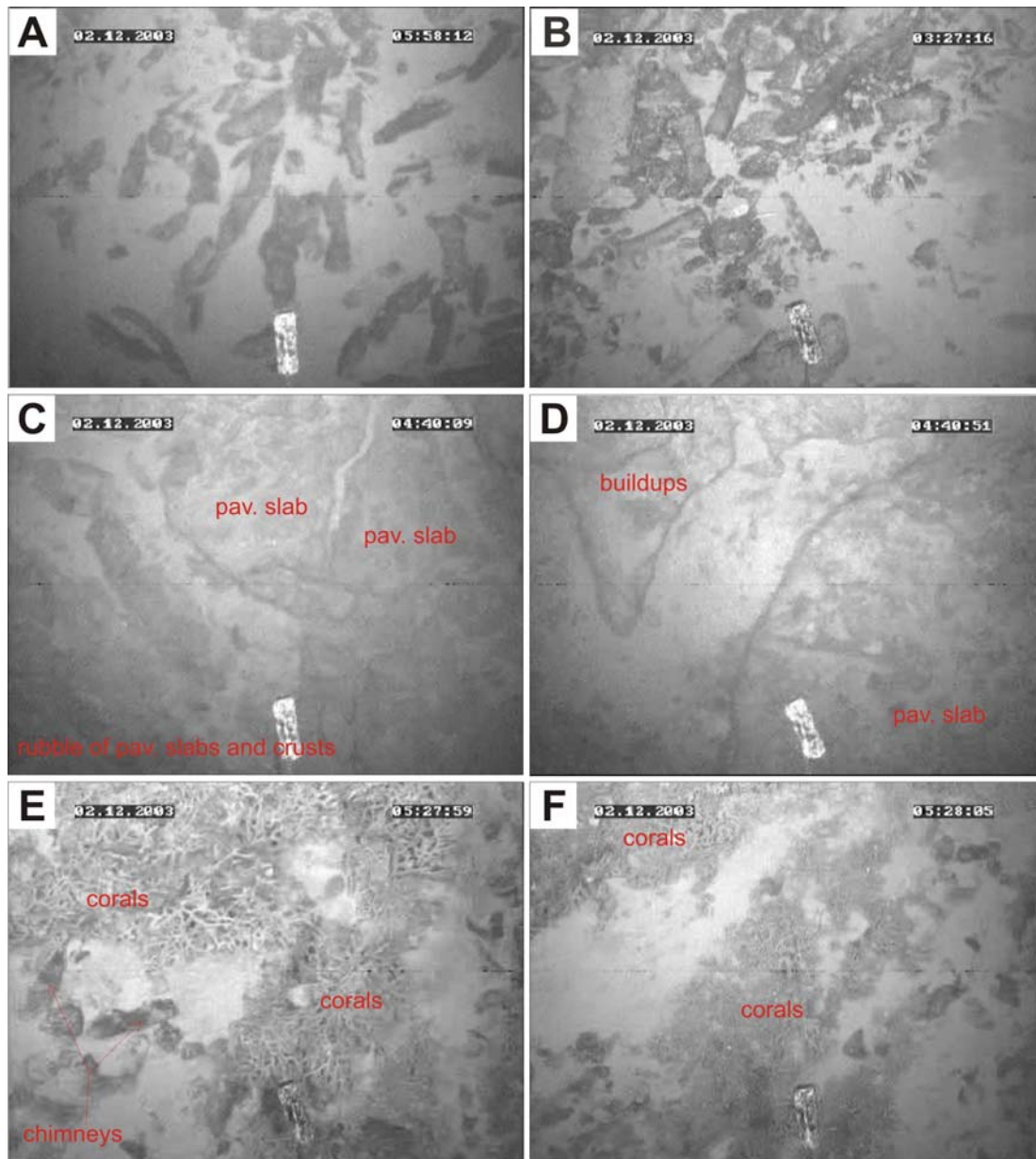


**Figure 4.29.** Still photograph taken with the video sledge OFOS16. (A-B) large number of chimneys and other carbonate rubble. (B-C) pavements, pavement slabs and mounded buildups. (E-F) corals and coral rubble in a chimneys field. Most probably the corals use the chimneys as hardground for fixation.

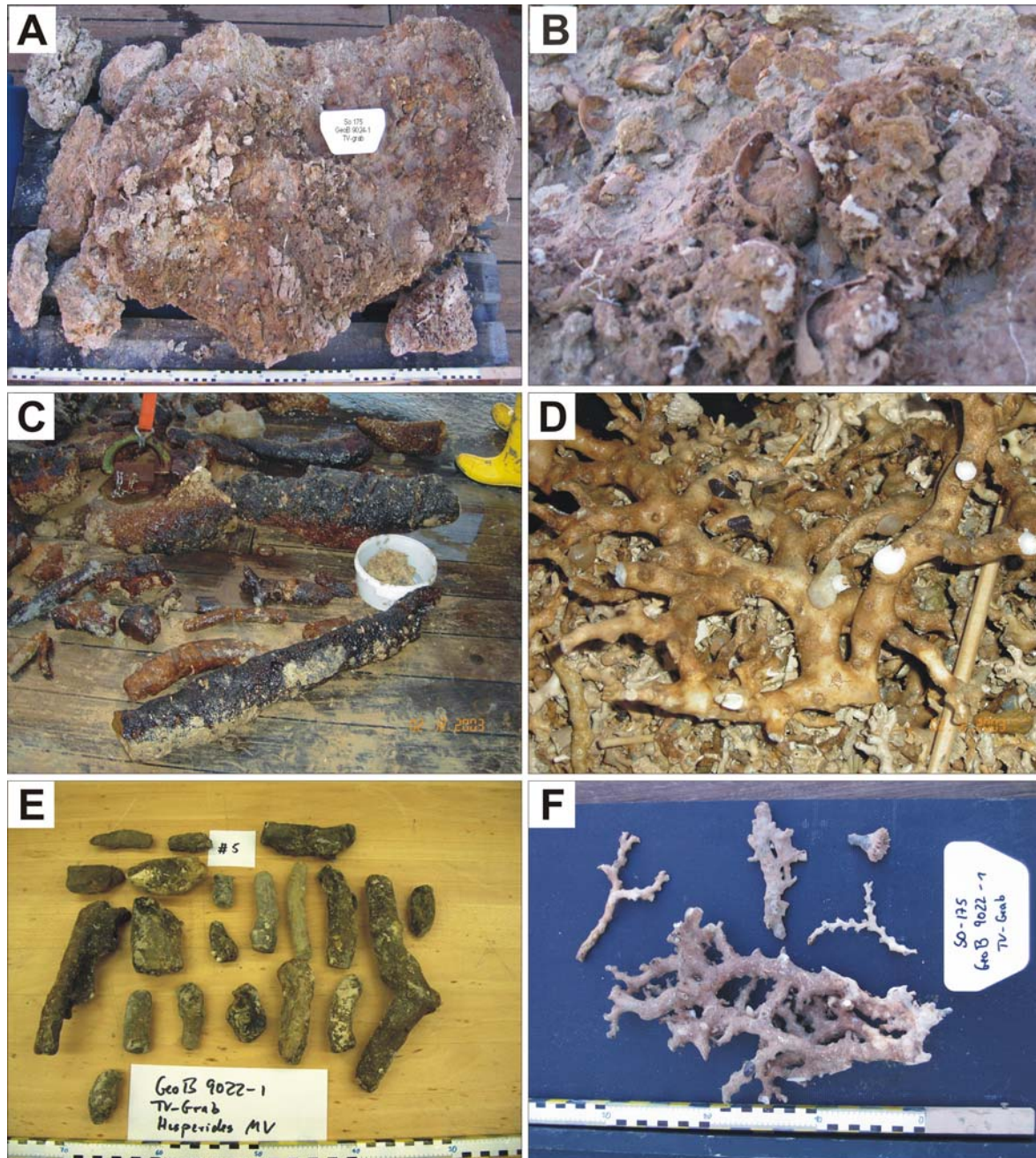


**Figure 4.30.** Photographs of samples collected by the TV-controlled grab during the GAP cruise. (A-B) station GeoB 9024. (C-D) station GeoB 9023. (E-F) station GeoB 9022. See Figure 4.24 for location of the sampling stations.

The upper part of the C1 slope was sampled with a TV-controlled grab GeoB 9023 (Figure 4.30). More than 300 kg of carbonate chimneys were collected, with cylindrical, mounded, branched, or mushroom shapes. Small corals, sponges, brachiopods and other little organisms were attached to the chimney pieces. The final part of the OFOS 17 profile corresponds to the pool-like structure at the base of the southern flank of C1 and the base

of the Hesperides MV complex. This depression has an oval shape and many current structures were observed during the video profiles, such as rippled sands, probably as consequence of the MO. The presence of the MO is also supported by the warmer seawater temperature and by the anomalous temperature gradients recorded in the heat flow stations (GeoB 9025-1, GeoB 9025-2 and ANA01-Sc15) in this area (Gardner *et al.*, 2001; Kopf *et al.*, 2004).

Gravity cores ANA00-Gc10 and ANA00-Gc11 at the summit of cone C3, and ANA00-Gc12 at the summit of cone C4, are characterized by the presence of mud breccia (Figure 4.31) that consists mainly of clasts up to 5 cm that were interpreted by Somoza *et al.* (2003) as clasts of the “blue” marls, characteristic of the Early-Middle Miocene prelistostromic unit M1 defined by Maldonado *et al.*, (1999); these are thought to be responsible for the formation of the marly diapirism (like in the GDR) that occurred in the central area of the Gulf of Cadiz (Maldonado *et al.*, 1999).

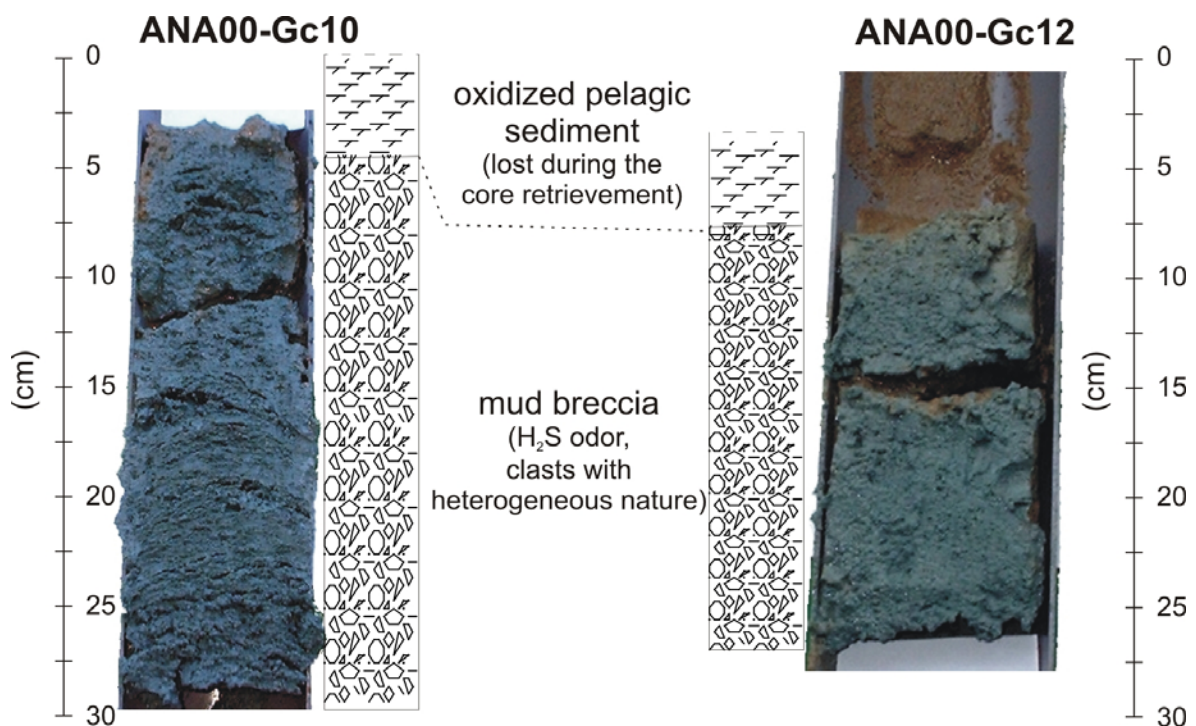


**Figure 4.31.** Gravity cores ANA00-Gc10 and ANA00-Gc12 retrieved during the Anastasya 2000 cruise, with mud breccia, which indicates the mud volcanic nature of Hesperides.

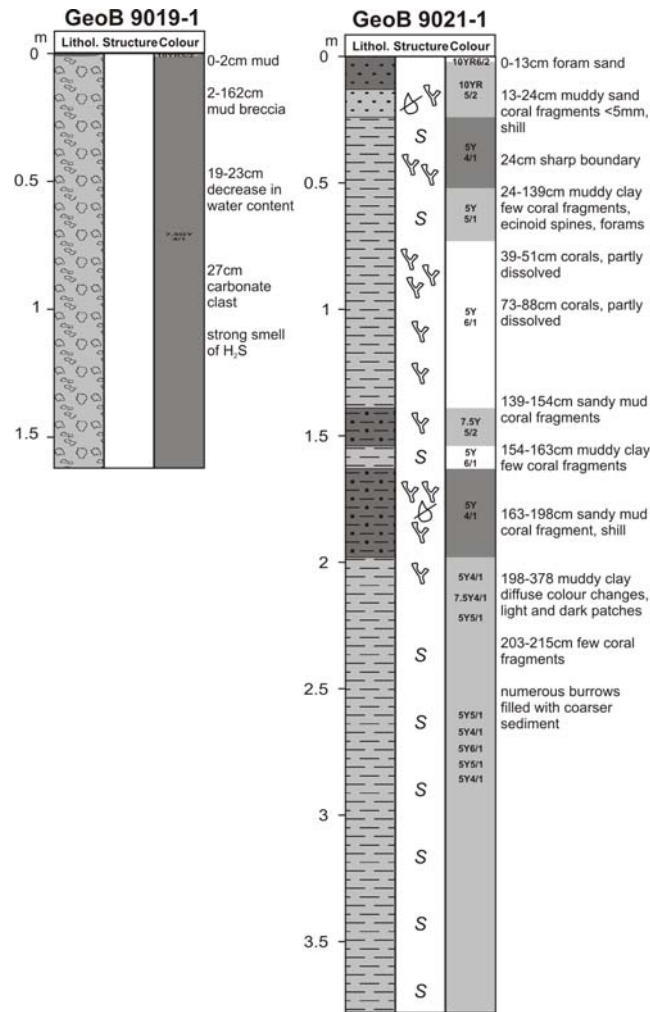


**Figure 4.32.** Gravity cores GeoB 9019 and GeoB 9021 retrieved during the GAP cruise (Kopf *et al.*, 2004) with mud breccia that indicate the mud volcano nature of the Hesperides.

Methane concentrations made on the three cores taken on the Hesperides MV cones (GeoB 9019, GeoB 9020, GeoB 9021) show low values (<0.2 mM), probably reflecting inactivity or slow rates of fluid venting, forming large amounts of carbonate crusts after mud volcano formation (Kopf *et al.*, 2004).

The heat flow station ANA01-Sc15 (Figure 4.33) was collected during the Anastasya survey in September 2001, in the pool-like depression at the base of the Hesperides MV southern of the cone C1 (see Figure 4.24 for location). At this station, the seafloor sediment temperature of 11.48°C indicates the presence of MO in this structure and the calculated thermal gradient of 79.85, heat flow of 106.55 mW/m<sup>2</sup> and a conductivity of 1.334 W/m-K allowed the estimation of the depth of the GHSZ at 1068 m, and an estimated thickness of the GHSZ of 40 m (Gardner *et al.*, 2001).

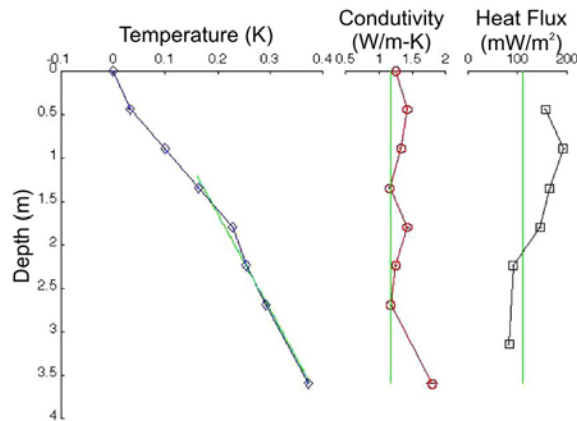


**Figure 4.33.** Heat flow station ANA01-Sc15 collected during the Anastasya survey in 2001 in the pool-like depression at the base of the Hesperides MV, south of cone C1 (see Figure 4.24 for location).

On the Hesperides MV, a transect of 10 heat flow stations (GeoB 9025-1 to GeoB 9025-10) was acquired (see Figure 4.24 for location). The stations shown non-linear thermal gradients (Figure 4.34), especially in the first 2 meters of the sedimentary column. These non-linear gradients, similar to the results from the Anastasya 2001 heat flow stations, were interpreted as the result of the seasonal variations of the bottom water temperature, as result of the presence and fluctuations of the MO. However, in some of the stations of the transect (GeoB 9025-1 and GeoB 9025-6), the heat flow measurements reached sufficient depth and the deepest sensors provided linear trends of the temperature, allowing the calculation of the heat flow. Therefore an heat flow value of  $73.3 \text{ mW/m}^2$  was estimated for station GeoB 9025-1 and an heat flow value of  $36.4 \text{ mW/m}^2$  was estimated for station GeoB 9025-6 (Kopf *et al.*, 2004).

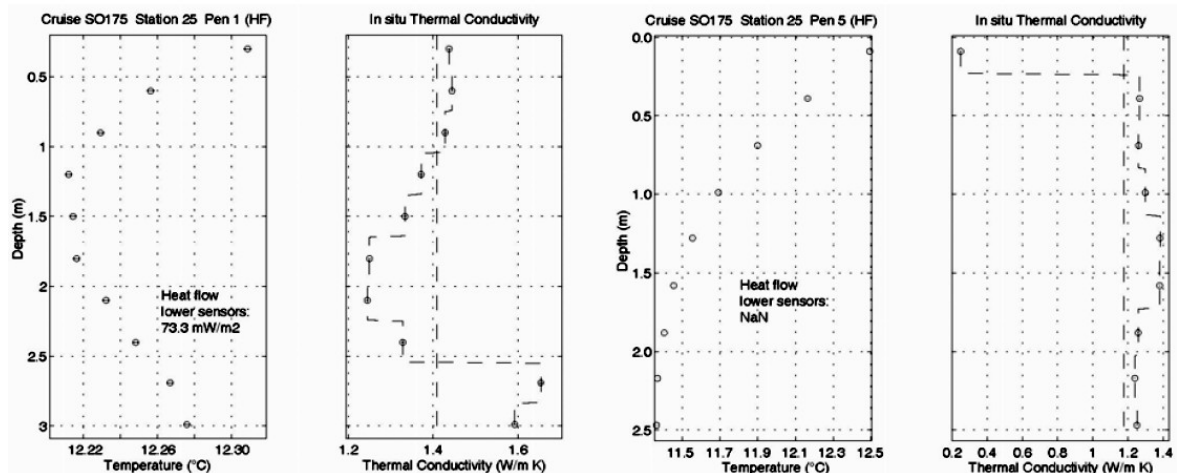


**Figure 4.34.** Heat flow stations GeoB 9025 collected during the GAP cruise (Kopf *et al.*, 2004) along a profile on the Hesperides MV, see Figure 4.24 for location.

### 4.3.2.2 Faro, Cibeles and Almazan

Faro, Cibeles and Almazan MVs are situated along a major positive relief arcuate structure, with 9 km in diameter and 13 km in length, that links the three MVs (Figure 4.35). This arcuate structure has slopes with gradients up to  $18^\circ$  and the highest gradients are found in the SW flank of the Cibeles MV (Figure 4.36B). Cibeles is located at the W limit of the arc, Faro MV is located in the central part of the arc, and Almazan is located at the E limit of the arc. The arcuate structure has highs ranging from 40 m up to a maximum of 120 m in relation to the surrounding high. The arcuate structure is interrupted by a NW-SE trend linear depression in between the Cibeles and the Faro MVs (Figure 4.35). The area inside the arcuate structure is characterized by a plateau with a smooth topography, with small depressions up to 20 m depth and a deeper moat at the border of the interior slope of the arc. This structure is characterized by a moderate to high backscatter reflectivity on the NRL Seamap imagery (Figure 4.36A).

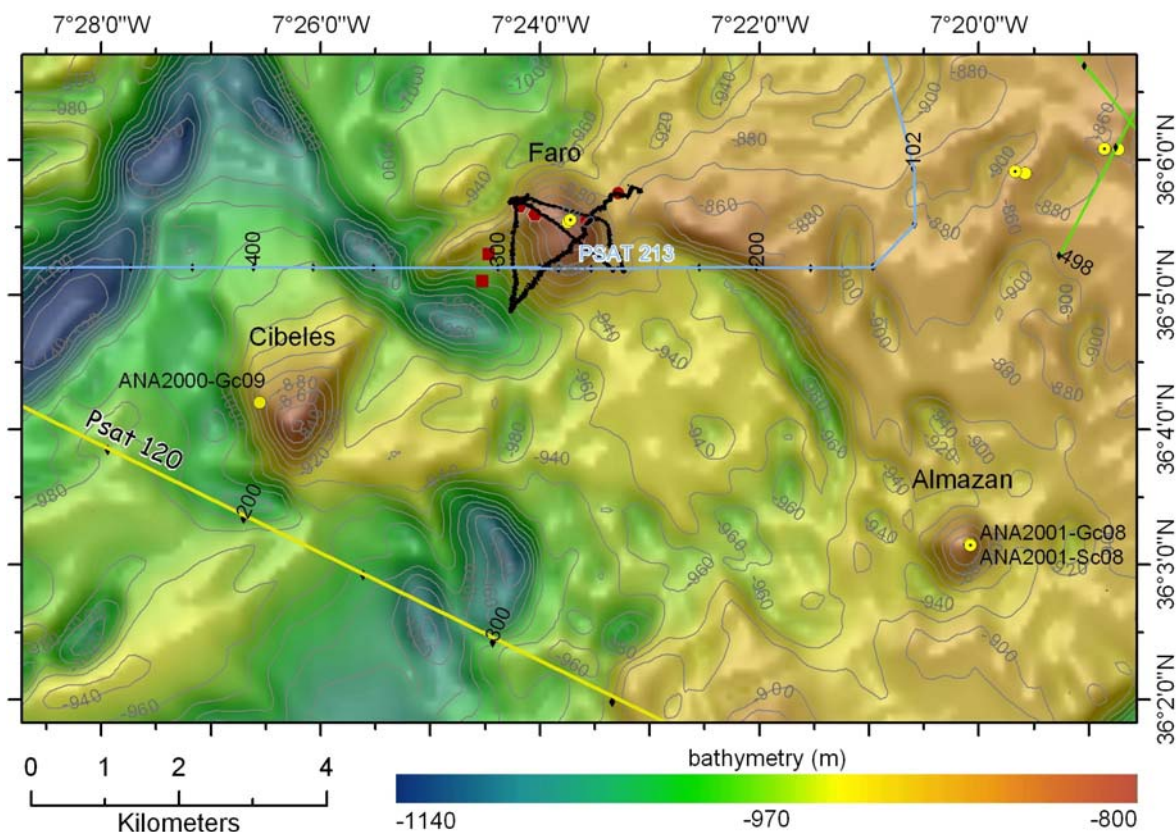


**Figure 4.35.** Bathymetry of the Faro, Cibeles and Almazan MV with the sampling stations and underwater OFOS track of station GeoB 9028. Bathymetry, with a slope gradient and a hillshade with illumination from the NW.

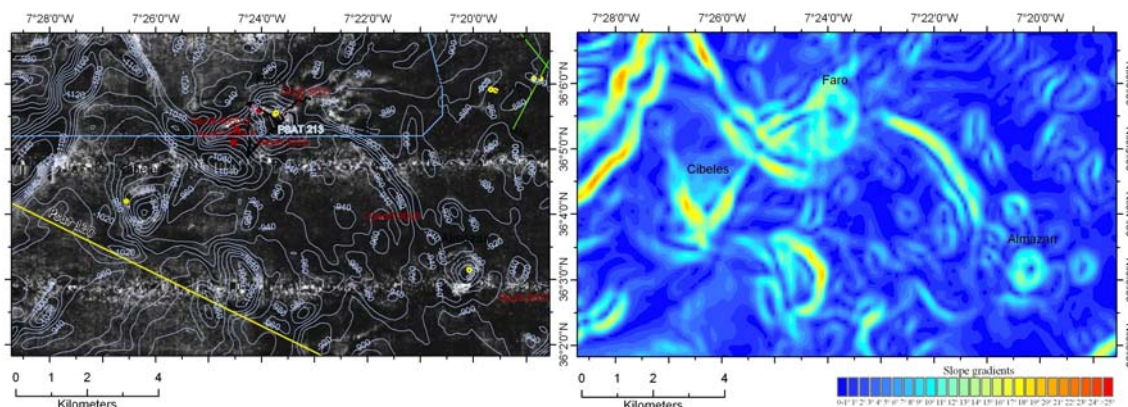


**Figure 4.36.** (A) NRL Seamap long-range side-scan sonar. (B) Slope gradient of the arcuate structure where the Cibeles, Faro and Almazan MVs are located.

The seismic profile TTR11-Psat 213 crosses the southern flank of the Faro MV and the arcuate structure, revealing the chaotic and indistinct seismic reflection pattern below the surface conical expression of the Faro MV, contrasting with the parallel reflections of the sedimentary basin sequences (Figure 4.37B). The arcuate structure is characterized by intense folding of the sediments in contact with the piercing structure (Figure 4.37B). On the seismic profile TTR09-Psat 120 (Figure 4.37A), which crosses the prolongation of the arc south of Cibeles, although the data quality is not of optimal resolution it is possible to interpret that in the prolongation of the arc and on the Cibeles MV, near shot point 230, the reflectors show an upward deformation similar but less intense than that observed on profile TTR11-Psat 213 over the arc's crest.

The Cibeles MV is located at the southwestern limit of the arc. It has a triangular pyramidal conical shape with asymmetric flanks. The steepest gradient flanks are the SW and the SE flanks with up to 18° slopes. The top is located at 860 m water depth and it has a relief of 150 m above the surrounding seafloor. The SE flank is characterized by a smooth depression resembling an erosive moat while at the base of the SW flank 60-70 m deep depressions are found. The MV edifice has a maximum diameter of about 2 km along the arcuate structure and a minimum diameter of 1.2 km in the NW-SE direction. A gravity core (ANA2000-Gc09) taken at the SW flank of the mud volcano allowed the recovery of 15 cm of oxidised brown muddy sands (Figure 4.42A), overlying 155 cm of grey clay muds with obvious indications of gas saturation, degassing structures and a strong H<sub>2</sub>S smell, that indicate the mud volcanic nature of this structure.

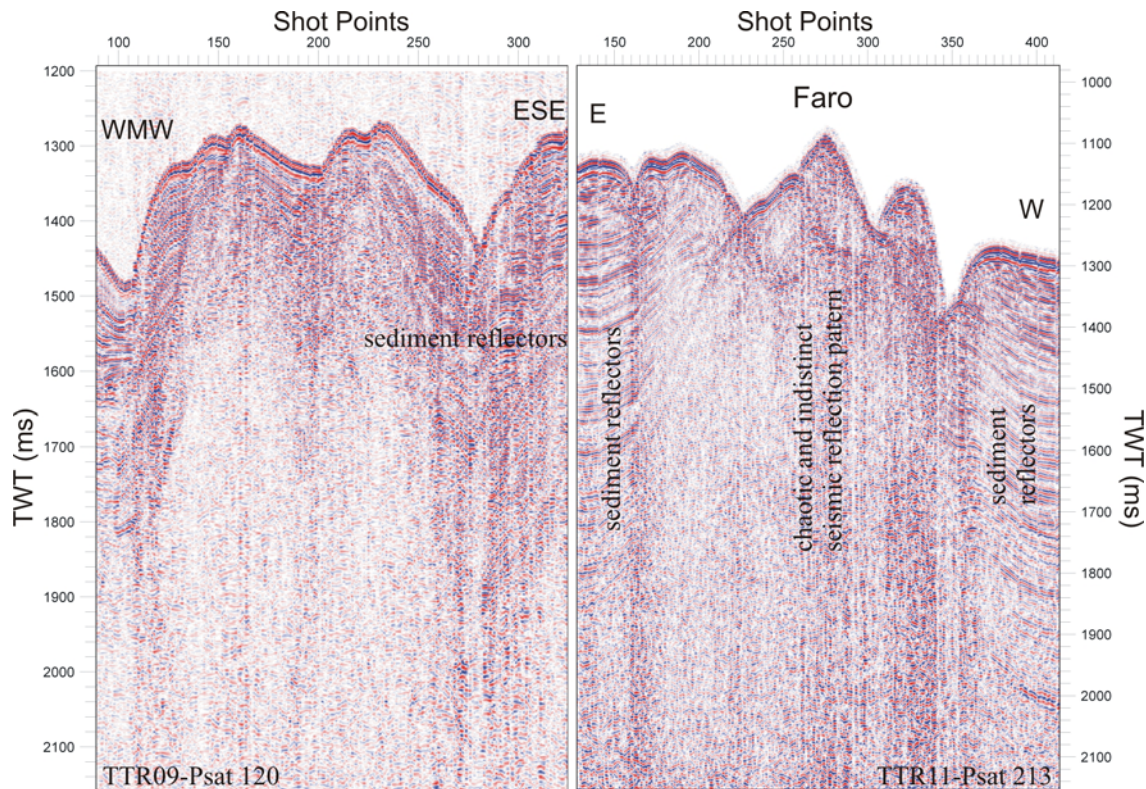


**Figure 4.37.** Single channel seismic lines TTR09-Psat 120 and TTR11-Psat 213. The location of the seismic lines is depicted in Figure 4.35. To be noted the chaotic and indistinct seismic reflection pattern below the surface conical expression of the Faro MV, contrasting with the parallel reflections of the sedimentary basin sequences.

The Almazan mud volcano is located in the easternmost part of the arc is characterized by a regular and symmetric conical morphology (Figure 4.35 and Figure 4.36B). The MV has a seabed diameter ranging from 1.0 to 1.2 km, a relief of 75 m above the surrounding seafloor (Figure 4.35) and steep flanks with slopes ranging from 8° to 14° (Figure 4.36B). The top of the MV is located at 845 m water depth. On the NRL Seamap imagery Almazan is characterized by moderate but differential backscatter intensity. The top has a stronger backscatter intensity than the flanks or the base of the MV. High resolution sparker seismic profiles acquired during the Tasyo campaign (Somoza *et al.*, 2003) show that the surface of the cone is characterized by high-reflectivity coherent reflectors and the interior of the MV is characterized by indistinct and chaotic seismic reflection pattern. The mud volcano feeder channel has been identified as a columnar disturbance with a chaotic and indistinct seismic reflection pattern below the crest of the mud volcano, with a diameter of 600 m (Somoza *et al.*, 2003) that cuts the well-stratified sedimentary sequences. The MV was sampled at its summit with a gravity core

(ANA2001-Gc08) which allowed the collection of a 107 cm long core with coarse bioclastic sandy sediments recovering mud breccia sediments with a strong H<sub>2</sub>S smell, high content of heterogeneous clayish clasts, gastropods and with intercalated layers with abundant coral and bivalve fragments (Diaz del Rio *et al.*, 2001). The heat flow station ANA2001-Sc08, performed at the summit of the Almazan MV, indicated a bottom water temperature of 10.22°C and allowed an estimation of a thermal gradient of 85.81, a heat-flow of 87.92 (mW/m<sup>2</sup>), and a conductivity of 1.025 (W/m-K) (Figure 4.38A). Based on these data the gas hydrate stability zone (GHSZ) can be estimated at a depth of 862 m with a thickness of 30 m (Gardner *et al.*, 2001).

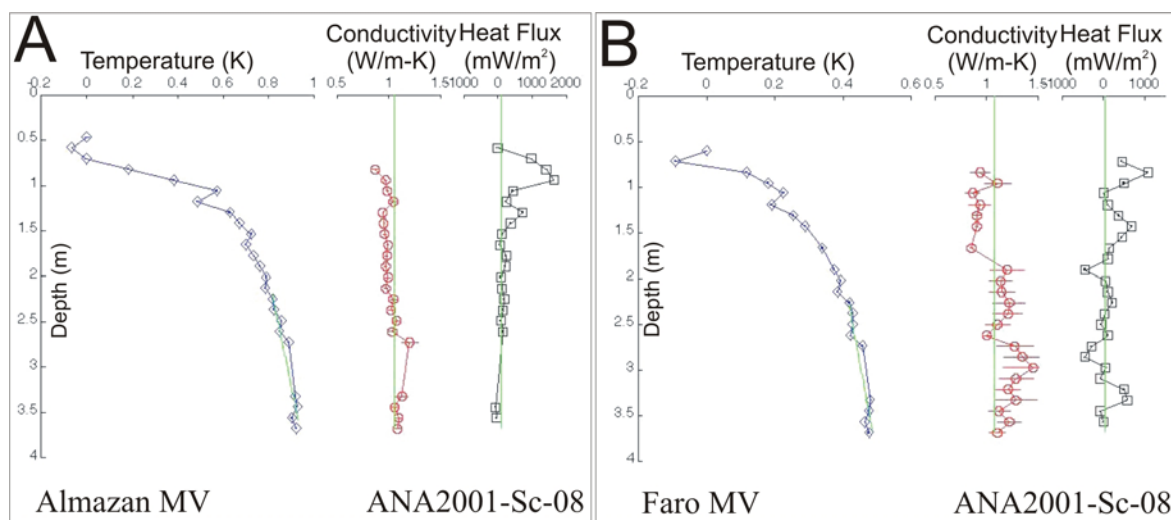


**Figure 4.38.** Heat-flow stations ANA01-Sc08 and ANA01-Sc14 collected, respectively, at the summit of Almazan and Faro MVs during the Anastasya survey in 2001 (Gardner *et al.*, 2001), see Figure 4.35 and Figure 4.39 for location.

The Faro MV is the largest feature in this arcuate structure, it has a conical shape with an oval regular section, with a maximum basal diameter of 1.4 km along the NNW-SSE direction and a minimum diameter of 1.2 km in the orthogonal direction. The summit of the Faro MV is located at 810 m water depth and represents a relief of 110 m in relation to the background bathymetric high of the centre of the arcuate structure (Figure 4.39). The MV has an asymmetric form with slopes of up to 16° (Figure 4.36B). Seismic reflection profiles over the mound show the chaotic seismic facies typical of the MVs (Figure 4.37B) and high resolution sparker seismic profiles of the Tasyo campaign allowed the identification of the MV feeder channel with an apparent diameter of 1 km at the base of the MV (Somoza *et al.*, 2003). The adjacent well-stratified sediments are folded with low

amplitude folds and show an upward flexure of the reflectors towards the MV as also observed towards the arcuate crest (Figure 4.37B).

One gravity core (ANA2001-Gc14) collected at the summit of the Faro MV allowed the retrieval of mud breccia with a strong H<sub>2</sub>S smell and heterometric clasts composed of sandstone, limestone, marlstone and some blue marlstone clasts, up to 5 cm in diameter, confirming the mud volcanic nature of the mound (Somoza *et al.*, 2003). Gravity cores collected in the upper slope on the NE flank (GeoB 9032) and at the base of the MV (GeoB 9031) allowed the retrieval of coral bearing sediments (Kopf *et al.*, 2004). Two multi-corer stations were performed in one location where a possible bacterial mat was interpreted on the video profile OFOS-28. However, due to the presence of hardgrounds of aragonite pavements the multi-cores GeoB 9029-1 did not allowed the collection of any sediment and core GeoB 9029-2 only retrieved 12 cm of mud breccia sediment with fragments of aragonite pavements and bioclasts.

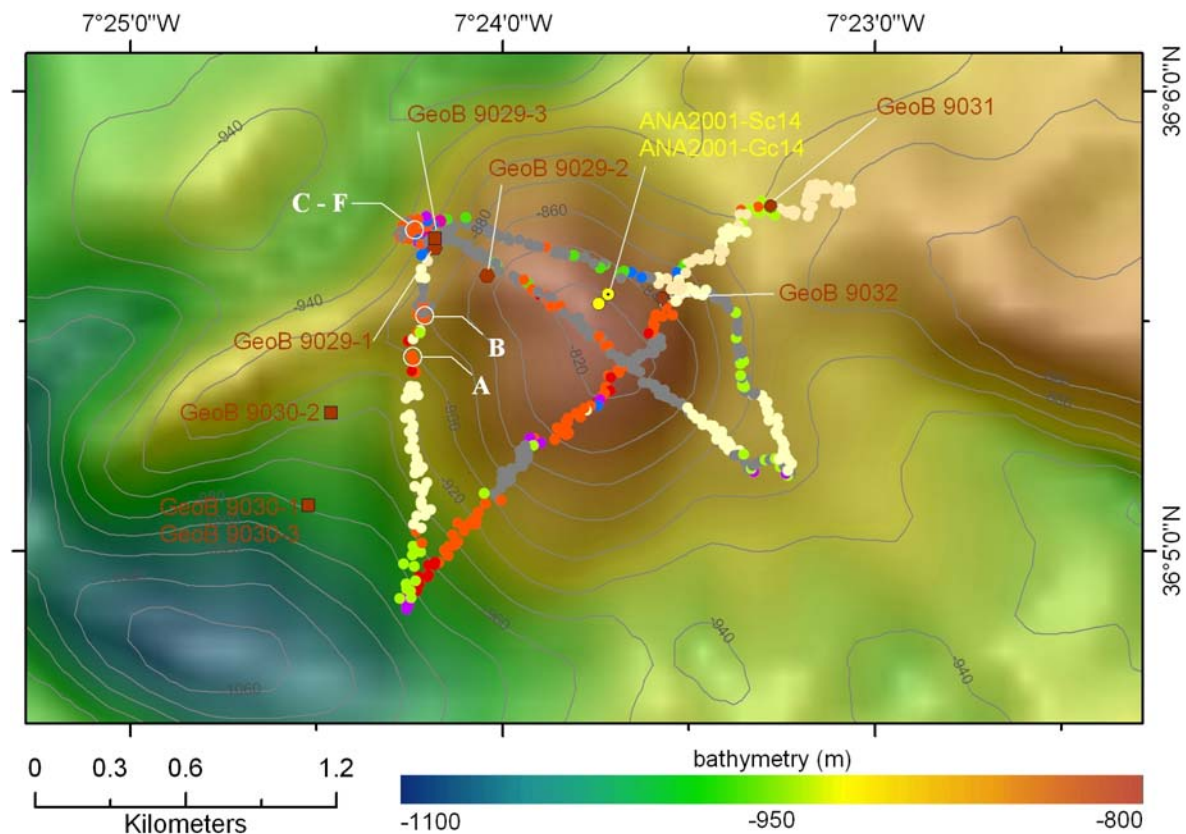


**Figure 4.39.** Bathymetry of the Faro MV with the sampling stations and the facies interpretation of the underwater OFOS track station GeoB 9028. Legend of the interpretation is depicted in Figure 4.40. Circles correspond to gravity cores, boxes correspond to TV-grab stations and hexagons correspond to TV-multicorer stations. Anastasya stations: heat-flow probe and gravity core, are plotted in yellow; GAP stations are plotted in brown; white letters represent the underwater seafloor pictures shown in Figure 4.41. (see text for description).

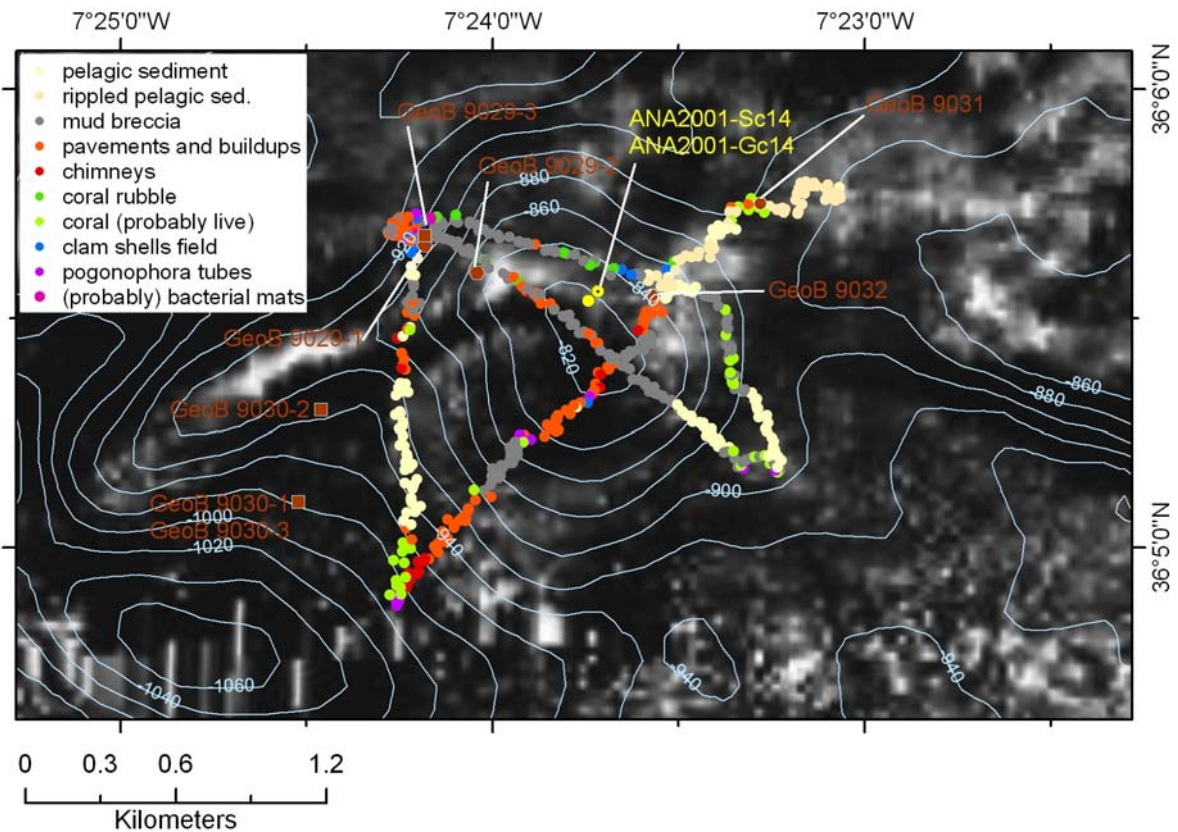


**Figure 4.40.** NRL Seamap long range SSS with the seafloor facies interpretation from the OFOS28 video observations.

The OFOS 28 track, illustrated in Figure 4.39 and Figure 4.40, is composed by a NE-SW profile crossing the summit of the Faro MV, followed by a S-N transect along the W flank, a NW-SE transect crossing the MV summit, a S-N transect along the E lower flank, and a ESE-WNW transect on the northern flank. The first transect with a NW-SE direction, began NW of the Faro mud volcano. The surrounding area and the lower flank of the MV are characterized by pelagic sediment with sandy and muddy patches, sometimes with ripples. Scattered corals occur especially at the base of the MV, where the gravity corer GeoB 9031 was collected, and at the lower flank, close to the intersection with the ESE-WNW transect in the area where the gravity corer GeoB 9032 was collected. These two cores here characterized by pelagic sediments with coral rubble and mud breccia at the base (Kopf *et al.*, 2004). Scarce fragments of carbonates forming small buildups and crusts were observed at the base of the depression close to the area where the gravity core GeoB 9031 was collected. In the upper slope of the NE flank of the MV the seafloor is characterized by the presence of carbonate crusts, forming slabs, pavements, buildups and

large blocks, some of them up to two meters in size. Scarce chimneys or pipe like carbonates are found scattered within the carbonate pavements. Corals and benthic fauna are frequently found attached to these carbonates. The northern flank near the summit area, close to the intersection with the NW-SE OFOS transect is characterized by mud breccia. The SW flank of the MV is characterized by dense occurrence of carbonates, forming crusts, pavements and slabs, sometimes forming buildups and large blocks with several meters in size and with some chimney fragments scattered lying in between the crusts. The seafloor has similar characteristics to those observed at the summit of Hesperides, but with a lower abundance of MDAC and less massive than on the Hesperides. The carbonates are frequently colonized by benthic fauna (corals). In some areas, pogonophora tube worms were found, occurring isolated or forming small patches. In the middle slope of the SW flank, an area of seafloor is covered by mud breccia. The summit and the upper SW flank, where the carbonates are more frequent is characterized by a stronger acoustic backscatter reflectivity (Figure 4.40). At the foot of the SW flank, the OFOS track continues to the north, and crosses the arcuate structure observed on the previous multibeam bathymetry. The area of the base of the MV, corresponding to less intense backscatter intensity on the NRL Seamap imagery than the summit of the MV, is characterized by muddy sediments showing patches of coarser grained sand, with scattered but abundant individual corals, hydrozoa and scarce carbonate crusts. The southern flank of the arcuate structure and its crest are characterized by the dense occurrences of carbonate crusts, slabs, pavements and buildups (Figure 4.41A-B), with scattered chimneys between the slabs. Individual corals are found attached to the carbonates. The northern flank of the arc is covered by mud breccia, sometimes recovered by pelagic sediments, often with rippled sand and muddy patches. When the profile reaches the base of the NW flank of the MV the seafloor is characterized by the occurrence of patches of dense accumulations of bivalves (Figure 4.41C-D) some of which most probably correspond to live Solemyidae due to their elongated shape and dark brown colours. However, Lucinoma shells seem to be the most abundant, as confirmed by the TV-Grab sample GeoB 9029-3, collected in this area. This area is also characterized by carbonate pavements and slabs. Some of these carbonate pavements are apparently covered by white bacterial mats (Figure 4.41E-F). Pogonophora tubes were also observed associated with the carbonates, bivalves and the bacterial mats. Two multicorer stations were acquired with the objective to collect samples of bacterial

mats. One station was performed in this area (GeoB 9029-1) for that purpose but due to the hard carbonate pavements such collections was not possible. A second multicorer station (GeoB 9029-2) was attempted in a closer location dominated by mud breccia sediments in order to estimate methane concentrations in the sediments but only 10 to 15 cm of mud breccia was collected. A TV-controlled grab station (GeoB 9029-3) aimed to sample the bacterial mat area and aragonite pavement samples were collected with mytilid bivalves related to *Calyptogena* sp., Solemyidae and *Lucinoma* shells. Pogonophora tubes were also collected but bacterial mats were not retrieved (Figure 4.42B). The chemosynthetic fauna that hosts bacterial symbionts (sulphide oxidizing bacteria in their gills) indicate active hydrocarbon gas expulsion in this area.

The OFOS 28 profile (Figure 4.40) along the track from the base of the NW slope to the summit of the MV was characterized by mud breccia material with pavements crusts and chimney carbonates that sometimes occur in denser patches, especially at the MV summit. The SE slope, the summit and the upper slope are characterized by mud breccia while the SE lower slope is dominated by pelagic sediment, sometimes with ripples indicating strong currents near the bottom. At the MV base the seafloor was again dominated by mud breccia with isolated corals and pogonophora occurring as isolated individuals, or in small patches.

The next section of the OFOS profile, with a S-N direction showed a pelagic sedimentary cover at the base of the MV and mud breccia material with isolated individual corals attached to some of the mud breccia clasts.

The last section of the OFOS profile, along the mid slope of the northern flank of the MV showed, in general, mud breccia sediments with patches of a pelagic sediment cover. Patches of coral rubble were also observed along this section of the OFOS track. It should be noted also the observation of an area with high density of shells and clam shells. This track ended at the previously surveyed area on the NW base of the MV, and once more carbonates pavements, slabs and buildups were observed; some of these pavements seem to host white bacterial mats. Pogonophora and clam fields were also found in between the pavement slabs.

Attempts to sample the southern flank of the arc (TV-Grab GeoB 9030-2) and the base of the MV (TV-Grab stations: GeoB 9030-1 and GeoB 9030-3) in areas where extensive carbonate pavements were observed associated with pogonophora tubes were

unsuccessful and only greyish mud and some branches of live coral (Figure 4.42E-F) were collected in sample GeoB 9030-3.

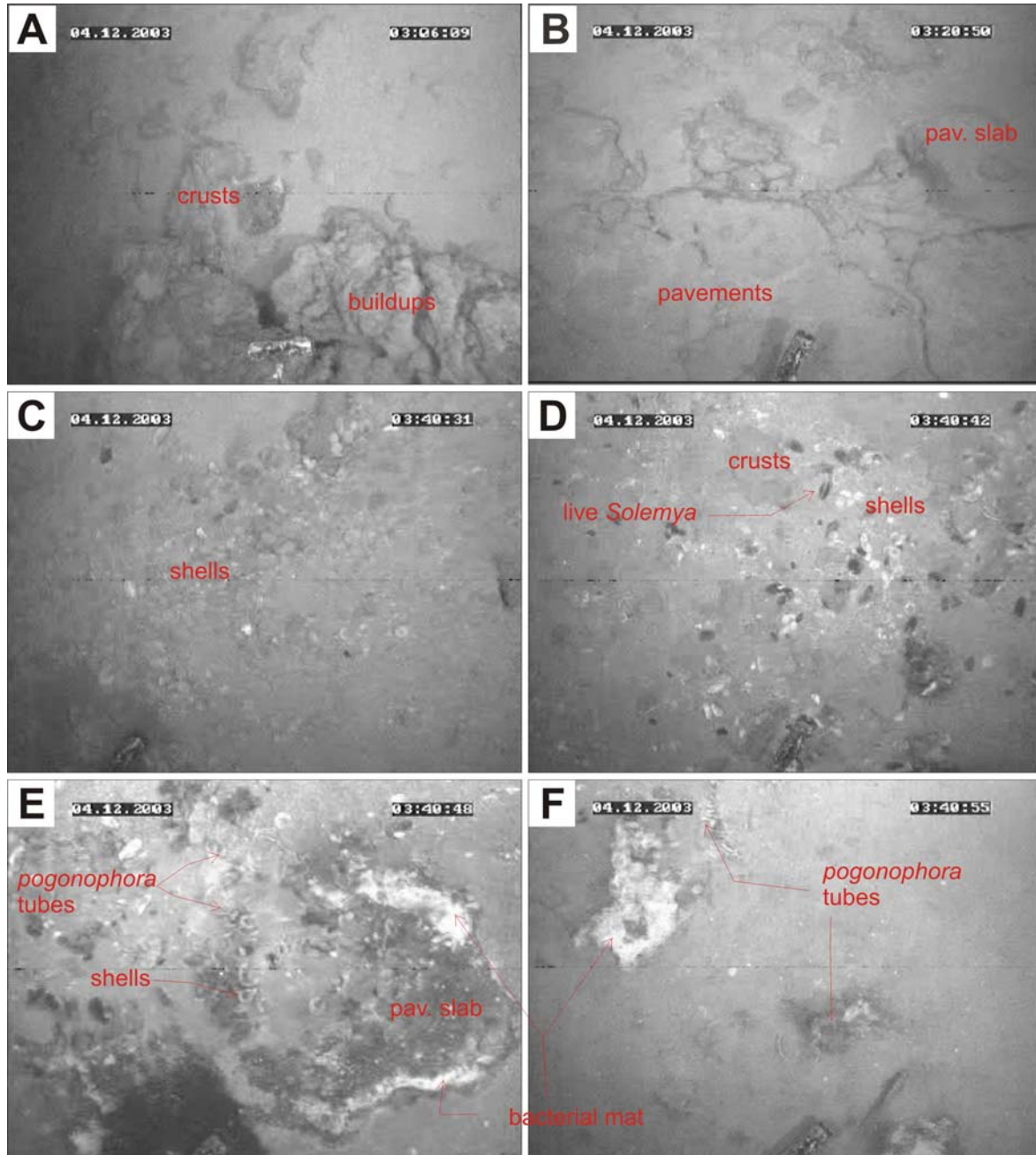


**Figure 4.41.** Photographs taken from the video profile OFOS28. (A-B) carbonate buildups, crusts, slabs and pavements. (C-D) Clam and shell fields with dead and live organisms. (E-F) Bacterial mats recovering pavement slabs and pogonophora tubes occurring as isolated individuals or in small clusters. See Figure 4.39 for location of the photographs. Pictures are about 1.5 m wide.

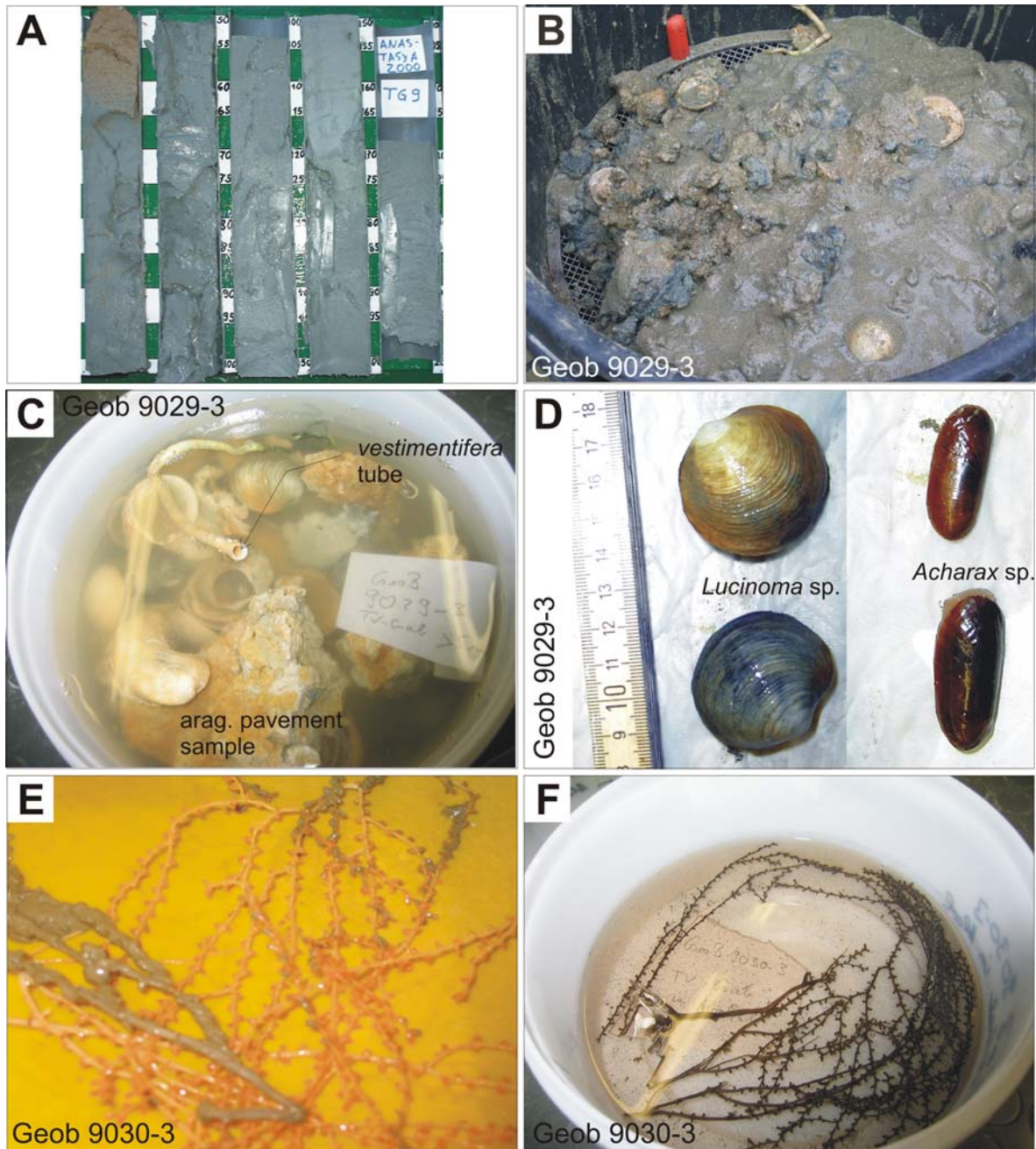


**Figure 4.42.** (A) gravity core ANA2000-Gc09 collected at the SW flank of the Cibeles MV. (B-F) Samples collected from Faro MV. (B) TV-Grab Geob 9029-3 with detail images illustrating Vestimentifera tubes, aragonite pavement samples and shells. Aragonite pavement samples and mytilid bivalves in (C), and live *Acharax* sp. and *Lucinoma* sp. bivalves in (D), are indicating active hydrocarbon gas escape. (E-F) live corals collected from the TV-Grab Geob 9030-3.

### 4.3.3 Mediterranean Outflow channels

#### 4.3.3.1 Cadiz Channel W of Iberico

The Cadiz channel, 7 km W of the Iberico cone was surveyed in an area of irregular bottom topography located at 1100 to 1050 m water depth. This area is characterized by strong acoustic backscatter intensity on the NRL Seemap 12 kHz side-scan sonar. It was surveyed with 30 kHz deep-towed MAK side-scan sonar, with seismics, with underwater TV video profiles and sampled by dredging (Figure 4.43).

On the high resolution deep-towed side-scan sonar (line TTR11-MAK42) this area is also characterized by a strong backscatter intensity and shows a pattern of sharp and near parallel shadows (Figure 4.44) indicative of bedding and faulting of outcrop rocks, similar to the pattern observed on the N-NW flank of the Iberico mud cone. This pattern is typical for the entire Cadiz channel but the eastern side of the channel, illustrated in Figure 4.44, is characterized by strong backscatter intensity. In this area the underwater video profile TTR11-TV 21 was acquired in order to characterize the seafloor in this rocky headwall of the channel. This profile was carried out in a South to North direction along the headwall of the Cadiz channel starting on a small high, crossing a small depression and ending at the crest of a small elevation, as illustrated in Figure 4.43. The seafloor along the underwater TTR11-TV 21 video profile was characterized by the occurrence of high density of carbonate rubble, mainly chimneys lying in the seabottom over outcropping claystone (as confirmed by the claystone sample retrieved from the dredge TTR11-339D). The chimneys occur lying at the seabottom (as illustrated in Figure 4.47A and B), very fragmented, oxidized and colonized by benthic fauna indicating a long period of permanence at the seafloor. Some buildups and slabs of pavements were also found (as illustrated in Figure 4.47E and F), especially close to the end of the profile. The rocky outcrops were composed of consolidated claystones that exhibit frequently, up to 1-2 m, scarps (as illustrated in Figure 4.47C and D) where the blocks of the outcropping rocks are found at their base. Layering of the rocky outcrops was observed as well as small patches of coral rubble. In general, the rocky outcrops had no pelagic sediment cover due to the strong bottom currents, as observed by the movement of the soft corals and by the movement of particulate matters on the video records. Only small patches of rippled sandy sediments were found.

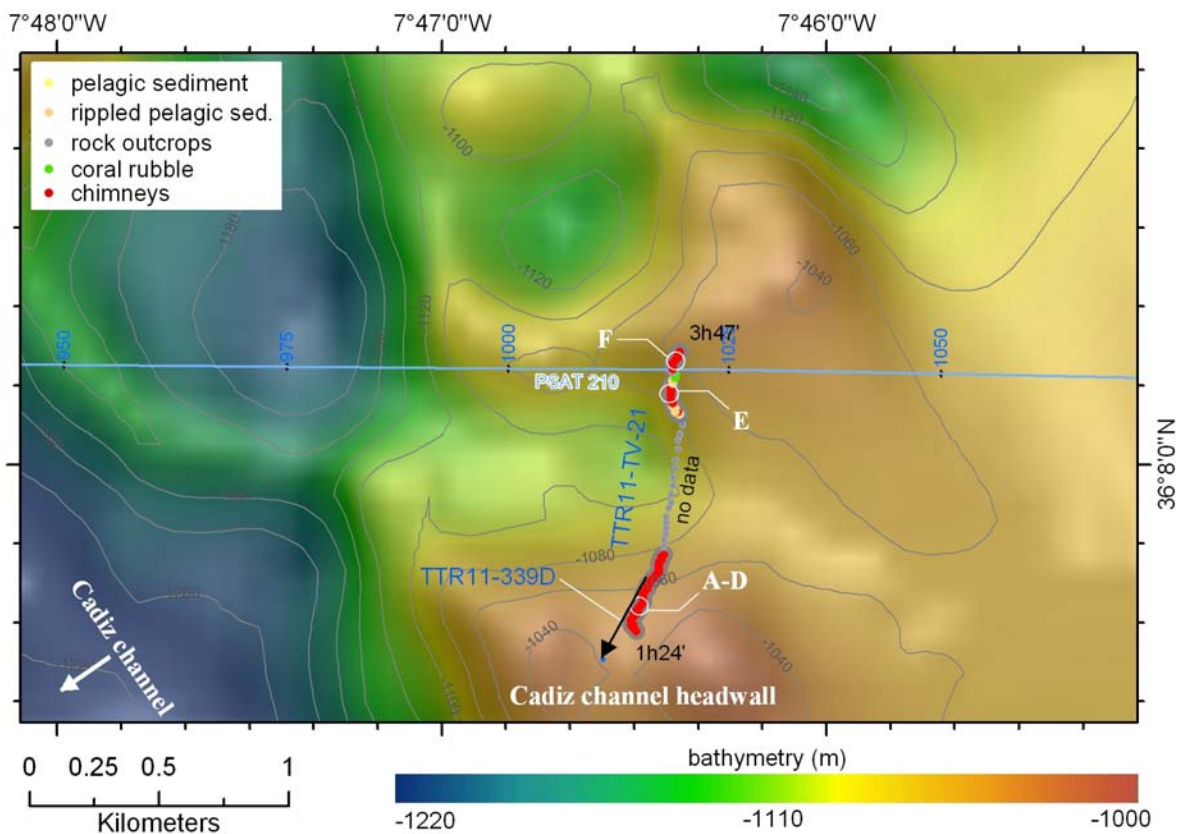


**Figure 4.43.** Bathymetry of the Cadiz Channel W of Iberico where the underwater profile TTR11-TV-21 was acquired which allowed the interpretation of the seabed nature. Bathymetry, with a slope gradient and a hillshade with illumination from the NW.

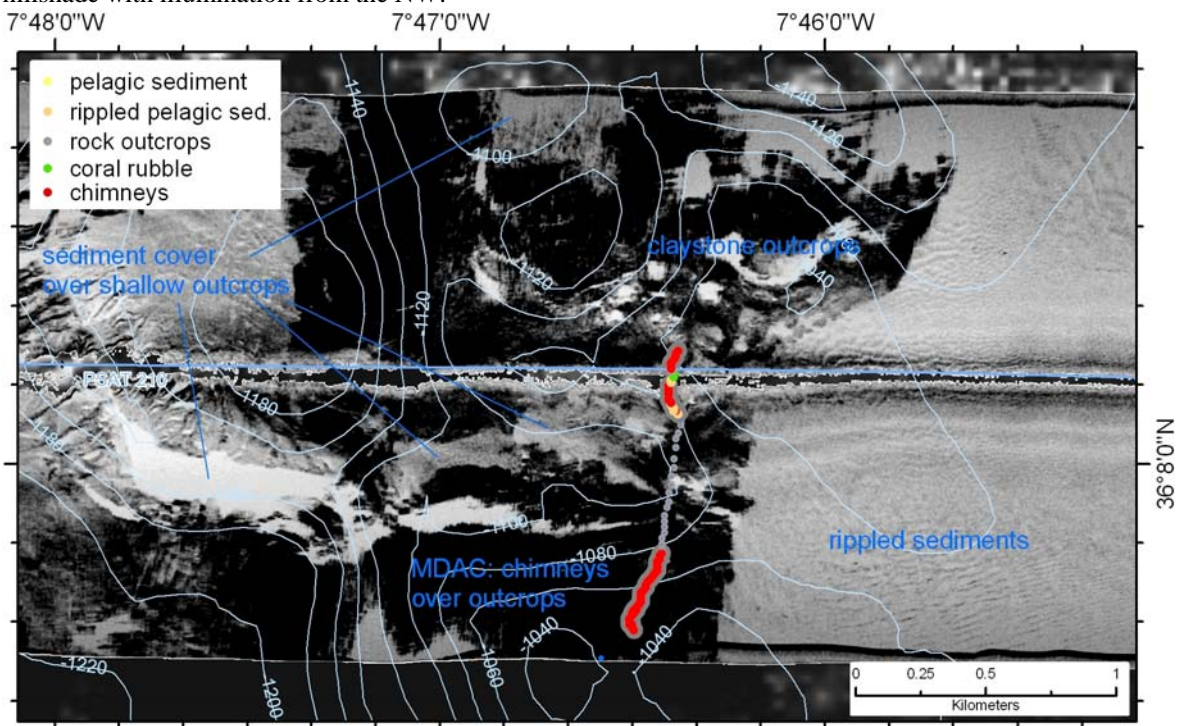


**Figure 4.44.** NRL Seamap long range SSC (low resolution) and TTR11-MAK41 SSC imagery (high resolution) with the bottom facies interpretation overlaid.

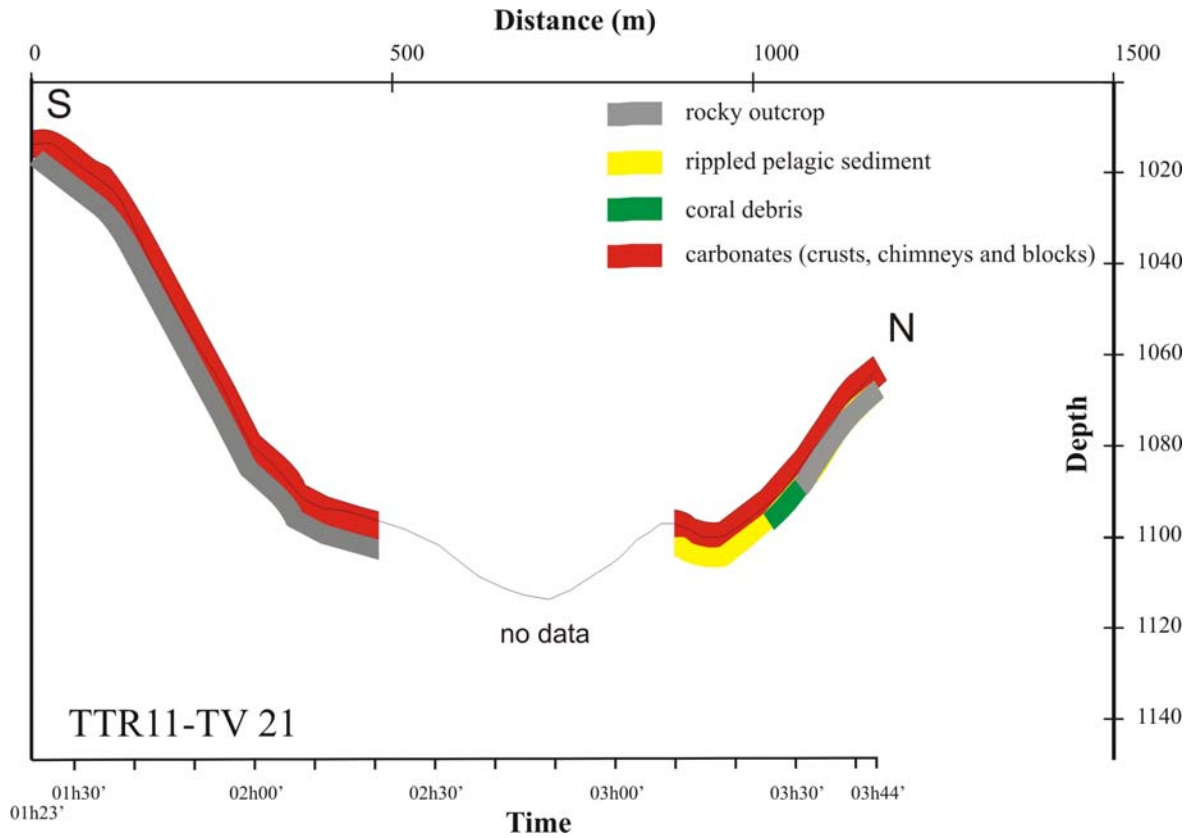


Figure 4.45. Bottom facies interpretation of the underwater TTR11-TV 21 video profile.

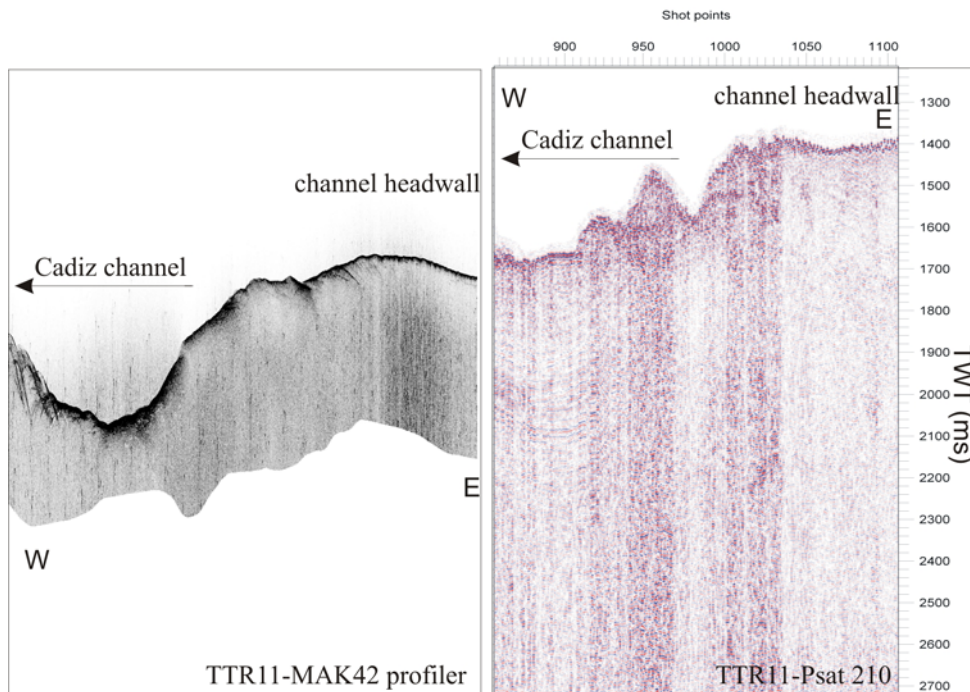
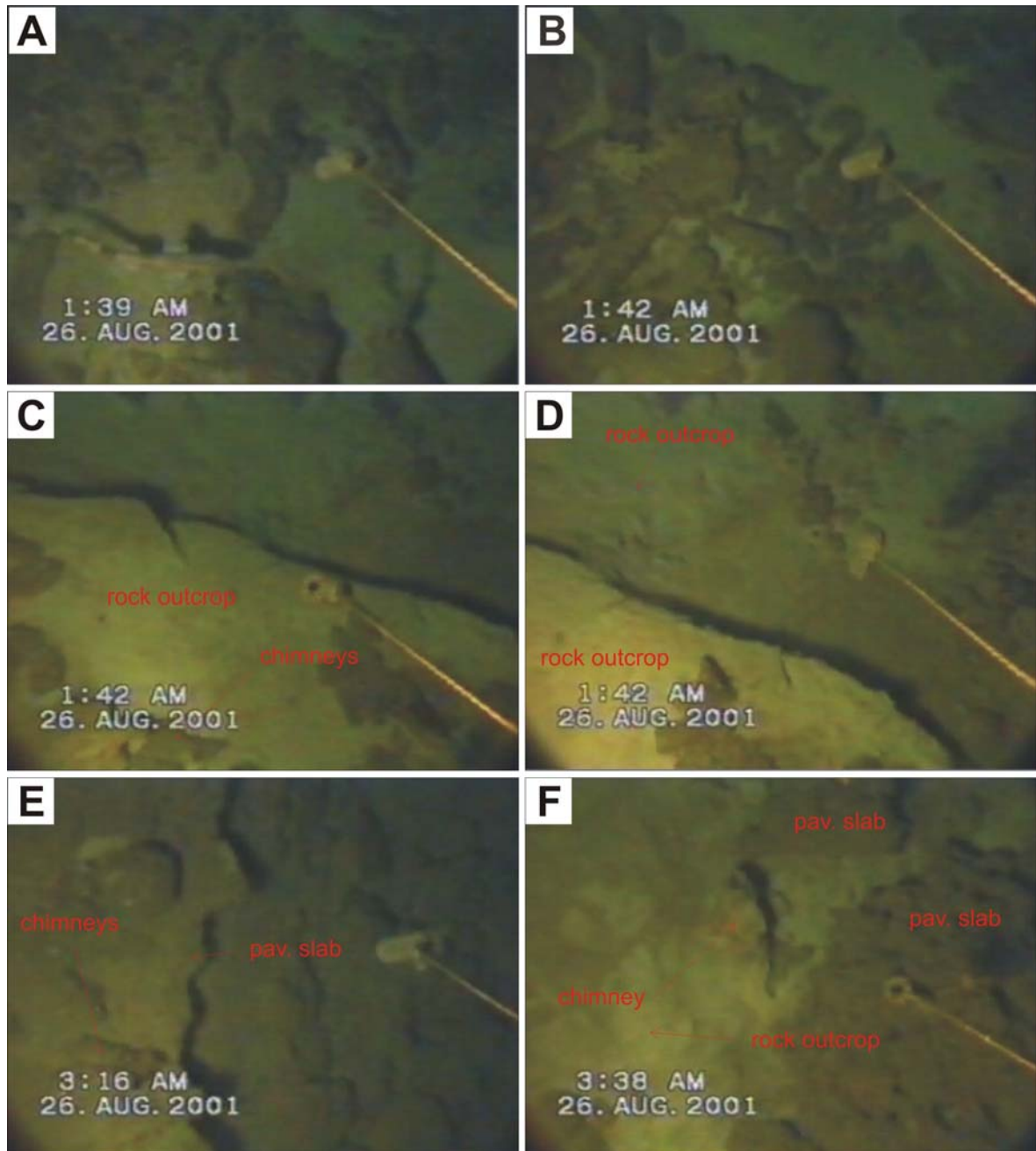


Figure 4.46. (A) 5 kHz profiler of the deep towed TTR11-MAK 42 illustrated in Figure 4.44. (B) seismic profile TTR11-Psat 210 whose location in shown in Figure 4.43.



**Figure 4.47.** Underwater pictures from the video profile TTR11-TV 21. Location of the pictures is plotted in Figure 4.43. (A-B) illustrate the aspect of the chimneys and carbonate rubble. (C-D) illustrate the aspect of the chimneys and carbonate rubble lying over the claystone rocky outcrops where meter-size scarps and faults are frequent along the channel scarp headwall. (E-F) illustrate the pavements, pavement slabs, chimneys and other carbonate rubble over the rocky outcrops. Pictures are about 1.5 m wide.



**Figure 4.48.** Samples collected by the dredge TTR11-339D, with dolomite chimneys and carbonate rubble, composed of fragments of the dolomite chimneys and crusts; also some fragments of claystone interpreted as fragments of the rocky outcrops.

## 4.4 Discussion

### 4.4.1 Fluid and gas escape manifestations in the Gulf of Cadiz

In the Gulf of Cadiz, the area of the accretionary wedge is characterised by an extensive occurrence of fluid escape structures (Figure 4.1) expressed by mud volcanoes, mud cones, diapiric ridges, pockmarks, MDAC and chemosynthetic ecosystems, related to hydrocarbon rich fluid venting (Pinheiro *et al.*, 2003; Somoza *et al.*, 2003; Rensbergen *et al.*, 2005b), that has been interpreted as indicators of depth gas rich overpressured sediments (Somoza *et al.*, 2000; Somoza *et al.*, 2001; Stadnitskaia *et al.*, 2006). The migration of these fluids through the sediments to the seafloor appears, in some places, to be controlled by faulting (Pinheiro *et al.*, 2005). Some of the mud volcanoes (Moroccan margin) are located along major NW-SE and NE-SW trending faults identifiable on the Naval Research Laboratory (NRL) side-scan imagery (Gardner, 2001). In other places the

mud volcanoes appear to be located at the intersection between the NW-SE strike-slip faults and trusts of variable orientation that reflect the Gibraltar Arc curvature (Pinheiro *et al.*, 2005).

The migration of fluids along these faults is possibly related both to along-slope gravitational sliding and to the tectonic transpressional deformation of the olistostromes and the accretionary complex, due to the Africa-Eurasia convergence (Somoza *et al.*, 2000; Somoza *et al.*, 2001), which induces in places transpressional tectonic movements of the shale/salt deposits of the olistostromes mass, generating salt/shale arched wedges. It has also been suggested that some of the widespread shallow fluid venting on the seafloor, particularly in the area of occurrence of carbonate chimneys of the south and southwest of the GDR and in the FR, could be explained by the destabilisation of gas hydrates rich sediments in contact to the MO (Somoza *et al.*, 2000; Somoza *et al.*, 2001).

Although a quantitative relationship between the fluid/gas expulsion and the geologic/biologic manifestation is not straightforward, it is clear that, qualitatively, the geologic and biologic responses are dependent on the fluid and gas compositions and on the flux rate and frequency of the eruption episodes. Data on the frequency, composition and impacts of the expulsion episodes, which imply a long term monitorization of the fluid escape structures, are difficult to collect and, not yet available for the GC. However, the seafloor features that result from fluid/gas escape give information on the nature of the fluids/gas being delivered to the seafloor, on the episodic nature of the processes, and on the duration of those events and the delivery rates (Roberts, 2001).

Roberts and Carney (1997) qualitatively correlated the different fluid escape structures with relative changes in the rate of vertical flux and expulsion of fluids and gases (hydrocarbons, pore waters and sediment) to the seafloor (Figure 4.49). The sediment-prone mud volcanism corresponds to the rapid flux end-member of the fluid escape feature spectrum. Mud volcanoes and mud flows composed of extruded fluidized sediments that consist of fine grained sediments and clasts from the underlying sediment layers. The opposite end-member of the spectrum of the fluid escape structures corresponds to the slow flux of gases and fluids. It is represented by mineral-prone structures, such as authigenic carbonates, of which dolomite crusts, nodules and chimneys and aragonite pavements types are represented in the GC. In this case, the processes of microbial mediated degradation of hydrocarbons (mainly methane) can produce calcium-

magnesium carbonates that form a variety of seafloor features including the hard-grounds, mound-like buildup structures and accumulations of conduit or pipe-like MDAC of variable dimensions. The intermediate flux rates are frequently associated with the occurrence of shallow subsurface gas hydrates, where the chemosynthetic communities are most common and well developed.

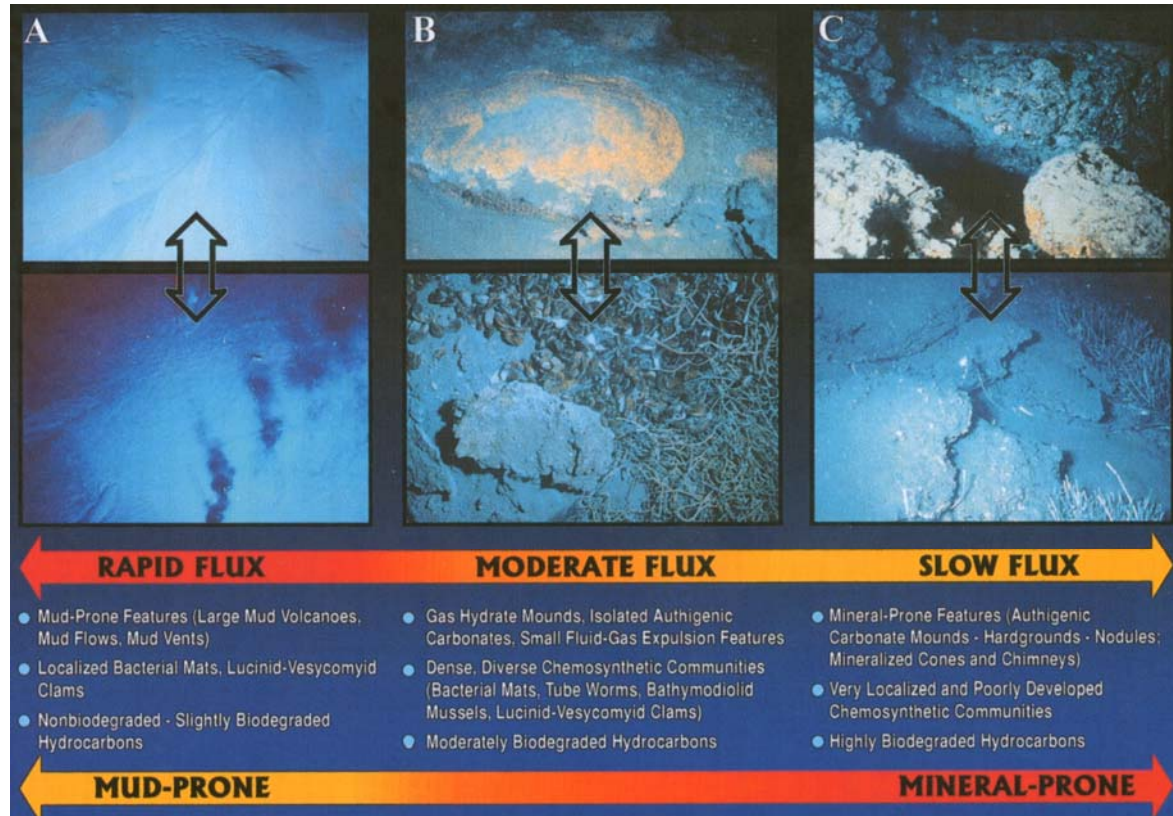


**Figure 4.49.** Schematic summary of the qualitative relationships between the flux of fluids and gases to the seafloor and the resultant escape structures (Roberts and Carney, 1997). (A) pictures illustrating the rapid flux (mud-prone) end-member corresponding to the mud volcanoes and mud flows. (B) pictures illustrating an intermediate case with moderate flux rates, corresponding to surface exposures or shallow gas hydrates and well-developed chemosynthetic ecosystems and local areas of occurrence of MDAC. (C) pictures corresponding to slow flux cases (mineral-prone case) characterized by a sparse or absent chemosynthetic communities and dominance of the MDAC, occurring as pavements, slabs, buildups, mounds, chimneys and other forms of lithified seafloor.

#### 4.4.2 MDAC occurrence and characterization

The MDAC from the Gulf of Cadiz have high variable morphologies and mineralogies but, as described in Chapter 5, two main lithologic types of MDAC have been identified in the collected samples: (I) dolomite-dominated carbonates and (II) aragonite-

dominate carbonates. All these MDAC indicate modern or recent methane seepage and its anaerobic oxidation (mediated by microbial activity) which leads to the precipitation of the authigenic carbonates (aragonite, calcite, Mg-calcite and dolomite) resulting in the cementation of the sediments and the formation of chimneys and other structures.

The different morphologies of the carbonate structures reflect different flow patterns through the sediments. If the flux of fluid enriched in methane is canalized through the sulphate reduction zone of the sedimentary column, using borrows or sediment heterogeneities as pathways, the sulphate-methane interface and consequently the precipitation of the authigenic carbonates will occur around these (sulphate semi-closed systems) fluid conduits, resulting in the lithification of the sediments and the formation of the dolomitic chimneys (as discussed in Chapter 5). Similar formation processes can be proposed for the formation of the dolomite dominated crusts, nodules and massive forms. The aragonite pavement types result from the oxidation of methane at or close to the seafloor resulting on the formation of buildups or small carbonate mounds or paving the seafloor with continuous hard-grounds or as crusts, slabs and blocs.

Seep sites and authigenic carbonate deposits were initially assumed to be isolated occurrences. With the increase of the detailed survey coverage they now have been encountered in several other locations (between 500 and 4000 m water depth), indicating that they are far more common features than previously anticipated (Figure 4.1).

The seafloor occurrences of these different MDAC, as described from the underwater observations, are discussed below.

#### **4.4.2.1 Dolomite crusts and chimneys**

The distribution of the MDAC, observed on underwater video profiles and by sample retrieval, is correlated with high backscatter acoustic intensities on the side-scan sonar imagery. The sites of occurrence of the MDAC are characterized by the strongest acoustic response, stronger than the backscatter from mud breccia and even from most of the rock outcrops that are frequently characterized by the occurrence of particular textural features that reflect some characteristic shadows, resulting from the layering and faulting patterns. This is illustrated e.g. on the Iberico mud cone (Figure 4.18) where is clear the distinction

between the strong acoustic backscatter of the MDAC, the intermediate acoustic intensity of the rocky outcrops, and the low backscatter reflectivity of the pelagic sediments.

The underwater video observations revealed that the dolomite crusts and chimneys occur as fields with high density of carbonate samples. These carbonate samples exhibit a large variety of shapes and sizes, such as pipe-like, tubular linear shapes, curved or helicoidal shapes, conical, branched, nodular, and massive irregular shapes. Their sizes are highly variable both in length and diameter. Chimneys with more than 3 m long and up to 0.5 m in diameter were observed. Those chimneys and crusts appear to be broken, sometimes intensely fragmented, forming carbonate rubble, and occur most of the times lying on the sea floor. It is very rare to find chimneys that are in the vertical position, protruding from the sediments.

Isolated individuals and small colonies of sea urchins, Cnidaria (Hydrozoa and Anthozoa), Mollusca (Gastropoda and Bivalvia burrows), Annelida (Polychaeta), Arthropoda (Decapoda), Brachiopoda, Echinodermata (Crinoidea, Asteroidea, Ophiuroidea, Echinoidea and Holothuroidea) are frequently found on the chimneys fields. However, no chemosynthetic organisms were found directly associated and in close relation with the dolomite chimneys crusts and nodules. Chemosynthetic communities were identified only at sites characterized by the occurrence of the aragonite pavement types. In the Hesperides, Faro and Student mud volcanoes, and off Gibraltar, occurrences of dolomite chimneys and aragonite pavements are found in close spatial proximity or even occur simultaneously. However, the observed field geometry relationships between the different MDAC indicate that they had distinct formation periods. The morphologic and textural characteristics of the aragonite pavement carbonates show indicators of a recent or present day formation while the dolomite carbonates, which occur as fragments and remobilized pieces, indicate older formation episodes. The benthic organisms found in the chimney fields use the carbonates as a hard ground for fixation. The chimneys exhibit variable but in general strong dark brown colours indicating oxy-hydroxide iron and manganese coatings. The benthic colonization of these carbonates and their oxidation coatings indicate that they are, in general, in contact with the seawater for a considerable amount of time.

Occasionally, and in especial on the video profile TTR15-TV69 in the Cadiz channel at the East of Lolita (Figure 4.7), chimneys occur in situ and do not completely outcrop

from the sedimentary formation where they were formed. Sometimes it was possible to recognize in some situations a sub-parallel orientation of some chimneys relative to the sedimentary layering, while others clearly have a sub-vertical orientation. The sub-vertical orientation of some of the chimneys was already suggested by the apparent layering interpreted from the granulometric and textural variations in some chimneys (Chapter 5). These observations, together with the large variety of the dolomite chimneys, suggest a complex plumbing system for the fluid percolation. In some situations the fluid percolates upwards, cutting the sedimentary layers, while in other cases the fluid also percolates horizontally along more permeable layers tending to form the slab-like crusts and branched chimneys. Some of the conduit type of chimneys can also result from horizontal flow.

The areas where the chimneys occur are systematically characterized by strong bottom currents. These currents, as evidenced by the transport of particulate matter, by the swing of soft corals and by the bent of the wait string attached to the video camera frame, are considered to have clearly the potential to erode the unconsolidated sediments in which the chimneys formed. In the northern area of the GC, in the GDR field, in the Tasyo field and in the ridges West of Gibraltar, these strong currents are related to the Mediterranean Outflow water (MO). In the Moroccan margin, strong currents were also observed at the Pen Duick escarpment and in the Vernarsky Ridge. While in this area the origin of these currents is not so clearly documented as related to the Mediterranean Outflow (MO), the presence of these structures in the upper and intermediate slope can be generated by these strong currents. Therefore it is possible to propose that strong bottom currents and the MO have an effective control on the outcrop of the dolomite crusts, nodules and chimneys. It is proposed that the locations where the dolomite chimneys occur are presently swept by the flowing of the MO and/or other strong bottom currents which can remobilize the unconsolidated sediment inside of which the chimneys were formed and therefore produce the collapse of the individual chimneys, explaining their present position on the seafloor. Considering this, it is possible to consider that the chimneys may be formed under the seafloor (as proposed based on the geochemical and mineralogical composition of the carbonates, and discussed in Chapter 5) and gradually exposed at the seafloor through erosion of the surrounding unconsolidated sediments, which causes them to lose sustentation and fall down on the seafloor. The oxidation and the iron and

manganese coating, as well as the colonization by the benthic fauna, began after the chimneys cropped out.

#### **4.4.2.2 Aragonite pavements**

Underwater video observations revealed that the aragonite pavement type of MDAC occur as (1) buildups and small mound-like buildups of variable dimensions, some up to 4-5 m high and several meters in length (e.g. see Figure 4.29); (2) as rough hard-grounds (up to 50-80 cm thick) that can pave the seafloor for several square meters, with a thin or absent sediment cover (e.g. see Figure 4.41B); (3) as crusts and slabs, similar to the pavements or; (4) as nodular masses of few cm size within superficial sediments. The mounds appear on the underwater video observations as accumulations of chaotically tilted and fractured blocks, separated by well-defined joints (e.g. Figure 4.29). According to Roberts (2001) The nodular masses, the hardgrounds and the crusts are most common in the intermediate to slow flux rate settings, while the mounded carbonates and the chimneys are interpreted to be more characteristic of slow flux rate environments.

Colonization of these pavements by benthic fauna (non chemosynthetic) is frequent but less intense than observed on some of the chimney fields. The aragonite pavements are characterized by having frequently associated chemosynthetic communities. Aggregates of clam shells, probably most of them dead, were identified on the seafloor observations at several places (e.g. Hesperides, Faro and Porto MVs). Live chemosynthetic fauna (*Calyptogena*, *Acharax* and pogonophora tube worms) were identified and sampled in close association with areas of aragonite pavements occurrence. Besides, shells of chemosynthetic fauna are also present cemented and incorporated in the carbonate samples, in the aragonite pavements sub-type: shell crusts (described in Chapter 5). Small bacterial mats and pogonophora tube worms were also observed in restricted areas of the Faro MV, in close association with the aragonite pavements (Figure 4.41E-F).

#### **4.4.3 Chemosynthetic fauna: occurrence and underwater observations**

In the Gulf of Cadiz, macro-scale chemosynthetic organisms were found in lower abundance when compared with other seepage areas as in the Gulf of Mexico where well developed macro-scale chemosynthetic communities were found in association with gas

hydrates (MacDonald *et al.*, 1988; Carney, 1994; Roberts, 2001; Bergquist *et al.*, 2003; MacDonald *et al.*, 2003). The chemosynthetic fauna in the Gulf of Cadiz include host invertebrates with bacterial symbionts such as the Calyptogena, Acharax and pogonophora tube worms. They were observed only in small areas correlated with recent or more intense active hydrocarbon venting sites.

The microbial communities in the Gulf of Cadiz include sulfate reducing bacteria, methanogenic bacteria, sulfide and methane-oxidizing bacteria and bacteria that oxidize heavier hydrocarbons (Niemann *et al.*, 2006; Santos *et al.*, 2006). The microbial communities are critical to carbon cycling in intermediate to slow seepage environments as they have an important role in the precipitation of the MDAC.

Small patches of probable bacterial mats were identified only at one location in the Faro mud volcano. They were not detected at the scales normally found in areas of intense and active seeps like in the Gulf of Mexico or in the East Mediterranean. This is interpreted as indicating a present day state of low or inactive fluid venting at the seafloor. This is also confirmed by the low to mid range microbial methane turnover and AOM activity in the measured mud volcanoes from the Gulf of Cadiz (Niemann *et al.*, 2006). Gas bubbles and sites of active fluid migration were observed only at two locations in the Mercator mud volcano crater, in areas of highly gas-saturated mud breccia.

#### **4.4.4 Characteristics of mud volcanoes, mud cones and diapiric ridges**

The mud volcanoes in the Gulf of Cadiz are morphologically characterized by a moat around part of the base of the mud volcano cone, this moat can be erosive and/or resultant from the collapse of the structure as result of the overburden and stress release after the eruptions. The mud volcanoes are also characterized by an irregular slope with radial outward sediment flows, terraces and/or depositional sediment flow escarpments (lobe fronts). The summit of the mud volcanoes is in general characterized by a crater depression, or shows a flat top, or sometimes a central dome. The mud volcanoes in the GC are characterized by positive topographic features with diameters up to 5.4 km and up to 255 m high, like the Al Idrissi MV (Rensbergen *et al.*, 2005a; Rensbergen *et al.*, 2005b). The mud volcano edifices are composed by the stacking of successive deposits of fluidised

sediments composed by clay material, water, gases and clasts or rock fragments from the different strata crossed by the mud volcano conduit and or from the source layer.

The mud volcanoes from the Gulf of Cadiz are characterized by the presence of mud breccia sediments, composed of a mixture of clay rich sediment with fragments of exotic rocks that have high variable sizes and nature (clasts). The most abundant clasts correspond to claystones from which a significant percentage correspond to the plastic mud and blue marls clasts interpreted as being of Early-Middle Miocene age and expressing the wedge front of the olistostrome/accretionary complex (Somoza *et al.*, 2001; Díaz-del-Río *et al.*, 2003).

The mud breccia sediments are also characterized by a high gas (essentially methane) content and also by high H<sub>2</sub>S contents. On mud volcanoes where gas hydrates were collected, the mud breccias exhibit a mousy like texture with high amounts of vacuoles and high water content. This texture results from the dissociation of gas hydrates. Gas hydrate pieces were collected from the cores only when they had sizes sufficient to resist to their dissociation during the time of their retrieval.

The study of the mud breccia and the clasts from mud volcanoes from the Gulf of Cadiz allowed the identification of microfossils indicating ages ranging from Upper Cretaceous, Eocene and Miocene-Pliocene (Ovsiannikov *et al.*, 2003; Pinheiro *et al.*, 2003). However, the complex tectonic evolution and structure of the Gulf of Cadiz and the location of the mud volcanoes within the accretionary wedge complex, where several melange/olistostrome bodies are present, which can contain a mixture of several source rocks. The accretionary wedge geometry with major and deep thrusts can also bring deeper strata to close to the surface or even at the surface, as observed on the diapiric ridges where the upper Miocene blue marls are exposed at the seafloor. Therefore, the oldest ages defined from the mud breccia clasts are not clear indicators of the deepest and the source layers of the mud volcanoes. Nevertheless, the seismic profiles, the age information of the mud breccia clasts and the pressure and temperature conditions estimated from the pore water geochemistry, suggest that the mud volcanoes are most probably deeply rooted.

The MVs from the Gulf of Cadiz, as other examples from onshore and submarine MVs, exhibit sedimentological and geometric characteristics supporting their episodic, rapid and sometimes violent expulsion events. As regards the GC mud volcanoes, these evidences are interpreted based on seismic, acoustic, morphologic and sedimentary

analysis. The identification of eruptive mud flow episodes are recognised from the different backscatter intensities between the more recent mud flows, with high acoustic backscatter, when compared with the moderated backscatter intensities of the older flows recovered by pelagic sediments (e.g. Figure 4.50A). The recognition of mud flows is also possible from detailed bathymetry of the mud volcanoes (Rensbergen *et al.*, 2005a). Episodes of mud flows deposition are also recognized from the christmas tree facies where an inter-fingerings of acoustic transparent or chaotic seismic facies, typical of mud breccia flows, intercalate with the coherent and continuous reflectors from the sedimentary layers. The intercalation of hemipelagic sediment layers within mud breccia flows, as recognised on the 3.76 m long gravity core GeoB 9037-1 collected on the slope of the Captain Arutyunov MV and shown in Figure 4.50B, allowed to recognise three individual layers of mud breccia, corresponding to different mud flows episodes intercalated with pelagic sediment that indicates MV inactive periods (Kopf *et al.*, 2004).

Mud volcanoes are characterized on the side-scan sonar by a stronger acoustic backscatter than the surrounding pelagic sediment cover. This stronger backscatter reflectivity is attributed to the presence of clasts on the mud breccia and also due to the occurrence of the MDAC that are also frequently found within the mud volcano edifice. The high reflectivity of the surface of the mud volcanoes is also evident on seismic profiles as the seafloor amplitude over them corresponds to a clear strong positive anomaly when compared to the surrounding pelagic sediments.

On the seismic profiles the mud volcanoes are generally characterized by acoustically opaque, chaotic and indistinct seismic patterns, which extend from the seafloor into the subsurface (e.g. Figure 4.25B). The general interpretation for these acoustic wipeout zones is that they result of the presence of free gas (bubbles) in the surface and near-surface sediments, or is the acoustic response of the mud breccia deposits that correspond to material that is structureless as result of the sediment remolding along the subsurface feeder channel and mud flows resulting from the mud extrusion and gas escaping. This is supported by the fact that some of the mud volcanoes that are inactive show this chaotic seismic pattern, indicating that this characteristic is maintained in the systems and therefore is not an evidence of present activity or of the presence of free gas within the MV. On seismic profiles, the gas-charged sediments are identified by the high

amplitude reflecting horizons and/or by acoustic wipe-out zones below (Hovland and Judd, 1988).

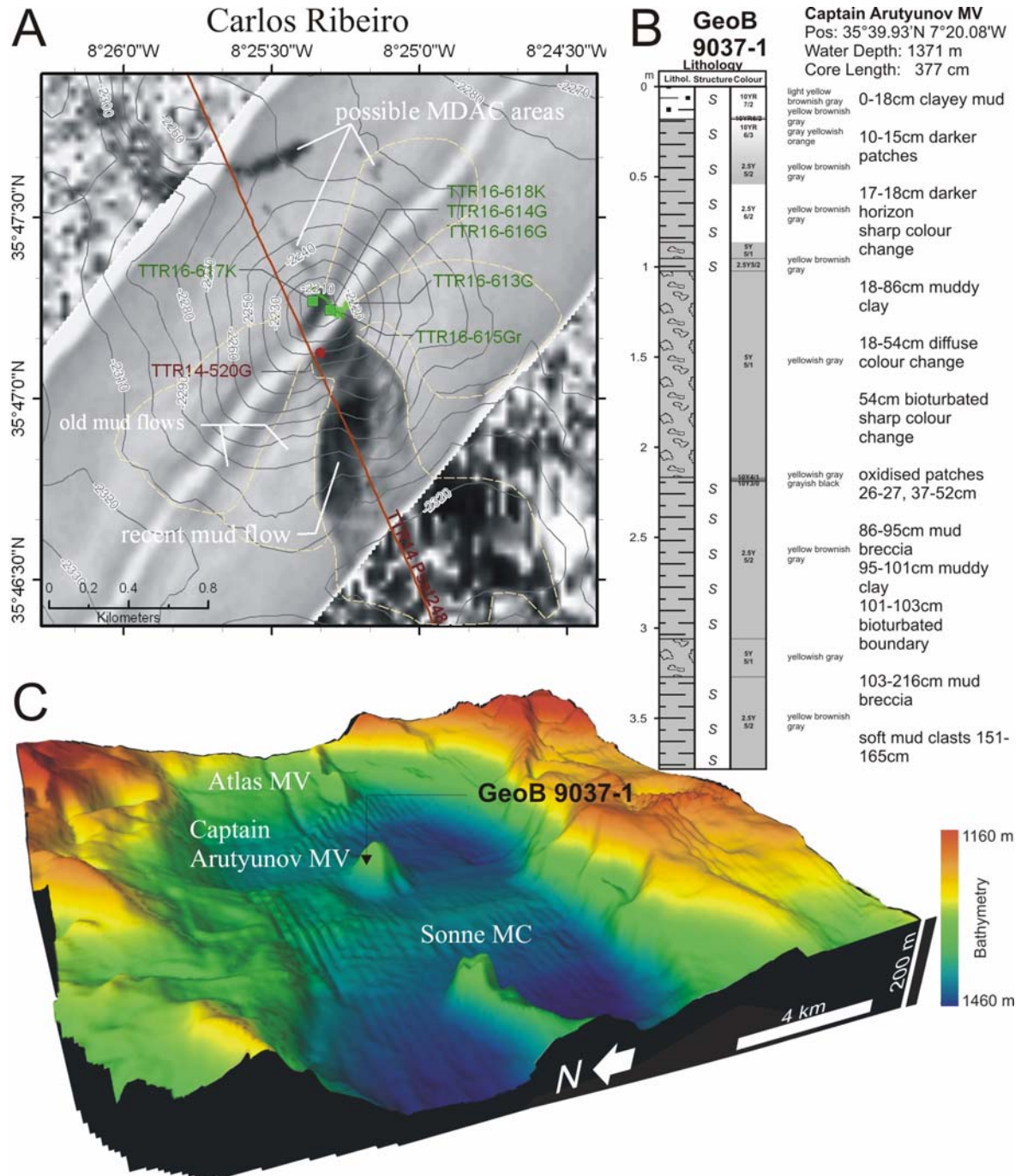


**Figure 4.50.** (A) Carlos Ribeiro MV showing a recent mud flow characterized by a strong backscatter MAK 1 side-scan sonar imagery. (B) Gravity core GeoB 9037-1 where is possible to recognize three mud flows. (C) bathymetry of the mini-basin where the Sonne mud cone, the Captain Arutyunov and the Atlas MVs are located. Also shown the location of gravity core GeoB 3937-1.

As the mud volcanoes correspond to rapid flux settings, a considerable heat is expected to be transported from deeper strata accompanying the extruded fluidized sediments, water and gases. Mud volcanoes on the deformation front of Barbados prism (Henry *et al.*, 1996) and in the Haakon Mosby mud volcano offshore Norway with high thermal gradient and heat flow of  $1000 \text{ mW m}^{-2}$  (Eldholm *et al.*, 1999) are examples of the highest heat flux settings. Other mud volcanoes, such as Mound Culebra offshore Costa Rica have heat flow values of  $35\text{-}50 \text{ mW m}^{-2}$ , 30-80% higher than the regional background values (Grevemeyer *et al.*, 2004). In the vicinity of mud volcanoes from the Mediterranean Ridge, heat flow values were observed to just slightly increase towards the mounds (Camerlenghi *et al.*, 1995).

The heat-flow measurements from the Gulf of Cadiz performed during the GAP and Anastasya 2001 cruises have recorded the only heat-flow values available from mud volcanoes in this area. Due to the presence of the MO that flows close to the seabottom at water depths between 400 and 1400 m, the heat-flow measurements are affected by the seasonal bottom water temperature variations. As the MO has significant seasonal variations, the transient changes in the temperature of the water column will cause temperature waves which will propagate from the seafloor downwards and therefore overprint the internal upward heat flux. An example of this effect is the record of the Hesperides MV that is characterized by non-linear gradients Figure 4.34. Nevertheless, heat-flow measurements from mud volcanoes in the Gulf of Cadiz recorded low heat-flow values in the Captain Arutyunov ( $17\text{-}22 \text{ mW m}^{-2}$ ), Hesperides ( $73\text{-}100 \text{ mW m}^{-2}$ ) and Ginsbug MVs (Gardner *et al.*, 2001; Kopf *et al.*, 2004). The Bonjardim was the mud volcano that showed higher heat-flow values ( $66\text{-}163 \text{ mW m}^{-2}$ ) pointing to a stronger activity in this structure than on the Captain Arutyunov, Hesperides and Ginsbug MVs (Kopf *et al.*, 2004).

#### **4.4.5 Temporal and spatial relationship between the MDAC, chemosynthetic organisms and the MV, MD and diapiric ridges**

The fluid escape structures from the Gulf of Cadiz represent a high degree of geologic and biologic variability associated with the type, intensity and duration of the fluxes. The rapid expulsions of fine-grained sediments during the MV mud flows

emplacement (and/or possibly accompanying by suspended sediments), will create environmental conditions that are hostile for the benthic fauna (Figure 4.51A and D). For filter feeders, the high suspended sediment loads overwhelm their respiratory systems and the mud flows can burry them or made their life difficult or impossible and preclude sulfide-producing anaerobic oxidation of hydrocarbons.

As rapid flux systems become progressively less active, these systems can start to acquire superficial features characteristic of moderate to slow and more fluid/gas dominated seepage. After a mud flow emplacement, if the mud breccia has enough high hydrocarbon (essentially methane) and a high sulfide content, these environments can be suitable for methane oxidizing and sulfate reducers to develop and carbonate precipitation will be induced and simultaneously the mat-forming bacteria *Beggiatoa* may colonize the surface of the mud flow. Lucinid and vesycomiid clams can then colonize the mud flows if the biodegradation of the incorporated hydrocarbons produces a sufficient sulfide source (Figure 4.51B). However, since the mud breccia expulsion events are episodic, any mud flow deposits have a limited hydrocarbon charge and therefore a limited sulfide-production potential. For this reason, infaunal lucinid clam communities establish themselves and quickly deplete the available sulfide source (Figure 4.51C). This is in agreement with their seafloor distribution as the clam shells superficial accumulations observed occur frequently scattered over the surface of extruded muds. Only in places where there is e.g. a tectonic focalization of the fluids and gases that can escape slowly to the seafloor, can these systems provide long term methane supply that can be stored as gas hydrates deposits at shallow depths, and/or fuel the methane oxidizers/sulfate reducers and subsequent sulfide oxidizers communities. These settings will also be associated with an intense MDAC formation. This can explain the location of the MDAC and larger chemosynthetic ecosystems that are most frequently found in the mud volcano crater or at its flanks where there is some focalization of fluid and gas seepage (Figure 4.51C).

Therefore, dormant or marginally active phases of the mud volcanoes may contain gas hydrates, authigenic carbonates and localized chemosynthetic communities. In fact, the mud volcanoes from which gas hydrates were collected from (Bonjardim, Captain Arutyunov and Ginsburg) or from which strong evidences of gas hydrates were identified, were also characterized by the presence of live chemosynthetic communities with lucinid-vesycomiid clams, pogonophora, vestimentifera tube worms and bathymodiolid mussels.

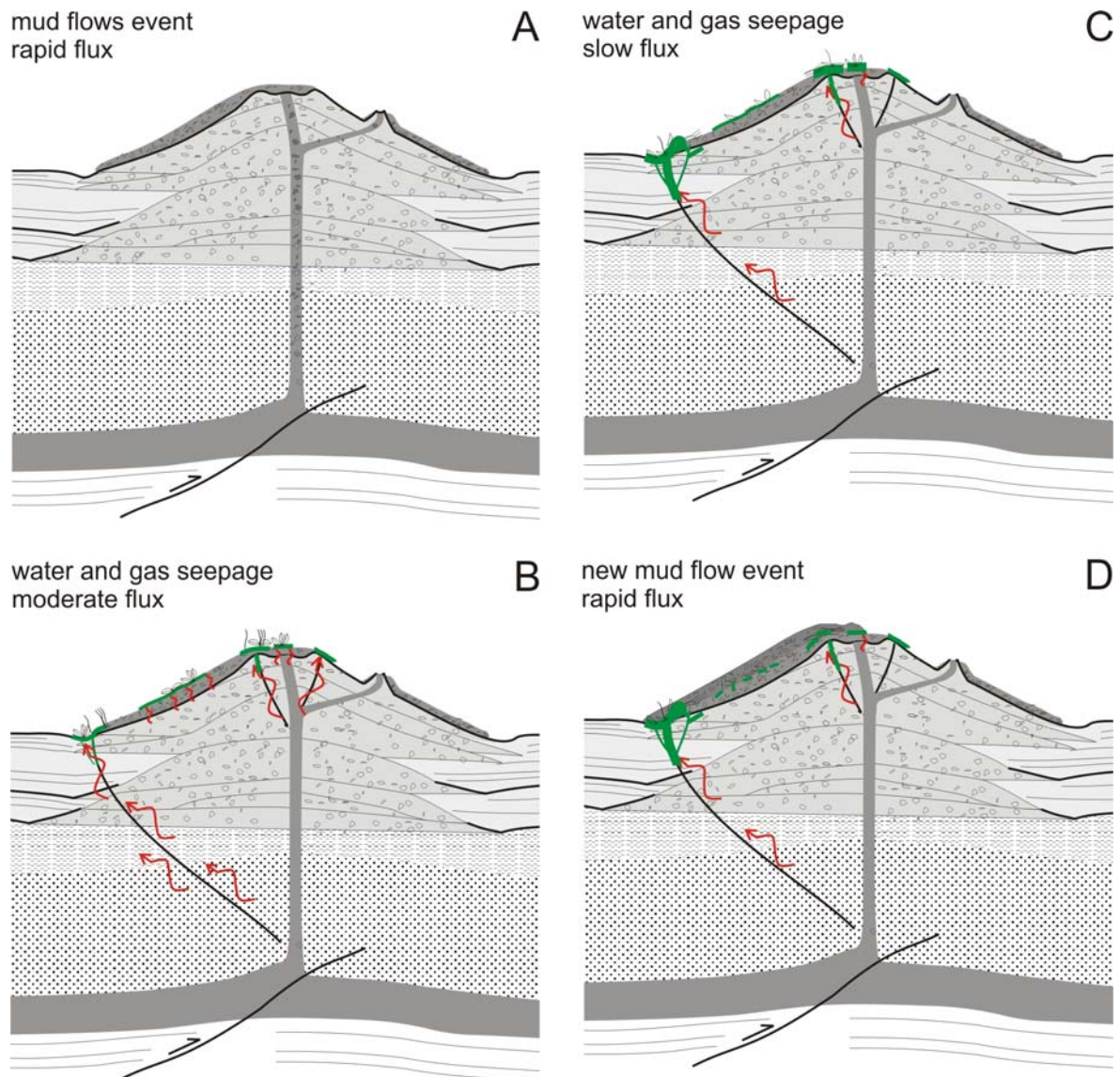


**Figure 4.51.** Schematic representation of a mud volcano illustrating a succession of different phases of its evolution. (A) phase of rapid flux with a mud-prone dominated event. (B) phase of intermediate flux with a flux dominated by water and gas and subsequent formation of MDAC, accumulation of gas hydrates and the establishment of large chemosynthetic communities. (C) phase of slow flux rate with a mineral-prone dominated features. (D) new phase of rapid flux with a mud-prone dominated event that covers the previous MDAC and chemosynthetic communities.

Through time, the mud volcanoes will successively go through different phases of activity, from a mud-prone phase of mud breccia extrusion with the rapid emplacement of mud flows, to a subsequent phase of moderate flux, dominated by water and gas can result in the accumulation of shallow gas hydrates, to the cementation of the mud breccia sediments and the formation of other types of MDAC and support of chemosynthetic

communities. A subsequent phase of reduced flux, dominated also by water and gas flux will result in further formation of MDAC and a decrease of the chemosynthetic communities.

In the Gulf of Cadiz the mud volcano fluids including gases are vertically focused by faults and by the mud volcano conduits, as the gas hydrates, MDAC and the chemosynthetic communities were found within the mud volcano edifices (Porto, Faro, Darwin, Fiuza, Yuma, Ginsburg, Jesus Braza, Kidd, Meknes, Mercator, Shouen and Student), mud cones (Iberico, Cornide), diapiric ridges (FR, GDR, Hormigas) and fault scarps (Pen Duick, Vernarsky ridge, Ridge W Gibraltar, Cadiz channel), and no regionally bottom-simulating reflectors were found until now.

## 4.5 Conclusions

The sites where MDAC occur are in close relation with mud volcanoes (MV) and mud cones (MC), within diapiric ridges, fault scarps and probably faults in the channels of the Mediterranean Outflow (MO), indicating that MV, MC, diapirs and faults are the preferential pathways for fluid escape. Underwater seafloor video observations suggest that the MO can have an effective control on the occurrence of the MDAC, promoting their formation (as discussed in Chapter 6). The MO has also a control on the occurrence of the different types of authigenic carbonates, as the dolomitic dominated MDAC mainly occur in places where the MO has a strong erosive effect (Magalhães *et al.*, 2005).

The MDAC chimneys have a large variability of shapes and sizes, such as pipe-like, tubular linear shapes, curved or helicoidal shapes, conical, branched, nodular and massive irregular shapes. Their sizes are highly variable both in length and diameter. Chimneys with more than 3 m long and up to 0.5 m in diameter were observed. These chimneys and crusts appear broken, sometimes intensely fragmented, forming carbonate rubble and they occur most of the times lying on the sea floor. It is very rare to find chimneys that are in a vertical position, protruding from the sediments.

The aragonite MDAC pavements occur as (1) buildups and small mound-like buildups of variable dimensions, some up to 4-5 m high and several meters in length; (2) as

rough hard-grounds that can pave the seafloor for several square meters, with a thin or absent sediment cover; (3) as crusts and slabs, similar to the pavements or; (4) as nodular masses of few cm size within superficial sediments.

The fluid escape structures from the Gulf of Cadiz (MV, MC, MDAC) and associated chemosynthetic communities, exhibit different phases of activity. They can represent a mud-prone phase of mud breccia extrusion with the rapid emplacement of mud flows. They can locally consist of phases of moderate flux, dominated by water and gas that can result in the accumulation of shallow gas hydrates, manifested by the cementation of the mud breccia sediments and the formation of other types of MDAC and by the support of chemosynthetic communities. Or they can consist of phases of reduced flux, dominated also by water and gas, which will result in further formation of MDAC and a decrease of the chemosynthetic communities.



## **Chapter 5. Methane-derived authigenic carbonates from the Gulf of Cadiz: Characterization and formation model**

### **5.1 Introduction**

During the TTR11 (Leg 3), TTR12 (Leg 2), TTR14 (Leg 1), TTR15 (Leg 4) and TTR16 (Leg 2) cruises, the area south and southwest of the Guadalquivir Diapiric Ridge (GDR), the Formosa Ridge (FR) and channels of the outflow of the Mediterranean water (MO), were surveyed with seismics, side-scan sonar, underwater TV and sampling. This area is characterized by a very strong backscatter on the available side scan sonar images and a very irregular seafloor, with morphological and sedimentological features related to fluid escape, as well as sedimentary structures associated with the MO (Figure 5.2). As described on the previous chapter, the GDR, the FR, on erosional features associated with the MO on the Cadiz Channel, in the Pen Duick and the Vernadsky Ridges and on some mud volcanoes and mud diapirs located on the pathway of the MO (Iberico, Faro, Hesperides, Student and Yuma) has been shown to be characterized by the presence of large fields of dolomite crusts and chimneys (Kenyon *et al.*, 2002; Magalhães *et al.*, 2002; Somoza *et al.*, 2002; Díaz-del-Río *et al.*, 2003; Kenyon *et al.*, 2003; Pinheiro *et al.*, 2003; Pinheiro *et al.*, 2004). Dense fields of dolomite chimneys and aragonite pavements were also discovered during the TTR14 cruise on the main channel of the MO in front of the Strait of Gibraltar. The re-examination of samples collected during the much earlier (1976) Hesperides cruise on the northern slope of the Guadalquivir Channel also showed the presence of similar dolomite chimneys. Aragonite and calcite crusts or pavements, typical from cold seeps, were also discovered and sampled, associated with the Pen Duick and the Vernadsky Ridges, within the Cadiz Channel and associated with several mud volcanoes: Jesus Baraza, Yuma, Ginsburg, Kid, Mercator, Fiuza, Darwin, Shouen, Adamastor, Meknes, Hesperides Faro and Porto (Figure 5.1).

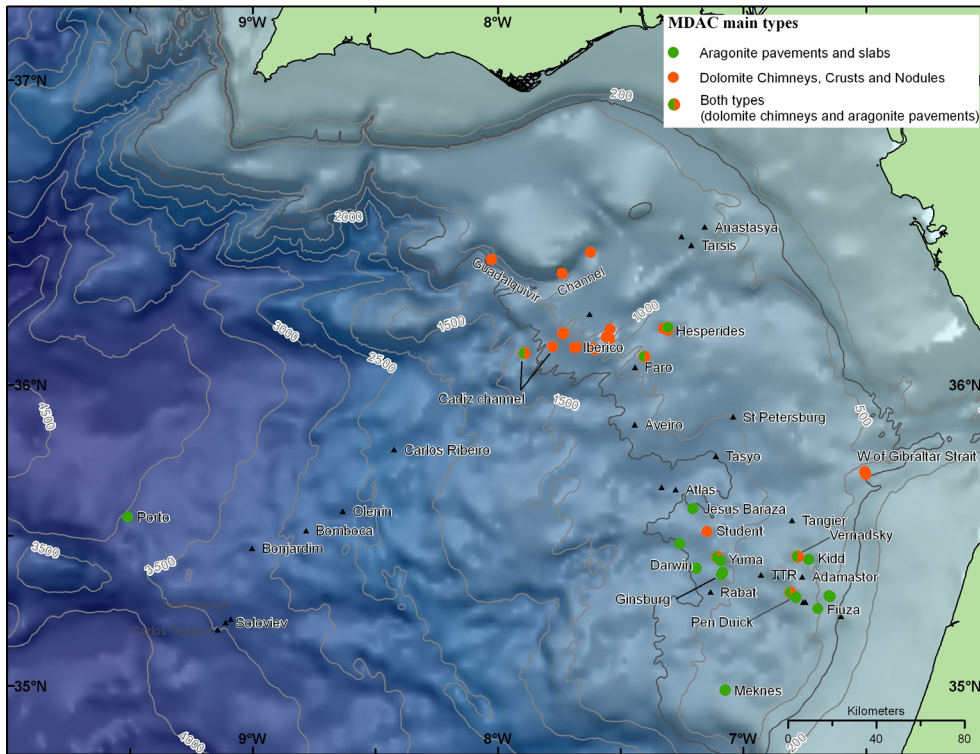


**Figure 5.1.** Map of the Gulf of Cadiz, showing the location of mud volcanoes, mud diapirs and carbonate crusts and chimneys.

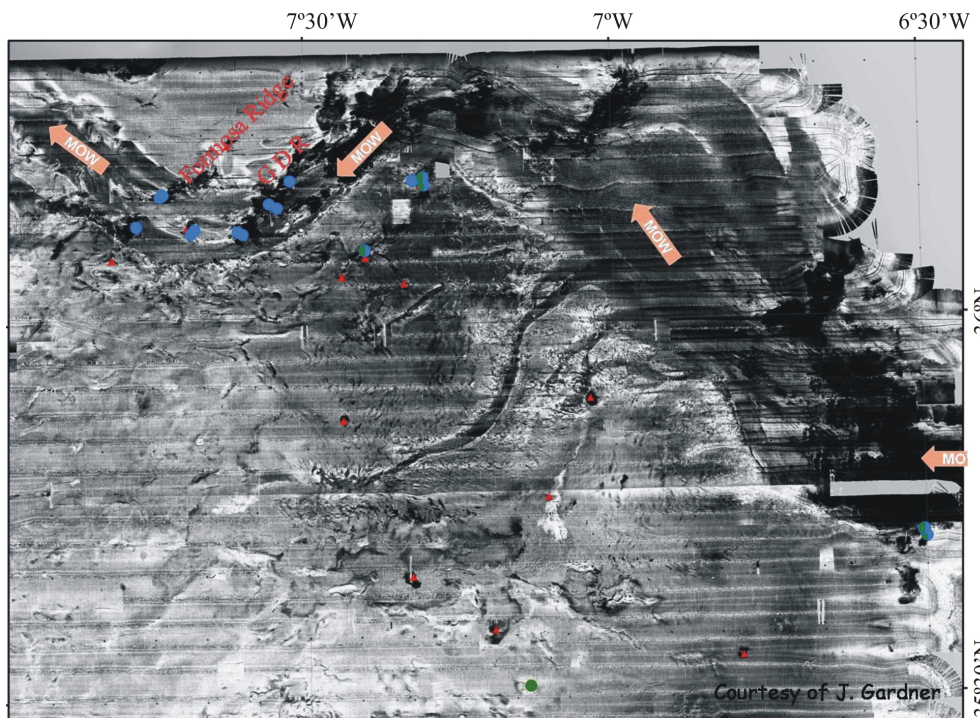


**Figure 5.2.** Area of the Guadalquivir Diapiric Ridge (GDR) and Formosa Ridge (FR) were the samples described in this study were collected. Also shown the location of underwater video camera profiles and the pathway of the Mediterranean Outflow Water (MO) that in this area runs near the sea bottom causing a strong erosive effect.

In this chapter, the different types of MDAC collected in the Gulf of Cadiz are described, together with their mineralogy, stable C and O isotopic composition, SEM and biomarker studies. The relationships between distinct geochemical environments and the resulting precipitated MDAC are investigated and a formation mechanism of the different carbonate lithologies is proposed.

## 5.2 Material and methods

The samples used in this study were collected by dredging and by TV controlled grab, on the main channels of the MO (Guadalquivir and Cadiz Channels, and in the MO channel in front of the Gibraltar Strait), on the GDR, on the FR, in the Pen Duick and the Vernadsky Ridges; in the Jesus Baraza, Yuma, Ginsburg, Kid, Mercator, Adamastor, Fiuza, Darwin, Shouen, Meknes, Faro, Hesperides and Porto mud volcanoes; and I the Iberico mud cone (Figure 5.1 and Figure 5.2).

Morphology and sizes of the authigenic carbonates were described on underwater video observations and on the retrieved samples. The petrography of the carbonates was examined in polished slabs and thin sections by standard petrographic and cathodoluminescence techniques.

Scanning electron microscope (SEM) observations were carried out, coupled with energy dispersive spectrometer X-ray elementary analysis (EDS), in fresh fractured surfaces and in samples etched with HCl 1% during 1-4 minutes before the SEM observations.

Bulk mineralogy and the relative abundance of different carbonate mineralogies in each sample were investigated by X-ray diffraction (XRD) on 134 powdered samples (Table 1). X-ray diffraction patterns were obtained using a Scintag X-ray diffractometer with  $\text{CuK}\alpha$  radiation (1.5405 Å wavelength); Scans were done from 5° to 60° 2 $\theta$  at 0.02°/sec, using 40 kV accelerating voltage and 30 mA current. As the intensity of the diffraction pattern of a mineral in a mixture is proportional to its concentration, estimates of the relative proportions of the minerals in a sample were made by measuring their relative peak areas. Peak identification and minerals relative abundance estimation were performed using the Scintag interpretation software and the MacDiff® software packages.

The peak areas were measured for the main peaks of the carbonate minerals aragonite (3.40 Å), calcite (< 8 mol% MgCO<sub>3</sub>, 3.036 to 3.012 Å), high-Mg calcite (8 to 30 mol% MgCO<sub>3</sub>, 3.012 to 2.946 Å), protodolomite (30 to 40 mol% MgCO<sub>3</sub>, 2.946 to 2.916 Å) and dolomite (40 to 55 mol% MgCO<sub>3</sub>, 2.916 to 2.871 Å). The Mg:Ca ratio of the carbonate minerals was calculated from the shift of the d-spacing of the (104) reflection peak of calcite and dolomite from the stoichiometric peak positions in the diffraction spectra (Goldsmith and Graf, 1958; Lumsden, 1979).

Samples for carbon and oxygen stable isotopic analyses were prepared by reacting at 90°C with 100% phosphoric acid on an automated carbonate device connected to a VG-PRISM mass spectrometer calibrated with NBS19, NBS 18 and NBS 20. The results are reported in the conventional δ ‰-notation with reference to VPDB (Vienna Peedee Belemnite). Analytical reproducibility of the method, based on repeated standards is better than ±0.1‰ for both carbon and oxygen. For temperature calculations of the dolomite samples, dolomite δ<sup>18</sup>O values were corrected for the analytical offset of +1.63‰, consequence of the unequal oxygen fractionation during the reaction to CO<sub>2</sub> (Rosenbaum and Sheppard, 1986).

Samples for <sup>87</sup>Sr/<sup>86</sup>Sr were dissolved in 20 ml, 1.0 N ultra pure acid acetic, centrifuged, and then decanted and evaporated dry. Then, they were re-dissolved in 20 ml of 5-N HNO<sub>3</sub> and loaded into columns containing the AG8 50W BioRad Sr-specific resin. The <sup>87</sup>Sr/<sup>86</sup>Sr composition of the carbonates (Arag, Calc, Mg-Calc and Dol) was determined using a VG-Sector 54 Thermal Ionization Mass Spectrometer. The analytical reproducibility of the method, based on repeated standards, is better than ±0.000060‰.

The carbonate and the organic carbon were determined using a LECO CHNS-932 elemental analyzer. Three replicates of powdered and homogenized bulk material (2 mg), collected with a micro-drill, were analyzed per sub-sample. The same set of sub-samples was later subjected to combustion for 8 h through a predefined stepwise increase in temperature up to 400°C, to remove organic carbon, and re-analyzed for inorganic carbon. The organic carbon content (C<sub>org</sub>) was determined by the difference between total carbon and the inorganic carbon concentration. Results are presented in weight percent (wt%). The relative precision of repeated measurements of both samples and standards was 0.03 wt%.

The sample preparation procedure used for extraction and purification of the lipid biomarkers is based on the method of Peckmann *et al.*, (2004) and described in detail in

Magalhães *et al.*, (2005). The freshly broken carbonate sample was decalcified (HCl 10%) and the dried residue was refluxed in 6% KOH in CH<sub>3</sub>OH (saponification reaction: 2 h). The supernatant was decanted and the residue was repeatedly extracted by ultrasonication in CH<sub>2</sub>Cl<sub>2</sub>/CH<sub>3</sub>OH (3:1 v:v), until the solvent become colorless. Subsequently, the combined supernatants were portioned in CH<sub>2</sub>Cl<sub>2</sub> versus water (pH 2). The resulting total extract was dried and separated by column chromatography (Merck silica gel 60, 0.063-0.200 mm; i.d.: 15 mm, length: 35 mm) into fractions containing: (1) hydrocarbons (20 ml or 3 column volumes of n-hexane); (2) Esters/ketones (20 ml of n-hexane/CH<sub>2</sub>Cl<sub>2</sub> 2:1); (3) Alcohols (20 ml of CH<sub>2</sub>Cl<sub>2</sub>/Aceton 9:1; (4) Fatty acids/Polars (20 ml of MeOH). The Esters/ketones and Alcohols fractions were dried and derivatised using pyridine and BSTFA (2:1) at 70°C (1 h). The polar fractions/Fatty acids were dried and transesterificated with Boron-Trifluoride methanol and then with KCl + hexane. Internal standard used for all fractions was Cholestane. A modification of the method, by doing a previous extraction with CH<sub>2</sub>Cl<sub>2</sub>/CH<sub>3</sub>OH (3:1; v:v) prior to decalcification, revealed to be efficient in cleaning dirt peaks on the dolomite chimney samples.

The hydrocarbon fraction was examined by combined gas chromatography-mass spectrometry (GC-MS) using a Varian CP-3800 GC/Saturn 2000 MS EI-mode, 70 eV) equipped with a 30 m fused silica capillary column (CP-Sil 8 CB Low Bleed, 0.25 mm ID, 0.25 µm film thickness). The carrier gas was He. The GC-temperature program used was: injection at 80°C, 5 min isothermal; from 80°C to 310°C at 4°C min<sup>-1</sup>; 20 min isothermal. Identification of the organic compounds was based on comparison of the mass spectra and of GC retention times with those of published data and of reference compounds.

Coupled GC-combustion-isotope ratio MS (GC-C-IRMS) was conducted using a Finnigan DeltaPlusXL mass spectrometer equipped with a HP6890GC and CuO/Ni/Pt combustion furnace operated at 940°C. Samples were injected splitless (1 min) onto a 30-m fused silica column (DB5-MS, 0.32 mm i.d., 0.25 µm film thickness) using a Gerstel Cooled Injection System (CIS4) programmed from 48°C (0 min) to 310°C (10 min) at 12°C sec<sup>-1</sup>. Carrier gas was He. The GC temperature program was: 3 min at 80°C; from 80°C to 310°C at 4°C min<sup>-1</sup>; 30 min at 310°C. GC-C-IRMS precision was checked using a standard alkane mix (n-C<sub>15</sub> to n-C<sub>29</sub>) with known isotopic composition. The stable carbon isotope composition is reported in the delta notation (δ<sup>13</sup>C) vs. the VPDB Standard.

Samples for XRD, Sr, total organic carbon, carbonate content, carbon and oxygen

stable isotope were extracted from transversal and longitudinal cuts and micro-drilled along radial and longitudinal profiles.

## 5.3 Results

### 5.3.1 Types and morphologies of the MDAC

Based on macroscopic, morphological and textural characteristics in hand specimens, the more than 134 studied individual carbonate samples have been classified into 2 main different types: (I) crusts, nodules and chimneys with the mineralogy dominated by dolomite and high Mg-calcite and (II) crusts, pavements or buildups with mineralogy dominated by aragonite. In each one of these types, sub-types were defined. On the dolomite type the following sub-types were identified: Dolomite crusts (DCr); Dolomite Chimneys (DCh); Nodules or irregular massive forms (Nod). On the aragonite build-up or pavement type (AragPav) the following sub-types were defined: Lithified mud volcano mud breccia (LMb); Shell crusts (SCr); Intraformational breccias (IBr); Lithified fragments of dolomite chimneys (LDChy); Stromatolitic layers (Str) and Fossilised biofilms (Fbf).

#### 5.3.1.1 Dolomite chimneys (DChy)

The terminology dolomite “chimney” is used in this work with a descriptive sense, indicating samples with a pipe-like or a conduit-like morphology. It is not used with a genetic connotation of the formation process in the water column as a resemblance with the hydrothermal vent chimneys. This term is preferred because it has always been used to describe such structures not only in the Gulf of Cadiz (Diaz-del-Rio *et al.*, 2001; Magalhães *et al.*, 2002; Somoza *et al.*, 2002; Díaz-del-Río *et al.*, 2003) but also in many other cold seepage areas (Kulm and Suess, 1990; Greinert *et al.*, 2001). The terminology of chimney is adequate to these samples if the term is considered with the meaning of a fluid conduit.

The recovered dolomite chimneys (DChy) are composed of compact, in general tightly carbonate-cemented, medium light grey to light brown colour sandstone/mudstone. Their shape is in general cylindrical or conical, exhibiting a wide range sizes from 10 to 70 cm in length and from 1 to 35 cm in diameter. During underwater video observations it

was possible to identify chimneys up to 4 m long and with a diameter up to 0.5 m. The mineralogy, as described in Table 5.1 and in more detail in section 5.3.3, is characterized by the presence of dolomite as the major constituent of the cement.

Based on their morphologies, several subtypes of chimneys were defined: (1) tubular (single or with 2 or 3 parallel tubes cemented together), (2) conical, (3) doughnut shaped, (4) spiral and (5) branched (Figure 5.3).

Relatively to the vent channel, some chimneys are completely filled, without any open and clear channel, while others show an open and sometimes large (up to half of the total diameter, c.a. 15 cm) vent orifice(s) that has the same shape than the chimney (straight, tortuous, ramified or helical). In general, the chimneys completely filled exhibit growth concentric ring layers. The outer walls of most of the chimneys (as the inner wall in the ones with an open channel) are iron oxide stained, with a dark red to dark brown colour. The chimneys that do not show any signs of this iron coating exhibit a pale yellow to medium light grey colour. Colonisation of the chimneys by fixed benthic fauna, like incrusting sponges (Porifera), corals, bivalve shells or brachiopod clusters is common, especially on the chimneys with the dark iron oxides coating. These samples are frequently nailed by scavenger burrows of 1 to 2 mm in diameter and several cm in length, forming sinusoidal holes coming from the sample exterior. No mollusc shells or fragment of heterotrophic organisms, intact or even corroded, are found cemented inside the chimneys. This is the opposite of what is observed on aragonite pavement samples or as it has been described on samples typical from active seeping sites e.g. Paull *et al.*, (1992) and Sibuet and Olu (1998).

The presence of iron and manganese oxy-hydroxides is interpreted as resulting from secondary oxidation of sulphur minerals (pyrite), occurring after exhumation of the samples, when they were in contact with the seawater, or in the oxidation zone of the sediment column. This exhumation is probably the result of erosion and sediment removal due to strong bottom water currents like the MO. This explains why some chimneys have different characteristics in the upper and the lower parts. Some samples present a reddish to brownish coloured upper part with higher frequency of holes, scavenging features and benthic fauna, more tightly cemented and more intensely coated with oxides, while the bottom part is less cohesive and less oxidized, as reflected by the more greyish colours. This is interpreted as the result of a longer period of contact of the upper oxidized part of

the sample with the seawater, during the progressive exhumation of the sample. Some samples like the one presented in Figure 5.4C clearly present oxidation fronts of growing intensity of the oxidation to the external part of the chimney and to the interior open vent channel. The internal material, not in contact to the exterior is less oxidized. This is indicating that the oxidation is a secondary process occurring with the change of the geochemical environment, probably related to the exhumation of the sample. Around burrows or scavenger channels, that promote the circulation of seawater within the sample, it is also possible to see similar oxidation fronts. The chimneys composed of finer grain size detrital fraction have lower porosity and lower permeability than the chimneys with a detrital fraction of silt to sand size. All these silty to sandy chimneys present higher oxidation intensities and only some scarce clayish chimneys are not oxidized.

Singular pyrite framboids or small pyrite clusters are observed by SEM on the non-oxidized dolomite chimneys, dolomite crusts and nodules. Pyrite is absent from the intensely oxidized samples. On the weak oxidized samples, pyrite, if observed, shows signs of oxidation forming rims of iron oxides (probably containing OH-groups). This is also visible on thin sections as brownish stain that is reflected on the reddish to brownish colour of the hand samples.

Some of the chimneys present a incipient layering perpendicularly to the vent direction, that in some situations is shown by fractures or weakness zones that contribute to the segmentation and division of the chimneys (if this segmentation is closely-spaced then the chimneys present a doughnut-shape where the length of the chimney is very small compared to the diameter). In other situations, the layering is revealed by a increasing of the diameter of the chimney (forming nodular protuberances) or changes on the granulometry of the detrital fraction (see Figure 5.4). In one sample, it was possible to consider that an dolomite crust was being formed perpendicularly to the chimney conduit, as the result of cementation along a conduit that crossed perpendicularly a more permeable layer and the fluid migration developed also along this layer and also promoting their cementation.

The helicoidally, curved and branched chimneys (Figure 5.3F and G) probably correspond to cemented borrow infills.

Based on the morphology, mineralogy, petrography and geochemistry, the dolomite chimneys are interpreted as corresponding to cemented fluid conduits. Depending on the

sediment properties and fluid flow rate, different regimes of fluid flow can be expected: (1) Migration through diffusion, that is expected to occur in the sediments with a higher grain size and that in general correspond to conduits with no open vent channels; (2) Migration through (hydraulic) fracturing, as migration of clusters, as a flow through a single channel or as a flow through a canalized network (Stöhr *et al.*, 2005). Burrows and other sedimentary structures and heterogeneities can be preferential pathways for this plumbing system. This flux regime in finer sediments will preferably maintain an open vent channel. This is supported by the observation that the chimneys with open vent channels are characterized by a finer detrital fraction.

#### **5.3.1.2 Dolomite crusts (DCr)**

Dolomite crusts (DCr) have planar shapes, up to 5 cm thick and up to 44 cm long (Figure 5.3A), although larger specimens were identifiable on underwater observations. They are generally covered by a dark red or dark brown coating of Mn/Fe oxy-hydroxides. Colonization of the crusts by fixed benthic fauna is common and more intense on crusts with more intense coating. The samples with more intense coating present scavenger burrows of 1 to 2 mm in diameter and several cm in length forming sinusoidal holes coming from the sample exterior.

The dolomite crusts are composed of pale yellowish to light brown (indicating the presence of Mn/Fe oxy-hydroxides) fine-grained and tightly cemented carbonate sandstone/mudstone, very homogeneous with no internal structure. Present in general, low porosity, just microporous and absence of macroporous or internal channels. Shells or biogenic components incorporated in the crust are absent (except for foraminifera and coccolithic tests). Based on the morphology, texture, mineralogy and geochemistry, the dolomite crusts are interpreted as cemented sedimentary layers.



**Figure 5.3.** Illustration of the different morphologic types of dolomite carbonate samples recovered. A: Dolomite crust type; B: Tubular DChy; C: Conical DChy; D: Spiral DChy; E: Branched DChy; F: Nodular or massive type (Nod).

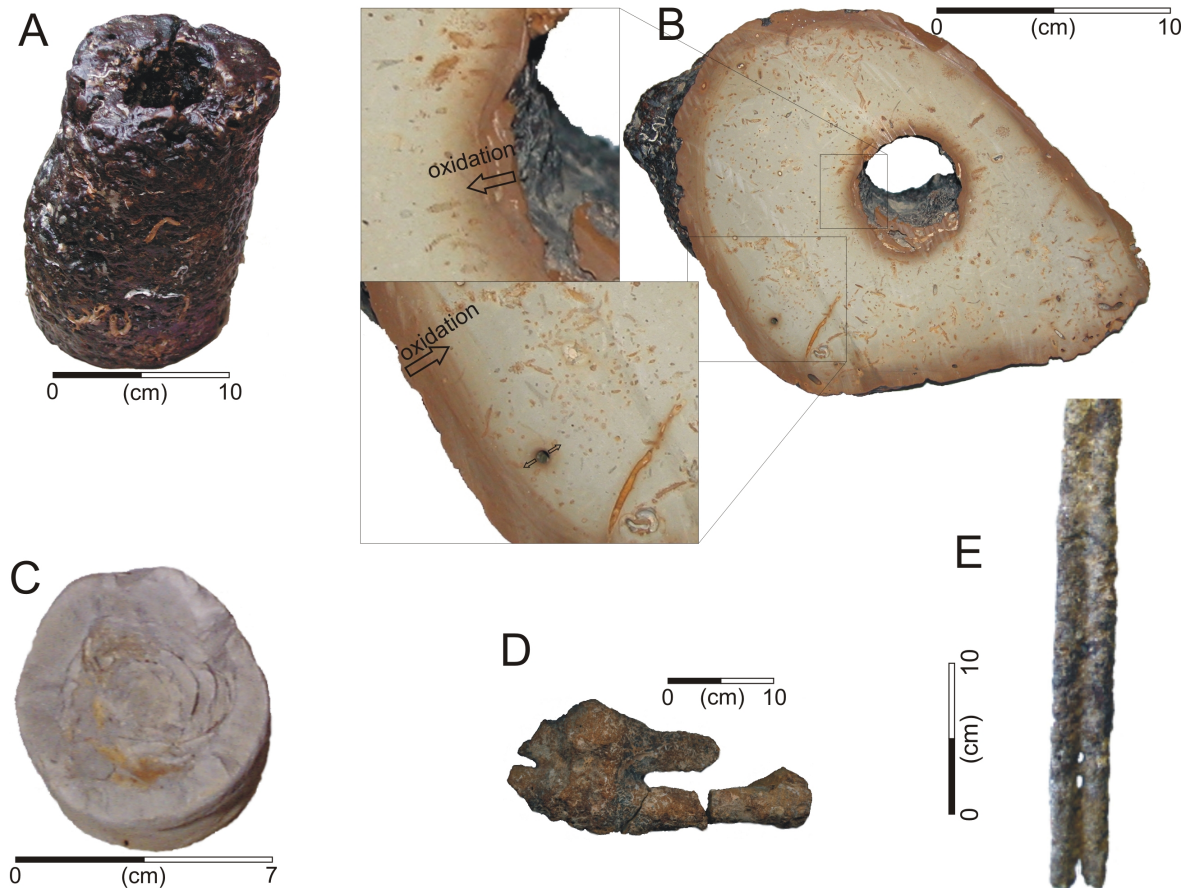


**Figure 5.4.** Illustration of the different types of vent channel. (A) open vent channel; (B) open vent channel exhibiting oxidation fronts spreading out from the exterior of the sample and from the interior open vent channel and also from open holes of burrows, as the one illustrated where is possible to observe the oxidation front spreading from this hole; (C) completely filled chimney sample exhibiting concentric grow layers; (D) chimney with 2 parallel vent channels that are jointed at a an intermediate length; (E) chimney with two parallel and open vent channels.

### 5.3.1.3 Dolomite nodules (Nod)

This type corresponds to nodular, massive, round or irregular forms (Figure 5.3H), composed of compact sandstone/mudstone. The texture, colour, mineralogy and petrography of this type is similar to the chimneys, with light brown or grey colours, often coated by dark brown Mn/Fe oxy-hydroxides. The presence of oxidation rims progressing from the exterior to the interior of the samples is frequently observed. These samples are characterized by a dense homogeneous matrix of terrigenous (detrital quartz, feldspar and clay minerals) and foraminifers, completely cemented by micrite to microsparite carbonate composed of mixtures of dolomite, calcite and high Mg-calcite. Like the chimneys they do

not include mollusc shells or fragments of heterotrophic organisms as part of the constituent material. The shells or organisms, when present, represent secondary colonization of the surface of the samples by benthic fauna. The size of the collected samples is up to 45 cm in diameter.

#### **5.3.1.4 Aragonite crusts and pavements (AragPav)**

Aragonite crusts and pavements are porous, whitish, light brownish grey to dark grey aragonite dominated carbonate. Their mineralogy is dominated by aragonite and calcite, cementing a detrital fraction of quartz, feldspars, clays, mud volcano mud breccia clasts, shell fragments, foraminifera and calcareous nannofossils. Aragonite crusts and pavements present in general tabular shapes (as revealed by the retrieved samples and by the underwater video observations) or irregular block like or build-up shapes. The samples collected are up to 50 cm in thickness and up to 1 m in length.

Different lithologic types of aragonite pavements were identified: *(i)* lithified mud volcano breccias; *(ii)* shell crusts; *(iii)* intraformational breccias; *(iv)* lithified fragments of dolomite chimneys/crusts; *(v)* stromatolitic layers; *(vi)* fossilised biofilms. Several subtypes can coexist at the same location and some times in the same sample.

##### ***5.3.1.4.1 Lithified mud volcano breccias (LMb)***

Lithified mud volcano breccias correspond to very porous, weak to moderated carbonate-cemented mud volcano breccias (Figure 5.5A). The collected samples present, in general, irregular block-like shapes, up to 50 cm in diameter. Most probably, the recovered shapes result from the fragmentation of the samples during the sampling process. Underwater video observations have shown that they form pavements with several square meters of rough seafloor (Figure 5.6B).

They present in general brownish colours, indicating a moderate oxidation environment, to dark grey or black colours, indicating a reduced environment. Some samples present an sharp interface of those different oxidation environments, the top part of the sample presenting a brownish colour, interpreted as corresponding to the seawater dominated environment, while the deeper part has a dark grey colour corresponding to subsurface anoxic sediment environment.

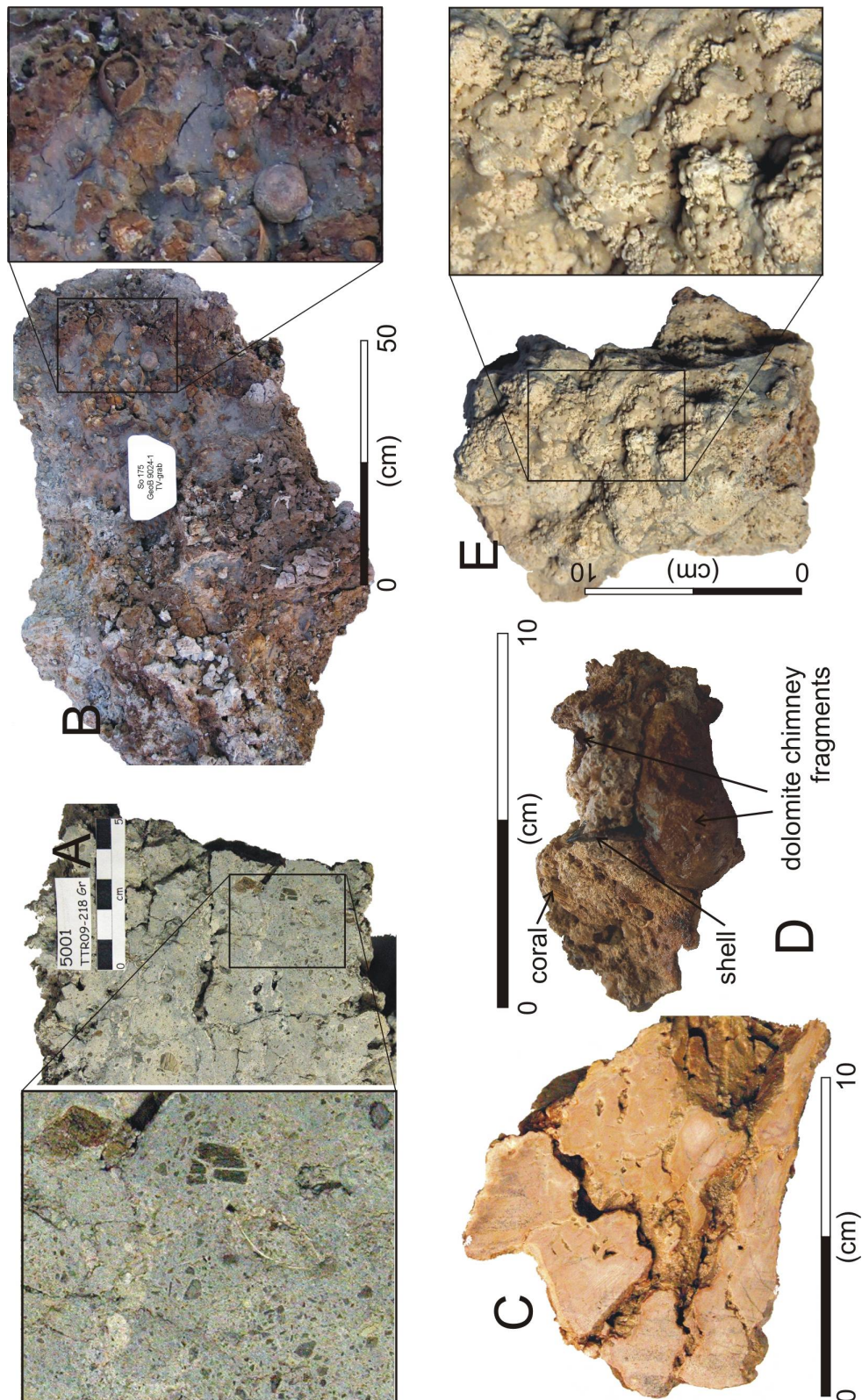


**Figure 5.5.** Illustration of the different aragonite pavement types. (A) Lithified mud volcano mud breccias (LMb); (B) Shell crusted (SCr); (C) intraformational breccias (IBr); (D) Lithified clasts of dolomite chimneys crusts fragments (LDChy); (E) Stromatolitic layers (SL).

Aragonite pavement LMb are characterized by distinctive mud volcano breccia clasts with up to 3 cm in diameter, sub-angular to very angular shapes, randomly oriented. These clasts are very similar to the ones that are characteristic of the mud breccia material collected on the various mud volcanoes in the Gulf of Cadiz.

Lithified mud volcano breccias are in general cement-supported. The matrix is composed of the clayish mud breccia clasts, silt to sand-size quartz and feldspar grains, coccolithids, radiolarians, diatoms and foraminifera skeletons, as well as detrital clay minerals. Singular pyrite crystals, or small clusters randomly distributed or arranged in short lamina, are also present. The cement is fine grained granular (micrite to sparitic) in generally poly-mineralic: aragonite, calcite and high Mg-calcite. Some LMb samples present stromatolitic layers of fibrous, botryoidal mono-mineralic cement (see section 5.3.1.4.5) composed of microspar to sparite aragonite needles 10 to 40  $\mu\text{m}$  across and up to 1 mm in length with less or no impurities of the detrital sediment matrix that are described in more detail as stromatolitic layers.

Frequent linear holes of tubular shape, with 2 to 8 mm in diameter, were interpreted as Pogonophora worm casts. Alternatively, the linear holes could also be interpreted as venting conduits along which fluid migration is focused and around which precipitation is enhanced. Live Pogonophora were retrieved with some of the LMb in sites of interpreted more intense or recent venting activity, as revealed by the live chemoautotrophic communities.

#### **5.3.1.4.2 Shell crusts (SCr)**

Shell crusts (Figure 5.5B) correspond to aragonite pavement samples with high amount of bioclasts, mainly of *Calyptogena* sp., Solemyidae and *Lucinoma*, *Acharax* shells and Pogonophora tube worms, incorporated in the fine grained granular (micrite to microspar) mono-mineral (aragonite) or poly-phase (aragonite, calcite, Mg-calcite) cement. Sessile organisms, like small corals, brachiopods and small sponges are also found attached, and some times incorporated into the crusts. Some of the *Acharax* shells are still enclosed by an intact periostracum indicating in situ cementation. Like on the LMb the SCr also show tubular holes (2 to 8 mm in diameter) interpreted as Pogonophora worm casts or as venting conduits along which fluid migration is focused and where the authigenic-

carbonate precipitation is enhanced. Incorporated Calyptogena, Acharax and open channels of Pogonophora casts indicate that the crust formation took place near or at the seafloor.

Shell crusts show different degrees of oxidation and different intensities of iron oxides coating. They have brownish colours, indicating moderate oxidation, or grey to black colours, indicating redox environment. Samples presenting a sharp interface between these two different degrees of oxidation are also found, with a top part of the sample presenting a brownish colour and colonized by benthic organisms, interpreted as corresponding to the seawater or oxic superficial sediment column. And with a deeper part presenting a dark grey colour with no signs of benthic organisms that is interpreted as corresponding to anoxic sub-superficial sediment column.

The crusts are grain or cement-supported, moderated to very strongly cemented with low to medium macro-porosity of irregular shaped and randomly interconnected open cracks and cavities up to 2 cm in diameter. Because this type presented the best densely cemented samples of all the different pavement types, the SCr correspond to the largest retrieved samples (up to 1 m in length and 40 cm thick). The underwater video observations revealed that they can form pavements with rough surfaces littering the seafloor for several meters or forming buildups.

#### ***5.3.1.4.3 Intraformational breccias (IBr)***

Intraformational breccias (Figure 5.5C) exhibit tabular crust morphologies that pave the seafloor or form irregular shaped buildups at the seafloor. These breccias are interpreted as sin-formational breccias, composed of chaotically oriented matrix-like carbonate intra-clasts (up to 3 cm in size, interpreted as fragments from previous aragonite pavements), bioturbation casts, rare shells and can also include poorly lithified mud breccia clasts typical of the lithified mud volcano breccia type.

Intraformational breccias are in general clast-supported with clay and silt size terrigenous sediment, in general intensely cemented by randomly oriented fibrous sparitic aragonite and/or fine grained granular poly-phase micrite to microspar aragonite, calcite and high Mg-calcite (this, more abundant in the intraclasts). They present medium to high porosity with abundant irregular shaped and randomly interconnected plumbing networks of mesopores, open cracks and cavities that lead to the pseudobrecciated collapse texture for this sample type. This lithologic type is interpreted as sin-formational i.e. the fractures

and pore spaces were formed during the cementation and maintained open. Some mesopores present a cover with stromatolitic layers of botryoidal white aragonite cements. Framboidal pyrite sometime occurring as layers, parallel to the stromatolitic lamina, are an indicator of the formation in anoxic microenvironments. Some of the pyrite shows a secondary oxidation phase indicating a change in environment.

This lithologic type is interpreted as indicating a superficial formation process. It can be explained by mechanisms involving gas hydrate formation and decomposition. This lithology corresponds to the intraformational breccias, gas hydrate carbonates and aragonite collapse breccias as defined by Bohrmann *et al.*, (1998) and Greinert *et al.*, (2001). The brecciation can also result from ascending fluids, bubbles and pressure build up, as a result of the accumulation of methane gas below the crust and subsequent violent gas escape, as described by Hovland *et al.* (1987) for MDAC in North Sea pockmarks. The growing of gas hydrate pieces or layers and subsequent decomposition produces large volume expansion that can also produce sediment disruption at the seafloor and brecciation, as described at the shallow seeps in the Cascadia Subduction zone Hydrate Ridge (Bohrmann *et al.*, 1998; Greinert *et al.*, 2001; Greinert *et al.*, 2002) and in the Gulf of Mexico (MacDonald *et al.*, 2003). One other mechanism can explain this lithology. The gas hydrates form layers and veins along which the cementation by carbonates is prevented. When the gas hydrate free host sediment is cemented the hydrate-bearing parts will build pores after the gas hydrate decomposition (that can occur in situ or during the sample recovery).

#### **5.3.1.4.4 *Lithified fragments of dolomite chimneys/crusts (LDChy)***

Lithified fragments of dolomite chimneys/crusts (LDChy) are clast supported breccias with dolomite clasts that have petrographic, mineralogical and isotopic characteristics of the dolomite nodules, crusts and chimneys. Therefore, these clasts are interpreted as fragments of dolomite chimneys (DChy) and crusts (DCr) that were cemented during secondary episodes of MDAC precipitation. The LDChy samples (Figure 5.5D) were collected by dredging the flank of the Guadalquivir Channel. The recovered specimens of this type consist on 3 fragments up to 12 cm in size, with irregular to sub rounded morphologies that are probably the result of the sampling operation by dredging. The clasts present up to 7 cm in size and are strongly stained with iron oxides. They

present in general sub-round shapes that indicate significant transport of the clasts by deep currents along the step flank of the Cadiz MO Channel or it can be a consequence of their original nodular shape of concretion-like morphologies. The pebbles are cemented by a porous and weakly to moderately lithified poly-phase carbonate of microspar aragonite and calcite. The cement has pale to light brown colours indicating variable degrees of oxidation.

#### **5.3.1.4.5 *Stromatolitic layers (SL)***

Stromatolitic layers are present in all the different lithologic aragonite pavement types (with exception for the LDChy) but, on the studied samples, their occurrence is more frequent on the intraformational breccias and on the lithified mud volcano breccias. It corresponds to stromatolitic laminas of an almost pure fibrous aragonite phase that recovers the internal surface of pore spaces, voids, tubular cavities and fractures (Figure 5.5E) of AragPav samples. These stromatolitic layers, up to 10 mm in thickness, present an external smooth surface with domal, isopachous layers of aggregates and botryoidal rims of sparite fibrous aragonite needles that grow in the direction of the centre of the cavities. The undulated laminas pattern, similar to the cauliflower-like structures of the stromatolites, grow on top and, in general, parallel to the cavities surfaces, on top of the fine grained (micritic to microsparitic) aragonite and calcite cement of the LMb, SCr and IBr. Because this fabric occurs associated with structures interpreted as fossilised biofilms, the SL formation is interpreted as induced by the encrustation of microbial mats.

The stromatolitic layers are similar to the ones reported by Greinert *et al.*, (2002) exhibiting inverted stromatolitic grow direction when compared with the true stromatolites. He emphasize that the stromatolites in methane-derived crusts grow in the direction of the source of energy, protruding downwards from shallow sediment horizons. AOM proceeds below pre-existing carbonate crusts and is aggregating downwards. The stromatolitic layers of the studied samples presents complex growth patterns. Along some cavities, the stromatolitic layers are growing in the direction of the centre of the cavity. When the shape of the pore (usually elongated pores up to 2x12 cm) of irregular to lenticular shape resemble the shape of the collected chunks of gas hydrates (from some mud volcanoes), these pores can be interpreted as relicts of gas hydrate pieces, veins or cavities filled with gas or methane rich pore fluids. In some larger cavities the botryoidal aragonite layers

aggregation occurs downward from the top of the cavity. In this situations the stromatolitic layers are interpreted as representing the roof of the cavities where the methane is being trapped, leading to a more intense AOM in this part of the cavity. So this fabric is expected to occur whenever the environmental conditions favours near surface gas hydrate formation/decomposition.

This fabric represents a second stage of mineralization of the aragonite pavements. The micritic to microspar calcite, Mg-calcite and fine grained aragonite precipitates, cementing the clay rich detrital matrix before the later stage of the fibrous aragonite stromatolitic layers formation.

#### ***5.3.1.4.6 Fossilised biofilms (Fbf)***

SEM and thin section observations of the aragonite pavements frequently show thin sheets and threads lying over and between the aragonite needles, sometimes evolving the aragonite needles or at the transition between different stromatolitic layers. These structures, are described and discussed in Chapter 8, are interpreted as fossilised microbial biofilms and mucous biofilms, relicts of micro-organisms. They were found exclusively associated with the stromatolitic layers, on top of the botryoidal aragonite layers or between different aragonite layers.

### **5.3.2 Occurrence and Underwater observations**

Seep sites and authigenic carbonate deposits were initially assumed to be isolated occurrences in the Gulf of Cadiz. The increasing detail and survey coverage during the last years allowed the recognition of various cold seeps and MDAC occurrences between 400 and 4000 m water depth, indicating that these features are far more common than previously anticipated (Figure 5.1 and Figure 5.2). The evaluation of the distribution of seafloor fluid seepage indicators observed on underwater video profiles and during sample retrieval by video controlled grab, and their correlation with sediment samples and acoustic characteristics on the seismic profiles and side-scan sonar backscatter images, indicate that the occurrence of the MDAC and the seep sites are in close relation with mud volcanoes, mud diapirs and probable deep routed faults. Such structures are the preferential pathways for fluid circulation and escape.

### 5.3.2.1 Dolomite crusts and chimneys

Dolomite chimneys, crusts and nodules occur as high density fields where they occur some times very fragmented and lying on the seafloor (Figure 5.6A). It is rare to find chimneys in a vertical position, protruding from the sediments. On a video line in the Cadiz MO Channel chimneys are reported to occur in situ and not completely extruded from the sedimentary formation where they formed (Chapter 9) and there it was possible to recognize in some situations a sub-parallel orientation of some chimneys relative to the sedimentary layering while other chimneys clearly present a sub-vertical orientation also supported by the apparent layering interpreted in some chimneys. The dolomite crusts, chimneys and nodule occurrences are restricted to areas characterized by moderated to strong bottom currents. Those are considered to be able to produce active erosion of the surrounding unconsolidated sediments within which the chimneys grew, inducing the exhumation of the chimneys and their consequent following down and fragmentation.

Large colonies of sea urchins, Cnidaria (Hydrozoa and Anthozoa), Mollusca (Gastropoda and Bivalvia burrows), Annelida (Polychaeta), Arthropoda (Decapoda), Brachiopoda, Echinodermata (Crinoidea, Asteroidea, Ophiuroidea, Echinoidea and Holothuroidea) use the carbonates as a hard ground for fixation. Unambiguous chemosynthetic communities were not identified at sites of exclusive occurrence of dolomite chimneys, crusts and nodules. Chemosynthetic communities were identified only at sites characterized by the occurrence of the aragonite pavement types. At the Hesperides, Faro and Student mud volcanoes, and off Gibraltar, occurrences of dolomite chimneys and aragonite pavements are found in close spatial proximity or simultaneously. However the observed field geometry relationships between the different MDAC indicate that they had distinct formation periods. The morphologic and textural characteristics of the aragonite pavement carbonates show indicators of a recent or present day formation while the dolomite carbonates, which occur as fragments and remobilized pieces, indicate older formation episodes.

### 5.3.2.2 Aragonite pavements

The aragonite pavements appear in the seafloor as buildups, some times with dimensions up to 2-4 m, or as rough hard-grounds (up to 50-80 cm thick) that can paving the seafloor for areas of several square meters, with a thin or absent sediment cover (Figure 5.6B).

Colonization of these pavements by benthic fauna is frequent. Aggregates of clam shells, probably most of them dead, were identified in several places. Live chemosynthetic fauna (Calyptogena, Acharax and Pogonofera tube worms) were identified and sampled in small areas and at sites where the venting activity is considered to be more recent or more intense. Small patches of probable bacterial mats were identified only at one location in the Faro mud volcano. They were not detected at the scales normally found in areas of intense and active seeps like in the Gulf of Mexico or in the East Mediterranean. This is interpreted as indicating a present day state of low or inactive fluid venting at the seafloor. This is also confirmed by the low to mid range microbial methane turnover and AOM activity in the measured mud volcanoes from the Gulf of Cadiz (Niemann *et al.*, 2006). Gas bubbles and sites of active fluid migration were observed only at two locations in the Mercator mud volcano crater, in areas of highly gas-saturated mud breccia.

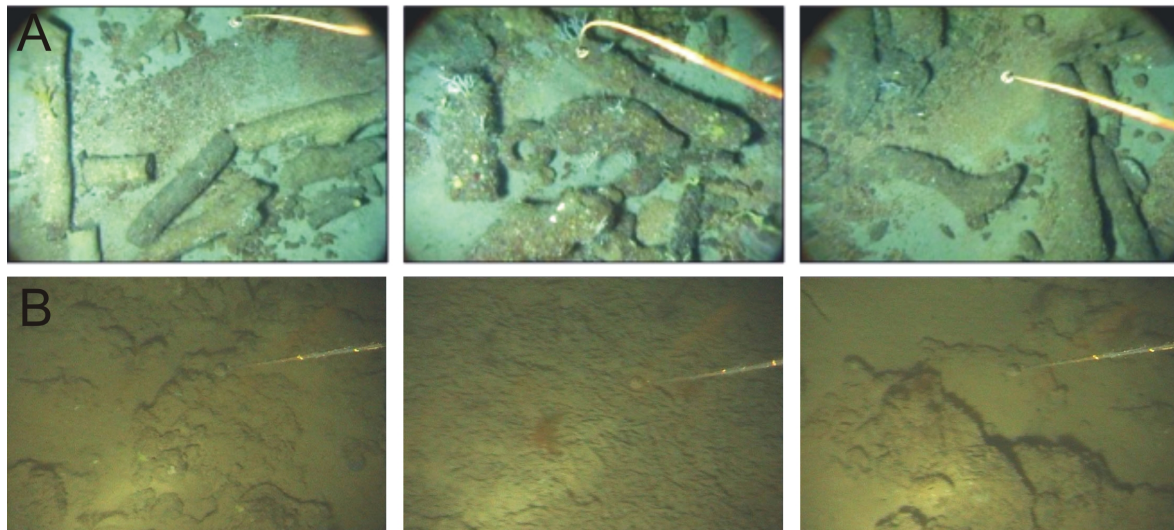


**Figure 5.6.** Bottom photographs taken from the R/V Prof. Logachev underwater video camera from the video profiles: TV AT-18 and TV AT-19 (B) on the Iberico mud diapir; TV AT-20 and TV AT-21 (A) on the MO channel; and TV AT-29 on the Formosa Ridge (C to H) (see location in Figure 5.2). The field of view is approximately 1m for picture A, approximately 2 m for B and approximately 2.5 m for pictures C to H.

**Table 5.1.** Mineralogy, carbonate content and stable isotopic composition of the different defined types of MDAC samples collected in the Gulf of Cadiz. (Complete table of values is given in Appendix B.

Relative percentages (wt%)						Mole Mg(%)				CaCO <sub>3</sub>	CaCO <sub>3</sub> fraction (wt%)					$\delta^{13}\text{C}$	$\delta^{18}\text{O}$
Arag	Calc	Mg-Calc	ProtDol	Dol	Detrital	Calc	Mg-Calc	ProtDol	Dol	(wt%)	Arag	Calc	Mg-Calc	ProtDol	Dol	(VPDB)	(VPDB)
<b>Dolomite Crust (N = 8)</b>																	
-	18	33	-	41	33	3	11	-	46	67	-	30	46	-	60	-29.23	3.89
-	(3-60)	(5-77)	-	(9-88)	(9-56)	(1-5)	(10-11)	-	(44-51)	(44-91)	-	(4-78)	(12-89)	-	(11-100)	(-46.88 to -8.42)	(3.08 to 5.47)
-	6	3	-	8	8	6	3	-	8	8	-	6	3	-	8	7	7
<b>Dolomite Chimney (N = 101)</b>																	
-	12	10	10	52	34	3	14	32	47	66	-	21	15	13	78	-33.41	4.22
-	(1-93)	(1-64)	(5-32)	(2-92)	(5-74)	(1-8)	(8-27)	(30-35)	(41-49)	(26-95)	-	(2-98)	(1-97)	(6-39)	(2-100)	(-45.55 to -14.70)	(0.81 to 6.77)
-	72	43	6	101	101	70	43	6	101	101	-	72	43	6	101	87	87
<b>Nodular or massive dolomite morphology (N = 4)</b>																	
-	31	-	29	47	27	4	-	37	45	73	-	41	-	52	61	-24.01	5.41
-	(7-75)	-	(29-29)	(11-81)	(13-45)	(2-8)	-	(37-37)	(43-46)	(55-87)	-	(8-87)	-	(52-52)	(13-92)	(-24.01 to -24.01)	(5.41 to 5.41)
-	4	-	1	3	4	4	-	1	3	4	-	4	-	1	3	1	1
<b>Aragonite Pavement - Lithified Mud Volcano Mud Breccia (N = 5)</b>																	
57	10	10	-	4	23	4	18	-	52	77	74	13	12	-	4	-24.29	3.92
(49-66)	(4-20)	(6-13)	-	(4-4)	(12-39)	(1-6)	(14-22)	-	(52-52)	(61-88)	(60-83)	(7-25)	(10-16)	-	(4-4)	(-27.56 to -21.70)	(3.17 to 4.34)
5	5	5	-	1	5	5	5	-	1	5	5	5	5	-	1	3	3
<b>Aragonite Pavement - In-situ Breccia (N = 4)</b>																	
70	16	19	-	-	10	3	13	-	-	90	78	17	20	-	-	-16.91	4.71
(57-87)	(4-31)	(19-19)	-	-	(6-14)	(2-5)	(13-13)	-	-	(86-94)	(62-96)	(4-36)	(20-20)	-	-	(-19.10 to -14.25)	(4.03 to 5.18)
4	4	1	-	-	4	4	1	-	-	4	4	4	1	-	-	4	4
<b>Aragonite Pavement - Shell Crust (N = 5)</b>																	
57	11	8	-	2	22	2	17	-	46	77	73	15	11	-	2	-42.23	3.42
(41-76)	(10-12)	(4-13)	-	(2-2)	(6-37)	(1-3)	(9-21)	-	(45-46)	(59-94)	(65-82)	(11-20)	(7-18)	-	(1-3)	(-48.13 to -31.28)	(3.06 to 3.74)
5	5	5	-	1	5	4	5	-	2	5	5	5	5	-	2	3	3

**Table 5.1** (Continuation)

Relative percentages (wt%)						Mole Mg(%)				CaCO <sub>3</sub>	CaCO <sub>3</sub> fraction (wt%)					$\delta^{13}\text{C}$	$\delta^{18}\text{O}$
Arag	Calc	Mg-Calc	ProtDol	Dol	Detrital	Calc	Mg-Calc	ProtDol	Dol	(wt%)	Arag	Calc	Mg-Calc	ProtDol	Dol	(VPDB)	(VPDB)
<b>Aragonite Pavement - Stromatolithic fabric (N = 3)</b>																	
80	7	5	-	-	11	3	18	-	-	89	90	7	6	-	-	-44.50	3.99
(73-85)	(4-10)	(5-5)	-	-	(8-18)	(1-6)	(18-18)	-	-	(82-92)	(89-92)	(4-10)	(6-6)	-	-	(-56.16 to -22.64)	(3.82 to 4.27)
3	3	1	-	-	3	3	1	-	-	3	3	3	1	-	-	3	3
<b>Shell / Corals / Carbonate tube worms casts, attached to the exterior of the samples (N = 6)</b>																	
46	48	77	-	13	11	5	13	-	46	91	49	53	86	-	15	0.09	2.44
(19-91)	(9-96)	(76-77)	-	(13-13)	(4-19)	(2-8)	(13-13)	-	(46-46)	(81-100)	(24-91)	(9-100)	(85-87)	-	(15-15)	(-3.30 to 2.09)	(2.24 to 2.57)
3	5	2	-	1	5	4	2	-	1	6	3	5	2	-	1	4	4
<b>Shells cemented inside the Aragonite Pavement (N = 3)</b>																	
39	19	8	-	18	18	3	17	-	55	82	49	23	10	-	22	-12.11	3.04
(34-46)	(10-25)	(6-9)	-	(9-26)	(14-26)	(1-4)	(15-18)	-	(54-55)	(74-86)	(40-62)	(14-30)	(7-12)	-	(12-30)	(-18.30 to -8.84)	(2.93 to 3.11)
3	3	2	-	3	3	2	2	-	3	3	3	3	2	-	3	3	3

Notes: N = number of studied samples. - = indicate that the mineral was not detected. Lithologic types defined according to the text. Arag = Aragonite. Calc = Calcite (mol Mg % < 8%). Mg-Calc = high Mg-Calcite (8% < mol Mg % < 30%). PrtDol = Protodolomite (30% < mol Mg % < 40%). Dol = Dolomite (40% < mol Mg % < 55%). Detrital = Detrital Fraction (Quartz, feldspar, clays and other minerals that compose the detrital fraction).

The  $\delta^{13}\text{C}$  and  $\delta^{18}\text{O}$  Stable isotopic values are reported in the conventional  $\delta$  ‰-notation with reference to VPDB. For the dolomite-type samples (>20% of dolomite),  $\delta^{18}\text{O}$  values are corrected for the analytical offset of +1.63‰, consequence of the unequal oxygen fractionation during the reaction to CO<sub>2</sub>.

### **5.3.3 Mineralogy, petrography and SEM**

#### **5.3.3.1 Dolomite crusts, chimneys and nodules**

Dolomite crusts, nodular and chimneys consist essentially of medium to tightly carbonate-cemented mudstones, siltstones, wackstones and sandstones (Figure 8.3, Chapter 8). Petrographic and XRD studies show that their mineralogical composition consists of dolomite, protodolomite, high-Mg calcite, calcite, quartz, feldspar and clays (Figure 5.8). The detrital fraction corresponds to a fossiliferous matrix with abundant bioclasts of planktonic foraminifera (globigerinoids), ostracods, pellets and silty terrigenous grains of quartz, calcite, feldspars and clays. Iron and manganese oxy-hydroxides are present in almost all the samples, staining them with a variable brownish colour depending on the degree of oxidation of the sample. On samples with low or no oxidation it is possible to recognize, on thin section and SEM, singular pyrite framboids or small pyrite clusters with oxidation rims of brownish iron oxides that probably contain OH-groups.

The degree of cementation corresponds to an almost complete infilling of the original pore space and therefore, all the different dolomite types show low porosity with absence of mega-porous and scarce fractures or cracks. The contacts between cemented grains are irregular, ranging from complete to inter-grain pore spaces with dimensions, in general, lower than 10  $\mu\text{m}$ , leaving little residual porosity. The cement is composed of micrite to micro-sparite equigranular rhombohedral calcite, high-Mg calcite, protodolomite and dolomite with dimensions of less than 15  $\mu\text{m}$  (Figure 8.4, Chapter 8). The texture varies from isolated rhombohedra and aggregates of interlocking subhedral to euhedral crystals on a tight mosaic of interlocking subhedral crystals. The individual dolomite rhombohedra have diameters in the range of 2-15  $\mu\text{m}$ , sometimes exhibiting serrated crystal faces. The contacts between detrital grains and the cement are dictated by the shape of the detrital grain. The carbonates are not observed dissolving or replacing the detrital grains.

No significant zoning of the individual dolomite crystals, either by petrographic, cathodoluminescence or SEM-EDS was observed. The carbonate cement shows no luminescence in cathodoluminescence observations. Since no textural evidence of calcite replacement by dolomite was observed, dolomite is considered to be primary authigenic micritic cement. Detailed description on the petrography and SEM observation of the dolomite dominated carbonates is presented in Chapter 8, section 8.3.1.1.

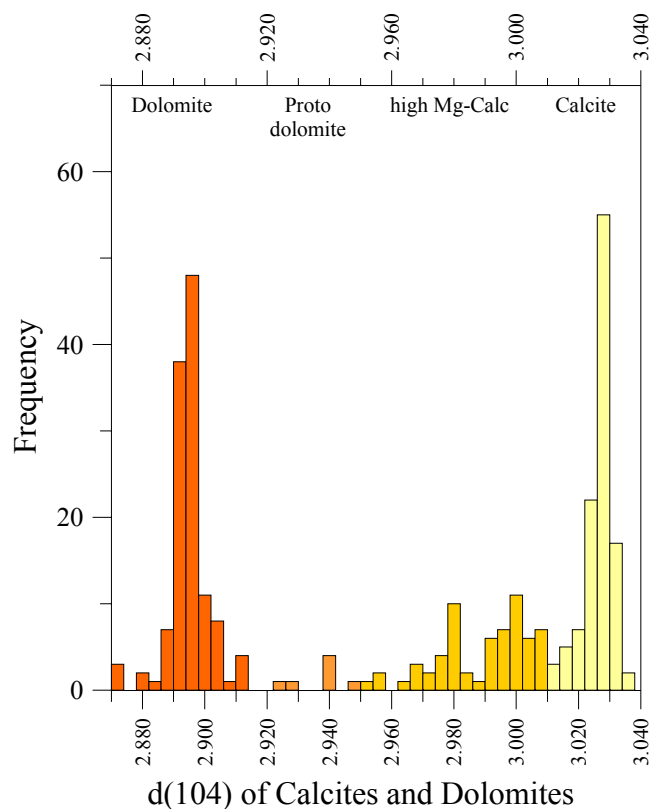


**Figure 5.7.** Frequency histogram of the distribution of the d(104) values for calcites and dolomites of the studied dolomite dominated samples.

After correction of the diffraction peaks of calcite and dolomite in function of the major diffraction peak of quartz, it is possible to recognize that the major diffraction peak of calcite d(104) differs from those of stoichiometric calcite  $d(104) = 3.035 \text{ \AA}$ . This shift can result from the  $\text{Ca}^{2+}$  substitution by  $\text{Mg}^{2+}$  and/or  $\text{Fe}^{2+}$  and  $\text{Mn}^{2+}$  (Goldsmith and Graf, 1958). EDS analyses performed during SEM observations indicate that, in general, only Ca and Mg were detected on the calcite and dolomite minerals. Fe was detected in some samples, representing relative proportions of less than 10% of the total (Ca + Mg + Fe). The Fe is most probably coming from the iron oxides. This is also supported by the cathodoluminescence microscopy observations that do not indicate the presence of significant amounts of Fe or Mn in the carbonate phases. Therefore, the shift of the d(104) dolomite diffraction peak is assumed to result from the Ca/Mg replacement. Estimates of the Mg/Ca ratios are reported in Figure 5.7, based on the Goldsmith and Graf (1958) equation, with a maximum error of 9 mol  $\text{MgCO}_3$  % (Goldsmith and Graf, 1958).

$$\text{Mg}(\text{mol}\%) = (1/0.00298) \times (3.035 - d) \quad (5.1)$$

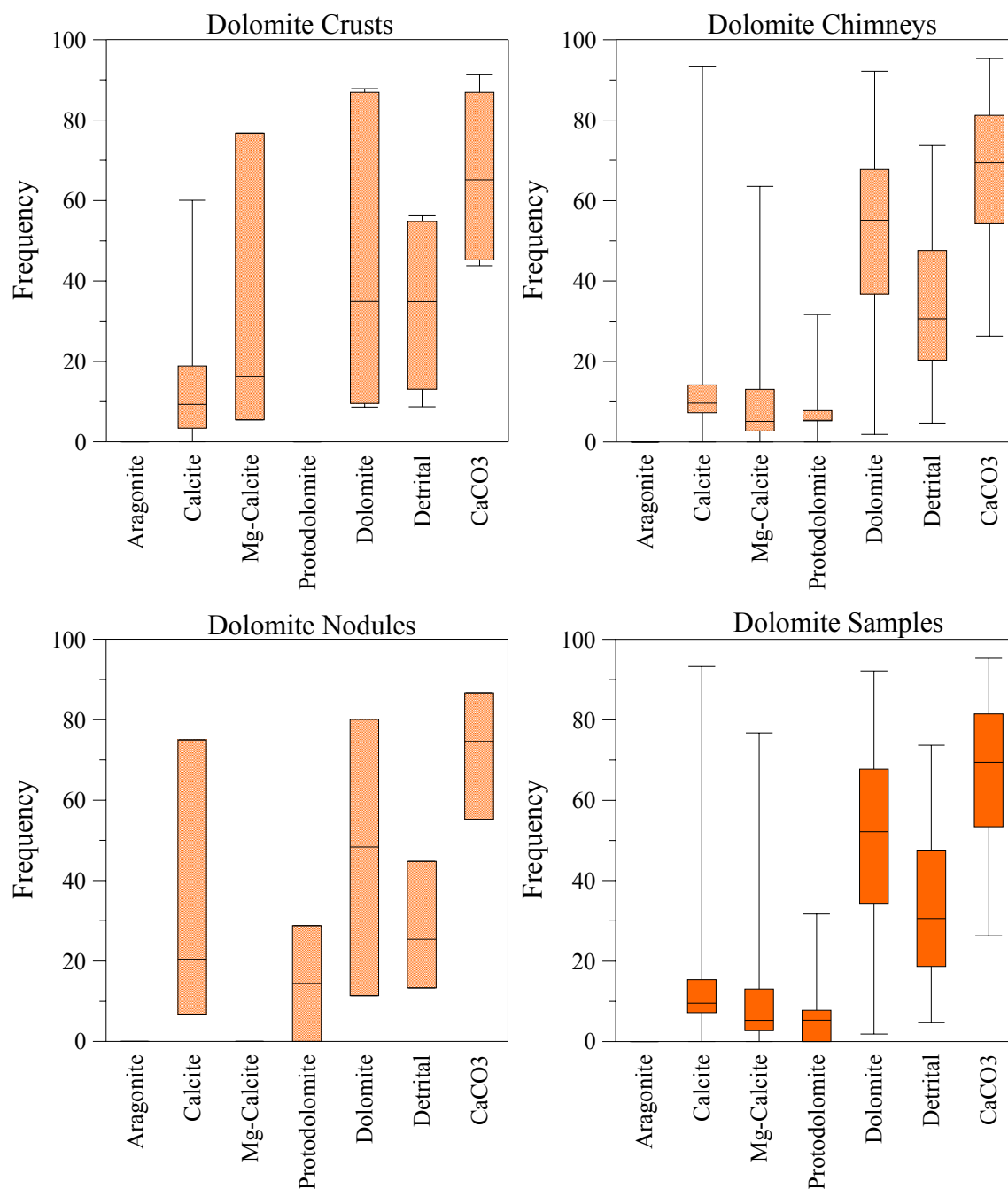


**Figure 5.8.** Box-whisker diagrams of the mineralogical composition and carbonate content of the dolomite dominated samples.

Dolomite is the dominant carbonate mineral with mean values of 60, 78 and 61 wt% on DCr, DChy and Nod, respectively (Figure 5.8). In some crusts and chimneys, dolomite forms the entire carbonate mineral fraction. The dolomite corresponds to fairly constant MgCO<sub>3</sub> content between 45 and 47 mol%. The dolomite content in the sediment collected within the carbonate samples is lower and possibly corresponds, at least partially, to

fragments of carbonate samples incorporated in the surrounding sediments. Sediment samples collected in the vicinity but out of the chimney fields show absence of dolomite. This confirms the petrographic and XRD observations that dolomite is the predominant authigenic mineral in the DCr, DChy and Nod samples. Protodolomite is present on the DChy and Nod samples (up to 32% wt%) with 30 to 37 mol% of  $\text{MgCO}_3$ . Calcite and Mg-calcite are the major constituents with up to 93% wt%. Calcite is the main carbonate mineral in the surrounding sediments and has a tendency to lower magnesium content on their lattice than in the calcite from the MDAC.

The detrital fraction, composed mainly of quartz, feldspars and clays, ranges from 5 to 92% wt% of the MDAC, with average values of 27, 33 and 34% wt% for Nod, DCr and DChy, respectively. In the surrounding sediments the non carbonate fraction corresponds to more than 50% wt% of the sediment.

SEM observations (as described in more detail in Chapter 8) allowed the identification of a high diversity of microbial induced fabrics such as: (1) microbial filaments; (2) high Mg-calcite and dolomitic crystal aggregates that mimetize microbial filaments through calcification, that these aggregates often incorporated in larger dolomite and calcite minerals; (3) carbonate rods with brush-like terminations; (4) carbonates with dumbbell-like and cauliflower structures (Figure 8.8 to 8.13, Chapter 8). Precipitation of similar crystal aggregates have been induced by bacterial activity in laboratory experiments using sulphate-reducing bacteria (Vasconcelos *et al.*, 1995; Warthmann *et al.*, 2000; Van Lith *et al.*, 2003a; Van Lith *et al.*, 2003b). These microbial filaments and structures match the typical size of the microbial filaments and structures observed on SEM, indicating that those are clearly related to the precipitation of the carbonates and do not correspond to any form of contamination. Therefore, and because of their low  $\delta^{13}\text{C}$  values, the structures observed on SEM are interpreted as representing an important involvement of microbial activity in the formation of the authigenic carbonate minerals.

### 5.3.3.2 Aragonite crusts and pavements

The petrography and mineralogy of the different aragonite crusts and pavements have common characteristics. The mineralogy is dominated by aragonite, with subordinate calcite and high Mg-calcite. Aragonite pavement samples are characterized by the absence or by minor amounts of dolomite (less than 4% wt%), identified only on two of the 17

studied samples. On shell fragments collected from a shell crust sample, dolomite was detected by XRD on 3 samples, with values ranging from 9 to 26% wt% (Figure 5.11). Therefore, the detected dolomite on the cement of the aragonite pavement sample can derive from the shells or can have an authigenic origin. Quartz, feldspars and clay minerals compose the detrital minerals of the host sediments, with amounts ranging from 6 to 39% wt% (Figure 5.10). It should be noted that the clastic fraction occurs in lower average amounts on the stromatolitic layers (11% wt%). Aragonite is more abundant in the carbonate samples than in the background sediment (6% wt%), confirming the petrographic observations that aragonite is the major authigenic mineral.

Pyrite was not detected on XRD but it was observed on thin sections and by SEM. Pyrite occurs as individual spheres, framboids and small pyrite clusters forming incipient layers or lineaments. In general, the pyrite is partially to almost completely oxidized to iron oxides and/or hydroxides, that on thin section form brownish rims and stains. The detailed mineralogy of the iron oxides was not determined.

The aragonite pavements and crusts have a higher porosity when compared to the dolomite crusts, chimneys and nodules. The aragonite pavement samples present large macro-porosity due to the large amount of voids, fractures, tubular and irregular cavities, some of them interconnected, but they also have higher inter-granular pore spaces.

On the authigenic cements of the aragonite pavement samples two distinct texture types can be defined (Figure 8.17, Chapter 8): fine grained texture, and stromatolitic fibrous texture. These two textures differ in porosity, mineral content and crystal shape.

The fine grained granular texture (Figure 8.17, Chapter 8) is characteristic of the cement of the lithified mud volcano mud breccias (LMb), of the shell crusts (SCr), of the intraformational breccias (IBr) and of the lithified fragments of dolomite chimneys/crusts (LDChy). This texture is characterized by a complex poly-phase mineralogy of granular and fibrous aragonite, calcite and Mg-calcite crystals. Aragonite is the dominant mineral but the relative proportion on the carbonate fraction is not as high as in the fibrous texture. The detrital components (quartz, feldspars and clays) and siliceous/calcareous microfossils are present here in higher proportions than on the fibrous texture. The fine grained aragonite and calcite ranges from micrite to microspar crystals. The detrital grains and clasts (of mud volcano mud breccia, fragments of dolomite chimneys, clasts of the intraformational breccias or shell fragments) are cemented and inter-grown by fibrous to

granular aragonite, calcite and Mg-calcite, suggesting that the aragonite precipitated within unconsolidated and very weakly compacted sediments. Pyrite is also found in these texture, as individual framboids and small clusters, partially to almost completely oxidized and dispersed on the fine grained mass.

Stromatolitic texture (Figure 5.5F) is representative of the stromatolitic layers (SL), described in section 5.3.1.4.5. It is characterized by up to 1.5 mm long fibrous aragonite needles, typically occurring in layers or radiating aggregates or bundles that recover the pore spaces, cavities and fracture walls in the different aragonite pavements. The stromatolitic texture in general does not completely fill the pore spaces, voids, fractures and tubular cavities. As described in section 5.3.1.4.6 and in Chapter 8, these layers are also characterized by the presence of microbial and mucous biofilms. The mineralogy is dominated by aragonite, with minor amounts of calcite and detrital fraction. Mg-calcite is absent or occurs as minor component. From thin section observation it is possible to recognise that the content of detrital grains in this texture is clearly less important or negligible when compared to the fine grained texture. Pyrite is found, in general, as framboids or small clusters aligned parallel to the stromatolitic layers, partially to almost completely oxidized.

The fibrous texture represents a later stage of authigenic carbonate formation that clearly has grown over the previous fine grained granular texture. It has not been observed any situation where the stromatolitic texture has been overlain by the fine grained granular texture.

SEM observations revealed a high diversity of microbial induced fabrics, such as microbial filaments (Figure 8.23, Chapter 8), microbial and mucous biofilm sheets and threads draped between aragonite needles (Figure 8.26, Chapter 8), aragonite batons, ball-capped batons (0.20-0.70  $\mu\text{m}$ ) and nanograins.

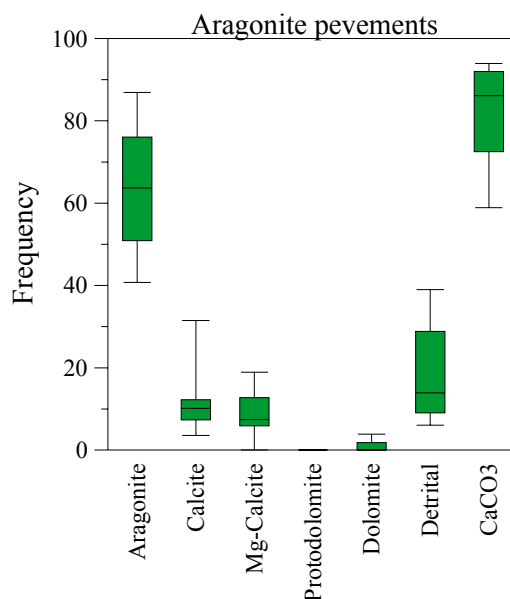


**Figure 5.9.** Box-whisker diagrams of the mineralogical composition and carbonate content of the aragonite dominated samples.

### 5.3.4 CaCO<sub>3</sub> and Total Organic Carbon

The carbonate content of the three dolomite-dominated MDAC lithologic types is very similar, with a mean value of 72% (wt%) and with values ranging from 32 to 93% (wt%). The carbonate content of these lithologic types is significantly higher than the mean CaCO<sub>3</sub> value of the background sediment (~34 wt%, Figure 5.11). Based on these observations, it can be concluded that the MDAC contain, on average, ~38 wt% of authigenic carbonate cement (although this value can reach a maximum of up to 60% wt%).

The carbonate content of the different aragonite crusts and pavements has average values ranging from 77 to 90% wt% (Figure 5.9). These values are significantly higher than the average CaCO<sub>3</sub> values in the background sediment (~30% wt%), indicating that the aragonite crusts and pavements contain 40 to 60% wt% of authigenic carbonate cement.

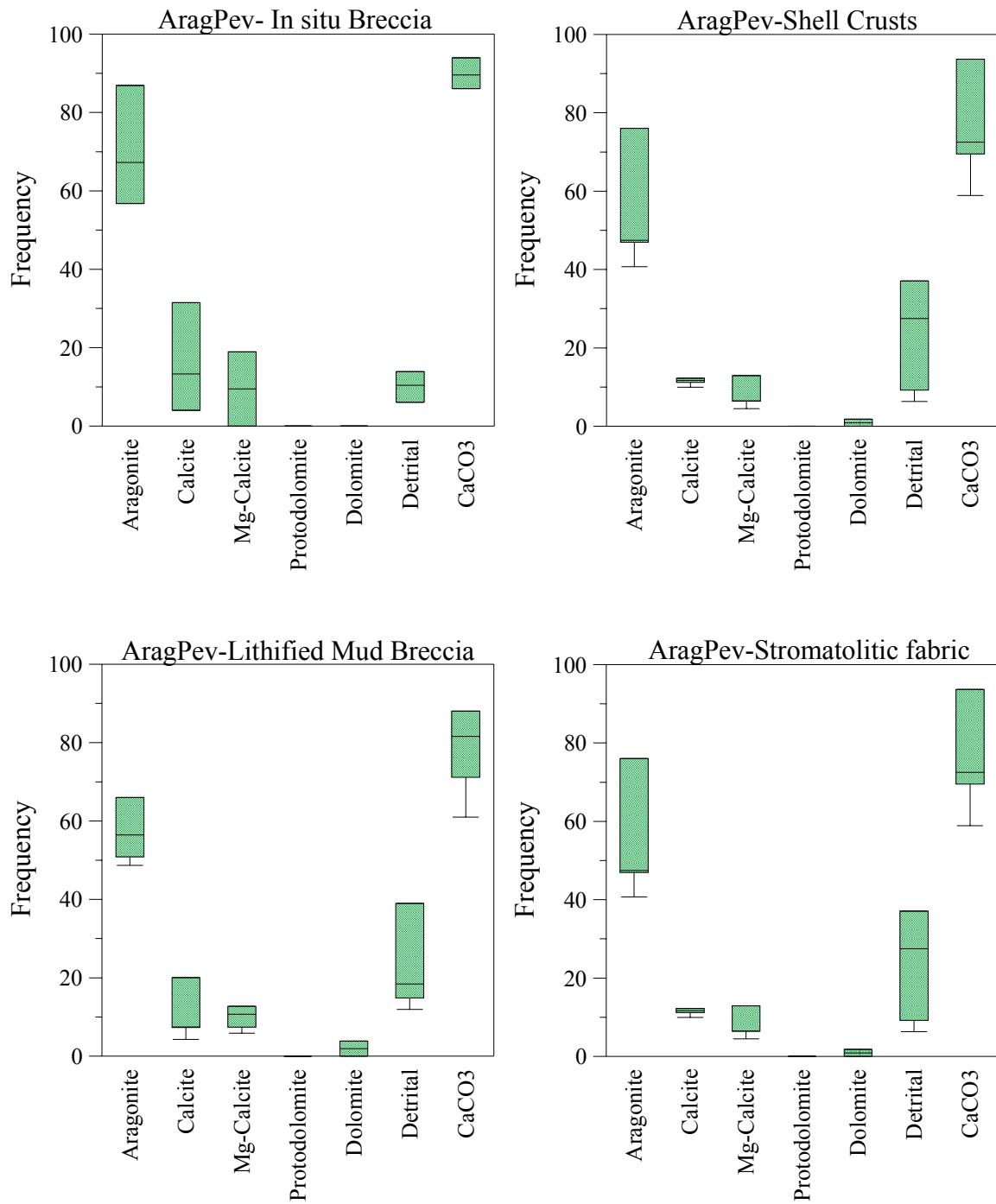


**Figure 5.10.** Box-whisker diagrams of the mineralogical composition and carbonate content of the different types of aragonite dominated samples.

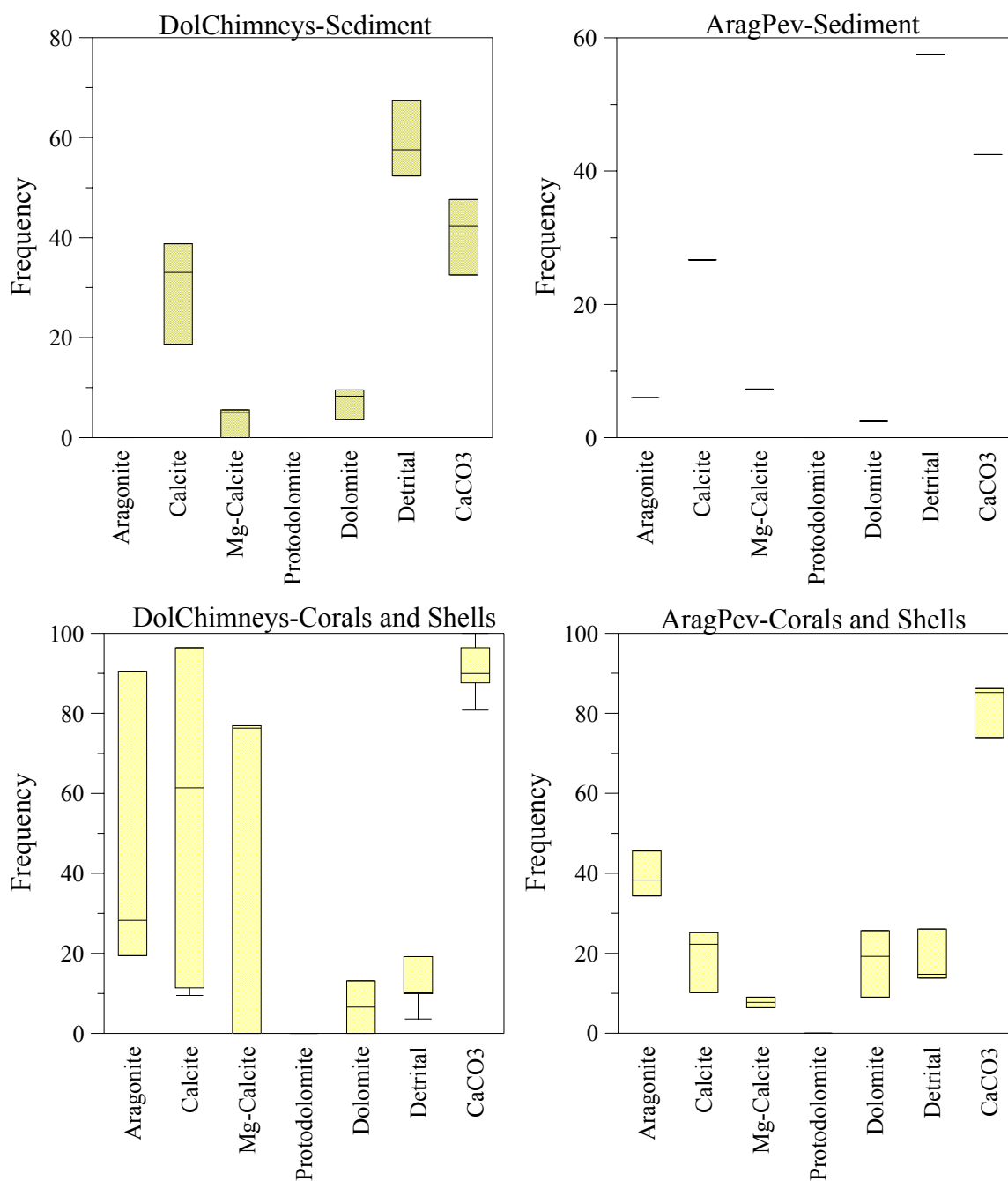


**Figure 5.11.** Box-whisker diagrams of the mineralogical composition and carbonate content of sediment samples collected at the places near the MDAC occurrences and of shells and corals collected from the MDAC.

As regards the organic carbon ( $C_{org}$ ) content of the MDAC samples, it is inferior to 0.4% (dry wt%) with an average value of about 0.1%. These values are lower than those characteristic of the pelagic sediments of the slope and rise of the Gulf of Cadiz, in general

in the range of 0.5% and 1.5% (DGM-INETI MarSed samples database, (Schonfeld, 2001). Pelagic sediments collected at the Iberico dome, where authigenic carbonates were collected, have organic carbon ( $C_{org}$ ) values of 0.88% (wt%). On the Tasyo, Carlos Ribeiro, Olenin and Bonjardim mud volcanoes, the mud volcano mud breccia shows values in the range between 0.12 and 0.96% (dry weight %). This may indicate that during the MDAC formation, part of the organic carbon available on the sediments was consumed.

### 5.3.5 C and O stable isotopes

Carbon and oxygen stable isotopes were measured on 117 bulk samples of dolomite crusts, chimneys, nodules, aragonite pavements and also on bivalve shells. The results of the measurements are presented on Figure 5.12. Carbon isotope results show depleted  $\delta^{13}C$  values between  $-56.2\text{‰}$  and  $-8.4\text{‰}$  VPDB indicating a methane-derived carbon source (Friedman and O'Neil, 1977). Dolomite lithologic types have  $\delta^{13}C$  values between  $-46.9\text{‰}$  and  $-8.4\text{‰}$  VPDB, whereas the aragonite lithologic types have values in the range of  $-56.2\text{‰}$  to  $-14.3\text{‰}$  VPDB. Within the different types of dolomite samples and within the different types of aragonite pavements there is not a significant and distinctive difference in the carbon isotopic composition.

Stable isotopic analyses of oxygen show  $\delta^{18}O$  values varying from  $0.8\text{‰}$  up to  $6.8\text{‰}$  VPDB (Figure 5.12). Dolomite lithologic types present  $\delta^{18}O$  values between  $0.8\text{‰}$  and  $6.8\text{‰}$  VPDB, while values of the aragonite lithologic types range from  $3.1\text{‰}$  to  $5.2\text{‰}$  VPDB and do not show any significant and distinctive variability of values between the different MDAC types.

Samples of biogenic calcite from corals and bivalve shells attached to the surface of dolomite chimneys yielded an  $\delta^{13}C$  average value of  $0.09\text{‰}$  VPDB, and a  $\delta^{18}O$  average value of  $2.44\text{‰}$  VPDB. The isotopic composition of shells collected from the aragonite shell crust type has average values of  $\delta^{13}C$  of  $-12.1\text{‰}$  VPDB and a  $\delta^{18}O$  average value of  $3.0\text{‰}$  VPDB.

Radial and longitudinal profiles of samples along the chimneys present in some cases a clear linear variation that in some other samples seems to be more complex.

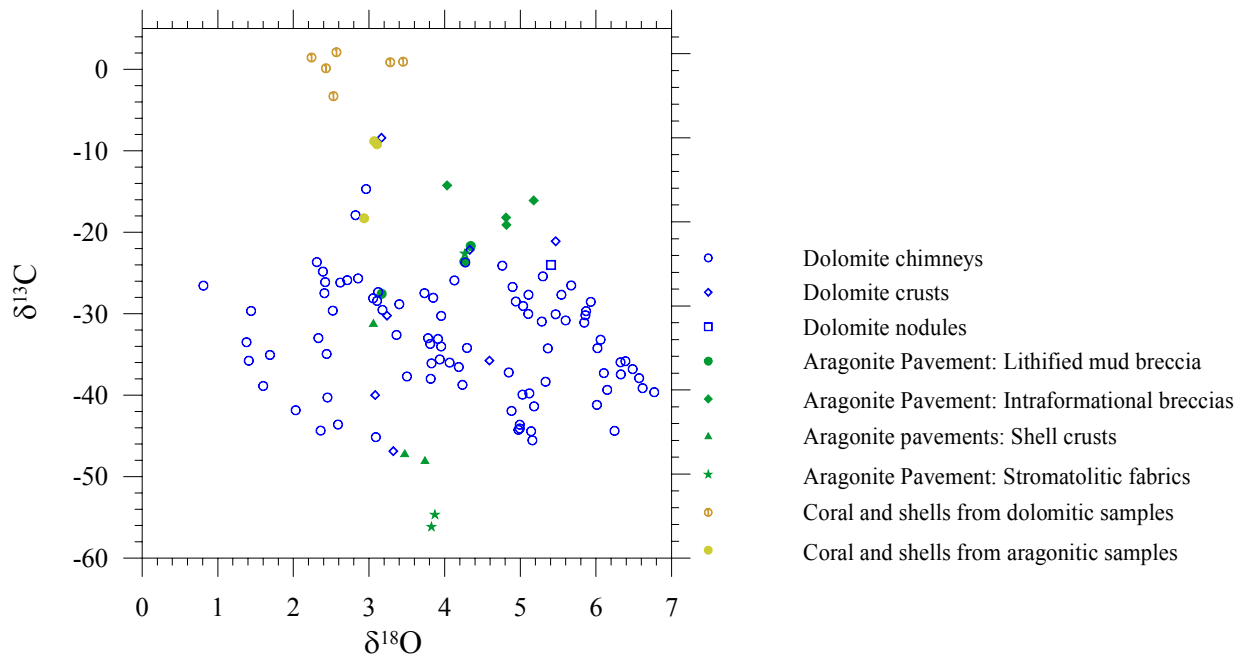


Figure 5.12. Isotopic composition of the authigenic carbonates.

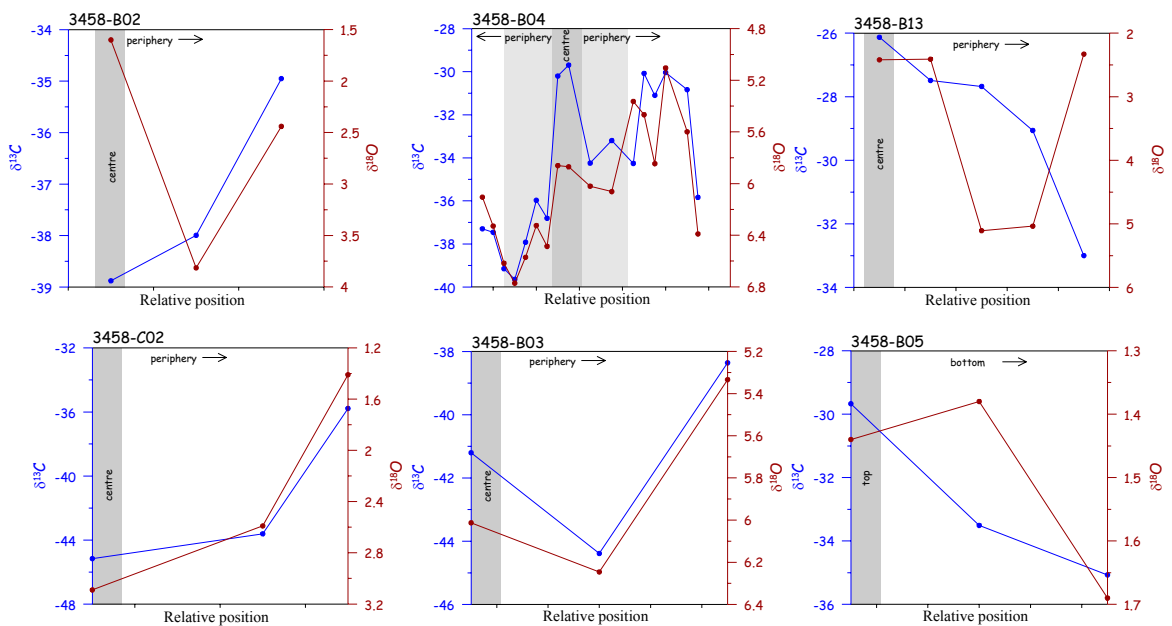


Figure 5.13. Radial and longitudinal profiles along dolomite chimneys.

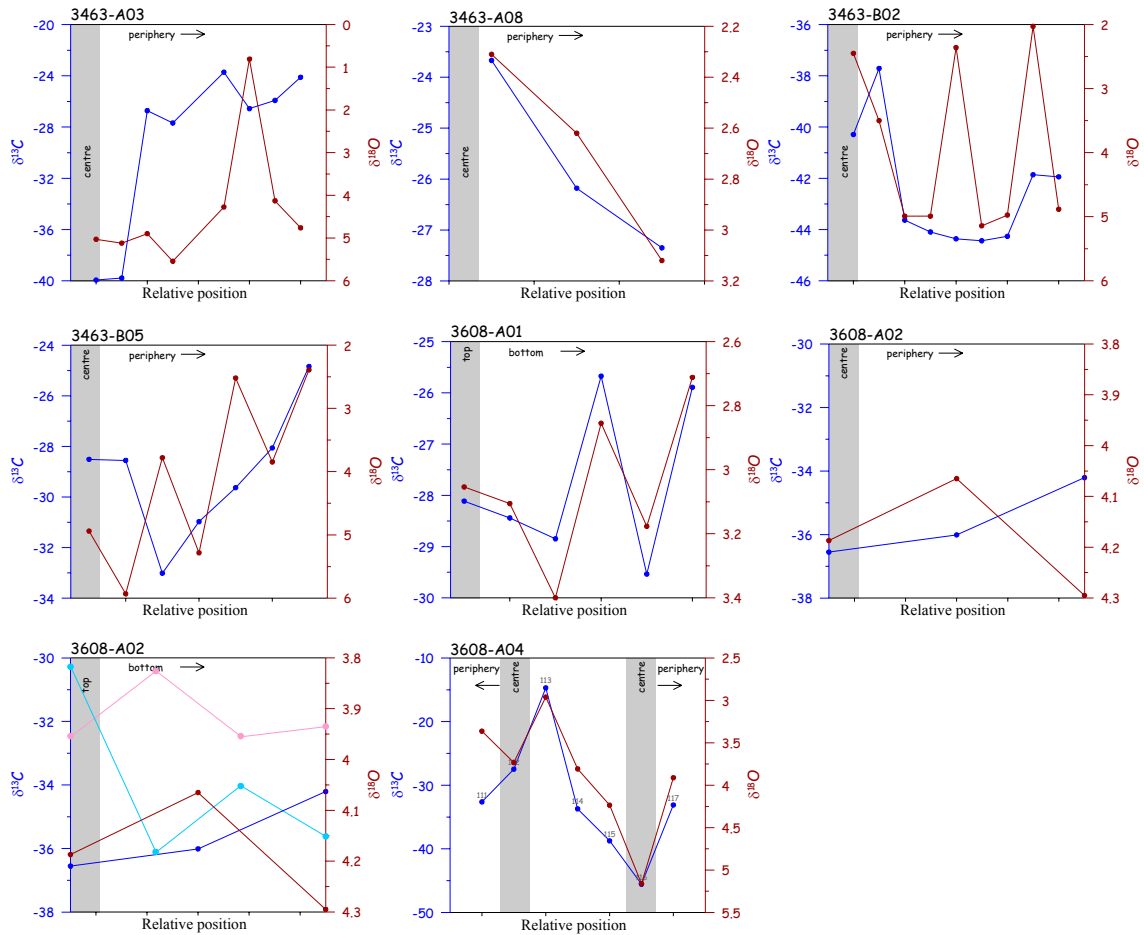


Figure 5.14. Radial and longitudinal profiles along dolomite chimneys.

### 5.3.6 Sr Isotopes and seawater Influence

The strontium isotopic composition of the carbonate minerals reflects the strontium isotopic composition of the water in which they formed (Hess *et al.*, 1986). The variation of the strontium isotopic composition of seawater is well defined (Elderfield, 1986; Farrell *et al.*, 1995). Thus, strontium isotopes can be used to constrain the source of the fluids of authigenic carbonates.

Table 5.2. Strontium isotope values of MDAC samples.

Sample	MDAC type	$^{87}\text{Sr}/^{86}\text{Sr}$	Error (2 $\sigma$ )
3458-A3	Dolomite Crust (DCr)	0.709191	$\pm 0.000060$
3463-A8c	Dolomite chimney (DChy)	0.709110	$\pm 0.000054$
3611-A1	Aragonite pavement (SCr)	0.709183	$\pm 0.000054$

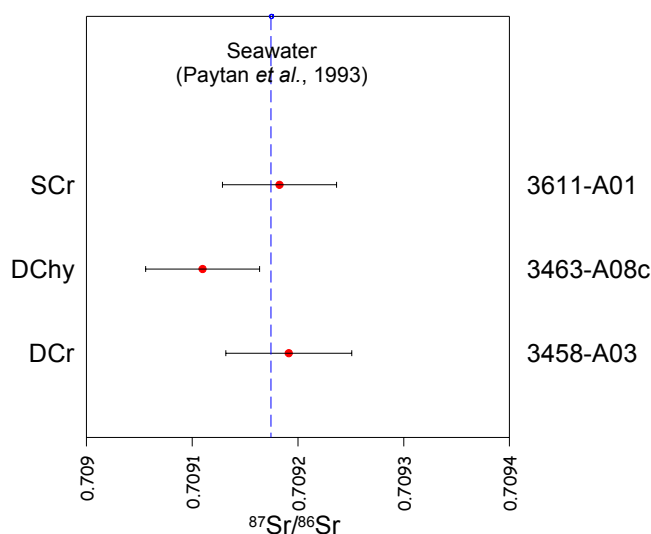


**Figure 5.15.** Strontium isotope values of MDAC samples with reference to the present day seawater strontium isotopic composition (Paytan *et al.*, 1993).

To evaluate the source of the fluids at the cold seeps where MDAC are formed, their strontium isotopic composition should be compared with the  $^{87}\text{Sr}/^{86}\text{Sr}$  values of the pore water in nearby sedimentary sections and with that of the venting fluids and of the pore water from sites of active seepage. Unfortunately this data are not available for the Gulf of Cadiz. The nearest DSDP sites (site 120 situated on the Gorringer Bank, site 135 located at the Horseshoe Abyssal Plain and sites 544-547 at the Moroccan margin) represent different geochemical environment, out of the accretionary complex setting. The available data of pore water  $^{87}\text{Sr}/^{86}\text{Sr}$  ratios, within the Gulf of Cadiz accretionary complex, are from the Bonjardim, Ginsburg and Captain Arutyunov mud volcanoes (MVs), that significantly differ from present day seawater composition, indicate different fluid sources for the different MVs (Hensen *et al.*, in press). Assuming that all the studied MDAC are recent in age (Pleistocene) only nominal variations in the strontium isotopic composition of the authigenic carbonates are to be expected if the carbonates have been formed at or very near the Pleistocene seafloor water. If there is an addition of strontium from deep fluids with different Sr isotopic compositions, as indicated from the analysed MV fluids (Hensen *et al.*, in press) then it is expected that the authigenic carbonates should have Sr isotopic compositions that differ from that of the present day seawater. If the source of Sr captured in the authigenic carbonates was carried by fluids moving upwards along deep faults, then the  $^{87}\text{Sr}/^{86}\text{Sr}$  values should reflect this deeper origin. The  $^{87}\text{Sr}/^{86}\text{Sr}$  ratios for the different

types of carbonate samples (dolomite chimneys and crusts and aragonite pavements) show values between 0.709110 and 0.709191 (Table 5.2 and Figure 5.15). These  $^{87}\text{Sr}/^{86}\text{Sr}$  ratios reflect the isotopic signature of the present day seawater of 0.709175 (Paytan *et al.*, 1993), indicating that all the authigenic carbonates were formed from seawater with Sr values similar to those of the present day seawater. Thus the  $^{87}\text{Sr}/^{86}\text{Sr}$  ratios of the analyses authigenic carbonates do not indicate an addition of Sr from deep-seated fluids.

### 5.3.7 Biomarker analyses

Specific  $^{13}\text{C}$ -depleted lipid biomarkers were identified in dolomitic chimney samples (Figure 5.16). These biomarkers include tail-to-tail linked acyclic isoprenoids such as  $^{13}\text{C}$ -depleted PMI (2,6,10,15,19-pentamethyleicosane;  $\delta^{13}\text{C}$ -values of -117 and -144‰) and squalane (2,6,10,15,19,23-hexamethyltetracosane;  $\delta^{13}\text{C}$ -values of -64 and -98‰). These compounds derive from archaea involved in the anaerobic oxidation of methane (AOM) (Peckmann and Thiel, 2004).

The aragonite crusts show better preserved biomarker patterns in comparison with the dolomite chimneys. PMI ( $\delta^{13}\text{C}$  value: -101‰) are accompanied by unsaturated derivatives with 1 to 3 double bonds (PMI $\Delta$ ; -75‰). Isotopically-depleted PMI represents the most widespread and persistent hydrocarbon biomarker for AOM-performing archaea (Peckmann and Thiel, 2004). Crocetane is present as one of the dominant peaks, strongly depleted in  $^{13}\text{C}$  (-132.27‰). Crocetane:1, the monounsaturated version of crocetane, is also present with a  $^{13}\text{C}$  ratio of -50‰. Squalane is present but not so depleted as in the previous biomarkers.

These results support the SEM observations, that indicate that the precipitation of the MDAC is microbially mediated, and show that Archaea have played an important role in the carbonate authigenesis at methane-seeps in the Gulf of Cadiz.

Lipid biomarker analysis and interpretation is discussed in more detail in Chapter 8.

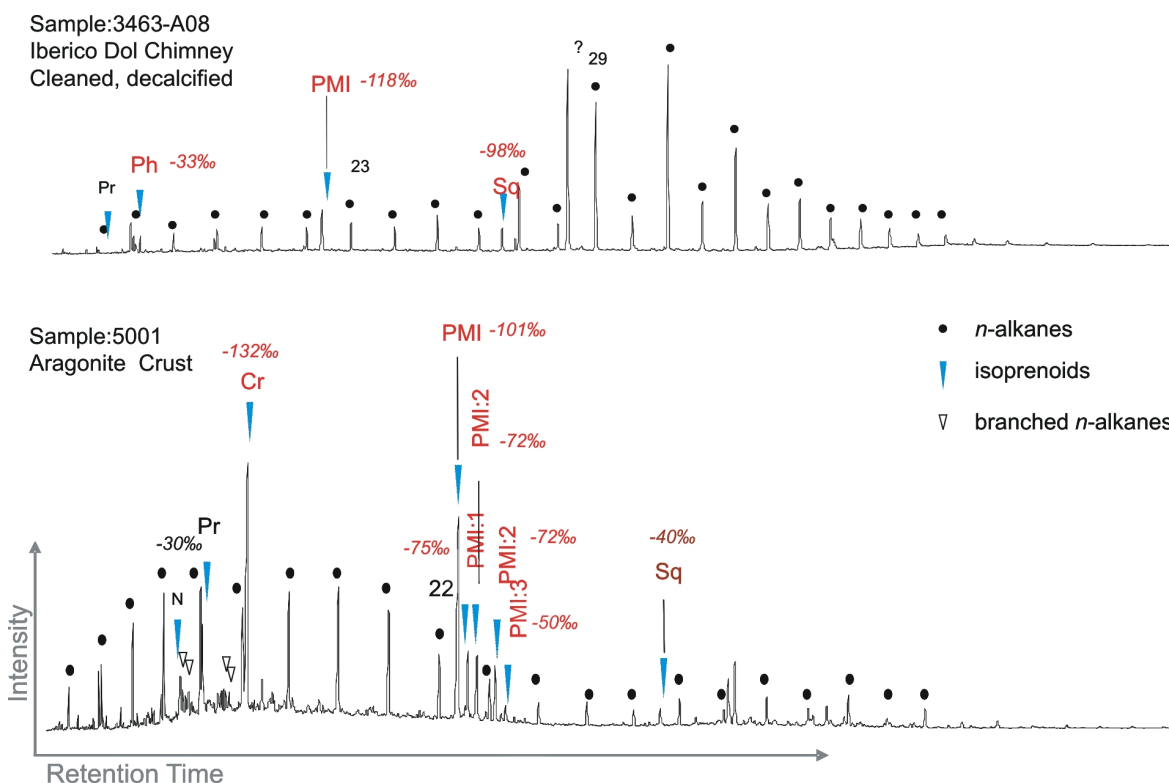


**Figure 5.16.** Hydrocarbon fraction gas chromatograms of a dolomite chimney (on top) and of an aragonite pavement (bottom). Isotope compositions of individual biomarkers are presented in  $\delta^{13}\text{C}$  ‰ relative to PDB.

## 5.4 Discussion

### 5.4.1 MDAC and their relation with MVs and deep faults

The methane rich fluids, regardless of their thermogenic or biogenic origin, must migrate from their site of formation to the seabed where, as indicated by the textural and isotopic composition, the carbonates were precipitated. Diffusive transport of methane under normal vertical compaction and in a region that is not characterized by a high ocean primary productivity neither with high sedimentation rates, is not likely to produce large amounts of light hydrocarbons to induce the precipitation of the authigenic carbonates. The Gulf of Cadiz corresponds to an accretionary wedge subjected to tectonically induced compaction, in addition to the normal gravitational loading (Gutscher *et al.*, 2002; Gutscher, 2004). The Gulf of Cadiz is also characterized by the occurrence of mud volcanoes and mud diapirs that are tectonic controlled by deep structures (Pinheiro *et al.*, in prep.). In these deformed sediments, the large-scale migration of fluids will be, most

probably, conditioned and favoured along the fault zones, dipping permeable beds and along the mud volcanoes and diapir conduits. The result of fluid advection along those discrete pathways will be localized at sites of abnormally high discharge. This is in agreement with the field relationships and with the geological distribution of the occurrences of the authigenic carbonates in the Gulf of Cadiz. The authigenic carbonates occur whether associated with mud volcanoes (Faro, Hesperides, Ginsburg, Mercator, Adamastor, Meknes, and Jesus Baraza), mud diapirs (Iberico, Cornide), fault scarps (Penn Duick escarpment) or along ridges (GDR, Formoza ridge). The occurrences along the Guadalquivir and Cadiz Channels, with the GDR and Formoza ridge, are probably, part of the same tectonic system of trusts that correspond to the N limit of the accretionary wedge (Figure 5.1 and Figure 5.2).

## **5.4.2 Estimation of fluids composition and evolution**

### **5.4.2.1 Estimation of Pore water composition**

The carbon isotopic composition of the authigenic carbonates ( $\delta^{13}\text{C} = -56.16\text{‰}$  to  $-8.42\text{‰}$  PDB, Figure 5.12) indicate that they originated from a moderate to extremely  $^{13}\text{C}$ -depleted reservoir. For isotopic light carbon signature, two principal sources can be considered: (1) decomposition of organic matter, that result in typical pore waters  $\delta^{13}\text{C}$  values of about  $-25\text{‰}$  PDB, and (2) methane ( $\text{CH}_4$ ) and higher hydrocarbons oxidation products (Rosenfeld and Silverman, 1959; Claypool and Kaplan, 1974).

Two potential sources of methane can be considered in the Gulf of Cadiz: thermogenic and biogenic. Typically, biogenic methane formed by  $\text{CO}_2$  reduction or by fermentative decomposition of organic matter by micro-organisms at shallow depths is extremely fractionated in  $^{13}\text{C}$ , typically with  $\delta^{13}\text{C}$ -values between  $-50\text{‰}$  and  $-110\text{‰}$  PDB (Claypool and Kaplan, 1974; Schoell, 1988). Thermogenic methane, in contrast, is isotopic less fractionated ranging from  $-50\text{‰}$  to  $-20\text{‰}$  PDB (Schoell, 1980, 1988).

Results from organic geochemical study of gas saturated mud breccia gravity cores from the Porto, Bonjardim, Captain Arutyunov, and Ginsburg mud volcanoes (MV) show a predominantly thermogenic origin for the hydrocarbon gases (Nuzzo *et al.*, 2005a, b; Stadnitskaia *et al.*, 2006; Hensen *et al.*, in press), but suggest distinctive fluid-generating environments and different secondary processes during transport (e.g., deep hydrocarbon

oxidation and mixing with brines) for the different sectors of the Gulf of Cadiz. For Porto, Bonjardim and Captain Arutyunov MVs the methane generation seems to be associated with deep hydrothermal activity (Hensen *et al.*, in press). While Ginsburg MV and other MVs in the Moroccan margin indicate conventional thermogenic origin. Observed values are: Bonjardim:  $\delta^{13}\text{C-CH}_4 = -47$  to  $-50\text{‰ VPDB}$ ,  $\text{C}_1/\text{C}_{2+} \sim 10$ ; Ginsburg:  $\delta^{13}\text{C-CH}_4 = -40$  to  $-42\text{‰ VPDB}$ ,  $\text{C}_1/\text{C}_{2+} \sim 20$  to  $100$ ; Captain Arutyunov:  $\delta^{13}\text{C-CH}_4 = -42$  to  $-52\text{‰ VPDB}$ ,  $\text{C}_1/\text{C}_{2+} \sim 1000$  (Nuzzo *et al.*, 2005a, b). The gas hydrate composition from the Ginsburg MV has methane to heavier hydrocarbons ratios ( $\text{C}_1/\text{C}_2\text{-C}_6$ ) up to 19% of  $\text{C}_{2+}$  and an inferred source of the gas in the hydrates enriched in  $\text{C}_2\text{-C}_6$  ( $\leq 5\%$ ) indicating a thermogenic origin of the gas (Mazurenko *et al.*, 2002). Therefore, the oxidation of higher hydrocarbons is another potential process that can occur and explain the observed data.

Diagenetic turnover of organic matter, which produces  $\delta^{13}\text{C}$  pore water values of approximately  $-20\text{‰ PDB}$ , is another process that can have an influence on the carbon isotopic signature of the authigenic carbonates. The total organic carbon content ( $\text{C}_{\text{org}}$ ) of pelagic sediments collected at or near the sites where the authigenic carbonates were collected from, shows values up to 0.88% (Figure 5.11). These values are in the range of the normal values of  $\text{C}_{\text{org}}$  reported from this area and represent typical low to moderated organic contents of this low to medium productivity margin (Schonfeld, 2001). As such, the  $\text{C}_{\text{org}}$  content of the pelagic sediments can generate microbial methane but, at the top sediments of the sedimentary column, the input from in situ organic matter oxidation to the pore water total carbon pool is not expected to be major.

Dissolved carbon from normal seawater and  $\text{HCO}_3^-$  derived from dissolution of carbonate tests, both with  $\delta^{13}\text{C}$  values  $\sim 0\text{‰ (PDB)}$  is another potential important source of carbon to the total carbon pool from which the carbonates were precipitated. Given that the strontium isotopic values indicated a seawater origin, it is to be expected that the seawater can also be an important source for the carbon.

The inference of the isotopic composition of the carbon pool from the carbonate mineral isotopic composition is complex, because the mineral composition may reflect mixing from the different carbon sources. Fractionation of the carbon will also depend on the extent to which the different carbon reservoirs are oxidized. However, it is possible to estimate the  $\delta^{13}\text{C}$  composition of the fluids from which the authigenic carbonates were precipitated from. As many samples have  $\delta^{13}\text{C}$  values heavier than biogenic methane,

mixing with other carbon sources is apparently common. The average  $\delta^{13}\text{C}$  values of the authigenic carbonates is very close to the average values of the gas hydrates and pore water gas composition collected from the mud volcanoes, that indicate in general a mixture of biogenic and thermogenic gases. Thus, it is possible to estimate that the authigenic carbonates most probably reflect a similar fluid composition. As such, the isotopic composition of the authigenic carbonates (Figure 5.12) reflects a major mixing of thermogenic and biogenic methane-rich fluids with non-methane carbon sources where most probably, seawater is the most important. A mixing of different proportions of biogenic and thermogenic methane is also to be considered, since this process is also observed on the gas composition of different mud volcanoes.

#### 5.4.2.2 Anaerobic oxidation of methane and carbonate precipitation

$\delta^{13}\text{C}$  values of the authigenic carbonates (Figure 5.12) are typical from carbonates formed at methane vents (Kulm *et al.*, 1986; Hovland *et al.*, 1987; Ritger *et al.*, 1987; Kulm and Suess, 1990; Paull *et al.*, 1992; Bohrmann *et al.*, 1998; Greinert *et al.*, 2001; Peckmann *et al.*, 2001a).

The textural relationship of the authigenic pyrite that is completely surrounded by the carbonate cement indicates that they are syn-genetic. The authigenic pyrite requires that the sediments were below the zone of oxic diagenesis. This implies anaerobic oxidation of methane (AOM) via sulphate reduction (SR) also supported by the biomarker evidence of AOM and SR in dolomite chimneys and in aragonite pavements (Figure 5.16).

During the upward migration the methane rich fluids, probably with minor amounts of reduced carbon-compounds, were anaerobically oxidized (AOM) in the Sulphate Reduction Zone (SRZ), according to the microbially mediated (Boetius *et al.*, 2000) net chemical reaction (Reeburgh, 1980):



AOM increases the alkalinity of the pore fluids and isotopic light methane carbon is converted to bicarbonate and partly controls whether aragonite, Mg-calcite or dolomite carbonates with light carbon isotopic ratio precipitates (Ritger *et al.*, 1987; Paull *et al.*, 1992). Sulphide is another product of coupling AOM + SR and accumulates in

concentrations equivalent to those of sulphate consumption. The sulphide produced will be precipitated as pyrite, dissolved in the seawater and an important amount will be consumed by sulphide-based communities such as *Siboglinum* sp., *Polybrachia* and *Oligograchia* (pogonophora), *Acharax* sp. (solemydae) and *Lucinoma* (Lucinidae) that were collected at the most active sites where authigenic carbonates were collected (Rodrigues and Cunha, 2005).

During the upward fluid migration, if sulphate is available at depth, it will promote methane oxidation and the pore waters which migrated from the zone of methanogenesis towards the seafloor can already contain substantial amounts of methane-derived CO<sub>3</sub> upon arrival at the top of the sediment column. The intense upward migration of methane (as gas or fluid) will move up the SRZ to close or, in extreme fluxes, to the seafloor. At the more active mud volcanoes (Bonjardim, Ginsburg, Gemini and Captain Arutyunov) the SMTZ lies at depths ranging between 20 and 200 cm bellow seafloor (Niemann *et al.*, 2006; Hensen *et al.*, in press). Similar SMTZ depths are characteristic of the more active sites from where authigenic carbonates were collected.

### **5.4.3 Carbonate mineralogy and geochemical environments**

Petrographic estimation of pre-cementation porosities suggests that the carbonate precipitation occurs near or very near the top of the sediment column. Carbonate precipitation and dissolution is influenced by the concentration of the cations Ca<sup>2+</sup> and Mg<sup>2+</sup> (Fe<sup>2+</sup>, Mn<sup>2+</sup>), the complex-forming anions SO<sub>4</sub><sup>2-</sup> and temperature (Burton, 1993; Morse *et al.*, 1997). These factors determine the development of the authigenic carbonates, their mineralogy and their isotopic signature. Hence, the different carbonate lithologies record distinct environments of formation.

Calcium and magnesium occur in sufficient amounts in the pore waters of the uppermost sediments to induce precipitation. The absence of a systematic and deeper pore water samples, and the scarceness of long gravity cores at the more active sites, make it difficult to assess the role of calcium and magnesium in the formation of the authigenic carbonates and to constrain the depth of the more active precipitation zone. The available data (Hensen *et al.*, in press) indicate a wide and variable depth of Ca-Mg depletion, that is

strongly associated with the methane and sulphate gradients. The Ca-Mg profiles seem to reflect the depth of the SMTZ zone.

The mineralogy of the authigenic carbonates is widely variable, and consists of dolomite, protodolomite, Mg-calcite and calcite in the dolomite crusts, nodules and chimneys (Figure 5.7), and aragonite, calcite and Mg-calcite in the aragonite pavements. There is a clear distinction between the two main morphologic types of samples: the dolomite-dominated mineralogy of the crusts, chimneys and nodules, and the aragonite-dominated mineralogy of the pavements. All the methane-derived authigenic carbonates are formed from diagenetic fluids that are, most probably, super-saturated with respect to all the carbonates phases that are found. Therefore the different mineralogies will be determined by the differences in mineral growth rate and the minor differences in the geochemical conditions that will favour one mineralogy in detriment of the other.

#### 5.4.3.1 Dolomite

Magnesium that in seawater is supersaturated for dolomite precipitation forms ion-complex  $\text{MgSO}_4^0$ , even at very low  $\text{SO}_4^{2-}$  concentrations (Baker and Kastner, 1981). Therefore,  $\text{SO}_4^{2-}$  is an effective inhibitor for dolomite precipitation, even at concentrations less than 5% of its value in seawater, which is the ultimate source of  $\text{SO}_4^{2-}$  for marine sediments. At methane seeps, where there is an efficient system of migration of sulphate-deficient and methane-enriched deep fluids, the SMTZ will be pulled upward and, according to equation (5.2), the seawater sulphate will be gradually consumed. As a result, the amount of  $\text{MgSO}_4^0$  decreases and free Mg ion increases, the Mg/Ca ratio increases and dolomite is preferentially precipitated (Baker and Kastner, 1981). According to equation (5.2), AOM also contributes to a higher  $\text{CO}_3$  super-saturation, that favours the incorporation of greater amounts of  $\text{MgCO}_3$  (Mackenzie *et al.*, 1983). In semi-closed systems, such as burrows, and along the methane-rich fluid migration conduits and pathways, the sulphate depletion should reach maximum values and those should be places of preferential dolomite precipitation.

The existence of pyrite provides evidence for an anoxic pore water environment. The presence of pyrite in the non-oxidized dolomite chimneys, dolomite crusts and nodules and its absence in the oxidized samples is not interpreted as lack of pyrite formation during the cementation of the chimneys. It is interpreted instead as the result of pyrite oxidation and

degradation to iron oxy-hydroxides after exhumation of the samples from the sediment. The higher oxidation intensities of the samples will indicate longer periods of permanence at the seafloor. This is also supported by the biomarker analyses that show a better preservation of organic compounds in the samples with lower oxidation intensities.

In conclusion, dolomite precipitation occurs at the sulphate-methane transition zone (SMTZ), preferably within semi-closed systems, such as the fluid conduits. Biomarker and SEM observations indicate that the microbial activity have and important role on the dolomite formation.

#### **5.4.3.2 Aragonite**

Aragonite formation is favoured over calcite in more aerobic environments, with high  $\text{SO}_4^{2-}$  concentrations and high Mg/Ca ratios, like in typical seawater values (Burton, 1993), and at low phosphate concentration and low organic matter oxidation (Burton and Walter, 1990). As such, on a more open system, like in environments very close to the seafloor, aragonite is preferentially formed. The precipitation of aragonite instead of calcite is favoured in seawater, as a result of the inhibiting effect of the hydrated Mg ions on the calcite structure. These environmental conditions should be met at or very close to the seafloor, when more intense and diffuse methane flux will move the SMTZ very close to the seafloor and the seeping methane-charged pore waters will meet bottom waters, and when SR coupled with AOM keep the rates of organic matter oxidation and phosphate production low. Therefore, the aragonite pavement samples that present a mineralogy dominated by aragonite, should have been formed in such a geochemical environment.

#### **5.4.3.3 Calcite and Mg-calcite**

The calcite d(104) values show a poly-modal distribution revealing the existence of different calcite sources: a low Mg-calcite, of biogenic origin, with d(104) values centred around 3.028 Å, and high Mg-calcites with d(104) values centred at 3.000 and 2.980 Å (Figure 5.7).

The high Mg-calcite precipitation will be promoted in environments not so influenciaded by the seawater such as those that promote the aragonite precipitation, and not in closed systems where dolomite is favoured.

#### 5.4.4 Biogeochemistry - the microbial factor

Although the exact biochemical pathway of AOM still remains unclear, molecular, isotopic and phylogenetic evidence revealed that AOM is performed by a consortium of methanotrophic archaea and sulphate-reducing bacteria (SRB) (Peckmann *et al.*, 1999; Boetius *et al.*, 2000; Elvert *et al.*, 2000; Peckmann *et al.*, 2001a; Peckmann *et al.*, 2001b). Therefore, this microbial activity has an active and important role on the definition of the bio-geochemical conditions that will lead to the precipitation of the authigenic carbonates. The presence of the AOM-SR consortium is revealed by the biomarkers present in the authigenic carbonates. These biomarkers have been identified on both aragonite pavements and dolomite chimneys.

In aragonite pavements the identification of microbial and mucous biofilms is frequent, occurring as a coating, draped between the aragonite fibres and needles of the stromatolitic layers. Also, aragonite batons, ball-capped batons and nanograins are observed. This indicates that microbial activity has played an important role in the micro-environmental conditions and most probably also on the formation of the authigenic carbonate minerals (Figure 8.23, Chapter 8).

In the cement of the dolomite crusts, nodules and chimneys, which consists of minor aggregates of rhombohedral calcite, high-Mg calcite and dolomite, up to 15  $\mu\text{m}$  in diameter, SEM observations allowed the identification of a large variety of microbial-induced fabrics, such as: (1) microbial filaments; (2) high Mg-calcite and dolomite crystal aggregates calcifying and mimetizing filaments and flattening themselves against dolomite and calcite minerals; (3) rods with brush-like terminations; (4) dumbbell-like and cauliflower structures (Figure 8.8 to 8.13, Chapter 8). Precipitation of similar crystal aggregates have been induced by bacterial activity in laboratory experiments using sulphate-reducing bacteria (Vasconcelos *et al.*, 1995; Warthmann *et al.*, 2000; Van Lith *et al.*, 2003a; Van Lith *et al.*, 2003b). The observed microbial filaments and structures in these aggregates match the typical size of the described features in the authigenic carbonates and are clearly constructive in origin. The filaments that are covered by the 50 nm to 1  $\mu\text{m}$  size rhombohedra of Mg-calcite or dolomite and that are being incorporated by larger 10-15 $\mu\text{m}$  dolomite rhombohedra, can be interpreted as corresponding to nucleation

points from where the dolomite precipitation started and from which it progressed. So, the organogenic dolomite formation model, proposed for dolomite formation in shallow coastal lagunal and shallow marine environments (Vasconcelos *et al.*, 1995; Vasconcelos and McKenzie, 1997; Wright, 2000; Warthmann *et al.*, 2005), or in organic rich and deep marine sediments (Meister, 2005), is also proposed on the formation of these MDAC. The SEM observations and the biomarker analysis show that microbes are an active key factor involved on the dolomite precipitation. They most probably promote the adequate geochemical conditions, creating optimal micro-environmental conditions, most probably around the microbial structures, from where the precipitation of the MDAC will be initiated.

#### **5.4.5 Formation of the different MDAC lithologies**

##### **5.4.5.1 Isotopic zonation**

The carbon and oxygen isotopic ratios of the dolomite chimneys show a wide but regular pattern (Figure 5.13 and Figure 5.14). Along radial profiles across the chimneys, the carbon isotopic ratios become, in general, heavy towards the periphery and whereas the oxygen isotopic ratios become lighter. This variation suggests temperature and/or pore fluid isotopic composition variations, reflecting the existence of changes in the sources of the fluid venting during the formation of the chimneys. Large chimneys have, in general, lighter carbon isotopic ratios than thinner chimneys.

##### **5.4.5.2 Formation of dolomite crusts, chimneys and nodules**

Considering the underwater video observations, the morphologic, mineralogic and textural characteristics, it is possible to propose that the dolomite chimneys were most probably formed in the sediments below the seafloor and were gradually exposed by the erosion of the surrounding layers of unconsolidated sediments. In Figure 5.17 is represented a schematic model for the formation of the different MDAC. As they lose sustentation they will fall down on the seafloor. The oxidation and the iron and manganese coating, as well as the colonization by the benthic fauna, begin after the chimneys are cropped out. The dolomite chimneys with the more intense oxidation reveal a longer time

of exposure to the seawater and correspond to samples exhumed from shallower depths in the sediment column. In contrast, the dolomite chimneys without or with only weak oxidation signs have a shorter period of exposure to the seawater and correspond to a formation deeper inside the sediment column. The Mediterranean Outflow (MO) appears to have an effective control on the areas of occurrence of the different types of authigenic carbonates. Dolomite crusts, nodules and chimneys occur in places where the MO has a strong erosive effect (Figure 5.2).

If the dolomite chimneys and crusts had formed above the seafloor, by upward growth of carbonates (analogous to the sulphide chimneys on hydrothermal vents) they should contain a very small detrital fraction that should be limited to the fine grained hemipelagic sediments. Moreover, they should not contain a similar detrital composition and a similar fabric to those of the surrounding pelagic sediments.

Based on the morphology, mineralogy, petrography and geochemistry, the dolomite crusts correspond to cemented sedimentary layers while the dolomite chimneys correspond to cemented fluid conduits. The dolomite chimneys are the result of expulsion of methane rich cold seep fluids along pathways of fluid escape formed by (hydraulic) fracturing or along sedimentary discontinuities such as borrows. The large variability of shapes of the chimneys (helicoïdal, parallel and branched) suggests a complex plumbing system and pathways for the fluid percolation. In some situations, the fluid percolates upwards, cutting the sedimentary layers (dolomite chimneys with variable diameter) while in other cases the fluid also percolates horizontally along more permeable layers, tending to form the slab-like crusts and branched chimneys. Some of the chimneys type can also result from horizontal flow along the conduits. When the fluid conduit crosses layers of different permeability (like layers of more sandy material), the penetration of the seeping fluid will increase and the chimney will develop nodules, mushroom-like or even crust like shapes.

The low cement porosity of the dolomite crusts, chimneys and nodular types compared to the aragonite pavements suggest that the cementation took place at a deeper level in the sediment column, most probably at the SMTZ, where AOM coupled with the SR is more intense. The formation of the aragonite pavements, with higher porosity, will most probably occur at the seafloor or very close to the seafloor.

It is proposed that the fluid with  $^{13}\text{C}$  depleted methane migrated laterally through a centred vent hole. Concentric precipitation of authigenic dolomite occurred by mixing of

the fluid penetrating radially outward from the vent hole with the ambient pore water (that the  $^{87}\text{Sr}/^{86}\text{Sr}$  values indicate to be present day seawater) in the surrounding sediments of the SRZ. Therefore, the carbon isotopic ratios of dolomite become progressively heavier with increasing distance from the vent hole. The same explanation applies to the oxygen isotopic ratios, with the heavy oxygen being supplied by the fluid and the lighter oxygen by the pore water fluids. Similarly, the large chimneys present the lightest carbon isotope ratios whereas the thinner chimneys have heavier values. When the cold seep flux is high, the power of the fluid penetration is also stronger and the isotopic dilution effect by the pore water will be weaker, for sediments with the same permeability. Therefore, large chimneys may have been formed with stronger cold seep flux than the thinner chimneys.

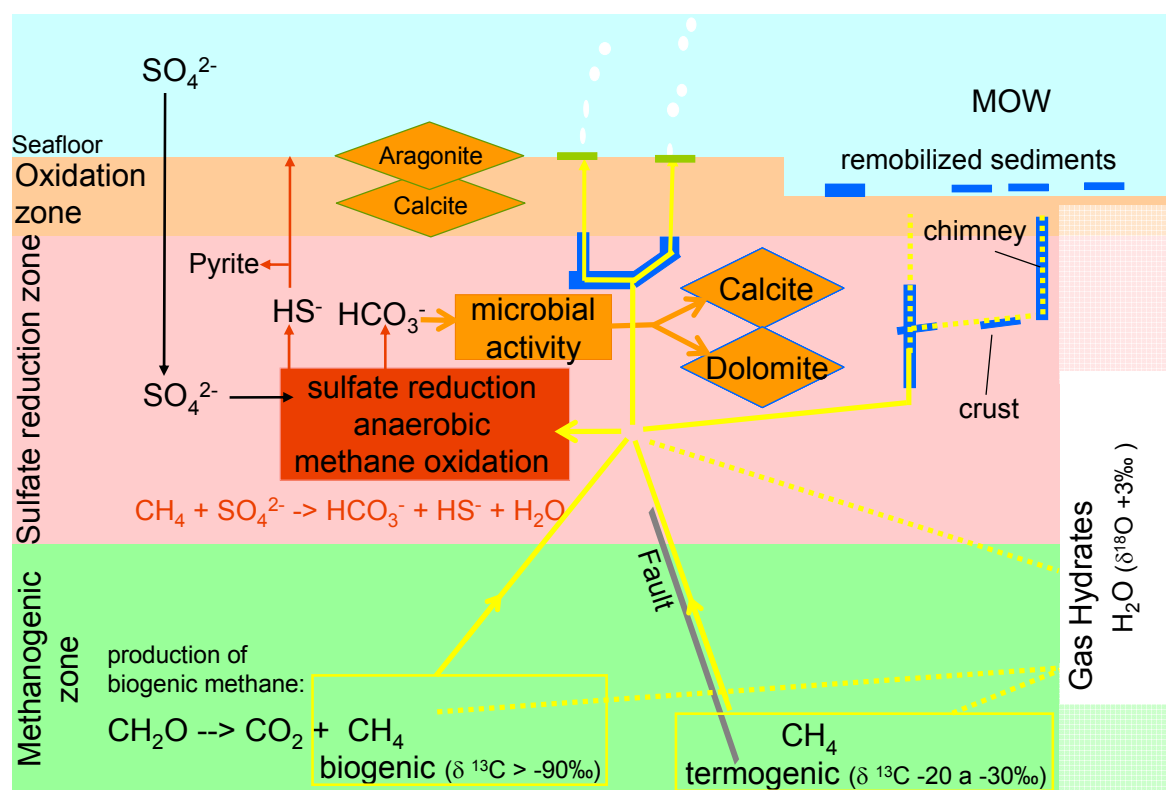


**Figure 5.17.** Proposed schematic model for the formation of the methane-derived authigenic carbonates in the Gulf of Cadiz.

The fluid/pore water penetration is dependent of the permeability of the surrounding sediments. Sediments with low permeability, like clay rich sediments will develop open vent channel chimneys and, in general, show lighter  $\delta^{13}\text{C}$  and heavier  $\delta^{18}\text{O}$ . Sediments with high permeability, such as silty to sandy sediments, in contrast will develop chimneys with closed vent channels and sometimes with concentric growth structures. The different

concentric rings can reflect different episodes of venting with different intensities and different fluid compositions, or mixing fronts between the methane rich fluid and the seawater pore water.

#### 5.4.5.3 Formation of the aragonite pavements

The incorporation of *Calyptogena* sp., *Acharax* sp., open channels of Pogonophora casts and the high porosity of the aragonite pavements indicate a formation near or at the sediment surface. Shell crusts indicate in situ cementation of, most probably, live chemosynthetic communities. Seafloor observations also support this as they show that seep sites are characterized by rough surfaces with crusts and slabs, forming pavements and buildups of cemented sediment. These pavements and buildups in the Gulf of Cadiz are observed associated with mud volcanoes, with the exception of the occurrences associated with the Pen Duick and Vernadski escarpments and in places on MO channels.

Field relationships from seafloor video observations show that they are in general related to methane venting at discrete portions of the mud edifice. They are found in places where fluid escape to the bottom water or to the top sediments, very close to the sediment-seawater interface, occurs or has probably occurred recently. These higher fluxes can fuel methane and sulphide chemosynthetic communities. At these sites, under anoxic but more intensely seawater ventilated environmental conditions, with higher sulphate concentrations, authigenic precipitation is dominated by aragonite and calcite. These can be the environmental conditions where shell crusts, lithified mud breccias (LMB) and intraformational breccias are formed (Figure 5.17).

An alternative hypothesis can be proposed to explain the vast extensions of the aragonite pavements of the LMB type, which does not involve active fluid venting in vast extensions. Both mechanisms are compatible and probably may correspond to different time episodes of the evolution of a seep system. After a mud volcano eruption, mud will be extruded producing flows that cover part or all the crater and eventually flow down the mud volcano flanks as a debris flows. This process produces reduced or insignificant mixing of bottom waters with the freshly emplaced mud breccia methane rich fluid, sulphate and oxygen depleted pore waters. After emplacement of the mud flow, methane oxidation will occur at the sediment-water interface and the oxidation front will progress downward according to the rates of methane flux due to the mud breccia compaction and

the downward diffusion of dissolved  $\text{SO}_4^{2-}$  and  $\text{O}_2$ . This diffusion of  $\text{SO}_4^{2-}$  and  $\text{O}_2$  is controlled not only by the chemical gradients but also by bioturbation and biologic activity. This process can result in the cementation of the mud volcano breccia, forming crust-like shaped LMB that pave extensive areas of mud volcano breccia flows.

The temporal alternation of active fluid venting and pore water methane-enriched mud flow emplacement can explain the breccification texture of the different aragonite pavement types. It can also explain the secondary precipitation episodes that characterize the stromatolitic layers. Gas hydrate formation/destabilization at shallow depths is also a process that is probably involved during high methane flux episodes and that can cause the breccification of the carbonate crusts.

The zonation represented by the different stages of cementation that characterize the formation of the stromatolitic layers can alternatively be caused by precipitation at different depths below the seafloor and/or in different geochemical microenvironments. The extrusive activity of the mud volcanoes can result on a vertical migration of MDAC formed at deeper environments that were brought close to or at the seafloor by mud breccia expulsions. This process can explain the lithified fragments of dolomite chimneys/crusts (LDChy), where dolomite mineralogy formed at confined environments, most probably at depth, at the SMTZ, was brought to the seafloor (by mud volcano activity or by erosion of the unconsolidated soft sediments) and later these fragments were re-cemented at shallow depths close or at the seafloor by aragonite precipitation. So, the LDChy correspond to two distinct time episodes of formation of MDAC in distinct geochemical environments.

The presence of small amounts of dolomite in one aragonite pavement sample can indicate that the sulphate depleted environmental conditions (SMTZ) that promote dolomite formation can be reached at a micro-environment scale conditions within the pore spaces, even in a near surface environment. Considering that the dolomite formation is a process that is mediated by microbial processes, this mediation will not biologically control the precipitation process, but preferentially biologically induce the alteration of the microenvironment surrounding the bacteria cells (Vasconcelos *et al.*, 2005), creating the optimal conditions for dolomite precipitation. These could result in the precipitation of dolomite in restricted microenvironments in an environment that is more propitious to the precipitation of aragonite.

## 5.5 Conclusions

MDAC from the Gulf of Cadiz occur in two main carbonate types: dolomite crusts nodules and chimneys; and aragonite pavements. All dolomite crusts nodules and chimneys are composed of dolomite, protodolomite, high Mg-calcite and calcite, while the pavements are composed of aragonite high Mg-calcite and calcite.

Thermogenic and microbial methane produced by microbial fermentation of organic matter forms methane gas and hydrate layers or nodules under the seafloor, where conditions are adequate. When pressure or temperature change, gas hydrates dissociates realising methane rich fluids with light carbon and heavy oxygen isotopic ratios. This methane reacts with sulphate at the Sulphate-Methane Transition Zone (SMTZ), through a process that is mediated by microbial activity, by a consortium of archaea and sulphate reducing bacteria, as described by Boetius et al. (2000), which is confirmed by the biomarker analyses.

As result of the AOM-SR net reaction (equation 2) the alkalinity is increased with light carbon isotopic ratios, the sulphate is consumed and carbonate precipitation is induced (aragonite, calcite, high-Mg calcite and dolomite). Precipitation of carbonates occurs when bicarbonate-rich, high alkalinity pore fluids become sufficiently enriched in calcium and magnesium ions supplied mainly from seawater, (according to the Sr isotopic composition). The precipitation of the authigenic carbonate minerals induces the lithification of the sediments and it is the mechanism assumed for the formation of the pavements, crusts and chimneys.  $\text{HS}^-$ , a product of this reaction will precipitate as pyrite or, together with methane which has not been completely consumed, will feed chemosynthetic communities at the seafloor, such as *Bathymodiolus* and *Calyptogena*, that are found cemented in the aragonite pavements (Figure 5.17).

The different morphologies and different carbonate types reflect different flow patterns through the sediments. If the flux of fluid enriched in methane is channelled through the SRZ of the sedimentary column, using borrows or sediment heterogeneities as pathways, the SMTZ and the consequently precipitation of the authigenic carbonates will be developed around these fluid conduits. Because this fluid conduits correspond to confined environments in relation to seawater influence, sulphate depletion can be reached and dolomite will be the dominant mineralogy. The lithification of the sediments will result

in the formation of the dolomite nodules, crusts and chimneys (Figure 5.17). As can be observed in the NRL Seamap image (Figure 5.2) The locations where the dolomite chimneys occur are presently swept by the flow of the Mediterranean undercurrent which can remobilize the unconsolidated sediment inside of which the chimneys here probably formed and therefore produce the collapse of the individual chimneys, explaining their present position on the seafloor.

Aragonite pavements represent precipitation of authigenic carbonates in a similar process to that of dolomite morphologies, but in an environment closer to the seafloor interface. The aragonite pavements will be formed at the sediment-seawater interface or close to it, as a product of the AOM-SR coupling process that can result from an active and discrete venting or from an more diffuse and low intensity venting process. Because these processes are more ventilated by seawater where high alkalinity is coupled with high sulphate concentrations, the mineralogy is dominated by aragonite.

The MDAC can be interpreted as a fossil record of extensive methane seepage in this particular area of the Gulf of Cadiz, spatially associated with probable deep fault systems, with mud volcanoes and diapirs, which constitute preferential pathways for fluid migration. They constitute a probably important natural methane sequestration process, on which microbial activity has played an important role on the formation of these MDAC.



## **Chapter 6. Origin, paleo-temperature and composition reconstruction of fluids associated with the formation of MDAC in the Gulf of Cadiz**

### **6.1 Introduction**

Carbon isotopic composition is used in MDAC as a proxy for the source of the bicarbonate ion of the carbonate. If methane oxidation is the main source of the bicarbonate then the  $\delta^{13}\text{C}$  value of the carbonate will be depleted in relation to the normal marine carbonate value (Figure 6.1).

The oxygen isotopic record in marine carbonates represents one of the most important proxies for past oceanographic reconstructions. Variations in the  $\delta^{18}\text{O}$  values of ocean seawater during glacial and interglacial periods are incorporated into the marine carbonates, that also record information of seawater temperature, according to the respective fractionation factors of the different carbonate phases (Friedman and O'Neil, 1977). Therefore, the different mineralogical fractionation effects must be considered in the interpretation of the MDAC isotopic data. In order to estimate the isotopic composition of the original pore waters and the temperature of formation of the MDAC, the isotopic composition has to be corrected for the effects of the different isotopic fractionation for the different mineralogy.

This study is focused on the analyses of the carbon, oxygen and strontium isotopic composition of the MDAC samples recovered from the Gulf of Cadiz. Carbon isotopes are used to constrain the carbon source and the composition of the fluids from which the MDAC were formed from. Oxygen isotopes in aragonite, calcite and dolomite are used to estimate  $\delta^{18}\text{O}$  isotopic composition of the fluids from which the different carbonate phases precipitated from and compared with the present day pore water isotopic composition and with estimated seawater  $\delta^{18}\text{O}$  isotopic composition and temperatures for glacial/interglacial

periods in order to understand the origin and evolution of the pore waters of the studied cold seeps and the geochemical environments in which the different MDAC lithologic types were formed.

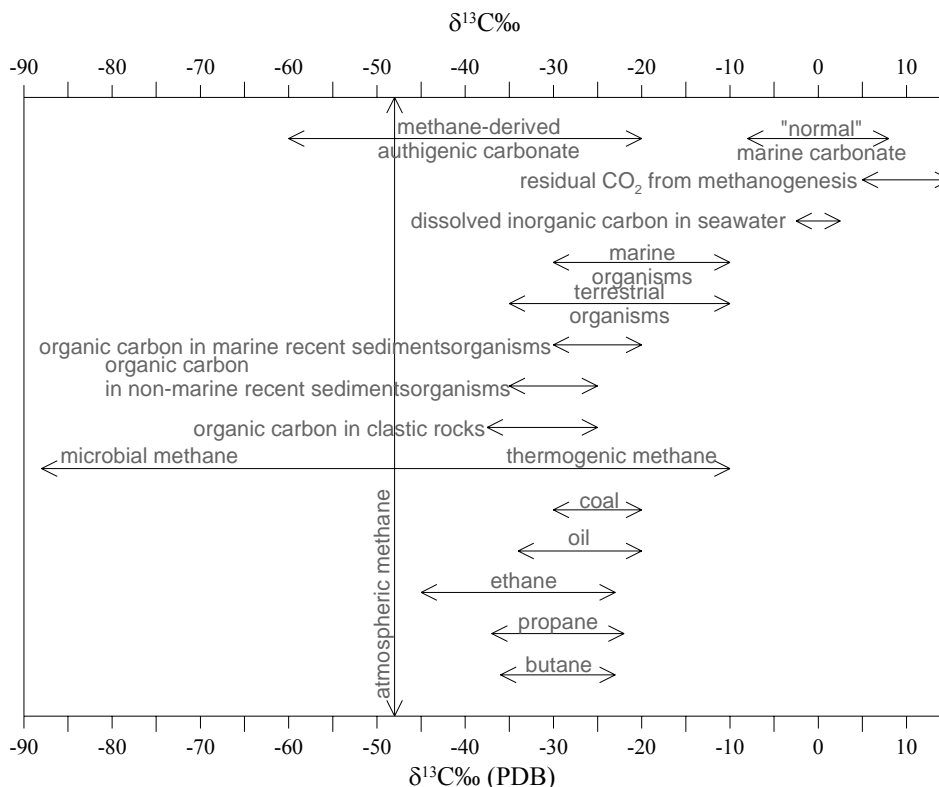


**Figure 6.1.** Carbon isotopic composition of some geologically important materials. Modified from (Hoefs, 1997)

### 6.1.1 Fractionation factor

Isotope fractionation is the partition of isotopes between two substances or two phases of the same substance with different isotope ratios. The main processes responsible for the isotopic fractionation are isotope exchange reactions and kinetic processes (which depend primarily on differences in reaction rates of isotopic molecules). Equilibrium isotope partitioning between minerals and fluids depends on the chemical composition and bond character of the mineral. This is well known for oxygen and carbon isotope fractionation between minerals and aqueous fluids (Kim and O'Neil, 1997).

The fractionation of oxygen and carbon isotopes differs between the different  $\text{CaCO}_3$  polymorphs. As an example, in aragonite,  $^{18}\text{O}$  is enriched by 1.0‰ and  $^{13}\text{C}$  by 1.7‰ relative to calcite (Romanek *et al.*, 1992; Bohm *et al.*, 2000). This is the result of the different vibrational behaviour of the carbonate ions, influenced by the structure of the

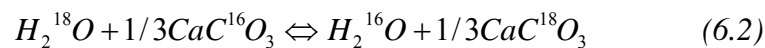
crystal lattice and the atomic coordination numbers. The denser aragonite lattice with its Ca<sup>(9)</sup>O coordination enhances the fractionation of oxygen and carbon compared to calcite Ca<sup>(6)</sup>O coordination. The isotope fractionation effects are mainly caused by thermodynamic (vibrational) behaviour of the C-O bonds in the carbonate ion (CO<sub>3</sub><sup>2-</sup>).

The oxygen isotopic ratio of the carbonates is determined principally by the δ<sup>18</sup>O of the fluid from which the carbonate precipitated, by the temperature of precipitation and by the carbonate mineralogy (each carbonate mineral has a different fractionation factor) (Friedman and O'Neil, 1977).

The fractionation factor (α) between two compounds (A and B) is defined as the ratio of the numbers of any two isotopes in the chemical compound A divided by the corresponding ratio for the other chemical compound B:

$$\alpha_{A-B} = R_A / R_B \quad (6.1)$$

For example, the fractionation factor for the exchange of <sup>18</sup>O and <sup>16</sup>O between water and CaCO<sub>3</sub> is expressed by the reaction:



With the fractionation factor α<sub>CaCO<sub>3</sub>-H<sub>2</sub>O</sub> defined as:

$$\alpha_{CaCO_3} = \frac{(^{18}O/^{16}O)_{CaCO_3}}{(^{18}O/^{16}O)_{H_2O}} \quad (6.3)$$

From theoretical and practical reasons the function 1000lnα is employed to characterize the fractionation factor.

### 6.1.2 The delta value (δ)

In isotope geochemistry the isotopic composition is commonly expressed in terms of δ values. The δ value is defined as the *per mil* proportion of the isotopic ratio measurement of a compound over the isotopic ratio of a standard sample.

In the case of the oxygen isotopes, the δ value is defined as:

$$\delta = \left( \frac{[^{18}O/^{16}O]_{sample}}{[^{18}O/^{16}O]_{standard}} - 1 \right) * 1000 \quad (6.3)$$

### 6.1.3 Oxygen isotopic standards

Two different  $\delta$  scales are generally used for the oxygen isotopes: the  $\delta^{18}\text{O}_{(\text{SMOW})}$  and the  $\delta^{18}\text{O}_{(\text{PDB})}$ , because of the two different categories of users who have been traditionally engaged on O-isotope studies.

The PDB standard is used in low temperature carbonate studies. It is referred to the Cretaceous Belemnite from the Pee Dee Formation in South California and was the laboratory working standard used at the University of Chicago in the early 1950s when the paleo-temperature scale was developed (McCrea, 1950; Epstein *et al.*, 1951, 1953). The original supply of this standard has long been exhausted and secondary standards, whose isotopic composition is considered calibrated to PDB, were introduced (Table 6.1); the new equivalent scale is referred to as the Vienna Pee Dee Belemnite (VPDB).

The Standard Mean Ocean Water (SMOW) scale is generally used for oxygen isotope analyses of non-carbonate phases such as waters, silicates, phosphates, sulphates and high-temperature carbonates. Similarly, the exhaustion of the original standard sample supply introduced the Vienna Standard Mean Ocean Water (VSMOW) scale, which is equivalent to the SMOW. Table 6.1 shows  $\delta^{18}\text{O}$  values for commonly used oxygen isotope standards on both scales.

**Table 6.1.**  $\delta^{18}\text{O}$  values of commonly used O-isotope standards (Hoefs, 1997).

Standard	Material	PDB scale	SMOW scale
NBS-18	Carbonatite	-23.00	(7.20)
NBS-19	Marble	-2.20	(28.64)
NBS-20	Limestone	-4.14	(26.64)
NBS-28	Quartz	(-20.67)	9.60
NBS-30	Biotite	(-25.30)	5.10
GISP	Water	(-53.99)	-24.75
SLAP	Water	(-83.82)	-55.50

*(parentheses denote calculated values)*

The conversion equations between  $\delta^{18}\text{O}_{(\text{SMOW})}$  and  $\delta^{18}\text{O}_{(\text{PDB})}$  and vice versa can be calculated by the Friedman and O'Neil (1977) equations (6.4) and (6.5):

$$\delta^{18}\text{O}_{(PDB)} = 0.97006 * \delta^{18}\text{O}_{(SMOW)} - 29.94 \quad (6.4)$$

$$\delta^{18}\text{O}_{(SMOW)} = 1.03086 * \delta^{18}\text{O}_{(PDB)} + 30.86 \quad (6.5)$$

Or the Coplen *et al.*, (1983) equations (6.6) and (6.7):

$$\delta^{18}\text{O}_{(PDB)} = 0.97002 * \delta^{18}\text{O}_{(SMOW)} - 29.98 \quad (6.6)$$

$$\delta^{18}\text{O}_{(SMOW)} = 1.03091 * \delta^{18}\text{O}_{(PDB)} + 30.91 \quad (6.7)$$

Throughout this work, the conversion from the PDB to the SMOW scale, and vice versa, is done according to the Coplen *et al.*, (1983) equations (6.6) and (6.7).

#### **6.1.4 Temperature equations**

To calculate the equilibrium formation temperatures and to estimate the isotopic composition of the fluids from which the carbonates precipitated from, different temperature equations have to be applied to the different carbonate minerals. The different proposed equations for the different carbonate mineralogy are presented and discussed the ones that best suit for the studied samples.

A compilation of the most significant oxygen isotope fractionation equation for different carbonates, calibrated by laboratory experiments and by analysis of natural samples, are presented in Table 6.2 and discussed in the following sections.

**Table 6.2.** Oxygen isotope fractionation factors for carbonates. Calibrations based on experiments or natural samples. Modified from (Chacko *et al.*, 2001).

#	Phases	Reference	Method	1000 ln $\alpha$	T (°C)	Comments
29	Aragonite/calcite - H <sub>2</sub> O	(McCrea, 1950)	Ex	$\delta^{18}O = 15.7(10^3/T) - 54.2$ (Florida seawater) $\delta^{18}O = 15.7(10^3/T) - 54.2$ (Cape Cod seawater)	-1.2 to 79.8	Slow precipitation by CO <sub>2</sub> degassing.
30	Calcite-H <sub>2</sub> O	(Epstein <i>et al.</i> , 1953)	Mx	$2.73(10^6/T^2) - 2.71$	7-30	Combination of data obtained from biogenic precipitation of calcite in tank experiments and analysis of natural samples. Regression line fit through data given in (Epstein <i>et al.</i> , 1953) after recalculation following the method outlined in (Tarutani <i>et al.</i> , 1969).
	Dolomite-calcite	(Engel <i>et al.</i> , 1958)	N	$\Delta_{\text{dol-calc}} = +5-9\text{‰}$		Based on analysis of co-existing calcite and dolomite in Leadville Limestone (Mississippian, Colorado) and in its hydrothermal and metamorphic phases.
	Dolomite-calcite	(Clayton and Epstein, 1958)	N	$\Delta_{\text{dol-calc}} = +5-9\text{‰}$		calcite and dolomite metamorphic assemblages
	Dolomite-calcite	(Friedman and Hall, 1963)	N	$\Delta_{\text{dol-calc}} = 0-1.8\text{‰}$		low-temperature hydrothermal dolomites. Interbedded limestone and dolomites and calcite-dolomite hydrothermal alteration zones
58	Dolomite-calcite	(Epstein <i>et al.</i> , 1963)	Ex	$\Delta_{\text{dol-calc}} = +0.9$	550	Dolomitization of natural calcite with CaCl <sub>2</sub> soln.
	Dolomite-calcite	(Degens and Epstein, 1964)	N	$\Delta_{\text{dol-calc}} = 0$ to +5-9‰		Holocene Dolomites
48	Dolomite-H <sub>2</sub> O	(Northrop and Clayton, 1966)	Ex	$3.20(10^6/T^2) - 2.00$	300-510	Direct exchange, 3-50% exchange. P=1 kbar.
51 52	CO <sub>2</sub> -calcite CO <sub>2</sub> -dolomite	(O'Neil and Epstein, 1966)	Ex	$1.93(10^6/T^2) + 3.92$ , Cal. $1.31(10^6/T^2) + 3.62$ , Dol.	350-610	Direct Exchange experiments using very large calcite to CO <sub>2</sub> ratio. Measured values may represent surface fractionations rather than true equilibrium fractionations. P=0.3 bars.
59	Dolomite-calcite	(Northrop and Clayton, 1966)	Ex	$0.50(10^6/T^2)$	300-510	Combination of dolomite-H <sub>2</sub> O experiments of Northrop and Clayton (1966) and calcite-H <sub>2</sub> O experiment of O'Neil (1963).
60	Dolomite-calcite	(O'Neil and Epstein, 1966)	Ex	$0.56(10^6/T^2) + 0.45$	350-610	Combination of CO <sub>2</sub> -calcite and CO <sub>2</sub> -dolomite experiments.
47	Dolomite-H <sub>2</sub> O	(Clayton <i>et al.</i> , 1968)	N	+34.5	20 ±5	Based on sedimentary dolomite from Deep Springs Lake, California.
31	Calcite-H <sub>2</sub> O	(O'Neil <i>et al.</i> , 1969)	Ex	$2.78(10^6/T^2) - 2.89$ Corrected in (Friedman and O'Neil, 1977)	0-500	0-25°C experiments involving controlled precipitation of carbonate minerals from bicarbonate solutions, P=1 atm. 200-500°C experiments involved exchange between carbonate minerals and ammonium chloride solutions, P=1kbar. 100% exchange in all experiments.

Table 2. Continued

#	Phases	Reference	Method	1000 ln $\alpha$	T (°C)	Comments
56	Aragonite/calcite/ Mg-calcite – H <sub>2</sub> O	(Tarutani <i>et al.</i> , 1969)	Ex	0.6 (aragonite-calcite)	0-25	Combination of data from experiments in which calcite or aragonite were slowly precipitated from aqueous bicarbonate solutions. Effect of polymorphism and Mg substitution on the Oxygen isotope fractionation.
50	Protodolomite- H <sub>2</sub> O	(Fritz and Smith, 1970)	Ex	+23.4 to +31.6 3.2(10 <sup>6</sup> /T <sup>2</sup> )-2.0	25- 78.6	Precipitated from a Ca-Mg-CO <sub>3</sub> soln. The equation is based on extrapolation to the 25°C datum of Clayton <i>et al.</i> , (1968).
61	Dolomite-calcite	(Sheppard and Schwarcz, 1970)	N	0.45(10 <sup>6</sup> /T <sup>2</sup> )-0.40	100- 650	Based on analysis of co-existing calcite and dolomite pairs in regionally metamorphosed marbles and calcareous schists. Temperatures derived from calcite-dolomite solvus thermometry.
31	Calcite-H <sub>2</sub> O	(Clayton <i>et al.</i> , 1975)	Ex	1.22-1.33(500°C) 0.01-0.10(700°C)	500, 700	Pressure effects investigated to 20 kbars in pure water.
	Mg-calcite	(Friedman and O'Neil, 1977)	Ex	$2.78(10^6/T^2) - 2.89 + 0.06 * Mol\%MgCO_3$		Oxygen isotope fractionation as function of temperature and the Mg mol% content in calcite.
49	Dolomite-H <sub>2</sub> O	(Matthews and Katz, 1977)	Ex	3.06(10 <sup>6</sup> /T <sup>2</sup> )-3.24	252- 295	Hydrothermal dolomitization of calcite or aragonite in the presence of Ca-Mg-Sr chloride solutions. P=1 atm.
	Protodolomite- H <sub>2</sub> O	(Irwin, 1980)	E	$T = 31.9 - 5.56(\delta^{18}O_{dolomite} - \delta^{18}O_{SMOW}) + 0.17(\delta^{18}O_{dolomite} - \delta^{18}O)$		Calculated based on the experimental data for the precipitation of protodolomite of Fritz and Smith (1970).
	Dolomite-calcite	(McKenzie, 1981)	N	$\Delta_{dol-calc} = 3.5\text{‰}$	~35° C	Modern calcite and dolomite formation in a sabkha environment.
57	Aragonite/calcite – H <sub>2</sub> O	(Grossman and Ku, 1986)	N	0.76-0.017T(°C)	0-25	Based on the analysis of aragonitic foraminifer <i>Hogelundia</i> and coexisting calcitic foraminifer <i>Uvigerina</i> . Large scatter about the regression line indicates that the apparent temperature dependence is not statistically significant.
	Aragonite – H <sub>2</sub> O	(Hudson and Anderson, 1989)	N	$t = 19.7 - 4.34(\delta^{18}O_{arag(PDB)} - \delta^{18}O_{w(SMOW)})$		Hudson and Anderson (1989) modified the Grossman and Ku equation to the $\delta^{18}O$ notation of the water in the SMOW scale, according to the Friedman and O'Neil (1977) equations
53	CO <sub>2</sub> -calcite	(Chacko <i>et al.</i> , 1991)	Ex	-0.038435+5.0077x -1.0703x <sup>2</sup> +0.15452x <sup>3</sup> -0.014366x <sup>4</sup> +0.00073624x <sup>5</sup> -0.000015567x <sup>6</sup> , where x=10 <sup>6</sup> /T <sup>2</sup>	400- 800	Direct exchange. 39-94% exchange. P=10 kbar. Equation represents theoretical calculations that closely fit the experimental data. The equation reproduces the calculated fractionations from 273-4000 K.
54	CO <sub>2</sub> -calcite	(Scheele and Hoefs, 1992)	Ex	5.92 – 2.31	500- 1200	Aragonite starting material inverted to calcite during the experiment. No equation given but fractionations generally larger than those given by Chacko <i>et al.</i> , (1991) by ~0.5‰.

Table 2. Continued

#	Phases	Reference	Method	1000 ln $\alpha$	T (°C)	Comments
	Aragonite – H <sub>2</sub> O	(Patterson <i>et al.</i> , 1993)	N	$18.56(1000/T_{(K)}) - 33.49$		Based on aragonite otoliths from freshwater fish that lived in waters of known temperature and isotopic composition.
55	CO <sub>2</sub> -calcite	(Rosenbaum, 1994)	Ex	3.30	900	Direct exchange. 97% exchange. P=12.5 kbar.
37	Calcite-H <sub>2</sub> O	(Kim and O'Neil, 1997)	Ex	$18.03(10^3/T) - 32.42$	10-40	Low-T controlled precipitation experiments.
	Aragonite – H <sub>2</sub> O	(Bohm <i>et al.</i> , 2000)	N	$18.45(1000/T_{(K)}) - 32.54$	3 to 28°C	Based on aragonitic sponge skeletons ( <i>Ceratoporella nicholsoni</i> ), molluscs and foraminifera from well constrained ambient seawater composition and temperature.
	Dolomite – H <sub>2</sub> O	(Vasconcelos <i>et al.</i> , 2005)	E	$2.73(10^6/T^2) + 0.26$	25, 30, 40 and 45°C	Experiments under anaerobic conditions with pure microbial stain of sulphate-reducing bacteria ( <i>Desulfovibrio</i> stain LV form1) and precipitated dolomite in a synthetic growth medium solution at 25, 30, 40 and 45°C
Notes: Ex = experimental; N = natural sample; Mx = mixed experimental and natural sample calibration; T in the equations in Kelvin and t in °C, unless otherwise indicated.						

#### 6.1.4.1 Calcite and Mg-Calcite

The temperature dependence of the oxygen isotopes fractionation during calcite precipitation was investigated since the pioneering theoretical and experimental work by McCrea (1950). Using two different seawaters, McCrea (1950) inorganically precipitated calcium carbonate by CO<sub>2</sub> degassing at a temperature (T) range from -1.2°C to 79.8°C, and obtained two different equations (6.8 and 6.9) describing the relationship between the isotopic composition of the calcite with the isotopic composition of the water and the temperature of formation.

$$\delta^{18}\text{O} = 15.7(10^3/T) - 54.2 \quad (\text{for Florida seawater}) \quad (6.8)$$

$$\delta^{18}\text{O} = 16.4(10^3/T) - 57.6 \quad (\text{for Cape Cod seawater}) \quad (6.9)$$

Epstein *et al.*, (1951; 1953) combining experimental data from foraminifera calcite precipitation and analysis of natural samples collected from known seawater-temperature environments, defined a new oxygen isotopic temperature fractionation equation (6.10 and 6.11). Epstein *et al.*, (1953) also proposed the use of the oxygen isotopes for paleo-temperature calculations and his oxygen isotope paleotemperature scale has been widely used in paleoceanography and paleoclimatology.

$$1000 \ln \alpha = 2.73(10^6/T^2) - 2.71 \quad (6.10)$$

$$\delta^{18}\text{O}_{\text{Cc(PDB)}} = e^{\left(\frac{2.73(10^6/T^2(K)) - 2.71}{1000}\right)} \times (1000 + \delta^{18}\text{O}_{\text{w(PDB)}}) - 1000 \quad (6.11)$$

$$t_{(^\circ\text{C})} = 16.5 - 4.3(\delta^{18}\text{O}_{\text{calc(PDB)}} - \delta^{18}\text{O}_{\text{w(SMOW)}}) + 0.14(\delta^{18}\text{O}_{\text{calc(PDB)}} - \delta^{18}\text{O}_{\text{w(SMOW)}})^2 \quad (6.12)$$

The temperature coefficient for CaCO<sub>3</sub>-water fractionation of Epstein *et al.*, (1953) is in agreement with one of the equations of McCrea (1950) and with their results. They both conclude that, at low temperatures (0-20°C), there is significant <sup>18</sup>O/<sup>16</sup>O fractionation, of up to a few *per mil*, between the different alkaline earth carbonate phases.

Several questions have been raised concerning the Epstein *et al.*, (1953) method. Among the most important are: the validity of the original calibrations; the influence on the equilibrium fractionation factor of the different CaCO<sub>3</sub> polymorphic phases; the chemical variability of biogenic shells or of the carbonate cements; the kinetic effects of both biological (vital effects) and chemical origin; the reliability of acid fractionation factors; and the recognition of the sometimes important diagenetic processes that alter the original isotopic composition.

O'Neil *et al.*, (1969) addressed some of these questions during their laboratory experiments of inorganic precipitation of alkaline-earth carbonates at high (200-500°C) and low temperatures (0-25°C) and calculated the fractionation equation (6.13):

$$1000 \ln \alpha = 2.78(10^6/T^2) - 2.89 \quad (6.13)$$

O'Neil *et al.*, (1969) identified differences of the isotopic fractionation with variable divalent cationic content on the carbonate phases. This dependence was quantified for the first time by Tarutani *et al.*, (1969), based on synthetic carbonate precipitation of calcite, aragonite and Mg-calcite from various bicarbonate solutions. The quantification of the effect of the MgCO<sub>3</sub> content in calcite on the oxygen isotopic fractionation has shown that, at 25°C, for each mol% of MgCO<sub>3</sub> the 1000ln $\alpha$  increases by 0.06‰ in relation to pure calcite (Tarutani *et al.*, 1969). Simultaneously, aragonite shows a small but significant <sup>18</sup>O enrichment of 0.6‰ in relation to calcite at 25°C (Tarutani *et al.*, 1969).

Friedman and O'Neil (1977) established the equation of the oxygen isotope fractionation as a function of temperature and the Mg mol% content in calcite:

$$1000 \ln \alpha = 2.78(10^6/T^2) - 2.89 + 0.06 * \text{Mol}\% \text{MgCO}_3 \quad (6.14)$$

$$\delta^{18}\text{O}_{\text{Cc}(PDB)} = e^{\left( \frac{2.78(10^6/T^2(K)) - 2.89 + 0.06 * \text{Mol}\% \text{MgCO}_3}{1000} \right)} \times (1000 + \delta^{18}\text{O}_{\text{w}(PDB)}) - 1000 \quad (6.15)$$

Kim and O'Neil (1997) proposed the equations (6.16 and 6.17) for calcite-water fractionation in inorganic precipitation over a low-temperature range (10-40°C):

$$1000 \ln \alpha = 18.03(10^3/T) - 32.42 \quad (6.16)$$

$$\delta^{18}\text{O}_{\text{Cc}(PDB)} = e^{\left( \frac{18.03(10^3/T(K)) - 32.42}{1000} \right)} \times (1000 + \delta^{18}\text{O}_{\text{w}(PDB)}) - 1000 \quad (6.17)$$

Several equations have also been proposed to calculate equilibrium fractionation for several specific biogenic calcitic and aragonitic species. Essentially, these equations are based and similar to those from Kim and O'Neil (1997) and Friedman and O'Neil (1977), showing different species-dependent vital effects contributions to the oxygen fractionation factors. As an example is the following equation by (Shackleton and Kennett, 1975a, b; Wefer and Berger, 1991):

$$t_{(eC)} = 16.9 - 4.38(\delta^{18}\text{O}_{\text{calc}(PDB)} - \delta^{18}\text{O}_{\text{w}(SMOW)}) + 0.10(\delta^{18}\text{O}_{\text{calc}(PDB)} - \delta^{18}\text{O}_{\text{w}(SMOW)})^2 \quad (6.18)$$

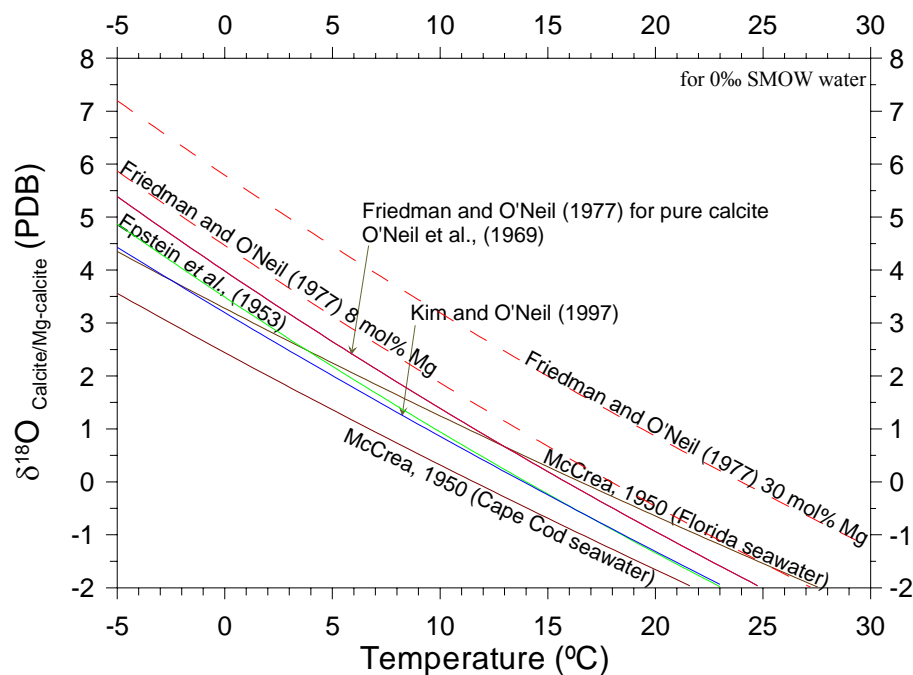


**Figure 6.2.**  $^{18}\text{O}$ -fractionation equations defined for calcite and Mg-calcite.

From all the different temperature oxygen fractionation equations for calcite, throughout this work, the Kim and O'Neil (1997) equation is used as the fractionation equation because it is considered to best represent the fractionation equation for calcite mineralogy, as it was defined for inorganic calcite and has been used successfully in a large range of paleo-temperature calculations in calcites from a large range of settings, including in cold seep carbonates. As can be observed from Figure 6.2, this equation curve corresponds to an average position in relationship to the several different equations defined for calcite. For Mg-calcite, the Friedman and O'Neil (1977) equation will be used, as the oxygen isotope fractionation as a function of temperature and the Mg mol% content in Mg-calcite. This equation is considered to best represent the fractionation equation for Mg-calcite mineralogy, as it has been used successfully in a large range of paleo-temperature calculations in Mg-calcites from a large range of settings, including in cold seep carbonates.

#### 6.1.4.2 Protodolomite and Dolomite

The failure to precipitate dolomite in the laboratory at low temperatures (Land, 1998) has not allowed the direct determination of the temperature-dependent oxygen isotopic fractionation factor between low temperature dolomite and the solution from which it

precipitates. In order to constrain this limitation indirect approaches have been employed. One approach consists in using natural coexisting calcite and dolomite. Assuming the precipitation in equilibrium from the same water and at the same temperature, the difference between the  $\delta^{18}\text{O}$  values of both minerals ( $\Delta^{18}\text{O}_{\text{dol-cal}}$ ) should be constant. As the calcite-water fractionation factor is known and the  $\Delta^{18}\text{O}_{\text{dol-cal}}$  values can be measured, the dolomite-water fractionation factor can therefore be indirectly calculated. Another approach consists on the extrapolation of the dolomite-water oxygen isotope fractionation determined from the high-temperature experiments to low-temperatures.

Isotopic studies of calcite and dolomite metamorphic assemblages predicted an equilibrium  $^{18}\text{O}$  enrichment in dolomite relative to calcite of 5-9‰ (Clayton and Epstein, 1958; Engel *et al.*, 1958; Sheppard and Schwarcz, 1970).

$$1000 \ln \alpha = 0.45(10^6/T^2) - 0.40 \quad (6.19) \quad (\text{Sheppard and Schwarcz, 1970})$$

Investigations by Clayton *et al.*, (1968) have shown that dolomite is strongly enriched in  $^{18}\text{O}$ , from 5 to 7‰ relative to calcite, and defined the dolomite fractionation equation (6.20) as:

$$1000 \ln \alpha = 3.2(10^6/T^2) - 2.0 \quad (6.20)$$

$$\delta^{18}\text{O}_{\text{Dol(PDB)}} = e^{\left(\frac{3.2(10^6/T^2(K)) - 2.0}{1000}\right)} \times (1000 + \delta^{18}\text{O}_{\text{w(PDB)}}) - 1000 \quad (6.21)$$

$$\delta^{18}\text{O}_{\text{w}} = \left( \frac{(1000 + \delta^{18}\text{O}_{\text{Dol(PDB)})}}{e^{\left(\frac{3.2(10^6/T^2(K)) - 2.0}{1000}\right)}} \right) - 1000 \quad (6.22)$$

The extrapolation of the laboratory determined isotope equilibrium of high-temperature dolomite experiments, to low-temperature (25°C) dolomite, indicates that dolomite in equilibrium with calcite would be enriched in  $^{18}\text{O}$  by 4-7‰ (Epstein *et al.*, 1963; Northrop and Clayton, 1966; O'Neil and Epstein, 1966).

$$1000 \ln \alpha = 0.56(10^6/T^2) + 0.45 \quad (6.23) \quad (\text{Epstein *et al.*, 1953})$$

Lower-temperature experimental work (25-78.6°C) by Fritz and Smith (1970) updated the results of Tarutani (1969) to higher contents of  $\text{MgCO}_3$ , and inferred that protodolomite should exhibit a fractionation factor that would lead to a  $^{18}\text{O}$  enrichment of dolomite between 2‰ and 4‰ relative to calcite.

From experimental data of precipitation of protodolomite by Fritz and Smith (1970),

Irwin (1980) calculated the fractionation equation (6.24) between protodolomite and water as a function of temperature.

$$t(^{\circ}\text{C}) = 31.9 - 5.55(\delta^{18}\text{O}_{\text{Proto}(PDB)} - \delta^{18}\text{O}_{\text{w}(SMOW)}) + 0.17(\delta^{18}\text{O}_{\text{Proto}(PDB)} - \delta^{18}\text{O}_{\text{w}(SMOW)})^2 \quad (6.24)$$

$$\delta^{18}\text{O}_{\text{w}(SMOW)} = \sqrt{\left(\frac{5.55 - 0.34 * \delta^{18}\text{O}_{\text{Proto}(PDB)}}{0.34}\right)^2 - \frac{31.9 - t - 5.55 * \delta^{18}\text{O}_{\text{Proto}(PDB)} + 0.17 * \delta^{18}\text{O}_{\text{Proto}(PDB)}^2}{0.17} - \frac{5.55 - 0.34 * \delta^{18}\text{O}_{\text{Proto}(PDB)}}{0.34}} \quad (6.25)$$

Holocene dolomites (Degens and Epstein, 1964) and low-temperature hydrothermal dolomites (Friedman and Hall, 1963) have very similar fractionation factors for dolomite and for coexisting calcites.

A study of modern calcite and dolomite formation in a sabkha environment with a temperature of  $\sim 35^{\circ}\text{C}$ , gave an equilibrium fractionation factor of 3.2‰ (McKenzie, 1981).

The extrapolation to the low-temperature dolomite-water oxygen isotope fractionation from the high-temperature experiments (Northrop and Clayton, 1966) has lead to the empirical equation (6.26).

$$1000 \ln \alpha = 3.20(10^6/T^2) - 2.0 \quad (6.26)$$

Matthews and Katz (1977) experimental oxygen isotope fractionation (6.27), measured during hydrothermal dolomitization of  $\text{CaCO}_3$  at a temperature range from  $252^{\circ}\text{C}$  to  $295^{\circ}\text{C}$ , indicated however a lower dolomite-water fractionation than the Northrop and Clayton (1966) calibration.

$$1000 \ln \alpha = 3.06(10^6/T^2) - 3.24 \quad (6.27)$$

In summary, the results of the various isotopic studies of calcite-dolomite pairs have indicated a wide range of the interpreted  $\Delta^{18}\text{O}_{\text{dol-cal}}$  values, ranging from  $\sim 0\text{‰}$  to  $9\text{‰}$ . The inconsistencies in these results, make it difficult to satisfactory characterize the environmental conditions of dolomite precipitation from its oxygen isotopic composition. The inconsistencies in the  $\Delta^{18}\text{O}_{\text{dol-cal}}$  values have been discussed and referred to by Land (1998) as the “ $\Delta$  problem.”

More recently, geomicrobiological research has introduced the microbial factor (Vasconcelos and McKenzie, 1997) to the complex and large number of interacting factors, such as thermodynamics, chemical kinetics, hydrology, host-rock mineralogy and texture (Hardie, 1987), that intervene in the process of dolomite formation. With the discovery of bacterial-mediated processes that induced the precipitation of dolomite at low temperatures (Vasconcelos, 1994; Vasconcelos *et al.*, 1995; Vasconcelos and McKenzie, 1997; Warthmann *et al.*, 2000), it become finally possible to calibrate the dolomite-water oxygen

isotope fractionation factor (Vasconcelos *et al.*, 2005). Experiments under anaerobic conditions with pure microbial stain of sulphate-reducing bacteria (*Desulfovibrio* stain LV form1) allowed the precipitation of dolomite in a synthetic growth medium solution at 25, 30, 40 and 45°C. These experiments allowed the calculation of the oxygen isotope fractionation equation (6.28), as a function of temperature (Vasconcelos *et al.*, 2005):

$$1000 \ln \alpha = 2.73(10^6/T^2) + 0.26 \quad (6.28)$$

During the microbial-mediated process of dolomite precipitation at low temperature it is assumed that dolomite precipitates in equilibrium with the solution and that the bacteria have a passive involvement in this process, with no vital effect on the precipitation itself and not affecting the isotopic composition. This assumption is corroborated by observations that indicate that the precipitation is not biologically controlled, but simply biologically induced by the alteration of the microenvironment surrounding the bacteria cells (Vasconcelos *et al.*, 2005).

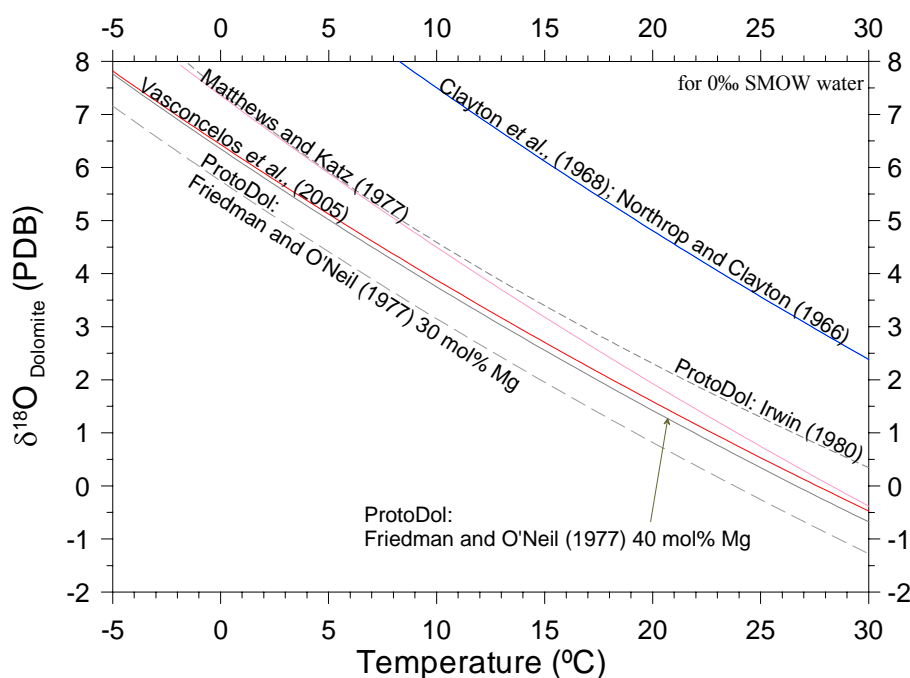


**Figure 6.3.**  $^{18}\text{O}$ -fractionation equations for dolomite and proto-dolomite.

From all the different temperature oxygen fractionation equations, the Vasconcelos *et al.*, (2005) equation is used in this work as the dolomite fractionation equation. This is the only equation experimentally calibrated for low temperatures, and the microbial induced precipitation process used for the calibration is the process considered to be involved on

the formation of the MDAC samples, as discussed in this study (Magalhães *et al.*, in preparation and Chapter 5).

### 6.1.4.3 Aragonite

In contrast to the investigations of inorganic precipitation of calcite and other types of carbonate phases, the oxygen isotopic fractionation during the formation of aragonite is frequently deduced from biogenic-produced material from corals, sponges, molluscs and foraminifers. Aragonite presents a heavier oxygen isotopic fractionation when compared to calcite (Kim and O'Neil, 1997).

The relation between the  $\delta^{18}\text{O}$  of aragonite ( $\delta^{18}\text{O}_c$  in ‰ PDB), the  $\delta^{18}\text{O}_w$  of the ambient water ( $\delta^{18}\text{O}_w$  in ‰ SMOW) and the temperature of precipitation ( $t$  in °C) has been calculated by Grossman and Ku (1986), through the equation:

$$t = 20.6 - 4.34(\delta^{18}\text{O}_{arag} - \delta^{18}\text{O}_w) \quad (6.28)$$

$$\delta^{18}\text{O}_{arag} = \frac{20.6 - t + 4.34\delta^{18}\text{O}_w}{4.34} \quad (6.29)$$

This equation was defined based on isotopic analyses on live and modern species of aragonitic foraminifera, gastropods and acaphopods at the 2.6–22.0°C ambient temperature range. Grossman and Ku (1986) observed that the aragonitic foraminifera *Hoeglundina elegans* was, on average,  $0.2 \pm 0.2\%$  depleted in  $^{18}\text{O}$  relative to the aragonitic molluscs. Comparing the aragonitic foraminifera species with the calcitic foraminifera *Uvigerina*, *Hoeglundina* was  $0.6 \pm 0.3\%$  enriched. This enrichment in  $^{18}\text{O}$  of aragonite relative to calcite is similar to that observed in previous experimental and theoretical studies.

Hudson and Anderson (1989) modified the Grossman and Ku equation into the  $\delta^{18}\text{O}$  notation of the water in the SMOW scale, according to the Friedman and O'Neil (1977) equations (6.4) and (6.5). As such, the Hudson and Anderson (1989), with temperature in °C, is:

$$t = 19.7 - 4.34(\delta^{18}\text{O}_{arag(PDB)} - \delta^{18}\text{O}_{w(SMOW)}) \quad (6.30)$$

$$\delta^{18}\text{O}_{arag(PDB)} = \frac{19.7 - t + 4.34\delta^{18}\text{O}_{w(SMOW)}}{4.34} \quad (6.31)$$

Patterson *et al.*, (1993) defined an aragonite equation on basis of aragonite otoliths from freshwater fish that live in waters of known temperature and isotopic composition.

They show a small difference (approximated 0.2‰) for the low-temperature calcite equation from Friedman and O'Neil (1977). (Temperature in K):

$$1000 \ln \alpha = 18.56(1000/T_{(K)}) - 33.49 \quad (6.32)$$

$$\delta^{18}\text{O}_{\text{arag}(PDB)} = e^{\left(\frac{18.56(1000/T_{(K)})-33.49}{1000}\right)} \times (1000 + \delta^{18}\text{O}_{w(PDB)}) - 1000 \quad (6.33)$$

Bohm *et al.*, (2000) based on aragonitic sponge skeletons (*Ceratoporella nicholsoni*) that precipitate a basal skeleton in oxygen and carbon isotopic equilibrium with ambient seawater, and combining it with temperature and cold water equilibrium values from molluscs and foraminifera, established a well constrained temperature equation for the aragonite precipitation very close to isotopic equilibrium, for a temperature range between 3 and 28°C.

$$1000 \ln \alpha_{\text{arag}} = 18.45(1000/T_{(K)}) - 32.54 \quad (6.34)$$

$$\delta^{18}\text{O}_{\text{arag}(PDB)} = e^{\left(\frac{18.45(1000/T_{(K)})-32.54}{1000}\right)} \times (1000 + \delta^{18}\text{O}_{w(PDB)}) - 1000 \quad (6.35)$$

$$T_{(^\circ\text{C})} = 20.0 - 4.42 * (\delta_{\text{arag}(PDB)} - \delta_{w(SMOW)}) \quad (6.36)$$

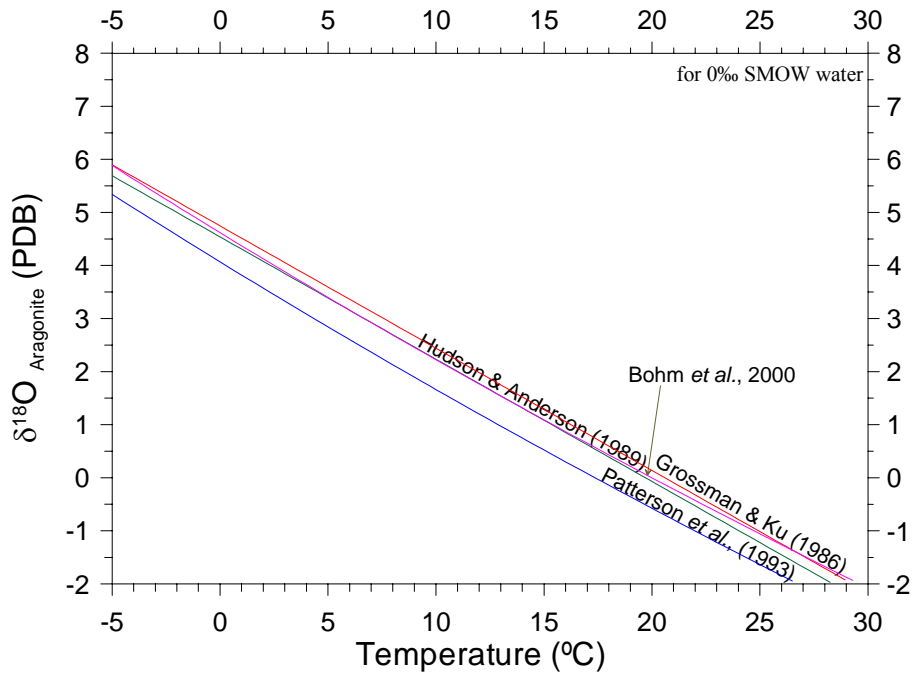


**Figure 6.4.**  $^{18}\text{O}$ -fractionation equations for aragonite.

From all the different temperature oxygen fractionation equations, in this work, the Bohm *et al.*, (2000) is used as the fractionation equation that best represents the

fractionation equation for the aragonite mineralogy.

#### 6.1.4.4 Comparison of the Aragonite with the Calcite fractionation equations

Comparing the calcite with the aragonite oxygen fractionation equations (Figure 6.5) it is clear that during aragonite precipitation the oxygen is more intensely fractionated to heavier values. The fractionation differences between the two phases ( $\Delta^{18}\text{O}_{\text{arag-calc}}$ ) exhibit a significant variability, function of the fractionation equation considered. The Kim and O'Neil (1997) proposed equation (6.16) for calcite and the Grossman and Ku (1986) equation (6.28) for aragonite present the large difference in the  $\Delta^{18}\text{O}_{\text{arag-calc}}$  of 1.60‰. However comparing the Patterson *et al.*, (1993) estimation for aragonite (6.32) with the Friedman and O'Neil (1977) equation (6.14), the fractionation difference  $\Delta^{18}\text{O}_{\text{arag-calc}}$  has the minimum value of 0.2‰.

The difference between the Bohm *et al.* (2000) fractionation equation for aragonite to the Kim and O'Neil (1997) fractionation equation for calcite shows a  $\Delta^{18}\text{O}_{\text{arag-calc}}$  of 1.40‰ and is considered the most probable fractionation difference that would be expected on the methane-derived authigenic calcite and aragonite, considering their formation in isotopic equilibrium.

Also to be noted is that the presence of Mg in the calcite lattice will move the oxygen fractionation equations towards a heavier isotopic values, as shown by the Friedman and O'Neil (1977) equations (grey lines in Figure 6.5). For 8 mol% of Mg in calcite, the  $\Delta^{18}\text{O}_{\text{arag-MgCalc}}$  is variable with the temperature, increasing from 0.20‰ at near 0°C and reaching 0.60‰ at 25°C. Therefore, the presence of Mg in the calcite lattice or the higher abundance of Mg-calcite in the carbonate mixture should result in smaller differences between the fractionation equations of aragonite and calcite and more similar isotopic values for aragonite and calcite.

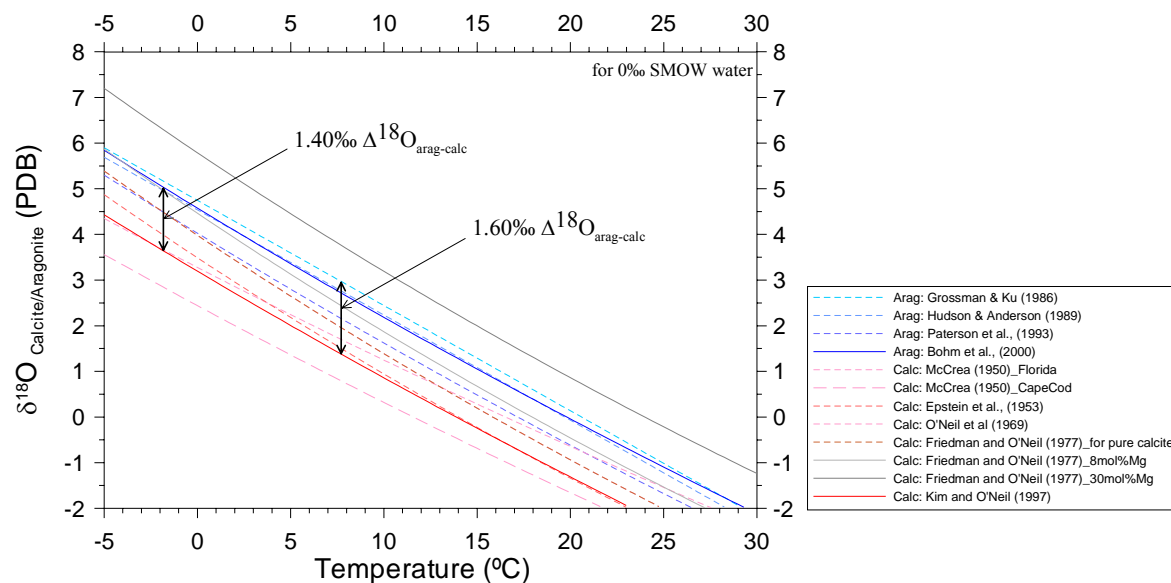


**Figure 6.5.** Differences in the oxygen isotopic fractionation ( $\Delta^{18}\text{O}_{\text{arag-calc}}$ ) of calcite (red lines) and aragonite (blue lines) in equilibrium with water with  $\delta^{18}\text{O} = 0\text{‰}$  SMOW, as a function of temperature. The difference between aragonite and calcite according to the Bohm *et al.*, (2000) and the Kim and O'Neil (1997) equations is 1.40‰. The maximum difference in the oxygen isotopic fractionation is 1.60‰ considering the Grossman and Ku (1986) equation for aragonite.

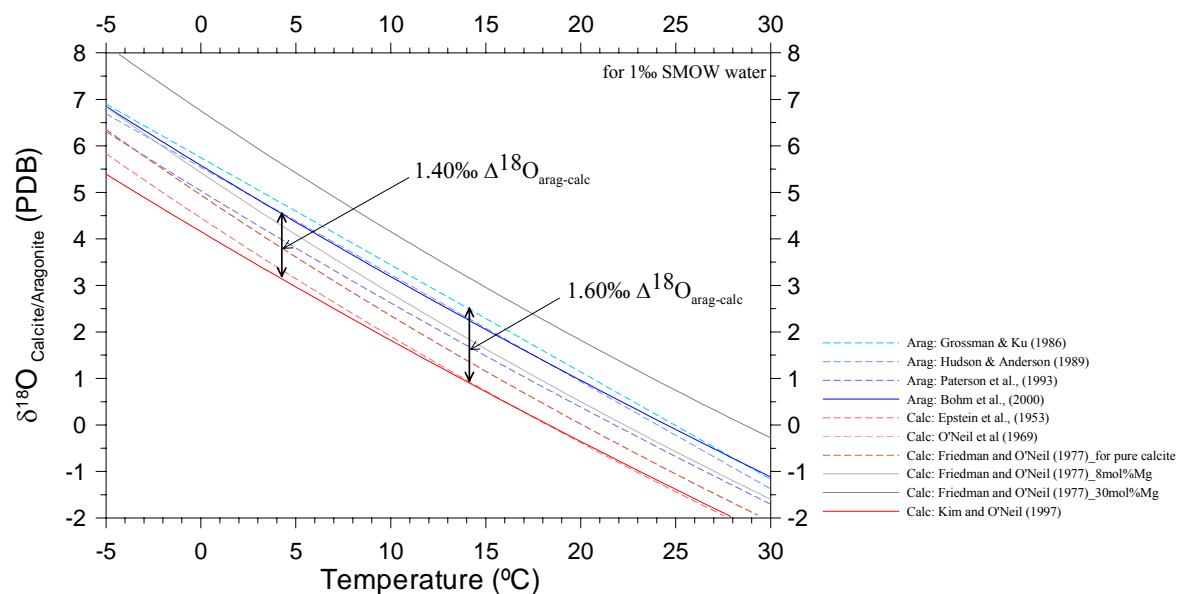


**Figure 6.6.** Differences in the oxygen isotopic fractionation ( $\Delta^{18}\text{O}_{\text{arag-calc}}$ ) of calcite (red lines) and aragonite (blue lines) in equilibrium with water with  $\delta^{18}\text{O} = 1\text{‰}$  SMOW, as a function of temperature. The difference between aragonite and calcite according to the Bohm *et al.*, (2000) and the Kim and O'Neil (1997) equations is 1.40‰. The maximum difference in the oxygen isotopic fractionation is 1.60‰ considering the Grossman and Ku (1986) equation for aragonite.

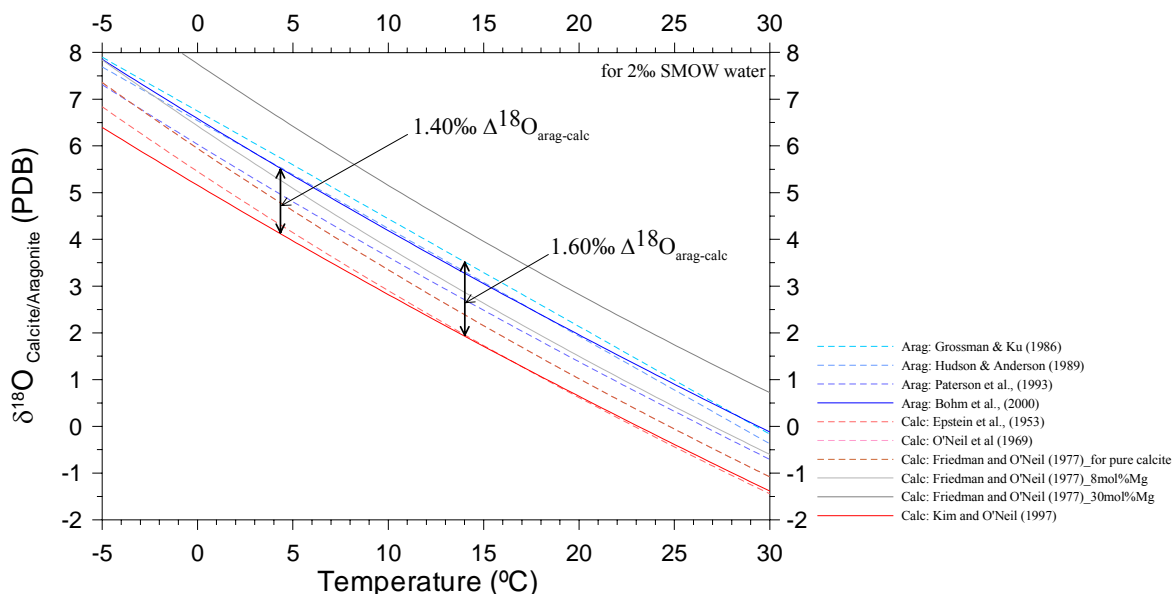


**Figure 6.7.** Differences in the oxygen isotopic fractionation ( $\Delta^{18}\text{O}_{\text{arag-calc}}$ ) of calcite (red lines) and aragonite (blue lines) in equilibrium with water with  $\delta^{18}\text{O} = 2\text{‰}$  SMOW, as a function of temperature. The difference between aragonite and calcite according to the Bohm *et al.*, (2000) and the Kim and O'Neil (1997) equations is 1.40‰. The maximum difference in the oxygen isotopic fractionation is 1.60‰ considering the Grossman and Ku (1986) equation for aragonite.

In conclusion, for coexisting calcite and aragonite, if both have precipitated in isotopic equilibrium, from the same solution (independently of its isotopic composition) and at the same temperature, aragonite is expected to be up to 1.60‰ more enriched in  $^{18}\text{O}$  than calcite. For higher Mg contents in calcite or if calcite is coexisting with Mg-calcite, then the oxygen isotopic difference between the calcite + Mg-calcite mixture and aragonite should be smaller.

#### 6.1.4.5 Comparison of the Dolomite with the Calcite fractionation equations

Comparing the Vasconcelos *et al.*, (2005) low-temperature experimental determination of the oxygen isotope fractionation of dolomite (6.28) with the Kim and O'Neil (1997) proposed equation (6.16) for calcite-water fractionation on inorganic precipitation at low temperature, the difference between the isotopic fractionation factors ( $\Delta^{18}\text{O}_{\text{dol-cal}}$ ) is temperature dependent: at 4°C this difference is 3.10‰ and at 14°C the difference is 2.98‰, more positive for dolomite (Figure 6.8). For the present objective, the slopes of equations (6.28), (6.14) and (6.16) can be considered identical and the ( $\Delta^{18}\text{O}_{\text{dol-cal}}$ ) value can be considered constant with temperature. In conclusion, for coexisting calcite and dolomite, if both have precipitated in isotopic equilibrium from the same solution at

the same temperature, dolomite is expected to be 3‰ more enriched in  $^{18}\text{O}$  than calcite.

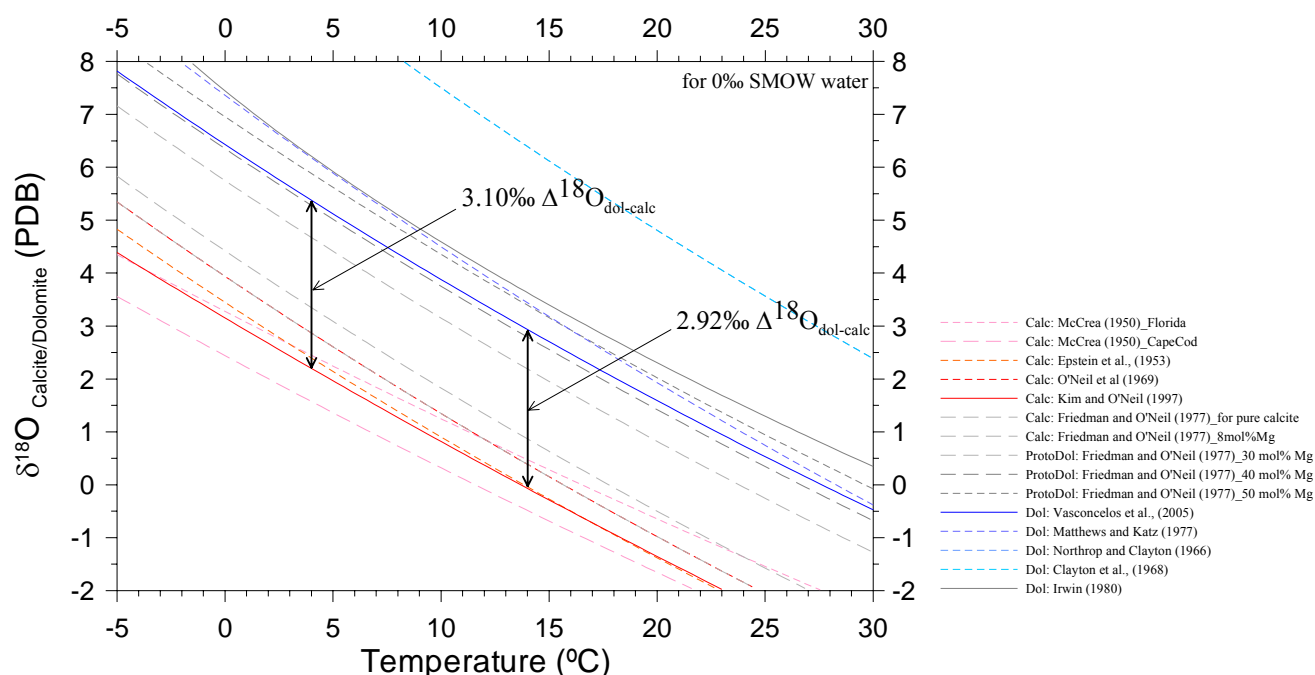


**Figure 6.8.** Differences in the oxygen isotopic fractionation ( $\Delta^{18}\text{O}_{\text{dol-calc}}$ ) of calcite (red lines) and dolomite (blue lines) in equilibrium with water with  $\delta^{18}\text{O} = 0\text{‰}$  SMOW, as a function of temperature.

## 6.2 Present day oceanographic conditions in the Gulf of Cadiz

In the Gulf of Cadiz,  $\delta^{18}\text{O}$  for the Mediterranean Outflow water (MO) ocean water show values in the range of +0.60 to +0.70‰ SMOW and present day  $\delta^{18}\text{O}$  values for NACW are in the range of +0.66 to +0.84‰ SMOW (A. Voelker personal communication).  $\delta^{18}\text{O}$  values of bottom water at the sites where MDAC were collected, vary from +0.5 to +1.5‰ SMOW (Mazurenko *et al.*, 2002). The bottom water temperature, depending if the sites where MDAC occur are under influence of the NACW or MW range from 6  $^{\circ}\text{C}$  to 12  $^{\circ}\text{C}$  respectively (CANIGO data base).

Based on seawater temperature reconstructions from benthic foraminifer from gravity cores in the Gulf of Cadiz it is possible to estimate a minimum sea-bottom water temperature of 4  $^{\circ}\text{C}$  for extreme conditions in glacial stages, and a maximum sea-bottom water temperature of 14  $^{\circ}\text{C}$  for extreme conditions in interglacial stages (Voelker *et al.*, 2006). These temperature intervals will be used for the interpretation of the oxygen

isotopic composition s of the MDAC. The interval of 8 to 12°C, that corresponds to the temperatures measured at the sites where the samples were collected, is considered the most probable temperature range of formation of the MDAC. The interval between 4°C and 14°C is considered as representing extreme lower and higher temperatures that could had be reached during extreme conditions such as the glacial periods (for the lower temperature) and the temperature of 14°C could be reached in times of enhanced MO influence.

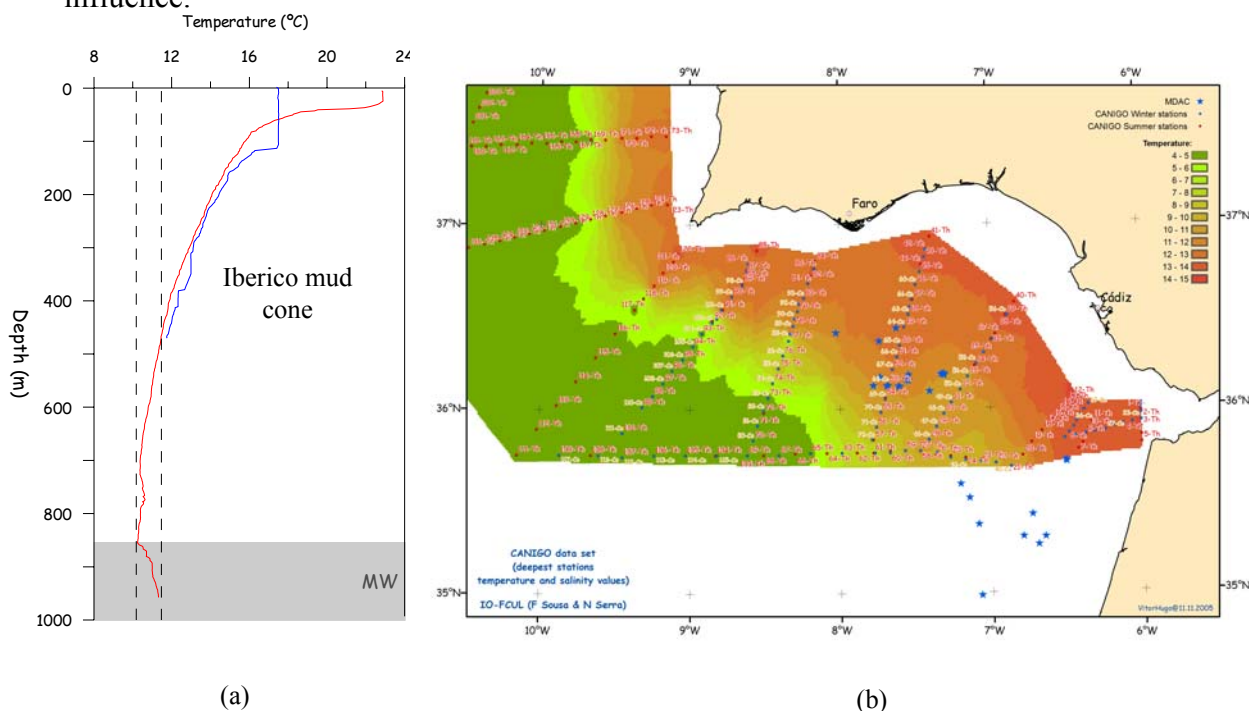


**Figure 6.9.** (a) Temperature profile close to the Iberico mud cone, where MDAC were collected. Data presented correspond to summer and winter profiles from the CANIGO data base and shows the two main water masses in the Gulf of Cadiz. At the depth range between 400 and 1600 meters, the NACW is characterized by temperatures ranging from 6 to 12°C. The MO is characterized by temperatures ranging from 10 to 14°C. (b) Map showing the location of sites where MDAC were collected and temperature values of the deepest CTD measurement from the CANIGO data set. To be noted the scarceness of measurements in the Moroccan margin. The temperature values on this margin were extrapolated from the temperature values from the northern part of the Gulf of Cadiz which most probably corresponds to an underestimation of the temperature values for the Morocco margin.

### 6.3 Methods

The samples used in this study were collected by dredging and by TV controlled grab, on the Iberico mud cone, on the main channels of the MO (Guadalquivir and Cadiz Channels), on the Guadalquivir Diapiric Ridge (GDR), on the Formosa Ridge (FR), at the

Penn Duick escarpment and on the Faro, Hesperides, Ginsburg, Mercator, Adamastor, Meknes and Jesus Baraza mud volcanoes (Figures 5.1 and 5.2 and Magalhães *et al.*, in prep). Add sites of the TTR16

The morphology and sizes of the authigenic carbonates were described on underwater video observations and on the retrieved samples. The petrography of the carbonates was examined in polished slabs and thin sections by standard petrographic and cathodoluminescence techniques. Scanning electron microscope (SEM) observations were carried out, coupled with energy dispersive spectrometer X-ray elementary analysis (EDS), in fresh fractured surfaces and in samples etched with HCl 10% during 3-4 minutes before the SEM observations.

Samples for XRD, Sr, total organic carbon, carbonate content, carbon and oxygen stable isotope were extracted from transversal and longitudinal cuts and micro-drilled along radial and longitudinal profiles.

Bulk mineralogy and the relative abundance of the different carbonate mineralogies in each sample were investigated by X-ray diffraction (XRD) on 134 powdered samples (Table 5.1). X-ray diffraction patterns were obtained using a Scintag X-ray diffractometer with  $\text{CuK}\alpha$  radiation (1.5405 Å wavelength). Scans were done from 5° to 60° 2θ at 0.02°/sec, using a 40 kV accelerating voltage and 30 mA current. As the intensity of the diffraction pattern of a mineral in a mixture is proportional to its concentration, estimates of the relative proportions of the minerals in a sample were made by measuring their relative peak areas. Peak identification and minerals relative abundance estimation were performed using the Scintag interpretation software and the MacDiff<sup>®</sup> software packages. The peak areas were measured for the main peaks of the carbonate minerals aragonite (3.40 Å), calcite (< 8 mol%  $\text{MgCO}_3$ , 3.036 to 3.012 Å), high Mg-calcite (8 to 30 mol%  $\text{MgCO}_3$ , 3.012 to 2.946 Å), protodolomite or Ca-dolomite (30 to 40 mol%  $\text{MgCO}_3$ , 2.946 to 2.916 Å) and dolomite (40 to 55 mol%  $\text{MgCO}_3$ , 2.916 to 2.871 Å). The Mg:Ca ratio of the carbonate minerals was calculated from the shift of the d-spacing of the (104) reflection peak of calcite and dolomite from the stoichiometric peaks positions in the diffraction spectra (Goldsmith and Graf, 1958; Lumsden, 1979).

Samples for carbon and oxygen stable isotopic analyses were prepared by reacting at 90°C with 100% phosphoric acid on an automated carbonate device connected to a VG-PRISM mass spectrometer calibrated with NBS19, NBS 18 and NBS 20. The results are

reported in the conventional  $\delta$  ‰-notation with reference to VPDB (Vienna Peedee Belemnite). Analytical reproducibility of the method, based on repeated standards is better than  $\pm 0.1$ ‰ for both carbon and oxygen. For temperature calculations of the dolomite samples, dolomite  $\delta^{18}\text{O}$  values were corrected for the analytical offset of  $+1.63$ ‰, consequence of the unequal oxygen fractionation during the reaction to  $\text{CO}_2$  (Rosenbaum and Sheppard, 1986). For the reconstruction of paleo-pore water temperatures and oxygen isotopic composition, the Kim and O'Neil (1997) equation was used for calcite, the Vasconcelos *et al.*, (2005) equation was used for dolomite and the Bohm *et al.*, (2000) equation was used for aragonite, as described in previous sections.

In order to determine the different isotopic composition of the different carbonate phases on selected MDAC samples, the organic acid ethylenedinitrilotetracetic acid (EDTA) was used. A detailed description of the leaching technique is described in Appendix C. Samples for EDTA were retrieved from the powdered samples collected with a micro-drill, each sample was spitted in two fractions. One sub-sample was used for XRD analysis and for carbon and oxygen isotopic analysis of the bulk carbonate. The second sub-sample was leached with 20 ml boiling 0.25 M EDTA solution at pH 11 during 24 hours in glass covered containers to avoid evaporation. The solvent level was maintained at 20 ml/g by adding distilled water. After 24 hours the sub-sample was taken out of the EDTA solution, washed in distilled water, freeze dried, examined with XRD and measured for carbon and oxygen isotopic composition.

Samples for  $^{87}\text{Sr}/^{86}\text{Sr}$  were dissolved in 20 ml, 1.0 N ultra pure acid acetic, centrifuged, and then decanted and evaporated dry. Then, they were re-dissolved in 20 ml of 5-N  $\text{HNO}_3$  and loaded into columns containing the AG8 50W BioRad Sr-specific resin. The  $^{87}\text{Sr}/^{86}\text{Sr}$  composition of the carbonates (Arag, Calc, Mg-Calc and Dol) was determined using a VG-Sector 54 Thermal Ionization Mass Spectrometer. The analytical reproducibility of the method, based on repeated standards, is better than  $\pm 0.000060$ ‰.

## 6.4 Results

### 6.4.1 Oxygen and carbon isotopes

#### 6.4.1.1 EDTA

The EDTA leaching technique was used to differentiate between coexisting calcite, high Mg-calcite and dolomite in a controlled and simple technique. Using a 0.25 M EDTA solution, a mixture of 74:26 dolomite:calcite+high Mg-calcite was altered to a 100:00 (wt%:wt%) mixture in 24 hours, as described in Appendix C. The selective separation of the coexisting carbonate minerals allowed the identification of different carbon and oxygen isotopic values for the different mineral phases.

On average, pure dolomite shows a constant depletion in  $\delta^{13}\text{C}$  of  $-5.49\text{‰} \pm 2.08\text{‰}$  (PDB) in relation to the bulk carbonate (Figure 6.10 and Figure C.9). Pure dolomite phase (obtained by EDTA leaching of 6 samples) shows an average  $\delta^{18}\text{O}$  isotopic composition of  $+5.69\text{‰} \pm 0.29$  (PDB) (Figure 6.10 and Table C.2). Extrapolated  $\delta^{18}\text{O}$  isotopic composition of pure dolomite from EDTA leaching of 6 samples (Figure 6.10 and Figure C.9) indicate an average value of  $+5.66\text{‰}$  (PDB).

The calculation of the  $\delta^{18}\text{O}$  isotopic composition of pure calcite or, of the mixture of calcite + high Mg-calcite (Table C.2., Appendix C), indicates a calculated value of  $+0.93\text{‰} \pm 0.67$  (PDB). The extrapolation from the linear best fit of the plot of the  $\delta^{18}\text{O}$  isotopic composition as a function of the dolomite content Figure 6.10 indicates an estimated composition for pure calcite phase, or to the mixture of calcite + high Mg-calcite of  $1.4\text{‰}$  (PDB). The calculated (Table C.2., Appendix C)  $\delta^{13}\text{C}$  for a pure calcite + high Mg-calcite mixture indicates a value of  $-9.83\text{‰} \pm 6.17$  (PDB). As such, all the estimations point to  $\sim 1.4\text{‰}$  (PDB) near seawater composition of the calcite phase and a positive  $\sim 5.7\text{‰}$  (PDB)  $\delta^{18}\text{O}$  isotopic composition of the dolomite.

The difference between the oxygen isotopic fractionation factors of the two end-members pure dolomite and pure calcite ( $\Delta^{18}\text{O}_{\text{dol-cal}}$ ) is  $4.2\text{‰}$  (PDB) or  $4.7\text{‰}$  (PDB), considering the different extrapolations. These values are significantly higher than the expected theoretical maximum limit value of  $3.1\text{‰}$  (PDB) for the temperature of  $4^\circ\text{C}$

(section 6.1.4.5, Figure 6.8).

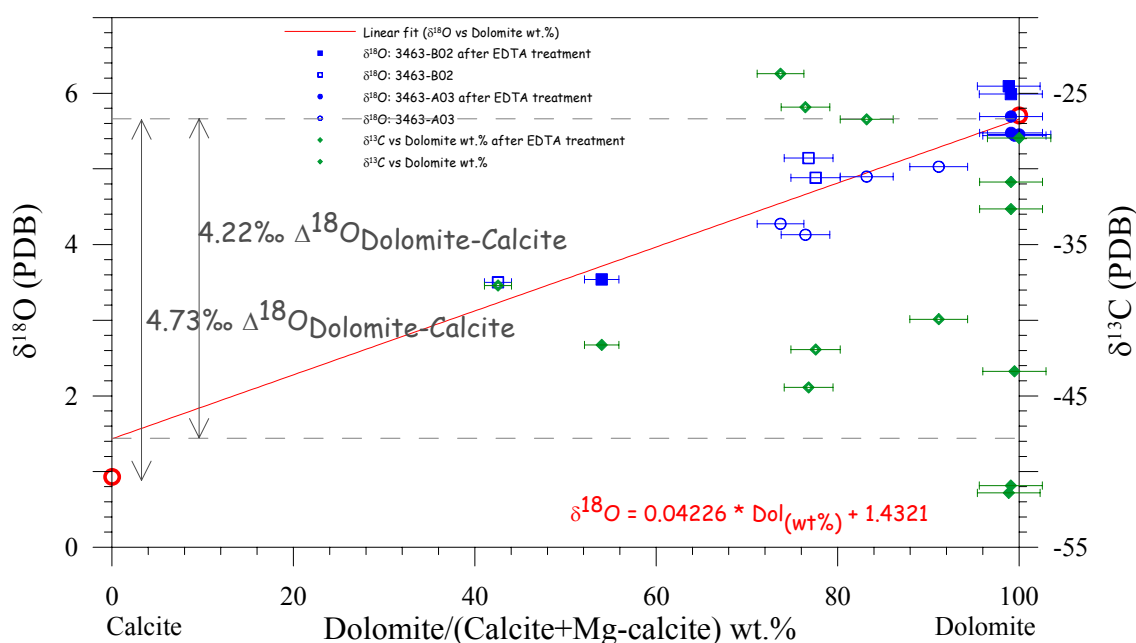


**Figure 6.10.** Correlation between the dolomite/(calcite + Mg-calcite) ratio and the  $\delta^{18}\text{O}$  values of the group of samples treated with EDTA leaching. Pure dolomite yields 5.6‰  $\delta^{18}\text{O}$  PDB, whereas  $^{18}\text{O}$  is strongly depleted in the calcite and Mg-calcite phases. There is no clear relationship between the mineralogy and the  $\delta^{13}\text{C}$  values.

#### 6.4.1.2 Calcite and Mg-calcite vs Dolomite in bulk samples of the dolomite crusts, chimneys and nodules

The samples of dolomite crusts, chimneys and nodular type are composed of calcite, high Mg-calcite, protodolomite and dolomite with different mineral proportions and with high variability of the C and O isotopic compositions. These values are reported in Table 5.1 and Figure 5.9. The high variability on the  $^{18}\text{O}$  values of bulk samples is the consequence of the different mineralogical composition (calcite/dolomite ratio), possible different temperature of formation and different pore fluids composition.

The bulk  $\delta^{18}\text{O}$  isotopic composition as function of the dolomite to carbonate ratio (Figure 6.11) shows a high variability with values ranging from 0.8 up to 6.8‰ (PDB). Samples with more than 95% of dolomite also show a high variability with  $\delta^{18}\text{O}$  values ranging from 3 to 6.8‰ (PDB). The linear best fit equation for all the samples has a poor coefficient of determination but, shows an median  $\delta^{18}\text{O}$  isotopic value of  $4.8\text{‰} \pm 2.2\text{‰}$  (PDB), value close to the 5.66‰ (PDB) value for the pure dolomite phase estimated from

the EDTA leaching technique.

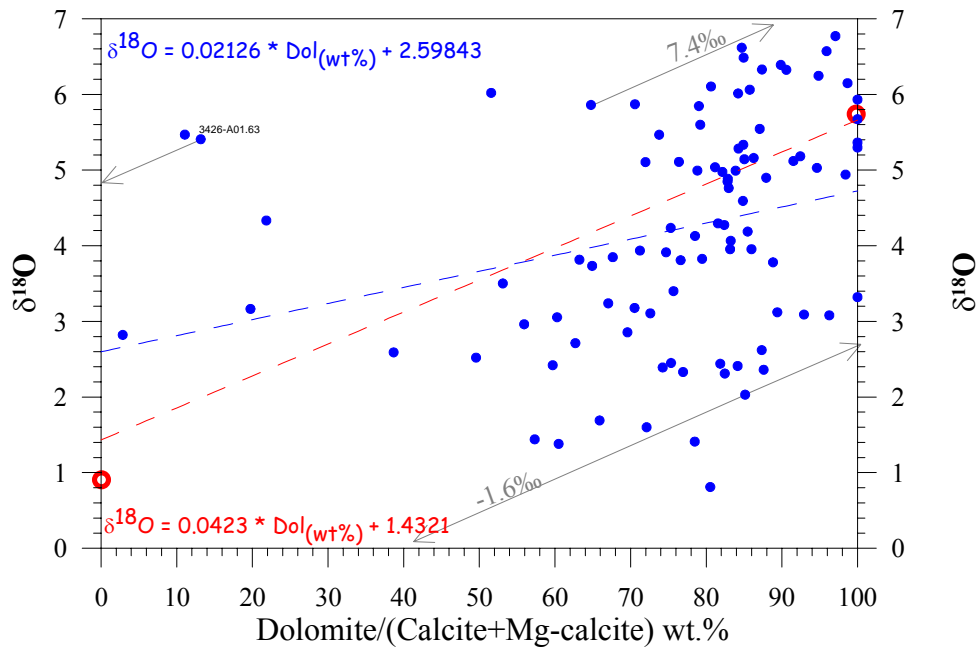


**Figure 6.11.** Correlation between the dolomite/calcite + Mg-calcite ratio and the  $\delta^{18}\text{O}$  values of the dolomite crusts, chimneys and nodular samples. Also plotted (in red dashed line) the trend line and the calculated (red circles) isotopic composition of the pure calcite and pure dolomite phases determined with the EDTA leaching methodology (Appendix C). Grey arrows indicate the considered extreme isotopic maximum and minimum values for the pure calcite and pure dolomite end-members.

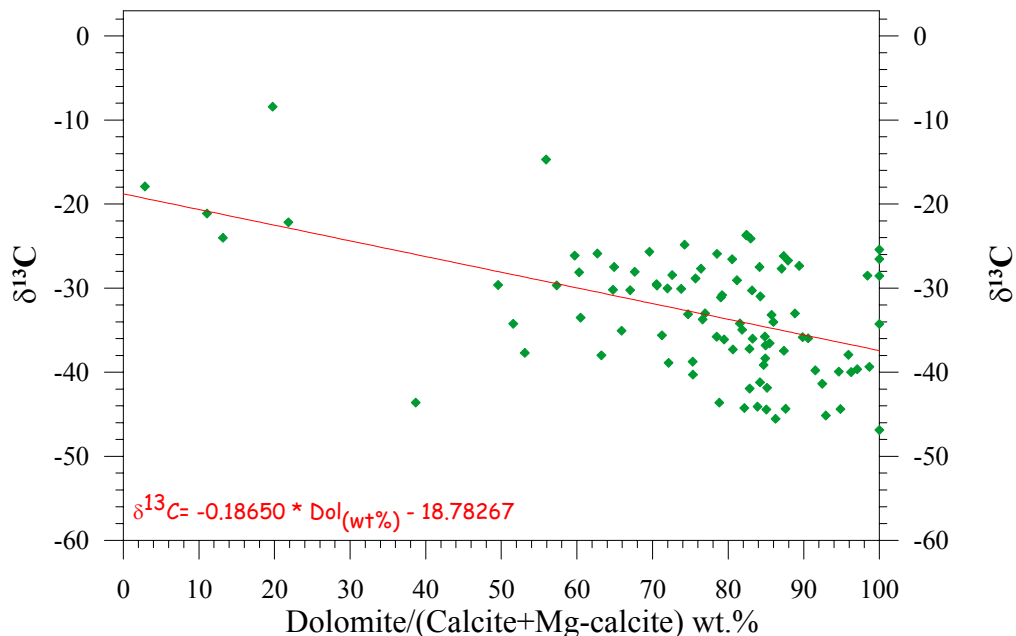


**Figure 6.12.** Correlation between the dolomite/calcite + Mg-calcite ratio and the  $\delta^{13}\text{C}$  values of the dolomite crusts, chimneys and nodular samples.

The  $\delta^{18}\text{O}$  isotopic composition of bulk samples with mineralogy dominated by

calcite (calcite + high Mg-calcite >80%) shows values ranging from 2.8 to 5.5‰ PDB (Figure 6.11). These values are higher than the estimated composition of the pure calcite phase (1.44‰ PDB) estimated from the EDTA leaching technique. The linear best fit equation for all the samples, that has a poor coefficient of determination, shows a median  $\delta^{18}\text{O}$  isotopic value of 2.6‰ (PDB) for the pure calcite phase. This value is higher than the 1.44‰ (PDB) estimated from the EDTA leaching technique.

The plot of the bulk  $\delta^{13}\text{C}$  isotopic composition of the dolomite chimneys crusts and nodules as function of their dolomite to carbonate ratio (Figure 6.12) indicates an evident trend with a  $\delta^{13}\text{C}$  value of  $-37\text{‰} \pm 10\text{‰}$  (PDB) for pure dolomite end-member and  $-18\text{‰} \pm 10\text{‰}$  (PDB) for calcite+Mg-calcite end-member. The extrapolations of the  $\delta^{13}\text{C}$  values for pure dolomite, based on the  $\delta^{13}\text{C}$  values of bulk and leached material (Figure C.12) indicate  $\delta^{13}\text{C}$  compositions ranging from  $-52\text{‰}$  to  $-28\text{‰}$  (PDB) for the pure dolomite phase, with an average value of  $-39\text{‰} \pm 10\text{‰}$  (PDB). The calcite and Mg-calcite phases  $^{13}\text{C}$  are heavier with the extrapolated values ranging from  $-2$  to  $-23\text{‰}$  (PDB) with an average value of  $-9.83\text{‰} \pm 6.17\text{‰}$  (PDB).

In conclusion, both EDTA and bulk samples clearly indicate for the calcite a closer to normal seawater isotopic composition, also seen on the oxygen isotopes; and a lighter carbon isotopic and heavier oxygen isotopic composition for dolomite.

### 6.4.1.3 Calcite and Mg-calcite vs Aragonite in aragonite pavements

Calcite, Mg-calcite and aragonite occur in samples of aragonite pavements, with different mineral proportions and with different C and O isotopic compositions. These values are reported in Table 5.1 and Figure 5.9. The high variability on the  $^{18}\text{O}$  values of bulk samples of aragonite pavements is the consequence of the different mineralogical composition (calcite/aragonite ratios) and possible also different temperature of formation and different pore fluid composition.

The aragonite pavement samples reveal a linear correlation between the mineral content i.e., the ratio aragonite/(calcite+Mg-calcite), and the  $\delta^{18}\text{O}$  composition (Figure 6.13). This correlation indicates a  $\delta^{18}\text{O}$  calculated isotopic composition of 2.3‰ (PDB) for the end-member pure calcite phase. The  $\delta^{18}\text{O}$  calculated isotopic composition of the end-member pure aragonite is 4.2‰ (PDB). This corresponds to a difference between the isotopic fractionation factors ( $\Delta^{18}\text{O}_{\text{arag-cal}}$ ) of 1.9‰ (PDB). This value is higher than the

expected theoretical maximum limit value of 1.6‰ (PDB) (Section 6.1.4.4, Figure 6.5).

There is no evident different correlation between the mineral content and the  $\delta^{18}\text{O}$  composition as function of the sample location but, samples from Hesperides and Ginsburg MVs are located slightly above the average trend line, while samples from Jesus Baraza, and Faro MVs are located above that line. It is not evident any clear correlation between the different aragonite types (lithified mud volcano breccias, intraformational breccias, shell crusts and stromatolitic fabric) and their  $\delta^{13}\text{C}$  and  $\delta^{18}\text{O}$  composition. It should however be noted that the intraformational breccias present the higher  $\delta^{13}\text{C}$  and  $\delta^{18}\text{O}$  values.

In relation to the carbon isotopic composition (Figure 6.14), there is no clear evidence of an isotopic trend with the mineralogical composition. Nevertheless it is of significance that shell samples collected within the aragonite pavements present heavier  $\delta^{13}\text{C}$  values than the shells collected from dolomite chimney samples. The aragonite pavement cements present a wide range of  $\delta^{13}\text{C}$  values from -14.2 to -56.2‰ (PDB).

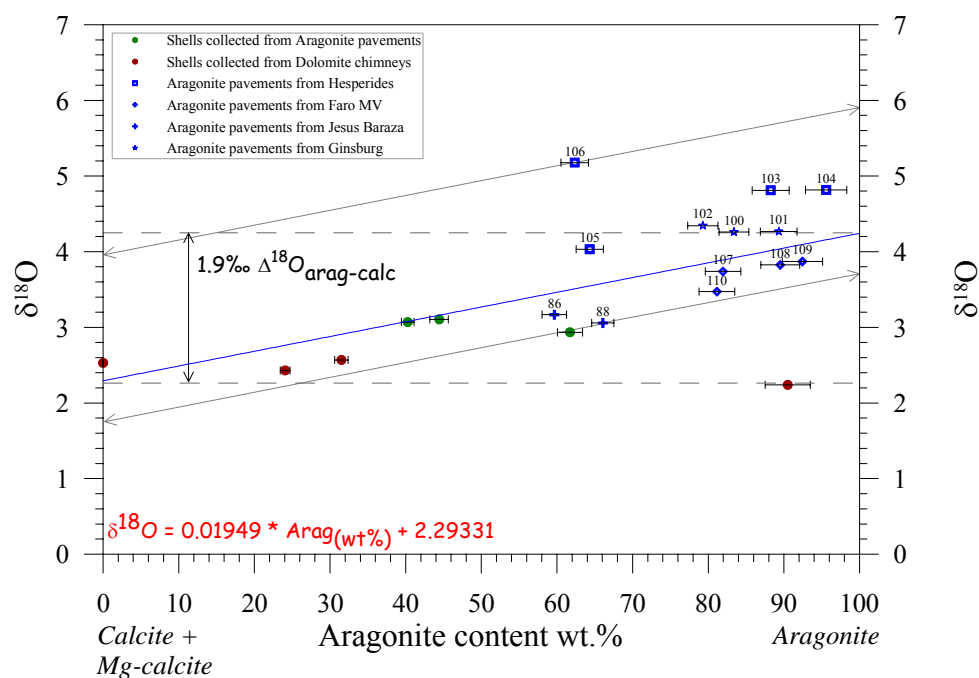


**Figure 6.13.** Correlation between the Aragonite/calcite+Mg-calcite ratio and the  $\delta^{18}\text{O}$  values for the aragonite pavement samples. A pure aragonite mineral yields about 4.2‰  $\delta^{18}\text{O}$  (PDB), whereas  $^{18}\text{O}$  is lighter in the pure calcite phase (2.3‰). Also plotted (in green) the isotopic composition of shells cemented within the shell pavement-type samples and corals and shells (dark brown colour) attached to the external surface of dolomite chimney samples. Labels on the Aragonite pavement samples correspond to the sample ID number see text for explanation.

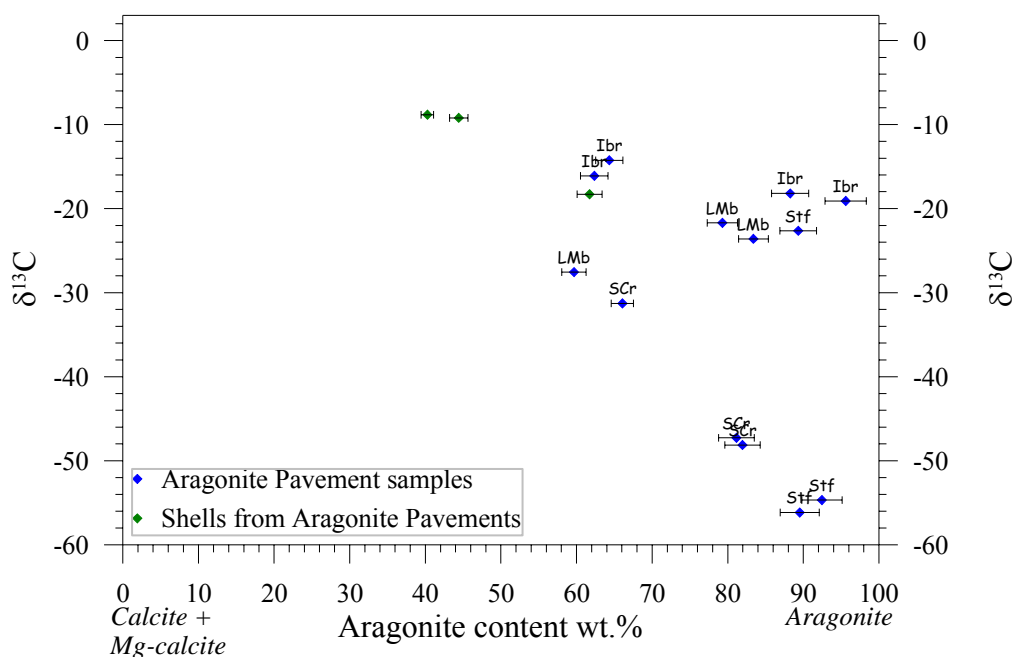


**Figure 6.14.** Aragonite pavement samples do not reveal any clear correlation between the Aragonite/calcite ratio and the  $\delta^{13}\text{C}$  values. Also plotted (in green) the isotopic composition of shells cemented within the shell pavement type samples. In dark brown colour is shown the isotopic composition of corals and shells attached to the external surface of dolomite chimney samples.

## 6.4.2 Strontium isotopes

The strontium isotopic composition of carbonate minerals reflects the strontium isotopic composition of the fluid in which they formed (Hess *et al.*, 1986). As the variation of the strontium isotopic composition of seawater through time is well defined (Elderfield, 1986; Farrell *et al.*, 1995), the strontium isotopes can be used to constrain the source of the fluids of authigenic carbonates.

$^{87}\text{Sr}/^{86}\text{Sr}$  ratios on the different types of carbonate samples (dolomite crusts and chimneys and aragonite pavements) show values between 0.709110 and 0.709191 (Table 6.3). The aragonite pavement carbonate  $^{87}\text{Sr}/^{86}\text{Sr}$  ratio clearly reflects the isotopic ratio of contemporaneous seawater of 0.709175 (Paytan *et al.*, 1993) indicating that the authigenic carbonates of the aragonite pavements were formed from fluids with Sr values similar to present day seawater. Dolomite chimney samples shows  $^{87}\text{Sr}/^{86}\text{Sr}$  values close to the contemporaneous seawater composition, but in spite of its large error value limits, the dolomite chimney sample (3463-A08) presents a  $^{87}\text{Sr}/^{86}\text{Sr}$  value (0.709110) that is lighter than the present day seawater composition (Figure 6.15 and Figure 6.16). However, the dolomite crust sample 3458-A03 has  $^{87}\text{Sr}/^{86}\text{Sr}$  values close to the contemporaneous

seawater composition. The difference on the strontium isotopic value of the dolomite chimney sample is interpreted as reflecting a contribution of older seawater composition (indicated by the age of  $245 \text{ ka} \pm 9.3\%$  obtained by U/Th, as discussed in chapter 7) or possibly a contribution from deeper strontium rich fluids (with compositions closer to the Bonjardim and Ginsburg MVs estimated end member pore fluids, Figure 6.15). The dolomite crust and the aragonite pavement, they both reflect a contemporaneous seawater composition. The  $^{87}\text{Sr}/^{86}\text{Sr}$  ratios of the Captain Arutyunov, Bonjardim and Ginsburg MVs clearly deviates from the present day seawater values (Figure 6.15). Thus the  $^{87}\text{Sr}/^{86}\text{Sr}$  ratios of the analysed authigenic carbonates do not indicate a clear and major addition of Sr from deep seated fluids, the MDAC preferably reflect contemporaneous seawater Sr composition. The dolomite chimney sample has a signal that supports a deeper seated fluids and/or an older seawater contribution that nevertheless corresponds to a minor contribution while the main Sr source is seawater.

**Table 6.3.** Strontium isotope values of MDAC samples.

Sample	MDAC type	$^{87}\text{Sr}/^{86}\text{Sr}$	Error (2 $\sigma$ )
3458-A3	Dolomite Crust (DCr)	0.709191	$\pm 0.000060$
3463-A8c	Dolomite chimney (DChy)	0.709110	$\pm 0.000054$
3611-A1	Aragonite pavement (SCr)	0.709183	$\pm 0.000054$

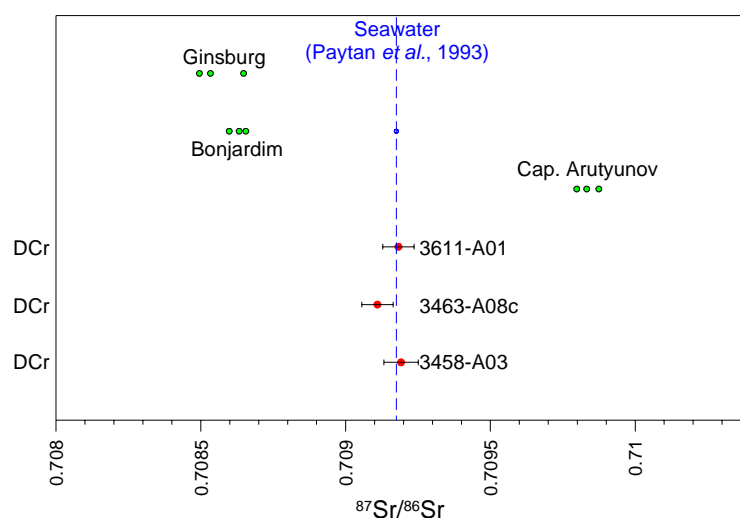


**Figure 6.15.** Strontium isotope values of MDAC samples plotted with reference to the seawater and to the pore fluids end member compositions from the Captain Arutyunov, Ginsburg and Bonjardim MVs (Hensen *et al.*, Submitted).

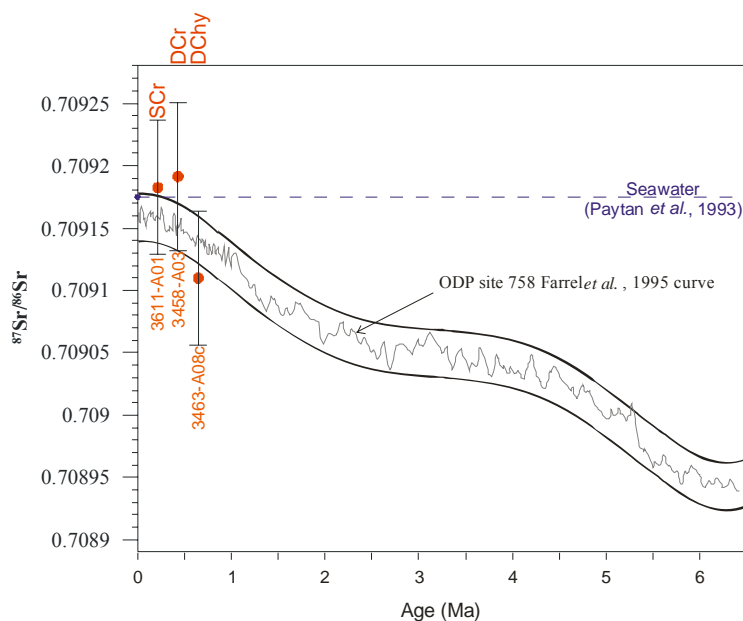


**Figure 6.16.** Strontium isotope values of MDAC samples plotted over the ODP site 758 Farrel *et al.*, (1995) seawater  $^{87}\text{Sr}/^{86}\text{Sr}$  reference curve and the respective confidence interval ( $\pm 19 \times 10^{-6}$  from 5-order fit of the curve). Dcr - Dolomite crust sample; Scr - stromatolitic crust of an aragonite pavement; Dchy - Dolomite chimney sample. To be noted that the Age axis is valid only for the Farrel *et al.*, (1995) seawater  $^{87}\text{Sr}/^{86}\text{Sr}$  reference curve, the age of the MDAC samples is not established and their position over the X axis on this plot is positioned only for reading convenience. On the graph is also plotted the Present day seawater strontium value from Paytan *et al.*, (1993).

## 6.5 Discussion

### 6.5.1 Methane rich pore waters

As discussed in chapter 5, the carbon isotopic composition of the authigenic carbonates ( $\delta^{13}\text{C} = -56.16\text{‰}$  to  $-8.42\text{‰}$  PDB, Figure 5.9 and Table 5.1) reflect the carbon source indicating that they were originated from pore fluids enriched in methane. Most probably, from a mixture of moderate to extremely  $^{13}\text{C}$ -depleted methane enriched fluids, given that  $\delta^{13}\text{C}$  values of gas hydrates and pore water are in the range  $-80$  to  $-20\text{‰}$  PDB (Stadnitskaia *et al.*, 2006; Niemann *et al.*, Submitted; Nuzzo *et al.*, Submitted), with normal seawater and  $\text{HCO}_3^-$  derived from dissolution of carbonate tests (characterized by  $\delta^{13}\text{C}$  values  $\sim 0\text{‰}$  PDB). Two potential sources of methane can be considered for the Gulf of Cadiz authigenic carbonates: thermogenic and biogenic.

As the mineral composition of the authigenic carbonates may reflect mixing from the

different carbon sources, the inference of the isotopic composition of the carbon pool from the carbonate mineral isotopic composition is complex. Fractionation of the carbon will also depend on the extent to which the different carbon reservoirs are oxidized. However, it is possible to estimate the  $\delta^{13}\text{C}$  composition of the fluids from which the authigenic carbonates were precipitated from. Since many samples have  $\delta^{13}\text{C}$  values heavier than biogenic methane, mixing with other carbon sources is necessary and apparently common. The gas hydrates and pore water gas compositions collected from mud volcanoes (MVs) in the Gulf of Cadiz indicate, in general, a mixture of biogenic and thermogenic gases, with secondary migration, mixing and microbial alteration of hydrocarbons (Stadnitskaia *et al.*, 2006). Thus, it is possible to recognize that the authigenic carbonates most probably reflect a similar fluid composition. As such, the isotopic composition of the authigenic carbonates reflects a major mixing of thermogenic and biogenic methane-rich fluids with non-methane carbon sources where, most probably, seawater is the most important.

### **6.5.2 Paleo-temperatures and fluid composition on dolomite crusts, chimneys and nodules**

To investigate whether the analysed  $\delta^{18}\text{O}$  isotopic values of the dolomite crusts, chimneys and nodules reflect equilibrium crystallization with the present day seawater temperatures and oxygen isotopic composition, the Vasconcelos *et al.*, (2005) low-temperature experimental determination of the oxygen isotope fractionation of dolomite (equation 6.28) and the Kim and O'Neil (1997) proposed equation (6.16) for calcite-water fractionation on inorganic precipitation at low temperature were used.

Pure calcite end-member phase have an estimated average oxygen isotopic composition of 1.4‰ PDB and a wide range of values estimated based on the EDTA and calculated based on the calcite-dolomite trend line (Figure 6.10 and Figure 6.11). Therefore, a minimum value of -1.6‰ (PDB) and a maximum value of 5.0‰ PDB can be defined. Pure dolomite end-member phase has an average oxygen isotopic composition of 5.7‰ PDB and a wide range of values with a minimum and maximum value estimated to be 2.7 and 7.4‰ PDB, respectively (Figure 6.11 and Table 6.4), based on the EDTA calculated calcite-dolomite trend line.

**Table 6.4.** Summary table of the minimum, maximum and average estimated values of oxygen isotopic composition of the end-members calcite and aragonite phases in the aragonite pavements and of the end-members calcite and dolomite of the dolomite crusts, chimneys and nodules.

Aragonite pavements			Dolomite crusts, chimneys and nodules			
	(PDB)	$\Delta^{18}\text{O}_{\text{Cal-Arag}}$		(PDB)	$\Delta^{18}\text{O}_{\text{Cal-Dol}}$	
Calcite	Minimum	1.7‰	1.9‰	Calcite	Minimum	-1.6‰
	Average	2.3‰		Calcite	Average	1.4‰
	Maximum	3.9‰		Calcite	Maximum	5.0‰
Aragonite	Minimum	3.6‰		Dolomite	Minimum	2.7‰
	Average	4.2‰		Dolomite	Average	5.7‰
	Maximum	5.9‰		Dolomite	Maximum	7.4‰

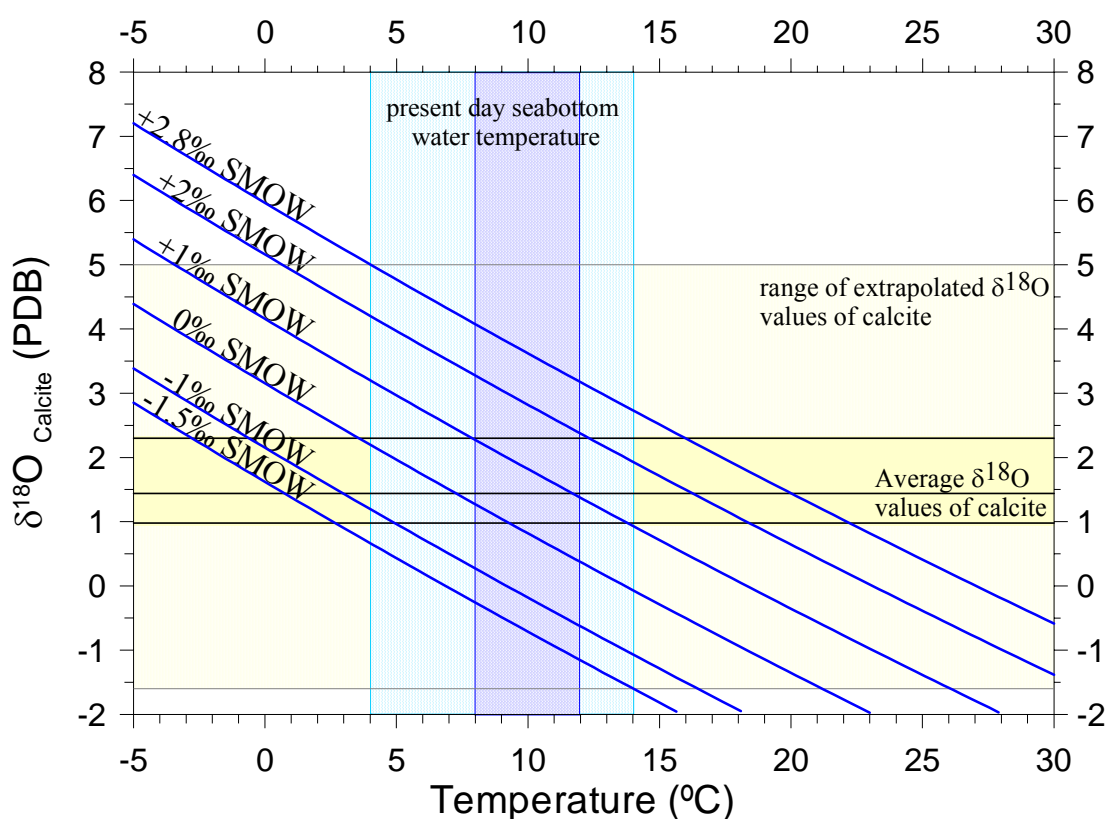


**Figure 6.17.** Plot showing the relation between oxygen isotope composition estimated for the end-member pure calcite of the dolomite crust, chimney and nodule samples, versus the temperature of precipitation with seawater oxygen isotope composition of -1.5, -1.0, 0, 1, 2, and 2.8‰ vs. SMOW. The relation is based on the equation given by Kim and O'Neil (1997).

### 6.5.2.1 Calcite and high Mg-calcite

Figure 6.17 illustrates the Kim and O'Neil (1997) relation between temperature and the  $\delta^{18}\text{O}$  of calcite, for seawater  $\delta^{18}\text{O}$  isotopic compositions ranging from -1.5 to +2.8‰ SMOW. Figure 6.18 illustrates the different temperature  $^{18}\text{O}$ -fractionation equations defined for calcite and/or Mg-calcite and the extrapolated range of  $\delta^{18}\text{O}$  values of the calcite end-member phase of the dolomite crusts, chimneys and nodules, assuming oxygen isotope compositions of the pore water changing from -2 to +3‰ SMOW. In both figures is also shown (by the blue rectangles) the present day temperature intervals that occur in the places where the MDAC were collected (dark blue, 8 to 12°C) and the temperature range (4 to 14°C) considered to represent extreme temperature limits that could occur in particular conditions as the glacial or intense periods of the MO.

From Figure 6.17 and Figure 6.18 it is evident that the extrapolated average oxygen isotopic values of calcite (1.4‰ PDB) can be explained by precipitation from normal seawater composition (0-1‰ SMOW) at the present day temperature range (8-12°C) that characterizes the different places where the MDAC were collected from. The average  $\delta^{18}\text{O}$  value (1.4‰ PDB) of the end-member calcite (that, as seen, represents the pelagic fraction carbonate) is identical to the measured values of clam shells and coral branches (2.8‰ PDB, Chapter 5, Table 5.1) that were collected from the external surface of dolomite chimneys which, as also indicated by their average  $\delta^{13}\text{C}$  value (0.36‰ PDB) were formed, most probably, in equilibrium with ambient bottom water. Therefore, the average isotopic composition of the calcite phase on the dolomite crusts, chimneys and nodules is interpreted as reflecting the dominance of the pelagic carbonate source on the total carbonate content of the samples. This pelagic calcite is characterized by isotopic compositions of 1-2‰ PDB and reflects precipitation from normal seawater at present day temperature conditions.

Samples with oxygen isotopic compositions that show a clear deviation from these average values correspond to samples where the pelagic calcite fraction is not dominant and the authigenic calcite that composes the cement is significantly controlling the isotopic composition of the total calcite phase. The extrapolated minimum and maximum limit values of oxygen isotopes of calcite and/or high Mg-calcite cannot be explained by precipitation from normal seawater composition (0-1‰ SMOW) at the present day temperature range, not even considering the minimum expected temperature during glacial

stages (4°C) or the maximum expected temperature of 14°C.

The minimum limit of -1.6‰ PDB of some calcites can be explained by precipitation from depleted pore waters, with  $\delta^{18}\text{O}$  of  $\leq -1.5\text{‰}$  SMOW (Table 6.5). Precipitation from normal seawater would require higher temperatures ( $>21^\circ\text{C}$ ). Such high temperatures are not expected to occur in the superficial sediments, since the thermal gradient measurements on some of the mud volcanoes in the Gulf of Cadiz indicate very low heat flow (Kopf *et al.*, 2004). Therefore, the minimum  $\delta^{18}\text{O}$  value of hypothetically pure calcite phase (-1.6‰ PDB) is interpreted as representing precipitation from a  $^{18}\text{O}$ -depleted source water ( $\leq -1.5\text{‰}$  SMOW). The most probable explanation for this depleted  $^{18}\text{O}$  pore waters is an important contribution from residual waters formed during the formation of methane hydrates. During the formation of gas hydrates, the  $^{18}\text{O}$ -rich water molecules are incorporated preferentially in the clathrate lattice leaving the remaining pore waters with increased ionic concentrations and with excess of  $^{18}\text{O}$ -depleted water molecules (Ussler and Paull, 1995; Ussler and Paull, 2001).

Given that temperatures less than 4°C are very improbable to occur, even considering glacial periods and with changes in the MO pathways and their absence at the sampling locations, the maximum limit value of 4.8‰ PDB on some samples can only be explained by precipitation from heavier pore waters. Alternatively, the maximum limit values of 4.8‰ PDB of some samples could be explained by precipitation from normal pore waters ( $\delta^{18}\text{O}_w$  up to 1‰ SMOW), if the mineralogy were composed with large dominance of high Mg-calcite with high amounts of mol% of Mg. However, this is not the case for all the samples. Some samples (c.a. 3426-A01.63) are composed of calcite (87% wt%) with 7.7% mol% Mg and dolomite (with 43% mol% Mg). Therefore, the maximum limit values (4.8‰ PDB) of some samples are preferably interpreted as resulting of the precipitation from  $^{18}\text{O}$ -enriched pore waters, with  $\delta^{18}\text{O}_w$  of at least 2.8‰ SMOW (Table 6.5) under seawater temperatures of 4°C. If the precipitation would occur under c.a. 8°C, then to explain the calcite isotopic composition it would be required that the fluids would have a composition of 3.8‰ SMOW (Table 6.5).

The variation of the oxygen isotopic composition in the North Atlantic associated with the last deglaciation is  $0.8 \pm 0.1\text{‰}$  (Waelbroeck *et al.*, 2002), the glacial to interglacial change in  $\delta^{18}\text{O}$  of the deep Atlantic ranges between 0.7 and 0.8‰ (Schrag *et al.*, 2002), and the change in global mean ocean  $\delta^{18}\text{O}$  between glacial and interglacial periods is

1.1±0.1‰ SMOW (Schrag *et al.*, 1996). In addition, the  $\delta^{18}\text{O}$  glacial-interglacial variations of the of bottom waters and of pore waters do not explain the calculated negative  $\delta^{18}\text{O}_w$  values ( $\leq -1.5\text{‰}$  SMOW). Therefore, the at least 2.8‰  $^{18}\text{O}$ -enriched pore waters cannot be explained as having an origin from fossil glacial pore waters. The heavier pore water composition ( $\delta^{18}\text{O}_w \geq 2.8\text{‰}$  SMOW) can be produced by fluids which contain deeply sourced clay-dehydration water, brine fluids or gas hydrate water resulting from the dissociation of gas hydrates. The hypothesis of the pore waters from which the authigenic carbonates had precipitated from have a significant contribution from hypersaline or brine fluid is considered to be less probable because no mineralogical indicators was detected as it would be expected and because the strontium isotopic records indicate instead an dominant seawater dominance of the source fluids. The brine fluids contribution also do not explain the calculated negative  $\delta^{18}\text{O}$  values that are required for some of the samples. In some of the places where the MDAC were collected, in some of them the MDAC formation process is presently active or very recent, and in the various mud volcanoes in the Gulf of Cadiz, never brine fluids were indicated in the pore water composition. The hypothesis of the source of the heavier oxygen isotopic composition as a result from deeply sourced clay-dehydration water is possible, but is not supported by the strontium isotopic composition of the carbonates. The negative  $\delta^{18}\text{O}$  values of the pore fluids that are estimated for some of the samples are also difficult to be explained by pore fluids with a clay-dehydration source.

In conclusion, given that some dolomite crust and chimney samples also indicate precipitation from  $\delta^{18}\text{O}$ -depleted water, the source of the heavier pore water composition is interpreted as resulting from the destabilization of gas hydrates. The estimated values of the  $\delta^{18}\text{O}$ -enrichment of the pore water from which some dolomite and calcites had precipitated from ( $\delta^{18}\text{O}_w \geq 2.8\text{‰}$  SMOW) corresponds to typical reported isotopic values of pore waters resulting from the destabilization of gas hydrates (Hesse and Harrison, 1981; Davidson *et al.*, 1983; Jenden and Gieskes, 1983).

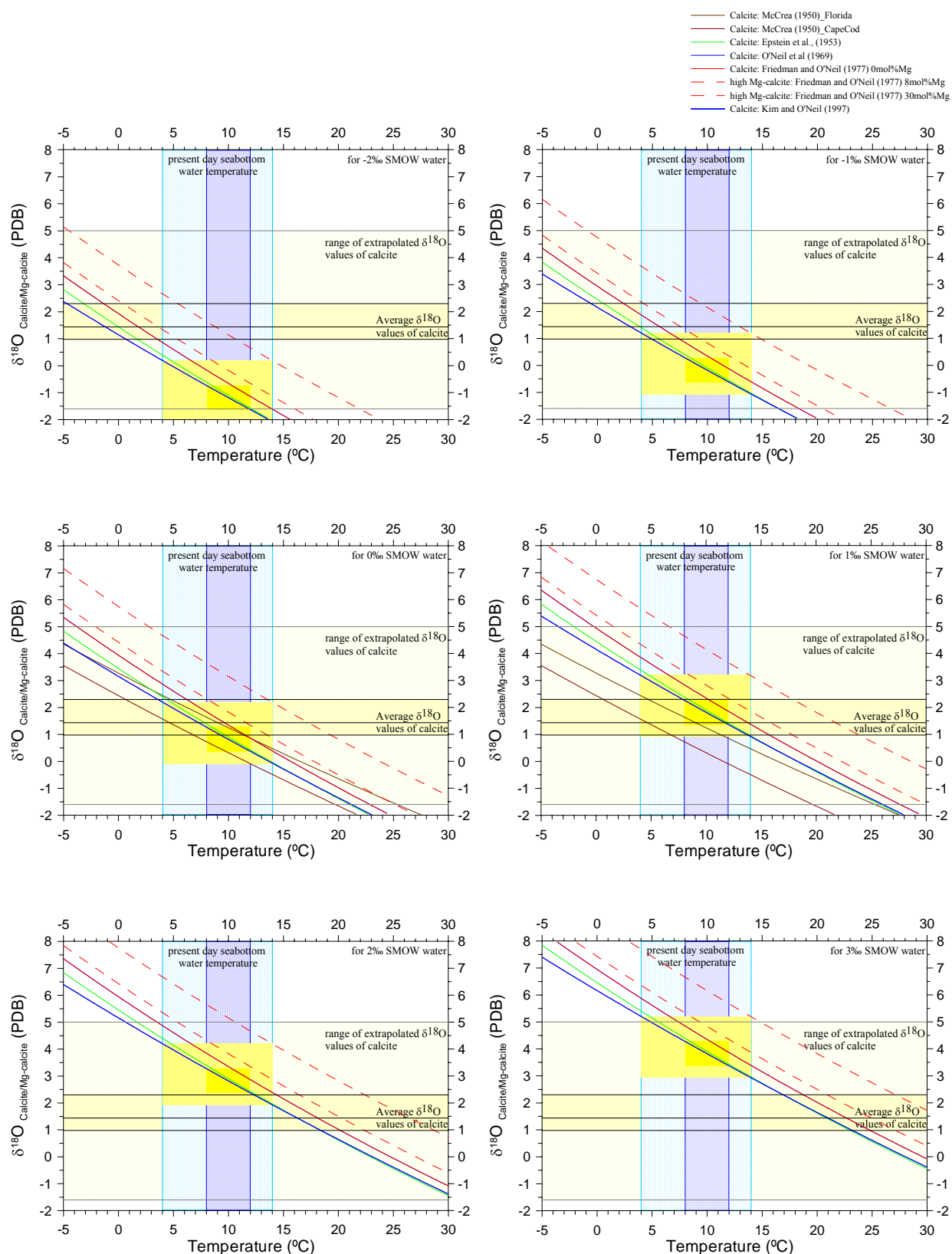


**Figure 6.18.** Different  $^{18}\text{O}$ -fractionation equations defined for calcite and Mg-calcite and the extrapolated range of  $\delta^{18}\text{O}$  values of the dolomite crusts, chimneys and nodules for different oxygen isotope compositions of water (-2 to +3% SMOW). Also shown in the plots the present day temperature range at the sites where the MDAC were collected.

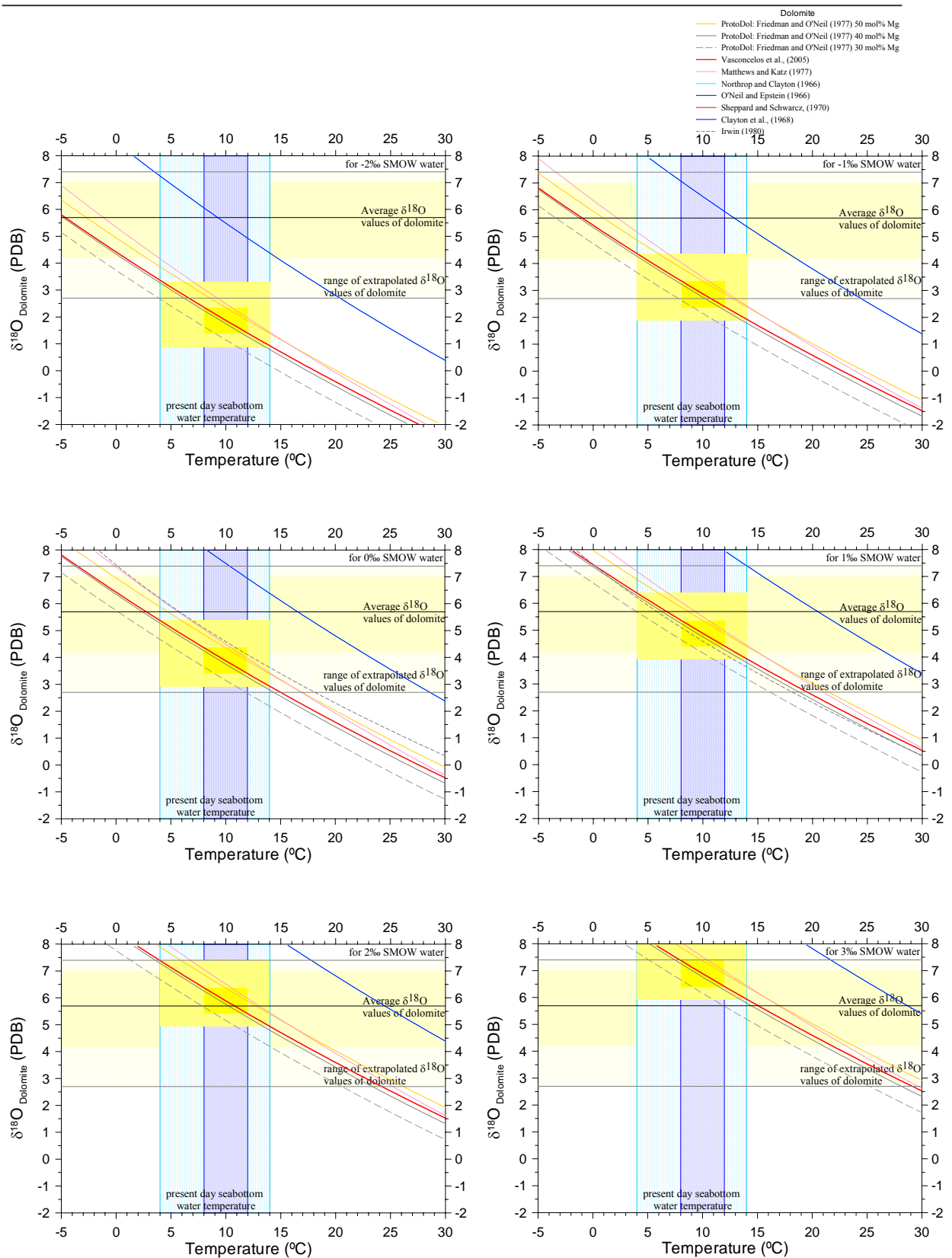


**Figure 6.19.** Different  $^{18}\text{O}$ -fractionation equations defined for protodolomite and dolomite and the extrapolated range of  $\delta^{18}\text{O}$  values of the dolomite crusts, chimneys and nodules for different oxygen isotope compositions of water (-2 to +3‰ SMOW). Also shown in the plots the present day temperature range at the sites where the MDAC were collected.

### 6.5.2.2 Protodolomite and dolomite

The Vasconcelos *et al.*, (2005) fractionation equation that relates the dolomite  $\delta^{18}\text{O}$  isotopic composition with the temperature of formation is illustrated in Figure 6.20 for  $\delta^{18}\text{O}_w$  of the pore fluids from which it precipitates ranging from -2 to +3‰ SMOW. Also shown is the present day seabottom water temperature range and the average isotopic composition and the estimated range of values of the pure dolomite end-member in samples of dolomite crusts, chimneys and nodules. Similarly, Figure 6.19 shows the different  $^{18}\text{O}$ -fractionation equations defined for dolomite for the same temperature and pore water oxygen isotopic compositions as in Figure 6.20 ranging from -2 to +3‰ SMOW.

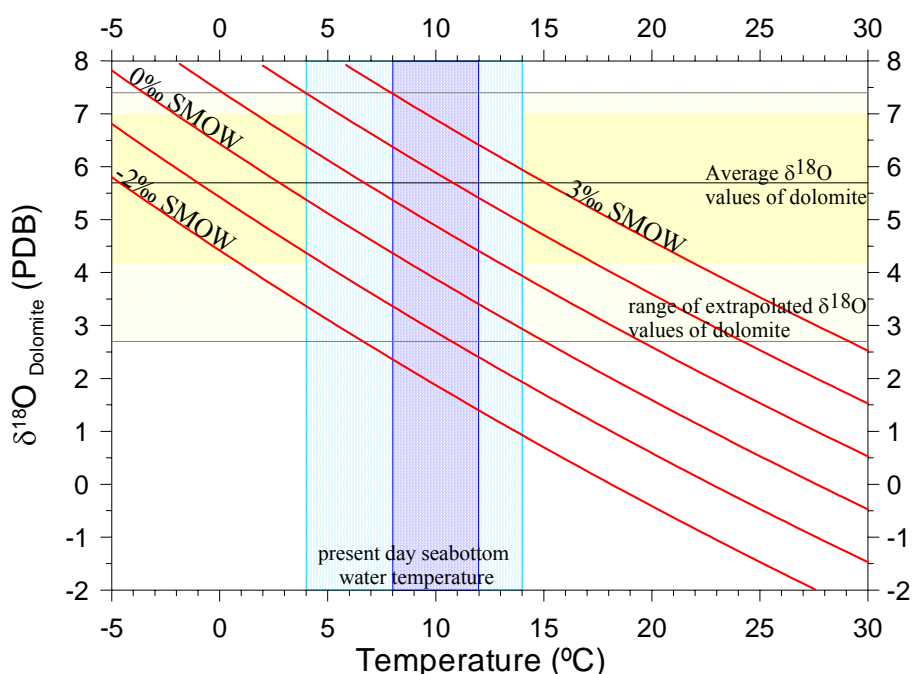


**Figure 6.20.** Plot showing the relation between oxygen isotope composition estimated for dolomite and temperature of precipitation, for oxygen isotope composition of seawater of -2, -1, 0, 1, 2, and 3‰ vs. SMOW. The relation is based on the equation given by Vasconcelos *et al.*, (2005).

From these plots it is possible to conclude that the average oxygen isotopic value of dolomite ( $\delta^{18}\text{O}$  of 5.7‰ PDB) can be explained by precipitation in isotopic equilibrium at the lower limit of present day seawater temperature (8°C) from a pore water with a normal or close to normal isotopic composition (1.3‰ SMOW), that is in the range of the isotopic composition of pore waters collected from some of the mud volcanoes (0.5 to 1.5‰ SMOW) from the Gulf of Cadiz (Mazurenko *et al.*, 2002). If the precipitation of the dolomite is considered to occur during glacial periods, with lower seabottom water

temperatures (down to 4°C) then the isotopic composition of the pore fluids can reach normal seawater composition of (0.3‰) close to 0‰ SMOW (Table 6.5).

The minimum values of dolomite isotopic composition (lower value of 2.7‰ PDB) cannot be explained by precipitation in isotopic equilibrium with normal seawater oxygen isotopic composition, even considering a wider temperature range up to 14°C. To precipitate dolomite with 2.7‰ PDB from normal seawater (as low as 0‰ SMOW) would require a temperature of more than 16°C, a value that is unlikely to occur at these water depths. These extreme low values of dolomite are thus interpreted as precipitation from slightly <sup>18</sup>O-depleted pore water -2.7 to -0.2‰ SMOW considering respectively temperatures of 4°C or 14°C. The more probable explanation for this depleted <sup>18</sup>O pore waters, as similar to the minimum limit of the calcite isotopic composition, is the result of dolomite precipitation from residual waters formed during the crystallization of gas hydrates.

**Table 6.5.** Dolomite crusts, chimneys and nodules estimated isotopic composition of seawater or pore fluid from which the end-members calcite and dolomite had precipitated considering several temperature values.

Dolomite crusts, chimneys and nodules						
Seawater or pore fluids isotopic composition			(‰ SMOW)	(‰ SMOW)	(‰ SMOW)	(‰ SMOW)
			T = 4°C	T = 8°C	T = 12°C	T = 14°C
Calcite	Minimum	-1.6‰ PDB	-3.8	-2.9	-1.8	-1.5
	Average	1.4‰ PDB	-0.8	0.15	1.0	1.5
	Maximum	5.0‰ PDB	2.8	3.8	4.6	5.1
Dolomite	Minimum	2.7‰ PDB	-2.7	-1.7	-0.7	-0.2
	Average	5.7‰ PDB	0.3	1.3	2.3	2.8
	Maximum	7.4‰ PDB	2.0	3.0	4.0	4.4

**Note:** Seawater pore fluids composition in blue are interpreted as residual waters formed during the crystallization of methane hydrates; Seawater pore fluids composition in green are interpreted as normal seawater compositions; Seawater pore fluids composition in red are interpreted as resulting from the destabilization of gas hydrates.

An extrapolated pure phase dolomite end-member maximum limit value of 7.4‰ PDB, (very close to the measured bulk values of several samples) can not be explained by precipitation under present day temperature conditions from a pore water fluids with normal or close to normal oxygen isotopic composition. Considering that seawater temperatures inferior of 4°C are not probable to occur in this area, such high  $\delta^{18}\text{O}$  dolomite values can only be explained by precipitation from <sup>18</sup>O-enriched fluids, ranging from 2 to 4‰ SMOW (Table 6.5), under temperatures ranging from 4 to 14°C (respectively). As interpreted for the heavier calcite values, such <sup>18</sup>O-enriched pore water fluids are

interpreted as resulting from the destabilization of gas hydrates, as it corresponds to typical reported isotopic values of pore waters resulting from the destabilization of gas hydrates (Hesse and Harrison, 1981; Davidson *et al.*, 1983; Jenden and Gieskes, 1983).

### 6.5.2.3 Dolomite crusts, chimneys and nodules carbonates

The observed average difference between the estimated isotopic compositions of the pure calcite and pure dolomite end-members (reported in Table 6.4) ranges from 4.2 to 4.7‰ (PDB). These values are clearly higher than the theoretical values expected according to the isotopic fractionation factors ( $\Delta^{18}\text{O}_{\text{dol-cal}}$ ) of 3.10‰ (at 4°C) and 2.98‰ (at 14°C), as defined by the Vasconcelos *et al.*, (2005) dolomite oxygen isotope fractionation equation (6.28) with the Kim and O'Neil (1997) proposed equation (6.16) for calcite. The large observed difference between the estimated and the theoretical equilibrium isotopic fractionation factors indicate that both minerals have not precipitated in isotopic equilibrium. According to the petrographic and XRD observations two different calcite phases can be distinguished: a pelagic calcite from the calcareous nanofossils and foraminifera shells; and an authigenic calcite that composes the cement with dolomite, proto-dolomite and high Mg-calcite (Figure 5.8.B). It is so to be expected that the dolomite phase and the pelagic calcite would not have been precipitated in isotopic equilibrium. Because the amount of pelagic  $\text{CaCO}_3$  of the background sediment is on average 34 wt% (Section 5.4, Table 5.1) the calculated isotopic composition of the calcite and high Mg-calcite estimated through the EDTA technique is strongly influenced by the pelagic calcite signal. Therefore, the estimated average oxygen isotopic composition value of the calcite end-member of 0.98 and 1.44‰ (PDB) is reflecting the larger amount of calcite of pelagic origin, like the foraminifera and coccolith shells precipitated from normal seawater.

The authigenic calcite and/or high Mg-calcite that composes the cement, occurs in variable proportions on the samples, and according to the petrographic observations it is expected to be formed in isotopic equilibrium with the dolomite phase and not in equilibrium with the pelagic calcite. The isotopic values of these authigenic calcite phases are interpreted as the ones that are shown to have isotopic compositions that stand away from the average values and that constitutes the extreme and wide range of estimated isotopic values (from -1.6 to + 5.0‰ PDB).

The values of the seawater or pore fluids from which the mineral has precipitated,

estimated from the average compositions of calcite and dolomite, are very similar, both indicating normal seawater composition.

Low isotopic value compositions of calcite and dolomite end-members indicate formation from pore fluids with  $^{18}\text{O}$ -depleted isotopic compositions, considering the same temperatures (-1.5‰ SMOW for calcite and -0.2‰ SMOW for dolomite), and are interpreted as precipitating from residual waters formed during the crystallization of methane hydrates.

Maximum estimated values for seawater or pore fluids from which the minerals precipitated were estimated from the maximum isotopic values of calcite and dolomite end-members, and for similar temperatures, correspond to similar seawater isotopic compositions (2.8‰ to 5.1‰ SMOW for calcite and 2.0 to 4.45‰ SMOW for dolomite). This is interpreted as precipitation from pore fluids formed during the destabilization of methane hydrates.

It should be noted that there is a significant difference of about 1‰ SMOW for the estimated pore fluids isotopic composition from with the calcite and dolomite precipitated. This difference was already been shown (in section 6.4.1.1) as revealed by the difference between the isotopic fractionation factors of the two end-members, pure calcite and pure dolomite (4.2‰ PDB), which is larger than the theoretical value of 3.1‰ PDB. Partially this difference can be explained by the presence of two end-members in the calcite faction, (as discussed in section 6.5.2): (1) the pelagic calcite, composed by the detrital carbonate and foraminifera and coccolith tests, that corresponds to a formation in isotopic equilibrium with normal seawater composition; and (2) the authigenic calcite that should have formed in isotopic equilibrium with the dolomite. Alternatively, this difference can also be interpreted as reflecting a larger range of  $\delta^{18}\text{O}_w$  compositions for calcite and more restricted optimal conditions favourable for dolomite precipitation. This is interpreted as an indication of a relatively large variability of the fluid composition during the sample formation and a different time and/or different fluid composition during the formation of the different authigenic carbonates. As already seen in chapter 5, section 5.5.1) dolomite, compared to the calcite and Mg-calcite, is expected to precipitate under more restricted geochemical environments (high alkalinity and low  $\text{SO}_4^{2-}$  environment conditions). The oxygen isotopic data is interpreted as indicating more restricted pore water compositions than the calcite precipitation. As illustrated in Figure 6.21, the minimum  $\delta^{18}\text{O}_w$  pore fluids

composition from which calcite is precipitating from is estimated to be more  $^{18}\text{O}$ -depleted (by about 1‰ SMOW) than for the minimum  $\delta^{18}\text{O}_w$  pore fluids composition from which dolomite is precipitating from. The maximum  $\delta^{18}\text{O}_w$  pore fluids composition for calcite precipitation indicates a heavier oxygen isotopic values than for dolomite.

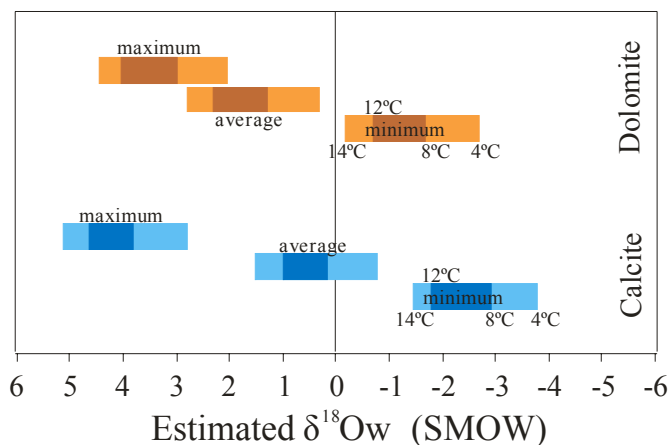


**Figure 6.21.** Plot showing the dolomite crusts, chimneys and nodules estimated average and extreme limit values of the isotopic composition of seawater or pore fluid from which the end-members calcite and dolomite had precipitated.

### 6.5.3 Paleo-temperatures and fluid composition on aragonite pavements

Aragonite pavement samples (Figure 6.13) reveal a linear correlation between the aragonite/calcite ratio and the  $\delta^{18}\text{O}$  values. Deviations of the  $\delta^{18}\text{O}$  values in bulk samples of the aragonite pavements are, to some extent, related to the respective mineral compositions and result from the different fractionation processes associated with the formation of low Mg-calcite, high Mg-calcite and aragonite. Calcite and aragonite precipitation from pore waters with different oxygen isotopic compositions or at different temperature are discussed in this section.

#### 6.5.3.1 Calcite and high Mg-calcite

The relation between  $\delta^{18}\text{O}$  of calcite, temperature and oxygen isotope composition of waters, from which calcite had precipitated, evaluated by the Kim and O'Neil (1997) equation is illustrated in Figure 6.22, with oxygen isotope composition of waters ranging from -2 to +3‰ SMOW. Figure 6.23 illustrates the different temperature  $^{18}\text{O}$ -fractionation equations defined for calcite and for Mg-calcite and the extrapolated range of  $\delta^{18}\text{O}$  values of the calcite end-member phase of the aragonite pavements, assuming oxygen isotope

compositions of the pore water ranging from -2 to +3‰ SMOW.

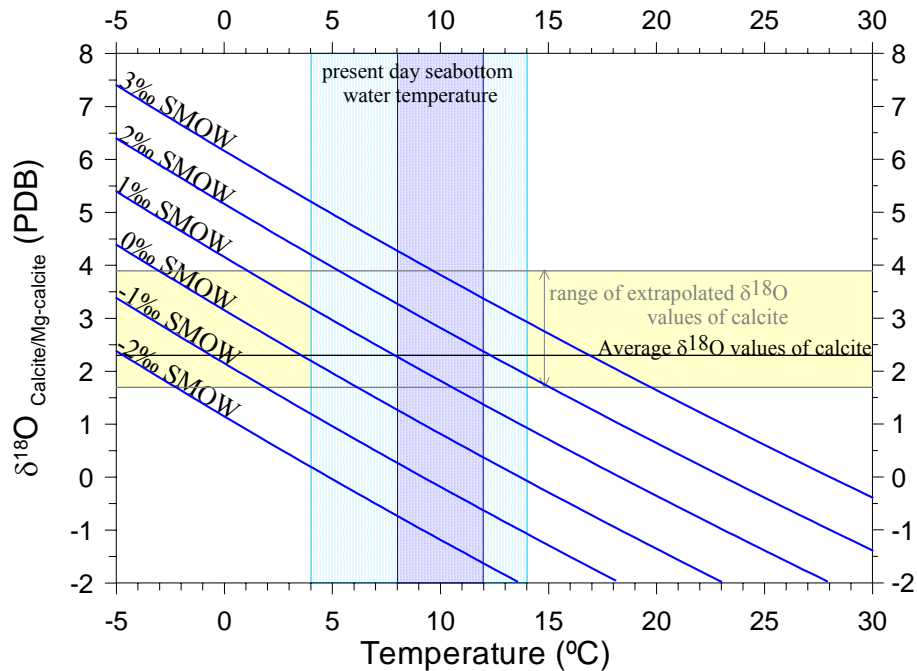


**Figure 6.22.** Plot showing the relation between oxygen isotope composition estimated for calcite and/or high Mg-calcite in aragonite pavement samples and temperature of precipitation with oxygen isotope composition of seawater are -2, -1, 0, 1, 2, and 3‰ vs. SMOW. The relation is based on the equation given by Kim and O'Neil (1997).

From Figure 6.22 and Figure 6.23, it is evident that the extrapolated average oxygen isotopic values of the end-member calcite (2.3‰ PDB) can be explained by the precipitation from normal seawater composition (0-1.5‰ SMOW) with temperature up to 10°C, considering low Mg-calcite as dominant over high Mg-calcite. This would imply that for temperatures of 11.48 °C (Gardner *et al.*, 2001) or 12.30°C (Kopf *et al.*, 2004) measured at the seafloor on the Hesperides MV, where aragonite pavements were retrieved from, the calcite end-member measurements, ranging from 2.8 to 4.0‰ PDB, values higher than the average value (2.3‰ PDB), this would imply a precipitation from <sup>18</sup>O-enriched pore water with a composition of at least 1.81‰ SMOW. This would require that the precipitation of calcite with the estimated average isotopic composition had precipitated from slightly <sup>18</sup>O-enriched pore waters or precipitated at lower ambient temperatures than the present day seabottom temperatures. However, some samples have significant amounts of high Mg-calcite in their carbonate composition, and one of the samples even has 4% of dolomite in the bulk composition (Chapter 5, Table 5.1). Alternatively, the presence of Mg-calcite can justify the apparent <sup>18</sup>O disequilibrium. According to Figure 6.23 the precipitation of calcite with δ<sup>18</sup>O values of 2.3‰ PDB can be

precipitated from normal seawater composition ( $\delta^{18}\text{O}_w$  from 0 to 1.5‰ SMOW) at the present day seabottom temperatures (4-10°C).

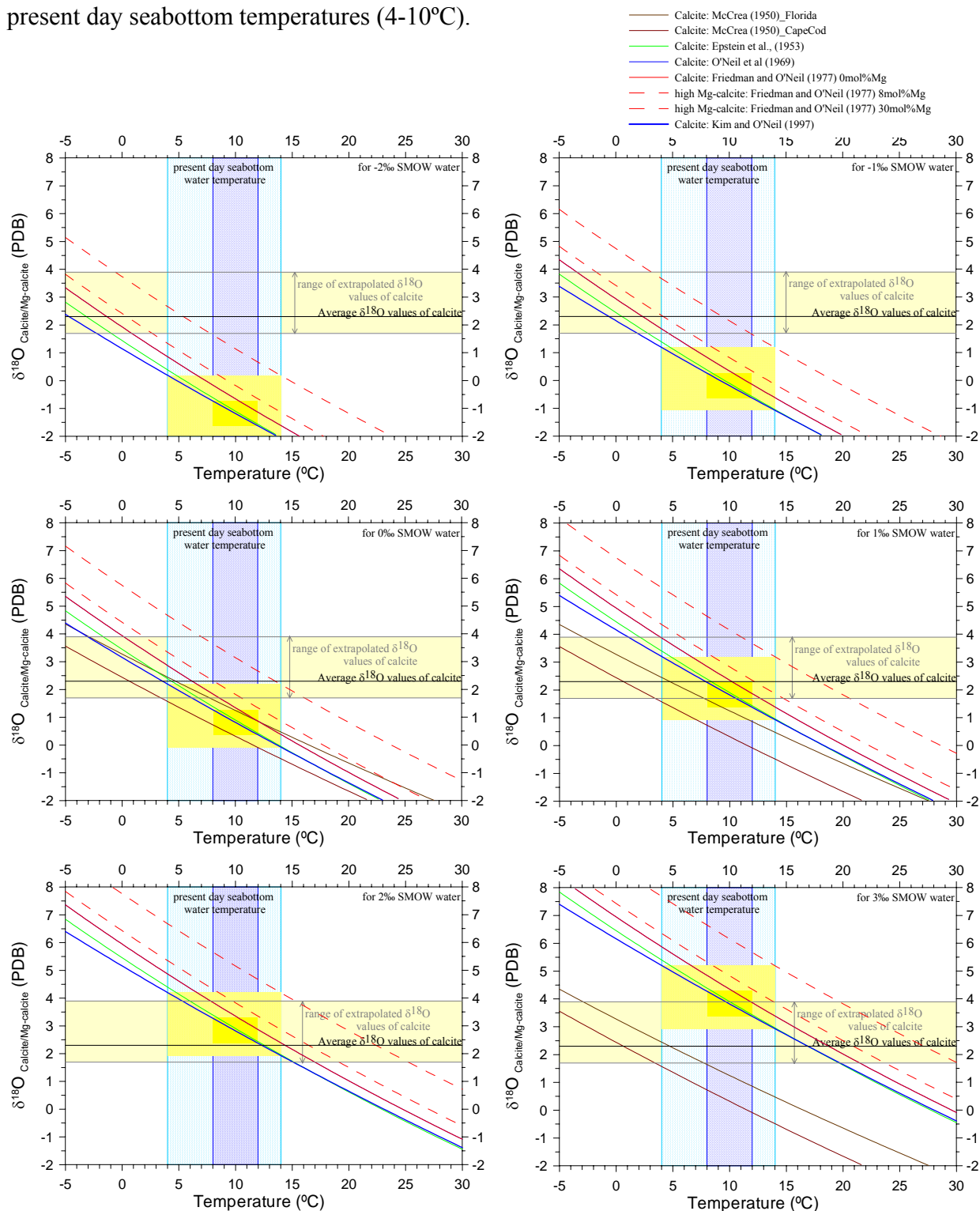


**Figure 6.23.** Different  $^{18}\text{O}$ -fractionation equations defined for calcite and Mg-calcite and the extrapolated range of  $\delta^{18}\text{O}$  values of the aragonite pavements for different oxygen isotope compositions of water -2 to +3‰ SMOW. Also shown in the plots the present day temperature range at the sites where the MDAC were collected.

The simultaneous occurrence of high Mg-calcite and calcite is a factor that can in some degree explain the oxygen isotopic variability of the estimated composition of the end-member calcite. However, the variability in the mineralogy composition does not totally explain the extreme minimum and maximum values estimated for the calcite end-member composition. The minimum value of 1.7‰ PDB estimated for the calcite end-member that corresponds to the estimated isotopic composition for the calcite end-member of sample 88 in Figure 6.13 (collected from Jesus Baraza MV) corresponds to a sample where the low Mg-calcite to high Mg-calcite is of about 1/1. Although no temperature measurements were collected at the Jesus Baraza MV it is assumed that it is within the temperature range of 8 to 12°C. As such, the calcite end-member  $\delta^{18}\text{O}$  value can be explained by precipitation from normal seawater under the present day ambient temperatures (Table 6.6 and Figure 6.22).

Given that temperatures inferior to 4°C are very improbable to occur, even considering glacial periods and with changes in the MO pathways and their absence at the sampling locations, the maximum limit value of 3.9‰ PDB on some samples can only be explained by precipitation from heavier pore waters. Alternatively, the maximum limit values of 3.9‰ PDB of some samples could be explained by precipitation from normal pore waters ( $\delta^{18}\text{O}_w$  up to 1‰ SMOW), if the mineralogy were composed with large dominance of high Mg-calcite with high amounts of mol% of Mg. Nevertheless, this is not the case for all the samples. Sample c.a. 106, shows the maximum estimated  $\delta^{18}\text{O}$  value of 3.9‰ PDB was collected at the Hesperides MV and is composed of calcite 18% wt% (with 3.4% mol% Mg) and high Mg-Calcite 20% wt% (with 13% mol% Mg). Mass balance calculations would require a pore water isotopic composition  $\geq 1.0$ ‰ SMOW and ambient temperature  $\leq 4$ °C (very inferior to the measured temperatures 11.48°C and 12.30°C) to be able to precipitate a 1:1 mixture of calcite:high Mg-calcite with a isotopic composition of 3.9‰ PDB. Considering an ambient temperature of 8°C a pore water with oxygen isotopic composition  $\geq 2.0$ ‰ SMOW would be required to precipitate a 1:1 mixture of calcite:high Mg-calcite with a isotopic composition of 3.9‰ PDB. Considering an ambient temperature of 12°C a pore water with oxygen isotopic composition  $\geq 2.8$ ‰ SMOW would be required to precipitate a 1:1 mixture of calcite:high Mg-calcite with a isotopic composition of 3.9‰ PDB. Therefore, the maximum limit values (3.9‰ PDB) of this sample is interpreted as resulting of the precipitation from  $^{18}\text{O}$ -enriched pore waters, with  $\delta^{18}\text{O}_w$  of at least 2.0‰

SMOW. As similar to the calcite and dolomite in the dolomite crusts, nodules and chimneys (section 6.5.2), the heavier pore water composition ( $\delta^{18}\text{O}_w \geq 2.0\text{‰}$  SMOW) is interpreted as resulting from the destabilization of gas hydrates, as it corresponds to typical reported isotopic values of pore waters resulting from the destabilization of gas hydrates (Hesse and Harrison, 1981; Davidson *et al.*, 1983; Jenden and Gieskes, 1983).

### 6.5.3.2 Aragonite

The oxygen isotopic fractionation equation of Bohm *et al.*, (2000) defined for aragonite is illustrated in Figure 6.25 for pore waters with isotopic compositions ( $\delta^{18}\text{O}_w$ ) ranging from -2 to 4‰ SMOW. The expected temperature range and the calculated isotopic composition of the pure end-member aragonite phase ( $\delta^{18}\text{O}_{\text{arg}}$ ) are also plotted. In Figure 6.24 are also plotted the other oxygen isotopic fractionation equations defined for aragonite and the same pore waters compositions range, temperature and pure phase aragonite end-member calculated compositions as in Figure 6.25.

From Figure 6.24 and Figure 6.25 it is evident that the extrapolated average value of the pure aragonite end-member (4.2‰ PDB) can be explained by precipitation from normal seawater, with isotopic compositions ranging from 0 to 1.5‰ SMOW only for ambient temperatures inferior to 7.8°C. Present day temperature values collected from places where aragonite pavements were collected indicate higher temperatures (11-12°C). Therefore, the extrapolated average value of the pure aragonite end-member can reflect precipitation during colder periods most probably when the MO was absent from the sites where the aragonite pavements are found and the ambient water was at least 4 °C colder than today. Alternatively these aragonite composition can be reflecting precipitation from  $^{18}\text{O}$ -enriched pore waters. Considering the calculated  $^{18}\text{O}$ -enriched pore waters during the precipitation of calcite mineralogy in the aragonite pavements, and considering the petrographic and textural characteristics of the aragonite pavements that indicate that the precipitation of the authigenic carbonates occurred very close or at the seafloor, where the seawater ( $\delta^{18}\text{O}_w \sim 0\text{‰}$  SMOW) should clearly dominate, then the hypothesis of precipitation of aragonite from  $\delta^{18}\text{O}$  enriched pore waters, with compositions ranging from 1.1‰ to 2‰ SMOW, is interpreted as the more probable.

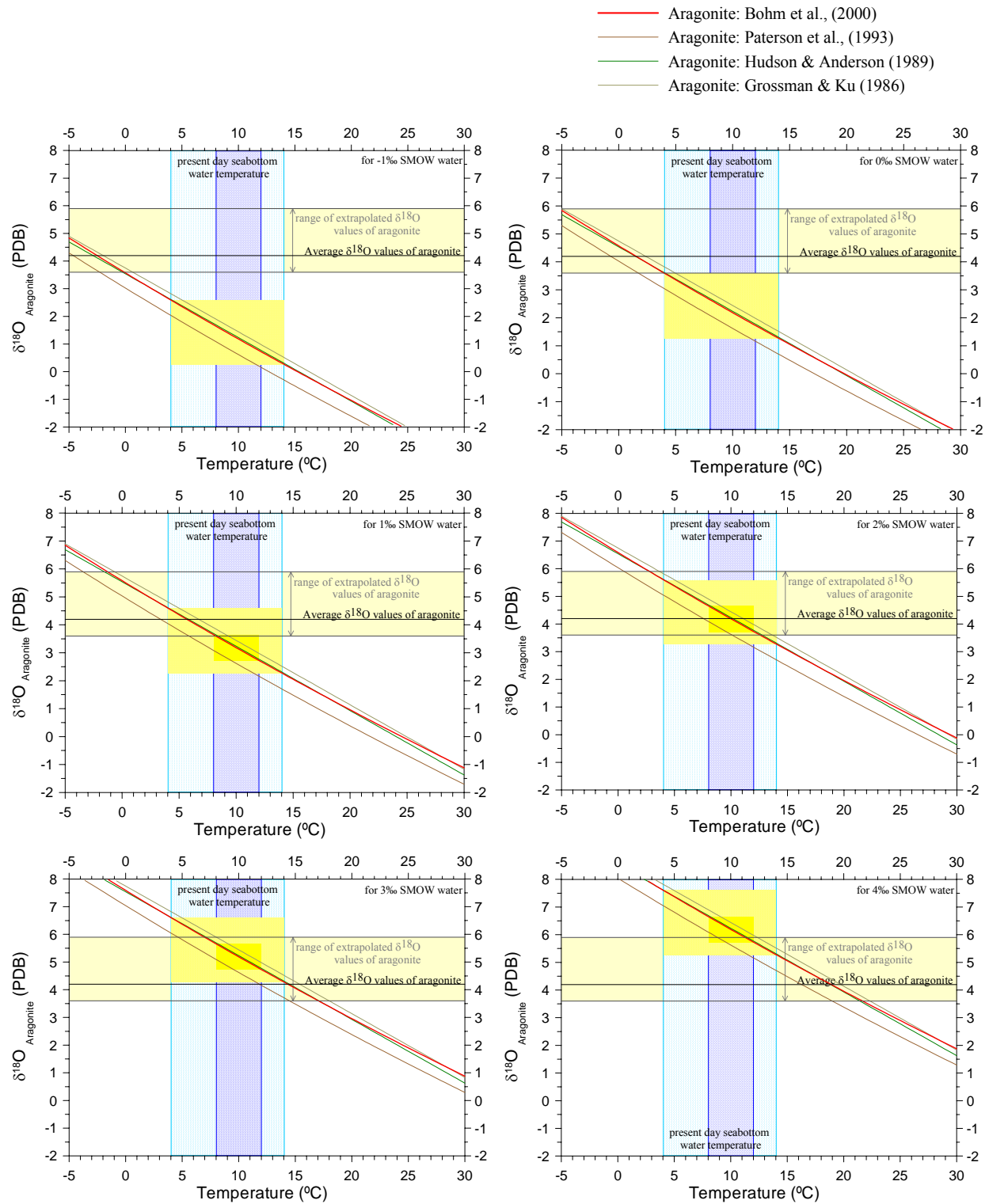


**Figure 6.24.** Different  $^{18}\text{O}$ -fractionation equations defined for aragonite and the extrapolated range of  $\delta^{18}\text{O}$  values of the aragonite pavements for different oxygen isotope compositions of water -2 to +3‰ SMOW. Also shown in the plots the present day temperature range at the sites where the MDAC were collected.

The minimum estimated value for the aragonite end-member ( $\delta^{18}\text{O}_{\text{arag}}=3.6\text{‰}$  PDB) indicates that a  $\delta^{18}\text{O}_w$  of 0‰ SMOW is only possible for temperatures of 4°C. The present day temperature range (8-12°C) suggests aragonite precipitation from pore water with

isotopic compositions in the range from 1.0 to 1.9‰ SMOW.

The maximum estimated value of the aragonite end-member ( $\delta^{18}\text{O}_{\text{arag}}=5.9\text{‰}$  PDB) can only be explained by precipitation from  $^{18}\text{O}$ -enriched pore waters. Even for the lower temperature acceptable for this area ( $4^{\circ}\text{C}$ ) the estimated isotopic compositions of the pore waters have to be significantly enriched (i.e.,  $+0.80\text{‰}$  SMOW). To the more realistic temperature range ( $8\text{-}12^{\circ}\text{C}$ ) the estimated composition of the pore water from which the aragonite precipitates from have compositions between  $3.2\text{‰}$  SMOW and  $4.2\text{‰}$  SMOW (Table 6.6).

As similar to the  $\delta^{18}\text{O}$ -enriched pore waters estimated for the heavier calcites and dolomites in the dolomite chimneys samples (sections 6.5.2.1 and 6.5.2.2) and the heavier calcite in the aragonite pavements (section 6.5.3.1), the enrichment in the heavy oxygen isotope ( $\delta^{18}\text{O}_{\text{w}} \geq 1.1\text{‰}$  SMOW) is interpreted as resulting from gas hydrate dissociation, which yields a cage water with an oxygen isotopic composition of up to  $+3\text{‰}$  SMOW (Hesse and Harrison, 1981; Davidson *et al.*, 1983; Jenden and Gieskes, 1983).

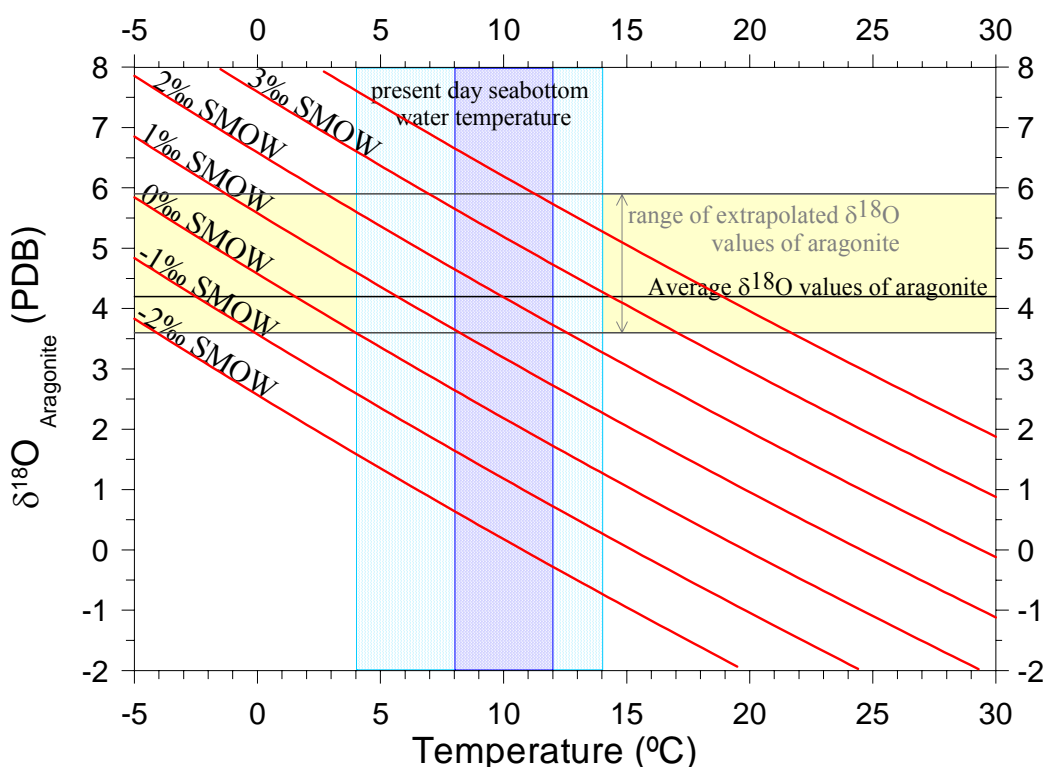


**Figure 6.25.** Plot showing the relation between oxygen isotope composition estimated for pure phase aragonite in aragonite pavement samples and temperature of precipitation with oxygen isotope composition of seawater are  $-2$ ,  $-1$ ,  $0$ ,  $1$ ,  $2$ ,  $3$  and  $4\text{‰}$  vs. SMOW. The relation is based on the equation given by Bohm *et al.*, (2000).

### 6.5.3.3 Aragonite pavement carbonates

The values of the seawater/pore waters from which the carbonate minerals precipitated, as estimated from the average compositions of calcite and aragonite indicate similar formation conditions (Figure 6.26) for both minerals. The estimated minimum oxygen isotopic values of the seawater or pore fluids, from which the pure phase end-members calcite and aragonite precipitated from, indicate a composition close to normal seawater values for the most probable temperature interval considered (more than -0.5‰ SMOW for more than 4°C for calcite and more than 0‰ SMOW for more than 4°C for aragonite). The estimated maximum oxygen isotopic values of the seawater or pore fluids from which the pore phase end-members calcite and aragonite had precipitated indicate  $^{18}\text{O}$  enriched pore fluids composition, even considering the lower assumed temperature limit of 4°C. This is interpreted as indicating (especially for aragonite) a precipitation from pore fluids formed during the destabilization of methane hydrates. The estimated average oxygen isotopic values of the seawater or pore fluids from which the pore phase end-members calcite and aragonite precipitated also indicates that aragonite had precipitated from a more  $^{18}\text{O}$  enriched pore fluid composition than the calcite phase.

An estimated  $\delta^{18}\text{O}$  of pure aragonite end-member mineral yields on average 4.2‰ (PDB), whereas  $^{18}\text{O}$  is strongly lighter in the pure calcite end-member (2.3‰ Figure 6.13). The difference between the two carbonate phases (1.9‰) is larger than the expected value due to the differences in the oxygen isotopic fractionation  $\Delta^{18}\text{O}_{\text{arag-calc}}$  value of 1.4‰, according to Figure 6.5. As seen in section 6.5.2.3, as discussed for the apparent non equilibrium between the calcite and dolomite phases in the dolomite crusts, chimneys and nodules, the larger difference (1.9‰) in the isotopic fractionation between calcite and aragonite can be due to the pelagic contribution of the detrital calcite and mainly from the foraminifera and coccoliths tests that represent isotopic compositions in equilibrium with normal seawater compositions and that have the effect of lowering the global isotopic composition of the total calcite phase. Admitting that both mineralogies were precipitated in or close to isotopic equilibrium with the pore fluids from which they precipitated, this implies that the calcite and the aragonite precipitation occurs in slightly different environmental conditions, most probably considerably different temperature and/or  $\delta^{18}\text{O}$  isotopic composition of the pore water fluids. Alternatively, if the effect of the pelagic calcite fraction is ignored, then for the same temperatures, the estimated oxygen isotopic

composition of the seawater or pore fluids from which calcite precipitates from is 0.5 to 0.6‰ (SMOW), more <sup>18</sup>O-depleted than the estimated composition of the pore fluids from which aragonite is precipitated from (Figure 6.26). This is interpreted as one of the reasons for the observed difference of 1.9‰ PDB (Figure 6.13) between the calcite and aragonite isotopic fractionation factors ( $\Delta^{18}\text{O}_{\text{arag-cal}}$ ) that is higher than the expected theoretical difference of 1.4‰ (PDB) (Section 6.1.4.4, Figure 6.5). Therefore, the precipitation of calcite and aragonite can alternatively be occurring, at similar temperatures but from pore fluids with slightly different oxygen isotopic compositions, with aragonite precipitating from an more <sup>18</sup>O-enriched (0.5 to 0.6‰) pore fluids that the calcite.

**Table 6.6.** Aragonite pavements estimated isotopic composition of seawater or pore fluid from with the end-members calcite and aragonite had precipitated considering several temperature values.

Aragonite pavement samples						
Seawater or pore fluids isotopic composition		(‰ SMOW)	(‰ SMOW)	(‰ SMOW)	(‰ SMOW)	
		T = 4°C	T = 8°C	T = 12°C	T = 14°C	
Calcite	Minimum	1.7‰ PDB	-0.5	0.4	1.3	1.8
	Average	2.3‰ PDB	0.1	1.1	2.0	2.4
	Maximum	3.9‰ PDB	1.7	2.6	3.5	4.0
Aragonite	Minimum	3.6‰ PDB	0.0	1.0	1.9	2.3
	Average	4.2‰ PDB	0.6	1.6	2.5	2.9
	Maximum	5.9‰ PDB	2.3	3.2	4.2	4.6

**Note:** Seawater pore fluids composition in blue are interpreted as residual waters formed during the crystallization of methane hydrates; Seawater pore fluids composition in green are interpreted as normal seawater compositions; Seawater pore fluids composition in red are interpreted as resulting from the destabilization of gas hydrates.

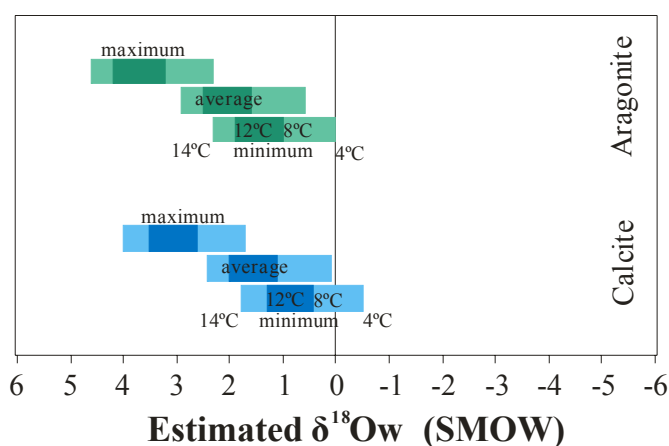


**Figure 6.26.** Plot showing the aragonite pavements estimated average and extreme limit values of the isotopic composition of seawater or pore fluid from with the end-members calcite and aragonite had precipitated.

As described in section 5.1.4, the aragonite pavement samples present several lithologic, textural and mineralogical indicators that suggest the influence of gas hydrates on the formation of these MDAC samples. The stromatolitic fabric, the presence of botryoidal textures composed of almost pure aragonite mineralogy, both infilling megapores and cavities are interpreted as resulting from aragonite precipitation in association with gas hydrates, similar to the descriptions of several other cold seeps MDAC (Bohrmann *et al.*, 1998; Greinert *et al.*, 2001). The structure of the intraformational breccias is interpreted as resulting from gas hydrate growth and decomposition, mechanism interpreted to be the responsible for the collapse and breccification of pre-existing crusts and pavements. Subsequent re-cementation produced the intraformational breccias. Both these evidences support the interpretation that the oxygen isotopic composition of the carbonates reflects, at least for some samples, the influence of gas hydrates decomposition on the formation of calcite and specially aragonite authigenic minerals of the aragonite pavements.

The dominance of aragonite in the matrix, occurring as pure aragonite stromatolitic layers and botryoids, that from the underwater observations that indicate their occurrence at the seafloor (Chapter 8) and the gas hydrate fabrics are interpreted as indicating a near-surface origin of the aragonite pavements. Here, the geochemical conditions with high alkalinity and higher sulphate concentrations stimulate aragonite precipitation (Burton, 1993; Savard *et al.*, 1996). The high alkalinity is interpreted as resulting from high methane oxidation rates, consequence of high methane concentrations from gas hydrate destabilization and high sulphate concentration from the intense seawater ventilation. Calcite formation is favoured at relatively lower alkalinity and lower sulphate concentrations, indicating an intra-sediment environment, with  $^{18}\text{O}$ -enriched pore water. Such conditions are suggested to be present after the decomposition of gas hydrates or in methane rich sediments, in a less ventilated environment as in intra-sediment environment where the sulphate has been partially consumed for the oxidation of the hydrate-methane via sulphate reduction and is not restored. If this mechanism evolves to a more confine system, most probably at a micro environmental scale, in consequence of the progressive cementation, it can lead to the total sulphate consumption and in cases of high alkalinity, probably after significant Ca removal during intense calcite and aragonite precipitation, these conditions can lead to the precipitation of high Mg-calcite or even to dolomite, in the

aragonite pavements. The presence of minor amounts of dolomite (4.4% of the total carbonate phase) in sample 3611-A01.92, can be interpreted as reflecting this mechanism.

#### 6.5.4 Comparison of aragonite pavements and dolomite crusts, chimneys and nodules

Comparing the estimated oxygen isotopic composition of the pore fluids from which the dolomite crusts, chimneys and nodules and the aragonite pavements probably formed (Figure 6.27) it is possible to infer that they formed in slightly different conditions.

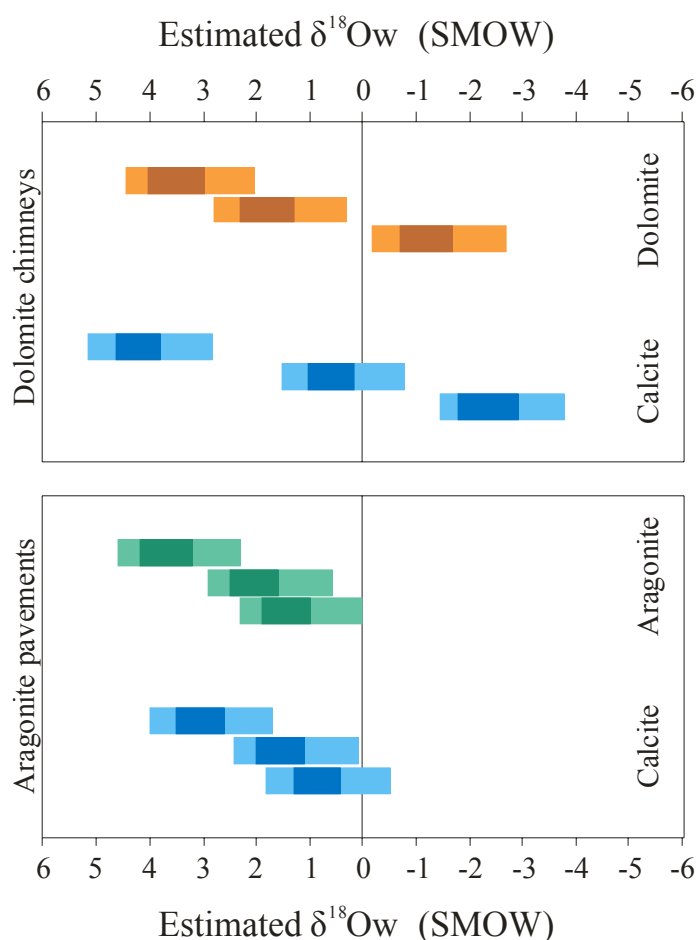


**Figure 6.27.** Plot comparing the estimated average and extreme limit values of the isotopic composition of seawater or pore fluid from which the end-members calcite – aragonite and calcite - dolomite had precipitated on the aragonite pavement samples (bottom frame) and the dolomite crusts, chimneys and nodules (top frame).

The dolomite chimneys formed in wider isotopic conditions, while the aragonite pavements were formed in more restricted  $^{18}\text{O}$  pore waters. Aragonite pavements were formed within pore water conditions close to normal seawater oxygen isotopic

compositions or from a  $^{18}\text{O}$ -enriched pore waters indicating a contribution from dissociated gas hydrates. The dolomite chimneys indicate similar normal seawater conditions, pore waters resulting from the destabilization of gas hydrates and precipitation from pore waters during gas hydrates formation. The smaller interval of variation of the estimated pore water composition of the aragonite pavements is interpreted as reflecting the more proximal and intense influence of seawater. The larger interval of variation of the estimated pore water composition of the dolomite chimneys is interpreted as reflecting a more distant and confined environment where the pore waters are able to evolve and differ more intensely away from the normal seawater isotopic composition.

## 6.6 Conclusions

Considering the present day temperature (ranging from 8 to 12 °C) and the extreme limits for temperature variation, considering the oxygen isotopic composition of the Gulf of Cadiz bottom water both for the NADW and the MO, and assuming that the oxygen isotopic ratio variations are the typical between glacial and interglacial stages, within the range from +0.5 to +1.5‰ SMOW, the isotopic composition of the original fluids from which the carbonates were precipitated were estimated according to the different mineral temperature of precipitation equations. Considering the minimum and maximum temperature limits, admitted to be possible to occur at these sites, not all the measured carbonate isotopic values are compatible with precipitation from normal seawater isotopic composition.

Aragonite pavements are estimated to be formed from normal seawater oxygen isotopic compositions and from a  $^{18}\text{O}$ -enriched pore waters indicating a contribution from dissociated gas hydrates. The aragonite pavement samples indicate a formation in environments near or at the sediment seawater interface, while the dolomite chimneys indicate a formation in more confined within the sediment column. The dolomite chimneys indicate formation conditions similar normal seawater and destabilization of gas hydrates but they also indicate precipitation from pore waters during gas hydrates formation.

The  $^{87}\text{Sr}/^{86}\text{Sr}$  ratios of the analyses of authigenic carbonates do not indicate a clear and major addition of Sr from deep seated fluids, but they preferably reflect the

contemporaneous seawater Sr composition. This is evident on the aragonite pavement and on the dolomite crust Sr isotopic signals. The dolomite chimney sample indicate signal that supports a contribution from a deeper seated fluids and/or an older seawater origin.



## **Chapter 7. U/Th Ages of dolomite chimneys from the Gulf of Cadiz: record of intense past fluid escape episodes**

### **7.1 Introduction**

The high abundance of fluid escape structures in the Gulf of Cadiz, expressed as mud volcanoes, mud diapirs, pockmarks, active seepage, modern and fossil cold seepage recorded by the precipitation methane-derived authigenic carbonates (MDAC), is an indicator that fluid seepage has been an active process in this area in the present and past geological record (e.g. Somoza *et al.*, 2002; Díaz-del-Río *et al.*, 2003; Magalhães *et al.*, 2003; Pinheiro *et al.*, 2003; Somoza *et al.*, 2003; Magalhães *et al.*, 2004; Rensbergen *et al.*, 2005).

Several hydrocarbon-rich fluid seepage indicators can be considered in the geologic record. Amongst those indicators, the more important are the MDAC that typically exhibit highly negative carbon isotopic signatures, with  $\delta^{13}\text{C}$  values ranging from -10 to -90‰ VPDB (Vienna Peedee Belemnite), depending on the microbial or thermogenic source origin of the methane. The carbon and oxygen isotopic signals from MDAC recovered from seepage areas are now being extensively used to investigate past fluid escape and episodes of gas hydrate destabilization in marine sediments (Dickens *et al.*, 1995; Hesselbo *et al.*, 2000; Krull and Retallack, 2000; Krull *et al.*, 2000). While there is still a discussion whether the  $\delta^{13}\text{C}$  signature in seep benthic foraminifera really reflects the surrounding pore water composition from which they have precipitated or if it was acquired later, after deposition, during diagenesis (Torres *et al.*, 2003; Martin *et al.*, 2004), the negative  $\delta^{13}\text{C}$  excursions recorded by benthic foraminiferal shells in cold seep sediments have been interpreted as indicating methane release episodes (Hill *et al.*, 2004; Mackensen *et al.*, 2006) some of these, proposed to be related with methane hydrate dissociation (e.g. Dickens *et al.*, 1997; Kennett *et al.*, 2000, 2003). Hydrocarbon seepage is also marked by

chemosynthetic communities like particular species of bivalves, tube worms and bacterial mats that derive their energy from the oxidation of advected reduced elements and/or hydrocarbon compounds (Sibuet and Olu, 1998).

In the Gulf of Cadiz, MDAC occur as seafloor crusts, pavements, build-ups, concretions, and conduit or chimney-like forms, and are associated with seepage of hydrocarbon-rich fluids (mainly methane, as discussed in Chapters 5 and 6). Their formation is triggered by the increase of alkalinity during anaerobic methane oxidation (AOM), coupled with sulphate reduction (SR) (e.g. Hovland *et al.*, 1987; Ritger *et al.*, 1987; Hovland and Judd, 1988; Paull *et al.*, 1992) in a process mediated by microbial activity (Boetius *et al.*, 2000). The mineralogy of these carbonates (aragonite, calcite, Mg-calcite, protodolomite and dolomite) records different geochemical and diagenetic environments during their formation process. In particular, there is clear evidence that the formation of some of these MDAC is associated with the dissociation of gas hydrates (Chapter 6), given the abnormal positive  $\delta^{18}\text{O}$  values of the constituent authigenic carbonate minerals.

Therefore, past fluid flow and gas hydrate formation/dissociation episodes can be reconstructed from the MDAC (e.g. Bohrmann *et al.*, 1998; Greinert *et al.*, 2001). Amongst all the different seepage structures, MDAC are those that probably better record the seepage activity at cold seeps. They can potentially record the fluid flow intensity, whether the fluid flow venting is a continuous process or if it occurs discontinuously, and the timing and age of the seeping episodes. Absolute dating of the MDAC can therefore provide the means for reconstructing the past fluid escape episodes, their frequency and evolution through time. Dating of the MDAC is also essential to constrain the external factors that can actively control the fluid flow and its intensity, such as tectonic events, mass-wasting processes, sea-level variations, gas hydrate formation/destabilisation, and also to assess the potential impact and significance of these processes in global climate change.

Conventional  $^{14}\text{C}$  dating techniques are not applicable to MDAC, as their carbon derives partially from thermogenic, old methane. The most suitable dating technique, also favourable due to its larger time window, is the U/Th dating technique, that was successfully applied to authigenic carbonates from the Hydrate Ridge (Teichert *et al.*, 2003). The  $^{230}\text{Th}$ - $^{234}\text{U}$ - $^{238}\text{U}$  system as also been proven to be adequate for dating a variety

of materials from Late Pleistocene to Holocene age (Broecker, 1963; Broecker *et al.*, 1968). Therefore, U/Th dating was employed here for the age determination of selected samples from MDAC dolomite chimneys from the Gulf of Cadiz.

In the following section, the analytical procedure developed with the objective of date the MDAC samples from the Gulf of Cadiz is described. The analytical processes and the age determination were performed at the IFM-Geomar in Kiel (Germany), during an author visit from October 25<sup>th</sup> to November 06<sup>th</sup> in 2004. The various U/Th dating approaches are also presented in this chapter, and their results discussed with the objective of reconstructing past fluid flow episodes and possible processes that might have controlled the formation of the MDAC.

## 7.2 Materials and methods

### 7.2.1 Samples used

In this work, two MDAC samples (3463-A03 and 3463-A08) were selected for dating (Table 7.1 and Figure 7.2). Both samples were collected by dredging on the Cadiz Channel, to the west of the Iberico mud cone during the TTR11 cruise, station TTR11-AT339D (Kenyon *et al.*, 2002). This sampling site is located on the pathway of the lower core of the Mediterranean Outflow (Figure 7.1.B), which flows in direct contact with the seafloor, producing a strong erosive effect, as discussed in Chapter 4. The selected samples for U/Th analysis belong to the dolomite chimneys type, as defined in Chapter 5. Sample 3463-A03 was taken from a chimney with two parallel cemented conduits with no internal open vent channels and with distinct concentric growth layers around the two cemented conduit axes. Sub-samples for age determination were collected at the centre of each of the conduit axes and in intermediate layers, in order to evaluate if the different axes correspond to separate or the same formation episode. Sample 3463-A08 as taken from a chimney with an open central vent channel, very homogeneous, with no detected concentric growth layers neither any longitudinal textural discontinuity along the chimney. Both samples were selected because of their mineral composition, with more than 65% of carbonate (Dolomite: 54 to 78%; Calcite: 3 to 13%), and because they show little or no oxidation, as revealed by their pale-yellow to pale-grey colours. This is interpreted as indicating that these chimneys were exposed to the seawater during a period of time not

long enough to produce their oxidation and consequently they should not have been affected by significant secondary alteration processes, and therefore their formation processes should be more preserved.

**Table 7.1.** MDAC samples used for U/Th dating.

Sample	Sub-sample	Location	Latitude (N)	Longitude (W)	Water depth (m)	Type (Chapter 5)
3463-A08	1	top, periphery	36° 07.591'	-7° 46.587'	1021	Dolomite
	2	top, intermediate				chimney, 2
	3	top, centre				conduits,
	4	middle, intermediate				medium
	5	bottom, intermediate				
3463-A03	6	Periphery channel 1	36° 07.591'	-7° 46.587'	1021	Dolomite
	7	Centre channel 1				chimney, low
	8	Intermediate				oxidation, open
	9	Periphery channel 2				vent channel
	10	Centre channel 2				

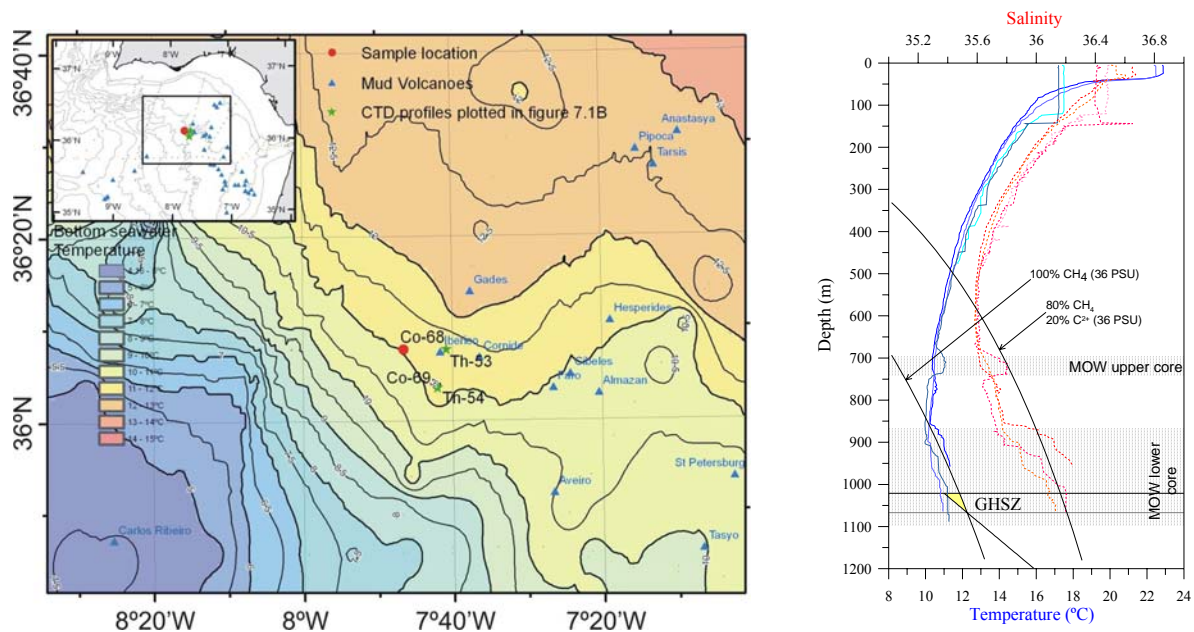


**Figure 7.1.** (A) Sample location and seabottom water temperature grid, calculated based on the deepest measurements from the CTD (stations Co-68 and Co-69 acquired during the winter at the same positions of the equivalent summer stations: Th-53 and Th-54) database from the CANIGO project (Ambar *et al.*, 2002). (B) CTD profiles closer to the sampling site, are plotted over the P-T stability domain of gas hydrates. To be noted that the sampling location are bathed by the lower core of the Mediterranean Outflow (MOW) with a temperature of 11°C, but the seasonal variations on the temperature values close to the seafloor are in the order of magnitude of 0.5°C to 1°C; therefore, the gas hydrate stability zone (GHSZ) plotted in the graph represents the temperature in winter conditions and it can be significantly reduced or even null during part of the year. In red are plotted the salinity profiles and in blue the temperature profiles.

From each sample, 5 sub-samples were collected by hand-drilling until ca. 29 to 36 mg of powder carbonate were obtained. The sub-samples were collected in order to define radial and longitudinal profiles along the chimneys (as illustrated in Figure 7.2). The powder material was treated for U/Th analysis according to the analytical procedures described in section 7.2.3.

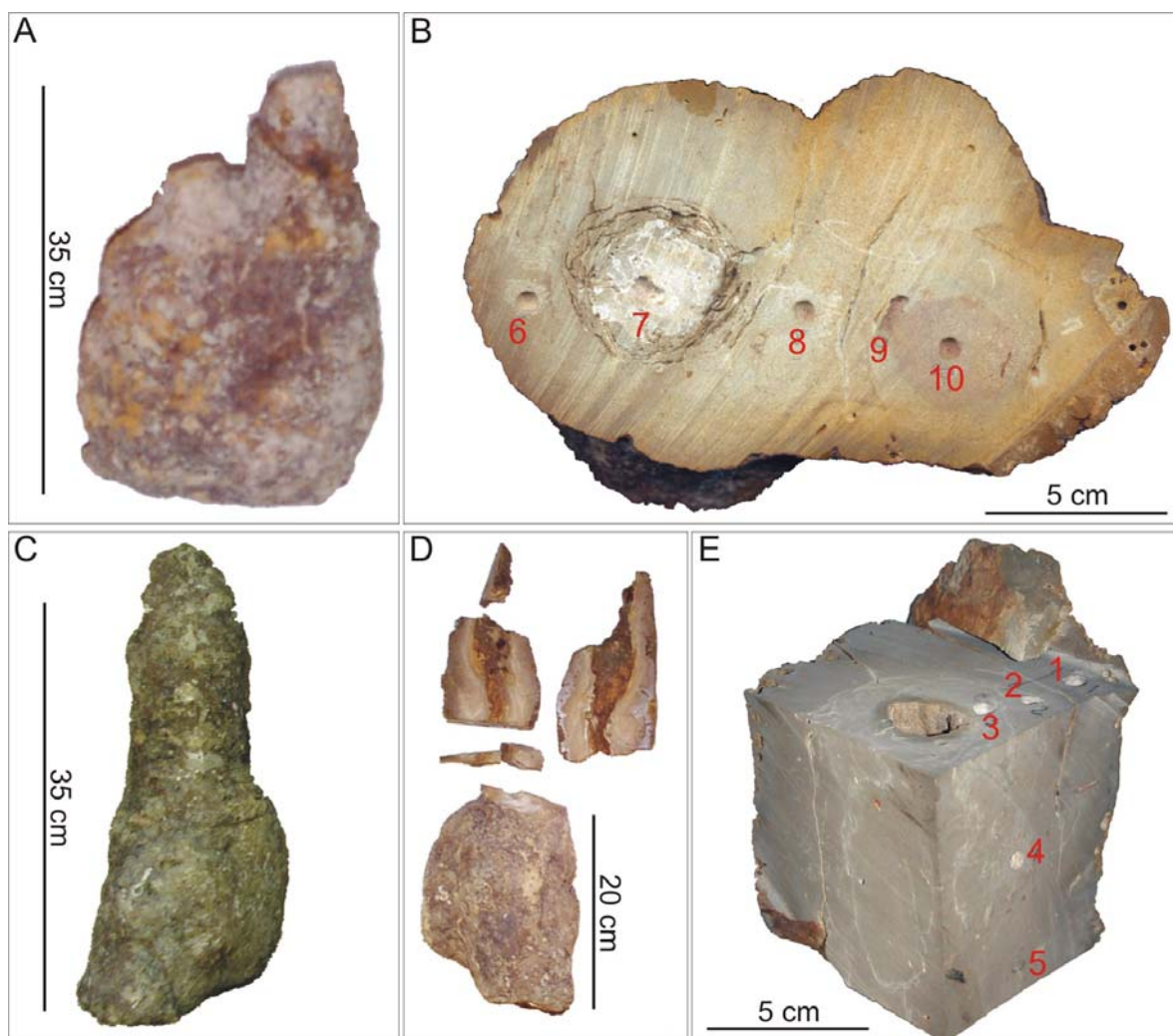


**Figure 7.2.** Samples analysed for U/Th age determination. (A) and (B): sample 3463-A03. (C), (D) and (E): sample 3463-A08. Numbers in (B) and (E) represent locations of analysed sub-samples collected with a hand micro-drilling.

## 7.2.2 Petrography, mineralogy and geochemistry of the authigenic carbonates

### 7.2.2.1 Petrography of the two dolomite chimneys

The two samples analysed for age determination have distinct petrographic characteristics. While sample 3463-A03 corresponds to a cemented sand-siltstone (Figure 7.3) with the detrital fraction being composed by sand to silty dominated terrigenous matrix and abundant bioclasts, sample 3463-A08 corresponds to a mud-wackstone with a detrital fraction composed mainly by clay fraction. Therefore, sediments that were on the origin of sample 3463-A03 have higher initial porosity and therefore higher initial permeability; the sample 3463-A08 has lower initial porosity and lower permeability.

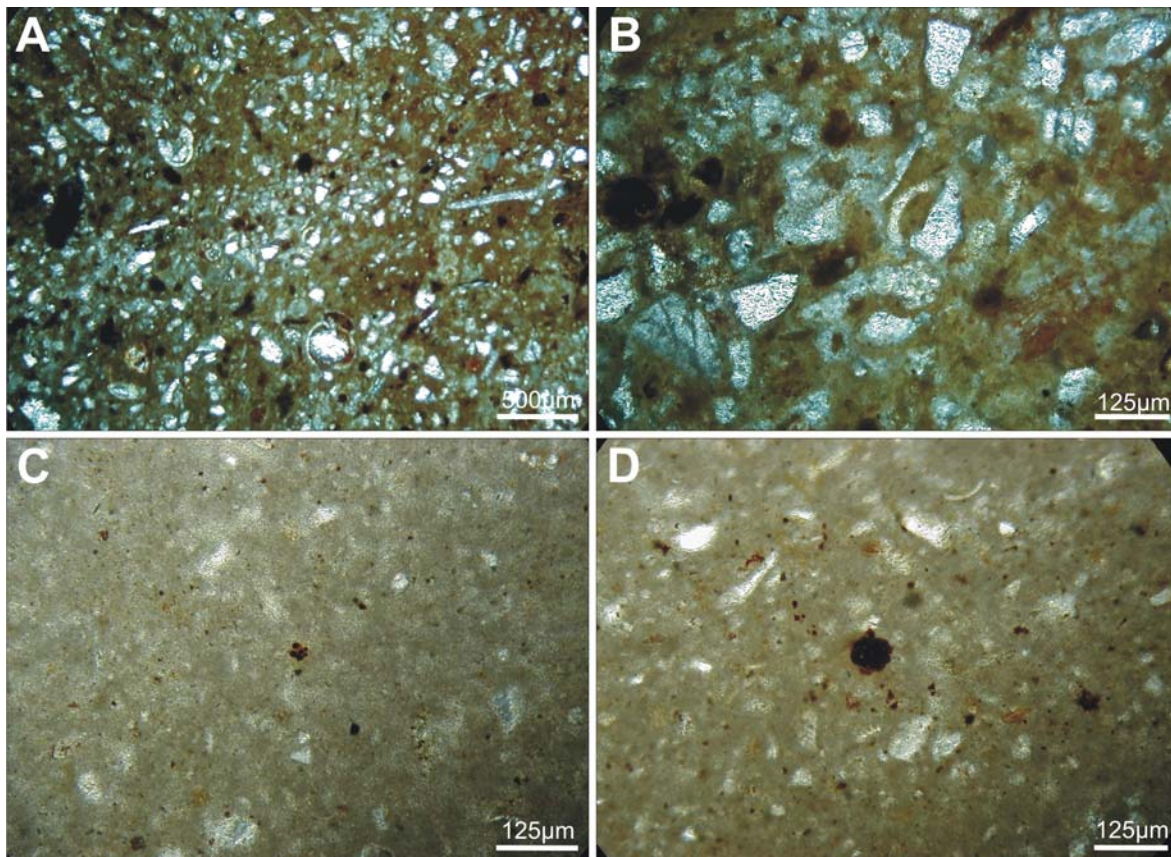


**Figure 7.3.** Thin section photomicrographs of dolomite chimney 3463-A03 (A and B) and sample 3463-A08 (C and D) where it is evident that sample 3463-A03 have a sand size grain supported texture while sample 3463-A08 that corresponds to a mudstone/wackstone have a cement/clay matrix supported texture. Therefore the initial permeability of sample 3463-A03 is much higher than sample 3463-A08.

### 7.2.2.2 XRD results

Semiquantitative abundance of the carbonate phases and mineralogical composition of the analysed samples was determined by X-ray diffraction (XRD) at the ETH Centre in Zurich, according to the methodology described in chapter 5, section 3. Their results are shown in Table 7.2. The detrital phase, reported in Table 7.2, consists of quartz, clay minerals and feldspars.

**Table 7.2.** Mineralogy and detrital fraction present in the analysed samples. See Figure 7.1 for location.

Sample	Sub-sample	Arag (%)	Calc (%)	Mg-calc (%)	Protodolomite (%)	Dolomite (%)	Detrital (%)
3463-A08	1	0.0	8.6	0.0	0.0	72.6	18.8
	2	0.0	10.5	0.0	0.0	72.8	16.7
	3	0.0	14.6	0.0	0.0	68.4	17.0
	4	0.0	11.9	0.0	0.0	71.3	16.8
	5	0.0	12.6	0.0	0.0	70.6	16.8
3463-A03	6	0.0	8.8	1.0	1.0	53.6	35.6
	7	0.0	2.7	1.9	0.0	78.3	17.2
	8	0.0	11.8	0.0	0.0	55.0	33.3
	9	<i>nm</i>	<i>nm</i>	<i>nm</i>	<i>nm</i>	<i>nm</i>	<i>nm</i>
	10	<i>nm</i>	<i>nm</i>	<i>nm</i>	<i>nm</i>	<i>nm</i>	<i>nm</i>

(*nm* = not measured).

### 7.2.2.3 Carbon and Oxygen Isotopic analysis

The carbon and oxygen stable isotopic composition of the analysed samples was determined at the ETH Centre in Zurich according to the methodology described in chapter 4, section 3 and the results are shown in Table 7.3. The estimated  $\delta^{18}\text{O}$  of pure phases was calculated based on the isotopic fractionation equation defined by the EDTA leaching technique, which was also used to calculate the pure phases, calcite and dolomite, and the  $\delta^{18}\text{O}$  composition in all the MDAC samples, according to figure 6.11 (chapter 6). The estimated  $\delta^{13}\text{C}$  of pure phases, calcite and dolomite, was calculated based on the isotopic fractionation equation defined by all the sample dataset, according to figure 6.12 (chapter 6). Theoretical  $\delta^{18}\text{O}$  compositions for pure calcite and dolomite phases were calculated for the present day temperature at the sampling sites (11°C), estimated from the CANIGO CTD dataset (Ambar *et al.*, 2002), as plotted in Figure 7.1, and the  $\delta^{18}\text{O}_{\text{SMOW}}$  isotopic values of seawater collected from the lower core of the Mediterranean Outflow (MO) at

locations close to the sampling site (Voelker, 2005). For calcite, the Kim and O'Neil (1997) fractionation equation (chapter 6) was used, and for dolomite the one proposed by Vasconcelos *et al.* (2005).

**Table 7.3.** Stable carbon and oxygen isotopic composition, estimated isotopic values of the calcite and dolomite pure phases and theoretical  $\delta^{18}\text{O}$  composition of pure calcite and dolomite phases, calculated for the present day temperature (Ambar *et al.*, 2002) and the  $\delta^{18}\text{O}_{\text{SMOW}}$  isotopic values of seawater collected from the lower core of the MO at locations close to the sampling site (Voelker, 2005).

Sample	Sub-sample	bulk sample $\delta^{13}\text{C}$ (VPDB)	bulk sample $\delta^{18}\text{O}$ (VPDB)	estimated $\delta^{13}\text{C}$ (VPDB) pure calcite	estimated $\delta^{13}\text{C}$ (VPDB) pure Dolomite	estimated $\delta^{18}\text{O}$ (VPDB) pure calcite	estimated $\delta^{18}\text{O}$ (VPDB) pure Dolomite	theoretical calcite $\delta^{18}\text{O}$ (VPDB)	theoretical dolomite $\delta^{18}\text{O}$ (VPDB)
								$t=11^\circ\text{C}; \delta^{18}\text{O}_{\text{fluid}}=0.6$ to $0.7$ ‰(SMOW)	$t=11^\circ\text{C}; \delta^{18}\text{O}_{\text{fluid}}=0.6$ to $0.7$ ‰(SMOW)
3463-A08	1	-27.4	3.1	-13.80	-32.45	0.05	4.28	1.19 to 1.29 ‰(VPDB)	4.24 to 4.34 ‰(VPDB)
	2	-26.2	2.6	-12.61	-31.26	-0.46	3.77		
	3	-23.7	2.3	-10.91	-29.56	-0.58	3.65		
	4	-25.3	2.5	-12.04	-30.69	-0.50	3.73		
	5	-24.9	2.5	-11.76	-30.41	-0.52	3.71		
3463-A03	6	-26.2	4.0	-16.02	-34.67	1.72	5.95	1.29 to 1.95 ‰(VPDB)	4.34 to 6.18 ‰(VPDB)
	7	-39.9	5.1	-25.26	-43.91	1.76	5.99		
	8	-23.7	4.3	-13.46	-32.11	1.95	6.18		
	9	nm	nm	nm	nm	nm	nm		
	10	nm	nm	nm	nm	nm	nm		

(nm = not measured).

### 7.2.3 Sample preparation and analytical methods

The analytical procedure for separation and purification of U and Th was similar to that described by Chen *et al.* (1986) and Edwards *et al.* (1987).

Approximately 30 mg of sample material was collected by hand-drilling. Powdered samples were dissolved with  $\text{HNO}_3$  acid until all carbonate was dissolved and spiked with 120  $\mu\text{l}$  of spike MIX 6, centrifuged, and the solution evaporated in a hot plate ( $90^\circ\text{C}$ ) overnight. It was then dissolved in 1N  $\text{HCl}$ , and 8 mg of Fe in chloride solution was added. The U and Th were then co-precipitated with the Fe by the addition of ammonium hydroxide until the color of the solution changed from yellow to clear. The mixture was

centrifuged and the supernatant discarded. The residue was then rinsed twice with distilled water, dissolved in concentrated HNO<sub>3</sub>, dried and re-dissolved in concentrated HNO<sub>3</sub> twice, dried and dissolved in 0.5 ml of 7N HNO<sub>3</sub>. This solution was loaded on an anion exchange column (Dowex AG 1 × 8 resin) with a volume of 0.5 ml previously washed with mili-Q water, HNO<sub>3</sub>-H<sub>2</sub>O (1:1), HCl 6N, and mili-Q water. Fe was eluted using 7N HNO<sub>3</sub>. The Th fraction was then eluted with 6N HCl and the U fraction with 1N HBr. The U fraction was dried three times and dissolved in 0.1N HNO<sub>3</sub>. An aliquot, containing ~ 3x 10<sup>10</sup> atoms of <sup>234</sup>U, was loaded on a graphite-coated zone refined Re filament. The Th fraction was further purified by drying it, dissolving it in HNO<sub>3</sub>, drying it again, and dissolving it in 0.15 ml of 7N HNO<sub>3</sub>. This solution was loaded on a column similar to the first column used but with a volume of 0.15 ml. A similar elution scheme was followed. The subsequent Th fraction was dried and dissolved in 0.1N HNO<sub>3</sub>.

Three analytical blanks, one ~100 mg of LICS, and a standard solution of HU1 with a proportion of U-Th of 1:1 were submitted to the same sample preparation methodology and measured with the samples for control. U and Th isotope measurements were performed with a <sup>233</sup>U/<sup>236</sup>U double spike and a <sup>229</sup>Th single spike by Thermal Ionisation Mass Spectrometry (TIMS) on a Finnigan MAT 262 RPQ, at IFM-Geomar in Kiel, Germany.

## 7.3 Results and Discussion

### 7.3.1 Constrains on the origin of the uranium in the MDAC

The U concentration in the carbonates depends on many factors, such as the U concentration on the precipitation fluids, the mineralogy, the mineral morphology, the temperature, and the geochemical conditions during mineral formation (Shen and Dunbar, 1995). The average U concentrations of the analysed MDAC are higher than the average value for modern seawater (Figure 7.4). Within the two chimney samples the U concentrations vary significantly. Sample 3463-A03 has similar values for the different sub-samples, from 0.64 to 3.24 µg/g, while the sub-samples from sample 3463-A08 show a larger variation of U concentration values, ranging from 0.26 to 28.10 µg/g (Figure 7.4 and Table 7.4). Sample 3463-A03 shows very similar  $\delta^{234}\text{U}$  values for the different sub-samples and sample 3463-A08 has a larger dispersion of the sub-sample values. Sub-

samples 3 and 5 of chimney 3463-A08 have abnormal high U concentrations, although abnormal mineral content was not detected on the XRD analysis; a detrital contribution may explain these high U values. Alternatively, high U concentrations on these sub-samples can result from an abnormal U content in the fluids from which these carbonates precipitated from. Although not statistically significant, these two sub-samples were collected closer to the open conduit of fluid percolation, and therefore may correspond to a more intense fluid composition signal. It should be noted that chimney 3463-A08 presents a much wider range of U concentration and  $\delta^{234}\text{U}$  values in its sub-samples than chimney 3463-A03 (Figure 7.6). Although sample 3463-A08 represents a shorter formation time-span than chimney 3463-A03 (see section 7.3.2), this can be interpreted as indicating a much more variable fluid composition during the time-span corresponding to the formation of the chimney 3463-A08.

As concerns  $\delta^{234}\text{U}$  values, all sub-samples in sample 3463-A03 have lower  $\delta^{234}\text{U}$  values than seawater (Figure 7.5). Again, sample 3463-A08 shows highly variable  $\delta^{234}\text{U}$  values, with sub-samples 3, 4 and 5 showing lower  $\delta^{234}\text{U}$  values than seawater but, with sub-samples 1 and 2 showing higher  $\delta^{234}\text{U}$  values than seawater (Figure 7.5).

U is highly soluble in oxic conditions and highly insoluble under anoxic conditions (Barnes and Cochran, 1990). Therefore, the U concentration of the dolomite chimneys that are formed as a result of AOM (chapter 5 and 6), *i.e.* precipitated from anoxic pore waters, are expected to have lower U concentrations than the authigenic carbonates precipitated from bottom waters, such as the aragonite-dominated MDAC or corals. The uranium concentration of pure aragonite (>97 wt.% aragonite) chemoherm carbonates reported by Teichert *et al.*, (2003), that are considered as being formed in highly seawater ventilated environments, most probably at or very close to the sediment/seawater interface (very similar to the aragonite pavement samples described in chapter 5), have mean U concentrations of  $5.2 \pm 0.8 \mu\text{g/g}$ . Modern (*D. cristagalli*) and fossil corals have reported average U concentration values of 3.85 and 3.78  $\mu\text{g/g}$ , respectively (Cheng *et al.*, 2000). These reported chemoherm and coral U concentration values are higher than the measured values of the analysed samples in this study (Figure 7.4) (with the exception of sub-samples 3 and 5 in sample 3463-A08, discussed above), supporting the formation model of the dolomite chimneys in an anoxic environment within the sedimentary column, as discussed in Chapter 5.

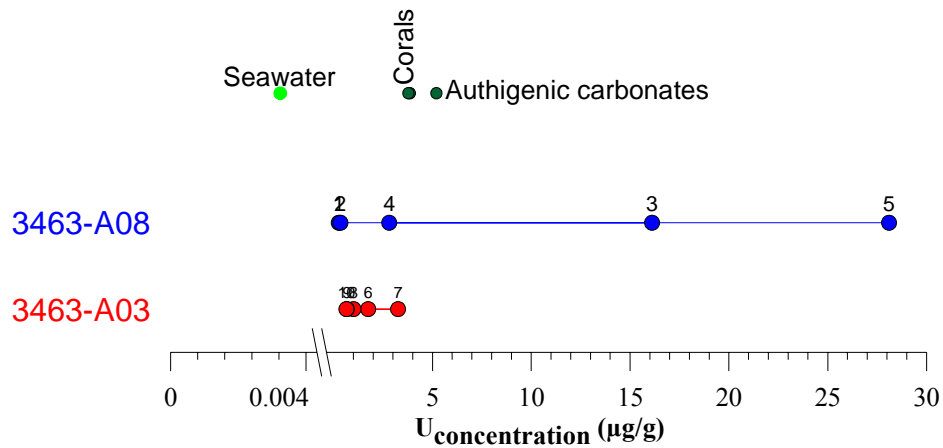


**Figure 7.4.** Uranium concentrations of the analysed samples, compared with modern seawater U concentration (c.a. 3.238 ng/g) from Chen *et al.*, (1986), uranium average values from fossil and modern corals (Cheng *et al.*, 2000), and aragonite authigenic carbonates (chemohermes) from Hydrate Ridge (Teichert *et al.*, 2003).

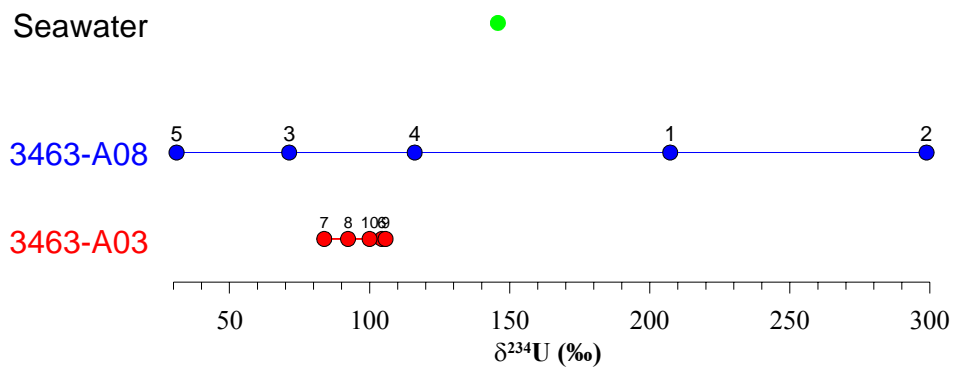


**Figure 7.5.**  $\delta^{234}\text{U}$  ratios of the analysed samples and  $\delta^{234}\text{U}$  average value from modern seawater, c.a.  $144 \pm 2\%$  (Chen *et al.*, 1986).

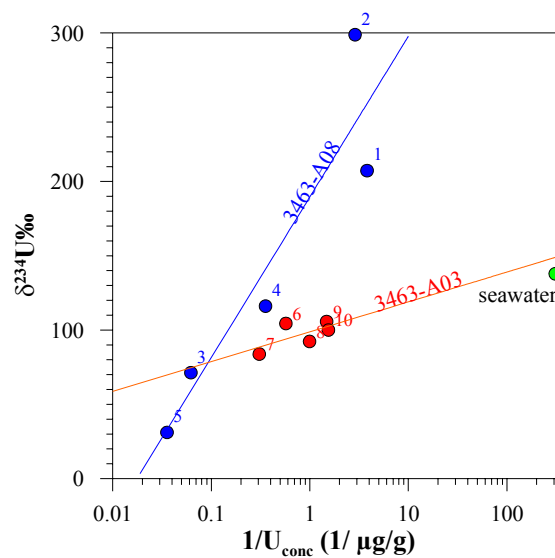


**Figure 7.6.** Inverse U concentration as a function of  $\delta^{234}\text{U}$  values in the analysed chimney samples. The seawater average value (Cheng *et al.*, 2000) is also plotted, for reference.

The U concentrations and the  $\delta^{234}\text{U}$  values of the authigenic carbonates are dependent on the U concentration and the  $\delta^{234}\text{U}$  composition of the fluids from which they precipitated from, but may also vary with several chemical factors, such as the redox conditions during the carbonate formation (Teichert *et al.*, 2003). In order to investigate if the seawater has an important contribution to the U fluid composition of the two analysed carbonates, the uranium concentration was plotted against the  $\delta^{234}\text{U}$  ratios in Figure 7.6.

The U concentration as a function of  $\delta^{234}\text{U}$  values of the analysed sub-samples of the two samples define two trend lines that are interpreted as representing mixing lines between different end-members. The slopes of the mixing lines depend on the composition of the fluids from which the authigenic carbonate precipitated, which may contain varying amounts of pore water fluids, methane rich fluids, and seawater. Most probably, two important contributions correspond to the pore water and the methane rich fluids. The seawater contribution is not a clear important end-member, as the two trend lines do not point to the seawater composition (Figure 7.6).

Considering this simplified model, it is possible to propose that sample 3463-A03 represents a carbonate precipitation from anoxic pore water fluids with a mixture of an enriched  $^{234}\text{U}$  fluid with a more depleted  $^{234}\text{U}$  fluid, both with a fairly constant  $\delta^{234}\text{U}$  composition. Sample 3463-A08, in contrast would represent a precipitation from a fluid that corresponds to a mixture of a low  $^{234}\text{U}$  concentration and low  $\delta^{234}\text{U}$  fluid, with a more enriched  $\delta^{234}\text{U}$  and higher concentration  $^{234}\text{U}$  fluid. Sample 3463-A03 points to an end-member composition close to the seawater composition. As this sample has a larger average grain size and therefore corresponds to lithified sediments with an original higher porosity and higher permeability, it is interpreted that, on this sample, the pore water and the seawater contribution is more important than on sample 3463-A08, which corresponds to a cemented mudstone with very low initial porosity and low permeability.

### 7.3.2 Age determination

The U/Th dating method is based on the Th insolubility leading that the carbonates precipitated from solution are free of Th but may contain U. Known the  $^{230}\text{Th}$  and  $^{234}\text{U}$  decay constants, the age of the carbonate phases can be calculated from the  $^{230}\text{Th}/^{234}\text{U}$  and

$^{234}\text{U}/^{238}\text{U}$  activity ratios, according to the equation:

$$^{230}\text{Th}/^{234}\text{U} = (^{238}\text{U}/^{234}\text{U})[1 - \exp(-\lambda t_0)] + [\lambda_0 / (\lambda_0 - \lambda_4)] \times (1 - ^{238}\text{U}/^{234}\text{U}) \times [1 - \exp(\lambda_4 - \lambda_0)t]$$

Where  $\lambda_0$  and  $\lambda_4$  are the decay constants for  $^{230}\text{Th}$  and  $^{234}\text{U}$ , respectively, and  $t$  is the age.

However, natural carbonate samples (such as the studied MDAC samples) contain detrital material of variable origin such as terrigenous fractions and clay minerals that can contribute with significant amounts of  $^{230}\text{Th}$  and  $^{234}\text{U}$  to the total sample, resulting in deviations of the observed  $^{230}\text{Th}/^{234}\text{U}$  ratio from that of the authigenically precipitated carbonate component alone, and if not corrected for, produces apparent erroneous age values. Various methods have been proposed to “correct” this detritus contamination. On this study, individual sub-sample ages were obtained by correcting the analysis of a single leachate for its contaminant  $^{230}\text{Th}$ . For each sample, from which 5 coeval sub-samples with differing detrital component were analysed to construct an “isochron”, as discussed above.

U and Th isotopic compositions of the authigenic carbonates and the corresponding  $^{230}\text{Th}/^{234}\text{U}$  ages, corrected for each sub-sample contaminant  $^{230}\text{Th}$ , are reported in Table 7.4 and Figure 7.7.

**Table 7.4.** U and Th isotopic compositions and  $^{230}\text{Th}/^{234}\text{U}$  ages determined for the authigenic carbonates analysed in this study.

(*npd*: ages could not be determined with this method)

Sample	Sub-Sample	$^{238}\text{U}$ ( $\mu\text{g/g}$ )	$^{230}\text{Th}$ ( $\text{pg/g}$ )	$^{230}\text{Th}/^{232}\text{Th}$ activity ratio	$\delta^{234}\text{U}$ ‰	$^{230}\text{Th}/^{234}\text{U}$ activity ratio	Age corrected (a)
3463-A08	1	0.2624 $\pm$ 0.0014	4.8 $\pm$ 0.1	0.9 $\pm$ 0.01	207.3 $\pm$ 9	0.9344 $\pm$ 0.01	244 866 $\pm$ 22 312
	2	0.3476 $\pm$ 0.0017	355.8 $\pm$ 2.8	1.6 $\pm$ 0.19	298.8 $\pm$ 6	48.5062 $\pm$ 0.13	<i>npd</i>
	3	16.1115 $\pm$ 0.0703	282.1 $\pm$ 6.5	68.1 $\pm$ 0.3	71.3 $\pm$ 2	1.0063 $\pm$ 0.35	<i>npd</i>
	4	2.8130 $\pm$ 0.0135	49.9 $\pm$ 1.1	14.3 $\pm$ 0.05	116.1 $\pm$ 4	0.9789 $\pm$ 0.06	246 184 $\pm$ 22 312
	5	28.1020 $\pm$ 0.1503	494.4 $\pm$ 14.7	104.6 $\pm$ 0.67	31.1 $\pm$ 5	1.0504 $\pm$ 0.82	244 870 $\pm$ 22 312
3463-A03	6	1.7488 $\pm$ 0.0079	27.8 $\pm$ 0.6	4.7 $\pm$ 0.04	104.4 $\pm$ 3	0.8852 $\pm$ 0.04	135 210 $\pm$ 7 792
	7	3.2603 $\pm$ 0.0145	53.7 $\pm$ 1.2	15.5 $\pm$ 0.06	83.8 $\pm$ 2	0.9356 $\pm$ 0.07	220 555 $\pm$ 16 721
	8	1.0068 $\pm$ 0.0046	17.3 $\pm$ 0.4	2.7 $\pm$ 0.02	92.3 $\pm$ 3	0.9702 $\pm$ 0.02	113 794 $\pm$ 7 088
	9	0.6758 $\pm$ 0.0037	11.9 $\pm$ 0.3	2.1 $\pm$ 0.02	105.7 $\pm$ 7	0.9795 $\pm$ 0.02	93 143 $\pm$ 6 193
	10	0.6473 $\pm$ 0.0035	11.3 $\pm$ 0.3	2.1 $\pm$ 0.02	100.0 $\pm$ 6	0.9784 $\pm$ 0.02	88 593 $\pm$ 5 925

Most of the samples have low  $^{230}\text{Th}/^{232}\text{Th}$  activity ratios ( $<20$ , with the exception of samples 3 and 5), and therefore corrections for the inherited  $^{230}\text{Th}$  were done using the  $^{230}\text{Th}$ ,  $^{232}\text{Th}$  and  $\lambda^{238}\text{U}$  activities to extrapolate the detritus contribution. It should be noted that the term detritus used here deviates from its sedimentological definition. The detritus phase here refers to all phases bearing Th isotopes initially incorporated into the sample. The U-series datation method is based on the large difference in solubility between U and Th. In most of the systems, such as the authigenic carbonate phases precipitation from natural solutions, they will have very low  $^{232}\text{Th}/^{238}\text{U}$  and  $^{230}\text{Th}/^{238}\text{U}$  ratios. The  $^{230}\text{Th}$  growth method for dating these carbonate phases may be employed with confidence by assuming  $^{230}\text{Th}/^{234}\text{U} = 0$ , at the time of formation. This is only possible in the cases in which the authigenic phases that contain U are essentially free of  $^{232}\text{Th}$ . In the case of the analysed MDAC samples, which contain significant amounts of non-authigenic carbonate minerals, such as biogenic fragments, quartz, feldspars and clays (15 to 35%), it should be expected the presence of non free  $^{232}\text{Th}$  from those allochthonous minerals. Therefore, the corrections to the initial  $^{230}\text{Th}$ ,  $^{238}\text{U}$  and  $^{234}\text{U}$  have to be made assuming that it is accompanied by the  $^{232}\text{Th}$ . Therefore, the correction value of the detritus  $^{230}\text{Th}$  contribution is assumed to be equal to the  $^{232}\text{Th}$  concentration.

The isochron method is the common approach to solve this problem. By analyzing three or more co-genetic samples with variable  $^{238}\text{U}/^{232}\text{Th}$ , it is possible to extrapolate the  $^{232}\text{Th}$ -free end-member isotopic ratios from a least-squares regression of the data on a pair of isotope-ratio diagrams that completely define the  $^{238}\text{U}$ - $^{234}\text{U}$ - $^{230}\text{Th}$ - $^{232}\text{Th}$  system. The isochron method allows the definition of the detrital correction from the several sub-samples of each chimney. Since five sub-samples of each sample were analysed, and assuming that the chimneys were formed rapidly, compared with their ages, the five co-genetic sub-samples have different authigenic carbonate/detritus ratios and so, variable  $^{230}\text{Th}$ - $^{234}\text{U}$ - $^{238}\text{U}$  isotope ratios. Four pairs of isotope-ratio or isochron diagrams could be used (Ludwig and Titterton, 1994): (1) the Rosholt type I isochron diagrams:  $^{230}\text{Th}/^{232}\text{Th} - ^{234}\text{U}/^{232}\text{Th}$  and  $^{234}\text{U}/^{232}\text{Th} - ^{238}\text{U}/^{232}\text{Th}$ ; (2) the Osmond type I isochron diagrams:  $^{230}\text{Th}/^{234}\text{U} - ^{232}\text{Th}/^{234}\text{U}$  and  $^{234}\text{U}/^{238}\text{U} - ^{232}\text{Th}/^{238}\text{U}$ ; (3) the Rosholt type II isochron diagrams:  $^{230}\text{Th}/^{232}\text{Th} - ^{238}\text{U}/^{232}\text{Th}$  and  $^{234}\text{U}/^{232}\text{Th} - ^{238}\text{U}/^{232}\text{Th}$ ; and (4) the Osmond type II isochron diagrams:  $^{230}\text{Th}/^{238}\text{U} - ^{232}\text{Th}/^{238}\text{U}$  and  $^{234}\text{U}/^{238}\text{U} - ^{232}\text{Th}/^{238}\text{U}$ .

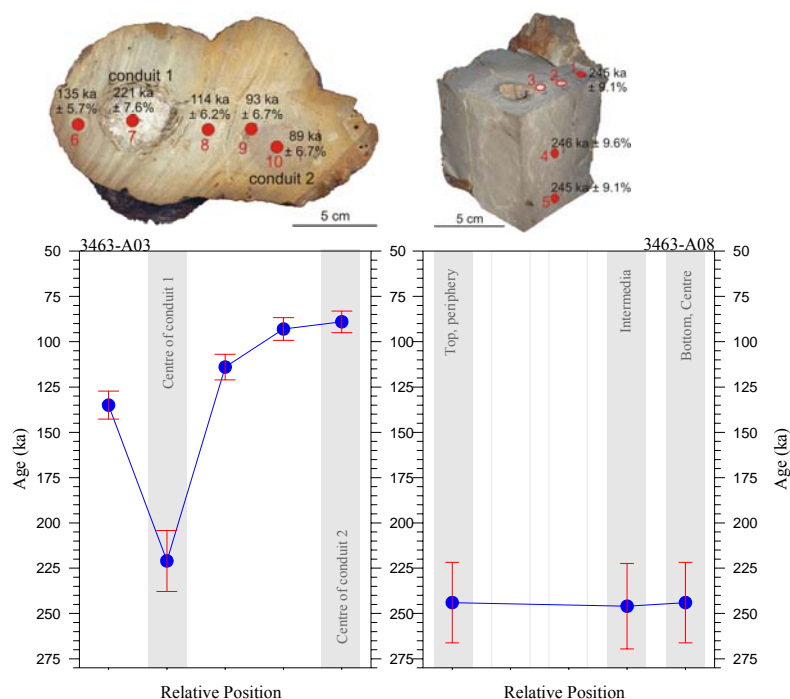


**Figure 7.7.** U/Th ages determined along radial and longitudinal profiles on the analysed samples.

In this study, the  $^{232}\text{Th}$ -free end-member, from which the age is calculated from, is given by either the slope in the Rosholt diagrams or by the intercept in the Osmond diagrams. It should be noted that analytical errors produce a scattering of the points around the theoretical strait lines. Additionally, scattering can also result from uranium and thorium open-system behaviour and/or the presence of multiple end-members.

In the isochron diagrams (Figure 7.8, Figure 7.9 and Figure 7.10), the mixing lines between any two components are strait lines with fairly good correlation coefficients, indicating that the assumed conditions for the use of this technique are adequate. The Rosholt isochrones for both samples show good correlation coefficients (0.999). The Osmond isochrones show a good correlation coefficient for sample 3463-A08 (0.95 and 0.71) but a more deficient correlation for sample 3463-A03 (0.71 and 0.36). This indicates that the assumed considerations are respected to a high degree for sample 3463-A08, but not so well for sample 3463-A03 and therefore the calculated ages with the isochron methods are reliable and the ages estimated by this method are expected to be closer to the real age of the pure authigenic carbonate phases.

The Osmond isochrones indicate a mean age of 360 ka for chimney 3463-A03 and a mean age of 247.8 ka for chimney 3463-A08, which is also very close to the ages determined for the sub-samples.

**Table 7.5.** Osmond isochrones ages determined for the analysed samples.

Sample	$^{230}\text{Th}/^{234}\text{U}$	$^{234}\text{U}/^{238}\text{U}$	min. Age	mean Age	max. Age
3463-A03	$0.986 \pm 0.028$	$1.074 \pm 0.046$	243 ka	360 ka	$\infty$
3463-A08	$0.9133 \pm 0.0027$	$1.0721 \pm 0.0052$	240.0 ka	247.8 ka	256.3 ka

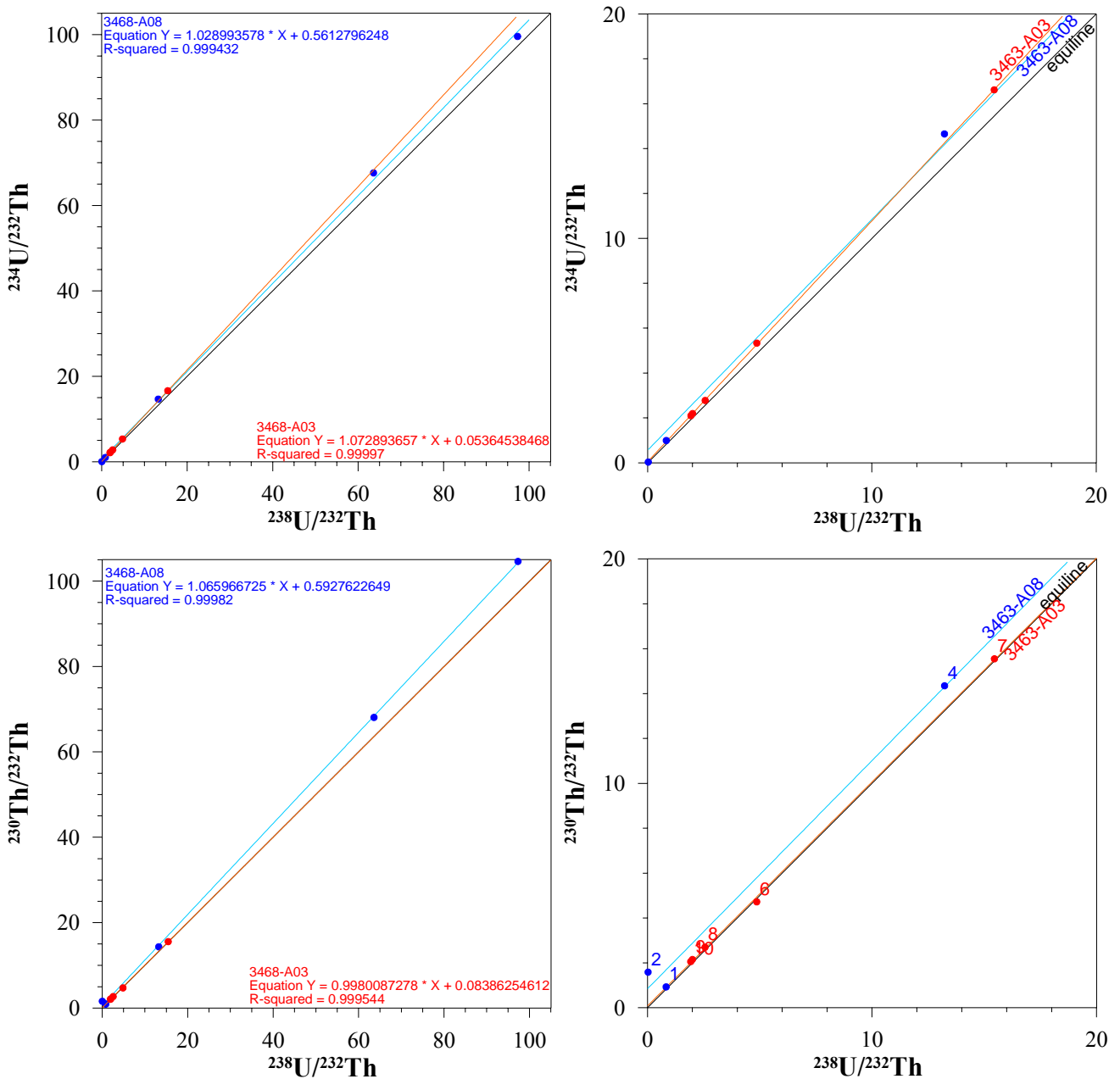


**Figure 7.8.** Rosholt type II isochron diagrams. To be noted the good linear correlation of the trend lines. To be noted that the graphs on the right correspond to a zoom of the lower values [0-20] of the graphs in the left.

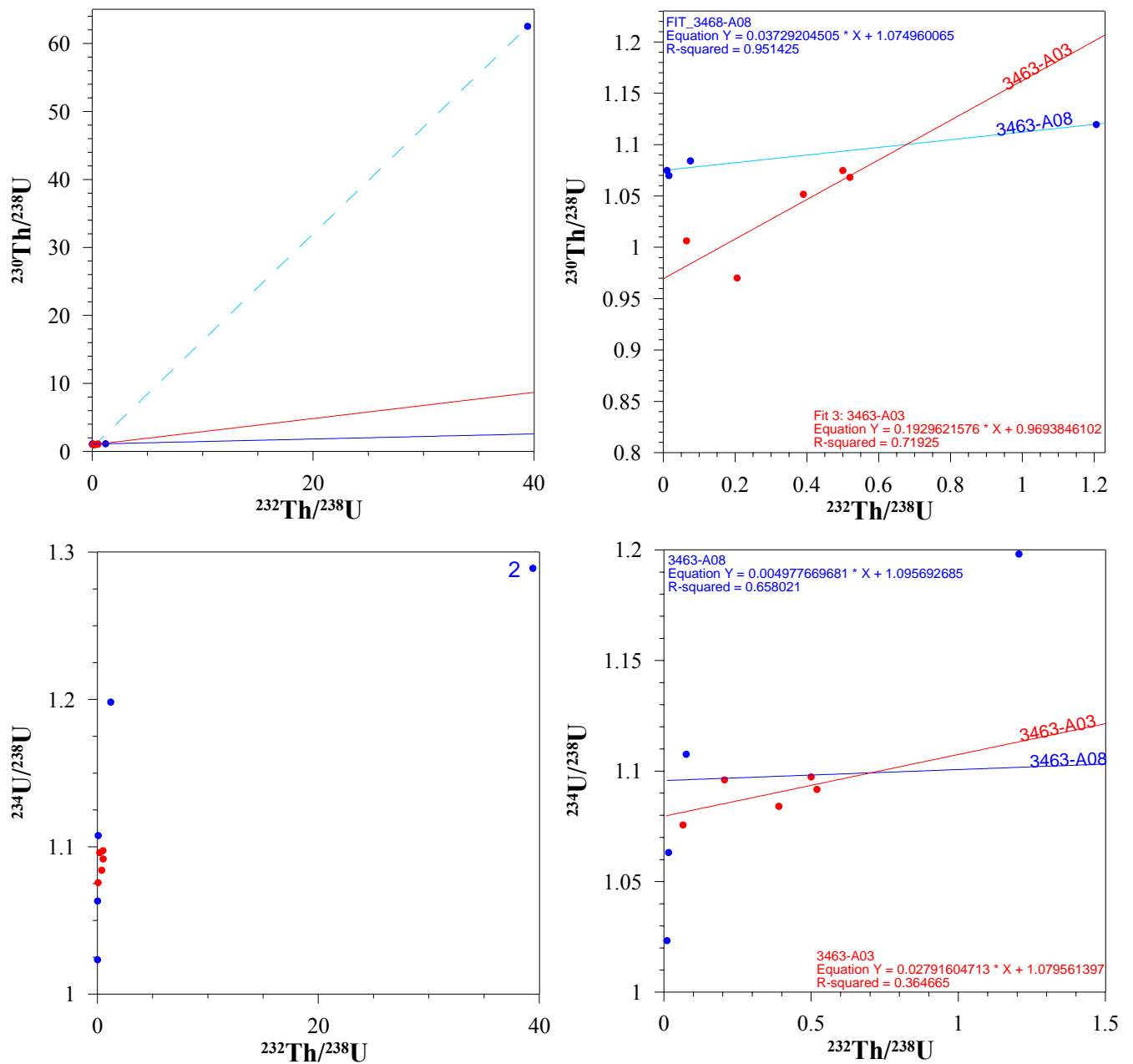


**Figure 7.9.** Osmond type II isochron diagrams. To be noted the reasonable linear correlation of the trend lines, with the exception of sample 3463-A03. To be noted that the graphs on the right correspond to a zoom of the lower values [0-1.2] of the graphs in the left.

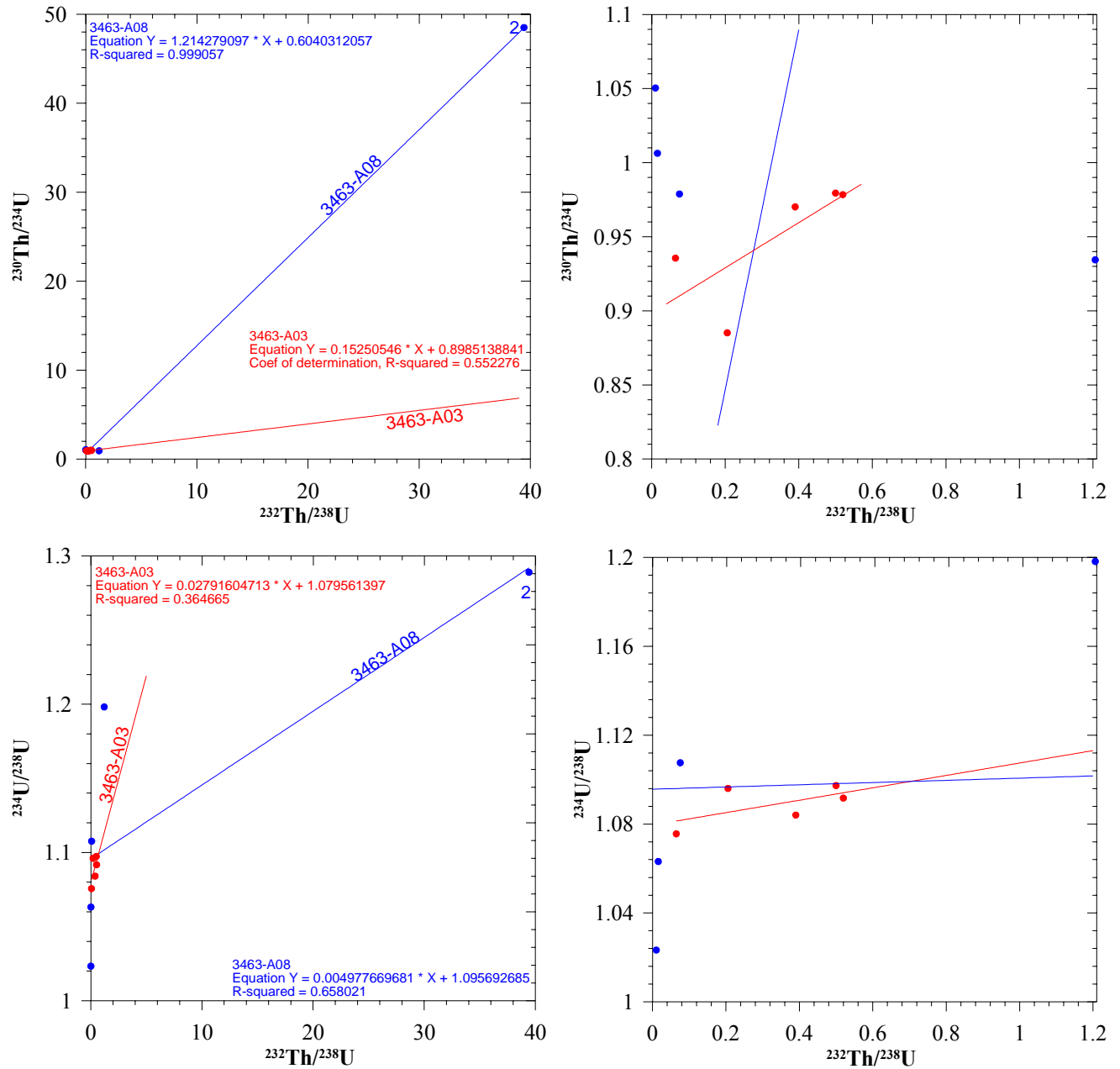


**Figure 7.10.** Osmond type isochron diagrams. To be noted the good linear correlation of the trend lines, with the exception of sample 3463-A03. To be noted that the graphs on the right correspond to a zoom of the lower values [0-1.2] of the graphs in the left.

### 7.3.2.1 Sample 3463-A08

The sub-samples collected from radial and longitudinal profiles along this chimney yield ages reported in Figure 7.11 and Table 7.4, ranging between 244 ka and 246 ka. This indicates a short formation time-span of  $\sim 4 \text{ ka} \pm 50 \text{ ka}$ , consistent with the homogeneous character of this sample. The estimated ages, while having associated considerable error values are statistically significant, indicating that the formation of the chimney occurs during a short episode of enhanced precipitation, indicating a high rate of carbonate formation (1 cm/ka). Given its textural homogeneity, this chimney was, most probably, formed continuously. Given that sub-samples 3, 4 and 5 were collected from a equal distance from the chimney centre, it is possible to propose that the growth of the chimney proceeds from the centre to the periphery.

The Osmond isochron age estimated for sample 3463-A08 is in very good agreement with the individual ages of the sub-samples (Table 7.4, Table 7.5 and Figure 7.11). The good linear correlation of the trend lines defined by the isochron techniques (Figure 7.8 to Figure 7.10) point to a good estimation of the ages by the isochron technique.

### 7.3.2.2 Sample 3463-A03

Sub-samples collected along a radial profile in sample 3463-A03 yielded ages ranging from 89 ka to 221 ka (Table 7.4 and Figure 7.11). Sample 3463-A03 corresponds to a chimney with two cemented parallel conduits. The centre of conduit 1 has an estimated age of 221 ka and a growing direction from the centre of the conduit to the periphery, with subsequent enlargement episodes (continuous or discontinuous). Conduit 2 has an estimated age of 89 ka and indicates an apparent growing direction from the exterior to the centre of the conduit. The ages of the sample as their heterogeneous texture indicates that the formation of the sample was, most probably, episodically, with a first fluid flow episode that induced the precipitation of conduit 1. Carbonate precipitation progressed radially from this conduit (most probably by discontinuous episodes). A latter fluid episode resulted in the precipitation of conduit 2. The grow rate on this sample is vary variable ranging from 2.6 mm/ka, considering just the conduit 1 zone (segment between sub-samples 6 and 7) to 0.6 mm/ka, considering the zone between the centre of the two conduits (sub-samples 7 and 10).

The age estimated by the Osmond isochron method for this sample indicates an age of 360 ka, with a lower limit of 243 ka and the maximum limit indicates more than 500 ka (Table 7.5 and Figure 7.9), above the upper limit of this dating technique. The discrepancy between the isochrone age and the  $^{230}\text{Th}/^{234}\text{U}$  ages of the different sub-samples is interpreted as resulting from the large time span along which the sample was formed, *i.e.* the condition of application of the isochron technique that the samples were formed in a short period of time compared to their age is not adequately verified. The period of formation (221 to 89 ka) represents a significant time span compared with the age of the sample (at least 60% of the maximum age). This is also reflected by the lower correlation coefficient of the isochron trend lines of sample 3463-A03 compared with sample 3463-A08 (Figure 7.8 to Figure 7.10).

### 7.3.2.3 Samples 3463-A03 and 3463-A08

As seen in chapters 5 and 6, the precipitation of the authigenic carbonates in the Gulf of Cadiz is closely linked with the supply of methane-rich fluids. The estimated ages indicate that during this interval, favourable conditions for enhanced methane flux throughout the sediments, and consequently carbonate precipitation, occur at specific time intervals. The estimated ages of the two samples indicate that the carbonate precipitation and the dolomite chimney formation occur in distinct intervals or episodes. These episodes occur in the same geological setting and within very closely spaced locations, and are interpreted as indicating that the fluid escape processes within this area of the Gulf of Cadiz has occurred during a long time-span (at least 150 ka), but the precipitation of the different samples occurs in shorter episodes. Most probably, there is an edification of a complex plumbing system along which the carbonate chimneys are formed. The plumbing system most probably would show global and local variability of the fluid flow intensity. The seepage intensity can have episodes of high intense flux and locally the flux can be localized and have spatial migrations. Some fluid conduits can be interrupted by complete clog of the fluid conduits as a result of carbonate cementation, or if the flux along them is diminished or deviated to other pathways and resumed latter, giving place to the formation of secondary conduits, such as those represented by sample 3463-A03. Variations in the regional tectonic stress field would correspond to changes with larger time scale periods; however it is possible to speculate that earthquakes and smaller scale tectonic stress regime

changes may produce the opening, enlargement or closure of different conduits for the supply of methane-rich fluids. Those small scale stress readjustments can have variations in the same time scale period of formation of the samples. In addition, sealevel variations, related to glacial-interglacial fluctuations, which have a time scale cyclicity of 100 ka, will most probably have significant control on the fluid flow regime and intensity in the upper portion of the sedimentary column. Therefore, the potential regional paleoceanographic control on the enhanced fluid flow episodes is investigated in the next section.

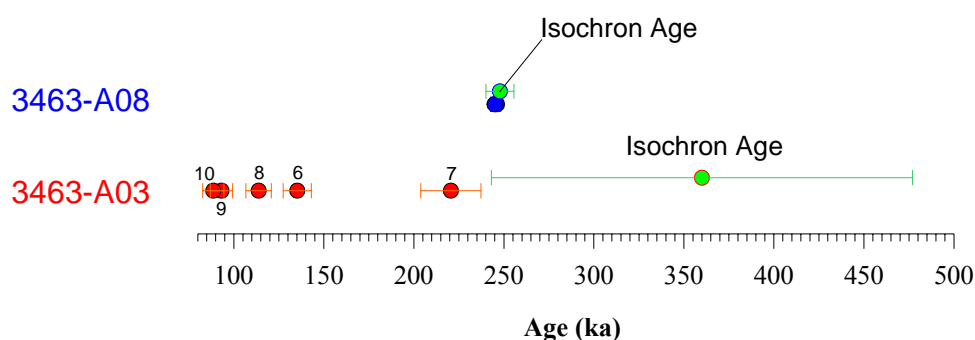


**Figure 7.11.**  $^{230}\text{Th}/^{234}\text{U}$  ages of individual sub-samples and isochron ages determined by the Osmond isochron method.

### 7.3.3 $^{230}\text{Th}/^{234}\text{U}$ ages of the MDAC and their relationship to the global sealevel record

Over the time scale of glacial-interglacial cycles, the corresponding sealevel variations may significantly influence fluid flow in continental margins. In the Gulf of Cadiz, between the 600 m and the 1200 m water depths, the MO controls the sedimentation (Hernandez-Molina *et al.*, 2003), the temperature of bottom water and the temperature in the upper sedimentary section (Figure 7.1). Glacial-interglacial changes have a strong influence in the MO flow pattern and the consequent temperature changes have the potential to dissociate possible gas hydrate occurrences in the top sediments or create favourable thermodynamic conditions for gas hydrate formation.

Considering just the pressure effect, the glacial sealevel lowering with the

consequent lowering of pressure would shift the bottom of the gas hydrate stability zone into shallower depths and consequently promote the dissociation of the existing gas hydrates. The enhanced decomposition of gas hydrates may then generate enhanced gas and fluid flow in cold seep areas, leading to an increased precipitation of methane-derived authigenic carbonates (as described in chapter 6). In addition, the decomposition of gas hydrates, as a consequence of the changes in the gas hydrate stability zone, releases considerable amounts of fresh water into the sediment pore space, thereby increasing the negative pressure gradient between the pore fluids and the seawater column, enhancing the fluid flow. For active fluid seepage, it is most crucial that the hydraulic pressure of the ascending fluids in the plumbing system within the sediments exceeds the pressure of the overlying seawater column, that corresponds to the sealevel (Carson and Screaton, 1998). Therefore, two scenarios can be distinguished when considering pore water pressure changes due to sealevel variations: (1) the seawater pressure exceeds the hydraulic pressure of the plumbing system below a methane fluid seepage site, inhibiting the rise of fluids; (2) the seawater pressure is lower than the hydraulic pressure of the plumbing system and vigorous fluid seepage occurs. It is therefore possible to propose that during glacial stages, which correspond to low sealevel, a negative pressure gradient is established between the pore water fluids or the plumbing system and the seawater pressure, triggering or leading to maximum fluid flow rates at methane seep sites, enhancing the precipitation of methane-derived authigenic carbonates. In contrast, during sealevel rise at the glacial to interglacial transitions, the seawater pressure increases and the pressure difference between the seawater column pressure and the hydraulic pressure in the plumbing system of the methane seep diminishes or is minimal. In this way, sealevel rise restricts fluid flow or stops it. Consequently, considering just the pressure effect, the carbonate precipitation during interglacial stages should be low or null and maximum precipitation should coincide with glacial maxima. This scenario is similar to the observed short-term tidal control on the fluid flow intensity variations in shallow water seep sites, where higher rates of fluid flow are measured coinciding with the low tides, whereas high tides are characterised by low or null flow rates (Boles *et al.*, 2001; Rollet *et al.*, 2006). The tidal effect on fluid flow intensity is still an effective process at deep locations up to 800 m water depth, as documented in the Hydrate Ridge (Tryon and Brown, 2001; Tryon *et al.*, 2002).

Vigorous fluid flow may nevertheless also occur during sealevel highstands as long as the hydraulic pressure exceeds the pressure of the height of the water column.

In the following discussion, the mentioned isotopic stages are referred to as Marine Isotopic Stages (MIS) and their timing is defined according to Martinson *et al.* (1987), Shackleton (2000) and the LR04 stack of Lisiecki and Raymo (2005).

The estimated ages of the sub-samples indicate formation (1) at the onsets of terminations 2 and 3, contemporary with rapid sealevel rise; (2) at the transition from stadial to interstadial, also corresponding to rapid sealevel rise; and (3) at the transition from interglacial (MIS 5.5) to stadial MIS 5.4 or from interglacial (MIS 5.3) to stadial 5.2, associated with periods of progressive sealevel lowering (Figure 7.12).

Sample 3463-A08 with an estimated age of 245-246 ka (260 ka according to the isochron dating technique) is associated with precipitation during termination 3, at the end of MIS 8 and beginning of MIS 7 (between 8.02 and 7.5), corresponding to precipitation during a period of a rapid sealevel rise (Figure 7.12).

The estimated age of 221 ka of the sub-sample 7 collected from the centre of conduit 1 in sample 3463-A03 correlates with the transition from a stadial (MIS 7.4) to an interstadial (MIS 7.3), during a time span corresponding to a rapid sealevel rise. Sub-sample 6 from the exterior of conduit 1, (sample 3463-A03) with an age of 135 ka, is related to the base of termination 2 and therefore the onset of a rapid sealevel rise. It is therefore evident that the centre and the periphery of conduit 1 are associated with two different fluid flow episodes. Sub-sample 8, in between the two conduits 1 and 2 in sample 3463-A08, correlates with MIS 5, namely the transition from interglacial (MIS 5.5) to stadial MIS 5.4 and consequently with a formation related to a progressive sealevel lowering. Sub-samples at the centre of conduit 2 (sub-sample 10) and at their periphery (sub-sample 9) corresponding to ages of 89 and 93 ka respectively, are contemporary with a period of progressive sealevel lowering, from the interstadial MIS 5.3 to the stadial MIS 5.2. Sub-samples at the centre and periphery of conduit 2 (sub-sample 10) and in between conduit 1 and 2 (sub-sample 9) can be interpreted as formed in result of the lowering of the seawater column pressure reduction and intensification of the fluid flux of methane-rich fluid and subsequent authigenic carbonate precipitation.

The ages of the MDAC sub-samples are therefore associated with periods of rapid sealevel changes: rapid sealevel rises (such as the terminations 2 and 3) or the interstadial

to stadial progressive sealevel lowering periods. This shows that the direct pressure variation of the seawater column is not the predominant factor controlling the fluid flow of the methane-rich fluids from which the carbonates precipitated. Therefore, the sealevel variation and seawater pressure conceptual model for controlling the fluid flow intensity at the cold seeps can not be used to explain the formation of most of the samples. As the pressure effect is not the most significant effect on controlling fluid flow, it is proposed that temperature changes are the preferable forcing factor on fluid flow intensity.

Glacial and interglacial changes induce changes in the MO intensity and the depth at which it flows at the seafloor (Faugères *et al.*, 1984; Llave *et al.*, 2006; Voelker *et al.*, 2006). During globally cooler conditions, as during the glacial stages, the MO was denser and therefore the centres of the MO cores were located deeper than at present. On the other hand, during warm periods the MO was less dense, favouring an increased intensity of the MO on upper slope areas (Llave *et al.*, 2006). Under present day conditions, corresponding to an interglacial stage, the sites where samples 3463-A03 and 3463-A08 were collected from are located under intense influence of the lower core of the MO (Figure 7.1). At present, the gas hydrate stability zone (GHSZ) is thin (46 m for 100% methane gas hydrate) or even nonexistent (100% methane gas hydrate), considering the upper temperature values of 12°C within the seasonal MO temperature variations. During glacial periods, it is proposed that the sampling sites are characterised by a weaker MO influence, or the MO position does not bath the sampling site locations. Therefore at these sites the seabottom water temperature and the temperature in the upper part of the sediment column should be inferior to the present day temperatures. The base of the GHSZ at the sampling sites during glacials should therefore be deeper than during the interglacial stages. Methane hydrates should therefore have stabilized and accumulated during glacial stages, when the MO had a weaker positive temperature influence at the sampling sites. At interglacial stages, especially at the glacial terminations, the MO rapidly increases its influence and the seafloor bottom water temperature and consequently the temperature in the upper sediments should increase, reducing the GHSZ and increasing gas hydrate dissociation, enhancing the methane-rich fluid flow at the top sedimentary column or even at the seafloor. Therefore, it is proposed that the MDAC precipitation is recording intense fluid flow episodes occurring during periods of higher temperature of the seabottom water and of the upper sediment column, as a result of greater influence of the MO at these sampling

sites. This increase in seabottom water temperature is, most probably, causing changes on the gas hydrate stability zone, causing its reduction, leading to gas hydrate dissociation and to its consequent release of methane-rich fluids which will induce the carbonate precipitation along the fluid conduits on the fluid pathways above the methane seepage sites.

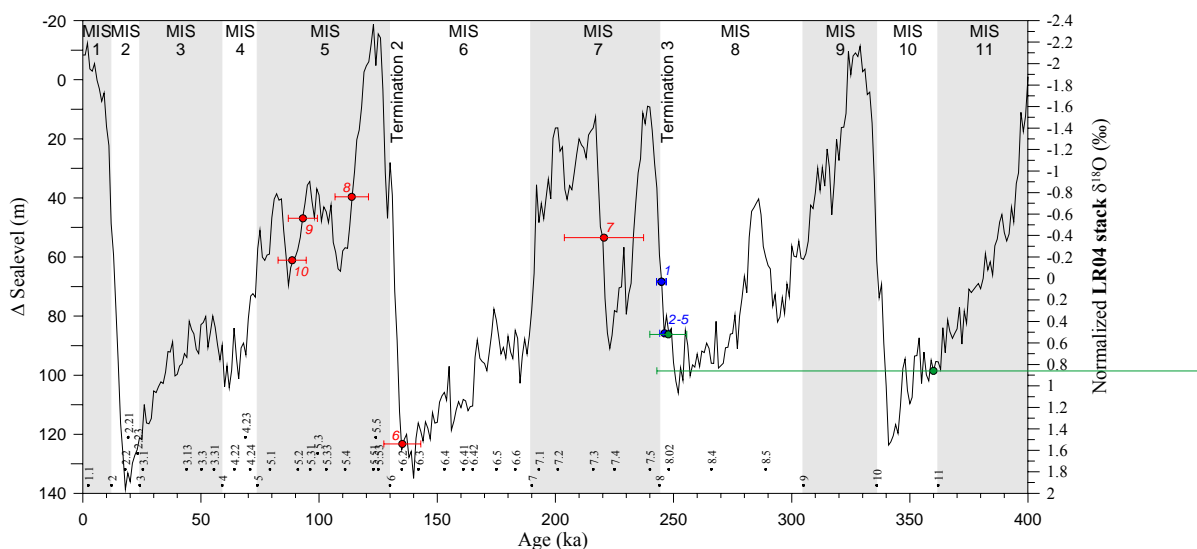


**Figure 7.12.** Ages of the two dolomite chimney samples projected over the  $\delta^{18}\text{O}_{\text{SMOW}}$  estimated sealevel variation curve. The sealevel variation curve is based on the assumption that the global seawater  $\delta^{18}\text{O}_{\text{SMOW}}$  variation resultant from glacial-interglacial ice volume change is of about 1‰ (Schrag *et al.*, 1996; Duplessy *et al.*, 2002) and that the entire sealevel scale is 125 m (Fairbanks and Matthews, 1978; Fairbanks, 1989). The plotted  $\delta^{18}\text{O}$  curve corresponds to the normalized “LR04” stack (Lisiecki and Raymo, 2005). The MIS ages and nomenclature are the ones defined by the SPECMAP, Martinson *et al.* (1987) and (Shackleton, 2000).

### 7.3.4 Potential controls on the $\delta^{18}\text{O}$ signal in the chimneys

The oxygen isotopic composition of the MDAC depends mainly on the mineralogy of the carbonate, the temperature of formation and on the isotopic composition of the fluids from which the carbonates precipitated from. Salinity and pH have minor effects, neglected in this discussion.

The analysed chimney samples are composed of a mixture of different carbonate phases where either calcite or dolomite is dominant (Table 7.2). In order to reconstruct the

temperature and the  $\delta^{18}\text{O}$  composition of the fluids from which the authigenic carbonates precipitated, it is necessary to calculate the isotopic composition of the different carbonate phases. Therefore, the bulk isotopic composition of the sub-samples were plotted as a function of their mineral content, and the isotopic composition of the pure calcite and dolomite were extrapolated using the correlation trend line calculated from a group of samples leached with EDTA, which allowed the total dissolution of the calcite and Mg-calcite phases until obtaining and analyse of the pure dolomite phase (Figure 6.10, in chapter 6). This allowed the estimation of the isotopic composition of the calcite and dolomite phases, as shown in Table 7.3 and in Figure 7.13.

Considering the present day bottom water temperature of 11°C, as determined from nearby CTD data of the CANIGO project (Figure 7.1), and the bottom water oxygen isotopic composition ranging from 0.6 to 0.7‰ SMOW at site SWIM04-42, at 35.88°N; 7.53°W (Voelker, 2005, Personal Communication), the expected isotopic composition of calcite should range from 1.19 to 1.29‰ VPDB, and dolomite should vary between 4.24 and 4.34‰ VPDB (Table 7.3), according to the Kim and O'Neil (1997) fractionation equation for calcite and the Vasconcelos *et al.* (2005) equation for dolomite. In sample 3463-A03, the estimated isotopic composition of calcite is enriched in  $^{18}\text{O}$  (0.43‰ up to 0.76‰ VPDB) relative to their expected modern conditions, while dolomite is 1.61 up to 1.94‰ VPDB enriched in  $^{18}\text{O}$  relative to their expected modern conditions. In sample 3463-A08, the estimated isotopic composition of calcite and dolomite are more depleted in  $^{18}\text{O}$  than expected for modern conditions. Calcite shows estimated values ranging from -0.58 to 0.05‰ VPDB, corresponding to a depletion of up to 1.87‰ VPDB, while dolomite shows estimated values ranging from 3.65 to 4.28‰ VPDB, corresponding to a depletion in  $^{18}\text{O}$  up to 0.69‰ VPDB. These significant discrepancies between the estimated isotopic compositions of the pure phases of calcite or dolomite and the theoretical values under modern temperature and bottom seawater isotopic compositions indicate that the temperature and isotopic compositions of the fluids from which the authigenic carbonates precipitated are significantly different from the present day conditions.

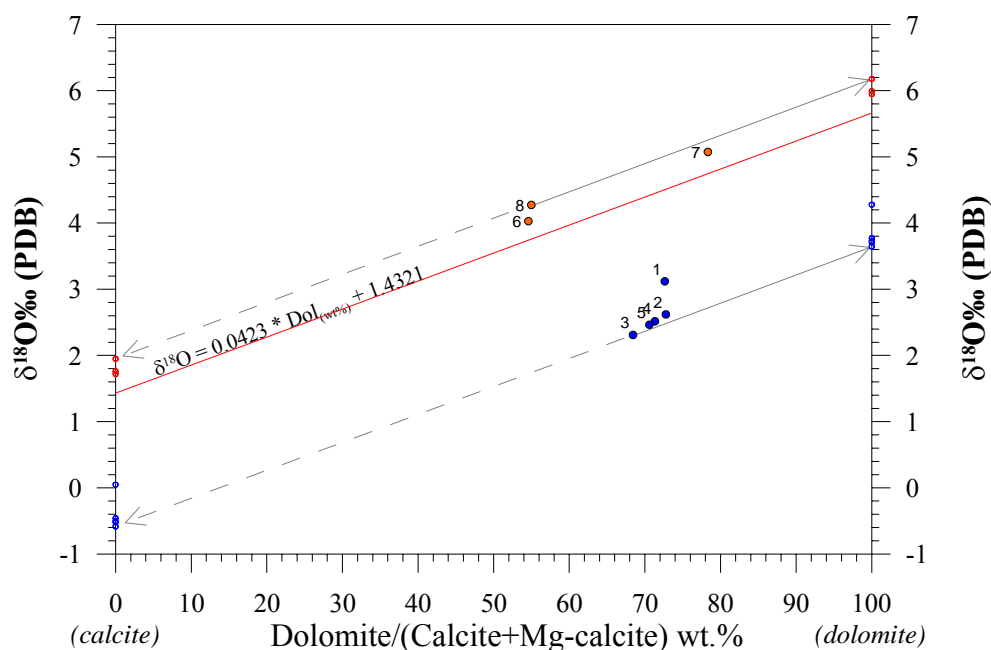


**Figure 7.13.** Mineralogy (dolomite/calcite ratio) and  $\delta^{18}\text{O}$  values of the analysed sub-samples and extrapolated values of calcite and dolomite pure phases. Red line represents the trend line that indicates the relationship of the estimated isotopic compositions of pure calcite and dolomite phases, calculated from the group of samples leached with EDTA, according to Figure 6.10 in chapter 6. Grey arrows point to the pure calcite and dolomite phases isotopic, minimum and maximum, estimated isotopic values.

The  $^{18}\text{O}$  composition of the fluids from which the authigenic carbonates precipitated, were estimated for the temperature range of 4 °C to 14°C, which corresponds to the values that are the estimated temperature range considered to be possible to occur between extreme glacial-interglacial settings at the locations from which the authigenic carbonates were collected from. The estimated fluid composition for the different temperatures is shown in Table 7.6 and Figure 7.14. Seawater  $\delta^{18}\text{O}_{\text{SMOW}}$  changes are a consequence of the glacial-interglacial cyclicity, as evidenced by the  $\delta^{18}\text{O}$  LR04 curve (Figure 7.12 and Figure 7.14). The exact value for the  $\delta^{18}\text{O}$  difference between glacial and interglacial periods is still under discussion, but estimates of the deep ocean water  $\delta^{18}\text{O}$  between the Last Glacial Maximum (LGM) and the Holocene (MIS1) points to a value of about 1.05‰ (Duplessy *et al.*, 2002). Although this 1.05‰ variation does not necessary apply for all the MIS, especially in the Gulf of Cadiz where the presence of the Mediterranean water can introduce significant variations on the bottom seawater  $\delta^{18}\text{O}$  composition, it is considered as a good approximation to the true value.

#### 7.3.4.1 Sample 3463-A03

In sample 3463-A03, the pure calcite and dolomite phases are estimated to precipitate from fluids that are significantly enriched in  $^{18}\text{O}$  compared to the expected composition of the seawater for the corresponding MIS (Table 7.6 and Figure 7.14). In Figure 7.14 the estimated fluid compositions are shifted towards heavier  $^{18}\text{O}$  values than the predicted by the  $\delta^{18}\text{O}$  LR04 curve. Sub-sample 8 indicates precipitation from fluids enriched in  $^{18}\text{O}$  (from 0.68‰ SMOW at 8°C up to 2.02‰ SMOW, at 14°C for calcite and from 0.8‰ SMOW at 4°C up to 3.24‰ SMOW at 14°C for dolomite). Calcite precipitation close to expected seawater composition is obtained with a precipitation temperature of 4°C. However, temperatures higher than 8°C are thought to be more plausible at these water depths for the correspondent sub-sample age. The estimated fluid composition values are too heavy (for 8°C, more than 1.2‰ SMOW heavier than the present day 0.6‰ SMOW seawater isotopic composition) to be explained by glacial-interglacial fluctuation of the seawater  $\delta^{18}\text{O}$  composition alone. Therefore these isotopic values are interpreted as including a significant contribution of heavier isotopic water resulting, most probably, from the destabilization of gas hydrates. Sub-samples 6 and 7 also indicate heavier isotopic composition of the fluids from which the authigenic dolomite precipitated, although this enrichment is not as significant as in sub-sample 8.

The precipitation of calcite can be explained by formation at a temperature of 4 to 8°C in sub-samples 6 and 7 *i.e.* at a temperature range close to the present day values (8 to 12°C). The dolomite estimated fluid composition indicates heavier  $^{18}\text{O}$  fluid composition or significantly lower temperature of precipitation (less than 4°C for sub-sample 7, and between 4 and 8°C for sub-sample 6). Considering the glacial-interglacial relative age of the sub-samples, it should be expected for sample 8 the highest temperature of precipitation and for sample 6 the lowest temperature of precipitation, as illustrated in Figure 7.14 (where the temperatures of precipitation considering a constant  $\delta^{18}\text{O}$  fluid composition value of 0.6‰ SMOW are plotted in magenta open circles for calcite and X symbols for dolomite). Sub-sample 8 however corresponds to the lowest estimated temperatures of precipitation (7.65°C for calcite and 3.24°C for dolomite) while sub-sample 6 corresponds to the highest temperature of formation (8.65°C for calcite and 4.10°C for dolomite). At the location where the samples were collected, the MO intensity is expected to be higher during the interglacial periods and weaker during glacials (as

discussed before). Therefore, the calculated relative temperatures are in opposite phase to those expected from the glacial-interglacial timing and the consecutive MO intensity. It is therefore interpreted that the predominant factor that is being reflected in the isotopic composition of the authigenic carbonates is the variation in the isotopic composition of the fluids from which the carbonates precipitated.

If one considers the precipitation of the authigenic carbonates from a constant fluid isotopic composition, then the authigenic calcite and dolomite compositions have to be explained by temperature variations. The estimated temperature of formation of the several sub-samples (plotted in Figure 7.14) indicates a variation that is not in agreement with the expected variation correspondent to the different MIS. Also the temperature amplitudes between the sub-samples (from 0.86°C up to 1.0°C) are much lower than the temperature amplitudes that would be expected from the very different formation stages of the sub-samples. These low temperature amplitudes are interpreted instead as reflecting a relatively constant temperature of the seeping fluids and that the oxygen isotopic variability of the authigenic calcite and dolomite preferentially reflects variations in the source fluid  $^{18}\text{O}$  composition, instead of temperature variations.

It should be noted that, while the different sub-samples from sample 3463-A03 correspond to a large time range (88 to 221 ka), corresponding to different MIS and to significant variability in the seawater  $\delta^{18}\text{O}$  composition, the isotopic values of the authigenic carbonates have relatively constant composition values. This is interpreted as reflecting a similar fluid composition that is not significantly controlled by the glacial-interglacial seawater isotopic variability but, most probably is mainly constrained by the pore water and seepage fluid compositions. As such, this sample seems to exhibit a contribution from pore waters resulting from dissolution of gas hydrates.

**Table 7.6.** Calculated  $\delta^{18}\text{O}_{\text{SMOW}}$  values of pure phases calcite and dolomite, for temperature values of 4, 8, 11, 12 and 14°C. For calcite, the Kim and O'Neil (1997) fractionation equation was used, and for dolomite the one by Vasconcelos *et al.* (2005).  $\delta^{18}\text{O}$  values of sub-samples 9 and 10 were not measured.

Sample	Sub-sample	Age (ka)	Calculated Fluid $\delta^{18}\text{O}_{\text{SMOW}}$ composition									
			Calcite					Dolomite				
			t=4°C	t=8°C	t=11°C	t=12°C	t=14°C	t=4°C	t=8°C	t=11°C	t=12°C	t=14°C
3463-A08	1	244.9	-2.14	-1.22	-0.54	-0.32	0.12	-1.09	-0.09	0.64	0.87	1.34
	2	247.8*	-2.65	-1.73	-1.05	-0.83	-0.39	-1.60	-0.60	0.13	0.37	0.83
	3	247.8*	-2.77	-1.85	-1.17	-0.95	-0.51	-1.72	-0.71	0.01	0.25	0.71
	4	246.2	-2.69	-1.77	-1.09	-0.87	-0.43	-1.64	-0.64	0.09	0.33	0.79
	5	244.9	-2.71	-1.79	-1.11	-0.89	-0.45	-1.66	-0.66	0.07	0.31	0.77
3463-A03	6	135.2	-0.48	0.45	1.13	1.35	1.79	0.57	1.58	2.3	2.54	3.01
	7	220.6	-0.44	0.49	1.17	1.39	1.83	0.61	1.61	2.34	2.58	3.05
	8	113.8	-0.25	0.68	1.36	1.58	2.02	0.8	1.8	2.53	2.77	3.24

\* isochron age

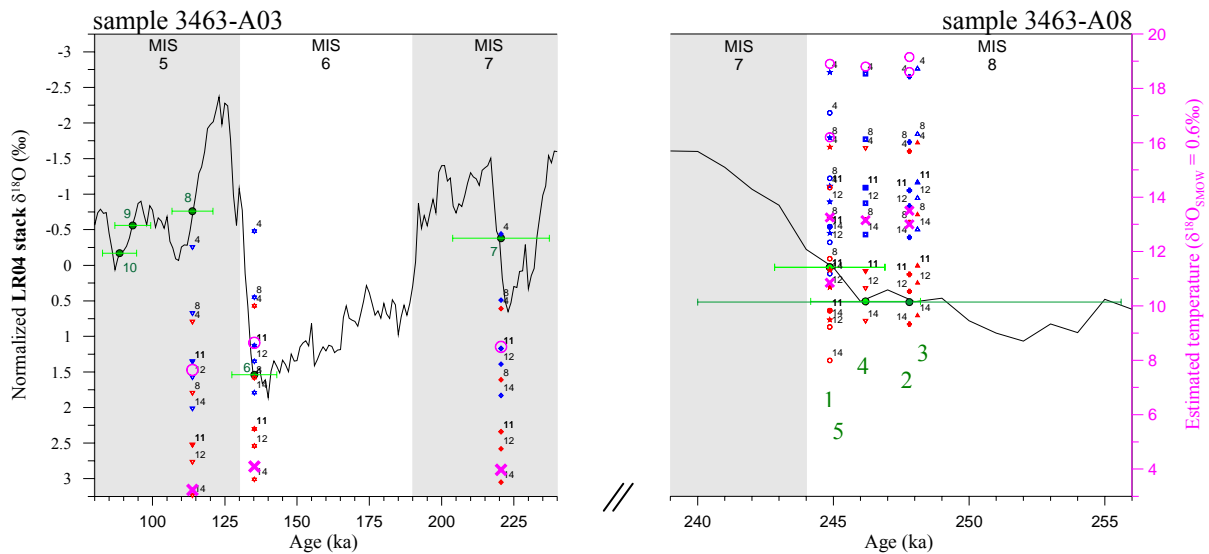


**Figure 7.14.** Plot of the determined ages of the analysed dolomite chimneys over the normalized  $\delta^{18}\text{O}_{\text{SMOW}}$  “LR04” stack curve (Lisiecki and Raymo, 2005). Age values are projected onto the normalized  $\delta^{18}\text{O}_{\text{SMOW}}$  curve. The estimated  $\delta^{18}\text{O}_{\text{SMOW}}$  fluid composition from which the calcite (in blue) and the dolomite (in red) pure phases end-members precipitated are plotted for fluid temperature values of 4, 8, 11, 12 and 14°C, respectively (Table 7.6). In magenta are plotted the temperatures of precipitation considering a constant  $\delta^{18}\text{O}$  fluid composition value of 0.6‰ (SMOW), the open circles correspond to calcite and the X symbols correspond to dolomite. Note the different age scale and the scale hiatus in the graph. Green numbers indicate sub-sample labels.

#### 7.3.4.2 Sample 3463-A08

In sample 3463-A08, the authigenic calcite and dolomite are estimated to precipitate from fluids significantly depleted in  $^{18}\text{O}$  relative to the expected composition of seawater at the corresponding MIS seawater composition (Table 7.6 and Figure 7.14). All sub-samples (1-5) indicate calcite precipitation from fluids depleted in  $^{18}\text{O}$  (from -2.77‰ SMOW at 4°C up to 0.12‰ SMOW at 14°C). For dolomite, the estimated fluid composition is heavier than the estimated fluid composition for calcite. This can be explained by a contribution from the detrital calcite fraction from the calcareous microfossils that should have a isotopic oxygen source distinct from the methane-derived authigenic calcite, or could indicate a slightly different fluid composition or a different temperature during the formation of the various authigenic carbonate phases (as already discussed in chapter 6). The estimated composition of the fluids from which the dolomite precipitated indicates fluid compositions ranging from -1.72‰ SMOW at 4°C up to 1.34‰ SMOW at 14 °C. These values correspond to fluids with compositions close to the seawater value expected for the corresponding MIS period for the several sub-samples, with the exception of sub-sample 1, which has a heavier isotopic fluid composition than the other sub-samples. Sample 3463-A08 does not therefore show a clear contribution from a heavier oxygen source, with the exception of dolomite from sub-sample 1; as such, the contribution from the dissociation of gas hydrates is not considered to be significant for the fluids from which this sample precipitated. Furthermore, it should be noted that all sub-samples in sample 3463-A08 have similar  $\delta^{18}\text{O}$  compositions. The similar isotopic compositions of the authigenic calcite and dolomite (maximum difference of 0.63‰) also support their similar age values. This can also be interpreted as reflecting a major contribution from a methane rich fluid with a constant composition. The contribution from seawater source fluids is interpreted as being minor since the composition trend of the authigenic calcite and dolomite does not have any similarity with the expected seawater isotopic trend illustrated by the  $\delta^{18}\text{O}$  LR04 curve (Figure 7.14).

If one considers the precipitation of the authigenic carbonates from a fluid with a constant isotopic composition (c.a. the present day 0.6‰ SMOW), then, in order to explain the calcite and dolomite  $\delta^{18}\text{O}$  compositions, the temperature of precipitation of the different sub-samples shows a variation that is not in agreement with the expected temperature variation correspondent to the MIS ages of the sub-samples. Temperature

amplitudes between the sub-samples (up to 2.65°C for dolomite and up to 2.95°C for calcite) would have to be considered to explain the authigenic calcite and dolomite compositions (Figure 7.14). As these temperature amplitudes are observed in sub-samples with very close ages, they are interpreted as being less probable to occur as a consequence of the glacial-interglacial variation during the correspondent short time span for this sample formation. These temperature amplitudes and the fact that they show a variation that is not in agreement with the one expected from the ages of the several sub-samples, are interpreted as indicating that the oxygen isotopic variability of the authigenic calcite and dolomite preferentially reflects variations in the fluid  $^{18}\text{O}$  compositions, instead of temperature variations.

The amount of data available is not yet sufficient to support a robust refinement of the proposed inferences concerning the fluid isotopic composition and their source and formation temperature. Further investigation has to be carried out in order to better constrain the use of the MDAC as a proxy for the reconstruction of the seep fluids composition and formation temperatures.

### **7.3.5 Formation model of the two chimneys**

The sample 3463-A03 that is characterized by high initial sediment porosity and high permeability it is proposed, according to the general formation model (as discussed in chapter 5), that this chimney will be formed by cementation resultant from the precipitation of authigenic carbonates as result of anaerobic methane oxidation coupled with sulphate reduction, at the reaction front between a percolating fluid (gas or solution) enriched in methane and the *in situ* interstitial sulphate enriched pore waters. The percolated methane-rich fluid would preferentially, for the case of sample 3463-A03, percolate through the sediment along a percolation pathway of higher interstitial porosity, cementing the original sediments along this pathway, without the requisition of an open vent conduit, as the initial permeability of the sediments are high. Therefore, the lithification resulted on a completely cemented conduit, which would correspond (approximately), to the centre of conduit 1 (Figure 7.7). Subsequent fluid flow episodes would kip using the same pathway but around this cemented hard nucleus. Therefore, this conduit would grow spreading out from the centre of conduit 1. If the cementation resulted in blocking of the fluid initial pathway,

latter fluid flow episodes have to follow different pathways that would again form a cemented nucleus with the cementation grow spreading out from this second conduit. When the two conduits are closely spaced than the unification of both could occur. To be noted that, these two or even more parallel conduits, can be contemporary or subsequent, like it is the proposed for sample 3463-A03. The space between two parallel conduits can exhibit authigenic carbonate minerals corresponding to a mixture of the two fluid episodes and therefore ages that would correspond to a mixture or intermediate ages.

The fluid pathways through out the sediments can be constrained and resulting from sedimentary discontinuities such as borrows. In fact many of the chimney samples resemble the shape and structure of many borrows and scavenger holes of many organisms where two parallel tubular holes are frequent.

The sample 363-A08 corresponds to the lithification of clay rich sediments. The permeability of the initial sediment material would be reduced when compared to the material that composed the unconsolidated sediment of sample 3463-A03. It is proposed that the unconsolidated sediment of sample 3463-A08 would have low or reduced permeability and therefore the percolation of any fluids throughout these sediments would require that the fluid would form a vent conduit that had to be open for the methane-rich fluid percolation. Therefore the AOM-SR reaction front and the precipitation of the authigenic cement would occur spreading out from the methane-rich fluid conduit, but would occur in a single episode and within an unique event, as indicated by the ages obtained from this sample. The precipitation would occur as long far as the AOM-SR reaction front would be able to progress away from the open vent conduit, into the sulphate zone. Once the cementation reach a complete cementation of the open vent conduit walls, it would block the laterally methane percolation and therefore the AOM-SR reaction would cessed. Therefore open vent chimneys would correspond to a single cemented episode. Subsequent episodes of fluid flow could induce the cement formation within the open vent conduit if the environment inside the conduit would go through a previous episode of refilling with sulphate that would feed new episode of AOM-SR reaction. This would result in chimneys with a concentric grow layers, having a younger core and an older periphery.

## 7.4 Conclusions

The estimated ages of the two dolomite chimneys analysed indicate that the precipitation of the authigenic carbonates occurs, from the centre or axis of the chimney to the periphery, during short intervals of time and the chimneys can grow during several discontinuous episodes, probably with longer periods with absence of precipitation. The chimneys that result from the precipitation during different episodes will be most probably evidence different grow layers or concentric rings.

The estimated ages of the sub-samples indicate formation at periods of rapid paleoclimatic changes. The samples point to precipitation during (1) the onsets of terminations 2 and 3, contemporary with rapid sealevel rises; (2) at the transition from stadial to interstadial, also corresponding to rapid sealevel rise; and (3) at the transition from interglacial (MIS 5.5) to stadial MIS 5.4 or from interglacial (MIS 5.3) to stadial 5.2, associated with periods of progressive sealevel lowering (Figure 7.12).

It is proposed that the MDAC precipitation are recording intense fluid flow episodes during periods of increased seabottom water temperature as a result of the increase of the MO influence at the locations where the samples were collected from. This increase in seabottom water temperature is, most probably, reducing the gas hydrate stability zone, leading to gas hydrate dissociation and consequent release of methane-rich fluids which will induce the carbonate precipitation along the fluid conduits on the fluid pathways above the methane seepage sites.

Estimated compositions of the fluids from which the authigenic precipitated indicate for sample 3463-A03 a precipitation from fluids that are significantly enriched in  $^{18}\text{O}$  compared to the expected composition of the seawater for the correspondent MIS. These isotopic values are interpreted as including a significant contribution of heavier isotopic water resulting, most probably, from the destabilization of gas hydrates. Sample 3463-A08, however, does not indicate a similar evolution; its precipitation is compatible with the expected correspondent MIS fluid isotopic composition.

## **Chapter 8. Biomarker and SEM evidences of microbial mediation in the formation of MDAC in the Gulf of Cadiz**

### **8.1 Introduction**

As described in detail in Chapter 5, two main lithologic types of MDAC were identified in the collected samples from the Gulf of Cadiz: (1) dolomite-dominated carbonates; and (2) aragonite-dominated carbonates. The dolomite-dominated carbonates form crusts, irregular massive or nodular aggregates, and chimneys (fluid conduits or filled burrows). The dolomite samples have been found along the Guadalquivir diapiric ridge (GDR), the Formoza Ridge, the Cadiz and the Guadalquivir Channels, in the Mediterranean Outflow (MO) channel in front of Gibraltar Strait, in the Pen Duick and Vernadsky ridges, in the Iberico mud cone, and in the Faro, Hesperides, Student and Yuma mud volcanoes (Magalhães *et al.*, 2002; Díaz-del-Río *et al.*, 2003; Magalhães *et al.*, 2005b). The aragonitic pavements form crusts or slabs that pave the seafloor for several square meters or form buildups and irregular blocks, up to 2 m high, at the seafloor. They have been found in the Pen Duick and Vernadsky ridges, within the Cadiz Channel, and also associated with several mud volcanoes: Porto, Jesus Baraza, Yuma, Ginsburg, Darwin, Shauen, Kidd, Mercator, Fiuza, Faro, Hesperides and Meknes (Figure 8.1).

As discussed in Chapters 5, 6 and 7, the formation of some of these MDAC in the Gulf of Cadiz is related to episodes of enhanced fluid seepage, at least during the last 250 ka, and some of them are related to episodes of gas hydrate formation and dissociation.

The precipitation of these authigenic carbonates (as described in Chapter 5), is similar to that described for modern environments throughout the world's oceans, at a variety of depths, associated with hydrocarbon seepage (e.g. Kulm *et al.*, 1986; Hovland *et al.*, 1987; Ritger *et al.*, 1987; Hovland and Judd, 1988; Kulm and Suess, 1990; Paull *et al.*, 1992; Aharon, 1994; Bohrmann *et al.*, 1998; Greinert *et al.*, 1999; Aloisi *et al.*, 2000;

Elvert *et al.*, 2000; Greinert *et al.*, 2000; Greinert *et al.*, 2001; Campbell *et al.*, 2002; Greinert *et al.*, 2002; Díaz-del-Río *et al.*, 2003). Their formation is assigned to the sulphate reduction zone or to the transition between the sulphate reduction zone and the methanogenic zone, where microbial sulphate reduction (SR) is coupled with anaerobic oxidation of methane (AOM) (Ritger *et al.*, 1987; Paull *et al.*, 1992; Hoehler *et al.*, 1994) according to the Reeburgh (1980) net equation (see Chapter 5). As a by-product of AOM, bicarbonate is produced with a consequent increase of the pore water fluid alkalinity, promoting the precipitation of the authigenic carbonates. AOM is a microbial-mediated process performed by a consortium of methanotrophic archaea and sulphate-reducing bacteria (SRB), occurring in anoxic environments, where sulphate is used as electron receptor (Hoehler *et al.*, 1994; Hinrichs *et al.*, 1999; Boetius *et al.*, 2000; Hinrichs *et al.*, 2000; Pancost *et al.*, 2000; Orphan *et al.*, 2001a; Orphan *et al.*, 2001b). The evidences for this process, as described for several modern cold seeps and gas hydrate occurrences, derive from archaeal biomarkers, such as Crocetane 2,6,11,15-tetramethylhexadecane (e.g. Thiel *et al.*, 1999; Boetius *et al.*, 2000; Elvert *et al.*, 2000; Hinrichs *et al.*, 2000; Pancost *et al.*, 2000; Elvert *et al.*, 2001; Orphan *et al.*, 2001a; Pancost *et al.*, 2001b; Thiel *et al.*, 2001a; Thiel *et al.*, 2001b; Hinrichs and Boetius, 2002; Michaelis *et al.*, 2002; Werne *et al.*, 2004; Pancost *et al.*, 2005), PMI (2,6,10,15,19-pentamethylcosane) and PMIA (e.g. Thiel *et al.*, 1999; Boetius *et al.*, 2000; Elvert *et al.*, 2000; Hinrichs *et al.*, 2000; Pancost *et al.*, 2000; Elvert *et al.*, 2001; Orphan *et al.*, 2001a; Pancost *et al.*, 2001b; Thiel *et al.*, 2001a; Thiel *et al.*, 2001b; Hinrichs and Boetius, 2002; Michaelis *et al.*, 2002; Werne *et al.*, 2004; Pancost *et al.*, 2005), Squalane (2,6,10,15,19,23-hexamethyltetracosane) and squalenes (Elvert *et al.*, 2000), that can have an archaeal source or can have a bacterial origin, Archaeol (2,3-di-O-phytanyl-sn-glycerol) (e.g. Boetius *et al.*, 2000; Elvert *et al.*, 2000; Pancost *et al.*, 2000; Elvert *et al.*, 2001; Orphan *et al.*, 2001a; Pancost *et al.*, 2001b; Hinrichs and Boetius, 2002; Michaelis *et al.*, 2002; Werne *et al.*, 2004; Pancost *et al.*, 2005), Hydroxyarchaeol (2-O-3-hydroxyphytanyl-3-O-phytanyl-sn-glycerol) (e.g. Boetius *et al.*, 2000; Pancost *et al.*, 2000; Orphan *et al.*, 2001a; Pancost *et al.*, 2001b; Hinrichs and Boetius, 2002; Michaelis *et al.*, 2002; Werne *et al.*, 2004; Pancost *et al.*, 2005), and Biphytanyl tetraethers (Thiel *et al.*, 1999; Pancost *et al.*, 2000; Pancost *et al.*, 2001b; Thiel *et al.*, 2001a; Thiel *et al.*, 2001b; Michaelis *et al.*, 2002; Pancost *et al.*, 2005). All these

archaeal biomarkers are characterized by extremely negative  $\delta^{13}\text{C}$  values (less than -100‰ VPDB).

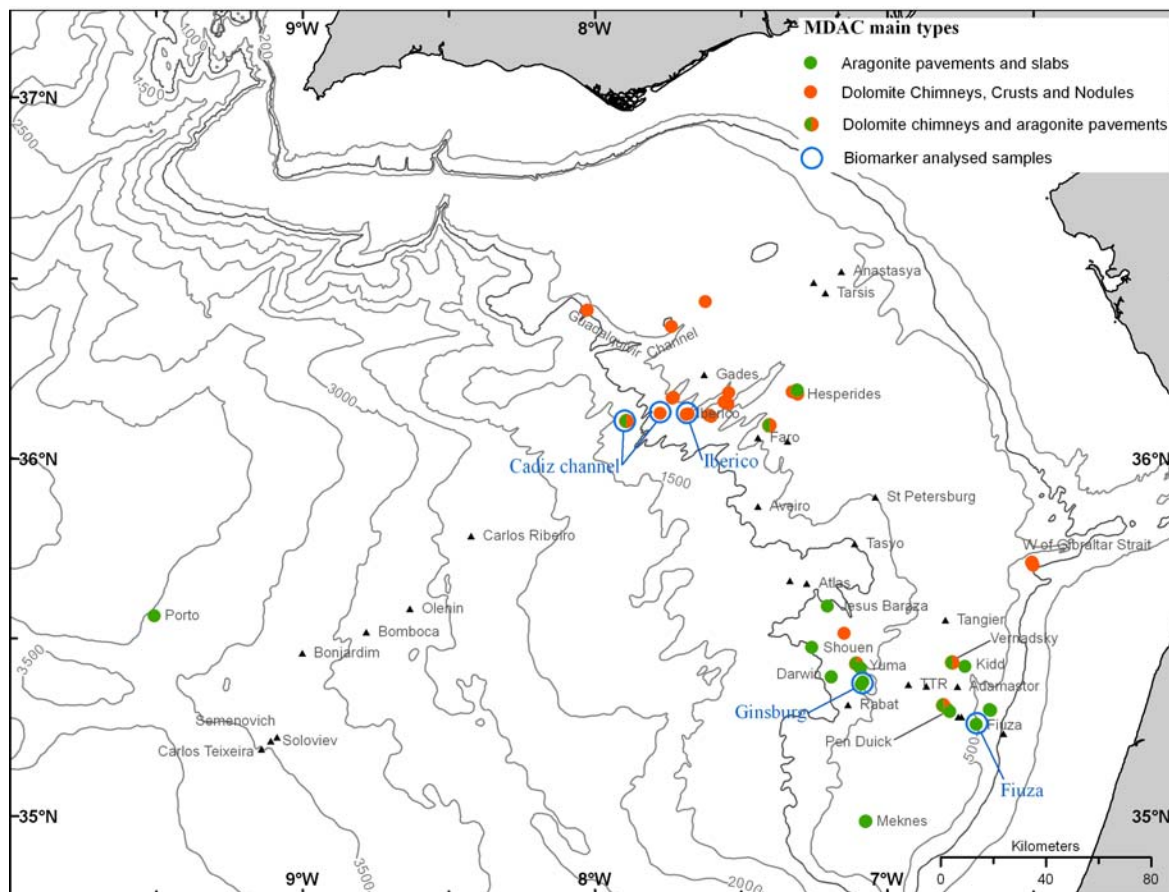


**Figure 8.1.** Occurrences of MDAC in the Gulf of Cadiz. The samples analysed for biomarkers in this work are highlighted with open blue circles. Black triangles indicate the location of known mud volcanoes.

Biomarkers for SRB are frequently identified associated with the archaeal biomarkers (Valentine and Reeburgh, 2000). Amongst these, alkyl diethers, 12-methyl-tetradecanoic acid, Mono- and dialkyl-glycerolethers (non isoprenoidal), n-, mono-methyl (i-, ai-, mid-chain), N-cyclohexyl and cyclopropyl carbon chains (e.g. Hinrichs *et al.*, 2000; Orphan *et al.*, 2001a; Pancost *et al.*, 2001a; Hinrichs and Boetius, 2002; Michaelis *et al.*, 2002; Werne *et al.*, 2004), and ester-bound fatty acids, such as n-, mono-methyl (i-, ai-, mid-chain), N-cyclohexyl, and cyclopropyl carbon chains are frequent (e.g. Boetius *et al.*, 2000; Hinrichs *et al.*, 2000; Pancost *et al.*, 2000; Orphan *et al.*, 2001a; Pancost *et al.*, 2001a; Thiel *et al.*, 2001a; Hinrichs and Boetius, 2002; Werne *et al.*, 2004).

In active cold seep sediments, genetic analysis shows that the observed archaea belong to either the clusters of AMNE-1 and AMNE-2, or those of the Methanomicrobiales/Methanosarcinales (Hinrichs *et al.*, 1999; Hinrichs and Boetius, 2002). The SRB are interpreted as most probably belonging to the Desulfocarcina/Desulfococcus group (Michaelis *et al.*, 2002). Direct morphological evidences of microbes at cold seeps have been shown via epifluorescence microscopy (Boetius *et al.*, 2000; Orphan *et al.*, 2001b) and *in situ* field surveys of putative *Beggiatoa* mats (Michaelis *et al.*, 2002).

In ancient methane seep deposits, evidences of past microbial activity include geochemical and biomarker signatures as well as morphologic evidences. The geochemical evidences for microbial involvement in the authigenic carbonate formation as a result of AOM include the association of authigenic carbonates with isotopic negative  $^{13}\text{C}$  values associated with pyrite (Cavagna *et al.*, 1999; Peckmann *et al.*, 2002; Shapiro and Fricke, 2002). Biomarkers indicative of archaea and their diagenetic products, such as PMI and  $\text{C}_{30}$  acyclic isoprenoids, are frequently associated with fossil hydrocarbon seep deposits (Peckmann *et al.*, 1999a). Morphologic signatures of microbial activity include the presence of early non-detrital micrite, thinly laminated micrite, micrite diffusive peloids with 0.1-1 mm in diameter (Campbell *et al.*, 2002), dumbbell-shaped crystal bundles (Van Lith *et al.*, 2003), laminated sediments, hollow dolomite crystals, dolomitic tubes with 15  $\mu\text{m}$  in diameter, cylindrical aggregates of framboidal pyrite with diameters of about 100  $\mu\text{m}$  (Cavagna *et al.*, 1999), dumbbell morphologies and body fossils of clotted microfabrics (Peckmann *et al.*, 2002), pinnate bacteria with 0.3  $\mu\text{m}$  in diameter and 1-1.5  $\mu\text{m}$  long, sheaths with 2-4  $\mu\text{m}$  in diameter or clusters of coccoids, up to 40 per cluster and each with 0.5-1  $\mu\text{m}$  in diameter (Shapiro, 2004).

A significant number of the MDAC occurrences in the Gulf of Cadiz are dolomite-dominated and occur in extensive areas of hundreds of square meters at the seafloor (Chapter 4). The study of these authigenic dolomite samples can bring new contributions to the dolomite problem, by evaluating if these samples support the so-called microbial factor, which proposes that microbial activity has an important role mediating the precipitation of dolomite under normal temperature conditions (Vasconcelos *et al.*, 1995; Warthmann *et al.*, 2000).

This chapter focuses on the microbial component of the MDAC from the Gulf of Cadiz, based on the petrography, scanning electron microscopy (SEM) and biomarker evidences of microbial activity preserved in these MDAC. The aragonite pavements are considered to represent very recent or present day formation of authigenic carbonates (Chapter 5), whereas the dolomite chimneys probably represent older formation episodes over a period spanning at least from 89 ka until 250 ka (see Chapter 7). The analysis of the different preserved microbial evidences can be used to track the degradation of the microbial signatures through time.

In order to attain these objectives, specific lipid biomarkers analyses were carried out at the Marine Biogeochemistry Laboratory of the Research Center for Ocean Margins (RCOM), of the Bremen University (Magalhães *et al.*, 2005a). SEM observations were carried out at the ETH Centre (Zurich) and in the University of Aveiro, together with petrographic observations, in order to investigate morphological evidences of the microbial activity.

## 8.2 Materials and Methods

The samples selected for identification of microbial evidences were chosen based on the best preservation potential of their organic content. Petrographic analysis was carried out on hand specimens and in thin sections with binocular microscope, petrographic microscope and cathodoluminescence. Scanning electron microscopy (SEM) and biomarker analysis were also performed in selected samples (listed in Table 8.1). The chimneys were selected based on their degree of oxidation. Because the oxidation is a secondary process that occurs after the exhumation of the samples from the sediments and because the oxidation will have a strong effect on the degradation of organic compounds, only the samples with none or with weak signs of oxidation were selected. Amongst these, samples 3463-A08 and 3722-A33 were selected (+ amostras da Luisa) (Figure 8.2), because they are compact, very homogeneous, massive, with no fractures, and do not show significant signs of alteration, and therefore have lower probabilities of being contaminated. Aragonite pavement samples were also selected in order to represent the different lithologic types and to obtain the best organic matter preservation. As such, only

aragonite pavement samples with weaker or no signs of oxidation were selected.

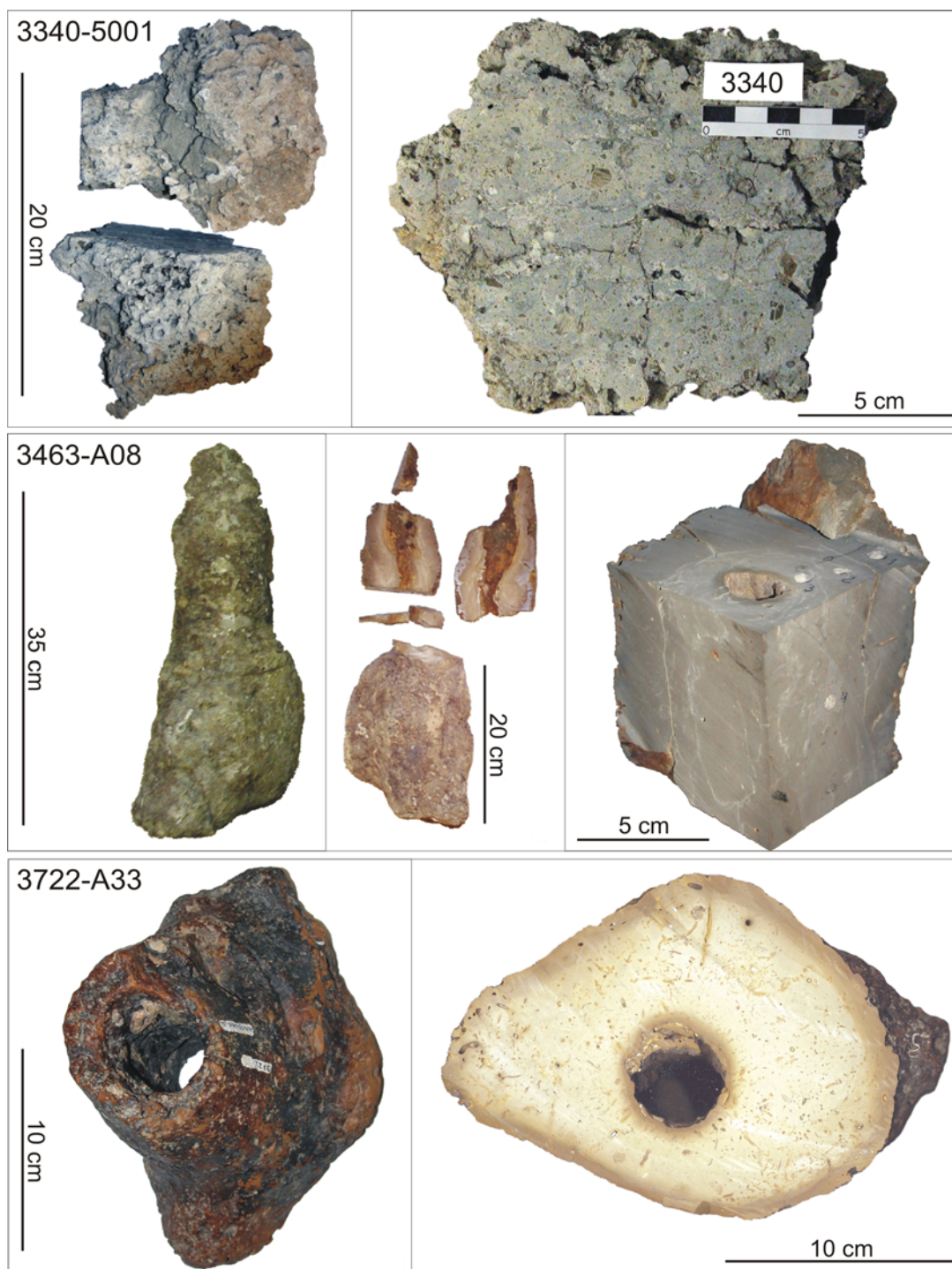


**Figure 8.2.** Samples analysed for biomarkers. Sample 3340-5001 (TTR09-218Gr): aragonite pavement, from which a sub-sample was collected for biomarker analyses, by cutting a 7 cm thick slice off the interior of the crust. Sample 3463-A08 (TTR11-339D-A08): dolomite chimney with no signs or very weak signs of oxidation. Sample 3722-A33 (ANA00-DA10.33): dolomite chimney with weak signs of oxidation in the internal chimney material. To avoid the oxidation fronts, sub-samples were collected by cutting a 7 cm thick slice in the internal, less oxidized area.

**Table 8.1.** Samples selected for biomarker analyses and SEM observations. (TS: thin section; SEM: scanning electron microscopy; BK: biomarker analysis)

Sample	Field N°	Sample location	Description	Work		
3458-A03	TTR11-335D	Iberico Mud Cone	Dolomite crust (section 5.4.1.2, Chapter 5) with a moderate degree of oxidation	TS		
3458-A05	TTR11-335D	Iberico Mud Cone	Dolomite crust (section 5.4.1.2, Chapter 5) with a moderate degree of oxidation	TS		
3458-B04	TTR11-335D	Iberico Mud Cone	Dolomite crust (section 5.4.1.2, Chapter 5) with a moderate degree of oxidation, very homogeneous and massive	TS	SEM	
3458-B05	TTR11-335D	Iberico Mud Cone	Dolomite crust (section 5.4.1.2, Chapter 5) with a moderate degree of oxidation, very homogeneous and massive	TS		
3458-B11	TTR11-335D	Iberico Mud Cone	Dolomite crust (section 5.4.1.2, Chapter 5) with a moderate degree of oxidation, very homogeneous and massive material	TS		BK
3458-B13	TTR11-335D	Iberico Mud Cone	Dolomite crust (section 5.4.1.2, Chapter 5) with a moderate degree of oxidation, very homogeneous and massive	TS	SEM	
3458-C02	TTR11-335D	Iberico Mud Cone	Dolomite crust (section 5.4.1.2, Chapter 5) with a moderate degree of oxidation, very homogeneous and massive	TS	SEM	
3463-A08	TTR11-339D	Cadiz Channel	Dolomite chimney (section 5.4.1.1, Chapter 5) with no significant signs of oxidation, very homogeneous and massive	TS		BK
3463-B02	TTR11-339D	Cadiz Channel	Dolomite crust (section 5.4.1.2, Chapter 5) with a moderate degree of oxidation, very homogeneous and massive	TS	SEM	
3463-B05	TTR11-339D	Cadiz Channel	Dolomite crust (section 5.4.1.2, Chapter 5) with a moderate degree of oxidation, very homogeneous and massive	TS	SEM	
3722-A33	ANA00-DA10.33	Iberico Mud Cone	Dolomite crust (section 5.4.1.2, Chapter 5) with a moderate degree of oxidation, homogeneous and massive material	TS		BK
3608-A01	TTR12-388Gr	Formoza Ridge	Dolomite crust (section 5.4.1.2, Chapter 5) with a moderate degree of oxidation, high porosity material with sand size detrital grains	TS	SEM	
3611-A01	TTR12-391Gr	Jesus Baraza MV	Aragonite pavement, shell crust type (section 5.4.1.4.2, Chapter 5)	TS	SEM	
3611-A02	TTR12-391Gr	Jesus Baraza MV	Aragonite pavement, shell crust type (section 5.4.1.4.2, Chapter 5)	TS	SEM	
3920	GeoB9023-1	Hesperides MV	Aragonite pavement with stromatolitic layers (section 5.4.1.4.5, Chapter 5)	TS	SEM	BK
3921-A62	GeoB9024-6	Hesperides MV	Aragonite pavement with stromatolitic layers (section 5.4.1.4.5, Chapter 5)	TS	SEM	
3921-A63	GeoB9024-6	Hesperides MV	Aragonite pavement with stromatolitic layers (section 5.4.1.4.5, Chapter 5)	TS		
3922-107	GeoB9029-3	Faro MV	Aragonite pavement with dark color and stromatolitic layers (section 5.4.1.4.5, Chapter 5)	TS	SEM	BK
3340-5001	TTR09-218Gr	Ginsburg MV	Aragonite pavement, lithified mud breccia type (section 5.4.1.4.1, Chapter 5)	TS	SEM	BK
	TTR14-566Gr	Fiuza MV	Aragonite pavement, lithified mud breccia type (section 5.4.1.4.1, Chapter 5)	TS		BK
	TTR15-599D.B01	Cadiz Channel	Dolomite chimney with weak oxidation, homogeneous, high porosity material (section 5.4.1.1, Chapter 5)	TS		BK
	TTR15-599D.C02	Cadiz Channel	Dolomite chimney with no significant oxidation, homogeneous, high porosity material (section 5.4.1.1, Chapter 5)	TS		BK
	TTR15-599D.D01	Cadiz Channel	Aragonite pavement, lithified mud breccia type (section 5.4.1.4.1, Chapter 5)	TS		BK

## 8.2.1 Petrography, SEM and EDS

The samples used for this study were cut in 7 cm thick slices, from which thin sections were prepared in three perpendicular planes. The chimney samples were cut parallel and perpendicular to the chimney axis.

SEM and energy dispersive spectrometer X-ray elementary analysis (EDS) were performed on slices cut from the samples, in which the external and the existing friable material or material containing penetrative fractures was removed. From these slices, chips with 1x1x5 cm were cut and cleaned in distilled water in an ultrasonic cleaner for 15 minutes. Then, the samples were etched in 1% HCl for 1 minute. After etching, the samples were rinsed in distilled water and immediately dried on a warm furnace (at 45°C), and gold or carbon coated. After coating the samples were kept isolated in a desiccator to avoid contamination. They were analysed on a Hitachi S4100 scanning electron microscope, operating at 15 kV and equipped with a backscattered electron detector (Rontec Energy Dispersive X-ray Spectrometer system, series M) with a window for light elements. All photomicrographs are secondary electron imaging scans at varying working distances. The SEM-EDS analyses were performed both at ETH in Zurich, and in the Ceramics Department of the University of Aveiro.

## 8.2.2 Lipid Biomarkers

### 8.2.2.1 Sample preparation

The aragonite pavements are considered to represent a more recent carbonate generation than the dolomite chimneys. Previous studies (Duarte, 2005; Niemann *et al.*, 2005; Niemann *et al.*, 2006) have already shown that the biomarker indicators are very abundant in this type of samples. Sample 3340 (Figure 8.2) was selected because it shows no signs of oxidation. From this aragonite pavement sample, 20 g of material was collected and prepared for biomarker extraction. As concerns the dolomite chimneys, 250 g of material was collected and prepared for biomarker extraction by fragmenting to small 5 cm thick slices from samples 3458-B11, TTR14-566Gr, TTR15-599D.B01, TTR15-599D.C02, TTR15-599D.D02, 3463-A08 and 3722-A33 (Figure 8.2), avoiding the periphery and fractured parts of the samples that can act as contamination sources.

The sample preparation procedure used for extraction and purification of the lipid biomarkers was based on the method of Peckmann *et al.* (2004). The analytical methodology used for the dolomite chimney samples is described in the flowchart of Figure D.2, Appendix D and the one used for the aragonite pavements is shown in the flowchart of Figure D.1, Appendix D.

### 8.2.2.2 Analytical procedure

The freshly broken carbonate samples were decalcified (HCl) and the dried residue was refluxed in 6% KOH in CH<sub>3</sub>OH (saponification reaction: 2 h). The supernatant was decanted and the residue was repeatedly extracted by ultrasonication in CH<sub>2</sub>Cl<sub>2</sub>/CH<sub>3</sub>OH (3:1; v:v) until the solvent became colourless. Subsequently, the combined supernatants were portioned in CH<sub>2</sub>Cl<sub>2</sub> versus water (pH 2). The resulting total extract was dried and separated by column chromatography (Merck silica gel 60, 0.063-0.200 mm; i.d.: 15 mm, length: 35 mm) into fractions containing: (1) hydrocarbons (20 ml or 3 column volumes of n-hexane); (2) esters/ketones (20 ml of n-hexane/CH<sub>2</sub>Cl<sub>2</sub> 2:1); (3) alcohol (20 ml of CH<sub>2</sub>Cl<sub>2</sub>/aceton 9:1; and (4) fatty acids/polars (20 ml of MeOH). The esters/ketones and alcohol fractions were dried and derivatised using pyridine and BSTFA (2:1) at 70°C (1 h). The polar fractions/fatty acids were dried and transesterificated with boron-trifluoride methanol and then with KCl + hexane. The internal standard used for all fractions was Cholestane. A modification of the method, which involved a previous extraction with CH<sub>2</sub>Cl<sub>2</sub>/CH<sub>3</sub>OH (3:1; v:v) prior to decalcification, proved to be efficient in cleaning dirt peaks on the dolomite samples.

### 8.2.2.3 Gas chromatography and coupled mass spectrometry (GC-MS)

The hydrocarbon fraction was examined by combined gas chromatography-mass spectrometry (GC-MS) using a Varian CP-3800 GC/Saturn 2000 MS EI-mode, 70eV) equipped with a 30 m fused silica capillary column (CP-Sil 8 CB Low Bleed, 0.25mm ID, 0.25 µm film thickness). The carrier gas was He. The GC-temperature program used was: injection at 80°C, 5 min isothermal; from 80°C to 310°C at 4°C min<sup>-1</sup>; 20 min isothermal. The identification of the organic compounds was based on comparison of the mass spectra and the GC retention times with those of published data and reference compounds.

Coupled GC-combustion-isotope ratio MS (GC-C-IRMS) was conducted using a Finnigan DeltaPlusXL mass spectrometer equipped with a HP6890GC and CuO/Ni/Pt

combustion furnace operated at 940°C. Samples were injected splitless (1 min) onto a 30 m fused silica column (DB5-MS, 0.32 mm i.d., 0.25 µm film thickness) using a Gerstel Cooled Injection System (CIS4) programmed from 48°C (0 min) to 310°C (10 min) at 12°C sec<sup>-1</sup>. The carrier gas was He. The GC temperature program used was: 3 min at 80°C; from 80°C to 310°C at 4°C min<sup>-1</sup>; 30 min at 310°C. The GC-C-IRMS precision was checked using a standard alkane mix (n-C15 to n-C29) with known isotopic composition. The stable carbon isotope compositions are reported in the delta notation ( $\delta^{13}\text{C}$ ) vs. the VPDB Standard.

## 8.3 Results

### 8.3.1 Petrographic and SEM evidences of bacterial activity

Although the organic remains of micro-organisms are not expected to be preserved in ancient microbial carbonates (Stolz *et al.*, 2001), because the organic compounds probably degrade very fast, especially in oxidizing conditions, evidences of microbial origin are expected to be preserved mainly as morphological structures. While the morphology and the mineralogy of particles larger than 10 µm are not expected to reveal microbial induced characteristics (Knorre and Krumbein, 2000), embedded microbes and particles with shapes similar to bacteria and which are only slightly larger than bacteria are interpreted as evidence that microbes were present when the carbonate formed. Whether the microbes just happened to be there or whether they actually induced the carbonate precipitation cannot be undoubtedly inferred from the morphological observations. However, if the corresponding sediment environmental physico-chemical conditions are suitable for microbial activity and if these appropriated microbial communities are proven to be involved in the carbonate precipitation, it is plausible to assume that these microbial evidences represent the direct involvement of those microbes in the carbonate formation. Indeed, it has been proposed that the microbes can induce an increase in carbonate alkalinity that will result in carbonate precipitation (Vasconcelos *et al.*, 1995; Boetius *et al.*, 2000; Castanier *et al.*, 2000; Folk and Chafetz, 2000; Knorre and Krumbein, 2000; Warthmann *et al.*, 2000; Hinrichs and Boetius, 2002; Van Lith *et al.*, 2003) and therefore they can function as nucleation sites (Knorre and Krumbein, 2000; Van Lith *et al.*, 2003). In this chapter, will be described many morphological evidences of microbial activity

found in the MDAC samples, such as peloid-like structures, filamentous structures and smaller scale features.

### 8.3.1.1 Dolomite chimneys

#### *Mineralogy and textural characterization*

As described in Chapter 5, the dolomite crusts, nodules and chimneys consist essentially of medium to tightly carbonate-cemented mudstones, siltstones, wackestones and sandstones (Figure 8.3 and Figure 8.4). The detrital fraction corresponds to a fossiliferous matrix with abundant bioclasts of planktonic and benthic foraminifera, ostracods, pellets and silty terrigenous grains of quartz, calcite, feldspars, apatite, zircon and clays. Iron and manganese oxy-hydroxides are present in almost all the samples, staining them with a variable brownish colour depending on the degree of oxidation of the sample. This is illustrated as example in Figure 8.3E, a thin section microphotograph of a transversal slice from a 3 cm thick chimney, showing the iron oxidation pervasive coating progressing from the exterior of the chimney (on the left of the image) and from their centre.

On non oxidized samples or with a weak oxidation degree it is possible to recognize authigenic pyrite, occurring as singular pyrite framboids  $<20\ \mu\text{m}$  (Figure 8.6), as framboidal aggregates  $<200\ \mu\text{m}$  (Figure 8.7B and C) isolated or forming groups, small pyrite grains ( $<5\ \mu\text{m}$  in size) isolated or forming clusters (Figure 8.3E and Figure 8.7A-C), and as euhedral pyrite single crystals (Figure 8.7B). Frequently, pyrite shows oxidation rims of brownish iron oxides probably containing OH-groups. Pyrite also occurs infilling foraminifera and other bioclasts chambers (Figure 8.3F); speckled on peloids (Figure 8.7A-C), generally associated with organic matter; disseminated in the carbonate matrix (Figure 8.7B-C); or filling inter-clast porosity. Sulphur isotopic compositions of the pyrite show negative  $\delta^{34}\text{S}$  values ( $-34\text{‰}$  CDT) (González *et al.*, 2006a, b). The presence of pyrite and their  $\delta^{34}\text{S}$  values indicate sulphate-reducing bacterial activity promoting the sulphide precipitation in anoxic sediment conditions. Pyrite replacement by Fe-Mn oxy-hydroxides (goethite and others) is observed and is frequent on samples with high oxidation intensity (Figure 8.3E-F and Figure 8.7D-F).

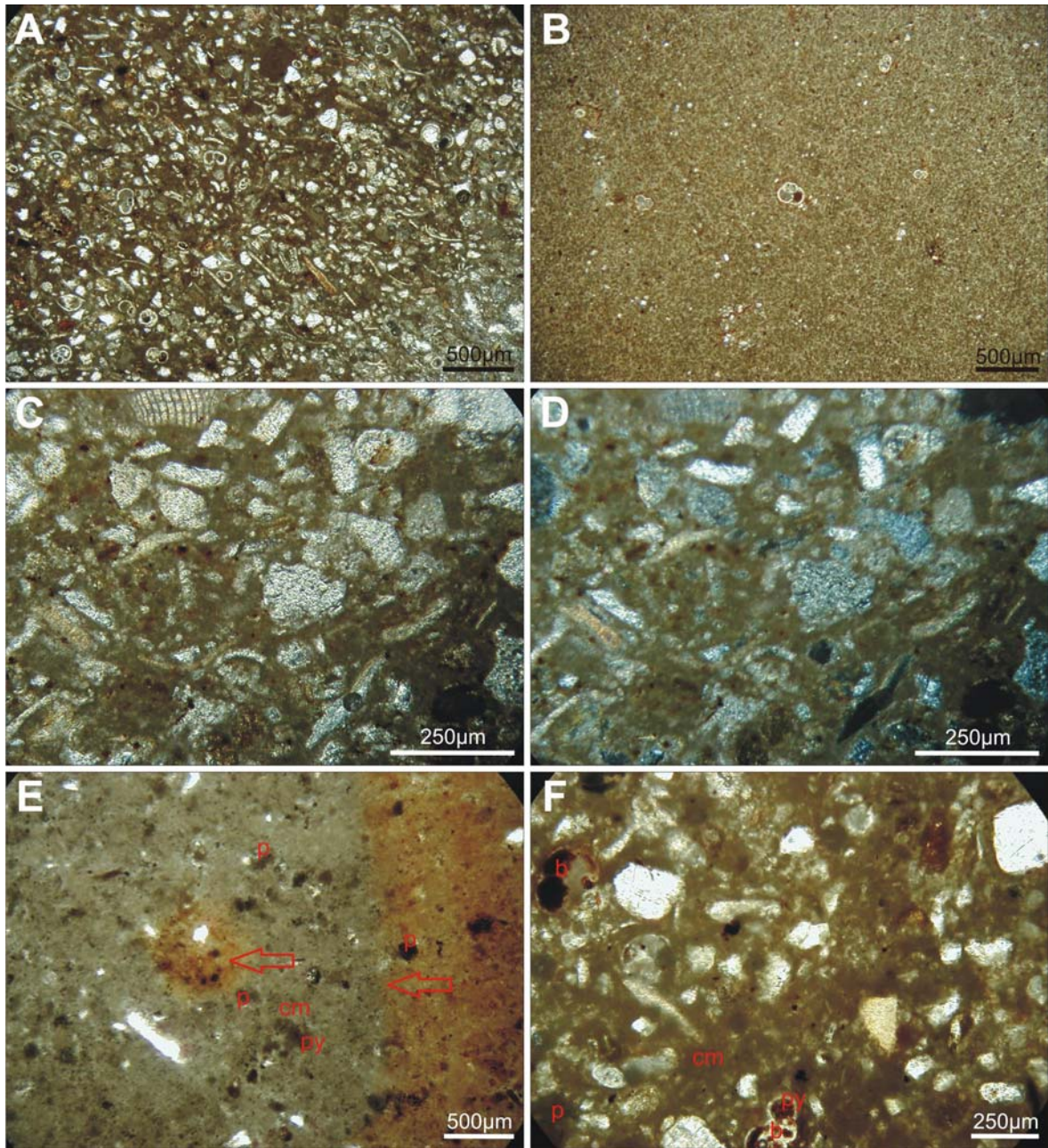


**Figure 8.3.** Dolomite chimneys general textural characteristics. Sandstone (A, C, D and F) and wackestone (B, E) thin section microphotographs, where it is possible to recognise that the detrital fraction, composed of bioclasts and terrigenous detritus, is cemented by a micrite to micro-spar carbonate cement with a peloidal and clotted microfabric. The detrital grains range from clast-supported to matrix-supported. The cement shows a clotted microfabric (cm) where peloidal-like structures (p) are identified. Pyrite (py), some times replaced by oxy-hydroxides, occurs speckled in the clotted micrite cement and within bioclasts (b) of foraminifera tests. All microphotographs are in plane-polarized light except for image D which is in crossed-polarized light.

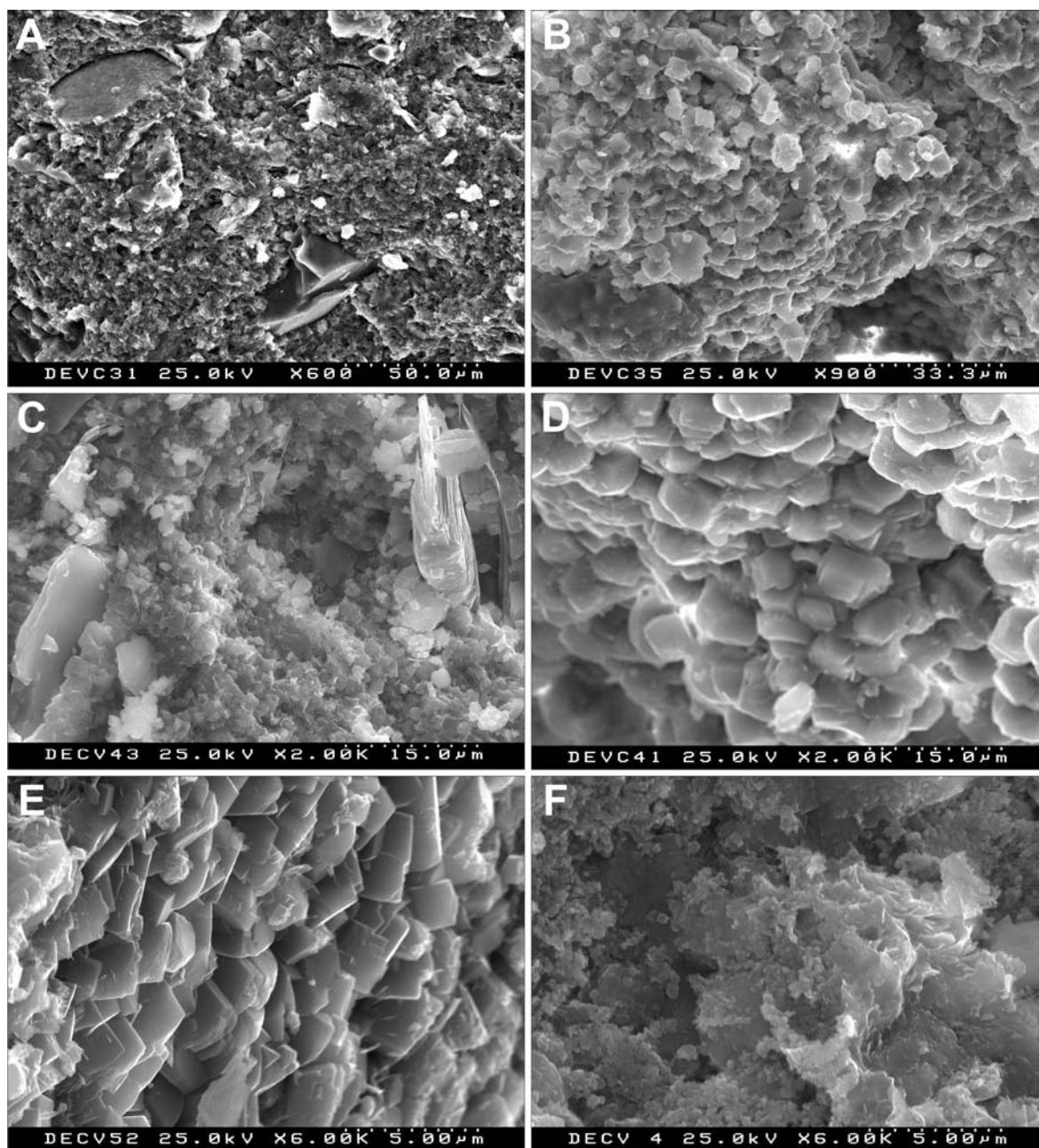


**Figure 8.4.** SEM imagery illustrating the general textural characteristics of the dolomite chimney samples. Authigenic calcite, high Mg-calcite and dolomite compose the cement whereas the detrital fraction is composed of quartz, feldspars, clays and bioclasts. (A to C) general characteristics where it is possible to recognise different detrital grains and the authigenic carbonate minerals with rhombohedra shapes less than 5  $\mu\text{m}$  in size. (D-E) details of euhedral carbonate minerals. (F) carbonate cement minerals with less than 0.5  $\mu\text{m}$  in size that have sub-round shapes, contrasting with the euhedral crystal shapes on the images (D) and (E). Scale and acquisition parameters of pictures are shown in the pictures footnotes.

The degree of authigenic carbonate cementation corresponds to an almost complete infilling of the original pore space and therefore the different samples of dolomite crusts,

chimneys and nodules show low porosity, with absence of mega-porous and scarce fractures or cracks. The contacts between the cemented grains are irregular, ranging from complete to inter-grain pore spaces with dimensions lower than 10  $\mu\text{m}$ , leaving little residual porosity. The cement is composed of micrite to micro-sparite equigranular rhombohedral calcite, high Mg-calcite, protodolomite and dolomite with dimensions in the range of 2-10  $\mu\text{m}$  (Figure 8.4 and Figure 8.5). The texture varies from isolated rhombohedra and aggregates of interlocking sub-euhedral to euhedral crystals, sometimes exhibiting serrated crystal faces. More rarely the cement carbonates show sub-round shapes with sizes  $< 0.5 \mu\text{m}$  (Figure 8.3F). The contacts between detrital grains and the cement are dictated by the shape of the detrital grain. The carbonates are not observed dissolving or replacing the detrital grains. EDS chemical analysis of the dolomite crystals indicate Ca and Mg as the dominant constituents. Fe is also frequently identified on the EDS chemical analysis, with a proportion that is in general inferior to 5% on point analysis performed on single cement crystals. Analyses performed over scanned areas show larger relative abundance of Fe, even when performed on dolomite crystals. This is interpreted as a consequence of the pervasive existence of iron oxy-hydroxides over most of the sample material (Figure 8.5). Although dolomite can contain Fe in its crystallographic structure, the analysed samples showed  $\text{Mg:Fe} > 4$ , and therefore are not interpreted as being ankerite. In general, the cement crystals have non-stoichiometric compositions and show an excess of Ca relative to the Mg; consequently a continuous range of carbonate phases with compositions ranging from dolomite, protodolomite and high Mg-calcite through calcite can be observed in the authigenic cement (this is also evidenced by the X-ray diffraction data, as discussed in Chapter 5).

All the cement minerals seem to be paragenetic. Cathodoluminescence does not reveal different generations in the micrite cement nor any compositional variability within the crystals. The cement exhibits non-luminescence dull to medium orange to brownish red colours.

Neither on the SEM observations nor in the petrographic observations, was it possible to recognise any signs of calcite dissolution, or calcite replacement by dolomite. Therefore, the cement dolomite, protodolomite, calcite and the high Mg-calcites are considered to be primary authigenic mineralogy.

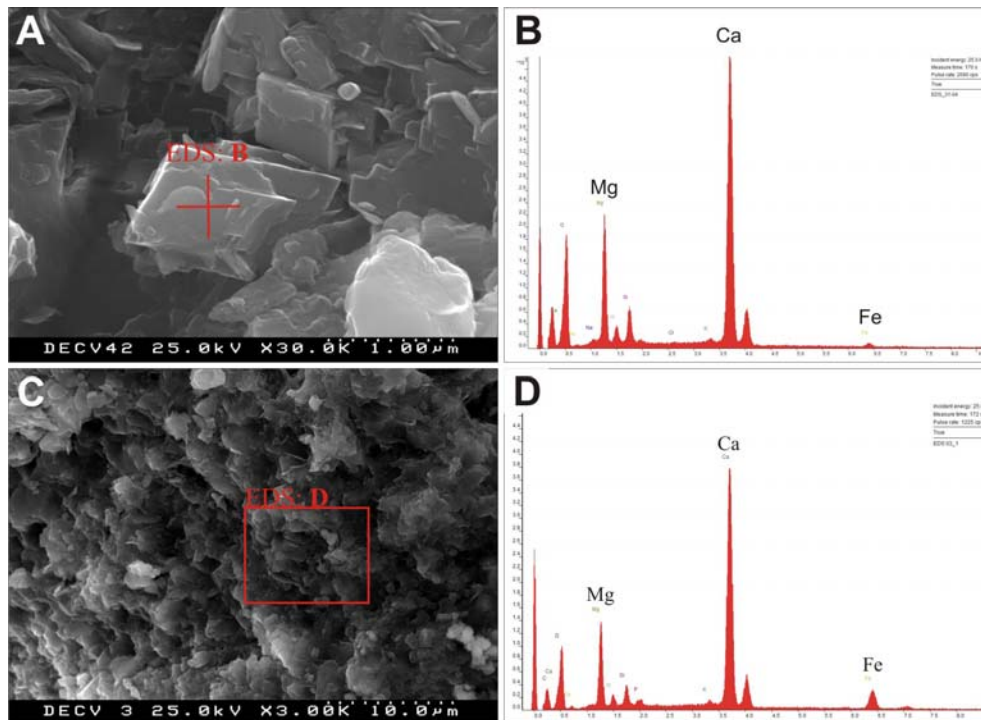


**Figure 8.5.** SEM imagery and EDS chemical composition of the authigenic dolomite and high Mg-calcites in the dolomite chimney samples. Note that the detection of Fe in the EDS chemical analysis is considered to result from the crystal structure and also from the iron oxy-hydroxides that pervasively exist coating the sample. Scale and acquisition parameters are shown in the pictures footnotes.

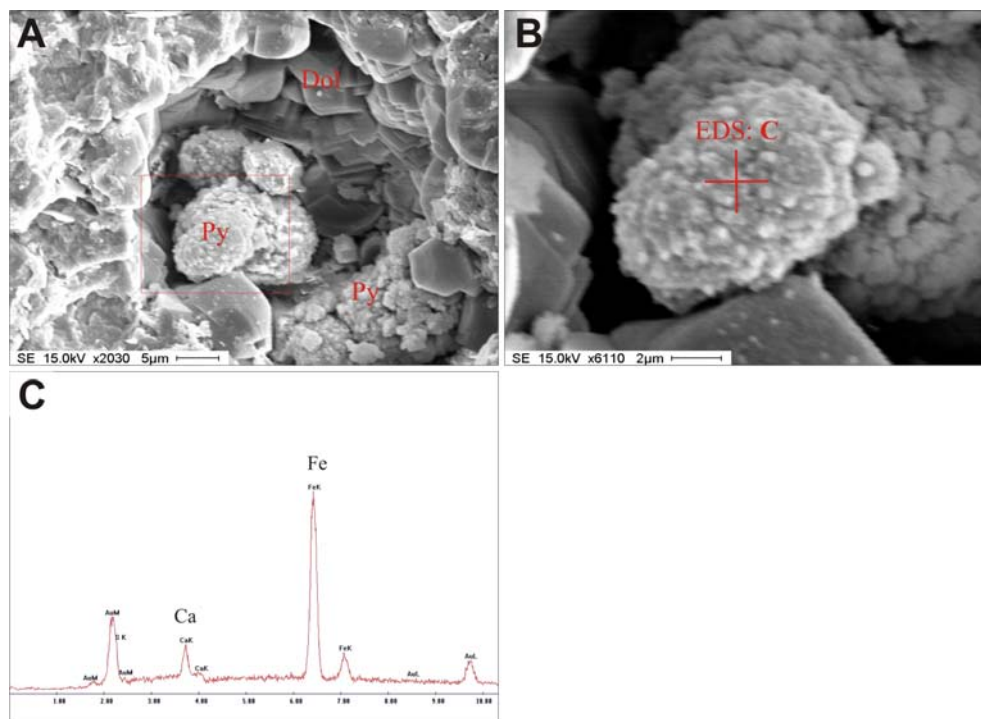


**Figure 8.6.** SEM imagery and EDS chemical composition of framboidal pyrite (Py) within dolomite chimney samples. The pyrite framboids are surrounded by euhedral dolomite crystals (Dol). (B) is a detailed image of the pyrite framboid in (A) where the EDS chemical analysis (C) was performed. Scale and acquisition parameters are shown in pictures footnotes.

The typical fabric of the dolomite chimneys includes the intrapelbiomicritic and pelmicrite which are diagnostic of a biotic origin and show equivalent characteristics to other methane seep cements described in several other places and in ancient seep deposits (Peckmann *et al.*, 2002; Shapiro and Fricke, 2002).

### ***Peloidal and clotted microfabrics***

The cement of the dolomite chimney samples frequently show peloids, peloid-like allochems and clotted microfabric (Figure 8.7). The peloid-like structures have variable sizes, generally range from 10 to 300  $\mu\text{m}$  in diameter, and are characterized, in thin section (Figure 8.7), by cloudy areas at their centres (clotted fabric) sometimes surrounded by a more clear exterior rims of micritic to micro-spar crystals of carbonate (calcite, high Mg-calcite or dolomite) or by indistinct and diffuse margins. The peloids are frequently speckled by pyrite which, in some cases can be the dominant phase. Similar fabric is also found at the interior of foraminifera tests (Figure 8.3F and Figure 8.6). Frequently the peloid-like texture assumes non-rounded shapes and can form irregular areas of the cement covering large extensions of the intergranular space (Figure 8.7). As the peloids can occur between and within the detrital material and the bioclasts, and given the lack of indications of transportation of the peloids, the peloidal fabric is interpreted as having an *in situ* origin and not as of fecal origin. The space between the peloidal clots is predominantly filled by micritic to micro-spar carbonate cement, and the cores of the peloids are composed of submicron to micron-sized anhedral carbonate grains. In thin section, the peloids display light brownish grey to dark colours and in cathodoluminescence they have non-luminescent dull to medium colours, that are interpreted as indicating remains of organic matter.

The peloids are therefore considered to represent bacterially induced precipitates where an association of micritic mineralogies, probably with more abundant microbial remains, composes the authigenic cement. Co-occurrence of pyrite within the peloids is frequent and indicates anaerobic conditions, where the organic compounds (most probably light hydrocarbons, such as methane) are anaerobically oxidized. The peloidal-like fabric of the dolomite chimneys, similar to the fabrics described in other active or fossil cold seep systems (Peckmann *et al.*, 2002) are, interpreted here as representing clusters or fragments of clusters of higher concentrations of microbial consortia.

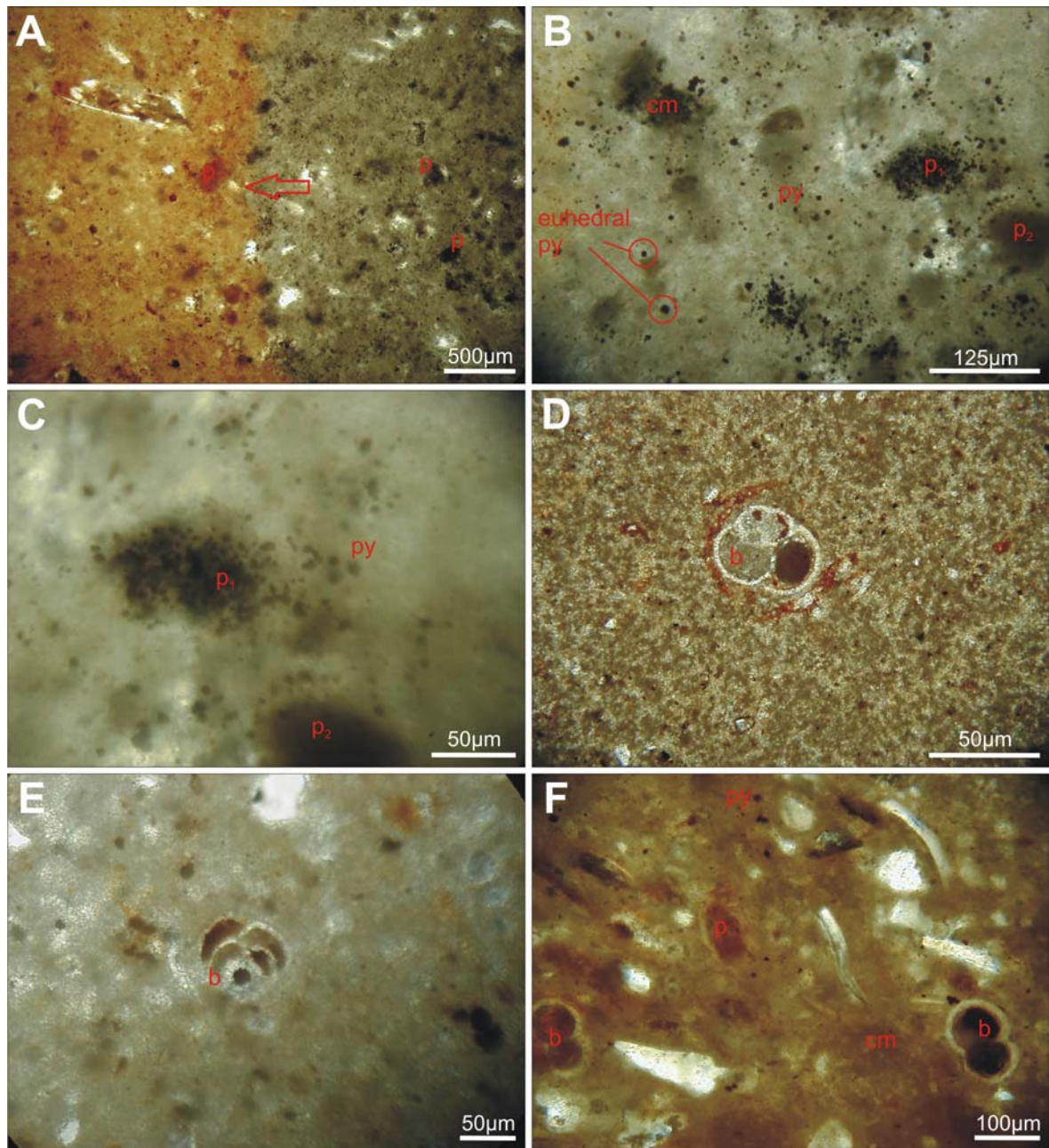


**Figure 8.7.** Thin section micrograph of peloidal and clotted microfabric in dolomite chimney samples. (A) peloidal and clotted microfabric on oxidized and non oxidized material. Arrow pinpoints the oxidation front. (B) peloidal (p) and clotted microfabric (cm) where is possible to recognise high density of speckled pyrite framboids (py) also present on the micrite cement. (C) detail image of (B) where the indistinct and diffuse margins of the peloid ( $p_1$ ) is compared with an more well defined margin of the peloid ( $p_2$ ). (D and E) shows micritic clots surrounded by micritic cement and also show foraminifera bioclasts with oxidized pyrite infillings. (F) peloidal and clotted microfabric of the cement where is possible to recognise speckled pyrite framboids (py). All microphotographs are in plane-polarized light.

### ***Microbial filaments***

Locally, high densities of unidentified filaments with diameters of about 0.5  $\mu\text{m}$  and up to 100  $\mu\text{m}$  long occur in the dolomite chimneys (Figure 8.8). These filaments form complex networks that appear to be cemented by the authigenic carbonate cement crystals (Figure 8.8C) and are therefore proposed to be contemporary of the carbonate cement formation and not as resulting from a later stage contamination.

Linear clusters of small crystals with sizes ranging from 0.1 to 2-3  $\mu\text{m}$  in diameter are also observed (Figure 8.9A-B). These structures are interpreted as being formed by calcification over filamentous structures (biomineralizations) since their size and shapes resemble bacterial morphologies. These calcified filaments are incorporated and surrounded by larger cement crystals and therefore are clearly contemporary to the cement precipitation (Figure 8.9B). Similar crystals clusters, not showing linear arrangements, are also observed on top of some larger crystals (Figure 8.9C). Individual crystals or sub-spherical particles with less than 0.1  $\mu\text{m}$  in diameter are also observed as being cemented and incorporated in the cement crystals as illustrated in (Figure 8.9D), where a fragment of a nanofossil appears to have been cemented and incorporated in a cemented crystal.

### ***Particles with shapes that possibly indicate a microbial origin***

Several other structures with a probable biogenic origin are also frequently observed on the dolomite chimney samples.

Associated with the filaments agglomerates of cocci, straight and curved rod-shaped and sub-spherical carbonate phases are also frequently found (Figure 8.8A-B pinpointed by black arrows, Figure 8.10A-C and Figure 8.11A pinpointed by white arrows). The rods and sub-spherical structures have sizes ranging from 0.1 to 1  $\mu\text{m}$  in diameter and are less than 3  $\mu\text{m}$  long. Because of their simple morphology the cocci and rods are possibly of bacterial origin, as their size and shapes are compatible with the size and shapes of bacteria. The rod-shaped agglomerates have very similar compositions to the calcitic micrite cement (Figure 8.10B and F) and the rods are locally being incorporated into the calcite cement crystals, as illustrated in Figure 8.10C and pinpointed by the arrows. It should be noted that these agglomerates of rod-shaped morphologies have a similar morphology to the radial structures illustrated in Figure 8.11B-E, but with significant differences. While the rods in the rod-shaped agglomerates have a random orientation, in the radial structures the rods are

parallel and have a regular divergent distribution. The radial structures have diameters ranging from 10 to 20  $\mu\text{m}$  and, similarly to the rod-shaped agglomerates, are interpreted as being biogenic in origin, although their nature is more difficult to determine. They can be sections of spicules or they can be bacterial in origin.

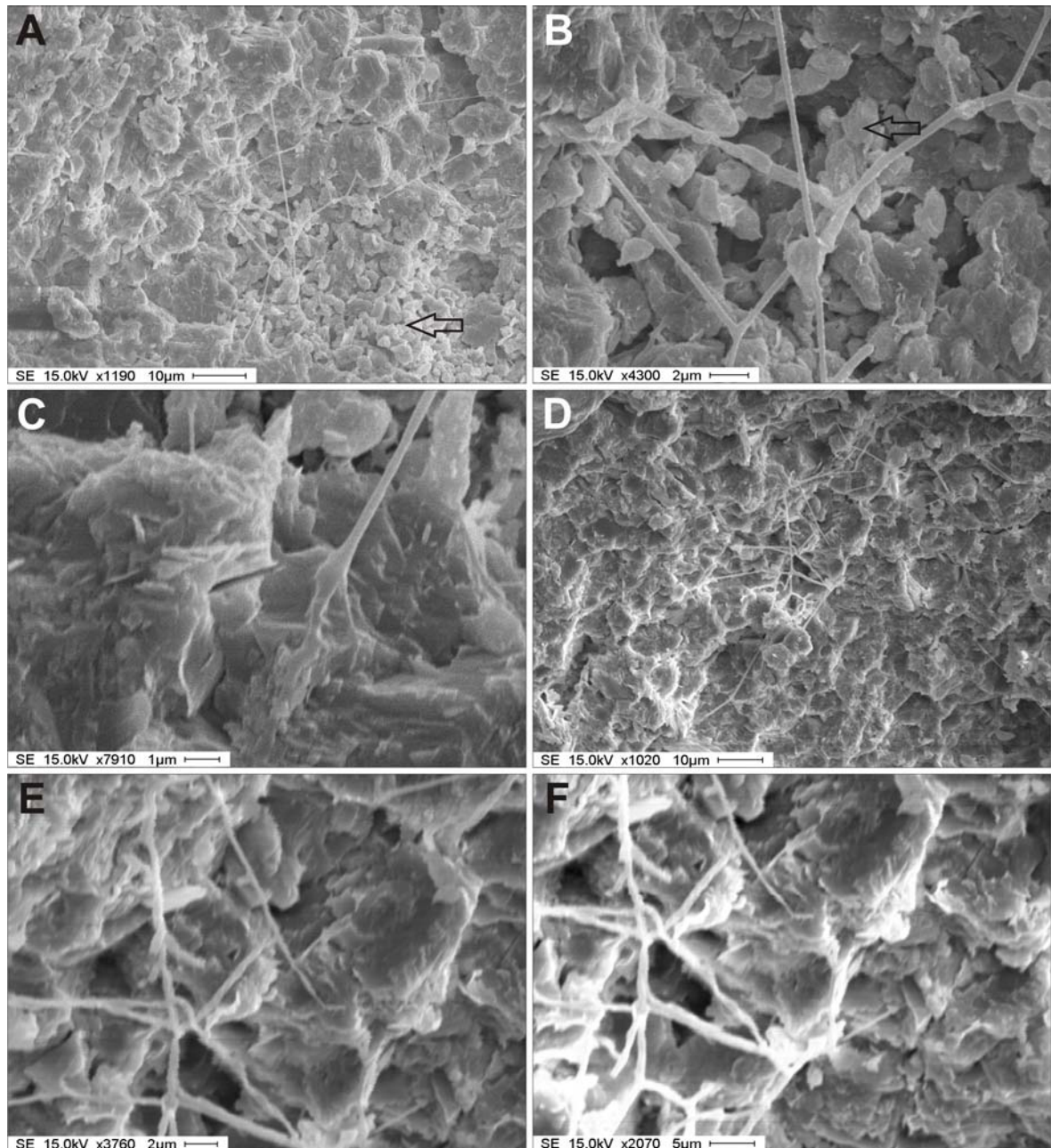


**Figure 8.8.** SEM imagery illustrating microbial filaments on dolomite chimney samples. (Scale and acquisition parameters are shown in pictures footnotes). See text for description and discussion.

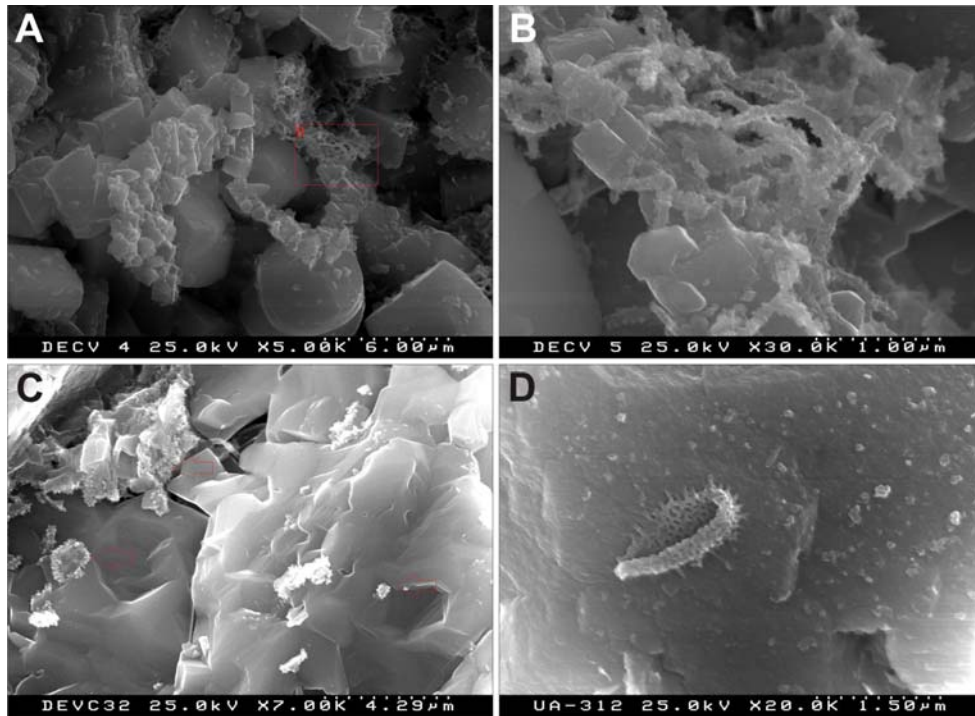


**Figure 8.9.** SEM imagery illustrating calcified structures on dolomite chimney samples that are interpreted to have a biological origin. (Scale and acquisition parameters are shown in pictures footnotes).

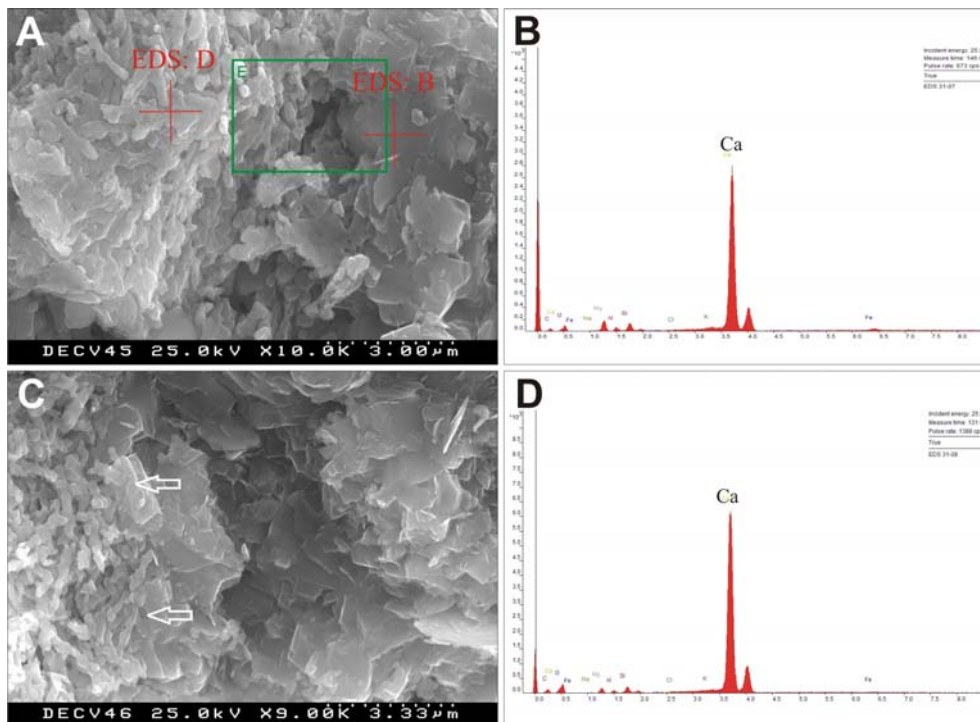


**Figure 8.10.** SEM imagery illustrating calcitic globular and rod-shaped structures (scale and acquisition parameters are shown on the pictures footnotes). (A and C) globular and rod-shaped structures that are possibly biological in origin. (C) is a detail image of (A) showing the boundary between the rod-shaped agglomerate and the cement. (B and D) EDS chemical analyses on (B) calcite cement crystal and (D) rod-shaped structures, indicating a calcite mineralogy. See text for discussion.

Linear filament structures with baton-shaped morphologies have also been identified on the dolomite chimney samples. As illustrated in Figure 8.12, these batons (pinpointed by the arrows) have a diameter of 0.1 to 0.2  $\mu\text{m}$ , and are 1-2  $\mu\text{m}$  long. Since they have bacterial equivalent sizes, they are interpreted as possible fossilised bacteria. Some of these batons are being incorporated into the cement carbonate crystals.

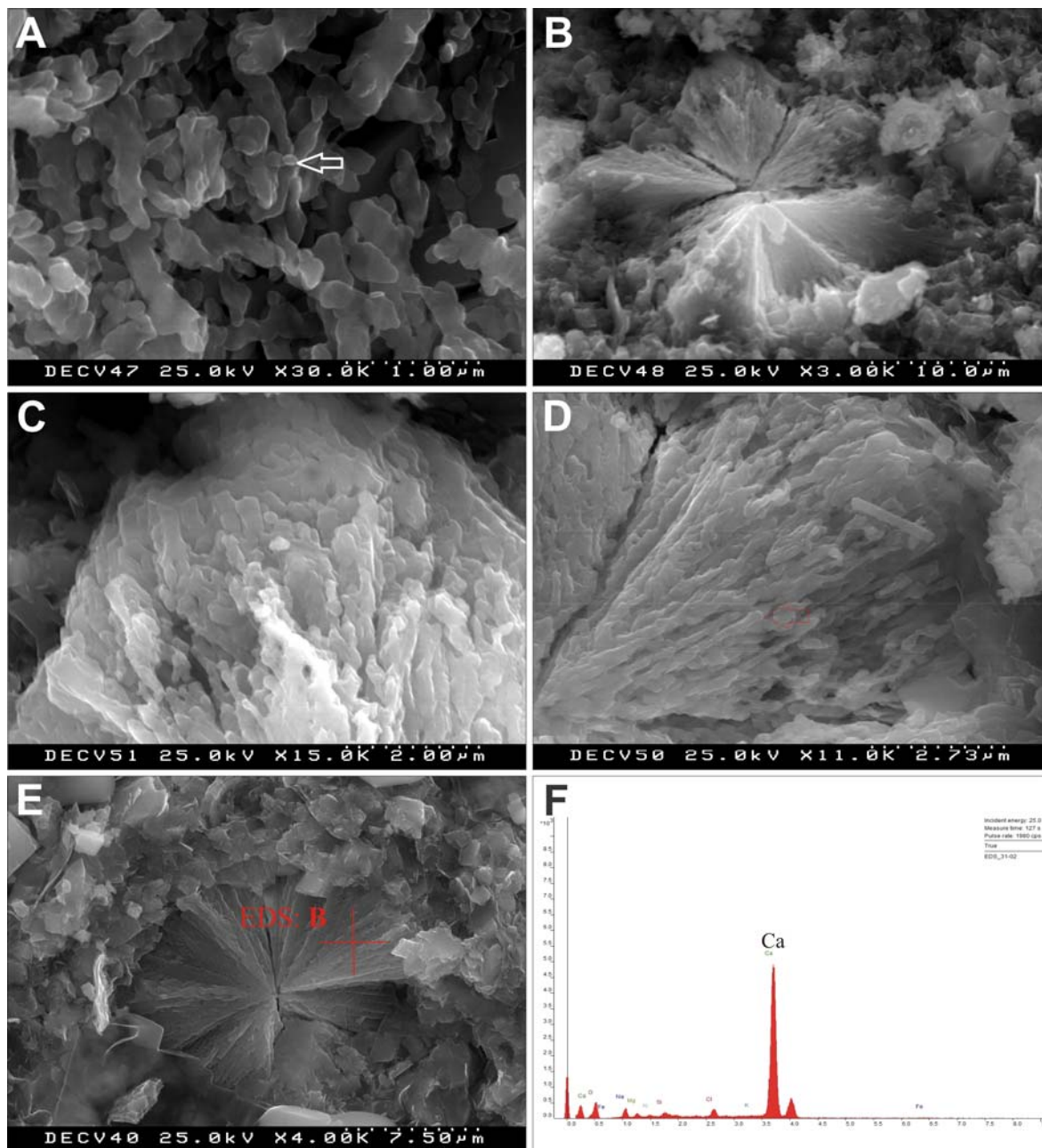


**Figure 8.11.** Dolomite chimney samples SEM imagery, illustrating the similarity between the (A) globular and rod-shaped structures that are possibly biological in origin and (B-E) the radial structures, possibly of sections of spiculas. (Scale and acquisition parameters are shown in pictures footnotes). See text for discussion.

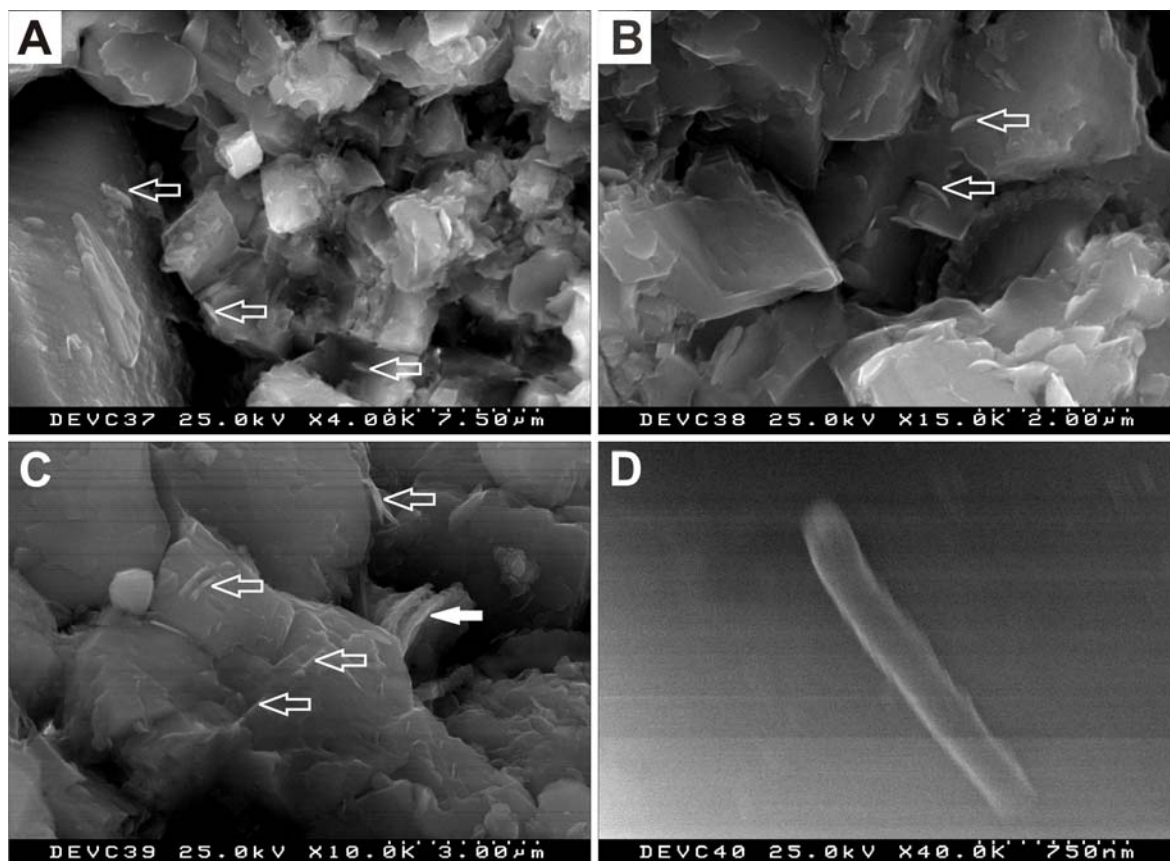


**Figure 8.12.** SEM imagery illustrating linear filamentous structures (batons) interpreted as possible fossilised bacteria. (Scale and acquisition parameters are shown in pictures footnotes). (A-C) baton like structures with bacterial equivalent sizes, some of which are being incorporated in the carbonate crystals. The structure pointed by the white arrow in (C) is a coccolith disk. (D) detail of one of the baton structures.

Several other globular and sub-spherical morphologies have also been observed on dolomite chimney samples. Globular morphologies that resemble dumbbells (illustrated in Figure 8.13A-B) 4-5  $\mu\text{m}$  long, were observed as sub-spherical particles with a diameter of 2-5  $\mu\text{m}$  (Figure 8.13C-D). Fragments of tubular morphologies with 10  $\mu\text{m}$  in diameter were also recognised (Figure 8.13E).

It was also possible to identify morphologies that resemble twisted clotted surfaces or sheaths, 2-3  $\mu\text{m}$  thick (Figure 8.13F), with globular grains, some of which are probably pyrite framboids (1-5  $\mu\text{m}$  in diameter) being cemented on these sheaths. These clotted surfaces are probably calcified biofilms and some of the globular grains on their surface are bacterial rods being cemented into the sheaths.

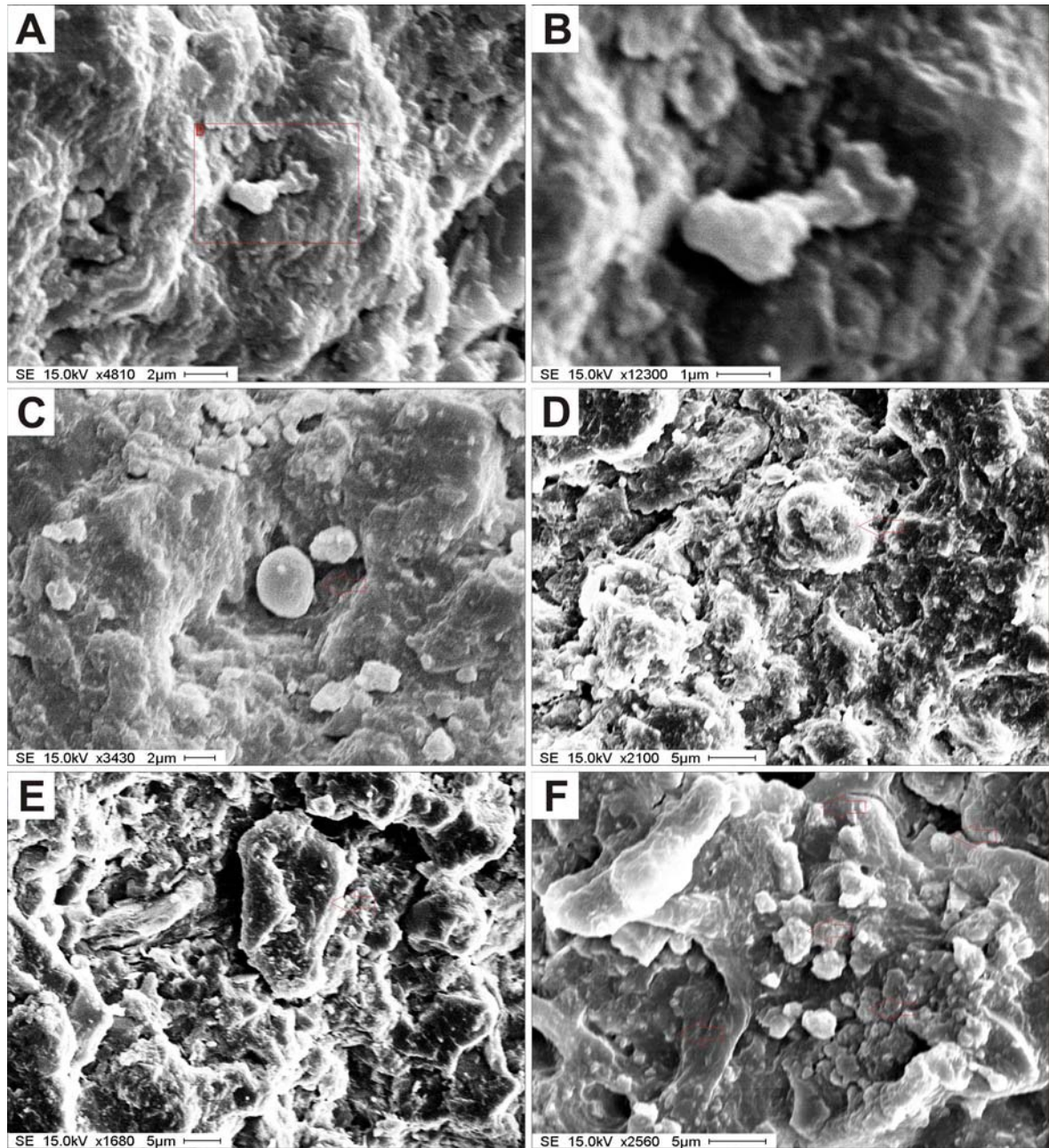


**Figure 8.13.** SEM imagery illustrating globular, tubular and dumbbell like structures that are interpreted to have a biological origin. (Scale and acquisition parameters of pictures are shown in pictures footnotes). (A-B) globular morphology possible a dumbbell ? (C-D) globular sub-spherical grains. (E) fragment of a tubular structure. (F) clotted surface with globular grains and pyrite framboids being cemented on these clotted surface.

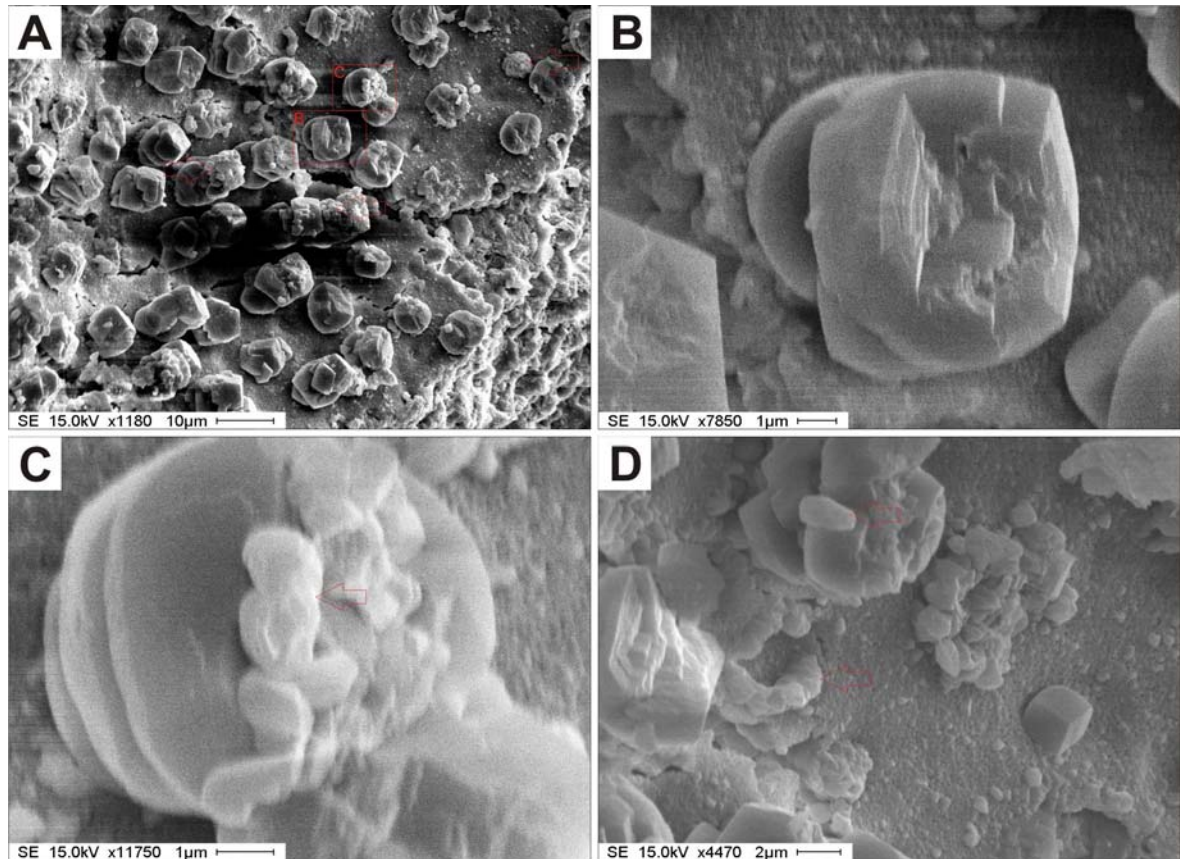


**Figure 8.14.** SEM imagery illustrating globular and structures that are interpreted to have a biological origin on dolomite crystals. (Scale and acquisition parameters of pictures are shown in picture footnote).

Over large euhedral cement crystal sub-rounded morphologies can be observed (Figure 8.14A-C) that, while speculative, can be biogenic in origin. Also difficult to interpret but also supporting a biogenic origin, these euhedral cement crystals are frequently found growing over a surface of sub-micron carbonate phase that cements the surface of some detrital grains. These carbonate surfaces have 2-4  $\mu\text{m}$  thick and exhibit a micro-rough texture. The euhedral crystals seem to be growing from this surface, which can be interpreted as a calcified biofilm.

In some of these euhedral cement crystals with 2-3  $\mu\text{m}$  in diameter are growing and incorporating sub-spherical agglomerates of euhedral crystals with 0.5  $\mu\text{m}$  size and possibly pyrite framboids (Figure 8.15B)

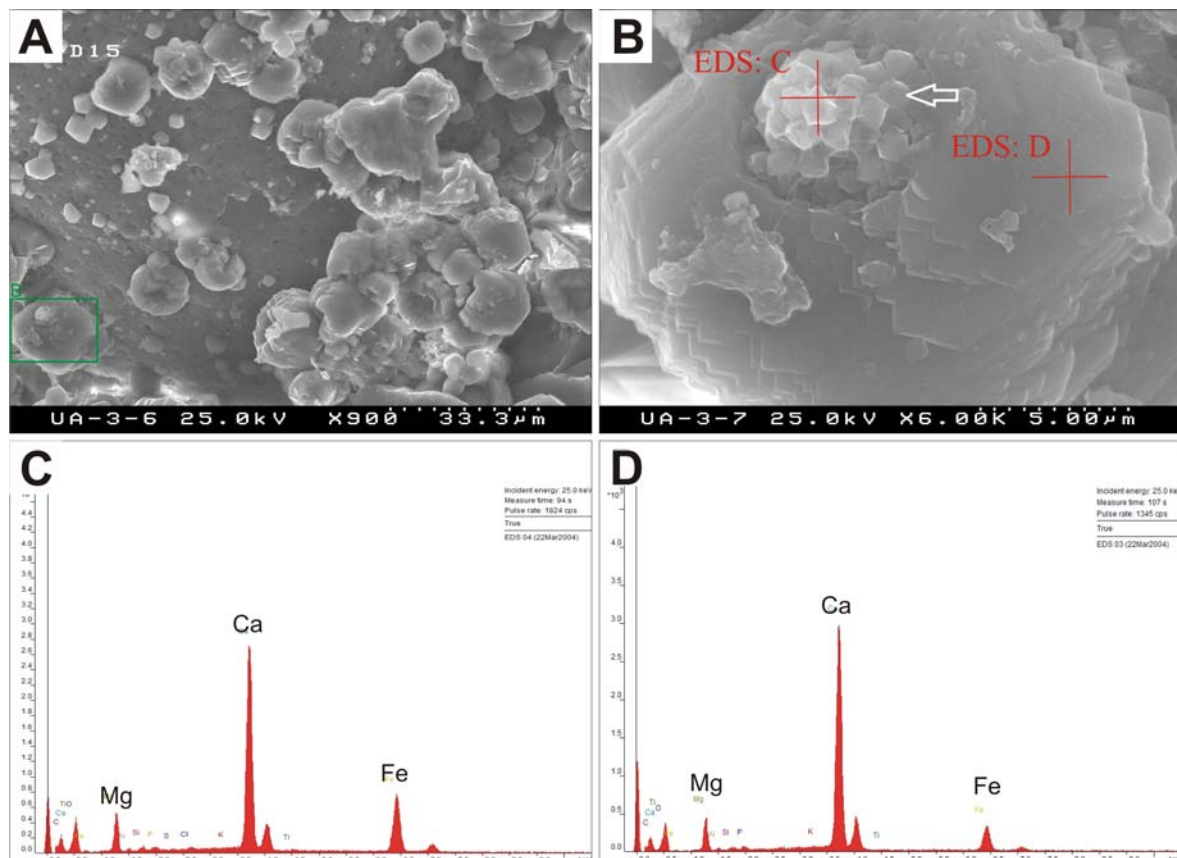


**Figure 8.15.** SEM imagery illustrating high Mg-calcite globular and framboidal structures that are interpreted to have a biological origin. (Scale and acquisition parameters are shown in pictures footnotes). (B) is a detail of the area framed by the green rectangle in (A). Arrow in (B) pinpoints a sub-spherical agglomerate of euhedral crystals that are being incorporated by the larger cement crystal. Both sub-spherical agglomerate and the large cement crystal have similar chemical compositions, as indicated by the EDS analysis presented in (C) and (D) respectively.

### 8.3.1.2 Aragonite pavements

#### *Mineralogy and textural characterization*

Aragonite pavement samples, in hand-species, are porous and whitish, light brownish grey to dark grey. Their mineralogy is dominated by aragonite and calcite, cementing a detrital fraction of quartz, feldspars, clays, mud volcano mud breccia clasts, shell fragments, foraminifera and calcareous nannofossils. Aragonite crusts and pavements are in general tabular (as revealed by the retrieved samples and on the underwater video observations) or form irregular block like or buildups at the seafloor. Different lithologic types of aragonite pavements have been identified (see Chapter 5): (i) lithified mud

volcano breccias; (ii) shell crusts; (iii) intraformational breccias; and (iv) lithified fragments of dolomite crusts and chimneys. Several of these sub-types can coexist at the same location and sometimes in the same sample.

The aragonite pavement samples, as illustrated for example in Figure 8.16, are characterized by a complex variety of macro and micro fabrics that developed at different times and where is possible to identify primary and later minerals. Dissolution horizons are also found in these samples, in opposition to the fabric of the dolomite crusts and chimneys, where no dissolution surfaces were found. The dissolution surfaces of the aragonite pavements indicate oxidation-reduction changes in the geochemical environment during their formation. The different aragonite pavements are characterized by the presence of two carbonate cement phases: the peloidal and clotted microfabrics, and the botryoidal and fibrous stromatolitic microfabric.

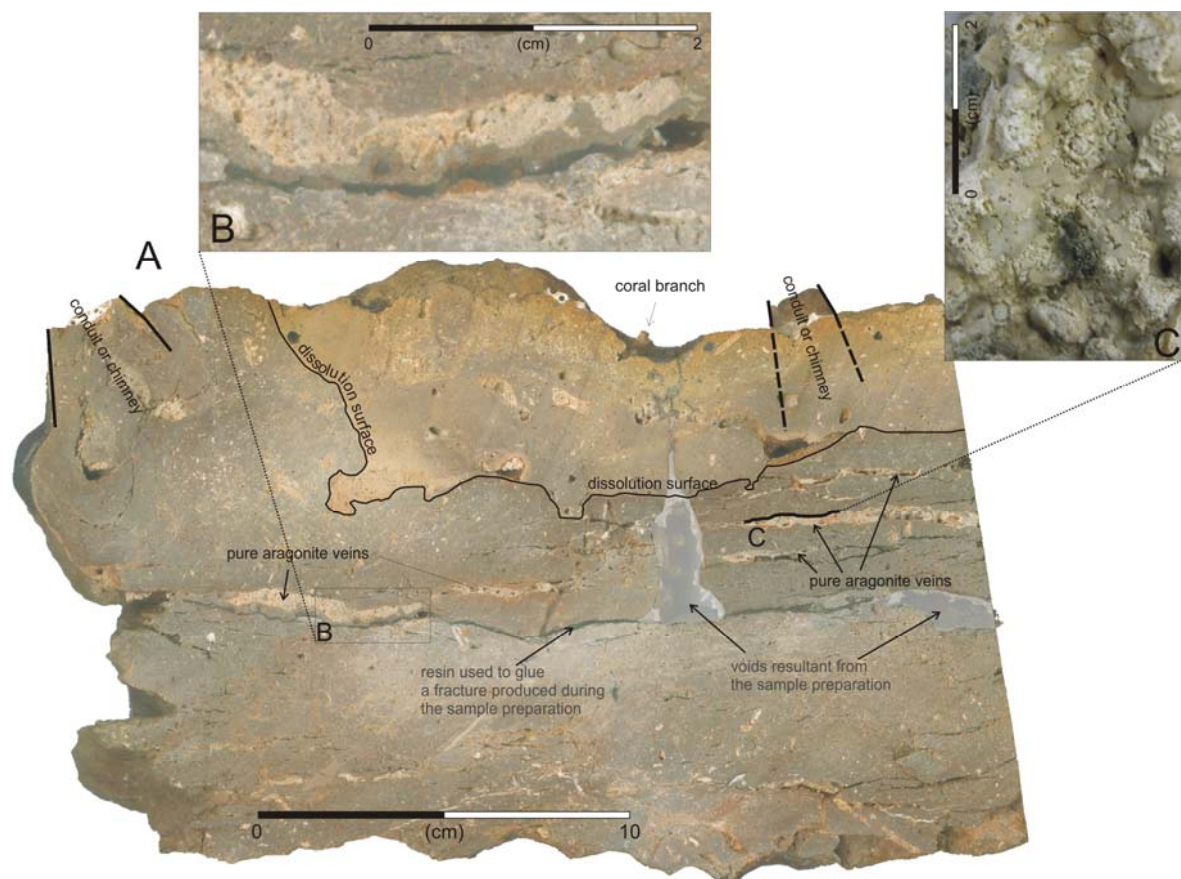


**Figure 8.16.** (A) Transversal cut of an aragonite pavement where is possible to recognise a dissolution surface and veins filled by pure aragonite cement (B) with botryoidal and stromatolitic layers (C).

***Peloidal and clotted microfabrics***

The peloidal and clotted microfabrics correspond to the earliest stage cement phase. It consists of clotted micrite and pelmicrite cement, composed of micritic clots with calcite, high Mg-calcite and aragonite (pointed by *cm* in Figure 8.17). It is very similar to the fabric of the dolomite chimneys. This fabric is characterized by an abundant detrital component, in general dominated by bioclasts of planktonic and benthic foraminifera, ostracods and nonofossils, with silty terrigenous grains of quartz, calcite, feldspars, apatite, zircon and clays. Iron and manganese oxy-hydroxides are present in some samples, staining them with a variable brownish colour depending on the degree of oxidation of the sample; however, in general the aragonite pavements with no signs of oxidation are the most frequent. This microfabric is characterized by the abundance of peloidal-like clotts, as illustrated in Figure 8.19. The aragonitic and calcitic micritic clots have irregular shapes and sizes, and a cloudy internal texture. The size of most clots ranges from 50 to 500  $\mu\text{m}$  in diameter. The clots form an important fraction of the carbonate cement and, in general, the space between the clots is filled by micrite to star aragonite and calcite cement, or by fibrous stromatolitic and botryoidal aragonite. Frequently, the interior of foraminifera bioclasts have similar clotted microfabric. In the clots and peloidal-like structures the occurrence of organic matter is interpreted to be significant.

Authigenic pyrite is abundant in this fabric, occurring as isolated framboids with up to 30  $\mu\text{m}$  in diameter, as framboidal aggregates (Figure 8.17) with up to 200  $\mu\text{m}$  in diameter, or as individual euhedral crystals. Pyrite occurs with high density in the clots and in the peloidal-like structures and it also often completely infills some foraminifera shells (Figure 8.19C, E-F). Pyrite, most probably associated with organic matter, occurs frequently as forming layers at the margins of material with clotted micritic fabric and on top of which aragonite needles grow, forming botryoidal and stromatolitic layers (Figure 8.17D and F pinpointed by the arrows).

The clotted pelmicrite fabrics are interpreted as being biogenic (microbial) related fabric.

***Botryoidal and fibrous stromatolitic microfabric***

The botryoidal and isopachous fibrous stromatolitic microfabrics correspond to a later cementation stage by acicular (almost pure) aragonite that fills the pore spaces,

fractures and open cracks, frequently forming botryoidal and stromatolitic layers (Figure 8.17 and Figure 8.18).

The botryoids are characterized by a radial texture of the aragonite needles (Figure 8.20A-C). that can have sizes ranging from 100 to 300  $\mu\text{m}$  in length. They grow over the clotted micrite cement and fill in the open porosity and open voids.

Fibrous stromatolitic microfabric characteristically occurs as infilling large porous, fractures and cavities. The stromatolitic microfabric is formed by isopachous aragonite needles, occurring as a single or as multiple layers that recover the cavities walls and form stromatolitic crusts. This microfabric is composed of almost pure aragonite and can have thicknesses of 100  $\mu\text{m}$  up to 0.9 cm and can fill cavities and fractures with a thickness of up to 2-3 cm. The nature and characteristics of the stromatolitic cavities are discussed below.

The stromatolitic layers, like the botryoidal fabric, represent a later cementation phase as they grow over the clotted micritic fabric, filling open spaces. In thin section, they frequently exhibit horizons or layers of clotted fabric within the aragonite needles layers or at the centre of the stromatolitic cavities (Figure 8.20C-F). These cloudy horizons are interpreted as possibly corresponding to levels with a high amount of organic content, probably corresponding to the calcified biofilms, such as the ones illustrated by SEM imagery on Figure 8.26.

#### ***Chaotic fabrics, dissolution horizons and stromatolitic cavities***

Samples of intraformational breccias, characterized by a chaotic fabric produced by *in situ* brecciation, and samples of lithified fragments of dolomite crusts and chimneys, are both characterized by the presence of mega-clasts (up to 12 cm) cemented by the authigenic aragonite and calcite cement described above. As described in Chapter 5, the clasts of the intraformational breccias are interpreted as fragments of previous semi-consolidated aragonite pavements that were fractured and later re-cemented. The fragmentation and the generation of the clasts can be interpreted as resulting from instability related to mud volcano activity, where episodes of mud breccia extrusion, gas and fluids emissions can fracture the aragonite pavements being formed close to the seafloor. Alternatively, gas hydrate formation and subsequent dissociation can also produce the fragmentation of the pavements, similar to the gas hydrate associated carbonates found in the Cascadia margin (Bohrmann *et al.*, 1998; Greinert *et al.*, 2001).

The intraformational breccia clasts frequently show signs of dissolution and corroded edges (Figure 8.18D, E and F). This puts in evidence that after an episode of MDAC formation, changes in the geochemical environment happened, leading to carbonate dissolution. Possibly this is evidencing a phase of aerobic oxidation of methane that induces an increase in the pore water CO<sub>2</sub> content and leads to the acidification of the pore waters leading to the dissolution conditions. After this episode, adequate conditions for anaerobic oxidation of methane occur, leading to a new episode of cementation of the mega-clasts by a new generation of authigenic carbonates.

In general, the degree of authigenic carbonate cementation is not pervasive and intergranular pore spaces are frequent; therefore, the aragonite pavements exhibit, in general, high porosity. The aragonite pavement samples frequently have voids, fractures and open cracks that are recovered or totally filled by crusts or layers of stromatolitic and botryoidal aragonite microfabrics, described above and illustrated in Figure 8.16, Figure 8.17A, Figure 8.18A and Figure 8.20. These cavities frequently have sheet to lenses shapes, occurring parallel to the stratification or to the global planar shape of the pavement sample. They can have thicknesses ranging from 1 mm to 2-3 cm and can extent for more than 12 cm in length. The shape of these voids and the subsequent aragonite layers resembles to the aspect of the gas hydrates chunks and layers that were recovered from mud volcanoes in the Gulf of Cadiz (Kenyon *et al.*, 2000, 2001, 2002, 2003; Pinheiro *et al.*, 2003; Kenyon *et al.*, 2006) and also from other settings (Suess *et al.*, 1999; Suess *et al.*, 2001). Therefore the stromatolitic and botryoidal aragonite fabrics are interpreted as the remains of lenses of gas hydrates layers that grow within the sediments, occurring as planar layers parallel to the stratification of the sediments as also suggested for similar sample fabrics (Bohrmann *et al.*, 1998). After the dissociation of these gas hydrate layers, their morphology is registered by the layers of almost pure aragonite illustrated in Figure 8.16.

The pelmicrite and intrapelsparite, with clotted cement fabric and aragonite botryoids, isopachous needles and stromatolitic layers or crusts observed in the aragonite pavements from the Gulf of Cadiz are also typical of other active and fossil methane seeps (Savard *et al.*, 1996; Bohrmann *et al.*, 1998; Campbell *et al.*, 2002; Shapiro and Fricke, 2002; Shapiro, 2002; Shapiro, 2004).

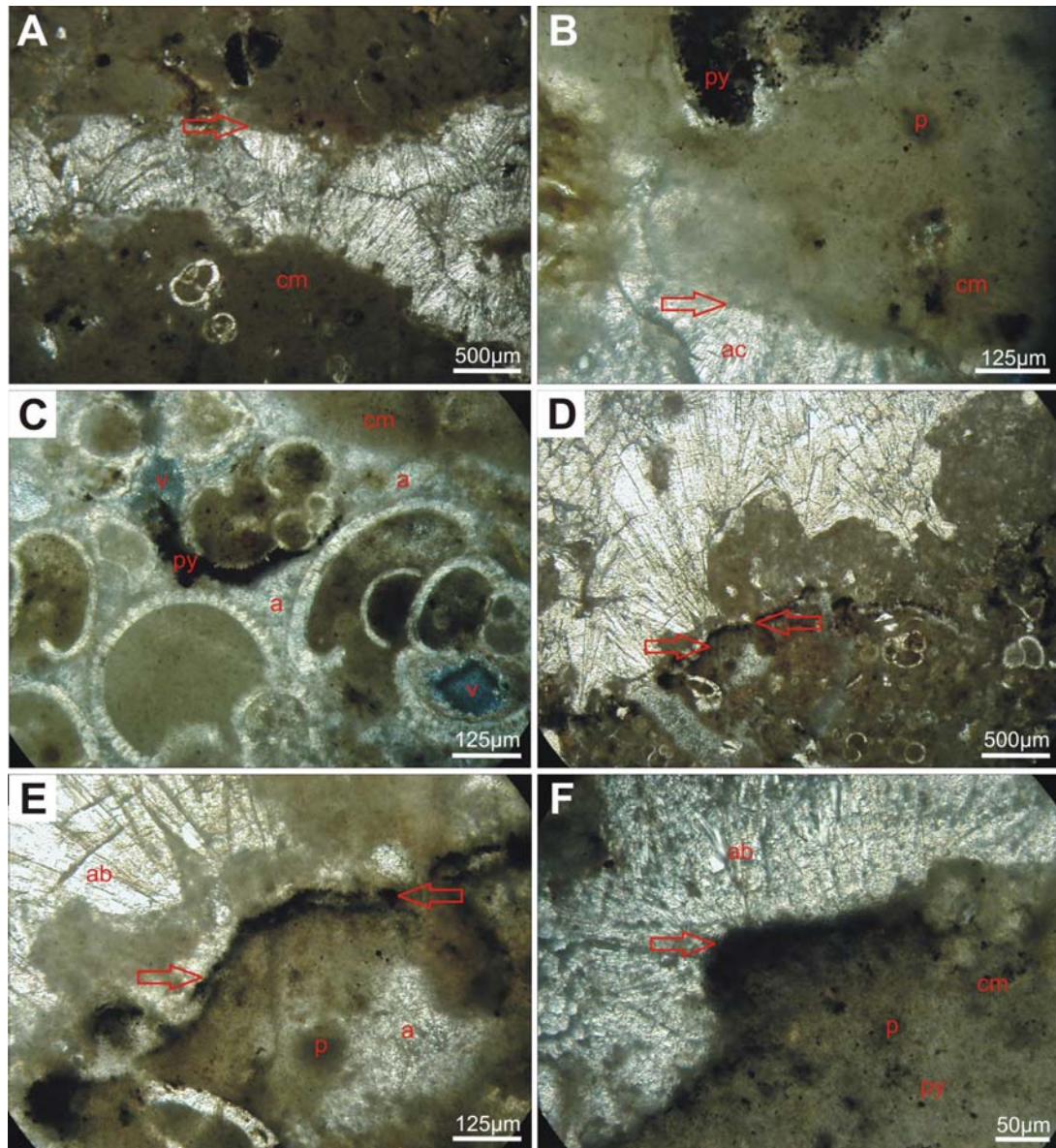


**Figure 8.17.** Thin section micrograph of the lithified mud volcano mud breccias and shell crusts. (A) shows the two carbonate cement phases: the clotted micrite or microbial pelmicrite cement (cm) composed of calcite, high Mg-calcite and aragonite; and a later cementation stage by acicular (almost pure) aragonite that fills the pore spaces, fractures and open cracks, frequently forming botryoidal cements. (B) detail of (A) where is possible to recognise clotted peloidal-like (p) microfabric of the aragonite and calcite cement that is very similar to the fabric of the dolomite chimneys illustrated in Figure 8.7B and C. Arrows in (A) and in (B) indicate coincident locations. (C) pyrite (py) and micritic to spar aragonite (a) cementing bioclasts and leaving some open voids (v). (D-F) details of the contact between the acicular aragonite and the peloidal clotted microfabric (cm) with abundant pyrite framboids and from where the botryoidal acicular aragonite initiates from. In some occasions this contact is characterized by intense pyrite (and organic matter) layer that can show locally finer intercalations of aragonite cement, as illustrated by the arrows in (E) and in Figure 8.18C. (E) is a detail image of (D). All microphotographs are in plane-polarized light except for images (C) and (F) that are crossed polarized light.

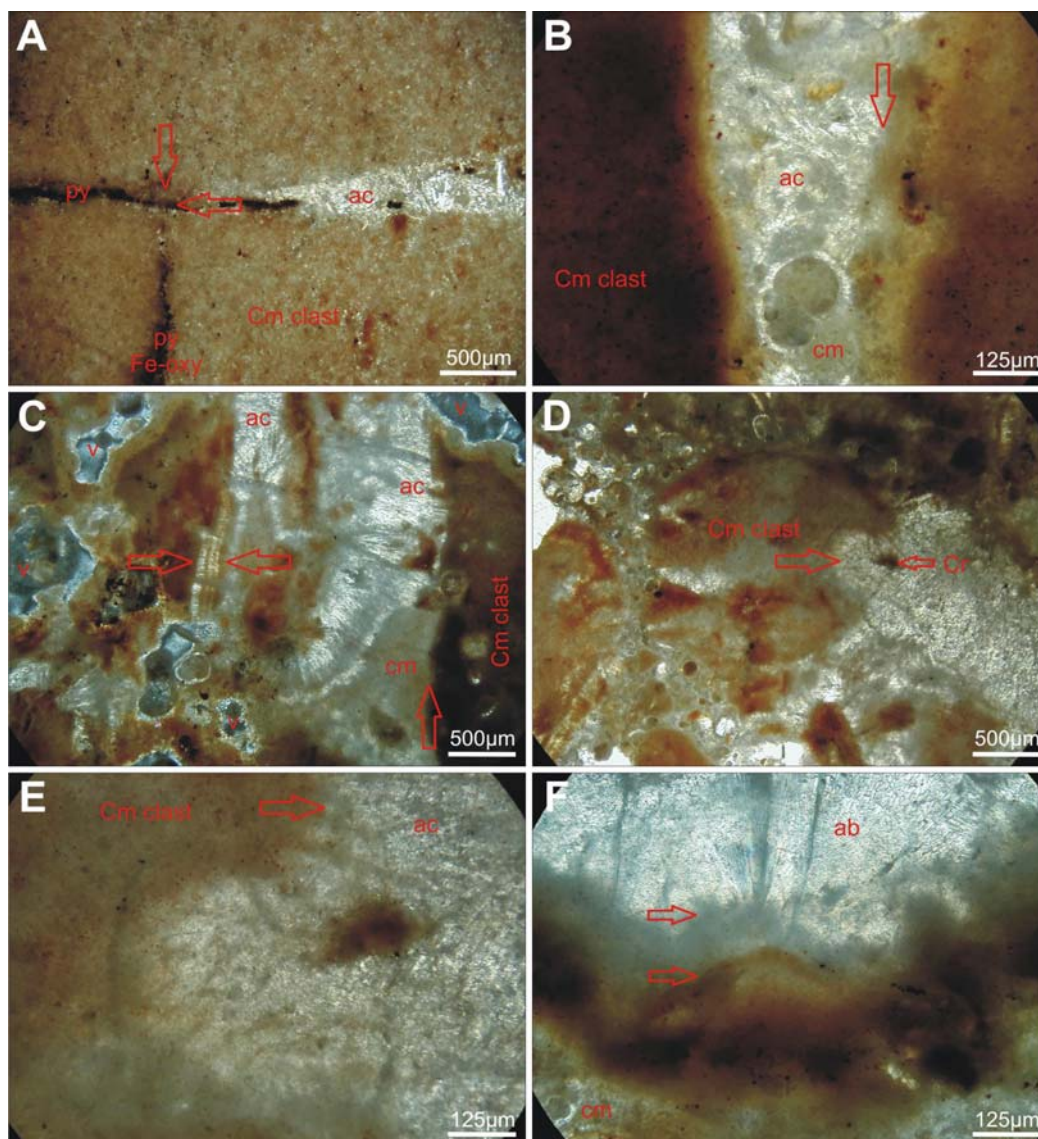


**Figure 8.18.** Thin section micrograph of aragonite pavement samples with re-cemented megaclasts (up to 3 cm size) of previous authigenic carbonate fragments. These samples correspond to the intraformational breccias (described in Chapter 5). (A) biopelmicrite megaclasts (Cm clast), interpreted as previously cemented mud to sands with textural characteristics as described on the dolomite chimneys and other aragonite pavements, fractured and cemented by acicular aragonite (ac) and pyrite (py) probably later replaced by oxy-hydroxids (Fe oxy) and also by clotted micritic cement (cm) with aragonite, calcite and Mg-calcite that can incorporate also bioclasts and other detrital components, as illustrated in (B) and (C). Voids and open cracks are also observed (C) Arrows in (C) pinpoint to the mega-clasts borders. Some of the mega-clasts show sub-rounded shapes (D) and frequently have signs of dissolution, pinpointed by the arrows in (D) and (E). (F) illustrates the radial botryoidal cement (ab) with radial aragonite fabric growing from the clotted pelmicrite cement (cm); to be noted the cloudy fabric at the base of the botryoidal aragonite that is also frequently observed at their ends and that is interpreted as resulting from the incorporation of organic matter of microbial origin. All microphotographs are in plane-polarized light except for images (C) that is crossed polarized light.

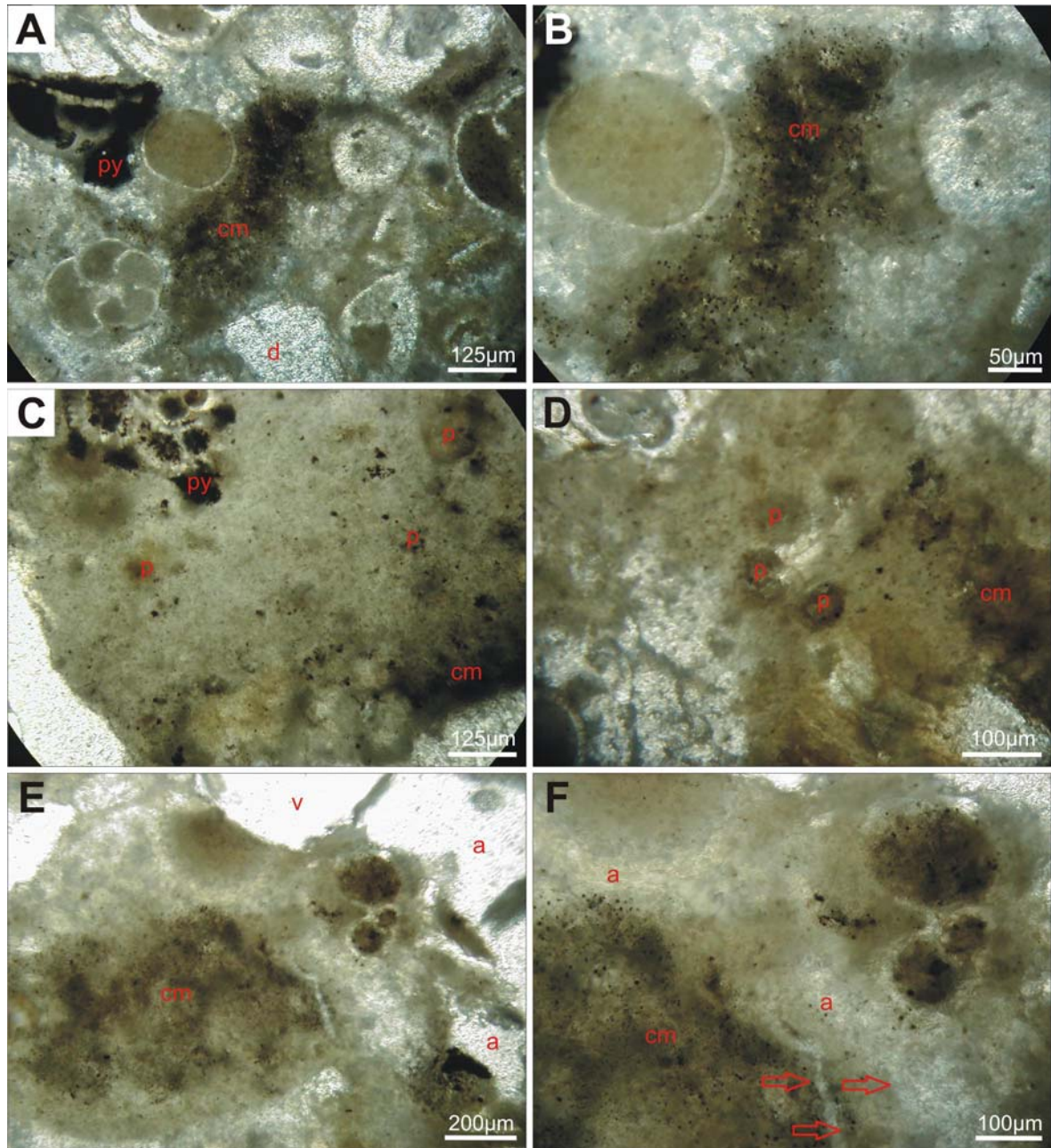


**Figure 8.19.** Thin section micrograph of aragonite pavement peloidal and clotted microfabrics. (A) Clots containing framboidal pyrite (smack black spots) cementing detrital grains (d) and bioclasts some of them containing pyritised interiors (py). (B) detail of the clot from (A). (C - F) clotted microfabric and micritic cement with peloidal-like structures and spackled by pyrite frambooids forming clusters or dispersed in the cement. Arrows in (F) pinpoint to intercalations of aragonitic layers in the clotted microfabric. All microphotographs are in plane-polarized light except for images (A) that is crossed polarized light.

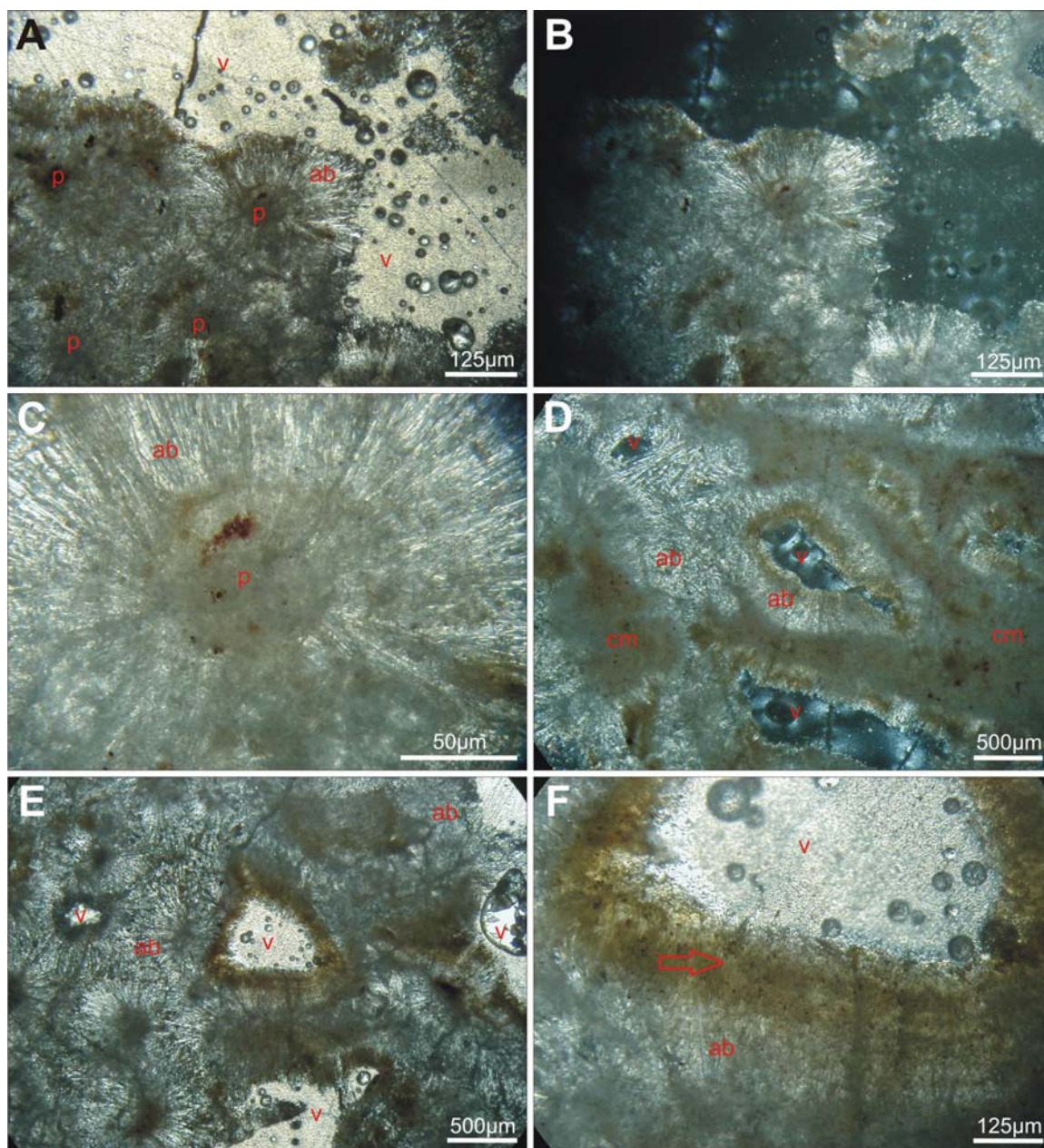


**Figure 8.20.** Thin section micrographs illustrating peloidal, clotted microfabric and aragonite botryoidal infilling voids, cavities and cracks of the lithified mud volcano breccias and shell crusts. (A and C) details of peloids (p) where botryoidal aragonite (ab) cement, with radial fabric, initiates and grow, infilling open spaces. (C) detail of a peloid from (A and B) where is possible to recognise the margin of the peloid and the initiation of the botryoidal aragonite, showing zoned concentric isopachous layers that are interpreted as being layers of higher organic matter content and pyrite. (D) botryoidal aragonite infilling of voids where is botryoidal aragonite grows over clotted micrite cement. (F) detail of image (E) showing the botryoidal infilling of open space showing zoned concentric isopachous layers of brownish yellowish material speckled by small black spots interpreted as pyrite. These layers are interpreted as corresponding to high content in organic mater probably the biofilms and preserved bacterial rods that are imagined by SEM images in Figure 8.22D and E and in Figure 8.26.

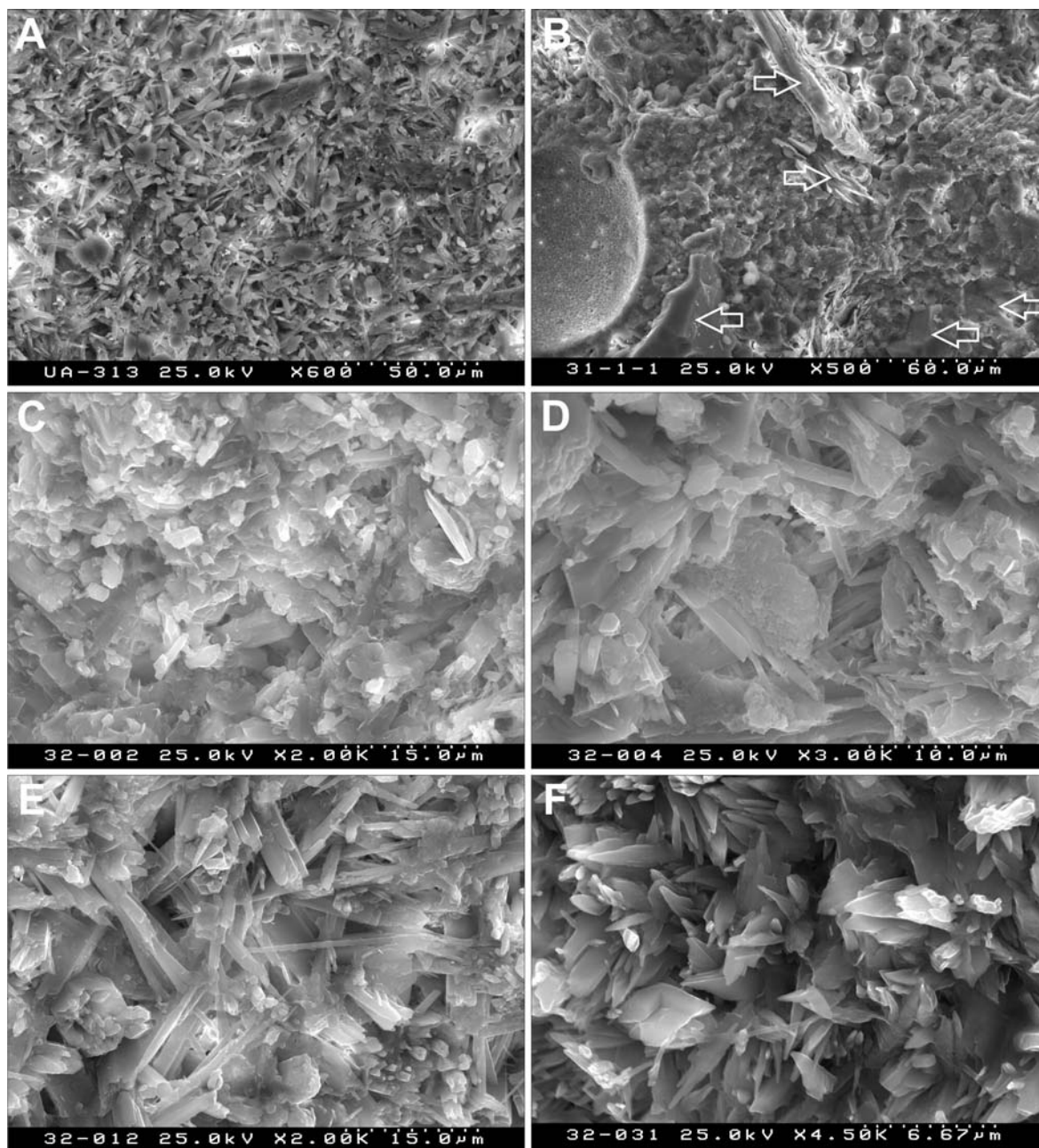


**Figure 8.21.** SEM imagery illustrating general textural characteristics of the micrite and pelmicritic fabric of the aragonite pavements. Arrows in (A) pinpoint detrital grains. (Scale and acquisition parameters are shown in pictures footnotes).

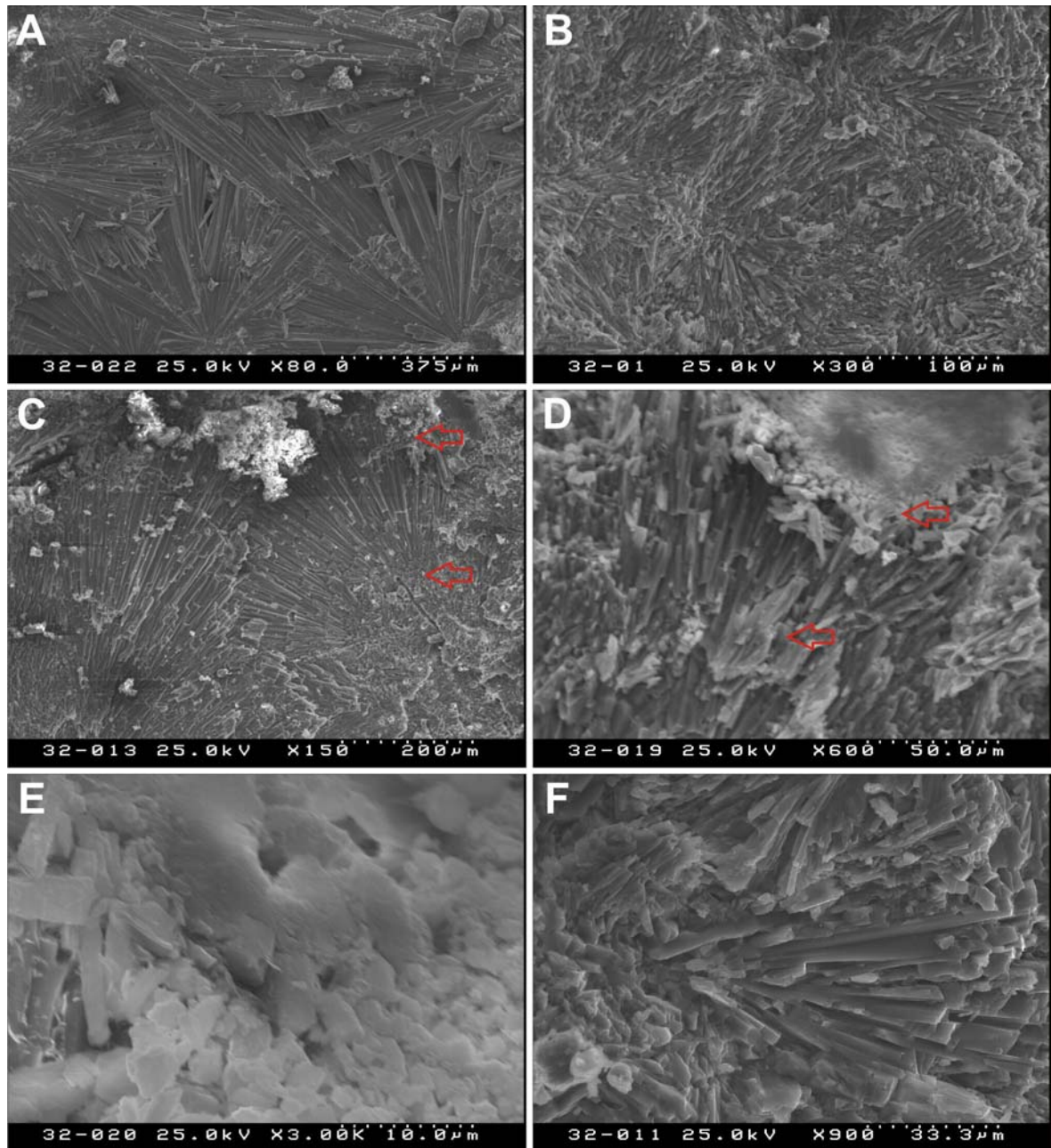


**Figure 8.22.** SEM imagery illustrating textural characteristics of the aragonite botryoidal and stromatolitic layers fabric of the aragonite pavements. (D) arrows pinpoint to different aragonite layers within the stromatolitic layer fabric (Scale and acquisition parameters are shown in pictures footnotes).

### ***Microbial filaments***

Unidentified filaments with diameters of about 1  $\mu\text{m}$  and up to 15  $\mu\text{m}$  in length were frequently observed by SEM within the aragonite pavement cements (Figure 8.23). Two distinct types of filaments can be identified: (1) strait linear filaments with a very smooth external surface, illustrated in Figure 8.23E-G, very similar to the filaments observed on the dolomitic crusts and chimney samples (8.3.1.1: Microbial filaments); and (2) sinuous filaments that have curve shapes and a more rough (unpolished) exterior (Figure 8.23A-D), some of them seem to being calcified, cemented and incorporated by the authigenic cement (Figure 8.23H). Some of these sinuous filaments are boll capped filaments or exhibit boll caps or coccoids (with  $< 1 \mu\text{m}$  in diameter) over them. Because the filaments, in particular the sinuous filaments have shapes and sizes similar to bacteria and are similar to the fossilized bacteria filaments enclosed in several modern seep carbonates (Peckmann *et al.*, 2001b; Shapiro, 2004; Reitner *et al.*, 2005), they are interpreted as fossilized microbial filaments. The microbial filaments can occur isolated between the aragonite fibers or as denser clusters, such as that in Figure 8.23H.

It was also possible to identify some open tubular structures, such as the one illustrated in Figure 8.24A with a similar diameter to the microbial filaments (of about 1  $\mu\text{m}$ ). Tubular holes with larger diameters of 3 to 5  $\mu\text{m}$  are also frequently observed, which are interpreted as scavenger holes by unidentified organisms (Figure 8.24B-D).

Individual coccoids or boll caps are spherical to sub-spherical structures with 0.5-1  $\mu\text{m}$  in diameter that occur isolated, associated with filaments or forming coccoid clusters. While many different processes, including abiogenic processes, can be considered to explain the formation of the spherical structures, their sizes are equivalent to the sizes of modern bacteria and archaea (Boetius *et al.*, 2000); their occurrence, associated with microbial filaments and biofilms, and their EDS chemical composition with higher carbon content, compared with the involved carbonate cement, suggests a biogenic origin for the coccoids.

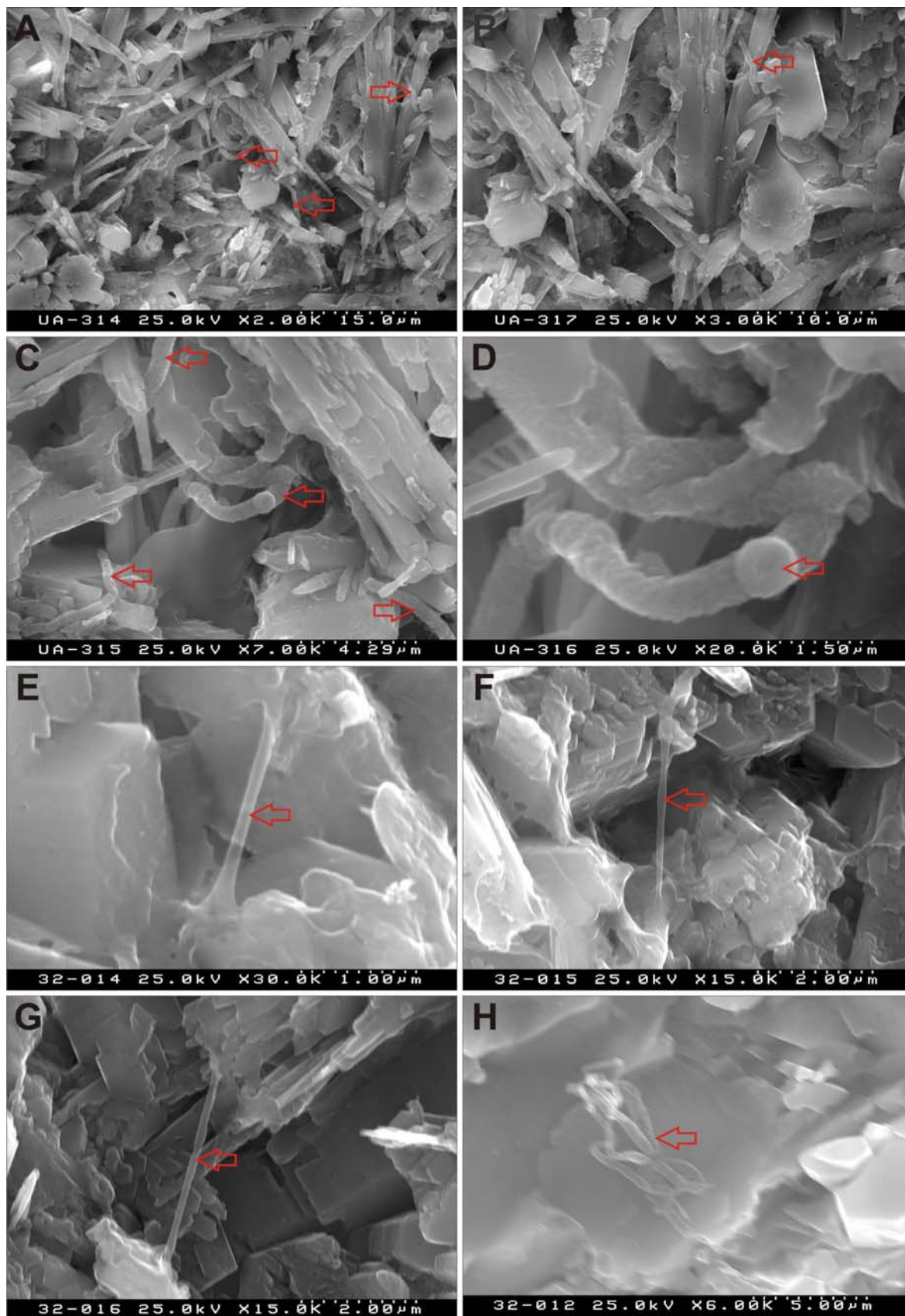


**Figure 8.23.** SEM imagery illustrating aragonite pavements microbial filaments. (Scale and acquisition parameters are shown in the pictures footnotes).

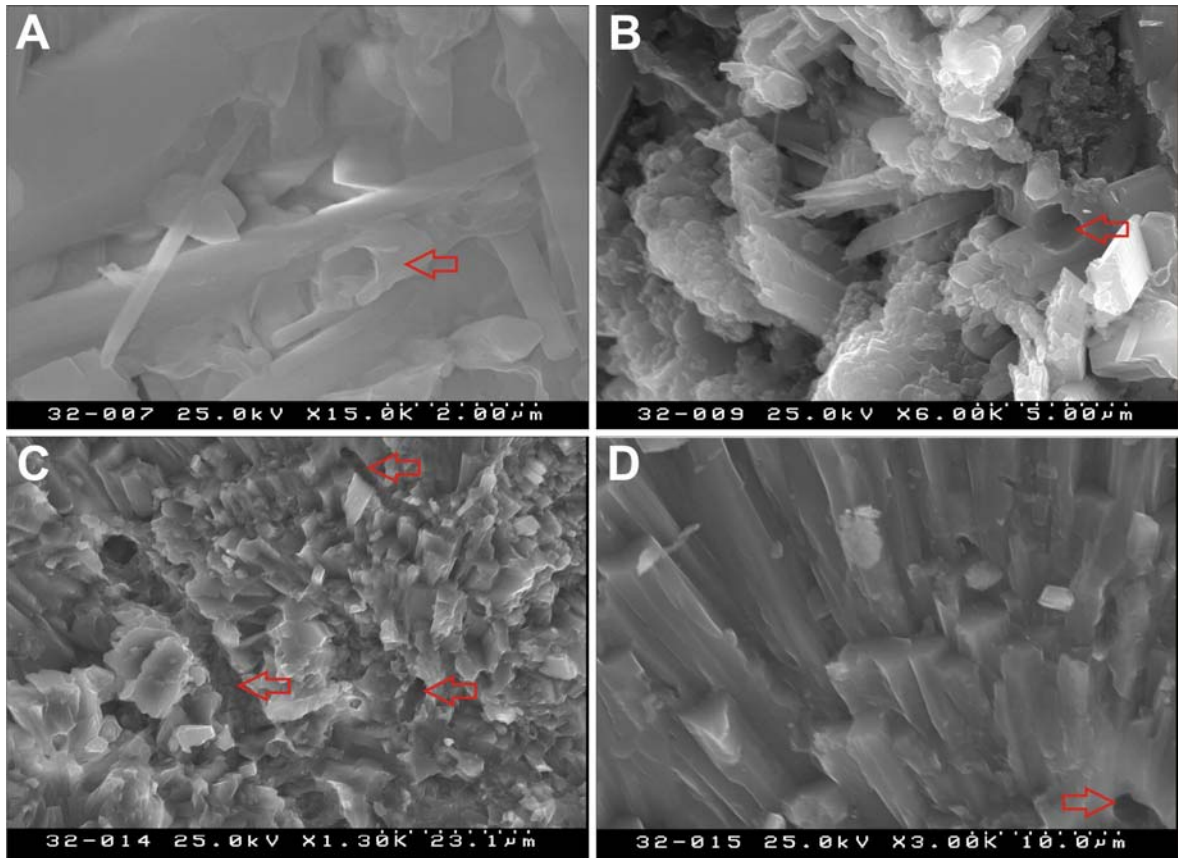


**Figure 8.24.** SEM imagery illustrating aragonite pavements tubular and microbial scavenger holes. (Scale and acquisition parameters are shown in pictures footnotes).

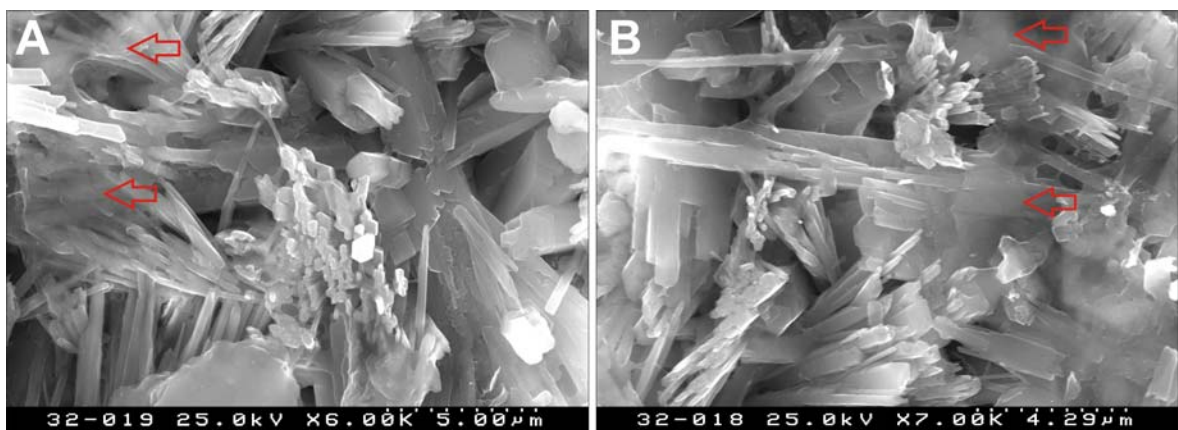


**Figure 8.25.** SEM imagery illustrating general textural characteristics of the aragonite pavement type with mucilage or calcified biomucous within the aragonite needles pinpointed by the arrows. (Scale and acquisition parameters are shown in pictures footnotes).

**Biofilms**

Between the aragonite needles of the zoned isopachous stromatolitic cement layers and the botryoidal aragonite, especially at the centre of the cavities, biofilms and biomucos also occur, as illustrated in Figure 8.25 and Figure 8.26 (pinpointed by the arrows). While the nature of these structures is not totally clear, a biogenic origin of these is proposed.

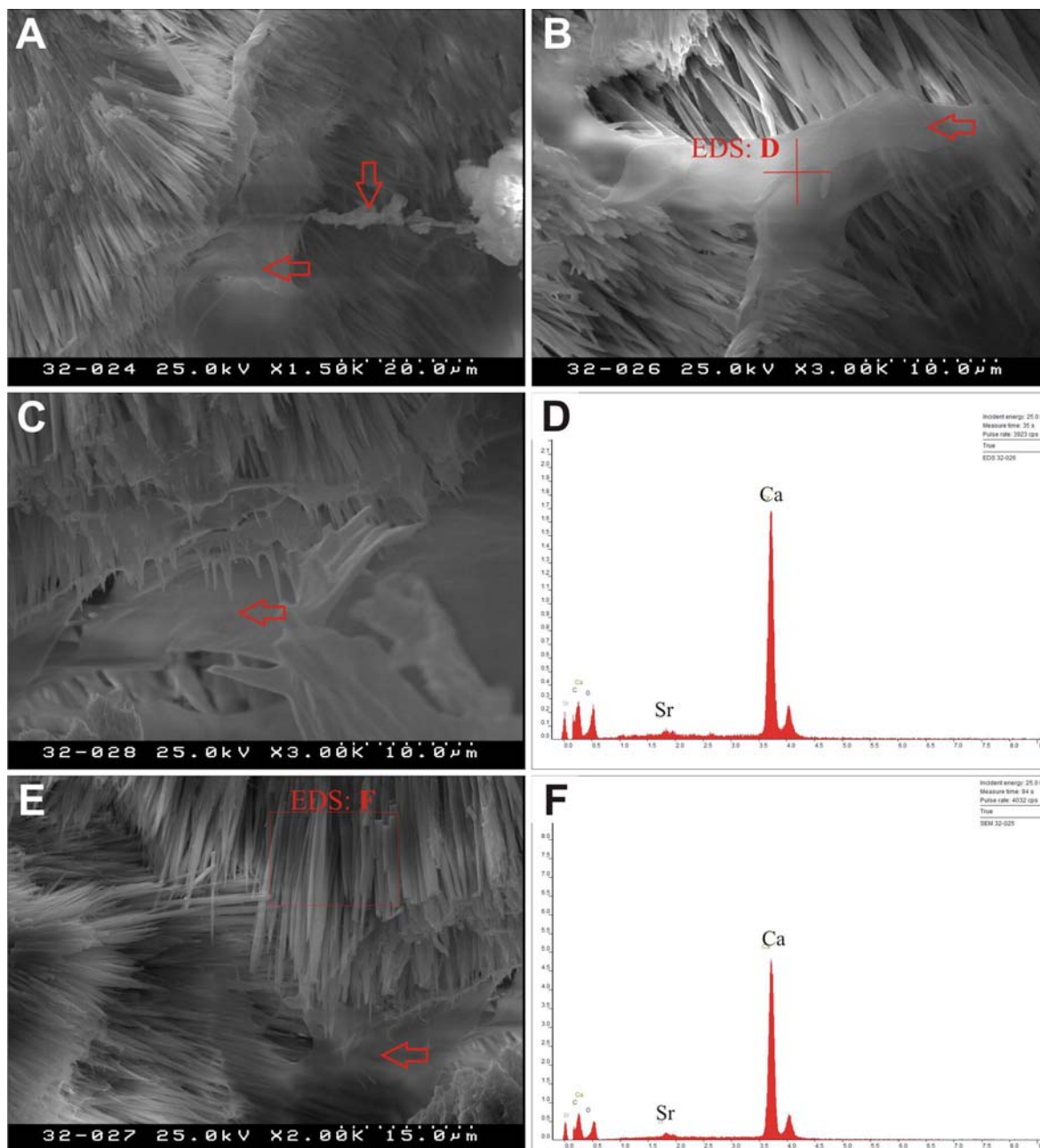


**Figure 8.26.** SEM imagery illustrating aragonite needles stromatolitic layer filing a cavity with biofilms and biomucos. (Scale and acquisition parameters are shown in pictures footnotes).

## 8.3.2 Lipid biomarkers

### 8.3.2.1 Dolomite chimneys

#### *Sample 3722-A33*

The chromatogram of this sample shows a large amount of dirt peaks, but some archaea-diagnostic biomarkers evidencing AOM were identified (Figure 8.27A and Table 8.2).

The peak of PMI, not very intense but clear, is identified and the carbon isotopic composition of this compound shows a depleted carbon isotopic ratio of -114‰ VPDB, which is a clear evidence for archaea-mediated AOM. PMI is produced by Archaea (Thiel *et al.*, 1999) especially by methanogens, thermoacidophilics and methanogens.

Squalane is present and depleted in  $^{13}\text{C}$  (-64‰ VPDB; Figure 8.27). Although squalane is not an unquestionable AOM marker, as it can have various sources, such strongly depleted  $^{13}\text{C}$  value indicates that methane must be the carbon source for this biomarker and it is most probably indicating AOM archaea. Possibly, squalane is a good and promising marker for the degradation of squalene, which is a polyunsaturated precursor of Squalane.

Crocoetane was not detected in this sample. The fact that this compound was detected on sample 3463-A08 (that presents a lower oxidation intensity), can be interpreted as an indicator of the degradation intensity. The degradation intensity in sample 3722-A33 is higher and therefore only the final and more resistant AOM markers remain.

Other small peaks of isoprenoids, such as Pristane are present but just in trace quantities that do not allow the measurement of the  $^{13}\text{C}$  isotopic composition. Aliphatic n-alkanes are also present: the short ones are produced by eukaryotes and the long ones by land plants. These compounds are allochthonous markers from eukaryotes and land plants. The uneven chains ( $\text{C}_{27}$ ,  $\text{C}_{29}$  and  $\text{C}_{31}$ ) predominate over the short ones, indicating relatively fresh biomarker material from the detrital organic mater.

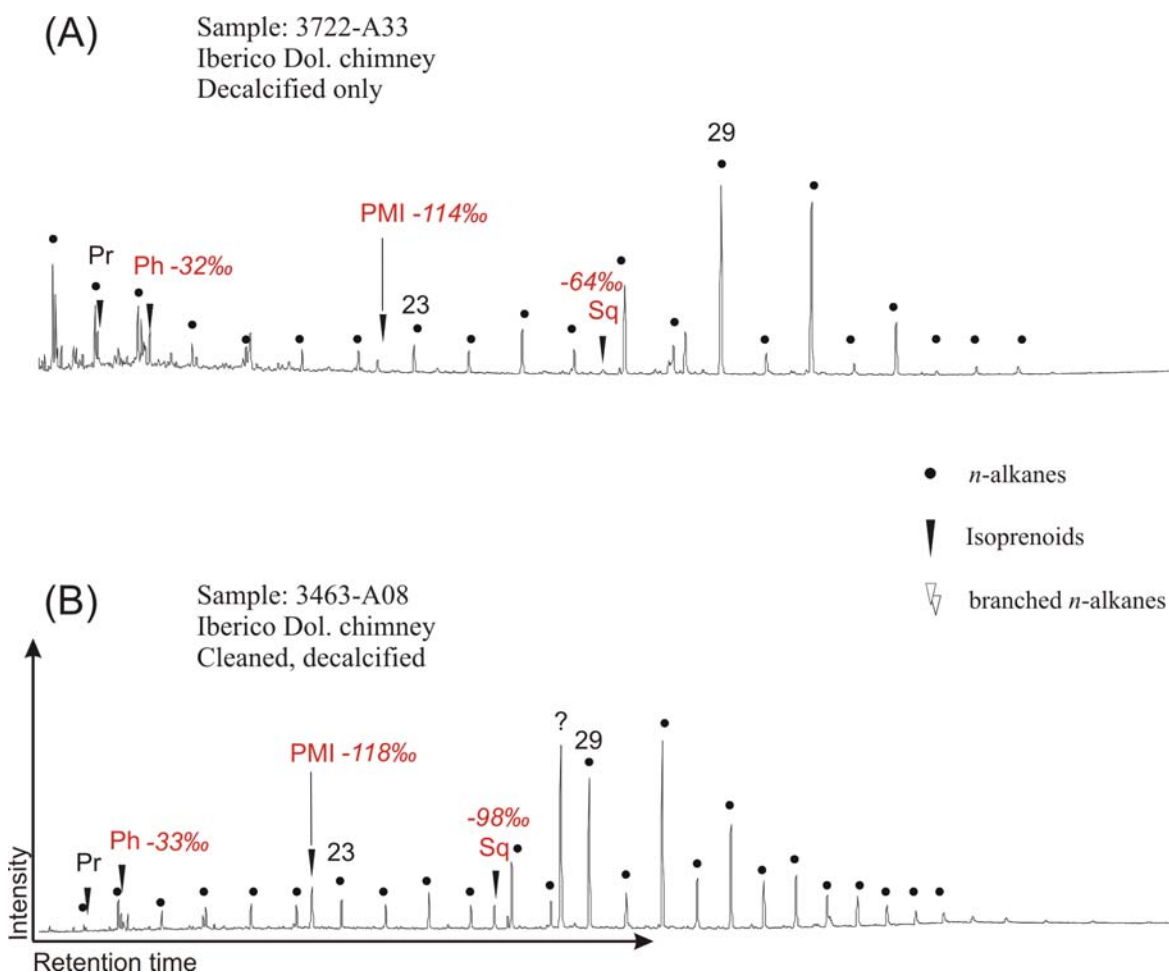


**Figure 8.27.** Gas chromatograms of hydrocarbon fractions obtained from samples 3722-A33 (A) and 3463-A08 (B). *n*-Alkanes are indicated by solid circles. Numbers represent total number of carbon atoms. (Hydrocarbon compounds: Pr= 2, 6, 10, 14-tetramethylpentadecane; Ph= 2, 6, 10, 14-tetramethylhexadecane; Cr= Crocetane; Cr:1, Cr:2 = Crocetane containing one or two double bonds, respectively; PMI= 2, 6, 10, 15, 19-pentamethylcosane; PMI:3, PMI:4, PMI:5 = pentamethylcosenes containing three, four or five double bonds, respectively; SI= internal standards; ?= unknown cyclic compounds). Italicized values in red indicate  $\delta^{13}\text{C}$  isotopic composition of individual biomarkers in ‰ VPDB.

### *Sample 3463-A08*

For the biomarker analysis of sample 3463-A08 (Figure 8.2) 250 g of material was collected by fragmenting slices of this sample to small pieces, keeping in mind to avoid the periphery of the chimney and parts of the sample with possible contamination. The analytical methodology used to process this sample is described in the flowchart of Figure D.2, Appendix D. The analytical procedure used for this sample includes a supplementary step that involves a previous extraction before the standard methodology normally used.

This first extraction step was performed to clean the dirt peaks before the decalcification. Only during the decalcification the biomarker compounds that we wish to analyse, will be liberated from the cement carbonate phase, and therefore concentrated in relation to the dirt compounds.

**Table 8.2.** Main biomarker compounds identified on the studied samples and their carbon isotopic compositions (values in ‰ VPDB). Diagnostic lipid biomarkers are highlighted in grey, red colour values identify probable AOM compounds. (*n.d.* = not detected).

GC/MS-RT	IRMS RT	Compound	Sample		
			3340	3463-A08	3722-A33
10.60	1160	<b>16</b>	-29.33	<i>n.d.</i>	-39.17
12.02	1311	<b>17</b>	-29.19	<i>n.d.</i>	-40.34
12.10	1326	<b>Pristane</b>	-29.54	<i>n.d.</i>	-36.40
13.66	1460	<b>18</b>	-29.40	-27.89	-33.39
13.80	1481	<b>Phytane/Crocetane</b>	-132.27	-33.56	-32.06
14.45	1534	<b>Crocetane:1</b>	-48.08	<i>n.d.</i>	<i>n.d.</i>
15.47	1608	<b>19</b>	-32.71	-31.53	-30.34
17.41	1755	<b>20</b>	-30.68	-28.21	-34.32
19.39	1898	<b>21</b>	-29.84	-30.43	-34.78
21.37	2035	<b>22</b>	-28.96	-32.58	-30.45
22.12	2104	<b>PMI</b>	-100.82	-117.79	-114.92
22.49	2125	<b>PMI:1</b>	-75.21	<i>n.d.</i>	<i>n.d.</i>
22.84	2144	<b>PMI:2</b>	-72.36	<i>n.d.</i>	<i>n.d.</i>
23.34	2175	<b>23</b>	-45.72	-31.32	-31.50
23.56	2187	<b>PMI:2</b>	-76.17	<i>n.d.</i>	<i>n.d.</i>
23.96	2212	<b>PMI:3</b>	-50.94	<i>n.d.</i>	<i>n.d.</i>
25.26	2298	<b>24</b>	-33.70	-32.33	-30.92
27.15	2423	<b>25</b>	-31.94	-34.02	-34.03
28.96	2543	<b>26</b>	-32.85	-31.71	-38.28
30.00	2619	<b>Squalane</b>	-39.60	-98.33	-63.94
30.75	2659	<b>27</b>	-33.79	-30.25	-32.21
32.46	2777	<b>28</b>	-38.18	-32.50	-31.58
32.89	2790	<b>Perylen</b>	<i>n.d.</i>	-26.07	-25.12
34.13	2886	<b>29</b>	-34.66	-33.66	-34.42
35.75	2991	<b>30</b>	-35.53	-31.85	-33.24
37.32	3099	<b>Hopan</b>	-34.35	-31.74	-33.67
37.35	3112	<b>31</b>	-43.44	<i>n.d.</i>	-19.05
38.85	3214	<b>32</b>	-36.64	-31.21	-36.75
40.33	3337	<b>33</b>	-36.05	-31.24	-31.44

The chromatogram for this sample (Figure 8.27B and Table 8.2) shows biomarkers evidencing AOM, similar to the previous dolomite chimney sample, but here the archaeal diagnostic biomarkers are present in larger amounts. The peak of PMI is more pronounced than in sample 3722-A33 and the carbon isotopic composition of this compound shows a depleted carbon isotopic ratio of -117‰ VPDB, which is a clear evidence of AOM.

Squalane shows a depleted  $^{13}\text{C}$  ratio (-98‰ VPDB). This depleted value indicates methanogenic archaea as the probable source. A possible explanation for the difference in the isotopic composition of squalane between the dolomite chimneys samples 3463-A08 and 3722-A33 might be that during the previous supplementary step of extraction, in sample 3463-A08, some of the “heavy” squalane was lost.

### 8.3.2.2 Aragonite pavements

#### Sample 3340

The aragonite pavement sample 3340 was prepared according to the standard analytical methodology described in the flowchart of Figure D.1, Appendix D. The amount of material used was 20 g.

This sample presents evidence not only of PMI (with  $^{13}\text{C}$  ratio of -100‰ VPDB), but also of mono-, di- and triunsaturated PMI. The isotopic ratios of the unsaturated PMI's are heavier than the saturated compounds, presenting values of -72‰ to -75‰ VPDB (Figure 8.28).

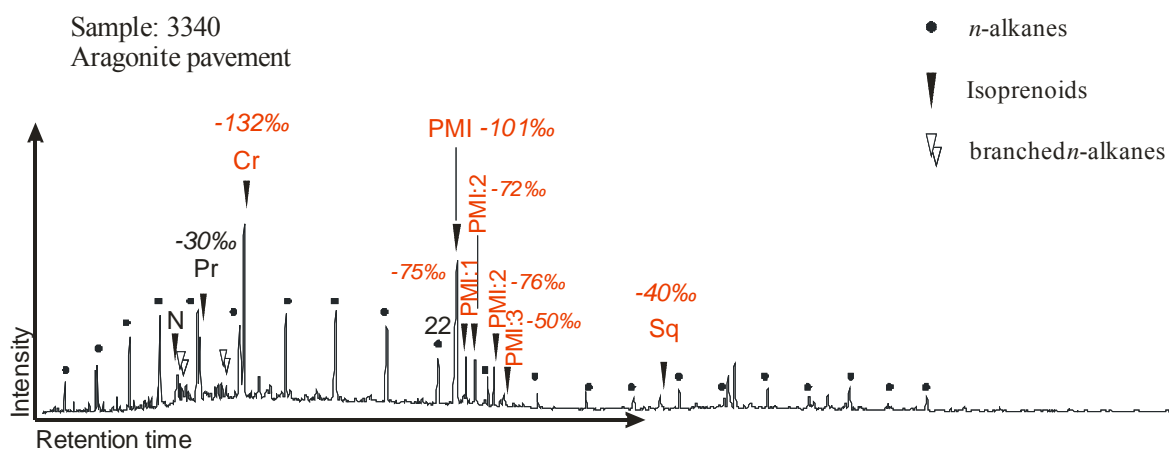


**Figure 8.28.** Gas chromatograms of hydrocarbon fractions obtained from the aragonite pavement sample 3340. *n*-Alkanes are indicated by solid circles. Numbers represent total number of carbon atoms. (Hydrocarbon compounds: Pr= 2, 6, 10, 14-tetramethylpentadecane; Ph= 2, 6, 10, 14-tetramethylhexadecane; Cr= Crocetane; Cr:1, Cr:2 = Crocetane containing one or two double bonds, respectively; PMI= 2, 6, 10, 15, 19-pentamethylcosane; PMI:3, PMI:4, PMI:5 = pentamethylcosenes containing three, four or five double bonds, respectively; SI= internal standards; ?= unknown cyclic compounds). Italicized values in red indicate  $\delta^{13}\text{C}$  isotopic composition of individual biomarkers in ‰ VPDB.

Crocetane is also present. It is one of the dominant peaks in the sample and presents very depleted isotopic  $^{13}\text{C}$  ratio (-132.27‰ VPDB). Crocetane:1, the monounsaturated version of crocetane, is also present with a  $^{13}\text{C}$  ratio of -50‰ VPDB. Squalane is present but it is not as depleted as in the dolomite chimney samples. Squalane presents a  $^{13}\text{C}$  ratio of -40‰ VPDB. The short-chain n-alkanes are more abundant than the long-chain alkanes. There is also a stronger presence of eukariotes and less input of terrestrial material in this sample. Therefore the terrestrial input on the aragonite pavements seems to be less than the terrestrial input on the dolomite chimneys.

### ***Sample GeoB 9029-3***

Aragonite pavement samples from the Faro mud volcano (MV) yielded archaeal biomarkers such as crocetane/phytane with depleted isotopic  $^{13}\text{C}$  values (-110‰ VPDB), and Archaeal sn2-hydroxyarchaeol, also depleted in  $^{13}\text{C}$  (Table 8.3). PMI (with a  $^{13}\text{C}$  ratio of -111‰ VPDB) as mono-, di- and triunsaturated PMI are also present in this sample, all with depleted isotopic  $^{13}\text{C}$  values.

Several bacterial lipid biomarkers, such as the i-C<sub>15:0</sub>; ai-C<sub>15:0</sub>; C<sub>16:1 $\omega$ 5</sub>; C<sub>17:1 $\omega$ 6</sub> that have been described as related to SRB (Elvert *et al.*, 2003), are present in this aragonite pavement sample. The bacterial lipid biomarkers that could be analysed are strongly depleted in  $^{13}\text{C}$ , with values ranging from -95 to -99‰ VPDB (Table 8.3).

In this sample, the archaeal and bacterial lipids biomarkers occur in similar concentrations (Niemann *et al.*, 2006).

### ***Sample GeoB 9023-1***

The aragonite pavement sample from Hesperides MV shows stronger oxidation intensity than the aragonite pavement from both Faro and Ginsburg MVs. Probably because of this, the bacterial fatty acids (FA) and the archaeal biomarkers from the Hesperides MV were found in much lower amount than in Faro MV.

The most common bacterial FAs in the Hesperides MV were the C<sub>16:0</sub> and C<sub>18:0</sub>, compounds, which are not associated with SRB. The lipid biomarkers associated with SRB (Elvert *et al.*, 2003) found in this sample were i-C<sub>15:0</sub>; ai-C<sub>15:0</sub> and C<sub>16:1 $\omega$ 5</sub>, showing  $\delta^{13}\text{C}$  values less depleted than those values recorded on samples from the Hesperides MV (Table 8.3).

**Table 8.3.** Main biomarker compounds identified on aragonite pavements collected from the Hesperides and Faro mud volcanoes (data from Duarte, 2005; Niemann *et al.*, 2006). Abundances of fatty acids were normalised to i-C<sub>15:0</sub>, archaeal diethers to archaeol and archaeal isoprenoidal hydrocarbons to PMI:0. Diagnostic lipid biomarkers are highlighted in grey. (*n.d.* = not detected).

Compound	Hesperides GeoB 9023-1		Faro GeoB 9029-3		
	Normalized abundance	$\delta^{13}\text{C}$ (‰VPDB)	Normalized abundance	$\delta^{13}\text{C}$ (‰VPDB)	
Bacterial fatty acids	C <sub>14:0</sub>	1.1	-31	2.3	-93
	i-C <sub>15:0</sub>	1.0	-39	1.0	-99
	ai-C <sub>15:0</sub>	1.5	-43	1.9	-95
	C <sub>15:0</sub>	0.3	-45	0.4	-96
	i-C <sub>16:0</sub>	0.2	<i>n.d.</i>	0.2	-87
	C <sub>16:1<math>\omega</math>9</sub>	<i>n.d.</i>	<i>n.d.</i>	0.1	-92
	C <sub>16:1<math>\omega</math>7</sub>	0.6	-27	1.8	-93
	C <sub>16:1<math>\omega</math>5</sub>	0.1	-41	0.7	-96
	C <sub>16:0</sub>	4.8	-27	1.6	-77
	10MeC <sub>16:0</sub>	<i>n.d.</i>	<i>n.d.</i>	1.0	-94
	i-C <sub>17:0</sub>	0.3	-32	0.3	-96
	ai-C <sub>17:0</sub>	0.5	-38	0.3	-99
	C <sub>17:1<math>\omega</math>7</sub>	0.5	-31	0.4	-93
	C <sub>17:1<math>\omega</math>6</sub>	<i>n.d.</i>	<i>n.d.</i>	0.1	<i>n.d.</i>
	cyC <sub>17:0<math>\omega</math>5,6</sub>	<i>n.d.</i>	<i>n.d.</i>	<i>n.d.</i>	<i>n.d.</i>
	C <sub>17:0</sub>	0.2	<i>n.d.</i>	0.1	<i>n.d.</i>
	C <sub>18:1<math>\omega</math>9</sub>	0.2	<i>n.d.</i>	0.3	-77
	C <sub>18:1<math>\omega</math>7</sub>	0.4	-37	1.5	-84
C <sub>18:0</sub>	1.8	-28	0.4	-67	
Archaeal lipids	Archaeol	1.0	-97	1.0	-114
	<i>sn</i> 2-hydroxyarchaeol	<i>traces</i>	<i>n.d.</i>	0.2	-111
	Crocetane/Phytane	0.5	-47	3.3	-110
	PMI:0	1.0	-87	1.0	-111
	$\Sigma$ PMI:1	0.3	<i>n.d.</i>	4.6	-113
	$\Sigma$ PMI:2	<i>n.d.</i>	<i>n.d.</i>	8.3	-113
	$\Sigma$ PMI:3	<i>n.d.</i>	<i>n.d.</i>	0.3	-101
<b>Concentration (<math>\mu\text{g g-dw}^{-1}</math>)</b>					
Bacterial fatty acids	i-C <sub>15:0</sub>	0.1	-	8.7	-
	ai-C <sub>15:0</sub>	0.2	-	16.8	-
	C <sub>16:1<math>\omega</math>5</sub>	0.0	-	6.1	-
	C <sub>17:1<math>\omega</math>6</sub>	<i>n.d.</i>	-	0.5	-
	cyC <sub>17:0<math>\omega</math>5,6</sub>	<i>n.d.</i>	-	<i>n.d.</i>	-
Archaea l lipids	Archaeol	2.4		41.6	
	<i>sn</i> 2-hydroxyarchaeol	0.0		8.3	
	Crocetane/Phytane	0.2		4.6	
	PMI:0	0.4		1.4	
<b>Putative origin</b>		AMNE1 Seep-SRB1(?)		AMNE1, Seep-SRB1 AMNE2, Seep-SRB1	

The archaeal biomarkers, similar to the SRB biomarkers, are found to be less abundant here than in the Faro MV sample. The most abundant archaeal biomarker is PMI (with depleted  $^{13}\text{C}$  isotopic value of  $-87\text{‰}$  VPDB). Mono-unsaturated PMI was also identified as crocetane/phytane, archaeal and just traces of *sn2*-hydroxyarchaeol (Table 8.3).

Comparing the abundance of the archaeal lipids and the diagnostic bacterial biomarkers, here the bacterial biomarkers were approximately an order of magnitude lower in concentration than the Archaeal lipids.

## 8.4 Discussion

### 8.4.1 Textural and fabric implications on the MDAC formation processes

The authigenic carbonate phases that compose the cement (aragonite, calcite and Mg-calcite in the aragonite pavements, and dolomite, Mg-calcite and calcite in the dolomitic crusts, chimneys and nodules) are characterized by depleted carbon isotopic compositions ( $\delta^{13}\text{C}$  values as low as  $-46.9\text{‰}$  VPDB, as described in Chapter 5), indicating that the precipitation of the authigenic carbonate minerals were induced by methane oxidation. The co-formation of the authigenic carbonates and authigenic pyrite with  $\delta^{34}\text{S}$  negative values (González *et al.*, 2006a, b) indicates an anaerobic geochemical environment with sulphate-reducing bacterial activity promoting the sulphide precipitation in anoxic sediment conditions. Therefore, the oxidation of methane that lead to the alkalinity increase and subsequent formation of the authigenic carbonates had to be reached through the anaerobic oxidation of methane (AOM).

As the dolomite chimneys, crusts and nodules do not evidence any signs of dissolution episodes and subsequent phase of cementation, this support the model (as proposed in Chapter 5) that the dolomite dominated MDAC are formed at a deeper locations within the sedimentary column.

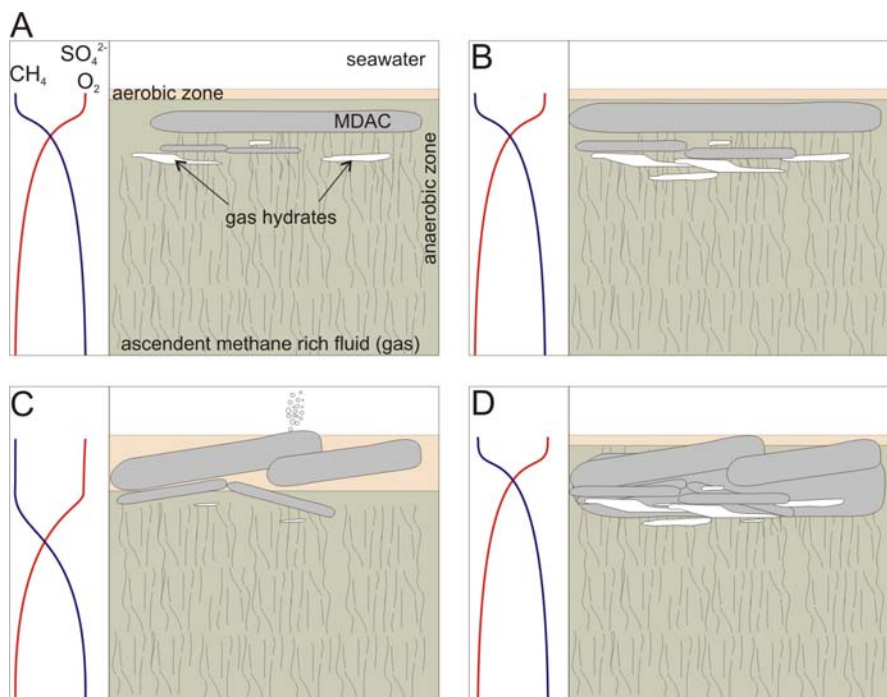


**Figure 8.29.** Schematic diagram illustrating the chemical environment during the formation of the authigenic carbonates (phase A and B). In (C) a change in the chemical environment occurs due to destabilization of gas hydrate layers that promotes the fracturation of the incipient aragonite pavements and subsequent ventilation of the system by seawater and consequent change of the environment to an oxic phase. This phase can be followed by a new phase (D) of authigenic carbonate formation leading to the re-cementation of the MDAC fragments.

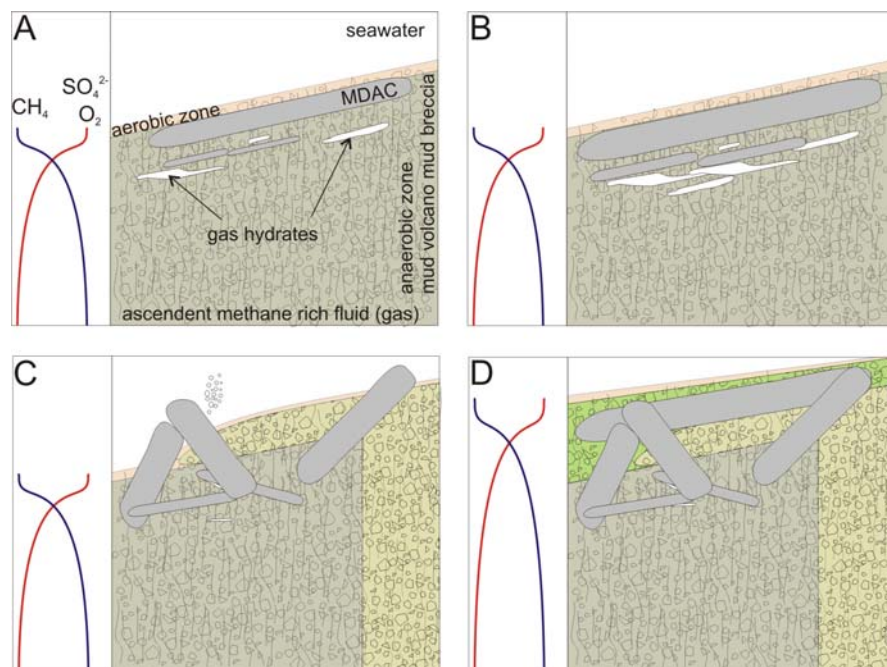


**Figure 8.30.** Schematic diagram illustrating the chemical environment during the formation of the authigenic carbonates considering multiple episodes of mud volcano mud breccia extrusion episodes.

The dolomite chimneys, crusts and nodules do not exhibit any textural or microfabric characteristics that indicate a change in the geochemical conditions (as dissolution episodes and subsequent phases of cementation). Some of them exhibit discontinuities not related to dissolution phases but interpreted as resulting from lithologic changes in the initial sediment from which the carbonate was formed or discontinuities that were interpreted as resulting most probably from variations on the cementation as consequence of variation of the methane flux supply. Therefore the dolomitic carbonates are interpreted as corresponding to a more confined environment of formation, most probably within the first meters of the sedimentary column (as discussed in Chapter 5).

As some of the aragonite pavements show frequent dissolution events, this is an indicator of the variability of the environmental conditions and probably of changes to aerobic conditions, with periods of aerobic methane oxidation that lead to increase in acidity of the pore waters and carbonate dissolution instead of carbonate formation. This is interpreted as indicating a more ventilated (by seawater) environment, most probably closer to the seafloor, during the formation of the aragonite pavements. These dissolution events can be interpreted as corresponding to episodes of increased seawater ventilation. These episodes can result from: (1) a mechanical destabilization of the system by dissociation of gas hydrate layers in the shallow subsurface (as illustrated in Figure 8.29); (2) mechanical destabilization of the system as result of mud breccia eruptions within a mud volcano (as illustrated in Figure 8.30) or (3) by a reduction of the methane flux, allowing the sulphate and oxygen diffusion from seawater deeper into the sediment column. The two first processes can lead to ruptures of the carbonate cap of the aragonite pavements, leading to their brecciation and consequent increase of seawater ventilation and changing the chemical environment from anoxic to oxic conditions.

#### **8.4.2 Microfabrics and microbial fossil evidences**

The petrographic and SEM observations discussed in this chapter revealed large amounts of structures and textures that clearly indicate microbial activity during the formation of the MDAC.

The carbonate cement of the MDAC, in both the dolomitic and aragonitic samples is characterized by a dominance of clotted microfabric that corresponds to the “structure

grumeleuse” described by Cayeux (1935) whose genesis and significance have been object of discussion (Shapiro, 2000; Peckmann *et al.*, 2002; Shapiro and Fricke, 2002; Shapiro, 2002; Shapiro, 2004). This term is used to designate aggregates of cloudy, irregular, micritic authigenic carbonate (aragonite, calcite, Mg-calcite and dolomite) cement, primary in origin and where authigenic pyrite and probably organic compounds are abundant. This microfabric has been recorded in association with several active and fossil seep carbonates (Shapiro, 2000; Peckmann *et al.*, 2001c; Peckmann *et al.*, 2002; Shapiro and Fricke, 2002; Shapiro, 2002). Furthermore, the presence of clotted microfabric in both aragonitic and dolomitic carbonated indicates that this fabric is not specific of a particular mineralogy but it is specific of a particular genesis. The clotted fabrics of different scales are interpreted as typical features of microbial origin (Burne and Moore, 1987; Shapiro, 2000; Shapiro and Awramik, 2000; Peckmann *et al.*, 2002; Shapiro and Fricke, 2002; Shapiro, 2002; Shapiro, 2004). Given their irregular shape, the spatial arrangement of the clots and the higher abundance of pyrite and organic compounds, the clots are interpreted as indicative of formation in microenvironments of geochemical adequate conditions that were controlled by microbial metabolism. Therefore this microfabric is interpreted as an evidence of microbial mediation in the formation of the authigenic carbonates, particularly in the initiation of the carbonate precipitation.

SEM observations of the cement of the dolomite crusts, chimneys and nodules (which consist of minor aggregates of rhombohedral calcite, high-Mg calcite and dolomite, up to 10  $\mu\text{m}$  in diameter) allowed the identification of a large variety of other microbial-induced morphologies and fabrics, such as: (1) microbial filaments; (2) high Mg-calcite and dolomite crystal aggregates calcifying and mimetizing filaments, some of them being incorporated by dolomite and calcite crystals; (3) rods with brush-like terminations; (4) structures that resemble dumbbell-like and cauliflower morphologies. The precipitation of dumbbell-like and cauliflower crystal aggregates have been induced by bacterial activity in laboratory experiments using sulphate-reducing bacteria (Vasconcelos *et al.*, 1995; Warthmann *et al.*, 2000). The observed microbial filaments and structures in the observed aggregates match the typical size of the features described in the bacterially laboratory authigenic carbonates precipitation experiments and are clearly constructive in origin. The filaments that are covered by the 50 nm to 1  $\mu\text{m}$  size rhombohedra of calcite, Mg-calcite or dolomite and that are being incorporated by larger (5-10  $\mu\text{m}$ ) dolomite rhombohedra can

be interpreted as corresponding to nucleation points from where the dolomite precipitation started and from which it progressed. The lack of any crystallographic form or indication of cleavage of the rods and brush-like terminations and the similarity of the size of these features with the typical bacteria sizes indicates to a biotic origin. Therefore, the organogenic dolomite formation model, proposed for dolomite formation in shallow coastal lagunall and shallow marine environments (Vasconcelos *et al.*, 1995) or in organic rich and deep marine sediments (Meister, 2005), is also proposed for the formation of the MDAC in the Gulf of Cadiz.

In the aragonite pavements, SEM observations also allowed the identification of similar microbial-induced morphologies and fabrics, such as: (1) microbial filaments; (2) rods with brush-like terminations; (3) aragonite batons, ball-capped batons and nanograins; (4) microbial and mucous biofilms occurring as a coating, draped between the aragonite fibres and needles of the stromatolitic layers; (5) the biotic origin of the pelmicrite clotted peloidal fabric; and (5) microbial filaments probably representing morphological bacteria remains.

Samples of aragonite pavements frequently have botryoidal and stromatolitic fabrics that recover or totally fill cavities, fractures and open pore spaces. This fabric is similar to the stromatolitic fabrics reported from several active seep carbonates (Greinert *et al.*, 2001; Peckmann *et al.*, 2001b; Greinert *et al.*, 2002) and to the stromatactoid fabric reported from several fossil seep carbonates (Peckmann *et al.*, 2001a; Peckmann *et al.*, 2002; Shapiro and Fricke, 2002). These reported stromatolitic and stromatactoid fabrics are described as infilling cavities and the cement (calcite or aragonite) grows in direction towards the source of energy (methane), which is downwards. This produces a smooth upper surface and an irregular lower surface of the reported stromatolitic and stromatactoid fabrics. In the aragonite samples from the Gulf of Cadiz, this growth criteria is not so clear and instead the stromatolitic and botryoidal layers seem to grow from the wall of the cavity towards their centre. Because much of the stromatolitic and botryoidal layers have shapes and sizes that resemble the shapes and sizes of the gas hydrate pieces collected from the mud breccia sediments in some mud volcanoes from the Gulf of Cadiz, the formation of the cavities (specially the sub-horizontal cavities and fractures) is interpreted as being generated by gas hydrate formation, inducing the fracturation of the unconsolidated or semi-cemented sediments. Subsequent dissociation of these gas hydrates and anaerobic oxidation of

resultant methane induced the precipitation of the stromatolitic and botryoidal layers. As the gas hydrate dissociation had to progress from the periphery of the gas hydrate chunks towards their centres, the authigenic cementations will also have the same trend.

#### **8.4.3 Biomarker significance**

Specific  $^{13}\text{C}$ -depleted lipid biomarkers have been identified in the dolomite chimney samples. These biomarkers include tail-to-tail linked acyclic isoprenoids such as PMI (2,6,10,15,19-pentamethyleicosane), pristane, phytane/croctane and squalane (2,6,10,15,19,23-hexamethyl-tetracosane). These compounds derive from archaea involved in the anaerobic oxidation of methane (AOM).

The aragonite crusts showed even better preserved biomarker patterns in comparison with the chimney dolomites. PMI ( $\delta^{13}\text{C}$  value: -101‰) are accompanied by unsaturated derivatives with 1 to 3 double bonds (PMI $\Delta$ ; -75‰). Isotopically-depleted PMI represents the most widespread and persistent hydrocarbon biomarker for AOM-performing archaea (Peckmann and Thiel, 2004). Croctane is present as one of the dominant peaks, strongly depleted in  $^{13}\text{C}$  (-132.27‰). Croctane:1, the monounsaturated version of croctane, is also present with a  $^{13}\text{C}$  ratio of -50‰. Squalane is present but not so depleted as in the previous biomarkers. Archaeol and hydroxyarchaeol were also detected with depleted in  $^{13}\text{C}$  compositions.

Bacterial lipid biomarkers, strongly depleted in  $^{13}\text{C}$ , with values ranging from -95 to -99‰ VPDB, that have been described as related with SRB, were identified on the aragonite pavement samples. The archaeal and bacterial lipids biomarkers occur in comparable concentrations (Niemann *et al.*, 2006).

Although the exact biochemical pathway of AOM still remains unclear, molecular, isotopic and phylogenetic evidence revealed that AOM is performed by a consortium of methanotrophic archaea and sulphate-reducing bacteria (SRB) (Peckmann *et al.*, 1999b; Boetius *et al.*, 2000; Elvert *et al.*, 2000; Peckmann *et al.*, 2001b; Peckmann *et al.*, 2001c). The biomarkers identified on both aragonite pavements and dolomite chimneys indicate the presence of an AOM-SR consortium. Therefore, this microbial activity has an active and important role on the definition of the bio-geochemical conditions that has lead to the precipitation of the authigenic carbonates.

## 8.5 Conclusions

The different types of MDAC from the Gulf of Cadiz include (as discussed in Chapter 5): dolomite crusts, dolomite nodules, chimneys or filled burrows, and aragonitic slabs or pavements. They all correspond to the cementation of sediments through the precipitation of authigenic carbonates and the different lithologic types correspond to different geochemical environments of formation. The dolomitic samples consist of microcrystalline dolomite cements with subordinate high and low magnesium calcite cementing a detrital pelagic fraction composed mainly of quartz and minor feldspar, clays, bioclasts of planktonic foraminifera (globigerinoids), ostracods, and pellets. The aragonite pavements form tabular to nodular precipitates consisting mainly of aragonite and calcite cementing mud volcano mud breccias, shells and clasts from previous generations of crusts, and detrital quartz, clays and bioclasts of planktonic foraminifera. Authigenic carbonates with depleted  $\delta^{13}\text{C}$  values indicate the oxidation of methane as the major carbon source. Authigenic pyrite also occurs, with  $\delta^{34}\text{S}$  negative values indicating an anaerobic geochemical environment with sulphate-reducing bacterial activity promoting sulphide precipitation in anoxic sediment conditions.

The presence of clotted microfabric in both aragonitic and dolomitic carbonate cements is interpreted as indicating microbial mediation in the formation of the authigenic carbonates, particularly in the initiation of the carbonate precipitation. This interpretation is also supported by other observable structures such as: microbial filaments; high Mg-calcite and dolomite crystal aggregates calcifying and mimetizing filaments, some of them being incorporated by dolomite and calcite crystals; rods with brush-like terminations; dumbbell-like and cauliflower morphologies; aragonite batons, ball-capped batons and nanograins; microbial and mucous biofilms forming coatings, draped between the aragonite fibres and needles of the stromatolitic layers; and microbial filaments probably representing morphological bacteria remains.

Specific  $^{13}\text{C}$ -depleted lipid biomarkers were identified in the dolomite chimney samples. They include tail-to-tail linked acyclic isoprenoids such as PMI (2,6,10,15,19-pentamethyleicosane) and squalane (2,6,10,15,19,23-hexamethyltetracosane). These compounds derive from archaea involved in the anaerobic oxidation of methane (AOM). The aragonite crusts showed even better preserved biomarker patterns in comparison with

the dolomite chimneys. PMI ( $\delta^{13}\text{C} = -101\text{‰ VPDB}$ ) is accompanied by unsaturated derivatives with 1 to 3 double bonds (PMI $\Delta = -75\text{‰ VPDB}$ ). Isotopically-depleted PMI represents the most widespread and persistent hydrocarbon biomarker for AOM-performing archaea. Bacterial lipid biomarkers strongly depleted in  $^{13}\text{C}$ , with values ranging from -95 to -99‰ VPDB, occur in comparable concentrations to the archaea lipid biomarkers, and have been described as related to sulphate-reducing bacteria (SRB).

The results of the SEM observations and biomarker analysis show that microbes, consortia of Archaea/SRB had an active key role in the formation of authigenic carbonates. An organogenic model is proposed not only for the dolomite precipitation but also for the formation of the remaining authigenic carbonates (aragonite, calcite and Mg-calcite). The microbial activity most probably created optimal micro-environmental geochemical conditions, most probably around the microbial structures, from where the precipitation of the MDAC is initiated.

The presence of the stromatolitic and botryoidal fabrics further support the indications that the formation and dissociation of gas hydrates was a process that was actively involved during the precipitation of the authigenic carbonates (Chapter 6).



## **Chapter 9. Main Conclusions, Future work and Open questions**

### **9.1 Main conclusions**

#### *Fluid escape structures in the Gulf of Cadiz*

The fluid escape structures from the Gulf of Cadiz show a high degree of geologic and biologic variability associated with the type, intensity and duration of the fluid fluxes. The fluid escape structures observed in the Gulf of Cadiz include active and inactive mud volcanoes, mud diapirs, pockmarks and hydrocarbon seeps recorded by the methane-derived authigenic carbonates (MDAC).

In the Gulf of Cadiz the fluids and gases are mainly vertically focused through faults and along the mud volcano conduits, since the gas hydrates, the MDAC and the chemosynthetic communities are essentially found within the mud volcano edifices (Porto, Faro, Darwin, Fiuza, Yuma, Ginsburg, Jesus Baraza, Kidd, Meknes, Mercator, Shouen and Student), the mud cones (Iberico, Cornide), the diapiric ridges (Formoza Ridge, Gudalquivir Diapiric Ridge and Hormigas Ridge) and the fault scarps (Pen Duick, Vernarsky ridge, Ridge W Gibraltar, Cadiz channel). Moreover, no regionally bottom simulating reflectors were found until now.

The fluid escape structures from the Gulf of Cadiz and associated chemosynthetic communities, exhibit different manifestations corresponding to different phases of activity. They can represent a mud-prone phase of mud breccia extrusion with the rapid emplacement of mud flows, or they can locally consist of phases of moderate fluid flux, dominated by water and gas, resulting in the accumulation of shallow gas hydrates, the cementation of the mud breccia sediments, the formation of other types of MDAC, and the support of associated chemosynthetic communities. Through time, a mud volcano can

successively go through different phases of activity with different manifestations (as proposed on the schematic model in Figure 4.51, Chapter 4).

### ***MDAC occurrences and their controls***

As interpreted from side-scan sonar imagery, observed in the underwater video observations and confirmed by sampling, the MDAC occur within the mud volcanoes and mud cones, on the diapiric ridges, or associated with faults, as described in Chapter 4. They occur as fields with a high density of carbonate samples.

The dolomite dominated MDAC (chimneys, crusts and nodules) show a large variability of shapes and sizes, including pipe-like, curved or helicoidal shapes, conical, branched, nodular, and massive irregular shapes. Their sizes are highly variable both in length and diameter. Chimneys with more than 3 m long and up to 0.5 m in diameter were observed. Most of these chimneys and crusts appear broken, sometimes intensely fragmented as carbonate rubble and occur most of the times lying on the sea floor. It is very rare to find chimneys that are in the vertical position, protruding from the sediments.

As concerns the aragonite dominated MDAC, they occur (1) as buildups and small mound-like buildups of variable dimensions, some up to 4-5 m high and several meters in length; (2) as rough hard-grounds that can pave the seafloor for several square meters, with a thin or absent sediment cover; (3) as crusts and slabs, similar to the pavements or; (4) as nodular centimetric masses within the superficial sediments.

### ***MDAC and their formation process***

As discussed in Chapter 5, all the MDAC from the Gulf of Cadiz indicate that they formed as the result of anaerobic oxidation of fluids enriched in methane. This methane can have two different and distinct origins: thermogenic or microbial origin. Under adequate pressure and temperature conditions this methane can be stored as hydrate layers or nodules within the sediments. When pressure or temperature changes these gas hydrates can dissociate, leading to pore fluids enrichment in methane with light carbon, and water

with heavier oxygen isotopes. This methane from the dissociation of the gas hydrates, together with microbial and thermogenic methane that migrated from deeper parts of the sedimentary column, when it reaches the sulphate-methane transition zone, is anaerobically oxidized (AOM) coupled with the reduction of sulphate (SR), through a process that is mediated by microbial activity by a consortium of archaea and sulphate reducing bacteria, as described by Boetius *et al.* (2000). As result of the AOM-SR net reaction the alkalinity in the pore fluids is increased, the sulphate is consumed and authigenic carbonate (aragonite, calcite, high-Mg calcite and dolomite) precipitation is induced. The precipitation of the authigenic carbonate minerals results in the lithification of the sediments and this is the mechanism assumed for the formation of the MDAC.

Also as a result of the AOM-SR net reaction  $\text{HS}^-$ , is produced an will precipitate as pyrite or, together with methane which has not been completely precipitated, will feed chemosynthetic communities at the seafloor, such as *Bathymodiolus* and *Calypptogena*, that are frequently found cemented in the aragonite pavements.

The different morphologies and different carbonate types reflect different flow patterns through the sediments. This is summarized on the schematic model proposed for the formation of the different MDAC shown in (Figure 5.17, Chapter 5). If the flux of fluid enriched in methane is canalized through the sulphate reducing zone (SRZ) of the sedimentary column, using borrows or sediment heterogeneities as pathways, a SMTZ with a strong gradient will be developed around these fluid conduits and consequently precipitation of the authigenic carbonates will be promoted around these conduits. Because these fluid conduits correspond to confined environments in relation to seawater influence, sulphate depletion can be reached and dolomite will be the dominant mineralogy to precipitate. The lithification of the sediments will result in the formation of the dolomite nodules, crusts and chimneys. The locations where the dolomite chimneys occur are presently swept by the flow of the Mediterranean undercurrent which can remobilize the unconsolidated sediments inside of which the chimneys were formed and therefore produce the collapse of the individual chimneys, explaining their present position on the seafloor.

Aragonite pavements represent precipitation of authigenic carbonates in a similar process to that of dolomite morphologies but, in an environment closer to the seafloor. The aragonite pavements will be formed at the sediment-seawater interface or close to it, as a product of the AOM-SR coupling process that can result from an active and discrete venting or from a more diffuse and low intensity venting process. Because these processes are more ventilated by seawater where high alkalinity is coupled with high sulphate concentrations, the mineralogy is dominated by aragonite.

Therefore, the widespread occurrence of MDAC can be interpreted as a fossil record of extensive methane seepage in this particular area of the Gulf of Cadiz, spatially associated with probable deep fault systems and with mud volcanoes and diapirs, that constitute preferential pathways for the fluid migration. They constitute a probable important natural methane sequestration process.

#### ***MDAC precipitation and estimated pore fluids composition***

Considering (1) the present day seabottom water temperatures, (2) the extreme limits for temperature variation during the glacial/interglacial cycles, (3) the oxygen isotopic composition of the Gulf of Cadiz bottom waters, both for the North Atlantic Deep Water and the Mediterranean Outflow water, and (4) assuming that the oxygen isotopic ratio variations are the typical between glacial and interglacial stages, the isotopic composition of the original fluids from which the carbonates precipitated were estimated according to the different mineral/temperature fractionation equations of precipitation. Considering the minimum and maximum temperature limits admitted to be possible to occur in the Gulf of Cadiz, not all the measured carbonate isotopic values are compatible with precipitation from normal seawater isotopic composition (as summarized in Figure 6.27, Chapter 6).

Aragonite pavements are estimated to have been formed from normal seawater oxygen isotopic compositions, or from  $^{18}\text{O}$ -enriched pore waters, indicating a contribution from the dissociation of gas hydrates.

Some dolomite chimneys indicate formation conditions from pore waters with oxygen isotopic compositions similar to normal seawater. However, others indicate a

formation from pore fluids with a contribution from destabilization of gas hydrates, or the precipitation from pore waters during gas hydrates formation (Figure 6.27, Chapter 6).

The  $^{87}\text{Sr}/^{86}\text{Sr}$  ratios of the authigenic carbonates do not indicate a clear and major addition of Sr from deep seated fluids, but they preferably reflect the contemporaneous seawater Sr composition.

### ***Dating of the dolomite chimneys formation***

The U/Th estimated ages of two dolomite chimneys, as described in Chapter 7, indicate that the precipitation of the authigenic carbonates occurs in short discontinuous intervals of time, most probably, intercalated with longer periods of absence of precipitation. The chimneys that result from the precipitation during different episodes will exhibit different grow layers or concentric rings.

The estimated ages along radial profiles on dolomite chimneys indicate formation at periods of rapid paleoceanographic changes. The ages obtained point to the precipitation during: (1) the onsets of glacial/interglacial cycles (termination 2 and 3), contemporary with rapid sealevel rises; (2) at the transition from stadial to interstadial, also corresponding to rapid sealevel rise; and (3) at the transition from interglacial (MIS 5.5) to stadial MIS 5.4 or from interglacial (MIS 5.3) to stadial 5.2, associated with periods of progressive sealevel lowering (Figure 7.12, Chapter 7).

It is proposed that the MDAC are the record of intense fluid flow episodes during periods of increased seabottom water temperature, most probably as a result of the increase of the Mediterranean Outflow influence at the locations where the samples were collected from. This increase in seabottom water temperature is, most probably, reducing the gas hydrate stability zone, leading to gas hydrate dissociation and the consequent release of methane-rich fluids which will induce the carbonate precipitation along the fluid conduits on the fluid pathways above the methane seepage sites.

### ***Microbial mediation on the formation of the MDAC***

As discussed in Chapter 8, the presence of clotted microfabric in both aragonite and dolomite dominated carbonate cements is interpreted as indicating a microbial mediation in the formation of the authigenic carbonates, particularly in the initiation of the carbonate precipitation. This interpretation is also supported by other observable structures such as: (1) microbial filaments; (2) high Mg-calcite and dolomite crystal aggregates calcifying filaments, some of them being incorporated by dolomite and calcite crystals; (3) rods with brush-like terminations; (4) aragonite batons, ball-capped batons and nanograins; (5) microbial and mucous biofilms forming coatings, draped between the aragonite fibres and needles of the stromatolitic layers; and (6) microbial filaments probably representing morphological bacteria remains.

Specific  $^{13}\text{C}$ -depleted lipid biomarkers were identified in the dolomite chimney samples. These include tail-to-tail linked acyclic isoprenoids such as PMI (2,6,10,15,19-pentamethyleicosane) and squalane (2,6,10,15,19,23-hexamethyltetracosane). These compounds derive from archaea involved in the anaerobic oxidation of methane. The aragonite crusts showed even better preserved biomarker patterns in comparison with the dolomite chimneys. Bacterial lipid biomarkers strongly depleted in  $^{13}\text{C}$  occur in comparable concentrations to the archaea lipid biomarkers, and have been described as related to sulphate-reducing bacteria.

The results of the SEM observations and biomarker analysis show that microbes, a consortia of Archaea/sulphate-reducing bacteria, had an active key role in the formation of the authigenic carbonates. An organogenic model is proposed not only for the dolomite precipitation but also for the formation of the remaining authigenic carbonates (aragonite, calcite and Mg-calcite). The microbial activity most probably created optimal micro-environmental geochemical conditions around the microbial structures, from where the precipitation of the MDAC is initiated.

The presence of the stromatolitic and botryoidal fabrics further support the indications that the formation and dissociation of gas hydrates were processes actively involved in the precipitation of the authigenic carbonates.

## 9.2 Future work and open questions

Natural gas hydrates (GH) were recovered and inferred to occur in several mud volcanoes in the Gulf of Cadiz. The proximity of this methane reservoir to the seafloor and its restricted thermodynamic stability domain has motivated large speculations about the release of methane from destabilized GH in response to climatic changes (MacDonald, 1990). Increases of seabottom temperature (as result of regional oceanographic condition changes) and decreases in pressure (e.g. through sea level changes) can destabilize gas hydrates, releasing methane into the near-surface environment and having an important impact on the carbon cycle (Buffett and Archer, 2004; Archer and Buffett, 2005). According to the clathrate gun hypothesis (Kennett *et al.*, 2003), episodic atmospheric methane emissions resulting from the destabilisation of GH reservoirs contributed significantly to the distinctive behaviour of late Quaternary climate.

The influence of GH destabilization on the carbon cycle depends on the volume of the GH reservoirs and on how the GH responds to changes in the oceanographic conditions (time scale of the methane release). If GH destabilization and fluid escape is slow, then the diffuse escape of methane will most probably result in its total oxidation in the sulphate-methane transition zone, leading to the precipitation of methane-derived authigenic carbonates (MDAC), or to its aerobic consumption by microbes, with negligible amounts being released to the seawater. If the fluid escape is fast enough, it will allow methane to be released directly to the water column and possibly also to the atmosphere. The principal mechanisms of rapid methane release are 1) mud volcano (MV) activity (e.g. Etiope *et al.*, 2004; Etiope and Milkov, 2004); 2) slumping at continental slopes (Mienert *et al.*, 1998); and 3) pervasive flow along fractures due to overpressured gas (Flemings *et al.*, 2003).

During the period of this research the several cruises and projects carried out in the Gulf of Cadiz (GC) allowed the discovery of 42 MVs (Pinheiro *et al.*, 2003; 2005). Gas hydrates were retrieved from some of them (Bonjardim, Captain Arutyunov and Ginsburg MVs) and inferred to occur in several others. Other fluid escape structures associated with the MVs, such as pockmarks and MDAC (Magalhães *et al.*, 2004) indicate active processes of dewatering of the sedimentary basin. According to the carbon isotopic composition of the GH, the presence of heavy hydrocarbons (Mazurenko *et al.*, 2002; Nuzzo *et al.*, 2005) and the isotopic composition of the authigenic carbonates (as concluded from the work

carried out from this thesis), the most active sites in the GC are characterized by high concentrations of light hydrocarbons, both of microbial and thermogenic origin. The implications of the identification of thermogenic light hydrocarbons in deeper parts of the sediment column and the evaluation of the potential source rocks are open questions to be investigated.

The Mediterranean Outflow water (MO) strongly influences the hydrology of the North Atlantic making the GC a highly sensitive region to paleoclimatic changes. The MV areas, in the upper and middle slope of the GC, are located under the influence of the MO. Possible influences of the MO on slope failure and GH destabilization have been proposed by Gardner (2001) and also from the results of the work carried out during this thesis.

It is now possible and evident that it would be of great importance to complete the inventory of GH occurrences in the GC and to model the GH stability field for the different ranges of gas compositions determined from MV pore waters and the known GH compositions. The spatial distribution of potential areas of GH occurrence and shallow gas accumulations need to be interpolated on a regional scale, with an estimation of potential volumes involved and the response of the potential regional reservoirs to environmental changes.

Specific structures such as the MV, mud cones, MDAC fields, pockmarks, landslides and erosive structures like some channels of the MO, should now be studied in detail. Modelling different scenarios, with extreme oceanographic conditions (glacial and interglacial maximums and variations in seabottom temperature, salinity, and oxygen content resulting from different MO strength and pathways) and their consequences on the GH stability field can now be investigated and understood. The determination of the responses of the different fluid escape structures to episodes of GH destabilization is also an important task that should be investigated.

A calculation of the GH stability domains should allow a reinterpretation of the available seismic data in order to identify the existence of possible bottom simulating reflectors (BSRs) in areas where they have not been recognized previously.

The implications of the presence of methane on the benthic faunal communities and on the geochemical characteristics of the sediments is also an important question to be investigated. With this objective, benthic foraminifera communities, from selected MVs where active fluid venting was recognised from this work, should be studied in order to

evaluate the isotopic composition of the benthic fauna and to establish criteria (isotopic and specific chemical fingerprints) that can be used to recognize fossil gas seeps on the geological record. This is also an open question that can be a test of the clathrate gun hypothesis, as the quantification of the  $\delta^{13}\text{C}$  excursion towards depleted values in the foraminifera tests from seep sites with moderate to slow flux rates where all the methane is consumed within the sediment, is pertinent.



## References

- Acosta, J., Uchupi, E., A.Munoz, Herranz, P., Palomo, C., Ballesteros, M. and ZEEWorking Group** 2003. Salt Diapirs, Salt Brine Seeps, Pockmarks and Surficial Sediment Creep and Slides in the Canary Channel off NW Africa. *Marine Geophysical Researches*, **24**: 41-57.
- Aharon, P., Graber, E.R. and Roberts, H.H.** 1992. Dissolved Carbon and Delta-C-13 Anomalies in the Water Column Caused by Hydrocarbon Seeps on the Northwestern Gulf of Mexico Slope. *Geo-Marine Letters*, **12**: 33-40.
- Aharon, P.** 1994. Geology and Biology of Modern and Ancient Submarine Hydrocarbon Seeps and Vents - an Introduction. *Geo-Marine Letters*, **14**: 69-73.
- Aiello, I.W., Garrison, R.E., Moore, J.C., Kastner, M. and Stakes, D.S.** 2001. Anatomy and origin of carbonate structures in a Miocene cold-seep field. *Geology*, **29**: 1111-1114.
- Aiello, I.W.** 2005. Fossil seep structures of the Monterey Bay region and tectonic/structural controls on fluid flow in an active transform margin. *Palaeogeography, Palaeoclimatology, Palaeoecology*, **227**: 124-142.
- Akhmanov, G.G., Silva, P., Erba, E. and Cita, M.B.** 2003. Sedimentary succession and evolution of the Mediterranean Ridge western sector as derived from lithology of mud breccia clasts. *Marine Geology*, **195**: 277-299.
- Aliyev, A.A.A., Guliyev, I.S. and Belov, I.S.** 2002. *Catalogue of recorded eruptions of mud volcanoes of Azerbaijan (for period of years 1810-2001)*, 89 pp.
- Aloisi, G., Pierre, C., Rouchy, J.-M., Foucher, J.-P., Woodside, J.M. and MEDINAUT Scientific Party** 2000. Methane-related authigenic carbonates of eastern Mediterranean Sea mud volcanoes and their possible relation to gas hydrate destabilisation. *Earth and Planetary Science Letters*, **184**: 321-338.
- Aloisi, G., Bouloubassi, I., Heijs, S.K., Pancost, R.D., Pierre, C., Damsté, J.S.S., Gottschal, J.C., Forney, L.J. and Rouchy, J.-M.** 2002a. CH<sub>4</sub>-consuming microorganisms and the formation of carbonate crusts at cold seeps. *Earth and Planetary Science Letters*, **203**: 195-203.
- Aloisi, G., Pierre, C., Rouchy, J.-M. and Faugères, J.-C.** 2002b. Isotopic evidence of methane-related diagenesis in the mud volcanic sediments of the Barbados Accretionary Prism. *Continental Shelf Research*, **22**: 2355-2372.
- Aloisi, G., Wallmann, K., Drews, M. and Bohrmann, G.** 2004. Evidence for the submarine weathering of silicate minerals in Black Sea sediments: Possible implications for the marine Li and B cycles. *G3 Geochemistry Geophysics Geosystems*, **5**: Q04007, doi:10.1029/2003GC000639.
- Ambar, I. and Howe, M.R.** 1979a. Observations of the Mediterranean Outflow .1. Mixing in the Mediterranean Outflow. *Deep-Sea Research Part a-Oceanographic Research Papers*, **26**: 535-554.
- Ambar, I. and Howe, M.R.** 1979b. Observations of the Mediterranean Outflow .2. Deep Circulation in the Vicinity of the Gulf of Cadiz. *Deep-Sea Research Part a-Oceanographic Research Papers*, **26**: 555-568.
- Ambar, I.** 1983. A Shallow Core of Mediterranean Water Off Western Portugal. *Deep-Sea Research Part a-Oceanographic Research Papers*, **30**: 677-680.
- Ambar, I., Armi, L., Bower, A. and Ferreira, T.** 1999. Some aspects of time variability of the Mediterranean Water off south Portugal. *Deep-Sea Research Part I-Oceanographic Research Papers*, **46**: 1109-1136.
- Ambar, I., Serra, N., Brogueira, M.J., Cabecadas, G., Abrantes, F., Freitas, P., Goncalves, C. and Gonzalez, N.** 2002. Physical, chemical and sedimentological aspects of the Mediterranean outflow off Iberia. *Deep-Sea Research Part II-Topical Studies in Oceanography*, **49**: 4163-4177.
- Archer, D. and Buffett, B.** 2005. Time-dependent response of the global ocean clathrate reservoir to climatic and anthropogenic forcing. *Geochemistry Geophysics Geosystems*, **6**: Q03002, doi:10.1029/2004GC000854.
- Argus, D.F., Gordon, R.G., Demets, C. and Stein, S.** 1989. Closure of the Africa Eurasia North America Plate Motion Circuit and Tectonics of the Gloria Fault. *Journal of Geophysical Research-Solid Earth and Planets*, **94**: 5585-5602.

- Armi, L. and Zenk, W.** 1984. Large Lenses of Highly Saline Mediterranean Water. *Journal of Physical Oceanography*, **14**: 1560-1576.
- Armi, L., Hebert, D., Oakey, N., Price, J.F., Richardson, P.L., Rossby, H.T. and Ruddick, B.** 1989. 2 Years in the Life of a Mediterranean Salt Lens. *Journal of Physical Oceanography*, **19**: 354-370.
- Aslan, A., Warne, A.G., White, W.A., Guevara, E.H., Smyth, R.C., Raney, J.A. and Gibeaut, J.C.** 2001. Mud volcanoes of the Orinoco Delta, Eastern Venezuela. *Geomorphology*, **41**: 323-336.
- Baker, P.A. and Kastner, M.** 1981. Constraints on the Formation of Sedimentary Dolomite. *Science*, **213**: 214-216.
- Baraza, J. and Ercilla, G.** 1996. Gas-charged sediments and large pockmark-like features on the Gulf of Cadiz slope (SW Spain). *Marine and Petroleum Geology*, **13**: 253-261.
- Baraza, J., Ercilla, G. and Nelson, C.H.** 1999. Potential geologic hazards on the eastern Gulf of Cadiz slope (SW Spain). *Marine Geology*, **155**: 191-215.
- Barber, A.J., Tjokrosapetro, S. and Charlton, T.R.** 1986. Mud Volcanos, Shale Diapirs, Wrench Faults, and Melanges in Accretionary Complexes, Eastern Indonesia. *Bulletin of the American Association of Petroleum Geologists*, **70**: 1729-1741.
- Barber, T. and Brown, K.** 1988. Mud diapirism: the origin of melanges in accretionary complexes? *Geology Today*, **May-June**: 89-94.
- Baringer, M.O.N. and Price, J.F.** 1999. A review of the physical oceanography of the Mediterranean outflow. *Marine Geology*, **155**: 63-82.
- Barnes, C.E. and Cochran, J.K.** 1990. Uranium Removal in Oceanic Sediments and the Oceanic U Balance. *Earth and Planetary Science Letters*, **97**: 94-101.
- Barnes, R.O. and Goldberg, E.D.** 1976. Methane Production and Consumption in Anoxic Marine-Sediments. *Geology*, **4**: 297-300.
- Bergquist, D.C., Ward, T., Cordes, E.E., McNelis, T., Howlett, S., Kosoff, R., Hourdez, S., Carney, R. and Fisher, C.R.** 2003. Community structure of vestimentiferan-generated habitat islands from Gulf of Mexico cold seeps. *Journal of Experimental Marine Biology and Ecology*, **289**: 197-222.
- Berndt, C., Bunz, S., Clayton, T., Mienert, J. and Saunders, M.** 2004. Seismic character of bottom simulating reflectors: examples from the mid-Norwegian margin. *Marine and Petroleum Geology*, **21**: 723-733.
- Blankenship, C.L.** 1992. Structure and paleogeography of the External Betic Cordillera, southern Spain. *Marine and Petroleum Geology*, **9**: 256-264.
- Boetius, A., Ravensschlag, K., Schubert, C.J., Rickert, D., Widdel, F., Gieseke, A., Amann, R., Jorgensen, B.B., Witte, U. and Pfannkuche, O.** 2000. A marine microbial consortium apparently mediating anaerobic oxidation of methane. *Nature*, **407**: 623-626.
- Bohm, F., Joachimski, M.M., Dullo, W.C., Eisenhauer, A., Lehnert, H., Reitner, J. and Worheide, G.** 2000. Oxygen isotope fractionation in marine aragonite of coralline sponges. *Geochimica Et Cosmochimica Acta*, **64**: 1695-1703.
- Bohrmann, G., Greinert, J., Suess, E. and Torres, M.** 1998. Authigenic carbonates from the Cascadia subduction zone and their relation to gas hydrate stability. *Geology*, **26**: 647-650.
- Boles, J.R., Clark, J.F., Leifer, I. and Washburn, L.** 2001. Temporal variation in natural methane seep rate due to tides, Coal Oil Point area, California. *Journal of Geophysical Research-Oceans*, **106**: 27077-27086.
- Bower, A.S., Serra, N. and Ambar, I.** 2002. Structure of the Mediterranean Undercurrent and Mediterranean Water spreading around the southwestern Iberian Peninsula. *Journal of Geophysical Research*, **107**: 3161, doi:10.1029/2001JC001007.
- Broecker, W.S.** 1963. A Preliminary Evaluation of Uranium Series Inequilibrium as a Tool for Absolute Age Measurement on Marine Carbonates. *Journal of Geophysical Research*, **68**: 2817-2834.
- Broecker, W.S., Thurber, D.L., Goddard, J., Ku, T.L., Matthews, R.K. and Mesolell, K.J.** 1968. Milankovitch Hypothesis Supported by Precise Dating of Coral Reefs and Deep-Sea Sediments. *Science*, **159**: 297-300.
- Brown, K. and Westbrook, G.K.** 1988. Mud Diapirism and Subcretion in the Barbados Ridge Accretionary Complex - the Role of Fluids in Accretionary Processes. *Tectonics*, **7**: 613-640.
- Brown, K.M.** 1990. The Nature and Hydrogeologic Significance of Mud Diapirs and Diatremes for Accretionary Systems. *Journal of Geophysical Research-Solid Earth and Planets*, **95**: 8969-8982.
- Brown, K.M., Saffer, D.M. and Bekins, B.A.** 2001. Smectite diagenesis, pore-water freshening, and fluid flow at the toe of the Nankai wedge. *Earth and Planetary Science Letters*, **194**: 97-109.
- Bryden, H.L. and Stommel, H.M.** 1984. Limiting processes that determine basic features of the circulation in the Mediterranean Sea. *Oceanologica Acta*, **7**: 289-296.

- Buffett, B. and Archer, D.** 2004. Global inventory of methane clathrate: sensitivity to changes in the deep ocean. *Earth and Planetary Science Letters*, **227**: 185-199.
- Bufo, E., Degaldeano, C.S. and Udias, A.** 1995. Seismotectonics of the Ibero-Maghrebian Region. *Tectonophysics*, **248**: 247-261.
- Bufo, E., Bezzeghoud, M., Udias, A. and Pro, C.** 2004a. Seismic sources on the Iberia-African plate boundary and their tectonic implications. *Pure and Applied Geophysics*, **161**: 623-646.
- Bufo, E., Martin-Davila, J. and Udias, A.** 2004b. Azores-Tunisia geodynamics - Introduction. *Pure and Applied Geophysics*, **161**: 473-476.
- Burne, R.V. and Moore, L.S.** 1987. Microbialites: organosedimentary deposits of benthic microbial communities. *Palaaios*, **2**: 241-254.
- Burns, S.J., McKenzie, J.A. and Vasconcelos, C.** 2000. Dolomite formation and biogeochemical cycles in the Phanerozoic. *Sedimentology*, **47**: 49-61.
- Burton, E.A. and Walter, L.M.** 1990. The role of pH in Phosphate Inhibition of Calcite and Aragonite Precipitation Rates in Seawater. *Geochimica et Cosmochimica Acta*, **54**: 797-808.
- Burton, E.A.** 1993. Controls on Marine Carbonate Cement Mineralogy - Review and Reassessment. *Chemical Geology*, **105**: 163-179.
- Cabral, J.** (Ed), 1995. *Neotectónica em Portugal Continental*. (Ed I.G.e. Mineiro), *Memórias do Instituto Geológico e Mineiro*, **31**. Instituto Geológico e Mineiro, Lisboa, 265 pp.
- Cacho, I., Grimalt, J.O., Sierro, F.J., Shackleton, N.J. and Canals, M.** 2000. Evidence for enhanced Mediterranean thermohaline circulation during rapid climatic coolings. *Earth and Planetary Science Letters*, **183**: 417-429.
- Camerlenghi, A., Cita, M.B., Della Vedova, B., Fusi, N., Mirable, L. and Pellis, G.** 1995. Geophysical evidence of mud diapirism on the Mediterranean Ridge accretionary complex. *Marine Geophysical Researches*, **17**: 115-141.
- Campbell, K.A. and Bottjer, D.J.** 1995. Brachiopods and Chemosymbiotic Bivalves in Phanerozoic Hydrothermal Vent and Cold Seep Environments. *Geology*, **23**: 321-324.
- Campbell, K.A., Farmer, J.D. and Des Marais, D.** 2002. Ancient hydrocarbon seeps from the Mesozoic convergent margin of California: carbonate geochemistry, fluids and palaeoenvironments. *Geofluids*, **2**: 63-94.
- Campbell, K.A.** 2006. Hydrocarbon seep and hydrothermal vent paleoenvironments and paleontology: Past developments and future research directions. *Palaeogeography, Palaeoclimatology, Palaeoecology*, **232**: 362-407.
- Carney, R.S.** 1994. Consideration of the Oasis Analogy for Chemosynthetic Communities at Gulf-of-Mexico Hydrocarbon Vents. *Geo-Marine Letters*, **14**: 149-159.
- Carson, B. and Screaton, E.J.** 1998. Fluid flow in accretionary prisms: Evidence for focused, time-variable discharge. *Reviews of Geophysics*, **36**: 329-351.
- Castanier, S., Métayer-Levrel, G.L. and Perthuisot, J.-P.** 2000. Bacterial Roles in the Precipitation of Carbonate Minerals. In: *Microbial Sediments* (Eds R.E. Riding and S.M. Awramik), pp. 32-39. Springer-Verlag, Berlin Heidelberg.
- Cavagna, S., Clari, P. and Martire, L.** 1999. The role of bacteria in the formation of cold seep carbonates: geological evidence from Monferrato (Tertiary, NW Italy). *Sedimentary Geology*, **126**: 253-270.
- Cayeux, L.** 1935. *Les Roches Sédimentaires de France; Roches Carbonatées*. Masson et Cie, Paris, 463 pp.
- Chacko, T., Mayeda, T.K., Clayton, R.N. and Goldsmith, J.R.** 1991. Oxygen and Carbon Isotope Fractionations between CO<sub>2</sub> and Calcite. *Geochimica et Cosmochimica Acta*, **55**: 2867-2882.
- Chacko, T., Cole, D.R. and Horita, J.** 2001. Equilibrium Oxygen, Hydrogen and Carbon Isotope Fractionation Factors Applicable to Geologic Systems. In: *Stable Isotope Geochemistry* (Eds J.W. Valley and D.R. Cole), *Reviews in Mineralogy and Geochemistry*, **43**, pp. 1-81. Mineralogical Society of America.
- Chen, J.H., Edwards, R.L. and Wasserburg, G.J.** 1986. U-238, U-234 and Th-232 in Seawater. *Earth and Planetary Science Letters*, **80**: 241-251.
- Cheng, H., Adkins, J., Edwards, R.L. and Boyle, E.A.** 2000. U-Th dating of deep-sea corals. *Geochimica et Cosmochimica Acta*, **64**: 2401-2416.
- Chérubin, L.M., Serra, N. and Ambar, I.** 2003. Low-frequency variability of the Mediterranean undercurrent downstream of Portimão Canyon. *Journal of Geophysical Research*, **108**: 3058, doi:10.1029/2001JC001229.
- Çifçi, G., Dondurur, D. and Ergun, M.** 2003. Deep and shallow structures of large pockmarks in the Turkish shelf, Eastern Black Sea. *Geo-Marine Letters*, **23**: 311-322.

- Cita, M.B., Ryan, W.B.F. and Paggi, L.** 1981. Prometheus mud breccia. An example of shale diapirism in the Western Mediterranean Ridge. *Annales Géologiques des Pays Héliéniques*, **30**: 543-569.
- Clari, P., Fornara, L., Ricci, B. and Zuppi, G.M.** 1994. Methane-Derived Carbonates and Chemosymbiotic Communities of Piedmont (Miocene, Northern Italy) - an Update. *Geo-Marine Letters*, **14**: 201-209.
- Claypool, G.E. and Kaplan, I.R.** 1974. The origin and distribution of methane in marine sediments. *Marine Science*, **3**: 99-139.
- Clayton, R.N. and Epstein, S.** 1958. The Relationship between O<sup>18</sup>-O<sup>16</sup> Ratios in Coexisting Quartz, Carbonate, and Iron Oxides from Various Geological Deposits. *Journal of Geology*, **66**: 352-373.
- Clayton, R.N., Jones, B.F. and Berner, R.A.** 1968. Isotope Studies of Dolomite Formation under Sedimentary Conditions. *Geochimica et Cosmochimica Acta*, **32**: 415-432.
- Clayton, R.N., Goldsmith, J.R., Karel, K.J., Mayeda, T.K. and Newton, R.C.** 1975. Limits on effect of pressure on isotopic fractionation. *Geochimica et Cosmochimica Acta*, **39**: 1197-1201.
- Clennell, M.B., Hovland, M., Booth, J.S., Henry, P. and Winters, W.J.** 1999. Formation of natural gas hydrates in marine sediments 1. Conceptual model of gas hydrates growth conditioned by host sediment properties. *Journal of Geophysical Research*, **104**: 22985-23003.
- Coffin, M.F., Gahagan, L.M. and Lawver, L.A.** 2000. World Tectonic Plate Boundaries. FGDC Metadata of the Present-day Plate Boundary Digital Data Compilation, University of Texas Institute for Geophysics, Texas.
- Coplen, T.B., Kendall, C. and Hopple, J.** 1983. Comparison of Stable Isotope Reference Samples. *Nature*, **302**: 236-236.
- Corliss, J.B., Dymond, J., Gordon, L.I., Edmond, J.M., Herzen, R.P.V., Ballard, R.D., Green, K., Williams, D., Bainbridge, A., Crane, K. and Vanandel, T.H.** 1979. Submarine Thermal Springs on the Galapagos Rift. *Science*, **203**: 1073-1083.
- Cunha, M., Rodrigues, C.F., Santos, P.R.d., Sá, C.V.d. and TTR14-Leg1 scientific party** 2005. The faunal assemblage of the Meknès mud volcano (North African margin off Morocco). Preliminary results of the TTR14 cruise in the Gulf of Cadiz. In: *International Conference and TTR14 Post-cruise meeting. Geosphere-Biosphere Coupling Processes: the TTR interdisciplinary approach towards studies of the European and N. African margins*, pp. 1, Marrakech, Morocco.
- Davidson, D.W., Leaist, D.G. and Hesse, R.** 1983. Oxygen-18 enrichment in the water of a clathrate hydrate. *Geochimica et Cosmochimica Acta*, **47**: 2293-2295.
- De Boever, E., Swennen, R. and Dimitrov, L.** 2006. Lower Eocene carbonate cemented chimneys (Varna, NE Bulgaria): Formation mechanisms and the (a)biological mediation of chimney growth? *Sedimentary Geology*, **185**: 159-173.
- De Lange, G.J. and Brumsack, H.-J.** 1998. Pore-water indications for the occurrence of gas hydrates in eastern-Mediterranean mud dome structures. In: *Ocean Drilling Program, Scientific Results* (Eds H.F. Robertson, K.-C. Emeis, C. Richter and A. Camerlenghi), **160**, pp. 569-574.
- Degens, E.T. and Epstein, S.** 1964. Oxygen and Carbon Isotope Ratios in Coexisting Calcites and Dolomites from Recent and Ancient Sediments. *Geochimica et Cosmochimica Acta*, **28**: 23-44.
- Delisle, G., von Rad, U., Andruleit, H., Daniels, C.H.v., Tabrez, A.R. and Inam, A.** 2002. Active mud volcanoes on- and offshore eastern Makran, Pakistan. *International Journal of Earth Sciences*, **91**: 93-110.
- Depreiter, D., Poort, J., Rensbergen, P.V. and Henriët, J.P.** 2005. Geophysical evidence of gas hydrates in shallow submarine mud volcanoes on the Moroccan margin. *JOURNAL OF GEOPHYSICAL RESEARCH*, **110**: doi:10.1029/2005JB003622.
- Des Marais, D.J., Donchin, J.H., Nehring, N.L. and Truesdell, A.H.** 1981. Molecular Carbon Isotopic Evidence for the Origin of Geothermal Hydrocarbons. *Nature*, **292**: 826-828.
- Dewey, J.F., Helman, M.L., Turco, E., Hutton, D.H.W. and Knott, S.** 1989. Kinematics of the western Mediterranean. In: *Alpine tectonics* (Ed M. Conrad), *Special Publication of the Geological Society of London*, **45**, pp. 265-283.
- Diaz del Rio, V., Somoza, L. and Anastasya 2001 scientific team** 2001. ANASTASYA-2001/09 Cruise report.
- Diaz-del-Rio, V., Somoza, L., Martinez-Frias, J., Hernandez-Molina, F.J., Lunar, R., Fernandez-Puga, M.C., Maestro, A., Terrinha, P., Llave, E., Garcia, A., Garcia, A.C. and Vazquez, J.T.** 2001. Carbonate chimneys in the Gulf of Cadiz: Initial report on their petrography and geochemistry. In: *International Conference and Ninth Post-Cruise Meeting of the Training-Through-Research Programme. Devoted to the TTR 10th Anniversary, Workshop Report N° 175*, pp. 53-54. UNESCO - Intergovernmental Oceanographic Commission (IOC), Moscow-Mozhenka, Russia.

- Díaz-del-Río, V., Somoza, L., Martínez-Frias, J., Mata, M.P., Delgado, A., Hernandez-Molina, F.J., Lunar, R., Martín-Rubí, J.A., Maestro, A., Fernández-Puga, M.C., León, R., Llave, E., Medialdea, T. and Vázquez, J.T. 2003. Vast fields of hydrocarbon-derived carbonate chimneys related to the accretionary wedge/olistostrome of the Gulf of Cádiz. *Marine Geology*, **195**: 177-200.
- Dickens, G.R., Oneil, J.R., Rea, D.K. and Owen, R.M. 1995. Dissociation of oceanic methane hydrate as a cause of the carbon isotope excursion at the end of the Paleocene. *Paleoceanography*, **10**: 965-971.
- Dickens, G.R., Castillo, M.M. and Walker, J.C.G. 1997. A blast of gas in the latest Paleocene: Simulating first-order effects of massive dissociation of oceanic methane hydrate. *Geology*, **25**: 259-262.
- Dimitrov, L. 2000. Pobitite Kamani - Lower Eocene Bubbling Reefs.
- Dimitrov, L. and Woodside, J. 2003. Deep sea pockmark environments in the eastern Mediterranean. *Marine Geology*, **195**: 263-276.
- Dimitrov, L.I. 2002. Mud volcanoes - the most important pathway for degassing deeply buried sediments. *Earth-Science Reviews*, **59**: 49-76.
- Dimitrov, L.I. 2003. Mud volcanoes - a significant source of atmospheric methane. *Geo-Marine Letters*, **23**: 155-161.
- Docherty, C. and Banda, E. 1995. Evidence for the Eastward Migration of the Alboran Sea Based on Regional Subsidence Analysis - a Case for Basin Formation by Delamination of the Subcrustal Lithosphere. *Tectonics*, **14**: 804-818.
- Duarte, J. 2005. *Biosphere/Geosphere Coupling Processes in Marine Sediments from Mud Volcanoes of the Gulf of Cadiz, SW Iberia*. Master Thesis, Universidade de Aveiro, Aveiro.
- Duplessy, J.C., Labeyrie, L. and Waelbroeck, C. 2002. Constraints on the ocean oxygen isotopic enrichment between the Last Glacial Maximum and the Holocene: Paleocyanographic implications. *Quaternary Science Reviews*, **21**: 315-330.
- Edwards, R.L., Chen, J.H. and Wasserburg, G.J. 1987.  $^{238}\text{U}$ - $^{234}\text{U}$ - $^{230}\text{Th}$ - $^{232}\text{Th}$  systematics and the precise measurement of time over the past 500,000 years. *Earth and Planetary Science Letters*, **81**: 175-192.
- Elderfield, H. 1986. Strontium isotope stratigraphy. *Palaeogeography Palaeoclimatology Palaeoecology*, **57**: 71-90.
- Eldholm, O., Sundvor, E., Vogt, P.R., Hjelstuen, B.O., Crane, K., Nilsen, A.K. and Gladchenko, T.P. 1999. SW Barents Sea continental margin heat flow and Has kon Mosby Mud Volcano. *Geo-Marine Letters*, **19**: 29-37.
- Elvert, M., Suess, E., Greinert, J. and Whiticar, M.J. 2000. Archaea mediating anaerobic methane oxidation in deep-sea sediments at cold seeps of the eastern Aleutian subduction zone. *Organic Geochemistry*, **31**: 1175-1187.
- Elvert, M., Greinert, J. and Suess, E. 2001. Carbon Isotopes of Biomarkers Derived from Methane-Oxidizing Microbes at Hydrate Ridge, Cascadia Convergent Margin. In: *Natural Gas Hydrates: Occurrence, Distribution, and Detection* (Eds C.K. Paull and W.P. Dillon), *Geophysical Monograph*, **124**, pp. 115-129. American Geophysical Union, Washington.
- Elvert, M., Boetins, A., Knittel, K. and Jorgensen, B.B. 2003. Characterization of specific membrane fatty acids as chemotaxonomic markers for sulfate-reducing bacteria involved in anaerobic oxidation of methane. *Geomicrobiology Journal*, **20**: 403-419.
- Emery, W.J. and Meincke, J. 1986. Global Water Masses - Summary and Review. *Oceanologica Acta*, **9**: 383-391.
- Engel, A.E.J., Clayton, R.N. and Epstein, S. 1958. Variations in Isotopic Composition of Oxygen and Carbon in Leadville Limestone (Mississippian, Colorado) and in Its Hydrothermal and Metamorphic Phases. *Journal of Geology*, **66**: 374-393.
- Epstein, S., Buchsbaum, R., Lowenstam, H.A. and Urey, H.C. 1951. Carbonate-Water Isotopic Temperature Scale. *Geological Society of America Bulletin*, **62**: 417-426.
- Epstein, S., Buchsbaum, R., Lowenstam, H.A. and Urey, H.C. 1953. Revised Carbonate-Water Isotopic Temperature Scale. *Geological Society of America Bulletin*, **64**: 1315-1325.
- Epstein, S., Graf, D.L. and Degens, E.T. 1963. Oxygen isotope studies on the origin of dolomite. In: *Isotope and cosmic chemistry* (Ed H. Craig), pp. 169-180.
- Fairbanks, R.G. and Matthews, R.K. 1978. Marine Oxygen Isotope Record in Pleistocene Coral, Barbados, West-Indies. *Quaternary Research*, **10**: 181-196.
- Fairbanks, R.G. 1989. A 17,000-Year Glacio-Eustatic Sea-Level Record - Influence of Glacial Melting Rates on the Younger Dryas Event and Deep-Ocean Circulation. *Nature*, **342**: 637-642.
- Farrell, J.W., Clemens, S.C. and Gromet, L.P. 1995. Improved Chronostratigraphic Reference Curve of Late Neogene Seawater Sr-87/Sr-86. *Geology*, **23**: 403-406.

- Faugères, J.-C., Gonthier, E. and Stow, D.A.V. 1984. Contourite drift molded by deep Mediterranean outflow. *Geology*, **12**: 296-300.
- Fiuzza, A.F.G. 1984. *Hidrologia e dinâmica das águas costeiras Portuguesas*. PhD Thesis, Universidade de Lisboa, Lisboa, 294 pp.
- Fiuzza, A.F.G., Hamann, M., Ambar, I., del Rio, G.D., Gonzalez, N. and Cabanas, J.M. 1998. Water masses and their circulation off western Iberia during May 1993. *Deep-Sea Research Part I-Oceanographic Research Papers*, **45**: 1127-1160.
- Folk, R.L. and Chafetz, H.S. 2000. Bacterially Induced Microscale and Nonoscale Carbonate Precipitates. In: *Microbial Sediments* (Eds R.E. Riding and S.M. Awramik), pp. 40-49. Springer-Verlag, Berlin Heidelberg.
- Foustoukos, D.I. and Seyfried Jr., W.E. 2004. Hydrocarbons in Hydrothermal Vent Fluids: The role of Chromium-Bearing Catalysts. *Science*, **304**: 1002-1005.
- Fowler, S.R., Mildenhall, J., Zalova, S., Riley, G., Elsley, G., Desplanques, A. and Guliyev, F. 2000. Mud volcanoes and structural development on Shah Deniz. *Journal of Petroleum Science and Engineering*, **28**: 189-206.
- Freitas, P.S. and Abrantes, F. 2002. Suspended particulate matter in the Mediterranean water at the Gulf of Cadiz and off the southwest coast of the Iberian Peninsula. *Deep-Sea Research Part II-Topical Studies in Oceanography*, **49**: 4245-4261.
- Friedman, I. and Hall, W.E. 1963. Fractionation of  $O^{18}/O^{16}$  between Coexisting Calcite and Dolomite. *Journal of Geology*, **71**: 238-243.
- Friedman, I. and O'Neil, J.R. 1977. Compilation of stable isotope fractionation factors of geochemical interest. Professional Paper, N° P 0440-KK, U. S. Geological Survey.
- Fritz, P. and Smith, D.G.W. 1970. Isotopic Composition of Secondary Dolomites. *Geochimica et Cosmochimica Acta*, **34**: 1161-1173.
- Gageonnet, R. and Lemoine, M. 1958. *Contribution à la connaissance de la géologie de la province portugaise de Timor*. Estudos, ensaios e documentos, **48**. Ministerio do Ultramar. Junta de Investigações do Ultramar, Lisboa, 136 pp.
- García, M., Hernandez-Molina, F.J., Diaz-del-Rio, V., Llave, E., Somoza, L., Vazquez, J.T. and Dias, J.A. 2003. The Gulf of Cadiz channels and valleys system: Oceanographic implications. In: *4<sup>th</sup> Symposium on the Atlantic Iberian Continental Margins* (Eds F. Vilas et al.), **Special Volume on the 4<sup>th</sup> Symposium on the Atlantic Iberian Continental Margins, Thalassas**, **19 (2a)**, pp. 43-45, Vigo Spain.
- García-Dueñas, V., Banda, E., Torne, M., Cordoba, D., Coimas, C., Gonzalezlodeiro, F., Maldonado, A., Munoz, M., Orozco, M., Degaldeano, C.S., Surinach, E., Tubia, J.M. and Vegas, R. 1994. A Deep Seismic-Reflection Survey across the Betic Chain (Southern Spain) - 1st Results. *Tectonophysics*, **232**: 77-89.
- Gardner, J., Jung, W.-y. and Somoza, L. 2001. The possible effect of the mediterranean outflow water (MOW) on gas hydrate dissociation in the Gulf of Cadiz. In: *2001 AGU Fall Meeting*, San Francisco, USA.
- Gardner, J.M. 2002. *Morphology, Sedimentology and Biology of Mud Volcanoes on the Moroccan Continental Margin*. PhD Thesis, The George Washington University, Washington, 157 pp.
- Gardner, J.M. 2001. Mud volcanoes revealed and sampled on the Western Moroccan continental margin. *Geophysical Research Letters*, **28**: 339-342.
- Gardner, J.V. and Kidd, R.B. 1983. Sedimentary processes on the Iberian continental margin viewed by long-range side-scan sonar. Part I: Gulf of Cadiz. *Oceanologica Acta*, **6**: 245-254.
- Gascard, J.C. and Richez, C. 1985. Water Masses and Circulation in the Western Alboran Sea and in the Straits of Gibraltar. *Progress in Oceanography*, **15**: 157-216.
- Gay, A., Lopez, M., Cochonat, P., Levache, D., Sermondadaz, G. and Seranne, M. 2006a. Evidences of early to late fluid migration from an upper Miocene turbiditic channel revealed by 3D seismic coupled to geochemical sampling within seafloor pockmarks, Lower Congo Basin. *Marine and Petroleum Geology*, **23**: 387-399.
- Gay, A., Lopez, M., Cochonat, P., Seranne, M., Levache, D. and Sermondadaz, G. 2006b. Isolated seafloor pockmarks linked to BSRs, fluid chimneys, polygonal faults and stacked Oligocene-Miocene turbiditic palaeochannels in the Lower Congo Basin. *Marine Geology*, **226**: 25-40.
- Gay, A., Lopez, M., Ondreas, H., Charlou, J.-L., Sermondadaz, G. and Cochonat, P. 2006c. Seafloor facies related to upward methane flux within a Giant Pockmark of the Lower Congo Basin. *Marine Geology*, **226**: 81-95.

- Gill, F.L., Harding, I.C., Little, C.T.S. and Todd, J.A. 2005. Palaeogene and Neogene cold seep communities in Barbados, Trinidad and Venezuela: An overview. *Palaeogeography, Palaeoclimatology, Palaeoecology*, **227**: 191-209.
- Gischler, E., Sandy, M.R. and Peckmann, J. 2003. *Ibergirhynchia contraria* (F.A. Roemer, 1850), and Early Carboniferous seep-related rhynchonellide brachiopod from the Harz Mountains, Germany - A possible successor to *Dzieduszyckia*? *Journal of Paleontology*, **77**: 293-303.
- Goedert, J.L., Peckmann, J. and Reitner, J. 2000. Worm tubes in an allochthonous cold-seep carbonate from Lower Oligocene rocks of Western Washington. *Journal of Paleontology*, **74**: 992-999.
- Goedert, J.L., Thiel, V., Schmale, O., Weldon, W., Michaelis, W. and Peckmann, J. 2003. The Late Eocene "Whiskey Creek" Methane-Seep Deposit (Western Washington State) Part I: Geology, Paleontology, and Molecular Geobiology. *Facies*, **48**: 223-240.
- Gold, T. and Soter, S. 1980. The Deep-Earth-Gas Hypothesis. *Scientific American*, **242**: 154-&.
- Goldsmith, J.R. and Graf, D.L. 1958. Relation between lattice constants and composition of the Ca-Mg Carbonates. *The American Mineralogist*, **43**: 84-101.
- González, F.J., Pinheiro, L.M., Magalhães, V.H., Ivanov, M., Somoza, L. and Merinero, R. 2006a. SULPHATE-REDUCING BACTERIA AS A NUCLEATION SITES FOR PYRITE IN CARBONATE CHIMNEYS FROM THE VERNADSKY RIDGE, MOROCCAN MARGIN OF THE GULF OF CADIZ. In: *Geological Processes on Deep-Water European Margins. International Conference and 15th Anniversary Training Through Reserach Post-Cruise Meeting* (Ed G.G. Akhmanov), pp. 31-34, Moscow /Zvenigorod, Russia.
- González, F.J., Pinheiro, L.M., Magalhães, V.H., Ivanov, M., Somoza, L. and Merinero, R. 2006b. Pyrite nucleation induced by sulphate-reducing bacteria in carbonate chimneys from the Vernadsky Ridge, Moroccan Margin (Gulf of Cadiz). In: *European Geosciences Union 2006* (Ed E.G. Union), *Geophysical Research Abstracts*, **8**, pp. EGU06-A-03759. European Geosciences Union, Vienna.
- Gonzalez-Fernandez, A., Cordoba, D., Matias, L.M. and Torne, M. 2001. Seismic crustal structure in the Gulf of Cadiz (SW Iberian Peninsula). *Marine Geophysical Researches*, **22**: 207-223.
- Graue, K. 2000. Mud volcanoes in deepwater Nigeria. *Marine and Petroleum Geology*, **17**: 959-974.
- Greinert, J. and Bohrmann, G. 1998. Carbonate precipitates at the Oregon accretionary margin : their relationship to vent fluids and the influence of gas hydrates. In: *Carbonate Mud Mounts and Cold Water Reefs Conference*, Gent, Belgium.
- Greinert, J., Derkachev, A., Suess, E., Obzhurov, A.I., Baranov, B.V. and Winckler, G. 1999. Gas venting, biota and carbonate mineralization along the Sakhalin shear zone, Sea of Okhotsk. In: *AAPG Meeting Pacific Section*, Monterey Bay.
- Greinert, J., Nadler, T. and GEOPECO working group 2000. Cold Vents and Carbonate Chemoherms in the Yaquina Basin, Peruvian Continental Margin: Visual, Mineralogical and Isotopic Investigations. In: *AGU Fall Meeting 2000*, San Francisco.
- Greinert, J., Bohrmann, G. and Suess, E. 2001. Gas Hydrate-Associated Carbonates and Methane-Venting at Hydrate Ridge: Classification, Distribution, and Origin of Authigenic Lithologies. In: *Natural Gas Hydrates: Occurrence, Distribution, and Detection* (Eds C.K. Paull and W.P. Dillon), *Geophysical Monograph Series*, **124**, pp. 99-113. American Geophysical Union, Washington.
- Greinert, J., Bohrmann, G. and Elvert, M. 2002a. Stromatolitic fabric of authigenic carbonate crusts: result of anaerobic methane oxidation at cold seeps in 4,850 m water depth. *International Journal of Earth Sciences*, **91**: 698-711.
- Greinert, J., Bollwerk, S.M., Derkachev, A., Bohrmann, G. and Suess, E. 2002b. Massive barite deposits and carbonate mineralization in the Derugin Basin, Sea of Okhotsk: precipitation processes at cold seep sites. *Earth and Planetary Science Letters*, **203**: 165-180.
- Greinert, J., Klauke, I. and Gimpel, P. 2002c. Side-Scan Sonar Investigations and Hydroacoustic "Bubble" Quantification in an Area of Surface-Near Gas Hydrate Occurrences: Recent Studies from Hydrate Ridge, Offshore Oregon. *The Institution of Electrical Engineers* 1143-1147.
- Greinert, J. and Nutz, B. 2004. Hydroacoustic experiments to establish a method for the determination of methane bubble fluxes at cold seeps. *Geo-Marine Letters*, **24**: 75-85.
- Greinert, J., Artemov, Y., Egorov, V., De Batist, M. and McGinnis, D. 2006. 1300-m-high rising bubbles from mud volcanoes at 2080 m in the Black Sea: Hydroacoustic characteristics and temporal variability. *Earth and Planetary Science Letters*, **244**: 1-15.
- Grevenmeyer, I., Kopf, A.J., Fekete, N., Kaul, N., Villinger, H.W., Heesemann, M., Wallmann, K., Spieß, V., Gennerich, H.-H., Müller, M. and Weinrebe, W. 2004. Fluid flow through active mud dome Mound Culebra offshore Nicoya Peninsula, Costa Rica: evidence from heat flow surveying. *Marine Geology*, **207**: 145-157.

- Grimison, N.L. and Chen, W.P.** 1986. The Azores-Gibraltar Plate Boundary - Focal Mechanisms, Depths of Earthquakes, and Their Tectonic Implications. *Journal of Geophysical Research-Solid Earth and Planets*, **91**: 2029-2047.
- Grossman, E.L. and Ku, T.-L.** 1986. Oxygen and carbon isotope fractionation in biogenic aragonite: Temperature effects. *Chemical Geology*, **59**: 59-74.
- Gutscher, M.-A., Malod, J., Rehault, J.-P., Contrucci, I., Klingelhoefer, F., Mendes-Victor, L. and Spakman, W.** 2002. Evidence for active subduction beneath Gibraltar. *Geology*, **30**: 1071-1074.
- Gutscher, M.-A.** 2004. What Caused the Great Lisbon Earthquake? *Science*, **305**: 1247-1248.
- Gutscher, M.-A., Baptista, M.A. and Miranda, J.M.** 2006. The Gibraltar Arc seismogenic zone (part 2): Constraints on a shallow east dipping fault plane source for the 1755 Lisbon earthquake provided by tsunami modeling and seismic intensity. *Tectonophysics*, **426**: 153-166.
- Hansen, L.B., Finster, K., Fossing, H. and Iversen, N.** 1998. Anaerobic methane oxidation in sulfate depleted sediments: effects of sulfate and molybdate additions. *Aquatic Microbial Ecology*, **14**: 195-204.
- Haq, B.U., Hardenbol, J. and Vail, P.R.** 1987. Chronology of Fluctuating Sea Levels since the Triassic. *Science*, **235**: 1156-1167.
- Hardie, L.A.** 1987. Dolomitization: A critical view of some current views. *Journal of Sedimentary Petrology*, **57**: 166-183.
- Hayward, N., Watts, A.B., Westbrook, G.K. and Collier, J.S.** 1999. A seismic reflection and GLORIA study of compressional deformation in the Gorringe Bank region, eastern North Atlantic. *Geophysical Journal International*, **138**: 831-850.
- Hedberg, H.D.** 1974. Relation of Methane Generation to Undercompacted Shales, Shale Diapirs, and Mud Volcanos. *Aapg Bulletin-American Association of Petroleum Geologists*, **58**: 661-673.
- Henriet, J.P., Mol, B.D., Pillen, S., Vanneste, M., Rooij, D.V., Versteeg, W., Croker, P.F., Shannon, P.M., Unnithan, V., Bouriak, S., Chachkine, P. and The Porcupine-Belgica 97 Shipboard Party** 2003. Gas hydrate crystals may help build reefs. *Nature*, **391**: 648-649.
- Henriet, J.-P. and Mienert, J.** (Eds) 1998. *Gas Hydrates: Relevance to World Margin Stability and Climate Change*. (Eds A.J. Fleet, A.C. Morton and M.R. A), *Geological Society Special Publications*, **137**. Geological Society, London, 331 pp.
- Henriet, J.-P., Versteeg, W. and Rooij, D.V.** 2005. BELGICA Cruise Report 05/12.
- Henry, P., Pichon, X.L., Lallemand, S., Foucher, J.-P., Westbrook, G. and Hobart, M.** 1990. Mud Volcano Field Seaward of the Barbados Accretionary Complex: A Deep-Towed Side Scan Sonar Survey. In: *Journal of Geophysical Research*, **95**, pp. 8917-8929.
- Henry, P., Le Pichon, X., Lallemand, S., Lance, S., Martin, J.B., Foucher, J.P., Fiala-Médioni, A., Rostek, F., Guilhaumou, N., Pranal, V. and Castrec, M.** 1996. Fluid flow in and around a mud volcano field seaward of the Barbados accretionary wedge: Results from Manon cruise. *Journal of Geophysical Research*, **101**: 20297-20323.
- Henry, P., Lallemand, S., Nakamura, K.-i., Tsunogai, U., Mazzotti, S. and Kobayashi, K.** 2002. Surface expression of fluid venting at the toe of the Nankai wedge and implications for flow paths. *Marine Geology*, **187**: 119-143.
- Henrys, S.A., Ellis, S. and Uruski, C.** 2003. Conductive heat flow variations from bottom-simulating reflectors on the Hikurangi margin, New Zealand. *Geophysical Research Letters*, **30**: 37.1-37.4.
- Hensen, C., Nuzzo, M., Hornibrook, E., Pinheiro, L.M., Bock, B., Magalhães, V.H. and Brückmann, W.** Submitted. Sources of mud volcano fluids in the Gulf of Cadiz - indications for hydrothermally altered fluids. *Geochimica et Cosmochimica Acta*.
- Hensen, C., Nuzzo, M., Hornibrook, E., Pinheiro, L.M., Bock, B., Magalhães, V.H. and Brückmann, W.** Submitted. Sources of mud volcano fluids in the Gulf of Cadiz - indications for hydrothermally altered fluids. *Geochimica et Cosmochimica Acta*.
- Hernández-Molina, F.J., Llave, E., Stow, D.A.V., García, M., Somoza, L., Vázquez, J.T., Lobo, F.J., Maestro, A., Río, V.D.d., León, R., Medialdea, T. and Gardner, J.** 2006. The contourite depositional system of the Gulf of Cadiz: A sedimentary model related to the bottom current activity of the Mediterranean outflow water and its interaction with the continental margin. *Deep-Sea Research Part II-Topical Studies in Oceanography*, **53**: 1420-1463.
- Hernandez-Molina, J., Llave, E., Somoza, L., Fernandez-Puga, M.C., Maestro, A., León, R., Medialdea, T., Barnolas, A., García, M., Diaz-del-Rio, V., Fernández-Salas, L.M., Vázquez, J.T., Lobo, F., Dias, J.A., Rodero, J. and Gardner, J.** 2003. Looking for clues to paleoceanographic imprints: A diagnosis of the Gulf of Cadiz contourite depositional systems. *Geology*, **31**: 19-22.
- Hess, J., Bender, M.L. and Schilling, J.G.** 1986. Evolution of the Ratio of Strontium-87 to Strontium-86 in Seawater from Cretaceous to Present. *Science*, **231**: 979-984.

- Hesse, R. and Harrison, W.E. 1981. Gas hydrates (clathrates) causing pore-water freshening and oxygen isotope fractionation in deep-water sedimentary sections of terrigenous continental margins. *Earth and Planetary Science Letters*, **55**: 453-462.
- Hesse, R., Frape, S.K., Egeberg, P.K. and Matsumoto, R. 2000. STABLE ISOTOPE STUDIES (Cl, O, AND H) OF INTERSTITIAL WATERS FROM SITE 997, BLAKE RIDGE GAS HYDRATE FIELD, WEST ATLANTIC. In: *Proceedings of the Ocean Drilling Program, Scientific Results* (Eds C.K. Paull, R. Matsumoto, P.J. Wallace and W.P. Dillon), **164**, pp. 129-137.
- Hesse, R. 2003. Pore water anomalies of submarine gas-hydrate zones as tool to assess hydrate abundance and distribution in the subsurface. What have we learned in the past decade? *Earth-Science Reviews*, **61**: 149-179.
- Hesselbo, S.P., Grocke, D.R., Jenkyns, H.C., Bjerrum, C.J., Farrimond, P., Bell, H.S.M. and Green, O.R. 2000. Massive dissociation of gas hydrate during a Jurassic oceanic anoxic event. *Nature*, **406**: 392-395.
- Higgins, G.E. and Saunders, J.B. 1974. Mud volcanoes - their nature and origin. In: *Contribution to the geology and paleobiology of the Caribbean and adjacent area* (Ed V.d.N.G.z. Basel), **84**, pp. 101-152, Basle.
- Hill, T.M., Kennett, J.P. and Valentine, D.L. 2004. Isotopic evidence for the incorporation of methane-derived carbon into foraminifera from modern methane seeps, Hydrate Ridge, Northeast Pacific. *Geochimica et Cosmochimica Acta*, **68**: 4619-4627.
- Hinrichs, K.U., Hayes, J.M., Sylva, S.P., Brewer, P.G. and DeLong, E.F. 1999. Methane-consuming archaeobacteria in marine sediments. *Nature*, **398**: 802-805.
- Hinrichs, K.U., Summons, R.E., Orphan, V., Sylva, S.P. and Hayes, J.M. 2000. Molecular and isotopic analysis of anaerobic methane-oxidizing communities in marine sediments. *Organic Geochemistry*, **31**: 1685-1701.
- Hinrichs, K.-U. and Boetius, A. 2002. The Anaerobic Oxidation of Methane: New Insights in Microbial Ecology and Biogeochemistry. In: *Ocean Margin Systems* (Eds G. Wefer et al.), pp. 457-477. Springer-Verlag, Berlin Heidelberg.
- Hinrichsen, H.H., Rhein, M., Kase, R.H. and Zenk, W. 1993. The Mediterranean Water Tongue and Its Chlorofluoromethane Signal in the Iberian Basin in Early Summer 1989. *Journal of Geophysical Research-Oceans*, **98**: 8405-8412.
- Hoefs, J. 1997. *Stable Isotope Geochemistry*. Springer, 201 pp.
- Hoehler, T.M., Alperin, M.J., Albert, D.B. and Martens, C.S. 1994. Field and Laboratory Studies of Methane Oxidation in an Anoxic Marine Sediment - Evidence for a Methanogen-Sulfate Reducer Consortium. *Global Biogeochemical Cycles*, **8**: 451-463.
- Hovland, M., Talbot, M.R., Qvale, H., Olausson, S. and Aasberg, L. 1987. Methane-Related Carbonate Cements in Pockmarks of the North-Sea. *Journal of Sedimentary Petrology*, **57**: 881-892.
- Hovland, M. and Judd, A.G. 1988. *Seabed Pockmarks and seepages. Impact on Geology, Biology and the Marine Environment*. Graham and Trotman, 293 pp.
- Hovland, M. 1990. Do carbonate reefs form due to fluid seepage? *Terra Nova*, **2**: 8-18.
- Hovland, M., Hill, A. and Stokes, D. 1997. The structure and geomorphology of the Dashgil mud volcano, Azerbaijan. *Geomorphology*, **21**: 1-15.
- Hovland, M. and Thomsen, E. 1997. Cold-water corals - are they hydrocarbon seep related? *Marine Geology*, **137**: 159-164.
- Hovland, M. and Gudmestad, O.T. 2001. Potential influence of gas hydrates on seabed installations. In: *Natural Gas Hydrates* (Eds C.K. Paull and W.P. Dillon), *Geophys. Monograph Ser.*, **124**, pp. 300-309. Am. Geophys. Union.
- Hovland, M., Macdonald, I.R., Rueslatten, H., Johansen, H.K., Naehr, T. and Bohrmann, G. 2005a. Chapopote Asphalt Volcano May Have Been Generated by Supercritical Water. *EOS Transactions, American Geophysical Union*, **86**: 397, 402.
- Hovland, M., Svensen, H., Forsberg, C.F., Johansen, H., Fichler, C., Fossa, J.H., Jonsson, R. and Rueslatten, H.K. 2005b. Complex pockmarks with carbonate-ridges off mid-Norway: Products of sediment degassing. *Marine Geology*, **218**: 191-206.
- Hudson, J.C. and Anderson, T.F. 1989. Ocean temperatures and isotopic compositions through time. In: *Environments and physiology of fossil organisms* (Eds E.N.K. Clarkson, G.B. Curry and W.D.I. Rolfe), **80**, pp. 183-192. Transactions of the Royal Society of Edinburgh.
- Huhnerbach, V. and Masson, D.G. 2004. Landslides in the North Atlantic and its adjacent seas: an analysis of their morphology, setting and behaviour. *Marine Geology*, **213**: 343-362.

- Huseynov, D.A. and Guliyev, I.S.** 2004. Mud volcanic natural phenomena in the South Caspian Basin: geology, fluid dynamics and environmental impact. *Environmental Geology*, **46**: 1012-1023.
- Iorga, M.C. and Lozier, M.S.** 1999a. Signatures of the Mediterranean outflow from a North Atlantic climatology 1. Salinity and density fields. *Journal of Geophysical Research*, **104**: 25,985-26,009.
- Iorga, M.C. and Lozier, M.S.** 1999b. Signatures of the Mediterranean outflow from a North Atlantic climatology 2. Diagnostic velocity fields. *J. Geophys. Res.*, **104**: 26,011-26,029.
- Irwin, H.** 1980. Early Diagenetic Carbonate Precipitation and Pore Fluid Migration in the Kimmeridge Clay of Dorset, England. *Sedimentology*, **27**: 577-591.
- Ivanov, M.K., Limonov, A.F. and Woodside, J.M.** (Eds) 1992. *Geological and geophysical investigations in the Mediterranean and Black Seas. Initial results of the "Training through-Research" Cruise of RV Gelendzhik in the Western Mediterranean and Black Sea (June-July 1991)*. (Ed UNESCO), UNESCO Reports in Marine Science, **56**. United Nations Educational, Scientific and Cultural Organization, 208 pp.
- Ivanov, M.K., Limonov, A.F. and van Weering, T.C.E.** 1996. Comparative characteristics of the Black Sea and Mediterranean Ridge mud volcanoes. In: *Marine Geology*, **132**, pp. 253-271.
- Ivanov, M.K. and Woodside, J.M.** 1996. Shallow Gas and Gas Hydrates on the Crimean Continental Margin, Black Sea. In: *Gas Hydrates: Relevance to World Margin Stability and Climatic Change. Abstracts Book. First Master Workshop* (Eds J.-P. Henriot and J. Mienert), pp. 46, Het Pand, Gent, Belgium.
- Ivanov, M.K., Limonov, A.F. and Woodside, J.M.** 1998. Extensive deep fluid flux through the sea floor on the Crimean continental margin (Black Sea). In: *Gas Hydrates: Relevance to World Margin Stability and Climate Change* (Eds J.-P. Henriot and J. Mienert), **137**, pp. 195-213. Geological Society, London.
- Jenden, P.D. and Gieskes, J.M.** 1983. Chemical and Isotopic Composition of Interstitial Water from Deep-Sea Drilling Project Site-533 and Site-534. *Initial Reports of the Deep Sea Drilling Project*, **76**: 453-461.
- Jiménez-Munt, I., Fernández, M., Torne, M. and Bird, P.** 2001. The transition from linear to diffuse plate boundary in the Azores-Gibraltar region: results from a thin-sheet model. *Earth and Planetary Science Letters*, **192**: 175-189.
- Jolivet, L., Augier, R., Robin, C., Suc, J.-P. and Rouchy, J.M.** 2006. Lithospheric-scale geodynamic context of the Messinian salinity crisis. *Sedimentary Geology*, **188-189**: 9-33.
- Jonk, R., Mazzini, A., Duranti, D., Parnell, J., Cronin, B. and Hurst, A.** 2003. Fluid escape from reservoirs: implications from cold seeps, fractures and injected sands - Part II. The fluids involved. *Journal of Geochemical Exploration*, **78-9**: 297-300.
- Jorgensen, N.O.** 1992. Methane-derived carbonate cementation of marine sediments from the Kattegat, Denmark: Geochemical and geological evidence. *Marine Geology*, **103**: 1-13.
- Judd, A., Davies, G., Wilson, J., Holmes, R., Baron, G. and Bryden, I.** 1997. Contributions to atmospheric methane by natural seepages on the UK continental shelf. *Marine Geology*, **137**: 165-189.
- Judd, A.G., Hovland, M., Dimitrov, L.I., García Gil, S. and Jukes, V.** 2002. The geological methane budget at Continental Margins and its influence on climate change. *Geofluids*, **2**: 109-126.
- Judd, A.G.** 2003. The global importance and context of methane escape from the seabed. *Geo-Marine Letters*, **23**: 147-154.
- Judd, A.G.** 2004. Natural seabed gas seeps as sources of atmospheric methane. *Environmental Geology*, **46**: 988-996.
- Kalinko, M.** 1964. Mud volcanoes, reasons of their origin, development and fading. *VNIIGRI*, **40**: 30-54.
- Kastner, M., Keene, J.B. and Gieskes, J.M.** 1977. Diagenesis of Siliceous Oozes. 1. Chemical Controls on Rate of Opal-a to Opal-Ct Transformation - Experimental Study. *Geochimica et Cosmochimica Acta*, **41**: 1041-1059.
- Kastner, M.** 1984. Control of Dolomite Formation. *Nature*, **311**: 410-411.
- Kastner, M., Elderfield, H. and Martin, J.B.** 1991. Fluids in Convergent Margins - What Do We Know About Their Composition, Origin, Role in Diagenesis and Importance for Oceanic Chemical Fluxes. *Philosophical Transactions of the Royal Society of London Series a-Mathematical Physical and Engineering Sciences*, **335**: 243-259.
- Kauffman, E.G., Arthur, M.A., Howe, B. and Scholle, P.A.** 1996. Widespread venting of methane-rich fluids Late Cretaceous in (Campanian) submarine springs (Tepee Buttes), Western Interior seaway, USA. *Geology*, **24**: 799-802.
- Kelly, S.R.A., Ditchfield, P.W., Doubleday, P.A. and Marshall, J.D.** 1995. An Upper Jurassic Methane-Seep Limestone from the Fossil Bluff Group Fore-Arc Basin of Alexander Island, Antarctica. *Journal of Sedimentary Research Section a-Sedimentary Petrology and Processes*, **65**: 274-282.
- Kennett, J.P., Hendy, I.L. and Behl, R.J.** 1996. Marine Clathrates and Rapid Climate Change, Santa Barbara Basin, California. In: *Gas Hydrates: Relevance to World Margin Stability and Climatic Change*.

- Abstracts Book. First Master Workshop* (Eds J.-P. Henriot and J. Mienert), pp. 6-7, Het Pand, Gent, Belgium.
- Kennett, J.P., Cannariato, K.G., Hendy, I.L. and Behl, R.J.** 2000. Carbon Isotopic Evidence for Methane Hydrate Instability During Quaternary Interstadials. *Science*, **288**: 128-133.
- Kennett, J.P., Cannariato, K.G., Hendy, I.L. and Behl, R.J.** 2003. *Methane hydrates in Quaternary climate change: the clathrate gun hypothesis*. AGU, 216 pp.
- Kenyon, N.H., Ivanov, M.K., Akhmetzhanov, A.M. and Akhmanov, G.G.** (Eds) 2000. *Multidisciplinary Study of Geological Processes on the North East Atlantic and Western Mediterranean Sea Margins. Preliminary results of geological and geophysical investigations during the TTR-9 cruise of R/V Professor Logachev June-July, 1999*. (Ed UNESCO), *Intergovernmental Oceanographic Commission (IOC) technical series*, **56**. UNESCO, Paris, 102 pp.
- Kenyon, N.H., Ivanov, M.K., Akhmetzhanov, A.M. and Akhmanov, G.G.** (Eds) 2001. *Interdisciplinary Approaches to Geoscience on the North East Atlantic Margin and Mid-Atlantic Ridge. Preliminary results of investigations during the TTR-10 cruise of RV Professor Logachev. July-August, 2000*. (Ed UNESCO), *Intergovernmental Oceanographic Commission (IOC) technical series*, **60**. UNESCO, Paris, 104 pp.
- Kenyon, N.H., Ivanov, M.K., Akhmetzhanov, A.M. and Akhmanov, G.G.** (Eds) 2002. *Geological Processes in the Mediterranean and Black Seas and North East Atlantic. Preliminary results of investigations during the TTR-11 cruise of RV Professor Logachev July-September, 2001*. (Ed UNESCO), *IOC Technical Series*, **62**. United Nations Educational, Scientific and Cultural Organization, Paris, 89 pp.
- Kenyon, N.H., Ivanov, M.K., Akhmetzhanov, A.M. and Akhmanov, G.G.** (Eds) 2003. *Interdisciplinary Geoscience Research on the NorthEast Atlantic Margin, Mediterranean Sea and Mid-Atlantic Ridge. Preliminary results of investigations during the TTR-12 cruise of RV Professor Logachev June-August, 2002*. (Ed UNESCO), *IOC Technical Series*, **67**. United Nations Educational, Scientific and Cultural Organization, Paris, 112 pp.
- Kenyon, N.H., Ivanov, M.K., Akhmetzhanov, A.M. and Akhmanov, G.G.** (Eds) 2006. *Interdisciplinary geoscience studies of the Gulf of Cadiz and Western Mediterranean basins. Preliminary results of investigations during the TTR-14 cruise of RV Professor Logachev July-September, 2004*. (Ed UNESCO), *IOC Technical Series*, **70**. United Nations Educational, Scientific and Cultural Organization, Paris, 115 pp.
- Kholodov, V.N.** 2002. Mud Volcanoes, Their Distribution Regularities and Genesis: Communication 1. Mud Volcanic Provinces and Morphology of Mud Volcanoes. *Lithology and Mineral Resources*, **37**: 197-209.
- Kim, S.-T. and O'Neil, J.R.** 1997. Equilibrium and nonequilibrium oxygen isotope effects in synthetic carbonates. *Geochimica et Cosmochimica Acta*, **61**: 3461-3475.
- King, L.H. and MacLean, B.** 1970. Pockmarks on the Scotian Shelf. *Geological Society of America Bulletin*, **81**: 3141-3148.
- Knorre, H.V. and Krumbein, W.E.** 2000. Bacterial Calcification. In: *Microbial Sediments* (Eds R.E. Riding and S.M. Awramik), pp. 25-31. Springer-Verlag, Berlin Heidelberg.
- Kopf, A., Robertson, A.H.F., Clennell, M.B. and Flecker, R.** 1998. Mechanisms of mud extrusion on the Mediterranean Ridge Accretionary Complex. *Geo-Marine Letters*, **18**: 97-114.
- Kopf, A., Robertson, A.H.F. and Volkman, N.** 2000. Origin of mud breccia from the Mediterranean Ridge accretionary complex based on evidence of the maturity of organic matter and related petrographic and regional tectonic evidence. *Marine Geology*, **166**: 65-82.
- Kopf, A., Klaeschen, D. and Mascle, J.** 2001. Extreme efficiency of mud volcanism in dewatering accretionary prisms. *Earth and Planetary Science Letters*, **189**: 295-313.
- Kopf, A. and Deyhle, A.** 2002. Back to the roots: boron geochemistry of mud volcanoes and its implications for mobilization depth and global B cycling. *Chemical Geology*, **192**: 195-210.
- Kopf, A., Bannert, B., Brückmann, W., Dorschel, B., Foubert, A.T.G., Grevemeyer, I., Gutscher, M.-A., Hebbeln, D., Heesemann, B., Hensen, C., Kaul, N.E., Lutz, M., Magalhães, V.H., Marquardt, M.J., Marti, A.V., Nass, K.S., Neubert, N., Niemann, H., Nuzzo, M., Poort, J.P.D., Rosiak, U.D., Sahling, H., J., S.v.D., Somoza, L.L., Thiebot, E. and Wilkop, T.P.** 2004. Report and preliminary results of Sonne Cruise SO175. MIAMI - BREMERHAVEN, 12.11 - 30.12.2003. 228, Bremen.
- Kopf, A.J.** 2002. Significance of mud volcanism. *Reviews of Geophysics*, **40**: B-1 - B-52.
- Kornacki, A.S., Kendrick, J.W. and Berry, J.L.** 1994. Impact of Oil and Gas Vents and Slicks on Petroleum-Exploration in the Deep-Water Gulf-of-Mexico. *Geo-Marine Letters*, **14**: 160-169.
- Krijgsman, W., Hilgen, F.J., Raffi, I., Sierro, F.J. and Wilson, D.S.** 1999. Chronology, causes and progression of the Messinian salinity crisis. *Nature*, **400**: 652-655.

- Krull, E.S. and Retallack, G.J.** 2000. delta C-13 depth profiles from paleosols across the Permian-Triassic boundary: Evidence for methane release. *Geological Society of America Bulletin*, **112**: 1459-1472.
- Krull, E.S., Retallack, G.J., Campbell, H.J. and Lyon, G.L.** 2000. delta C-13(org) chemostratigraphy of the Permian-Triassic boundary in the Maitai Group, New Zealand: evidence for high-latitudinal methane release. *New Zealand Journal of Geology and Geophysics*, **43**: 21-32.
- Kugler, H.G.** 1933. Contribution to the knowledge of sedimentary volcanism. *J. Inst. Petrol. Technologists*, **19**: 743-772.
- Kugler, H.G.** 1975. *Volcanism, Sedimentary*, pp. 854-856.
- Kulm, L.D., Suess, E., Moore, J.C., Carson, B., Lewis, B.T., Ritger, S.D., Kadko, D.C., Thornburg, T.M., Embley, R.W., Righ, W.D., Massoth, G.J., Langseth, M.G., Cochrane, G.R. and Scamman, R.L.** 1986. Oregon Subduction Zone: Venting, Fauna, and Carbonates. *Science*, **231**: 561-566.
- Kulm, L.D. and Suess, E.** 1990. Relationship between Carbonate Deposits and Fluid Venting - Oregon Accretionary Prism. *Journal of Geophysical Research-Solid Earth and Planets*, **95**: 8899-8915.
- Kuramoto, S.i., Ashi, J., Greinert, J., Gulick, S., Ishimura, T., Morita, S., Nakamura, K.-i., Okada, M., Okamoto, T., Rickert, D., Saito, S., Suess, E., Tsunogai, U. and Tomosugi, T.** 2001. Surface Observations of Subduction Related Mud Volcanoes and Large Thrust Sheets in the Nankai Subduction Margin ; Report on YK00-10 and YK01-04 Cruises. *JAMSTEC J. Deep Sea Res.*, **19**: 131-139.
- Kvenvolden, K.A.** 1993. Gas Hydrates - Geological Perspective and Global Change. *Reviews of Geophysics*, **31**: 173-187.
- Kvenvolden, K.A. and Lorenson, T.D.** 2000. A Global Inventory of Natural Gas Hydrate Occurrence (Ed USGS).
- Kvenvolden, K.A. and Lorenson, T.D.** 2001. A Global Inventory of Natural Gas Hydrate Occurrence. USGS.
- Lancelot, Y. and Ewing, J.I.** 1972. 27. Correlation of natural gas zonation and carbonate diagenesis in Tertiary sediments from the North-West Atlantic. In: *Initial Reports of the Deep Sea Drilling Project, Volume XI* (Eds C.D. Hollister et al.), *Initial Reports of the Deep Sea Drilling Project, XI*, pp. 791-799. U.S. Government Printing Office, Washington.
- Land, L.S.** 1998. Failure to Precipitate Dolomite at 25 °C from Dilute Solution Despite 1000-Fold Oversaturation after 32 Years. *Aquatic Geochemistry*, **4**: 361-368.
- Lavrushin, V.Y., Dubinina, E.O. and Avdeenko, A.S.** 2005. Isotopic Composition of Oxygen and Hydrogen in Mud-Volcanic Waters from Taman (Russia) and Kakheta (Eastern Georgia). *Lithology and Mineral Resources*, **40**: 123-137.
- Le Pichon, X., Foucher, J.P., Boulegue, J., Henry, P., Lallemand, S., Benedetti, M., Avedik, F. and Mariotti, A.** 1990. Mud Volcano Field Seaward of the Barbados Accretionary Complex - a Submersible Survey. *Journal of Geophysical Research-Solid Earth and Planets*, **95**: 8931-8943.
- Leme, J.C.d.A.** 1968. Breve ensaio sobre a geologia da província de Timor. In: *Curso de Geologia do Ultramar*, **1**, pp. 107-164. Junta de Investigação do Ultramar, Lisboa.
- León, R., Somoza, L., Medialdea, T., Maestro, A., Díaz-del-Río, V. and Fernández-Puga, M.d.C.** 2006. Classification of sea-floor features associated with methane seeps along the Gulf of Cádiz continental margin. *Deep-Sea Research II -Topical Studies in Oceanography*, **53**: 1464-1481.
- Levin, L.A.** 2005. Ecology of cold seep sediments: Interactions of fauna with flow, chemistry and microbes. *Oceanography and Marine Biology: An Annual Review*, **43**: 1-46.
- Limonov, A.F., Woodside, J.M. and Ivanov, M.K.** (Eds) 1994. *Mud volcanism in the Mediterranean and Black Seas and shallow structure of the Eratosthenes Seamount. Initial results of the geological and geophysical investigations during the Third UNESCO-ESF "Training through-Research" Cruise of RV Gelendzhik (June-July 1993)*. (Ed UNESCO), *UNESCO Reports in Marine Science*, **64**. United Nations Educational, Scientific and Cultural Organization, Paris, 173 pp.
- Limonov, A.F., Woodside, J.M., Cita, M.B. and Ivanov, M.K.** 1996. The Mediterranean Ridge and related mud diapirism: a background. *Marine Geology*, **132**: 7-19.
- Limonov, A.F., van Weering, T.C.E., Kenyon, N.H., Ivanov, M.K. and Meisner, L.B.** 1997. Seabed morphology and gas venting in the Black Sea mudvolcano area: Observations with the MAK1 deep-tow sidescan sonar and bottom profiler. *Marine Geology*, **137**: 121-136.
- Lisiecki, L.E. and Raymo, M.E.** 2005. A Pliocene-Pleistocene stack of 57 globally distributed benthic  $\delta^{18}\text{O}$  records. *Paleoceanography*, **20**: PA1003; doi:10.1029/2004PA001071.
- Llave, E., Hernandez-Molina, F.J., Somoza, L., Diaz-del-Rio, V., Stow, D.A.V., Maestro, A. and Dias, J.A.** 2001. Seismic stacking pattern of the Faro-Albufeira contourite system (Gulf of Cadiz): a Quaternary record of paleoceanographic and tectonic influences. *Marine Geophysical Researches*, **22**: 487-508.

- Llave, E., Schonfeld, J., Hernandez-Molina, F.J., Mulder, T., Somoza, L., Diaz del Rio, V. and Sanchez-Almazo, I. 2006. High-resolution stratigraphy of the Mediterranean outflow contourite system in the Gulf of Cadiz during the late Pleistocene: The impact of Heinrich events. *Marine Geology*, **227**: 241-262.
- Lollar, B.S., Frappe, S.K., Weise, S.M., Fritz, P., Macko, S.A. and Welhan, J.A. 1993. Abiogenic methanogenesis in crystalline rocks. *Geochimica et Cosmochimica Acta*, **57**: 5087-5992.
- Lollar, B.S., Westgate, T.D., Ward, J.A., Slater, G.F. and Lacrampe-Couloume, G. 2002. Abiogenic formation of alkanes in the Earth's crust as a minor source for global hydrocarbon reservoirs. *Nature*, **416**: 522-524.
- Loneragan, L. and White, N. 1997. Origin of the Betic-Rif mountain belt. *Tectonics*, **16**: 504-522.
- Loubere, P. 1987. Changes in Mid-Depth North-Atlantic and Mediterranean Circulation During the Late Pliocene - Isotopic and Sedimentological Evidence. *Marine Geology*, **77**: 15-38.
- Ludwig, K.R. and Titterton, D.M. 1994. Calculation of (230)Th/U Isochrons, Ages, and Errors. *Geochimica et Cosmochimica Acta*, **58**: 5031-5042.
- Lumsden, D.N. 1979. Discrepancy between thin-section and X-ray estimates of dolomite in limestone. *Journal of Sedimentary Petrology*, **49**: 429-435.
- MacDonald, G.J. 1990. Role of Methane Clathrates in Past and Future Climates. *Climatic Change*, **16**: 247-281.
- MacDonald, I., Carney, R. and Wilkinson, D. 1988. Gulf of Mexico chemosynthetic communities at oil seeps: estimating total density. *The Institution of Electrical Engineers* 90-95.
- MacDonald, I.R., Leifer, I., Sassen, R., Stine, P., Mitchell, R. and Guinasso, N. 2002. Transfer of hydrocarbons from natural seeps to the water column and atmosphere. *Geofluids*, **2**: 95-107.
- MacDonald, I.R., Sager, W.W. and Peccini, M.B. 2003. Gas hydrate and chemosynthetic biota in mounded bathymetry at mid-slope hydrocarbon seeps: Northern Gulf of Mexico. *Marine Geology*, **198**: 133-158.
- MacDonald, I.R., Bohrmann, G., Escobar, E., Abegg, F., Blanchon, P., Blinova, V., Bruckmann, W., Drews, M., Eisenhauer, A., Han, X., Heeschen, K., Meier, F., Mortera, C., Naehr, T., Orcutt, B., Bernard, B., Brooks, J. and Faragó, M.d. 2004. Asphalt Volcanism and Chemosynthetic Life in the Campeche Knolls, Gulf of Mexico. *Science*, **304**: 999-1002.
- Mackensen, A., Wollenburg, J. and Licari, L. 2006. Low  $\delta^{13}\text{C}$  in tests of live epibenthic and endobenthic foraminifera at a site of active methane seepage. *Paleoceanography*, **21**: PA2022, doi:10.1029/2005PA001196.
- Mackenzie, F.T., Bischoff, W., Bischof, F., Loijens, M., Schonmaker, J. and Wollast, R. 1983. Magnesium calcites: Low temperature occurrence, solubility, and solid-solution behavior. In: *Carbonates: Mineralogy and chemistry. Reviews in Mineralogy* (Ed R.J. Reeder), *Reviews in Mineralogy*, **11**, pp. 97-144.
- Madelain, F. 1970. Influence de la topographie du fond sur l'écoulement méditerranéen entre le détroit de Gibraltar et le cap Saint-Vincent. In: *Cahiers océanographiques* (Ed S.H.d.l. Marine), **XXII**, pp. 43-61. Service Hydrographique de la Marine, Paris.
- Magalhães, V., Vasconcelos, C., Gaspar, L., Monteiro, H., Pinheiro, L., Ivanov, M., Díaz-del-Río, V. and Somoza, L. 2003. Methane related authigenic carbonates, chimneys and crusts from the Gulf of Cadiz. In: *EGS-AGU-EUG Joint Assembly* (Ed E.G. Society), *Geophysical Research Abstracts*, **5**, pp. 12842. European Geophysical Society, Nice, France.
- Magalhães, V., Pinheiro, L.M., Rensbergen, P.V., Roque, C., León-Buendía, R., Bouriak, S., Kopf, A., Gardner, J. and Ivanov, M. 2004. Fluid escape structures in the Gulf of Cadiz. Evidence of structural control from combined seismic reflection and sidescan sonar interpretation. In: *European Geosciences Union, 1st General Assembly* (Ed E.G. Union), Nice, France.
- Magalhães, V.H., Bobos, J., Gaspar, L., Pinheiro, L.M., Monteiro, H. and Ivanov, M.K. 2002a. Mineralogy and geochemistry of Carbonate chimneys from the Gulf of Cadiz: preliminary results. In: *Geosphere/Biosphere/Hydrosphere Coupling Processes, Fluid Escape Structures and Tectonics at Continental Margins and Ocean Ridges - TTR11 Post-Cruise Meeting and International Conference* (Eds M.R.d. Cunha, L.M. Pinheiro and A. Suzyumov), pp. 31, Aveiro, Portugal.
- Magalhães, V.H., Bobos, J., Gaspar, L., Pinheiro, L.M., Monteiro, H. and Ivanov, M.K. 2002b. Mineralogy and geochemistry of Carbonate chimneys from the Gulf of Cadiz: preliminary results. In: *Geosphere/Biosphere/Hydrosphere Coupling Processes, Fluid Escape Structures and Tectonics at Continental Margins and Ocean Ridges. International Conference and Tenth Post-Cruise Meeting of the Training-Through-Research Programme* (Eds M.R. Cunha, L.M. Pinheiro and A. Suzyumov), **Workshop Report N° 183**, pp. 18. UNESCO - Intergovernmental Oceanographic Commission (IOC), Aveiro, Portugal.

- Magalhães, V.H., Birgel, D. and Peckmann, J.** 2005a. Lipid Biomarker analysis at the Marine Biogeochemistry Laboratory of the Research Center for Ocean Margins (rcom) at the Bremen University. INGMARDEP xx/FCT/2005 - xx.03.2005, National Institute of Engineering, Technology and Innovation, Alfragide.
- Magalhães, V.H., Birguel, D., Peckmann, J., Srisawang, B., Pinheiro, L.M., Vasconcelos, C., McKenzie, J.A. and Ivanov, M.K.** 2005b. Authigenic carbonate chimneys and crusts from the Gulf of Cadiz: Biomarker evidence of archaea mediating anaerobic oxidation of methane. In: *International Conference and TTR14 Post-cruise meeting. Geosphere-Biosphere Coupling Processes: the TTR interdisciplinary approach towards studies of the European and N. African margins*, pp. 1, Marrakech, Morocco.
- Magalhães, V.H., Pinheiro, L.M. and Ivanov, M.K.** 2005c. Methane-derived authigenic carbonates in the Gulf of Cadiz: Cartography, distribution and controls. In: *2005 AGU Fall Meeting* (Ed AGU), **86**, pp. OS33C-1484. AGU, San Francisco.
- Magalhães, V.H., Pinheiro, L.M., Ivanov, M.K., Díaz-del-Río, V., Somoza, L. and Gardner, J.** 2005d. Distribution of mud volcanism and seepage-related authigenic carbonates in the Gulf of Cadiz. In: *European Geosciences Union, General Assembly 2005* (Ed E.G. Union), *Geophysical Research Abstracts*, **7**, pp. 05589, Vienna, Austria.
- Makogon, Y.F., Trebin, F.A., Trofimuk, A.A., Tsarev, V.P. and Cherskii, N.V.** 1971. Detection of Natural Gas Deposit in Solid (Gas-Hydrated) State. *Doklady Akademii Nauk Sssr*, **196**: 205-.
- Maldonado, A. and Nelson, C.H.** 1999. Interaction of tectonic and depositional processes that control the evolution of the Iberian Gulf of Cadiz margin. *Marine Geology*, **155**: 217-242.
- Maldonado, A., Somoza, L. and Pallarés, L.** 1999. The Betic orogen and the Iberian-African boundary in the Gulf of Cádiz: geological evolution (central North Atlantic). *Marine Geology*, **155**: 9-43.
- Martin, J.B., Day, S.A., Rathburn, A.E., Perez, M.E., Mahn, C. and Gieskes, J.** 2004. Relationships between the stable isotopic signatures of living and fossil foraminifera in Monterey Bay, California. *G3 Geochemistry Geophysics Geosystems*, **5**: Q04004, doi:10.1029/2003GC000629.
- Martinson, D.G., Pisias, N.G., Hays, J.D., Imbrie, J., Moore, T.C. and Shackleton, N.J.** 1987. Age Dating and the Orbital Theory of the Ice Ages: Development of a High-Resolution 0 to 300,000-Year Chronostratigraphy. *Quaternary Research*, **27**: 1-29.
- Masclé, J., Zitter, T., Bellaiche, G., Droz, L., Gaullier, V., Loncke, L. and Party, P.S.** 2001. The Nile deep sea fan: preliminary results from a swath bathymetry survey. *Marine and Petroleum Geology*, **18**: 471-477.
- Masson, D.G. and Berndt, C.** 2006. R.R.S. CHARLES DARWIN CRUISE 178 (14th MARCH -11th APRIL, 2006). 3D seismic acquisition over mud volcanoes in the Gulf of Cadiz and submarine landslides in the Eivissa Channel, western Mediterranean Sea, NATIONAL OCEANOGRAPHY CENTRE, SOUTHAMPTON.
- Matsumoto, R.** 1990. Vuggy carbonate crust formed by hydrocarbon seepage on the continental shelf of Baffin Island, northeast Canada. *Geochemical Journal*, **24**: 143-158.
- Matthews, A. and Katz, A.** 1977. Oxygen isotope fractionation during the dolomitization of calcium carbonate. *Geochimica et Cosmochimica Acta*, **41**: 1431-1438.
- Matthiesen, S. and Haines, K.** 2003. A hydraulic box model study of the Mediterranean response to postglacial sea-level rise. *Paleoceanography*, **18**: 1084, doi:10.1029/2003PA000880.
- Mauffret, A., Mougout, D., Miles, P.R. and Malod, J.A.** 1989. Results from Multichannel Reflection Profiling of the Tagus Abyssal Plain (Portugal) - Comparison with the Canadian Margin. In: *Extensional Tectonics and Stratigraphy of the North Atlantic Margins* (Ed A.J.a.B. Tankard), **46**, pp. 379-393. Am. Assoc. Petrol. Geol.
- Mazurenko, L.L., Soloviev, V.A., Belenkaya, I., Ivanov, M.K. and Pinheiro, L.M.** 2002. Mud volcano gas hydrates in the Gulf of Cadiz. *Terra Nova*, **14**: 321-329.
- Mazzini, A., Jonk, R., Duranti, D., Parnell, J., Cronin, B. and Hurst, A.** 2003. Fluid escape from reservoirs: implications from cold seeps, fractures and injected sands - Part I. The fluid flow system. *Journal of Geochemical Exploration*, **78-9**: 293-296.
- McCrea, J.M.** 1950. On the Isotopic Chemistry of Carbonates and a Paleotemperature Scale. *Journal of Chemical Physics*, **18**: 849-857.
- McKenzie, J.A.** 1981. Holocene Dolomitization of Calcium-Carbonate Sediments from the Coastal Sabkhas of Abu Dhabi, U.A.E.: A Stable Isotope Study. *Journal of Geology*, **89**: 185-198.
- Medialdea, T., Vegas, R., Somoza, L., Vazquez, J.T., Maldonado, A., Diaz-del-Rio, V., Maestro, A., Cordoba, D. and Fernandez-Puga, M.C.** 2004. Structure and evolution of the "Olistostrome" complex of the Gibraltar Arc in the Gulf of Cadiz (eastern Central Atlantic): evidence from two long seismic cross-sections. *Marine Geology*, **209**: 173-198.

- Meister, P.** 2005. *Linking the Formation of Dolomite and other Early Diagenetic Minerals with Microbial Activity in Deep-Sea Sediments: Results from ODP Leg 201, Peru Margin and Eastern Equatorial Pacific*. PhD Thesis, Swiss Federal Institute of Technology Zurich, Zürich, Switzerland, 187 pp.
- Michaelis, W., Seifert, R., Nauhaus, K., Treude, T., Thiel, V., Blumenberg, M., Knittel, K., Gieseke, A., Peterknecht, K., Pape, T., Boetius, A., Amann, R., Jørgensen, B.B., Widdel, F., Peckmann, J., Pimenov, N.V. and Gulin, M.B.** 2002. Microbial Reefs in the Black Sea Fueled by Anaerobic Oxidation of Methane. *Science*, **297**: 1013-1015.
- Milkov, A.V.** 2000. Worldwide distribution of submarine mud volcanoes and associated gas hydrates. *Marine Geology*, **167**: 29-42.
- Milkov, A.V.** 2004. Global estimates of hydrate-bound gas in marine sediments: how much is really out there? *Earth-Science Reviews*, **66**: 183-197.
- Morales, J., Serrano, I., Jabaloy, A., Galindo-Saldivar, J., Zhao, D., Torcal, F., Vidal, F. and Gonzales-Lodeiro, F.** 1999. Active continental subduction beneath the Betic Cordillera and the Alboran Sea. *Geology*, **27**: 735-738.
- Morse, J.W., Wang, Q.W. and Tsio, M.Y.** 1997. Influences of temperature and Mg:Ca ratio on CaCO<sub>3</sub> precipitates from seawater. *Geology*, **25**: 85-87.
- Mougenot, D. and Vanney, J.-R.** 1982. Les Rides de Contourites Plio-Quaternaires de la Pente Continentale Sud-Portugaise, *Bull. Inst. Géol. Bassin d' Aquitaine, Bordeaux. Actes Colloque International CNRS, Bordeaux, Sept. 1981, N° 31*, pp. 131-139.
- Mulder, T., Voisset, M., Lecroart, P., Drezén, E.L., Gonthier, E., Hanquiez, V., res, J.-C.F., Habgood, E., Hernandez-Molina, F.J., Estrada, F., Llave-Barranco, E., Poirier, D., Gorini, C., Fuchey, Y., Voelker, A., Freitas, P., Sanchez, F.L., Fernandez, L.M., Kenyon, N.H. and Morel, J.** 2003. The Gulf of Cadiz: an unstable giant contouritic levee. *Geo-Marine Letters*, **23**: 7-18.
- Nelson, C.H., Baraza, J. and Maldonado, A.** 1993. Mediterranean Undercurrent Sandy Contourites, Gulf of Cadiz, Spain. *Sedimentary Geology*, **82**: 103-131.
- Niemann, H., Duarte, J., Hensen, C., Elvert, M., Magalhães, V.H., Boetius, A. and Pinheiro, L.M.** 2005. Diverse Microbial Communities mediate Anaerobic Oxidation of Methane at Mud Volcanoes in the Gulf of Cadiz. In: *European Geosciences Union, General Assembly 2005* (Ed E.G. Union), *Geophysical Research Abstracts*, **7**, pp. 08197. European Geosciences Union, Vienna, Austria.
- Niemann, H., Duarte, J., Hensen, C., Omeregíe, E., Magalhães, V.H., Elvert, M., Pinheiro, L.M., Kopf, A. and Boetius, A.** 2006. Microbial methane turnover at mud volcanoes of the Gulf of Cadiz. *Geochimica et Cosmochimica Acta*, **70**: 5336-5355 doi:10.1016/j.gca.2006.08.010.
- Niemann, H., Duarte, J., Hensen, C., Omeregíe, E., Magalhães, V.H., Elvert, M., Pinheiro, L.M. and Boetius, A.** Submitted. Microbial methane turnover at mud volcanoes of the Gulf of Cadiz. *Geochimica et Cosmochimica Acta*.
- Northrop, D.A. and Clayton, R.N.** 1966. Oxygen-isotope fractionations in systems containing dolomite. *Journal of Geology*, **74**: 174-196.
- Nuzzo, M., Hensen, C., Hornibrook, E.R.C., Brückmann, W., Magalhães, V.H., Parkes, R.J. and Pinheiro, L.M.** 2005a. Origin of mud volcano fluids in the Gulf of Cadiz (E-Atlantic). In: *European Geosciences Union, General Assembly 2005* (Ed E.G. Union), *Geophysical Research Abstracts*, **7**, pp. 06264. European Geosciences Union, Vienna, Austria.
- Nuzzo, M., Hensen, C., Hornibrook, E.R.C., Brückmann, W., Magalhães, V.H., Parkes, R.J. and Pinheiro, L.M.** 2005b. Origin of mud volcano fluids in the Gulf of Cadiz (E-Atlantic). In: *IODP meeting (Brest)*, Brest.
- Nuzzo, M., Hensen, C., Hornibrook, E.R.C., Bock, B., Magalhães, V.H., Brückmann, W., Parkes, R.J. and Pinheiro, L.M.** Submitted. Mud volcanism in the Gulf of Cadiz: insights into an active collisional setting through anomalous pore fluids and light hydrocarbon gases. *Geology*.
- Nuzzo, M., Hensen, C., Hornibrook, E.R.C., Bock, B., Magalhães, V.H., Brückmann, W., Parkes, R.J. and Pinheiro, L.M.** Submitted to *Geology*. Mud volcanism in the Gulf of Cadiz: insights into an active collisional setting through anomalous pore fluids and light hydrocarbon gases. *Geology*.
- Olu, K., Lance, S., Sibuet, M., Henry, P., Fiala-Médioni, A. and Dinét, A.** 1997. Cold seep communities as indicators of fluid expulsion patterns through mud volcanoes seaward of the Barbados accretionary prism. *Deep-Sea Research I*, **44**: 811-841.
- Olu-Le Roy, K., Sibuet, M., Fiala-Medioni, A., Gofas, S., Salas, C., Mariotti, A., Foucher, J.P. and Woodside, J.** 2004. Cold seep communities in the deep eastern Mediterranean Sea: composition, symbiosis and spatial distribution on mud volcanoes. *Deep-Sea Research Part I-Oceanographic Research Papers*, **51**: 1915-1936.

- O'Neil, J.R. 1963. *Oxygen isotope fractionation studies in mineral systems*. PhD Thesis, University of Chicago.
- O'Neil, J.R. and Epstein, S. 1966. Oxygen Isotope Fractionation in System Dolomite-Calcite-Carbon Dioxide. *Science*, **152**: 198-201.
- O'Neil, J.R., Clayton, R.N. and Mayeda, T.K. 1969. Oxygen isotope fractionation in divalent metal carbonates. *Journal of Chemical Physics*, **51**: 5547-5558.
- Orange, D.L., Greene, H.G., Reed, D., Martin, J.B., McHugh, C.M., Ryan, W.B.F., Maher, N., Stakes, D. and Barry, J. 1999. Widespread fluid expulsion on a translational continental margin: Mud volcanoes, fault zones, headless canyons, and organic-rich substrate in Monterey Bay, California. *Geological Society of America Bulletin*, **111**: 992-1009.
- Orphan, V.J., Hinrichs, K.-U., III, W.U., Paull, C.K., Taylor, L.T., Sylva, S.P., Hayes, J.M. and DeLong, E.F. 2001a. Comparative Analysis of Methane-Oxidizing Archaea and Sulfate-Reducing Bacteria in Anoxic Marine Sediments. *Applied and Environmental Microbiology*, **67**: 1922-1934.
- Orphan, V.J., House, C.H., Hinrichs, K.U., McKeegan, K.D. and DeLong, E.F. 2001b. Methane-consuming archaea revealed by directly coupled isotopic and phylogenetic analysis. *Science*, **293**: 484-487.
- Ovsyannikov, D.O., Sadekov, A.Y. and Kozlova, E.V. 2003. Rock fragments from mud volcanic deposits of the Gulf of Cadiz: an insight into the Eocene-Pliocene sedimentary succession of the basin. *Marine Geology*, **195**: 211-221.
- Pancost, R.D., Damste, J.S.S., de Lint, S., van der Maarel, M.J.E.C., Gottschal, J.C. and Party, M.S.S. 2000. Biomarker evidence for widespread anaerobic methane oxidation in Mediterranean sediments by a consortium of methanogenic archaea and bacteria. *Applied and Environmental Microbiology*, **66**: 1126-1132.
- Pancost, R.D., Bouloubassi, I., Aloisi, G., Damste, J.S.S. and Party, M.S.S. 2001a. Three series of non-isoprenoidal dialkyl glycerol diethers in cold-seep carbonate crusts. *Organic Geochemistry*, **32**: 695-707.
- Pancost, R.D., Hopmans, E.C., Damsté, J.S.S. and The Medinaut shipboard Scientific party 2001b. Archaeal lipids in Mediterranean Cold Seeps: Molecular proxies for anaerobic methane oxidation. *Geochimica et Cosmochimica Acta*, **65**: 1611-1627.
- Pancost, R.D., Zhang, C.L., Tavacoli, J., Talbot, H.M., Farrimond, P., Schouten, S., Sinninghe Damste, J.S. and Sassen, R. 2005. Lipid biomarkers preserved in hydrate-associated authigenic carbonate rocks of the Gulf of Mexico. *Palaeogeography, Palaeoclimatology, Palaeoecology*, **227**: 48-66.
- Parkes, R.J., Webster, G., Cragg, B.A., Weightman, A.J., Newberry, C.J., Ferdelman, T.G., Kallmeyer, J., Jorgensen, B.B., Aiello, I.W. and Fry, J.C. 2005. Deep sub-seafloor prokaryotes stimulated at interfaces over geological time. *Nature*, **436**: 390-394.
- Patterson, W.P., Smith, G.R. and Lohmann, K.C. 1993. Continental and paleothermometry and seasonality using the isotopic composition of aragonite otoliths of freshwater fishes. In: *Climate Change in Continental Isotope Records* (Eds P.K. Swart, K.C. Lohmann, J.A. McKenzie and S. Savin), *Geophysical Monograph Series*, **78**, pp. 191-202. American Geophysical Union.
- Paull, C.K., Chanton, J.P., Neumann, A.C., Coston, J.A., Martens, C.S. and Showers, W. 1992. Indicators of Methane-Derived Carbonates and Chemosynthetic Organic Carbon Deposits: Examples from the Florida Escarpment. *Palaios*, **7**: 361-375.
- Paytan, A., Kastner, M., Martin, E.E., Macdougall, J.D. and Herbert, T. 1993. Marine barite as a monitor of seawater strontium isotope composition. *Nature*, **366**: 445-449.
- Pecher, I.A., Minshull, T.A., Singh, S.C. and Huene, R.v. 1996. Velocity structure of a bottom simulating reflector offshore Peru: Results from full waveform inversion. *Earth and Planetary Science Letters*, **139**: 459-269.
- Peckmann, J., Paul, J. and Thiel, V. 1999a. Bacterially mediated formation of diagenetic aragonite and native sulfur in Zechstein carbonates (Upper Permian, Central Germany). *Sedimentary Geology*, **126**: 205-222.
- Peckmann, J., Thiel, V., Michaelis, W., Clari, P., Gaillard, C., Martire, L. and Reitner, J. 1999b. Cold seep deposits of Beauvoisin (Oxfordian; southeastern France) and Marmorito (Miocene; northern Italy): microbially induced authigenic carbonates. *International Journal of Earth Sciences*, **88**: 60-75.
- Peckmann, J., Walliser, O.H., Riegel, W. and Reitner, J. 1999c. Signatures of Hydrocarbon Venting in a Middle Devonian Carbonate Mound (Hollard Mound) at the Hamar Laghdad (AntiAtlas, Morocco). *Facies*, **40**: 281-296.
- Peckmann, J., Gischler, E., Oschmann, W. and Reitner, J. 2001a. An Early Carboniferous seep community and hydrocarbon-derived carbonates from the Harz Mountains, Germany. *Geology*, **29**: 271-274.

- Peckmann, J., Reimer, A., Luth, U., Luth, C., Hansen, B.T., Heinicke, C., Hoefs, J. and Reitner, J. 2001b. Methane-derived carbonates and authigenic pyrite from the northwestern Black Sea. *Marine Geology*, **177**: 129-150.
- Peckmann, J., Taviani, M., Thiel, V., Aharon, P., Michaelis, W. and Reitner, J. 2001c. Microbial signatures of Miocene methane-derived carbonates from the Romagna Apennine, Italy. In: *21st IAS-Meeting of Sedimentology*, Davos, Switzerland.
- Peckmann, J., Goedert, J.L., Thiel, V., Michaelis, W. and Reitner, J. 2002. A comprehensive approach to the study of methane-seep deposits from the Lincoln Creek Formation, western Washington State, USA. *Sedimentology*, **49**: 855-873.
- Peckmann, J., Goedert, J.L., Heinrichs, T., Hoefs, J. and Reitner, J. 2003. The Late Eocene "Whiskey Creek" Methane-Seep Deposit (Western Washington State) Part II: Petrology, Stable Isotopes, and Biogeochemistry. *Facies*, **48**: 241-254.
- Peckmann, J. and Thiel, V. 2004. Carbon cycling at ancient methane-seeps. *Chemical Geology*, **205**: 443-467.
- Peckmann, J., Thiel, V., Reitner, J., Taviani, M., Aharon, P. and Michaelis, W. 2004. A Microbial Mat of a Large Sulfur Bacterium Preserved in a Miocene Methane-Seep Limestone. *Geomicrobiology Journal*, **21**: 247-255.
- Peckmann, J., Little, C.T.S., Gill, F. and Reitner, J. 2005. Worm tube fossils from the Hollard Mound hydrocarbon-seep deposit, Middle Devonian, Morocco: Palaeozoic seep-related vestimentiferans? *Palaeogeography Palaeoclimatology Palaeoecology*, **227**: 242-257.
- Perez, F.F., Rios, A.F., Castro, C.G. and Fraga, F. 1998. Mixing analysis of nutrients, oxygen and dissolved inorganic carbon in the upper and middle North Atlantic ocean east of the Azores. *Journal of Marine Systems*, **16**: 219-233.
- Perez-Belzuz, F., Alonso, B. and Ercilla, G. 1997. History of mud diapirism and trigger mechanisms in the Western Alboran Sea. *Tectonophysics*, **282**: 399-422.
- Pfannkuche, O. and Fahrteilnehmer 2006. Maria S. Merian Cruise 1 Leg 3 weekly reports, IFG-Geomar.
- Pierre, F.D., Clari, P., Cavagna, S. and Bicchi, E. 2002. The Parona chaotic complex: a puzzling record of the Messinian (Late Miocene) events in Monferrato (NW Italy). *Sedimentary Geology*, **152**: 289-311.
- Pinheiro, L.M., Ivanov, M.K., Sautkin, A.P., Akhmanov, G.G., Magalhães, V.H., Volkonskaya, A., Monteiro, H., Somoza, L., Gardner, J., Hamouni, N. and Cunha, M.R.d. 2003. Mud volcanism in the Gulf of Cadiz: results from the TTR-10 cruise. *Marine Geology*, **195**: 131-151.
- Pinheiro, L.M., Magalhães, V.H. and Monteiro, J.H. 2004. Vulcanismo de lama, hidratos de metano e potenciais ocorrências de hidrocarbonetos na Margem Sul Portuguesa profunda. *Revista Nação e Defesa, Instituto de Defesa Nacional*, **108**, 2ª Série: 139-155.
- Pinheiro, L.M., Ivanov, M., Kenyon, N.H., Magalhães, V., Somoza, L., Gardner, J., Kopf, A., Rensbergen, P.V., Monteiro, J.H. and Euromargins-MVSEIS Team 2006. Structural control of mud volcanism and hydrocarbon-rich fluid seepage in the gulf of Cadiz: Recent results from the TTR-15 cruise. In: *Fluid Seepages / Mud Volcanism in the Mediterranean and Adjacent Domains. CIESM Workshop Monographs n°29* (Eds J. Mascle, D. Sakellariou and F. Briand), pp. 53-58, Bologna, Italy.
- Price, J.F., Baringer, M.O., Lueck, R.G., Johnson, G.C., Ambar, I., Parrilla, G., Cantos, A., Kennelly, M.A. and Sanford, T.B. 1993. Mediterranean Outflow Mixing and Dynamics. *Science*, **259**: 1277-1282.
- Price, J.F. and Baringer, M.O. 1994. Outflows and Deep-Water Production by Marginal Seas. *Progress in Oceanography*, **33**: 161-200.
- Prior, D.B., Doyle, E.H. and Kaluza, M.S. 1989. Evidence for Sediment Eruption on Deep Sea Floor, Gulf of Mexico. In: *Science*, **243**, pp. 517-519.
- Puga, M.D.C.F. 2004. *Diapirismo y Estructuras de Expulsión de Gases Hidrocarburos en el Talud Continental deo Golfo de Cádiz*. Tesis Doctoral, Facultad de Ciencias del Mar, Universidad de Cadiz, Puerto Real, Cadiz, 336 pp.
- Rad, U.v., Rosch, H., Berner, U., Geyh, M., Marchig, V. and Schulz, H. 1996. Authigenic carbonates derived from oxidized methane vented from the Makran accretionary prism off Pakistan. *Marine Geology*, **136**: 55-77.
- Reeburgh, W.S. 1980. Anaerobic methane oxidation: rate depth distributions in Skan Bay sediments. *Earth and Planetary Science Letters*, **47**: 345-352.
- Reed, D.L., Silver, E.A., Tagudin, J.E., Shipley, T.H. and Vrolijk, P. 1990. Relations between Mud Volcanos, Thrust Deformation, Slope Sedimentation, and Gas Hydrate, Offshore North Panama. *Marine and Petroleum Geology*, **7**: 44-54.

- Reitner, J., Peckmann, J., Blumenberg, M., Michaelis, W., Reimer, A. and Thiel, V. 2005. Concretionary methane-seep carbonates and associated microbial communities in Black Sea sediments. *Palaeogeography, Palaeoclimatology, Palaeoecology*, **227**: 18-30.
- Rensbergen, P.V., Morley, C.K., Ang, D.W., Hoan, T.Q. and Lam, N.T. 1999. Structural evolution of shale diapirs from reactive rise to mud volcanism: 3D seismic data from the Baram delta, offshore Brunei Darussalam. *Journal of the Geological Society London*, **156**: 633–650.
- Rensbergen, P.V., Depreiter, D., Pannemans, B. and Henriët, J.-P. 2005a. Seafloor expression of sediment extrusion and intrusion at the El Arraiche mud volcano field, Gulf of Cadiz. *JOURNAL OF GEOPHYSICAL RESEARCH*, **110**: doi:10.1029/2004JF000165.
- Rensbergen, P.V., Depreiter, D., Pannemans, B., Moerkerke, G., Rooij, D.V., Marsset, B., Akhmanov, G., Blinova, V., Ivanov, M., Rachidi, M., Magalhães, V., Pinheiro, L., Cunha, M. and Henriët, J.-P. 2005b. The El Arraiche mud volcano field at the Moroccan Atlantic slope, Gulf of Cadiz. *Marine Geology*, **219**: 1-17.
- Richardson, P.L., Walsh, D., Armi, L., Schroder, M. and Price, J.F. 1989. Tracking 3 Meddies with Sofar Floats. *Journal of Physical Oceanography*, **19**: 371-383.
- Ridd, M.F. 1970. Mud Volcanoes in New-Zealand. *American Association of Petroleum Geologists Bulletin*, **54**: 601-616.
- Ritger, S., Carson, B. and Suess, E. 1987. Methane-derived authigenic carbonates formed by subduction-induced pore-water expulsion along the Oregon/Washington margin. *Geological Society of America Bulletin*, **98**: 147-156.
- Roberts, D.G. 1970. The Rif-Betic orogen in the Gulf of Cadiz. *Marine Geology*, **9**: M31-M37.
- Roberts, H.H. and Aharon, P. 1994. Hydrocarbon-Derived Carbonate Buildups of the Northern Gulf-of-Mexico Continental-Slope - a Review of Submersible Investigations. *Geo-Marine Letters*, **14**: 135-148.
- Roberts, H.H. and Carney, R. 1997. Evidence of episodic fluid, gas and sediment venting on the northern Gulf of Mexico continental slope. *Economic Geology and the Bulletin of the Society of Economic Geologists*, **92**: 863-879.
- Roberts, H.H. 2001. Fluid and Gas Expulsion on the Northern Gulf of Mexico Continental Slope: Mud-Prone to Mineral-Prone Responses. In: *Natural Gas Hydrates: Occurrence, Distribution, and Detection* (Eds C.K. Paull and W.P. Dillon), *Geophysical Monograph*, **124**, pp. 145-161. American Geophysical Union, Washington.
- Robertson, A., Emeis, K.C., Richter, C., BlancValleron, M.M., Bouloubassi, I., Brumsack, H.J., Cramp, A., DeLange, C.J., DiStefano, E., Flecker, R., Frankel, E., Howell, M.W., Janecek, T.R., JuradoRodriguez, M.J., Kemp, A.E.S., Koisumi, I., Kopf, A., Major, C.O., Mart, Y., Pribnow, D.F.C., Rabaute, A., Roberts, A., Rullkotter, J.H., Sakamoto, T., Spezzaferrri, S., Staerker, T.S., Stoner, J.S., Whiting, B.M. and Woodside, J.M. 1996. Mud volcanism on the Mediterranean Ridge: Initial results of Ocean Drilling Program Leg 160. *Geology*, **24**: 239-242.
- Robertson, A.H.F. and Kopf, A. 1998. Origin of clasts and matrix within the Milano and Napoli mud volcanoes, Mediterranean Ridge accretionary complex. In: *Proc. ODP, Scientific Results* (Eds A.H.F. Robertson, K.-C. Emeis, C. Richter and A. Camerlenghi), **160**, pp. 575-596.
- Rodrigues, C.F. and Cunha, M. 2005. Common chemosynthetic species in the Gulf of Cadiz: Some data on their spatial distribution. In: *International Conference and TTR14 Post-cruise meeting. Geosphere-Biosphere Coupling Processes: the TTR interdisciplinary approach towards studies of the European and N. African margins*, pp. 1, Marrakech, Morocco.
- Rogerson, M., Rohling, E.J., Weaver, P.P.E. and Myurray, J.W. 2005. Glacial to interglacial changes in the settling depth of the Mediterranean Outflow plume. *Paleoceanography*, **20**: doi: 10.1029/2004PA001106.
- Rollet, N., Logan, G.A., Kennard, J.M., O'Brien, P.E., Jones, A.T. and Sexton, M. 2006. Characterisation and correlation of active hydrocarbon seepage using geophysical data sets: An example from the tropical, carbonate Yampi Shelf, Northwest Australia. *Marine and Petroleum Geology*, **23**: 145-164.
- Romanek, C.S., Grossman, E.L. and Morse, J.W. 1992. Carbon Isotopic Fractionation in Synthetic Aragonite and Calcite - Effects of Temperature and Precipitation Rate. *Geochimica Et Cosmochimica Acta*, **56**: 419-430.
- Rooij, D.V., Depreiter, D., Bouimetarhan, I., Boever, E.D., Rycker, K.D., Foubert, A., Huvenne, V., Réveillaud, J., Staelens, P., Vercruysse, J., Versteeg, W. and Henriët, J.-P. 2005. First Sighting of Active Fluid Venting in the Gulf of Cadiz. *EOS*, **86**: 509-511.
- Rosenbaum, G., Lister, G.S. and Duboz, C. 2002. Reconstruction of the tectonic evolution of the western Mediterranean since the Oligocene. *Journal of the Virtual Explorer*, **8**: 107 - 126.

- Rosenbaum, J. and Sheppard, S.M.F. 1986. An Isotopic Study of Siderites, Dolomites and Ankerites at High-Temperatures. *Geochimica et Cosmochimica Acta*, **50**: 1147-1150.
- Rosenbaum, J.M. 1994. Stable isotope exchange between carbon dioxide and calcite at 900°C. *Geochimica et Cosmochimica Acta*, **58**: 3747-3753.
- Rosenfeld, W.D. and Silverman, S.R. 1959. Carbon Isotope Fractionation in Bacterial Production of Methane. *Science*, **130**: 1658-1659.
- Royden, L.H. 1993. Evolution of Retreating Subduction Boundaries Formed During Continental Collision. *Tectonics*, **12**: 629-638.
- Sager, W.W., MacDonald, I.R. and Hou, R. 2003. Geophysical signatures of mud mounds at hydrocarbon seeps on the Louisiana continental slope, northern Gulf of Mexico. *Marine Geology*, **198**: 97-132.
- Santos, L., Almeida, A., Coelho, F., Cunha, A., Lima, E., Loureiro, N., Matos, P., Salvador, S. and Pinheiro, L. 2006. Distribution, activity, and diversity of microbial communities from sediments of the mud volcano Mercator (Gulf of Cadiz). In: *Geological Processes on Deep-Water European Margins. International Conference and 15th Anniversary Training Through Reserach Post-Cruise Meeting* (Ed G.G. Akhmanov), pp. 83-86, Moscow /Zvenigorod, Russia.
- Sanz de Galdeano, C. 1990. Geologic Evolution of the Betic Cordilleras in the Western Mediterranean, Miocene to the Present. *Tectonophysics*, **172**: 107-119.
- Sartori, R., Torelli, L., Zitellini, N., Peis, D. and Lodolo, E. 1994. Eastern Segment of the Azores-Gibraltar Line (Central-Eastern Atlantic) - an Oceanic Plate Boundary with Diffuse Compressional Deformation. *Geology*, **22**: 555-558.
- Sassen, R., Losh, S.L., Cathles III, L., Roberts, H.H., Whelan, J.K., Milkov, A.V., Sweet, S.T. and DeFreitas, D.A. 2001a. Massive vein-filling gas hydrate: relation to ongoing gas migration from the deep subsurface in the Gulf of Mexico. *Marine and Petroleum Geology*, **18**: 551-560.
- Sassen, R., Sweet, S.T., Milkov, A.V., DeFreitas, D.A., Kennicutt II, M.C. and Roberts, H.H. 2001b. Stability of Thermogenic Gas Hydrate in the Gulf of Mexico: Constrains on Models of Climate Change. In: *Natural Gas Hydrates: Occurrence, Distribution, and Detection* (Eds C.K. Paull and W.P. Dillon), *Geophysical Monograph*, **124**, pp. 131-143. American Geophysical Union, Washington.
- Sassen, R., Milkov, A.V., Ozigul, E., Roberts, H.H., Hunt, J.L., Beeunas, M.A., Chanton, J.P., DeFreitas, D.A. and Sweet, S.T. 2003a. Gas venting and subsurface charge in the Green Canyon area, Gulf of Mexico continental slope: evidence of a deep bacterial methane source? *Organic Geochemistry*, **34**: 1455-1464.
- Sassen, R., Milkov, A.V., Roberts, H.H., Sweet, S.T. and DeFreitas, D.A. 2003b. Geochemical evidence of rapid hydrocarbon venting from a seafloor-piercing mud diapir, Gulf of Mexico continental shelf. *Marine Geology*, **198**: 319-329.
- Sassen, R., Roberts, H.H., Carney, R., Milkov, A.V., DeFreitas, D.A., Lanoil, B. and Zhang, C. 2004. Free hydrocarbon gas, gas hydrate, and authigenic minerals in chemosynthetic communities of the northern Gulf of Mexico continental slope: relation to microbial processes. *Chemical Geology*, **205**: 195-217.
- Sauter, E.J., Muyakshin, S.I., Charlou, J.-L., Schlüter, M., Boetius, A., Jerosch, K., Damm, E., Foucher, J.-P. and Klages, M. 2006. Methane discharge from a deep-sea submarine mud volcano into the upper water column by gas hydrate-coated methane bubbles. *Earth and Planetary Science Letters*, **243**: 354-365.
- Sautkin, A., Talukder, A.R., Comas, M.C., Soto, J.I. and Alekseev, A. 2003. Mud volcanoes in the Alboran Sea: evidence from micropaleontological and geophysical data. *Marine Geology*, **195**: 237-261.
- Savard, M.M., Beauchamp, B. and Veizer, J. 1996. Significance of aragonite cements around Cretaceous marine methane seeps. *Journal of Sedimentary Research*, **66**: 430-438.
- Scheele, N. and Hoefs, J. 1992. Carbon isotope fractionation between calcite, graphite and CO<sub>2</sub>: An experimental study. *Contribution to Mineral Petrology*, **112**: 35-45.
- Schiermeier, Q. 2003. Rapid climate change: Gas leak! *Nature*, **423**: 681-682.
- Schippers, A., Neretin, L.N., Kallmeyer, J., Ferdelman, T.G., Cragg, B.A., Parkes, R.J. and Jorgensen, B.B. 2005. Prokaryotic cells of the deep sub-seafloor biosphere identified as living bacteria. *Nature*, **433**: 861-864.
- Schluter, H.U., Prexl, A., Gaedicke, C., Roeser, H., Reichert, C., Meyer, H. and von Daniels, C. 2002. The Makran accretionary wedge: sediment thicknesses and ages and the origin of mud volcanoes. *Marine Geology*, **185**: 219-232.
- Schoell, M. 1980. The hydrogen and carbon isotopic composition of methane from natural gases of various origins. *Geochimica et Cosmochimica Acta*, **44**: 649-661.
- Schoell, M. 1988. Multiple Origins of Methane in the Earth. *Chemical Geology*, **71**: 1-10.

- Schonfeld, J.** 1997. The impact of the Mediterranean Outflow Water (MOW) on benthic foraminiferal assemblages and surface sediments at the southern Portuguese continental margin. *Marine Micropaleontology*, **29**: 211-236.
- Schonfeld, J. and Zahn, R.** 2000. Late Glacial to Holocene history of the Mediterranean Outflow. Evidence from benthic foraminiferal assemblages and stable isotopes at the Portuguese margin. *Palaeogeography, Palaeoclimatology, Palaeoecology*, **159**: 85-111.
- Schonfeld, J.** 2001. Benthic foraminifera and pore-water oxygen profiles: A re-assessment of species boundary conditions at the western Iberian Margin. *Journal of Foraminiferal Research*, **31**: 86-107.
- Schrag, D.P., Hampt, G. and Murray, D.W.** 1996. Pore fluid constraints on the temperature and oxygen isotopic composition of the glacial ocean. *Science*, **272**: 1930-1932.
- Schrag, D.P., Adkins, J.F., McIntyre, K., Alexander, J.L., Hodell, D.A., Charles, C.D. and McManus, J.F.** 2002. The oxygen isotopic composition of seawater during the Last Glacial Maximum. *Quaternary Science Reviews*, **21**: 331-342.
- Serra, N., Ambar, I. and Kase, R.H.** 2005. Observations and numerical modelling of the Mediterranean outflow splitting and eddy generation. *Deep Sea Research Part II: Topical Studies in Oceanography*, **52**: 383-408.
- Shackleton, N.J. and Kennett, J.P.** 1975a. Late Cenozoic oxygen and carbon isotopic changes at DSDP Site 284: Implications for glacial history of the northern hemisphere and Antarctica. In: *Initial Reports of the Deep Sea Drilling Project*, **29**, pp. 801-808.
- Shackleton, N.J. and Kennett, J.P.** 1975b. Paleotemperature history of the Cenozoic and the initiation of Antarctic glaciation: oxygen and carbon isotope analyses in DSDP Sites 277, 279 and 281. In: *Initial Reports of the Deep Sea Drilling Project*, **29**, pp. 743-755.
- Shackleton, N.J.** 2000. The 100,000-year ice-age cycle identified and found to lag temperature, carbon dioxide, and orbital eccentricity. *Science*, **289**: 1897-1902.
- Shapiro, R. and Fricke, H.** 2002. Tepee Buttes: Fossilized methane-seep ecosystems. In: *High Plains to Rio Grande Rift: Late Cenozoic Evolution of Central Colorado* (Eds E.M. Leonard and et al), pp. 94-101.
- Shapiro, R.S.** 2000. A Comment on the Systematic Confusion of Thrombolites. *Palaios*, **15**: 166-169.
- Shapiro, R.S. and Awramik, S.M.** 2000. Microbialite Morphostratigraphy as a Tool for Correlating Late Cambrian-Early Ordovician Sequences. *The Journal of Geology*, **108**: 170-180.
- Shapiro, R.S.** 2002. Are Proterozoic cap carbonates and isotopic excursions a record of gas hydrate destabilization following Earth's coldest intervals?: Comment. *Geology*, **30**: 761-762.
- Shapiro, R.S.** 2004. Recognition of Fossil Prokaryotes in Cretaceous Methane Seep Carbonates: Relevance to Astrobiology. *Astrobiology*, **4**: 438-449.
- Shen, G.T. and Dunbar, R.B.** 1995. Environmental Controls on Uranium in Reef Corals. *Geochimica et Cosmochimica Acta*, **59**: 2009-2024.
- Sheppard, S.M.F. and Schwarcz, H.P.** 1970. Fractionation of Carbon and Oxygen Isotopes and Magnesium between Coexisting Metamorphic Calcite and Dolomite. *Contributions to Mineralogy and Petrology*, **26**: 161-198.
- Shipley, T.H., Houston, M.H., Buffler, R.T., Shaub, F.J., Mcmillen, K.J., Ladd, J.W. and Worzel, J.L.** 1979. Seismic Evidence for Widespread Possible Gas Hydrate Horizons on Continental Slopes and Rises. *The American Association of Petroleum Geologists Bulletin*, **63**: 2204-2213.
- Shipley, T.H. and Didyk, B.M.** 1982. Occurrence of Methane Hydrates Offshore Southern Mexico. *Initial Reports of the Deep Sea Drilling Project*, **66**: 547-555.
- Sibuet, M., Juniper, S.K. and Pautot, G.** 1988. Cold-Seep Benthic Communities in the Japan Subduction Zones - Geological Control of Community-Development. *Journal of Marine Research*, **46**: 333-348.
- Sibuet, M. and Olu, K.** 1998. Biogeography, biodiversity and fluid dependence of deep-sea cold-seep communities at active and passive margins. *Deep-Sea Research II*, **45**: 517-567.
- Singh, S.C., Minshull, T.A. and Spence, G.D.** 1993. Velocity Structure of a Gas Hydrate Reflector. *Science*, **260**: 204-207.
- Sloan, E.D.** 1998. *Clathrate Hydrates of Natural Gases*, **73**. Marcel Dekker, Inc., New York, USA, 705 pp.
- Somoza, L., Maestro, A. and Lowrie, A.** 1999. Allochthonous Blocks as Hydrocarbon Traps in the Gulf of Cadiz. In: *Offshore Technology Conference*, pp. 571-576.
- Somoza, L., Diaz-del-Rio, V., Hernandez-Molina, F.J., León, R., Lobato, A., Dias, J.A., Rodero, J. and team, T.** 2000. New discovery of a mud-volcanoe field related to gas venting in the Gulf of Cadiz: Imagery of multibeam data and ultra-high resolution seismic. In: *3º Simpósio sobre a Margem Ibérica Atlântica* (Eds J.A. Dias and Ó. Ferreira), pp. 397-398. CIACOMAR, Faro.
- Somoza, L., Ivanov, M.K., Pinheiro, L.M., Maestro, A., Lowrie, A., Vazquez, J.T., Gardner, J., Medialdea, T. and Fernandez-Puga, M.C.** 2001. Structural and tectonic control of fluid seeps and mud

- volcanoes in the Gulf of Cadiz. In: *International Conference and Ninth Post-Cruise Meeting of the Training-Through-Research Programme. Devoted to the TTR 10th Anniversary* (Eds G.G. Akhmanov and A. Suzyumov), *Intergovernmental Oceanographic Commission (IOC) Workshop Report, Workshop Report N° 175*, pp. 41-42. UNESCO/IOC, Moscow-Mozhenka, Russia.
- Somoza, L., Gardner, J.M., Díaz-del-Río, V., Vázquez, J.T., Pinheiro, L.M., Hernández-Molina, F.J. and TASYO/ANASTASYA shipboard scientific parties** 2002. Numerous Methane Gas-related Sea Floor Structures Identified in Gulf of Cadiz. *EOS*, **83**: 541-549.
- Somoza, L., Díaz-del-Río, V., León, R., Ivanov, M., Fernández-Puga, M.C., Gardner, J.M., Hernández-Molina, F.J., Pinheiro, L.M., Rodero, J., Lobato, A., Maestro, A., Vázquez, J.T., Medialdea, T. and Fernández-Salas, L.M.** 2003. Seabed morphology and hydrocarbon seepage in the Gulf of Cádiz mud volcano area: Acoustic imagery, multibeam and ultra-high resolution seismic data. *Marine Geology*, **195**: 153-176.
- Srivastava, S.P., Roest, W.R., Kovacs, L.C., Oakey, G., Lévesque, S., Verhoef, J. and Macnab, R.** 1990. Motion of Iberia since the Late Jurassic - Results from Detailed Aeromagnetic Measurements in the Newfoundland Basin. *Tectonophysics*, **184**: 229-260.
- Stadnitskaia, A., Ivanov, M.K., Blinova, V., Kreulen, R. and van Weering, T.C.E.** 2006. Molecular and carbon isotopic variability of hydrocarbon gases from mud volcanoes in the Gulf of Cadiz, NE Atlantic. *Marine and Petroleum Geology*, **23**: 281-296.
- State Oil of the Republic of Azerbaijan (SOCAR)** 1996. Engineering geology of the seabed in the Guneshli, Chirag and Azeri field areas, Azerbaijan International Oil (AIOC).
- Stewart, F.J., Newton, I.L.G. and Cavanaugh, C.M.** 2005. Chemosynthetic endosymbioses: adaptations to oxic-anoxic interfaces. *Trends in Microbiology*, **13**: 439-448.
- Stöhr, M., Boetius, A. and Khalili, A.** 2005. Flow and transport in permeable sediments induced by gas seepage. In: *European Geosciences Union 2005, Geophysical Research Abstracts*, **7**, pp. 07548. European Geosciences Union, Vienna, Austria.
- Stolz, J.F., Feinstein, T.N., Salsi, J., Visscher, P.T. and Reid, R.P.** 2001. TEM analysis of microbial mediated sedimentation and lithification in modern marine stromatolites. *American Mineralogist*, **86**: 826-833.
- Suess, E., Carson, B. and Ritger, S.D.** 1985. Biological communities at vent sites along the subduction zone off Oregon. *Biological Society Washington Bulletin*, **6**: 475-484.
- Suess, E., Bohrmann, G., von Huene, R., Linke, P., Wallmann, K., Lammers, S., Sahling, H., Winckler, G., Lutz, R.A. and Orange, D.** 1998. Fluid venting in the eastern Aleutian subduction zone. *Journal of Geophysical Research-Solid Earth*, **103**: 2597-2614.
- Suess, E., Torres, M.E., Bohrmann, G., Collier, R.W., Greinert, J., Linke, P., Rehder, G., Trehu, A., Wallmann, K., Winckler, G. and Zuleger, E.** 1999. Gas hydrate destabilization: enhanced dewatering, benthic material turnover and large methane plumes at the Cascadia convergent margin. *Earth and Planetary Science Letters*, **170**: 1-15.
- Suess, E., Torres, M.E., Bohrmann, G., Collier, R.W., Rickert, D., Goldfinger, C., Linke, P., Heuser, A., Sahling, H., Heeschen, K., Jung, C., Nakamura, K., Greinert, J., Pfannkuche, O., Trehu, A., Klinkhammer, G., Whiticar, M.J., Eisenhauer, A., Teichert, B. and Elvert, M.** 2001. Sea Floor Methane Hydrates at Hydrate Ridge, Cascadia Margin. In: *Natural Gas Hydrates: Occurrence, Distribution, and Detection* (Eds C.K. Paull and W.P. Dillon), *Geophysical Monograph*, **124**, pp. 87-98. American Geophysical Union, Washington.
- Talukder, A.R.** 2003. PhD Thesis, University of Granada, Granada, 251 pp.
- Tarutani, T., Clayton, R.N. and Mayeda, T.K.** 1969. The effect of polymorphism and magnesium substitution on oxygen isotope fractionation between calcium carbonate and water. *Geochimica et Cosmochimica Acta*, **33**: 987-996.
- Teichert, B.M.A., Eisenhauer, A., Bohrmann, G., Haase-Schramm, A., Bock, B. and Linke, P.** 2003. U/Th Systematics and Ages of Authigenic Carbonates from Hydrate Ridge, Cascadia Margin: Recorders of Fluid Flow Variations. *Geochimica et Cosmochimica Acta*, **62**: 3845-3857.
- Teixeira, C.** 1950. Os vulcões de lama de Timor. *Estudos Coloniais*, **1**: 1-17.
- Terrinha, P., Matias, L., Vicente, J., Duarte, J., Luís, J., Pinheiro, L., Lourenço, N., Diez, S., Rosas, F., Magalhães, V., Valadares, V., Zitellini, N., Mendes Víctor, L. and MATESPRO Team** Submitted to Geology. Sea floor morphology and active tectonics of the Gulf of Cadiz Africa-Iberia transpressive boundary: new evidence from multibeam bathymetry and seismic reflection data. *Geology*, **Submitted**.
- Thauer, R.K.** 1998. Biochemistry of methanogenesis: a tribute to Marjory Stephenson. *Microbiology-Sgm*, **144**: 2377-2406.

- Thiebot, E. and Gutscher, M.-A.** 2006. The Gibraltar Arc seismogenic zone (part 1): Constraints on a shallow east dipping fault plane source for the 1755 Lisbon earthquake provided by seismic data, gravity and thermal modeling. *Tectonophysics*, **426**: 135-152.
- Thiel, V., Peckmann, J., Seifert, R., Wehrung, P., Reitner, J. and Michaelis, W.** 1999. Highly isotopically depleted isoprenoids: Molecular markers for ancient methane venting. *Geochimica et Cosmochimica Acta*, **63**: 3959–3966.
- Thiel, V., Peckmann, J., Richnow, H.H., Luth, U., Reitner, J. and Michaelis, W.** 2001a. Molecular signals for anaerobic methane oxidation in Black Sea seep carbonates and a microbial mat. *Marine Chemistry*, **73**: 97–112.
- Thiel, V., Peckmann, J., Schmale, O., Reitner, J. and Michaelis, W.** 2001b. A new straight-chain hydrocarbon biomarker associated with anaerobic methane cycling. *Organic Geochemistry*, **32**: 1019–1023.
- Thomson, J., Nixon, S., Summerhayes, C.P., Schonfeld, J., Zahn, R. and Grootes, P.** 1999. Implications for sedimentation changes on the Iberian margin over the last two glacial/interglacial transitions from (Th-230(excess))(0) systematics. *Earth and Planetary Science Letters*, **165**: 255-270.
- Thunell, R., Rio, D., Sprovieri, R. and Vergnaud-Grazzini, C.** 1991. An overview of the post-Messinian paleoenvironmental history of the Mediterranean. *Palaeoceanography*, **6**: 143–164.
- Torelli, L., Sartorit, R. and Zitellini, N.** 1997. The giant chaotic body in the Atlantic Ocean off Gibraltar: new results from a deep seismic reflection survey. *Marine and Petroleum Geology*, **14**: 125-138.
- Torres, M.E., Mix, A.C., Kinports, K., Haley, B., Klinkhammer, G.P., McManus, J. and de Angelis, M.A.** 2003. Is methane venting at the seafloor recorded by delta C-13 of benthic foraminifera shells? *Paleoceanography*, **18**: doi:10.1029/2002PA000824.
- Torres-Roldan, R.L., Poli, G. and Peccerillo, A.** 1986. An Early Miocene Arc-Tholeiitic Magmatic Dike Event from the Alboran Sea - Evidence for Precollisional Subduction and Back-Arc Crustal Extension in the Westernmost Mediterranean. *Geologische Rundschau*, **75**: 219–234.
- Tortella, D., Torne, M. and PerezEstaun, A.** 1997. Geodynamic evolution of the eastern segment of the Azores-Gibraltar zone: The Goringe Bank and the Gulf of Cadiz region. *Marine Geophysical Researches*, **19**: 211-230.
- Tryon, M.D. and Brown, K.M.** 2001. Complex flow patterns through Hydrate Ridge and their impact on seep biota. *Geophysical Research Letters*, **28**: 2863-2866.
- Tryon, M.D., Brown, K.M. and Torres, M.E.** 2002. Fluid and chemical flux in and out of sediments hosting methane hydrate deposits on Hydrate Ridge, OR, II: Hydrological processes. *Earth and Planetary Science Letters*, **201**: 541-557.
- Ussler, W. and Paull, C.K.** 1995. Effects of Ion-Exclusion and Isotopic Fractionation on Pore-Water Geochemistry During Gas Hydrate Formation and Decomposition. *Geo-Marine Letters*, **15**: 37-44.
- Ussler, W. and Paull, C.K.** 2001. Ion Excursion Associated With Marine Gas Hydrate Deposits. In: *Natural Gas Hydrates: Occurrence, Distribution, and Detection* (Eds C.K. Paull and W.P. Dillon), *Geophysical Monograph*, **124**, pp. 41-51. American Geophysical Union, Washington.
- Valentine, D.L. and Reeburgh, W.S.** 2000. New perspectives on anaerobic methane oxidation (Minireview). *Environmental Microbiology*, **2**: 477-484.
- Van Lith, Y., Warthmann, R., Vasconcelos, C. and McKenzie, J.A.** 2003a. Sulphate-reducing bacteria induce low-temperature Ca-dolomite and high Mg-calcite formation. *Geobiology*, **1**: 71-79.
- Van Lith, Y., Warthmann, R., Vasconcelos, C. and McKenzie, J.A.** 2003b. Microbial fossilization in carbonate sediments: a result of the bacterial surface involvement in dolomite precipitation. *Sedimentology*, **50**: 237-245.
- Van Rooij, D., Huvenne, V., Moerkerke, G. and Henriët, J.-P.** 2002. Cruise Report: Belgica 02/12 CADIPOR, Gulf of Cadiz, Renard Centre of Marine Geology, Ghent University, Ghent.
- Vanne, J.-R. and Mougnot, D.** 1981. *La Plate-forme Continentale du Portugal et des provinces adjacentes: Analyse Geomorphologique*. Memórias dos Serviços Geológicos de Portugal, **28**. Direcção Geral de Geologia e Minas, Lisboa, 86 pp.
- Vasconcelos, C.** 1994. *Modern dolomite precipitation and diagenesis in a coastal mixed water system (Lagoa Vermelha, Brazil): A microbial model for dolomite formation under anoxic conditions*. PhD thesis, Swiss Federal Institute of Technology Zurich - ETH, Zurich, 134 pp.
- Vasconcelos, C., McKenzie, J.A., Bernasconi, S., Grujic, D. and Tien, A.J.** 1995. Microbial mediation as a possible mechanism for natural dolomite formation at low temperatures. *Nature*, **377**: 220-222.
- Vasconcelos, C. and McKenzie, J.A.** 1997. Microbial mediation of modern dolomite precipitation and diagenesis under anoxic conditions (Lagoa Vermelha, Rio de Janeiro, Brazil). *Journal of Sedimentary Research*, **67**: 378-390.

- Vasconcelos, C., McKenzie, J.A., Warthmann, R. and Bernasconi, S.M. 2005. Calibration of the  $\delta^{18}\text{O}$  paleothermometer for dolomite precipitated in microbial cultures and natural environments. *Geology*, **33**: 317-320.
- Vázquez, J.T., Medialdea, T., Maestro, A., Somosa, L., Diaz-del-Rio, V., Vegas, R., Catalán, M. and Fernandez-Puga, M.C. 2000. Tectónica Compressiva en el Golfo de Cádiz. In: *3º Simpósio sobre a Margem Ibérica Atlântica* (Eds J.A. Dias and Ó. Ferreira), pp. 389-390. CIACOMAR, Faro.
- Vázquez, J.T., Medialdea, T., Fernandez-Puga, M.C., Barranco, E.L., Hernandez-Molina, F.J., Somoza, L., Vegas, R., Diaz-del-Rio, V., Maestro, A. and Terrinha, P. 2003. Terminación de las unidades aloctonas de Cadiz sobre el Banco del Guadalquivir. Deformaciones asociadas. In: *4<sup>th</sup> Symposium on the Atlantic Iberian Continental Margins* (Eds F. Vilas et al.), **Special Volume on the 4<sup>th</sup> Symposium on the Atlantic Iberian Continental Margins, *Thalassas*, 19 (2a)**, pp. 77-78, Vigo Spain.
- Vernette, G., Mauffret, A., Bobier, C., Briceno, L. and Gayet, J. 1992. Mud Diapirism, Fan Sedimentation and Strike-Slip Faulting, Caribbean Colombian Margin. *Tectonophysics*, **202**: 335-349.
- Voelker, A. 2005. Iberian margin water isotopic compositions, pp. Unpublished data from AV of water isotopic composition on the Iberian margin, data from the Paleol and the Swim cruises.
- Voelker, A.H.L., Lebreiro, S.M., Schönfeld, J., Cacho, I., Erlenkeuser, H. and Abrantes, F. 2006. Mediterranean outflow strengthening during northern hemisphere coolings: A salt source for the glacial Atlantic? *Earth and Planetary Science Letters*, **245**: 39-55.
- Vogt, P.R., Gardner, J. and Crane, K. 1999. The Norwegian-Barents-Svalbard (NBS) continental margin: Introducing a natural laboratory of mass wasting, hydrates, and ascent of sediment, pore water, and methane. *Geo-Marine Letters*, **19**: 2-21.
- von Rad, U., Berner, U., Delisle, G., Doose-Rolinski, H., Fechner, N., Linke, P., Luckge, A., Roeser, H.A., Schmaljohann, R., Wiedicke, M. and SONNE 122/130 Scientific Parties 2000. Gas and fluid venting at the Makran accretionary wedge off Pakistan. *Geo-Marine Letters*, **20**: 10-19.
- Waelbroeck, C., Labeyrie, L., Michel, E., Duplessy, J.C., McManus, J.F., Lambeck, K., Balbon, E. and Labracherie, M. 2002. Sea-level and deep water temperature changes derived from benthic foraminifera isotopic records. *Quaternary Science Reviews*, **21**: 295-305.
- Wallmann, K., Linke, P., Suess, E., Bohrmann, G., Sahling, H., Schluter, M., Dahlmann, A., Lammers, S., Greinert, J. and Mirbach, N.v. 1997a. Quantifying fluid flow, solute mixing, and biogeochemical turnover at cold vents of the eastern Aleutian subduction zone. *Geochimica et Cosmochimica Acta*, **61**: 5209-5219.
- Wallmann, K., Linke, P., Suess, E., Bohrmann, G., Sahling, H., Schluter, M., Dahlmann, A., Lammers, S., Greinert, J. and von Mirbach, N. 1997b. Quantifying fluid flow, solute mixing, and biogeochemical turnover at cold vents of the eastern Aleutian subduction zone. *Geochimica et Cosmochimica Acta*, **61**: 5209-5219.
- Warthmann, R., Lith, Y.v., Vasconcelos, C., McKenzie, J.A. and Karpoff, A.M. 2000. Bacterially induced dolomite precipitation in anoxic culture experiments. *Geology*, **28**: 1091-1094.
- Warthmann, R., Vasconcelos, C. and McKenzie, J.A. 2005. Lithifying microbial mats in Lagoa Vermelha, Brazil: A model system for Precambrian carbonate formation? In: *European Geosciences Union 2005, Geophysical Research Abstracts*, **7**, pp. 01630. European Geosciences Union, Vienna, Austria.
- Wefer, G. and Berger, W.H. 1991. Isotope paleontology: growth and composition of extant calcareous species. *Marine Geology*, **100**: 207-248.
- Wellsbury, P., Goodman, K., Cragg, B.A. and Parkes, R.J. 2000. The geomicrobiology of deep marine sediments from Blake Ridge containing methane hydrate (sites 994, 995, and 997). In: *Proceedings of the Ocean Drilling Program, Scientific Results* (Eds C.K. Paull, R. Matsumoto, P.J. Wallace and W.P. Dillon), **164**, pp. 379-391.
- Werne, J.P., Haese, R.R., Zitter, T., Aloisi, G., Bouloubassi, I., Heijs, S., Fiala-Medioni, A., Pancost, R.D., Sinninghe Damste, J.S., de Lange, G., Forney, L.J., Gottschal, J.C., Foucher, J.P., Mascle, J., Woodside, J. and MEDINAUT MEDINETH Shipboard Sci Party 2004. Life at cold seeps: a synthesis of biogeochemical and ecological data from Kazan mud volcano, eastern Mediterranean Sea. *Chemical Geology*, **205**: 367-390.
- Westbrook, G.K. and Smith, M.J. 1983. Long Decollements and Mud Volcanos - Evidence from the Barbados Ridge Complex for the Role of High Pore-Fluid Pressure in the Development of an Accretionary Complex. *Geology*, **11**: 279-283.
- Whiticar, M.J. 1999. Carbon and hydrogen isotope systematics of bacterial formation and oxidation of methane. *Chemical Geology*, **161**: 291-314.
- Whitman, W.B., Coleman, D.C. and Wiebe, W.J. 1998. Prokaryotes: The unseen majority. *Proceedings of the National Academy of Sciences of the United States of America*, **95**: 6578-6583.

- Wiedicke, M., Neben, S. and Spiess, V.** 2001. Mud volcanoes at the front of the Makran accretionary complex, Pakistan. *Marine Geology*, **172**: 57-73.
- Wiedicke, M., Sahling, H., Delisle, G., Faber, E., Neben, S., Beiersdorf, H., Marchig, V., Weiss, W., von Mirbach, N. and Afiat, A.** 2002. Characteristics of an active vent in the fore-arc basin of the Sunda Arc, Indonesia. *Marine Geology*, **184**: 121-141.
- Woodside, J.M., Ivanov, M.K. and Limonov, A.F.** (Eds) 1997a. *Neotectonics and fluid flow through seafloor sediments in the Eastern Mediterranean and Black Seas. Part I: Eastern Mediterranean Sea. Preliminary results of geological and geophysical investigations during the ANAXIPROBE/TTR-6 cruise of R/V Gelendzhik, July-August 1996.* (Ed UNESCO), *Intergovernmental Oceanographic Commission technical series*, **48**. United Nations Educational, Scientific and Cultural Organization, Paris, 128 pp.
- Woodside, J.M., Ivanov, M.K. and Limonov, A.F.** (Eds) 1997b. *Neotectonics and fluid flow through seafloor sediments in the Eastern Mediterranean and Black Seas. Part II: Black Sea. Preliminary results of geological and geophysical investigations during the ANAXIPROBE/TTR-6 cruise of R/V Gelendzhik, July-August 1996.* (Ed UNESCO), *Intergovernmental Oceanographic Commission technical series*, **48**. United Nations Educational, Scientific and Cultural Organization, Paris, 226 pp.
- Woodside, J.M., Ivanov, M.K., Limonov, A.F. and Expeditions, S.S.o.t.A.** 1998. Shallow gas and gas hydrates in the Anaximander Mountains region, eastern Mediterranean Sea. In: *Gas Hydrates: Relevance to World Margin Stability and Climate Change* (Eds J.-P. Henriot and J. Mienert), **137**, pp. 177-193. Geological Society, London.
- Wright, D.T.** 2000. Benthic Microbial Communities and Dolomite Formation in Marine and Lacustrine Environments - A New Dolomite Model. In: *Marine Authigenesis: From Global to Microbial* (Eds C.R. Glenn, L. Prévôt-Lucas and J. Lucas), *Special Publication*, **66**, pp. 7-20, Oklahoma, USA.
- Yamano, M., Foucher, J.P., Kinoshita, M., Fisher, A., e, R.D.H. and ODP Leg 131 Shipboard Scientific Party** 1992. Heat flow and fluid flow regime in the western Nankai accretionary prism. *Earth and Planetary Science Letters*, **109**: 451-462.
- Yefremova, A.G. and Zhizhchenko, B.P.** 1974. Occurrence of crystal hydrates of gas in sediments of modern marine basins. *Doklady Akademii Nauk SSSR*, **214**: 1179-1181.
- Yusifov, M. and Rabinowitz, P.D.** 2004. Classification of mud volcanoes in the South Caspian Basin, offshore Azerbaijan. *Marine and Petroleum Geology*, **21**: 965-975.
- Zenk, W. and Armi, L.** 1990. The Complex Spreading Pattern of Mediterranean Water Off the Portuguese Continental-Slope. *Deep-Sea Research Part a-Oceanographic Research Papers*, **37**: 1805-1823.

## **Publications**

Articles in journals included in Science Citation Index published during the work developed in this thesis, to which the Author had contributed. The complete articles are included in the CD-ROM of the Appendixes.

- Pinheiro, L.M., Ivanov, M.K., Sautkin, A.P., Akhmanov, G.G., **Magalhães, V.H.**, Volkonskaya, A., Monteiro, H., Somoza, L., Gardner, J., Hamouni, N. and Cunha, M.R. 2003. Mud volcanism in the Gulf of Cadiz: results from the TTR-10 cruise. *Marine Geology*, 195: 131-151.
- Rensbergen, P.V., Depreiter, D., Pannemans, B., Moerkerke, G., Rooij, D.V., Marsset, B., Akhmanov, G., Blinova, V., Ivanov, M., Rachidi, M., **Magalhães, V.**, Pinheiro, L., Cunha, M. and Henriot, J.-P. 2005. The El Arraiche mud volcano field at the Moroccan Atlantic slope, Gulf of Cadiz. *Marine Geology*, 219: 1-17.
- Hensen, C., Nuzzo, M., Hornibrook, E., Pinheiro, L.M., Bock, B., **Magalhães, V.H.** and Brückmann, W. in press. Sources of mud volcano fluids in the Gulf of Cadiz - indications for hydrothermally altered fluids. *Geochimica et Cosmochimica Acta*.
- Niemann, H., Duarte, J., Hensen, C., Omoregie, E., **Magalhães, V.H.**, Elvert, M., Pinheiro, L.M., Kopf, A. and Boetius, A. 2006. Microbial methane turnover at mud volcanoes of the Gulf of Cadiz. *Geochimica et Cosmochimica Acta*, 70: 5336-5355 doi:10.1016/j.gca.2006.08.010.



fauna that includes several species of molluscs, polychaetes, pogonophoran worms, crustaceans, echinoderms and some fragments of dead coral (*Madrepora* and *Lophelia*). Carbonate crusts were recovered from the Student mud volcano. The Ginsburg mud volcano, discovered during the previous TTR-9 cruise, was revisited and gas hydrates recovered once again. A new mud volcano was also discovered in the Spanish margin, Tasyo, where evidence was found of coral build-ups on the hard substratum of the mud volcanic edifice.

© 2002 Elsevier Science B.V. All rights reserved.

*Keywords:* mud volcanoes; gas hydrates; hydrocarbon seepage; cold seeps; chemosynthetic communities; Gulf of Cadiz; South Portuguese margin; South Spanish margin; Northwest Moroccan margin

## 1. Introduction

A considerable quantity of work on the topics of mud volcanism, submarine gas hydrates, cold seeps and hydrocarbon-rich fluid venting has been done over more than two decades, both by industry and academia (see, for example, references in Ginsburg and Soloviev, 1998, and in Milkov, 2000). A particular effort has been put into understanding the role of tectonics in the occurrence of mud volcanism, particularly in compressional regimes (e.g. Westbrook and Smith, 1983; Barber et al., 1986; Limonov et al., 1996; Galindo-Zaldivar et al., 1996; Woodside et al., 1997; Çifçi et al., 1997; Suess et al., 1999). Also, in the last few years, the international scientific community has devoted much attention to the widespread occurrence of gas hydrates (mainly methane, which is a greenhouse gas) in the ocean sub-bottom sediments and their importance to global carbon fluxes, climate change, slope instabilities and as a potential energy resource for the future (e.g. Hovland and Judd, 1988; Mienert et al., 1996; Dickens et al., 1997; Judd et al., 1997; Nisbet and Piper, 1998; Ginsburg and Soloviev, 1998; Henriot and Mienert, 1998; Baraza et al., 1999; Milkov, 2000; Paull and Dillon, 2001).

The occurrence of mud volcanism, cold seepage, hydrocarbon venting and gas hydrates in the Gulf of Cadiz has been intensively investigated since 1996 (Baraza and Ercilla, 1996; Baraza et al., 1999; Gardner, 2001; Kenyon et al., 2000; Ivanov et al., 2000, 2001; Somoza et al., 2000; Mazurenko et al., 2001). Within the framework of the UNESCO/IOC Training Through Research Program, two research cruises have investigated the Gulf of Cadiz for this specific purpose: TTR-9, in 1999, and TTR-10, in 2000. Dur-

ing the TTR-9 cruise (Gardner, 2001; Kenyon et al., 2000), a large mud volcano field was discovered in the Moroccan and Spanish margins of the Gulf of Cadiz. This discovery was based on the interpretation of a side-scan sonar mosaic and multibeam bathymetry (SEAMAP) acquired in that area by the Marine Physics Branch of the Naval Research Laboratory (NRL), Washington, DC, USA, in cooperation with the Hawaii Mapping Group and the Naval Oceanographic Office, in 1992. This was followed by three other cruises: (1) two cruises in the Spanish and Portuguese sectors of the Gulf of Cadiz, within the framework of the Spanish Tasyo project, where, besides new mud volcanoes, carbonate chimney structures related to fluid venting were recovered (Somoza et al., 2000, 2003); (2) the TTR-10 cruise (Leg 2).

In this paper we present the results of the TTR-10, Leg 2. The main objective of this cruise was to investigate several seafloor structures observed on the NRL side-scan mosaic, that occur in the South Portuguese, the Western Moroccan and the Spanish margins of the Gulf of Cadiz. These often exhibit a significant morphological expression on the multibeam bathymetry and were interpreted as mud volcanoes. They were investigated with seismic profiling, long-range side-scan sonar (OKEAN), hull-mounted 3.5-kHz profiler, TV grab and were confirmed by coring to be mud volcanoes (Fig. 1). This work complements the previous work done in the Moroccan and Spanish margins during the TTR-9 cruise.

## 2. Geological setting

The Gulf of Cadiz has had a very complex geological history and has undergone several episodes

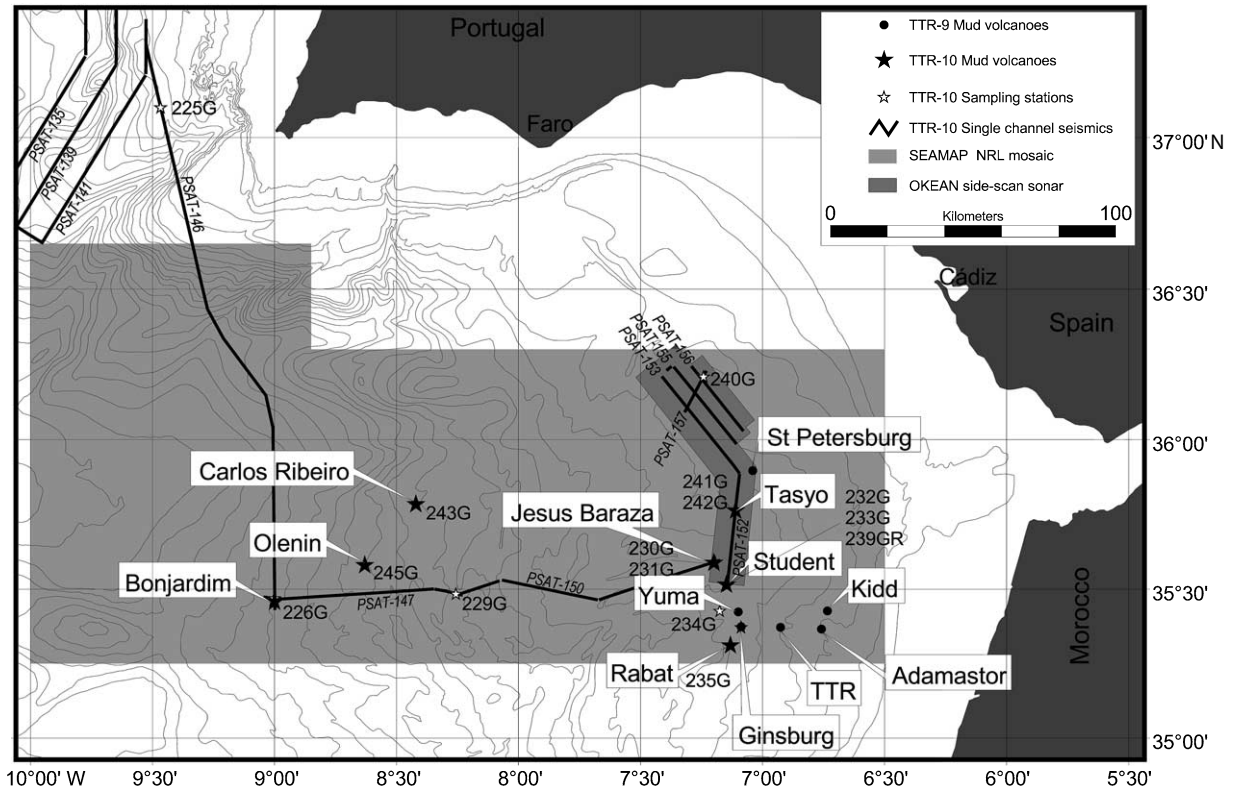


Fig. 1. Map of South Iberia and Gulf of Cadiz, showing the location of the mud volcanoes discovered in the area during the TTR-9 (circles) and the TTR-10 cruises (stars). Also shown the area covered by the NRL side-scan mosaic (shaded gray) and the main core locations, the single-channel seismic lines and the OKEAN side-scan sonar coverage obtained during the TTR-10 cruise.

of rifting, compression and strike-slip motion, since the Triassic (Wilson et al., 1989; Dewey et al., 1989; Maldonado et al., 1999). During the Mesozoic and the Early Cenozoic, the area was undergoing rifting, with the formation of half-graben structures and carbonate platforms (Maldonado et al., 1999). The westward migration of the Gibraltar arc during the Late Tortonian caused the Gulf of Cadiz to form as a forearc basin and induced the emplacement of an olistostrome, in an accretionary wedge-type depositional environment, strongly deforming the sediments derived from the South Iberian and North African margins of Thetys (Maldonado and Comas, 1992; Maldonado et al., 1999) (Fig. 2). The end of the emplacement of the olistostrome took place in the Late Miocene and coincided with an accelerated tectonic subsidence and the development of thick

progradational and aggradational depositional sequences.

Throughout this area, extensive mud volcanism (Fig. 2), mud diapirism, carbonate mounds and chimney structures related to hydrocarbon-rich fluid venting are observed (Somoza et al., 2003). The observed mud volcanism has been interpreted as indicating the existence at depth of gas-rich overpressured sediments (Somoza et al., 2000). The migration of these fluids through the sediments to the seafloor appears, in some places, to have been controlled by faulting, since some of the mud volcanoes are located along major NW–SE and NE–SW trending faults identifiable on the NRL side-scan imagery (Gardner, 2001). The migration of the fluids along these faults is possibly related both to along-slope gravitational sliding and to the tectonic compression of the

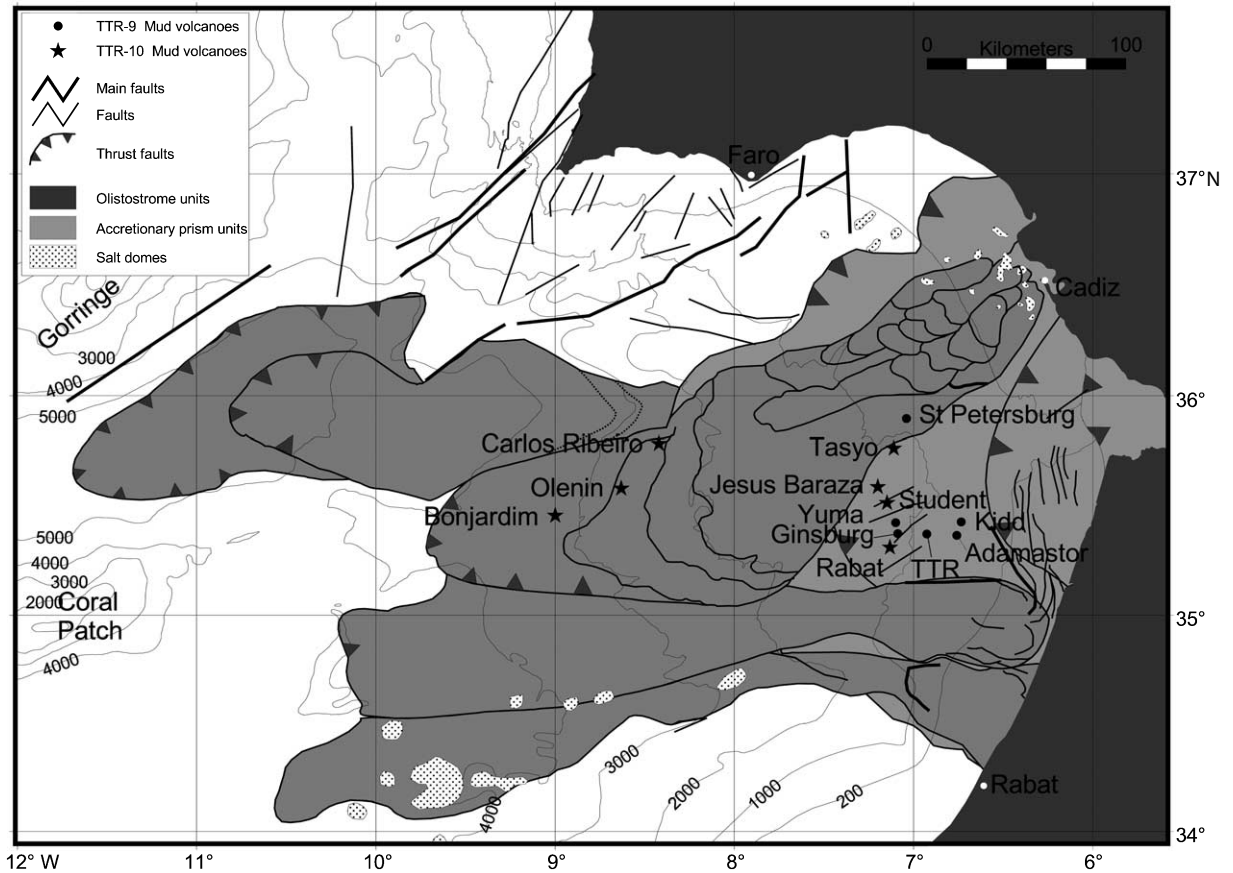


Fig. 2. Geological setting of the study area. (Modified from Maldonado et al., 1999; Somoza et al., 1999). A simplified bathymetry and the location of the mud volcanoes discovered during the TTR-9 and TTR-10 cruises are also shown.

olistostrome and accretionary complex of the Gulf of Cadiz, due to the Africa–Eurasia convergence (Somoza et al., 2000). It has also been suggested that some of the widespread shallow fluid venting on the seafloor, particularly in the Northern Gulf of Cadiz, could be explained by the destabilization of gas hydrate-rich sediments in contact with the Mediterranean Outflow Water (MOW) (Somoza et al., 2000).

### 3. Geophysical data acquisition

During the TTR-10 cruise, additional geophysical surveys with airgun single-channel seismic, OKEAN side-scan sonar and 3.5-kHz profiler

were carried out in the areas chosen for bottom sampling (Fig. 1).

#### 3.1. Seismic reflection profiles

Single-channel seismic reflection profiles were acquired in the Gulf of Cadiz area during the TTR-10 cruise. The source consisted of one 3.5-l airgun, at a pressure of 120 bar (12 MPa), towed at a depth of approximately 2–2.5 m and fired every 10 s (i.e. approximately every 30 m). The streamer consisted of one active section, 7.5 m long, with 16 hydrophones, towed at a depth of approximately 2.5–3 m. The offset between the seismic source and the middle of the hydrophone array was 180 m. The signals were analogue-fil-

Table 1  
Location of the cores (G) and the TV-grab station (GR), obtained during the TTR-10 cruise

Core N.	Latitude	Longitude	Depth (m)	Site
AT-226G	35°27.603'N	09°00.023'W	3059	Bonjardim mud volcano
AT-227G	35°27.851'N	09°00.028'W	3060	Bonjardim mud volcano
AT-228G	35°28.234'N	09°00.030'W	3150	Bonjardim mud volcano
AT-229G	35°29.129'N	08°15.442'W	1962	diapiric structure
AT-230G	35°35.539'N	07°11.693'W	1159	Jesus Baraza mud volcano
AT-231G	35°35.452'N	07°12.048'W	1091	Jesus Baraza mud volcano
AT-232G	35°30.849'N	07°08.744'W	940	Student mud volcano
AT-233G	35°31.068'N	07°08.964'W	955	Student mud volcano
AT-234G	35°25.724'N	07°10.556'W	1140	diapiric structure
AT-235G	35°18.858'N	07°07.997'W	1060	Rabat mud volcano
AT-236G	35°22.409'N	07°05.328'W	910	Ginsburg mud volcano
AT-237G	35°22.410'N	07°05.343'W	910	Ginsburg mud volcano
AT-238G	35°22.409'N	07°05.330'W	910	Ginsburg mud volcano
AT-239GR	35°30.853'N	07°08.816'W	955	Student mud volcano
AT-240G	36°12.624'N	07°14.540'W	845	submarine channel
AT-241G	35°45.967'N	07°06.720'W	1100	Tasyo mud volcano
AT-242G	35°45.962'N	07°06.684'W	1098	Tasyo mud volcano
AT-243G	35°47.217'N	08°25.313'W	2200	Carlos Ribeiro mud volcano
AT-244G	35°47.221'N	08°25.333'W	2200	Carlos Ribeiro mud volcano
AT-245G	35°35.007'N	08°37.901'W	2614	Olenin mud volcano
AT-246G	35°27.610'N	09°00.030'W	3060	Bonjardim mud volcano

tered to 50–250 Hz during the acquisition stage. The sample interval was 1 ms and the record length 3 s. The data were acquired digitally using software developed by Moscow State University (MSU). Preliminary processing was done on board with RadExPro software, provided to the Unesco MSU Centre for Marine Geosciences by GSD Productions, Moscow, Russia. The basic processing sequence, after the definition of the source-receiver geometry, consisted of the application of static shift corrections, amplitude recovery by spherical divergence correction, and Butterworth bandpass filtering (20–230 Hz).

### 3.2. OKEAN side-scan coverage

Due to time constraints and also to the fact that the NRL mosaic provided excellent detail in the western part of the survey, where the geology appears to be simpler, only the eastern part of the study area (Lines PSAT 152–156) was surveyed with the long-range 10-kHz OKEAN side-scan sonar available on the *Professor Logachev* (Fig. 1). In this area, the geology is very complex

with a strong mix of tectonic and sedimentary features. This survey was necessary to provide a more detailed image of the sites selected for coring. It covers the Tasyo mud volcano and part of the Tasyo field in the north.

## 4. Bottom sampling results

A total of 21 sites in the South Portuguese, the Western Moroccan and the Spanish margins of the Gulf of Cadiz were chosen for sampling (see location in Table 1). The precise sampling location was based on the interpretation of the NRL mosaic, complemented by additional seismic, 3.5-kHz profiler and OKEAN side-scan imagery. Twenty gravity cores were taken, with a total recovery of 36.87 m. One site was investigated with a TV-controlled grab system (Student mud volcano). The location of the 13 most important cores is depicted in Fig. 1. Macrofauna was recovered from the top 30 cm of each gravity core and from sieved sediments of the grab sample. The listing of the taxa recovered is shown in Table 2.

Table 2  
Taxonomical list of the macrofauna collected during TTR-10 in the mud volcanoes of the Gulf of Cadiz

Taxa	Sampling stations
Porifera	
undetermined species	S (239-GR)
Cnidaria	
Hydrozoa	S (232-G, 239-GR); R (235-G)
Anthozoa	S (233-G, 239-GR)
Sipuncula	
undetermined species	T (242-G); S (239-GR)
Annelida	
Polychaeta	
<i>Nothria hispanica</i>	(241-G)
Maldanidae	B (246-G)
undetermined species	S (233-G; 239-GR)
Pogonophora	
<i>Oligobrachia</i> sp.	B (246-G); CR (244-G)
<i>Polybrachia</i> sp.	B (227-G)
<i>Siboglinum</i> sp.	JB (231-G); S (232-G, 239-GR); R (235-G); G (236-G, 237-G, 238-G)
undetermined species	B (226-G; 227-G); CR (243-G)
Mollusca	
Gastropoda	
undetermined species	S (239-GR)
Bivalvia	
Cuspidariidae	S (239-GR)
<i>Limopsis</i> sp.	S (232-G, 239-GR)
Thyasiridae	CR (243-G)
Arthropoda	
Pycnogonida	
<i>Hedgepethia atlantica</i>	S (239-GR)
Crustacea	
Cirripedia	S (239-GR)
<i>Procampylaspis</i> sp.	S (239-GR)
<i>Liropus</i> cf. <i>elongatus</i>	S (239-GR)
Tanaidacea sp. 1	B (228-G)
Tanaidacea sp. 2	S (239-GR)
Anthuridae	S (239-GR)
<i>Munidopsis</i> sp.	S (232-G)
Echinodermata	
Echinidae	S (239-GR)
Ophiuridae	S (239-GR)

Portuguese sector: Bonjardim (B) and Carlos Ribeiro (CR); Spanish sector: Tasyo (T); Moroccan sector: Jesus Baraza (JB), Student (S), Rabat (R) and Ginsburg (G).

#### 4.1. The South Portuguese field

Several structures observed on the NRL SEA-MAP mosaic of the deep South Portuguese margin of the Gulf of Cadiz (water depths between

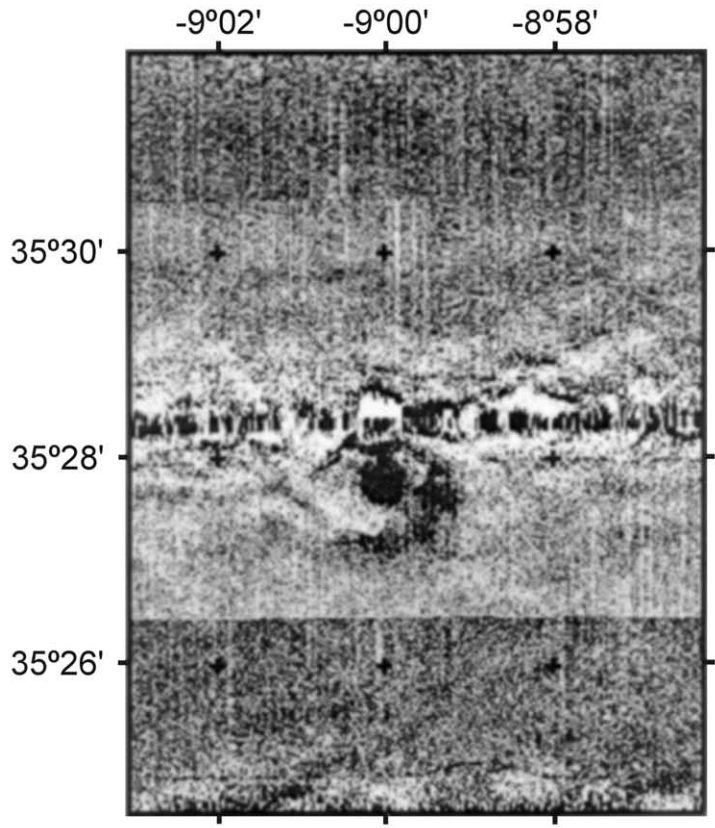
ca. 2000 and 3200 m) were interpreted as either mud volcanoes or gas seepage structures. Four sites, expressed by high reflectivity sub-circular spots, were chosen for bottom sampling. Three of them were confirmed by coring to be new mud volcanic structures and were named: Bonjardim, Carlos Ribeiro and Olenin.

##### 4.1.1. The Bonjardim mud volcano

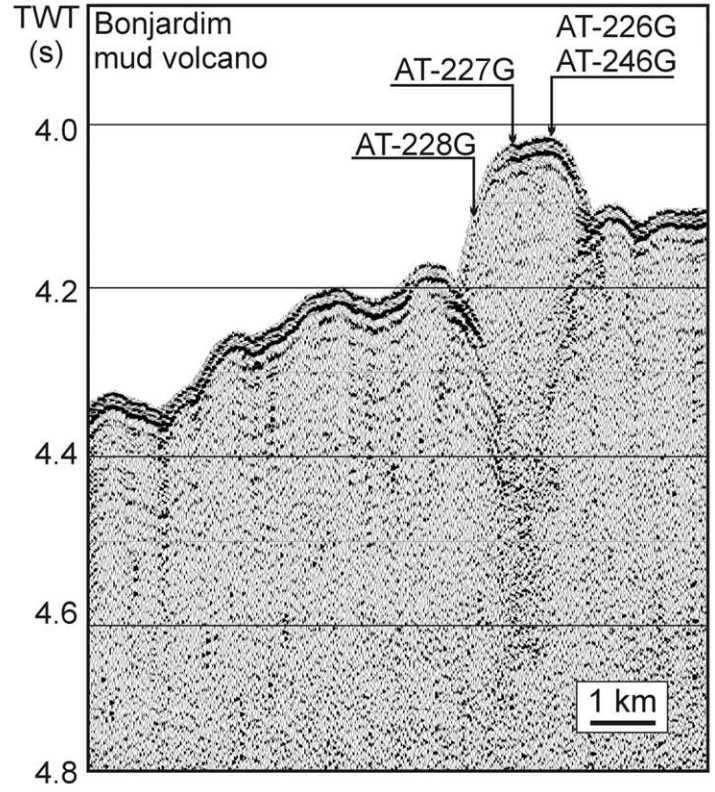
This was the first structure, presumed to be a mud volcano, investigated during the TTR-10 cruise. It is located at 35°27.6'N and 09°00.0'W. On the NRL side-scan mosaic, it appears as an approximately circular, isolated feature, with a diameter of ca. 1 km and a strong backscatter (Fig. 3a). The single-channel seismic profiles PSAT-146 and PSAT-147 reveal that it has a height of approximately 100 m (Fig. 3b) with a seafloor depression at the rim of the cone. Four cores were taken on this structure, all of which recovered mud breccia and confirmed it to be a mud volcano.

The first core, AT-226G, was taken from the top of the Bonjardim mud volcano, at a depth of 3059 m (Fig. 3b). The recovery consisted of 151 cm of mud breccia matrix, supporting angular and subangular clasts of variable size (from millimetric to 3 cm) and lithology, mainly represented by brownish gray mudstone. There was no pelagic veneer, and only the uppermost few cm of the mud volcanic deposits were oxidized, suggesting that this mud volcano was recently active. Different layers of mud breccia were observed along the core, alternating lighter and water saturated with darker and more consolidated mud breccia. This may indicate different flows and stages of activity of the volcano. A strong H<sub>2</sub>S smell was detected and Pogonophora (two undetermined species) were recovered from this core.

The second core, AT-227G (234 cm), was taken from a terrace just below the top of the mud volcano, at a depth of 3066 m (Figs. 1 and 3); the mud breccia recovered was very similar to the one previously sampled (although it was more homogenous) but the top 42 cm comprised a marly sediment, soupy in the first 6 cm and then bioturbated and rich in Foraminifera. A strong H<sub>2</sub>S smell was present and a Pogonophora-rich



(a)



(b)

Fig. 3. Bonjardim mud volcano. (a) Side-scan image (NRL mosaic); (b) single-channel seismic profile across the structure (southern end of Line PSAT 146). See Fig. 1 for location. Also shown are the locations of the cores taken during the TTR-10 cruise (AT-226G, AT-227G, AT-228G and AT-246G).

(mainly *Polybrachia* sp.) layer was observed at the very top of the core, indicating active fluid venting. Foraminifera and empty polychaete tubes were also recovered from this core.

A third core, AT-228G (283 cm), was taken from the flank of the mud volcano, at a depth of 3150 m, in order to define the extension of the mud flows (Fig. 3). The recovery consisted of a thick intercalation of olive brown pelagic marl and brown marly turbidites enriched in Foraminifera, easily distinguishable due to the sharp boundaries and the coarser texture. Bioturbation activity was very strong throughout the whole core. No mud breccia was recovered. One crustacean (Tanaidacea) and empty Pogonophora tubes were recovered from this core.

Finally, one last core, AT-246G (306 cm), was taken, at a depth of 3060 m, on the top of the Bonjardim mud volcano, in an attempt to recover gas hydrates. The recovery was comparable to that of the station AT-226G, with a 12-cm layer of soupy and oxidized structureless mud breccia at the top, with angular and subangular clasts of different size and lithology. The contact between the oxidized and the unoxidized parts was very sharp. Between 135 and 156 cm, an interval of darker mud breccia was observed. Gas hydrates, in the form of small crystals, were finally sampled and found below 156 cm. A strong H<sub>2</sub>S smell was evident and some small pyrite crystals were observed. Foraminifera, Pogonophora (*Oligobrachia* sp.) and polychaete fragments (Malidanidae) were recovered from this core.

#### 4.1.2. The Carlos Ribeiro mud volcano

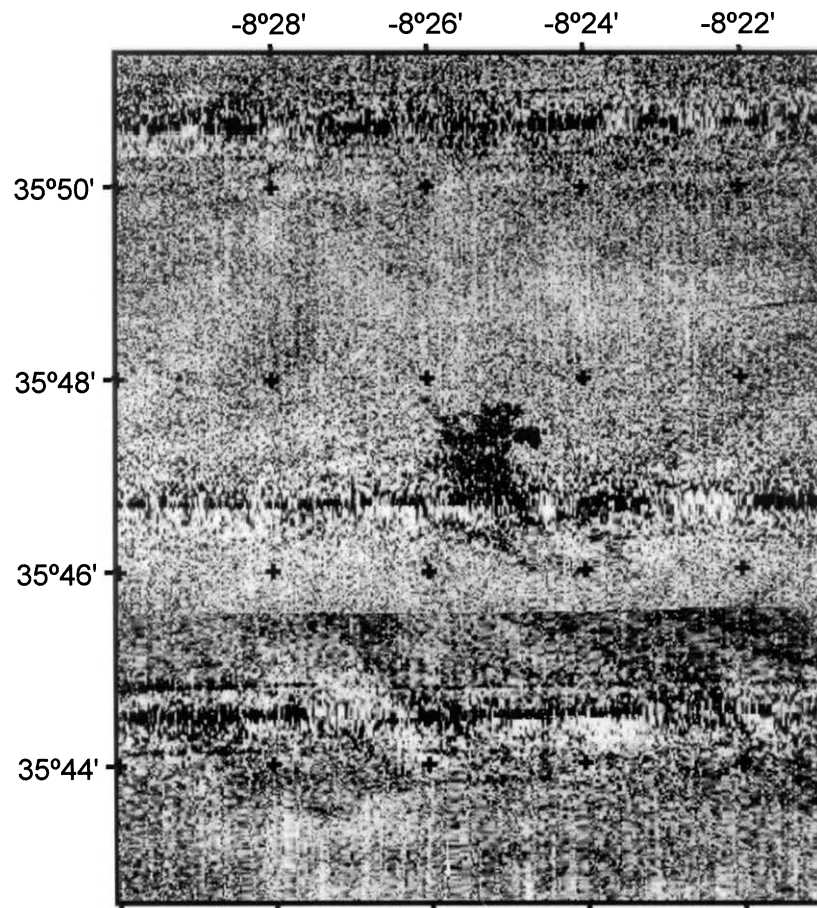
The next mud volcano in the South Portuguese margin that was investigated during the TTR-10 cruise was named Carlos Ribeiro, after a famous Portuguese geologist (1813–1882). It is located at 35°47.217'N and 08°25.313'W, at a depth of 2200 m. It is expressed as a high reflectivity sub-circular spot on the NRL SEAMAP mosaic (Fig. 4a). The 3.5-kHz profiler confirms its conical shape, with a height of approximately 80 m and a diameter of ca. 1.5 km (Fig. 4b).

Two cores, separated by approximately 30 m, were taken from the top of this structure: AT-243G and AT-244G (Fig. 4; Table 1). The cores

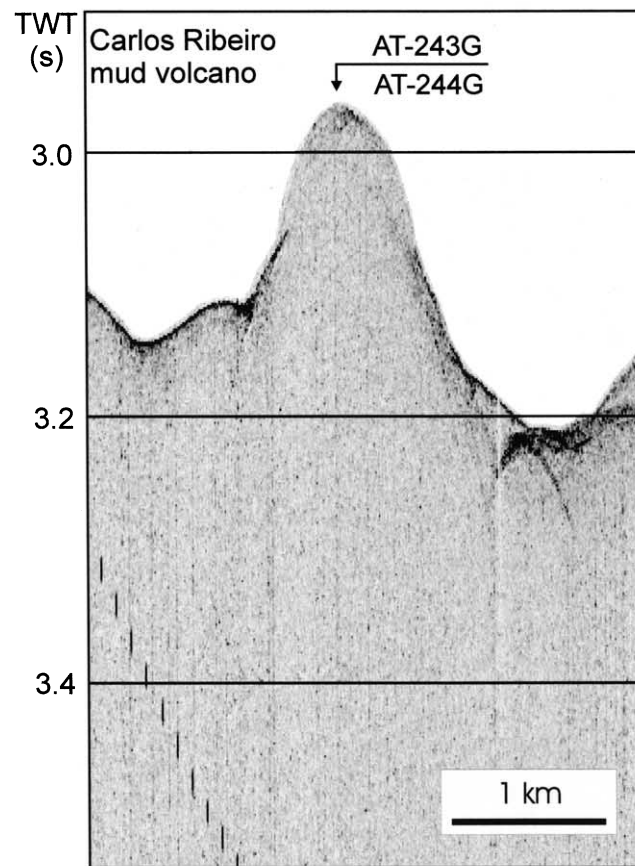
are similar, showing almost no pelagic sediments on top, and a succession of gray structureless very poorly sorted mud breccia, slightly oxidized and bioturbated at the very top (only a few cm thick on core AT-244G); this indicates that this is a recently active structure. The mud breccia recovered is highly gasified, with an intense H<sub>2</sub>S smell. The clasts are subangular or angular rock fragments of different lithologies and shapes, with variable sizes sometimes reaching 15 cm. Among them was found one fragment of semi-consolidated claystone with a thin bitumenous pellicule at the surface. The strong H<sub>2</sub>S smell throughout both cores and the lack of a pelagic veneer at the top of both successions confirms an intense recent activity of this mud volcano. Some empty shells and one live bivalve (Thyasiridae), Foraminifera, empty Thecosomata shells and Pogonophora (*Oligobrachia* sp. and another undetermined species) were recovered from this site.

#### 4.1.3. The Olenin mud volcano

The next structure to be investigated was the Olenin mud volcano (Figs. 1 and 5), named after a famous Russian scientist (1923–1982). On the SEAMAP mosaic, it appears as a dome-like structure with high reflectivity, located at approximately 35°45'N and 08°26'W, on a slope. It was surveyed with a 3.5-kHz profiler. Two crossing profiles were collected, and one core, AT-245G, was taken near the summit of this structure (Fig. 5). The 287 cm of core recovered is mainly represented by pelagic yellowish brown and olive gray marl with olive brown and gray clay. The sediments were bioturbated and contained a silty and foraminiferal admixture. Several oxidized layers were observed throughout the core and traces of a reduction front were described for the lowermost part of the succession, suggesting possible past fluid venting in the site. A minor part of the core consisted of two thin layers of mud volcanic deposits: one at the 60–65-cm and the other at the 210–210-cm intervals. They both were characterized by sharp irregular contacts and contained millimetric to centimetric subangular clasts of different lithologies in a silty clayey matrix. The fauna recovered from this site included Foraminifera, empty Thecosomata shells and a few frag-



(a)



(b)

Fig. 4. Carlos Ribeiro mud volcano. (a) Side-scan image (NRL mosaic); (b) 5.1-kHz profile across this structure. See Fig. 1 for location. Also shown are the locations of the two cores (AT-243G and AT-244G) taken during the TTR-10 cruise.

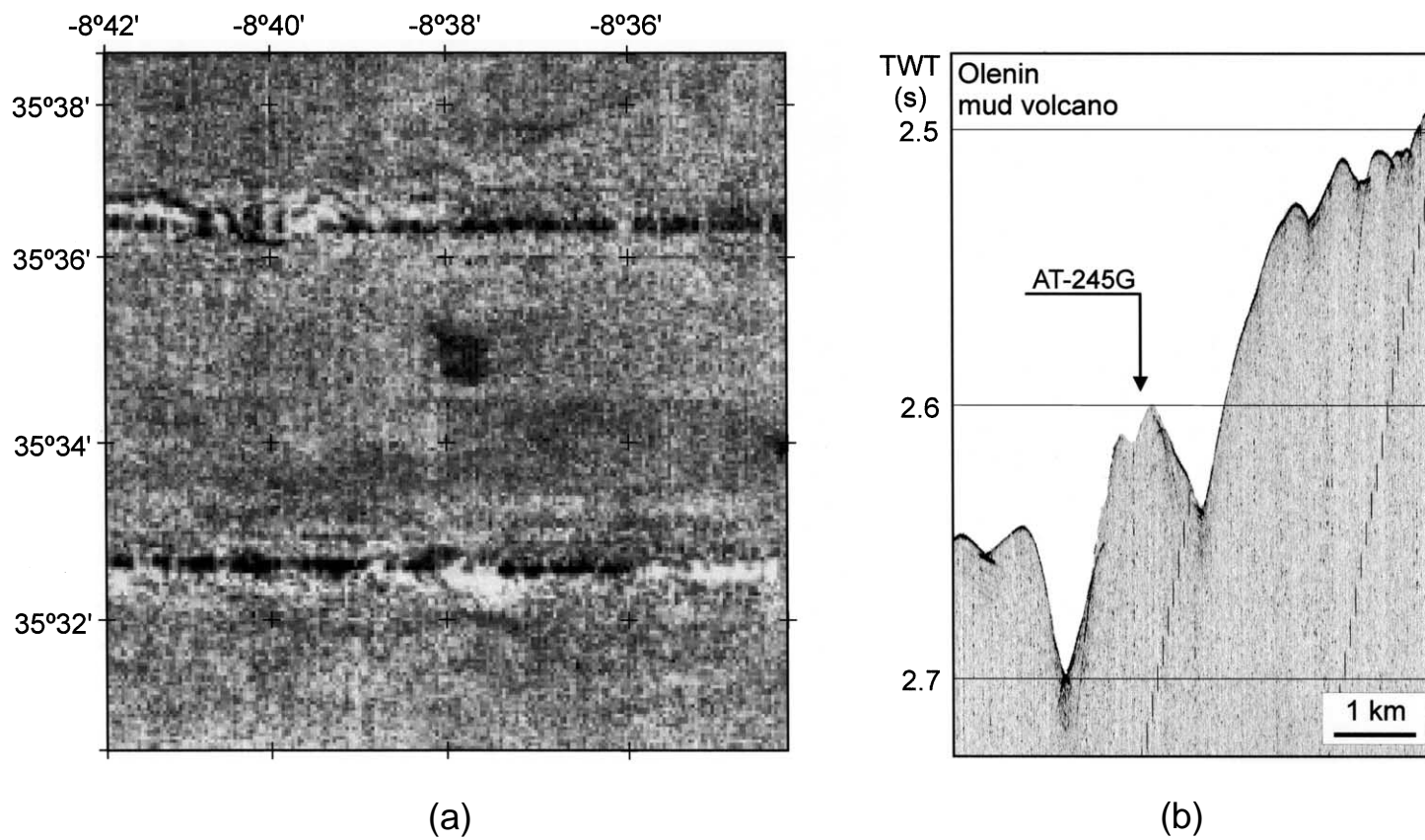


Fig. 5. Olenin mud volcano. (a) Side-scan image (NRL mosaic); (b) 5.1-kHz profile across this structure. See Fig. 1 for location. Also shown is the location of the AT-245G core taken during the TTR-10 cruise.

ments of empty pogonophoran tubes. It has been interpreted as a small, non-active vent/volcano.

#### 4.1.4. Dome-shaped structure. Mud volcano?

One dome-shaped structure was also observed on the OKEAN side-scan sonar records and on the seismic profile PSAT-148, at approximately 35°29'N, 08°15'W (Fig. 1). One core, AT-229G, was taken in this structure. A hemipelagic succession of alternating light olive brown and strongly bioturbated marl rich in Foraminifera and more grayish, also intensively bioturbated marl was recovered. Although no mud breccia was recovered from this site, a mud volcanic origin of the dome-like structure cannot be excluded. Empty tubes of Pogonophora and Polychaeta were also retrieved from this site.

## 4.2. The Spanish field

In the Spanish field, several occurrences of gas seepage and mud volcanism were discovered during the TTR-9 (Kenyon et al., 2000) and TTR-10 cruises. In the northern part of this sector, a significant amount of very high quality data, including multibeam bathymetry, high resolution seismics, coring and dredging, was collected in the Tasyo field (Somoza et al., 1999, 2003). During the TTR-9 cruise, a very interesting mud volcano was discovered in this area – the St. Petersburg mud volcano (Gardner, 2001; Kenyon et al., 2000). During the TTR-10 cruise, another dome-like structure, discovered during the Spanish Geological Institute expedition in 1999 (L. Somoza, personal communication) was investigated: the Tasyo mud volcano.

### 4.2.1. The Tasyo mud volcano

The Tasyo mud volcano is located approximately at 35°45'N and 07°05'W. During the TTR-10 cruise, both OKEAN and seismics were used to investigate this structure prior to coring. The seismic Line PSAT-152 crossed the TASYO mud volcano (Figs. 1 and 6).

Two cores were taken on the top of this mud volcano (Table 1). The first core, AT-241G (Fig. 6), at a depth of 1100 m, penetrated carbonate-rich superficial sediments (marls with dead corals

– *Lophelia*), overlying a mud breccia with gas vesicles. Empty shells of Thecosomata and other gastropods, Sipuncula (undetermined species) and Polychaeta (*Nothria hispanica*), were recovered from this site. The second core, AT-242G, at a water depth of 1100 m, penetrated marls and mud breccia like AT-241G, with Foraminifera, although with less dead corals (*Lophelia*). The two cores recovered showed a marly unit on the top, of differing thickness. In both cases the yellowish brown marl was found to be rich in Foraminifera and contained a coral-supported layer at about 15 cm below the top of the core. In the core AT-241G, coral fragments showed up again in the lower part of the marly unit between 50 and 69 cm, where the sediment appeared to be more grayish and enriched in Foraminifera. The second half of these cores was a homogenous and structureless mud breccia with a large number of clasts of different roundness and size (in some cases up to 9 cm in size). Both cores showed evidence of a possible development of coral build-ups on hard substrate, namely carbonate crusts at the surface of the mud volcanic edifice.

## 4.3. The Western Moroccan field

In the Western Moroccan field, where the Yuma, Ginsburg, Kidd, Adamastor and TTR mud volcanoes were discovered during the TTR-9 cruise (Gardner, 2001; Kenyon et al., 2000), five sites were chosen for bottom sampling (see location in Fig. 1). Three new mud volcanoes were discovered: Jesus Baraza, Student and Rabat. Three cores were also taken from the previously known Ginsburg mud volcano, and more gas hydrates were recovered from them.

### 4.3.1. The Jesus Baraza mud volcano

This was the second structure to be cored during the TTR-10 cruise. It also proved to be a mud volcano and was named Jesus Baraza, after a recently deceased Spanish geologist who worked intensively on methane seeps. On the side-scan mosaic it shows up as a circular feature with a strong backscatter (Fig. 7a). On the seismic profiles (eastern end on Line PSAT-151; Fig. 1) it shows as a prominent high with a maximum height above

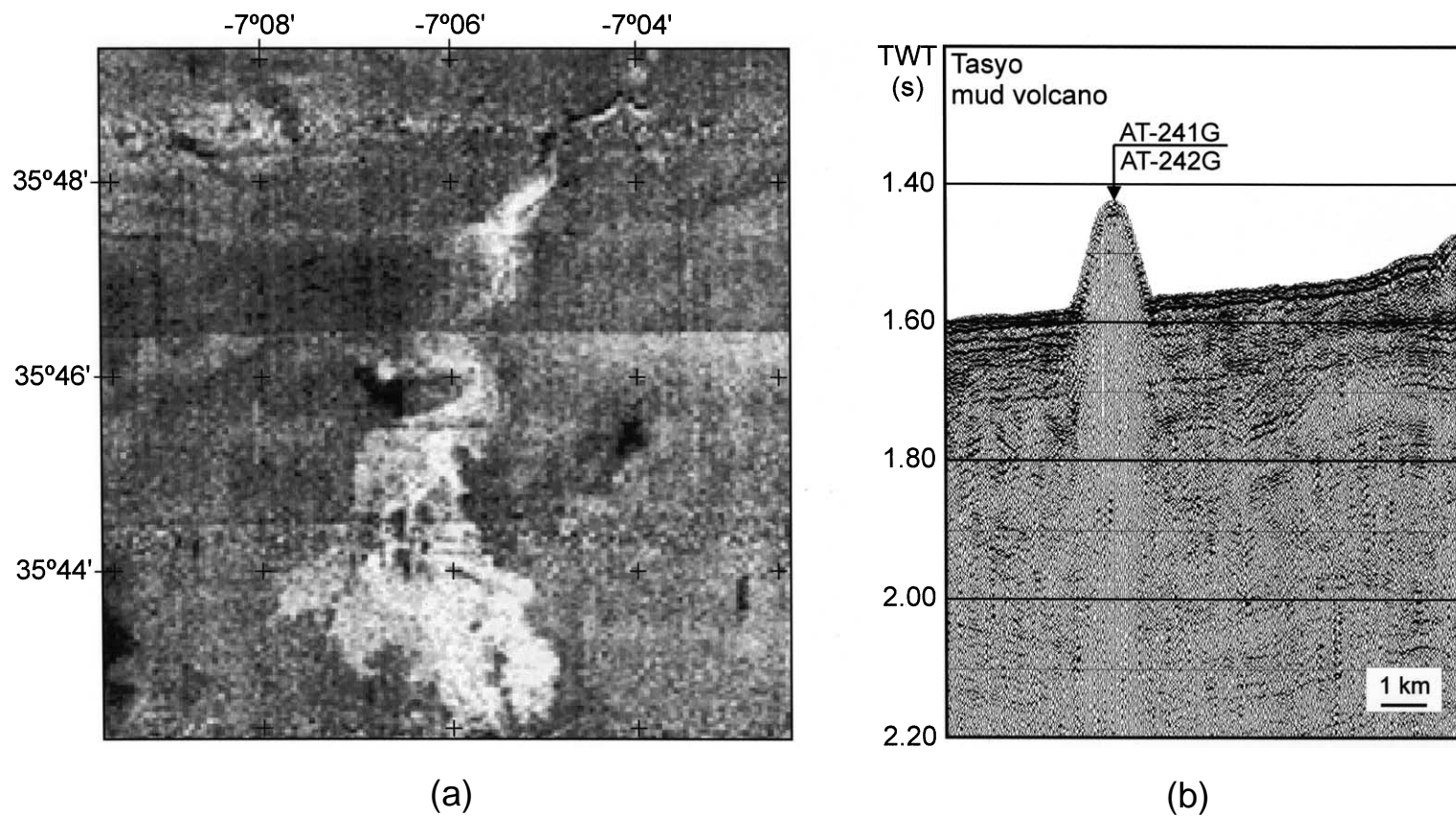
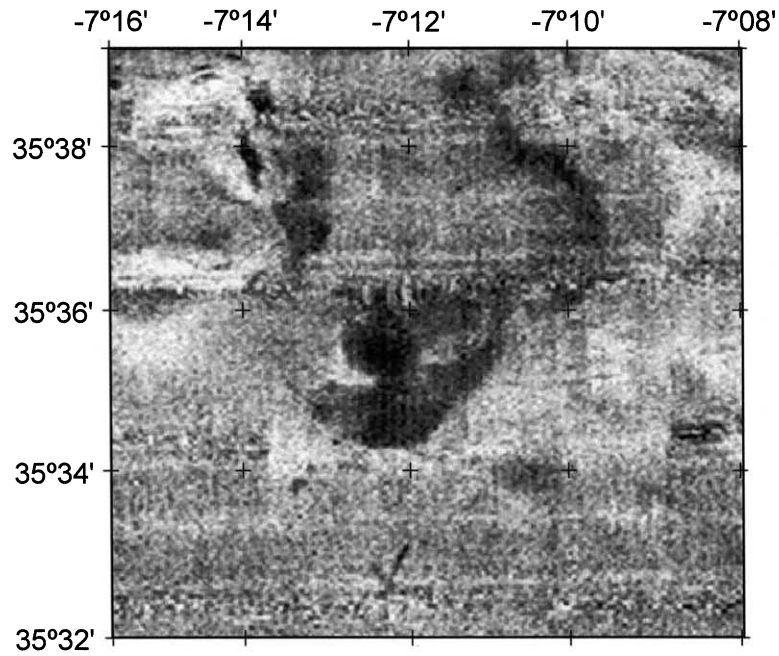
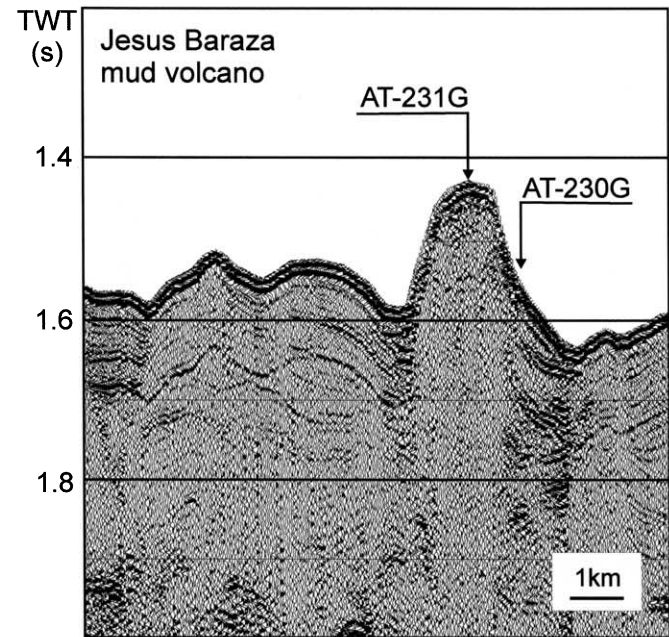


Fig. 6. Tasyo mud volcano. (a) Side-scan image (NRL mosaic); (b) single-channel seismic profile across the structure (Line PSAT 152). See Fig. 1 for location. Also shown is the location of the AT-242G core taken during the TTR-10 cruise.



(a)



(b)

Fig. 7. Jesus Baraza mud volcano. (a) Side-scan image (NRL mosaic); (b) single-channel seismic profile across the structure (Line PSAT 151). See Fig. 1 for location. Also shown are the locations of the two cores AT-230G and AT-231G taken during the TTR-10 cruise.

seafloor of about 150 m (Fig. 7b). Two cores were collected in this mud volcano.

The first core, AT-230G, was taken from the flank of the mud volcano, at the base of the slope, at a water depth of 1159 m. A hemipelagic marly succession was recovered with bioturbation and Foraminifera distributed throughout the whole core. The usual few centimeters of soupy and water-saturated brownish marl were found at the top, with the sediment becoming more consistent downcore. Slump structures were visible below 120 cm, where darker layers and burrows were tilted and bent in an oblique orientation. No mud breccia was recovered. This indicates that hemipelagic and slump deposition was prevalent on this slope for a relatively long period. Only a few specimens of Foraminifera and empty Thecosomata shells were recovered from this core.

The second core, AT-231G, at a water depth of 1091 m, sampled the top of the mud volcano. The first 4 cm consisted of light brown soupy and water-saturated marl very rich in Foraminifera, with a few Pogonophora (*Siboglinum* sp.). The rest of the core could be subdivided in two main units. The first unit (4–27 cm) showed structureless water-saturated brownish mud breccia with clayey matrix and numerous clasts of different color, roundness and lithology. The oxidation of this interval and the bioturbation with burrows, filled with sediment from the upper marl layer, might indicate that the mud volcano has not been active recently. The second unit (27–1254 cm) presented the same mud breccia found above but more consolidated and without oxidation or bioturbation. A strong H<sub>2</sub>S smell was detected. The mud breccia unit was relatively well stratified, with several intervals representing different mud flows. Mud breccia flows therefore occurred on this mud volcano but they did not reach the site of the first of these two cores.

#### 4.3.2. Student. Another mud volcano?

Two cores, AT-232G and AT-233G, and one TV-controlled grab station (AT-239GR) were taken on this high reflectivity, sub-circular feature observed on both the NRL mosaic and the OKEAN sonar mosaic obtained during the TTR-9 cruise (Fig. 8). They confirmed that this

structure is related to cold seepage, and it was named Student. A carbonate crust and dead corals (*Madrepora* and *Lophelia*) were retrieved from the top part of the cores.

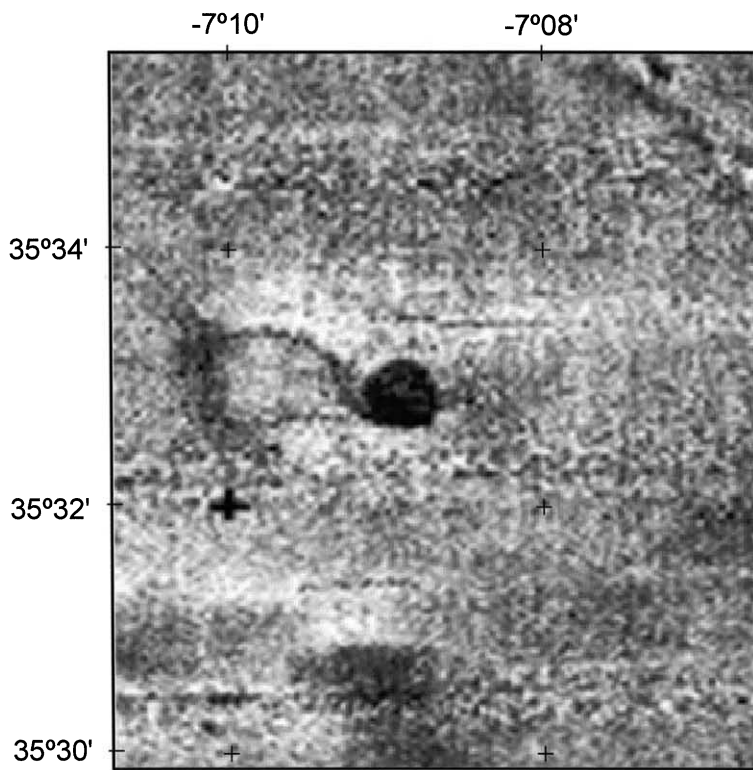
The first core, AT-232G, showed a poor recovery, with only some material in the core catcher. It was represented by gray mud enriched in Foraminifera, with numerous dead coral branches of *Lophelia* cf. *pertusa* and *Madrepora* cf. *oculata* and abundant fragments of mollusc shells and echinoderm spikes. Many Pogonophora (*Siboglinum* sp.), some hydroids, one decapod (*Munidopsis* sp.) and one bivalve (*Limopsis* sp.), were also recovered. Three carbonate crusts were collected.

The second core, AT-233G, recovered 36 cm of yellowish brown and grayish brown marl, very enriched in Foraminifera with fragments of bivalve shells and dead coral branches (*Madrepora* and *Lophelia*). One anthozoan, a polychaete fragment and a juvenile pogonophoran (probably *Siboglinum* sp.), were collected from this sample. A carbonate crust (5 cm in size) was also found in the middle of the recovered sequence.

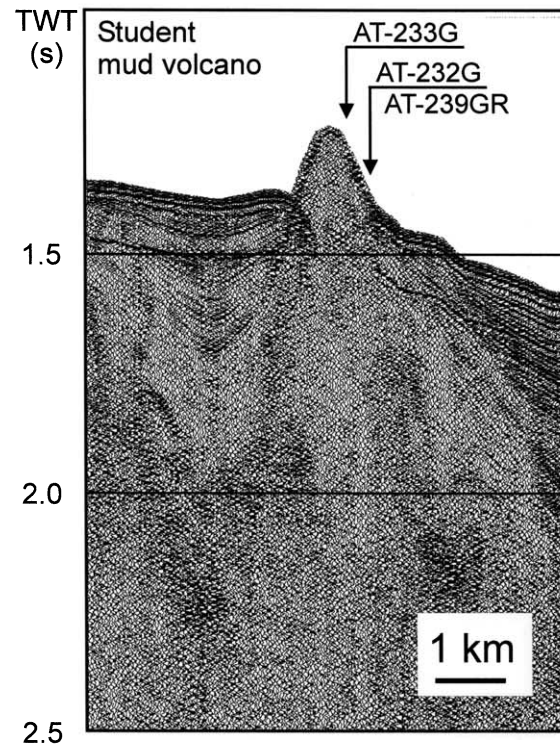
Finally, one grab station (AT-239GR), positioned with a TV camera, recovered carbonate crusts and marls. A video profile across this structure confirmed the assumption about recent seepage in the area, and showed the presence of gas-related carbonate build-ups, dense clam beds (probably *Solemya mediterranea*), living coral, and coral debris. A number of yellowish and grayish brown porous carbonate crusts were collected, reaching 50 cm in size. The fauna recovered from this sample was very abundant and diversified: 50 specimens belonging to 17 different taxa were collected. These included Porifera, Cnidaria (Hydrozoa and Anthozoa), Sipuncula, Polychaeta, Pogonophora (*Siboglinum* sp.), Mollusca (undetermined gastropod, Cuspidariidae-like bivalves, *Limopsis* sp.), Pycnogonida (*Hedgpepthia atlantica*), Crustacea (Cirripedia, the cumacean *Procampylaspis* sp., the amphipod *Liropus* cf. *elongatus*, a tanaid and an anthurid isopod) and Echinodermata (undetermined species of Echinidae and Ophiuridae).

#### 4.3.3. The Rabat mud volcano

This mud volcano (see Fig. 1 for location) ap-



(a)



(b)

Fig. 8. Student mud volcano. (a) Side-scan image (NRL mosaic); (b) seismic profile across the structure (Line PSAT 146). See Fig. 1 for location.



Fig. 9. Gas hydrates recovered from the Ginsburg mud volcano during the TTR-10 cruise.

pears on the NRL side-scan mosaic as another circular feature. One core, AT-235G, was taken from the top of this structure. 288.5 cm of sediment was recovered. The first 19 cm consisted of yellowish brown marl intensively bioturbated and water-saturated for the first 6 cm. Foraminifera, Pogonophora (*Siboglinum* sp.), shell-coral debris and dead coral (*Lophelia*) were found throughout this interval. From 19 to 129 cm the core showed the same marl but with a grayish color becoming darker towards the bottom. Coral debris were present throughout this interval. Bioturbation was extremely intense, with large burrows filled with soupy, sandy silty clay, presumably from an underlying interval. The rest of the core was mud breccia, with a color varying from gray to dark gray; the intervals separated by sharp boundaries were interpreted as different mud flows. Surprisingly the mud breccia showed intense bioturbation; this, together with the existence of a marly sediment upper cover, appears to indicate that the mud volcano has been inactive for a relatively long period of time.

#### 4.3.4. The Ginsburg mud volcano

Three cores were collected and gas hydrates re-

trieved from the top of the Ginsburg mud volcano (see location in Fig. 1), discovered during the TTR-9 cruise (Gardner, 2001; Kenyon et al., 2000): AT-236G, AT-237G and AT-238G. The recovery varied from 145 to 182 cm and they all showed the same lithology: a structureless, gray, very gassified mud breccia with a thin oxidized interval at the very top. The target, to recover gas hydrate crystals, was successfully accomplished in core AT-238G, from which ice-like gas hydrates up to 5 cm in size (Fig. 9) were collected from the interval below 150 cm. These were stored in a cold laboratory for later geochemical analyses. According to the data obtained during the TTR-9 and TTR-10 cruises, the Ginsburg mud volcano appears to be presently the most active mud volcano in the Gulf of Cadiz. Foraminifera and Pogonophora (*Siboglinum* sp.) were recovered from this site.

#### 4.3.5. Diapir-like structure. Mud volcano?

One core, AT-234G, was also taken from the top of dome-shaped structure shown as a high reflectivity spot on both the NRL mosaic and the OKEAN side-scan data from the TTR-9 cruise. 241 cm of a marly succession was recov-

ered, showing an intensive bioturbation throughout the core and the presence of Foraminifera, shells and dead coral fragments at some intervals. The lower half of the succession was represented by an unusual intercalation of oxidized and reduced lamina and was characterized by an intense H<sub>2</sub>S smell. All this evidence seems to indicate the existence of fluid venting through the seafloor. Although no more cores were taken from this structure, its gas escape origin was confirmed. Thus, this site clearly deserves further investigation.

### 5. Micropaleontological investigation of the matrix from the mud volcanic deposits

Micropaleontological studies were carried out on board, to date the matrix of the mud volcanic deposits using calcareous nannofossils. Samples from the matrix of the mud breccia were taken from the Bonjardim, Carlos Ribeiro, Jesus Baraza, Rabat, Ginsburg and Tasyo mud volcanoes for preliminary determination of the time range. Smear slides were prepared from raw samples and examined under the microscope. The method of calcareous nannofossils identification of Perch-Nielsen (Bolli et al., 1985) was applied to coccoliths.

Calcareous nannofossils from different ages have been found in the matrix of the mud breccias. Preservation of the calcareous nannofossils is moderate to poor. They seem to be partially dissolved, which makes it difficult to identify small forms. Relatively large coccoliths show good preservation. In general, discoasters are found to be damaged and at times their arms broken, making their identification difficult. Some representatives of the discoasters show overcalcification patterns that obscure important features and cause complications during the process of identification and classification of species.

Some Upper Cretaceous species are common in the samples from the mud volcanoes. In each sample, four to six species of Upper Cretaceous coccoliths were identified in the mud volcanoes of the Moroccan and the Spanish margins. The most abundant species are *Micula decussata* and *Watz-*

*naueria barnesae*. These species could have been derived from a hemipelagic source or from slope sediment by the process of re-sedimentation. They are also present in the pelagic sediments observed on the superficial sediments of some mud volcanoes. Thus, the presence of these species is not conclusive evidence of an Upper Cretaceous age. Only the mud volcanoes discovered in the South Portuguese margin show an assemblage of Upper Cretaceous coccoliths. It is possible that Upper Cretaceous deposits are located near the roots of the mud volcanoes on the Portuguese margin.

Paleocene species occur only sporadically in only two sediment samples. The most probable explanation for this is the absence of significant Paleocene deposits near the roots of the studied mud volcanoes. Calcareous nannofossils, typical of Eocene deposits, are found in abundance. Among them *Reticulofenestra umbilica*, *R. hillae*, *Discoaster barbendiensis*, *D. saipanensis*, *Ericsonia formosa* are frequently observed in smear slides. Based on these nannofossils it is confirmed that there are Eocene deposits in the roots of the mud volcanoes. There are also some transitional species through the Oligocene (*D. deflandrei*, *Cycli-cargolithus floridanus*, *C. abisectus*, *Dictyococites bisectus*). However, the presence of the Oligocene sediments cannot be confirmed because of lack of evidence of marker species. The most abundant species in the matrix are Miocene–Pliocene coccoliths and discoasters. There are numerous species in all the samples of the matrix that were studied. The following species were observed most frequently in the smear slides: *Discoaster variabilis*, *D. druggii*, *D. pansus*, *Reticulofenestra pseudoumbilica*, *R. gelida*, *Reticulofenestra* spp., *Dictyococites* spp., *Sphenolithus heteromorphus*, *Calcidiscus macintyreii*; several other species were also present. The presence of Miocene–Pliocene species suggests that sediments of these ages have been actively involved in the process of mud volcanism in the region.

Quantitative analysis of the coccoliths was carried out in the samples of matrix from mud breccia in core AT-227G. Amongst the 145 specimens of calcareous nannofossils, 45 are from the Upper Cretaceous (mainly *Micula decussata* 26, *Watznaueria barnesae* 15, *Cribrospherella ehrinbergii*

5, etc.), 25 specimens are from the Eocene (*Ericsonia formosa* 7, *Reticulofenestra umbilica* 5, *R. hillae* 3), 15 specimens are transitional from the Upper Eocene through the Oligocene to the lower Miocene, and 37 specimens are from the Miocene–Pliocene (mainly different types of *Discosters*, small *Reticulofenestra*, *R. pseudoumbilica*, *R. gelida* and *Dictyococithes* sp.). The other species are recent coccoliths namely *Emiliania huxley*, *Gephyrocapsa* sp., *Coccolithus pelagicus*, *Calcidiscus leptoporus*, *Rhabdosphaera claviger* and *Syracosphaera pulchra*.

## 6. Discussion and conclusions

From the combined results of the TTR-9, TTR-10 and Tasyo cruises, there is now vast evidence of extensive cold seepage, carbonate mound formation including cold-water coral communities (*Lophelia* skeletons), hydrocarbon-rich gas venting and mud diapirism in the South Portuguese, Spanish and Western Moroccan margins of the Gulf of Cadiz (Baraza and Ercilla, 1996; Baraza et al., 1999; Kenyon et al., 2000, 2001; Ivanov et al., 2000; Somoza et al., 2000, 2003; Gardner, 2001; Mazurenko et al., 2001). This has been interpreted as indicating the existence of gas-rich overpressured sediments at depth and the migration of these fluids through the sediments and/or along major faults to the seafloor (Somoza et al., 2000).

As regards the tectonic control of the location of the mud volcanoes, the NRL SEAMAP mosaic shows that some of these structures are aligned along major fault structures, probably strike-slip, with two main orientations: NW–SE and a conjugate NE–SW set (Gardner, 2001). Therefore, although some of the widespread shallow fluid venting on the seafloor in the northern part of the Gulf of Cadiz may be explained by the destabilization of gas hydrate-rich sediments in contact with the warmer MOW (Somoza et al., 2000), a significant number of the mud volcanoes in the deeper areas of the basin appear to be controlled by major faults that acted as conduits for the fluids. The overpressure in the sediments at depth is possibly related to fast sediment supply, along-

slope gravitational sliding and to the tectonic compression of the olistostrome and accretionary complex caused by the Africa–Eurasia convergence (Somoza et al., 2000).

There is also strong evidence that the mud volcanoes located in the western and deeper parts of the Gulf of Cadiz are the most active, with the exception of the Ginsburg mud volcano, on the Moroccan sector. Gas hydrates were recovered from both the Bonjardim and the Ginsburg mud volcanoes. The significance of this is not yet fully understood but is possibly related to the distribution of the tectonic stress in this area.

The typical structures related to fluid venting in this area are conical mud volcanoes with diameters ranging from several tens of meters to ca. 4 km and heights that can reach 200 m (Ivanov et al., 2000). In some of the cores recovered from these structures (e.g. Bonjardim mud volcano), a strong H<sub>2</sub>S smell could be felt. This, together with the lack of a pelagic veneer and abundant Pogonophora at the very top of the core, appears to indicate active venting. Evidence of multiple flows was also observed on several mud volcanoes.

As regards the age of the gas-rich layer, the oldest clasts found in the cores are of Upper Cretaceous age (Bonjardim, Carlos Ribeiro and Tasyo), particularly in the Portuguese sector, although the majority of the clasts are of Eocene/Miocene age. Since the study area is an accretionary complex with an olistostrome emplacement, this does not necessarily imply that the overpressured gas-rich mud layer is older, because the Upper Cretaceous clasts may belong to the overlying olistostrome and come from the eastern nappes. Further research is necessary to clarify this problem.

Carbonate crusts and cold-water coral communities were found only in the eastern sectors of the Gulf of Cadiz, i.e. the Spanish and Moroccan sector. Seepage contributes to the enrichment of dissolved organic carbon in the water column which seemingly favors the development of such communities (Hovland et al., 1998). However, the presence of a hard substrate in some of the mud volcanoes, namely the existence of carbonate crusts or mud breccias, may be crucial to the initial settlement of the coral larvae. This question



ELSEVIER

Marine Geology 195 (2003) 131–151



[www.elsevier.com/locate/margeo](http://www.elsevier.com/locate/margeo)

## Mud volcanism in the Gulf of Cadiz: results from the TTR-10 cruise

L.M. Pinheiro<sup>a,b,\*</sup>, M.K. Ivanov<sup>c</sup>, A. Sautkin<sup>c</sup>, G. Akhmanov<sup>c</sup>,  
V.H. Magalhães<sup>b</sup>, A. Volkonskaya<sup>c</sup>, J.H. Monteiro<sup>b</sup>, L. Somoza<sup>d</sup>,  
J. Gardner<sup>e</sup>, N. Hamouni<sup>f</sup>, M.R. Cunha<sup>g</sup>

<sup>a</sup> Departamento de Geociências, Universidade de Aveiro, 3800 Aveiro, Portugal

<sup>b</sup> Departamento de Geologia Marinha, Instituto Geológico e Mineiro, Alfragide, Portugal

<sup>c</sup> UNESCO Centre on Marine Geology and Geophysics, Moscow State University, Geology Faculty, Moscow, Russia

<sup>d</sup> Division de Geologia Marina, Instituto Geologico y Minero, Madrid, Spain

<sup>e</sup> Naval Research Office, Washington, DC, USA

<sup>f</sup> Mohamed 5 University, Rabat, Morocco

<sup>g</sup> Departamento de Biologia, Universidade de Aveiro, 3800 Aveiro, Portugal

Received 25 March 2002; accepted 5 November 2002

### Abstract

A new deep water mud volcano field (between 2000 and 3500 m water depth) was discovered in the deep South Portuguese margin, as well as several new mud volcanoes in the South Spanish and Western Moroccan margins of the Gulf of Cadiz, during the TTR-10 (Training Through Research, UNESCO/IOC) cruise, in July/August 2000. This work followed the discovery of a large mud volcano field in the Gulf of Cadiz, first investigated during the TTR-9 cruise [Gardner (2001) *Geophys. Res. Lett.* 28, 339–342; Kenyon et al. (2000) IOC, Technical series no. 56]. The discoveries were made based on a SEAMAP side-scan sonar mosaic and multibeam bathymetry (SEABEAM) collected in the area by the Naval Research Laboratory (NRL), Washington, DC, USA, in 1992, kindly released for this purpose. Single-channel seismics, long-range side-scan sonar (OKEAN), TV-controlled grab, hull-mounted 3.5-kHz profiler and coring were used to investigate several seafloor features observed on the side-scan sonar imagery, in the South Iberia, Spanish and Moroccan margins of the Gulf of Cadiz, which were confirmed to be mud volcanoes. The typical structures related to fluid venting in the Gulf of Cadiz are essentially represented by conical mud volcanoes with diameters ranging from several tens of meters to 4 km and heights that can reach 200 m. Some of these structures appear to be aligned along major conjugate NE–SW and NW–SE trending faults that can be identified on the side-scan sonar imagery. The new field discovered in the South Portuguese margin is the deepest in the Gulf of Cadiz area and includes three new mud volcanoes – Bonjardim, Olenin and Carlos Ribeiro – which seem to be quite active, with near-surface gas hydrate occurrence and a high saturation in H<sub>2</sub>S and hydrocarbon gases (mainly methane) in the mud breccia and overlying pelagic sediments. Gas hydrates were recovered from the Bonjardim mud volcano. An intensely gassified mud breccia, with one fragment of semi-consolidated claystone with a thin bituminous veneer at the surface, was recovered from the Carlos Ribeiro mud volcano. The fauna recovered consists mainly of pogonophoran worms belonging to several species and undetermined species of Foraminifera. Three new mud volcanoes were also discovered in the NW Moroccan margin: Rabat, Student and Jesus Baraza. These show a richer

\* Corresponding author. Fax: +351-234370605. E-mail address: [imp@geo.ua.pt](mailto:imp@geo.ua.pt) (L.M. Pinheiro).

also deserves further investigation. The fauna collected in the Moroccan sector exhibited a high diversity that can be explained mainly by the high habitat heterogeneity due to the availability of different substrates (soft muddy sediments, carbonated crust, dead coral beds).

The macrofauna collected in the Gulf of Cadiz included several species of pogonophoran worms belonging to the genera *Siboglinum*, *Polybrachia* and *Oligobrachia*. Variations in the species distribution are mainly depth-related with a higher diversity occurring at the deeper Portuguese mud volcanoes. Thyasirid bivalves (one living specimen and several empty shells), whose complex burrow systems oxygenate the sediments to a depth of more than 8 cm, were also recovered in the Portuguese sector. Video footages from the Moroccan sector, collected during this cruise, showed evidence of dense clam beds (probably *Solemya mediterranea*). These pogonophoran and bivalve species are known to contain bacterial symbionts and form chemosynthetic communities that are sustained by fluid expulsion through mud volcanoes (Southward, 1985, 1986; Southward et al., 1981; Sibuet and Olu, 1998).

Chemoautotrophic organisms may interact with the sediment properties: high levels of bioturbation are associated with the dense beds of the bivalves that can cause significant changes in the chemical characteristics of the sediment due to the activity of their symbionts (Dando and Southward, 1986). On the other hand these organisms respond to the environment characteristics and may also be used as indicators of fluid emission: variations in the density of Pogonophora (number of tubes per m<sup>2</sup>) can be related to the intensity or chemistry and regularity or persistence of fluid emissions in seepage areas (Sibuet and Olu, 1998). No Pogonophora were recovered from the Spanish field, while the highest densities were found at the Student, Ginsburg (Moroccan sector) and Bonjardim (Portuguese sector) mud volcanoes. This biological information agrees with the geological evidence of recent activity especially in the two latter volcanoes.

Based on all the available data, the main conclusions that can be drawn from the bottom sam-

pling results, integrated with the geophysical data and the preliminary work carried out, can be summarized as follows:

- A large variety of sediment types present in the Gulf of Cadiz area were recovered and described, implying a superposition of different depositional environments in this region of very complex geology and fluid fluxes.

- The mud volcanism is a widespread phenomenon in the Gulf of Cadiz and six new mud volcanoes were discovered in the area during the TTR-10 cruise. Most of them were proven to be recently active, in particular Bonjardim, Carlos Ribeiro and Ginsburg. Gas hydrates were recovered from Bonjardim and Ginsburg.

- The mud volcanism of the Gulf of Cadiz is characterized by a zonal pattern in terms of the mud breccia lithology typical of different mud volcanoes. In general, relatively thin mud breccia flows, intensively bioturbated at the top, and semi-consolidated clasts within matrix with high carbonate content are characteristic of the mud volcanoes sampled on the Spanish and Moroccan margins of the Gulf of Cadiz. Non-stratified thick stiff mud breccia, only occasionally bioturbated, and numerous well lithified clasts within matrix lacking significant carbonate admixture were found to be typical of the mud volcanoes from the Portuguese margin of the Gulf of Cadiz.

- The co-existence of coral-rich carbonate build-ups and mud volcanic activity was confirmed to be widely present in the Gulf of Cadiz. However, this co-existence appears to be restricted to the shallower Spanish and Moroccan sectors (900–1200 m) and apparently absent on the deeper Portuguese sector (2200–3200 m).

- Faunal communities probably sustained by hydrocarbon-rich fluid emission through mud volcanoes were also widely present in the Gulf of Cadiz.

- Differences in composition and structure of the chemosynthetic-based communities in the mud volcanoes may be related to the intensity or chemistry, or to the regularity or persistence of the hydrocarbon-rich fluid emission. These differences may be used as indicators of temporal variations in the activity of the mud volcanoes.

## Acknowledgements

The authors thank the NRL, Washington, DC, USA, for kindly having released their SEAMAP mosaic and multibeam bathymetry for the TTR-10 cruise. We also wish to thank Eve Southward and Roger Bamber, for the identification of the Pogonophora and Pycnogonida, respectively, and Alan Judd, Martin Hovland and Jean-Paul Foucher, for their careful revision of this paper, which helped us to greatly improve the overall quality of the final version. Finally, we thank the Captain and crew of the R/V *Professor Logachev* for a splendid time on board and for the quality of data acquired during the whole cruise. Contributions by J. Gardner to this project were supported by the Office of Naval Research PE #0601153N. This work and the shiptime of TTR-10 were funded jointly by the UNESCO/IOC, the University of Moscow and the Portuguese Geological and Mining Institute (through the INGMAR Project – PLE/4/98, financed by the Portuguese Foundation for Science and Technology – FCT).

## References

- Baraza, J., Ercilla, G., 1996. Gas-charged sediments and large pockmark-like features in the Gulf of Cadiz (SW Spain). *Mar. Pet. Geol.* 13, 253–261.
- Baraza, J., Ercilla, G., Nelson, C.H., 1999. Potential geologic hazards on the eastern Gulf of Cadiz slope (SW Spain). *Mar. Geol.* 155, 191–215.
- Barber, A.J., Tjokrosapetro, S., Charlton, T.R., 1986. Mud volcanoes, shale diapirs, wrench faults and mélanges in accretionary complexes, Eastern Indonesia. *Am. Assoc. Petrol. Geol. Bull.* 70, 1729–1741.
- Bolli, H.M., Saunders, J.B., Perch-Nielsen, 1985. *Plankton Stratigraphy*, vol. 1, Planktic Foraminifera, Calcareous Nannofossils and Calpionellids. Cambridge University Press.
- Çiğçi, G., Limonov, A., Dimitrov, L., Gainanov, V., 1997. Mud volcanoes and dome-like structures at the Eastern Mediterranean Ridge. *Mar. Geophys. Res.* 19, 421–438.
- Dando, P.R., Southward, A.J., 1986. Chemoautotrophy in bivalve molluscs of the genus *Thyasira*. *J. Mar. Biol. Assoc. UK* 66, 915–929.
- Dewey, J.F., Helman, M.L., Turco, E., Hutton, D.H.W., Knott, S.D., 1989. Kinematics of the western Mediterranean. In: Coward, M. (Ed.), *Alpine Tectonics*. Spec. Publ. Geol. Soc. London, 45, pp. 265–283.
- Dickens, G.R., Castillo, M.M., Walker, J.C.G., 1997. A blast of gas in the latest Paleocene: simulating first-order effects of massive dissociation of oceanic methane hydrate. *Geology* 25, 259–262.
- Galindo-Zaldívar, J., Nieto, L., Woodside, J., 1996. Structural features of mud volcanoes and the fold system of the Mediterranean Ridge, south of Crete. *Mar. Geol.* 132, 95–112.
- Gardner, J., 2001. Mud volcanoes revealed and sampled on the Western Moroccan continental Margin. *Geophys. Res. Lett.* 28, 339–342.
- Ginsburg, G.D., Soloviev, V.A., 1998. *Submarine Gas Hydrates*. VNIIOKeangeologia, St. Petersburg, 216 pp.
- Henriet, J.-P., Mienert, J., 1998. Gas Hydrates: Relevance to World Margin Stability and Climatic Change. Special Publication of the Geological Society of London, 137, 338 pp.
- Hovland, M., Judd, A., 1988. Seabed Pockmarks and Seepages. Impact on Geology, Biology and the Marine Environment. Graham and Trotman, 296 pp.
- Hovland, M., Mortensen, P.B., Brattegard, T., Strass, P., Rokoengen, K., 1998. Ahermatypic coral banks off mid-Norway: evidence for a link with seepage of light hydrocarbons. *Palaios* 13, 189–200.
- Ivanov, M.K., Pinheiro, L.M., Henriët, J., Gardner, J., Akhmanov, G., 2000. Some evidences of the relationship between carbonate mound formation and cold seepage in the Gulf of Cadiz. Proceedings AGU Fall Meeting, American Geophysical Union, Fall Meet. Suppl., AGU, 81(48), Abstract OS51E-05.
- Ivanov, M.K., Pinheiro, L.M., Stadniskaya, A., Blinova, V., 2001. Hydrocarbon Seeps on the Deep Portuguese Margin. EUG XI, Abstract Volume, 160.
- Judd, A., Davies, G., Wilson, J., Holmes, R., Baron, G., Bryden, I., 1997. Contributions to atmospheric methane by natural seepages on the UK continental shelf. *Mar. Geol.* 140, 427–455.
- Kenyon, N.H., Ivanov, M.K., Akhmetzhanov, A.M., Akhmanov, G.G., 2000. Multidisciplinary Study of Geological Processes on the North East Atlantic and Western Mediterranean Sea Margins. IOC, Technical series no. 56.
- Limonov, A.F., Woodside, J.M., Cita, M.B., Ivanov, M.K., 1996. The Mediterranean Ridge and related mud diapirism: a background. *Mar. Geol.* 132, 7–19.
- Maldonado, A., Comas, M.C., 1992. Geology and geophysics of the Alboran Sea: an introduction. *Geomar. Lett.* 12, 61–65.
- Maldonado, A., Somoza, L., Pallarés, L., 1999. The Betic orogen and the Iberian–African boundary in the Gulf of Cadiz: geological evolution (central North Atlantic). *Mar. Geol.* 155, 9–43.
- Mazurenko, L.L., Soloviev, V.A., Ivanov, M.K., Pinheiro, L.M., Gardner, J.M., 2001. Composition of Gas-Hydrate Forming Fluids in the Gulf of Cadiz. EUG XI, Abstract Volume, 160.
- Mienert, J., Posewang, J., Baumann, M., 1996. Geophysical signature of gas hydrates along the Northeastern Atlantic Margin: possible hydrate-bound margin instabilities and

- possible transfer of methane from Oceanosphere to Atmosphere. In: Henriot, J.-P., Mienert, J. (Eds.), *Gas Hydrates: Relevance to World Margin Stability and Climatic Change*. Tutorial Book. First Master Workshop. Het Pand, Gent, pp. 106–122.
- Milkov, A., 2000. Worldwide distribution of submarine mud volcanoes and associated gas hydrates. *Mar. Geol.* 167, 29–42.
- Nisbet, E.G., Piper, D.J.W., 1998. Giant submarine landslides. *Nature* 392, 329–330.
- Paull, C., Dillon, W.P., 2001. *Natural Gas Hydrates: Occurrence, Distribution and Detection*. Geophysical Monograph Series, 124, 315 pp.
- Sibuet, M., Olu, K., 1998. Biogeography, biodiversity and fluid dependence of deep-sea cold-seep communities at active and passive margins. *Deep-Sea Res. II* 45, 517–567.
- Somoza, L., Ivanov, M.K., Pinheiro, L.M., Maestro, A., Lowrie, A., Vasquez, J.T., Gardner, J., Leon, R., Fernandez-Puga, M.C., 2000. Structural and tectonic control of fluid seeps and mud volcanoes in the Gulf of Cadiz. Proceedings of the TTR-10 Post Cruise Meeting, Mozenka, Moscow.
- Somoza, L., Diaz-del-Rio, V., Léon, R., Ivanov, M.K., Fernández-Puga, M.C., Lobato, A., Maestro, A., Hernández-Molina, F.J., Gardner, J.M., Rodero, J., Pinheiro, L.M., Vásquez, J.T., Medialdea, T., Fernández-Salas, L.M., 2003. Seabed morphology and hydrocarbon seepage in the the Gulf of Cadiz mudvolcano area: imagery of multibeam data and ultra-high resolution data. *Mar. Geol.* S0025-3227(02)00686-2.
- Somoza, L., Diaz-del-Rio, V., Hernández-Molina, F.J., Léon, R., Lobato, A., Lobo, F., Rodero, J. and the TASYO Team, 1999. New discovery of a mud volcano field related to gas venting in the Gulf of Cadiz: imagery of multibeam data and ultra-high resolution seismics. Proceedings of the 5th Symposium on the Iberian Atlantic Margin, Faro, pp. 397–398.
- Southward, A.J., Southward, E.C., Dando, P.R., Rau, G.H., Felbeck, H., Flugel, H.J., 1981. Bacterial symbionts and low  $^{13}\text{C}/^{12}\text{C}$  ratios in tissues of Pogonophora indicate unusual nutrition and metabolism. *Nature London* 293, 616–620.
- Southward, E.C., 1985. Pogonophora. In: Laubier, L., Monniot, C. (Ed.), *Peuplements profonds du Golfe de Gascogne*. Éd. IFREMER, pp. 369–373.
- Southward, E.C., 1986. Gill symbionts in Thyasirid and other bivalve molluscs. *J. Mar. Biol. Assoc. UK* 66, 889–914.
- Suess, E., Torres, M.E., Bohrmann, G., Collier, R.W., Greinert, J., Linke, P., Rehder, G., Trehu, A., Wallmann, K., Winckler, G., Zuleger, E., 1999. Gas hydrate destabilization: enhanced dewatering, benthic material turnover and large methane plumes at the cascadia convergent margin. *Earth Planet. Sci. Lett.* 170, 1–15.
- Westbrook, G.K., Smith, M.J., 1983. Long decollements and mud volcanoes: evidence from the Barbados Ridge complex for the role of high pore-fluid pressure in the development of an accretionary complex. *Geology* 11, 279–283.
- Wilson, R.C.L., Hiscott, M.G., Gradstein, F.M., 1989. The Lusitanian Basin of West Central Portugal. Mesozoic and Tertiary tectonic, stratigraphy and subsidence history. In: Tankard, A.J., Balkwill, H.R. (Eds.), *Extensional Tectonics and Stratigraphy of the North Atlantic Margins*. AAPG Mem. 46, pp. 341–361.
- Woodside, J.M., Ivanov, M.K., Limonov, A.F., 1997. Neotectonics and Fluid Flow through Seafloor Sediments in the Eastern Mediterranean and Black Seas, Parts I and II. *IOC Tech. Ser.*, 48.





ELSEVIER

Marine Geology 219 (2005) 1–17

**MARINE  
GEOLOGY**

INTERNATIONAL JOURNAL OF MARINE  
GEOLOGY, GEOCHEMISTRY AND GEOPHYSICS

www.elsevier.com/locate/margeo

## The El Arraiche mud volcano field at the Moroccan Atlantic slope, Gulf of Cadiz

Pieter Van Rensbergen<sup>a,\*</sup>, Davy Depreiter<sup>a</sup>, Bart Pannemans<sup>a</sup>, Geert Moerkerke<sup>a</sup>,  
David Van Rooij<sup>a</sup>, Bruno Marsset<sup>b</sup>, Grigorii Akhmanov<sup>c</sup>, Valentina Blinova<sup>c</sup>,  
Michael Ivanov<sup>c</sup>, Merouane Rachidi<sup>d</sup>, Vitor Magalhaes<sup>e</sup>,  
Luis Pinheiro<sup>e</sup>, Marinha Cunha<sup>f</sup>, Jean-Pierre Henriët<sup>a</sup>

<sup>a</sup>*Renard Centre of Marine Geology, Ghent University, Krijgslaan 281-S8, 9000 Ghent, Belgium*

<sup>b</sup>*IFREMER, Brest, France*

<sup>c</sup>*UNESCO-MSU Centre for Marine Geoscience, Moscow State University, Moscow, Russia*

<sup>d</sup>*Mohamed V University, Rabat, Morocco*

<sup>e</sup>*Departamento de Geosciências, Universidade de Aveiro, Aveiro, Portugal*

<sup>f</sup>*Departamento de Biologia, Universidade de Aveiro, Aveiro, Portugal*

Received 21 April 2004; received in revised form 13 April 2005; accepted 19 April 2005

---

### Abstract

The El Arraiche field is a new mud volcano field discovered near the Moroccan shelf edge in the Gulf of Cadiz that consists of 8 mud volcanoes in water depths from 200 to 700 m. The largest mud volcano in the field (Al Idrissi mud volcano) is 255 m high and 5.4 km wide. The cluster was discovered during a survey with the RV Belgica and studied further during Leg 2 of the TTR 12 survey onboard the R/V Prof Logachev. The 2002 surveys yielded detailed multibeam bathymetry over a 700 km<sup>2</sup> study area, dense grids of high-resolution seismic data, deep-tow sub bottom profiles, sidescan sonar mosaics over the major structures. Selected video imagery lines, video guided grab samples, dredge samples, gravity cores, and box cores were collected for groundtruthing purposes. Eight mud volcanoes in water depths from 200 to 700 m cluster around two, sub-parallel anticlines and associated active extensional faults. Rock clasts and regional seismic data locate the El Arraiche field over a Late Miocene–Pliocene extensional basin. The onset of mud volcanic activity is estimated at about 2.4 Ma and probably roots in the Cretaceous–Miocene accretionary wedge. Stacked outflows are visible up to a depth of about 500 m below the sea floor. The occurrence of long-lived mud volcanoes bear witness to continued overpressure generation at depth, either by in situ oil and gas generation or by focussed flow and accumulation in the area. Geochemical analyses of pore water from cores demonstrate the presence of thermogenic hydrocarbon processes. The activity of the mud volcanoes is indicated by the thickness of hemi-pelagic sediments covering extruded mud breccia, the

---

\* Corresponding author. Tel.: +32 9 2644590; fax: +32 9 2644967.

E-mail address: pieter\_vanrensbergen@yahoo.com (P. Van Rensbergen).

occurrence of seep-typical fauna, the degree of mixing between thermogenic and biogenic hydrocarbon processes, or the depth to the base of the sulphate reduction zone. Given its structural setting and the evidence of thermogenic and biogenic hydrocarbons, the area has promising hydrocarbon potential but remains untested.

© 2005 Elsevier B.V. All rights reserved.

*Keywords:* mud volcanoes; hydrocarbons; Gulf of Cadiz; Morocco; Atlantic margin

## 1. Introduction

Since the first mud volcano was discovered in the Gulf of Cadiz in 1999 (Gardner, 2000, 2001), 30 or more mud volcanoes were identified in the span of three years (Pinheiro et al., 2002; Somoza et al., 2003), together with vast fields of hydrocarbon-derived pockmarks and other features related to fluid escape (Barazza and Ercilla, 1996). As such, the Gulf of Cadiz (Fig. 1) has, in a very short time, become one of the prime targets to study these submarine features and the associated sedimentary, biological and biochemical processes.

In May 2002 a new mud volcano cluster was discovered (Fig. 2) near the Moroccan shelf edge offshore of the city of Larache during a survey with RV Belgica and studied further during Leg 2 of the TTR 12 survey on board of RV Prof Logachev. The El Arraiche mud volcano cluster (Fig. 2) consists of 8 mud volcanoes in water depths from 200 to 700 m. The largest mud volcano in the field (Al Idrissi mud volcano) is 255 m high and 5.4 km wide and the smallest mud volcanoes (Lazarillo de Tormes and Don Quichote mud volcanoes) are only 500 m wide and 25 m high. The surveys yielded detailed multibeam bathymetry over the entire area, dense grids of high-resolution seismic

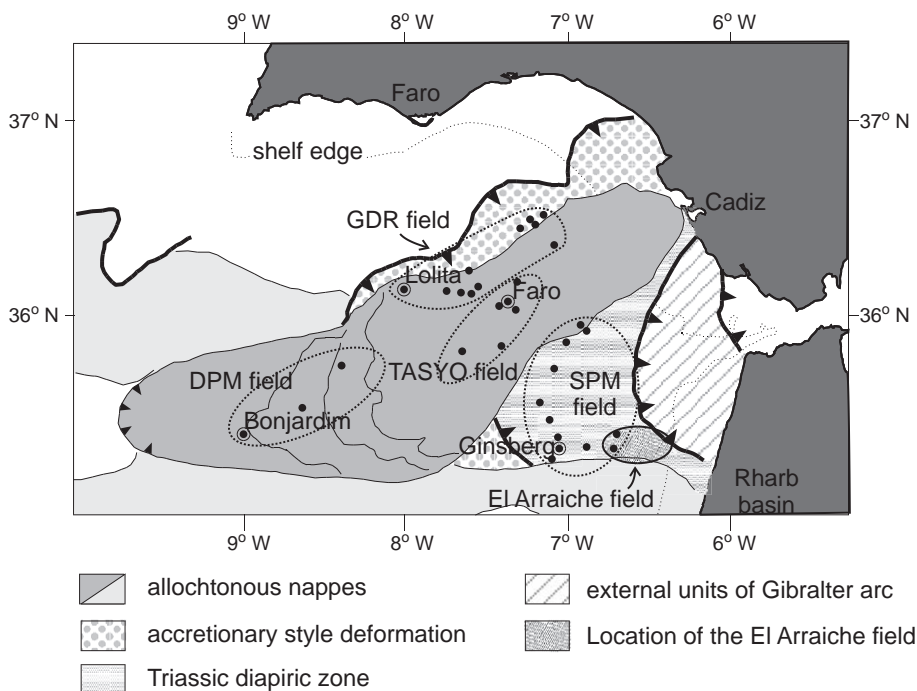


Fig. 1. Mud volcano provinces of the Gulf of Cadiz in their structural setting (based on Maldonado et al., 1999; Somoza et al., 2003). GDR=Guadalquivir ridge, DPM=Deep Portuguese margin, SPM=Spanish Moroccan margin.

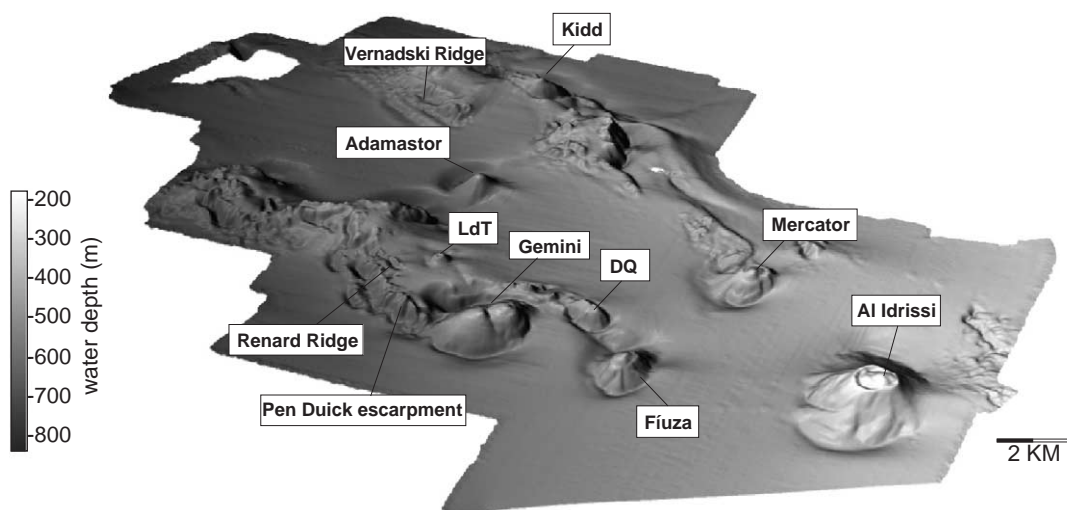


Fig. 2. 3D morphology of the El Arraiche mud volcano field at the Moroccan Atlantic margin derived from multibeam bathymetry. Al Idrissi is the largest mud volcano, 255 m high and 5.4 km in diameter. Don Quichote (DQ) and Lazarillo de Tormes (LdT), the smallest mud volcanoes, are only about 25 m high.

data, a few very high-resolution deep-towed sub-bottom profiles, side scan sonar data over the major structures, selected video imagery, video guided grab samples, dredge samples and gravity cores. Integration of data sets allows studying these long-lived mud volcanoes in detail, and moreover, macro as well as micro level studies over selected places from the regional scales down to microscopic scales.

Mud volcanoes in the Gulf of Cadiz are closely associated with accretionary wedge-type setting related to the convergence of the African and Eurasian plate boundaries and gravitational thin-skinned tectonics over a Triassic salt decollement, also commonly known as the olistostrome unit (Somoza et al., 2003). The newly discovered El Arraiche field is part of a larger cluster of mud volcanoes (the Spanish Moroccan Field, Gardner, 2001) that lies within the accretionary realm but outside the active olistostrome units (Fig. 1). Like other mud volcanoes in the Gulf of Cadiz (Somoza et al., 2002), the El Arraiche mud volcanoes evidence episodic expulsion of liquidized sediment thought to be related to the episodic migration of hydrocarbons. This paper describes the main characteristics of the mud volcanoes in the El Arraiche field and discusses their origin, structural setting and the implications for the hydrocarbon potential of this area offshore Morocco.

## 2. Geological setting

The Gulf of Cadiz is situated between  $9^{\circ}$  W to  $6^{\circ}$   $45'$  W and  $34^{\circ}$  N to  $37.15'$  N enclosed by the Iberian peninsula and Morocco, west of Gibraltar. The bathymetry is steadily increasing from 200 m at the shelf edge to depths of over 4 km in the Horseshoe and Seine abyssal plains. Geologically, the setting of the Gulf of Cadiz is extremely complex and still under debate (Sartori et al., 1994; Maldonado et al., 1999; Gutscher et al., 2002). One of the most important structures is the large olistostrome complex (or allochthonous nappes) that were emplaced in the Tortonian in an accretionary wedge-type environment (Maldonado et al., 1999; Medialdea et al., 2004). The main part of the olistostrome unit occupies the central part of the Gulf of Cadiz as a lobe-shaped structure that extends over 300 km into the ocean (Fig. 1, Maldonado et al., 1999), its extent seems not yet well defined (Maldonado et al., 1999; Somoza et al., 1999; Medialdea et al., 2004; Maestro et al., 2003). The study area is situated south of the main olistostrome unit where thick Late Miocene–Pliocene sedimentary series were deposited in extensional basins at the back of advancing allochthonous sheets (Medialdea et al., 2004). Mio–Pliocene depocentres are bordered by shallow ridges characterized by large and active normal faults (Flinch, 1993), probably super-

posed on relict Miocene thrust anticlines (Maldonado et al., 1999) or Triassic salt diapir structures (Berástegui et al., 1998; Somoza et al., 2003).

All mud volcanoes and other fluid escape features have been found within the realm of the accretionary prism units. They cluster in several mud volcano fields (Somoza et al., 2003, Fig. 1): the Guadalquivir Diapir Ridge (GDR) mud volcano field is located at the north-western side of the Guadalquivir Ridge at the margin of the Tortonian olistostrome unit and at the main thrust belt in this area. It is a dense field with 11 identified mud volcanoes, mud cones and large fluid escape structures in water depths from 380 to 1560 m (Somoza et al., 2003). The term “mud cone” refers to conical shaped hills without proof of mud breccia (Somoza et al., 2003) but is further used here to indicate the mud volcanic hill. The largest structure, the Lolita mud cone, occurs in a water depth of 1560 m and is 316 m high and 5.7 km wide. The Tasyo mud volcano field is separated from the GDR mud volcano field by the Cadiz undercurrent channel. It lies over the north-central part of the main olistostrome unit and consists of 8 mud volcanoes or mud cones amidst many other unidentified circular sea floor structures. The largest structure, the Faro mud volcano, is 190 m high and 2.6 km wide and set in a water depth of 795 m. The Deep Portuguese Margin (DPM) mud volcano field occupies the distal part of the main olistostrome unit in water depths between about 2 to 3.2 km. Only three mud volcanoes have been discovered in this large area but many other features that resemble mud volcanoes or mud cones still need to be studied. The largest in this mud volcano field is probably the Bonjardim mud volcano that was encountered in a water depth of about 3060 m. It is about 100 m high and about 1 km in diameter (Pinheiro et al., 2002). The Spanish-Moroccan (SPM) mud volcano field lies within the “Triassic Diapiric” structural zone (Somoza et al., 2003), south of the main olistostrome unit, in a water depth of about 600 to 1200 m. The largest structure in this area is probably the Ginsburg mud volcano that is over 200 m high and about 4 km in diameter in a water depth of about 1200 m (Gardner, 2000, 2001).

The El Arraiche mud volcano field is located at the south-eastern continuation of the Spanish-Moroccan mud volcano field, offshore the city of Larache. The mud volcano field is located within the accretionary

prism structure but outside the realm of the main olistostrome units. Exploration well LAR-1 is located about 8 km east of the study area.

### 3. Data

The multibeam survey on board R/V Belgica used a Kongsberg EM 1002, extended with a deep water module. Maximum sailing speed was 6 knots, with a swath width of 750 m in shallow water (<500 m) and 500 m in deep water. The acquired data was corrected and cleaned with the Kongsberg packages Merlin and Neptune. The footprint at 400 m is  $15 \times 15$  m. In total 700 km<sup>2</sup> was covered.

A total of 62 high-resolution seismic profiles (Fig. 3) were acquired in three dense grids with a line spacing of about 1 km centred on the Mercator, Al Idrissi and Gemini mud volcanoes. The seismic acquisition used a SIG sparker (80 electrodes) with an energy of 500 J and a SIG surface single channel streamer. In some cases a water gun (15 in.<sup>3</sup>) or a GI-gun (SODERA 35 in.<sup>3</sup> generator and 35 in.<sup>3</sup> injector) were used. Along 5 lines the IFREMER deep-tow Chirp source (650–2000 Hz) was tested with the IFREMER deep-tow 2-channel streamer (of which only one channel was used during this campaign), with excellent results in terms of penetration and resolution. Seismic profiles were digitally recorded using the Elics Delph system. Data processing (swell-filter, band pass filter, deconvolution and signal amplification) used the Landmark Promax processing software. Interpretation and mapping was done using Seismic Microsystems' Kingdom Suite.

During the TTR 12 survey side scan sonar imagery over the main features (Fig. 3) was acquired using the deep-towed hydro-acoustic complex Mak-1, with an operating frequency of 30 kHz, and a sub bottom profiler operating at 5 kHz. The Vernadsky Ridge, the deeper part of the Renard Ridge and the Mercator mud volcano were surveyed with one sidescan sonar line each, Al Idrissi and Gemini mud volcanoes and the upper Renard Ridge were each covered by a mosaic of three lines. Based on the side scan sonar data, 6 transects were chosen for a deep-towed TV-line, for a total of 15 h. Based on the TV-lines, TV-guided grab samples were taken (Fig. 3). Dredge samples of mud breccia at the sea floor were taken on Mercator and Al

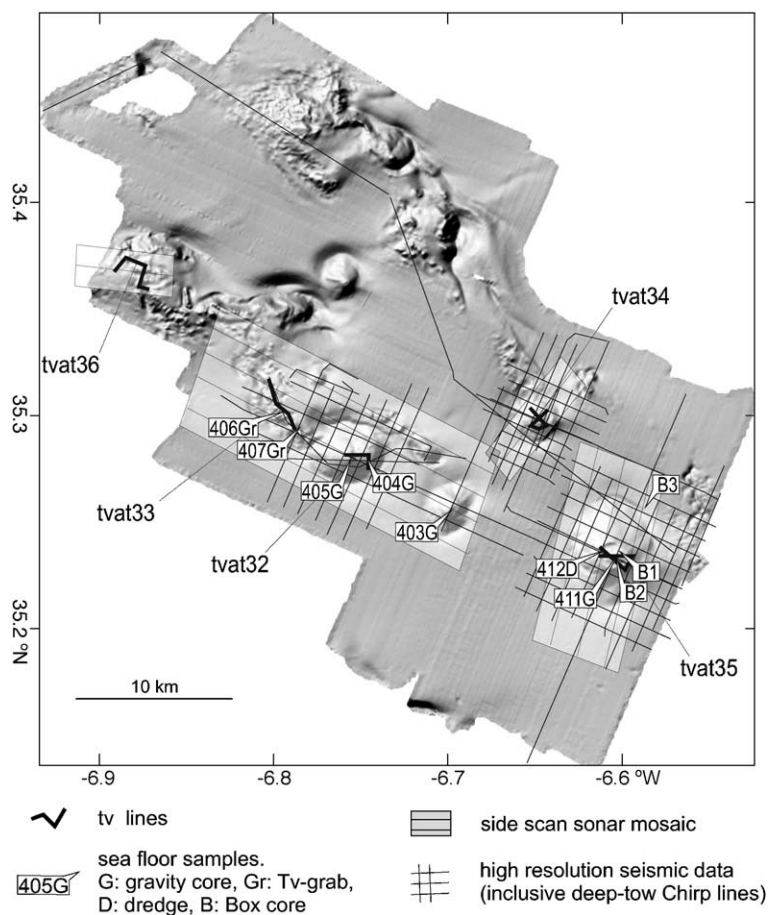


Fig. 3. Shaded bathymetry map of the El Arraiche mud volcano field with localisation of the available seismic data, side scan sonar mosaics, TV-lines, and sea floor samples.

Idrissi mud volcanoes. In the craters of the main mud volcanoes (Mercator, Al Idrissi, Gemini, and Fiúza) the subsurface was sampled by gravity cores. Four additional box cores are also available from the R/V Belgica survey. The technical details of the equipment and core analysis strategies during TTR12 survey are listed in the cruise report Kenyon et al. (2003). Geochemical sampling was performed on all gravity cores within the El Arraiche mud volcano field at irregular intervals of about 10 to 30 cm, depending on the lithology. Geochemical sampling and analysis procedures are described by De Mol et al. (1998) and Stadnitskaia et al. (2002). This paper uses measurements of methane concentrations and the ratio between methane concentration and the concentration in high hydrocarbons ( $C_1/C_{2+}$ ).

#### 4. Data description and interpretation

The El Arraiche mud volcano field (Fig. 2) consists of at least 8 mud volcanoes of varying size that are clustered around two sub-parallel sea floor ridges, the Vernadsky and Renard ridges, both with steep fault escarpments. The ridges rise up in water depths of about 700 m and stretch to the shelf edge. Most mud volcanoes occur on top of the Renard ridge (Lazarillo de Tormes mud volcano, Gemini mud volcano, Don Quichote mud volcano and Fiúza mud volcano). The Kidd mud volcano is situated on top of the Vernadsky Ridge. Isolated mud volcanoes occur between the ridges (Adamastor mud volcano, Mercator mud volcano, Al Idrissi mud volcano).

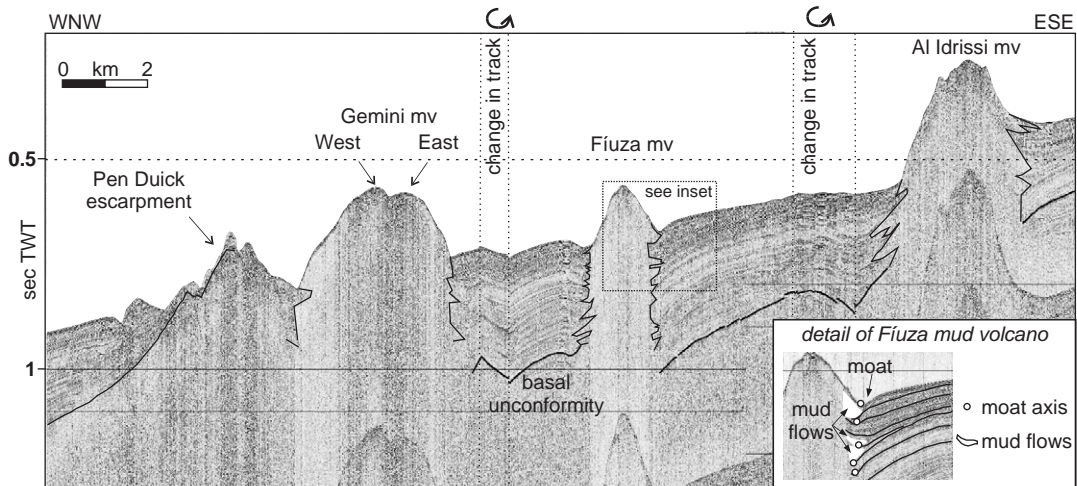


Fig. 4. General high-resolution seismic line (sparker source) over Al Idrissi, Fiúza and Gemini mud volcanoes. The mud volcanoes are characterized by a reflection-free seismic facies that shows stacked outflow lenses within a stratified series of hemi-pelagic sediments above a regional unconformity. The inset shows a detail of interfingering mud flows that accumulate in moats at the base of the Fiúza mud volcano cone.

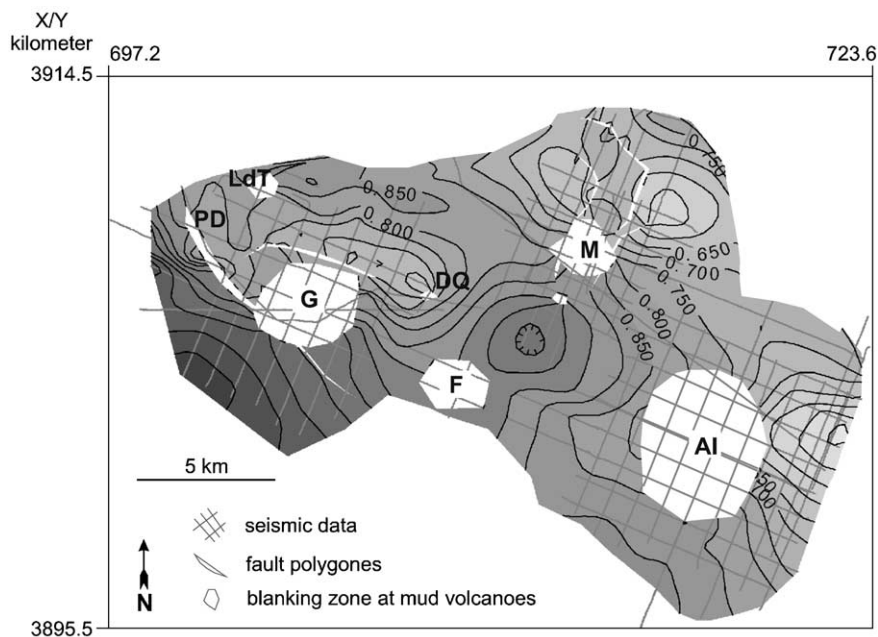


Fig. 5. Time-structure map of the basal unconformity (Fig. 4) mapped on basis of the high-resolution seismic data. The age of the basal unconformity is estimated 2.4 Ma, an upper estimate for the onset of mud volcanism. Indicated abbreviations are AI=Al Idrissi, M=Mercator, G=Gemini, F=Fiúza, DQ=Don Quichote, LdT=Lazarillo de Tormes, PD=Pen Duick escarpment. Contouring is in milliseconds TWT below sea level.

Table 1  
General morphological characteristics of the main mud volcanoes of the El Arraiche field

Name	Water depth top (m)	Height (m)	Slope			Crater Max depth (m)	Slope		Moat		Quadrant
			Width base (km)	Width top (km)	Overall angle (°)		Height (m)	Diameter (km)	Max depth (m)	Radius (km)	
Al Idrissi	197	111–255	4.3–5.4	1.2–1.5	5–8	17	14–42	1.9–2.3	2.85	16	
Mercator	350	51–141	2.45–1.82	0.98–1.1	5.5–10	2	22–38	0.65–0.8	1.3	9	
Gemini W	423	170–252	4.1–2.3	1.1	5.5–8.5	No crater	23–27	0.52–0.87	1.5–1.9	12	
Gemini E	423	117–169	4.1–2.3	0.95–1.3	5–10.5	No crater	13–23	0.7–0.87	0.95–1.25	3	
Fiúza	393	97–143	2.9–2.1	0.75–0.8	6–10	No crater	27	0.5–0.7	1.1–1.6	36	

The mud volcanoes stand out as conical hills on the sea floor with varying slope profiles (Van Rensbergen et al., 2005), mud breccia deposits were found at their top. On the seismic data, the mud volcanoes are characterized by a reflection-free seismic facies that shows stacked outflow lenses within a stratified series of hemi-pelagic sediments above a regional unconformity (Fig. 4). This basal unconformity is mapped in Fig. 5 and is used to document the structural setting of the mud volcanoes. The following paragraphs will describe each of the mud volcanoes. Statistical and descriptive information on the mud volcanoes can be found in Table 1.

#### 4.1. Al Idrissi mud volcano

Al Idrissi mud volcano is the largest and shallowest mud volcano in the field, situated just below the shelf edge in water depths of about 420 m (Fig. 2). It appears to be located on a westward plunging anticline (Fig. 5), visible in the bathymetry and on seismic data at the eastern side of the Al Idrissi mud volcano but almost entirely disappears at its western side. Deep moats at the base occur at the northern and southern side of the mud cone but they are absent over the plunging anticline at the western and eastern sides. The mud volcano is 225 m high, up to 5.4 km wide at its base and 1.5 km wide at the top (Table 1). It is almost circular at the base and has an eye-shaped crater at the top. The crater is up to 17 m deep at the western side, the eastern part is occupied by a central dome-shaped elevation, maximum 42 m above the crater floor. The flanks of the mud volcano are dominated by down slope mud flows. On the side scan sonar mosaic (Fig. 6), mud flows have an even texture but return high backscatter in contrast to the pelagic slope sediments. Backscatter contrast is lower on the southern and eastern flanks probably where pelagic sediments drape the mud extrusions. Core 411G (Fig. 7) and box cores B1 and B2 at the top and at the northern flank of the central dome reveal a sandy layer at the surface of 3–5 cm thick with a sharp and irregular limit separating it from a mud breccia. In core 411G (Fig. 7) this mud breccia is a stiff structureless clay with claystone clasts up to 1 cm. The small clasts encountered at the central dome is in contrast with rock clasts found at the crater floor. Here, up to 0.5 m large rocks were dredged. They

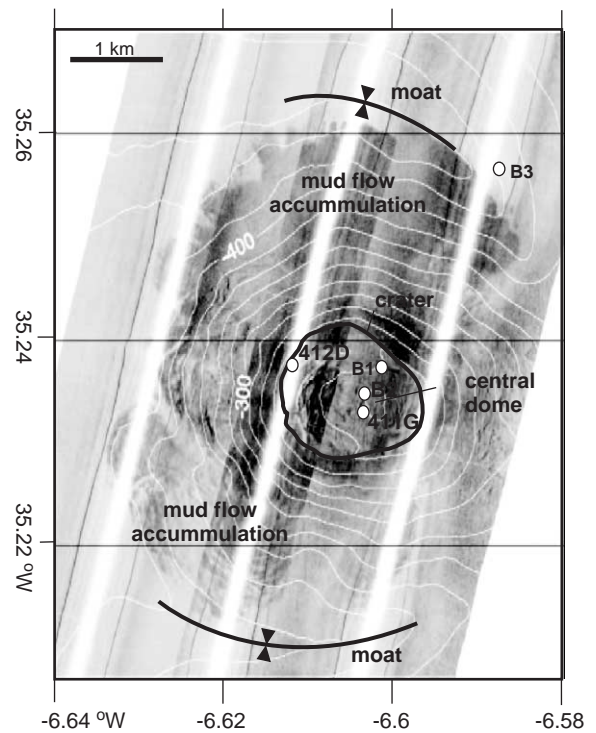


Fig. 6. Side scan sonar mosaic over the Al Idrissi mud volcano with superimposed bathymetry. This mud volcano is 225 m high, 5.4 km wide at its base and 1.5 km wide at the top. The flanks of the mud volcano are dominated by down slope mud flows with high backscatter that contrast with pelagic slope sediments with low backscatter.

are mainly of Upper Miocene and Pliocene age and composed of coarse to fine grained sandstones and siltstones, some with biotritus in a calcite cement (Akhmanov et al., 2002).

#### 4.2. Mercator mud volcano

The Mercator mud volcano is set at the southern flank of the Vernadsky Ridge within a 2 km wide, N–S oriented, collapse zone. This collapse zone is L-shaped and turns 90 degrees west, north of the Mercator mud volcano (Figs. 2 and 5). The mud volcano is an asymmetric mud volcano (Fig. 8) with a moat along its southern and western side. It is 141 m high at the southern side, 90 m high at the northern side and only 51 m high at its eastern side (Table 1). It has a maximum diameter of 2.45 km at the base and 1.1 km at its top. Side scan sonar data show a semi-concentric pattern related to the fronts of mud flow lobes, rather

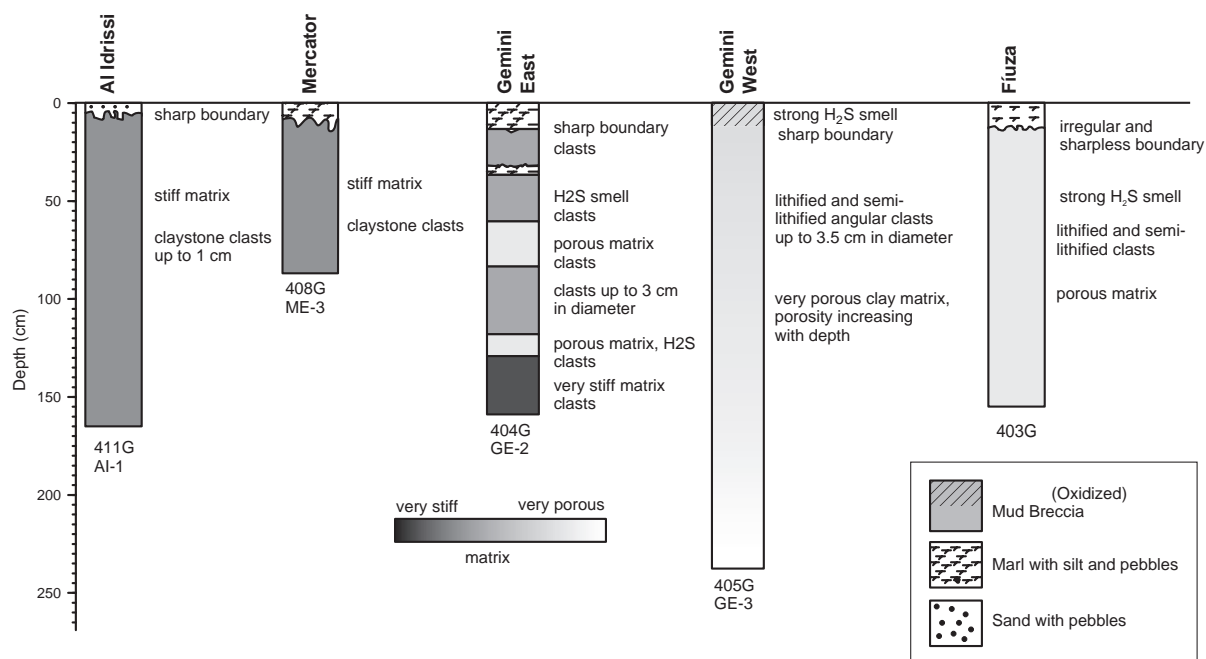


Fig. 7. Description of gravity cores located at the crests of the main mud volcanoes. The localisation of the cores is indicated on Fig. 3. Cores have widely varying fluid contents. Inactive mud volcanoes are covered by a hemi-pelagic drape.

than a radial outward mud flow pattern. A 2 m deep rimmed crater occurs at the northern side but is absent at the southern side. The top of the mud volcano consists of a crater and a 38 m high central dome. Solitary blocks ( $\pm 10$  cm in diameter) occur. Core 408 (Fig. 7) yielded a grey, structureless, slightly silty clay with clay stone clasts, covered by 8 cm of oxidized marl. The seismic data (Fig. 9) show a smaller buried structure, interpreted as a buried mud volcano occurs south of Mercator mud volcano within the same collapse zone.

#### 4.3. Gemini mud volcano

The Gemini mud volcano occurs south of the large fault escarpments at the sea floor that bound the southern flank of the Renard Ridge (Fig. 2). It consists of two mud volcanoes in one large oval-shaped mud cone (Fig. 10). The entire mud volcano is up to 252 m high, 4.1 km long to 2.3 km wide at the base, the maximum diameter at the top of the eastern part (Gemini East) is 1.3 km and the maximum diameter of the western part (Gemini West) is 0.9 km (Table 1). The summits of both Gemini East and Gemini West consist of a flat crater area with a central dome of respectively

23 and 27 m above the flat crater area. Core 404G at the eastern summit (Fig. 7) reveals 12 cm of bio-turbated marl (hemi-pelagic mud), on top of different layers of mud breccia. Another marl layer with a thickness of 4 cm occurs at 32 cm depth. The mud breccia is gray and very gas-saturated, with randomly distributed rock clasts. At the western summit is no hemi-pelagic sediment. Core 405G (Fig. 7) shows a gray mud breccia with a strong H<sub>2</sub>S smell. The surface layer (11 cm) is an oxidized, heavily bioturbated mud breccia. Moats are present parallel to the long axis of the mud volcano.

#### 4.4. Other mud volcanoes

Fiúza mud volcano is a smaller mud volcano east of Gemini (Fig. 10). It is located at the western termination of the Renard Ridge and possibly at the southern continuation of the collapse depression that host the Mercator mud volcano but no faults could be traced in either direction to its location. The mud volcano is maximum 143 m high, 2.2 km wide at the base and has a flat top of up to 0.75 km wide with a central dome of 27 m high and maximum 0.7 km wide (Table 1). Core 403G (Fig. 7) at the top of the mud volcano retrieved a

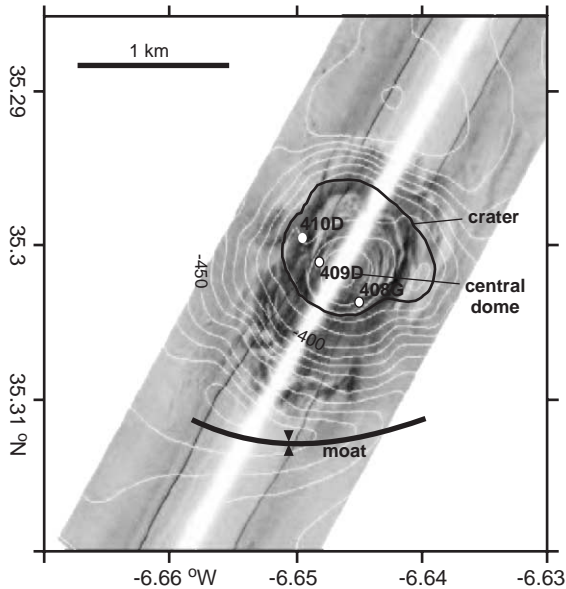


Fig. 8. Side scan sonar image of the Mercator mud volcano with superimposed bathymetry. This asymmetric mud volcano is 140 m high at the southern side but only 90 m high at the northern side. It has a diameter of 1.84 km at the base and 0.5 km at its top. Side scan sonar data show a semi-concentric pattern of mud flow lobe fronts in the crater and on the slope, different from radial outward mud flow pattern at Al Idrissi mud volcano.

homogeneous mud breccia covered by 12 cm of pelagic marl. A semi-circular moat occurs around the base of the mud volcano. Moats are also prominent at deeper levels on seismic data.

Kidd and Adamstor mud volcanoes have been described earlier by Gardner and Shashkin (2000). Adamstor is 2 km wide at the base and about 160 m high. Kidd is sitting on the edge of a fault escarpment, it is about 4 km wide but its height is difficult to measure (between 60 to 160 m). The smaller Don Quichote and Lazarillo de Tormes mud volcanoes occur at the crest of fault blocks on top of the Renard Ridge. Lazarillo de Tormes mud volcano, is 500 m wide and 25 m high. No cores were taken at these mud volcanoes. In general, both mud volcano setting seem associated with extensional faults at the crest of the Renard Ridge anticline.

#### 4.5. Interpretation

On seismic sections, the mud volcanoes consist of a columnar zone without coherent acoustic information, about the width of the mud volcanic cone (Fig. 4). Large mud flows emerging from this central zone are also free of reflections, but show a sharp transi-

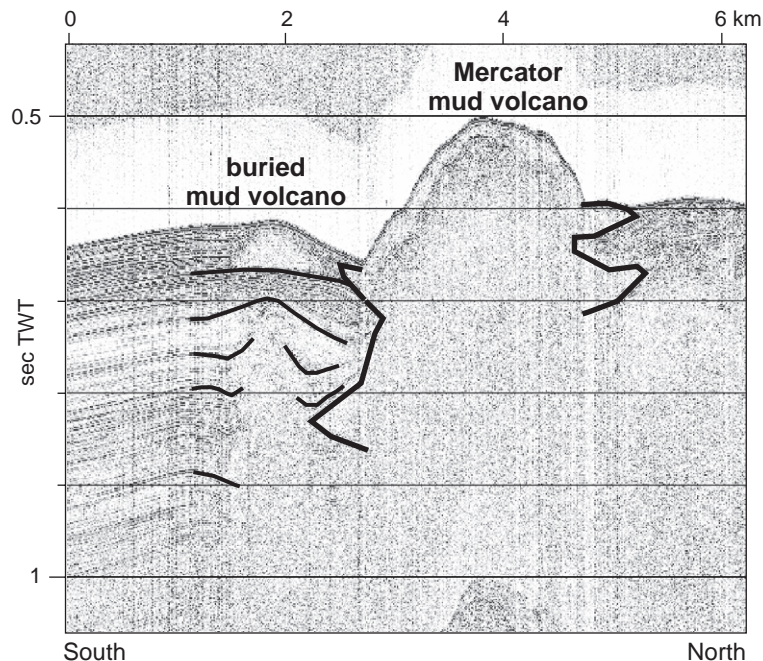


Fig. 9. Seismic line through the Mercator mud volcano and a smaller buried mud volcano just south of it.

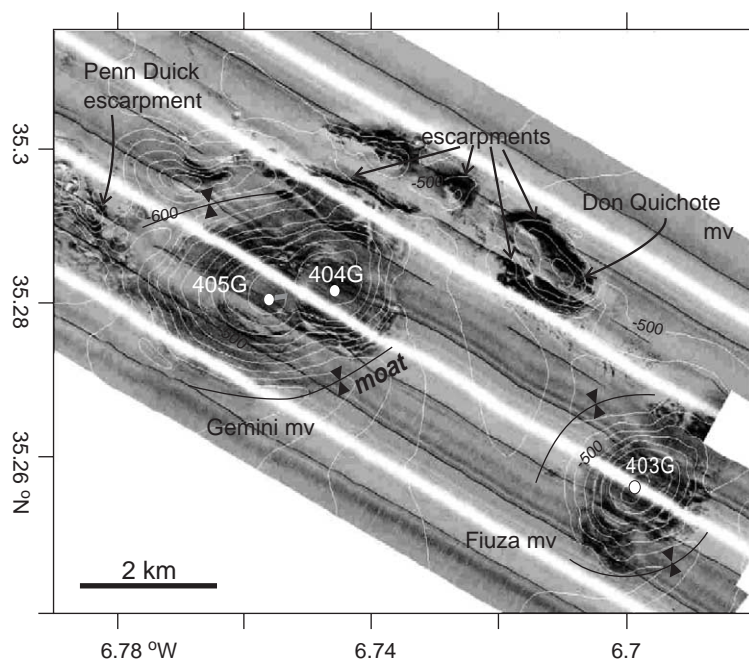


Fig. 10. Side scan sonar mosaic over the Gemini and Fiúza mud volcanoes with superimposed bathymetry. The entire mud volcano is about 200 m high, 4.88 km long to 2.5 km wide at the base, the diameter at the top of the eastern part is 0.9 km and the diameter of the western part is 0.6 km. The summits consist of a flat area with a central dome of respectively 20 and 30 m above the flat top. Fiúza mud volcano is 60 m high, 2.2 km wide at the base and has a flat top of about 600 m wide with a central dome of 10–18 m high and about 300 m wide.

tion to the surrounding sediments. The mud flow deposits are typically lens-shaped, convex at the top and often fill a moat at the base of the mud volcano. In the subsurface, the same pattern returns at several levels bounded by local unconformities (Fig. 4). Stacked outflow lenses produce the typical Christmas-tree morphology of long-lived mud volcanoes, similar to other mud volcanoes in the Gulf of Cadiz (Somoza et al., 2002). On the seismic data only the tips of the largest outflow deposits are visible and probably represent only the largest extrusion events. The lateral dimensions of feeder channel and outflow deposits in the subsurface cannot be measured due to acoustic blanking under almost the entire width of the present-day mud volcano. 3D seismic data in other mud volcanic provinces have demonstrated that the width of the feeder channel is probably much smaller than the zone affected by acoustic blanking or by chaotic reflections (Van Rensbergen et al., 1999).

Moats at the base of mud volcanoes are mostly interpreted as subsidence rims related to volume reduc-

tion caused by degassing and sediment removal (Prior et al., 1989; Camerlenghi et al. 1995). However, high-resolution seismic profiles across these moats show the details of a cut-and-fill facies, indicating erosion by currents. Somoza et al. (2002) also suggest that the moats are caused by erosional currents deflected by the mud volcano cone. For the El Arraiche mud volcano field, Van Rensbergen et al. (2005) suggest erosion in combination with subsidence; subsidence rims can be deepened by current or smoothed by sediment fill. The subsidence rims do not evolve into sediment withdrawal synclines but are filled by mud flows and layered hemi-pelagic sediments and re-appear higher in the section at a slightly different position.

Episodic mud extrusion created vertical columns of remoulded mud up to 500 m below the top of the mud volcanoes. The deepest observed occurrence of mud extrusion deposits is underlain by a regional unconformity. The unconformity, between 450 and 1250 ms TWT (or about 350 and 900 m below sea level), bears witness to a wide-spread erosional event and is the base for a seemingly continuous succession of deep

water sediments. This basal unconformity is interpreted to correspond to an important sea level low stand at 2.4 Ma (Hernández-Molina et al., 2002). This estimated date is well within the age limits obtained by correlation with a near-by industrial well LAR-1 (Flinch et al., 1996), and yields a reasonable sedimentation rate of about 10 cm/ka. The interpreted age (2.4 Ma) of the regional unconformity can be regarded as an upper estimate for the duration of the mud volcano activity in the El Arraiche field.

The time–structure map of this basal unconformity (Fig. 5) shows the structural highs and younger normal faults at the crests. Fault interpretation from the seismic sections is difficult due to the fact that data quality at the mud volcanoes and ridges is not optimal. The bathymetry data show much better the geometry of active faults. Steep escarpments are drawn from sea floor dip maps on the shaded relief map of the study area together with structural information from the seismic

data in Fig. 11. Numerous extensional faults create steep escarpments, in places more than 100 m high, with rapidly varying strike. They are interpreted as collapse faults related to the uplift of the anticlines. Also the Vernadsky Ridge and Renard Ridge anticlines are not continuous structures but appear almost as an ‘en-echelon’ succession of curved sections, disrupted by 2–3 km wide NW–SE trending deformation zones. From the seismic data, it appears that these deformation zones are associated with increased subsidence and collapse of the anticlines.

## 5. Discussion

### 5.1. Origin of El Arraiche mud volcano field

There is little information about the deep-seated feeder system of the El Arraiche field. High-resolution

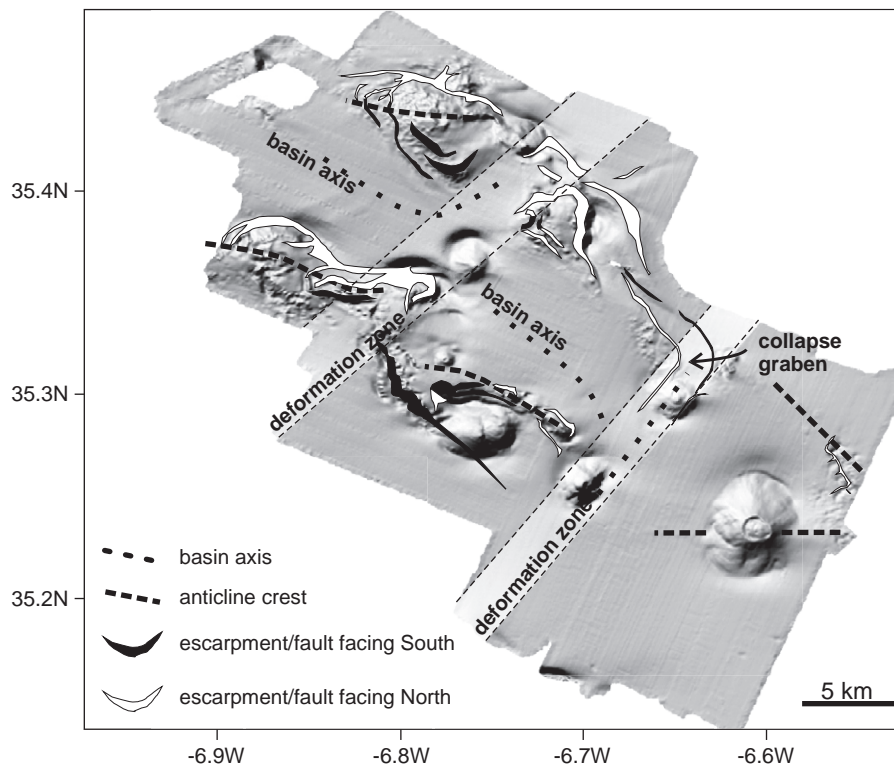


Fig. 11. The localisation of anticlines, basins, and faults from the time–structure map in Fig. 5 drawn on a shaded illumination map of the sea floor at the El Arraiche mud volcano field. In the western part of the study area, good seismic coverage is missing and structures are interpreted from detailed sea floor analysis. Faults have rapidly varying strike and throw, anticlines are discontinuous, and seem compartmentalized by NE–SW trending collapse zones.

seismic profiles only penetrate the upper 500 m and in this case only image the extrusive part of the mud volcano system. Moreover, the subsurface immediately below the mud volcanoes is almost entirely blanked. Only mud breccia clasts from the mud volcanoes bear witness of the stratigraphy that was traversed by the mud volcano feeder system. Petrographic studies of mud breccia clasts retrieved from Al Idrissi and Mercator mud volcanoes by Akhmanov et al. (2002) situate the mud volcano field over an Upper Miocene–Pliocene sedimentary basin. Smaller limestone clasts indicate that the mud volcano feeder system probably roots in or below Upper Cretaceous–Miocene rocks, similar to the other mud volcano fields in the Gulf of Cadiz (Akhmanov et al., 2002; Ovsyannikov et al., 2003).

Upper Miocene–Pliocene clasts were of exceptionally large size, which indicates the shallow position of Upper Miocene–Pliocene rocks in this area. On basis of the near-by exploration well LAR-1 and its correlation with industrial 2D seismic lines (Flinch, 1993), the top Pliocene and top Miocene at the Al Idrissi mud volcano are estimated to occur respectively at about 150 and 900 m below the sea floor. The base of the Upper Miocene was not encountered in the 2400 m deep LAR-1 drill hole. Hence, the distance of vertical transport of the large blocks ranges from 370 m (the depth to top Pliocene plus the height of the mud volcano) to over a kilometre.

The source of overpressure seems to be, at least partly, related to pore fluid volume expansion during thermogenic gas generation (Barker, 1990). The large mud volcanoes (Al Idrissi, Gemini, Mercator and Fiúza) bears witness of repetitive sediment extrusion

and growth since they appeared about 2.4 Ma ago. Gas generation in Mesozoic source rocks and focussed fluid flow along the basal detachment of the accretionary wedge both provide possible sources for sustained and repeated fluid injection into the overburden sediments, probably increased by periods of tectonic compression. Geochemical analysis of gravity cores on the mud volcanoes (Table 2) yielded hydrocarbon gasses from thermogenic origin in the crater of Gemini West and gasses from mixed thermogenic/biogenic in the craters of Fiúza and Gemini East mud volcanoes, the latter was interpreted by Bileva and Blinova (2002) as evidence for a longer period of inactivity. Hydrocarbon gasses with thermogenic signature were also retrieved from Ginsberg mud volcano, down slope of the El Arraiche field (Mazurenko et al., 2002).

### 5.2. Mud volcano activity

The notion of present-day activity of mud volcanoes depends on whether fluid or sediment expulsion is considered. Both processes occur at mud volcanoes and they are closely related given that fluid flow is the main cause of subsurface sediment mobilisation (see discussion by Van Rensbergen et al., 2003). But both fluid seepage and sediment extrusion activity are difficult to assess and conclusions can diverge as is illustrated below. Table 2 summarizes the indications of mud volcano activity for the main mud volcanoes in the El Arraiche field. The time since the last sediment extrusion is indicated by the thickness of hemi-pelagic sediments that cover mud breccia at the crater. Our observations indicate that most recent

Table 2

Overview of indicators of mud volcanic activity. Average  $C_1/C_{2+}$  ratio is calculated for the measurements below the sulphate reduction zone (SRZ)

	Thickness pelagic drape	Thickness SRZ	Maximum methane concentration	$C_1/C_{2+}$ ratio (average)	Seep fauna	Interpretation
Al Idrissi	No	55 cm	564 (ml/l) (at 161 cm)	1700	No seep fauna observed	Large flux of biogenic gas
Mercator	8 cm	≥ 80 cm	0.6 (ml/l) (at 61 cm)	–	Pogonophora	Very low flux
Gemini east	11 cm	90 cm	504 (ml/l) (at 153 cm)	888	Pogonophora	Low gas flux of mixed origin
Gemini west	No	45 cm	875 (ml/l) (at 201 cm)	27	Pogonophora	Large flux of thermogenic gas
Fiúza	12	35 cm	109 (ml/l) (at 71 cm)	803	No seep fauna observed	Moderate gas flux of mixed origin

crater-wide sediment extrusion occurred at Al Idrissi and Gemini West mud volcanoes. At Mercator mud volcano, recent extrusion seems to have occurred only in a narrow zone at the crest of the central dome (Van Rensbergen et al., 2005). The activity of gas seepage can be deduced from the depth of the sulfate reduction zone (SRZ) and by the occurrence of typical seep fauna. Al Idrissi and Gemini West are the most active mud volcanoes; there is no or little pelagic drape, the SRZ is shallowest and the methane concentrations in the sediments are high. It is remarkable that the  $C_1/C_{2+}$  ratio at Al Idrissi is typical for biogenic methane whereas Gemini West has  $C_1/C_{2+}$  ratio typical for thermogenic methane.

### 5.3. Structural control on mud volcano occurrences and its implications for hydrocarbon exploration

The Vernadsky Ridge anticline and the anticline below Al Idrissi mud volcano continue into the shelf area where they were mapped by Flinch (1993) on basis of regional seismic lines. Flinch et al. (1996) mapped listric faults over Miocene thrust anticlines that bound large Pliocene extensional basins (Fig. 12). Similar Pliocene extensional basins have been identified on regional seismic lines in the central Gulf of Cadiz (IAM-T3 line in Gracia et al., 2003 and in Medialdea et al., 2004). They formed at the back of the advancing sheets (Medialdea et al., 2004), probably facilitated by the mobilisation of Triassic evaporites and Miocene shales (Maestro et al., 2003).

The structural setting of the El Arraiche field is thus very different from the GDR, Tasyo and DPM mud volcano fields in the Gulf of Cadiz and the geographical division in mud volcano fields also has geological relevance. A generalized line drawing along a NW–SE transect illustrates the structural setting of the different mud volcano fields (Fig. 12). The GDR mud volcano field is located at the north-western margin of the Tortonian olistostrome and at the major fold and thrust belt in this area (Gracia et al., 2003). Large thrust faults are known to focus fluid flow at the base of the accretionary system. These fluids are likely to move upwards along stacked steep inverse faults at the front thrust zone (GDR field) or at thrust anticlines within the olistostrome unit (TASYO field en DPM field). At places, mud volcanoes are interpreted to overlie diapirs of Miocene plastic marly clays of the olistostrome unit (Maldonado et al., 1999; Somoza et al., 2003). The olistostrome unit is densely fractured, thrust anticlines are not continuous and very irregular, hence mud volcano distribution seems random. Pinheiro et al. (2002) indicate that mud volcanoes seemed aligned along a conjugate fault system with NW–SE and NE–SW direction, probably strike-slip faults. In any case, the influence of the intensely deformed allochthonous units on the distribution of mud volcanoes and fluid escape features is dominant. The SPM mud volcano field and the El Arraiche field are located outside the main olistostrome unit. Here, most compressional structures are buried below a thick, continuous, Plio–Pleistocene sequence that

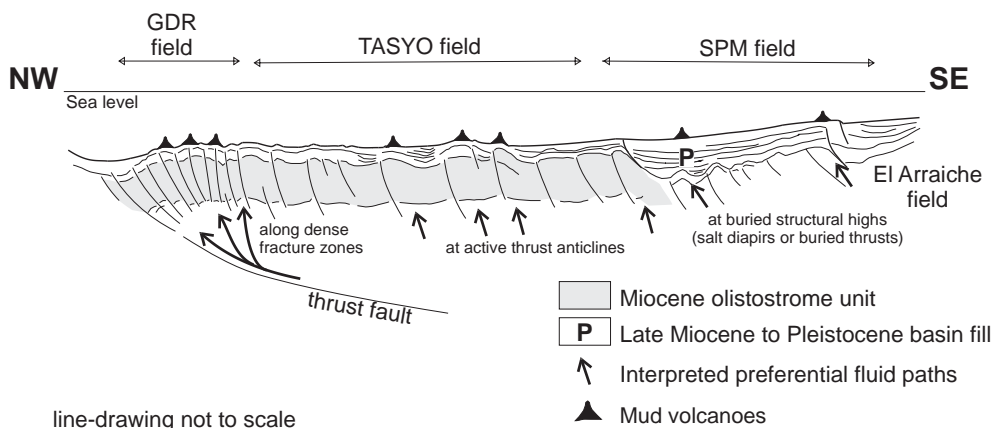


Fig. 12. General structural cross section of the Gulf of Cadiz showing the main mud volcano fields in their structural setting (based on Gracia et al., 2003; Flinch, 1993).

seals accretionary complex structures of Miocene age (Gracia et al., 2003).

The mud volcanoes seem to be located within extensional fault zones, which facilitate vertical upward fluid and sediment injections. The exact location of the mud volcanoes depends on the local and regional stress directions. Mercator mud volcano, the buried mud volcano south of Mercator mud volcano, and Fiúza mud volcano seem to occur within a NE–SW trending deformation zone. Kidd and Adamastor mud volcanoes, and probably a smaller one just south of Adamastor, also appear to occur within a NE–SW oriented deformation zone, almost parallel to the collapse depression that host the Mercator mud volcano (Fig. 11). Sediment injections will occur along fault sections or fractures perpendicular to the direction of minimum horizontal stress (Tingay et al., 2003). Since the anticlines are most likely compressional structures, sediment injections are expected to occur along fault zones perpendicular to the anticline.

Hydrocarbon exploitation in the Gulf of Cadiz only occurs at the Spanish shelf where Spain's largest gas field, the Poseidon field, produced >500 million Nm<sup>3</sup> of natural gas in 2002 (Mineco, 2003). The Moroccan and Portuguese margins are largely under explored, only 5 wildcats were drilled at the Portuguese margin in the Algarve basin (IGM, 2003) and 1 at the Moroccan shelf offshore the city of Larache (ONAREP, 2003). In the entire Gulf of Cadiz only 7 exploration wells were drilled at water depths >200 m. The main hydrocarbon source rock is Early to Middle Jurassic oil and gas prone shale. Oil generation was estimated to occur since Toarcian times (ONAREP, 2003). The most important reservoir rocks are Jurassic reefal build-ups and Cretaceous deltaic sands. In the deep water areas Tertiary turbidites and carbonates are considered to be possible reservoir rocks (ONAREP, 2003). Hydrocarbon exploration in the Gulf of Cadiz is hampered by the intense deformation and nappes emplacement since the Tortonian. Mud volcanoes in the entire Gulf of Cadiz seem to root in Cretaceous to Miocene rocks (Akhmanov et al., 2002), below or within the olistostrome units. Somoza et al. (1999) suggest large possible hydrocarbon accumulations below the salt-floored olistostrome units. In the central part of the Gulf of Cadiz the structural deformation extends up to the sediment surface and controls the distribution of mud volcanoes in the GDR, Tasyo

and DPM mud volcano fields. This may indicate a redistribution of hydrocarbon fluids from deeper sources along several fault-controlled pathways through the allochthonous complex. In the SPM and the El Arraiche mud volcanoes fields, most of accretionary wedge thrust anticlines are sealed by a thick Pliocene section and may host considerable hydrocarbon accumulations. The area offshore El Arraiche remains poorly tested for hydrocarbon accumulations but seems to have very good potential.

## 6. Conclusions

The newly discovered El Arraiche field at the Moroccan Atlantic margin, Gulf of Cadiz, consists of 8 mud volcanoes of varying size and shape just below the Moroccan shelf edge. The largest mud volcano, Al Idrissi mud volcano, is 225 m high and 5.3 km in diameter, the smallest observed mud volcano is only 25 m high and 500 m wide. The mud volcanoes seem to be associated with extensional faults with quickly varying throw and strike that compartmentalize anticlinal ridges. The anticlines can be traced regionally and bound extensional basins that formed during the Late Miocene.

The El Arraiche mud volcano field is part of a larger cluster of mud volcanoes (the Spanish Moroccan Field, Gardner, 2001) that lie within the accretionary realm but outside the active olistostrome units. This distinction is clear on regional seismic lines (Gracia et al., 2003; Medialdea et al., 2004) but it also has bearings on the composition and the size of rock clasts in the mud volcanoes (Akhmanov et al., 2002). As other mud volcanoes in the Gulf of Cadiz (Somoza et al., 2002), the El Arraiche mud volcanoes are long-lived structures thought to be related to the episodic migration of hydrocarbons. Onset of mud volcanic activity in the El Arraiche field is estimated at about 2.4 Ma. Since the Upper Pliocene, episodic expulsion of liquidized sediment created vertical piles of extruded mud of up to 500 m thick.

The occurrence of large mud volcanoes bears witness of continued overpressure generation at depth, either by in situ oil and gas generation or by focussed flow and accumulation in the area. The activity of the mud volcanoes is indicated by the thickness of hemipelagic sediments covering extruded mud breccia, the

occurrence of seep-typical fauna, the degree of mixing between thermogenic and biogenic hydrocarbons, or the depth of the sulphate reduction zone. These indications give variable results. Gemini West and Al Idrissi mud volcanoes are most active, as they lack a hemipelagic sediment drape, feature a shallow sulphate reduction zone, high concentrations of methane, and living Pogonophora worms. The ratio of methane concentration over the concentration of higher homologues gives a biogenic gas source in case of the Al Idrissi mud volcano and a thermogenic signature for the Gemini West crater. The eastern twin crater, Gemini East, was the least active, covered by 12 cm of hemi-pelagic mud. Given its structural setting and the evidence of thermogenic hydrocarbons, the area has promising hydrocarbon potential but remains untested.

### Acknowledgement

The study frames into ESF's MVSeis and Mound-force projects. The R/V Belgica CADIPOR survey was partly funded by the GOA project Porcupine-Belgica. The survey during TTR 12 was funded by a FWO-Flanders research grant to PVR. PVR is funded by FWO-Flanders. DD and DVR are funded by IWT. The technical and scientific crew of R/V Belgica and R/V Logachev are gratefully acknowledged. The deployment of the deep-tow chirp sonar was part of a collaborative venture with IFREMER. The seismic data were interpreted using Seismic Microsystems' Kingdom Suite with a University Grant. Joan Gardner suggested valuable improvements to the manuscript.

### References

- Akhmanov, G.G., Ivanov, M.K., Henriot, J.P., Sarantzev, E.S., 2002. The El Arraiche diapiric field and its "exotic" mud volcanic deposits recovered during the TTR-12 cruise in the Gulf of Cadiz, IOC Workshop Report, vol. 187, p. 9.
- Barazza, J., Ercilla, G., 1996. Gas-charged sediments and large pockmark features on the Gulf of Cadiz slope (SW Spain). *Mar. Pet. Geol.* 13 (2), 253–261.
- Barker, C., 1990. Calculated volume and pressure changes during the thermal cracking of oil to gas in reservoirs. *AAPG Bull.* 74, 1404–1413.
- Berástegui, X., Banks, C.J., Puig, C., Taberner, C., Waltham, D., Fernández, M., 1998. Lateral diapiric emplacement of Triassic evaporites at the southern margin of the Guadalquivir Basin, Spain. In: Mascle, A., Puigdefábregas, C., Luterbacher, H., Fernandez, M. (Eds.), *Cenozoic Foreland Basins of Western Europe*, Geol. Soc. Spec. Publ., vol. 134, pp. 49–68.
- Bileva, E., Blinova, V., 2002. Geochemical characteristics of hydrocarbon gasses from mud volcanoes of the Gulf of Cadiz. IOC Workshop Report, vol. 187, p. 12.
- Camerlenghi, A., Cita, M.B., Dellavedova, B., Fusi, N., Mirabile, L., Pellis, G., 1995. Geophysical evidence of mud volcanism on the Mediterranean Ridge. *Mar. Geophys. Res.* 17 (2), 115–141.
- De Mol, B., Stadnitskaya, A., Swennen, R., Belenkaya, I., Cave, R., 1998. Geochemical sampling. In: Kenyon, N.H., Ivanov, M.K., Akhmetzhanov, A.M. (Eds.), *Cold Water Carbonate Mounds and Sediment Transport on the Northeast Atlantic Margin: Preliminary Results of Geological and Geophysical Investigations During the TTR-7 Cruise of R/V Professor Logachev in Co-operation with the CORSAIRES and ENAM 2 Programmes, July–Aug. 1997*, IOC Technical Series, vol. 52. UNESCO, pp. 15–20.
- Flinch, J.A. 1993. Tectonic evolution of the Gibraltar Arc. Unpublished PhD thesis, Rice University, Houston.
- Flinch, J.A., Bally, A.W., Wu, S., 1996. Emplacement of a passive margin evaporitic allochthon in the Betic Cordillera of Spain. *Geology* 24, 67–70.
- Gardner, J.M., 2000. Gulf of Cadiz/Moroccan margin, mud diapirism and mud volcanism study, introduction and geological setting. In: Kenyon, N.H., Ivanov, M.K., Akhmetzhanov, A.M., Akhmanov, G.G. (Eds.), *Multidisciplinary Study of Geological Processes on the North East Atlantic and Western Mediterranean Margins*, UNESCO Intergovernmental Oceanographic Commission Technical Series, vol. 56, p. 56.
- Gardner, J.M., 2001. Mud volcanoes revealed and sampled on the Western Moroccan continental margin. *Geophys. Res. Lett.* 28 (2), 339–342.
- Gardner, J.M., Shashkin, P., 2000. Gulf of Cadiz/Moroccan margin (leg 2). Mud diapirism and mud volcanism study. Side scan sonar. In: Kenyon, N.H., Ivanov, M.K., Akhmetzhanov, A.M., Akhmanov, G.G. (Eds.), *Multidisciplinary Study of Geological Processes on the North East Atlantic and Western Mediterranean Margins*, IOC Technical Series, vol. 56.
- Gracia, E., Danobeitia, J., Verges, J., Bartolome, R., Cordoba, D., 2003. Crustal architecture and tectonic evolution of the Gulf of Cadiz (SW Iberian margin) at the convergence of the Eurasian and African plates. *Tectonics* 22 (4), 1033.
- Gutscher, M.A., Malod, J., Rehault, J.P., Contrucci, I., Klingelhoefer, F., Mendes-Victor, L., Spakman, W., 2002. Evidence for active subduction beneath Gibraltar. *Geology* 30 (12), 1071–1074.
- Hernández-Molina, F.J., Somoza, L., Vázquez, J.T., Lobo, F., Fernández-Puga, M.C., Llave, E., Daiz-del Río, V., 2002. Quaternary stratigraphic stacking patterns on the continental shelves of the southern Iberian Peninsula: their relationship with global climate and palaeoceanographic changes. *Quat. Int.* 92, 5–23.
- IGM 2003. <http://www.igm.ineti.pt/departam/npep/default.htm>.
- Kenyon, N.H., Ivanov, M.K., Akhmetzhanov, A.M., Akhmanov, G.G., (Eds.), 2003. *Interdisciplinary Geoscience Research on the North East Atlantic Margin, Mediterranean Sea, and Mid Atlantic Ridge During the TTR-12 Cruise of RV Professor*

- Logachev, June–August 2002, IOC Technical Series, vol. 67. UNESCO (156 pp.).
- Maestro, A., Somoza, L., Medialdea, T., Talbot, C.J., Lowrie, A., Vázquez, J.T., Díaz-del-Río, V., 2003. Large-scale slope failure involving Triassic and Middle Miocene salt and shale in the Gulf of Cadiz (Atlantic Iberian Margin). *Terra Nova* 15, 380–391.
- Maldonado, A., Somoza, L., Pallarés, L., 1999. The betic orogen and the Iberian–African boundary in the Gulf of Cadiz: geological evolution. *Mar. Geol.* 155, 9–43.
- Mazurenko, L.L., Soloviev, V.A., Belenkaya, I., Ivanov, M.K., Pinheiro, L.M., 2002. Mud volcano gas hydrates in the Gulf of Cadiz. *Terra Nova* 14, 321–329.
- Medialdea, T., Vegas, R., Somoza, L., Vázquez, J.T., Maldonado, A., Díaz-del-Río, V., Maestro, A., Córdoba, D., Fernández-Puga, M.C., 2004. Structure and evolution of the “Olistostrome” complex of the Gibraltar Arc in the Gulf of Cádiz (eastern Central Atlantic): evidence from two long seismic cross-sections. *Mar. Geol.* 209, 173–198.
- Mineco 2003. <http://www.cne.es/documentos/petroleo/estadisticas/>.
- ONAREP 2003. <http://www.onhym.com/onarep/>.
- Ovsyannikov, D.O., Sadekov, A.Yu., Kozlova, E., 2003. Rock fragments from mud volcanic deposits of the Gulf of Cadiz: an insight into the Eocene–Pliocene sedimentary succession of the basin. *Mar. Geol.* 3273, 1–11.
- Pinheiro, L.M., Ivanov, M.K., Sautkin, A., Akhmanov, G., Magalhães, V.H., Volkonskaya, A., Monteiro, J.H., Somoza, L., Gardner, J., Hamouni, N., Cunha, M.R., 2002. Mud volcanism in the Gulf of Cadiz: results from the TTR-10 cruise. *Mar. Geol.* 3269, 1–21.
- Prior, D.B., Doyle, E.H., Kaluza, M.J., 1989. Evidence for sediment eruption on deep-sea floor, Gulf of Mexico. *Science* 243, 517–519.
- Sartori, R., Torelli, L., Zitellini, N., Peis, D., Lodolo, E., 1994. Eastern segment of the Azores–Gibraltar line (central-eastern Atlantic): an oceanic plate boundary with diffuse compressional deformation. *Geology* 22, 555–558.
- Somoza, L., Maestro, A., Lowrie, A., 1999. Allochthonous Blocks as Hydrocarbon Traps in the Gulf of Cadiz. *Offshore Technology Conf. Proc. OTC-12202*, pp. 571–577.
- Somoza, L., Gardner, J.M., Díaz-del-Río, V., Vázquez, J.T., Pinheiro, L.M., Hernández-Molina, F.J. the TASYO/Anastasya shipboard parties, 2002. Numerous methane gas-related sea floor structures identified in the Gulf of Cádiz. EOS, p. 541.
- Somoza, L., Díaz-del-Río, V., León, R., Ivanov, M., Fernández-Puga, M.C., Gardner, J.M., Hernández-Molina, F.J., Pinheiro, L.M., Rodero, J., Lobato, A., Maestro, A., Vázquez, J.T., Medialdea, T., Fernández-Salas, L.M., 2003. Seabed morphology and hydrocarbon seepage in the Gulf of Cádiz mud volcano area: acoustic imagery, multibeam and ultra-high resolution seismic data. *Mar. Geol.* 195, 153–176.
- Stadnitskaia, A., Blinova, V., Poludetkina, E., 2002. Hydrocarbon gas sampling. In: Kenyon, N.H., Ivanov, M.K., Akhmetzhanov, A.M., Akhmanov, G.G. (Eds.), *Geological Processes in the Mediterranean and Black Seas and North East Atlantic; Preliminary Results of Investigations during the 11th Training-Through-Research (TTR-11) Cruise of RV Professor Logachev, July–September, 2001*, IOC Technical Series, vol. 62. UNESCO, pp. 34–39.
- Tingay, M.R.P., Hillis, R.R., Morley, C.K., Swarbrick, R.E., Okpere, E.C., 2003. Pore pressure/stress coupling in Brunei Darussalam—implications for shale injection. In: Van Rensbergen, P., Hillis, R.R., Maltman, J., Morley, C.K. (Eds.), *Subsurface Sediment Mobilisation*, Special Publication of the Geological Society of London, vol. 216, pp. 369–379.
- Van Rensbergen, P., Morley, C.K., Ang, D.W., Hoan, T.Q., Lam, N.T., 1999. Structural evolution of shale diapirs from reactive rise to mud volcanism: 3D seismic data from the Baram delta, offshore Brunei Darussalam. *J. Geol. Soc. Lond.* 156, 633–650.
- Van Rensbergen, P., Hillis, R.R., Maltman, J., Morley, C.K., 2003. Subsurface sediment mobilization, introduction. In: Van Rensbergen, P., Hillis, R.R., Maltman, J., Morley, C.K. (Eds.), *Subsurface Sediment Mobilisation*, Special Publication of the Geological Society of London, vol. 216, pp. 1–8.
- Van Rensbergen, P., Depreiter, D., Pannemans, B., Henriët, J.P., 2005. Seafloor expression of sediment extrusion and intrusion at the El Arraiche mud volcano field, Gulf of Cadiz. *J. Geophys. Res.* 110 (F2), F02010. (24 May).



## Microbial methane turnover at mud volcanoes of the Gulf of Cadiz

H. Niemann<sup>a,b,\*</sup>, J. Duarte<sup>c</sup>, C. Hensen<sup>d</sup>, E. Omoregie<sup>a,g</sup>, V.H. Magalhães<sup>c,e</sup>,  
M. Elvert<sup>f</sup>, L.M. Pinheiro<sup>c</sup>, A. Kopf<sup>f</sup>, A. Boetius<sup>a,g</sup>

<sup>a</sup> Max Planck Institute for Marine Microbiology Bremen, Celsiusstr.1, 28359 Bremen, Germany

<sup>b</sup> Alfred Wegener Institute for Polar and Marine Research, 27515 Bremerhaven, Germany

<sup>c</sup> Geosciences Department and CESAM, University of Aveiro, Campus de Santiago, 3810-193 Aveiro, Portugal

<sup>d</sup> Leibniz Institute of Marine Sciences, IfM-GEOMAR, 24148 Kiel, Germany

<sup>e</sup> Department National Institute of Engineering, Technology and Innovation, Alfragide, 2720-866 Amadora, Portugal

<sup>f</sup> Research Center Ocean Margins, University of Bremen, 28359 Bremen, Germany

<sup>g</sup> International University Bremen, 28759 Bremen, Germany

Received 1 August 2005; accepted in revised form 3 August 2006

### Abstract

The Gulf of Cadiz is a tectonically active area of the European continental margin and characterised by a high abundance of mud volcanoes, diapirs, pockmarks and carbonate chimneys. During the R/V SONNE expedition “GAP–Gibraltar Arc Processes (SO-175)” in December 2003, several mud volcanoes were surveyed for gas seepage and associated microbial methane turnover. Pore water analyses and methane oxidation measurements on sediment cores recovered from the centres of the mud volcanoes Captain Arutyunov, Bonjardim, Ginsburg, Gemini and a newly discovered, mud volcano-like structure called “No Name” show that thermogenic methane and associated higher hydrocarbons rising from deeper sediment strata are completely consumed within the seabed. The presence of a distinct sulphate–methane transition zone (SMT) overlapping with high sulphide concentrations suggests that methane oxidation is mediated under anaerobic conditions with sulphate as the electron acceptor. Anaerobic oxidation of methane (AOM) and sulphate reduction (SR) rates show maxima at the SMT, which was found between 20 and 200 cm below seafloor at the different mud volcanoes. In comparison to other methane seeps, AOM activity ( $<383 \text{ mmol m}^{-2} \text{ year}^{-1}$ ) and diffusive methane fluxes ( $<321 \text{ mmol m}^{-2} \text{ year}^{-1}$ ) in mud volcano sediments of the Gulf of Cadiz are low to mid range. Corresponding lipid biomarker and 16S rDNA clone library analysis give evidence that AOM is mediated by a mixed community of anaerobic methanotrophic archaea and associated sulphate reducing bacteria (SRB) in the studied mud volcanoes. Little is known about the variability of methane fluxes in this environment. Carbonate crusts littering the seafloor of mud volcanoes in the northern part of the Gulf of Cadiz had strongly  $^{13}\text{C}$ -depleted lipid signatures indicative of higher seepage activities in the past. However, actual seafloor video observations showed only scarce traces of methane seepage and associated biological processes at the seafloor. No active fluid or free gas escape to the hydrosphere was observed visually at any of the surveyed mud volcanoes, and biogeochemical measurements indicate a complete methane consumption in the seafloor. Our observations suggest that the emission of methane to the hydrosphere from the mud volcano structures studied here may be insignificant at present.

© 2006 Elsevier Inc. All rights reserved.

### 1. Introduction

Constraining global sources and sinks of the greenhouse gas methane, and understanding the climate change

coupled to variations in atmospheric methane, are important rationales of current biogeochemical research. Anthropogenic sources as well as natural emission from wetlands contribute significantly to the global emission of methane to the atmosphere, but the role of the ocean in global methane fluxes is not well understood (Reeburgh, 1996; Judd et al., 2002). Recently, marine mud volcanism has been identified as an important escape pathway for methane

\* Corresponding author. Fax: +49 421 2028690.

E-mail address: [hniemann@mpi-bremen.de](mailto:hniemann@mpi-bremen.de) (H. Niemann).

and higher hydrocarbons (Dimitrov, 2002; Judd et al., 2002; Dimitrov, 2003). Mud volcanism is caused by various geological processes at continental margins such as tectonic accretion and faulting, rapid burial of sediments and emission of gases and fluids. Such processes may lead to high pore fluid pressures and sediment instabilities, and consequently cause mud extrusions. Since subsurface muds and shales of productive continental margins often contain methane and other hydrocarbons of thermogenic and/or microbial origin, mud flows can be accompanied by gas expulsion (Milkov, 2000; Kopf, 2002; Charlou et al., 2003; Somoza et al., 2003). Mud volcanoes (MVs) are structurally diverse, ranging in shape from amorphous mud pies to conical structures, and in size from a few metres to kilometres in diameter, attaining heights of up to a few 100 m (Dimitrov, 2002; Kopf, 2002). While there are only 650–900 known terrestrial mud volcanoes (Kopf, 2003), global estimates for marine mud volcanoes range between 800 and 100,000 (Milkov, 2000; Dimitrov, 2002, 2003; Kopf, 2003; Milkov et al., 2003). It is unknown how many of these submarine mud volcanoes are actively emitting methane to the hydrosphere. As a result, global estimates of methane emissions from these structures vary considerably. Recent estimates suggest that terrestrial and shallow water mud volcanoes contribute between 2.2 and 6 Tg year<sup>-1</sup> of methane to the atmosphere (Dimitrov, 2003; Milkov et al., 2003) and that 27 Tg year<sup>-1</sup> of methane may escape from deep water mud volcanoes (Milkov et al., 2003). Revised estimates of the total methane emission from MVs ranges between 35 and 45 Tg year<sup>-1</sup> (Etioppe and Milkov, 2004), 30 and 70 Tg year<sup>-1</sup> (Etioppe and Klusman, 2002), and—when using only known MVs and correcting for size of the edifice—between 0.3 (Kopf, 2003) and 1.4 Tg year<sup>-1</sup> (Kopf, 2002). Clearly, a better understanding of mud volcano activity and methane turnover at these structures is needed, to evaluate the contribution of mud volcanism to the total annual methane emission to the atmosphere (535 Tg year<sup>-1</sup>, Judd et al., 2002).

The main sink for methane in the ocean is the anaerobic oxidation of methane (AOM) with sulphate as the terminal electron acceptor (Barnes and Goldberg, 1976; Reeburgh, 1976; Iversen and Jørgensen, 1985; Hinrichs and Boetius, 2002; Nauhaus et al., 2002; Treude et al., 2003). This process is mediated by archaea, operating most likely in cooperation with sulphate reducing bacteria (SRB) (Hinrichs et al., 1999; Boetius et al., 2000; Orphan et al., 2001). So far, two groups of anaerobic methanotrophic archaea (ANME-1, ANME-2) have been identified (Hinrichs et al., 1999; Boetius et al., 2000; Orphan et al., 2001; Michaelis et al., 2002; Knittel et al., 2005). They usually occur together with SRB from a distinct, yet uncultivated cluster within the *Desulfosarcina/Desulfococcus* group (Seep-SRB1; Knittel et al., 2003). Generally, microbial methane oxidation is characterised by a strong discrimination against the heavy, stable carbon isotope <sup>13</sup>C, leading to a significant depletion in the <sup>13</sup>C-content of metabolites

and biomass (Reeburgh and Heggie, 1977; Whiticar et al., 1986; Summons et al., 1994; Elvert et al., 1999; Thiel et al., 1999; Whiticar, 1999; Orphan et al., 2001). Such conspicuous isotope signatures of lipid biomarkers for the archaeal and bacterial partners in AOM mediating communities have been a main tool in studying the diversity and functioning of cold seep ecosystems (Hinrichs et al., 1999; Pancost et al., 2000; Elvert et al., 2001; Orphan et al., 2001; Michaelis et al., 2002; Elvert et al., 2003; Blumenberg et al., 2004; Elvert et al., 2005; Niemann et al., 2005). Active mud volcanoes in the Mediterranean Sea, e.g. Napoli, Amsterdam and Kazan (Pancost et al., 2000; Aloisi et al., 2002; Haese et al., 2003; Werne et al., 2004); the Black Sea, e.g. Dvurechenskii and Odessa (Bohrmann et al., 2003; Stadnitskaia et al., 2005); and the Barents Sea, e.g. Håkon Mosby (Vogt et al., 1997a,b; Damm and Budéus, 2003; De Beer et al., 2006) are characterised by steep gradients of pore water solutes due to upward fluid and gas flow and high rates of AOM and sulphate reduction (SR). Several of these geo-bio-systems were also found to support enormous biomasses of chemosynthetic symbiotic tubeworms and bivalves, which are fuelled by methane and/or sulphide, and mats of giant sulphide oxidising bacteria, (Southward et al., 1981; Fisher, 1990; Olu et al., 1997a; Gebruk et al., 2003).

During the UNESCO program “Training through Research (TTR)” with R/V Prof. Logachev, numerous mud volcanoes hosting methane-hydrate were discovered in the Gulf of Cadiz (Kenyon et al., 2000; Gardner, 2001; Kenyon et al., 2001; Mazurenko et al., 2002; Somoza et al., 2002; Pinheiro et al., 2003). However, the geochemical and microbiological activity of these potential seep structures and the occurrence of methane emission to the hydrosphere remained unknown. As part of the Gibraltar Arch Project (GAP), we studied several mud volcanoes with the aid of seafloor video imaging as well as video-guided sampling of sediments and carbonate crusts during a cruise with R/V Sonne in 2003 (SO-175). The main goals of this investigation were to survey the occurrence of methane seepage at mud volcanoes in the Gulf of Cadiz, to compare the distribution and magnitude of AOM by rate measurements and diffusive flux calculations, as well as to identify the key methanotrophs using lipid biomarker and 16S rDNA methods.

## 2. Materials and methods

### 2.1. Geological setting and videographic observations

The Gulf of Cadiz is located west of the Gibraltar Arc, between Iberia and the African plate (Fig. 1). This area has experienced a complex tectonic history with several episodes of extension, strike-slip and compression related to the closure of the Tethys Ocean, the opening of the N-Atlantic, and the African–Eurasian convergence since the Cenozoic (Maldonado et al., 1999). During the Tortonian, a large olistostome body made of eroded material from

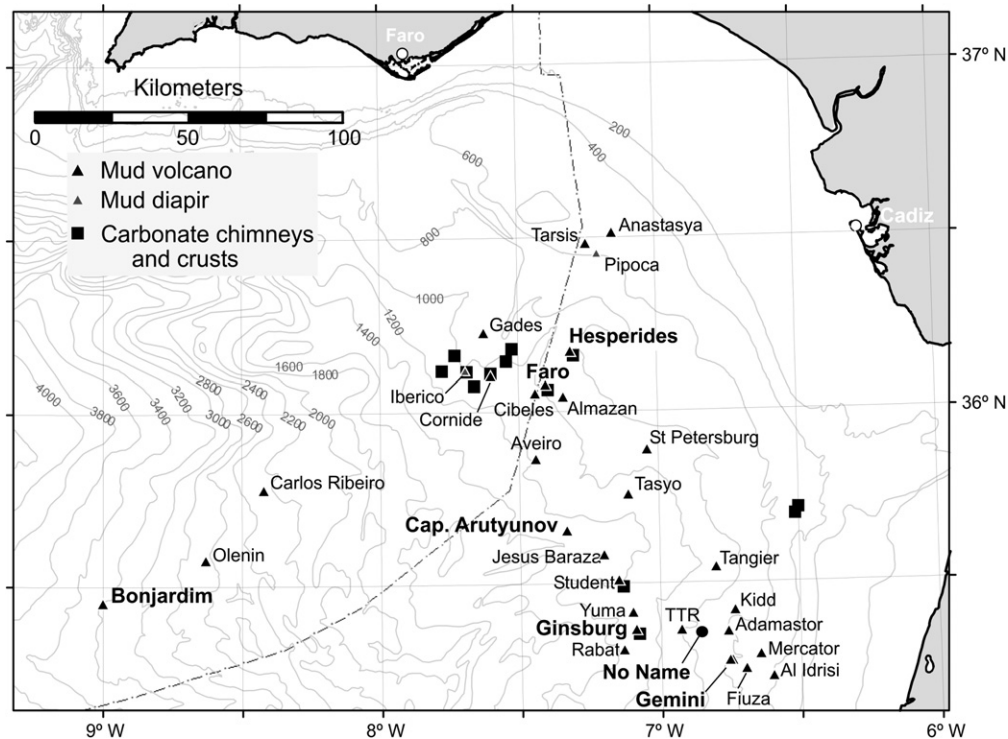


Fig. 1. Bathymetric chart of the Gulf of Cadiz showing the locations of known mud volcanoes, diapirs and areas where carbonate chimneys and crusts were discovered. The structures studied during the SO-175 expedition are in bold face letters.

the Betic Cordillera (Spain) and Rif Massif (Morocco) was emplaced west of the Straits of Gibraltar (Maldonado and Comas, 1992; Somoza et al., 2003). Due to the ongoing compression, these rapidly deposited sediments dewater intensely and form MVs and fluid escape structures (Diaz-Del-Rio et al., 2003). The Gulf of Cadiz has been intensely surveyed with geophysical tools, leading to the discovery of the first MVs, mud diapirs and pockmarks in 1999 (Kenyon et al., 2000; Gardner, 2001; Pinheiro et al., 2003). In addition, an extensive field of mud volcanoes and diapiric structures covered with carbonate chimneys and crusts was discovered along or in close proximity of the main channels of the Mediterranean outflow water (Kenyon et al., 2000, 2001; Diaz-Del-Rio et al., 2003; Somoza et al., 2003; Kopf et al., 2004).

In the present study, Captain Arutyunov (Capt. Arutyunov), Bonjardim, Ginsburg, Gemini, Hesperides and Faro MV and a newly discovered structure termed “No Name”, were investigated (Fig. 1, Table 1). Prior to biogeochemical sampling, a few transects across the selected MVs were surveyed with the video-sled Ocean Floor Observation System (OFOS), or with a video-guided multiple-corer (MUC, Table 1). Both systems are equipped with powerful lamps and a video camera. Video observations were made from a vertical perspective at ca. 1–2 m above the sea bottom to monitor an area of approximately 1 m<sup>2</sup>. The systems were passively towed at minimum speed (<1.84 km h<sup>-1</sup>) along 2–3 transects of 1–3 km crossing the rim and apex of the edifices with a total bottom observation time of approxi-

mately 8 h per mud volcano (Table 1, Kopf et al., 2004). The video-guided MUC was also used to select representative sampling positions and to retrieve undisturbed surface sediments (next section).

## 2.2. Sample collection and storage

Sediments from several mud volcanoes were sampled by gravity coring in the central crater region (Table 1, Fig. 2), retrieving up to 5 m of sediment. Additionally, surface sediments of Capt. Arutyunov and Bonjardim MV were obtained with a video-guided MUC because the top decimetres of sediment cover are often lost during gravity core retrieval. Video-guided MUC sampling enabled the retrieval of undisturbed surface sediments of up to 50 cm sediment depth. With this method, the seafloor can be observed when the MUC is towed at minimum speed at about 1–2 m above bottom. The MUC is launched immediately when targeted seafloor structures are observed. Compared to the gravity core, MUC-cores contained a broader horizon of hemipelagic surface sediments providing further evidence for a loss of surface sediments during gravity coring. To account for this loss, we aligned the depth of gravity cores obtained from Capt. Arutyunov and Bonjardim MV according to the vertical sulphate profiles of MUC-cores recovered from one site, assuming that sulphate concentrations are mainly a function of depth in proximate cores. According to this procedure, the top of the gravity cores recovered from Capt. Arutyunov and Bonjardim

Table 1  
Mud volcanoes investigated during the cruise SO-175

Structure	Relief [m]	Diam. [km]	Water depth [m]	Device	Core/Grab	Lat. N	Long. W	Applied methods
CAMV	80	2.0	1315	MUC	GeoB 9036-2	35° 39.72'	07° 19.98'	V, CH <sub>4</sub> , SO <sub>4</sub> <sup>2-</sup> , C <sub>2+</sub> , H <sub>2</sub> S, F, R, L, D
				GC	GeoB 9041-1	35° 39.70'	07° 19.97'	CH <sub>4</sub> , SO <sub>4</sub> <sup>2-</sup> , C <sub>2+</sub> , H <sub>2</sub> S
Bonjardim	100	1.0	3090	MUC	GeoB 9051-1	35° 27.72'	08° 59.98'	V, CH <sub>4</sub> , SO <sub>4</sub> <sup>2-</sup> , C <sub>2+</sub> , H <sub>2</sub> S, R, L
				GC	GeoB 9051-2	35° 27.61'	09° 00.03'	CH <sub>4</sub> , SO <sub>4</sub> <sup>2-</sup> , C <sub>2+</sub> , H <sub>2</sub> S, F, R, L
Ginsburg	150	4.0	910	GC	GeoB 9061-1	35° 22.42'	07° 05.29'	V, CH <sub>4</sub> , SO <sub>4</sub> <sup>2-</sup> , H <sub>2</sub> S, F
Gemini	200	4.9	435	GC	GeoB 9067-1	35° 16.92'	06° 45.47'	CH <sub>4</sub> , SO <sub>4</sub> <sup>2-</sup> , H <sub>2</sub> S, F
No Name	150	3.7	460	GC	GeoB 9063-1	35° 21.99'	06° 51.92'	CH <sub>4</sub> , SO <sub>4</sub> <sup>2-</sup> , H <sub>2</sub> S, F
Hesperides	160	3.0	690	Grab	GeoB 9023-1	36° 10.73'	07° 18.39'	V, L
Faro	190	2.6	810	Grab	GeoB 9029-3	36° 05.68'	07° 24.12'	V, L

The water depth refers to the highest elevation of the mud volcanoes. V, video observations; CH<sub>4</sub>, methane concentration measurements; SO<sub>4</sub><sup>2-</sup>, sulphate concentration measurements; C<sub>2+</sub>, concentration measurements of higher hydrocarbons; F, diffusive methane and sulphate flux calculation; R, AOM and SR rate measurements; L, lipid analyses; D, DNA analysis.

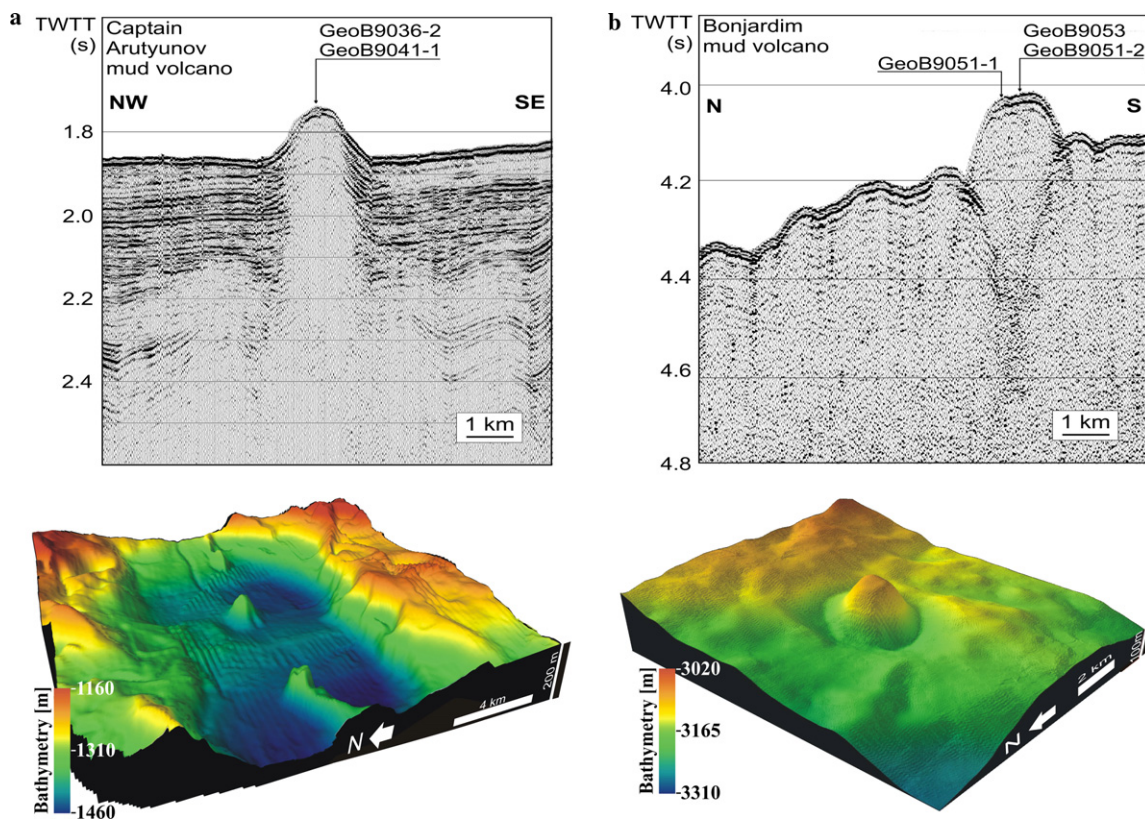


Fig. 2. Seismic images and 3D images of multibeam bathymetry of Captain Arutyunov (a) and Bonjardim mud volcano (b). Seismic images show the central conduit below the mud volcanoes and sampling position of the cores recovered during the SO-175 expedition. Captain Arutyunov and Bonjardim MV are conical shaped structures with a relief of 80 and 100 m and a diameter of ca. 2 and 1 km, respectively. Colours denote the bathymetry (m below sea surface). Seismic images were modified after Kenyon et al. (2001) (a) and Pinheiro et al. (2003) (b).

MV were from 40 to 12.5 cm sediment depth, respectively. Aligning proximate core sections is an approach to account for a loss of an unknown quantity of surface sediments during gravity coring. However, this can be problematic if the spatial variability of geochemical gradients is high.

Upon recovery, gravity cores were sectioned into 1 m pieces, which were cut longitudinally into halves, just before sub sampling. All cores were immediately transferred

into a cold room and subsampled for concentration measurements of pore water constituents (methane, sulphate, sulphide), AOM and SR rate measurements as well as for lipid biomarker and 16S rDNA analyses (Table 1). Sediments for measurements of methane and sulphate concentrations and turnover rate measurements were subsampled vertically with push cores (acrylic core liners, 26 mm diameter,  $n = 3$ ) from MUC-cores (Jørgensen, 1978; Treude et al., 2003). Gravity cores were subsampled by plugging

glass tubes (60 mm length, 10 mm diameter,  $n = 5$ ) into selected ca. 10 cm wide sediment horizons (every 20–30 cm). The tubes were then sealed with butyl rubber stoppers to prevent gas loss during the anaerobic incubation. Sediment samples for pore water extraction, biomarker and 16S rDNA analyses were collected from 2 cm sections of MUC-cores and from ca. 10 cm wide sediment horizons (every 20–30 cm) of gravity core sections. Directly after subsampling, pore water from these sediment horizons was extracted by pressure filtration (5 bars) through Teflon squeezers provided with 0.2  $\mu\text{m}$  cellulose acetate filters according to previous works (Reeburgh, 1967; Niewöhner et al., 1998; Hensen et al., 2003). Subsequently, the pore water was immediately fixed (next section). Lipid and DNA samples were stored in cleaned glass vials at  $-20^\circ\text{C}$  until extraction in the home laboratory. Carbonate crusts from Hesperides and Faro MV were collected with a video-guided grab-sampler (Table 1). Because Hesperides MV consist of six individual cones, the grab sample was taken from the apex of the highest (north-eastern) summit. The grab-sampler allows to retrieve samples down to a depth of ca. 0.5 m below seafloor (bsf). The videographic observation and sampling procedure is similar to the technique used for video-guided coring as explained above. Upon recovery, carbonate crusts for lipid biomarker analyses were transferred into plastic bags and stored at  $-20^\circ\text{C}$  until extraction.

### 2.3. Methane concentrations

Methane concentrations in sediments were determined according to the “head space” method from 5 ml sediment fixed with 10 ml NaOH (2.5%, w/v) in glass vials (20 ml) as described previously by Treude and co-workers (2003). A vertical resolution of 2 cm was chosen for surface samples from MUC-cores, and of 20–30 cm for subsurface samples from gravity cores. The concentrations presented here are *ex situ* methane concentrations. As a result of depressurisation and warming of the core during sediment retrieval, concentrations above 1.4 mM (saturation at 1 bar and  $4^\circ\text{C}$ ) would have led to degassing during retrieval and sediment subsampling. Also, dissociation of gas hydrates upon recovery may lead to biased methane concentrations in the cores. We tried to minimise the problem by (a) subsampling immediately after opening the core, and (b) subsampling of deeper sediments below the longitudinal opening plane of the gravity core with glass syringes. Methane concentrations were determined shortly after the cruise (<2 month) from 200  $\mu\text{l}$  aliquots of the head space using a gas chromatograph (5890A, Hewlett Packard) equipped with a packed stainless steel Poropak-Q column (6 ft., 0.125 in, 80/100 mesh, Agilent Technologies) and a flame ionisation detector (Treude et al., 2003). The carrier gas was helium at a flow rate of 30 ml  $\text{min}^{-1}$ . The column temperature was  $40^\circ\text{C}$ . The chromatography system was calibrated for a concentration range of 0.001–5 mM methane (final concentration in the sediment). Sediment samples from Capt.

Arutyunov and Bonjardim MV were additionally analysed for the concentrations of the higher hydrocarbons ( $\text{C}_{2+}$ ) ethane, propane, isobutene and butane ( $\Sigma\text{butane}$ ) using the above-described chromatography setting with a temperature gradient. Subsequent to injection at  $40^\circ\text{C}$ , the temperature was increased at a rate of  $2^\circ\text{C min}^{-1}$  to  $200^\circ\text{C}$  and held for 20 min. Identity and concentrations of methane and  $\text{C}_{2+}$ -compounds were determined with standards of known hydrocarbon compositions.

### 2.4. Sulphate and sulphide concentrations

Sulphate and sulphide concentrations were analysed according to modified methods from Cline (1969) and Small et al. (1975), respectively, as described elsewhere (Grasshoff et al., 1983). Briefly, sulphide concentrations were determined immediately after pore water squeezing by adding 1 ml of pore water to 50  $\mu\text{l}$  of a zinc acetate gelatine solution. Zinc acetate gelatine solution consists of 50 mg gelatine and 261 mg ZnAc dissolved in 25 ml  $\text{O}_2$ -free water. Sulphide was quantitatively removed as ZnS and kept in colloidal solution. After adding 10  $\mu\text{l}$  of 4% *N,N*-dimethyl-1,4-phenylenediamine-dihydrochloride dissolved in 6 N HCl (w/v), the concentration was determined photometrically by measuring the absorbance after 1 h at 670 nm. Sulphate concentrations were determined on 2 ml subsamples of filtered pore water using a Sykam-S ion chromatography system equipped with an anion exchange column (LCA A14). 7.5 mM  $\text{Na}_2\text{CO}_3$ -solution was used as an eluent at a flow rate of 1.75 ml  $\text{min}^{-1}$ . Samples were diluted by 1:54 with the eluent prior to injection. Sulphate concentrations were determined with a Sykam S3110 conductivity detector.

### 2.5. Diffusive flux calculations

Diffusive fluxes were calculated to compare areal rates of AOM and SR, to estimate the activity of Ginsburg and Gemini mud volcano as well as the No Name structure and to compare the surveyed systems to other seeps in the world oceans. This approach bears several problems, namely potential artefacts in the *ex situ* concentrations of porewater species due to degassing, the assumption of steady state in the porewater system, and the alignment of sediment cores. At Bonjardim mud volcano, the alignment of pore water profiles was discontinuous, while the resolution of pore water gradients was not well resolved at Ginsburg and Gemini mud volcano. Where possible, we determined two concentration gradients: one from the aligned profile and the other from the profile of the gravity core in order to provide a possible range of the sulphate and sulphide fluxes.

Local fluxes ( $J$ ) were calculated from the vertical profiles of pore water constituents (methane, sulphate, sulphide) according to Fick's first law of diffusion assuming steady state conditions (e.g. Niewöhner et al., 1998; Berner, 1980 and references therein):

$$J = -\phi D_s \frac{\delta C}{\delta x} \quad (1)$$

where  $D_s$  is the diffusion coefficient in the sediments (in  $\text{cm}^2 \text{year}^{-1}$ ),  $\phi$  the porosity (in %) and  $\frac{\delta C}{\delta x}$  the local concentration gradient (in  $\text{cm}^{-4}$ ).  $\frac{\delta C}{\delta x}$  was determined from the depth intervals where the concentration change was maximal.  $D_s$  was determined from the molecular diffusion coefficient after Boudreau (1997)

$$D_s = \frac{D_0}{1 - \ln(\phi)^2} \quad (2)$$

For each mud volcano,  $D_0$  values were corrected for temperature (3–12 °C, depending on the actual bottom water temperature), resulting in values ranging between 291 to 392, 178 to 244 and 356 to 434 for methane, sulphate and sulphide, respectively (Boudreau, 1997).  $\phi$  was determined from the weight loss per volume of wet sediment after drying to stable weight at 60 °C. In general,  $\phi$  decreased with depth showing values of 57–76% in the top sections and 51–60% in the bottom sections of the retrieved MUC- and GC-cores (data shown for the SMT, Table 2).

#### 2.6. *Ex situ* AOM and SR rate measurements

Sediment for turnover rate measurements recovered from Capt. Arutyunov and Bonjardim MV were incubated on board according to previously described methods (Jørgensen, 1978; Treude et al., 2003; Treude et al., 2005). Briefly, 25  $\mu\text{l}$   $^{14}\text{CH}_4$  (dissolved in water, 2.5 kBq) or 5  $\mu\text{l}$   $^{35}\text{SO}_4^{2-}$  tracer (dissolved in water, 50 kBq) were injected into butyl rubber sealed glass tubes from gravity core subsampling, and in 1 cm intervals into small push cores (whole core injection) used for MUC-core subsampling. Incubations were carried out for 24 h at *in situ* temperature in the dark. Subsequently, incubated AOM and SR rate samples were fixed in 25 ml NaOH (2.5%, w/v) and 25 ml zinc acetate solution (20%, w/v), respectively. Further processing of AOM and SR rate samples was performed according to Treude et al. (2003) and references therein. Turnover rates were calculated according to the following formulas:

$$\text{AOM} = \frac{^{14}\text{CO}_2}{^{14}\text{CH}_4 + ^{14}\text{CO}_2} \times \frac{\text{conc. CH}_4}{\text{incubat. Time}} \quad (3)$$

$$\text{SRR} = \frac{\text{TRI}^{35}\text{S}}{^{35}\text{SO}_4^{2-} + \text{TRI}^{35}\text{S}} \times \frac{\text{conc. SO}_4^{2-}}{\text{incubat. Time}} \quad (4)$$

Here,  $^{14}\text{CO}_2$ ,  $^{35}\text{SO}_4^{2-}$  and  $\text{TRI}^{35}\text{S}$  are the activities (Bq) of carbon dioxide, sulphate and total reduced sulphur species, respectively, whereas conc.  $\text{CH}_4$  and conc.  $\text{SO}_4^{2-}$  are the concentrations of methane and sulphate (per volume of fresh sediment) at the beginning of the incubation. To compare *ex situ* microbial rates with the diffusive fluxes of methane and sulphate, AOM and SR rates were integrated over depth (0–80 cm below seafloor) from the alignments of cores 9036-2 and 9041-4 as well as 9051-1 and 9051-2, respectively. *Ex situ* rate measurements may differ from *in situ* rates due to the effect of depressurisation on concentrations of gaseous and dissolved components.

#### 2.7. Extraction of sediment and carbonate samples and preparation of derivatives

Sediments from Capt. Arutyunov and Bonjardim MV as well as carbonate crusts from Hesperides and Faro MV were analysed for lipid biomarker signatures. The extraction procedure and preparation of fatty acid methyl esters (FAMES) was carried out according to previously described methods (Gillian et al., 1981; Elvert et al., 2003; Niemann et al., 2005). Briefly, total lipid extracts (TLE) were obtained from ca. 20 g of wet sediment and from authigenic carbonates disintegrated with HCL (2 M) prior to extraction. The TLE was extracted by subsequent ultrasonication using organic solvents of decreasing polarity (dichloromethane/methanol (1:2, v/v), dichloromethane/methanol (2:1 v/v), dichloromethane). Internal standards of known concentration and carbon isotopic compositions were added prior to extraction. Fatty acid moieties present in glyco and phospholipids were cleaved by saponification with methanolic KOH-solution. After extraction of the neutral lipid fraction from this mixture, fatty acids (FAs) were methylated with  $\text{BF}_3$  in methanol yielding FAMES. Double bond positions of monoenoic FAs were determined

Table 2  
Concentrations gradients, diffusive fluxes and *ex situ* AOM and SR rates integrated over depth

Structure	Core GeoB	Porosity [%]	Conc. gradient [ $\mu\text{mol cm}^{-4}$ ]			Diffusive fluxes [ $\text{mmol m}^{-2} \text{year}^{-1}$ ]			Microbial turnover [ $\text{mmol m}^{-2} \text{year}^{-1}$ ]		
			CH <sub>4</sub>	SO <sub>4</sub> <sup>2-</sup>		Sulphide	CH <sub>4</sub>	ΣSO <sub>4</sub> <sup>2-</sup>	ΣSulphide	AOM	SR
				SO <sub>4</sub> <sup>2-</sup>	Sulphide						
Capt. Arutyunov	9036-2	56	0.40	-1.12	0.63	407	708	702	383	577	
Bonjardim	9051-2	58	0.09	-0.76, -1.67*	0.23, 0.73* (-0.07)	76	388, 867‡	299, 795‡	36	690	
Ginsburg	9061-1	60	0.05	-0.92 (0.35)	0.32 (-0.15)	55	852	565			
Gemini	9067-1	56	0.02	-0.61	0.12 (-0.09)	21	388	272			
No Name	9063-1	57	0.03	-0.11	0.04 (-0.06)	29	74	108			

A negative concentration gradient indicates downward directed flux; a positive value indicates upward flux. Flux values are given without algebraic signs. \* and ‡ denote gradients and total sulphate fluxes determined from aligning multiple- and gravity cores. Gradients in brackets indicate upward diffusing sulphate and downward diffusing sulphide, respectively.

by analysis of dimethyl disulphide adducts according to methods described elsewhere (Nichols et al., 1986; Moss and Lambertfair, 1989).

Neutral lipids were further separated into hydrocarbons, ketones and alcohols on a SPE silica glass cartridge (0.5 g packing) with solvents of increasing polarity (*n*-hexane/dichloromethane (95:5, v/v), *n*-hexane/dichloromethane (2:1, v/v), dichloromethane/acetone (9:1, v/v)) (Niemann et al., 2005). Alcohols were derivatised with bis(trimethylsilyl)trifluoroacetamide (BSTFA) forming trimethylsilyl (TMS) ethers prior to analyses.

## 2.8. Gas chromatography

Concentrations of single lipid compounds were determined by gas chromatography analysis using a Varian 30 m apolar CP-Sil 8 CB fused silica capillary (0.25 mm internal diameter [ID], film thickness 0.25  $\mu\text{m}$ ) in a Hewlett Packard 6890 Series gas chromatograph equipped with an on column injector and a flame ionisation detector. Initial oven temperature was 80 °C. Subsequently to injection, the initial temperature was increased to 130 °C at a rate of 20 °C  $\text{min}^{-1}$ , then raised to 320 °C at a rate of 4 °C  $\text{min}^{-1}$  and held at 320 °C for 30 min. The carrier was helium at a constant flow of 2 ml  $\text{min}^{-1}$  and the detector temperature was set to 310 °C. Concentrations were calculated relative to internal standards present within the respective lipid fraction.

## 2.9. Gas chromatography-mass spectrometry (GC-MS), gas chromatography-isotope ratio mass spectrometry (GC-IRMS)

Identity and stable carbon isotope ratios of individual compounds were determined by GC-MS and GC-IRMS analysis, respectively. Instrument specifications and operation modes of the GC-MS and GC-IRMS units were set according to Elvert et al. (2003). Identities of acquired mass spectra were compared to known standards and published data. Stable isotope ratios are given in the  $\delta$ -notation against Pee Dee Belemnite.  $\delta^{13}\text{C}$ -values of FAs and alcohols were corrected for the introduction of additional carbon atoms during derivatisation. Internal standards were used to monitor precision and reproducibility during measurements. Reported  $\delta^{13}\text{C}$ -values have an analytical error of  $\pm 1\%$ .

## 2.10. DNA extraction and clone library construction

Total community DNA was extracted from sediments (ca. 1 g) collected from the SMT of Capt. Arutyunov MV (30–40 cm) using the FastDNA spin kit for soil (Q-Biogene, Irvine, California, USA). Samples were bead-beat in a Fastprep machine (Q-Biogene, Irvine, California, USA) at speed 4.5 for 30 s. All other steps in the DNA extraction procedure were performed according to the manufacturer's recommendations. Almost full-length

archaeal and bacterial 16S rRNA genes were amplified from sediments samples using the primers 20f (Massana et al., 1997) and Uni1392R (Lane et al., 1985) for *Archaea* and GM3F (Muyzer et al., 1995) and GM4R (Kane et al., 1993) for *Bacteria*. Polymerase chain reactions (PCRs) were performed with TaKaRa Ex Taq (TaKaRa, Otsu Japan), using 2.5 U of enzyme, 1 $\times$  Buffer, 4 mM of  $\text{MgCl}_2$ , 4 mM of each dNTP, 1  $\mu\text{M}$  of each primer and 2  $\mu\text{l}$  of template in a 50  $\mu\text{l}$  reaction. PCRs were performed in a Mastercycler machine (Eppendorf, Hamburg, Germany), with the following cycling conditions: 95 °C for 2 min, then 30 cycles of 95 °C for 30 s, 60 °C (*Archaea*) or 50 °C (*Bacteria*) for 30 s and 72 °C for 3 min, followed by a final incubation step at 72 °C for 10 min. PCR products were visualised on an agarose gel, and the 16S band excised. PCR products were purified using the QIAquick Gel Extraction Kit (Qiagen, Hilden, Germany). Two microliters of purified DNA were ligated in the pGEM T-Easy vector (Promega, Madison, WI) and transformed into competent *E. coli* TOP10 cells (Invitrogen, Carlsbad, CA) according to the manufacturer's recommendations. Transformation reactions were plated on LB-agarose plates. Overnight cultures were prepared from individual colonies picked from these plates using the Montage Plasmid Miniprep 96 kit (Millipore, Billerica, USA). Purified plasmids were sequenced in one direction, with either the 958R (*Archaea*) or GM1F (*Bacteria*) primers using the BigDye Terminator v3.0 Cycle Sequencing kit (Applied Biosystems, Foster City, USA). Samples were sequenced on an Applied Biosystems 3100 Genetic Analyser (Foster City, USA). A total of 39 archaeal and 47 bacterial clones were partially sequenced ( $\sim 0.5$  kb). Using the ARB software package, the sequences were calculated into existing phylogenetic trees by parsimony without allowing a change in the tree topology. Representative sequences of each cluster were then fully sequenced ( $\sim 1.3$  kb) and matched against the NCBI database (<http://www.ncbi.nlm.nih.gov/BLAST>). Sequences were submitted to the Genbank database (<http://www.ncbi.nlm.nih.gov/>) and are accessible under the following Accession Nos.: DQ004661–DQ004676 and DQ004678–DQ004680.

## 3. Results

### 3.1. Field observations

A detailed description of seafloor video observations, sedimentology and sampling locations is provided in the cruise report of R/V SONNE expedition SO-175 (Kopf et al., 2004). The mud volcanoes Capt. Arutyunov, Bonjardim, Ginsburg, Gemini, and Faro studied here are cone shaped structures with a relief of up to 200 m and a maximum diameter of 4.9 km (Fig. 2a, b; Table 1). Hesperides MV has comparable dimensions but is composed of six individual cones. A new structure was discovered east of the TTR MV and termed "No Name" (Fig. 1). Video observations of the mud volcanoes Capt. Arutyunov, Bon-

jardim, Ginsburg, Hesperides, and Faro did not reveal indications for recent gas, fluid or mud expulsion during the transects across the central craters of each structure. The centres of Capt. Arutyunov, Bonjardim and Ginsburg MV were covered with light beige sediments (shown for Capt. Arutyunov MV, Fig. 3a). At Capt. Arutyunov MV, some sediment stretches were scattered with accretions, interpreted as mud clasts, which may indicate past mud eruptions (Fig. 3b). At Ginsburg MV, a few small carbonate crusts (<0.5 m) were observed on the seafloor. Beside these observations, no other distinctive geological or biological features indicating gas or fluid seepage were visible on video images at Ginsburg MV. Surface sediments recovered from Capt. Arutyunov MV contained very thin tubeworms (diameter <1 mm), which extended down to 20 cm into the sediment. These were not visible on video images due to their low abundance and small diameter. Tubeworms are regarded as indicator species for reduced environments because the known species harbour methane or sulphide oxidising symbionts, indicating sulphide and/or methane availability in the sediments (Southward et al., 1981, 1986; Schmaljohann and Flugel, 1987; Sibuet and Olu, 1998; Kimura et al., 2003; Southward et al., 2005). The central areas of Hesperides and Faro MV were littered with fragments of carbonate chimneys and carbonate crusts (shown for Hesperides MV, Fig. 3c). Both, chimneys and crusts were ranging in size from several centimetres to metres in length and diameter, respectively. At Faro MV, a few, small patches covered with microbial mats possibly consisting of filamentous sulphide oxidising bacteria were

observed (Fig. 3d). Moreover, TV-guided grab samples recovered from this MV also contained a few specimens of the deep-dwelling chemosynthetic clam *Acharax* sp. usually harbouring sulphide oxidising bacteria in their gills (Felbeck, 1983; Krueger and Cavanaugh, 1997; Peek et al., 1998; Sibuet and Olu, 1998). Video observations were not carried out at Gemini MV and the “No Name” structure.

The MUC-cores retrieved from Capt. Arutyunov and Bonjardim MV contained yellowish, muddy sediments in the top sections from 0 to 20 and 0 to 40 cm bsf, respectively. The bottom sections of the MUC-cores contained mud breccia, a mud matrix with clasts extruded from greater depth below these edifices (Cita et al., 1981; Akhmanov and Woodside, 1998). The gravity cores retrieved from these MVs as well as those retrieved from Ginsburg and Gemini also contained mud breccia. The gravity core recovered from the “No Name” structure contained a matrix of cold water coral fragments and greyish mud but no mud breccia. Hence, the relation of the “No Name” geostructure to mud volcanism remains unknown. Grab samples from Hesperides and Faro MV contained carbonate fragments and mud breccia. After recovery, the temperature in the top sediment section (~1 m) at Bonjardim MV was ca. 3 °C. In contrast, the temperature was considerably higher at Capt. Arutyunov (12 °C), Ginsburg MV, Gemini MV and the “No Name” structure (10 °C, respectively) most probably as a result of the warm Mediterranean outflow water, which contributes to the bottom water at these MVs.

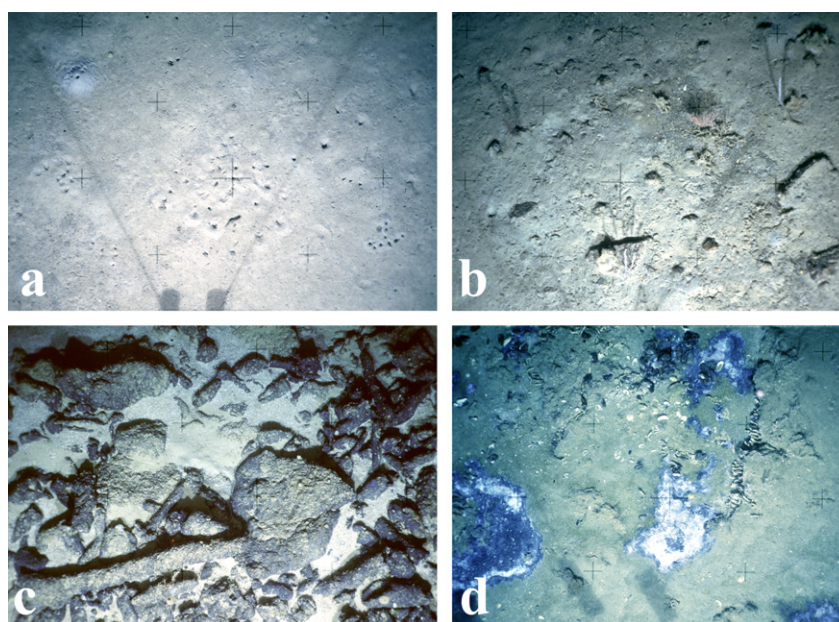


Fig. 3. Seafloor images (ca. 1 m<sup>2</sup>) of Capt. Arutyunov (a,b), Hesperides (c) and Faro MV (d). The surface of Capt. Arutyunov, Bonjardim, Ginsburg MV were found to be covered by pelagic sediments as shown in (a). The holes are burrows of crabs. Some sediment stretches at Capt. Arutyunov MV contained accretions that are interpreted as clasts (b) indicating past mud flows. Hesperides and Faro mud volcano were littered with carbonate chimneys and crusts as shown for Hesperides MV in (c). At Faro mud volcano, also a few dark sediment patches probably covered with whitish, giant sulphide-oxidizing bacteria were observed (d).

### 3.2. Captain Arutyunov MV

#### 3.2.1. Methane, C<sub>2+</sub>, sulphate and sulphide

Methane concentrations in surface sediments (0–20 cm, Fig. 4a) were <0.001 mM indicating a complete consumption of methane rising from deeper sediment strata. A distinct SMT was observed in the lower half of the MUC-core section (25–40 cm bsf.) with *ex situ* methane concentrations above saturation at atmospheric pressure, and sulphate concentrations dropping below 0.5 mM. The steepest gradients of methane and sulphate found in this zone amounted to 0.4 and  $-1.12 \mu\text{mol cm}^{-4}$ , respectively (Fig. 4a, Table 2). Small gas hydrate chips were found throughout the whole gravity core section from 44 to 235 cm bsf (1941-1). Similar to methane, concentrations of C<sub>2+</sub>-compounds decreased across the SMT (Fig. 4b). Hydrocarbons in the sediment comprised methane (>99%), ethane (<0.4%), propane (<0.07%) with trace amounts of butane and isobutene present indicating a thermogenic origin of these gases (Nuzzo et al., 2005; Stadnitskaia et al., 2006 and references therein). Sulphide concentrations peaked in the SMT with 4.8 mM at 39 cm bsf (Fig. 4d). The steepest sulphide gradient was  $0.63 \mu\text{mol cm}^{-4}$  (Fig. 4d, Table 2). A downward sulphide gradient could not be determined because highest sulphide concentrations were observed in the lowest sediment horizon of the MUC-core at Capt. Arutyunov MV. Unfortunately, the sulphide profile could not be aligned with the gravity core section.

#### 3.2.2. AOM, SR rates and diffusive fluxes

AOM and SR rates at Capt. Arutyunov MV were highest in the SMT at 39 cm bsf with maximum values of 11 and  $25 \text{ nmol cm}^{-3} \text{ d}^{-1}$ , respectively (Fig. 4c). AOM and SR rates sharply decreased above and below this horizon. Replicate AOM and SR rate measurements showed a stan-

dard error of 33% and 37% of the average value, respectively. The areal integration resulted in 1.8 higher SR rates compared to AOM (Table 2). The areal AOM and SR rate were in good agreement with diffusive flux calculations showing a 1.7-fold higher sulphate flux compared to the methane flux. The sulphide flux to the surface (upward flux) was comparable to the total downward flux of sulphate (Table 2).

#### 3.2.3. Lipid biomarker

Diagnostic archaeal and bacterial lipid concentrations were strongly increased in sediments at the SMT (Fig. 4e, g). Here, stable carbon isotope analysis revealed highest depletion in <sup>13</sup>C with minimum values of  $-92\text{‰}$  (*sn2*-hydroxyarchaeol) in archaeal specific diether lipids and  $-82\text{‰}$  (cyC<sub>17:0ω5,6</sub>) in bacterial specific FAs (Table 3, Fig. 4f, g) indicating the incorporation of methane derived carbon in archaeal and bacterial biomass (sample from 31 cm bsf). The concentration of both archaeal and bacterial lipids decreased just above and below this sediment horizon. At the SMT, the ratio of *sn2*-hydroxyarchaeol relative to archaeol was 1.6:1 (Table 3). Other diagnostic archaeal isoprenoidal hydrocarbons such as 2,6,11,15-tetramethylhexadecane (crocetane) could not be quantified due to an unresolved complex mixture of hydrocarbons (UCM) in all of the hydrocarbon fractions. Similarly, specific archaeal diethers and bacterial FAs could not be resolved from this background below 40 cm sediment depth. The concentrations of diagnostic archaeal lipids were roughly one order of magnitude lower in comparison to specific bacterial FAs.

The FA fraction in sediments at the SMT was dominated by the FAs C<sub>16:1ω5</sub> and cyC<sub>17:0ω5,6</sub> which are putatively specific for SRB involved in AOM (Elvert et al., 2003) and contained comparably high amounts of the FA C<sub>17:1ω6</sub>

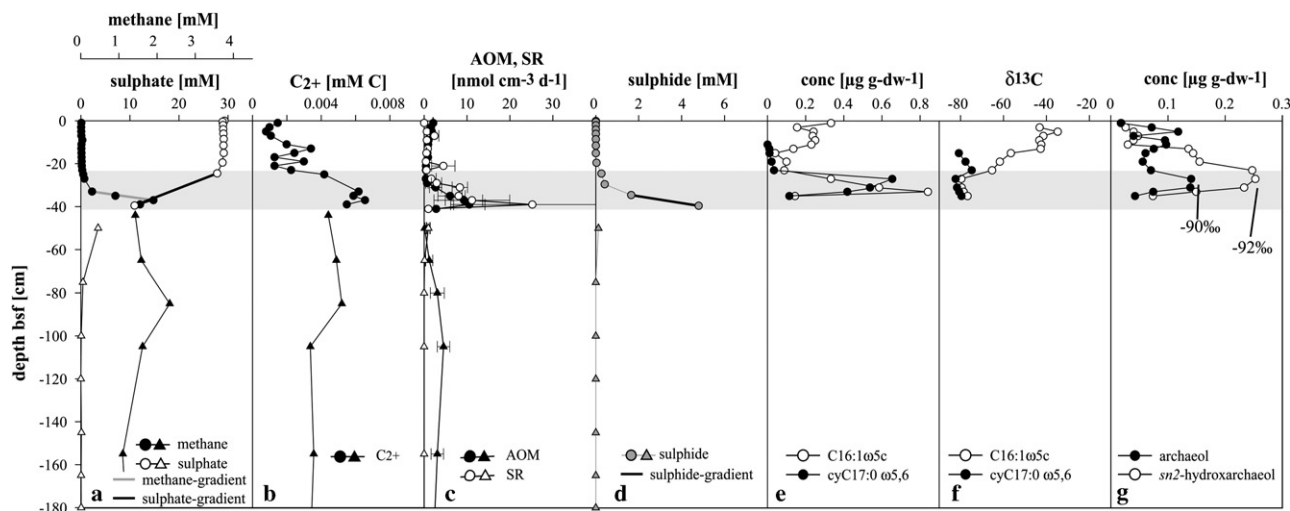


Fig. 4. Captain Arutyunov mud volcano. A distinct SMT, highlighted in grey, was found between 25 and 40 cm bsf (a). At this horizon, concentrations of higher hydrocarbons also decline (b). Note that AOM and SR rates (c), sulphide concentrations (d), concentrations (e) and stable carbon isotope values of diagnostic, bacterial fatty acids (f) and concentrations of isoprenoidal diethers (g) all peak at the SMT. (a) and (d) illustrate steepest gradients determined for methane, sulphate and sulphide (bold lines). Circles represent multiple-corer and triangles gravity corer samples. Errors are given as standard errors.

Table 3

Bacterial fatty acids, archaeal diether and isoprenoidal hydrocarbons analysed in sediments at the SMT of Captain Arutyunov and Bonjardim MV as well as in carbonate crusts from Hesperides and Faro MV

	Sediment		Carbonate		
	Captain Arutyunov	Bonjardim	Hesperides	Faro	
Normalised abundance ( $\delta^{13}\text{C}$ -values)	<b>Bacterial fatty acids</b>				
	C14:0	1.3 (-75)	2.0 (-37)	1.1 (-31)	2.3 (-93)
	i-C15:0	1.0 (-71)	1.0 (-42)	1.0 (-39)	1.0 (-99)
	ai-C15:0	1.3 (-73)	8.4 (-47)	1.5 (-43)	1.9 (-95)
	C15:0	0.6 (-73)	1.4 (nd)	0.3 (-45)	0.4 (-96)
	i-C16:0	0.2 (-73)	nd	0.2 (nd)	0.2 (-87)
	C16:1 $\omega$ 9	0.7 (-65)	nd	nd	0.1 (-92)
	C16:1 $\omega$ 7	0.8 (-67)	14.6 (-34)	0.6 (-27)	1.8 (-93)
	C16:1 $\omega$ 5	7.7 (-80)	8.4 (-49)	0.1 (-41)	0.7 (-96)
	C16:0	2.4 (-67)	7.8 (-21)	4.8 (-27)	1.6 (-77)
	10 MeC16:0	0.3 (-67)	nd	nd	1.0 (-94)
	i-C17:0	0.3 (-69)	nd	0.3 (-32)	0.3 (-96)
	ai-C17:0	0.1 (nd)	1.1	0.5 (-38)	0.3 (-99)
	C17:1 $\omega$ 7	0.9 (-68)	1.9	0.5 (-31)	0.4 (-93)
	C17:1 $\omega$ 6	1.9 (-74)	nd	nd	0.1 (nd)
	cyC17:0 $\omega$ 5,6	7.1 (-82)	nd	nd	nd
	C17:0	nd	nd	0.2 (nd)	0.1 (nd)
	C18:1 $\omega$ 9	1.0 (-27)	6.4 (-27)	0.2 (nd)	0.3 (-77)
	C18:1 $\omega$ 7	0.9 (-31)	13.7 (-31)	0.4 (-37)	1.5 (-84)
C18:0	0.2 (-25)	3.5 (-25)	1.8 (-28)	0.4 (-67)	
<b>Archaeal lipids</b>					
Archaeol	1.0 (-90)	1.0 (-81)	1.0 (-97)	1.0 (-114)	
sn2-hydroxyarchaeol	1.7 (-92)	0.7 (-83)	tr	0.2 (-111)	
Croacetane / Phytane			0.5 (-47)	3.3 (-110)	
PMI:0			1.0 (-87)	1.0 (-111)	
$\Sigma$ PMI:1			0.3 (nd)	4.6 (-113)	
$\Sigma$ PMI:2			nd	8.3 (-113)	
$\Sigma$ PMI:3			nd	0.3 (-101)	
Concentration [ $\mu\text{g g}^{-1}$ dw $^{-1}$ ]	<b>Bacterial fatty acids</b>				
	i-C15:0	0.08	0.01	0.1	8.7
	ai-C15:0	0.1	0.09	0.15	16.77
	C16:1 $\omega$ 5	0.6	0.09	0.01	6.05
	C17:1 $\omega$ 6	0.14	nd	nd	0.5
	cyC17:0 $\omega$ 5,6	0.56	nd	nd	nd
	<b>Archaeal lipids</b>				
	Archaeol	0.14	0.4	2.39	41.58
	sn2-hydroxyarchaeol	0.23	0.3	0.02	8.31
	Croacetane / Phytane			0.23	4.59
PMI:0			0.44	1.4	
Putative origin	ANME2 Seep-SRB1	ANME1 Seep-SRB1 & ANME2 Seep-SRB1	ANME1 Seep-SRB1 (?)	ANME1 Seep-SRB1 & ANME2 Seep-SRB1	

Abundances of fatty acids were normalised to i-C15:0, archaeal diethers to archaeol and archaeal isoprenoidal hydrocarbons to PMI:0. Specific lipid components are highlighted in grey.

(Table 3). Both, C16:1 $\omega$ 5 and cyC17:0 $\omega$ 5,6 were the most  $^{13}\text{C}$ -depleted FAs. However, all other FAs in the C14–C17 range carried significantly  $^{13}\text{C}$ -depleted isotope signatures as well with values ranging between  $-65\%$  (C16:1 $\omega$ 9) and  $-75\%$  (C14:0). C18-FAs were comparably enriched in  $^{13}\text{C}$  with  $\delta^{13}\text{C}$ -values ranging between  $-25\%$  (C18:0) and  $-31\%$  (C18:1 $\omega$ 7) most likely indicating a planktonic origin of these compounds. Concentrations of mono- and dialkyl glycerol ethers (MAGEs and DAGEs, respectively), presumably of bacterial origin (Pancost et al., 2001), were low in all samples recovered during cruise SO-175. Thus, a detailed analysis of these compounds was not carried out. However, sediments at the SMT of Capt. Arutyunov MV comprised comparably high contents of MAGEs relative to DAGEs

with  $\delta^{13}\text{C}$ -values ranging from  $-65\%$  to  $-85\%$  (data not shown). The MAGEs comprised a suite of alkyl moieties, which is comparable to those of the fatty acids found at Capt. Arutyunov MV. The suite of fatty acids extracted from the tubeworms comprised dominant amounts of the FAs C16:1 $\omega$ 7 and C18:1 $\omega$ 7 and to a lesser degree C16:0 and C18:0 with uniform  $\delta^{13}\text{C}$ -values of about  $-40\%$ , indicating chemoautotrophic carbon fixation (data not shown). The alcohol and hydrocarbon fractions were not analysed.

### 3.2.4. Phylogenetic diversity

An archaeal and a bacterial clone library was constructed to study the 16S rDNA-based microbial diversity in sediments at the SMT of Capt. Arutyunov MV (30–40 cm bsf). The 16S rDNA archaeal clone library consisted of nine phylogenetic groups (Table 4). Closest relatives of these groups were found among seep-endemic, uncultured microorganisms. The majority of sequences obtained were related to the ANME-2 group (59% ANME-2a, 3% ANME-2c of all archaeal sequences) which is known to mediate AOM (Boetius et al., 2000; Orphan et al., 2002; Knittel et al., 2005). The second most abundant group (18% of all archaeal sequences) was found to belong to the ANME-1 cluster which is also known to mediate AOM (Hinrichs et al., 1999; Michaelis et al., 2002; Orphan et al., 2002). The bacterial clone library consisted of 10 uncultivated bacterial lineages. Similar to the archaeal sequences, the next relatives of all bacterial 16S rDNA sequences belonged to uncultivated organisms that are commonly found at methane seeps (Knittel et al., 2003; Table 4). The closest relatives of the most abundant cluster of sequences (81%) belonged to the Seep-SRB1 group which comprises the bacterial partners of ANME-1 and ANME-2 (Knittel et al., 2003). Other phylogenetic groups of *Bacteria* were represented by single sequences (<2%).

### 3.3. Bonjardim MV

#### 3.3.1. Methane, C<sub>2+</sub>, sulphate and sulphide

A distinct SMT was observed in the top metre of the gravity core section with *ex situ* methane concentrations above saturation at atmospheric pressure and sulphate concentrations dropping below 0.2 mM. After aligning the sulphate profile of the gravity core with the MUC-core section, the actual depth of the SMT was determined between 45 and 70 cm bsf (Fig. 5a). Methane concentrations in surface sediments (0–52 cm sediment depth) were <0.001 mM indicating a complete consumption of methane in the SMT. As the two core sections overlapped, concentration gradients were determined from the gravity core section and also from aligned profiles in the overlapping zone (Fig. 5a, d). The steepest methane and sulphate gradients in the gravity core section were determined with 0.09 and  $-0.76 \mu\text{mol cm}^{-4}$ , respectively (Fig. 5a, Table 2). Aligning the gravity core and MUC-core sections, the steepest sulphate gradient was  $-1.67 \mu\text{mol cm}^{-4}$ . Methane concentrations declined

Table 4  
Archaeal and bacterial 16S rDNA clone libraries obtained from sediments of the SMT of Captain Arutyunov MV

Phylogenetic group	Clones	Representative clone	Next relative	Sequence similarity (%)	
<i>Archaea</i>					
Euryarchaeota	ANME-2a	39	CAMV300A948 (DQ004662)	Uncultured cold seep archaeal clone BS-K-H6 (AJ578128)	99
	ANME-2c	1	CAMV301A975 (DQ004668)	Uncultured hydrocarbon seep archaeal clone C1_R019 (AF419638)	99
	ANME-1	7	CAMV300A952 (DQ004664)	Uncultured hydrocarbon seep archaeal clone HydCal61 (AJ578089)	99
	Marine benthic group D	1	CAMV300A963 (DQ004667)	Uncultured hydrothermal vent archaeal clone pMC2A203 (AB019737)	98
	Marine benthic group D	1	CAMV300A951 (DQ004663)	Uncultured contaminated aquifer archaeal clone WCHD3-02 (AF050616)	90
	Marine benthic group D	1	CAMV301A980 (DQ004669)	Uncultured hydrothermal vent archaeal clone VC2.1 Arc6 (AF068817)	87
	Unclassified archaea	1	CAMV300A960 (DQ004666)	Uncultured cold seep archaeal clone BS-SR-H5 (AJ578148)	98
	Unclassified archaea	3	CAMV301A993 (DQ004661)	Uncultured hydrothermal vent archaea clone NT07-CAT-A24 (AB111475)	80
Crenarchaeota	Marine benthic group B	1	CAMV300A958 (DQ004665)	Uncultured archaeal clone BS-K-D4 (AJ578124)	99
<i>Bacteria</i>					
$\delta$ Proteobacteria	Seep-SRB1	47	CAMV300B922 (DQ004675)	Uncultured hydrocarbon seep bacterial clone Hyd89-04 (AJ535240)	99
	Desulfobulbacteraceae	1	CAMV301B937 (DQ004679)	Uncultured Echinocardium cordatum hindgut bacterial clone Del 7 (AY845643)	96
	Desulfobulbaceae	1	CAMV300B921 (DQ004674)	Uncultured hydrocarbon seep bacterial clone Hyd89-51 (AJ535252)	99
$\gamma$ Proteobacteria	Stenotrophomonas	1	CAMV301B944 (DQ004671)	Stenotrophomonas maltophilia (AB008509)	99
Clostridia	Clostridiales	1	CAMV300B902 (DQ004670)	Uncultured bacterial clone DR9IPCB16SCT8 (AY604055)	98
Spirochaetes	Spirochaeta	1	CAMV301B941 (DQ004680)	Uncultured Spirochaeta sp. (AF424377)	96
	Spirochaeta	1	CAMV300B915 (DQ004672)	Uncultured spirochete clone IE052 (AY605138)	96
	Unclassified bacteria	1	CAMV300B916 (DQ004673)	Uncultured hydrocarbon seep bacterial clone Hyd24-12 (AJ535232)	97
	Unclassified bacteria	1	CAMV301B934 (DQ004678)	Uncultured hydrocarbon seep bacterial clone 1B-41 (AY592596)	93
	Unclassified bacteria	1	CAMV300B923 (DQ004676)	Uncultured hydrocarbon seep bacterial clone GCA025 (AF154106)	98

The Archaeal clone library is dominated by sequences belonging to the ANME-2 cluster and the bacterial library by sequences belonging to the Seep-SRB1 cluster.

below the depth at which the two core sections overlap (Fig. 5a). Hence, no further concentration gradient was determined. In comparison to Capt. Arutyunov MV,  $C_{2+}$ -concentrations were high with values of  $>0.25$  mM at a sediment depth below 1 m (Fig. 5b). Similar to methane, concentrations of  $C_{2+}$ -compounds decreased across the SMT indicating a consumption of these compounds. Gaseous hydrocarbons comprised methane ( $>81\%$ ), ethane ( $<14\%$ ), propane ( $<4.5\%$ ) and  $\Sigma$ butane ( $<0.4\%$ ) indicating a thermogenic origin of these gases (Stadnitskaia et al., 2006). Sulphide concentrations peaked in the SMT with 5.3 mM at 52.5 cm bsf (Fig. 5d). In the gravity core section, the steepest sulphide gradients

were determined as 0.23 (upward) and  $-0.07$  (downward)  $\mu\text{mol cm}^{-4}$ , respectively (Table 2). Aligning the two core sections, the steepest (upward) sulphide gradient was determined with  $0.73 \mu\text{mol cm}^{-4}$ .

### 3.3.2. AOM, SR rates and diffusive fluxes

AOM and SR rates were highest in the SMT at 58 cm bsf with maximum values of 2.6 and  $15.4 \text{ nmol cm}^{-3} \text{ d}^{-1}$ , respectively (Fig. 5c). Comparably low values of AOM and SR rates were measured in over- and underlying sediment horizons. Replicate AOM and SR rate measurements showed a high standard error of 92% and 85% of the average value, respectively, possibly indicating a high small

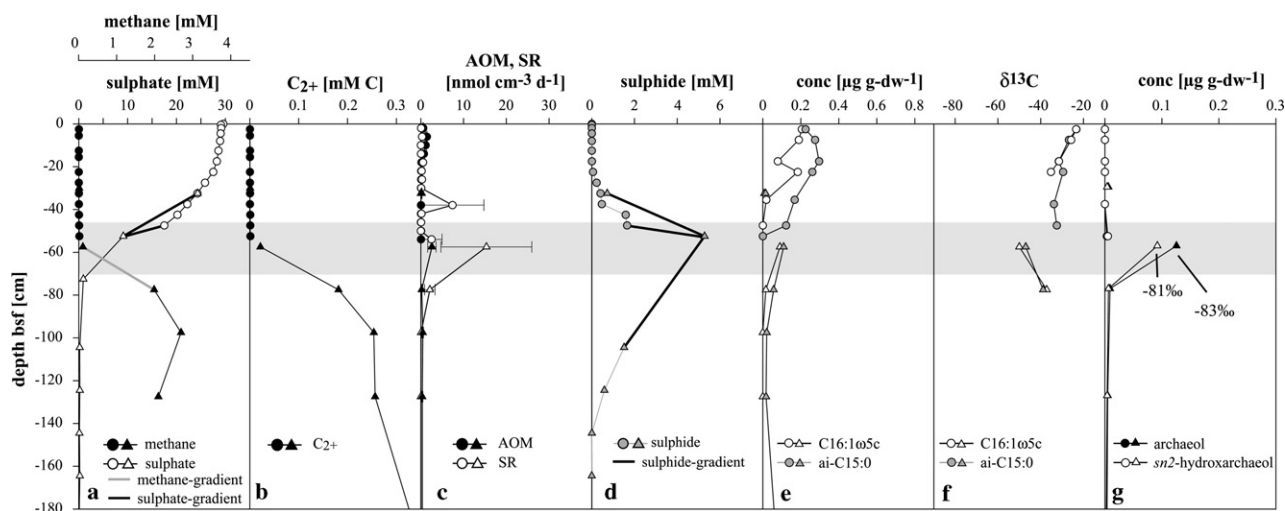


Fig. 5. Bonjardim mud volcano. A distinct SMT, highlighted in grey, was found between 50 and 70 cm bsf (a). At this horizon, concentrations of higher hydrocarbons also decline (b). Note that concentrations of  $C_{2+}$ -compounds are  $\sim 35$ -fold higher compared to Captain Arutyunov MV. AOM and SR rates (c), sulphide concentrations (d), concentrations (e) and stable carbon isotope values of diagnostic, bacterial fatty acids (f) and concentrations of isoprenoidal diethers (g) peak at the SMT. (a) and (d) illustrate steepest gradients determined for methane, sulphate and sulphide (bold lines). Concentration gradients for sulphate and sulphide were determined from concentration profiles of the gravity core samples as well as from aligned gravity core and multiple-corer concentration profiles. Circles represent multiple-corer and triangles gravity corer samples. Errors are given as standard errors.

scale variability on a metre scale. The 19-fold higher areal SR compared to AOM suggests a decoupling of these two processes (Table 2). Accordingly, the concentration gradients (determined from unaligned and aligned profiles) translate to a 5.1–11-fold higher diffusive downward flux of sulphate compared to the upward flux of methane. The cumulative sulphide flux (upward and downward) accounted for 77–92% of the sulphate flux.

### 3.3.3. Lipid biomarker

A moderate increase of diagnostic archaeal and bacterial lipid concentrations was observed at the SMT in sediments of Bonjardim MV (Fig. 5e, g). At this horizon ( $-57$  cm bsf), stable carbon isotope analysis revealed highest depletions in  $^{13}C$  with minimum values of  $-83\%$  (*sn2*-hydroxyarchaeol) in archaeal diether lipids and  $-49\%$  ( $C_{16:1\omega5}$ ) in bacterial FAs (Table 3, Fig. 5f, g). At the SMT, the ratio of *sn2*-hydroxyarchaeol relative to archaeol was 0.7:1 and therefore lower in comparison to Capt. Arutyunov MV (Table 3). Similar to Capt. Arutyunov MV, other diagnostic archaeal isoprenoidal hydrocarbons could not be measured due to a high UCM background. Equally high amounts of the FAs  $C_{16:1\omega5}$  and ai- $C_{15:0}$ , both of which were the most  $^{13}C$ -depleted FAs (Table 3), were detected in sediments at the SMT. The FA cy $C_{17:0\omega5,6}$ , which was abundant at Capt. Arutyunov MV could not be detected in sediments of Bonjardim MV. Furthermore, dominant FAs such as  $C_{16:1\omega7}$ ,  $C_{16:0}$ ,  $C_{18:1\omega9}$  and  $C_{18:1\omega7}$  carried  $\delta^{13}C$ -signatures  $\geq -34\%$ , indicating that AOM was not the main energy and carbon delivering process to the microbial community. In contrast to Capt. Arutyunov MV, the concentrations of diagnostic archaeal lipids were roughly 4-fold higher compared to specific bacterial FAs

(Table 3). A further analysis of the diversity of microbial organism using 16S rDNA methods was not carried out at Bonjardim MV.

## 3.4. Ginsburg MV, Gemini MV and “No Name”

### 3.4.1. Methane, sulphate and sulphide

The SMT was located in the upper metre of the sediment cores retrieved from Ginsburg and Gemini MV and at 2–3 m bsf at the “No Name” structure, respectively (Fig. 6a, c, e). Methane concentrations in sediments overlying the SMT at these structures were  $<0.001$  mM, and reached *ex situ* concentrations above (Gemini MV and “No Name”) and just below saturation (1.3 mM, Ginsburg MV) below the SMT. Sediments retrieved from Ginsburg MV had a distinct smell of petroleum below 40 cm bsf. No depth corrections were made as only gravity cores were taken from these MVs. The actual depth of the SMTs was therefore most likely 10–40 cm below the sediment depth indicated in Fig. 6. In contrast to the observed depletion of sulphate to concentrations  $<0.4$  mM below the SMT at Gemini MV and the “No Name” structure, sulphate concentrations showed a minimum between 30 and 70 cm and an increase to values  $\geq 17$  mM with depth below 90 cm at Ginsburg MV. The total diffusive sulphate flux was therefore calculated from both, the upward and the downward gradients at Ginsburg MV. At Ginsburg MV, Gemini MV and the “No Name” structure, methane and downward sulphate gradients ranged from 0.02 to 0.05 and  $-0.11$  to  $-0.92 \mu\text{mol cm}^{-4}$ , respectively (Table 2). The upward sulphate gradient at Ginsburg MV was  $0.35 \mu\text{mol cm}^{-4}$ . Sulphide concentrations peaked in the SMTs with values between 4.7 and 7.6 mM (Fig. 6b, d, f)

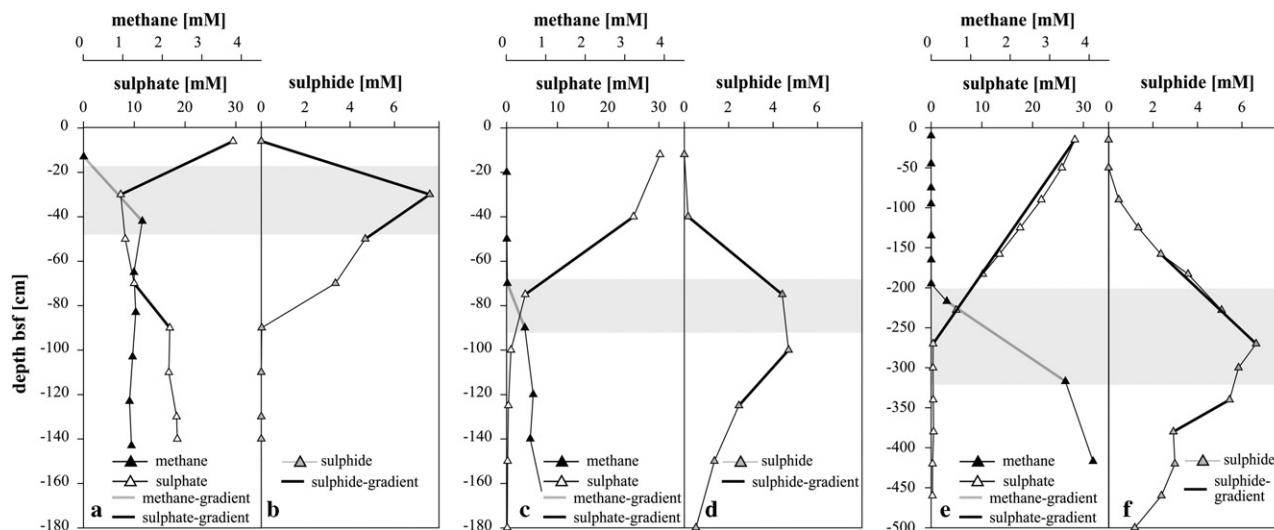


Fig. 6. The SMT, highlighted in grey, was found in the top most m at Ginsburg (a) and Gemini (c) and between 2 and 3 m at No Name MV (e; note the different scale chosen for depth). In these horizons, also sulphide concentrations peak (b, d, f). Bold lines illustrate steepest gradients determined for methane, sulphate and sulphide.

and steepest gradients were determined with values between 0.04 to 0.32 (upward) and  $-0.06$  to  $-0.15$  (downward)  $\mu\text{mol cm}^{-4}$ , respectively (Table 2).

### 3.4.2. Diffusive fluxes

The diffusive flux calculations from pore water profiles of Ginsburg MV, Gemini MV and the “No Name” structure indicate that the diffusive sulphate fluxes exceeded the methane fluxes (by 15.5-, 18.5- and 2.5-fold, respectively, according to the calculation). This suggests a decoupling of AOM and SR at these structures similar to the observations made at Bonjardim MV (Table 2). The calculated cumulative (upward + downward) sulphide flux accounted for 66%, 70% and 146% of the sulphate fluxes at Ginsburg MV, Gemini MV and the “No Name” structure, respectively. The composition of the microbial community was not investigated here.

### 3.5. Lipid biomarkers of carbonate crusts

Exposed carbonate crusts were observed at the mud volcanoes Ginsburg, Hesperides and Faro. Additionally, high amounts of broken carbonate chimneys were found at Hesperides and Faro MV. Both crusts and chimney pieces were absent at Capt. Arutyunov MV, Bonjardim MV and the “No Name” structure according to our visual inspections. We could retrieve crust samples from the summits of Hesperides and Faro MV for further analyses of the lipid signatures of the crusts.

#### 3.5.1. Hesperides MV

Carbonate crusts of Hesperides MV contained archaeal and bacterial lipids diagnostic for methanotrophic communities and processes. Archaeal lipids were strongly depleted in  $\delta^{13}\text{C}$  with minimum values of  $-97\text{‰}$  (archaeol) whereas bacterial FAs were only moderately depleted with mini-

mum values of  $-43\text{‰}$  (ai- $\text{C}_{15:0}$ , Table 3). Only trace amounts of *sn*2-hydroxyarchaeol were detected among the archaeal diethers. Isoprenoidal hydrocarbons were dominated by 2,6,10,15,19-pentamethylcosane (PMI:0) and contained comparably low amounts of a crocetane/2,6,10,14-tetramethylhexadecane (phytane) mixture and  $\Sigma\text{PMI:1}$  (comprising 2 isomers). The FA fraction in the carbonate was dominated by  $\text{C}_{16:0}$  followed by  $\text{C}_{18:0}$  with  $\delta^{13}\text{C}$ -values  $> -28\text{‰}$  (Table 3). FAs putatively specific for SRB involved in AOM such as  $\text{C}_{16:1\omega 5}$ , i- $\text{C}_{15:0}$  and ai- $\text{C}_{15:0}$  (Elvert et al., 2003; Blumenberg et al., 2004), were approximately 3–4.8 times lower in concentration compared to  $\text{C}_{16:0}$ . However, in contrast to abundant FAs, stable carbon isotope compositions of i- $\text{C}_{15:0}$ , ai- $\text{C}_{15:0}$  and  $\text{C}_{16:1\omega 5}$  showed a moderate depletion in  $^{13}\text{C}$  (Table 3). Moreover, in comparison to specific archaeal lipids, diagnostic bacterial FAs were roughly an order of magnitude lower in concentration.

#### 3.5.2. Faro MV

All archaeal and bacterial lipids found in the carbonate crust of Faro MV were strongly depleted in  $^{13}\text{C}$  (Table 3) with minimum  $\delta^{13}\text{C}$ -values of  $-114\text{‰}$  (archaeol) in diagnostic archaeal diether lipids and  $-99\text{‰}$  (i- $\text{C}_{15:0}$ ) in specific bacterial FAs (Table 3). Archaeal diether lipids were dominated by archaeol and contained comparably low amounts of *sn*2-hydroxyarchaeol. Isoprenoidal hydrocarbons were dominated by PMI:2 (9 isomers) followed by PMI:1 (2 isomers) and relatively high amounts of crocetane/phytane. Specific FAs showed comparably small differences in abundance and  $\delta^{13}\text{C}$ -values (Table 3). However, ai- $\text{C}_{15:0}$  was the most dominant FA with a roughly 2-fold higher concentration compared to i- $\text{C}_{15:0}$  and  $\text{C}_{16:1\omega 5}$ . The FA  $\text{cyC}_{17:0\omega 5,6}$  was not detected. Concentrations of specific FAs were comparable to specific archaeal lipids.

## 4. Discussion

### 4.1. Evidence of methane-driven geochemical and biological activity at mud volcanoes of the Gulf of Cadiz

Active marine mud volcanoes have been identified as important escape pathways of hydrocarbon gases and may even contribute to atmospheric green house gases (Dimitrov, 2002; Judd et al., 2002; Kopf, 2002; Damm and Budéus, 2003; Dimitrov, 2003; Sauter et al., 2006). However, high methane fluxes reaching surface sediments may support high biomasses of methane-oxidizing microorganisms, and via their sulphide production also thiotrophic, giant bacteria and other chemosynthetic fauna which form a filter against gas emission to the hydrosphere (Olu et al., 1997b; Sahling et al., 2002; Werne et al., 2002; Boetius and Suess, 2004; Milkov et al., 2004; Cordes et al., 2005). Furthermore, methane venting is often associated with the precipitation of authigenic carbonates which sequester methane derived CO<sub>2</sub> at the seafloor (Aloisi et al., 2000; Kopf, 2002; Boetius and Suess, 2004; Hensen et al., 2004). These carbonates may also serve as paleo-indicators of previously active phases of quiescent or fossil seeps (Ritger et al., 1987; Peckmann et al., 1999; Thiel et al., 1999).

The Gulf of Cadiz is characterised by numerous mud volcanoes (Fig. 1) which have been intensely surveyed since their discovery in 1999 (Kenyon et al., 2000, 2001; Somoza et al., 2002; Pinheiro et al., 2003). Among the findings indicative of high past and present methane seepage are the occurrence of hydrate-bearing sediments, authigenic carbonates and seep related biota at several mud volcanoes (Gardner, 2001; Diaz-Del-Rio et al., 2003; Pinheiro et al., 2003; Somoza et al., 2003). Yet, the present activity of these structures in relation to methane emission to the hydrosphere remains unknown. The observations during cruise SO-175 revealed only few traces of methane reaching surface sediment horizons (here referring to the upper decimetres bsf reachable by biota) at the centres of the mud volcanoes Capt. Arutyunov, Bonjardim, Ginsburg and Hesperides, and the “No Name” structure. No visible fluid or gas escape to the hydrosphere was detected with video observations, indicating that the mud volcanoes may be relatively inactive and that the methane flux may be consumed within subsurface sediment horizons. In contrast, highly active seep systems such as Hydrate Ridge, the Gulf of Mexico or Håkon Mosby Mud Volcano show maximal methane consumption and sulphide production at the sediment surface, and emit methane into the hydrosphere through focused gas and fluid escape pathways, despite the high methane and sulphate turnover rates consuming substantial fractions of the methane flux (Boetius et al., 2000; Damm and Budéus, 2003; Treude et al., 2003; Joye et al., 2004; De Beer et al., 2006; Sauter et al., 2006).

The high sulphide fluxes from anaerobic methane consumption at active seeps are utilised by thiotrophic communities, e.g. mats of giant bacteria like *Beggiatoa* sp., various chemosynthetic bivalves like *Calyplogena* sp., *Acharax* sp.,

*Bathymodiolus* sp. and by several siboglinid tubeworm species (Sibuet and Olu, 1998). Such communities often colonise large areas at highly active seeps. Furthermore, these organisms are adapted to different geochemical settings and can be used as indicators for high methane fluxes and turnover in surface sediments. Three types of indicator communities were so far observed at low abundances at the investigated mud volcanoes. Some small (ca. 20 cm diameter) blackish sediment patches covered with white bacterial mats were observed by towed camera systems at Faro MV indicating locally elevated fluxes of sulphide (likely AOM-derived) reaching the surface of the seafloor (Fig. 6d). Few specimen of the deep-dwelling thiotrophic bivalve *Acharax* sp. were recovered from Faro MV and previously from Ginsburg MV (Gardner, 2001). Members of the family *Solemyidae* to which *Acharax* sp. belongs are mostly deep burrowing and occur in seep habitats with low or moderate methane and sulphide fluxes where they can take up sulphide through their foot from subsurface accumulations (Sibuet and Olu, 1998; Sahling et al., 2002; Treude et al., 2003). At Hydrate Ridge for instance, *Acharax* sp. mines subsurface sediments for sulphide pockets below 15 cm sediment depth (Sahling et al., 2002). As a third indicator species, tubeworms were recovered from Capt. Arutyunov and previously observed at Bonjardim MV (Pinheiro et al., 2003). As adult animals, these worms are lacking a mouth, gut and anus and are hence depending on energy and carbon sources provided by symbiotic, thiotrophic or methanotrophic bacteria (Southward et al., 1981; Dando et al., 1994; Gebruk et al., 2003; Southward et al., 2005). At Capt. Arutyunov MV, the moderate <sup>13</sup>C-depletion of worm-derived membrane lipids (ca. -40‰) indicates a thiotrophic or mixed methanotrophic/thiotrophic feeding mode of the tubeworm symbionts. This is concluded on the basis of the δ<sup>13</sup>C-value of -48‰ of the source methane (Nuzzo et al., 2005). Aerobic methanotrophic bacteria are characterised by a considerable depletion in the <sup>13</sup>C-content of membrane lipids in comparison to source methane (Hanson and Hanson, 1996), which was not reflected in the tubeworm isotope signature.

### 4.2. Hotspots of hydrocarbon turnover at the mud volcanoes of the Gulf of Cadiz

The observed patterns of seep related biota is in good agreement with the observed geochemical gradients. All mud volcanoes investigated here showed a complete depletion of methane and sulphate within the subsurface SMT. At Capt. Arutyunov and Bonjardim MV, the SMT was positioned at 25–40 cm and 45–70 cm bsf, respectively (Figs. 4, 5a), and reflected in elevated AOM and SR rates within this zone. Generally, integrated rate measurements were comparable to the diffusive fluxes at Capt. Arutyunov and Bonjardim MV (Table 3). Also, concentration measurements of methane and sulphate and the resulting estimates of diffusive methane and sulphate fluxes at Ginsburg MV, Gemini MV and the

“No Name” structure indicate that sulphate-dependent AOM is a widespread microbial process in the centres of the mud volcanoes of the Gulf of Cadiz. However, as we cannot exclude a potential advective transport component in sediments of the surveyed mud volcanoes and due to shortcomings in the vertical resolution of pore water profiles, the estimates of fluxes presented here should be considered with caution.

With respect to methane fluxes and microbial turnover rates at the time of our investigation, Capt. Arutyunov MV was the most active of the investigated structures followed by Bonjardim, Ginsburg and Gemini MV, while “No Name” was the least active structure (Table 2). Furthermore, highest turnover rates and fluxes coincided with the shallowest SMT comparing all investigated MVs. Hence, compared to other marine gas seeps and methane-rich environments, the Gulf of Cadiz MVs investigated here showed a low or medium range in methane turnover rates, reflecting the relatively low methane fluxes. At the Namibian continental slope, the north western Black Sea and Chilean shelf and the western Argentinean basin for instance, the SMT is located several metres bsf and methane fluxes are low with values usually  $<55 \text{ mmol m}^{-2} \text{ year}^{-1}$  (Niewöhner et al., 1998; Jørgensen et al., 2001; Hensen et al., 2003; Treude et al., 2005). These values are comparable to Ginsburg and Gemini MV as well as to the “No Name” structure. The AOM activity and diffusive methane fluxes at Capt. Arutyunov and Bonjardim MV were substantially higher than those at Ginsburg MV, Gemini MV and the “No Name” structure. However, areal rates and diffusive fluxes at Capt. Arutyunov and Bonjardim MV are still two orders of magnitude lower in comparison to other cold seeps, which bear gas hydrates at their stability limit such as Håkon Mosby Mud Volcano, Hydrate Ridge and the Gulf of Mexico. In such environments with active fluid flow ( $>100 \text{ cm year}^{-1}$ ) and gas emission via ebullition, methane fluxes were estimated with values  $>8.5 \text{ mol m}^{-2} \text{ year}^{-1}$  (Torres et al., 2002; Luff and Wallmann, 2003; De Beer et al., 2006) and AOM reached values  $>4 \text{ mol m}^{-2} \text{ year}^{-1}$ , i.e.  $>0.5 \text{ } \mu\text{mol cm}^{-3} \text{ d}^{-1}$  (Treude et al., 2003; Joye et al., 2004).

*In vitro* experiments with sediment slurries and *ex situ* tracer injection assays have previously shown that AOM and SR are in a 1:1 molar stoichiometry if methane is the sole carbon source (Nauhaus et al., 2002; Treude et al., 2003). In spite of the putative loss of methane during subsampling, the deviation from the 1:1 stoichiometry between AOM and SR as well as between the sulphate and methane fluxes (Table 2) indicates the presence of electron donors other than methane for SR at the investigated MVs. SRR were always highest at the depth of the SMT but just above detection limit in the overlying sediments of Capt. Arutyunov and Bonjardim MV (Figs. 4, 5c). Hence, a substantial contribution to SR by pelagic organic matter input can be ruled out. However, our data provide evidence for the presence of other hydrocarbons beside methane in the subsurface sediments of several mud volcanoes. Sulphate

reducing bacteria can use a variety of short and long chain alkanes and complex aliphatic and aromatic compounds (Rueter et al., 1994; Widdel and Rabus, 2001). At Capt. Arutyunov and Bonjardim MV the presence of complex hydrocarbons is indicated by the strong unresolved complex mixture (UCM) of hydrocarbons in sediment samples from the SMT and deeper sediment horizons. Furthermore,  $\text{C}_2\text{--C}_4$  compounds declined at the depth of the SMT (Figs. 4, 5b), indicating their consumption in this zone. At Bonjardim MV, the deviation between AOM and SR was higher compared to Capt. Arutyunov MV coinciding with higher concentrations of  $\text{C}_{2+}$  compounds. Furthermore, Mazurenko et al. (2002) observed a composition of hydrocarbon gases at Ginsburg MV similar to those detected at Bonjardim MV. Nuzzo et al. (2005) and Stadnitskaia et al. (2006) showed that methane is commonly of a thermogenic origin at mud volcanoes in the Gulf of Cadiz. Hence, SR fuelled by higher hydrocarbons could be an important microbial process in the MV sediments of the Gulf of Cadiz in addition to methane oxidation. Similar results were obtained in a study of cold seeps of the Gulf of Mexico where SR rates exceed AOM rates up to 10-fold, fuelled by a variety of hydrocarbons and petroleum in the sediments (Joye et al., 2004).

In conclusion, our biogeochemical measurements as well as biological and geological observations indicate that elevated methane fluxes are associated with the centres of the MVs studied during cruise SO-175. However, at the investigated sites, all methane was consumed anaerobically in subsurface sediments and we could not observe any emission of methane to the hydrosphere. However, there is evidence for extensive fluid and/or gas escape in the past as indicated by the widespread occurrence of massive carbonate chimneys and crusts (Diaz-Del-Rio et al., 2003; Somoza et al., 2003) of which at least the latter bear AOM signals. Another geological evidence for temporally varying activities of mud volcanism in the Gulf of Cadiz are the typical “Christmas tree” structures observed on high-resolution seismic profiles (Somoza et al., 2002, 2003). Such patterns are probably caused by eruptive events followed by phases of dormancy. This so-called multiphase activity is a common behaviour in many terrestrial mud volcanoes (e.g. Lokbatan MV; Aliyev et al., 2002; Kholodov, 2002; Dimitrov, 2003). It is therefore possible that mud volcanism in the Gulf of Cadiz is in a transient state of low activity at present.

#### 4.3. Identity of methane oxidising communities in sediments and carbonate crusts

Fingerprinting of diagnostic lipids is a common tool for the chemotaxonomic identification of microorganisms (Madigan et al., 2000; Boschker and Middelburg, 2002). This approach has been used extensively to examine anaerobic methanotrophic organisms, because the carbon isotope fractionation associated with AOM leads to specific, very depleted  $\delta^{13}\text{C}$ -signatures of lipid biomarkers (Hinrichs

et al., 1999; Elvert et al., 2001; Blumenberg et al., 2004). The dominance of bacterial and archaeal lipids with low  $\delta^{13}\text{C}$ -values in sediments and carbonates indicate that AOM is a major biomass-generating process at the investigated MVs. Differences in the abundances of specific archaeal isoprenoidal diethers, hydrocarbons and bacterial FAs, as well as varying  $\Delta\delta^{13}\text{C}$ -values of these lipids (compared to source methane) indicate that several phylogenetic groups of methanotrophic communities mediate AOM in the Gulf of Cadiz. Elevated concentrations and associated low  $\delta^{13}\text{C}$ -signatures of specific archaeal and bacterial membrane lipids corresponded with elevated AOM and SR rates in sediments of the SMT at Capt. Arutyunov and Bonjardim MV (Figs. 4, 5e–g, Table 3). In combination with 16S rDNA analysis, the biomarker patterns give evidence that AOM is mediated by a microbial community consisting of methanotrophic archaea and SRB phylogenetically related to those which were previously found at other methane seeps (Boetius et al., 2000; Michaelis et al., 2002; Orphan et al., 2002; Teske et al., 2002; Niemann et al., 2005). Furthermore, the presence of a similar suite of  $^{13}\text{C}$ -depleted lipids in abundant authigenic carbonates recovered from Hesperides and Faro MV (Table 3) indicates higher activities and a more widespread microbial methane turnover in the past.

#### 4.3.1. Methanotrophic archaea

Previous publications revealed dominant amounts of *sn2*-hydroxyarchaeol relative to archaeol in ANME-2 dominated habitats, whereas the reverse was observed in ANME-1 dominated systems (Blumenberg et al., 2004; Elvert et al., 2005; Niemann et al., 2005). Moreover, ANME-2 communities were found to comprise high contents of crocetane, whereas it seems to be present at low concentrations in ANME-1 (Elvert et al., 1999; Boetius et al., 2000; Blumenberg et al., 2004). Stable carbon isotope fractionations were found to be higher in ANME-2 compared to ANME-1 dominated habitats (Orphan et al., 2002) with  $\Delta\delta^{13}\text{C}$ -values (archaeol relative to the source methane) ranging between 34 to 53‰ and 11 to 37‰, respectively (Hinrichs et al., 1999; Boetius et al., 2000; Elvert et al., 2001; Orphan et al., 2002; Teske et al., 2002; Blumenberg et al., 2004; Niemann et al., 2005).

In the Gulf of Cadiz, a high *sn2*-hydroxyarchaeol to archaeol ratio of 1.7:1 was detected at Capt. Arutyunov MV indicating that this system is dominated by ANME-2 archaea (Blumenberg et al., 2004; Elvert et al., 2005). Accordingly, a high  $\Delta\delta^{13}\text{C}$ -value of 42‰ of archaeol compared to the source methane (−48‰, Nuzzo et al., 2005) was observed. Furthermore, the dominance of ANME-2 compared to ANME-1 sequences in the clone library from Capt. Arutyunov MV suggests a dominance of ANME-2 in this SMT. However, the SMT of Capt. Arutyunov MV also contained other typical seep associated 16S rDNA sequences, including crenarcheota of the Marine Benthic Group B, which are often found at methane seeps, but whose function remains unknown (Knittel et al., 2005).

At Bonjardim MV, a lower *sn2*-hydroxyarchaeol to archaeol ratio of 0.7:1 combined with lower  $\Delta\delta^{13}\text{C}$ -values between the biomarkers (e.g. archaeol, 31.5‰) relative to the source methane (−49.5 to −51‰, Nuzzo et al., 2005; Stadnitskaia et al., 2006) lie between published values from systems dominated by either ANME-1 or ANME-2 (Blumenberg et al., 2004; Elvert et al., 2005; Niemann et al., 2005). This suggests a mixed ANME community in these sediments. Similar characteristics have been observed in carbonate crusts at Faro MV. At this mud volcano, substantial amounts of  $^{13}\text{C}$ -depleted crocetane were detected giving additional indications for an involvement of ANME-2 in AOM at the time of carbonate precipitation. At Hesperides MV, only trace amounts of *sn2*-hydroxyarchaeol were detected, and thus indicate the dominance of ANME-1 communities. No distinct environmental preferences have been found for either group, most likely because the taxonomic level investigated comprises a relatively large diversity of microorganisms.

#### 4.3.2. Sulphate reducing bacteria

At many different cold seep settings, ANME-1 and ANME-2 archaea have been found in consortium with SRB of the Seep-SRB1 cluster belonging to the *Desulfosarcina/Desulfococcus* group (Knittel et al., 2003). However, this cluster apparently comprises physiologically different ecotypes that are distinguished by very specific FA patterns according to their association to either ANME-1 or to ANME-2 (Elvert et al., 2003; Blumenberg et al., 2004). FA signatures in environmental systems dominated by ANME-1/Seep-SRB1 communities comprise high contents of ai-C<sub>15:0</sub> relative to i-C<sub>15:0</sub> (Blumenberg et al., 2004; Elvert et al., 2005), whereas systems dominated by ANME-2/Seep-SRB1 communities comprise the unusual FA cyC<sub>17:1 $\omega$ 5,6</sub> and dominant contents of C<sub>16:1 $\omega$ 5</sub> but almost balanced ratios of ai-C<sub>15:0</sub> relative to i-C<sub>15:0</sub> (Elvert et al., 2003; Blumenberg et al., 2004).

The dominance of the unusual FAs C<sub>16:1 $\omega$ 5</sub> and cyC<sub>17:1 $\omega$ 5,6</sub> and an almost equal ratio of the iso- and anteiso-branched C<sub>15:0</sub> FAs in sediments of the SMT at Capt. Arutyunov MV are in very good agreement with the archaeal lipid data and published lipid signatures of the Seep-SRB1 ecotype associated with ANME-2. This finding is also in accordance with the predominance of Seep-SRB1 sequences in the bacterial clone library. As expected from the detection of potentially diverse ANME communities at Bonjardim MV, the FA signature shows characteristics of both SRB ecotypes previously identified as bacterial partners in AOM. The high ratio of ai-C<sub>15:0</sub> compared to i-C<sub>15:0</sub> (8.4:1) is indicative for the Seep-SRB1 ecotype associated with ANME-1 while the high abundance of C<sub>16:1 $\omega$ 5</sub> indicates the ecotype associated with ANME-2. This finding is similar to results obtained from a carbonate crust at Faro MV where a comparable fatty acid pattern has been detected. At Bonjardim MV, however, several FAs carry  $\delta^{13}\text{C}$ -signatures that are comparable to the source methane and do not show any fractionation. This suggests

a contribution to carbon biomass from processes other than methane consumption. A similar mixture of carbon sources to biomass could also explain the unspecific signature of FAs in the carbonate of Hesperides MV.

Another striking difference is the comparably high lipid concentration in the carbonate recovered from Faro compared to that recovered from Hesperides MV. A rather recent formation of the sampled carbonate from Faro MV appears likely, as these were stained black from sulphide and recovered together with some living specimens of the chemosynthetic bivalve *Acharax* sp. A possible explanation for the difference in AOM-derived lipid contents could be that the sampled carbonate crust from Hesperides is older than that recovered from Faro MV and has been exposed to oxic sea water and lipid diagenesis for a longer time which is indicated by the dominant abundance of saturated FAs relative to unsaturated FAs. This may also explain the dominance of PMI's with higher degrees of saturation at Hesperides compared to Faro MV assuming that the diagenetic alteration of unsaturated isoprenoid hydrocarbons is similar to that of FAs.

## 5. Conclusions

At the centres of the mud volcanoes Captain Arutyunov, Bonjardim, Ginsburg, Gemini and Faro as well as at the “No Name” structure, several indications for a slow upward fluid and gas flux were found. Our data suggest a complete consumption of methane and higher hydrocarbons in the sediments of the studied mud volcanoes at depths of 20–300 cm below seafloor. We found no indication of hydrocarbons reaching near surface sediments or the hydrosphere except from the visual observation of small patches of reduced sediments covered by giant sulphide-oxidizing bacteria indicating localised near-surface AOM activities. However, with respect to the limited extent of video surveys and sediment sampling in this study, a potential seepage of hydrocarbons into the water column can not be ruled out. The overlap of methane and sulphate depletion with sulphide production shows that methane oxidation processes are mediated microbially under anaerobic conditions. Correspondingly, AOM and SR rates show a peak in a distinct, narrow SMT in the subsurface sediments of the mud volcano centres. Highest turnover rates and fluxes coincided with the shallowest SMT depths with Capt. Arutyunov MV as the most active system in the study area, followed by the mud volcanoes Bonjardim, Ginsburg and Gemini, and finally the “No Name” structure. In comparison to other gas seeps, methane fluxes and turnover rates are low to mid range in the Gulf of Cadiz. In addition to AOM, the anaerobic oxidation of higher hydrocarbons could be an important process fuelling SR. Lipid biomarker patterns and 16S rDNA clone sequences from the sediments and carbonates of the AOM hotspots provide evidence that both of the previously described ANME-1/Seep-SRB1 and ANME-2/Seep-SRB1 communities mediate AOM at mud volcanoes in the Gulf of Cadiz.

The finding of their lipid signatures in carbonate crusts at the centres of the investigated mud volcanoes indicates that at least some of the vast amounts of carbonates littering mud volcanoes and diapiric ridges in the northern part of the Gulf of Cadiz are linked to methane seepage.

## Acknowledgments

The authors thank the captain and crew as well as the shipboard scientific community of the R/V SONNE for their help at sea. We also thank Tomas Wilkop, Imke Müller and Viola Beier for technical assistance with laboratory analyses. Scientific exchange and collaboration were supported by the CRUP-ICCTI/DAAD Portuguese/German Joint Action *Geosphere/Biosphere Coupling Processes in the Gulf of Cadiz* (A-15/04; Boetius, Pinheiro). This work was also supported by the ESF Eurocores/Euromargins MVSEIS project (01-LEC\_EMA24F; PDCTM72003/DIV/40018-MVSEIS), as well as by the IRCCM (International Research Consortium on Continental Margins at International University Bremen, Germany), the Max Planck Society and the project MUMM (Mikrobielle Umsatzraten von Methan in gashydrathaltigen Sedimenten, FN 03G0608A) supported by the German Ministry of Education and Research (BMBF). This is publication GEOTECH-234 of the program GEOTECHNOLOGIEN of the BMBF and German Research Foundation (DFG).

*Associate editor:* Donald E. Canfield

## References

- Akhmanov, G., Woodside, J., 1998. Mud volcanic samples in the context of the mediterranean ridge mud diapiric belt. In: Robertson, A.H.F., Emeis, K.-C., Richter, C., Camerlenghi, A. (Eds.), Proceedings of the Ocean Drilling Program, Scientific Results. Ocean Drilling Program, College Station, TX.
- Aliyev, A.A., Guliyev, I.S., Belov, I.S., 2002. Catalogue of recorded eruption of mud volcanoes of Azerbaijan (for period of years 1810–2001). Nafta Press, Baker.
- Aloisi, G., Bouloubassi, I., Heijs, S.K., Pancost, R.D., Pierre, C., Damste, J.S.S., Gottschal, J.C., Forney, L.J., Rouchy, J.M., 2002. CH<sub>4</sub>-consuming microorganisms and the formation of carbonate crusts at cold seeps. *Earth Planet. Sci. Lett.* **203**, 195–203.
- Aloisi, G., Pierre, C., Rouchy, J.-M., Foucher, J.-P., Woodside, J., Party, T.M.S., 2000. Methane-related authigenic carbonates of eastern Mediterranean Sea mud volcanoes and their possible relation to gas hydrate destabilisation. *Earth Planet. Sci. Lett.* **184**, 321–338.
- Barnes, R.O., Goldberg, E.D., 1976. Methane production and consumption in anoxic marine-sediments. *Geology* **4**, 297–300.
- Berner, R.A., 1980. Early Diagenesis—a Theoretical Approach. Princeton University Press, Princeton, New Jersey.
- Blumenberg, M., Seifert, R., Reitner, J., Pape, T., Michaelis, W., 2004. Membrane lipid patterns typify distinct anaerobic methanotrophic consortia. *Proc. Natl. Acad. Sci. USA*, 101.
- Boetius, A., Ravensschlag, K., Schubert, C., Rickert, D., Widdel, F., Gieseke, A., Amann, R., Jørgensen, B.B., Witte, U., Pfannkuche, O., 2000. A marine microbial consortium apparently mediating anaerobic oxidation of methane. *Nature* **407**, 623–626.

- Boetius, A., Suess, E., 2004. Hydrate Ridge: a natural laboratory for the study of microbial life fueled by methane from near-surface gas hydrates. *Chem. Geol.* **205**, 291–310.
- Bohrmann, G., Ivanov, M., Foucher, J.P., Spiess, V., Bialas, J., Greinert, J., Weinrebe, W., Abegg, F., Aloisi, G., Artemov, Y., Blinova, V., Drews, M., Heidersdorf, F., Krabbenhoft, A., Klauke, I., Krastel, S., Leder, T., Polikarpov, I., Saburova, M., Schmale, O., Seifert, R., Volkonskaya, A., Zillmer, M., 2003. Mud volcanoes and gas hydrates in the Black Sea: new data from Dvurechenskii and Odessa mud volcanoes. *Geo-Mar. Lett.* **23**, 239–249.
- Boschker, H.T.S., Middelburg, J.J., 2002. Stable isotopes and biomarkers in microbial ecology. *FEMS Microbiol. Ecol.* **40**, 85–95.
- Boudreau, B.P., 1997. Diagenetic Models and their Implementation: Modelling Transport and Reactions in Aquatic Sediments. Springer, Berlin.
- Charlou, J.L., Donval, J.P., Zitter, T., Roy, N., Jean-Baptiste, P., Foucher, J.P., Woodside, J., 2003. Evidence of methane venting and geochemistry of brines on mud volcanoes of the eastern Mediterranean Sea. *Deep-Sea Res. Pt. I* **50**, 941–958.
- Cita, M.B., Ryan, W.B.F., Paggi, L., 1981. Prometheus Mud Breccia: an example of shale diapirism in the western Mediterranean Ridge, Annales Ge'ologiques Des Pays Helle'niques.
- Cline, J.D., 1969. Spectrophotometric Determination of Hydrogen Sulfide in Natural Waters. *Limnol. Oceanogr.* **14**, 454–458.
- Cordes, E.E., Arthur, M.A., Shea, K., Arvidson, R.S., Fisher, C.R., 2005. Modelling the mutualistic interactions between tubeworms and microbial consortia. *Plos. Biol.* **3**, 497–506.
- Damm, E., Budéus, G., 2003. Fate of vent-derived methane in seawater above the Hakon Mosby mud volcano (Norwegian Sea). *Mar. Chem.* **82**, 1–11.
- Dando, P.R., Bussmann, I., Niven, S.J., O'hara, S.C.M., Schmaljohann, R., Taylor, L.J., 1994. A methane seep area in the Skagerrak, the habitat of the pogonophore *Siboglinum poseidoni* and the bivalve mollusc *Thyasira sarsi*. *Mar. Ecol.-Prog. Ser.* **107**, 157–167.
- De Beer, D., Sauter, E., Niemann, H., Kaul, N., Foucher, J.P., Witte, U., Schluter, M., Boetius, A., 2006. In situ fluxes and zonation of microbial activity in surface sediments of the Hakon Mosby Mud Volcano. *Limnol. Oceanogr.* **51**, 1315–1331.
- Diaz-Del-Rio, V., Somoza, L., Martinez-Frias, J., Mata, M.P., Delgado, A., Hernandez-Molina, F.J., Lunar, R., Martin-Rubi, J.A., Maestro, A., Fernandez-Puga, M.C., Leon, R., Llave, E., Medialdea, T., Vazquez, J.T., 2003. Vast fields of hydrocarbon-derived carbonate chimneys related to the accretionary wedge/olistostrome of the Gulf of Cadiz. *Mar. Geol.* **195**, 177–200.
- Dimitrov, L.I., 2002. Mud volcanoes—the most important pathway for degassing deeply buried sediments. *Earth-Sci. Rev.* **59**, 49–76.
- Dimitrov, L.I., 2003. Mud volcanoes—a significant source of atmospheric methane. *Geo-Mar. Lett.* **23**, 155–161.
- Elvert, M., Boetius, A., Knittel, K., Jørgensen, B.B., 2003. Characterization of specific membrane fatty acids as chemotaxonomic markers for sulfate-reducing bacteria involved in anaerobic oxidation of methane. *Geomicrobiol. J.* **20**, 403–419.
- Elvert, M., Greinert, J., Suess, E., Whiticar, M.J., 2001. Carbon isotopes of biomarkers derived from methane-oxidizing microbes at hydrate ridge, Cascadia convergent margin. In: Paull, C.K., Dillon, W.P. (Eds.), *Natural Gas Hydrates: Occurrence, Distribution, and Dynamics*. American Geophysical Union, Washington DC.
- Elvert, M., Hopmans, E.C., Treude, T., Boetius, A., Hinrichs, K.-U., 2005. Spatial variations of archaeal-bacterial assemblages in gas hydrate bearing sediments at a cold seep: Implications from a high resolution molecular and isotopic approach. *Geobiology* **3**, 195–209.
- Elvert, M., Suess, E., Whiticar, M.J., 1999. Anaerobic methane oxidation associated with marine gas hydrates: superlight C-isotopes from saturated and unsaturated C<sub>20</sub> and C<sub>25</sub> irregular isoprenoids. *Naturwissenschaften* **86**, 295–300.
- Etiopé, G., Klusman, R.W., 2002. Geologic emissions of methane to the atmosphere. *Chemosphere* **49**, 777–789.
- Etiopé, G., Milkov, A.V., 2004. A new estimate of global methane flux from onshore and shallow submarine mud volcanoes to the atmosphere. *Environ. Geol.* **46**, 997–1002.
- Felbeck, H., 1983. Sulfide oxidation and carbon fixation by the gutless clam *solemya-reidi*—an animal bacteria symbiosis. *J. Comp. Physiol.* **152**, 3–11.
- Fisher, C.R., 1990. Chemoautotrophic and methanotrophic symbioses in marine-invertebrates. *Rev. Aquat. Sci.* **2**, 399–436.
- Gardner, J.M., 2001. Mud volcanoes revealed and sampled on the Western Moroccan continental margin. *Geophys. Res. Lett.* **28**, 339–342.
- Gebruk, A.V., Krylova, E.M., Lein, A.Y., Vinogradov, G.M., Anderson, E., Pimenov, N.V., Cherkashev, G.A., Crane, K., 2003. Methane seep community of the Hakon Mosby mud volcano (the Norwegian Sea): composition and trophic aspects. *Sarsia* **88**, 394–403.
- Gillian, F.T., Johns, R.B., Verheyen, T.V., Nichols, P.D., Esdaile, R.J., Bavor, H.J., 1981. Monounsaturated fatty acids as specific bacterial markers in marine sediments. *Adv. Org. Geochem.*
- Grasshoff, K., Ehrhardt, M., Kremling, K., 1983. *Methods of seawater analysis*. Verlag Chemie, Weinheim.
- Haese, R.R., Meile, C., Van Cappellen, P., De Lange, G.J., 2003. Carbon geochemistry of cold seeps: methane fluxes and transformation in sediments from Kazan mud volcano, eastern Mediterranean Sea. *Earth Planet. Sci. Lett.* **212**, 361–375.
- Hanson, R.S., Hanson, T.E., 1996. Methanotrophic bacteria. *Microbiol. Rev.* **60**, 439.
- Hensen, C., Wallmann, K., Schmidt, M., Ranero, C.R., Suess, E., 2004. Fluid expulsion related to mud extrusion off Costa Rica—a window to the subducting slab. *Geology* **32**, 201–204.
- Hensen, C., Zabel, M., Pfeifer, K., Schwenk, T., Kasten, S., Riedinger, N., Schulz, H.D., Boetius, A., 2003. Control of sulfate pore-water profiles by sedimentary events and the significance of anaerobic oxidation of methane for the burial of sulfur in marine sediments. *Geochim. Cosmochim. Acta* **67**, 2631–2647.
- Hinrichs, K.-U., Boetius, A., 2002. The anaerobic oxidation of methane: new insights in microbial ecology and biogeochemistry. In: Wefer, G., Billert, D., Hebbeln, D. (Eds.), *Ocean Margin System*. Springer-Verlag, Berlin.
- Hinrichs, K.-U., Hayes, J.M., Sylva, S.P., Brewer, P.G., Delong, E.F., 1999. Methane-consuming archaeobacteria in marine sediments. *Nature* **398**, 802–805.
- Iversen, N., Jørgensen, B.B., 1985. Anaerobic methane oxidation rates at the sulfate–methane transition in marine sediments from Kattegat and Skagerrak (Denmark). *Limnol. Oceanogr.* **30**, 944–955.
- Jørgensen, B.B., 1978. A comparison of methods for the quantification of bacterial sulphate reduction in coastal marine sediments. I. Measurements with radiotracer techniques. *Geomicrobiol. J.* **1**, 11–27.
- Jørgensen, B.B., Weber, A., Zopf, J., 2001. Sulfate reduction and anaerobic methane oxidation in Black Sea sediments. *Deep-Sea Res. Pt. I* **48**, 2097–2120.
- Joye, S.B., Boetius, A., Orcutt, B.N., Montoya, J.P., Schulz, H.N., Erickson, M.J., Lugo, S.K., 2004. The anaerobic oxidation of methane and sulfate reduction in sediments from Gulf of Mexico cold seeps. *Chem. Geol.* **205**, 219–238.
- Judd, A.G., Hovland, M., Dimitrov, L.I., Gil, S.G., Jukes, V., 2002. The geological methane budget at continental margins and its influence on climate change. *Geofluids* **2**, 109–126.
- Kane, M.D., Poulsen, L.K., Stahl, D.A., 1993. Monitoring the enrichment and isolation of sulfate-reducing bacteria by using oligonucleotide hybridization probes designed from environmentally derived 16s ribosomal-Rna sequences. *Appl. Environ. Microbiol.* **59**, 682–686.
- Kenyon, N.H., Ivanov, M.K., Akhmetzhanov, A.M., Akhmanov, G., 2001. Interdisciplinary Approaches to Geoscience on the North East Atlantic Margin and Mid-Atlantic Ridge. IOC Technical Series No. 60.
- Kenyon, N.H., Ivanov, M.K., Akhmetzhanov, A.M., Akhmanov, G.G., 2000. Multidisciplinary Study of Geological Processes on the North

- East Atlantic and Western Mediterranean Margins. IOC Technical Series No. 56.
- Kholodov, V.N., 2002. Mud volcanoes: distribution regularities and genesis (Communication 2. geological–geochemical peculiarities and formation model). *Lithol. Miner. Resour.* **37**, 293–310.
- Kimura, H., Sato, M., Sasayama, Y., Naganuma, T., 2003. Molecular characterization and in situ localization of endosymbiotic 16S ribosomal RNA and RuBisCO genes in the pogonophoran tissue. *Mar. Biotechnol.* **5**, 261–269.
- Knittel, K., Boetius, A., Lemke, A., Eilers, H., Lochte, K., Pfannkuche, O., Linke, P., Amann, R., 2003. Activity, distribution, and diversity of sulfate reducers and other bacteria in sediments above gas hydrate (Cascadia margin, Oregon). *Geomicrobiol. J.* **20**, 269–294.
- Knittel, K., Lösekann, T., Boetius, A., Kort, R., Amann, R., 2005. Diversity and distribution of methanotrophic archaea at cold seeps. *Appl. Environ. Microbiol.* **71**, 467–479.
- Kopf, A., Bannert, B., Brückmann, W., Dorschel, B., Foubert, A.T.G., Grevemeyer, I., Gutscher, M.A., Hebbeln, D., Heesemann, B., Hensen, C., Kaul, N.E., Lutz, M., Magalhaes, V.H., Marquardt, M.J., Marti, A.V., Nass, K.S., Neubert, N., Niemann, H., Nuzzo, M., Poort, J.P.D., Rosiak, U.D., Sahling, H., Schneider Von Deimling, J., Somoza, L., Thiebot, E., Wilkop, T.P., 2004. Report and preliminary results of Sonne Cruise SO175, Miami–Bremerhaven, 12.11–30.12.2003. Fachbereich Geowissenschaften der Universität Bremen.
- Kopf, A.J., 2002. Significance of mud volcanism. *Rev. Geophys.* **40**, B1–B49.
- Kopf, A.J., 2003. Global methane emission through mud volcanoes and its past and present impact on the Earth's climate. *Int. J. Earth Sci.* **92**, 806–816.
- Krueger, D.M., Cavanaugh, C.M., 1997. Phylogenetic diversity of bacterial symbionts of *Solemya* hosts based on comparative sequence analysis of 16S rRNA genes. *Appl. Environ. Microbiol.* **63**, 91–98.
- Lane, D.J., Pace, B., Olsen, G.J., Stahl, D.A., Sogin, M.L., Pace, N.R., 1985. Rapid-determination of 16s ribosomal-Rna sequences for phylogenetic analyses. *Proc. Natl. Acad. Sci. USA* **82**, 6955–6959.
- Luff, R., Wallmann, K., 2003. Fluid flow, methane fluxes, carbonate precipitation and biogeochemical turnover in gas hydrate-bearing sediments at hydrate ridge, Cascadia margin: numerical modeling and mass balances. *Geochim. Cosmochim. Acta* **67**, 3403–3421.
- Madigan, M.T., Martinko, J.M., Parker, J., 2000. *Brock Biology of Microorganisms*. Prentice-Hall Inc..
- Maldonado, A., Comas, M.C., 1992. Geology and geophysics of the Alboran Sea—an introduction. *Geo-Mar. Lett.* **12**, 61–65.
- Maldonado, A., Somoza, L., Pallares, L., 1999. The Betic orogen and the Iberian–African boundary in the Gulf of Cadiz: geological evolution (central North Atlantic). *Mar. Geol.* **155**, 9–43.
- Massana, R., Murray, A.E., Preston, C.M., Delong, E.F., 1997. Vertical distribution and phylogenetic characterization of marine planktonic Archaea in the Santa Barbara Channel. *Appl. Environ. Microbiol.* **63**, 50–56.
- Mazurenko, L.L., Soloviev, V.A., Belenkaya, I., Ivanov, M.K., Pinheiro, L.M., 2002. Mud volcano gas hydrates in the Gulf of Cadiz. *Terra Nova* **14**, 321–329.
- Michaelis, W., Seifert, R., Nauhaus, K., Treude, T., Thiel, V., Blumenberg, M., Knittel, K., Gieseke, A., Peterknecht, K., Pape, T., Boetius, A., Amann, R., Jorgensen, B.B., Widdel, F., Peckmann, J.R., Pimenov, N.V., Gulin, M.B., 2002. Microbial reefs in the Black Sea fueled by anaerobic oxidation of methane. *Science* **297**, 1013–1015.
- Milkov, A.V., 2000. Worldwide distribution of submarine mud volcanoes and associated gas hydrates. *Mar. Geol.* **167**, 29–42.
- Milkov, A.V., Sassen, R., Apanasovich, T.V., Dadashev, F.G., 2003. Global gas flux from mud volcanoes: a significant source of fossil methane in the atmosphere and the ocean. *Geophys. Res. Lett.*, 30.
- Milkov, A.V., Vogt, P.R., Crane, K., Lein, A.Y., Sassen, R., Cherkashev, G.A., 2004. Geological, geochemical, and microbial processes at the hydrate-bearing Hakon Mosby mud volcano: a review. *Chem. Geol.* **205**, 347–366.
- Moss, C.W., Lambertfair, M.A., 1989. Location of double-bonds in monounsaturated fatty-acids of campylobacter-cryaerophila with dimethyl disulfide derivatives and combined gas chromatography-mass spectrometry. *J. Clin. Microbiol.* **27**, 1467–1470.
- Muyzer, G., Teske, A., Wirsén, C.O., Jannasch, H.W., 1995. Phylogenetic relationships of *Thiomicrospira* species and their identification in deep-sea hydrothermal vent samples by denaturing gradient gel electrophoresis of 16S rDNA fragments. *Arch. Microbiol.* **164**, 165–172.
- Nauhaus, K., Boetius, A., Kruger, M., Widdel, F., 2002. In vitro demonstration of anaerobic oxidation of methane coupled to sulphate reduction in sediment from a marine gas hydrate area. *Environ. Microbiol.* **4**, 296–305.
- Nichols, P.D., Guckert, J.B., White, D.C., 1986. Determination of monounsaturated fatty acid double-bond position and geometry for microbial monocultures and complex consortia by capillary GC-MS of their dimethyl disulphide adducts. *J. Microbiol. Methods* **5**, 49–55.
- Niemann, H., Elvert, M., Hovland, M., Orcutt, B., Judd, A.G., Suck, I., Gutt, J., Joye, S.B., Damm, E., Finster, K., Boetius, A., 2005. Methane emission and consumption at a North Sea gas seep (Tommeliten area). *Biogeosciences* **2**, 335–351.
- Niewöhner, C., Hensen, C., Kasten, S., Zabel, M., Schulz, H.D., 1998. Deep sulfate reduction completely mediated by anaerobic methane oxidation in sediments of the upwelling area off Namibia. *Geochim. Cosmochim. Acta* **62**, 455–464.
- Nuzzo, M., Hensen, C., Hornibrook, E., Brueckmann, W., Magalhaes, V.H., Parkes, R.J., Pinheiro, L.M., 2005. Origin of Mud Volcano Fluids in the Gulf of Cadiz (E-Atlantic) EGU General Assembly, Vienna.
- Olu, K., Lance, S., Sibuet, M., Henry, P., Fialamedioni, A., Dinert, A., 1997a. Cold seep communities as indicators of fluid expulsion patterns through mud volcanoes seaward of the Barbados accretionary prism. *Deep-Sea Res. Pt. I* **44**, 811.
- Olu, K., Lance, S., Sibuet, M., Henry, P., Fiala-Médioni, A., Dinert, A., 1997b. Cold seep communities as indicators of fluid expulsion patterns through mud volcanoes seaward of the Barbados accretionary prism. *Deep-Sea Res. Pt. I* **44**, 811–841.
- Orphan, V.J., House, C.H., Hinrichs, K.U., Mckeegan, K.D., Delong, E.F., 2001. Methane-consuming archaea revealed by directly coupled isotopic and phylogenetic analysis. *Science* **293**, 484–487.
- Orphan, V.J., House, C.H., Hinrichs, K.U., Mckeegan, K.D., Delong, E.F., 2002. Multiple archaeal groups mediate methane oxidation in anoxic cold seep sediments. *Proc. Natl. Acad. Sci. USA* **99**, 7663–7668.
- Pancost, R.D., Bouloubassi, I., Aloisi, G., Damste, J.S.S., 2001. Three series of non-isoprenoidal dialkyl glycerol diethers in cold-seep carbonate crusts. *Org. Geochem.* **32**, 695–707.
- Pancost, R.D., Sinninghe Damsté, J.S., De Lint, S., Van Der Maarel, M.J.E.C., Gottschal, J.C., Party, T.M.S.S., 2000. Biomarker evidence for widespread anaerobic methane oxidation in Mediterranean sediments by a consortium of methanogenic archaea and bacteria. *Appl. Environ. Microbiol.* **66**, 1126–1132.
- Peckmann, J., Thiel, V., Michaelis, W., Clari, P., Gaillard, C., Martire, L., Reitner, J., 1999. Cold seep deposits of Beauvoisin (Oxfordian; southeastern France) and Marmorito (Miocene; northern Italy): microbially induced authigenic carbonates. *Int. J. Earth Sci.* **88**, 60–75.
- Peek, A.S., Feldman, R.A., Lutz, R.A., Vrijenhoek, R.C., 1998. Cospeciation of chemoautotrophic bacteria and deep sea clams. *Proc. Natl. Acad. Sci. USA* **95**, 9962–9966.
- Pinheiro, L.M., Ivanov, M.K., Sautkin, A., Akhmanov, G., Magalhaes, V.H., Volkonskaya, A., Monteiro, J.H., Somoza, L., Gardner, J., Hamouni, N., Cunha, M.R., 2003. Mud volcanism in the Gulf of Cadiz: results from the TTR-10 cruise. *Mar. Geol.* **195**, 131–151.
- Reeburgh, W.S., 1967. An improved interstitial water sampler. *Limnol. Oceanogr.* **12**, 163.
- Reeburgh, W.S., 1976. Methane consumption in Cariaco Trench waters and sediments. *Earth Planet. Sci. Lett.* **28**, 337–344.

- Reeburgh, W.S., 1996. "Soft spots" in the global methane budget. In: Lidstrom, M.E., Tabita, F.R. (Eds.), *Microbial Growth on C<sub>1</sub> Compounds*. Kluwer Academic Publishers, Dordrecht.
- Reeburgh, W.S., Heggie, D.T., 1977. Microbial methane consumption reactions and their effect on methane distributions in freshwater and marine environments. *Limnol. Oceanogr.* **22**, 1–9.
- Ritger, S., Carson, B., Suess, E., 1987. Methane-derived authigenic carbonates formed by subduction-induced pore-water expulsion along the Oregon/Washington margin. *Geol. Soc. Am. Bull.* **98**, 147–156.
- Rueter, P., Rabus, R., Wilkes, H., Aeckersberg, F., Rainey, F.A., Jannasch, H.W., Widdel, F., 1994. Anaerobic oxidation of hydrocarbons in crude-oil by new types of sulfate-reducing bacteria. *Nature* **372**, 455–458.
- Sahling, H., Rickert, D., Lee, R.W., Linke, P., Suess, E., 2002. Macrofaunal community structure and sulfide flux at gas hydrate deposits from the Cascadia convergent margin, NE Pacific. *Mar. Ecol.-Prog. Ser.* **231**, 121–138.
- Sauter, E.J., Muyakshin, S.I., Charlou, J.-L., Schluter, M., Boetius, A., Jerosch, K., Damm, E., Foucher, J.-P., Klages, M., 2006. Methane discharge from a deep-sea submarine mud volcano into the upper water column by gas hydrate-coated methane bubbles. *Earth Planet. Sci. Lett.* **243**, 354–365.
- Schmaljohann, R., Flugel, H.J., 1987. Methane-oxidizing bacteria in pogonophora. *Sarsia* **72**, 91–99.
- Sibuet, M., Olu, K., 1998. Biogeography, biodiversity and fluid dependence of deep-sea cold-seep communities at active and passive margins. *Deep-Sea Res. Pt. II* **45**, 517–567.
- Small, H., Stevens, T.S., Bauman, W.C., 1975. Novel ion-exchange chromatographic method using conductimetric detection. *Anal. Chem.* **47**, 1801–1809.
- Somoza, L., Diaz-Del-Rio, V., Leon, R., Ivanov, M., Fernandez-Puga, M.C., Gardner, J.M., Hernandez-Molina, F.J., Pinheiro, L.M., Rodero, J., Lobato, A., Maestro, A., Vazquez, J.T., Medialdea, T., Fernandez-Salas, L.M., 2003. Seabed morphology and hydrocarbon seepage in the Gulf of Cadiz mud volcano area: Acoustic imagery, multibeam and ultra-high resolution seismic data. *Mar. Geol.* **195**, 153–176.
- Somoza, L., Diaz-Del-Rio, V., Vazquez, J.T., Pinheiro, L.M., Hernandez-Molina, F.J., 2002. Numerous methane gas-related sea floor structures identified in Gulf of Cadiz. *EOS* **83**, 541–547.
- Southward, A.J., Southward, E.C., Dando, P.R., Barrett, R.L., Ling, R., 1986. Chemoautotrophic function of bacterial symbionts in small pogonophora. *J. Mar. Biol. Assoc. UK* **66**, 415–437.
- Southward, A.J., Southward, E.C., Dando, P.R., Rau, G.H., Felbeck, H., Flugel, H., 1981. Bacterial symbionts and low <sup>13</sup>C/<sup>12</sup>C ratios in tissues of Pogonophora indicate unusual nutrition and metabolism. *Nature* **293**, 616–620.
- Southward, E.C., Schulze, A., Gardiner, S.L., 2005. Pogonophora (Annelida): form and function. *Hydrobiologia* **535–536**, 227–251.
- Stadnitskaia, A., Ivanov, M.K., Blinova, V., Kreulen, R., Van Weering, T.C.E., 2006. Molecular and carbon isotopic variability of hydrocarbon gases from mud volcanoes in the Gulf of Cadiz, NE Atlantic. *Mar. Petrol. Geol.* **23**, 281–296.
- Stadnitskaia, A., Muyzer, G., Abbas, B., Coolen, M.J.L., Hopmans, E.C., Baas, M., Van Weering, T.C.E., Ivanov, M.K., Poludetkina, E., Damste, 2005. Biomarker and 16S rDNA evidence for anaerobic oxidation of methane and related carbonate precipitation in deep-sea mud volcanoes of the Sorokin Trough, Black Sea. *Mar. Geol.* **217**, 67–96.
- Summons, R.E., Jahnke, L.L., Roksandic, Z., 1994. Carbon isotopic fractionation in lipids from methanotrophic bacteria: relevance for interpretation of the geochemical record of biomarkers. *Geochim. Cosmochim. Acta* **58**, 2853–2863.
- Teske, A., Hinrichs, K.U., Edgcomb, V., Gomez, A.D., Kysela, D., Sylva, S.P., Sogin, M.L., Jannasch, H.W., 2002. Microbial diversity of hydrothermal sediments in the Guaymas basin: evidence for anaerobic methanotrophic communities. *Appl. Environ. Microbiol.* **68**, 1994–2007.
- Thiel, V., Peckmann, J., Seifert, R., Wehrung, P., Reitner, J., Michaelis, W., 1999. Highly isotopically depleted isoprenoids: molecular markers for ancient methane venting. *Geochim. Cosmochim. Acta* **63**, 3959–3966.
- Torres, M.E., Mcmanus, J., Hammond, D.E., De Angelis, M.A., Heeschen, K.U., Colbert, S.L., Tryon, M.D., Brown, K.M., Suess, E., 2002. Fluid and chemical fluxes in and out of sediments hosting methane hydrate deposits on hydrate ridge, OR, I: hydrological provinces. *Earth Planet. Sci. Lett.* **201**, 525–540.
- Treude, T., Boetius, A., Knittel, K., Wallmann, K., Jorgensen, B.B., 2003. Anaerobic oxidation of methane above gas hydrates at hydrate ridge, NE Pacific Ocean. *Mar. Ecol.-Prog. Ser.* **264**, 1–14.
- Treude, T., Niggemann, J., Kallmeyer, J., Wintersteller, P., Schubert, C.J., Boetius, A., Jorgensen, B.B., 2005. Anaerobic oxidation of methane and sulfate reduction along the Chilean continental margin. *Geochim. Cosmochim. Acta* **69**, 2767–2779.
- Vogt, P.R., Cherkashev, A., Ginsburg, G.D., Ivanov, G.I., Crane, K., Lein, A.Y., Sundvor, E., Pimenov, N.V., Egorov, A., 1997a. Haakon mosby mud volcano: a warm methane seep with seafloor hydrates and chemosynthesis-based ecosystem in late quaternary slide valley, Bear Island Fan, Barents Sea passive margin. *EOS Trans. Am. Geophys. Union Suppl.* **78**, 187–189.
- Vogt, P.R., Cherkashev, G., Ginsburg, G., Ivanov, G.I., Milkov, A., Crane, K., Lein, A., Sundvor, E., Pimenov, N.V., Egorov, A., 1997b. Haakon mosby mud volcano provides unusual example of venting. *EOS Trans. Am. Geophys. Union Suppl.* **78** (549), 556–557.
- Werne, J.P., Baas, M., Damste, J.S.S., 2002. Molecular isotopic tracing of carbon flow and trophic relationships in a methane-supported benthic microbial community. *Limnol. Oceanogr.* **47**, 1694–1701.
- Werne, J.P., Haese, R.R., Zitter, T., Aloisi, G., Bouloubassi, L., Heijs, S., Fiala-Medioni, A., Pancost, R.D., Damste, J.S.S., De Lange, G., Forney, L.J., Gottschal, J.C., Foucher, J.P., Mascle, J., Woodside, J., 2004. Life at cold seeps: a synthesis of biogeochemical and ecological data from Kazan mud volcano, eastern Mediterranean Sea. *Chem. Geol.* **205**, 367–390.
- Whiticar, M.J., 1999. Carbon and hydrogen isotope systematics of bacterial formation and oxidation of methane. *Chem. Geol.* **161**, 291–314.
- Whiticar, M.J., Faber, E., Schoell, M., 1986. Biogenic methane formation in marine and freshwater environments: CO<sub>2</sub> reduction vs. acetate fermentation—isotope evidence. *Geochim. Cosmochim. Acta* **50**, 693–709.
- Widdel, F., Rabus, R., 2001. Anaerobic biodegradation of saturated and aromatic hydrocarbons. *Curr. Opin. Biotechnol.* **12**, 259–276.





ELSEVIER

Available online at www.sciencedirect.com

Geochimica et Cosmochimica Acta xxx (2007) xxx–xxx

**Geochimica**

www.elsevier.com/locate/gca

## Sources of mud volcano fluids in the Gulf of Cadiz—indications for hydrothermal imprint

Christian Hensen <sup>a,\*</sup>, Marianne Nuzzo <sup>b</sup>, Edward Hornibrook <sup>b</sup>, Luis M. Pinheiro <sup>c,d</sup>,  
Barbara Bock <sup>a</sup>, Vitor H. Magalhães <sup>c,d</sup>, Warner Brückmann <sup>a</sup>

<sup>a</sup> Leibniz-Institute of Marine Sciences, IFM-GEOMAR, Wischhofstr. 1–3, D-24148 Kiel, Germany

<sup>b</sup> Bristol Biogeochemistry Research Centre, Department of Earth Sciences, University of Bristol, UK

<sup>c</sup> CESAM and Geosciences Department, Universidade de Aveiro, Aveiro, Portugal

<sup>d</sup> Marine Geology Department, INETI, Alfragide, Portugal

Received 16 February 2006; accepted in revised form 20 November 2006

### Abstract

Mud volcanism in the Gulf of Cadiz occurs over a large area extending from the shelf to more than 3500 m water depth and is triggered by compressional stress along the European–African plate boundary, affecting a deeply faulted sedimentary sequence of locally more than 5 km thickness. The investigation of six active sites shows that mud volcano (MV) fluids, on average, are highly enriched in CH<sub>4</sub>, Li, B, and Sr and depleted in Mg, K, and Br. The purity of the fluids is largely controlled by the intensity of upward directed flow. Flow rates could be constrained by numerical modelling and vary between <0.05 and 15 cm yr<sup>-1</sup>. Application of δD–δ<sup>18</sup>O systematics identifies clay mineral dehydration, most likely within Mesozoic and Tertiary shales and marls, as the major source of fluids. Hence, Cl and Na in the pore fluids are mostly depleted below seawater values, following a general trend of dilution. However, deviations from this trend occur and are likely caused by the dissolution of halite in evaporitic deposits. Other secondary processes overprinting the original fluid composition may occur along the flow path, such as dissolution of anhydrite or gypsum and/or the formation of calcite and dolomite. Different sources of fluids are also indicated by variations in <sup>87</sup>Sr/<sup>86</sup>Sr, which range from 0.7086 to 0.7099 at the different sites. Dehydration may be induced primarily by overburden and tectonic compression; however, very high concentrations of Li and B, specifically at Captain Arutyunov MV (CAMV) indicate additional leaching at temperatures above 150 °C, which could be explained by the injection of hot fluids along deep penetrating, major E–W strike-slip fault systems. This hypothesis is supported by the occurrence of generally thermogenic, but significantly CH<sub>4</sub>-enriched, light volatile hydrocarbon gases at CAMV which cannot be explained by shallow microbial methanogenesis. Li and Li/B ratios from different types of hot and cold vents are used to infer that high temperature signals seem to be preserved at various cold vent locations and indicate a closer coupling of both systems in continental margin environments than outlined in previous studies.

© 2006 Published by Elsevier Inc.

### 1. Introduction

Mud volcanism provides an important, but poorly constrained transport pathway for fluids along continental margins. Several thousands of mud volcanoes (MVs) may occur in deep-water areas along continental margins (Milkov, 2000; Milkov et al., 2003) so that the expulsion

of sedimentary fluids at continental margins may play a significant role for global fluid and element budgets (Aloisi et al., 2004a). Fluid expulsion is generally coupled to tectonic activity controlling episodic fault displacements (Moore and Vrolijk, 1992). Mud volcanoes and other types of cold vent systems are offering a window into otherwise obscured deep structural and diagenetic processes as geochemical interactions of the rising fluid with surrounding sediment and rock may significantly alter the chemistry of the pore fluids. Such diagenetic processes may involve

\* Corresponding author. Fax: +49 431 6002928.

E-mail address: chensen@ifm-geomar.de (C. Hensen).

the degradation of organic matter and the formation of gas hydrates (e.g. Martin et al., 1993; Buffett and Archer, 2004; Hensen and Wallmann, 2005), mineral dissolution/precipitation reactions and transformation processes of clay minerals and volcanic ashes (Chan and Kastner, 2000; Brown et al., 2001; Dählmann and De Lange, 2003) and high-temperature reactions with oceanic or continental crust (Martin et al., 1991; You and Gieskes, 2001; Von Damm et al., 2005). Negative chloride anomalies are typically reported from many modern accretionary prisms (Moore and Vrolijk, 1992); however, depending on the geologic and structural setting, the overlap of a number of these processes may lead to the formation of geochemically distinct fluids with an eventually complex history. This problem has been addressed by a number of studies (e.g. Martin et al., 1996; Suess et al., 1998; Fryer et al., 1999; Haese et al., 2003; Aloisi et al., 2004a; Hensen et al., 2004;) which have helped to improve our knowledge of key processes involved. Moreover, any rising fluid may be subject a large number of processes occurring simultaneously or successively under regionally changing environmental conditions. Hence, in many cases there is no unambiguous solution for the origin of a specific fluid. In some cases ODP drilling data provided valuable information bridging the gap between subsurface processes and sea floor observations. In order to proceed towards a more general understanding

of deep structural control on cold venting more systematic investigations from various tectonic settings are required.

Although the Gulf of Cadiz is, at present, target area of a number of European projects, geochemical data published to date are mostly limited to thermogenic hydrocarbon gases and CH<sub>4</sub> clathrates from MVs situated on the Moroccan Margin (Mazurenko et al., 2003; Depreiter et al., 2005; Van Rensbergen et al., 2005; Stadnitskaia et al., 2006). Here, we provide the first comprehensive data set on the geochemistry of mud volcano fluids in the Gulf of Cadiz. We combine analysis of pore water and gas geochemistry with information on regional geology to unravel the origin of the fluids in this compressive margin, which may be undergoing active subduction, as suggested recently by (Gutscher et al., 2002).

## 2. Study area and geological background

The Gulf of Cadiz is located in a structurally complex convergent tectonic setting in which the boundary between the African and Eurasian plates is concealed beneath thick (~7 km) Mio-Pliocene sedimentary deposits (e.g. Medialdea et al., 2004). In this area the Africa–Eurasia plate boundary strikes from the right-lateral Gloria Fault and Bank of Goringe thrust to the west, to the Alboran Sea, east of the Strait of Gibraltar (Fig. 1). The region is seismically active (Buforn et al., 1995; Ribeiro et al., 1996) and

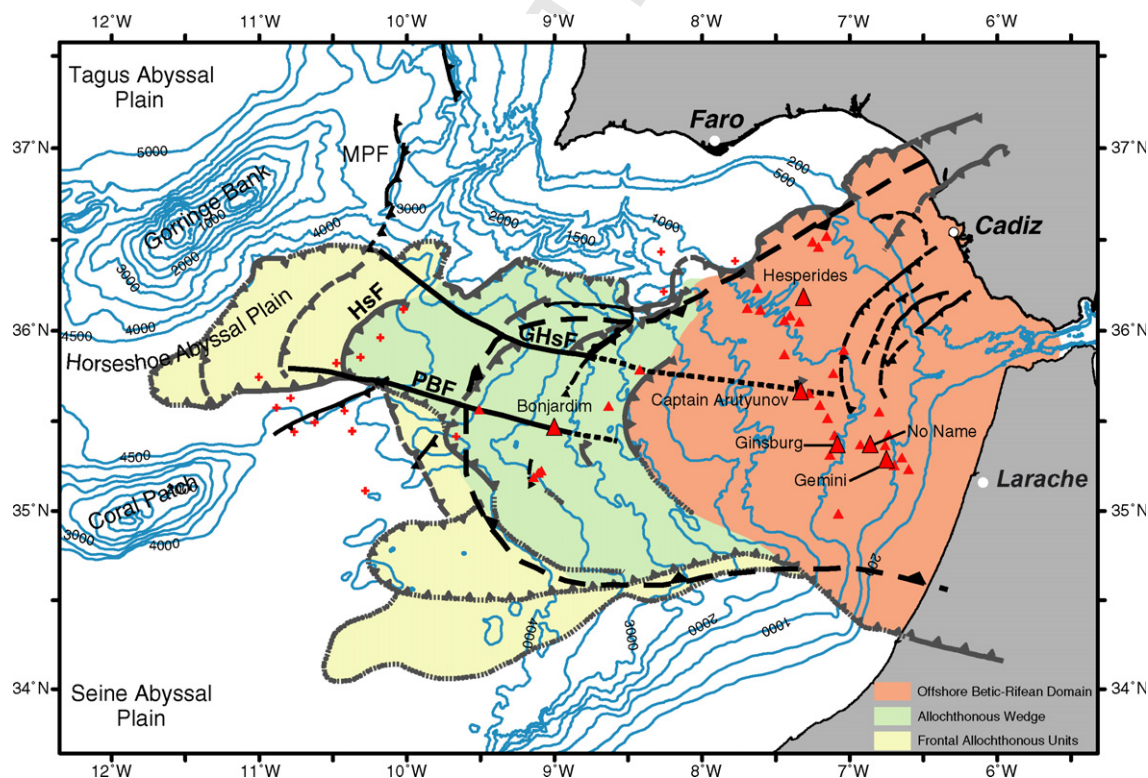


Fig. 1. Simplified structural geology map of the Gulf of Cadiz, modified after (Medialdea et al., 2004) and complemented with interpretations based on the Matespro bathymetric survey (Duarte et al., 2005), showing the Betic–Rifean Domain, the Allochthonous Wedge, the Frontal Allochthonous Units, major faults (black), the locations of Captain Arutyunov, Bonjardim, Ginsburg, Gemini, Hesperides, and No Name MVs (large triangles), and other MVs (small triangles) in the region. Major tectonic features include the Marques de Pombal (MPF), Porto-Bonjardim (PBF), Horseshoe (HsF), and Goringe-Horseshoe (GHsF) Fault. Crosses are basement highs. The large thrust fault outline (dashed line) indicates the edge of the accretionary wedge as suggested by (Gutscher, 2004). Bathymetric contours are from the GEBCO 2003 database.

99 was the epicentre of an >8.5 magnitude earthquake in 1755  
 100 which, combined with an associated tsunami, decimated  
 101 the city of Lisbon, Portugal (Baptista et al., 1988). The  
 102 NE sector is marked by a conjugate set of NW–SE and  
 103 NE–SW strike–slip faults (Fig. 1) that control diapiric ridges  
 104 and together with major WNW–ESE strike–slip faults  
 105 are thought to accommodate the NW-directed plate convergence  
 106 (e.g. Argus et al., 1989; Pinheiro et al., 2005) in  
 107 a broad deformation zone (Morel and Meghraoui, 1996)  
 108 that has been described as a diffuse plate boundary (Sartori  
 109 et al., 1994). It has been proposed previously that plate  
 110 convergence in the region is accommodated along major  
 111 deeply rooted Paleozoic wrench faults reactivated under  
 112 Plio-Quaternary transpressive convergence (Meghraoui  
 113 et al., 1996; Morel and Meghraoui, 1996). The formation  
 114 of the Arc of Gibraltar and expulsion of thick nappes to  
 115 the west in the Gulf of Cadiz were initiated by a change  
 116 in the main convergence direction during the Mid- to  
 117 Upper-Miocene (Maldonado et al., 1999). Several studies  
 118 have suggested that westward progression of the Arc of  
 119 Gibraltar into the Gulf of Cadiz ceased before the Pliocene  
 120 (e.g. Lonergan and White, 1997; Maldonado et al., 1999),  
 121 however, Gutscher et al. (2002) and Gutscher (2004) pro-  
 122 posed that E–W subduction remains active and is driven  
 123 by the rollback of a relic of subducted Thethian oceanic  
 124 crust beneath the Arc of Gibraltar (Fig. 1).

125 Mud volcanoes (MVs) were first discovered and sampled  
 126 in the Gulf of Cadiz in 1999 (Gardner, 2001) and since then  
 127 have been extensively investigated during several research  
 128 cruises (Pinheiro et al., 2003, 2005). Folding, mud volca-  
 129 nism, and diapirism in the region result from neo-tectonism  
 130 (Grácia et al., 2003) and MVs are located either along ma-  
 131 jor strike–slip faults or at the intersection of these faults  
 132 with arcuate thrusts associated with the formation of the  
 133 Gibraltar Arc (Pinheiro et al., 2003, 2005).

### 134 3. Material and methods

135 In December 2003, an extensive scientific programme  
 136 was conducted on the German research vessel *RV Sonne*  
 137 (cruise SO 175-2; Kopf and participants, 2004). Sediments,  
 138 fluids, and gases were sampled from active MVs through-  
 139 out the Gulf (Fig. 1 and Table 1). Surface indications for  
 140 active seepage of methane-rich fluids were not observed  
 141 at any of the sites during this cruise, i.e. there was an

absence of typical chemosynthetic fauna (Kopf and partic- 142  
 ipants, 2004), but widespread evidence for anaerobic oxida- 143  
 tion of methane (AOM) occurring in the shallow 144  
 subsurface (Niemann et al., 2006). The sites sampled were 145  
 Captain Arutyunov MV (CAMV, GeoB 9036-2, 9041-1, 146  
 9072-1), Ginsburg MV (GeoB 9061-1), Bonjardim MV 147  
 (GeoB 9051-1, 9051-2), Gemini MV (GeoB 9067-1), Un- 148  
 named MV (9063-1), and Hesperides MV (GeoB 9021-1). 149  
 Sediments consist mainly of gas-saturated homogeneous 150  
 mud breccias with low organic carbon content (Table 1). 151  
 Samples from Ginsburg MV were characterized by a dis- 152  
 tinct smell of petroleum. Gas hydrates, which have been 153  
 previously recovered from various sites (Mazurenko 154  
 et al., 2003; Pinheiro et al., 2003, 2005), were retrieved only 155  
 at CAMV. 156

#### 3.1. Sediment sampling 157

Gravity cores generally were taken after prior investi- 158  
 gation with a video sled (OFOS—ocean floor observation 159  
 system) and sampling of shallow surface sediments using 160  
 a video-guided multi-corer (Niemann et al., 2006). The 161  
 cores were segmented in pieces of 1 m and cut lengthwise 162  
 in a cooled laboratory at about 6 °C. Sediment samples 163  
 for pore water and gas analyses were collected within 164  
 1–2 h after retrieval. Although it is a well-known fact 165  
 that most (up to 95%) of the light hydrocarbon gases 166  
 are lost during core recovery, the remaining methane is 167  
 highly enriched above background values and can be 168  
 used for reliable flux calculations (Niewöhner et al., 169  
 1998) and isotope analyses (Wallace et al., 2000). Pore 170  
 waters were squeezed using a pressure filtration system 171  
 at pressures up to 5 bar and filtered through 0.45 µm cel- 172  
 lulose acetate membrane filters. Pore water samples were 173  
 then immediately analysed onboard or sub-sampled for 174  
 subsequent analysis. Sediment samples for pore water 175  
 hydrocarbon gas analysis were extruded and disaggregat- 176  
 ed in sealed 35 ml vials containing 10 ml of a 10%-KCl 177  
 solution to stop all microbial activity (Bowes and Horn- 178  
 ibrook, 2006). 179

#### 3.2. Pore water analysis 180

Onboard analyses were performed for the most sensitive 181  
 parameters (alkalinity, H<sub>2</sub>S, and NH<sub>4</sub>) immediately after 182

Table 1  
 Location of the gravity cores and general characteristics of the MV study sites

Site	Core Number GeoB	Latitude (°N)	Longitude (°W)	Water depth (m)	Average TOC (wt%)	Bottom water T (°C)
Captain	9041-1	35°39.7'	7°19.97'	1316	0.35	9.3
Arutyunov MV	9072-1	35°39.71'	7°19.95'	1321	0.34	
Hesperides MV	9021-1	36°10.99'	7°18.38'	701	0.22	12
Bonjardim MV	9051-2	35°27.61'	9°00.03'	3087	0.27	3.1
Ginsburg MV	9061-1	35°22.42'	7°05.29'	912	0.29	10
No Name MV	9063-1	35°21.99'	6°51.92'	598	0.36	13 <sup>a</sup>
Gemini MV	9067-1	35°16.92'	6°45.47'	435	0.30	15 <sup>a</sup>

<sup>a</sup> Estimated.

183 pore water separation. Total alkalinity was determined by  
184 titration (Ivanenkov and Lyakhin, 1978), whereas dis-  
185 solved  $\text{NH}_4$  and total  $\text{H}_2\text{S}$  were determined using standard  
186 photometric procedures (Grasshoff et al., 1983). The  
187 remaining pore waters were later analysed in the shore-  
188 based laboratory at IFM-GEOMAR for dissolved anions  
189 ( $\text{SO}_4^{2-}$ ,  $\text{Cl}^-$ ,  $\text{I}^-$ ,  $\text{Br}^-$ ) and cations ( $\text{Na}^+$ ,  $\text{K}^+$ ,  $\text{Li}^+$ ,  $\text{Mg}^{2+}$ ,  
190  $\text{Ca}^{2+}$ ,  $\text{Sr}^{2+}$ ,  $\text{Ba}^{2+}$ , B (boric acid), Si (silicic acid)) using  
191 ion chromatography and optical ICP, respectively. Sub-  
192 samples for dissolved element analyses (by ICP) were acid-  
193 ified immediately after pore water squeezing to prevent any  
194 precipitation of minerals due to depressurisation and  
195 degassing.

196 Sediment porosity was calculated from the water con-  
197 tent (weighing fresh and freeze-dried samples) assuming a  
198 dry solid density of  $2.65 \text{ g cm}^{-3}$ . Total organic carbon  
199 was determined by flash combustion of freeze-dried and  
200 ground using a Carlo Erba element analyser (NA1500)  
201 with a relative standard deviation of about 1% for replicate  
202 measurements. All analytical procedures applied on board  
203 and at IFM-GEOMAR laboratories are described else-  
204 where (Luff and Wallmann, 2003; Aloisi et al., 2004a)  
205 and documented in detail at [http://www.ifm-geomar.de/index.php?id=mg\\_analytik&L=](http://www.ifm-geomar.de/index.php?id=mg_analytik&L=).

207 Strontium isotopes were measured by thermal ionisation  
208 mass spectrometry (TRITON at IFM-GEOMAR) after Sr  
209 separation via ion exchange chromatography using a Sr-  
210 specific resin. The average  $^{87}\text{Sr}/^{86}\text{Sr}$  value for NBS 987  
211 run during this study ( $n = 12$ ) was  $0.710249 \pm 0.000020$   
212 ( $2\sigma$ ). Stable oxygen and hydrogen isotope composition of  
213 pore waters were measured by mass spectrometry at the  
214 GCA Laboratory in Sehnde (Germany) with a precision  
215 of 0.3‰ (oxygen) and 3.1‰ (hydrogen) using lab-internal,  
216 IAEA-calibrated standards (SLW:  $\delta^{18}\text{O} = -8.35\text{‰}$  V-  
217 SMOW,  $\delta\text{D} = -58.4\text{‰}$  V-SMOW; GRW:  $\delta^{18}\text{O} =$   
218  $-33.59\text{‰}$  V-SMOW,  $\delta\text{D} = -258.2\text{‰}$  V-SMOW).

### 219 3.3. Gas analysis

220 Light hydrocarbon gases were stripped from samples  
221 onboard by agitation of sediment in vials followed by an  
222 equilibration period of 48 h. Headspace gas was removed  
223 and stored for transport by injection into crimp-top vials  
224 previously filled with a  $\text{pH} \sim 1$ , 10% KCl solution. Light  
225 hydrocarbon gas abundances were measured using a Vari-  
226 an 3400 gas chromatograph (GC) equipped with a PLOT Q  
227 capillary column (0.32 mm  $\times$  30 m) and a flame ionisation  
228 detector (FID). Calibration standards for methane consist-  
229 ed of a range of BOC (UK) alpha-gravimetric mixtures and  
230 for  $\text{C}_2$  to  $\text{C}_6$  homologues a range of SCOTTY (UK)  
231 standards.

232 Analyses of  $^{13}\text{C}/^{12}\text{C}$  ratios in  $\text{CH}_4$  and  $\text{C}_2\text{H}_6$  were con-  
233 ducted by GC-combustion isotope ratio mass spectrometry  
234 (GC-C-IRMS) at Bristol University using a Thermoelec-  
235 tron XP mass spectrometer. Light hydrocarbon gases were  
236 separated on a PLOT Q capillary column (0.32 mm  $\times$  30 m)  
237 and combusted to  $\text{CO}_2$  at 1000 °C in a ceramic reactor con-

taining Cu and Pt wires. A high purity blend of 1%  $\text{O}_2$  in  
238 helium was fed into the reactor at  $0.2 \text{ ml min}^{-1}$  to ensure  
239 complete combustion. Calibration standards consisted of  
240 BOC (UK) alpha-gravimetric gas mixtures that had been  
241 analysed for  $\delta^{13}\text{C}$  at external laboratories and a  $\delta^{13}\text{C}$ -  
242  $\text{CO}_2$  gas standard from Oztech Corporation (USA). Stable  
243 isotope ratios are reported in the standard delta ( $\delta$ ) nota-  
244 tion in units of permil (‰) relative to Vienna Pee Dee  
245 Belemnite (VPDB). 246

### 247 3.4. Geochemical modelling

248 Rates of upward fluid flow, pore water mixing and  
249 AOM were determined by applying a reactive transport  
250 model running on Mathematica® Version 5.0 (Schmidt  
251 et al., 2005). The model considers molecular diffusion and  
252 advection of dissolved  $\text{SO}_4$ ,  $\text{CH}_4$ , Cl, and B. We applied  
253 the general differential equation: 254

$$255 \phi \cdot \frac{\partial [C]}{\partial t} = \partial \left( \frac{\phi \cdot D_{\text{sed}} \cdot \frac{\partial [C]}{\partial x}}{\partial x} \right) - \phi \cdot v \cdot \frac{\partial [C]}{\partial x} - \phi \cdot R_{\text{AOM}} \\ 256 - \phi \cdot \alpha(x) \cdot (C(x) - C(0)), \quad (1) \quad 257$$

258 where  $t$  is time (yr),  $x$  is sediment depth (cm),  $[C]$  is the con-  
259 centration of the dissolved pore water species  
260 ( $\text{mmol dm}^{-3}$ ),  $D_{\text{sed}}$  is the diffusion coefficient in the sedi-  
261 ments ( $\text{cm}^2 \text{ yr}^{-1}$ ; corrected for tortuosity; (Boudreau,  
262 1997),  $\phi$  is the sediment porosity (unitless),  $v$  is the velocity  
263 of upward fluid flow ( $\text{cm yr}^{-1}$ ),  $R_{\text{AOM}}$  is the rate of AOM  
264 (in  $\mu\text{mol dm}^{-3} \text{ yr}^{-1}$ ),  $\alpha(x)$  is the depth-dependent pore  
265 water-mixing coefficient ( $\text{yr}^{-1}$ ), and  $(C(x) - C(0))$  is the dif-  
266 ference between the concentration at any depth and in  
267 seawater.

The rate of AOM is calculated as:

$$268 R_{\text{AOM}} = k_{\text{AOM}} \cdot [\text{SO}_4] \cdot [\text{CH}_4], \quad (2) \quad 269$$

270 where  $k_{\text{AOM}}$  is the rate constant ( $\text{dm}^3 \text{ mmol}^{-1} \text{ yr}^{-1}$ ).

271 Sediment porosity changes with depth due to sediment  
272 compaction. The depth profile is approximated by fitting  
273 the measured porosity data with:

$$274 \phi = (\phi_{\text{top}} - \phi_{\text{bot}}) \cdot \text{Exp}(-\text{const} \cdot x) + \phi_{\text{bot}}, \quad (3) \quad 275$$

276 where  $\phi_{\text{bot}}$  and  $\phi_{\text{top}}$  are the porosity at the base of each  
277 core and at the sediment surface, and const is the attenua-  
278 tion coefficient for the exponential decrease of porosity  
279 with depth.

280 At most of the sites surficial mixing of seawater into the  
281 sediment is observed within the first meter of the sediment.  
282 This process can be identified by unusually weak gradients  
283 in the upper part of pore water profiles and seems to be  
284 common in the vicinity of cold seeps. It is likely caused  
285 by density differences (inducing convection cells) between  
286 upward flowing fluid and seawater or by flow effects  
287 around morphological elevations (e.g. Henry et al., 1996;  
288 Schmidt et al., 2005; Haese et al., 2006). For the simulation  
289 of this fluid-mixing process a rate law formulation with a  
290 depth-dependent mixing coefficient has been applied: 291

$$291 \quad \alpha(x) = \frac{\alpha'}{(1 + \text{Exp}[(x - x_{\text{mix}})/k])}, \quad (4)$$

292 where  $\alpha'$  is the pore water-mixing coefficient ( $\text{yr}^{-1}$ ),  $x_{\text{mix}}$  is  
 293 the depth of the mixed layer (in cm), and  $k$  determines the  
 294 thickness of the transition layer between the mixed and  
 295 the non-mixed proportion of the sediment column (in  
 296 cm).

297 Boundary conditions were defined for the sediment sur-  
 298 face (0 cm) and the base of each respective core. The model  
 299 was run to steady state beginning from arbitrary initial  
 300 conditions. The upward flow and mixing rates were deter-  
 301 mined by fitting the model to the measured pore water geo-  
 302 chemical data.

## 4. Results

### 4.1. Fluid geochemistry

#### 4.1.1. Major ions

306 Concentration–depth plots of major ions for all study  
 307 sites are shown in Fig. 2a and b. Apart from Hesperides  
 308 MV pore waters generally become depleted in  $\text{SO}_4$  within  
 309 30–300 cm below the sediment surface, followed by an in-  
 310 crease in  $\text{CH}_4$  below the  $\text{SO}_4$ – $\text{CH}_4$  transition (AOM) zone  
 311 (Fig. 2a). In cores 9072-1 (CAMV) and 9061-1 (Ginsburg  
 312 MV)  $\text{SO}_4$  is present even below the AOM which will be  
 313 discussed in more detail in Sections 5.1 and 5.2.2 Ca is

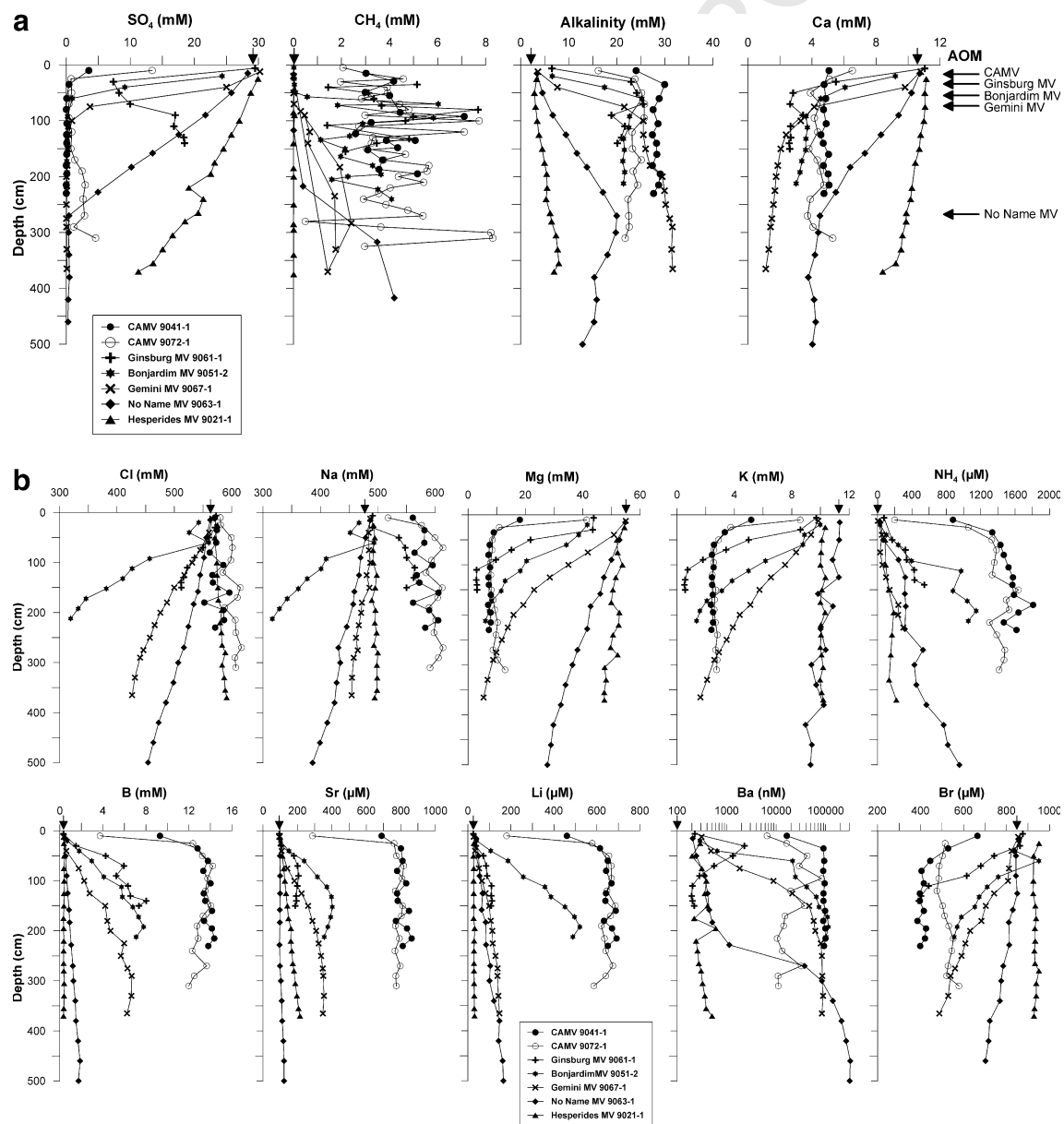


Fig. 2. (a) Pore water profiles of  $\text{SO}_4$ ,  $\text{CH}_4$ , alkalinity, and Ca at all investigated sites. Vertical arrows indicate seawater values. Horizontal arrows indicate depth of AOM. (b) Pore water profiles of various elements at all investigated sites. Vertical arrows indicate seawater values.

314 generally depleted, accompanied by a simultaneous in-  
 315 crease in alkalinity, from the AOM zone to the base of  
 316 the cores at all sites (Fig. 2a). Although significant differ-  
 317 ences exist between the sites, there is a general decrease  
 318 in Mg, K, and Br as well as an increase in Sr, Li, B, Ba,  
 319 and NH<sub>4</sub> concentrations (Fig. 2b). The behaviour of Na  
 320 and Cl is not uniform. Whereas Cl-concentrations of the  
 321 fluids at CAMV and Hesperides MV are slightly enriched  
 322 with respect to seawater, Cl is depleted at all other sites.  
 323 The same trends are observed for Na with the exception  
 324 of Ginsburg MV where Na and Cl show opposite trends  
 325 with depth. These major characteristics are summarized  
 326 in Table 2.

#### 327 4.1.2. Isotope data

328 Pore water samples from various depths in each core  
 329 have been used to characterize the stable oxygen- and  
 330 hydrogen-isotope systematics of the fluids. The results are  
 331 summarized in a  $\delta^{18}\text{O}$ - $\delta\text{D}$  plot (Fig. 3), which shows a  
 332 clear negative trend. Usually, the deepest sample from each  
 333 core shows the strongest deviation from seawater composi-  
 334 tion. Samples from different depths of CAMV cores (9041-  
 335 1, 9072-1) plot in the upper left panel of Fig. 3, indicating  
 336 the uniformity of fluid composition and a lack of dilution  
 337 by seawater. For comparison, the field of  $\delta^{18}\text{O}$ - $\delta\text{D}$  data  
 338 from eastern Mediterranean mud volcanoes (Dählmann  
 339 and De Lange, 2003) has been included in Fig. 3. The larg-  
 340 est offset from seawater composition occurs at Captain  
 341 Arutyunov and Ginsburg MVs.

342 One sample from the base of each core from Captain  
 343 Arutyunov, Ginsburg, and Bonjardim MVs has been used  
 344 for determination of <sup>87</sup>Sr/<sup>86</sup>Sr ratios. The results (Fig. 4)  
 345 show that fluids from CAMV clearly contain more radio-  
 346 genic Sr than Ginsburg and Bonjardim MVs.

#### 347 4.2. Dissolved hydrocarbon gases

348 The abundances of dissolved methane to pentane,  
 349 and the  $\delta^{13}\text{C}$  values of methane and its homologues

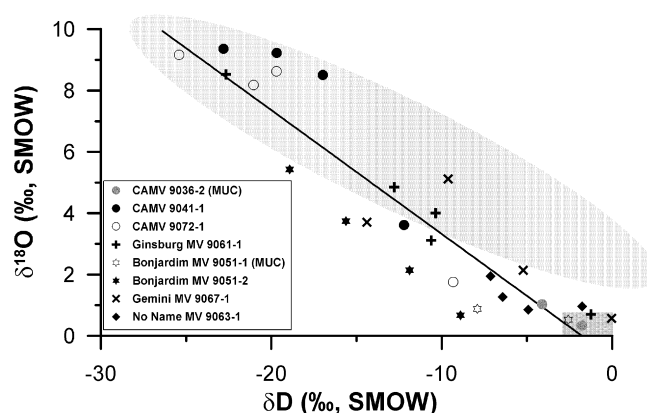


Fig. 3.  $\delta\text{D}$  vs.  $\delta^{18}\text{O}$ -H<sub>2</sub>O values from various core depths at all sampled sites with exception of Hesperides MV. Additional surface samples from two multicorer cores at CAMV (9036-2) and Bonjardim MV (9051-1) are included. The observed negative trend clearly indicates clay mineral dehydration as the major fluid source. In general, the lowermost samples in each core show the strongest enrichment in  $\delta^{18}\text{O}$  and depletion in  $\delta\text{D}$ ; closer to the sediment-water interface dilution by seawater is overprinting the fluid signature. The shaded ellipse corresponds to data reported by (Dählmann and De Lange, 2003) from eastern Mediterranean MVs. The shaded rectangle indicates the composition of seawater.

were measured to assess the origin of light hydrocarbon 350  
 gases in MV fluids. In spite of considerable loss in con- 351  
 centration during core recovery, the measured methane 352  
 concentrations are still highly elevated above seawater 353  
 values and appropriately reflect the in situ trend in shal- 354  
 low sediment layers (Fig. 2a). In fact, investigations by 355  
 (Wallace et al., 2000) did not show systematic deviations 356  
 between the  $\delta^{13}\text{C}$ -values of methane from standard (de- 357  
 gassed) and pressurized cores, implying that fractiona- 358  
 tion due to degassing is negligible. The overall results 359  
 are summarized in Table 3. Gases at Bonjardim and 360  
 Ginsburg MVs appear to possess clearly thermogenic 361  
 signatures, exhibiting low CH<sub>4</sub>/(C<sub>2</sub>H<sub>6</sub> + C<sub>3</sub>H<sub>8</sub>) ratios 362  
 and <sup>13</sup>C-enriched CH<sub>4</sub> and C<sub>2</sub>H<sub>6</sub>. Gas in pore fluids 363  
 at CAMV is unusual because it has a high CH<sub>4</sub>/ 364

Table 2

Overview of element enrichments (+) and depletions (-) with respect to seawater at the study sites

Parameter	CAMV	Hesperides MV	Bonjardim MV	Ginsburg MV	Gemini MV	No Name MV
Na	+	+	-	+	-	-
Cl	+	+	-	-	-	-
Ca	-	(-)	-	-	-	-
Mg	-	-	-	-	-	-
K	-	o	-	-	-	-
Sr	+++	+	+	++	+	o
Li	+++	o	+++	+	+	+
B	+++	o	++	++	++	+
Br	-	o	-	-	-	-
NH <sub>4</sub>	++	+	+	+	+	+
SO <sub>4</sub> (at depth)	o/+	AOM not reached	o	++	o	o
Ba	+	(+)	+	(+)	+	+
CH <sub>4</sub>	+	(+)	+	+	+	+

Slight changes are indicated parentheses and changes by 'o'. For Sr, Li, and B, a more differentiated scheme is provided in order to more clearly portray differences in fluid chemistry.

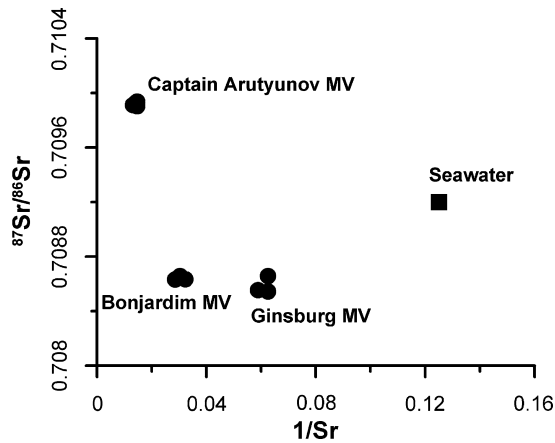


Fig. 4.  $^{87}\text{Sr}/^{86}\text{Sr}$  systematics of end member pore fluids from Captain Arutyunov, Ginsburg, and Bonjardim MVs. Pore fluids at CAMV contain more radiogenic Sr compared to seawater, whereas Ginsburg and Bonjardim MVs are affected by less radiogenic sources.

365 ( $\text{C}_2\text{H}_6 + \text{C}_3\text{H}_8$ ) ratio and also relatively positive  $\delta^{13}\text{C}$ -  
366  $\text{CH}_4$  values.

## 367 5. Discussion

### 368 5.1. Fluid advection and mixing processes

369 The purity of the geochemical signature of the pore  
370 water is dependent on the overall advection rate of the  
371 upward migrating fluid and irrigation processes in the  
372 subsurface sediments. In order to derive quantitatively  
373 well-constrained estimates of the advection rate we per-  
374 formed numerical model runs with conservative (Cl, B)  
375 and reacting parameters ( $\text{SO}_4$ ,  $\text{CH}_4$ ). Under environmental  
376 conditions met in the uppermost surface layers, Cl and B  
377 can be considered as geochemically conservative and hence  
378 their depth profiles provide useful parameters to estimate  
379 upward rates of fluid flow (Martin et al., 1996; Aloisi  
380 et al., 2004a; Haese et al., 2006). The consistency of flux  
381 rates can be checked by simultaneously modelling reactive  
382 solutes (e.g.,  $\text{SO}_4$  and  $\text{CH}_4$ ). In addition, the transition zone  
383 of  $\text{SO}_4$  and  $\text{CH}_4$  (AOM; Fig. 2a) is a perfect measure of the  
384 depth of near-surface mixing and oxidation processes in the  
385 vicinity of a vent site. A more detailed discussion of AOM  
386 at Gulf of Cadiz MVs is given in (Niemann et al., 2006).

387 All model parameters used to produce the fitted curves  
388 shown in Fig. 5 are summarized in Table 4. In general,  
389 good and internally consistent curve fits for Cl, B, and  
390  $\text{SO}_4$  could be produced for all sites. The scatter in Cl-pro-  
391 files below 50 cm bsf at CAMV is attributed to the occur-  
392 rence of gas hydrate at this site, and hence the maximum  
393 Cl-concentration measured in each of the cores has been  
394 used as the lower boundary (maximum) concentration in  
395 the model. In these cases, B is a more reliable parameter be-  
396 cause pore water concentrations are less affected by the  
397 presence of gas hydrates due to the high concentration dif-  
398 ference between seawater and MV pore fluid. The location  
399 of the AOM zone and the resulting reaction rates in the

Table 3  
Summary of end member gas geochemistry data for selected MV sites in the Gulf of Cadiz

Site	Core	$\text{CH}_4$ (mM)	$\delta^{13}\text{C}-\text{CH}_4$ (‰)	$\delta^{13}\text{C}-\text{C}_2\text{H}_6$ (‰)	$\delta^{13}\text{C}-\text{C}_3\text{H}_8$ (‰)	$\delta^{13}\text{C}-\text{C}_4\text{H}_{10}$ (‰)	$\delta^{13}\text{C}-\text{C}_4\text{H}_{10}$ (‰)	$\text{C}_1/(\text{C}_2 + \text{C}_3)$
Hesperides MV	GeoB 9021	$8 \pm 2 \cdot 10^{-3}$ (n = 5)	n.a.	n.a.	—	—	—	—
No Name MV	GeoB 9063	n.a.	n.a.	n.a.	—	—	—	n.a.
Bonjardim MV	GeoB 9051	$2.9 \pm 1.3$ (n = 12)	$-49.6 \pm 0.7$ (n = 10)	$-28.1 \pm 0.1$ (n = 4)	$-24.6 \pm 0.4$ (n = 4)	$-26.7 \pm 0.8$ (n = 3)	$-23.8 \pm 0.4$ (n = 4)	$14 \pm 3$ (n = 10)
Ginsburg MV	GeoB 9061	$4.2 \pm 2.1$ (n = 7)	$-40.9 \pm 0.4$ (n = 11)	$-22.5$ (n = 1)	$-22.1$ (n = 1)	$-24.1$ (n = 1)	—	$40 \pm 14$ (n = 11)
CAMV	GeoB 9041	$4.2 \pm 1.3$ (n = 10)	$-48.4 \pm 0.3$ (n = 15)	—	—	—	—	$1020 \pm 302$ (n = 15)
CAMV	GeoB 9072	$4.5 \pm 1.8$ (n = 26)	$-48.3 \pm 1.5$ (n = 32)	—	—	—	—	$1125 \pm 510$ (n = 32)
CAMV (gas hydrates)	GeoB 9036	$48.9 \pm 7.4$ (n = 3)	$-52.0 \pm 0.4$ (n = 3)	$-24.0$ (n = 1)	—	—	—	$852 \pm 145$ (n = 3)

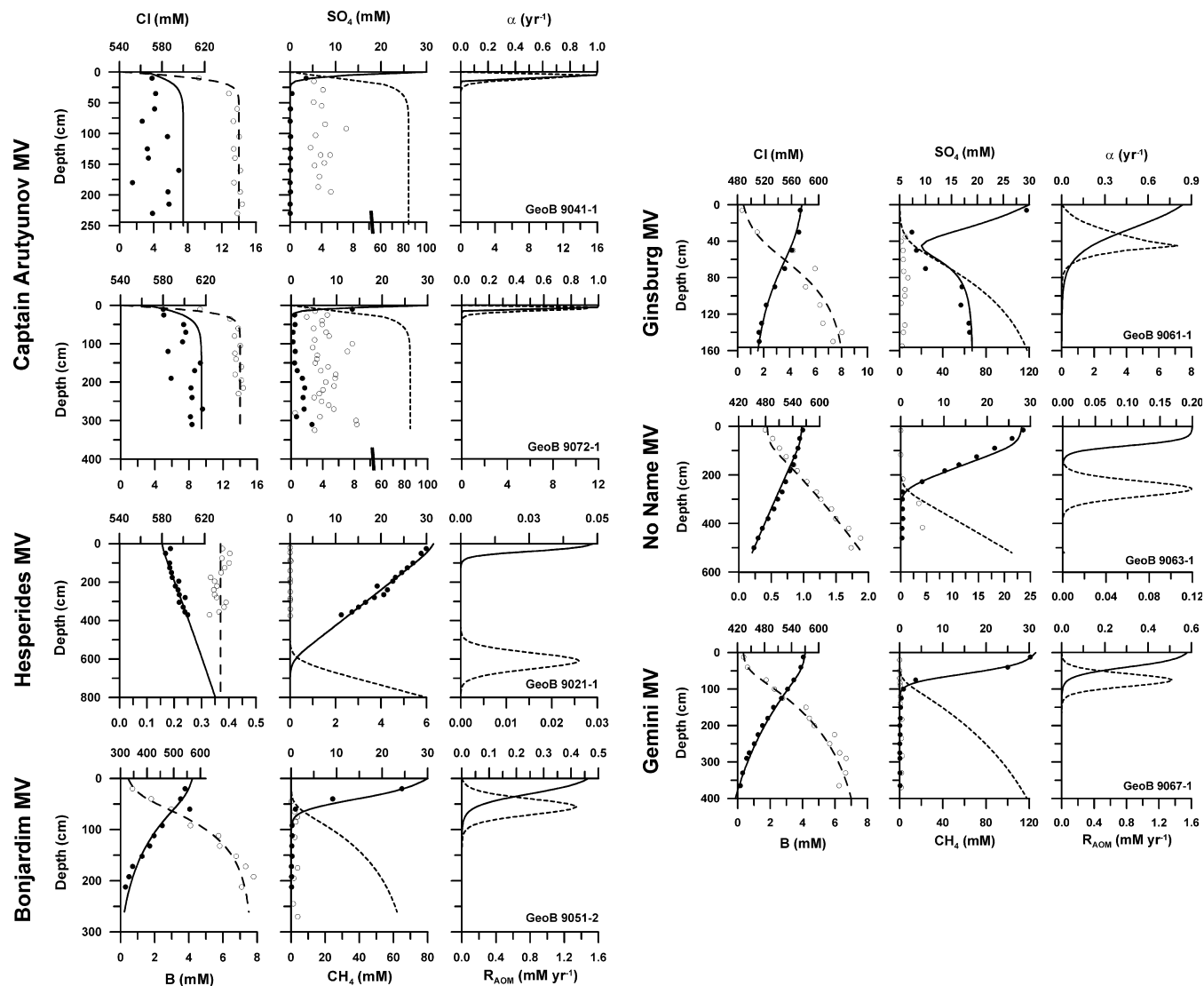


Fig. 5. Results of numerical modelling (solid lines: Cl, SO<sub>4</sub>,  $\alpha$ ; dashed lines: B and CH<sub>4</sub>, R<sub>AO</sub>M) for the various cores investigated in this study (core reference in the right-hand plots). Measured data are represented by closed circles for Cl and SO<sub>4</sub> and open circles for B and CH<sub>4</sub>, respectively. Note the different horizontal scales in the various plots.

405 model are strongly dependent on methane concentrations  
 406 prescribed at the lower boundary (CH<sub>4</sub>(B)). With the  
 407 exceptions of Hesperides and No Name MVs (GeoB  
 408 9021-1 and GeoB9063-1, respectively), the CH<sub>4</sub>(B) concentration  
 409 corresponds to (CAMV; GeoB9041 and  
 410 GeoB9072), or is slightly below the ambient methane solubility  
 411 with respect to gas hydrate stability (Tishchenko  
 412 et al., 2005). As outlined above (Section 3.1), the large discrepancy  
 413 between measured and modelled concentrations is due to the significant  
 414 decrease of methane solubility and degassing during core recovery.  
 415 Hence, the MV fluids are probably saturated with CH<sub>4</sub> at all sites,  
 416 except at Hesperides and No Name MVs, where upward fluid flow  
 417 rates are low and SO<sub>4</sub> penetrates deeply into the sediment so  
 418 that saturation levels of dissolved CH<sub>4</sub> cannot be expected  
 419 within the core depth.

421 Shallow near-surface gradients of all solutes are explained  
 422 by active admixing of bottom water, which seems

423 to be a typical feature at cold vents (Henry et al., 1996; 423  
 424 Schmidt et al., 2005; Haese et al., 2006). Due to the elevated  
 425 advective flow velocities, the mixing zone is very thin in  
 426 the CAMV cores and only resolved by multicorer sampling  
 427 (Niemann et al., 2006). Overall, flux rates decrease from  
 428 CAMV to Hesperides MV in the order listed in Table 4  
 429 (from left to right). This decrease is in accordance with  
 430 the preservation of the fluid signal: the higher the advective  
 431 flux, the lower is the admixing of seawater and hence the  
 432 purer the fluid composition. Effective diffusive exchange  
 433 between pore fluids and bottom water is limited to the upper-  
 434 most centimetres of the sediment when the flow rates  
 435 exceed a threshold of some centimetres per year (Luff and  
 436 Wallmann, 2003).

437 The unusual situation of high sulphate levels in rising  
 438 fluids at Ginsburg MV required inhibition of AOM in  
 439 the model below the maximum mixing depth in order to  
 440 produce consistent results. The coexistence of SO<sub>4</sub> and

Table 4  
Properties and boundary conditions used for numerical modelling

Parameter	Symbol	Core No.		Ginsburg MV (9061-1)	Bonjardim MV (9051-2)	Gemini MV (9067-1)	No Name MV (9063-1)	Hesperides MV (9021-1)
		Captain Arutyunov MV 9041-1	9072-1					
Column length (cm)		250	320	160	260	400	520	800
Upward fluid flow (cm yr <sup>-1</sup> )	$v$	15	10	3	1.3	0.6	0.1	(<0.05)
Porosity (sediment surface)	$\phi_{top}$	0.65	0.65	0.65	0.65	0.64	0.7	0.62
Porosity (lower boundary)	$\phi_{bot}$	0.57	0.62	0.57	0.57	0.52	0.57	0.5
Attenuation coefficient (cm <sup>-1</sup> )	const	0.05	0.05	0.05	0.05	0.02	0.05	0.02
Rate constant of AOM (dm <sup>3</sup> mmol <sup>-1</sup> yr <sup>-1</sup> )	$k_{AOM}$	0.1	0.1	0.5	0.1	0.1	0.1	0.1
Mixing coefficient (yr <sup>-1</sup> )	$\alpha'$	—	—	2.5	0.5	0.6	0.2	0.05
Depth of the mixed layer (cm)	$x_{mix}$	10	10	20	30	40	80	40
Mixed layer coefficient (cm)	$k$	1	1	12	12	12	12	12
Chloride (sediment surface) (mmol dm <sup>-3</sup> )	Cl(0)	565	565	575	570	570	560	580
Chloride (lower boundary) (mmol dm <sup>-3</sup> )	Cl(B)	600	607	510	315	415	450	630
Boron (sediment surface) (mmol dm <sup>-3</sup> )	B(0)	0.4	0.4	0.44	0.44	0.34	0.44	0.37
Boron (lower boundary) (mmol dm <sup>-3</sup> )	B(B)	14	14	8	7.5	7	1.9	0.37
Sulphate (sediment surface) (mmol dm <sup>-3</sup> )	SO <sub>4</sub> (0)	30	30	30	30	31.5	28	31.5
Sulphate (lower boundary) (mmol dm <sup>-3</sup> )	SO <sub>4</sub> (B)	0	0	0	0	0	0	0
Methane (sediment surface) (mmol dm <sup>-3</sup> )	CH <sub>4</sub> (0)	0	0	0	0	0	0	0
Methane (lower boundary) (mmol dm <sup>-3</sup> )	CH <sub>4</sub> (B)	85	85	130	62	120	21.4	6

CH<sub>4</sub> in the deeper part of the core further indicates that AOM must be attenuated along the flow path, because microbes may fail to find favourable growth conditions within the flowing medium.

Seawater intrusion at Ginsburg MV cannot account for the SO<sub>4</sub> enrichment in MV fluids as they are almost entirely depleted of K and Mg (Fig. 2). We suspect that high SO<sub>4</sub> levels are caused by dissolution of anhydrite or gypsum at greater depth (see also Section 5.2.2). In contrast to Ginsburg MV (GeoB9061-1), the very slight increase of sulphate at CAMV (GeoB 9072-1) can be readily attributed to a <10% admixing of seawater as it is accompanied by a similar increase of K and Mg and an obvious decrease of Ba-levels (Fig. 2). These hypotheses are further substantiated by the calculation of saturation levels ( $\Omega$ ) for barite (using average Ba and SO<sub>4</sub> concentrations of the cores 9072-1 and 9061-1 below the AOM and the solubility constant for barite in seawater provided by (Aloisi et al., 2004b) which indicate highly supersaturated fluids at CAMV ( $\Omega > 3$ ) and undersaturated fluids ( $\Omega < 0.5$ ) at Ginsburg MV. Since precipitation kinetics of barite are relatively slow (Aloisi et al., 2004b) supersaturation is indicative of a non-equilibrated system (recent seawater admixing into Ba-rich fluid) whereas the undersaturated fluids may have had sufficient time for equilibration due to the deep source of SO<sub>4</sub>.

## 5.2. Origin of the fluids

### 5.2.1. Evidence for clay mineral dehydration

As demonstrated by numerical modelling, the most active sites of fluid advection are GeoB 9041-1 and 9072-1 located at CAMV. The compilation  $\delta D$  and  $\delta^{18}O$  values of pore water samples from all investigated sites (Fig. 3) reveals a clear negative correlation which is typical for water that has been released by clay mineral dehydration, most likely by the transformation of smectite to illite (Sheppard and Gilg, 1996; Dählmann and De Lange, 2003). This observation is in accordance with data from Mediterranean Ridge mud volcanoes (Fig. 3) and earlier observations at Yuma and Ginsburg MVs in the Gulf of Cadiz (Mazurenko et al., 2003), although interpreted differently by the latter authors. The major temperature field for this process ranges between 60 and 150 °C (Freed and Peacor, 1989; Chan and Kastner, 2000). Applying an average geothermal gradient of 30 °C per km, the upper limit of formation depth would be approximately 5 km bsf, which comprises the lower sedimentary units deposited on basement rocks (Medialdea et al., 2004).

Due to the complex stratigraphic and tectonic development in this area it is difficult to unambiguously identify the "source rocks". Potential sedimentary sources to be considered belong to the Sub-Betic and other Mesozoic units as well as the so-called Allochthonous Unit of the Gulf of Cadiz (AUGC) comprising mainly Tertiary and Mesozoic shales and marls, which are overlain by up to 1 km of Plio-Quaternary hemipelagic sediments and pene-

496 trated by deep-reaching faults (Medialdea et al., 2004; Pin-  
 497 heiro et al., 2005). An abundance of smectite has been  
 498 reported in sediments affected by terrigenous input  
 499 (Chamley, 1989; Reicherter and Pletsch, 2000). However,  
 500 the clear stable isotopes signal (Fig. 3) strongly suggests  
 501 that the release of freshwater at greater depth is the quan-  
 502 titatively dominant process of fluid formation in this area.  
 503 The upward migration of the overpressured fluids occurs  
 504 under tectonic control, causing the liquefaction of sedi-  
 505 ments and the formation of mud volcanoes, which appear  
 506 to be located along deep strike-slip faults and thrusts, or  
 507 at fault intersections (Pinheiro et al., 2005; Fig. 1).

### 508 5.2.2. Overprinting of the fluid signature by secondary 509 processes

510 In principle, the release of mineral-bound water results  
 511 in a general freshening of pore fluids reflected by decreased  
 512 concentrations of Na and Cl, and other major solutes  
 513 (Fig. 2). Such a dilution trend is also depicted in Fig. 6.  
 514 However, deviations from the mixing line between seawater  
 515 and fluid suggest the occurrence of additional processes  
 516 leading to coeval and subsequent overprinting of the fluid  
 517 composition. Whereas Na is relatively enriched with re-  
 518 spect to Cl, Mg, and K are considerably depleted. Similar  
 519 observations have been reported from mud volcano sites  
 520 at different continental margins around the world (Martin  
 521 et al., 1996; Aloisi et al., 2004a; Godon et al., 2004).

522 Relative Na enrichments over Cl are thought to be a di-  
 523 rect consequence of the transformation of smectite to illite

524 where Na is released into solution. The increase in Na is then  
 525 a simple function of the relative amount of Na to H<sub>2</sub>O in the  
 526 smectite. This, however, is difficult to estimate since the Na-  
 527 H<sub>2</sub>O ratio of natural smectites is a quite variable factor.  
 528 Considering, for the moment, only those sites where the  
 529 pore water chlorinity indicates freshening, there is a clear  
 530 trend in Na increase in the order: No Name MV (~seawater  
 531 dilution) < Bonjardim MV < Gemini MV < Ginsburg MV.  
 532 In simple terms, this would mean that the Na content in the  
 533 original smectite would have shown an increase in the same  
 534 order of sites. This relation is more clearly illustrated in  
 535 Fig. 7. Assuming that the observed dilutions with respect  
 536 to seawater are caused by “dissolution” of a typical smectite  
 537 (montmorillonite) containing 15 wt% of water (Sheppard  
 538 and Gilg, 1996), the relative amount of Na in the smectites  
 539 can be calculated by matching the observed endmember  
 540 concentration in each core. In the same order of MVs as given  
 541 above this would be 0.004, 0.007, 0.028, and 0.12 mol Na  
 542 per mol of smectite.

543 Specifically for Ginsburg MV these observations are,  
 544 however, inconsistent with isotope data (Fig. 3) and mod-  
 545 elled advection rates (Fig. 5 and Table 4) as, in theory, the  
 546 degree of freshening should be in accordance with the iso-  
 547 tope signal and with the rate of fluid flow. Hence, this obvi-  
 548 ous contradiction at Ginsburg MV suggests that other  
 549 processes release Na into solution, preferentially without  
 550 altering the isotope ratios of oxygen and hydrogen.

551 The incongruent dissolution of Na-feldspars (albite to  
 552 kaolinite; Eq. (5)) could be considered as one possibility,

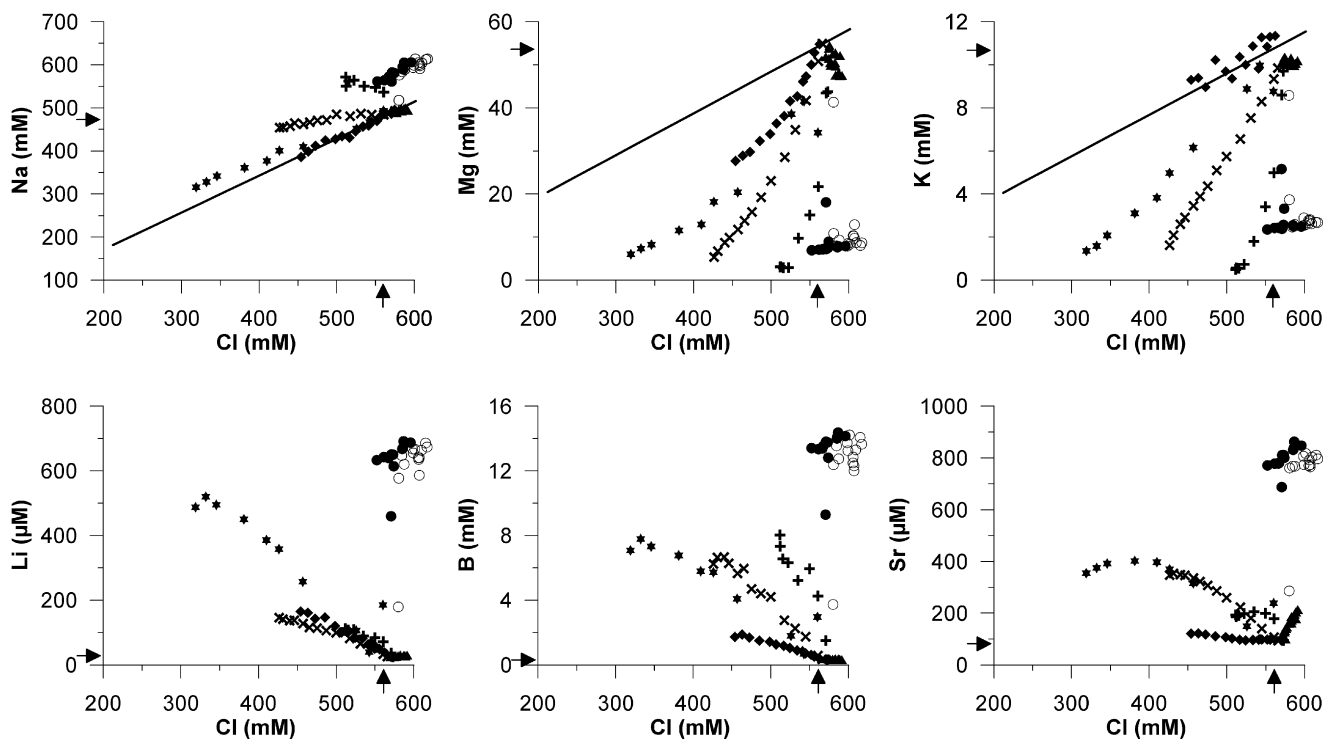


Fig. 6. Fluid property plots of Cl vs. Na, Mg, K (upper panel) and Li, B, Sr (lower panel). See Fig. 2 for symbols. The solid lines in the upper panel plots indicate freshening (dilution) of seawater with constant element ratio. Arrows indicate seawater values.

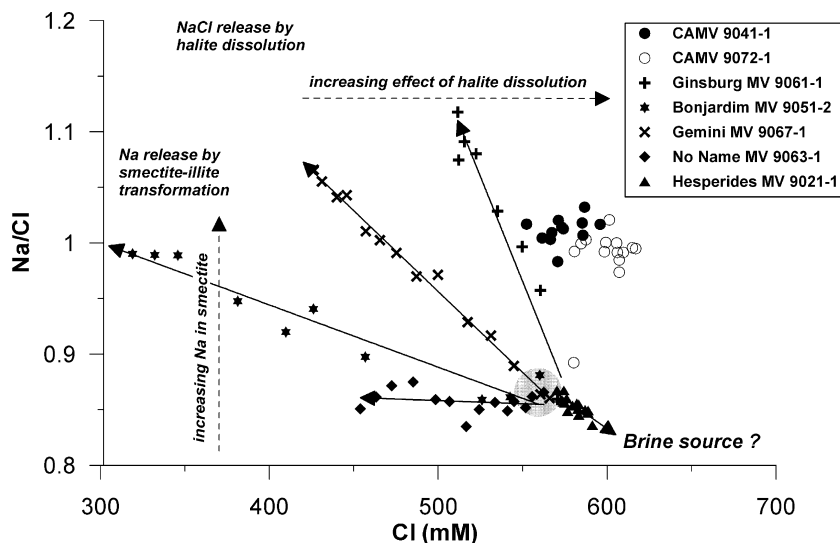
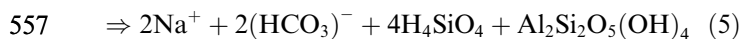
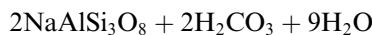


Fig. 7. Plot of Cl vs. Na/Cl indicating potential processes overprinting the primary composition of the fluids at various MV sites.

553 which, at the same time, could additionally account for in- 589  
 554 creased levels of alkalinity. 590

555



558 Unfortunately, this process would theoretically counteract 591  
 559 the observed  $\delta\text{D}$  trend (Fig. 3) and the freshening of the flu- 592  
 560 id as it consumes considerable amounts of water. 593

561 However, we believe that all observations discussed 594  
 562 above can be consistently explained by the simple addition 595  
 563 of NaCl (from leaching of halite) to a freshened fluid. In 596  
 564 contrast to the sites exhibiting pore water freshening, fluids 597  
 565 from Captain Arutyunov are enriched in both Na and Cl 598  
 566 (Fig. 7) and the approximately constant Na/Cl ratio of 1 599  
 567 at CAMV indicates the dissolution of halite (e.g. Bernas- 600  
 568 coni, 1999). However, typical brines resulting from leach- 601  
 569 ing of halite usually exhibit much higher concentrations 592  
 570 of NaCl. This implies that the measured concentration of 593  
 571 600 mM can only be explained by a mild leaching of NaCl. 594  
 572 Adding some NaCl to seawater would, however, not yield a 595  
 573 fluid with a Na/Cl ratio of 1. Taking into account that this 596  
 574 site exhibits the highest advection rates in combination 597  
 575 with the clearest  $\delta\text{D}$  and  $\delta^{18}\text{O}$  signal of all sites within 598  
 576 the study area, we may conclude that a strongly freshened 599  
 577 fluid is dissolving halite at depth. For such a low salinity 600  
 578 fluid only slight additions of Na released during clay min- 601  
 579 eral transformation are needed in order to shift the NaCl  
 580 ratio from 0.87 (in seawater) to about 1. In the same  
 581 way, the opposite trends at Ginsburg MV (Cl-depletion  
 582 and Na-enrichment) can be sufficiently explained, by sim-  
 583 ply leaching less NaCl by a freshened, but slightly more  
 584 Na-enriched original fluid. In order to obtain an approxi-  
 585 mation to the original Cl concentration at Ginsburg MV  
 586 and CAMV we used the obvious relation between Cl and  
 587  $\delta^{18}\text{O}$  at those sites, which are not affected by halite dissolu-  
 588 tion. As data from Gemini MV may also indicate some off-

set, we only used seawater and concentrations from No 589  
 Name and Bonjardim MVs to produce the exponential fit 590  
 shown in Fig. 8. From this relation we can deduce that origi- 591  
 nal Cl concentrations of freshened fluids at may have 592  
 been between 250 mM (Ginsburg MV) and  $\sim 230$  mM 593  
 (CAMV) and about 270–370 mM Cl have been added by 594  
 leaching of halite, respectively. In addition, we (re)-calcu- 595  
 lated the molar Na fractions of smectites that would be re- 596  
 quired to produce the measured Na/Cl ratios at Gemini 597  
 MV (0.02), Ginsburg MV (0.012), and CAMV (0.075). 598  
 The considerably decreased Na fractions at Gemini and 599  
 Ginsburg MVs further support the hypothesis since they 600  
 imply less regional variability of natural smectites in the 601

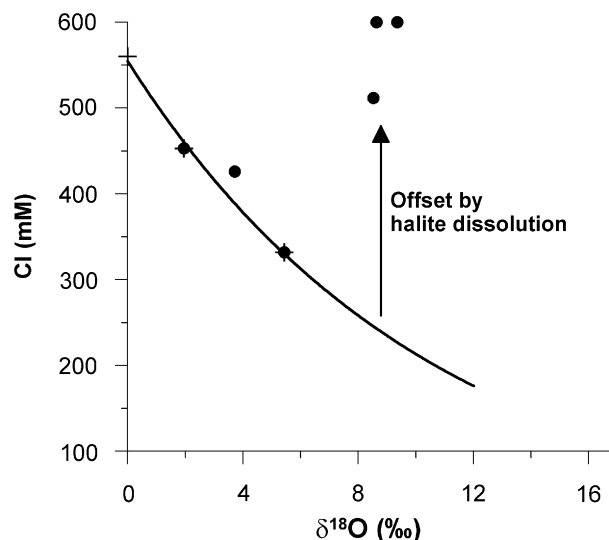


Fig. 8. Reconstruction of original Cl concentrations from  $\delta^{18}\text{O}$  values in the freshened fluid before overprinting by halite dissolution. The exponential fit function is obtained using values of seawater and the sites unaffected by halite dissolution (No Name MV, Bonjardim MV;  $\text{Cl} = e^{(-0.0955 \cdot \delta^{18}\text{O})} \cdot 554.37$ ). Arrow indicates offset created by halite dissolution at CAMV and Ginsburg MV.

602 working area. In addition, data from a very recent cruise  
603 by RV Merian in May 2006 revealed the unequivocal evi-  
604 dence for the existence of strongly saline brines in mud vol-  
605 cano fluids in the Gulf of Cadiz. Nearly NaCl-saturated  
606 and strongly SO<sub>4</sub>-enriched (80 mM) have been reported  
607 from Mercator MV (some 30 km east of Ginsburg MV to-  
608 wards the Moroccan coast; M. Haeckel, pers. comm., RV  
609 Maria S. Merian cruise MSM01/3, 2006). As outlined in  
610 Section 5.1, elevated pore water SO<sub>4</sub> concentrations at Gin-  
611 burg MV most likely result from leaching of gypsiferous  
612 clays and brecciae that generally cap deposition centres in  
613 the Gharb Basin (Maestro et al., 2003; Medialdea et al.,  
614 2004).

615 In contrast, slightly decreasing Na/Cl ratios at Hesperides  
616 MV (Fig. 7) may indicate evaporated seawater or resid-  
617 ual brines as a potential source in Hesperides MV (e.g.  
618 (McCaffrey et al., 1987). However, low advection rates at  
619 Hesperides MV cause a weak geochemical signal and  
620 hence, this interpretation is more speculative and will not  
621 be discussed in more detail.

622 Mg and K are strongly depleted in pore fluids at all sites  
623 (with the exception of K in No Name MV fluids; Fig. 6). In  
624 principle, the level of depletion is a function of advection  
625 rates, where the greatest advection produces the largest  
626 composition offset from seawater. The most likely explana-  
627 tion for the K-depletion in MV fluids is its integration into  
628 illite during clay mineral transformation (Martin et al.,  
629 1996; Aloisi et al., 2004a; Godon et al., 2004). Moreover,  
630 K is considered to be a major factor controlling the kinetics  
631 of smectite to illite transformation and the lack of K may  
632 even cause incomplete reaction (Spinelli and Underwood,  
633 2004; Cuadros, 2006). This case is strengthened by the  
634 strong correlation of K with either increasing δ<sup>18</sup>O, as  
635 depicted in Fig. 9, or with decreasing δD. In contrast, there  
636 is no correlation between Na and δ<sup>18</sup>O–H<sub>2</sub>O values result-  
637 ing from dissolution of halite affecting Na and Cl levels in  
638 pore water as outlined above.

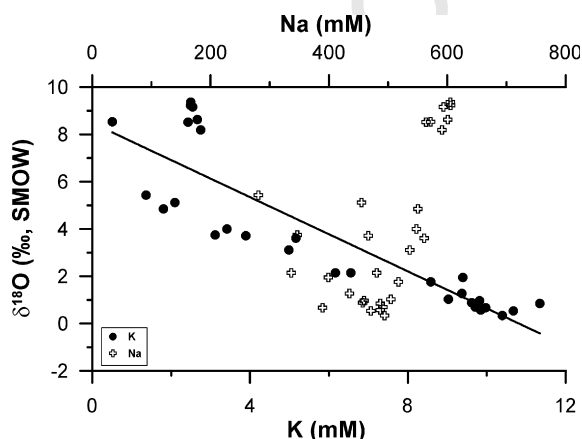


Fig. 9. Plot of K and Na vs. δ<sup>18</sup>O demonstrating that the K-depletion is likely related to an early stage of fluid generation (formation of illite), whereas the scatter in Na indicates subsequent overprinting at various sites.

The depletion in Mg and Ca at all sites (Fig. 2) can be ascribed to carbonate precipitation at any depth below core penetration. Although calcium carbonate precipitation related to AOM can be assumed, Ca-depletion below the AOM zone is typical for all sites. Hence, low Ca concentrations controlled by high levels of alkalinity (generated by organic matter breakdown and submarine weathering processes) are an inherent feature of the upward migrating fluids before reaching the surface sediments. The slight curvature of the Mg concentration depth profile (Fig. 2) or in the Mg vs. Cl plot shown in Fig. 6 does indicate the occurrence of co-precipitation of authigenic Mg-calcite related to AOM, although low Mg-levels are most probably largely controlled by the dolomitisation of widespread Tertiary and Mesozoic carbonates (Maldonado et al., 1999; Medialdea et al., 2004) deeper within the mud volcanoes.

### 5.2.3. High temperature imprint in the fluid signature

The most obvious enrichments observed are those in B, Li, and Sr (Figs. 2 and 6). B- and Li-enriched fluids are well-known from numerous locations along active continental margins worldwide (You et al., 1993; Martin et al., 1996; Chan and Kastner, 2000; Haese et al., 2003; Aloisi et al., 2004a; Hensen et al., 2004) and may be primarily released from clay minerals (Brumsack and Zuleger, 1992). Under experimental conditions simulating hydrothermal alteration of hemipelagic sediments Li is enriched preferentially over B as temperatures increase above 150 °C (You et al., 1995; Chan et al., 1999; You and Gieskes, 2001). The B/Li ratio in the Gulf of Cadiz fluids is consistently >10; however, Li concentrations as high as 700 μM and B abundances up to 15 mM are amongst the highest levels reported to date from offshore cold seep environments (Aloisi et al., 2004a; Godon et al., 2004; Haese et al., 2006). Hence, the low ratios instead may be caused by different mechanisms of Li and B release or different source-rock potentials, rather than being an indicator of low temperature alteration. For comparison, vent fluids at the convergent margin off Costa Rica are thought to be derived from sources having temperatures up to 150 °C; here, only B, but no Li enrichments were detected (Hensen et al., 2004). Similar results are reported from freshened mud volcano fluids of the Mediterranean Ridge (De Lange and Brumsack, 1998; Haese et al., 2006; Haese, personal communication). In contrast, fluids detected along distinct fault zones at ODP site 1040 at the Costa Rica margin (Chan and Kastner, 2000) are similar in composition to the vent fluids but are enriched in Li up to 300 mM. This finding rather suggests that deep and shallow fluid systems at the Costa Rica convergent margin are less well connected and the transmission of any original high temperature signal may be affected by the amount of mixing with other fluids and various reactions occurring along the flow path. However, following the results of (You and Gieskes, 2001), we propose that Li-enrichments—at least above certain threshold value—are indica-

695 tive for geochemical reactions occurring at temperatures  
696 above 150 °C. This hypothesis is further strengthened by  
697 data from other vent locations: higher Li, but lower B val-  
698 ues have been reported from MV fluids in the Black Sea  
699 (Aloisi et al., 2004a) and Barbados accretionary complex  
700 (Godon et al., 2004). Similar Li enrichments at the Peru  
701 convergent margin observed by (Martin et al., 1991) have  
702 been ascribed to alteration of oceanic basement at moder-  
703 ate to high temperatures. Enrichments in B of up to 15 mM  
704 are atypical for hydrothermal fluids; hence such extreme  
705 levels must be caused by extensive leaching of sedimentary  
706 B. This may also include the release of lattice-bound B,  
707 which makes up a significant part of the sedimentary B res-  
708 ervoir and which is remobilised at temperatures of approx-  
709 imately 300 °C (You and Gieskes, 2001; Kopf et al., 2003).

710 Because Li is only highly enriched at Captain Arutyunov  
711 and Bonjardim MVs, but B-levels are elevated at all  
712 sites where advection rates exceed 0.1 cm yr<sup>-1</sup> (Table 4  
713 and Fig. 6) we hypothesize that the fluid, which is predom-  
714 inantly derived from clay mineral dehydration, has been  
715 subject to injection of basement derived fluids, which are  
716 likely Li-enriched and may additionally contribute to high-  
717 er levels of B and Li from leaching of clays at temperatures  
718 >150 °C. Interestingly vent fluids from mid-ocean ridges  
719 buried beneath sedimentary cover (Von Damm et al.,  
720 1985, 2005) reach similar levels. This is illustrated by the  
721 compilation of Li and B concentrations of various hydro-  
722 thermal and cold vent sites in Fig. 10. Low-temperature  
723 alteration sites (I) are characterised by high B/Li ratios  
724 and low (<100 µM) Li concentrations, high-temperature al-  
725 tered cold vent (II) and sediment covered hydrothermal  
726 vent sites (IV) show low B/Li ratios accompanied by high  
727 (>350 µM) Li concentrations, and hydrothermal vents at

728 ridge crests (III) lack a significant B component revealing  
729 Li/B ratios <1. Thus, CAMV in particular may represent  
730 the cool end member of a hydrothermal injection system  
731 beneath a thick sedimentary cover, resulting in the enrich-  
732 ment of B versus Li (Chan et al., 1999). The fact that we do  
733 not observe typical hydrothermal signals, like K and Ca  
734 enrichments, can be ascribed to subsequent depletion by  
735 smectite-illite transformation and calcium carbonate pre-  
736 cipitation, respectively. As discussed above, both processes  
737 are unambiguously occurring in the subsurface of the mud  
738 volcano sites and, moreover, the supply of K is well known  
739 to be limiting for the smectite-to-illite reaction (e.g. Boles  
740 and Franks, 1979; Cuadros, 2006). Overall, Mg depletions  
741 are also well in line with the impact of hydrothermal solu-  
742 tions, even though low Mg levels are also a likely result of  
743 dolomite precipitation.

744 This general hypothesis is supported by additional  
745 observations. For example, B and Li enrichments correlate  
746 generally with Sr suggesting a common release mechanism  
747 during fluid formation. Sr-enriched fluids are typically  
748 considered to result from carbonate recrystallisation,  
749 which may reduce the Sr content of carbonate minerals  
750 by as much as an order of magnitude (Morse and Mac-  
751 kenzie, 1990). Mesozoic and Tertiary carbonates are wide-  
752 spread in the Gulf of Cadiz and may provide potential Sr-  
753 sources at all sites investigated. However, analyses of  
754 <sup>87</sup>Sr/<sup>86</sup>Sr ratios suggest that Sr originated from disparate  
755 fluid sources at the different MV sites (Fig. 4). Fluids at  
756 Bonjardim and Ginsburg MVs contain less-radiogenic  
757 Sr, which at Ginsburg MV (GeoB9061) may be related  
758 to dissolution of Tertiary and Cretaceous carbonates  
759 and evaporites (Burke et al., 1982; Banner, 2004) as sug-  
760 gested by the high sulphate levels at this site. However, be-

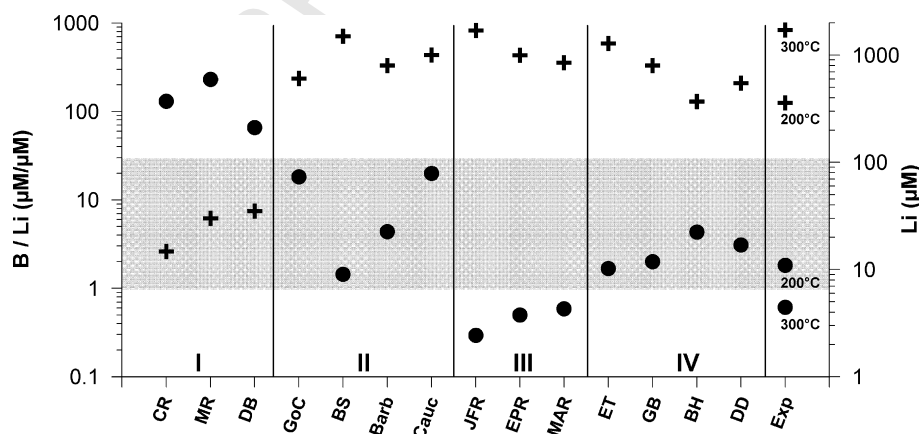


Fig. 10. Average B/Li ratios (dots) and Li concentrations (crosses) from selected cold vents (I, II), hydrothermal vents (III), sediment covered hydrothermal vents (IV), and hydrothermal experiments. There is a conspicuous similarity between fluids of fields II and IV, which are characterised by average Li/B ratios >1 (shaded rectangle) and corresponding high Li concentrations (>350 mM), implying that a high temperature imprint is preserved in certain cold vent areas. Data from hydrothermal experiments (Exp) at 200 and 300 °C (You and Gieskes, 2001) are presented for comparison. CR, Costa Rica (Hensen et al., 2004); MR, Mediterranean Ridge (De Lange and Brumsack, 1998; Haese et al., 2006); DB, Derugin Basin, Sea of Ochotsk (K. Wallmann, unpublished data); GoC, Gulf of Cadiz, average values of CAMV and Bonjardim MV (this study); BS, Dvurechenskii MV, Black Sea (Aloisi et al., 2004a); Barb, Barbados MVs (Dia et al., 1995; Godon et al., 2004); Cauc, Caucasian MVs (Kopf et al., 2003); JFR, Juan de Fuca Ridge; EPR, East Pacific Rise; MAR, Mid Atlantic Ridge (all Von Damm, 1990); ET, Escabana Trough; GB, Guaymas Basin; BH, Bent Hill, Middle Valley; DD, Dead Dog, Middle Valley (all Von Damm et al., 2005).

761 cause Bonjardim MV likely is underlain by oceanic crust  
 762 (Gutscher, 2004; Medialdea et al., 2004) and Li is more  
 763 enriched at this site,  $^{87}\text{Sr}/^{86}\text{Sr}$  ratios may rather point to  
 764 leaching of oceanic crust imprinting on the fluid composi-  
 765 tion. The radiogenic signature at CAMV suggests that sig-  
 766 nificant interaction has occurred between fluids and  
 767 continental crust material. This finding is supported by  
 768 deep seismic studies, which have shown that the eastern  
 769 part of the Gulf of Cadiz is underlain by thick continental  
 770 crust covered by the Betic–Rifean Allochthonous Units  
 771 (Gonzalez-Fernandez et al., 2001; Medialdea et al., 2004;  
 772 Zeyen et al., 2005). As shown in Figs. 2 and 6, fluids from  
 773 CAMV (and to some degree from Bonjardim MV also)  
 774 exhibit a strong correlation between Li, B, and Sr and  
 775 are offset from the other sites. Since Sr is also relatively  
 776 enriched (with respect to seawater) in continental crust  
 777 and terrigenous sediments (shales), this finding supports  
 778 the hypothesis of simultaneous “leaching” of these ele-  
 779 ments from clay minerals at moderate to high tempera-  
 780 tures. Overall, the observations are consistent with data  
 781 from the convergent margin off Chile where different  
 782  $^{87}\text{Sr}/^{86}\text{Sr}$  ratios of Li-enriched fluids are interpreted to  
 783 be caused by interaction with different crustal sources  
 784 (Martin et al., 1991).

785 Likewise, the molecular and isotopic composition of  
 786 light volatile hydrocarbon gases in expulsion fluids at  
 787 CAMV is unusual. The gases have a clear thermogenic ori-  
 788 gin at Ginsburg and Bonjardim MVs (Table 3). The com-  
 789 position of CAMV gas also indicates a thermogenic  
 790 origin, as shown by the stable carbon isotope signature  
 791 of ethane in gas hydrates recovered at this site (Table 3).  
 792 However, the high enrichment in methane cannot result  
 793 from an admixture of migrated thermogenic gas and shal-  
 794 low microbial methane, due to very low microbial  
 795 methanogenic activity in the shallow sediments (M. Nuzzo,  
 796 unpublished data). This finding is in agreement with sedi-  
 797 ment TOC abundances that never exceed  $\sim 0.5\%$  (Table  
 798 1) and generally low fluid concentrations of  $\text{NH}_4$  and Br  
 799 (Fig. 2b, Table 2; (Martin et al., 1993). A catagenic origin  
 800 of the methane expelled at CAMV is thus a more likely  
 801 hypothesis, consistent with fluid geochemical indications  
 802 for temperatures in excess of  $150^\circ\text{C}$ . In this line of evi-  
 803 dence, increased  $\text{NH}_4$  concentrations at CAMV (Fig. 2)  
 804 could be the result of the thermal alteration of organic  
 805 material as reported from sediment covered hydrothermal  
 806 vents (Thornton and Seyfried, 1987).

807 Expulsion of hydrothermally affected fluids at Bonjar-  
 808 dim and Captain Arutyunov MVs, but not at Ginsburg  
 809 MV is consistent with the locations of these edifices in dif-  
 810 ferent structural environments within the Gulf of Cadiz.  
 811 Bonjardim and Captain Arutyunov MVs appear to be sit-  
 812 uated along major crustal strike–slip faults associated with  
 813 the Africa/Eurasia Plate Boundary (Duarte et al., 2005),  
 814 for which no evidence exists at Ginsburg MV (Fig. 1). It  
 815 has indeed been shown that stress is released at strike–slip  
 816 faults, thus focussing the expulsion of deep over-pressured  
 817 fluids (Behrens, 1988; Tobin et al., 1993). The emplacement

of Bonjardim and Captain Arutyunov MVs may actually  
 be the result of intersecting strike–slip and thrust faults,  
 which reduces compression and favours stress release by  
 fluid advection (Chamot-Rooke et al., 2005). In contrast  
 to Bonjardim and Captain Arutyunov MVs, fluids at Gins-  
 burg MV likely are expelled along extensional and thrust  
 faults, similar to other MVs of the Moroccan margin  
 (Van Rensbergen et al., 2005).

Theoretically, the continuous rise of warm fluids should  
 be accompanied by an increased heat flow, which is not the  
 case since average geothermal gradients at all sites are  
 about  $20\text{--}40^\circ\text{C}$  per km (Kopf and participants, 2004).  
 However, comparatively low overall advection rates (Table  
 4) and insignificant emissions of methane into the overlying  
 seawater (Niemann et al., 2006) are indicative for low pres-  
 ent day expulsion rates. Variations in the activity of the  
 mud volcanoes have been suggested earlier for this region  
 (Pinheiro et al., 2003) and are in agreement with observa-  
 tions from various convergent margin settings where fluid  
 advection along deep fault zones has been identified as a  
 highly dynamic process which is subject to significant vari-  
 ations over time (e.g. Moore and Mascle, 1987; Martin  
 et al., 1991; Saffer and Bekins, 1999; Hensen and Wall-  
 mann, 2005). Since a heat pulse equilibrates much faster  
 in surface sediments compared to a geochemical signal as  
 soon as the supply is disconnected, the present day geo-  
 chemical composition of the fluids may be represent an im-  
 print of the latest fluid pulse.

## 6. Conclusions

Fluid geochemistry at MVs in the Gulf of Cadiz indi-  
 cates that major fluid formation and overpressuring is  
 caused by clay mineral dehydration at several kilometres  
 depth and temperatures of up to  $150^\circ\text{C}$ , which is in agree-  
 ment with the occurrence of thermogenic methane and simi-  
 lar observations at numerous cold vent areas worldwide  
 (e.g. Martin et al., 1996; Dählmann and De Lange, 2003;  
 Hensen et al., 2004). Quantitatively, the fluid composition  
 can be largely explained by the transformation of smectite  
 to illite; however a number of subsequent processes mask-  
 ing the primary fluid composition could be either proven or  
 strongly implied. These processes include the dissolution of  
 halite as well as anhydrite or gypsum, the precipitation of  
 calcium carbonate and dolomite, and potentially the  
 admixing of evaporated brines.

Very strong enrichments of the minor elements Li and B  
 (CAMV and Bonjardim MV) suggest high temperature  
 alterations ( $>150^\circ\text{C}$ ) related to fluid mobilisation along  
 fault systems cutting deeply into the underlying basement.  
 Element enrichments may be caused by elevated concentra-  
 tions in rising hydrothermal fluids and/or additional leach-  
 ing of these elements from the sediments at higher  
 temperatures. A compilation of various hot and cold vent  
 sites (Fig. 10) suggests that strong Li enrichments in combi-  
 nation with moderate B/Li ratios may be a good indicator for

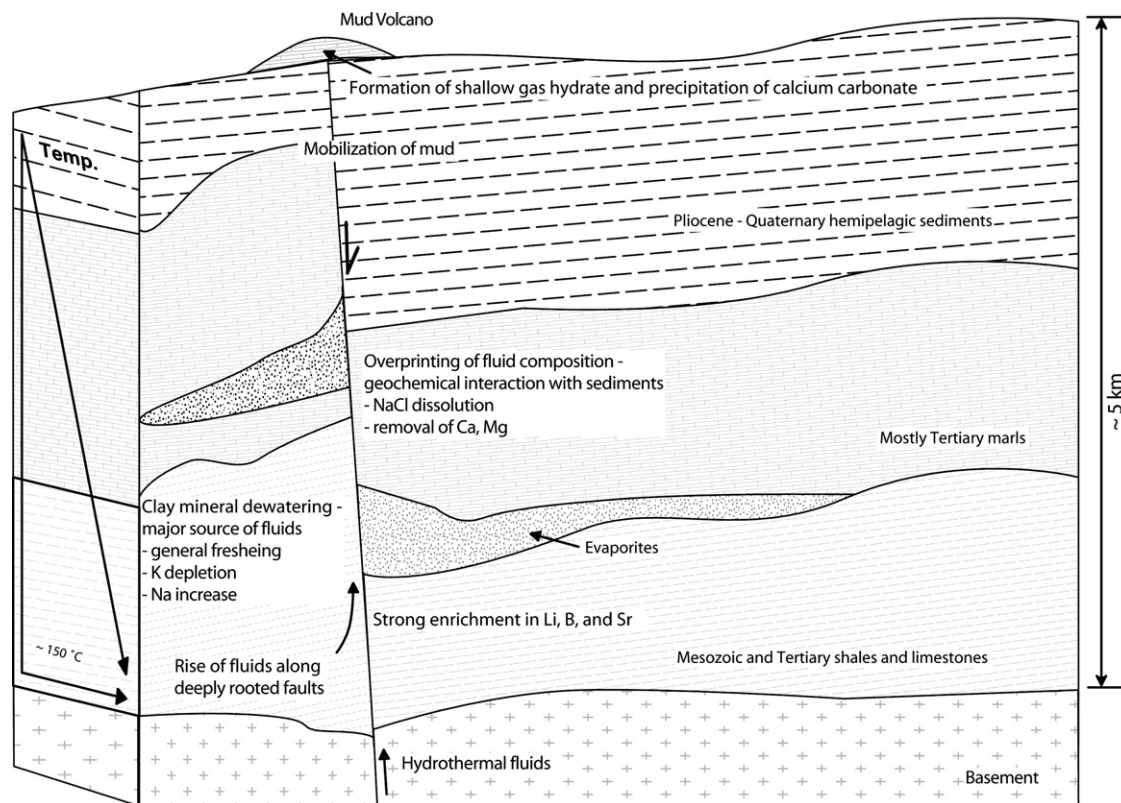


Fig. 11. Sketch illustrating an idealized sequence of MV fluid forming processes in the Gulf of Cadiz.

872 this type of processes. At least at CAMV, this observation is  
873 in line with the composition of  $\text{CH}_4$ -enriched, light volatile  
874 hydrocarbon gases. In addition, correlations between Li,  
875 B, and Sr, particularly at Bonjardim MV and CAMV, sug-  
876 gest that elevated Sr concentrations result from long-term  
877 leaching of crustal rocks and sediments, whereas differences  
878 in  $^{87}\text{Sr}/^{86}\text{Sr}$  ratios may be caused by differences in the nature  
879 of underlying crustal material (oceanic vs. continental).

880 All processes discussed in this study are summarized in  
881 a simplified diagram (Fig. 11) showing the suggested flow  
882 path of the fluids along major faults cutting through an  
883 idealized sequence of sedimentary rocks in the Gulf of  
884 Cadiz (after Medialdea et al., 2004). Although the occur-  
885 rence of a number of processes cannot be resolved unam-  
886 biguously, the suggested interpretation provides a  
887 comprehensive overview and raises the important question  
888 to what extent higher temperature reactions, perhaps in  
889 underlying basement, are linked to the processes control-  
890 ling mud volcanism and seepage of cold vents in general.  
891 However, the overall driving force of mud volcanism in  
892 the Gulf of Cadiz is—as in many accretionary and non-  
893 accretionary margins—clearly caused by clay mineral  
894 transformation.

## 895 Acknowledgments

896 We thank the officers, crew, and shipboard scientific  
897 party of RV Sonne for support at sea during expedition  
898 SO-175. Thanks to Kristin Nass, Mathias Marquardt,

and Nadja Neubert for assistance in pore water sampling  
and processing on board and Bettina Domeyer, Anke Bley-  
er, and Regina Surberg for analyses performed at IFM-  
GEOMAR. Marianne Nuzzo and Ed Hornibrook thank  
the DGM-INETI (Alfragide, Portugal) for use of laborato-  
ry space before and after the RV Sonne cruise. Klaus Wall-  
mann is thanked for many fruitful discussions on this topic.  
The manuscript benefited significantly from comments by  
Giovanni Aloisi and two anonymous reviewers. This work  
was supported by the Sonderforschungsbereich 574 at  
Christian-Albrechts-Universität, Kiel (SFB publication  
N° 103), Fundação para a Ciência e a Tecnologia (Lisbon,  
Portugal), EU-METROL, and the Eurocores/Euromargins  
MVSEIS Project (01-LEC-EMA24F; PDCTM72003/DIV/  
40018).

Associate editor: Jeffrey C. Alt

## References

- Aloisi, G., Drews, M., Wallmann, K., Bohrmann, G., 2004a. Fluid  
expulsion from the Dvurechenskii mud volcano (Black Sea).  
Part I. Fluid sources and relevance to Li, B, Sr, I and  
dissolved inorganic nitrogen cycles. *Earth Planet. Sci. Lett.* **225**,  
347–363.
- Aloisi, G., Wallmann, K., Bollwerk, S.M., Derkachev, A., Bohrmann,  
G., Suess, E., 2004b. The effect of dissolved barium on biogeo-  
chemical processes at cold seeps. *Geochim. Cosmochim. Acta* **68** (8),  
1735–1748.
- Argus, D.F., Gordon, R.G., Demets, C., Stein, S., 1989. Closure of the  
Africa–Eurasia–North America plate motion circuit and tectonics of  
the Gloria fault. *J. Geophys. Res.* **94**, 5585–5602.

- 929 Banner, J.L., 2004. Radiogenic isotopes: systematics and applications to  
930 earth surface processes and chemical stratigraphy. *Earth-Sci. Rev.* **65**,  
931 141–194.
- 932 Baptista, M.A., Heitor, S., Miranda, J.M., Miranda, P., Mendes Vitor, L.,  
933 1988. The 1755 Lisbon tsunami; evaluation of the tsunami parameters.  
934 *J. Geodyn.* **25** (2), 143–157.
- 935 Behrens, E.W., 1988. Geology of a continental slope oil seep, Northern  
936 Gulf of Mexico. *AAPG Bull.* **72** (2), 105–114.
- 937 Bernasconi, S.M. 1999. Interstitial water chemistry in the Western  
938 Mediterranean: results from leg 161. *Proceedings of the Ocean Drilling  
939 Program, Scientific Results* **161**, pp. 423–432.
- 940 Boles, J.R., Franks, S.G., 1979. Clay diagenesis in Wilcox sandstones of  
941 southwest Texas: implications of smectite diagenesis on sandstone  
942 cementation. *J. Sed. Petrol.* **49**, 55–70.
- 943 Boudreau, B.P., 1997. *Diagenetic models and their implementation:  
944 modelling transport and reactions in aquatic sediments*. Springer, Berlin,  
945 Heidelberg.
- 946 Bowes, H.L., Hornibrook, E.R.C., 2006. Emission of highly <sup>13</sup>C-depleted  
947 methane from an upland blanket mire. *Geophys. Res. Lett.* **33**, L04401.  
948 doi:10.1029/2005GL025209.
- 949 Brown, K.M., Saffer, D.M., Bekins, B.A., 2001. Smectite diagenesis, pore  
950 water freshening, and fluid flow at the toe of the Nankai wedge. *Earth  
951 Planet. Sci. Lett.* **194**, 97–109.
- 952 Brumsack, H.-J., Zuleger, E., 1992. Boron and boron isotopes in pore  
953 waters from ODP Leg 127, Sea of Japan. *Earth Planet Sci. Lett.* **113**,  
954 427–433.
- 955 Buffett, B., Archer, D., 2004. Global inventory of methane clathrate:  
956 sensitivity to changes in the deep ocean. *Earth Planet. Sci. Lett.* **227**,  
957 185–199.
- 958 Buforn, E., Sanz de Galeano, C., Udias, A., 1995. Seismotectonics of  
959 Ibero-Maghrebian region. *Tectonophysics* **248**, 247–261.
- 960 Burke, W.H., Denison, R.E., Hetherington, E.A., Koepnik, R.B., Nelson,  
961 H.F., Otto, J.B., 1982. Variation of seawater <sup>87</sup>Sr/<sup>86</sup>Sr throughout  
962 Phanerozoic time. *Geology* **10**, 516–519.
- 963 Chamley, H., 1989. *Clay sedimentology*. Springer-Verlag, Berlin.
- 964 Chamot-Rooke, N., Rabaute, A., Kreemer, C., 2005. Western Mediter-  
965 ranean Ridge mud belt correlates with active shear strain at the prism-  
966 backstop geological contact. *Geology* **33** (11), 861–864.
- 967 Chan, L.-H., Kastner, M., 2000. Lithium isotopic compositions of pore  
968 fluids and sediments in the Costa Rica subduction zone: implications  
969 for fluid processes and sediment contribution to the arc volcanoes.  
970 *Earth Planet Sci. Lett.* **183**, 275–290.
- 971 Chan, L.H., Leeman, W.P., You, C.-F., 1999. Lithium isotopic compo-  
972 sition of Central American volcanic arc lavas: implications for  
973 modification of subarc mantle by slab-derived fluids. *Chem. Geol.*  
974 **160**, 255–280.
- 975 Cuadros, J., 2006. Modeling of smectite illitization in burial diagenesis  
976 environments. *Geochim. Cosmochim. Acta* **70**, 4181–4195.
- 977 Dählmann, A., De Lange, G.J., 2003. Fluid-sediment interactions at  
978 Eastern Mediterranean mud volcanoes: a stable isotope study from  
979 ODP Leg 160. *Earth Planet. Sci. Lett.* **212**, 377–391.
- 980 De Lange, G.J., Brumsack, H.-J., 1998. Pore-water indications for the  
981 occurrence of gas hydrates in eastern mediterranean mud dome  
982 structures. *Proceedings of the Ocean Drilling Program, Scientific  
983 Results* **160**, pp. 569–574.
- 984 Depreiter, D., Poort, J., Van Rensbergen, P., Henriët, J.P., 2005.  
985 Geophysical evidence of gas hydrates in shallow submarine mud  
986 volcanoes on the Moroccan margin. *J. Geophys. Res.* **110**, B10103.  
987 doi:10.1029/2005JB003622.
- 988 Dia, A.N., Castrec, M., Boulégue, J., Boudou, J.P., 1995. Major and trace  
989 element and Sr isotope constraints on fluid circulations in the  
990 Barbados accretionary complex. Part I: Fluid origin. *Earth Planet.  
991 Sci. Lett.* **134**, 69–85.
- 992 Duarte, J.C., Rosas, F., Pinheiro, L.M., Matias, L.M., Carvalho, A.M.,  
993 Terrinha, P., Ivanov, M., 2005. Interpretation of recent sedimentary  
994 and tectonic structures off SW Iberia from multibeam bathymetry,  
995 seismic reflection and experimental modelling. in: *Geophysical  
996 Research Abstracts*, vol. 7, 07867. European Geosciences Union 2005.
- Freed, R.L., Peacor, D.R., 1989. Variability in temperature of the smectite/  
illite reaction in Gulf Coast sediments. *Clay Miner.* **24**, 171–180.
- Fryer, P., Wheat, C.G., Mottl, M.J., 1999. Mariana blueschist mud  
volcanism: implications for conditions within the subduction zone.  
*Geology* **27** (2), 103–106.
- Gardner, J.M., 2001. Mud volcanoes revealed and sampled on the western  
Morrocan continental margin. *Geophys. Res. Lett.* **28** (2), 339–342.
- Godon, A., Jendrzewski, N., Castrec-Rouelle, M., Dia, A., Pineau, F.,  
Boulegue, J., Javoy, M., 2004. Origin and evolution of fluids from mud  
volcanoes in the Barbados accretionary complex. *Geochim. Cosmo-  
chim. Acta* **68** (9), 2153–2165.
- Gonzalez-Fernandez, A., Cordoba, D., Matias, L., Torne, M., 2001.  
Seismic crustal structure in the Gulf of Cadiz (SW Iberian Peninsula).  
*Mar. Geophys. Res.* **22**, 207–223.
- Gràcia, E., Danobeitia, J., Verges, J., PARCIFAL-TEAM, 2003. Map-  
ping active faults offshore Portugal (36°N–38°N): implications for  
seismic hazard assessment along the southwest Iberian margin.  
*Geology* **31**(1), pp. 83–86.
- Grasshoff, K., Ehrhardt, M., Kremling, K., 1983. *Methods of Seawater  
Analysis*. Verlag Chemie.
- Gutscher, M.-A., 2004. What caused the Great Lisbon earthquake?  
*Science* **305**, 1247–1248.
- Gutscher, M.-A., Malod, J., Rehault, J.-P., Contrucci, I., Klingelhofer,  
K., Mendes-Victor, L., Spakman, W., 2002. Evidence for active  
subduction beneath Gibraltar. *Geology* **30** (12), 1071–1074.
- Haese, R., Hensen, C., De Lange, G.J., 2006. Pore water geochemistry of  
eastern Mediterranean mud volcanoes: implications for fluid transport  
and fluid origin. *Mar. Geol.* **225**, 191–208.
- Haese, R.R., Meile, C., Van Cappellen, P., De Lange, G.J., 2003. Carbon  
geochemistry of cold seeps: methane fluxes and transformation in  
sediments from Kazan mud volcano, eastern Mediterranean Sea. *Earth  
Planet. Sci. Lett.* **212**, 361–375.
- Henry, P., Le Pichon, X., Lallemand, S., Lance, S., Martin, J.B., Foucher,  
J.-P., Fiala-Médioni, A., Rostek, F., Guilhaumou, N., Pranal, V.,  
Castrec, M., 1996. Fluid flow in and around a mud volcano field  
seaward of the Barbados accretionary wedge: results from Manon  
cruise. *J. Geophys. Res.* **101** (B9), 20297–20323.
- Hensen, C., Wallmann, K., 2005. Methane formation at Costa Rica  
continental margin—constraints for gas hydrate inventories and cross-  
décollement fluid flow. *Earth Planet. Sci. Lett.* **236**, 41–60.
- Hensen, C., Wallmann, K., Schmidt, M., Ranero, C.R., Suess, E., 2004.  
Fluid expulsion related to mud extrusion off Costa Rica continental  
margin—a window to the subducting slab. *Geology* **32**, 201–204.
- Ivanenkov, V.N., Lyakhin, Y.I., 1978. Determination of total alkalinity in  
seawater. In: Bordovsky, O.K., Ivanenkov, V.N. (Eds.), *Methods of  
Hydrochemical Investigations in the Ocean (in Russian)*. Nauka Publ.  
House, pp. 110–114.
- Kopf, A., Deyhle, A., Lavrushin, V.Y., Polyak, B.G., Gieskes, J.M.,  
Buachidze, G.I., Wallmann, K., Eisenhauer, A., 2003. Isotopic  
evidence (He,B,C) for deep fluid and mud mobilization from mud  
volcanoes in the Caucasus continental collision zone. *Int. J. Earth Sci.*  
**92**, 407–425.
- Kopf A. and Participants a. c., 2004. Report and preliminary results of  
Sonne cruise SO-175, Miami-Bremerhaven, 12.11.-30.12.2003. Beri-  
chte, Fachbereich Geowissenschaften, Universität Bremen, No. 228.
- Lonergan, L., White, N., 1997. Origin of the Betic-Rif mountain belt.  
*Tectonics* **16** (3), 504–522.
- Luff, R., Wallmann, K., 2003. Fluid flow, methane fluxes, carbonate  
precipitation and biogeochemical turnover in gas hydrate-bearing  
sediments at Hydrate Ridge, Cascadia Margin: numerical modeling  
and mass balances. *Geochim. Cosmochim. Acta* **67** (18), 3403–3421.
- Maestro, A., Somoza, Luis, Medialdea, Teresa, Talbot, Christopher J.,  
Lowrie, Allen, Vazquez, Juan, Diaz-del-Rio, V., 2003. Large-scale  
slope failure involving Triassic and Middle Miocene salt and shale in  
the Gulf of Cadiz (Atlantic Iberian Margin). *Terra Nova* **15**, 380–391.
- Maldonado, A., Somoza, L., Pallares, L., 1999. The Betic orogen and the  
Iberian-African boundary in the Gulf of cadiz: geological evolution  
(central North Atlantic). *Mar. Geol.* **155**, 9–43.

- 1065 Martin, J.B., Gieskes, J.M., Torres, M.E., Kastner, M., 1993. Bromine  
1066 and iodine in Peru margin sediments and pore fluids: implications for  
1067 fluid origins. *Geochim. Cosmochim. Acta* **57**, 4377–4389.
- 1068 Martin, J.B., Kastner, M., Elderfield, H., 1991. Lithium: sources in pore  
1069 fluids of Peru slope sediments and implications for oceanic fluxes. *Mar.*  
1070 *Geol.* **102**, 281–292.
- 1071 Martin, J.B., Kastner, M., Henry, P., Le Pichon, X., Lallement, S., 1996.  
1072 Chemical and isotopic evidence for sources of fluids in a mud volcano  
1073 field seaward of the Barbados accretionary wedge. *J. Geophys. Res.* **101**  
1074 (B9), 20325–20345.
- 1075 Mazurenko, L.L., Soloviev, V.A., Gardner, J.M., Ivanov, M.K., 2003.  
1076 Gas hydrates in the Ginsburg and Yuma mud volcano sediments  
1077 (Moroccan margin): results of chemical and isotopic studies of pore  
1078 water. *Mar. Geol.* **195**, 201–210.
- 1079 McCaffrey, M.A., Lazar, B., Holland, H.D., 1987. The evaporation of  
1080 seawater and the coprecipitation of Br<sup>-</sup> and K<sup>+</sup> with halite. *J.*  
1081 *Sediment. Petrol.* **57**, 928–937.
- 1082 Medialdea, T., Vegas, R., Somoza, L., Vazquez, J.T., Maldonado, A.,  
1083 Diaz-del-Rio, V., Maestro, A., Cordoba, D., Fernandez-Puga, M.C.,  
1084 2004. Structure and evolution of the ‘olistostrome’ complex of the  
1085 Gibraltar Arc in the Gulf of Cadiz (eastern Central Atlantic):  
1086 evidence from two long seismic cross-sections. *Mar. Geol.* **209**, 173–  
1087 198.
- 1088 Meghraoui, M., Morel, J.-L., Andrieux, J., Dahmani, M., 1996. Tectonic  
1089 plio-quadernaire de la chaîne tello-rifaine et de la mer d’Alboran.  
1090 Une zone complexe de la convergence continent–continent. *Bull. Soc.*  
1091 *Geol. France* **167** (1), 141–157.
- 1092 Milkov, A.V., 2000. Worldwide distribution of submarine mud volcanoes  
1093 and associated gas hydrates. *Mar. Geol.* **167**, 29–42.
- 1094 Milkov, A.V., Sassen, R., Apanasovich, T.V., Dadashev, F.G., 2003.  
1095 Global gas flux from mud volcanoes: a significant source of fossil  
1096 methane in the atmosphere and the ocean. *Geophys. Res. Lett.* **30** (2),  
1097 1037. doi:10.1029/2002GL016358.
- 1098 Moore, J.C., Mascle, A., 1987. Expulsion of fluids from depth along a  
1099 subduction zone decollement horizon. *Nature* **326**, 785–788.
- 1100 Moore, J.C., Vrolijk, P., 1992. Fluids in accretionary prisms. *Rev.*  
1101 *Geophys.* **30** (2), 113–135.
- 1102 Morel, J.-L., Meghraoui, M., 1996. Goringe-Alboran-Tell tectonic zone: a  
1103 transpression system along the Africa–Eurasia plate boundary. *Geol-*  
1104 *ogy* **24** (8), 755–758.
- 1105 Morse, J.W., Mackenzie, F.T., 1990. *Geochemistry of Sedimentary*  
1106 *Carbonates*. Elsevier, Amsterdam.
- 1107 Niemann, H., Duarte, J., Hensen, C., Omereg, E., Magalhães, V.H.,  
1108 Elvert, M., Pinheiro, L.M., Boetius, A., Kopf, A., 2006. Microbial  
1109 methane turnover at mud volcanoes of the Gulf of Cadiz. *Geochim.*  
1110 *Cosmochim. Acta* **70**, 5336–5355.
- 1111 Niewöhner, C., Hensen, C., Kasten, S., Zabel, M., Schulz, H.D., 1998.  
1112 Deep sulfate reduction completely mediated by anaerobic methane  
1113 oxidation in sediments of the upwelling area off Namibia. *Geochim.*  
1114 *Cosmochim. Acta* **62** (3), 455–464.
- 1115 L.M. Pinheiro, Ivanov, M., Kenyon, N., Magalhães, V.H., Somoza, L.,  
1116 Gardner, J.M., Kopf, A., Van Rensbergen, P., Monteiro, J.H.,  
1117 Euromargins-MVSEIS-Team., 2005. Structural control of mud volca-  
1118 nism and hydrocarbon-rich fluid seepage in the Gulf of Cadiz: results  
1119 from the TTR-15 and other previous cruises. *CIESM Workshop*  
1120 *Monograph*, 28.
- 1121 Pinheiro, L.M., Ivanov, M.K., Sautkin, A., Akhmanov, G., Magalhães,  
1122 V.H., Volkonskaya, A., Monteiro, J.H., Somoza, L., Gardner,  
1123 J.V., Hamouni, N., Cunha, M.R., 2003. Mud volcanism in the  
1124 Gulf of Cadiz: results from the TTR-10 cruise. *Mar. Geol.* **195**,  
1125 131–151.
- 1126 Reicherter, K.R., Pletsch, T.K., 2000. Evidence for a synchronous circum-  
1127 Iberian subsidence event and its relation to the African–Iberian plate  
1128 convergence in the Late Cretaceous. *Terra Nova* **12** (3). doi:10.1046/  
1129 j.1365-3121.2000.123276.x.
- 1130 Ribeiro, A., Cabral, J., Baptista, R., Matias, L., 1996. Stress pattern in  
1131 Portugal mainland and the adjacent Atlantic region, West Iberia.  
1132 *Tectonics* **15** (2), 641–659.
- Saffer, D.M., Bekins, B.A., 1999. Fluid budgets at convergent plate  
1133 margins: implications for the extent and duration of fault zone  
1134 dilation. *Geology* **27**, 1095–1098.
- Sartori, R., Torelli, I., Zitellini, N., Peis, D., Lodolo, E., 1994. Eastern  
1136 segment of the Azores-Gibraltar line (Central-Eastern Atlantic): an  
1137 oceanic plate boundary with diffuse compressional deformation.  
1138 *Geology* **22**, 555–558.
- Schmidt, M., Hensen, C., Mörz, T., Müller, C., Grevemeyer, I.,  
1140 Wallmann, K., Mau, S., Kaul, N., 2005. Methane hydrate accumu-  
1141 lation in “Mound 11” mud volcano, Costa Rica forearc. *Mar. Geol.*  
1142 **216**, 83–100.
- Sheppard, S.M.F., Gilg, H.A., 1996. Stable isotope geochemistry of clay  
1144 minerals. *Clay Miner.* **31**, 1–24.
- Spinelli, G.A., Underwood, M.B., 2004. Character of sediments entering  
1146 the Costa Rica subduction zone: Implications for partitioning of water  
1147 along the plate interface. *The Island Arc* **13**, 432–451.
- Stadnitskaia, A., Ivanov, M.K., Blinova, V., Kreulen, R., van Weering,  
1149 T.C.E., 2006. Molecular and carbon isotopic variability of hydrocar-  
1150 bon gases from mud volcanoes in the Gulf of Cadiz, NE Atlantic. *Mar.*  
1151 *Petrol. Geol.* **23** (3), 281–296.
- Suess, E., Bohrmann, G., Von Huene, R., Linke, P., Wallmann, K.,  
1153 Lammers, S., Sahling, H., Winckler, G., Lutz, R.A., Orange, D., 1998.  
1154 Fluid venting in the eastern Aleutian subduction zone. *J. Geophys. Res.*  
1155 **103** (B2), 2597–2614.
- Thornton, E.C., Seyfried Jr., W.E., 1987. Reactivity of organic-rich  
1157 sediment in seawater at 350 °C, 500 bars: experimental and theoretical  
1158 constraints and implications for the Guaymas Basin hydrothermal  
1159 system. *Geochim. Cosmochim. Acta* **51**, 1997–2010.
- Tishchenko, P., Hensen, C., Wallmann, K., Wong, C.S., 2005. Calculation  
1161 of the stability and solubility of methane hydrate in seawater. *Chem.*  
1162 *Geol.* **219**, 37–52.
- Tobin, H.J., Moore, J.C., Mackay, M.E., Orange, D.L., Kulm, L.D.,  
1164 1993. Fluid flow along a strike-slip fault at the toe of the Oregon  
1165 accretionary prism: implications for the geometry of frontal accretion.  
1166 *Geol. Soc. Am. Bull.* **105** (5), 569–582.
- Van Rensbergen, P., Depreiter, D., Pannemans, B., Moerkerke, G., Van  
1168 Rooij, D., Marsset, B., Akhmanov, G., Blinova, V., Ivanov, M.,  
1169 Rachidi, M., Magalhães, V., Pinheiro, L.M., Cunha, M., Henriot, J.-  
1170 P., 2005. The El Arraiche mud volcano field at the Moroccan Atlantic  
1171 slope, Gulf of Cadiz. *Mar. Geol.* **219**, 1–369.
- Von Damm, K.L., 1990. Seafloor hydrothermal activity: black smoker  
1173 chemistry and chimneys. *Ann. Rev. Earth Planet. Sci.* **18**, 173–204.
- Von Damm, K.L., Edmond, J.M., Measures, C.I., Grant, B., 1985.  
1175 Chemistry of submarine hydrothermal solutions at Guaymas Basin,  
1176 Gulf of California. *Geochim. Cosmochim. Acta* **49** (11), 2221–2237.
- Von Damm, K.L., Parker, C.M., Zierenberg, R.A., Lilley, M.D., Olson,  
1178 E.J., Clague, D.A., McClain, J.S., 2005. The Escanaba Trough, Gorda  
1179 Ridge hydrothermal system: Temporal stability and seafloor  
1180 complexity. *Geochim. Cosmochim. Acta* **69** (21), 4971–4984.
- Wallace, P.J., Dickens, G.R., Paull, C.K., Ussler III, W., 2000. Effects of  
1182 core-retrieval and degassing on the carbon isotope composition of  
1183 methane in gas hydrate and free gas-bearing sediments from the Blake  
1184 Ridge. In: Paull, C.K., Matsumoto, R., Wallace, P.J., Dillon, W.P.  
1185 (Eds.), *Proc. ODP, Sci. Res.*, vol. 164, pp. 101–112.
- You, C.-F., Gieskes, J.M., 2001. Hydrothermal alteration of hemi-pelagic  
1187 sediments: experimental evaluation of geochemical processes in shal-  
1188 low subduction zones. *Appl. Geochem.* **16**, 1055–1066.
- You, C.-F., Spivack, A.J., Gieskes, J.M., Rosenbauer, R., Bischoff, J.L.,  
1190 1995. Experimental study of boron geochemistry: implications for fluid  
1191 processes in subduction zones. *Geochim. Cosmochim. Acta* **59** (12),  
1192 2435–2442.
- You, C.-F., Spivack, A.J., Smith, J.H., Gieskes, J.M., 1993. Mobilization  
1194 of boron in convergent margins: implications for the boron geochem-  
1195 ical cycle. *Geology* **21**, 207–210.
- Zeyen, H., Ayarza, P., Fernandez, M., Rimi, A., 2005. Lithospheric  
1197 structure under the western African–European plate boundary: a  
1198 transect across the Atlas Mountains and the Gulf of Cadiz. *Tectonics*  
1199 **24** (2). doi:10.1029/2004TC001639.



## **Appendix A. Geophysical data acquisition and processing, sample collection and underwater observations**

A large number of methodologies and techniques, commonly used in marine geology and geophysics, were used to identify seafloor structures which based on their size, shape and backscatter intensity, potentially represent mud volcanoes or seeps. Ground-truthing through coring, dredging and sampling with TV-controlled grabs together with underwater seafloor video observations were used to confirm the nature of these structures. In this appendix the scientific cruises which contributed with data for this thesis are briefly presented. The several geophysical, sampling and underwater observation techniques are described, the instrumentation used is presented and a brief overview of the data processing is described.

### **A.1 Oceanographic cruises**

The work and results presented in this PhD Thesis are based on data collected in 18 scientific cruises: TTR09, TTR10, TTR11A, TTR11, TTR12, TTR14, TTR15, TTR16, Tasyo, Anastasya-2000, Anastasya-2001, GAP, Cadipor, Cadisar-1 and 2, Matespro and Delila-1 and 2. The author participated on 10 of these cruises: TTR10, TTR11A, TTR11, TTR14, TTR15, TTR16, Anastasya-2001, GAP, Cadipor and Matespro.

TTR09 Leg 2 cruise (30 June - 16 July 1999) onboard the marine geology research and survey vessel Professor Logachev, operated by the Russian *Polar Marine Geosurvey Expedition*, from St Petersburg. The vessel is 104.5 m in length, 16 m wide, a draught of 6.66 m, has a net tonnage of 1351 ton, a displacement of 5700 ton and is powered by two 3500 hp diesel engines. TTR09-Leg 2 was devoted to the study of the fluid escape structures in the Gulf of Cadiz with Joan Gardner and M. K. Ivanov as co-chief scientists. The work developed during this cruise involved single and multichannel seismic acquisition, long range side-scan sonar (OKEAN) and deep towed side-scan sonar

(OREtech 30 and 100 kHz), 5.1 kHz acoustic profiler, underwater video system and sampling with gravity corer, box corer, TV-guided grab and dredge (Kenyon *et al.*, 2000). These equipments are described in the following sections.

TTR10-Leg 1 cruise (10 - 24 July 2000) onboard the R/V Professor Logachev, was devoted to the study of the fluid escape structures in the Gulf of Cadiz, coordinated by L. M. Pinheiro and M. K. Ivanov as co-chief scientists. The work developed during this cruise involved single and multichannel seismic acquisition, long range side-scan sonar (OKEAN) and deep towed side-scan sonar (OREtech 30 and 100 kHz), 5.1 kHz acoustic profiler, underwater video system and sampling with gravity corer, box corer, TV-guided grab and dredge (Kenyon *et al.*, 2001).

TTR11 Leg A cruise onboard the R/V Professor Logachev (10 - 16 June 2001), was devoted to the installation and test of new deep towed side scan sonar MAK system, underwater video system and seismic reflection system and the study of the fluid escape structures in the Gulf of Cadiz.

TTR11 Leg 3 cruise, onboard the R/V Professor Logachev (21 August - 3 September 2001), was devoted to the study of the fluid escape structures in the Gulf of Cadiz with co-chief scientists M. K. Ivanov, L. M. Pinheiro and N. Kenyon. The work developed during this cruise involved single and multichannel seismic acquisition, long range side-scan sonar (OKEAN) and deep towed side-scan sonar (MAK, 30 and 100 kHz), 5.1 kHz acoustic profiler, underwater video system and sampling with gravity corer, box corer, TV-guided grab and dredge (Kenyon *et al.*, 2002).

The ANASTASIA 2000 cruise onboard the R/V Cornide de Saavedra (4 - 20 September 2000) was devoted to the investigation of collection of samples for paleoceanography, study of the contourite system, study of mud volcanoes and other fluid escape structures in the Gulf of Cadiz with L. Somoza and V. Dias del Rio as co-chief scientists. The work developed during this cruise involved sediment sample collection with box corer, gravity corer and dredge, sparker and TOPAS seismic profiles acquisition.

The ANASTASIA 2001/09 cruise onboard the R/V Cornide de Saavedra (4 - 19 September 2001) was devoted to the investigation of the methane-derived authigenic carbonates (MDAC) occurrences, study of the contourite system and heat flow measurements in the Gulf of Cadiz. This cruise was part of the Spanish Tasyo project developed under co-chief of L. Somoza and V. Dias del Rio (Somoza *et al.*, 2002). The

work developed during this cruise involved sediment sample collection with box corer, gravity corer and dredge, underwater photography and heat flow measurements.

The CADIPOR cruise (16 - 28 May 2002) on board the RV Belgica, organized by the Gent University, Prof. Dr. Jean-Pierre Henriët. This cruise was devoted to the bathymetric, and seismic study of the mud volcanoes in the Moroccan Margin of the Gulf of Cadiz (Van Rooij *et al.*, 2002). The work developed during this cruise involved sediment sample collection with box corer, single and multichannel seismics and deep-towed seismics (chirp).

The GAP (Gibraltar Arc Processes), SO-175 cruise (26 November - 22 December 2003) onboard the R/V Sonne. During this cruise the activities were concentrated on the investigation of gas hydrates, methane-derived authigenic carbonates (MDAC) and the tectonic regime in the Gulf of Cadiz (Kopf *et al.*, 2004). The work developed during this cruise involved sediment sample collection with multi-corer, gravity corer and TV controlled grab, underwater video survey with OFOS (Ocean Floor Observation System), swath bathymetry, multichannel seismics, parametric parasound echosounding and heat flow measurements.

The MATESPRO (Major Tectonic and Sedimentary Processes in the Portuguese Margins) multibeam cruise, onboard the R/V D Carlos I (14 June – 10 July 2004) was devoted to multibeam survey in the South Portuguese Margin. This cruise had L. Matias and P. Terrinha (Univ. Lisbon) as chief scientist (Matias *et al.*, 2004; Terrinha *et al.*, 2004).

The TTR 14, Leg 1 (25 July – 10 August 2004) onboard the R/V Professor Logachev was devoted to the study of the fluid escape structures in the Gulf of Cadiz, and was coordinated by L. M. Pinheiro and M. K. Ivanov. The work developed during this cruise involved single and multichannel seismic acquisition, long range side-scan sonar (OKEAN) and deep towed side-scan sonar (MAK, 30 and 100 kHz), 5.1 kHz acoustic profiler, underwater video system and sampling with gravity corer, box corer, TV-guided grab and dredge.

The TTR 15, Leg 4 (19 July – 5 August 2005) onboard the R/V Professor Logachev was devoted to the study of the fluid escape structures in the Gulf of Cadiz, and was coordinated by L. M. Pinheiro and M. K. Ivanov. The work developed during this cruise involved single and multichannel seismic acquisition, long range side-scan sonar (OKEAN) and deep towed side-scan sonar (MAK, 30 and 100 kHz), 5.1 kHz acoustic

profiler, underwater video system and sampling with gravity corer, box corer, TV-guided grab and dredge.

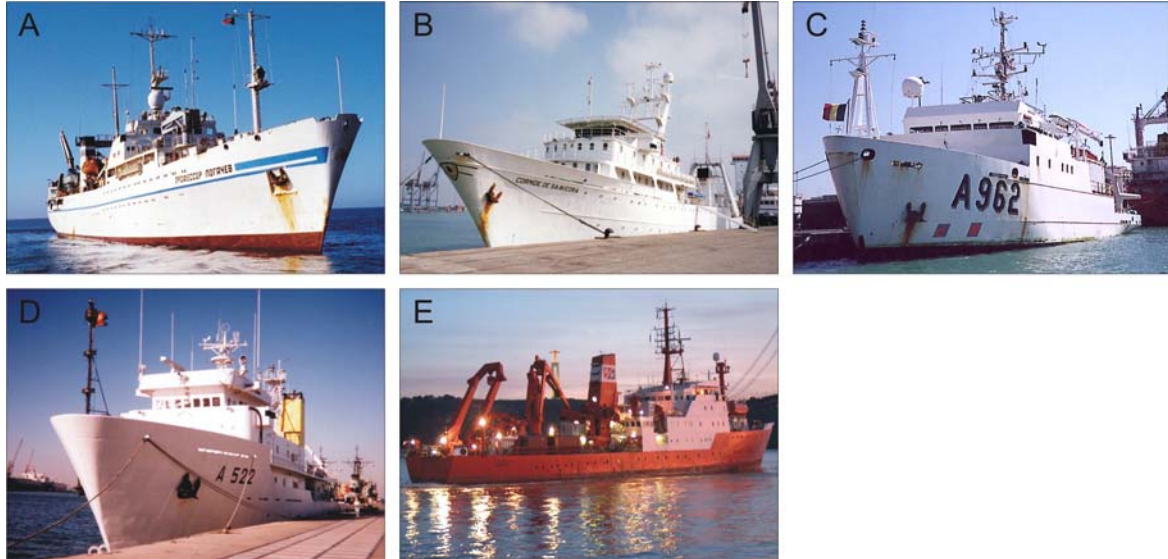


**Figure A.1.** Research vessels used in some of the cruises that allowed the collection of data used in this work. **(A)** Professor Logachev used on the TTR09 to TTR16 cruises. **(B)** R/V Cornide de Saavedra where the Anastasya cruises were performed. **(C)** R/V Belgica where the cruises Cadipor 1 and 2 were performed. **(D)** R/V D. Carlos I used during the swath bathymetry surveys Matespro and Delila 1. **(E)** R/V Sonne, GAP cruise.

## A.2 Navigation

Positioning during the TTR cruises was acquired with an Ashtech GG24 DPS + GLONASS receiver, allowing an optimal static accuracy of  $\pm 35$  cm (75 cm at 95% confidence limits). The normal accuracy, under normal satellite configuration, in the Gulf of Cadiz area is assumed as ca. 5 m.

Underwater navigation during deep towed operations, such as the deep towed side-scan sonar (MAK1 and OREtech), deep-towed video system and TV-controlled grab was based on the Sigma-1001 hydroacoustic system. This system consists on a pinger fitted at the deep-towed equipment, operating between 7-15 kHz and four stationary hull-mounted acoustic receivers, spaced 14 m apart. The signal emitted by the deep-towed pinger is tracked on board and accurate x,y position of the device is computed in relation to the vessel, taking into account the vessel roll, trim and speed. The error of the estimated

position of the deep-towed equipment by this system usually does not exceed 1-2% of the water depth.

For gravity corer seabed sampling, the error in positioning is normally 5% of the accuracy of the vessel position, due to their rapid deployment.

Navigation on board the D. Carlos I (Matespro and Delila 1 cruises), Sonne, Cornide de Saavedra and Belgica was carried out using both Global Positioning System (GPS) and Differential Global Positioning System (DGPS), installed in one or in multiple positions of the vessel. The two systems were used in order to allow the necessary accuracy in position determination, as well as the necessary yaw corrections to be used by the multibeam systems.

### **A.3 Multibeam bathymetry and backscatter reflectivity**

#### **A.3.1 Matespro and Delila 1 cruises (NRP D. carlos I)**

##### **A.3.1.1 Data acquisition**

The NRP D Carlos I is equipped with a SIMRAD EM 120 multibeam system and bathymetric echo sounders: Marimatech E-Sea Sound 206S (15 kHz), an Atlas Deso 20 (33 and 210 kHz) profiler and acoustic Doppler current profiler: RDI Ocean Surveyor (38 and 150 kHz). The SIMRAD EM 120 nominal sonar frequency is 12 kHz with an angular coverage sector of up to 150 degrees and 191 beams per ping as narrow as 1 degree. Achievable swath width on a flat bottom will normally be approximately six times the water depth. The transmit fan is split into several individual sectors with independent active steering according to vessel roll, pitch and yaw. This places all soundings on a “best fit” to a line perpendicular to the survey line, thus ensuring a uniform sampling of the bottom and 100% coverage. The sectors are frequency coded (11.25 to 12.60 kHz), and they are all transmitted sequentially at each ping. The sector steering is fully taken into account when the position and depth of each sounding is calculated, as is the refraction due to the sound speed profile, vessel attitude and installation angles. Pulse length and range sampling rate are variable with depth for best resolution, and in shallow waters due care is taken to account for near field effects. The ping rate is mainly limited by the round trip travel time in the water up to a ping rate of 5 Hz.

The system depth accuracy is very high due to the narrow beams and a high sampling rate is used (2 kHz). The expected total system RMS accuracy (assuming good external sensor data) is: 0.2% of depth (from nadir up to 45 degrees), 0.3% of the depth (up to 60 degrees), and 0.5% of the depth (between 60 and 70 degrees). More information about this system can be found at the system manufacturer site: [www.kongsberg.com](http://www.kongsberg.com).

The MATESPRO and Delila 1 Multibeam surveys were performed according to an Order 3 Hydrographic Survey Standard (Standards for Hydrographic Surveys, 1998). This means that accurate and true sound velocity profiles had to be acquired during the survey and that all areas were covered by verification lines crossing the main survey direction at 90 degrees. The verification lines covered 10% of the surveyed area. In order to minimize vertical and lateral errors associated with the external beams, and depending on the state of the sea, an maximum opening angle of 120° (and in some cases 60-70°) was used instead of maximum angular range of 150°, restricting the coverage to a maximum of 14 km wide swath to gain an more continuous spacing of beams on the ocean floor.

The distribution of the water masses in the Gulf of Cadiz is a crucial aspect for the conversion of the recorded SIMRAD EM120 travel times into depth values. This is particularly important in the Gulf of Cadiz where there is a strong influence on the sound velocity along the water column as a result of the presence of the saline and warm Mediterranean outflow water (MOW). Therefore, sound velocity profiles (SVP) were performed at the rate of 1 per day during the Matespro and Delila 1 cruises. During the GAP cruise, CTDOS (Conductivity, Temperature, Depth, Oxygen, Salinity), CTD (Conductivity, Temperature, Depth) were used, while XBTs were used during the RV Belgica Cadipor cruise, to calculate the sound velocity profiles on the water column. Climatological profiles of the Gulf of Cadiz region were also used to constrain the water column sound velocity.

#### **A.3.1.2 Data processing**

The processing of the multibeam data consists in a sequence of procedures that were performed by the dedicated software package CARIS-HIPS. The steps generally used are:

- i)* Conversion of the raw data from the native acquisition format to the application format
- ii)* Quality control of the raw data
- iii)* Automatic removal of outliers with dedicated filters/procedures

- iv) Manual/semi-automatic removal of outliers
- v) Generation of cruise grids
- vi) Integration with other available data sets.

The processing of the Matespro raw data was performed using the CARIS-HIPS software packaged (by the *Instituto Hidrografico* processing team). The backscatter data recorded by the SIMRAD EM-120 system was recovered and processed first by the MB-System (J. Luis, Univ. Algarve) and by the CARAIBES package (S. Diez, UTM-CSIC, Barcelona).

The grids cleaned were then converted and imported into the ArcGIS GIS system and integrated with the regional GIS database.

### **A.3.2 GAP cruise (RV Sonne)**

During the R/V Sonne GAP cruise, a Simrad EM120 multibeam echosounder was used for continuous mapping of the seafloor.

To convert the recorded travel times into depth several water velocity profiles were obtained with the shipboard CTD. During this cruise, handling of the bathymetric data was done by the ship's navigation system administrators. Each beam was corrected for ray bending using the appropriate sound velocity profile and the ship's motion, and finally stored with GPS position. To generate the bathymetric maps the data were averaged using the nearest neighbour gridding algorithm, using and displayed with the GMT mapping software (Wessel and Smith, 1991, 1995). However, data were not edited for clean bad beams. The final gridded data was converted into ArcGIS format and integrated in the GIS database of the Gulf of Cadiz.

## **A.4 Seismic profiles**

### **A.4.1 PSAT seismic profiles**

#### **A.4.1.1 Data acquisition**

Single channel seismic reflection profiles were acquired throughout the TTR cruises. The seismic source consisted of two 3.5 litre airguns, at a pressure of 150 atm. The airguns were towed at a depth of approximately 3.5 meters and were shot every 10 seconds

(approximately every 30 meters). The streamer consisted of one active section, 25 meters long, with 50 hydrophones, towed at a depth of approximately 3.5 meters. The offset between the seismic source and the centre of the live hydrophone array was 230 meters. Throughout the seismic acquisition, the average ship's speed was about 6.5 knots.

The data was acquired digitally using the MSU developed software and preliminary processed with the RadExPro software, which was provided to the UNESCO MSU Centre for Marine Geosciences by GDS Productions, Moscow. The trace length is 8s and the sampling rate is 1 ms. The signals were filtered analogically 30-250 Hz in the acquisition stage. The preliminary on board processing was carried out using both the RadExPro software and the SPW processing system (Seismic Processing Workshop). The basic processing sequence consisted of static shifts correction, amplitude recovery by spherical divergence correction and simple bandpass filtering (5-20-250-300 Hz). Signature deconvolution and phase-shift migration were also applied to some of the seismic lines to attenuate the bubble pulse and to better image the near-surface geological structure.

#### **A.4.1.2 Post-cruise data processing**

Post cruise processing of the seismic data collected during the TTR10, 11, 12, 14 and 15 cruises within the Gulf of Cadiz was performed in collaboration with Dr Serguei Bouriak using the SPW processing software (Bouriak, 2003).

The principal aim of the processing was to prepare the data sets for structural interpretation, attempting to enhance the traceability of deep reflections, with recovering of their true geometry. The processing flow included predictive deconvolution, time-variant Butterworth filtering, spherical divergence correction, muting, automatic gain control, and phase shift migration, as well as some additional subsidiary procedures (e.g. automatic trace edit) when necessary. Some lines, where the water depths variations were significant, required flattening of the seafloor with static shifts prior to time-variant filtering, with posterior recovery of the initial topography. A characteristic example of an SPW processing flow used for the processing of the data sets is shown on Figure A.2

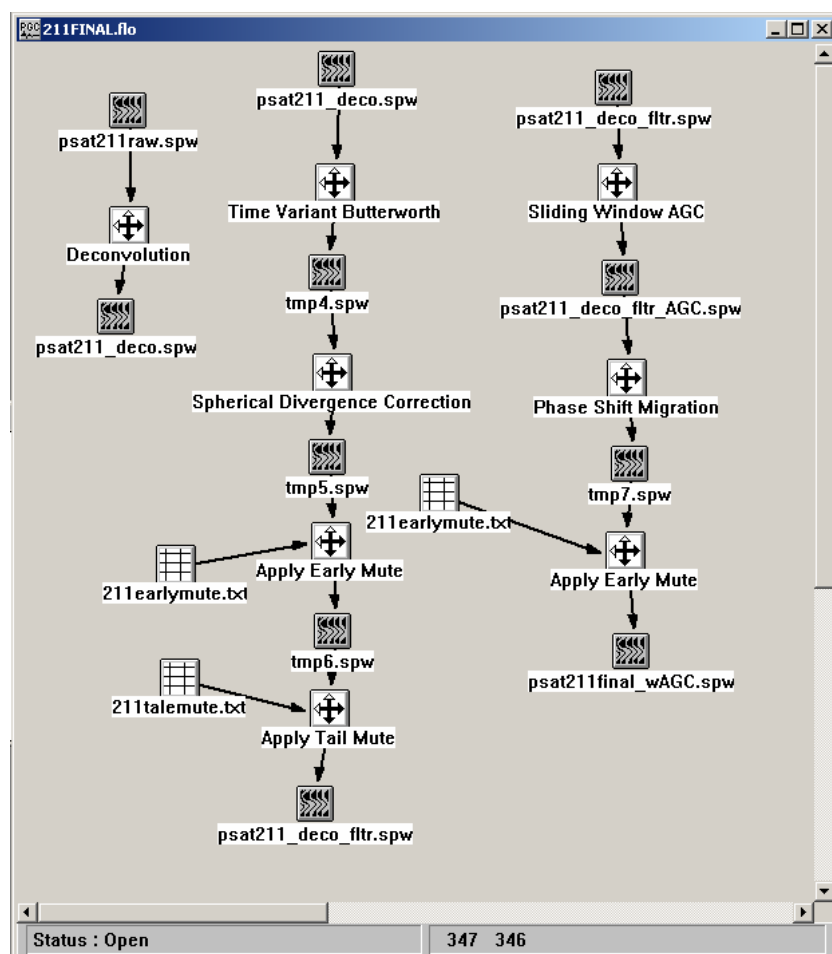


Figure A.2. SPW processing flow for TTR11 psat211 line.

#### A.4.2 Multichannel seismic

Multichannel seismic reflection (MCS) were acquired during the GAP cruise using one GI gun of 1.7 l and a 100 m active length streamer with 16 channels.

During the TTR15-leg 4 multichannel seismic profiles were acquired using the Bremen University multichannel seismic system, designed to acquire high resolution seismic data.

The main seismic source for the survey was a Soderia GI-Gun, in true GI-Mode with 2x1.7 l chamber volume. The trigger interval was 12 to 16 seconds, resulting on an average shot point spacing ranging from 31 to 41 m at 5 knots ship speed (when operating in parallel to the OKEAN) and 12 to 16 m at 2 knots ship speed (when operating in parallel to MAK). The gun was shot at a mean pressure of 120-150 bar.

The multichannel seismic streamer was towed with 3 MultiTrak Remote Units (MTCBirds) attached, used to keep the streamer in 3 m depth. The streamer included a

lead-in and 2 active sections of 50 m length each. A 30 m long deck cable connected the streamer to the recording system. The 2 active sections (SYNTRON) were each subdivided, giving 8 hydrophone groups in total. Each of the 6.25 m long hydrophone groups is again subdivided into 5 subgroups of different length. One of the subgroups was a high-resolution hydrophone with pre-amplifier. A programming module distributes the subgroups of 4 hydrophone groups, *i.e.* a total of 20 groups to 5 channels. To adapt the system to the water depth, deep water programming modules (instead of module 1, which could not be removed) were selected, so that every second 6.25 m hydrophone group was completely used with all 13 hydrophones.

The data acquisition system, developed at the working group marine technology/environmental research at the University of Bremen consists of a Pentium IV based PC (3 GHz, 1GB RAM, Windows XP) with two NI6052E 16bit AD-converters. Each ADC was connected to a 32 channel multiplexer (NI-SCXI1102-C) with onboard preamplification and anti-alias filter. The system therefore provides a maximum of 64 channels at maximum sampling rate of 10 kHz per channel. The acquisition software was also a custom development and provides nearly continuous recording of the 64 channels with data storage in demultiplexed SEG-Y to hard disk. The software, allows online quality control by displaying shot gathers and an online profile plot using brute channel stacks of arbitrary channels. Data were recorded at 4 kHz over lengths of 4 - 6 seconds depending on water depth with a delay of 0 s, resulting in 16000 – 24000 samples per trace.

On-board post-processing of the data was carried out with the Seismic processing software Vista 5.1. The main target of the processing was to enhance the signal to noise ratio. The following processing flow was routinely applied to the data. First, a wide bandpass filter of 5-800 Hz was used to allow trace editing. After removing bad traces, an f-k filter was applied. The filter design consists in the k-domain of two outside end rejections zones, which depends on the noise character of the data. In the frequency domain a rejection above 200 Hz was chosen. As a next step, spherical divergence was corrected, followed by a common-shot stack. For some profiles with obvious diffraction hyperbolae, an f-k migration was used with estimated shot spacing and a constant velocity model. After processing, the data were printed and exported as SEG-Y.

## **A.5 Side-scan Sonar**

### **A.5.1 NRL Seamap side-scan sonar mosaic**

During the NRL KANE cruise, low frequency 12 KHz side-scan sonar data was collected using the Seamap system, which was developed and built by the Hawaii Mapping Research Group and operated by the U.S. Naval Oceanographic Office (NAVO).

### **A.5.2 OKEAN**

The OKEAN long range side-scan sonar (Figure A.3A) operates at a frequency of 9.5 kHz was used in all the TTR cruises in the Gulf of Cadiz as a first reconnaissance surveying equipment. Its resolution is equivalent to the backscatter imagery of the EM12 swath bathymetry system and also similar to the NRL Seabeam side-scan sonar system. The OKEAN fish is towed 40 to 80 m behind the ship at a few meters depth below the sea surface, at a vessel speed of about 6 knots. The swath depends on the water depth, but in the surveyed areas, were in general either 7 or 15 km.

The data was digitally recorded onboard, filtered and processed by the acoustic scientific teams and the imagery was then georeferenced and integrated into the ArcGIS database.

### **A.5.3 OREtech**

The OREtech deep-towed side-scan sonar fish (Figure A.3B) was towed over selected seabed features at a near constant altitude of 130 m or at about 40-45 m above the seafloor, depending of the mode of operation at 30 or 100 kHz respectively. The fish is also equipped with a 6 kHz subbottom echosounder. The swath coverage was of 2 km or 500 m wide depending on the operation frequency of 30 or 100 kHz, respectively. The data was digitally recorded onboard, filtered, processed and georeferenced using the underwater navigation acquired during the operations by the acoustic scientific teams. The imagery was then integrated into the ArcGIS database.

During the TTR09 and TTR10 a total of 34 km of survey lines with OREtech were acquired in the Gulf of Cadiz.

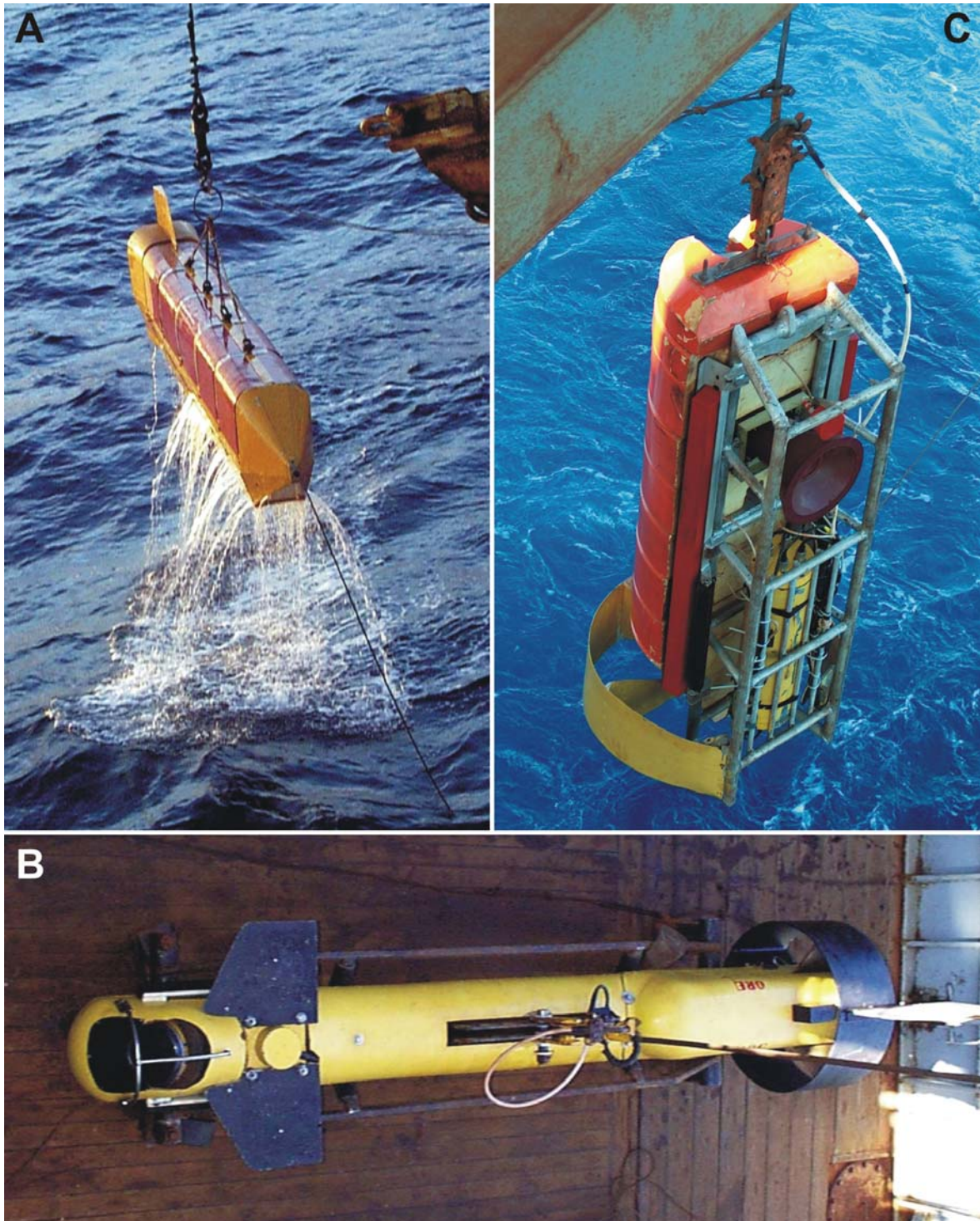


**Figure A.3** Side-scan sonar equipments used on board the R/V Professor Logachev. (A) OKEAN side-scan sonar fish used in all the TTR cruises. (B) OREtech deep-towed side-scan sonar used during the TTR09 and TTR10 cruises. (C) MAK-1M deep-towed side-scan sonar used from the TTR11 to the TTR16 cruises.

#### **A.5.4 MAK-1M**

The MAK-1M is a high resolution deep-towed side-scan sonar system used on board the R/V Professor Logachev during the TTR cruises in the Gulf of Cadiz since 2001. The MAK-1M fish is also equipped with a subbottom profiler, operating at a frequency of 5 kHz. The maximum swat coverage is 2 km (1 km per side) for a towing altitude of 150 m above the seafloor and operating at a frequency of 30 kHz. The resolution of the system ranges from 7 to 1 m across and along the track. The resolution is maximum near the nadir. During the TTR11 to the TTR16 the fish was towed at a nearly constant altitude of about 100-150 m above the seafloor at a speed of 1.5-2 knots for 30 kHz surveys and at about 50 m above the seafloor for 100 kHz surveys.

The data was onboard recorded digitally and processed by the acoustic scientific team. Time variant gain was applied to the data during acquisition. Onboard processing of the data included slant-range-to-ground-range (SLT) correction, geometric correction of the profiles for recovery of the real seafloor topography and smoothing average filtering of sonar and profiler record. The sonar individual lines were geometrically corrected for the towing speed of the fish and converted into a standard bitmap image format. Some image processing routines, such as histogram equalization and curve adjustment were used to improve the dynamic range of the imagery. Geographic georeferentiation of the obtained imagery was performed according to the positioning of the tow-fish underwater navigation acquired during the operation. The georeferenced imagery was then integrated into the ArcGIS database.

During the TTR cruises a total of 578 km of MAK-1M deep-towed side-scan sonar lines were acquired.

### **A.6 Sub-bottom profiler**

#### **A.6.1 TTR hull-mounted acoustic profiler**

During the TTR cruises in the Gulf of Cadiz a hull-mounted 3.5 kHz profiler was routinely used in most of the operations, with continuous paper output and digital record of selected portions of the data.

### **A.6.2 Parametric parasound**

The parametric parasound system works also as a low-frequency sediment echosounder and was routinely recorded during most of the GAP cruise. The system uses the parametric effect, which produces additional frequencies through non-linear acoustic interaction of finite amplitude waves. The system emits simultaneously two sound waves of similar frequencies (18 and 22 kHz); as a result, a signal of the difference frequency (4 kHz) is generated. The footprint size of this signal is much smaller than in the conventional systems and both vertical and lateral resolution are significantly improved. The recorded signal is recorded in the native Paradigma format.

### **A.7 Heat flow measurements**

Heat flow measurements were acquired during the GAP and during the Anastasya-2001 cruises. During the GAP cruise, a Lister type with a violin bow design heat flow probe was used. The heat flow probe from the University of Bremen was used to obtain temperature gradients and *in situ* thermal conductivities by a pulsed heat source method. The operations consisted on several probe penetrations at small distances (usually 300 m on top of mud volcanoes and 1000 to 2000 m apart for regional heat flow studies) along a profile. Each penetration consisted of raising the probe about one hundred meters above the sea floor from the previous penetration, slowly moving the ship to the next penetration site and dropping the probe into the sediment for the next penetration. Once the probe is in the sediment, it is left undisturbed for 7 minutes for equilibrium temperature measurements (time needed to allow the extrapolation to the equilibrium temperature after the frictional disturbance of the penetration) and another 7 minutes, if a thermal conductivity measurement is made.

Miniaturised autonomous temperature data loggers were used to obtain thermal gradient at selected gravity corer stations. The miniaturised temperature loggers were attached to the gravity corer at 1.1 m intervals and measured the sediment temperature.



**Figure A.4.** Heat flow probes. **(A)** Lister type heat flow probe with a violin bow design used in the GAP cruise and of the same type as the one used during the Anastasya-2001 cruise. **(B)** mini-temperature logger installed on a gravity corer.

## A.8 Underwater video observations

During the TTR cruises a deep-towed underwater video system was used for seabed observations. The system consists of an onboard and an underwater unit. The onboard unit consists of a control, a recording and an amplifier unit. Signal and power transmission is done through the traction coaxial cable. The underwater unit (Figure A.5A) is composed of a frame with the light unit, a high-pressure housing containing an analogical and a digital camera, and a power supply unit.

Visualization and recording of the seafloor observations is done in real time. The control of the distance of the camera to the seafloor is done by the winch operator in order to maintain a constant distance of 1.5 to 2 m. The distance of the camera to the seafloor is evaluated with a 1.5 m long cable with a weight that is observed in most of the seafloor pictures.

The underwater video unit is also equipped with an echo sounder and pinger that were used for underwater navigation. Therefore, the underwater video system, similarly to

the deep-towed side-scan sonar systems (OREtech and MAK), is acquired with underwater navigation control.

During the GAP cruise, on board the R/V Sonne, underwater video observations were performed using the Ocean Floor Observation System (OFOS). The OFOS (Figure A.5B) is equipped with two video cameras (colour and black and white) a still camera, a light system, a CTD, a compass, pitch and roll sensors, and a pinger that is used to calculate the OFOS underwater navigation. The video streams are transmitted in real time to the on-board command and display unit where they are analogical recorded, digitized and recorded. Ship navigation and underwater navigation of the OFOS is recorded in the logging system of the ship. The OFOS is towed at a distance of about 1.5 m above the seafloor and is manually adjusted by the winch operator. To assist on keeping a constant distance to the seafloor a weight on a 2 m long cable is attached to the bottom of the OFOS frame. Three laser pointers are used to scale the video images. The two outside laser points are parallel and 20 cm apart, and the laser in between the two is pointing at an oblique angle, to provide an estimate of the absolute distance to the seafloor.

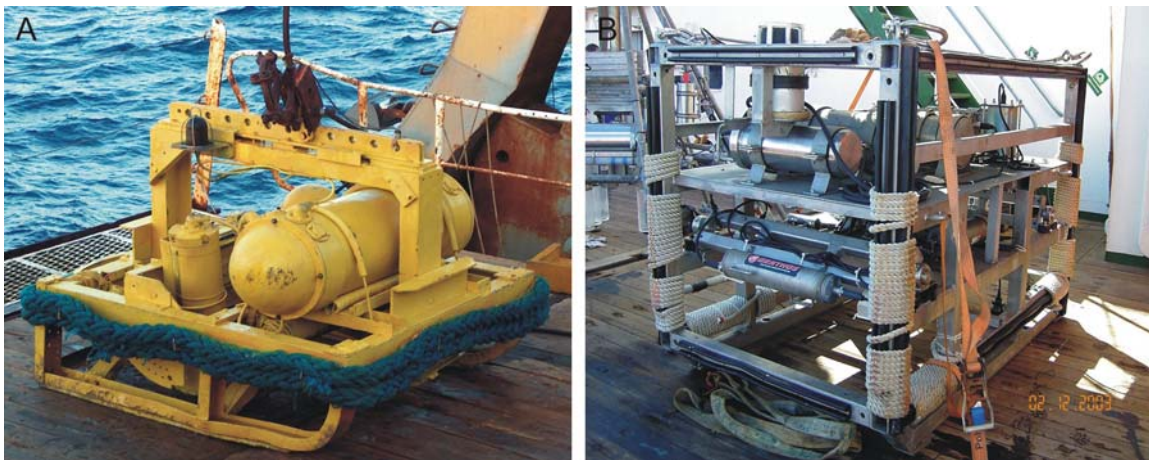


**Figure A.5** Underwater video systems. **(A)** TTR underwater video unit. In the picture is possible to recognise mounted in the frame the light system and the high-pressure housing containing the power supply. **(B)** OFOS system used during the GAP cruise.

## A.9 Gravity cores

Gravity cores were retrieved during the TTR cruises with a 6 m long gravity corer, deployed with a 1500 kg weight. An internal plastic liner with 14.7 cm in diameter is housed in the gravity corer.

After the gravity core is on deck and the removal of the core catcher, the internal plastic liner containing the sediment core is taken out and the sediment material is immediately retrieved with a piston extruder. The core sediment is segmented in sections of 60 to 70 cm long, immediately longitudinally opened in two identical sections and examined for occurrences of gas hydrates or intense degassing. Gas hydrates, if present, are removed and stored in cold containers.

One half of the open core is labelled, photographed and described on deck. Lithological logs with indication of lithology, colours and sedimentary structures along the core are constructed by the sedimentology teams. Core logs are shown throughout this thesis and all core logs are compiled in the respective cruise reports. The reported colours correspond to the Munsel Colour Charts. Magnetic susceptibility was routinely measured with a Bartington Instruments MS2E1 probe. The magnetic susceptibility reflects the presence of magnetic material and is strongly influenced by the grain size, heavy minerals content and is inversely related to the carbonate content and diagenetic ferric mineral reduction. The magnetic susceptibility is also a function of temperature and negative temperature anomalies associated with the destabilization of gas hydrates are easily detected on the magnetic susceptibility record.

The other half of the core is then available for sediment sampling. Samples for gas geochemistry, pore water samples, micropaleontological sub-samples and coccolith smear slides are routinely taken.

During the GAP cruise, gravity cores were collected with a 12 m long gravity corer of 12 cm in diameter. The gravity core liners after retrieval on board were split in 1.5 m long sections and immediately scanned on a MST core logger. The MST measured properties were: wet bulk density, P-wave velocity, magnetic susceptibility and natural gamma radiation. After the MST measurements, the core liner was split and the core longitudinally divided in two. One half was photographed, described and stored for archive. The other half was sub-sampled.

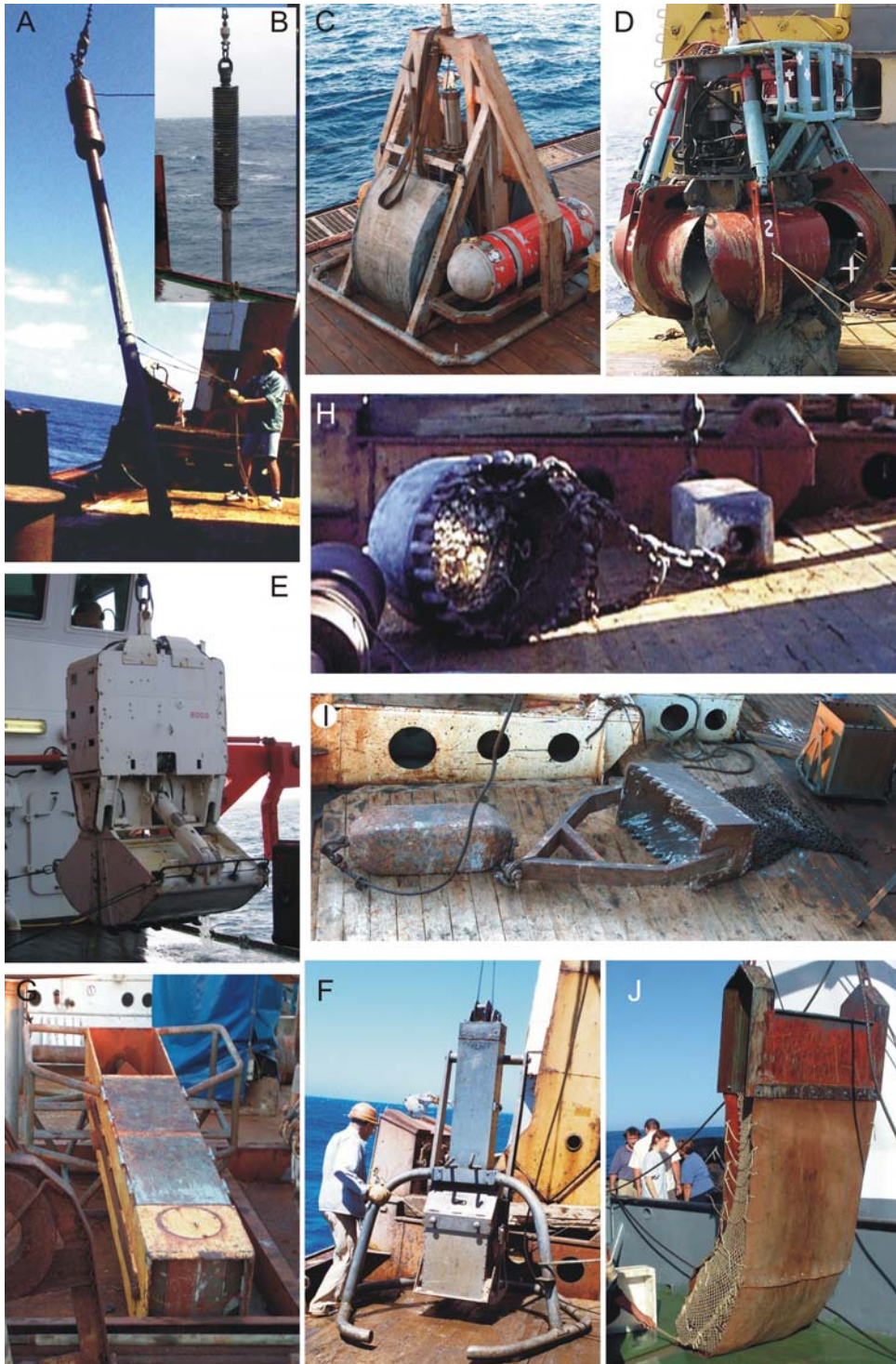


**Figure A.6.** Sampling devices used during the several cruises whose where used for this thesis. **(A)** Gravity corer used onboard the R/V Professor Logachev during the TTR cruises. **(B)** Gravity corer used onboard the R/V Sonne, GAP cruise. **(C)** TV-controlled grab used onboard the R/V Professor Logachev during the TTR10, 11, 12 and 15 cruises. **(D)** TV-controlled grab used onboard the R/V Professor Logachev during the TTR09, and TTR14 cruises. **(E)** TV-controlled grab used onboard the R/V Sonne, GAP cruise. **(F)** Box corer used onboard the R/V Professor Logachev during the TTR cruises. **(G)** Kasten box corer used onboard the R/V Professor Logachev during the TTR14 and TTR15 cruises. **(H)** circular dredge and **(I)** rectangular dredge used onboard the R/V Professor Logachev during the TTR cruises. **(J)** dredge used onboard the R/V Cornide de Saavedra during the Anastasya cruises.

### **A.10 TV controlled grabs**

Onboard the R/V Professor Logachev two different TV-controlled grabs were used. The DG-1 Grab system, illustrated in Figure A.6C, consists on a 1500 kg system operating up to 6000 m water depth with a maximum interior volume of 0.4 m<sup>3</sup>. The GTVD-2 is an orange peel grab Figure A.6D that operates up to 6000 m water depth, has 3.2 tons and an interior volume of 1.1 m<sup>3</sup>. Both systems have a video camera fitted, and power and light units, allowing real time visualization of the seafloor during the grab operation. The onboard unit allows the visualization and record of the video images for selection of the sampling site. Underwater positioning and navigation of the TV-grab is registered by the underwater navigation system. During the GAP cruise a tv-controlled grab (Figure A.6E) was also used to select and collect large volumes of surface sediments from the seafloor.

### **A.11 Box-cores**

Box cores were collected using a Reineck square box with 50x50x50 cm (Figure A.6F). Box cores were collected when samples of undisturbed seabed were needed. After retrieval, the box core was opened removing a side panel, the surface and side were photographed, described and sub-samples were then collected.

### **A.12 Kasten box-cores**

The Kasten corer was used on board the R/V Professor Logachev during the TTR14, TTR15 and TTR16 cruises in the Gulf of Cadiz (Figure A.6G). It was used when large amount and deeper (> 0.5 m) sediment material was needed or due to inefficiency of the other sampling equipments, in general due to the presence of large pebbles or carbonate crusts at the seabed. It consists on a square section corer with dimensions of 0.39x0.39x180 m.

After retrieving the kasten corer, it was opened through removing a side panel, the surface and side were photographed and described, and sub-samples were then collected.

### **A.13 Dredges**

The dredges used during the TTR cruises consist of a circular steel gate of 1 m<sup>2</sup> section (Figure A.6H) and a rectangular section (50x100 cm) dredge (Figure A.6I), both with chain meshes that were trailed behind a 0.5 ton weight, 3 m in front of the dredge gate. The mesh size was about 5 cm. The dredge was trailed up-slope at about 0.5 knots on sites previously monitored with the 3.5 kHz hull-mounted echosounder, high resolution side-scan sonar or underwater TV observations. The dredge was used to collect hard rock material such as most of the authigenic carbonate samples. After sample retrieved the samples were photographed, washed and described onboard. In Figure A.6J is illustrated the dredge used during the Anastasia cruises onboard the RV Cornide de Saavedra.

## **Appendix B. Analytical results**

A large number of analytical methodologies and techniques were used on the work developed for this thesis. The several analytical methods and their results are described and reported in the several chapters of the thesis. In this Appendix are reported the analytical results tables that due to their size are not suitable to be presented within the text.

In this Appendix are tabled the results of the carbonate mineralogy, as defined from the X-ray diffraction and corrected with the total organic carbon and the total carbonate content measured with the LECO CHNS-932 elemental analyser (description of this method is given in Chapter 5). Carbon and oxygen stable isotopes are also reported in this appendix (description of this method is given in Chapter 5). The results are presented grouped according to the different lithological types of MDAC as defined and described in Chapter 5.

**Table B.1.** Carbonate mineralogy, carbon and oxygen stable isotopes of MDAC samples, by lithologic type.

Sample	Field	Sample	Relative percentages (wt%)						Mole Mg(%)				CaCO <sub>3</sub> LECO	CaCO <sub>3</sub> fraction (wt%)					$\delta^{13}\text{C}$ ‰	$\delta^{18}\text{O}$ ‰	
ID	N°	Location	Arag	Calc	Mg- Calc	Prot Dol	Dol	Detrit al	Calc	Mg- Calc	Prot Dol	Dol	(wt%)	Arag	Calc	Mg- Calc	Prot Dol	Dol	(VPDB)	(VPDB)	
<b>Dolomite Crust</b>																					
3426- B1.64	TTR10-239Gr	Student			77		10	14				11	44	86.3				89	11	-21.12	5.47
3458- A03.14	TTR11-335D	Iberico					87	13					46	86.9				100		-46.88	3.32
3458- A05.15	TTR11-335D	Iberico		3			88	9	5				47	91.3		4		96		-39.99	3.08
3463- B06.69	TTR11-339D	Iberico		9			40	51	2				46	48.8		19		81			
3463- B06.71	TTR11-339D	Iberico		8			45	47	3				47	53.4		15		85		-35.76	4.59
3609- C01.84	TTR12-389D	Formoza		19	16		9	56	1	11			44	43.8		43	37	20		-8.42	3.16
3609- C02.85	TTR12-389D	Formoza		9	5		30	55	2	10			45	45.2		21	12	67		-30.24	3.24
3630- C01.90	TTR12-410D	Mercator		60			17	23	4				51	76.9		78		22		-22.17	4.33

**Table B.1.** (Continuation)

Sample ID	Field N°	Sample Location	Relative percentages (wt%)						Mole Mg(%)				CaCO <sub>3</sub> LECO (wt%)	CaCO <sub>3</sub> fraction (wt%)					$\delta^{13}\text{C}$ ‰ (VPDB)	$\delta^{18}\text{O}$ ‰ (VPDB)
			Arag	Calc	Mg- Calc	Prot Dol	Dol	Detrit al	Calc	Mg- Calc	Prot Dol	Dol		Arag	Calc	Mg- Calc	Prot Dol	Dol		
<b>Dolomite Chimney</b>																				
628.61	HE.76.35	Guadalquivir Bank					52	48				48	52.4					100	-26.54	5.67
631-A.62	HE.76.40	Guadalquivir Bank					85	15				46	85.1					100	-25.42	5.30
3458- B02.19	TTR11-335D	Iberico		23			60	17		4		44	83.3		28			72	-38.88	1.60
3458- B02.96	TTR11-335D	Iberico		13	10		40	36		2	13	43	63.7		21	16		63	-38.00	3.82
3458- B02.20	TTR11-335D	Iberico		16			71	13		3		45	86.5		18			82	-34.95	2.44
3458- B02.20	TTR11-335D	Iberico		26			5	69		2		48	31.0		85			15		
3458- B03.52	TTR11-335D	Iberico			13		67	21			11	49	79.3		16			84	-41.20	6.01
3458- B03.53	TTR11-335D	Iberico			3		64	33			9	48	67.3		5			95	-44.39	6.25
3458- B03.54	TTR11-335D	Iberico		10			56	34		6		47	66.0		15			85	-38.36	5.33
3458- B04.118	TTR11-335D	Iberico			11	5	66	19			12	32	48	81.5		13	6	81	-37.30	6.11
3458- B04.119	TTR11-335D	Iberico		4	5		61	30		6	12		48	70.0		5	7	87	-37.46	6.33
3458- B04.120	TTR11-335D	Iberico			5	6	62	27			11	32	48	72.8		7	8	85	-39.15	6.62
3458- B04.121	TTR11-335D	Iberico			2		66	32			27		48	68.4		3		97	-39.65	6.77
3458-	TTR11-335D	Iberico			3		67	31			8		48	69.4		4		96	-37.92	6.57



Authigenic Carbonates and Fluid Escape Structures in the Gulf of Cadiz

---

3458- B04.132	TTR11-335D	Iberico		7	62	31		11	48	68.5		10	90	-35.84	6.39
3458- B05.05	TTR11-335D	Iberico	27		37	36	3		43	64.1	43		57	-29.67	1.44
3458- B05.06	TTR11-335D	Iberico	22		34	44	3		44	56.2	40		60	-33.51	1.38
3458- B05.07	TTR11-335D	Iberico	20		39	40	3		44	59.6	34		66	-35.07	1.69
3458- B13.21	TTR11-335D	Iberico		37	55	8		10	47	92.3		40	60	-26.13	2.42
3458- B13.22	TTR11-335D	Iberico	13		68	19	3		46	81.3	16		84	-27.49	2.41
3458- B13.49	TTR11-335D	Iberico	9	4	44	42	5	22	46	57.9	16	7	76	-27.68	5.11
3458- B13.50	TTR11-335D	Iberico	9	3	50	38	3	19	46	62.0	14	4	81	-29.06	5.04
3458- B13.23	TTR11-335D	Iberico	18		61	21	3		46	79.3	23		77	-33.00	2.33
3458- C02.16	TTR11-335D	Iberico	7		86	7	1		41	92.9	7		93	-45.16	3.09
3458- C02.16	TTR11-335D	Iberico	8		71	20	3		46	79.7	10		90		
3458- C02.17	TTR11-335D	Iberico		50	32	18		14	45	81.6		61	39	-43.61	2.59
3458- C02.18	TTR11-335D	Iberico	17		61	22	2		46	77.7	22		78	-35.78	1.41
3458- C02.18	TTR11-335D	Iberico	14		56	30	3		46	69.8	20		80		
3458-C02- Pr	TTR11-335D	Iberico	21		47	31	2		47	68.8	31		69		
3463-	TTR11-339D	Iberico		2	88	10		10	41	90.0		2	98		

Appendix B. Analytical results

---

A03.08															
3463-	TTR11-339D	Iberico	5		81	14	5		47	86.0	5		95	-39.94	5.03
A03.08															
3463-	TTR11-339D	Iberico	3	3	68	26	3	27	47	74.3	4	4	92	-39.79	5.12
A03.08															
3463-	TTR11-339D	Iberico	8		61	30	3		47	69.6	12		88	-26.72	4.90
A03.09															
3463-	TTR11-339D	Iberico	7		45	48	4		48	51.6	13		87	-27.68	5.54
A03.09															
3463-	TTR11-339D	Iberico		5	5	49	40	9	30	48	60.1	9	9	82	
A03.09															
3463-	TTR11-339D	Iberico	9		41	50	3		49	49.5	18		82	-23.71	4.27
A03.IP															
3463-	TTR11-339D	Iberico	13		52	35	1		46	64.7	19		81	-26.56	0.81
A03.10															
3463-	TTR11-339D	Iberico	10		38	52	3		48	48.3	21		79	-25.92	4.13
A03.10															
3463-	TTR11-339D	Iberico	8		38	54	2		48	45.9	17		83	-24.11	4.76
A03.10															
3463-	TTR11-339D	Iberico	12		71	17	4		47	82.8	14		86		
A06.40															
3463-	TTR11-339D	Iberico	13		66	20	3		47	79.6	17		83		
A06.41															
3463-	TTR11-339D	Iberico	15		73	12	8		46	88.0	18		82	-23.67	2.31
A08.11															
3463-	TTR11-339D	Iberico	11		74	16	2		46	84.4	13		87	-26.18	2.62
A08.12															
3463-	TTR11-339D	Iberico	9		75	16	3		48	84.0	11		89	-27.35	3.12
A08.13															
3463-	TTR11-339D	Iberico	19		59	21	2		46	78.9	25		75	-40.29	2.45
B02.24															

Authigenic Carbonates and Fluid Escape Structures in the Gulf of Cadiz

---

3463- B02.24	TTR11-339D	Iberico	18	13	35	34	1	18	43	66.4	27	20	53	-37.71	3.50
3463- B02.46	TTR11-339D	Iberico	11	4	56	29	2	17	46	71.0	16	5	79	-43.63	4.99
3463- B02.47	TTR11-339D	Iberico	9	2	58	31	2	13	47	68.9	13	3	84	-44.09	4.99
3463- B02.25	TTR11-339D	Iberico	10		70	21	3		47	79.4	12		88	-44.36	2.36
3463- B02.25	TTR11-339D	Iberico	12		67	21	2		46	78.9	15		85	-44.44	5.14
3463- B02.48	TTR11-339D	Iberico	8	2	45	46	2	23	46	54.3	15	3	82	-44.26	4.98
3463- B02.26	TTR11-339D	Iberico	12		69	18	2		46	81.6	15		85	-41.86	2.03
3463- B02.26	TTR11-339D	Iberico	12		58	30	3		48	70.1	17		83	-41.94	4.88
3463- B05.01	TTR11-339D	Iberico	1		86	12	2		46	87.5	2		98	-28.51	4.94
3463- B05.43	TTR11-339D	Iberico			92	8			46	92.2			100	-28.55	5.93
3463- B05.02	TTR11-339D	Iberico	9		68	24	3		47	76.3	11		89	-33.01	3.78
3463- B05.44	TTR11-339D	Iberico	5	3	44	48	1	26	49	52.2	10	6	84	-30.97	5.28
3463- B05.03	TTR11-339D	Iberico	15	13	28	44	3	20	46	56.4	27	23	50	-29.63	2.52
3463- B05.45	TTR11-339D	Iberico	11	3	31	54	2	23	46	46.2	25	8	68	-28.06	3.85
3463- B05.04	TTR11-339D	Iberico	17		48	35	3		46	65.2	26		74	-24.84	2.39
3463-	TTR11-339D	Iberico	9		68	23	2		47	77.1	12		88		

Appendix B. Analytical results

---

B07.38														
3463-	TTR11-339D	Iberico	27		51	22		41	77.6		35		65	
B07.39														
3722-	ANA00-DA10.7	Iberico		1	92	7	18	48	92.8		1	99	-39.36 6.15	
A07.32														
3722-	ANA00-DA10.33	Iberico	7		82	12	2	46	88.3		8	92	-41.38 5.18	
A33.33														
3726-	ANA01-DA18-A01	Cornide	12		58	30	1	45	70.0		17	83	-37.22 4.85	
A01.67														
3726-	ANA01-DA18-A02	Cornide		64	2	35	9	49	65.4		97	3	-17.91 2.82	
A02.34														
3727-	ANA01-DA19-D3	GDR	93		2	5	3	48	95.3		98	2		
D03.31														
3608-	TTR12-388Gr	Formoza	23		34	43	3	48	57.0		40	60	-28.11 3.05	
A01.72														
3608-	TTR12-388Gr	Formoza	7		19	74	3	47	26.3		27	73	-28.44 3.11	
A01.73														
3608-	TTR12-388Gr	Formoza	9		28	63	1	46	37.2		24	76	-28.85 3.40	
A01.74														
3608-	TTR12-388Gr	Formoza	9		22	69	2	47	31.2		30	70	-25.67 2.86	
A01.75														
3608-	TTR12-388Gr	Formoza	8	4	30	57	3	12	49	42.9	19	10	71	-29.54 3.18
A01.76														
3608-	TTR12-388Gr	Formoza	13		22	66	2	47	34.4		37	63	-25.89 2.71	
A01.77														
3608-	TTR12-388Gr	Formoza	6		33	62	2	48	38.5		15	85	-36.55 4.19	
A02.78														
3608-	TTR12-388Gr	Formoza	6		30	64	2	47	36.2		17	83	-36.01 4.07	
A02.79														
3608-	TTR12-388Gr	Formoza	8		36	55	2	47	44.7		18	82	-34.21 4.30	
A02.80														

Authigenic Carbonates and Fluid Escape Structures in the Gulf of Cadiz

---

3608- A02.81	TTR12-388Gr	Formoza	7		28	64	2		47	35.5	21		79	-36.11	3.83
3608- A02.82	TTR12-388Gr	Formoza	5		29	66	2		48	33.5	14		86	-34.03	3.95
3608- A02.83	TTR12-388Gr	Formoza	12		30	58	4		47	41.7	29		71	-35.62	3.94
3608- A02.70	TTR12-388Gr	Formoza	8		38	55	2		47	45.2	17		83	-30.28	3.95
3608- A04.111	TTR12-388Gr	Formoza												-32.61	3.36
3608- A04.112	TTR12-388Gr	Formoza	10	4	25	62	2	12	45	37.9	25	10	65	-27.49	3.73
3608- A04.113	TTR12-388Gr	Formoza	10	3	17	69	3	8	46	30.5	33	11	56	-14.70	2.96
3608- A04.114	TTR12-388Gr	Formoza	7		24	69	2		46	30.7	23		77	-33.72	3.81
3608- A04.115	TTR12-388Gr	Formoza	6	2	26	66	4	12	47	34.2	18	6	75	-38.74	4.24
3608- A04.116	TTR12-388Gr	Formoza	6	2	48	45	1	9	47	55.1	10	4	86	-45.55	5.16
3608- A04.117	TTR12-388Gr	Formoza	7		22	71	3		46	29.1	25		75	-33.11	3.91

---

**Table B.1.** (Continuation)

Sample ID	Field N°	Sample Location	Relative percentages (wt%)					Mole Mg(%)				CaCO <sub>3</sub> LECO (wt%)	CaCO <sub>3</sub> fraction (wt%)					$\delta^{13}\text{C}$ ‰ (VPDB)	$\delta^{18}\text{O}$ ‰ (VPDB)	
			Arag	Calc	Mg- Calc	Prot Dol	Dol	Detrit al	Calc	Mg- Calc	Prot Dol		Dol	Arag	Calc	Mg- Calc	Prot Dol			Dol
<b>Nodular or massive dolomite morphology</b>																				
3426- A1.63	TTR10- 239Gr	Student	75				11	14		8			43	86.4		87		13	-24.01	5.41
3458- B25.42	TTR11-335D	Iberico	7				80	13		3			46	86.7		8		92		
3463- B03.35	TTR11-339D	Iberico	26				29	45		2		37	55.2		48		52			
3463- B03.36	TTR11-339D	Iberico	14				48	37		2		45	62.8		23		77			
<b>Aragonite Pavement - Lithified Mud Volcano Mud Breccia</b>																				
3611- A01.86	TTR12- 391Gr	Jesus Baraza	49	20	13			18		3	14			81.6	60	25	16		-27.56	3.17
3611- A01.86	TTR12- 391Gr	Jesus Baraza	64	11	11			15		6	22			85.2	75	13	13			
3611- A01.92	TTR12- 391Gr	Jesus Baraza	66	7	11		4	12		1	14		52	88.1	75	8	12	4		
3340.100	TTR09- 218Gr	Ginsbur g	51	4	6			39		4	19			61.0	83	7	10		-23.60	4.26
3340.102	TTR09- 218Gr	Ginsbur g	56	7	7			29		5	18			71.2	79	10	10		-21.70	4.34

**Table B.1.** (Continuation)

Sample ID	Field N°	Sample Location	Relative percentages (wt%)						Mole Mg(%)				CaCO <sub>3</sub> LECO (wt%)	CaCO <sub>3</sub> fraction (wt%)					$\delta^{13}\text{C}$ ‰ (VPDB)	$\delta^{18}\text{O}$ ‰ (VPDB)
			Arag	Calc	Mg- Calc	Prot Dol	Dol	Detrit al	Calc	Mg- Calc	Prot Dol	Dol		Arag	Calc	Mg- Calc	Prot Dol	Dol		
<b>Aragonite Pavement - In-situ Breccia</b>																				
3921- A62.103	GeoB9024-06	Hesperides	76	10			14	3				86.1	88	12				-18.20	4.81	
3921- A62.104	GeoB9024-06	Hesperides	87	4			9	5				90.9	96	4				-19.10	4.82	
3921- A63.105	GeoB9024-06	Hesperides	57	31			12	2				88.3	64	36				-14.25	4.03	
3921- A63.106	GeoB9024-06	Hesperides	59	16	19		6	3	13			94.0	62	17	20			-16.10	5.18	
<b>Aragonite Pavement - Shell Crust</b>																				
3611- A02.88	TTR12- 391Gr	Jesus Baraza	47	12	13		27	3	19	46		72.5	65	16	18	1		-31.28	3.06	
3611- A02.88	TTR12- 391Gr	Jesus Baraza	47	12	10		31	1	18			69.5	68	18	15					
3611- A02.99	TTR12- 391Gr	Jesus Baraza	41	12	4		2	37	3	21	45	58.9	69	20	8	3				
3922.107	GeoB9029-3	Faro	74	10	6		9		9			90.8	82	11	7			-48.13	3.74	
3922.110	GeoB9029-3	Faro	76	11	6		6	2	20			93.7	81	12	7			-47.28	3.47	

**Table B.1.** (Continuation)

Sample ID	Field N°	Sample Location	Relative percentages (wt%)						Mole Mg(%)				CaCO <sub>3</sub> LECO (wt%)	CaCO <sub>3</sub> fraction (wt%)					$\delta^{13}\text{C}$ ‰ (VPDB)	$\delta^{18}\text{O}$ ‰ (VPDB)
			Arag	Calc	Mg- Calc	Prot Dol	Dol	Detrit al	Calc	Mg- Calc	Prot Dol	Dol		Arag	Calc	Mg- Calc	Prot Dol	Dol		
<b>Aragonite Pavement - Stromatolithic fabric</b>																				
3340.101	TTR09- 218Gr	Ginsbur g	73	4	5		18	1	18			81.9	89	4	6		-22.64	4.27		
3922.108	GeoB9029-3	Faro	83	10			8	6				92.2	90	10			-56.16	3.82		
3922.109	GeoB9029-3	Faro	85	7			8	4				92.0	92	8			-54.69	3.87		
<b>Sediment from the chimneys</b>																				
3458-C02- iS	TTR11-335D	Iberico		19	6		8	67	2	16		47	32.6		57	17		26		
3458-C02- iS2	TTR11-335D	Iberico		33	5		10	52	2	19		46	47.7		69	11		20		
3458-C02- S3	TTR11-335D	Iberico		39			4	58	1			50	42.4		91			9		
<b>Sediment from Aragonite Pavements</b>																				
3611- A02.98	TTR12- 391Gr	Jesus Baraza	6	27	7		2	58	1	19		49	42.5	14	63	17		6		
<b>Shell / Corals / Carbonate tube worms casts, attached to the exterior of the samples</b>																				
3458- B03.55	TTR11-335D	Iberico	28	62			10		6				89.8	32	68			2.09	2.57	
3463- A06.58	TTR11-339D	Iberico		96			4		3				96.4		100					
3463- A08.57	TTR11-339D	Iberico		11	76		12		13				87.7		13	87				

Authigenic Carbonates and Fluid Escape Structures in the Gulf of Cadiz

3463- B02.56	TTR11-339D	Iberico			77		13	10		13		46	90.1		85	15	-3.30	2.53
3726- A02.59	ANA01- DA18-A02	Cornide	19	61				19	8				80.8	24	76		0.12	2.43
3869- A01.60	ANA01- DA20-A1	GDR	91	9					2				100.0	91	9		1.44	2.24

**Shells cemented inside the Aragonite Pavement**

3611- A01.87	TTR12- 391Gr	Jesus Baraza	38	22	6		19	14	1	15		54	86.2	44	26	7	22	-9.20	3.11
3611- A02.89	TTR12- 391Gr	Jesus Baraza	34	25			26	15				55	85.2	40	30		30	-8.84	3.07
3611- A02.94	TTR12- 391Gr	Jesus Baraza	46	10	9		9	26	4	18		55	73.9	62	14	12	12	-18.30	2.93

Blank columns indicate that the mineral was not detected.

Notes: Sample ID = Laboratory record number. Field Number = Cruise sample station number. Sample Location = Structure where the sample was collected from. Lithologic type defined according to the text. Arag = Aragonite. Calc = Calcite (mol Mg % < 8%). Mg-Calc = high Mg-Calcite (8% < mol Mg % < 30%). PrtDol = Protodolomite (30% < mol Mg % < 40%). Dol = Dolomite (40% < mol Mg % < 55%). Detrital = Detrital Fraction, Quartz, feldspar, clays and other minerals that compose the detrital fraction.

The  $\delta^{13}\text{C}$  and  $\delta^{18}\text{O}$  Stable isotopic values are reported in the conventional  $\delta$  ‰-notation with reference to VPDB. For the dolomite samples (>20% of dolomite),  $\delta^{18}\text{O}$  values are corrected for the analytical offset of +1.63‰, consequence of the unequal oxygen fractionation during the reaction to  $\text{CO}_2$ .



## **Appendix C. EDTA Differentiation of calcite and high Mg-calcite from dolomite for stable isotope measurements**

### ***C.1 Introduction***

Methane-derived authigenic carbonates (MDAC) collected from the Gulf of Cadiz consists of complex mixtures of aragonite, calcite, high Mg-calcite, protodolomite and dolomite phases (Chapter 5). A selective separation of the coexisting carbonate minerals is required for accurate phase-specific determination of oxygen and carbon isotope composition of the methane-derived authigenic carbonates. As the studied samples are characterized by mineralogies that range in size from micrite to microsparite (Chapter 5), a physical separation of the coexisting carbonate minerals is difficult and in general not possible to be applied, making the chemical separation as the more adequate method.

Chemical separation techniques based on time-dependent extraction of CO<sub>2</sub> by reaction of the carbonate minerals at 25°C with 100% phosphoric acid is widely used to achieve carbonate phase-specific carbon and oxygen isotope analysis (Alaasm *et al.*, 1990). But this method is difficult to use in complex carbonate mixtures of high Mg-calcite and dolomite.

Other method to obtain phase-specific carbon and oxygen isotopic compositions is based of the equation C.1, where  $\delta_{total}$  and  $\delta_{dolomite}$  are measured and  $\delta_{calcite}$  can be calculated using the fraction of dolomite in the bulk material ( $X$ ) as measured from XRD.

$$\delta_{total} = X \times \delta_{dolomite} + (1 - X) \times \delta_{calcite} \quad (C.1)$$

This approach is used with success for the separation of calcite from dolomite. The pure dolomite fraction can be obtained from dolomite-calcite mixtures by leaching with 5% acetic acid solution. The time dependent CO<sub>2</sub> extraction and the acetic acid dissolution of calcite and aragonite leaving the dolomite phase solute provides reasonable results on the isotopic calculation of the coexisting calcium carbonates (McKenzie, 1976). However,

these methods are also not successful in separating coexisting high Mg-calcite, protodolomite and dolomite, as the MDAC from the Gulf of Cadiz.

The organic acid ethylenedinitrilotetraceticacid (EDTA) is known to be an alternative to dissolve calcite, based on the fact that calcite is more water soluble than dolomite and thus forms stronger complexes with EDTA (Glover, 1961; Bodine and Fernald, 1973). EDTA present the following order of effectiveness as a solvent: calcite > high Mg-calcite > dolomite > magnesite (Bodine and Fernald, 1973).

In this appendix, is described the use of the EDTA and the leaching technique to separate calcite and Mg-calcite from dolomite in selected samples of MDAC. This method developed at the ETH, Zurich (Van Lith, 2001) proved to be efficient, allowing the separation of dolomite from complex mixtures of calcite, high Mg-calcite and dolomite, by slow dissolution of the calcite and high Mg-calcite fraction in a boiling 0.25 M of ethylenedinitrilotetraceticacid (EDTA) solution with pH 11. The carbon and oxygen isotopic composition of the bulk carbonate and of the dolomite fraction were analyzed and the isotopic composition of calcite phase could then be calculated.

## ***C.2 Methods***

The samples used in this study were selected from the collection of MDAC retrieved from the Gulf of Cadiz (Chapter 5). Samples for XRD, carbon and oxygen stable isotope were extracted from transversal and longitudinal cuts and micro-drilled along radial and longitudinal profiles of two selected dolomite chimneys.

Bulk mineralogy and the relative abundance of different carbonate mineralogies in each sample were investigated by X-ray diffraction (XRD) on 134 powdered samples (Table 5.1 in Chapter 5). X-ray diffraction patterns were obtained using a Scintag XDS2000 X-ray diffractometer with CuK $\alpha$  radiation (1.5405 Å wavelength) at the Geological Institute of the ETH Zurich. Scans were done from 5° to 60° 2 $\theta$  at 0.02°/sec, using 40 kV accelerating voltage and 30 mA current. As the intensity of the diffraction pattern of a mineral in a mixture is proportional to its concentration, estimates of the relative proportions of the minerals in a sample were made by measuring their relative

peak areas. Peak identification and minerals relative abundance estimation were performed using the Scintag interpretation software and the MacDiff<sup>®</sup> software packages. Error associated with the mineralogy content determination is estimated to be 7%. The Mg:Ca ratio of the carbonate minerals was calculated from the shift of the d-spacing of the (104) reflection peak of calcite and dolomite from the stoichiometric peak positions in the diffraction spectra (Goldsmith and Graf, 1958; Lumsden, 1979).

$$\text{mole\%MgCO}_3 = 100 - (d_{104} \times 333.33 - 911.99) \quad (\text{C.2})$$

The peak areas were measured for the main peaks of the carbonate minerals: calcite (< 8 mol% MgCO<sub>3</sub>, 3.036 to 3.012 Å), high Mg-calcite (8 to 30 mol% MgCO<sub>3</sub>, 3.012 to 2.946 Å), protodolomite or Ca-dolomite (30 to 40 mol% MgCO<sub>3</sub>, 2.946 to 2.916 Å) and dolomite (40 to 55 mol% MgCO<sub>3</sub>, 2.916 to 2.871 Å).

Carbon and oxygen isotopes in powdered bulk samples and in EDTA leaching residue were analysed at the Geological Institute of the ETH Zurich. Samples for carbon and oxygen stable isotopic analyses were prepared by reacting at 90°C with 100% phosphoric acid on an automated carbonate device connected to a VG-PRISM mass spectrometer calibrated with NBS19, NBS 18 and NBS 20. The results are reported in the conventional δ ‰-notation with reference to VPDB (Vienna Peedee Belemnite). Analytical reproducibility of the method, based on repeated standards is better than ±0.1‰ for both carbon and oxygen. For temperature calculations of the dolomite samples, dolomite δ<sup>18</sup>O values were corrected for the analytical offset of +1.63‰, consequence of the unequal oxygen fractionation during the reaction to CO<sub>2</sub> (Rosenbaum and Sheppard, 1986).

After retrieve the powdered samples by micro-drill, each sample was spitted in two fractions. One sub-sample was used for XRD analysis and for carbon and oxygen isotope analyse of the bulk carbonate. The second sub-sample was leached with 20 ml boiling 0.25 M EDTA solution at pH 11 during 24 hours in glass covered containers to avoid evaporation. The solvent level was maintained at 20 ml/g by adding distilled water. After 24 hours the sub-sample was taken out of the EDTA solution, washed in distilled water, freeze dried, examined with XRD and measured for carbon and oxygen isotopic composition.

### C.3 Results and Discussion

#### C.3.1 XRD results

The high Mg content in the calcite (< 8 mol% MgCO<sub>3</sub>, 26.50 to 29.63 2θ degrees), Mg-calcite (8 to 30 mol% MgCO<sub>3</sub>, 29.63 to 30.31 degrees), and the Ca-content in the protodolomite or Ca-dolomite (30 to 40 mol% MgCO<sub>3</sub>, 30.31 to 30.63 degrees) and in the dolomite (40 to 55 mol% MgCO<sub>3</sub>, 30.63 to 31.12 degrees) phases of the MDAC from the Gulf of Cadiz caused significant shifts of the respective 2θ peaks in the X-ray diffractogram relative to the standard 2θ peaks of pure calcite, Mg-calcite, protodolomite and stoichiometric dolomite (Figure C.1 to Figure C.7).

EDTA leaching method proved to be efficient as a dissolving calcite and Mg-calcite leaving dolomite intact when the bulk dolomite:(calcite + Mg-calcite) is high. The 0.25 M EDTA solution allowed the leaching of a mixture of 74:26 dolomite:(high Mg-calcite + calcite) to a 100:0 (wt%:wt%) mixture in 24 hours (Figure C.3). Sample 3463-B02.24, with a original dolomite:(high Mg-calcite + calcite) ration of 43:57 was not able to completely dissolve the calcite + Mg-calcite mixture and lead to a residue with 54:46 ratio (Figure C.5). Similar experiments (Van Lith, 2001) have demonstrated that when the start material contained more than 60% high Mg-calcite, the difference in solubility is not sufficient to significantly enrichment of the sample in dolomite. In these situations a longer reaction time have to be used. In conclusion mixtures with high amounts of dolomite (such as samples: 3463-A03.08, 3463-A03.09, 3463-A03.95, 3463-A03.10, 3463-B02.25, 3463-B02.26) resulted in a good dissolution of calcite and Mg-calcite and a complete purification of the dolomite carbonate phase (Table C.2).

Due to a more controlled and slower dissolution reaction rate, the EDTA is a good alternative to the weak acid method to separate carbonate minerals for accurate phase-specific isotope measurements.

**Table C.1.** Mineral content prior and after EDTA leaching and mole% MgCO<sub>3</sub> in the present carbonate phases.

Sample	Bulk sample								after EDTA							
	Detrital	Calcite	mol%Mg	Mg-calc	mol%Mg	Dol	mol%Mg	Dol:Calc	Detrital	Calcite	mol%Mg	Mg-calc	mol%Mg	Dol	mol%Mg	Dol:Calc
3463-A03.08	14.0	4.6	5.4	3.0	17.5	78.4	46.6	91:9	10.9	0.5	4.0	0.0	0.0	88.6	47.0	99:1
3463-A03.09	48.4	6.7	3.7	2.0	18.2	42.9	48.3	83:17	27.5	0.6	4.7	0.0	0.0	71.9	47.7	99:1
3463-A03.IP	50.5	8.7	3.0	4.3	18.3	36.5	48.7	74:26	30.2	0.0	0.0	0.0	0.0	69.8	47.7	100:0
3463-A03.10	51.7	10.4	3.0	1.0	20.1	37.0	48.3	76:24	27.5	0.0	0.0	0.6	15.8	71.9	47.7	99:1
3463-B02.24	33.6	18.1	1.3	20.1	18.5	28.3	43.3	43:57	29.5	13.2	2.0	19.2	21.1	38.1	45.3	54:46
3463-B02.25	21.1	11.8	2.0	6.5	18.0	60.6	46.3	77:23	19.9	0.0	0.0	0.9	13.1	79.1	45.6	99:1
3463-B02.26	29.9	12.0	3.4	3.7	21.3	54.4	48.3	78:22	19.5	0.7	2.0	0.0	0.0	79.8	46.3	99:1

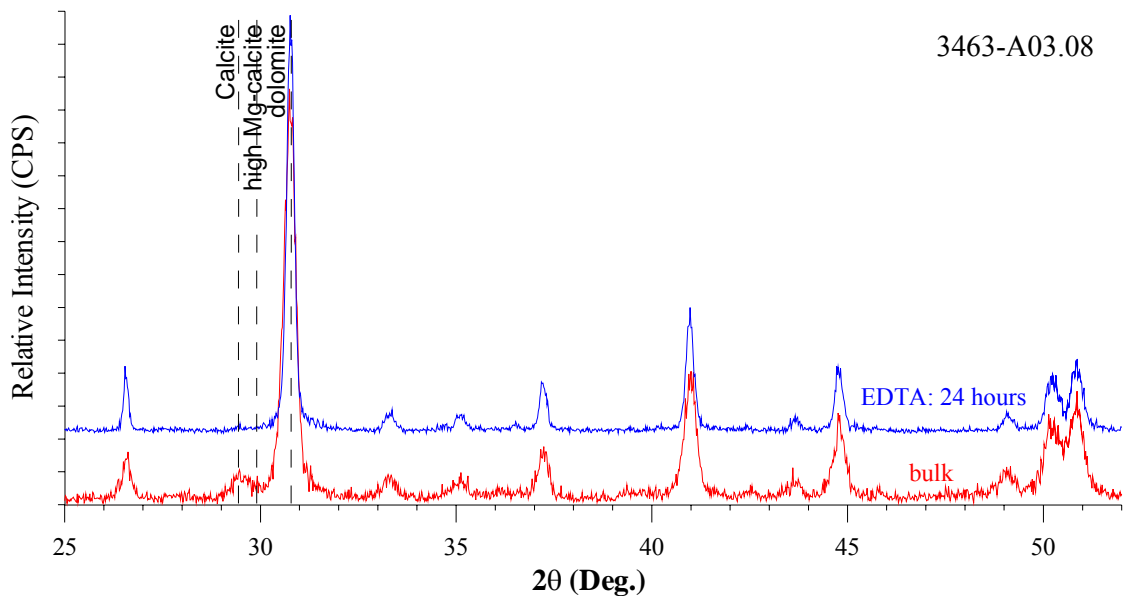


**Figure C.1.** X-ray diffraction pattern of high Mg-calcite – dolomite carbonate mixture of a dolomite chimney sample (3463-A03). The sample was leached with a 0.25 M EDTA solution of pH 11 and aliquots were taken after 24 hours. The  $2\theta$  positions for high Mg-calcite and dolomite are marked on the graphs. To be noted that the calcite peak almost completely disappears with the EDTA leaching.

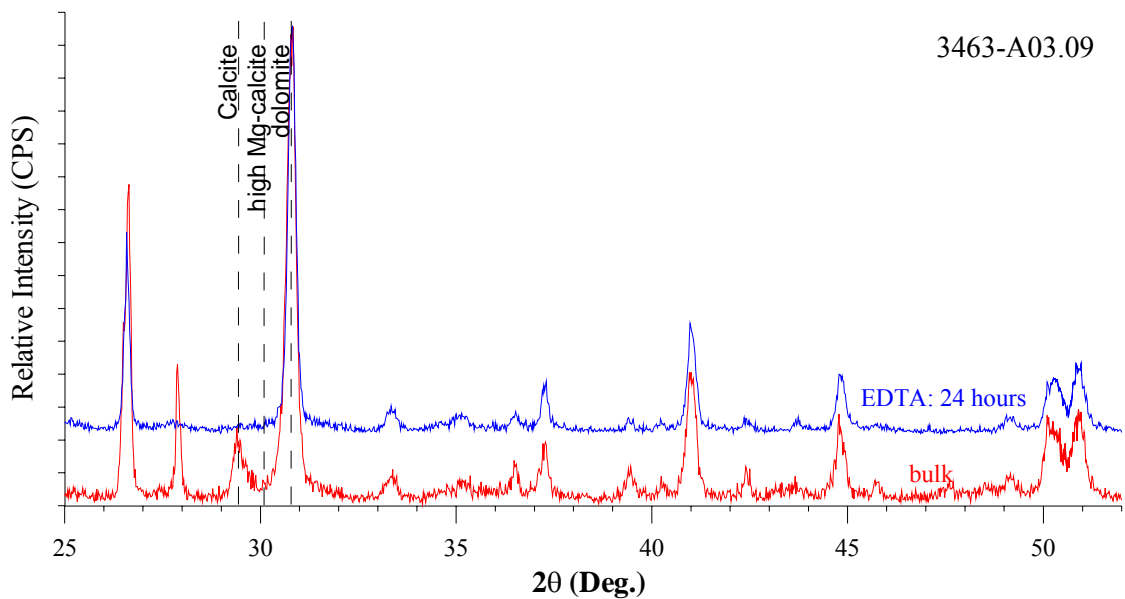


**Figure C.2.** X-ray diffraction pattern of high Mg-calcite – dolomite carbonate mixture of a dolomite chimney sample (3463-A03). The sample was leached with a 0.25 M EDTA solution of pH 11 and aliquots were taken after 24 hours. The  $2\theta$  positions for high Mg-calcite and dolomite are marked on the graphs.

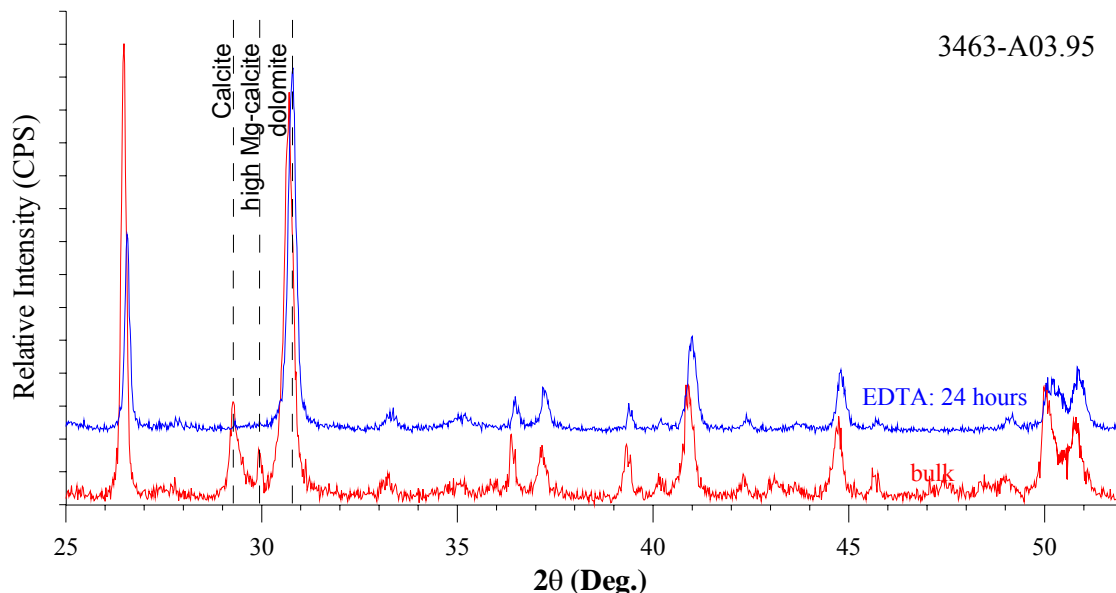


**Figure C.3.** X-ray diffraction pattern of high Mg-calcite – dolomite carbonate mixture of a dolomite chimney sample (3463-A03). The sample was leached with a 0.25 M EDTA solution of pH 11 and aliquots were taken after 24 hours. The  $2\theta$  positions for high Mg-calcite and dolomite are marked on the graphs.

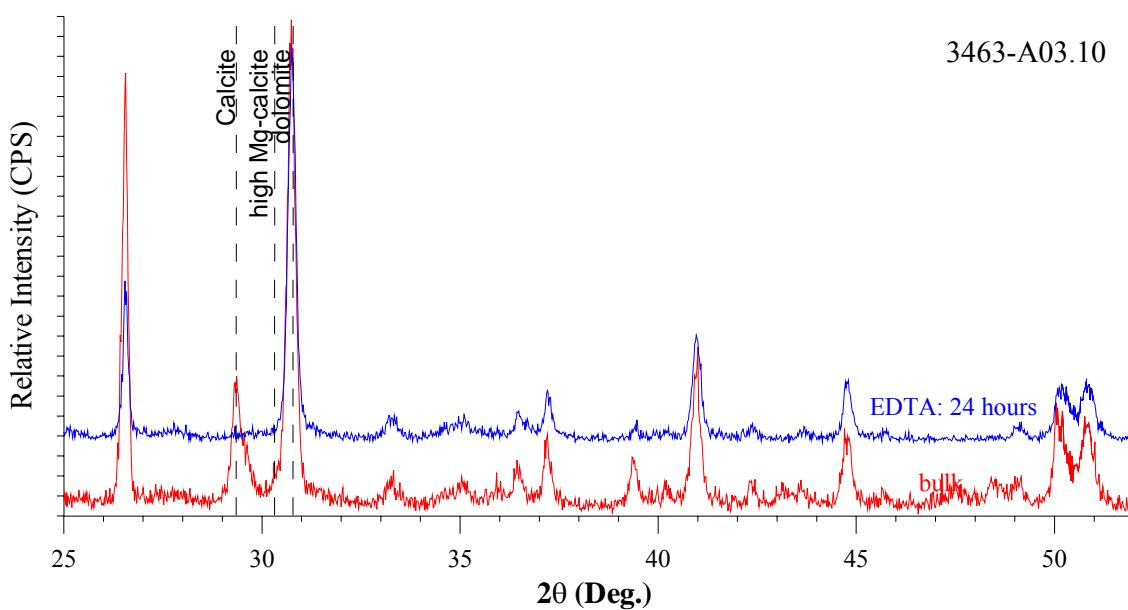


**Figure C.4.** X-ray diffraction pattern of high Mg-calcite – dolomite carbonate mixture of a dolomite chimney sample (3463-A03). The sample was leached with a 0.25 M EDTA solution of pH 11 and aliquots were taken after 24 hours. The  $2\theta$  positions for high Mg-calcite and dolomite are marked on the graphs.

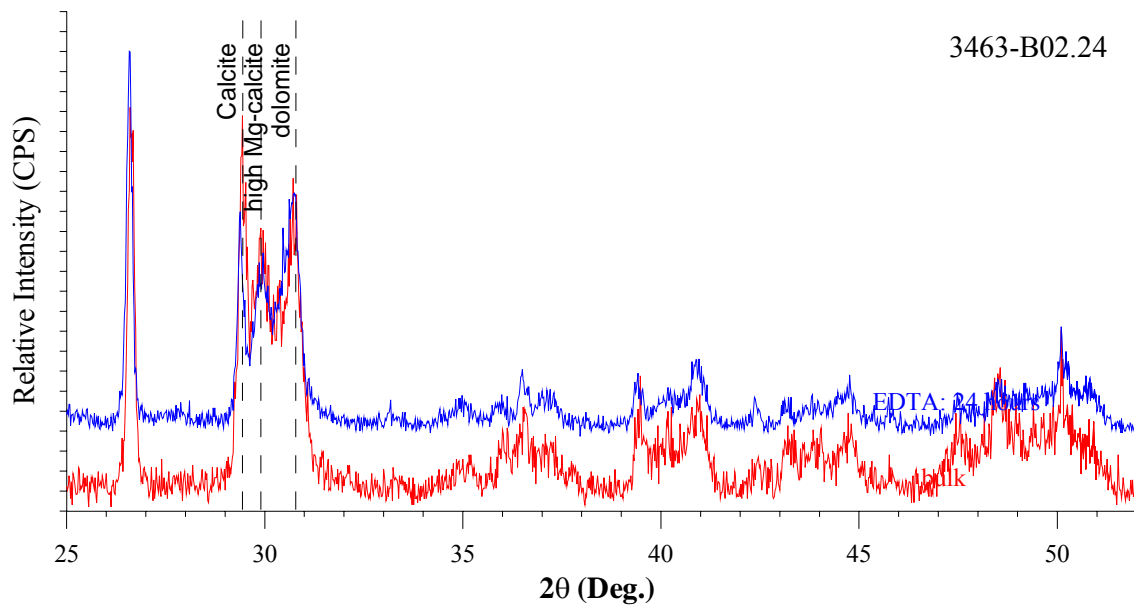


**Figure C.5.** X-ray diffraction pattern of high Mg-calcite – dolomite carbonate mixture of a dolomite chimney sample (3463-A03). The sample was leached with a 0.25 M EDTA solution of pH 11 and aliquots were taken after 24 hours. The  $2\theta$  positions for high Mg-calcite and dolomite are marked on the graphs.

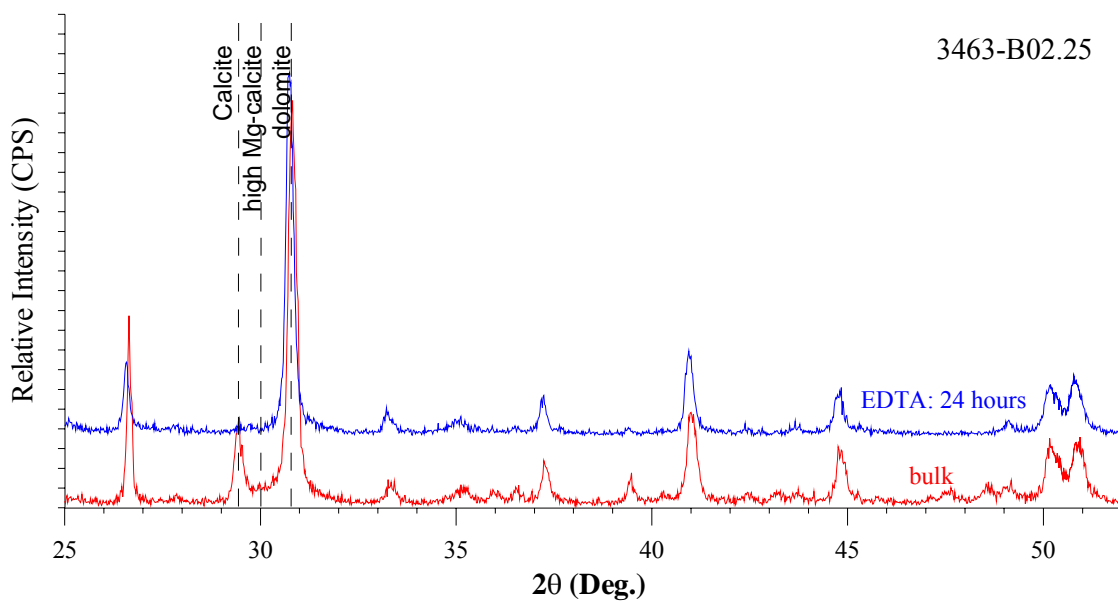


**Figure C.6.** X-ray diffraction pattern of high Mg-calcite – dolomite carbonate mixture of a dolomite chimney sample (3463-A03). The sample was leached with a 0.25 M EDTA solution of pH 11 and aliquots were taken after 24 hours. The  $2\theta$  positions for high Mg-calcite and dolomite are marked on the graphs.

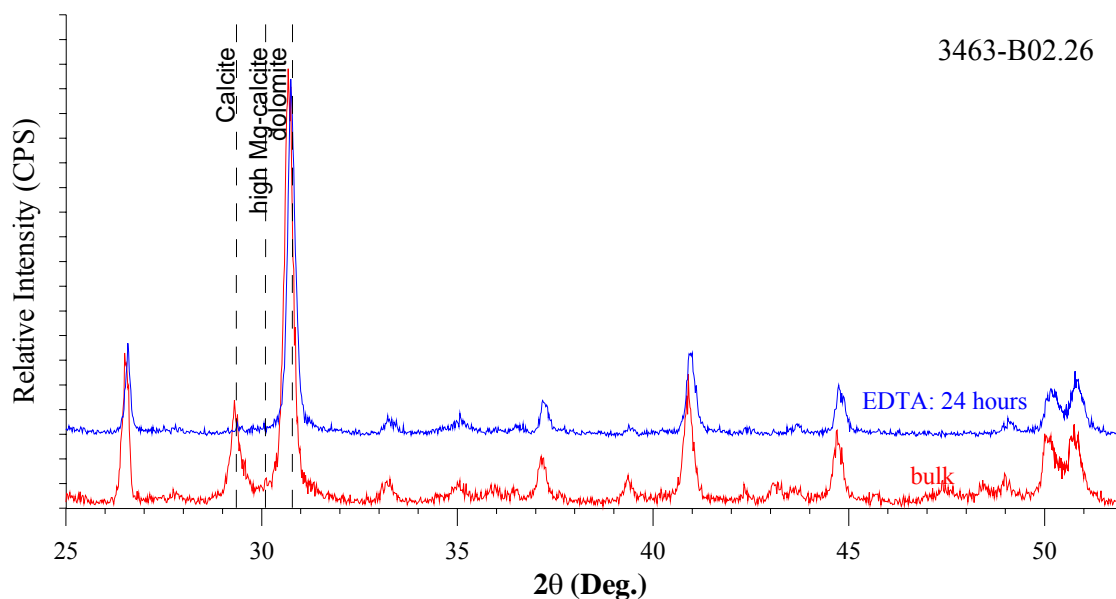


**Figure C.7.** X-ray diffraction pattern of high Mg-calcite – dolomite carbonate mixture of a dolomite chimney sample (3463-A03). The sample was leached with a 0.25 M EDTA solution of pH 11 and aliquots were taken after 24 hours. The  $2\theta$  positions for high Mg-calcite and dolomite are marked on the graphs.

### C.3.2 Carbon and Oxygen Isotopic analysis

Carbon and oxygen isotopic composition of the purified dolomite fraction after EDTA leaching shows a significant different stable isotopic values from the bulk material (Figure C.8). The dolomite fraction have consistently lighter carbon isotopic values and heavier oxygen isotopic values. This difference between the different carbonate phases, can reach 25% for the original  $\delta^{13}\text{C}$  bulk sample value and up to 27% of the original  $\delta^{18}\text{O}$  bulk sample value. This puts in evidence the relevance of separating the coexistent carbonate mineralogies for accurate temperature calculations and to evaluate the fluid compositions and the potential influence of heavy water from decomposition of gas hydrates, as discussed in Chapter 6.

The  $\delta^{18}\text{O}$  isotopic composition of pure dolomite fraction shows an average value of  $+5.69\text{‰} \pm 0.28$  (PDB) while the mixture of the different carbonates presents lower values. This is evident in the  $\delta^{18}\text{O}$  isotopic values function of the dolomite/(calcite + Mg-calcite) ratios in Figure C.9. The extrapolation of the regression line to a pure calcite composition indicates a oxygen isotopic value of 1.4‰ (PDB). The application of equation C.1 to the estimation of the isotopic values of the pure mixture of calcite and high Mg-calcite is shown in Table C.2. The estimated  $\delta^{18}\text{O}$  isotopic composition of calcite+high Mg-calcite

(to be noted that there is a clear higher abundance of calcite in this mixture), is ranging from -0.14 to +1.92‰, corresponding to isotopic values close to 0‰ *i.e.* values close to normal seawater composition. Indicating the precipitation from close to normal seawater fluids. So, most probably, the calcite phase (to be noted that there is a clear higher abundance of calcite in relation to Mg-calcite) correspond to pelagic calcite material from foraminifera and other calcite tests precipitated from normal seawater.

**Table C.2.** EDTA leaching method results. Efficiency of the leaching technique and stable carbon and oxygen isotope composition of the bulk, dolomite and high Mg-calcite fractions obtained with 0.25 M EDTA treatment.

Sample	Bulk sample			Dolomite			Calcite + high Mg-Calcite	
	Dol:Cal	$\delta^{13}\text{C}$	$\delta^{18}\text{O}$	after EDTA			(calculated)	
				Dol:Calc	$\delta^{13}\text{C}$	$\delta^{18}\text{O}$	$\delta^{13}\text{C}$	$\delta^{18}\text{O}$
3463-A03.08	91:9	-39.94	5.03	99:1	-43.38	5.44	-5.15	0.86
3463-A03.09	83:17	-26.72	4.90	99:1	-30.87	5.69	-6.48	1.02
3463-A03.95	74:26	-23.71	4.27	100:0	-27.96	5.46	-11.61	0.91
3463-A03.10	76:24	-25.92	4.13	99:1	-32.65	5.48	-4.60	-0.14
3463-B02.24	43:57	-37.71	3.50	54:46 *	-41.64	3.54	-34.75	3.47
3463-B02.25	77:23	-44.44	5.14	99:1	-51.41	6.09	-21.09	1.97
3463-B02.26	78:22	-41.94	4.88	99:1	-50.93	5.99	-10.08	0.97
Average		-33.78	4.73		-39.53	5.69	-9.83	0.93
Standard Deviation		9.29	0.42		10.41	0.29	6.17	0.67

Notes: Mg-calcite isotopic values calculated according to equation C.1

\* reaction stopped after 6 hours.

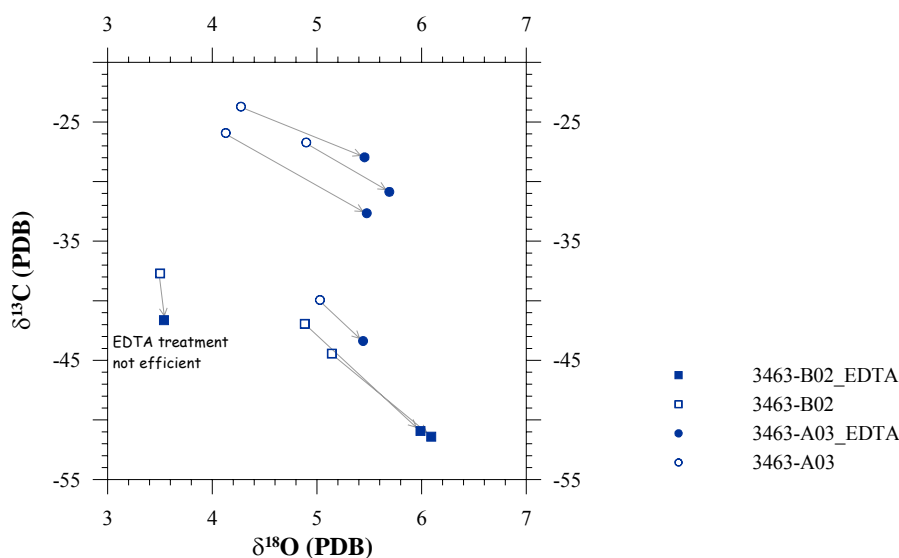


**Figure C.8.** Carbon and Oxygen isotopic composition of bulk samples (open symbols) and after EDTA leaching (filled symbols). All the samples exception to the sample 3463-B02.24 where the leaching process was not successfully completed, present a similar trend on the isotopic shift.

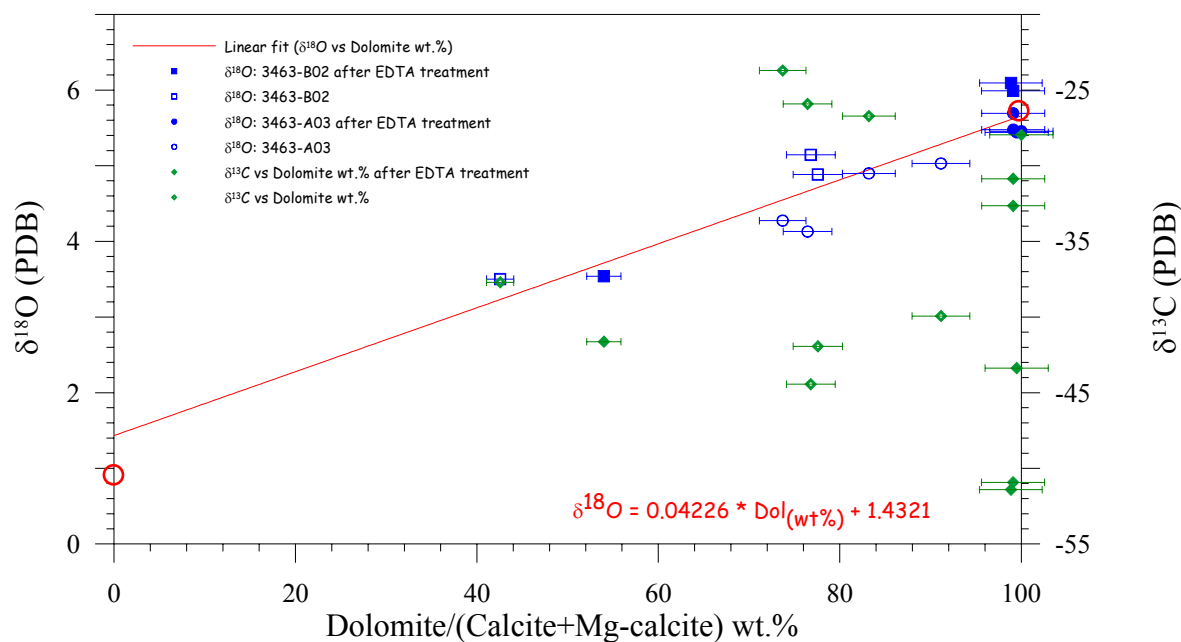


**Figure C.9.** Group of samples treated with EDTA leaching reveal linear correlation between the dolomite/(calcite + Mg-calcite) ratio and the  $\delta^{18}\text{O}$  values. Pure dolomite yields 5.6‰  $\delta^{18}\text{O}$  PDB, whereas  $^{18}\text{O}$  is strongly depleted in the calcite and Mg-calcite phases. There is no clear relationship between the mineralogy and  $\delta^{13}\text{C}$  values.

This trend is not so evident for all the dolomite chimneys crusts and nodules samples (Figure C.10). Although the  $\delta^{18}\text{O}$  isotopic composition of the enriched dolomite samples clearly present heavier isotopic values than the samples more enriched in calcite. This is interpreted as an indication of precipitation of dolomite from fluids that are different from the normal seawater composition from which calcite is dominantly precipitated from. These oxygen isotopic differences between dolomite and calcite+high Mg-calcite reveal different fluid compositions of the fluids from which the different carbonates had precipitated. These differences are discussed in detail in chapter 5.

The  $\delta^{13}\text{C}$  isotopic composition of dolomite shows consistently lighter values than the carbonate bulk mixture. The leached samples show a fairly constant depletion in  $\delta^{13}\text{C}$  of  $-5.76\text{‰} \pm 2.15\text{‰}$  (PDB) *i.e.* similar rate of  $\delta^{13}\text{C}$  variation as a function of the dolomite content. But a global variation on the carbon isotopic composition as a function of the dolomite content (Figure C.9) is not observed on the EDTA leached samples. But such a trend is clearly evident for all the dolomite chimneys crusts and nodules samples (Figure C.11). There is a clear evidence of more depleted carbon values for dolomite-dominated samples with an average value of  $-39\text{‰} \pm 10\text{‰}$  (PDB) for the extrapolated pure dolomite

carbon isotopic composition. The extrapolated  $\delta^{13}\text{C}$  for a pure calcite + high Mg-calcite mixture indicate a value of  $-18\text{‰}$  (PDB).

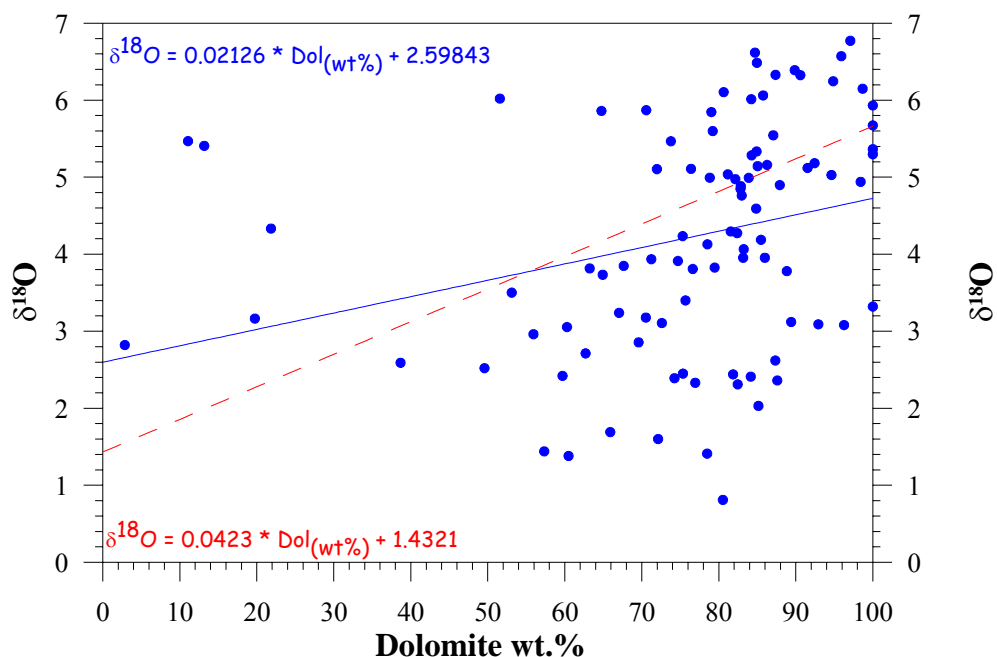


**Figure C.10.** Plot of the dolomite/(calcite + Mg-calcite) ratio and the  $\delta^{18}\text{O}$  values on all the samples of dolomite crusts, chimneys and Nodules. The correlation is not clear probably because of the high compositional variability of the samples but the general trend calculated from the EDTA leaching (red dashed line) can be inferred indicating heavier values toward higher abundance of dolomite and lighter oxygen isotopic values toward the dominated calcite samples.

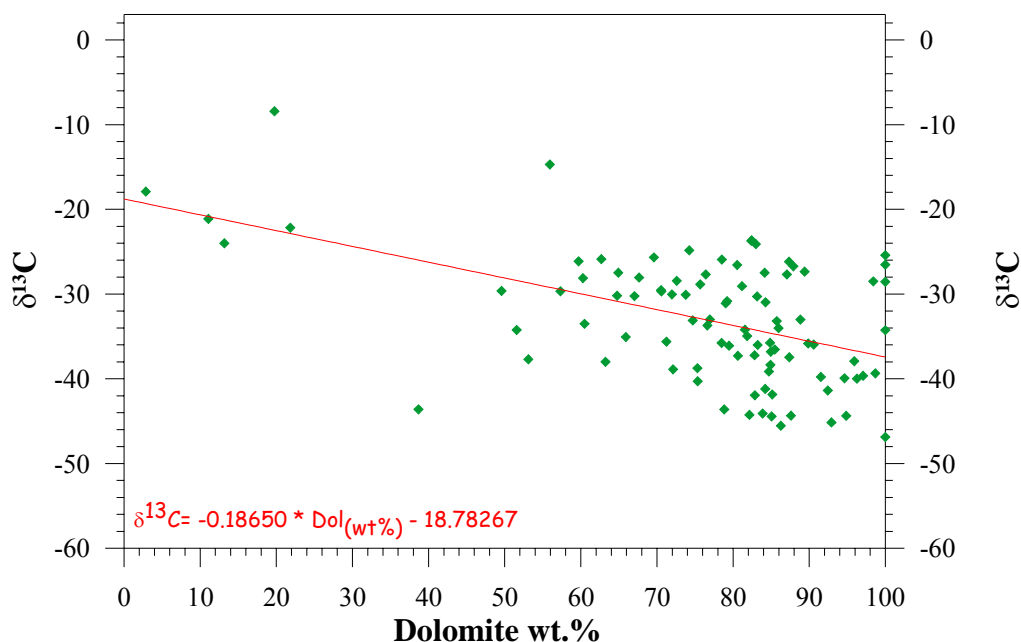


**Figure C.11.** Dolomite crusts, chimneys and Nodules reveal linear correlation between the dolomite/(calcite + Mg-calcite) ratio and the  $\delta^{13}\text{C}$  values. Pure dolomite yields  $-38 \pm 0.1\text{‰}$   $\delta^{13}\text{C}$  (PDB), whereas  $^{13}\text{C}$  is strongly enriched in the calcite and Mg-calcite phases.

The extrapolations of the  $\delta^{13}\text{C}$  values for pure dolomite and pure calcite phases, based on the  $\delta^{13}\text{C}$  values of bulk and leached material (Figure C.12) indicate  $\delta^{13}\text{C}$  compositions ranging from -57‰ to -28‰ (PDB) for pure dolomite phase. For the calcite and Mg-calcite phases  $^{13}\text{C}$  is strongly enriched with the extrapolated values ranging from -2 to -23‰ (PDB). Comparing these values with the function obtained by the linear fit for all bulk samples from Figure C.11 the end-members isotopic compositions (-38‰  $\pm$  10‰ (PDB) for pure dolomite and -18‰ (PDB) for a pure calcite + high Mg-calcite mixture) is within these values. The calculated  $^{13}\text{C}$  composition for the end-member calcite (Table C.2) presents an average value of -9.83‰  $\pm$  6.17‰ (PDB).

In conclusion both EDTA and bulk samples clear indicate a closer to the normal seawater isotopic composition, as also seen on the oxygen isotopes, for the calcite and a lighter isotopic composition for dolomite. This is interpreted as different carbon isotopic composition of the original fluids for the different samples. These differences are discussed in detail in chapter 6, but most probably is resulting from a mixture, with variable proportions of the carbon sources (biogenic, thermogenic and seawater carbon pools).

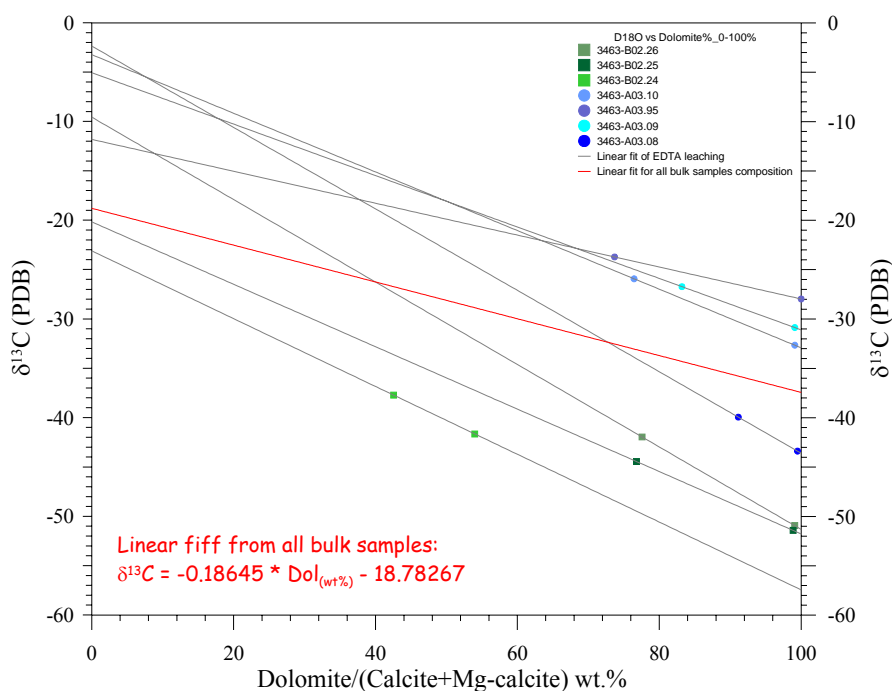


**Figure C.12.** Plot of the extrapolations of the  $\delta^{13}\text{C}$  values for pure dolomite and pure calcite phases, based on the  $\delta^{13}\text{C}$  values of bulk and leached material. Also is plotted the function obtained by the linear fit for all bulk samples from Figure E.11. The extrapolated  $\delta^{13}\text{C}$  values for pure dolomite phase ranges from -57‰ to -28‰ (PDB), whereas  $^{13}\text{C}$  is strongly enriched in the calcite and Mg-calcite phases with the extrapolated values ranging from -2 to -23‰ (PDB).

## ***C.4 Conclusions***

In summary, EDTA leaching technique was used to differentiate between coexisting calcite Mg-calcite and dolomite in a controlled and simple technique. Using a 0.25 M EDTA solution, a mixture of 74:26 dolomite:calcite+high Mg-calcite was altered to a 100:00 (wt%:wt%) mixture in 24 hours. Due to a more controlled and slower dissolution reaction rate, the EDTA is a good alternative to the weak acid method to separate carbonate minerals for accurate phase-specific isotope measurements.

The selective separation of the coexisting carbonate minerals allowed the identification of different carbon and oxygen isotopic values of the different mineral phases. Pure dolomite shows on average  $\delta^{18}\text{O}$  isotopic composition of  $+5.69\text{‰} \pm 0.29$  (PDB). On average, pure dolomite shows a constant depletion in  $\delta^{13}\text{C}$  of  $-5.49\text{‰} \pm 2.08\text{‰}$  (PDB) in relation to the bulk carbonate. Extrapolated  $\delta^{18}\text{O}$  isotopic composition of pure calcite or a mixture of calcite + high Mg-calcite (no dolomite) indicate a calculated value of  $+0.93\text{‰} \pm 0.67$  (PDB). The extrapolation from the linear best fit of the plot of the  $\delta^{18}\text{O}$  isotopic composition as function of dolomite proportion indicates to a estimated composition for pure calcite phase or to the mixture of calcite + high Mg-calcite of  $1.4\text{‰}$  (PDB). So, all the indications point to near seawater composition of the calcite phase and a positive  $\delta^{18}\text{O}$  isotopic composition of the dolomite. The extrapolated  $\delta^{13}\text{C}$  for a pure calcite + high Mg-calcite mixture indicate a value of  $-18\text{‰}$  (PDB).

These differences in isotopic composition of the different mineral phases reveal different fluid composition of the fluids from which the carbonates had precipitated from and are discussed in chapter 6.



## **Appendix D. Biomarkers: samples preparation and analysis**

### ***D.1 Introduction***

In this Appendix is described the sample preparation and analytical procedure for biomarker analysis. The lipid biomarkers analyses were carried out by the author in the Marine Biogeochemistry Laboratory of the Research Center for Ocean Margins (RCOM), of the Bremen University (Magalhães *et al.*, 2005) in collaboration with Prof. Jorn Peckmann and Dr Daniel Birgel of the RCOM.

The samples selected for biomarker analysis were chosen based on previous petrographic and mineralogical descriptions in order to analyse samples representative of the different types of methane-derived authigenic carbonates (MDAC) identified in the Gulf of Cadiz. As the oxidation processes is effective in reducing the preservation of the organic compounds present in the carbonate, the selected samples were the ones that showed lower oxidation degree and the most massive and un-altered characteristics. In Table D.1 are listed the samples selected for biomarker analysis at the RCOM centre.

The aragonite pavements are considered to represent a more recent carbonate than the dolomite chimneys and previous studies (Duarte, 2005; Niemann *et al.*, 2005; Niemann *et al.*, 2006) have already shown that the biomarker indicators are abundant in this type of samples. The aragonite pavement sample 3340 (Figure 8.2) was selected because it shows no signs of oxidation. From this aragonite pavement sample, 20 g of material was collected and prepared for biomarker extraction. From the dolomite chimney samples 3463-A08 and 3722-A33 (Figure 8.2), 250 g of material was collected and prepared for biomarker extraction by fragmenting to small 5 cm thick slices, avoiding the periphery and fractured parts of the samples that can act as contamination sources.

These results were complemented with lipid biomarker analyses performed at the Max Planck Institute for Marine Microbiology Bremen by L. Santos and H. Niemann

(Santos *et al.*, 2006) and the results are presented in Chapter 8.

The analytical procedure described in this Appendix is similar to the analytical procedure of the samples analysed at the Max Plank Institute for Marine Microbiology Bremen.

**Table D.1.** Samples selected for biomarker analyses and SEM observations. (TS: thin section; SEM: scanning electron microscopy; BK: biomarker analysis)

Sample	Field N°	Sample location	Description
3458-B11	TTR11-335D	Iberico Mud Cone	Dolomite crust (section 5.4.1.2, Chapter 5) with a moderate degree of oxidation, very homogeneous and massive material
3463-A08	TTR11-339D	Cadiz Channel	Dolomite chimney (section 5.4.1.1, Chapter 5) with no significant signs of oxidation, very homogeneous and massive
3722-A33	ANA00-DA10.33	Iberico Mud Cone	Dolomite crust (section 5.4.1.2, Chapter 5) with a moderate degree of oxidation, homogeneous and massive material
3340-5001	TTR09-218Gr	Ginsburg MV	Aragonite pavement, lithified mud breccia type (section 5.4.1.4.1, Chapter 5)

### ***D.1 Sample preparation***

The sample preparation procedure used for extraction and purification of the lipid biomarkers was based on the method of Peckmann *et al.* (2004). The analytical methodology used for the dolomite chimney samples is described by the flowchart in Figure D.2 and for the aragonite pavements the analytical methodology used is described in the flowchart of Figure D.1.

The freshly broken carbonate samples were decalcified (HCl) and the dried residue was refluxed in 6% KOH in CH<sub>3</sub>OH (saponification reaction: 2 h). The supernatant was decanted and the residue was repeatedly extracted by ultrasonication in CH<sub>2</sub>Cl<sub>2</sub>/CH<sub>3</sub>OH (3:1; v:v) until the solvent became colourless. Subsequently, the combined supernatants were portioned in CH<sub>2</sub>Cl<sub>2</sub> versus water (pH 2). The resulting total extract was dried and separated by column chromatography (Merck silica gel 60, 0.063-0.200 mm; i.d.: 15 mm, length: 35 mm) into fractions containing: (1) hydrocarbons (20 ml or 3 column volumes of n-hexane); (2) esters/ketones (20 ml of n-hexane/CH<sub>2</sub>Cl<sub>2</sub> 2:1); (3) alcohol (20 ml of CH<sub>2</sub>Cl<sub>2</sub>/acetone 9:1); (4) fatty acids/polars (20 ml of MeOH). The esters/ketones and alcohol fractions were dried and derivatised using pyridine and BSTFA (2:1) at 70°C (1 h). The polar fractions/fatty acids were dried and transesterificated with boron-trifluoride methanol and then with KCl + hexane. The internal standard used for all fractions was Cholestane. A modification of the method by doing a previous extraction with CH<sub>2</sub>Cl<sub>2</sub>/CH<sub>3</sub>OH (3:1; v:v) prior to decalcification proved to be efficient in cleaning dirt peaks on the dolomite

samples. Above are described the analytical sequence procedure used.

## ***D.2 Decalcification***

The first step in this process is the dissolution (decalcification) of the carbonate fraction, using the following procedure:

1. The carbonate piece of the sample to analyse is first crushed into small chips. In the case of the hard dolomitic chimneys, the sample was cut into smaller slices and crushed with a silicic acid mortar and pestle;
2. The beaker where the sample was placed for reaction was cleaned with DCM<sup>1</sup> (CH<sub>2</sub>Cl<sub>2</sub>) by washing the beaker twice, not forgetting also to wash the edges of the recipient.
3. The small chips of the sample were cleaned 2 or 3 times with acetone to prevent and eliminate any possible contamination during the handling of the sample by dust or any other contaminant.
4. Cleaning the separatory funnel with Millipore water and DCM 3 times, having special attention on cleaning the lead and the stopper of the funnel. Filling the funnel with HCl 10% vol. and placing it to decant over the beaker with the sample covered with Millipore water.
5. The decalcification reaction is started by adding water and then adding the acid (HCl 10% vol.) onto the sample, drop by drop, shaking with a magnum. Once the reaction diminishes more acid is added, controlling the pH of the solution so that it will not be more acid than 2. The reaction needs to be kept until a sufficient amount of sample is dissolved. The control of the reaction is done by “eye control”; once the bubbling of the acid stops or diminishes more acid is added to the solution.
6. Centrifuging the sample: once the reaction is kept for sufficient time and enough material is dissolved, the solution is centrifuged for 10 minutes at 2000 rpm. The supernatant is discarded and the residue is dried overnight on the oven at 50°C.

---

<sup>1</sup> DCM - DiCloroMethane (CH<sub>2</sub>Cl<sub>2</sub>) is used as a solvent of organic matter so it can be used to clean the glass material. DCM is also be used to clean the samples themselves.

### ***D.3 Saponification***

Saponification was done with 6% KOH in MeOH, through the addition of 30 ml of KOH in MeOH 6% to the sample (solid phase), a closed vial, and by letting it to react for 2 hours in ultrasonic bath at 40°C. After the saponification reaction, the supernatant was collected in a centrifuge tube.

### ***D.4 Extraction***

1. Three times with DCM:MeOH (3:1):
  - i.* after saponification the material was moved to the centrifuge tubes.
  - ii.* addition of 30 ml of DCM:MeOH (3:1)
  - iii.* placing the tube in the ultrasonic cleaner bath for 15 minutes
  - iv.* centrifuging for 5 minutes at 2000 rpm (the weight of the centrifuge tubes is balanced with DCM:MeOH (3:1)
  - v.* placing the solution on a separatory funnel, previously cleaned with DCM (2x)
  - vi.* repeating of steps *ii* to *v*, 3 times.
2. Extraction of organic phases vs. Water (pH2):
  - i.* addition of 30 ml of DCM
  - ii.* addition of water in the same volume of the volume of DCM:MeOH (3:1) used for the 3 steps of 1.*i* to 1.*vi* (c.a. 40 ml H<sub>2</sub>O)
  - iii.* addition of HCl 10%vol. (4-5 drops) to obtain a solution with pH=2
  - iv.* shaking.
3. Drying with Na<sub>2</sub>SO<sub>4</sub>
  - i.* cleaning a funnel and 1 evaporation tube with DCM (2x)
  - ii.* placing combusted glass wool on the gorge of the funnel and about 5 spoons of Na<sub>2</sub>SO<sub>4</sub> on top of the glass wool
  - iii.* placing the solution on the separatory funnel (steps 1 and 2)
  - iv.* shaking the separatory funnel with the solution and the DCM and let the DCM drop slowly on the column funnel, so that the solution drops down homogeneously over the salt, avoiding the perforation of the Na<sub>2</sub>SO<sub>4</sub>. Once all the DCM is drained, the salt is washed with 10 ml DCM to guarantee that all the solution with organic compounds is washed to the evaporation tube and none is

retained in the  $\text{Na}_2\text{SO}_4$  or in the glass wool.

v. Evaporation of the DCM with  $\text{N}_2$  gas flux. The evaporator uses evaporation tubes with 1 ml bottom “nipple-tube”. Settings of the  $\text{N}_2$  evaporator were: (1) pressure = 1.8 Psi or 1.2 bar; (2) Mode: automatic sensor; (3) bath temperature:  $37^\circ\text{C}$ .

vi. Activation of the respective cell number that contains the sample.

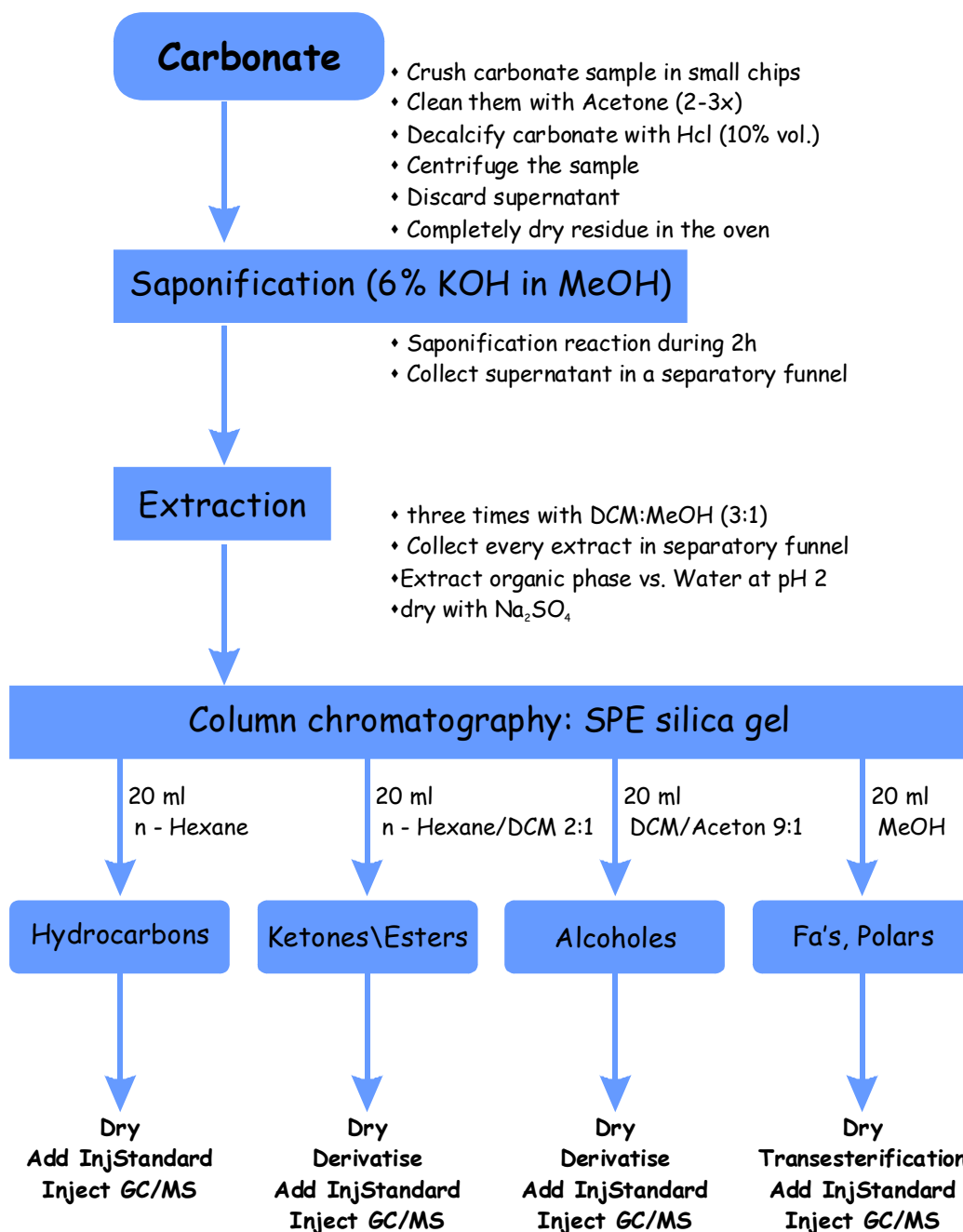


**Figure D.1.** Flowchart of the analytical procedure for biomarker analyses of cold seep carbonates. Modified from Peckmann *et al.* (2004).

## ***D.5 Column chromatography***

1. Preparation of 4 (5 ml) vials to collect the 4 different fractions: Hydrocarbons, Esters, Alcohols and Fatty Acids.
2. Cleaning of the column:
  - i.* Filling the column with DCM and let the solvent flow through the column.
  - ii.* Filling the column with Hexane and let the solvent flow through the column.  
Repeating this operation 3 times.
3. Placing 1 ml of the sample solution (attention not to allow the column to dry out). The ceramic of the column has to be always wet with the different solvents.
4. filling with 20 ml of Hexane and collection of the first fraction: hydrocarbons.
5. filling with 20 ml of Hexane/DCM 2:1 and collection of the first fraction: ketones/esters.
6. filling with 20 ml of DCM/Aceton 9:1 and collection of the first fraction: alcohols.
7. filling with 20 ml of MeOH and collection of the first fraction: fatty acids, polars.

After the column chromatography, the solutions are dried on a N<sub>2</sub> flux evaporator (using the one for small vials). The vial with the hydrocarbons fraction should not be totally dried out and a little amount of solvent has to be preserved. Vials fractions of esters, alcohols and FA can be totally dried out.

With a pipette, the solutions are transferred to the small vials that will be used on the automatic auto sampler of the chromatograph.

The solution is dried and once it is totally dried the standards and solvents are added. Fraction F1: addition of the solvent and the internal standard. Fractions F2 and F3 have to be derivatised. F4 has to be Transesterificated.

### **F1 - Hydrocarbons**

- i.* addition of 150 µl of solvent: Hexane + 50 µl of Internal Standard: Cholestane.
- ii.* analysis on the GC-MS and/or storing the vials in a -30°C refrigerator.

**F2 + F3 - Ketones/Esters + Alcohols. Derivatasing:**

- i.* addition of 100  $\mu$ l pyrodine + 50  $\mu$ l BSTFA.
- ii.* keeping the reaction for 1 hour, at 70°C in the oven with the vials closed.
- iii.* evaporation of the reaction vials with N<sub>2</sub> flux.
- iv.* addition of 150  $\mu$ l of solvent: Hexane + 50  $\mu$ l of Internal Standard: Cholestane.
- v.* analysis on the GC-MS and/or storing the vials in a -30°C refrigerator.

**F4 - FA. Transesterification:**

- i.* evaporation of the F4 vial with N<sub>2</sub> flux.
- ii.* addition of 1 ml of Boron-Trifluoride Methanol.
- iii.* evaporating with N<sub>2</sub> flux.
- iv.* addition of KCl 1 ml + Hexane and shaking it in a vortex.
- v.* extraction of the solvent with a pipette.
- vi.* repetition of the extraction steps (iv and v) 3 times.
- vii.* evaporation with N<sub>2</sub> flux.
- viii.* addition of 150  $\mu$ l of solvent: Hexane + 50  $\mu$ l of Internal Standard: Cholestane.
- ix.* analysis on the GC-MS and/or storing the vials in a -30°C refrigerator.

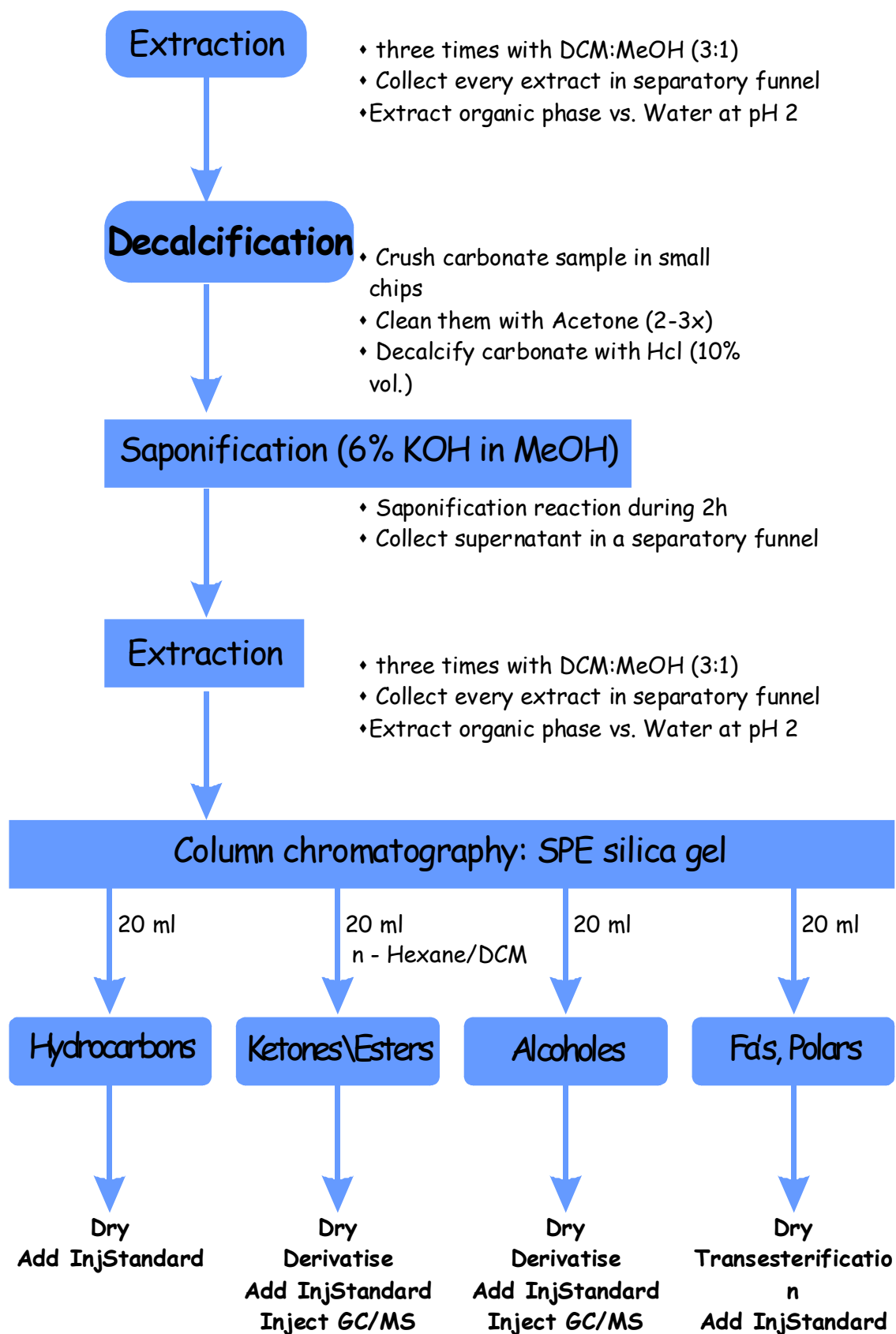


**Figure D.2.** Flowchart of the analytical procedure of biomarker analyses with a previous extraction, used on the dolomite chimney 3463-A08.

### ***D.5 Gas chromatography and coupled mass spectrometry (GC-MS)***

The hydrocarbon fraction was examined by combined gas chromatography-mass spectrometry (GC-MS) using a Varian CP-3800 GC/Saturn 2000 MS EI-mode, 70eV) equipped with a 30 m fused silica capillary column (CP-Sil 8 CB Low Bleed, 0.25mm ID, 0.25  $\mu\text{m}$  film thickness). The carrier gas was He. The GC-temperature program used was: injection at 80°C, 5 min isothermal; from 80°C to 310°C at 4°C min<sup>-1</sup>; 20 min isothermal. The identification of the organic compounds was based on comparison of the mass spectra and the GC retention times with those of published data and reference compounds.

Coupled GC-combustion-isotope ratio MS (GC-C-IRMS) was conducted using a Finnigan DeltaPlusXL mass spectrometer equipped with a HP6890GC and CuO/Ni/Pt combustion furnace operated at 940°C. Samples were injected splitless (1 min) onto a 30 m fused silica column (DB5-MS, 0.32 mm i.d., 0.25  $\mu\text{m}$  film thickness) using a Gerstel Cooled Injection System (CIS4) programmed from 48°C (0 min) to 310°C (10 min) at 12°C sec<sup>-1</sup>. The carrier gas was He. The GC temperature program used was: 3 min at 80°C; from 80°C to 310°C at 4°C min<sup>-1</sup>; 30 min at 310°C. The GC-C-IRMS precision was checked using a standard alkane mix (n-C<sub>15</sub> to n-C<sub>29</sub>) with known isotopic composition. The stable carbon isotope compositions are reported in the delta notation ( $\delta^{13}\text{C}$ ) vs. the VPDB Standard.